

LIQUID FILM COATING

JOIN US ON THE INTERNET VIA WWW, GOPHER, FTP OR EMAIL:

WWW: <http://www.thomson.com>

GOPHER: <gopher.thomson.com>

FTP: <ftp.thomson.com>

EMAIL: findit@kiosk.thomson.com

A service of **I(T)P[®]**

LIQUID FILM COATING

Scientific principles and their
technological implications

Edited by

Stephan F. Kistler

*Imation Corporation
Oakdale
Minnesota
USA*

and

Peter M. Schweizer

*ILFORD AG
Fribourg
Switzerland*



SPRINGER-SCIENCE+BUSINESS MEDIA, B.V.

First edition 1997

© 1997 Springer Science+Business Media Dordrecht
Originally published by Chapman & Hall in 1997
Typeset in 10/12pt Times by AFS Image Setters Ltd, Glasgow

ISBN 978-94-010-6246-6 ISBN 978-94-011-5342-3 (eBook)
DOI 10.1007/978-94-011-5342-3

Apart from any fair dealing for the purposes of research or private study, or criticism or review, as permitted under the UK Copyright Designs and Patents Act, 1988, this publication may not be reproduced, stored, or transmitted, in any form or by any means, without the prior permission in writing of the publishers, or in the case of reprographic reproduction only in accordance with the terms of the licences issued by the Copyright Licensing Agency in the UK, or in accordance with the terms of licences issued by the appropriate Reproduction Rights Organization outside the UK. Enquiries concerning reproduction outside the terms stated here should be sent to the publishers at the London address printed on this page.

The publisher makes no representation, express or implied, with regard to the accuracy of the information contained in this book and cannot accept any legal responsibility or liability for any errors or omissions that may be made.

A catalogue record for this book is available from the British Library

Library of Congress Catalog Card Number: 96-86101

 Printed on permanent acid-free text paper, manufactured in accordance with ANSI/NISO Z39.48-1992 (Permanence of Paper).

CONTENTS

Colour plates appear between pages 228 and 229

List of contributors	vii
Notation	ix
Introduction	1
1. Coating science and technology: an overview <i>Stephan F. Kistler and Peter M. Schweizer</i>	3
Part One: Physics and material interactions of coating processes	17
2. Capillary hydrodynamics and interfacial phenomena <i>Steven J. Weinstein and Harvey J. Palmer</i>	19
3. Wetting: static and dynamic contact lines <i>Terence D. Blake and Kenneth J. Ruschak</i>	63
4. Surfactants: static and dynamic surface tension <i>Yves-M. Tricot</i>	99
5. Coating rheology: component influence on the rheological response and performance of water-borne coatings in roll applications <i>J. Edward Glass and Robert K. Prud'homme</i>	137
6. The fate of thin liquid films after coating <i>Haroon S. Khesghi</i>	183
Part Two: Methods of investigating coating processes	207
7. Experimental methods <i>Peter M. Schweizer</i>	209
8. Asymptotic methods for the mathematical analysis of coating flows <i>Marc K. Smith</i>	251
9. Advances in computational methods for free-surface flows <i>Kostas N. Christodoulou, Stephan F. Kistler and P. Randall Schunk</i>	297

Part Three: Theory and practice of coating processes	367
10. Analysis and design of internal coating die cavities	369
<i>Robert B. Secor</i>	
Chapter 11: Premetered coating processes	399
11a Slot coating <i>Franz Durst and Hans-Günter Wagner</i>	401
11b Slide coating <i>Jules Hens and Willy Van Abbenyen</i>	427
11c Curtain coating <i>Kimiaki Miyamoto and Yoshinobu Katagiri</i>	463
11d Surfactant effects in coating processes <i>P. Randall Schunk and L.E. Scriven</i>	495
Chapter 12: Self-metered coating processes	537
12a Knife and roll coating <i>Dennis J. Coyle</i>	539
12b Meniscus roll coating <i>Philip H. Gaskell and Michael D. Savage</i>	573
12c Elastohydrodynamic coating systems <i>Ferdinand R. Pranckh and Dennis J. Coyle</i>	599
12d High-speed blade coating <i>Cyrus K. Aidun and Nick G. Triantafillopoulos</i>	637
13. Free-meniscus coating processes	673
<i>P. Randall Schunk, Alan J. Hurd and C. Jeffrey Brinker</i>	
14. Spin coating	709
<i>Ronald G. Larson and Timothy J. Rehg</i>	
15. Control and optimization of coating processes	735
<i>Peter M. Schweizer</i>	
Index	769

CONTRIBUTORS

CYRUS K. AIDUN

Georgia Institute of Technology,
Institute of Paper Science and Technology,
Atlanta, Georgia, USA.

TERENCE D. BLAKE

Kodak Limited,
Research Division,
Harrow, UK.

C. JEFFREY BRINKER

Sandia National Laboratories,
Ceramics Synthesis and Inorganic Chemistry
Department,
Albuquerque, New Mexico, USA.

KOSTAS N. CHRISTODOULOU

E.I. Du Pont De Nemours & Co.,
Scientific Computing Division,
Wilmington, Delaware, USA.

DENNIS J. COYLE

General Electric Co.,
Corporate R&D,
Niskayuna, New York, USA.

FRANZ DURST

Friedrich-Alexander-Universität,
Lehrstuhl für Strömungsmechanik,
Erlangen, Germany.

PHILIP H. GASKELL

The University of Leeds,
Department of Mechanical Engineering,
Leeds, UK.

J. EDWARD GLASS

North Dakota State University,
Polymers and Coatings Department,
Fargo, North Dakota, USA.

JULES HENS

Agfa-Gevaert N.V.,
Research Laboratories,
Mortsel, Belgium
(retired).

ALAN J. HURD

Sandia National Laboratories,
Ceramics Processing Science Department,
Albuquerque, New Mexico, USA.

YOSHINOBU KATAGIRI

Fuji Photo Film Co., Ltd.,
Production Engineering & Development
Division,
Minami-ashigara-shi, Kanagawa-ken, Japan.

HAROON S. KHESHGI

Exxon Research and Engineering Company,
Corporate Research,
Annandale, New Jersey, USA.

STEPHAN F. KISTLER

3M Company,
Data Storage Products Division,
St. Paul, Minnesota, USA.
(Current affiliation: Imation Corp.,
Oakdale, Minnesota, USA.)

RONALD G. LARSON

Lucent Technologies, Bell Laboratories,
Murray Hill, New Jersey, USA.
(Current affiliation: University of Michigan,
Department of Chemical Engineering,
Ann Arbor, Michigan, USA.)

KIMIAKI MIYAMOTO
Fuji Photo Film Co., Ltd.,
Production Engineering & Development Division,
Minami-ashigara-shi, Kanagawa-ken, Japan.

HARVEY J. PALMER
University of Rochester,
Department of Chemical Engineering,
Rochester, New York, USA.

FERDINAND R. PRANCKH
Avery Dennison,
Corporate Process Technology,
Pasadena, California, USA.
(Current affiliation: HPM Corp.,
Mount Gilead, Ohio, USA.)

ROBERT K. PRUD'HOMME
Princeton University,
Department of Chemical Engineering,
Princeton, New Jersey, USA.

TIMOTHY J. REHG
Allied Signal Inc.,
Aerospace Equipment Systems,
Torrance, California, USA.

KENNETH J. RUSCHAK
Eastman Kodak Company,
Emulsion Coating Technologies,
Rochester, New York, USA.

MICHAEL D. SAVAGE
The University of Leeds,
School of Mathematics,
Leeds, UK.

P. RANDALL SCHUNK
Sandia National Laboratories,
Department of Computational Fluid Dynamics,
Albuquerque, New Mexico, USA.

PETER M. SCHWEIZER
ILFORD AG,
Engineering Department,
Fribourg, Switzerland.

L. E. (SKIP) SCRIVEN
University of Minnesota,
Department of Chemical Engineering and
Materials Science,
Minneapolis, Minnesota, USA.

ROBERT B. SECOR
3M Company,
Engineering Systems and Technology
Laboratory,
St. Paul, Minnesota, USA.

MARC K. SMITH
Georgia Institute of Technology,
The George W. Woodruff School of Mechanical
Engineering,
Atlanta, Georgia, USA.

NICK G. TRIANTAFILLOPOULOS
GenCorp Polymer Products,
Latex Laboratories,
Akron, Ohio, USA.

YVES-M. TRICOT
ILFORD AG,
R&D Department,
Fribourg, Switzerland.

WILLY VAN ABBENYEN
Agfa-Gevaert N.V.,
Research Laboratories,
Mortsel, Belgium.

HANS-GÜNTHER WAGNER
BASF AG,
Ludwigshafen, Germany.

STEVEN J. WEINSTEIN
Eastman Kodak Company,
Emulsion Coating Technologies,
Rochester, New York, USA.

NOTATION

In each chapter, all the symbols are defined in the text where they first appear. The following list defines the symbols most commonly used throughout the book. The list is by no means complete, and a particular symbol may have more than one meaning, depending on its local definition. Also, given the large number of authors and the wide range of subject matters covered, some inconsistencies were nearly impossible to avoid. As a general rule, upper-case letters denote dimensional variables, and lower-case letters are used for dimensionless quantities; dimensionless groups are given by two-letter symbols, the first one being upper case. Apart from a few well-marked exceptions, SI units are used throughout the book.

A	surface area [m^2] or Hamacker constant [J]	h_∞	Young's modulus [N/m^2] or dilational surface elasticity modulus [N/m]
a	Langmuir constant [mol/cm^3]	H	elasticity number [$El \equiv \mu UL^2/D = 12(1 - v^2)\mu UL^2/\{E\delta^3\}$]
Bo	Bond number [$Bo \equiv \rho g L^2/\sigma$]	H_∞	surface elasticity number [$[Es \equiv \mathcal{R}T\Gamma^*/\mu U]$]
C	concentration [mol/cm^3] or capacitance [A s/V]	H_G	force [N]; may also be used as a general-purpose function
C_i	concentration of species i [mol/cm^3]	h	focal length [m]
C_b	bulk concentration [mol/cm^3]	h_∞	activity coefficient [$-$]
C_s	sub-surface concentration [mol/cm^3]	H_∞	gravitational acceleration of [$[g = 9.81 \text{ m/s}^2]$]
C^*	reference concentration [mol/cm^3]	G'	Gibbs free energy [J] or shear modulus [N/m^2]
c_i	dimensionless concentration of species i [$c_i \equiv C_i/C^*$]	G''	loss modulus [N/m^2]
Ca	capillary number [$Ca \equiv \mu U/\sigma$]	h	elastic modulus [N/m^2]
Ca_{AE}	critical capillary number at onset of air entrainment [$Ca_{AE} \equiv \mu U_{AE}/\sigma$]	h_∞/L	dimensionless film thickness [$[h \equiv H/L]$]
D	diffusion coefficient [m^2/s] or bending stiffness [$D \equiv E\delta^3/\{12(1 - v^2)\}$]	h_∞/L	dimensionless final wet thickness of coated film [$[h_\infty \equiv H_\infty/L]$]
D_i	binary diffusion coefficient of species i [m^2/s]	H	film thickness or height [m]
		H_∞	final wet thickness of coated film [m]
		H_G	coating gap [m]
		H_∞	reference thickness (e.g., film thickness down an inclined slide, half gap in roll coating, etc.) [m]
		\mathcal{H}	mean curvature of surface [m^{-1}]
		I_o	incident radiant energy [J]
		I_t	transient radiant energy [J]
		J	Jacobian
		J	Jacobian matrix
		L	characteristic, macroscopic length scale [m]
		L_δ	length of boundary layer [m]
		L_σ	capillary length [$[L_\sigma \equiv \sqrt{\sigma/\rho g}]$]
		M	change of momentum per unit width [kg/s^2]

M	mass matrix	$V(t)$	volume of fluid body [m^3]
<i>n</i>	power law index, or index of refraction	V_s	surface velocity [m/s]
n	unit normal to a surface	V^*	volumetric flow rate [m^3/s]
<i>p</i>	dimensionless pressure [$p \equiv PL/\mu U$]	W	coating width in cross-web direction [m]
Δp	dimensionless pressure difference (e.g., bead vacuum) [$\Delta p \equiv \Delta PL/\mu U$]	W_A	work of adhesion [J/m^2]
<i>P</i>	pressure [N/m^2]	We	Weber number [$We \equiv \rho U^2 L/\sigma$]
ΔP	pressure difference (e.g., bead vacuum) [N/m^2]	X	coordinate in main flow direction [m]
P_A	ambient pressure [N/m^2]	Y	coordinate normal to film flow [m]
P_v	sub-ambient pressure underneath coating bead [N/m^2]	Z	transverse (cross-web) coordinate [m]
Po	liquid property number [$Po \equiv \sigma(\rho/\mu^4 g)^{1/3}$]	x, y, z	dimensionless coordinates [$X/L, Y/L, Z/L$]
<i>q</i>	dimensionless flow rate per unit coating width [$q \equiv Q/(UL)$]	<i>Greek letters</i>	
<i>Q</i>	volumetric flow rate per unit coating width [m^3/s]	α	eigenvalue, impingement angle or application angle
<i>R</i>	residual	β	angle of inclination (measured from horizontal)
R	residual vector	γ	angle of solid corner (e.g., at static separation line)
<i>R</i>	radius [m]	$\dot{\gamma}$	shear rate [s^{-1}]
R_h	hydraulic radius [m]	$\dot{\gamma}_o$	reference shear rate [s^{-1}]
R_m	mean radius of curvature [m]	Γ	surface excess concentration (adsorption density) [mol/m^2]
\mathcal{R}	universal gas constant [$\mathcal{R} = 8.31 \text{ J K}^{-1} \text{ mol}^{-1}$]	Γ_i	surface concentration (adsorption density) of species <i>i</i> [mol/m^2]
<i>Re</i>	Reynolds number [$Re \equiv \rho UL/\mu$]	Γ_o	equilibrium adsorption density [mol/m^2]
<i>S</i>	arc length [m] or spreading coefficient [mN/m]	Γ^*	reference surface concentration [mol/m^2]
<i>s</i>	dimensionless arc length [$s \equiv S/L$]	Γ_∞	maximum surface excess concentration (adsorption density) [mol/m^2]
Sc_i	Schmidt number for species <i>i</i> [$[Sc_i \equiv \mu/\rho\mathcal{D}_i]$]	δ	thickness of substrate, blade or boundary layer [m]
Sc_s	surface Schmidt number [$[Sc_s \equiv \mu/\rho\mathcal{D}_s]$]	ε	small parameter
<i>St</i>	Stokes number [$St = \rho g L^2/\mu U$]	$\dot{\varepsilon}$	extension rate [s^{-1}]
<i>t</i>	time or surface age [s]	ε_o	dielectric constant of vacuum [A s/(V m)]
t	unit tangent to a surface	ε_s	dielectric constant of material [A s/(V m)]
<i>T</i>	absolute temperature [K]	η	non-Newtonian viscosity [Pa s]
T	total stress tensor	η_o	non-Newtonian viscosity at reference shear rate [Pa s]
<i>u, v</i>	dimensionless velocity components [$-$]	K	curvature of curve [m^{-1}]
<i>U</i>	coating/web speed [m/s]		
U_{AE}	critical coating speed at onset of air entrainment [m/s]		
<i>V</i>	alternative characteristic velocity (e.g., impingement velocity in curtain coating, metering roll velocity in reverse roll coating, etc.) [m/s]		

κ	dimensionless curvature of curve [$\kappa = KL$]	θ_E	Young's equilibrium contact angle
κ_m	dimensionless mean curvature of surface [$\kappa_m = \mathcal{H}L$]	θ_R	recently receded/receding static contact angle
λ	wavelength [m] or dimensionless flow rate in roll coating [—]	θ_o	apparent static contact angle (dynamic value extrapolated to zero speed)
λ_η	viscosity ratio [$\lambda_\eta \equiv \mu_2/\mu_1$]	θ_w	local contact angle imposed as mathematical boundary condition
λ_ρ	density ratio [$\lambda_\rho \equiv \rho_2/\rho_1$]	σ	surface tension [N/m]
μ	Newtonian viscosity [Pa s]	σ_{eq}	equilibrium surface tension [N/m]
μ_s	surface dilational viscosity [N s/m]	σ_s	solvent surface tension [N/m]
ν	Poisson's ratio [—] or frequency [s^{-1}]	σ_{12}	interfacial tension between two liquids [N/m]
π	surface pressure [J/m ²]	σ_T	tension in substrate or blade [N/m]
Π	disjoining pressure [N/m ²]	τ	viscous stress [N/m ²]
ρ	density [kg/m ³]	τ_w	wall shear stress [N/m ²]
ϕ^i	finite-element basis function	ξ, ζ	isoparametric coordinates
ψ^i	finite-element basis function	Ω	frequency [s^{-1}]
θ	contact angle	ω	dimensionless frequency [$\omega \equiv \Omega L/U$]
θ_A	recently advanced/advancing static contact angle		
θ_D	apparent dynamic contact angle		

INTRODUCTION

COATING SCIENCE AND TECHNOLOGY: AN OVERVIEW

Stephan F. Kistler and Peter M. Schweizer

1

In industrial coating processes, one or several liquid layers are deposited on a solid substrate, often a flexible web, and are subsequently dried or cured to form solid films that serve specific functions. Figure 1.1 shows a much simplified schematic with the most essential components of an industrial coating line. At the heart of such processes is the displacement of a gas previously in contact with the substrate by a liquid film. The wet thickness of the coated films is typically on the order of 1 to 100 microns, or more. This range of wet film thickness explains the choice of the book title, namely *Liquid Film Coating*. The purpose is to distinguish the coating processes discussed in the volume at hand from another class of coating processes often referred to as 'thin film coating'. There, films with thicknesses

in the sub-micron to Angstrom range are applied by sputtering or chemical vapor deposition (CVD) to produce, for example, anti-reflection coatings on glass, one-way mirrors, etc.

Coating processes as considered in this book are employed in many industries that manufacture a vast number of different products, including paper of various grades and surface finishes, packaging materials, printed matter like books, newspapers, catalogues, etc., photoreceptors for xerographic reproduction processes, multilayer silver-halide photographic films and papers, non-silver imaging products, magnetic storage media such as audio and video tapes as well as computer discs, optical storage media such as audio and photo compact discs, fibers and wires, labels, protective and decorative paintings, photoresist

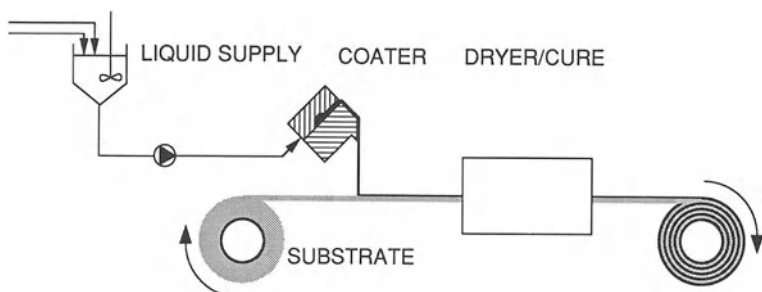


Figure 1.1 Simplified schematic of industrial liquid film coating process.

4 Coating science and technology: an overview

coatings for the manufacture of microelectronics such as printed circuits, solar cells, ceramic components made from sol/gels, sensors, medical products like transdermic systems which release active substances into the skin from a thin band-aid-like applicator, textiles, sand paper, adhesive tapes and many more.

Liquid films may be applied in one or several layers, either simultaneously or in multiple coating passes. Moreover, the substrate may be coated on just one or on both sides, again, either in one or in subsequent passes. Coating solutions are based on water or organic solvents. The latter are no longer attractive for ecological reasons. However, in spite of enormous efforts by various coating industries to substitute water for organic solvents, many desired product properties can, to date, only be achieved with organic solvents which, for many specialty applications, remain in common use.

The economic importance of the U.S. coating industry has been estimated by the US Department of Commerce (1994) to be about \$20 000 000 million per annum. This immense figure represents the value of coated products, coating process hardware, and other products in which coating is a key technology. The large value generated by the coating industry and the ever increasing demands on film thickness uniformity as well as on productivity and yield of the coating processes justify the need for a sound and basic understanding of coating technology.

The origins of coating technology are rooted in different industry segments associated with different product lines. Moreover, coating is a complex multi-disciplinary matter, comprising aspects of wetting, spreading, adhesion, fluid mechanics, rheology, mathematics and others. It is therefore not surprising that a consolidation of disciplines and open communications between various industry segments did not take place for a long time. Consequently, coating technology remained an art for the better part of the 20th century. First signs of turning coating from art into science appeared in the land-mark paper by Landau and Levich (1942). For small capillary numbers, these authors derived a rigorous mathematical analysis of the viscous, surface

tension and static pressure forces in liquid film deposition as it may occur in dip or extrusion coating. By matching the film profile downstream to a static meniscus region upstream, they were able to derive a simple relationship for the final film thickness as a function of liquid properties and coating speed. A major thrust of coating research began in the early 1970s under the leadership of Professor L. E. (Skip) Scriven at the University of Minnesota. He not only started teaching about interfacial phenomena, but he also initiated a comprehensive research program of various coating methods, thereby emphasizing and developing experimental methods, theoretical models, as well as analytical and numerical techniques for solving the models. It was perhaps the availability of more advanced mathematical methods, more potent computers, and more refined measurement tools that triggered an avalanche effect in coating research and development in the early 1980s.

Today, industrial and academic research laboratories all over the world communicate and collaborate with each other, as is evident in the international coating conferences organized, for example, by the Technical Association of the Pulp and Paper Industry (TAPPI), the American Institute of Chemical Engineers (AIChE), the Society for Imaging Science and Technology (IS&T) and the Society of Chemical Engineers in Japan (SCEJ); short courses and workshops on various topics related to coating technology, offered, for example, by AIChE's Continuing Education Department, the Center for Interfacial Engineering at the University of Minnesota, and the Universities of Erlangen (Germany) and Bradford (England); close collaboration between universities and industrial companies, manifested by engineering research centers such as the Center for Interfacial Engineering at the University of Minnesota; technical journals devoted to liquid film coating technology, including the *Journal of Coating Technology*, *Coating* (in German), and *Industrial Coating Research* (in Japanese and English); and a rapidly growing number of publications in other professional journals related to fluid mechanics, colloid and surface science, rheology, etc.

In spite of all the activity in coating process research, there is no preceding comprehensive text that summarizes results obtained in various places around the world and published in different technical journals. In particular, there is no single text that systematically interprets all the physical mechanisms that control coating processes, and that explains implications of scientific principles on industrial coating applications. This is not to say that no books or reviews on coating technology have been written in the past. However, they all focus on either coating equipment (Higgins 1965; Booth 1970; Weiss 1977; Satas 1984); on just a few particular coating methods (Middleman 1977; Ruschak 1985); or on particular aspects of coating technology such as numerical methods (Kistler and Scriven 1983), process control (Frost and Gutoff 1991), or wettability (Blake 1984; Berg 1993). The recent volumes edited by Cohen and Gutoff (1992) and Benkreira (1993) emerged from short courses on coating technology. They cover a wide range of topics, but make no attempt at being comprehensive or consistent in approach and thus provide only snap-shots of recent progress made in the selected subject areas.

The multi-author book at hand, in contrast, seeks to provide a systematic up-to-date guide to the literature, a critical assessment of the current state of knowledge, and an outlook on directions for future developments, all written by recognized experts in their respective fields. The book is intended primarily for scientists, engineers and technical managers at industrial companies, universities and government laboratories who are engaged in research and development of coating processes, coated products and advanced materials. The book is also intended to be valuable as a text for self-study, or as a reference for class-room lectures.

The overall aim of the book is to provide the interested researcher or engineer with the information needed to address, in a systematic and scientifically sound manner, the challenges most commonly faced in industrial coating practice. When a new product is being developed or an existing one is modified in a significant way, the challenge is to select a coating method from a

wide range of available methods or to invent a new one. Then, of course, the details of the coating equipment must be specified and designed, and feasibility of the process selected must be demonstrated for a desired range of operating conditions. For an existing product, on the other hand, the most pressing issues are often to expand the range of successful operation, for instance to higher coating speeds, thinner wet layers, or more layers coated simultaneously; to eliminate coating imperfections or defects that degrade product quality; and to increase the yield, or the fraction of salable material from an entire lot coated. Coating engineers, together with formulation chemists, also respond to never-ending quests to improve the performance of the final products which, in some instances in very subtle ways and in others to a significant extent, depend on careful control of the micro-structure or surface properties imparted on the coated layers by the coating flow process upstream. Altogether, most of the activities of industrial coating-process research and development amount to a gigantic optimization procedure, with seemingly countless independent variables for the design and operation of the process as well as the chemical composition of the coated products, and with many, often conflicting target functions for both manufacturability and ultimate product performance. Rapidly intensifying competitive pressures on a world-wide basis, furthermore, demand that the optimization addresses not only technological refinement, but also economical viability.

All in all, the challenges listed make apparent that future refinements in coating technology become increasingly intricate and difficult. In addition, the challenges must be met in ever shorter time periods. All this puts a premium on being able to identify and analyze the physical mechanisms that decide between success and failure of a coating process rather than relying on an empirical approach based mostly on trial and error. In liquid film coating of the sort considered in the book at hand, many of the essential mechanisms are those of viscous free-surface flows, and these are the main subject of

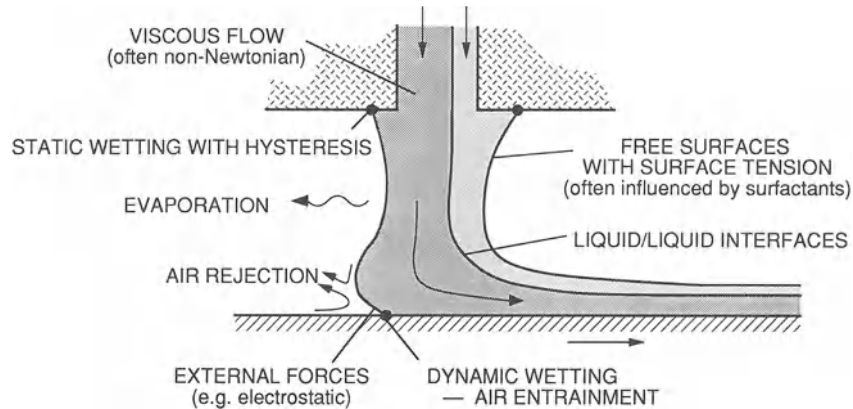


Figure 1.2 Cursory overview of physical mechanisms involved in liquid film coating (the figure shows a hypothetical coating process for two-layer coating).

the book. Figure 1.2 shows a schematic of a free-surface flow that is prototypic of the flows encountered in liquid film coating. It includes many of the features that contribute to the technological complexity of coating-flow processes yet, at the same time, make for interesting and rewarding fluid mechanics problems. Because of the small thickness scales of the coated wet films, Reynolds numbers rarely exceed 100 and so the difficulties associated with turbulence are usually not of concern, at least in the liquid phase. Significant complications and resulting mathematical nonlinearities, however, arise from the free surfaces between the coating flow and the surrounding gas, and from interfaces between stratified layers in multilayer coating. Primarily because of the free surfaces and interfaces, coating flows are susceptible to numerous hydrodynamic instabilities that, all too often, lead to catastrophic failure of the process to deposit a uniform liquid layer. The stability of coating flows is also extremely sensitive to non-Newtonian behavior of the coating solutions, sometimes strongly influenced by small traces of a non-Newtonian component whose effect can barely be detected in rheological tests. Likewise, surface-active substances, either added on purpose or present because of contamination, can drastically alter the equilibrium of forces at the free surfaces and thereby affect coating flows and their stability.

Catastrophic coating failure may also stem from the inability of the coating liquid to displace sufficient amounts of air previously in contact with the substrate, a process that takes place at what is called a dynamic wetting line. Both flow stability and successful air displacement may, quite often, be enhanced by the application of external forces, such as those from an electrostatic field or an external pressure difference applied between two free surfaces of a coating flow. Even when the flow is stable, however, imperfections in coated liquid films may arise from a wide variety of mechanisms. These include inhomogeneities, foreign matter or contaminants arriving with the coating solution or the substrate; disturbances induced by equipment vibrations, uncontrolled air flow, or evaporation; various wetting phenomena such as the uneven advance of a static contact line past a sharp corner, or patchy charge distributions arriving on a non-conductive substrate. Coating flaws may also stem from flow instabilities that grow only to modest amplitudes during liquid film application and partially decay further downstream. In some instances, coating imperfections can be alleviated by spontaneous self-leveling of the liquid film after coating. In other cases, however, small imperfections or defects may grow between coating and drying to gross flaws in the film or even dry patches. In either case, surface-active components

can have a significant effect on the formation and fate of defects. The ultimate properties of the coated product, finally, depend not only on the coating flow mechanics upstream, but also on the mechanisms that constitute drying and solidification downstream, including diffusion, evaporation and other forms of mass transfer, phase behavior, particle migration and orientation, film-internal stress buildup, and many more.

The goal of the book at hand is not only to review the mechanisms that control the deposition of liquid films on solid substrates, but also to bridge the gap between scientific principles and practical implementation on an industrial scale. Part One (Chapters 2–6) reviews the underlying physical principles and important material properties. The discussion is at a fairly advanced level, but is complemented with plenty of references to introductory texts. Part Two (Chapters 7–9) gives a comprehensive treatise of the most sophisticated experimental and mathematical methods available today to investigate coating processes. The techniques are described in sufficient detail to give the reader a realistic picture for what is involved, and a helpful guide for where to look for more details. Part Three (Chapters 10–15) finally provides an in-depth overview of a wide range of industrial coating processes. Special emphasis is placed on combining scientific principles with results from sophisticated methods of analysis to give the reader a solid knowledge of the operating behavior of various coating techniques, and an appreciation for how many phenomena that commonly prevent successful coating can be traced back to fundamental mechanisms.

In Part One, Chapter 2 by Weinstein and Palmer recounts the capillary hydrodynamics and interfacial phenomena that are all-important in coating flows. The main emphasis is on a careful derivation of the complete set of governing equations and boundary conditions for a rigorous mathematical analysis of liquid film coating; identification of dimensionless groups and closely related, limiting flow regimes; and a set of well-chosen sample problems that are worked out in detail to reinforce the physical insights

into some of the key mechanisms at work in liquid film coating. For a more phenomenological approach to interfacial hydrodynamics, the reader may also want to consult the review by Berg (1982). Issues of wettability, associated with contact lines where liquid/gas interfaces meet solid surfaces, are touched upon in Chapter 2 but are treated in depth in Chapter 3 by Blake and Ruschak. These authors give an authoritative review and assessment of the current level of understanding of both static and dynamic wetting. At the same time, they keenly focus on the issues most relevant in industrial coating practice, namely how to control the pinning and uniformity of static contact lines, and how to avoid deleterious air entrainment at dynamic wetting lines. Chapter 4 by Tricot addresses the subject of surfactant effects in coating, for which Chapter 2 also lays some of the foundations. Apart from an overview of the classical concepts in surfactancy, the main focus in Chapter 4 is on material properties of aqueous surfactant formulations. In particular, the chapter discusses experimental methods to accurately measure static and dynamic surface tension, and the application of such measurements to systematically optimize surfactant systems for improved coating performance (the issue of how surfactants actually affect the coating flow mechanics is taken up in detail in Chapter 11d of Part Three). Chapter 5 by Glass and Prud'homme covers the sometimes dramatic effects of non-Newtonian liquid behavior in coating flows. All in all, this subject is still rather poorly understood, perhaps because of the complicated deformation fields encountered in most coating processes, and the complex rheological behavior of many coating formulations. The chapter reviews some of the most important non-Newtonian material properties and related constitutive models, and illustrates the interactions between material structure, rheological behavior and actual coating performance for selected coating systems. For additional, more general information, many excellent texts are available on constitutive theory (e.g., Larson 1988), non-Newtonian fluid mechanics (Bird, Armstrong and Hassager 1987), and rheological measurements

8 Coating science and technology: an overview

(Barnes, Hutton and Walters 1989; Macosko 1994). Chapter 6 by Kheshgi concludes Part One with a concise overview of the mechanisms that control the fate of liquid films after coating. These include surface leveling which can heal coating irregularities; de-wetting which can result from the nucleation and growth of dry patches; diffusion, mass transfer, and phase transitions which are associated with drying; and stress build-up from solvent removal and other mechanisms that can cause cracking, crazing, peeling and curling of coated films.

In Part Two on methodology for coating process investigations, Chapter 7 by Schweizer discusses experimental equipment and design, flow visualization and measurement instrumentation, and on-line inspection techniques. The focus is on methods suitable for coating process studies in an R&D environment as well as methods used for scale-up and production purposes, and on illustrating the application of these methods for particular case studies. Chapter 8 by Smith introduces approximate methods of conventional mathematical analysis of coating flows. It starts with simple lubrication-flow analysis and then treats in depth more systematic perturbation methods that seek to exploit, by way of asymptotic expansions, the simplifications made possible by limiting parameter regimes or simple flow geometries. Carefully developed examples show when and how asymptotic methods can be applied to analyze steady flow fields as well as transient behavior and related stability. Chapter 9 by Christodoulou, Kistler, and Schunk reviews recent advances in numerical methods of computer-aided mathematical analysis of coating flows. The main emphasis is on finite-element methods which, over the last fifteen years, have become remarkably powerful and which, at present, are the preferred choice. The chapter also highlights alternative methods for computational free-surface flow analysis which, for certain applications, may offer distinct advantages.

As has been pointed by many others before (e.g., Scriven (1984); Churchill (1992)) – and as is apparent throughout the volume at hand – the three methods covered in Part Two are

complementary rather than competitive. Experiments on pilot coaters are indispensable to demonstrate feasibility of a process or to generate sample product. Experiments, either on pilot coaters or cleverly designed table-top devices, are also invaluable to identify the mechanisms by which coating processes fail or defects form, for they provide the ultimate validation for any hypothesis or theory. Experiments alone, however, often cannot fully explain cause-and-effect relationships. They can also be very costly and, in some instances, visualizing essential small-scale features of a coating flow can be exceedingly difficult if not impossible. Conventional methods of mathematical analysis, such as simple lubrication–flow models or more systematic methods based on asymptotic expansions, have a keen ability to zero in on the essential mechanisms while, at the same time, indicating which mechanisms may be secondary and can be ignored. For problems that are simple enough, classical methods of flow analysis furthermore produce closed form solutions which reveal important trends from simple inspection of the mathematical expressions, or from quick numerical evaluation. The applicability of these methods, on the other hand, is usually restricted to idealized flow configurations that may have to be much simpler than the coating process of practical interest. In addition, the validity of the asymptotic expansions is usually restricted to limiting regimes. These limitations are not a factor with computational methods. In their most sophisticated form available today, such methods not only predict the mostly two-dimensional base flows in successful coater operation at realistic conditions, but also the stability of the computed flow states and the susceptibility of stable coating flows to external disturbances. Computational methods – and asymptotic methods where applicable – have the ability to visualize details of the flow fields that are difficult to measure in experiments; unravel the nonlinear behavior of free-surface flows and, thereby, isolate key mechanisms and stability limits that are difficult to understand from experimental data; evaluate many more designs and configurations than could realistically be

tested; and explore wider parameter ranges than may be accessible with existing equipment. In spite of their power and promise, however, computational methods have limitations as well. For one, difficulties associated with dynamic wetting lines, non-Newtonian flow behavior, and other specific material effects still seriously hamper predictive capabilities. In addition, systematic exploration of wide parameter ranges can be costly and time-consuming, and a large number of output files and color plots do not guarantee that important trends are recognized, especially by inexperienced users with limited background in coating flow mechanics.

Part Three covers the theory and practice of a wide range of industrially significant coating processes. A casual survey of various coating configurations might suggest that the possibilities of inventing or modifying coating systems are limitless. A more thoughtful analysis, however, reveals that all existing coating methods – and, most likely, all that will be developed from here on – are merely permutations of the sequence or geometric arrangement in which the key tasks of a coater are performed (Scriven 1991; Benjamin and Scriven 1991). These tasks are the distribution of the liquid in the cross-web direction and associated control of the coated film thickness in that direction; the control of the coating thickness in down-web direction; the deposition of the liquid on the substrate, which includes the displacement of the air previously in contact with the substrate; and the formation of the free surface that bounds the coated film.

In a wide range of coating configurations, the first task is performed by the internal distribution cavity and metering slot of a coating die or another feed device that spreads the coating liquid from a single inlet port to a slot-shaped outlet that extends in the cross-web direction. Chapter 10 by Secor discusses the analysis and design of die internals. The chapter surveys methods of die design, focusing on a fairly simple, yet very effective approximate method that readily accounts for non-Newtonian effects; addresses mechanical and thermal aspects of die design; identifies various flow regimes; and concludes

with illustrative examples and practical design considerations for some of the most common die geometries.

Chapter 11 covers pre-metered coating processes in which the amount of liquid applied to the web per unit area is predetermined by a fluid metering device upstream, such as a precision gear pump, and the remaining task of the coating device is to distribute that amount as uniformly as possible in both the down-web and cross-web direction. In slot or extrusion coating, discussed by Durst and Wagner in Chapter 11a, one or several layers of coating liquid emerge from a coating die in close proximity to the moving web and bridge the gap between the die and web to form a coated film. In slide coating, covered by Hens and Van Abbenyen in Chapter 11b, one or several liquid layers are metered onto an inclined plane to form a falling-film flow that is picked up by the moving web across a narrow gap between the lip at the end of the incline and the web. In curtain coating, which Miyamoto and Katagiri review in Chapter 11c, the coating die is mounted at a considerable height above the point of coating and the coating liquid(s) fall as an unsupported sheet onto the moving web. The key features that differentiate the three pre-metered coating methods are the length of the liquid bridge that needs to be established between the coating device and the moving substrate; the orientation of gravity with respect to the main direction of flow in the liquid bridge; and the amount of momentum the coating liquid carries toward the substrate. Resulting from these distinguishing features are different operating limits and characteristic coating defects, to be explained in detail in Chapters 11a through 11c. In spite of significant physical and practical differences, however, the three pre-metered coating methods share many similarities. In particular, they involve two free surfaces, two static contact lines, and one dynamic wetting line (for an example, see Fig. 1.2 above). One free surface forms the liquid film; it separates at a static contact line from a stationary solid piece that is part of the coating die. The other free surface also starts at a static contact line on the coating die and terminates at a dynamic wetting line

where most of the air previously in contact with the substrate is displaced by the coating liquid. All three pre-metered coating processes are furthermore suitable for single- and multi-layer capability; and the stability of the flow is often assisted by externally applied forces, most commonly an ambient air pressure difference across the liquid bridge.

Because of the many similarities between slot, slide, and curtain coating, Chapters 11a, 11b, and 11c all follow in essence the same structure: they first specify the design and other important aspects of the coater set-up; they then discuss the hydrodynamics that make up successful coater operation; they move on to identify operability limits past which the process fails catastrophically; they assess susceptibility to external disturbances within the window of successful operation, which can have a significant effect on final coating quality; and they conclude with an overview of practical considerations, showing how specific solutions proposed in the patent literature or elsewhere can be rationalized from a fundamental understanding of the process.

Chapter 11d by Schunk and Scriven discusses surfactant effects in coating flows. This chapter is included as part of Chapter 11 because it focuses primarily on pre-metered coating processes of the sort used in the manufacture of water-based photographic materials. Building on the information given in Chapter 4, Chapter 11d presents a comprehensive mathematical theory of the action of surface-active materials, and reviews analyses of surfactant effects in coating and related free-surface flows. The bulk of the chapter, however, is dedicated to three particular case studies intended to show how care must be taken in interpreting dynamic surface tension data, how surfactants influence falling film-flow stability, and how they alter the local force balance in the dynamic wetting region of a slide coating flow.

Chapters 12 and 13 treat self-metered coating processes in which the final wet thickness of the coated film is mostly controlled by the interactions of the fluid flow with the coating applicator, rather than the amount of liquid supplied to the coater head as in pre-metered processes. Self-

metered coating processes, in turn, can be divided into those in which the coated film thickness is metered primarily by a narrow gap between the web and a solid member upstream of the film forming region; and processes in which the meniscus at which the film forms also performs the metering task via the action of capillarity. Self-metered coating processes with a narrow metering gap can be subdivided further into those where the solid boundaries of the applicator are rigid; and those where one or more solid members are flexible and, hence, deform in response to fluid pressure or external loads. The latter class is referred to as elastohydrodynamic.

Chapter 12a by Coyle describes knife, forward-roll, and reverse-roll coating. These processes are prototypical of configurations with narrow, rigid metering gaps in which the coating thickness depends mainly on the interplay of viscous forces with the geometry of the coating device and the relative speed of its surfaces. The chapter shows how much of the operating behavior can be understood from the classical theory of hydrodynamic lubrication between slowly converging and diverging surfaces (Reynolds 1886; see also Chapter 8). The chapter also explains the physical cause and mathematical analysis of various flow instabilities – including the much celebrated ribbing instability that can arise in a wide range of coating methods. The chapter furthermore assembles operating diagrams for the three processes covered; and discusses how coating non-uniformities may arise from various disturbances, contaminants, and also ancillary flows such as those associated with feeding. Chapter 12c by Pranckh and Coyle follows a similar program for elastohydrodynamic coating systems, addressing blade, membrane, tensioned-web, squeeze-roll and gravure coating. In addition, Chapter 12c provides the theoretical background in solid mechanics needed to understand elastohydrodynamic coating systems (see also Dowson and Higginson (1966)). Chapter 12d by Aidun and Triantafyllopoulos focuses on blade coating in greater depth, specializing on paper coating in which speeds in excess of 25 m/s are not unheard of. The chapter deals with the special

issues that arise from the rough, porous substrate and the high speeds, in particular as they pertain to applying the fluid, managing hydrodynamic instabilities, and avoiding air entrainment. The chapter furthermore addresses specific coating defects and microstructures that arise from the particulate coating solutions and their viscoelastic properties, as well as from the porous and strongly hydrophilic substrate.

Chapter 12b by Gaskell and Savage, like Chapter 12a, considers coating with rigid rollers, but specializes in a particular regime referred to as meniscus roll coating in which the liquid film arriving at the nip between the rollers is much thinner than the roll separation. In this regime, capillarity plays a dominant role. The coated film thickness is not metered by the gap between the rollers, but the process is self-metered in the sense that the final film thickness depends on the speed ratio between the rollers, and is influenced by capillarity. Chapter 12b uncovers a wealth of structures in meniscus-roll-coating flows, and focuses on identifying different flow regimes and related flow transitions in-between.

Meniscus roll coating is in some ways closely related to dip coating, which is the subject of Chapter 13 by Schunk, Hurd and Brinker. Dip coating is the withdrawal of a substrate, either a continuous web or individual pieces of substrate material, from a liquid pool. It is the archetype of a self-metered coating process, for the coated film thickness is controlled entirely by the capillary hydrodynamics involved in the film deposition. Chapter 13 begins with a review of the classical and well-known results on dip coating, but then stresses that, at low coating speeds, the mass transport by evaporation of volatile components can compete with the hydrodynamics in controlling the meniscus profile and setting the final film thickness. The chapter furthermore establishes important links between coating flow processes and resulting microstructures by considering modern applications of dip coating in advanced materials processing, namely the deposition of Langmuir–Blodgett films and sol-gel films. For the latter, the chapter summarizes a comprehensive computational analysis of fluid flow and mass

transport in both the liquid and the gas phase, including the volume changes associated with evaporation and condensation. The results reveal possible effects of the drying environment on the microstructure of the final sol-gel films, and are exemplary of the type of future work needed to expand the scope of coating flow mechanics from the deposition of uniform films to the formation of films with controlled microstructure.

Chapter 14 by Larson and Rehg reviews another specialized coating process for advanced materials processing, namely spin coating. The chapter identifies the relative importance of hydrodynamics and evaporation, explains why on flat substrate surfaces uniform films are rather easy to achieve, and isolates the key factors that favor leveling or planarization of spin-coated films on surfaces with textured topography. The last case is of particular importance in the microelectronics industry, and the chapter gives due consideration to the specific material properties of the photoresist solutions used in that particular application.

Chapter 15 by Schweizer, finally, seeks to put much of the information contained in the volume at hand into perspective by consolidating it into the frameworks of control and optimization. The chapter briefly reviews some of the elementary concepts of control theory and argues for a more systematic application of these concepts in coating technology. The chapter also recounts the fundamental principles behind optimization, and illustrates how they can and should be applied at various levels, including micro-optimization of a single detail of a coating flow, such as a wetting line position; overall optimization of an entire process step, such as flow distribution within a coating die; global optimization of an entire manufacturing process to maximize, for instance, productivity or yields; combined process and product optimization; and last, but not least, economic optimization addressing unit costs of the coated product.

Even though the book at hand treats a wide range of coating configurations and associated physical mechanisms, it does not cover all aspects

of coating technology. As mentioned above, the book focuses on the fundamentals of the actual deposition process and, for that reason, ignores all ancillary technologies, such as fluid preparation and delivery, web handling and cleaning, air flow management and clean-room conditioning, or calendering and other forms of post-processing. For a practical guide on how to condition, pump, filter, and de-gass coating solutions, the reader should consult the review by Schweizer (1992). Kheboian (1992) gives practical advise on web-handling but, unfortunately, his treatise does not attempt to review the growing scientific literature that is available on the mechanics involved in web transport and winding (e.g. Good 1993). Similarly, for most other supporting technologies involved in coating, there exist no preeminent scientific reviews, and the reader must be satisfied with the general overviews in some of the books cited above (Booth 1970; Weiss 1977; Satas 1984), or dig into the literature themselves.

Even within its intended scope of treating the scientific principles of liquid film coating, the book at hand is not exhaustive in its coverage of coating technology, for it ignores some specialized, yet very common application methods, such as spray coating (for a cursory introduction, see Satas 1984). This process involves interesting fluid-flow, heat- and mass-transfer phenomena associated with atomization, evaporation, impingement, spreading and coagulation of liquid droplets (e.g. Lefebvre (1988); Trapaga and Szekely (1991); Coeling (1993); Fukai *et al.* (1993)).

In addition, the book pays insufficient attention to some important mechanisms in liquid film coating – mostly due to the lack of a sufficiently large body of scientific literature at the time the outline of the book was planned back in 1990. One class of such mechanisms is related to the three-dimensional phenomena associated with the edges of coated layers, and the transient phenomena that arise during splice passage, start-up and termination of coating processes. Because these phenomena are very complex, much of the know-how on the quality of coated edges, coatability of splices, and controlled start-up of liquid film coating is based on empirical

work that is documented in numerous patents rather than scientific investigations. Noteworthy exceptions are the recent papers by Katagiri (1992), who applied the finite-element method to predict the three-dimensional flow along an edge guide of a falling curtain (see Chapter 11c), and by Brandon *et al.* (1994), who successfully employed finite-element methods for transient and stability analysis to guide the invention of an improved procedure for splice passage in slide coating.

Another mechanism that is not covered in sufficient depth is the all-important effect of electrostatic charges. Coating practitioners have long known about the deleterious effects on coating quality from uncontrolled charges carried by polyester webs and other substrates – as well as their safety hazards – and have devised practical means to cope with the problem (e.g. Keers 1984). On the other hand, electrostatic fields applied on purpose can also be used to great advantage to assist dynamic wetting and other functions of a coating process, as described in a vast number of patents following the pioneering works of Chappel (1934) and Nadeau (1956). Scientific investigations into the physical mechanisms at work have a well-established foundation in the theory of electrohydrodynamics (e.g., Melcher and Taylor (1969)), but are only now beginning to appear in the public domain (e.g., Feng and Scriven (1992)).

A somewhat related aspect of liquid film coating that the book fails to address in an up-front manner is the influence of the substrate surface. Those with industrial coating experience know all too well that some substrates simply ‘coat much better’ than others. They also know of various attempts to influence the success of a coating process by applying ‘priming’ or ‘subbing’ layers to the film, or devising other on-line treatments such as corona discharge. Curiously, with the exception perhaps of Chapter 3, the discussion of these effects is confined to a few parenthetical remarks well-hidden in the main text. The reason is probably our incomplete understanding of the physics of dynamic wetting, which remains one of the most prominent

unresolved issues in coating flow hydrodynamics.

Another aspect of liquid film coating that, given recent developments, receives insufficient attention in the present collection of review articles is that of drying and other methods of solidification. Chapter 6 by Kheshgi provides a concise and insightful summary of the most important mechanisms and identifies different drying regimes. And Chapters 13 and 14 analyze in detail specific coating flows accompanied by simultaneous evaporation. None of the chapters, however, does full justice to the significant progress that has been made in recent years in advancing the basic understanding of solvent removal, polymerization and other cross-linking reactions, or changes in colloidal stability and phase behavior in liquid films undergoing drying and/or solidification. For a lucid assessment of the key issues involved, results available today, and future research directions, the interested reader may want to look at the recent paper by Cairncross, Francis and Scriven (1996). On the other hand, the reader looking for a description of drying equipment or advice on how to dimension dryer ovens based on macroscopic mass and energy balances may want to consult Cohen (1992).

Closely related to drying and solidification is, of course, the formation of microstructure, i.e. the distribution and physico-chemical state of individual chemical compounds, the concentration, agglomeration, flocculation and orientation of particles, porosity, surface texture, and many other attributes of coated films that are essential for their ultimate performance as a useful product. Chapter 13 reports a special case study in which the final film microstructure has been linked to drying and even coating upstream. More generally, however, none of the chapters in the book at hand – nor any other review we are aware of – synthesizes a coherent picture of the many intricate ways in which the materials in a coating formulation, and also the substrate, interact with the coating and drying process to form the ultimate microstructure. Controlled microstructure formation is an exciting research area of coating process fundamentals which, due to

never-ending refinements in experimental and analytical instrumentation and rapid advances in computer power, should see dramatic progress in the near future on both the experimental and the theoretical side.

A further aspect of liquid film coating that is not treated in a separate chapter in the book at hand is the issue of coating defects. Most chapters make reference to various hydrodynamic instabilities that produce gross defects. Some also discuss coating nonuniformities induced by ongoing disturbances, such as mechanical vibrations, pump pulsations, speed fluctuations, etc. Many chapters furthermore mention various characteristics of coating flows, such as enclosed recirculations or poorly controlled static wetting lines, that supposedly cause streaks or other down-web striations. With the exception of Chapters 6 and 15, however, there are very few explicit explanations of specific mechanisms that cause the many seemingly random defects that plague every-day coating practice, and predictably foul up ‘quality circles’ in their industrious quest for making ‘defect-free coating’ a reality. Hansen and Pierce (1974) and Gutoff and Cohen (1995) provide helpful overviews of defects in liquid film coating.

In fact, it is perhaps the biggest shortcoming of the hydrodynamic principles behind liquid film coating – which constitute the bulk of the material in this book – that, at best, they explain various defects but that, in many cases, they are unable to predict the frequency at which defects occur or recommend fool-proof remedies. This is not to say that hydrodynamic studies of coating are not extremely helpful. They must be performed, however, with the humbling awareness that some aspects of liquid film coating technology may evade rigorous prediction from physical principles for some time to come – and thereby remain, for the moment, being art rather than science. Still, a considerable amount of fundamental knowledge in liquid film coating has been accumulated over the years, and we hope this book makes a contribution by providing a comprehensive consolidation of the knowledge available today.

ACKNOWLEDGMENTS

We are grateful to Marjorie Spencer from Van Nostrand Reinhold for her initiative and encouragement to write this book and for her valuable guidance during the early stages of the project. We are thankful to all participating authors for their fine contributions and for their exemplary commitment to carry this large project to the end. We appreciate the generosity of 3M Company and Ilford AG for providing the means for extensive communications between Minnesota and Switzerland by phone, fax and express mail. Most of all, we thank our wives, Karen and Sue, for their patience during six long years, and for their encouragement to keep on going, particularly when we were tempted not to do so.

REFERENCES

- Barnes, H. A., Hutton, J. F. and Walters, K. 1989. *An Introduction to Rheology*. Amsterdam and New York: Elsevier.
- Benjamin, D. F., Scriven, L. E. and colleagues. 1991. Coating flows: form and function. *Ind. Coating Res.* 1: 1–37.
- Benkreira, H. (ed.) 1993. *Thin Film Coating*. Boca Raton: CRC Press.
- Berg, J. C. 1982. Interfacial hydrodynamics: an overview. *Canad. Metall. Quart.* 21: 121–136.
- Berg, J. C. (ed.) 1993. *Wettability*. New York: Marcel Dekker.
- Bird, R. B., Armstrong, R. C. and Hassager, O. 1987. *Dynamics of Polymeric Liquids – Volume 1: Fluid Dynamics*. 2nd edn. New York: Wiley.
- Blake, T. D. 1984. Wetting. In *Surfactants*, ed. T. F. Tadros, pp. 221–275. London: Academic Press.
- Booth, G. L. 1970. *Coating Equipment and Processes*. New York: Lockwood.
- Brandon, N. C., Hackler, M. A., Hirshburg, R. I. and Christodoulou, K. N. 1994. Coatable splice process in photographic film coating: theoretical prediction and experimental investigation of process latitude. Paper read at *AIChe Spring National Meeting*, Atlanta, GA, April 17–21.
- Cairncross, R. A., Francis, L. F. and Scriven, L. E. 1996. Predicting drying in coatings that react and gel: Drying regime maps. *AIChe J.* 42: 55–67.
- Chappell, F. R. 1934. Spreading, extruding, or like operations. US Patent 2,052,131.
- Churchill, S. W. 1992. The role of analysis in rate processes. *Ind. Eng. Chem. Res.* 31: 643–658.
- Coeling, K. J. 1993. Spray coating. In *Kirk-Othmer Encyclopedia of Chemical Technology*, Volume 6, 4th edn, eds J. I. Kroschwitz and M. Howe-Grant, pp. 661–669. New York: Wiley.
- Cohen, E. D. 1992. Thin film drying. In *Modern Coating and Drying Technology*, eds E. D. Cohen and E. B. Gutoff, pp. 266–298. New York: VCH.
- Cohen, E. D. and Gutoff, E. B. 1992. Introduction. In *Modern Coating and Drying Technology*, eds E. D. Cohen and E. B. Gutoff, pp. xv–xx. New York: VCH.
- Cohen, E. D. and Gutoff, E. B. (eds). 1992. *Modern Coating and Drying Technology*. New York: VCH.
- Dowson, D. and Higginson, G. R. 1966. *Elasto-Hydrodynamic Lubrication*. Oxford: Pergamon Press.
- Feng, J. Q. and Scriven, L. E. 1992. Electrostatic effects in continuous liquid coating. Paper read at *AIChe Spring National Meeting*, New Orleans, LA, March 30–April 2.
- Frost, P. J. and Gutoff, E. B. 1991. *The Application of Statistical Process Control to Roll Products*. North Quincy: P. J. Associates.
- Fukai, J., Zhao, Z., Poulikakos, D., Megaridis, C. M. and Miyatake, O. 1993. Modeling of the deformation of a liquid droplet impinging on a flat surface. *Phys. Fluids A – Fluid Dynamics* 5: 2588–2599.
- Good, J. K. (ed.) 1993. *Proceedings of the First International Conference on Web Handling* (Web Handling Research Center, Oklahoma State University, May 19–22, 1991). Stillwater, Oklahoma: Oklahoma State University.
- Gutoff, E. B. and Cohen, E. D. 1995. *Coating and Drying Defects*. New York: John Wiley.
- Hansen, C. M. and Pierce, P. E. 1974. Surface effects in coating processes. *Ind. Eng. Chem. Prod. Res. Develop.* 13: 218–225.
- Higgins, D. G. 1965. Coating methods. In *Encyclopedia of Polymer Science and Technology*, Volume 3, eds H. F. Mark, N. G. Gaylord and V. M. Bikales, pp. 765–807. New York: Wiley.
- Katagiri, Y. 1992. Analysis of edge effects in curtain coating. Paper read at *AIChe Spring National Meeting*, New Orleans, LA, March 29–April 2.
- Keers, J. J. 1984. Static electricity. In *Web Processing and Converting Technology and Equipment*, ed. D. Satas, pp. 511–523. New York: Van Nostrand Reinhold.
- Kheboian, G. I. 1992. Drive systems for off-machine coaters. In *Modern Coating and Drying Technology*, eds E. D. Cohen and E. B. Gutoff, pp. 193–266. New York: VCH.
- Kistler, S. F. and Scriven, L. E. 1983. Coating flows. In *Computational Analysis of Polymer Processing*, eds J. R. A. Pearson and S. M. Richardson, pp. 243–299. London and New York: Applied Science Publishers.
- Landau, L. and Levich, B. 1942. Dragging of a liquid by a moving plate. *Acta Physico-Chim. USSR* 17: 42–54.

- Larson, R. G. 1988. *Constitutive Equations for Polymer Melts and Solutions*. Boston: Butterworths.
- Lefebvre, A. H. 1988. *Atomization and Sprays*. New York: Hemisphere.
- Macosko, C. W. (ed.) 1994. *Rheology: Principles, Measurements, and Applications*. New York: VCH.
- Melcher, J. R. and Taylor, G. I. 1969. Electrohydrodynamics: a review of the role of interfacial shear stresses. *Ann. Rev. Fluid Mech.* **1**: 111–146.
- Middleman, S. 1977. *Fundamentals of Polymer Processing*. New York: McGraw-Hill.
- Nadeau, G. F. 1956. Method for coating a liquid photographic emulsion on the surface of a support. US Patent 2,952,559.
- Reynolds, O. 1886. On the theory of lubrication and its application to Mr. Beauchamp Tower's experiments, including an experimental determination of the viscosity of olive oils. *Philos. Trans. Roy. Soc. Lond. A.* **177**: 157–234.
- Ruschak, K. J. 1985. Coating flows. *Ann. Rev. Fluid Mech.* **17**: 65–89.
- Satas, D. (ed.) 1984. *Web Processing and Converting Technology and Equipment*. New York: Van Nostrand Rheinhold.
- Schweizer, P. M. 1992. Fluid handling and preparation. In *Modern Coating and Drying Technology*, eds E. D. Cohen and E. B. Gutoff, pp. 23–61. New York: VCH.
- Scriven, L. E. 1984. Coating flows and coating rheology research. Introductory remarks read at *Annual Review of Coating Flows and Coating Rheology Research Program*, University of Minnesota, Minneapolis, September 20 and 21.
- Scriven, L. E. 1991. Bringing fundamentals to bear on choosing a coating method. In *Proceedings of the IS&T Symposium on Coating Technologies for Imaging Materials* (St. Paul, Minnesota, May 12–17), eds J. G. Truong and E. D. Cohen, pp. 79–85. Springfield, Virginia: IS&T – The Society for Imaging Science and Technology.
- Trapaga, G. and Szekely, J. 1991. Mathematical modeling of the isothermal impingement of liquid droplets in spraying processes. *Metall Trans.* **22B**: 901–914.
- U.S. Department of Commerce. 1994. 1994 U.S. Industrial Outlook. Bureau of Industrial Economics, U.S. Government Printing Office.
- Weiss, H. L. 1977. *Coating and Laminating Machines*. Milwaukee, WI: Converting Technology Co.

PART ONE

**PHYSICS AND MATERIAL INTERACTIONS
OF COATING PROCESSES**

CAPILLARY HYDRODYNAMICS AND INTERFACIAL PHENOMENA

2

Steven J. Weinstein and Harvey J. Palmer

2.1 INTRODUCTION

In coating processes, one or more liquid layers is typically applied, either individually or simultaneously, onto a substrate; after coating, these liquid layers are ultimately transformed into a solid coated structure via chilling, drying, or some other means. For much of a coating process, then, the layers are in liquid form. To understand the advantages and limitations of such processes, it is imperative to have a fundamental understanding of the physical principles governing fluid flow. In many cases, these principles can be expressed concisely in mathematical form, allowing the suitability of various coating operations for a desired product application to be assessed from a theoretical point of view. Once the agreement between theory and experiment is established for a given process, the need to perform experiments to explore the effect of process variables is greatly diminished; the use of a theoretical analysis can often represent significant savings in time and money in evaluating various coating options.

In this chapter, the underlying physics of fluid flow is discussed, and the associated governing equations and boundary conditions are presented. A distinguishing feature of coating flows, as compared with many other flow configurations, is the existence of fluid–fluid interfaces (i.e. gas–liquid or liquid–liquid). Interfaces have a marked effect on fluid flows, and therefore much

attention in this chapter will be given to the specific physics involved with their appearance.

2.2 PRELIMINARY CONCEPTS

Before considering the conservation laws which govern fluid flow, it is necessary to define what is meant by a fluid. A precise, all-encompassing definition of a fluid itself is difficult, in that the particular physical configuration in which a material is found may impact the way in which it behaves from a classification point of view. We define a fluid in the following way. The material in question is placed between two parallel plates, and a constant external force, F , is applied to the top plate tangent to its surface while the bottom plate is held stationary. We define a fluid as a material which continually deforms in such a configuration, albeit with some resistance. This is in contrast to a solid, for which the distortion of a material eventually ceases even though the constant external force is applied. Some materials have characteristics of both fluids and solids, such as those fluids that also exhibit elastic behavior, according to the above definition. Generally speaking, the equations of fluid mechanics can also handle these materials as fluids, provided the correct relation between force and distortion is employed. For practical coating flows, those materials being identified by phase as liquids and gases are fluids.

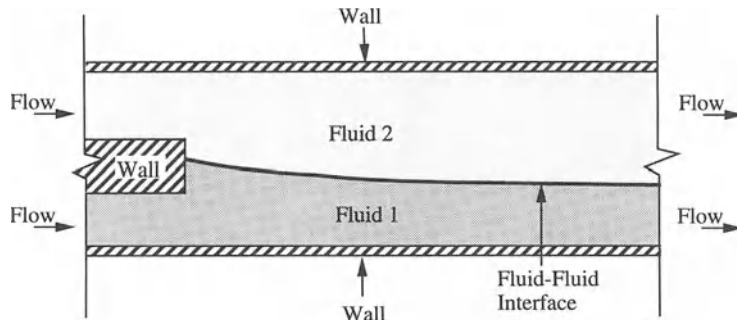


Figure 2.1 Multiphase flow configuration used to motivate the governing equations and boundary conditions.

In the above phenomenological approach to material characterization, the observed distortion of the material determines its classification. This is consistent with the fact that fluid mechanics provides a macroscopic description of fluid motion, where average properties such as fluid density and viscosity have physical meaning. Thus, attention is confined to length scales larger than those of molecular dimension. Once the length scale of a flow field is reduced to approximately ten times the distance between the molecules comprising a material, the appropriateness of modeling the material as a fluid is in question. The smallest ‘body’ of fluid which can be envisioned, but still within the constraints of a macroscopic continuum, is called a fluid point. The equations of fluid mechanics govern the motion of fluid points.

2.3 MATHEMATICAL DESCRIPTION OF FLUID FLOW

To help motivate the mathematical treatment of coating flows, let us consider the physical configuration shown in Fig. 2.1, which is meant to embody some arbitrary portion of a coating process. Here, two immiscible fluid layers are flowing in the domain as shown, where either of the top or bottom walls may be moving. We now

proceed to identify the equations and boundary conditions which govern the interfacial fluid flow. The equations to be presented are quite general and can be used for any flow configuration; they are not restricted to the flow domain shown in Fig. 2.1.

Multiphase flows, such as shown in Fig. 2.1, are a combination of flows of single fluid phases,* which are linked through contact at interfaces. Thus, in defining the governing equations of fluid mechanics, which embody conservation of mass and Newton’s laws of motion, the flow of a single-fluid phase is examined. The unique character imparted to the flow by the interface and solid boundaries enters the fluid mechanical description as boundary conditions, which are presented subsequent to the consideration of the governing conservation equations for a single fluid phase.

2.3.1 CONSERVATION EQUATIONS

2.3.1.1 Conservation of mass

All the equations of fluid mechanics can be derived by applying conservation laws to collections of fluid points, called material bodies, which by definition always consist of the same fluid points as the boundaries of the material body distort and translate with time (Whitaker 1968). Consider the motion of an arbitrary material body, which can be viewed as being imbedded entirely in one of the fluid layers shown in

*In a fluid flow consisting of more than one fluid, it is common to refer to each fluid as a phase, regardless of whether it is a gas or a liquid.

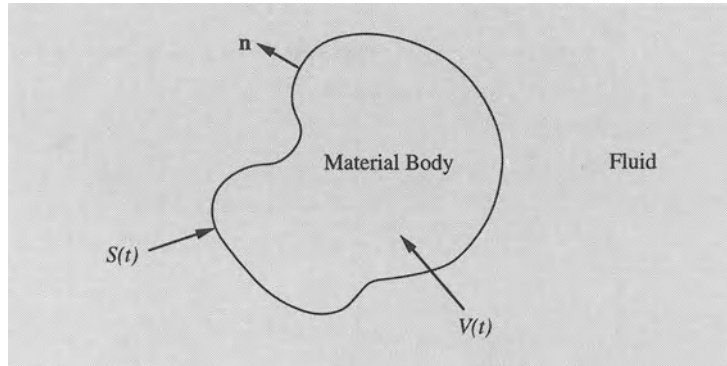


Figure 2.2 Arbitrary material body for a single fluid phase.

Fig. 2.1. Let the volume of the material body be denoted as $V(t)$, where t denotes time (Fig. 2.2). Further, let the fluid density be denoted by ρ , which is parameterized as $\rho = \rho(\mathbf{X}, t)$ where the spatial location within the material body is denoted by the coordinates of the vector \mathbf{X} ; we note here that the convention to be used in what follows is that quantities in boldface denote vectors and tensors. For a given differential volume element of the body, dV , the associated mass is given by ρdV ; thus, the total mass M of the body is obtained as the sum of those differential elements as

$$M = \int_{V(t)} \rho dV$$

As by definition, all the fluid points always remain in the material body, it is clear that

$$\frac{dM}{dt} = \frac{d}{dt} \int_{V(t)} \rho dV = 0 \quad (2.1)$$

Equation (2.1) is an integral form of conservation of mass.

To apply equation (2.1), it is necessary to know how the boundaries of the material body change with time, as is evident from the time-dependent integration domain. This form, however, is often inconvenient, as an assessment of the density distribution and velocity field for a specific region

in space with equation (2.1) requires knowledge of where the boundary of the body was at a previous time and where it will be at a later time. Rather, it is usually more desirable to examine the consequences of conservation of mass for volumes whose surfaces can deform arbitrarily in time (which also includes the case where the boundaries are fixed in time). Such arbitrarily deforming volumes are often referred to as control volumes.

The change in perspective from a material body to a control volume is afforded by the well-known Reynolds transport theorem (Whitaker 1968):

$$\frac{d}{dt} \int_{V(t)} \Phi dV = \int_{V(t)} \frac{\partial \Phi}{\partial t} dV + \int_{S(t)} \Phi \mathbf{U} \cdot \mathbf{n} dS \quad (2.2)$$

where $S(t)$ denotes the boundary of $V(t)$, \mathbf{U} is the velocity vector of the fluid parameterized as $\mathbf{U} = \mathbf{U}(\mathbf{X}, t)$, \mathbf{n} is the unit outward normal to the surface $S(t)$, and Φ is a quantity (scalar or vector) to which the theorem is applied. With the aid of (2.2), equation (2.1) can be rewritten as

$$\int_{V(t)} \frac{\partial \rho}{\partial t} dV + \int_{S(t)} \rho \mathbf{U} \cdot \mathbf{n} dS = 0 \quad (2.3)$$

which relates the rate of change of the mass of an arbitrary control volume of interest, $V(t)$, to

the rate of material flow in and out through its boundary $S(t)$.

The local differential form of the mass conservation law can be derived directly from (2.3) with the help of the divergence theorem:

$$\int_{S(t)} \mathbf{r} \cdot \mathbf{n} dS = \int_{V(t)} \nabla \cdot \mathbf{r} dV \quad (2.4)$$

where \mathbf{r} is any vector. Applying (2.4) to the surface integral in (2.3) produces the following result:

$$\int_{V(t)} \left[\frac{\partial \rho}{\partial t} + \nabla \cdot \rho \mathbf{U} \right] dV = 0 \quad (2.5)$$

To obtain the final differential form, we argue that, for a given fluid, the choice of $V(t)$ can be made arbitrarily, and thus all material bodies must satisfy (2.5). This implies that the integrand in (2.5) is identically zero. Thus, the local differential form of conservation of mass is given by

$$\frac{\partial \rho}{\partial t} + \nabla \cdot \rho \mathbf{U} = 0 \quad (2.6)$$

Equation (2.6) is commonly referred to as the continuity equation.

For coating flows, the density of the fluids involved can be considered to be constant. In the constant-density case, equation (2.6) becomes

$$\nabla \cdot \mathbf{U} = 0 \quad (2.7)$$

The physical interpretation of this local equation can best be made by utilizing the integral forms, from which (2.7) was derived. For a constant density fluid, equation (2.1) yields

$$\frac{dV(t)}{dt} = 0 \quad (2.8)$$

Equation (2.8) indicates that the volume of any arbitrary material body in the fluid does not change with time; that is, the fluid is incompressible. Thus, we see that (2.7) embodies the fact that velocity components must be related in a unique way to achieve a constant volume as a material body is distorted.

2.3.1.2 Conservation of linear momentum

Conservation of mass places one constraint on fluid motion, but to achieve flow there must be some driving force. The relation between applied force and fluid flow is described by Newton's second law of motion, which states that the time rate of change of the momentum of a body, \mathbf{L} , is equal to the net force on the body, \mathbf{F}_{net} .

$$\frac{d\mathbf{L}}{dt} = \mathbf{F}_{\text{net}} \quad (2.9)$$

As Newton's second law is valid for both deformable and undeformable material bodies, the equations of fluid motion can be derived, as for conservation of mass, by summing external forces on an arbitrary deformable material body as it moves in space. Referring again to Fig. 2.1, attention is confined to a material body moving entirely in one of the fluid layers. Note that it is assumed that the motion of the material body is observed in a frame of reference which is not accelerating, as (2.9) is valid only for such cases.

Using the material body notations shown in Fig. 2.2, the linear momentum associated with a differential element, dV , of an arbitrary material body, $V(t)$, is given by $\rho \mathbf{U} dV$ and the total linear momentum for the body, \mathbf{L} , is thus given by

$$\mathbf{L} = \int_{V(t)} \rho \mathbf{U} dV \quad (2.10)$$

Our material body may be acted upon by both body forces, \mathbf{F}_B , and surface forces, \mathbf{F}_S . Although there are several possible body forces, such as those due to magnetic and electrical fields acting on ferro-magnetic fluids, attention will be restricted here to the most common of such body forces in coating flows, namely that due to gravity. Denoting \mathbf{g} as the constant gravitational acceleration vector, the body force is

$$\mathbf{F}_B = \int_{V(t)} \rho \mathbf{g} dV \quad (2.11)$$

The surface force, \mathbf{F}_S , acts on the bounding

surface of the material body, and depends upon the identity of the fluid in contact with the material body, the type of motion the fluid is experiencing (i.e., static, laminar, or turbulent), and the orientation and shape of the surface $S(t)$. The surface force can be expressed in terms of the surface traction vector, \mathbf{t}_s , which gives the local force per area on a differential surface element, as

$$\mathbf{F}_s = \int_{S(t)} t_s dS \quad (2.12)$$

Upon substitution of (2.10), (2.11), and (2.12) into (2.9), we obtain a general form of conservation of linear momentum for a material body:

$$\frac{d}{dt} \int_{V(t)} \rho \mathbf{U} dV = \int_{S(t)} \mathbf{t}_s dS + \int_{V(t)} \rho \mathbf{g} dV \quad (2.13a)$$

A more useful form of the above conservation equation can be obtained by explicitly determining the form of the surface traction vector. It can be shown that there exists a stress-tensor, \mathbf{T} , which when operated on the unit outward normal, \mathbf{n} , yields the surface traction vector (Whitaker 1968) as

$$\mathbf{t}_s = \mathbf{n} \cdot \mathbf{T} \quad (2.13b)$$

As for the case of conservation of mass, it is desirable to have a differential equation which describes the response of the fluid to applied forces pointwise in a given domain. The local form can be derived from the integral form by following the approach used to obtain the local form for conservation of mass. First, the Reynolds transport theorem (2.2) is applied to the volume integral on the left-hand side of (2.13a), to yield

$$\begin{aligned} \int_{V(t)} \frac{\partial \rho \mathbf{U}}{\partial t} dV + \int_{S(t)} \rho \mathbf{U} \mathbf{U} \cdot \mathbf{n} dS &= \int_{S(t)} \mathbf{n} \cdot \mathbf{T} dS \\ &+ \int_{V(t)} \rho \mathbf{g} dV \end{aligned} \quad (2.14)$$

Recall that the transport theorem changes our

perspective from a material body (whose boundary distorts so as to always contain the same fluid points) to that of a control volume (whose surface can deform arbitrarily in time). Note that this process leads to a convection term, which in this case is the convection of momentum through the boundaries of the arbitrary volume (the surface integral on the left-hand side of (2.14)). Thus, we see that convective transport of momentum is an artifact of changing from a balance of forces on a material body, to a balance of forces on an arbitrary region of space.

The next step is to apply the divergence theorem (2.4) to the two surface integrals in (2.14) to convert them to volume integrals (the divergence theorem is valid for vectors and tensors alike) and to rewrite (2.14) under a single volume integral:

$$\int_{V(t)} \left[\frac{\partial \rho \mathbf{U}}{\partial t} + \nabla \cdot \rho \mathbf{U} \mathbf{U} - \nabla \cdot \mathbf{T} - \rho \mathbf{g} \right] dV = 0 \quad (2.15)$$

Then, as in conservation of mass, it is argued that the choice of $V(t)$ within the fluid is arbitrary, and all such bodies satisfy (2.15). Consequently, the integrand of (2.15) is identically zero:

$$\frac{\partial \rho \mathbf{U}}{\partial t} + \nabla \cdot \rho \mathbf{U} \mathbf{U} = \nabla \cdot \mathbf{T} + \rho \mathbf{g} \quad (2.16)$$

A more widely used local form of conservation of linear momentum can be obtained by employing the vector identity $\nabla \cdot \rho \mathbf{U} \mathbf{U} = \rho \mathbf{U} \cdot \nabla \mathbf{U} + \mathbf{U} \nabla \cdot \rho \mathbf{U}$ to the left-hand side of (2.16), and simplifying the result by invoking conservation of mass (2.6):

$$\rho \frac{D \mathbf{U}}{Dt} = \nabla \cdot \mathbf{T} + \rho \mathbf{g} \quad (2.17a)$$

where the operator D/Dt , commonly referred to as the substantial derivative, is defined as

$$\frac{D}{Dt} = \frac{\partial}{\partial t} + \mathbf{U} \cdot \nabla \quad (2.17b)$$

At this point, it is important to note that the physical meaning of the differential terms in

(2.17a) may be deduced by relating them to the corresponding integral terms in (2.13a). In particular, recall that the integral term on the left-hand side of (2.13a) gives the rate of change of momentum in the body. Thus, the left-hand side of (2.17a) represents the time rate of change of momentum of a fluid point, i.e. mass times the acceleration, where we identify the total derivative in (2.17a) as the acceleration of a fluid point as its trajectory is followed through space. The correspondence between the integral and differential terms containing the stress tensor indicates that forces exerted on the surface of a material body as it moves through space are translated into local variations in the internal stress of that body. Furthermore, according to the differential and integral balances, these stresses can give rise to a localized fluid motion inside the material body. The gravity term on the right-hand side of (2.17a), which incorporates the local influence of the gravity body force exerted on a material body, provides an additional source of fluid motion as well.

In order to use the differential or integral forms of conservation of linear momentum, it is necessary to relate the stress tensor \mathbf{T} to the type of fluid and its motion. Such a relationship is called a constitutive relation. Generally speaking, these relations are determined experimentally. Any constitutive relation can be postulated; however, the justification for such a postulate ultimately lies in the agreement between the resulting theoretical predictions and the experimental observations for the particular fluid. It turns out that in all constitutive relations relevant to coating flows the surface forces are a sum of pressure forces and viscous forces. For a positive pressure, the pressure force on a differential element acts inward and normal to the element. Thus, all stress tensors can be written as

$$\mathbf{T} = -P\mathbf{I} + \boldsymbol{\tau} \quad (2.18)$$

where \mathbf{I} and $\boldsymbol{\tau}$ are the identity and viscous stress tensors, respectively. As a consequence, efforts to identify constitutive relations are focused on determining the appropriate form of the viscous stress. Substituting (2.18) into (2.17) yields the

final local form of conservation of linear momentum:

$$\rho \left[\frac{\partial \mathbf{U}}{\partial t} + \mathbf{U} \cdot \nabla \mathbf{U} \right] = -\nabla P + \nabla \cdot \boldsymbol{\tau} + \rho \mathbf{g} \quad (2.19)$$

One commonly used constitutive relation, which is often used in the examination of coating flows, is that of a Newtonian fluid of constant viscosity, μ :

$$\boldsymbol{\tau} = -\frac{2}{3}\mu(\nabla \cdot \mathbf{U})\mathbf{I} + \mu[\nabla \mathbf{U} + (\nabla \mathbf{U})^T] \quad (2.20a)$$

where the superscript ‘T’ denotes the transpose of the quantity in parentheses. Because, as stated previously, coating operations typically involve liquids whose densities are constant, equation (2.7) is valid, and thus (2.20a) becomes

$$\boldsymbol{\tau} = \mu[\nabla \mathbf{U} + (\nabla \mathbf{U})^T] \quad (2.20b)$$

The quantity in brackets is the rate of strain tensor; thus, (2.20b) states that the local viscous stress on a fluid point is proportional to the local rate of strain. Substituting this relationship into (2.19) yields the well-known Navier–Stokes equation (which is valid for a fluid of constant density and viscosity from the above assumptions):

$$\rho \left[\frac{\partial \mathbf{U}}{\partial t} + \mathbf{U} \cdot \nabla \mathbf{U} \right] = -\nabla P + \mu \nabla^2 \mathbf{U} + \rho \mathbf{g} \quad (2.21)$$

There are other important constitutive relationships which are relevant to coating flows, although they typically are more complicated than (2.20). For example, fluids may exhibit shear-thinning behavior in one or more parts of a coating process; for such cases the general form given by (2.20) is valid, although the viscosity itself is dependent on the magnitude of the local rate of strain. Different constitutive equations may also be necessary when fluid elements exhibit viscoelastic behavior as fluid elements are stretched in a coating process. These cases are considered in more detail in Chapter 5. Note that the conservation equation (2.19) is valid for any of these cases, once the appropriate form of $\boldsymbol{\tau}$ is utilized.

2.3.1.3 Various limiting cases of governing equations

The differential equations derived above, namely conservation of mass and momentum, describe the motion of each individual fluid phase found in a coating process. The basic forces which can affect fluid flow in a given fluid phase are embedded in the conservation of momentum equation (2.19); that is, surface forces due to pressure and viscous stresses, and body forces due to gravity, where the net sum of these forces determines the inertia of a material body of fluid. There are often portions of a coating flow field in which one or more of these forces dominates over others; in other parts of the same flow field, these same forces may become negligible compared with those previously neglected. It is thus often possible to consider the flow field found in a complex coating process as a combination of simpler, less complex flow fields having different balances of these forces. Such an approach is useful because it allows for a coating flow field to be understood and examined as a series of component parts, for which the physics is more clear; this can endow the practicing coating engineer with intuition needed to modify coating processes to achieve a desired result. Furthermore, from a mathematical point of view, numerical techniques are often necessary to solve (2.7) and (2.19) with the appropriate boundary conditions (which have yet to be described). Numerical solutions are often quite time consuming to obtain owing to the nonlinear terms found in (2.19), the interdependence of the velocity components through mass conservation (2.7), and the complex flow geometries often encountered in a coating process. By identifying regions of the flow in which certain forces dominate, small terms in (2.19) can be neglected, and less-intensive numerical calculations can be used to solve the approximate equations; in some cases, these equations are simple enough that analytic solutions can be obtained. We note here that approximations must be made to both governing equations and boundary conditions in a self-consistent manner; in what follows, we only consider some different

flow regimes associated with the governing equations (2.7) and (2.19); the presentation of boundary conditions, as well as their simplifications in various limits are left until Sections 2.3.2 and 2.4, respectively (for a more comprehensive examination of various flow regimes, see Schlichting 1979).

To motivate our discussion, consider the simplified coating process shown in Fig. 2.3. Here, a large fluid reservoir is connected to a coating die (hopper) through a pipe of diameter D as shown. The fluid reservoir is open to the atmosphere having pressure P_A , and the fluid level in the reservoir is maintained at a height H . The hopper itself is shown in cross-section, and has a width W which is oriented into Fig. 2.3. Fluid enters the cavity of the coating hopper through the inlet, is distributed widthwise in the cavity, flows through the slot, and forms a two-dimensional liquid sheet (henceforth called a curtain), also of width W , which is subsequently coated on a substrate moving at speed U . We assume that the fluid being delivered is Newtonian, and so we utilize the Navier–Stokes equation (2.21) instead of (2.19), although the general arguments can be used when other constitutive relations are employed. We furthermore will assume that the flow is at a steady state, i.e., there is no time dependence in (2.21).

Let us begin by considering the flow in the reservoir itself. As indicated in Fig. 2.3, the constant height of the fluid in the reservoir, as well as the reservoir width, are extremely large compared with the radius of the pipe connected to the reservoir. Thus, there is almost no apparent fluid motion in the reservoir, except in the vicinity of the pipe. Under such conditions, we can expect that the flow terms in (2.21) are small compared with those due to pressure and gravity, and thus the equation governing the flow in the reservoir simplifies to

$$\nabla P = \rho g \quad (2.22a)$$

This equation can be integrated directly to obtain the pressure field in the reservoir:

$$P = P_A + \rho g X \quad (2.22b)$$

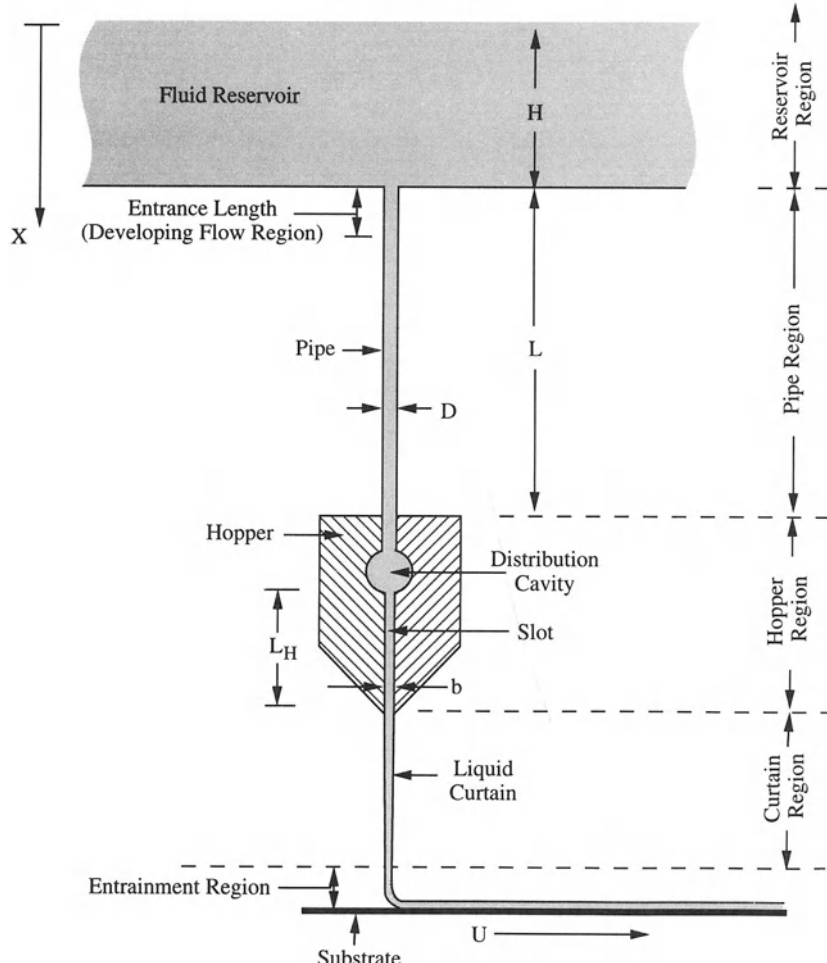
Atmosphere P_A 

Figure 2.3 The simplified coating process used to motivate the discussion of various limiting forms of the governing equations.

where X represents the vertical distance below the liquid surface (as shown in Fig. 2.3). In obtaining (2.22b), the relation $\mathbf{g} = g\hat{\mathbf{i}}$ has been employed, where g is the magnitude of the gravity vector, $\hat{\mathbf{i}}$ is the unit vector in the X -direction, and $X = 0$ is the location of the air–fluid interface. Equation (2.22b) is the well-known expression for the hydrostatic pressure in a fluid, which arises due to its weight.

In the pipe region of Fig. 2.3, there are a few

aspects of the flow to be considered. To begin, we recall that the flow of a Newtonian fluid in a straight pipe can be described by the well-known Poiseuille relation between volumetric flow rate, Q , and pressure drop across the pipe, ΔP , which is given by

$$Q = \frac{\pi R^4 (\Delta P + \rho g L)}{8 \mu L} \quad (2.23)$$

where L is the axial pipe length, and $R = D/2$ is

the pipe radius. Such a flow is characterized by a precise balance between the pressure, viscous and gravity terms in (2.21); the absence of density in (2.23), except in the hydrostatic pressure term, indicates that fluid inertia does not influence the flow. The Poiseuille relation provides a valid description of the flow field only if the fluid flow is laminar, i.e., the flow proceeds in an orderly fashion, in which fluid elements proceed along parallel streamlines. This is the case when the pipe Reynolds number, Re , is less than a minimum critical value:

$$Re = \frac{\rho V D}{\mu} < 2300 \quad (2.24)$$

where V is the average of the fluid velocity in the pipe and D is the inner diameter of the pipe. For flows which violate this criteria, small disturbances which naturally arise in a process (such as vibrations) can induce instabilities in the laminar flow; these instabilities grow, and the orderly streamline pattern of laminar flow is lost. In its place, a time-fluctuating turbulent flow arises. We note here that the time-dependent nature of turbulence often precludes the use of extremely high Reynolds number flows in a coating process. For example, if the turbulence occurs in a region of the coating process which is near the location where fluid layers are deposited on the substrate, the time-dependent flow can induce undesirable thickness variations in the coated fluid layers.

Another important assumption in using the Poiseuille relation (2.23) is that the pipe is long enough for the laminar flow to arrange itself into a fully developed configuration; when fully developed, the flow is in the X -direction only and the velocity field is independent of axial distance X from the reservoir. Near the inlet to the pipe in Fig. 2.3, of course, there is some axial distance, called the entrance length, over which the flow adjusts to the influence of the pipe walls as it enters the pipe from the reservoir. Here, the fluid velocity profile does indeed change with axial location, and the flow is termed a developing flow. Because of this flow rearrangement, the

relationship between the pressure gradient and the volumetric flow rate is different from that predicted by the Poiseuille relation (2.23). We note here that developing flows will arise in any portion of a flow process in which the geometry suddenly changes; in the current example, they arise in the vicinity of the junction between every region in Fig. 2.3.

Let us now consider the forces at play in the specific developing flow region associated with the flow into the pipe from the reservoir. An expanded view of this region is shown in Fig. 2.4a. In this region, the pressure, viscous and gravity forces must be important, since we know that the developing flow field must ultimately approach the limit of fully developed Poiseuille flow at the end of the developing region, in which these forces precisely balance. However, in the entrance region to the pipe, fluid streamlines are converging and the flow is not unidirectional; that is, there is both an axial and a radial component of fluid velocity, denoted by U_x and U_r , respectively. The interrelationship between these components is given by the continuity equation (2.7) expressed in cylindrical coordinates

$$\frac{1}{r} \frac{\partial}{\partial r} (r U_r) = - \frac{\partial U_x}{\partial X} \quad (2.25)$$

where r is the radial location in the pipe. Equation (2.25) shows that the presence of a radial component of velocity causes the velocity in the axial direction, U_x , to vary with axial location X ; that is, the fluid will accelerate or decelerate. Thus the inertial terms in (2.21), which quantify the acceleration of fluid points (see discussion following (2.17)), may be important in the developing flow region. Downstream, where the radial component of velocity U_r approaches zero and the flow becomes fully developed, equation (2.25) indicates that U_x is independent of axial location X ; this indicates that the flow is no longer accelerating, and inertial terms in (2.21) disappear.

The relative importance of the viscous and inertial terms in the developing flow region can be inferred from a simple dimensional analysis

28 Capillary hydrodynamics and interfacial phenomena

of the viscous and inertia terms in (2.21). To this end, we scale $\mathbf{U} \sim V$, $\nabla \sim 1/D$ and thus obtain

$$Re \sim \frac{\rho \mathbf{U} \cdot \nabla \mathbf{U}}{\mu V^2 \mathbf{U}} \quad (2.26)$$

where Re is the Reynolds number given by (2.24). Thus, for small Reynolds numbers, fluid inertia is negligible compared with viscous forces; for large Reynolds numbers, the opposite is true. When Re is small, an approximate form of (2.21) can be used to analyze the developing flow, in which the inertial terms of (2.21) are neglected:

$$\nabla P = \mu V^2 \mathbf{U} + \rho \mathbf{g} \quad (2.27)$$

Flow fields satisfying (2.27) are termed creeping flows. For a creeping flow, the length of the developing flow region is relatively small, being on the order of a few pipe diameters.

On the other hand, for high Reynolds numbers,

this entrance length and the associated flow can be greatly influenced by fluid inertia. Under such circumstances thin boundary layers form along the walls of the pipe, in which the viscous drag of the walls affects the flow (Fig. 2.4a). In these regions, all of the forces represented in (2.21) are important, although the velocity gradients in the radial direction dominate the magnitude of the viscous terms. In the interior of the pipe away from the influence of these boundary layers, viscous effects are negligible, and thus the governing equation (2.21) becomes

$$\rho \mathbf{U} \cdot \nabla \mathbf{U} = -\nabla P + \rho \mathbf{g} \quad (2.28)$$

Equation (2.28) is called Euler's equation, which governs the flow of fluids considered to be inviscid. It is not until the influence of the viscous forces actually reach the center of the pipe, i.e. the boundary layer thickness is on the order of

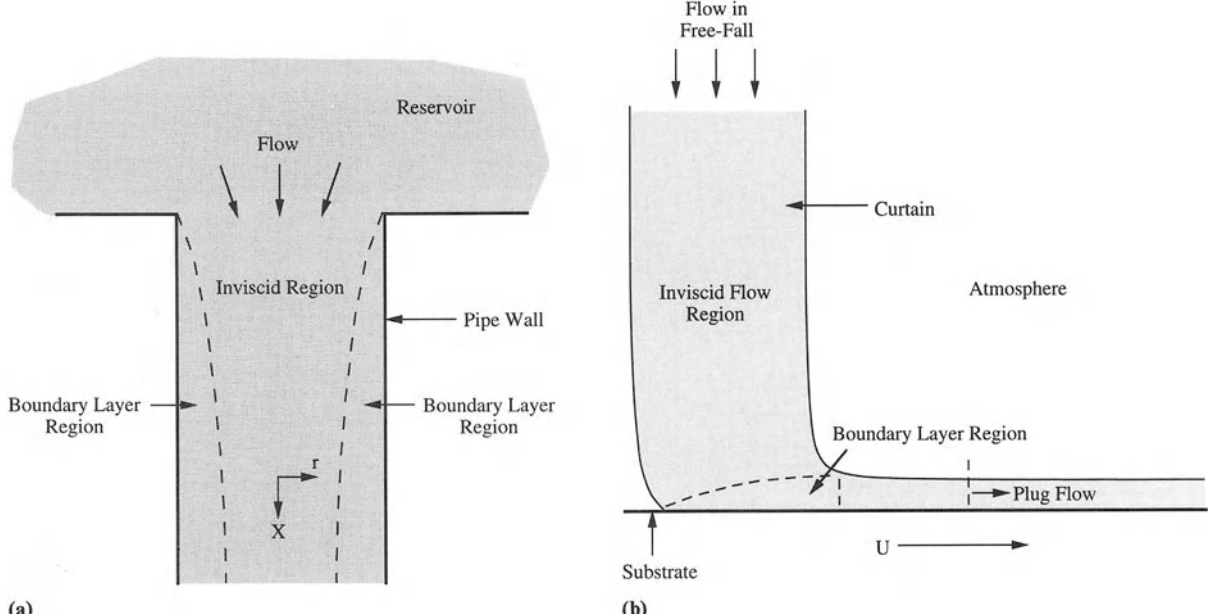


Figure 2.4 Details of the coating process illustrated in Fig. 2.3: (a) the developing flow region found as fluid moves from the reservoir into the pipe under conditions of high Reynolds number, where thin boundary layers form along the pipe walls; (b) the entrainment region near the moving substrate, under conditions of relatively high substrate speed relative to the impingement speed of the curtain.

the pipe radius and the inviscid region disappears, that the flow can rearrange and become fully developed. Because the boundary layers are initially quite thin, the distance it can take for the flow to become fully developed can be significantly larger than for the creeping flow case.

We now consider some important simplifications to Euler's equation which are relevant to the developing flow. If we choose the perspective of moving along a fluid streamline, which by definition is everywhere tangent to the velocity vector, then Euler's equation can be integrated along that given streamline in the inviscid region to obtain Bernoulli's equation:

$$\frac{V^2}{2} + \frac{P}{\rho} - gX = K \quad (2.29)$$

where V is the magnitude of the velocity vector \mathbf{U} , and K is a constant. In general, the constant in (2.29) varies with position in the fluid, depending only on the particular streamline. For the current problem, however, we note that in the reservoir itself the hydrostatic equation (2.22) is identical in form to (2.29) when V is small; as the inviscid region in the pipe does link directly with the flow in the pressure reservoir, we deduce that the constant in Bernoulli's equation is precisely the atmospheric pressure P_A for all locations in the central inviscid region of the pipe.

When the Bernoulli constant K does not vary from streamline to streamline in the fluid, as in the current case, the flow itself is irrotational, i.e., it satisfies

$$\nabla \times \mathbf{U} = 0 \quad (2.30a)$$

which implies the existence of a scalar velocity potential ϕ as

$$\mathbf{U} = \nabla \phi \quad (2.30b)$$

Combining this equation with conservation of mass (2.7), it is seen that the velocity potential satisfies Laplace's equation, i.e.

$$\nabla^2 \phi = 0 \quad (2.30c)$$

Flows satisfying (2.30) are termed potential flows.

Note that once the velocity potential is determined by solving to (2.30c), the pressure in the flow can be extracted directly using (2.29); this pressure provides a driving force for the flow in the viscous boundary layers near the pipe walls at high Reynolds numbers.

Returning to Fig. 2.3, after flowing through the pipe region, the fluid enters the hopper region. In the hopper itself, the role of the cavity is to distribute fluid uniformly widthwise (i.e., into Fig. 2.3) so that the local volumetric flow rate does not vary across the hopper; this is because flow non-uniformities ultimately can lead to undesirable thickness variations in fluid layers on a substrate after coating. To accomplish this, a hopper is typically designed such that the resistance to flow in the slot is much higher than that in the cavity itself so that any lateral pressure variations incurred as the flow distributes widthwise in the cavity will be a negligible percentage of the mean pressure in the cavity. Thus, a hopper typically has a cavity of large cross-sectional area, a small slot height, b , and a large slot length, L_H . Furthermore, the width of the hopper, W , which determines the ultimate coated width of the fluid on the substrate, is typically on the order of L_H or larger. In the ideal case where the cavity pressure is constant, a constant pressure drop ΔP is applied across the slot in the flow direction, as the hopper is opened to the atmosphere. For such a flow, the volumetric flow rate, Q , is related to the constant pressure drop as

$$Q = \frac{b^3 \Delta P W}{12\mu L_H} \quad (2.31)$$

We note here that this expression is the planar analogue of the fully-developed Poiseuille relation, which gives a balance between viscous, pressure and gravitational forces. As b is very small, the pressures generated inside the hopper can be quite large for moderate flows.

We acknowledge here that the flow in the hopper is almost never perfectly uniform, owing in part to the fact that there is always a pressure variation in the hopper cavity as the fluid is

distributed widthwise*. When this occurs, there is a widthwise component of velocity which is imparted to the fluid in the slot, and the flow is no longer unidirectional in the X -direction, as described by (2.31). As discussed previously, once a flow is no longer unidirectional, the prospect arises for inertial effects to become important in the flow field. We now deduce the magnitude of inertial effects in the slot. It is intuitive that velocity gradients across the narrow gap will be much larger than those in the flow direction itself, owing to the viscous drag of the walls. In fact, for a characteristic slot flow velocity V , the viscous terms in (2.21) will have magnitude $\mu V/b^2$, where b is the slot height, while the inertial terms will have magnitude $\rho V^2/L_H$, where L_H is the slot length. Consequently, the Reynolds number characterizing such a flow, as defined by (2.26) is given by

$$Re = \frac{\rho V b^2}{L_H \mu} \quad (2.32)$$

Based on the previously described slot geometry, the Reynolds number given by (2.32) will be small in a typical hopper, indicating that inertial effects are negligible in the slot. Thus the flow in the slot is governed most generally by the creeping flow equations, given by (2.27), although these equations can be simplified further by noting that viscous terms in (2.27) are dominated by the velocity gradients across the gap. Note that a detailed discussion of the design of coating hoppers is considered in Chapter 10.

Before leaving our discussion of the hopper slot, we consider the complications to the flow which can arise when the hopper slot height, b , varies from position to position. Such a variation might occur due to the internal pressure loading on the hopper itself, causing a distortion in the slot cross-section, or due to errors in the fabrication

* Although the internal hopper geometry can be adjusted to counteract these pressure variations, such adjustments can only assure uniformity for one particular flow rate and fluid type. A single hopper may be called on to deliver many different fluids and/or flows; the effect of pressure variations corresponding to these different conditions cannot be cancelled by the same hopper geometry.

and assembly of the hopper. When the slope of the opposing surfaces of the slot is small (e.g., b varies slowly with X), the flow field in the hopper can again be described by the creeping flow equations (2.27), with the simplification that the viscous terms are dominated by the velocity gradients across the gap. Furthermore, the flow profile across the gap itself looks identical to that in a slot of constant height, except that the location of the slot walls is adjusted locally. This local variation in wall location yields a modification to the pressure gradients in the slot as well. These flow characteristics are predicted by utilizing the hydrodynamic theory of lubrication, which is examined extensively in Chapter 8. We comment here that, more generally, this theory is widely used to analyze various coating flows with fluid–fluid interfaces, which typically have small characteristic aspect ratios similar to those for the slot described above, and for which the slope of the fluid streamlines is small.

After emanating from the hopper, the fluid enters the curtain region, in which a liquid curtain of width W (extending into Fig. 2.3) is formed. In this region, the viscous drag of the air on the fluid is negligible under typical conditions, and thus there is no mechanism by which velocity gradients perpendicular to the streamwise flow can be maintained. As is typical of all transitions in flow geometry, the fluid flow issuing from the hopper must adjust to this new environment, with its absence of viscous drag at the boundaries. Consequently, there is an entrance length equal to several times the hopper slot height b over which the flow rearranges itself from the parabolic, Poiseuille flow in the hopper slot to the fully-developed, flat velocity profile (no velocity gradients) in the curtain. This flat velocity profile is termed plug flow.

Because the fully developed curtain flow is plug at all streamwise locations, the flow field in the curtain region of Fig. 2.3 is effectively inviscid and is governed by Euler's equation (2.28), as well as Bernoulli's equation (2.29) along each streamline. Let us reposition the coordinate system from the reservoir region (as shown in Fig. 2.3) into the curtain region, such that $X = 0$

is located at the position below the hopper where the curtain flow first achieves plug flow. If we denote the curtain speed there as V_0 , then the Bernoulli constant in (2.29) will be

$$K = \frac{V_0^2}{2} + \frac{P_A}{\rho} \quad (2.33a)$$

which is the same for all streamlines at $X = 0$, and hence, throughout the whole curtain. We also note that the pressure experienced by the fluid in the curtain is essentially atmospheric across the thickness of the curtain; i.e., $P = P_A$ everywhere. Substituting this into Bernoulli's equation (2.29) and utilizing the Bernoulli constant (2.33a) results in the following relationship for the velocity in the curtain:

$$V^2 = V_0^2 + 2gX \quad (2.33b)$$

Flows which satisfy (2.33b) are said to be in free-fall.

The curtain itself ultimately impinges on the moving substrate in the entrainment region, as shown in Fig. 2.3. Under conditions where the substrate speed, U , is significantly greater than the impingement speed of the curtain, the viscous effects of the substrate motion are confined to a boundary layer in the vicinity of the web, as shown in Fig. 2.4b. Outside of this boundary layer, the fluid flow is inviscid and smoothly links with the free-fall flow valid in the curtain region above the web. We have already discussed the features of boundary layer flows and inviscid flows in the context of the developing flow in the pipe, and the basic physics is essentially the same in this impingement region. Eventually, all the fluid flow in the curtain is entrained in the boundary layer (i.e., the inviscid region disappears), and ultimately, downstream on the web, all of the fluid moves at precisely the web speed U . This ultimate plug flow profile arises due to the lack of viscous drag of the air on the fluid.

The above example indicates how the importance of various terms of the complete governing equation (2.21) can change throughout a coating process, and how markedly different flows can arise when different terms dominate. The import-

ance of various terms can often be identified by utilizing a dimensional analysis, such as that used in obtaining estimates for the Reynolds number in (2.26) and (2.32) in the above discussion, and assessing the magnitude of the resulting dimensionless groups. Such an approach is also utilized in Section 2.4, where we examine various limiting cases of the boundary conditions at fluid–fluid interfaces and their potential impact on coating flows. A formal framework for approximating dimensionless equations in various limits is afforded by the powerful technique of asymptotics, which is discussed extensively in Chapter 8.

2.3.2 BOUNDARY CONDITIONS

In the previous discussion, we described how a flow field can change depending upon the relative importance of various terms in the mass and momentum conservation equations. In that discussion, we determined the magnitude of these terms by using arguments which implicitly depended upon the interaction of the fluid flow with the solid walls and air which bounded the flow domain. This underscores the physical importance that the boundaries of a flow domain play on a fluid flow itself. To emphasize this point further, we note that the integral and differential forms of the conservation laws derived thus far are generally applicable to each phase of a single-phase flow. Thus, for the domain shown in Fig. 2.1, conservation of mass and conservation of linear momentum are applied to each layer separately. Clearly then, for the case in which two distinct fluid phases come in contact, the unique character of the resulting fluid flow is determined by the conditions applied along the fluid–fluid interface, such as shown in Fig. 2.1. The physical information introduced via the boundaries fulfills a mathematical requirement that boundary conditions are necessary to uniquely solve the governing differential equations of fluid mechanics. In what follows, we consider the various boundary conditions which are generally applicable to both single-phase and multi-phase coating flows.

2.3.2.1 The kinematic boundary condition: conservation of mass across the boundaries of the flow domain

The kinematic boundary condition provides a constraint on a fluid flow such that conservation of mass is satisfied across the boundaries of the flow domain. The general condition is obtained in a manner that resembles our derivation of the continuity equation (2.6). In particular, we start by focusing our attention on an arbitrary deformable material body $V(t)$ as it moves in space. However, in contrast to the previous approach to the conservation laws, the body is now positioned such that it straddles the interface between two fluids, as shown in Fig. 2.5 (Slattery 1967).

Because $V(t)$ is a material body, its mass, M , is independent of time, and thus the mass conservation condition (2.1) is necessarily satisfied. Unfortunately, because the density is discontinuous in $V(t)$, we cannot use the Reynolds transport theorem (2.2) to adapt this equation to the perspective of an arbitrary control volume. Instead, we must rewrite (2.1) as the sum of three integrals: one for phase 1, one for phase 2, and one for the interface itself:

$$\frac{d}{dt} \int_{V(t)} \rho dV = \frac{d}{dt} \int_{V_1(t)} \rho_1 dV + \frac{d}{dt} \int_{V_2(t)} \rho_2 dV + \frac{d}{dt} \int_{A(t)} \Gamma dS = 0 \quad (2.34)$$

where $V_1(t)$ and $V_2(t)$ are the volumes occupied by phases 1 and 2 within the material body at time t , $A(t)$ is the interfacial area in $V(t)$, and Γ represents any excess mass per unit area associated with the interface itself. Although $V(t)$ is a material body, $V_1(t)$ and $V_2(t)$ are not, because generally speaking mass can transfer across the interface (e.g., the case of solvent evaporation from the coating during flow). For such arbitrary volumes, the time derivatives in (2.34) can be brought inside each integral with the help of the general transport theorem (Whitaker 1968), which is written for the density of each phase as

$$\frac{d}{dt} \int_{V_j(t)} \rho_j dV = \int_{V_j(t)} \frac{\partial \rho_j}{\partial t} dV + \int_{S_j(t)} \rho_j \mathbf{w}_j \cdot \mathbf{n} dS \quad (2.35)$$

where for the current problem $j = 1$ or 2 , and \mathbf{w}_i

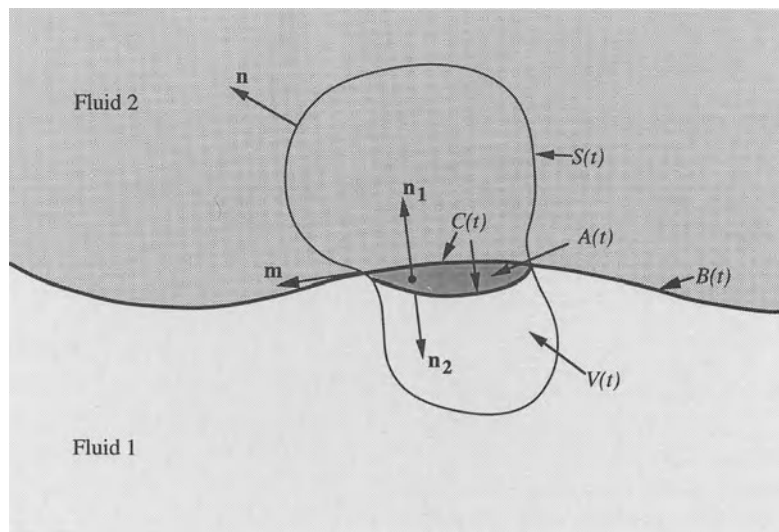


Figure 2.5 Arbitrary material body straddling an interface $B(t)$ that separates two fluid phases.

is the velocity of the surfaces $S_j(t)$, which bounds $V_j(t)$, as it deforms in time. In addition, \mathbf{n} is the unit outward normal to the surface $S_j(t)$. A comparison of (2.35) with (2.2) reveals that the Reynolds transport theorem is a special case of the general transport theorem; the Reynolds transport theorem applies to a material body whose surface, by definition, moves with the local velocity of the fluid (i.e., $\mathbf{w}_j = \mathbf{U}_j$) so that the body itself always consists of the same fluid points, while the general transport theorem applies to a body whose boundary motion is, in general, different from that of the local fluid velocity.

Employing (2.35) in the integrals in (2.34), we obtain

$$\int_{V_1(t)} \frac{\partial \rho_1}{\partial t} dV + \int_{S_1(t)} \rho_1 \mathbf{w}_1 \cdot \mathbf{n} dS + \int_{V_2(t)} \frac{\partial \rho_2}{\partial t} dV + \int_{S_2(t)} \rho_2 \mathbf{w}_2 \cdot \mathbf{n} dS = 0 \quad (2.36)$$

where we have neglected the mass of the interface, as it is small relative to the terms shown in (2.36). Note that $S_1(t)$ can be represented as the sum of the surface area of $V(t)$ that resides in phase 1, denoted as $A_1(t)$, plus the interfacial area, $A(t)$, separating the two phases in the material body. Similarly, $S_2(t)$ equals $A_2(t)$ plus $A(t)$, where $A_2(t)$ is that portion of the surface of the body residing in phase 2. Using this definition, we note that along the surfaces $A_1(t)$ and $A_2(t)$, the boundary velocity is equal to the local fluid velocity, i.e. $\mathbf{w}_j = \mathbf{U}_j$ in each phase; this is because, taken together, these surfaces comprise the outer boundary of the material body across which no fluid points can move (Fig. 2.5). On the other hand, the interface $A(t)$ is not in general a material boundary (i.e., fluid may pass across it). Thus, the local fluid velocity at the interface may be different from the rate of displacement of the interface itself. For this reason, we designate the rate of displacement of the interface as \mathbf{U}_σ to distinguish it from the local fluid velocity at the interface, \mathbf{U}_j . Consequently, $\mathbf{w}_1 = \mathbf{w}_2 = \mathbf{U}_\sigma$ along $A(t)$. The rate of displacement of the interface is

defined in the direction normal to the surface; thus $\mathbf{U}_\sigma = U_\sigma \mathbf{n}$ where U_σ is the magnitude of the vector \mathbf{U}_σ . Using these facts, we can separate each surface integral in (2.36) into two parts, to obtain the following result:

$$\begin{aligned} & \int_{V_1(t)} \frac{\partial \rho_1}{\partial t} dV + \int_{A_1(t)} \rho_1 \mathbf{U}_1 \cdot \mathbf{n} dS + \int_{A(t)} \rho_1 \mathbf{U}_\sigma \cdot \mathbf{n}_1 dS \\ & + \int_{V_2(t)} \frac{\partial \rho_2}{\partial t} dV + \int_{A_2(t)} \rho_2 \mathbf{U}_2 \cdot \mathbf{n} dS \\ & + \int_{A(t)} \rho_2 \mathbf{U}_\sigma \cdot \mathbf{n}_2 dS = 0 \end{aligned} \quad (2.37)$$

where \mathbf{n} is the outward unit normal to the surface of the material body $S(t)$, and \mathbf{n}_1 and \mathbf{n}_2 are the unit normals to the interface $A(t)$ pointing into phases 2 and 1, respectively, where $\mathbf{n}_1 = -\mathbf{n}_2$ (as indicated in Fig. 2.5).

To reduce equation (2.37) to its local, differential form, the volume integrals are rewritten by employing the continuity equation (2.6) and the divergence theorem (2.4) to obtain

$$\begin{aligned} \int_{V_1(t)} \frac{\partial \rho_1}{\partial t} dV &= - \int_{V_1(t)} \nabla \cdot \rho_1 \mathbf{U}_1 dV \\ &= - \int_{A_1(t)} \rho_1 \mathbf{U}_1 \cdot \mathbf{n} dS - \int_{A(t)} \rho_1 \mathbf{U}_1 \cdot \mathbf{n}_1 dS \end{aligned} \quad (2.38a)$$

$$\begin{aligned} \int_{V_2(t)} \frac{\partial \rho_2}{\partial t} dV &= - \int_{V_2(t)} \nabla \cdot \rho_2 \mathbf{U}_2 dV \\ &= - \int_{A_2(t)} \rho_2 \mathbf{U}_2 \cdot \mathbf{n} dS - \int_{A(t)} \rho_2 \mathbf{U}_2 \cdot \mathbf{n}_2 dS \end{aligned} \quad (2.38b)$$

If we now combine (2.38) with (2.37) and rearrange, the following equation is obtained:

$$\begin{aligned} & \int_{A(t)} \{ \rho_1 (\mathbf{U}_1 - \mathbf{U}_\sigma) \cdot \mathbf{n}_1 \\ & + \rho_2 (\mathbf{U}_2 - \mathbf{U}_\sigma) \cdot \mathbf{n}_2 \} dS = 0 \end{aligned} \quad (2.39)$$

Because the above equation must hold for arbitrary

34 Capillary hydrodynamics and interfacial phenomena

choices of the material volume, it follows that the integrand must be identically zero:

$$\rho_1(\mathbf{U}_1 - \mathbf{U}_\sigma) \cdot \mathbf{n}_1 - \rho_2(\mathbf{U}_2 - \mathbf{U}_\sigma) \cdot \mathbf{n}_1 = 0 \quad \text{at the interface.} \quad (2.40)$$

where in writing (2.40), we have explicitly used the fact that $\mathbf{n}_1 = -\mathbf{n}_2$ along $A(t)$.

Equation (2.40) is the general form of the kinematic boundary condition (also called the jump mass balance), and it applies at both permeable and impermeable boundaries. If, for example, phase 1 is an impenetrable solid, its normal component of velocity, $\mathbf{U}_1 \cdot \mathbf{n}_1$, will be identical to the normal component of the rate of displacement of the surface, $\mathbf{U}_\sigma \cdot \mathbf{n}_1 = U_\sigma$. Thus, (2.40) simplifies to the intuitively pleasing result that

$$\mathbf{U}_2 \cdot \mathbf{n}_1 = U_\sigma \quad \text{at the surface,} \quad (2.41a)$$

meaning that the fluid velocity normal to the solid surface is the same as the rate of displacement of the solid surface itself. If, on the other hand, phase 1 is also a fluid, so that the solid boundary is replaced with a fluid–fluid interface across which there is no mass transfer, then (2.40) indicates that phase 1 satisfies

$$\mathbf{U}_1 \cdot \mathbf{n}_1 = U_\sigma \quad \text{at the interface,} \quad (2.41b)$$

while for phase 2, equation (2.41a) is still valid.

Let us now consider the application of (2.41) to an impermeable fluid–fluid interface with a shape as shown in Fig. 2.1. Here, the thickness of fluid 1 is parameterized as $Y = H(X, Z, t)$, where X is the horizontal coordinate measured in the flow direction, Y is the vertical coordinate measured upwards from the bottom wall, and the Z direction is oriented out of Fig. 2.1. From vector calculus, we know that the normal vector to the surface is determined by the relation $\mathbf{n}_1 = \nabla B / |\nabla B|$, where the vertical bars denote the length of the vector, and $B = Y - H(X, Z, t) = 0$. Thus,

$$\mathbf{n}_1 = \frac{\nabla B}{|\nabla B|} = \frac{\hat{\mathbf{j}} - \frac{\partial H}{\partial X}\hat{\mathbf{i}} - \frac{\partial H}{\partial Z}\hat{\mathbf{k}}}{\left[1 + \left(\frac{\partial H}{\partial X}\right)^2 + \left(\frac{\partial H}{\partial Z}\right)^2\right]^{1/2}} \quad (2.42)$$

where $\hat{\mathbf{i}}$, $\hat{\mathbf{j}}$, and $\hat{\mathbf{k}}$ are unit vectors in the X , Y , and Z directions, respectively. Also, the magnitude of the rate of displacement of the surface, U_σ , is given by the relationship

$$U_\sigma = -\left\{ \frac{\partial H}{\partial t} \right\} \hat{\mathbf{j}} \cdot \mathbf{n}_1 \equiv \left\{ \frac{\partial B}{\partial t} \right\} \hat{\mathbf{j}} \cdot \mathbf{n}_1 \equiv \frac{\partial B}{|\nabla B|} \quad (2.43)$$

Combining (2.41) with (2.42) and (2.43), we obtain the following general expression for the kinematic condition at a fluid interface with negligible mass transfer:

$$\mathbf{U}_2 \cdot \nabla B = \frac{\partial B}{\partial t} \quad (2.44a)$$

$$\mathbf{U}_1 \cdot \nabla B = \frac{\partial B}{\partial t}. \quad (2.44b)$$

In component form, the kinematic boundary condition (2.44) is thus written as

$$U_Y - U_X \frac{\partial H}{\partial X} - U_Z \frac{\partial H}{\partial Z} = \frac{\partial H}{\partial t} \quad \text{at } X = H(Y, Z, t) \quad (2.45)$$

where U_X , U_Y , and U_Z are the components of \mathbf{U} in the $\hat{\mathbf{i}}$, $\hat{\mathbf{j}}$, and $\hat{\mathbf{k}}$ directions, respectively. In writing (2.45), the subscripts denoting the phase have been neglected, as the result is generally valid for either phase. Equation (2.45) places a restriction on the fluid flow adjacent to a deforming interface, consistent with its impenetrability. Notice that interfacial movement, which superficially appears as a rate of displacement in the $\hat{\mathbf{j}}$ direction, $\partial H / \partial t$, actually resolves itself into a fluid flow that has X , Y and Z components of velocity at the interface. It is only when the fluid interface is horizontal, that the vertical component of fluid velocity equals the rate of vertical displacement of the interface, $\partial H / \partial t$.

Generally speaking, the kinematic boundary condition for an impenetrable surface (2.44) is adequate for describing coating flows, even if interphase mass transfer is taking place, as long as the mass transfer process does not significantly alter the thickness of the coating flow in the region of interest. When the local interphase

mass flux is significant, (2.40) provides a complete description of the interrelationship between the local fluid velocities normal to the interface and the rate of interfacial displacement. In particular, if we consider a flat interface that appears stationary from our frame of reference, U_σ equals zero and (2.40) simplifies to the following result:

$$\rho_2(\mathbf{U}_2 \cdot \mathbf{n}_1) = \rho_1(\mathbf{U}_1 \cdot \mathbf{n}_1) \quad (2.46)$$

which states that the mass flux leaving phase 1 must equal the mass flux entering phase 2.

2.3.2.2 The no-slip condition

Thus far we have discussed a relationship between the normal component of velocity in each phase at an interface, and its relationship to the rate of displacement of the interface itself. There is also a need to constrain the motion of fluid points in each phase along an interface. A widely used assumption in viscous flows is that the tangential component of velocity is continuous across bounding surfaces; this assumption is applied to both solid surfaces and fluids alike. In other words, the tangential component of velocity for phase 1 is assumed to equal the tangential component of velocity of phase 2 on their surface of contact. That is,

$$\mathbf{U}_1 \cdot \mathbf{t} = \mathbf{U}_2 \cdot \mathbf{t} \quad (2.47)$$

where \mathbf{t} is a tangent to the interface. If the bounding surface is a solid, typically the motion of the solid is prescribed as \mathbf{U}_s , and (2.47) is written as:

$$\mathbf{U}_1 \cdot \mathbf{t} = \mathbf{U}_s \cdot \mathbf{t} \quad (2.48)$$

We comment here that this condition yields flow predictions in excellent agreement with experiment for a wide range of physical configurations. There is one notable exception, however, where mathematical analyses of flow which utilize this boundary condition run into difficulties; namely, flow fields involving a moving fluid–fluid interface where the interface makes contact with a solid wall. Even in such cases, however, the no-slip condition can be employed over the bulk of the domain, the mathematical difficulties being

restricted to the region in the close vicinity of the line of contact between the interface and the solid surface. As fluid–fluid interfaces are imbedded in virtually all coating flows, the mathematical difficulties associated with the use of (2.47) are quite relevant. This issue will be discussed in more detail in Chapter 3.

2.3.2.3 Combined application of kinematic and no-slip conditions to an impermeable fluid–fluid interface

The preceding two boundary conditions, in conjunction with the previously derived local conservation equations, are all that is necessary to describe flow of a single fluid phase in contact with a rigid solid boundary. For multiple phase flow, these boundary conditions apply as well. Consider for example the fluid–fluid interface shown in Fig. 2.1. Because the no-slip condition applies at the interface, equation (2.47) holds. Furthermore, the kinematic boundary condition must apply for both fluids at the fluid–fluid interface. In multilayer coating flows, such as that implied by Fig. 2.1, the rate of mass transfer, if any, between the various layers is usually small enough to have a negligible impact on the flow profiles, and thus the kinematic condition for an impermeable surface is given by (2.41). Combining (2.41a and b), we obtain

$$\mathbf{U}_2 \cdot \mathbf{n} = \mathbf{U}_1 \cdot \mathbf{n} \text{ at the interface,} \quad (2.49)$$

where we have removed the subscript on the normal vector written in (2.41); it is understood here that \mathbf{n} is a unit normal to the surface. The conditions (2.47) and (2.49) together imply that

$$\mathbf{U}_1 = \mathbf{U}_2 \text{ at the interface,} \quad (2.50)$$

i.e., the velocity must be continuous across the impermeable interface. Note, however, that (2.50) says nothing about the impenetrability restriction which must arise at the fluid–fluid interface. Thus, the kinematic boundary condition for one of the phases (given by (2.41a) or (2.41b)) must be applied together with (2.50) to provide essential information about the movement of the interface as well as the two bulk phases at the interface.

2.3.2.4 The dynamic boundary condition: the balance of interfacial stresses

Thus far, the boundary conditions discussed have addressed purely kinematic (motion) considerations. The way in which stresses transmit across an interface or, equivalently, the way in which forces balance on an interface needs to be considered as well. In what follows, the balance of forces on a material body containing two distinct fluid phases is considered. The local or differential form of such a force balance yields the desired stress boundary condition at the interface.

The approach taken is identical to that for conservation of linear momentum. External forces are summed on an arbitrary deformable material body as it moves in space. However, because we want to develop a stress balance at an interface, we position our material body such that it straddles the interface between two fluids (see Fig. 2.5 and our derivation of the kinematic boundary condition). Those forces already identified for a material body consisting of a single phase, namely the body force and surface force given by (2.11) and (2.12) respectively, are of identical form for the new material body; similarly, the momentum accumulation term given by (2.9) and (2.10) is of identical form as well. However, because our material body now consists of two separate phases, each with its own distinct physical properties, an evaluation of the applicable integral terms require that each integral be divided into three integrals, one for each phase and one for the interface itself.

If the interface does not exert some sort of force on the material body shown in Fig. 2.5, then the single-phase integral conservation law (2.13) is valid. Indeed, there are a number of physical situations for which this is true, such as in fluid–fluid systems where the same solvent is employed in each phase. More generally, however, flow and interfacial phenomena are observed that can be explained only if the interface is presumed to exert a force on the material body. To account for this force, the balance (2.13) must include an additional term, which acts only along

the line of contact between the interface and the boundary of the material body. Denoting $B(t)$ as the location of the interface, the line of contact is given by the intersection of $B(t)$ with the surface of the material body $S(t)$; this intersection is denoted by $C(t)$ in Fig. 2.5.

The force, \mathbf{F}_σ , that the interface exerts at the line of intersection $C(t)$, can be expressed in terms of the line traction vector, \mathbf{t}_σ , which gives the local force per unit length on a differential line element, dC :

$$\mathbf{F}_\sigma = \int_{C(t)} \mathbf{t}_\sigma dC \quad (2.51)$$

We note here that the expression for the line force \mathbf{F}_σ is entirely analogous to that for the surface force given by (2.12). The total force balance can be written directly, by employing (2.9) and including as an additional term (2.51) in the right-hand side of (2.13):

$$\begin{aligned} \frac{d}{dt} \int_{V(t)} \rho \mathbf{U} dV &= \int_{S(t)} \mathbf{n} \cdot \mathbf{T} dS \\ &+ \int_{V(t)} \rho \mathbf{g} dV + \int_{C(t)} \mathbf{t}_\sigma dC \quad (2.52a) \end{aligned}$$

The equation above is an integral form of conservation of linear momentum for a body consisting of two fluid phases and an interface. A more useful form of this conservation equation can be obtained by explicitly determining the form of the line traction vector. In an analogous way to the surface traction vector defined in (2.13b), it can be shown that there exists an interfacial stress tensor, \mathbf{T}_σ , which when operated on the unit vector, \mathbf{m} , yields the line traction vector as

$$\mathbf{t}_\sigma = \mathbf{m} \cdot \mathbf{T}_\sigma \quad (2.52b)$$

where \mathbf{m} is perpendicular to $C(t)$ and tangent to the interface $B(t)$ (see Fig. 2.5).

The initial motivation for obtaining (2.52) was to derive a boundary condition to apply at the interface when considering the local differential equations governing fluid flow. To this end, we

are led to derive a local form of (2.52), with attention focused on the interface itself. A general expression for the local form of the balance of stresses at the interface can be obtained by following the procedure used in the previous section for the derivation of the kinematic boundary condition; that is, by breaking up the integrals of (2.52) into parts that apply to each of the two phases and the interface, and then using the general transport theorem in conjunction with the momentum equation (2.17) for each phase.

An alternative, intuitive approach is to apply (2.52) to a material body drawn about the interface, whose local thickness is given by Δn , and whose top and bottom surfaces have areas $A_2(t)$ and $A_1(t)$, respectively, as shown in Fig. 2.6. Now, consider the limit as $\Delta n \rightarrow 0$. In such a limit, $A_1(t), A_2(t) \rightarrow A(t)$, where $A(t)$ is the area of the resulting surface, with sides 1 and 2 embedded in the interface $B(t)$. In this limit, the material body has no volume, and thus the volume integral contributions to (2.52) are zero*. Equation (2.52) can be written for a material body by denoting \mathbf{n}_1 and \mathbf{n}_2 as the normal to the interface which points into fluids 2 and 1, respectively (see Fig. 2.6), and noting that $\mathbf{n}_2 = -\mathbf{n}_1$ at each point along $A(t)$. The result is

$$\int_{A(t)} \mathbf{n}_1 \cdot (\mathbf{T}_2 - \mathbf{T}_1) dS + \int_{C(t)} \mathbf{m} \cdot \mathbf{T}_\sigma dC = 0 \quad (2.53)$$

The procedure to obtain the local form of (2.53) is to combine both integrals under a single one. This can be done with the divergence theorem for a surface

$$\int_{C(t)} \mathbf{m} \cdot \mathbf{T}_\sigma dC = \int_{A(t)} \nabla_{II} \cdot \mathbf{T}_\sigma dS$$

* Note that the left-hand side of equation (2.52) is negligible only if either the mass density of the two phases are the same or the rate of mass transfer across the interface is negligible. Otherwise, there will be a finite rate of change in the total linear momentum of the body due to the phase change associated with interphase mass transfer, as the size of one phase in $V(t)$ grows at the expense of the other, even for vanishingly small values of Δn . In ignoring the body force term, we are assuming that the excess mass at the interface associated with the interfacial adsorption of surfactant is insufficient to contribute measurably to the force at the interface.

which yields

$$\int_{A(t)} [\mathbf{n}_1 \cdot (\mathbf{T}_2 - \mathbf{T}_1) + \nabla_{II} \cdot \mathbf{T}_\sigma] dS = 0 \quad (2.54)$$

Here, ∇_{II} is the divergence operator resolved in the tangential plane, which is related to the three-dimensional divergence operator as

$$\nabla_{II} = \nabla - \mathbf{n}_1 (\mathbf{n}_1 \cdot \nabla) \quad (2.55)$$

Then, it is argued that as $A(t)$ is arbitrary, the integrand must be zero such that (2.54) holds for all material bodies that incorporate part of the interface. Consequently,

$$\mathbf{n}_1 \cdot (\mathbf{T}_2 - \mathbf{T}_1) + \nabla_{II} \cdot \mathbf{T}_\sigma = 0 \quad \text{at the interface.} \quad (2.56)$$

The result (2.56) is called the ‘dynamic boundary condition’, so called because its origin lies in a force balance. Basically, it says that if the interface has the ability to exert a force on a material body, which is characterized by a non-zero value of \mathbf{T}_σ , then a jump in stress across the interface arises. On the other hand, if the interface has no force-inducing properties, then $\mathbf{T}_\sigma = 0$ and (2.56) becomes

$$\mathbf{n}_1 \cdot (\mathbf{T}_2 - \mathbf{T}_1) = 0 \quad \text{at the interface,} \quad (2.57)$$

which indicates that the stress is continuous across the interface.

As in the case of the surface stress tensor \mathbf{T} , a constitutive relation must be defined to relate \mathbf{T}_σ to physical quantities associated with the interface (*cf.*, Scriven (1960), and the justification for any such relation lies again in the agreement between theory and experiment. The simplest of such constitutive relations is given by

$$\mathbf{T}_\sigma = \sigma \mathbf{I}_{II}, \quad (2.58a)$$

where σ is the surface tension and \mathbf{I}_{II} is the identity tensor in the tangential plane, defined in terms of the three-dimensional identity tensor, \mathbf{I} , as

$$\mathbf{I}_{II} = \mathbf{I} - \mathbf{n}_1 \mathbf{n}_1 \quad (2.58b)$$

Substituting (2.58) into (2.56), applying various

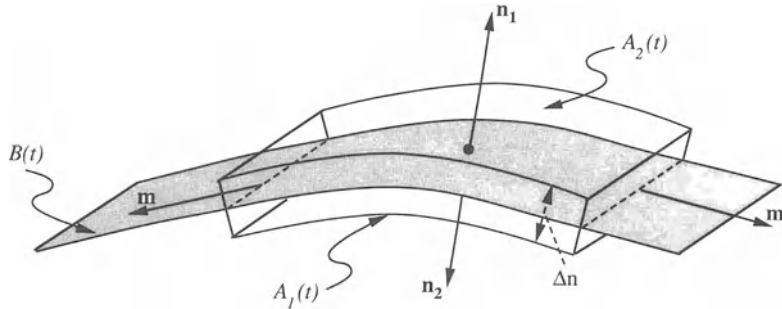


Figure 2.6 Material body used to derive the local form of the dynamic boundary condition.

tensor identities, and employing (2.18) yields

$$(P_1 - P_2)\mathbf{n}_1 + \mathbf{n}_1 \cdot (\tau_2 - \tau_1) + \nabla_{\mathbf{H}}\sigma - \frac{\sigma\mathbf{n}_1}{R_m} = 0$$

at the interface. (2.59a)

In (2.59), R_m is the mean radius of curvature of the interface, which is related to the unit outward normal as

$$\frac{1}{R_m} = \nabla_{\mathbf{H}} \cdot \mathbf{n}_1 \quad (2.59b)$$

For the case of zero flow, the only nonzero terms in (2.59a) are in the normal direction, and (2.59a) becomes

$$P_1 - P_2 = \frac{\sigma}{R_m} \quad \text{at the interface.} \quad (2.60)$$

The simplest constitutive relation (2.58) accounts for the effect of surface tension on the pressure jump across a curved interface, as originally described by Young and Laplace (see Adamson 1990). Without any further generalization, the constitutive relation (2.58) also explains the origin of Marangoni flows through the inherent dependence of σ on temperature and the interfacial concentration of surfactants (this is discussed in section 2.3.2.5), which gives rise to gradients in surface tension (i.e., nonzero values of $\nabla_{\mathbf{H}}\sigma$ in (2.59a)). Sufficient experimental evidence exists to suggest that the influence of surfactants on interfacial flows can go beyond that suggested by the $\nabla_{\mathbf{H}}\sigma$ term in equation (2.59a). Namely, surface-active agents can impart to the interface

intrinsic viscous and elastic properties. These features can be accounted for through more complex constitutive relations for \mathbf{T}_{σ} .

At this point, let us give a physical interpretation of the mean radius of curvature R_m in (2.59). The mean radius of curvature of an interface at a given point may be visualized by first erecting two perpendicular planes whose line of intersection is coincident with the outward normal at that point (Fig. 2.7). The intersection of the interface with each plane yields a curve. The mean radius of curvature is related to the curvature of these two curves at the point of interest. The curvature of each curve is determined by fitting a circle to the curve at the point (called the osculating circle) such that the first and second derivatives of the circle at the point equal the derivatives for the curve. If we denote the radii of the two osculating circles as R_1 and R_2 , then the mean radius of curvature at the point of interest is given as

$$\frac{1}{R_m} = \pm \left(\frac{1}{R_1} + \frac{1}{R_2} \right) \quad (2.61)$$

where the appropriate choice of sign is discussed below. A special feature of this definition is that the value of R_m is independent of the choice of the two perpendicular planes, as long as their line of intersection incorporates the outward normal to the surface at the point of interest. Thus, the orientation of these two planes can be chosen arbitrarily, in a manner that simplifies the evaluation of R_m .

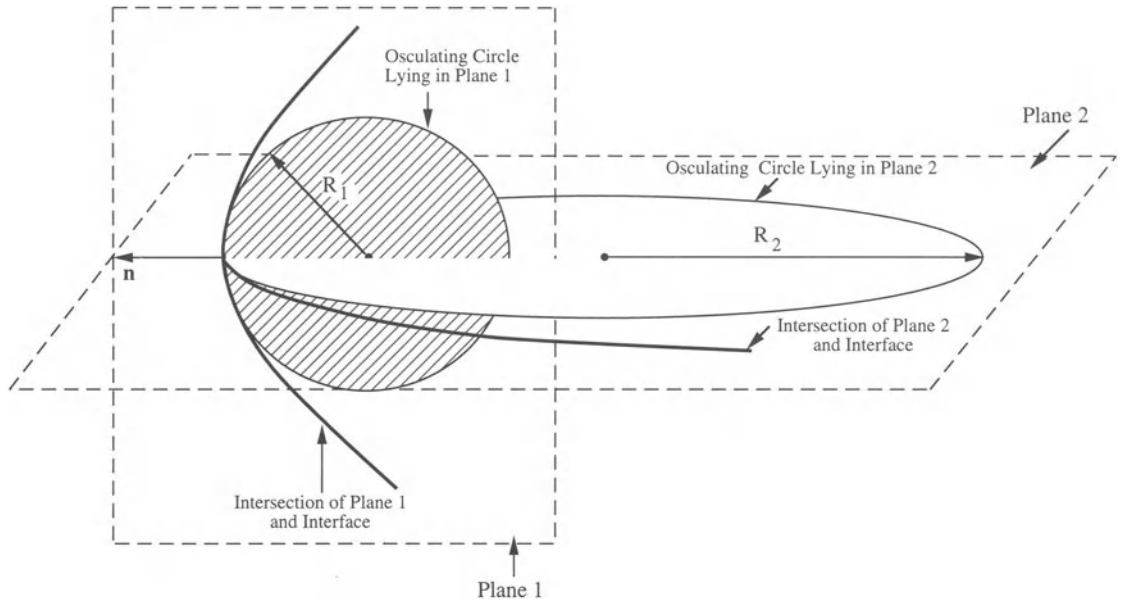


Figure 2.7 The principal radii of curvature, R_1 and R_2 , used to determine the mean radius of curvature.

Let us now apply (2.61) to a few simple cases. For the case of a sphere of radius R , the above procedure yields $R_1 = R_2 = R$ at every point on the spherical surface; thus $R_m = \pm R/2$. For the case of an infinitely long right circular cylinder of radius R , orient one of the planes in the axial direction, so that it includes the axis of the cylinder. Consequently, the perpendicular plane intersects the cylindrical surface on a circle of radius R , while the axial plane intersects the surface on a straight line ($R = \infty$). Thus, $R_1 = R$ and $R_2 = \infty$, yielding $R_m = \pm R$. Finally, for the case of a flat surface, the intersection of all perpendicular planes with the surface yields a straight line. Therefore, $R_1 = R_2 = \infty$ and $1/R_m = 0$.

The sign of (2.61) depends on the configuration of the problem in question. For example, consider the case of a spherical, static air bubble of radius R in a liquid, where the constant internal and external pressures are P_1 and P_2 , respectively. According to the equation of Young and Laplace

(see Adamson 1990), the internal air pressure is higher than the external liquid pressure. To choose the correct sign of R_m for this case, we embed it in (2.60). Noting the direction of the pressure and surface tension forces on a material body drawn to include a portion of the spherical interface (see Fig. 2.8), it is clear that the surface tension forces must oppose the higher pressure inside the bubble. Thus, the positive sign for R_m is chosen:

$$P_1 - P_2 = \frac{2\sigma}{R}$$

We note here that in any physical configuration, even those including fluid flow, the correct sign of the mean radius of curvature can always be identified by imagining that the problem is static and making sure that the pressure drop across the interface is consistent with its curvature. Alternatively, as the mean radius of curvature is defined in terms of the normal vector by (2.59b),

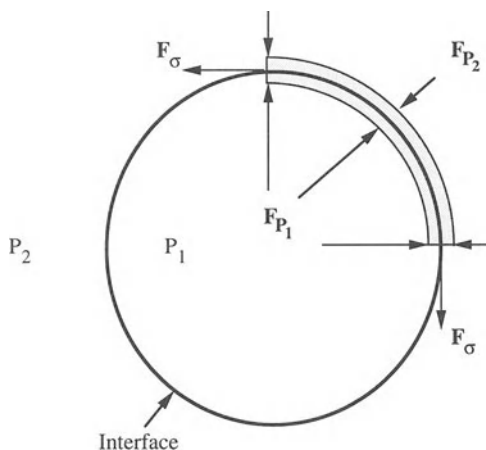


Figure 2.8 Force balance on a portion of a spherical interface. Here, F_{P_1} and F_{P_2} are the pressure forces exerted on the body due to the internal and external pressures P_1 and P_2 , respectively, and F_σ denotes the surface tension forces exerted on the body.

the correct sign will naturally arise by using this definition.

The importance of considering both principal radii in the mean radius of curvature is seen by considering the case of an axisymmetric soap film pinned to the surface of two wire rings, as illustrated in Fig. 2.9. The important feature of

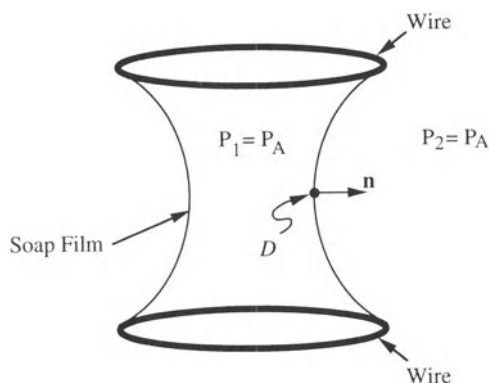


Figure 2.9 Shape of an axisymmetric soap film having identical internal and external pressures P_1 and P_2 , respectively.

this problem is that the soap film is exposed to a constant atmospheric pressure P_A everywhere (i.e., no films span the circular openings at either end). Therefore, the interior and exterior pressures, P_1 and P_2 , are identical; thus $1/R_m = 0$, in accordance with (2.60). But it is obvious, from the axisymmetric geometry of the soap film, that the film is curved. To resolve the dilemma, consider in particular the point D on the film, which is equidistant from the two rings. Now construct two perpendicular planes at D such that one contains the vertical axis of the film while the other is parallel to the wire rings. The intersection of the first plane with the film results in a curved line that is visualized in Fig. 2.9 as the ‘soap film’, whose radius of curvature at D is denoted as R_1 . The intersection of the second plane with the soap film results in a circle whose radius, R_2 , is smaller than that of the rings. The important point to recognize is that the sense of each curve is opposite to the other: the first curves inward while the second curves outward. Thus, the condition $1/R_m = 0$ is met because $R_2 = -R_1$ at D, as well anywhere else along the surface*. As a consequence, soap films freely suspended from curved wires invariably have saddle-like shapes.

The mathematical relationship between the mean radius of curvature and the parameterization of a given surface is a complicated nonlinear function of the interface shape. For example, for a surface parameterized as $Y = H(X, Z, t)$, the corresponding mean radius of curvature is given by (2.62).

* Note that for all other points on the film, the second plane will make an oblique angle with the planes containing the wire rings, as the second plane must intersect the axial plane along the outward normal to the film at the point of interest. Thus, the intersection of the soap film with this second plane will yield a curve whose curvature at each point, $1/R_2$, will vary with vertical position in a complex way. Note that, because R_2 varies with vertical position, the shape of the soap film in the vertical plane, as illustrated in Figure 2.9, is not circular.

$$\frac{1}{R_m} = \pm \frac{\frac{\partial^2 H}{\partial X^2} \left[1 + \left(\frac{\partial H}{\partial Z} \right)^2 \right] + \frac{\partial^2 H}{\partial Z^2} \left[1 + \left(\frac{\partial H}{\partial X} \right)^2 \right] - 2 \frac{\partial^2 H}{\partial X \partial Z} \frac{\partial H}{\partial X} \frac{\partial H}{\partial Z}}{\left[1 + \left(\frac{\partial H}{\partial X} \right)^2 + \left(\frac{\partial H}{\partial Z} \right)^2 \right]^{3/2}} \quad (2.62)$$

For the simple cylindrical, spherical, and flat interface cases described above where $1/R_m$ is constant, (2.62) can be solved exactly for the surface parameterization, despite its nonlinearity. For most other cases, however, the appearance of such a formidable mathematical expression in the dynamic boundary condition makes interfacial systems under both static and dynamic conditions extremely difficult to solve exactly.

2.3.2.5 Surface stresses derived from gradients in surface tension

As mentioned above, the surface stress balance presented in equation (2.59) is based on the simplest constitutive relationship for the surface stress tensor (2.58); that is, an interface whose sole mechanical property is interfacial tension σ . Nevertheless, such an interface can have a profound effect on the fluid dynamics of multiphase systems through the inherent dependence of interfacial tension on temperature and solute concentration. In problems involving heat and/or mass transfer, for example, the possibility exists for local spatial variations in temperature and/or concentration to develop along the interface, which in turn will create local gradients in the interfacial tension (i.e., nonzero values of $\nabla_{II}\sigma$ in (2.59a)). As can be seen from (2.59a), such gradients in σ appear as tangential surface stresses that can drive fluid flows in the adjacent phases. In particular, this is the mechanism by which Marangoni flows are initiated during interphase heat and/or mass transfer in fluid–fluid systems.

Gradients in the interfacial tension occur because the local value of the interfacial tension σ depends upon the local interfacial conditions; namely the local surface temperature and the local value of the surface excess of solute i adsorbed at the interface, Γ_i . Thus, with the aid of partial differentiation, we can rewrite the interfacial tension gradient term as a combination

of temperature and surface concentration gradients along the interface:

$$\nabla_{II}\sigma = \frac{\partial\sigma}{\partial T}\nabla_{II}T + \frac{\partial\sigma}{\partial\Gamma_i}\nabla_{II}\Gamma_i \quad (2.63)$$

The common assumption is that σ in (2.59a) and (2.63) is the equilibrium tension, and thus its dependence on T and Γ_i pointwise along the interface can be determined from equilibrium surface tension measurements. In particular, the equilibrium surface tension decreases linearly with increasing temperature, typical values of $(\partial\sigma/\partial T)$ being of the order of -1×10^{-4} N/m °C. For dilute solutions of surface-active solutes, the Gibbs adsorption equation (Adamson 1990) provides the following relationship between surface tension and surface excess:

$$\Gamma_i = -\left(\frac{C_i}{RT}\right)\left(\frac{\partial\sigma}{\partial C_i}\right)_T \quad (2.64)$$

where R is the gas constant and C_i is the molar concentration of species i in the bulk fluid. Furthermore, for dilute solutions, the surface tension decreases linearly with increasing bulk solute concentration. Thus, it follows from (2.64) that

$$\Gamma_i = \beta C_i \quad (2.65)$$

and

$$\frac{\partial\sigma}{\partial\Gamma_i} = -RT \approx -2500 \text{ N m/mole} \quad (2.66)$$

Note that β is a constant which represents the distribution coefficient for species i between the interface and the bulk phase, its value being strongly dependent on the molecular nature of the solute. For a mildly surface-active substance such as octanol in water (with $C_i < 0.1$ mM at 25°C), β equals 1.9×10^{-5} m; for aqueous solutions of a homologous series of organic solutes, the value of β increases by a factor of ~ 3 for each

CH_2 group added to the hydrocarbon chain (Traube's Rule; see Adamson 1990).

One of the most important effects of surfactants on fluid flows results from the convective redistribution of surfactant in the interface. When an interface is accelerated or stretched in the direction of flow, surfactant material in the interface is swept downstream, thereby creating a region of higher tension upstream. The net effect is an interfacial tension gradient that opposes the flow (see Section 2.4.2 for a model problem illustrating this effect). Because of the strong dependence of σ on Γ_i , only modest amounts of convective redistribution are needed to produce large forces which tend to oppose flow. Thus, it is not unusual to discover interfaces that resist viscous stresses and remain immobile, in a fashion that resembles a solid boundary, even when only small amounts of surfactant are present in the system. To account for the effect of convective redistribution of surfactant in the interface, an interfacial mass balance on the solute is needed. This solute balance is obtained in precisely the same way as the kinematic boundary condition (2.40), except that the accumulation of solute at the interface must be retained in the final form of the integral equation.

The result is:

$$\begin{aligned} \frac{\partial \Gamma_i}{\partial t} + \frac{\Gamma_i}{2a} \frac{\partial a}{\partial t} + \nabla_{\text{II}} \cdot (\Gamma_i \mathbf{U}_{\text{II}}) + D_s \nabla_{\text{II}}^2 \Gamma_i \\ = \rho_{i_1} (\mathbf{U}_1 - \mathbf{U}_{\sigma}) \cdot \mathbf{n}_1 - \rho_{i_2} (\mathbf{U}_2 - \mathbf{U}_{\sigma}) \cdot \mathbf{n}_1 \\ + (\mathbf{J}_{i_1} - \mathbf{J}_{i_2}) \cdot \mathbf{n}_1 \end{aligned} \quad (2.67a)$$

where a is the determinant of the surface metric tensor which characterizes the shape of the surface, D_s is the coefficient of diffusive transport within the interface itself, and \mathbf{J}_{i_1} and \mathbf{J}_{i_2} are the respective diffusive fluxes of species i in phases 1 and 2 at the interface. In addition, ρ_{i_1} and ρ_{i_2} are the mass concentrations of species i in phases 1 and 2 at the interface. We note here that ρ_i in either phase (written generally for either phase without the subscript 1 or 2) equals the corresponding molar concentration, C_i (introduced in (2.64)), times the molecular weight of species i .

Recall that \mathbf{U}_{σ} is the rate of displacement of the interface as defined in the context of equation (2.37). The velocity \mathbf{U}_{II} in (2.67a) is the velocity along the interface which is given by

$$\mathbf{U}_{\text{II}} = \mathbf{I}_{\text{II}} \cdot \mathbf{U} \quad (2.67b)$$

where \mathbf{I}_{II} is defined in (2.58b), and \mathbf{U} is the fluid velocity in either phase at the interface. We note here that for the case of negligible surface concentration, (2.67a) reduces to (2.40) for each component i . From left to right, the terms in (2.67a) account for the local rate of accumulation of solute at the interface, the rate of change in the local surface concentration due to local increases/decreases in the interfacial area owing to the motion of a curved surface normal to itself, the rate of convective redistribution of solute in the interface, the rate of surface diffusion, the rate of convective transport to/from the bulk phases to the interface, and the local diffusive flux to the interface from the bulk phases.

In the vast majority of coating flow applications, the flow is steady and the surface is not deforming normal to itself. Furthermore, the bulk concentration of surfactant is extremely low. Thus, (2.67) can be simplified, to

$$\mathbf{U}_{\text{II}} \cdot \nabla_{\text{II}} \Gamma_i = -\Gamma_i \nabla_{\text{II}} \cdot \mathbf{U}_{\text{II}} + (\mathbf{J}_{i_1} - \mathbf{J}_{i_2}) \cdot \mathbf{n}_1 \quad (2.68)$$

where the vector identity $\nabla_{\text{II}} \cdot (\Gamma_i \mathbf{U}_{\text{II}}) = \mathbf{U}_{\text{II}} \cdot \nabla_{\text{II}} \Gamma_i + \Gamma_i \nabla_{\text{II}} \cdot \mathbf{U}_{\text{II}}$ has been utilized in obtaining this form. Equation (2.68) is usually the starting point for all analyses of surfactant effects on coating flows. According to (2.68), gradients in interfacial concentration caused by convective redistribution (i.e., nonzero values of $\nabla_{\text{II}} \cdot \mathbf{U}_{\text{II}}$) are moderated by mass transfer from the bulk phases: the faster the rate of exchange between the interface and the bulk phases, the more uniform the interfacial concentration and the smaller the effect of the surfactant on the flow field.

In summary, the effects of surfactants on coating flows are accounted for by the $\nabla_{\text{II}} \sigma$ term in the interfacial stress balance (2.59a). The local value of this term requires knowledge of the gradient in Γ_i (see (2.63)), which in turn is

described by an interfacial mass balance (2.67) or (2.68). In applying these equations, knowledge of bulk diffusive fluxes in each phase to/from the interface are needed, and these are obtained from Fick's law

$$\mathbf{J}_i = -D_i \nabla \rho_i \quad (2.69a)$$

coupled with the equation of solute conservation for each phase

$$\frac{\partial \rho_i}{\partial t} + \mathbf{U} \cdot \nabla \rho_i = -\nabla \cdot \mathbf{J}_i + r_i \quad (2.69b)$$

Here, D_i is the molecular diffusivity of species i , and r_i is the rate of production of species i per unit volume by chemical reaction. To solve (2.69), a boundary condition on ρ_i is needed at the interface. Either local equilibrium at the interface is assumed and an equilibrium adsorption relationship such as (2.65) is applied, or the flux of solute into the interface is specified according to an adsorption/desorption reaction rate model such as

$$\text{diffusive flux} = \mathbf{J}_{i_1} \cdot \mathbf{n}_1 = k_1 \rho_i - k_{-1} \Gamma_i$$

where k_1 and k_{-1} are adsorption and desorption rate constants. A more detailed discussion of surfactant effects on coating flows can be found in Chapter 11d.

2.3.2.6 Disjoining pressure: modification to the dynamic boundary condition for ultra-thin films

The body forces, surface forces, and line forces discussed thus far involve measurable macroscopic quantities such as density, viscosity and surface tension. As mentioned previously, a continuum approach inherently considers length scales larger than that of molecular dimension so that these properties have meaning. However, we must acknowledge that these fluid properties do have a molecular origin, and in particular, in the vicinity of a fluid–solid or fluid–fluid boundary, the molecular interactions will be different from those in the bulk fluid away from these boundaries. These interactions can be due to, for example, long-range intermolecular forces such as Lon-

don–van der Waals dispersion forces and electrostatic forces.

Consider as an example, the air–liquid–solid system shown in Fig. 2.10a, which indicates the location of the boundary regions. The thickness of a boundary region is the distance over which long-range intermolecular forces act. Since the intermolecular forces vary with distance as either the air or solid is approached, physical properties such as density and viscosity will also vary, and will be different from those measured in the bulk liquid phase. Consequently, the pressure tensor is anisotropic in the boundary regions; i.e., the pressure measured relative to a plane parallel to the solid is different from the pressure measured relative to a plane perpendicular to the solid. Outside of these boundary regions, physical properties are simply bulk liquid properties in the classical sense, and the pressure tensor is isotropic.

For the vast majority of coating flow problems, the length scale of a typical liquid film is orders of magnitude greater than the thickness of these

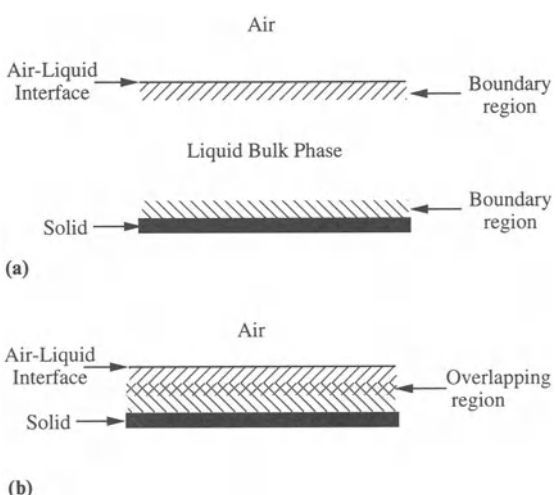


Figure 2.10 The origin of disjoining pressure: (a) a thin fluid layer whose thickness is greater than the range of intermolecular forces; (b) a fluid layer that has been thinned to the point where the interfacial boundary regions (hatched) have begun to overlap, thereby eliminating the region in the film that has bulk fluid properties.

boundary regions. On this length scale, the macroscopic manifestation of the anisotropic boundary region near the air–liquid interface is interfacial tension (Derjaguin, Churaev and Muller 1987), which is lumped into the interfacial stress tensor, \mathbf{T}_σ , in the dynamic boundary condition (2.56); furthermore, the properties of the liquid are interpreted in the classical sense. On the other hand, if the liquid layer is made progressively thinner to the point where its dimension approaches the length scale of long-range intermolecular forces (on the order of $0.1 \mu\text{m}$ or less), the boundary regions themselves constitute a significant portion of the domain, and may begin to overlap (Fig. 2.10b). In this case, the concept of bulk properties will no longer be meaningful. Even in such cases, however, the total thickness of the liquid layer often is large enough that it can be modelled in the context of the continuum assumption.

The net effect of the overlap of these boundary regions is an attractive or repulsive force between the air–liquid interface and the solid. When the force is attractive, fluid has a tendency to be squeezed out from between the solid and the interface. If the force is repulsive, fluid has a tendency to accumulate between the solid and air–liquid interface. The net force per unit area is called the disjoining pressure (Derjaguin, Churaev and Muller 1987), and it can be lumped into the dynamic boundary condition as an extra pressure term. In particular, for a static interface configuration, the pressure drop given by (2.60) can be modified to incorporate the disjoining pressure, Π , as

$$P_1 - P_2 - \Pi = \frac{\sigma}{R_m} \quad \text{at the interface} \quad (2.70)$$

The pressure relationship given by (2.70) is typically the starting point for analyses involving the flow occurring in ultra-thin films. Its physical significance can be elucidated by considering the situation illustrated in Fig. 2.11. Here, a static ultra-thin layer of fluid is suspended between two supports and is in direct communication with a bulk phase of the same fluid. Although the opposing interfaces of the layer are flat (i.e.,

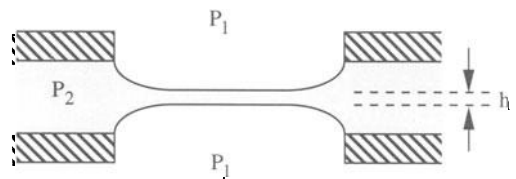


Figure 2.11 Schematic diagram of an ultra-thin fluid film in equilibrium with its bulk phase.

$R_m = \infty$) for most of the region between the supports, there is a pressure drop across each interface. Namely, a pressure, P_1 , in excess of the fluid pressure, P_2 , must be applied to maintain a given degree of separation, h , between the two interfaces (assuming that the excess force is repulsive).

As the thickness of the liquid layer determines the degree to which the boundary regions near the solid and air–liquid interface will interact, the disjoining pressure is a function of the film thickness as well as the temperature, pressure, and composition of the system. In addition, the disjoining pressure is a function of the particular forces being exerted in the layer, i.e., dispersion and electrostatic. If the interface and solid surfaces are uncharged, so that the net force between the interfaces is due solely to the London–van der Waals dispersion force, the relationship between disjoining pressure and layer thickness, h , is given by

$$\Pi = \frac{A}{6\pi h^3} \quad (2.71)$$

where A is the Hamaker constant, whose magnitude depends on the degree of polarizability of the molecules in the interfacial region. Other relationships are available to incorporate additional effects (Derjaguin, Churaev and Muller 1987). In addition, it should be noted here that once an overlap of the boundary regions occurs, the surface tension itself will be dependent on the film thickness. From a practical point of view, however, thermodynamic arguments typically indicate that this thickness effect is small, and it is reasonable to interpret the surface tension in (2.70) as that in the conventional, macroscopic sense.

Measurement indicates that the Hamaker constant is typically on the order of 10^{-20} J. Thus, from equations (2.70) and (2.71), we can deduce that disjoining pressure will be significant only for film thicknesses less than approximately $0.1\text{ }\mu\text{m}$. Consequently, its effect need not be considered in most hydrodynamic models of coating flows. On the other hand, at high coating speeds, the potential exists for entraining an ultrathin layer of air between the coating and the substrate. The tendency of this air layer to collapse or break up into tiny air bubbles is acutely influenced by the disjoining pressure of the layer (see Chapter 3). Similarly, the process by which a continuous liquid coating on a solid substrate breaks up into a patchwork of wet and dry areas inevitably involves the formation of an ultrathin film as a crucial intermediate step (see Chapter 6). Thus, the disjoining pressure also plays a key role in the hydrodynamic stability of thin liquid films, with applications that include not only coatings but also soap films and coalescence phenomena. A more thorough treatment of disjoining pressure and its role in coating flows will be presented in Chapter 6.

2.3.2.7 Contact angles

The mathematical expression for the curvature, such as that shown in (2.62), has interfacial derivatives, implying that additional boundary conditions are needed to determine the interfacial parameterization. In coating processes, it is common for one or more fluid–fluid interface to come in contact with a solid boundary, such as is shown in Fig. 2.1. The line of such contact is called a contact line, and the angle of intersection, θ , is called the contact angle; both of these are shown for an air–liquid system in Figure 2.12a. The location of the contact line, or the variation in the contact angle along this line, provide necessary boundary conditions to solve for interface shapes (Dussan V. 1979). We now discuss the basic properties of the contact angle. For the purposes of discussion, we will restrict attention to air–liquid systems, as they are common in coating flows, although the discussion

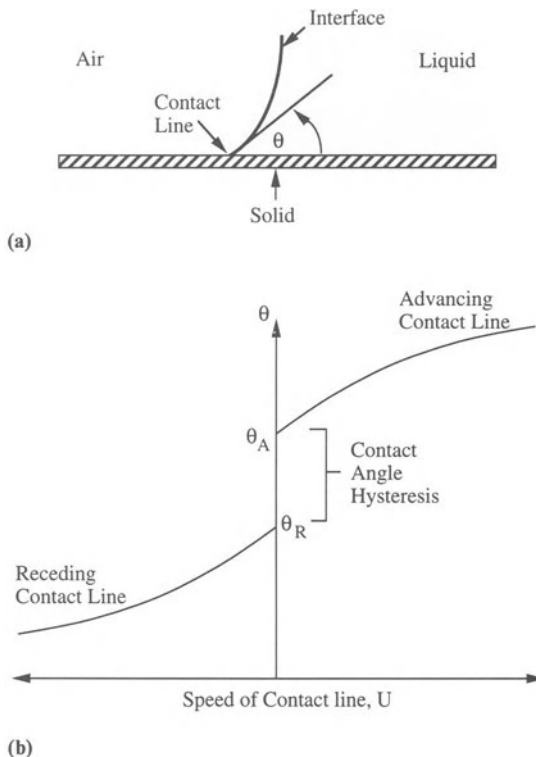


Figure 2.12 The contact angle: (a) cross-section of an air–liquid–solid system, indicating the contact angle, θ ; (b) the dependence of the contact angle on the speed of the contact line.

is valid for any fluid–fluid system whose interface exhibits interfacial tension.

In a static case in which there is no fluid flow, the contact angle is intimately affected by the identity of the solid surface (including its finish), the fluids and the interface. Thus, changing the material properties of the system is likely to change the value of this angle. In a case where the contact line moves, the contact angle (which is now referred to as a dynamic contact angle) is still affected by the material properties. However, experimentally observed dynamic contact angles, often called apparent contact angles, are also dependent upon the flow field found in the measurement domain. There have been some attempts at obtaining submicroscopic contact angles, which are also called actual contact

angles, which are supposed to be truly material properties that are independent of the macroscopic fluid flow (so they can be utilized in other geometrical configurations). However, as these contact angles cannot be experimentally observed, mathematical analyses which make some assumption about the flow in the vicinity of the contact line must be employed to extract their values from the observed interface shapes. It is thus difficult to assess whether the assumptions made in such analyses are correct. An extensive discussion of these issues is presented in Chapter 3; in that chapter, it is shown that from a practical point of view, the apparent contact angle is typically most useful to model coating flows.

We now discuss the properties of the apparent contact angle, which is henceforth simply called the contact angle. For a given material system and flow geometry, it has been found experimentally that the speed of the contact line, U , is related to the contact angle by a curve as shown in Fig. 2.12b. By convention, positive values of the contact line speed correspond to cases where liquid is displacing air, the contact angle being measured through the liquid as shown in Fig. 2.12a. The contact line in such a case is called an advancing contact line. On the other hand, negative contact line speeds are associated with receding contact lines, for which air displaces the liquid. It should be noted that, in either case, the contact line motion is always defined normal to the contact line in the plane of the solid, and the local value of the contact angle in this normal direction determines the local speed of the contact line.

In Fig. 2.12b, there are two angles which characterize the advancing and receding contact lines. The first, θ_A , is called the critical advancing contact angle, and is the angle above which the contact line moves towards the air. The second angle is the critical receding contact angle, denoted as θ_R , which is the angle below which the contact line will move towards the liquid. An important feature of such a curve is that $\theta_A \neq \theta_R$; i.e., there exists a range of angles over which there is no contact line motion. This range of angles is termed contact angle hysteresis, and it exists in virtually all material systems, at least to some

extent. The implication of contact angle hysteresis is profound. Force balances show that it would be impossible for stationary drops to exist on inclined surfaces without hysteresis. Furthermore, for a given static horizontal drop, the wide variety of shapes often seen are also attributable to the existence of hysteresis.

An implication of the contact-angle-versus-speed curve is that the mathematical solution to a static contact line problem may be obtained for a large range of values of θ , but not all of those solutions are physically realizable. In order to achieve a static contact line, it is necessary that all contact angles along the contact line lie within the hysteresis range; if they do not, then there will be contact line motion in those sections whose contact angles lie outside the hysteresis region. Thus, when solving for an interface shape in which no contact line motion is intended, it is important to specify contact angles which lie in the hysteresis region. In some cases, the location of the contact line along a solid is used as a boundary condition instead of the contact angle. To assure that the interface is static for these cases, it is important that the resultant angles along the contact line, extracted from the mathematical solution, fall within the hysteresis region.

Finally, we close this section by emphasizing that the need to specify constraints on the interface itself, such as the value of the contact angle or the location of the contact line, is intimately related to the appearance of the curvature term in the dynamic boundary condition. In those cases where the interface has zero surface tension, or in cases where the curvature operator is neglected through approximation, an equation system will be overspecified if contact angle or contact line boundary conditions are imposed on the interface without relaxing constraints elsewhere in the domain.

2.3.2.8 Additional constraints for a well-posed problem

The boundary conditions presented above are fundamental to the flow of multiple fluid phases.

Let us now summarize, in general form, the system of equations and boundary conditions which are applicable to the flow configuration shown in Fig. 2.1. For each fluid phase, the governing equations which apply are the continuity equation (2.6) and conservation of linear momentum (2.19). At the solid surfaces, the kinematic condition (2.40) and no-slip condition (2.48) apply. At the fluid–fluid interface, the kinematic boundary condition (2.40), the no-slip condition (2.47), and dynamic boundary condition (2.56) are imposed. If, in addition, the interface has surface tension, a contact angle condition or contact line location must be specified to constrain interfacial shape.

It should be noted that the governing conservation equations, in their most general form, require that boundary conditions be identified on all boundaries of the domain, and as of yet, we have not specified constraints along the inflow and outflow boundaries of the domain shown in Fig. 2.1. Boundary conditions applied at these locations can take various forms which depend upon the particular problem posed. We might treat the domain in the flow direction as being infinite, and such inflow and outflow boundary conditions would assure the correct limiting form of the flow field for the problem of interest. In other cases, for the purpose of computation, we might decide to approximate the domain of interest as being finite, and in this case, appropriate inflow and outflow boundary conditions would be obtained by looking at the fully developed flow fields upstream and downstream of the domain of interest, but applying them at a finite location for which the flow solution is still insensitive to the precise location of the conditions. Additional conditions are required if the flow is transient, as initial conditions for the fluid and interface must be specified as well.

2.4 MODEL PROBLEMS: THE EFFECTS OF FLUID–FLUID INTERFACES ON FLOW

With the equations and boundary conditions identified, we can now further examine the

physical implications of the presence of an interface when there is fluid motion. Generally, flow calculations involving interfaces are quite complicated, owing to the fact that the interface location is intimately coupled with the flow field, as can be seen from the boundary conditions derived previously. An interface location is not known *a priori* and must be determined as part of the solution to the problem. The complex mathematical structure of such problems can often obscure the relatively simple physics associated with the presence of the interface. In analyzing complex flow situations, it is often desirable to view the flow field as a combination of much simpler flow fields in which the physical mechanisms involved are clear. In addition, it is also important to examine limiting cases for which the mathematical solution of fluid flow is relatively simple, and to apply the intuition gained to cases where such limits are not strictly valid but the underlying physical mechanisms are essentially the same. The goal of the remaining part of this chapter is to provide a physical understanding of the basic concepts associated with interfacial fluid flow using both of these approaches.

The unique physical character of flow fields involving interfaces enters through the dynamic boundary condition (2.59a and b), and so it is natural to begin the discussion with this condition. To this end, it is useful to resolve (2.59a) into its normal and tangential components. For any point along an interface between phases 1 and 2, it takes one unit normal vector \mathbf{n}_1 (which is defined, following the convention established in Fig. 2.6, to be the unit outward normal to phase 1) and two linearly independent tangent vectors, \mathbf{t}_α and \mathbf{t}_β , to characterize the surface. Thus, (2.59a) can be written in component form as

$$\mathbf{n}_1 \cdot (P_1 - P_2) + [\mathbf{n}_1 \cdot (\tau_2 - \tau_1)] \cdot \mathbf{n}_1 = \frac{\sigma}{R_m}$$

at the interface (2.72a)

$$\mathbf{t}_\alpha \cdot [\mathbf{n}_1 \cdot (\tau_2 - \tau_1) + \nabla_{\mathbf{n}} \sigma] \cdot \mathbf{t}_\alpha = 0$$

at the interface (2.72b)

$$\mathbf{t}_\beta \cdot [\mathbf{n}_1 \cdot (\tau_2 - \tau_1) + \nabla_{II} \sigma] \cdot \mathbf{t}_\beta = 0$$

at the interface (2.72c)

where the definition of ∇_{II} , given by (2.55), has been used in eliminating the del operator in (2.72a).

2.4.1 IMPLICATIONS OF THE NORMAL STRESS BALANCE AT THE INTERFACE

We have already seen that in a static problem, surface tension is responsible for creating a pressure drop across a curved interface, as given by (2.60). The physical effect of surface tension in statics is confined to (2.72a), where viscous stresses are zero when there is no fluid motion. When viscous stresses are significant, the relationship between the pressure drop and the mean radius of curvature is altered. Given the intimate linkage between the flow field and the interface location, it is important to ask under what conditions the interface has a static-looking shape. In the context of such a case, given the complex form of the mean radius of curvature (as shown in 2.62), it is also useful to identify those conditions under which the mean radius of curvature is essentially constant, as the evaluation of the pressure drop across such an interface shape is easily determined by the dynamic boundary condition. Both of these cases are examined in what follows, in the context of two important dimensionless groups – the capillary and the Bond numbers.

2.4.1.1 The limit of small capillary numbers

Consider a meniscus between air and a Newtonian liquid formed between two parallel plates separated by a distance b , as shown in Fig. 2.13, where the interface is moving upwards with a constant shape at a steady speed U . The coordinate system is oriented as shown, where the plates are infinitely long in the Z -direction (which is oriented into the figure), and gravity acts in the $-X$ -direction. With the coordinate system fixed on the interface, the interface location is time independent. It is denoted as $X = H(Y)$, and $Y = \pm b/2$ denotes the locations of the surfaces of the two plates. In

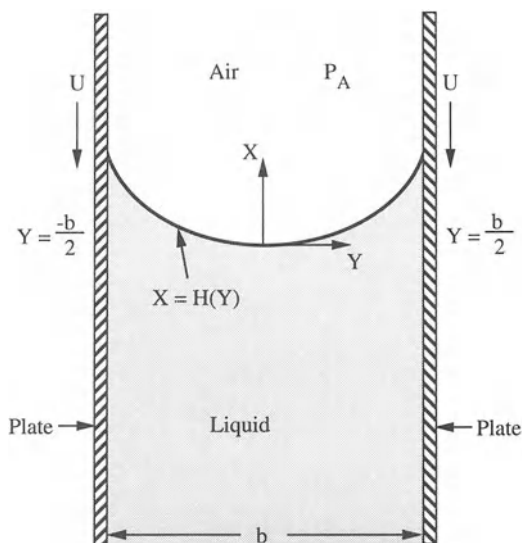


Figure 2.13 Air–liquid interface moving between parallel planes at a speed U .

such a frame of reference, the plates move at a velocity $-U\hat{\mathbf{i}}$, where $\hat{\mathbf{i}}$ is the unit vector in the X -direction. We assume that the viscous effects of the air on the film are negligible, i.e. $\tau_2 = 0$ in (2.72); we denote the constant air pressure as P_A . As all the fluid dynamics is thus limited to the liquid phase, we will not explicitly write the subscripts on the flow variables.

It is clear from (2.72a) that, if the viscous stresses in the liquid are negligible, the relationship between the pressure drop across the interface and the mean radius of curvature is of the same form as for a static problem. This does not necessarily imply, however, that the interface will have a static shape; rather, a static shape will be obtained only if the pressure drop obtained from the equation of motion is hydrostatic; i.e., it is governed by (2.22). With this limit in mind, let us determine the order of magnitude of terms in (2.72a) and (2.21) by choosing appropriate scales for all the variables as follows. The velocity and length are scaled with U and b , respectively, and the viscous stresses with $\mu U/b$. In anticipation of a limit where a static-looking shape is obtained, the pressures are scaled with σ/b . Then, with

dimensionless variables defined as

$$p = \frac{Pb}{\sigma}, p_A = \frac{P_A b}{\sigma}, r_m = \frac{R_m}{b}, \bar{\tau} = \frac{\tau b}{\mu U},$$

$$\bar{\nabla} = b\nabla, \bar{t} = \frac{tU}{b}, \mathbf{u} = \frac{\mathbf{U}}{U}, x = \frac{X}{b}, y = \frac{Y}{b}$$

where

$$h(y) \equiv h\left(\frac{Y}{b}\right) \equiv \frac{H(Y)}{b}$$

the normal component of the dynamic boundary condition (2.72a) becomes

$$(p - p_A) - Ca [\mathbf{n}_1 \cdot \bar{\tau}] \cdot \mathbf{n}_1 = \frac{1}{r_m} \quad \text{at } x = h(y) \quad (2.73a)$$

where

$$Ca = \frac{\mu U}{\sigma} \quad (2.73b)$$

The equation of motion (2.21) becomes

$$Re Ca \left[\frac{\partial \mathbf{u}}{\partial t} + \mathbf{u} \cdot \bar{\nabla} \mathbf{u} \right] = -\bar{\nabla} p + Ca \bar{\nabla}^2 \mathbf{u} - (Bo) \hat{\mathbf{i}} \quad (2.73c)$$

where the gravity vector, whose magnitude is denoted by g , has been written as $\mathbf{g} = -g\hat{\mathbf{i}}$, and

$$Re = \frac{\rho U b}{\mu}, \quad Bo = \frac{\rho g b^2}{\sigma} \quad (2.73d)$$

The dimensionless group defined in (2.73b), namely Ca , is called the capillary number, which is a ratio of viscous to surface tension forces. In (2.73d), Re is the Reynolds number, which is a ratio of inertial forces to viscous forces, and Bo is the Bond number, which is a ratio of gravitational forces to surface tension forces. Inspection of the equation of motion (2.73c) shows that the quantity $Re Ca$ actually characterizes the relative effect of inertia, in that it determines the magnitude of the left-hand side of (2.73c). This quantity is called the Weber number, We , which is thus defined as

$$We = Re Ca = \frac{\rho U^2 b}{\sigma} \quad (2.73e)$$

As the Weber number is independent of viscosity, it is the preferred dimensionless group for interfacial problems in which viscous effects are small and the resulting flow is dominated by fluid inertia. For problems in which the flow is relatively slow, so that viscous effects and surface tension effects are most important (as in the sample problem of Fig. 2.13), the Reynolds number as written explicitly in (2.73c) is often more conventional, as the relative sizes of viscous and inertial forces are compared in this single dimensionless group.

From (2.73), it is clear that in the limit as $Ca \rightarrow 0$, with all other groups held fixed,

$$p - p_A = \frac{1}{r_m} \quad \text{at } x = h(y) \quad (2.74a)$$

$$\bar{\nabla} p = -(Bo) \hat{\mathbf{i}} \quad (2.74b)$$

The system (2.74) is a dimensionless version of (2.22) and (2.60); thus, in the limit of small capillary number, the shape of the interface can be calculated as if it were static. The capillary number quantifies the relative importance of viscous forces (due to fluid flow) to surface tension forces in distorting the interface away from its static-looking shape. We note here that there is an important distinction between the dynamic problem and the static problem in the small Ca limit. At small but nonzero capillary numbers, the interface may be moving at some speed even though the interface has a static-looking shape; the dynamic contact angle indicates that the interface is moving. For the configuration shown in Fig. 2.13, the appropriate contact angle corresponding to the speed U is chosen from a relationship such as that shown in Fig. 2.12b, where the contact angle resides along the advancing portion of the curve.

2.4.1.2 The effect of the Bond number for small capillary numbers

We now consider those conditions under which the interface can have a constant mean radius of curvature. To continue our arguments, let us simplify the system (2.74). Integration of (2.74b)

yields

$$p = p_R(\bar{t}) - (Bo)x \quad (2.75a)$$

where $p_R(\bar{t})$ is in general a time-dependent function which arises from integration, and which acts as a reference pressure in the fluid. Substitution of (2.75a) into (2.74a) yields the equation that is solved for the interface shape:

$$p_R(\bar{t}) - p_A - (Bo)h(y) = \frac{1}{r_m} \quad (2.75b)$$

Inspection of this equation reveals that the reference pressure p_R in the fluid must be an absolute constant in order for r_m to be time-independent. Furthermore, equation (2.75b), obtained in the limit of small capillary number, indicates that it is not possible, as long as gravity is acting, to obtain an air–liquid interface of constant mean radius of curvature at low capillary numbers. Rather, the interface shape approaches a constant curvature only when the Bond number approaches zero. In the present example, this can be accomplished, according to the definition of the Bond number in (2.73d), by decreasing the spacing between the two plates while holding the physical properties of the system fixed. On the other hand, it is evident from (2.73a) that the limit $Bo \rightarrow 0$ is insufficient to ensure that the interface will have a constant mean radius of curvature as fluid flow also distorts the shape of the interface, through viscous stresses in proportion to the capillary number. However, for many problems of practical interest, the capillary number is usually low enough to permit the assumption that r_m is constant, provided the Bond number is also small. It is important to realize that in such cases the shape of the interface (the value of r_m) will not be the shape obtained for the case of zero fluid motion because, with finite fluid flow, the dynamic contact angle at solid boundaries will inevitably be different from that in the static state.

The Bond number can be interpreted physically by rewriting it as

$$Bo = \frac{\rho g b}{\sigma/b} \quad (2.76)$$

which, as written, explicitly indicates that Bo is a ratio of gravitational force to surface tension force. A small Bond number implies that the surface tension forces dominate, with the interfacial shape tending towards constant curvature (see 2.75b)), while large Bond numbers are characteristic of systems in which gravity tends to distort the interface shape away from such a condition.

A natural question to ask at this point is to what shape does gravity tend to distort the interface at low capillary numbers? An answer to this question can be obtained mathematically by looking at the large Bond number limit, where the gravity forces dominate the surface tension forces as characterized by (2.76). A large Bond number can be obtained in our illustrative example (Fig. 2.13) by increasing the spacing of the plates. For such a limit, the scaling of the pressures used to arrive at (2.75) is not appropriate, as gravity forces will dominate and pressure differences will be more closely associated with hydrostatic effects rather than capillary effects. Thus, we redefine the dimensionless pressures as

$$p = \frac{P}{\rho g b}, \quad p_A = \frac{P_A}{\rho g b}$$

causing equation (2.75b) to become

$$p_R - p_A - h(y) = \frac{1}{Bo r_m} \quad (2.77)$$

where the fact that p_R is a constant has been used. Now, as $Bo \rightarrow \infty$, we see that $h(y)$ approaches a constant, as the right-hand side of (2.77) drops out in that limit. In other words, the interface is driven towards a constant height, flattening out as gravity forces increase their dominance over surface tension forces.

We have already stated that problems in which an interface makes contact with a solid boundary, a contact angle-speed relationship must be imposed provided that the interface has a tension. For large but finite Bond number, the interface flattens according to (2.77), but it cannot flatten uniformly near the wall unless the contact angle

that the interface makes with the wall fortuitously equals 90° . Thus, in the vicinity of the contact line at the wall, there will be a region of high curvature. We will now consider a relatively simple analysis of this region, which leads to an important length scale often used in coating flows and which provides an alternative interpretation of the Bond number.

Let us focus on the region of fluid near the plate at $Y = -b/2$ in Fig. 2.13, where angle of contact with the wall is specified. This region is shown in more detail in Fig. 2.14, for a large Bond number. Note that from the wall, the interface becomes horizontal and is coincident with the $X = 0$ plane, consistent with the above physical description of the large Bond number limit. Consider a force balance on the rectangular material body shown in Fig. 2.14. The body is drawn with sufficient length to meet the location where the interface becomes horizontal. Furthermore, the body has width W in the Z -direction (oriented into the figure) and is of height d in the X -direction, where d is the height that the meniscus rises above the $X = 0$ plane. Note that the body is drawn close to, but not intersecting, the solid plate, and so it lies completely within the liquid and air. The general force balance for the body in Fig. 2.14 is given by (2.52) which, to be consistent with the small capillary limit, is

written in dimensional form as

$$0 = \int_{S(t)} -P\mathbf{n} dS + \int_{V(t)} \rho g dV + \int_{C(t)} \sigma \mathbf{m} dC \quad (2.78)$$

In obtaining (2.78), we have utilized the constitutive relation (2.58) which introduces the surface tension.

We now proceed to evaluate the terms in the force balance. In order to determine the first integral in (2.78), the local pressure field given by (2.75a) is employed, which is rewritten in dimensional form as

$$P = P_R(t) - (\rho g)X \quad (2.79a)$$

where $P_R(t)$ is a time-dependent function arising as a result of integration. This function is evaluated by using (2.75b), noting that the interface far away from the wall has zero curvature and is coincident with the $X = 0$ plane. In that region, $1/R_m = 0$, and thus

$$P_R(t) = P_A \quad (2.79b)$$

We now evaluate the pressure integral, using the notation shown in Fig. 2.14. The pressure integrals on sides 3 and 4 cancel as they are both at atmospheric pressure and act in opposite directions. The pressure on side 2 is atmospheric

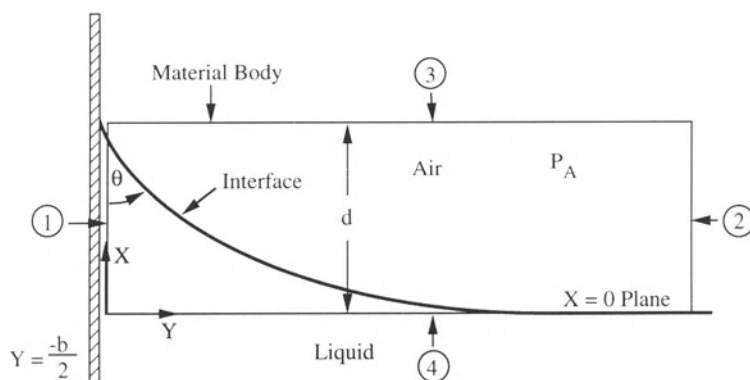


Figure 2.14 Material body used to analyze end effect in the large Bond number, low capillary number limit.

acting in the $-Y$ -direction, while on side 1 the pressure is hydrostatic given by (2.79), acting in the $+Y$ -direction. The resulting pressure integral is

$$\int_{S(t)} -P \mathbf{n} dS = -\frac{1}{2} \rho g d^2 W \hat{\mathbf{j}} \quad (2.80)$$

where $\hat{\mathbf{j}}$ is the unit vector oriented in the $+Y$ -direction. Let the volume of liquid which is lifted above the $X = 0$ plane be denoted as V_σ ; with this definition, the volume integral in (2.78) becomes

$$\int_{V(t)} \rho g dV = -\rho g V_\sigma \hat{\mathbf{i}} \quad (2.81)$$

Finally, we evaluate the line integral due to surface tension in (2.78). At the intersection of side 2 with the interface, the vector $\mathbf{m} = \hat{\mathbf{j}}$. At the intersection of side 1 with the interface, the vector \mathbf{m} is given in terms of the contact angle θ (as shown in Fig. 2.14):

$$\mathbf{m} = \hat{\mathbf{i}} \cos \theta - \hat{\mathbf{j}} \sin \theta$$

Both line integrals act along a line of length W , to yield

$$\int_{C(t)} \sigma \mathbf{m} dC = \sigma W (\hat{\mathbf{j}}(1 - \sin \theta) + \hat{\mathbf{i}} \cos \theta) \quad (2.82)$$

Substituting (2.80)–(2.82) into equation (2.78) and separating the $\hat{\mathbf{i}}$ and $\hat{\mathbf{j}}$ components yields the following result:

$$\hat{\mathbf{i}}: \quad V_\sigma = \frac{\sigma W \cos \theta}{\rho g} \quad (2.83a)$$

$$\hat{\mathbf{j}}: \quad d = \sqrt{\frac{\sigma}{\rho g}} \sqrt{2(1 - \sin \theta)} \quad (2.83b)$$

The force balance and result (2.83) indicate that it is the action of surface tension which provides the force necessary to oppose gravity and lift the fluid above the $X = 0$ plane shown in Fig. 2.14. Note that, in the derivation of (2.83), the shape of the interface was not considered; however, the fluid underneath the interface inside

the material body experiences a hydrostatic pressure less than atmospheric for $X > 0$, as can be seen from (2.79). This indicates that the interface itself must curve inward as drawn in Fig. 2.14, to be consistent with the way in which surface tension moderates a pressure drop, although the precise shape must be determined by solving the local equations (see Princen 1969).

For a given angle θ , the first square root in (2.83b) determines the height of rise of the fluid up the wall. The quantity

$$L_\sigma = \sqrt{\frac{\sigma}{\rho g}} \quad (2.84)$$

is called the capillary length, and is often used as a length scale in flow problems involving interfaces. With the definition (2.84), the Bond number in (2.73d) can be written as

$$Bo = \left(\frac{b}{L_\sigma} \right)^2 \quad (2.85)$$

where b again denotes the gap spacing in Fig. 2.13. We have already indicated that when the Bond number is large, the interface flattens, at least away from the walls. For a given material system, the height of rise along the plates shown in Fig. 2.14 is approximately the same regardless of the gap, as characterized by the capillary length L_σ in (2.84), provided that $b \gg L_\sigma$ (i.e., $Bo \gg 1$ in (2.85)). As the plate spacing is decreased such that $b \rightarrow L_\sigma$ (i.e., Bo is of order 1 in (2.85)) the end effects at each plate increasingly interact, and the region between them can no longer be approximated as being flat; thus, the reference pressure P_R in the fluid changes. Eventually, as b is further decreased such that $b \ll L_\sigma$ (i.e. $Bo \ll 1$ in (2.85)), surface tension effects dominate and the circular interface shape is approached. These limits on the interface shapes, for high and low Bond numbers at low capillary number, are shown in Fig. 2.15.

2.4.1.3 The limit of large capillary numbers

The above discussion on the effect of the capillary number and Bond numbers has been restricted

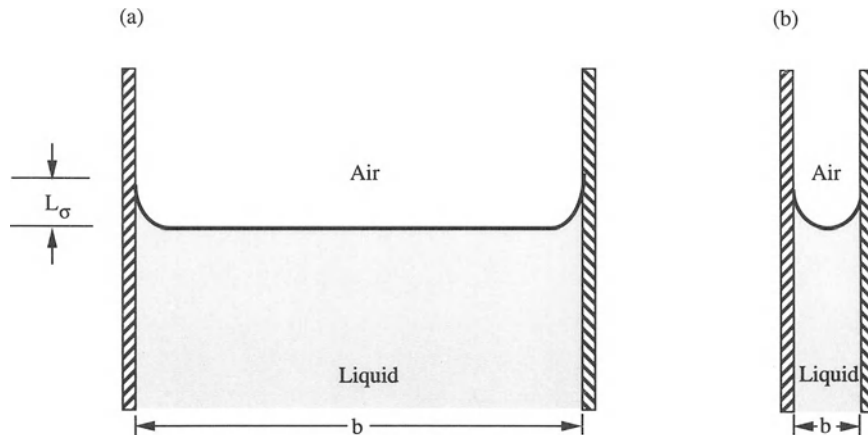


Figure 2.15 The effect of the Bond number on the interface shape in the low capillary number limit: (a) $Bo \gg 1$; (b) $Bo \ll 1$.

to low capillary numbers. For high capillary numbers, viscous forces dominate over surface tension forces, and thus the pressure scale chosen in (2.73) is not appropriate. Instead, the new dimensionless pressures are written as

$$p = \frac{Pb}{\mu U}, p_A = \frac{P_A b}{\mu U} \quad (2.86)$$

and with (2.86), equations (2.73a) and (2.73c) become

$$(p - p_A) - [\mathbf{n}_1 \cdot \bar{\tau}] \cdot \mathbf{n}_1 = \frac{1}{Car_m} \quad \text{at the interface} \quad (2.87a)$$

$$Re \left[\frac{\partial \mathbf{u}}{\partial t} + \mathbf{u} \cdot \nabla \mathbf{u} \right] = -\nabla p + \nabla^2 \mathbf{u} - St \hat{\mathbf{i}} \quad (2.87b)$$

where $St = \rho g b^2 / (\mu U)$ is called the Stokes number, which gives a ratio of gravitational to viscous forces. The important point to note in (2.87a) is that in the limit of infinite capillary number, the term including the mean radius of curvature disappears. For cases where the surface tension is identically zero (corresponding to Ca being infinite), we have already noted that the loss in the mean radius of curvature term dictates that boundary conditions at the contact line cannot be imposed. However, for large but finite capillary

number, the contact-angle boundary condition can still be imposed, but its effects are confined largely to the vicinity of the contact line, as it is in the large Bond number case discussed above. Finally, we note that for large capillary number, the pressure field can be quite complex and is far from hydrostatic, being governed by (2.87b).

2.4.1.4 Surface tension-induced pressure variations as a source of flow

For many practical cases, the flow field being analyzed does not fall into one of the two capillary and Bond number regimes just discussed. However, despite this fact, we can use the above discussion to assess qualitatively the effect of surface tension on the pressure in a fluid. Consider, for example, the case of a wavy air–liquid interface with surface tension as shown in Fig. 2.16. From (2.73a), it is evident that at moderate capillary numbers, viscous effects can be viewed as modifying the effect of the static-looking interfacial curvature on the pressure drop across the interface. Nevertheless, we can often qualitatively determine the pressure field in the fluid relative to atmospheric pressure by examining the curvature of the interface and viewing the pressure drop as being due to a static interface. For example, in Fig. 2.16, the pressures relative

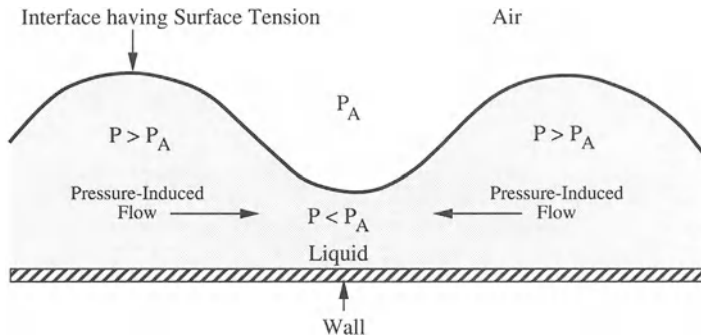


Figure 2.16 Qualitative pressures underneath a curved interface and the corresponding induced flow.

to atmospheric will be as indicated, even at moderate capillary numbers, and the resulting pressure gradients induced by such curvatures will provide the driving force for the indicated fluid motion.

2.4.2 IMPLICATIONS OF THE TANGENTIAL STRESS BALANCE AT THE INTERFACE

To understand the physics associated with the tangential components of the interfacial stress balance (2.72b,c), let us apply the dynamic boundary condition to a completely flat air–liquid interface. The coordinate system is as shown in Fig. 2.17 (the Z -direction, not shown, extends out of the figure), the interface is assumed to be located for all time at $Y = 0$, and there is no mass transfer across the interface. We will assume that the left-hand side of the interface experiences a higher temperature than the right-hand side, as shown in the figure. Furthermore, we will assume that the viscosity of the air is negligible and the air pressure is a constant, P_A . Let us denote the liquid as phase 1 in (2.72) and the air as phase 2. Where clarity is necessary, variables in the liquid phase are subscripted with a 1; otherwise, as all the dynamics is limited to the liquid phase, variables will be unsubscripted.

Recall that the surface tension of the liquid–air interface is a function of temperature, T , where typically $\partial\sigma/\partial T < 0$ (see (2.63) and associated discussion). Thus, the different temperatures at

the two ends of the domain will give rise to a surface tension gradient along the surface. Our goal is to assess the effect of such a surface tension gradient on the fluid flow; for purposes of discussion, we will restrict attention to incompressible Newtonian fluids governed by the constitutive relation (2.20b). For the domain as specified, we denote the unit outward normal vector to the liquid phase in the + Y -direction as $\hat{\mathbf{j}}$, and the two independent unit tangent vectors in the + X and + Z -directions as $\hat{\mathbf{i}}$ and $\hat{\mathbf{k}}$, respectively. To simplify the analysis, we will assume that the fluid is unbounded in the Z -direction and that liquid temperature varies only in the X -direction; thus there is no Z dependence in the problem.

Since the interface is flat, there are no curvature effects to motivate consideration of the normal stress balance at the interface. Instead, the heart of this model problem is the balance of the tangential stresses in the $\hat{\mathbf{t}}$ -direction, as described by (2.72b) with $\mathbf{t}_\alpha = \hat{\mathbf{i}}$. The terms in this equation are evaluated as follows. Because the viscosity of the air is assumed to be negligible, $\tau_2 = 0$; thus, the jump in tangential stress across the interface in Fig. 2.17 becomes

$$[\mathbf{n}_1 \cdot (\tau_2 - \tau_1)] \cdot \hat{\mathbf{i}} = [\hat{\mathbf{j}} \cdot (-\tau_1)] \cdot \hat{\mathbf{i}} = -[\tau_{1_{xy}} \hat{\mathbf{i}} + \tau_{1_{yy}} \hat{\mathbf{j}}] \cdot \hat{\mathbf{i}} = -\tau_{1_{xy}} \quad (2.88a)$$

where $\tau_{1_{xy}}$ is a component of the viscous stress tensor, which is expressed in terms of the $\hat{\mathbf{i}}$ and

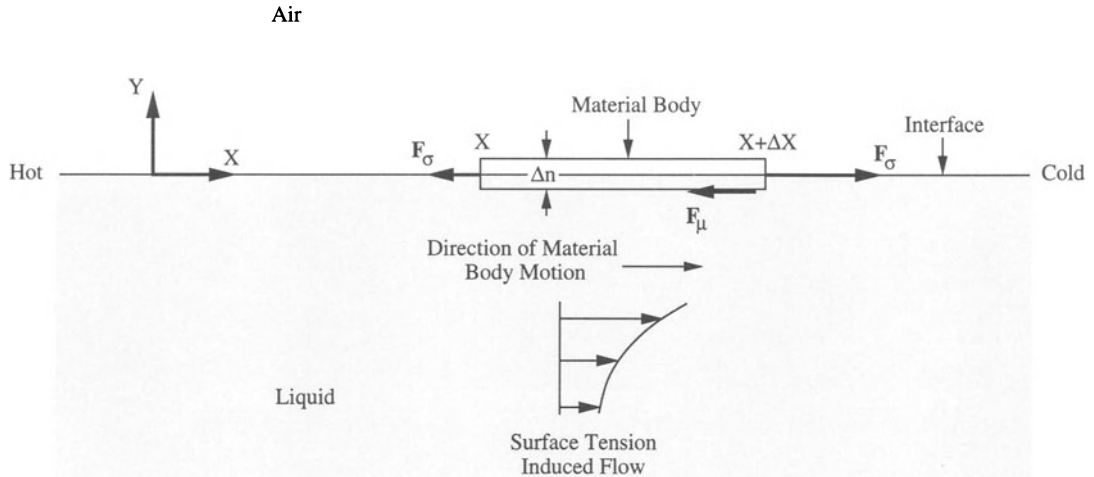


Figure 2.17 Flat interface on which dynamic boundary condition is applied. The action of forces in the X -direction is shown for a differential element of a surface. Here, F_σ and F_μ denote the surface tension and shear forces acting on the material body, where the direction and magnitude of the forces are as indicated by the vectors.

$\hat{\mathbf{j}}$ velocity components denoted respectively by U_X and U_Y , as

$$\tau_{1_{xx}} = \mu \left(\frac{\partial U_X}{\partial Y} + \frac{\partial U_Y}{\partial X} \right) \quad (2.88b)$$

Equation (2.88b) can be simplified by using the kinematic boundary condition (2.40). Along $Y = 0$, the kinematic condition yields $U_Y = 0$ for all X , implying that $\partial U_Y / \partial X$ is equal to zero. Using the definition (2.55), we obtain

$$\nabla_{II} = \nabla - \hat{\mathbf{j}}(\hat{\mathbf{j}} \cdot \nabla) = \frac{\partial}{\partial X} \hat{\mathbf{i}} + \frac{\partial}{\partial Z} \hat{\mathbf{k}}$$

Thus, the contribution of surface tension gradients to the tangential stress balance in the $\hat{\mathbf{i}}$ direction becomes

$$\nabla_{II} \sigma \cdot \hat{\mathbf{i}} = \frac{\partial \sigma}{\partial X} \quad (2.88c)$$

Equating (2.88b) and (2.88c) in accordance with (2.72b) yields the desired balance of tangential stresses at the interface:

$$\mu \frac{\partial U_X}{\partial Y} = \frac{\partial \sigma}{\partial X} \quad \text{at } Y = 0 \quad (2.89)$$

The result (2.89) indicates that viscous stresses balance the surface tension gradient along the free surface. To see this more clearly, consider a force balance on an element of the flat surface of length ΔX and width ΔZ , as shown in Fig. 2.17, where the thickness of the body, Δn , is negligible. For such a body, the force balance (2.53) applies; with the constitutive relation (2.58), the force balance is written explicitly as

$$\int_z^{z+\Delta Z} \int_x^{x+\Delta X} \hat{\mathbf{j}} \cdot (\mathbf{T}_2 - \mathbf{T}_1) dX dZ + \int_z^{z+\Delta Z} \sigma|_X (-\hat{\mathbf{i}}) dZ + \int_z^{z+\Delta Z} \sigma|_{X+\Delta X} \hat{\mathbf{i}} dZ = 0 \quad (2.90a)$$

Let us now simplify (2.90a) focusing attention on the tangential balance of forces, i.e., those in the X -direction. By assumption, there are no variations in flow in the Z -direction. Thus, as in (2.88) above,

$$[\hat{\mathbf{j}} \cdot (\mathbf{T}_2 - \mathbf{T}_1)] \cdot \hat{\mathbf{i}} = [(P_1 - P_A) \hat{\mathbf{j}} + -\hat{\mathbf{j}} \cdot \tau_1] \cdot \hat{\mathbf{i}}$$

$$= -\tau_{1_{xx}} = -\mu \left(\frac{\partial U_X}{\partial Y} \right) \quad (2.90b)$$

where we have utilized (2.18) in writing this expression. Substituting (2.90b) into (2.90a), the $\hat{\mathbf{i}}$ component of (2.90a) can be rewritten as

$$\begin{aligned} (\sigma|_{X+\Delta X} \Delta Z) \hat{\mathbf{i}} - (\sigma|_X \Delta Z) \hat{\mathbf{i}} \\ = \left(\int_X^{X+\Delta X} \mu \frac{\partial U_x}{\partial Y} dX \right) \Delta Z \hat{\mathbf{i}} \quad (2.90c) \end{aligned}$$

By inspection, we see that the result (2.90c) is an integrated form of the local condition (2.89). This result can be simply expressed as

$$\mathbf{F}_\sigma|_{X+\Delta X} - \mathbf{F}_\sigma|_X = -\mathbf{F}_\mu \quad (2.90d)$$

where \mathbf{F}_σ and \mathbf{F}_μ are the surface tension and viscous shear forces in the X -direction acting on the material body, respectively, and are defined by the terms in corresponding locations in (2.90c). As indicated by (2.90d) and as indicated by the vectors drawn in Fig. 2.17, the net surface tension force on the material body must be opposed by the retarding shear force due to fluid viscosity. Such a shear force can be generated only if there is a gradient in fluid velocity in (2.90c), which implies that fluid flow occurs.

Because surfactants reduce the surface tension of the interface, just as an increase in temperature does (see (2.63)–(2.66) and associated discussion), we can use the above reasoning to explain how the addition of a surfactant to a locality on the interface can also induce interfacial motion radially outward from the point where the surfactant is introduced. But in coating flows, surfactants are more often responsible for damping out flow disturbances, by imparting a rigidity to the interface with respect to tangential motion.

The retardation of interfacial flows by surfactants can be explained by considering what happens if our fluid layer in Fig. 2.17 contains some surface-active solute of molar concentration C_i . Before a temperature gradient is imposed along the interface to induce flow, the interface is in chemical equilibrium with the bulk liquid, which means that the surface concentration of solute, Γ_i , is in equilibrium with the bulk concentration, and a relationship such as (2.65) is satisfied. When the temperature gradient is imposed on the interface, the resulting fluid

motion will convect the solute in the system, and the effect of this convective transport may be assessed with the aid of (2.68). For the current problem, we are assuming that the interface is flat, there is no flow in the Z -direction and the surfactant does not transfer into the air (i.e., the surfactant is non-volatile); thus (2.68) is written as

$$U_x \frac{\partial \Gamma_i}{\partial X} = -\Gamma_i \frac{\partial U_x}{\partial X} - D_i \frac{\partial C_i}{\partial Y} \quad (2.91)$$

where the third term of (2.91) is the diffusive flux of species i to the interface from the liquid phase, obtained by employing Fick's law (2.69a) (after noting that the mass concentration ρ_i is related to the molar concentration C_i by the molecular weight of the species i).

The surfactant affects the resultant fluid flow only if the right-hand side of (2.91) is nonzero, as variations of Γ_i in the X -direction are required to adjust the magnitude of the surface tension gradient $\partial\sigma/\partial X$ in (2.89) through equation (2.63). Since the system was originally at chemical equilibrium, C_i was independent of position. Thus, nonzero values of $\partial\Gamma_i/\partial X$ must derive from accelerations or decelerations of the interface (i.e., nonzero values of $\partial U_x/\partial X$). Based on this observation, we can conclude that the presence of surfactant will have no effect on the flow if the fluid layer is unbounded (so that Γ_i is at its equilibrium concentration at either end of the system) and the flow in the X -direction is uniform.

In practice, coating flows are usually bounded or involve regions where fluid–fluid interfaces are stretched or compressed. Even in the case where a liquid layer issues from a two-dimensional slot and forms a liquid curtain, such as shown in Fig. 2.3, the interface is bounded in that it originates at the slot exit. In the curtain itself and close to the slot, surfactant is adsorbing into the interface from the liquid phase, because the interface has not had an opportunity to equilibrate with the bulk liquid, and the interface is accelerating in reaction to the sudden transition from the no-slip condition in the slot to zero viscous stresses from the air.

Returning to Fig. 2.17, we can introduce a

retarding effect of surfactants on the flow by adding a solid wall to our system, downstream of the material body, as shown in Fig. 2.18. Now, as the interface and the liquid below move in the positive X -direction due to the imposed temperature gradient, surfactant is carried downstream where it accumulates near the solid wall. The explicit details of the spatial variation of surfactant in the interface ($\partial\Gamma_i/\partial X$) near the wall is determined by the recirculation flow that must occur in this region. For the purposes of our discussion, it is only important to recognize that surfactant accumulates because the interface must decelerate as it approaches the wall. Thus, $\partial U_x/\partial X$ is negative and $\partial\Gamma_i/\partial X$ is positive in accordance with (2.91). If the surfactant is soluble, its high interfacial concentration near the wall will promote desorption of surfactant into the bulk liquid to compensate for the steady convective transport of surfactant in the interface from upstream. By this mechanism, a steady-state concentration profile of surfactant is established in the interface where $\partial\Gamma_i/\partial X > 0$.

Now, with the force balance ideas used in Fig. 2.17, let us examine how this concentration gradient can impart a rigidity to the interface through its effect on surface tension. Consider again a thin material body with sides ΔX and ΔZ in the interface, now positioned near the end wall as shown in Fig. 2.18. As the geometry and assumptions are the same as in the previous example, the general force balance given in (2.90) is valid. The one feature that is new in this problem (as compared with the discussion of Fig. 2.17) is that surface tension is now a function of both temperature and interfacial concentration, and both are functions of X . If we assume that the length of the body ΔX is small, then we can approximate the surface tension at $X + \Delta X$ by a Taylor series expansion:

$$\sigma|_{X+\Delta X} \sim \sigma|_X + \left(\frac{\partial\sigma}{\partial T}\right)_X \Delta T + \left(\frac{\partial\sigma}{\partial\Gamma_i}\right)_X \Delta\Gamma_i \quad (2.92a)$$

where

$$\Delta T = T|_{X+\Delta X} - T|_X \text{ and } \Delta\Gamma_i = \Gamma_i|_{X+\Delta X} - \Gamma_i|_X$$

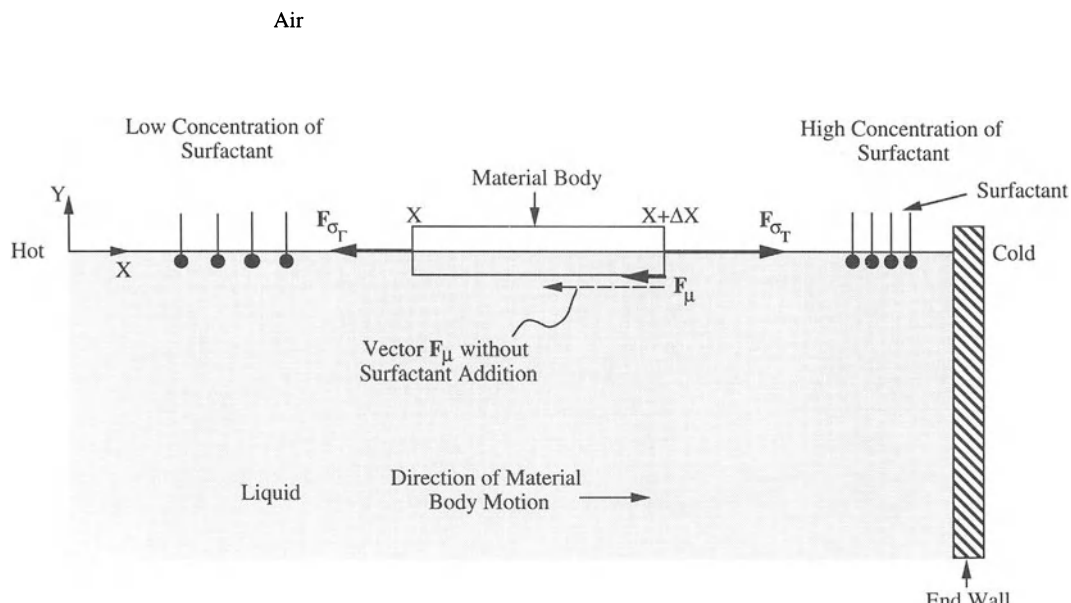


Figure 2.18 Force balance on a differential element of the surface, demonstrating the effect of surfactant addition when there is a temperature-induced surface tension gradient. Here, F_{σ_T} and F_{σ_r} denote the net surface tension forces due to temperature and surfactant gradients, respectively, while F_μ is the shear force

Thus, equation (2.90c) becomes

$$\begin{aligned} \left(\frac{\partial\sigma}{\partial T}\right)_x \Delta T \Delta Z \hat{i} + \left(\frac{\partial\sigma}{\partial \Gamma_i}\right) \Delta \Gamma_i \Delta Z \hat{i} \\ = \mu \left(\frac{\partial U_x}{\partial Y}\right)_x \Delta X \Delta Z \hat{i} \quad (2.92b) \end{aligned}$$

which, upon inspection, is seen to be identical to (2.89) once the chain rule of differentiation is applied and terms are rearranged.

We can express the result (2.92b) simply as

$$\mathbf{F}_{\sigma_T} + \mathbf{F}_{\sigma_\Gamma} = -\mathbf{F}_\mu \quad (2.92c)$$

where \mathbf{F}_{σ_T} and $\mathbf{F}_{\sigma_\Gamma}$ are the net surface tension forces due to temperature and surfactant gradients acting on the material body in the X -direction, respectively, and are defined by the terms in corresponding locations in (2.92b). Note that it is the use of the force balance (2.90c), coupled with the Taylor series expansion (2.92a), that allows the interpretation of \mathbf{F}_{σ_T} and $\mathbf{F}_{\sigma_\Gamma}$ as being net forces. As an increase in surfactant concentration decreases surface tension, the quantity $\partial\sigma/\partial\Gamma_i$ is negative; recall that the quantity $\partial\sigma/\partial T$ is negative as well. Furthermore, $\Delta T < 0$, indicating that the first term on the left-hand side of (2.92b) is a positive quantity; consequently \mathbf{F}_{σ_T} is oriented in the direction as shown in Fig. 2.18. The temperature gradient thus provides the driving force for flow. On the other hand, $\Delta\Gamma_i > 0$, and thus the second term on the left-hand side of (2.92b) is negative.

Consequently, $\mathbf{F}_{\sigma_\Gamma}$ is oriented in the direction as shown in Fig. 2.18, indicating that the presence of surfactant gives rise to a surface tension force which opposes \mathbf{F}_{σ_T} . Thus, the shear force \mathbf{F}_μ , and the resulting temperature-induced flow, is reduced through surfactant addition. Because surface tension is several orders of magnitude more sensitive to changes in surfactant concentration than to changes in temperature, it takes very little surfactant to diminish significantly or even eliminate a flow produced by a temperature gradient.

It should be noted that the importance of surfactants to coating flows is not restricted to damping out surface-tension-driven flows due to temperature gradients. Any local disturbance

which produces a dilation or compression of the interface will produce a redistribution of surfactant and thus generate surface-restoring forces that will tend to damp out these disturbances. We close this discussion by noting that in some cases surface contamination which may occur, for example, due to airborne particles, can play the role of a surfactant in a system. The presence of such contaminants may lead to an unanticipated Marangoni flow in a coating process while the fluid layers are still mobile; this flow can ultimately disturb the final layer thicknesses on the moving substrate. Thus, while we can take advantage of the surface-tension dependence on surfactant concentration to enhance the quality of a coating by damping out undesired flows, this same sensitivity requires that surface contamination be controlled in a coating process.

2.4.3 COMBINED EFFECT OF THE NORMAL AND TANGENTIAL COMPONENTS OF THE INTERFACIAL STRESS BALANCE

The model problems presented in Sections 2.4.1 and 2.4.2 illustrate how the interface acts in two principal ways, as embodied in the dynamic boundary condition. First, the normal component of the dynamic boundary condition indicates that surface tension causes a jump in pressure across a curved interface, where the sense of the pressure drop can be obtained by using intuition about the curvature of a pressurized container (or by rigorously using the curvature definition in (2.59b) in conjunction with (2.59a)). The addition of fluid motion complicates, but does not invalidate, this physical interpretation. In regard to the pressure drop induced by surface tension, the interface can be viewed, in some sense, as an elastic impermeable membrane. Furthermore, as suggested in Fig. 2.16, interfacial curvatures in a problem can act to produce a pressure gradient and induce motion. We have also seen that surface tension gradients can act to induce fluid flow or to oppose an existing fluid motion. In this respect, it is the fact that the fluid points are free to move along the interface which gives rise to such effects.

Thus far, the normal and tangential components of the dynamic boundary condition have been examined separately in different model problems. We now examine a model problem which explicitly demonstrates how these components operate together and affect fluid flow. Let us consider the case where a Newtonian liquid layer of constant thickness covers a stationary horizontal solid surface, as shown in Fig. 2.19. Let the interface be located at $Y = H$ for all time, where the coordinate system is as indicated in the figure (the Z -direction, not shown, is oriented out of the figure), and there is no mass transfer across the interface. A linear temperature gradient is applied to the bottom surface, which in turn induces a temperature variation in the liquid and the interface. Let the fluid be of high thermal diffusivity (heat transfers extremely easily by conduction), and assume that the flow which occurs is slow, so that convective heat transport is negligible relative to conduction. In this limiting case, the flow field is uncoupled from the temperature field, and it can be shown that the temperature in the fluid and along the air–liquid interface is identical to the linear temperature variation along the wall. Thus, we write the temperature variation everywhere in the domain as

$$T = T_0 - KX$$

where it is assumed that the constant K is greater than zero, i.e., the left-hand side of the domain is hotter than the right-hand side, as shown in

Fig. 2.19. Let us also assume that the surface tension decreases linearly with increasing temperature as

$$\sigma = \sigma_0 - \beta(T - T_0)$$

where β is a positive constant, and thus

$$\sigma = \sigma_0 + \beta KX \quad (2.93)$$

The goal is to determine the motion within the liquid induced by such a surface tension gradient. We will assume that the length of the domain, L , is large compared with the film thickness H . Thus, on the length scale H , the domain looks infinite in the X -direction, and it is reasonable to assume that the motion of the fluid is everywhere parallel to the solid surface, i.e. the component of velocity in the Y -direction, U_Y , is zero everywhere in the liquid. Furthermore, we will assume that there are no velocity variations in the Z -direction, and the velocity component in that direction, U_Z , is zero. At this point, we will not specify constraints on the ends of the domain in the X -direction, but instead these will be examined through the course of the problem.

Based on the above assumptions, we begin by writing $U_X = U_X(X, Y)$. The continuity equation (2.7) for this case is

$$\frac{\partial U_X}{\partial X} = 0$$

which implies that $U_X = U_X(Y)$. With this sim-

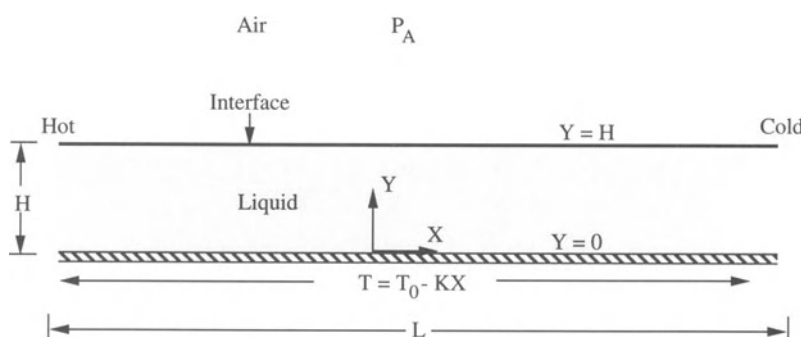


Figure 2.19 Liquid layer of constant thickness over a stationary, horizontal solid surface which is also heated.

plification, the Navier–Stokes equations (2.21) become, in component form,

$$\hat{i}: \frac{\partial P}{\partial X} = \mu \frac{d^2 U_x}{dY^2} \quad (2.94a)$$

$$\hat{j}: \frac{\partial P}{\partial Y} = -\rho g \quad (2.94b)$$

$$\hat{k}: \frac{\partial P}{\partial Z} = 0 \quad (2.94c)$$

The no-slip condition at the solid surface is

$$U_x = 0 \quad \text{at} \quad Y = 0 \quad (2.95a)$$

and the dynamic boundary condition at the free surface is,

$$P = P_A \quad \text{at} \quad Y = H \quad (2.95b)$$

$$\mu \frac{\partial U_x}{\partial Y} = \frac{\partial \sigma}{\partial X} = \beta K \quad \text{at} \quad Y = H \quad (2.95c)$$

where we have used the results for the flat interface (2.89) derived previously, as well as (2.93). We note here that, because the flow is always parallel to the solid surface and interface, the kinematic boundary condition at both surfaces is automatically satisfied, and so it is not explicitly written.

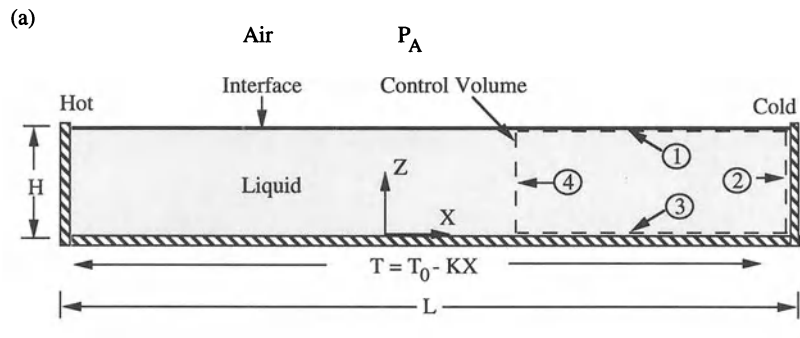
We begin by solving for the pressure field. From (2.94c), the pressure is not Z -dependent, and thus $P = P(X, Y)$. Integrating (2.94b) and applying (2.95b), we find that the pressure field is purely hydrostatic:

$$P = P_A + \rho g(H - Y) \quad (2.96a)$$

Thus, (2.94a) becomes

$$\frac{d^2 U_x}{dY^2} = 0$$

which when integrated, subject to (2.95a) and



(b)

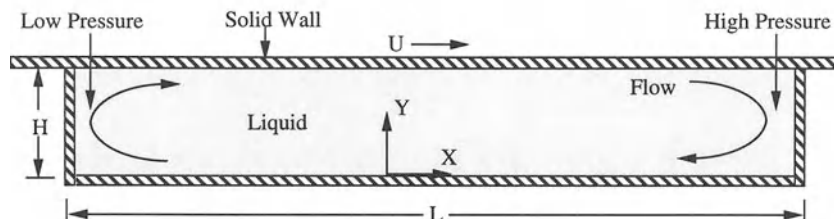


Figure 2.20 Effect of placing end walls on the domain shown in Fig. 2.19: (a) control volume on which mass is conserved; (b) configuration where a solid plate replaces the interface as a means for driving flow.

(2.95c), yields the desired result:

$$U_x = \frac{\beta K}{\mu} Y \quad (2.96b)$$

We note here that if, in the same geometry, a solid plate moving in the X -direction with a speed U replaces the air–liquid interface, and the pressure at the two ends of the domain in the X -direction are equal and hydrostatic, then the solution (2.96b) is valid with the quantity U/H replacing the group $\beta K/\mu$ in (2.96b). Thus, the action of a surface tension gradient along the surface acts as a solid plate which drags fluid along. Let us suppose, however, that we consider a domain which is closed at the ends as shown in Fig. 2.20a. Although we viewed the domain in this problem as being infinite on the length scale H , we acknowledge that the domain does indeed have a finite length, and the fact that the domain is closed on the ends will have an effect on the velocity field. The effect of end walls can be incorporated via a mass balance on control volume extending up to the end wall as shown in Fig. 2.20a. Here, the kinematic boundary conditions along sides 1, 2 and 3 of the domain dictate that the normal velocity at every point along these sides is identically zero; consequently, to conserve mass, there is no net flow along side 4 of the body, and

$$\int_0^H U_x dY = 0 \quad (2.97)$$

Clearly, (2.96b) does not satisfy (2.97) unless there is no flow at all. Thus, (2.96b) is not an appropriate solution for the case where ends are placed on the problem.

To understand the implication of this fact more fully, let us consider the identical configuration where the air–liquid interface is replaced with a solid wall, moving at a speed U , for the case where the domain is closed on the ends (see Fig. 2.20b). The governing equations for such a case are given by (2.94), subject to (2.95a), the no-slip condition at the moving wall (i.e. $U_x = U$), and the no-flux constraint (2.97). The solution

for the pressure field and velocity field under such conditions yields

$$P = \frac{6U\mu}{H^2} X + P_R - \rho g Y \quad (2.98a)$$

and

$$U_x = \frac{U}{H^2} (3Y^2 - 2HY) \quad (2.98b)$$

where P_R is a constant reference pressure in the fluid. This result indicates that, when a solid plate replaces the interface, the pressure in the fluid increases with X when the domain is closed at the ends. This is consistent with the physical intuition that fluid must turn around near the ends of the domain, where a higher pressure affords the force necessary to do so (Fig. 2.20b). When a flat interface is present (previous case), it is not possible for such a pressure profile to develop, as the dynamic condition (2.95b) will not allow pressure variations in the X -direction. The interface in the above cases sets both the pressure in the fluid (through the normal component of the dynamic condition) as well as the motion of the fluid (through the tangential component). On the other hand, the solid surface does not moderate a pressure drop and only induces motion. This is an important distinction between interface and confined flow problems.

The question then arises as to how the interface compensates for the requirement of fluid turning around when there are end constraints in the above problem. The answer to the question is that our assumption about the shape and orientation of the interface is in error. Because the channel is long relative to the thickness of the film, it is generally not feasible to develop interfacial curvatures that can provide the pressure gradient needed to drive the recirculation through the action of surface tension in the normal force balance. Rather, the interface remains relatively flat, but it becomes inclined to the horizontal as shown in Fig. 2.21, the film thickness being greater at the colder end of the channel, with the slope of the interface providing the gradient in hydrostatic pressure needed to drive the

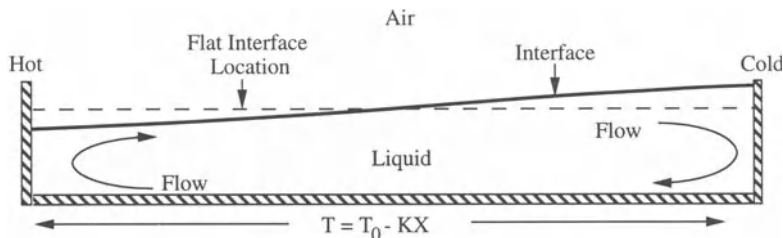


Figure 2.21 Interfacial distortion which can induce backflow to conserve mass for the domain shown in Fig. 2.20a.

recirculation through the action of gravity. It is possible, however, to imagine a physical situation similar to Fig. 2.19 where interfacial curvature and surface tension provide the needed pressure gradient to produce the recirculatory flow. For example, in the absence of gravity, such as on a space station, any recirculating flow process involving liquids with fluid interfaces will contain such interfacial curvature effects. We note here that if the slope of this interface is small, the above described physics can be predicted by utilizing the hydrodynamic theory of lubrication, introduced in Section 2.3.1, and presented in more detail in Chapter 8.

From a more practical viewpoint, in a gravitational field, the role of interfacial curvature will become important in situations where the Bond number becomes small (i.e., $Bo < 1$); in other words, the lateral bounds on the fluid flow would have to be of the same order of magnitude as the thickness of the layer. This situation is realized in coating flows with interfacial waves whose wavelength is of the same scale as the film thickness. For more complicated flow fields, the effect of gravity in the above arguments is augmented via competition with fluid inertia and

viscous forces in the equation of motion, which also compete with surface tension forces through the dynamic boundary condition.

REFERENCES

- Adamson, A. W. 1990. *Physical Chemistry of Surfaces*. 5th edn. New York: Wiley-Interscience.
- Derjaguin, B. V., Churaev, N. V. and Muller, V. M. 1987. *Surface Forces*. New York: Plenum. See also Derjaguin, B. V. 1989. *Theory of Stability of Colloids and Thin Films*. New York: Plenum.
- Dussan, V. E. B. 1979. On the spreading of liquids on solid surfaces: static and dynamic contact lines. *Ann. Rev. Fluid Mech.* **11**: 371–400.
- Princen, H. M. 1969. Shapes of interfaces, drops, and bubbles. In *Surface and Colloid Science*, Volume 2, ed. E. Matijevic, pp. 1–84. New York: Wiley-Interscience.
- Schlichting, H. 1979. *Boundary Layer Theory*. 7th edn. New York: McGraw-Hill.
- Scriven, L. E. 1960. Dynamics of a fluid interface: equation of motion for Newtonian surface fluids. *Chem. Engng Sci.* **12**: 98–108.
- Slattery, J. C. 1967. General balance equation for a phase interface. *Indust. Engng Chem. Fund.* **6**: 108–115; *ibid.* 1968. **7**: 672.
- Whitaker, S. 1968. *Introduction to Fluid Mechanics*. New Jersey: Prentice-Hall.

WETTING: STATIC AND DYNAMIC CONTACT LINES

3

Terence D. Blake and Kenneth J. Ruschak

3.1 STATIC AND DYNAMIC WETTING IN COATING PROCESSES

Wetting is basic to coating. Initially air contacts the solid, and during coating the liquid displaces the air from the moving solid surface so that none is visible in the coated film. Thus, coating is a process of dynamic wetting. For uniform coating, the wetting line must remain straight and advance steadily. At sufficiently high speeds, however, the wetting line becomes segmented and unsteady as a thin air film forms between the solid and liquid. The air film disrupts the uniformity of the coated film, and often air bubbles appear in the coating. Dynamic wetting failure limits coating speed.

Static wetting also affects the coating process, though less directly. There is a need to control where the liquid spreads. Leakage of liquid from the applicator or coated surface can produce contamination and waste. If the wetting lines at the edges of the coated film migrate, the width changes and the uniformity at the edges degrades.

The intent of this chapter is to present results for static and dynamic wetting that are applicable to coating processes, to illustrate their use, and to indicate their limitations. Attention is restricted to liquid/air/solid systems. The essentials of static wetting are covered first, because the theory for dynamic wetting has developed as a generalization of the static case. Whereas the physics of static wetting is well enough developed for many

applications, that of dynamic wetting is uncertain. In practical coating processes, the speed limits imposed by dynamic wetting failure are usually determined empirically. Nevertheless, the known features and trends of dynamic wetting can be useful.

Static and dynamic wetting have been reviewed from a more fundamental perspective by Dussan V. (1979), de Gennes (1985), Schrader and Loeb (1992), and Berg (1993). Adamson (1982) is a basic resource for general surface chemistry. The closely related topic of capillary hydrodynamics is extensively developed in books by Miller and Neogi (1985) and Levich (1962).

Coating flows are of sufficiently small scale that capillary forces are usually important. The surface tension of the liquid/air interface, σ , characterizes the magnitude of capillary forces. If R is the characteristic radius of curvature of a meniscus, then pressures due to surface tension are of order σ/R . Pressures due to the gravitational field are of order $\rho g R$, where ρ is the density of the liquid and g the gravitational acceleration. If capillary and gravitational pressures are in balance, then the characteristic radius of curvature is the capillary length, $L_c = \sqrt{(\sigma/\rho g)}$. The length scales R and L_c are often compared through the Bond number, $Bo = \rho g R^2/\sigma = (R/L_c)^2$. For large Bo , surface tension has negligible influence on meniscus shape. For small Bo , the variation of hydrostatic pressure has negligible influence. If

there is flow with a characteristic speed U , the viscous pressures are of order $\mu U/R$, where μ is viscosity, and capillary forces are important when the capillary number, $Ca = \mu U/\sigma$, is of order unity or smaller. Similarly, inertial pressures are of order ρU^2 , and capillary forces are important when the Weber number, $We = \rho U^2 R/\sigma$, is of order unity or smaller. In a coating flow, Bo is not likely to exceed unity, but Ca and We can be large or small, with significant implications for dynamic wetting.

3.2 STATIC MENISCI AND STATIONARY WETTING LINES

When there is no flow, the Young–Laplace equation governs meniscus shape (Chapter 2). Surface tension supports a pressure difference across a curved meniscus, with the higher pressure on the concave side.

$$2\sigma\mathcal{H} = P - P_A \quad (3.1)$$

Here P is the pressure in the liquid, P_A the pressure in the air, and \mathcal{H} the mean curvature, positive for liquid on the concave side of the meniscus. The pressure in the liquid is hydrostatic, increasing linearly in the direction of gravity. The pressure in the less dense air is sensibly uniform. If $Bo \ll 1$, then the pressure in the liquid can be considered uniform as well, and the meniscus has a uniform mean curvature.

Physical insight into the Young–Laplace equation follows from considering the pressure inside a small liquid drop of radius R . For $Bo \ll 1$, the drop is spherical. A balance of forces on one hemisphere of the drop yields the relationship between the pressure inside the drop and its radius. The pull of surface tension is tangent to the meniscus at the equator and so is $2\pi R\sigma$, the circumference at the equator times the value of surface tension. The ambient pressure exerts no net force, and so the net pressure force on the hemisphere is $(P - P_A)\pi R^2$, the gage pressure in the liquid times the cross-sectional area at the equator. Equating these forces gives $(P - P_A) = 2\sigma/R$, where $1/R$ is the mean curvature of the sphere.

As a result of the curvature term, the Young–Laplace equation is a nonlinear, second-order, partial differential equation. One boundary condition is required at the edge of a meniscus. Usually, the static contact angle is prescribed where the meniscus intersects a solid surface.

3.2.1 THE STATIC CONTACT ANGLE

Under ideal conditions, a liquid at rest intersects a solid at a unique angle (Fig. 3.1). The static contact angle θ_E is the angle at which the meniscus intersects the solid as measured through the liquid. The angle is measured in the plane defined by the unit vector normal to the meniscus and that normal to the solid. Young's equation relates θ_E and the surface tension of the liquid to the surface tensions of the solid/liquid and solid/air interfaces for conditions of thermodynamic equilibrium and a perfectly flat, homogeneous solid surface. With σ_{SL} the surface tension of the solid/liquid interface and σ_{SA} that of the solid/air interface, Young's equation is

$$\sigma \cos(\theta_E) = \sigma_{SA} - \sigma_{SL} \quad (3.2)$$

The contact angle thus defined is that for which no change in free energy accompanies a virtual displacement of the wetting line.

If the surface tension of the solid/air interface exceeds that of the solid/liquid interface by more than the surface tension of the liquid, then the liquid spontaneously spreads on the solid to form a film. Such behavior, often called complete wetting, is an indication of strong intermolecular forces of attraction between the liquid and solid. These forces give rise to a pressure, the disjoining

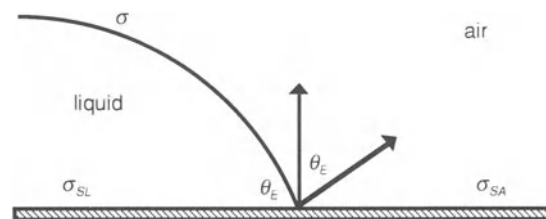


Figure 3.1 Equilibrium wetting line and contact angle.

pressure, which opposes film thinning. Disjoining pressures may have components arising from both short-range and long-range molecular forces. The former include polar interactions such as hydrogen bonds, while the latter comprise van der Waals dispersion forces. A completely wetting liquid spontaneously spreads by means of a precursor film that moves ahead of the main body of the liquid. For low-viscosity liquids like water on strongly polar substrates like glass, disjoining pressures are high and the precursor film may spread at velocities up to 0.1 m/s. Nevertheless, such rapid spreading is uncommon, and precursor films are therefore of limited significance to industrial coating processes.

The contact angle can be measured directly using low-power optics or computed from measurement of the force exerted on the solid by the meniscus. It can also be inferred by fitting a measured meniscus profile to a solution of the Young–Laplace equation and computing the angle of intersection with the surface of the solid.

3.2.2 CONTACT-ANGLE HYSTERESIS

According to Young's equation, the contact angle is a unique property of the solid/liquid/air system under consideration. In practice, however, a range of contact angles is usually possible, and this effect is called contact-angle hysteresis. Two generally accepted causes of hysteresis are roughness and surface heterogeneity, as reviewed by Blake and Haynes (1973) and, more recently, by Johnson and Dettre (1993). For rough surfaces, Young's equation may still apply on the scale of the roughness, but the apparent contact angle measured on the macroscopic scale usually differs from that existing on the microscopic scale. For heterogeneous surfaces, there cannot be a unique contact angle. Microscopic surface roughness and heterogeneity make possible multiple equilibrium configurations which appear as hysteresis on the macroscopic scale. Jansons (1985) has developed the mathematics relating the microscopic and macroscopic contact angles for nonideal surfaces.

Quantifying the extent of hysteresis requires

measurement of the so-called advancing and receding contact angles. These terms imply motion and are misleading when applied to the static case (Huh and Scriven 1971), but the usage is firmly established. The advancing angle θ_A is the largest contact angle achievable before the wetting line begins to move in the direction of the air phase. The receding contact angle θ_R is the smallest contact angle achievable before the wetting line begins to move in the direction of the liquid phase. A measurement is usually made by causing the wetting line to move and determining the angle once movement has ceased.

Young's equation (3.2) provides a theoretical basis for the contact angle but is of little direct practical use because the surface tension of the solid cannot be measured directly and is usually subject to considerable uncertainty. In addition, the solids encountered in practice seldom meet the equation's assumptions, as evidenced by the nonuniqueness of the contact angle. So, θ_A and θ_R are usually the contact angles that are experimentally determined, while θ_E can be difficult or impossible to determine and relate to θ_A and θ_R . Even experimental measurement of θ_A and θ_R is sometimes troublesome: chemical species such as surfactants may diffuse among the phases, porous surfaces may draw in liquid by capillary action, or the liquid and solid may react chemically. As an example, we have attempted to measure the contact angle of water on a dried coating of gelatin, which sorbs water in a fraction of a second (Joos 1992). The wetted gelatin swells, and the wetting line, at the boundary between the dry and wetted areas, sticks and shows massive hysteresis. Once it breaks free, the wetting line moves a considerable distance before coming to rest. In this case, the measurement and interpretation of the advancing contact angle are at best uncertain.

Even on uncomplicated surfaces, poor measuring technique may overestimate hysteresis. Equilibrium must be achieved before measurement is made. A common mistake is to take measurements while the wetting line is in slow but detectable motion. Wetting line speeds as small as 10 $\mu\text{m}/\text{s}$ can cause the contact angle to change

significantly from its static value and become a dynamic contact angle.

In general, hysteresis reduces wetting line mobility. The wetting line does not move toward the air if the contact angle is less than the advancing contact angle or toward the liquid if the contact angle is greater than the receding angle. At the wetting line of a static meniscus, the contact angle θ can therefore assume any value between θ_A and θ_R :

$$\theta_R \leq \theta \leq \theta_A \quad (3.3)$$

If the solid has an edge, the wetting line may preferentially locate along it (Oliver, Huh and Mason 1977). In effect, an edge augments hysteresis and thereby further reduces wetting-line mobility. Fig. 3.2 shows a wetting line positioned on an edge with included angle γ . The wetting line remains on the edge for a range of contact angles given by Gibbs' inequality

$$\theta_R \leq \theta \leq \theta_A + 180^\circ - \gamma \quad (3.4)$$

The sharper the angle, the greater the apparent hysteresis. In the design of coating applicators, edges are commonly exploited to 'pin' a wetting line.

3.2.3 EXAMPLES OF STATIC MENISCI WITH A WETTING LINE

Except for special cases, the Young–Laplace equation cannot be solved in closed form. Two applications follow showing how the static contact angle can affect the equilibrium configuration of the liquid. In the first example, the contact angle determines the extent of spreading of a liquid. In the second example, the contact angle can be inconsistent with meniscus shape so that no equilibrium configuration is possible; the wetting line therefore moves giving rise to a dynamic contact angle.

3.2.3.1 Application to capillary rise and wicking

A simple example of capillary hydrostatics relevant to coating operations is meniscus rise in a capillary tube (Fig. 3.3). The tube is inclined at an angle β to the horizontal, and one end contacts a pool of liquid. The inside radius of the capillary R_C is sufficiently small ($Bo \ll 1$) that the variation in hydrostatic pressure along the meniscus is negligible. In this case, the meniscus

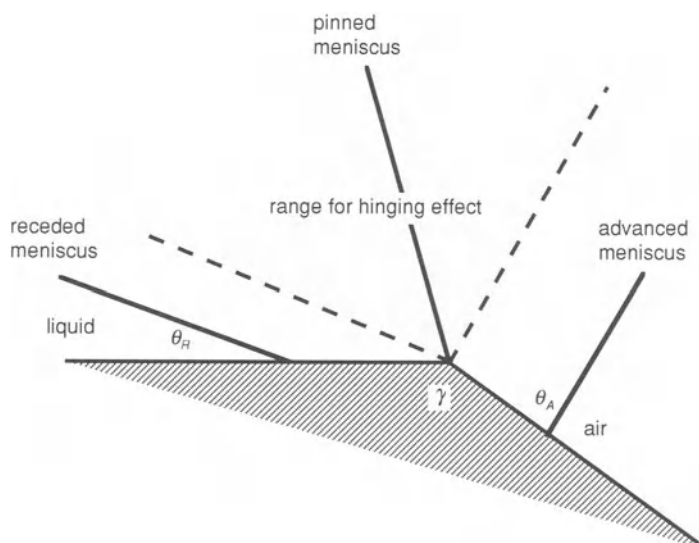


Figure 3.2 Conditions for a wetting line to advance or retreat from an edge.

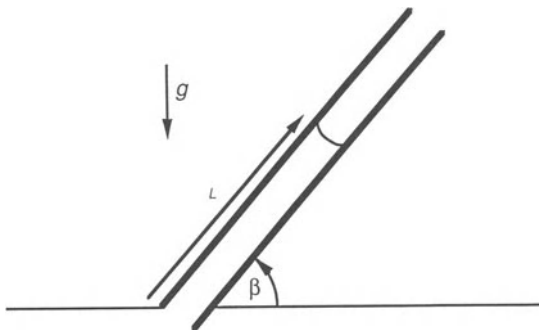


Figure 3.3 The rise of a meniscus in a capillary tube.

is a spherical cap of radius R , and the Young–Laplace equation (3.1) is simply $2\sigma/R = P - P_A$. The contact angle, presumed constant along the wetting line, determines the radius as $R_C/\cos\theta$, where the contact angle θ satisfies condition (3.3). So, the pressure in the liquid at the meniscus is below atmospheric by $2\sigma \cos\theta/R_C$. The equilibrium distance of the meniscus along the capillary from the surface of the pool, L_∞ , must be consistent with the hydrostatic pressure field in the liquid. Equating the pressure drop across the meniscus to the hydrostatic pressure drop between the pool surface and the meniscus gives

$$L_\infty = \frac{2\sigma \cos\theta}{\rho g R_C \sin\beta} \quad (3.5)$$

Note that the meniscus is above the surface of the pool only for $\theta < 90^\circ$, in which case the liquid is said to wet the surface of the capillary. Because of contact-angle hysteresis, L_∞ is larger if the meniscus falls toward its equilibrium position than if it rises; this is because $\theta_R < \theta_A$. The displacement of the meniscus along the capillary is large for low angles of inclination and is unbounded for a horizontal capillary. The displacement also increases with decreasing capillary radius.

The wicking of liquid through narrow cracks and crevices is a mechanism by which liquid can spontaneously move long distances and leak from coating hardware. The rate of wicking for

a circular cylinder is given below by equation (3.12). Tightly fitting parts reduce flow rate but do not stem flow (unless flow rate is so low that solidification occurs by drying or some other mechanism, creating a total blockage). Tightly fitting parts can also be expensive and difficult to use and maintain. Capillary wicking can be prevented by making the hardware from non-wetting material or by applying a nonwetting coating to parts so that $\theta_A > 90^\circ$, but surface contamination may defeat this approach. Capillary breaks can be designed into hardware to halt spreading. In this case, geometry is such that the meniscus achieves an equilibrium configuration, and the liquid progresses no farther.

3.2.3.2 Application to a meniscus that is asymptotically planar

A more complicated example is a two-dimensional meniscus that is planar at large distances from the wetting line. The plane approached by the meniscus is initially presumed to be horizontal; how this restriction can be relaxed is described later. The meniscus can represent the surface of a pool or the edge of a film of uniform thickness. Coordinate Y is measured vertically from the plane. The horizontal coordinate of the meniscus is $F(Y)$, and the Young–Laplace equation may be written

$$\sigma \frac{F_{YY}}{(1 + F_Y^2)^{3/2}} = \rho g Y \quad (3.6)$$

The term on the left is meniscus curvature, and that on the right is the hydrostatic pressure in the liquid. Upon introducing the dimensionless variables $y = Y/L_\sigma$ and $f = F/L_\sigma$, where L_σ is the capillary length, this equation becomes

$$\frac{f_{yy}}{(1 + f_y^2)^{3/2}} = \frac{d}{dy} \left\{ \frac{f_y}{(1 + f_y^2)^{1/2}} \right\} = y \quad (3.7)$$

A first integration, for $y > 0$ and with boundary

condition $f_y \rightarrow -\infty$, $y \rightarrow 0^+$, gives

$$f_y = \frac{\frac{y^2}{2} - 1}{y \sqrt{\left(1 - \frac{y^2}{4}\right)}} \quad (0 < y < 2) \quad (3.8)$$

A second integration, with the arbitrary condition that $f = 0$, $y = \sqrt{2}$ (the meniscus is invariant to a horizontal translation), completes the solution.

$$f = \sqrt{2} - \sqrt{(4 - y^2)} + \ln \left[\frac{1}{y} (2 + \sqrt{(4 - y^2)}) \right] - \ln [1 + \sqrt{2}] \quad (3.9)$$

The meniscus shape is plotted in Fig. 3.4.

A solution for $y < 0$ is $f(-y)$, which is a reflection across the horizontal axis. This solution can describe the edge of a film resting on a horizontal, solid surface (Fig. 3.5). The contact angle and the dimensionless asymptotic film thickness, $h_\infty = H_\infty/L_\sigma$, are related as follows (see equation (3.8)):

$$\theta = \frac{\pi}{2} + \tan^{-1} \left\{ \frac{\frac{h_\infty^2}{2} - 1}{h_\infty \sqrt{\left(1 - \frac{h_\infty^2}{4}\right)}} \right\} \quad (3.10)$$

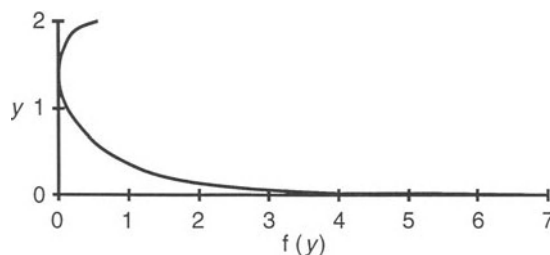


Figure 3.4 Plot of equation (3.9), the shape of a static meniscus that asymptotes to a horizontal plane.



Figure 3.5 The edge of a horizontal layer.

A given film thickness corresponds to one contact angle, which must satisfy condition (3.3) for equilibrium. Otherwise, θ is a dynamic contact angle, and the wetting line moves (see Section 3.3). Low levels of contact-angle hysteresis favor wetting-line motion and an unsteady meniscus. In the absence of significant hysteresis, the edges of coatings tend to be dynamic.

If the solid surface is inclined at an angle β to the horizontal as shown in Fig. 3.6, then the component of gravity parallel to the incline, $g \sin \beta$, drives a rectilinear flow parallel to the wetting line that exerts no stress on the meniscus. The component of gravity perpendicular to the incline, $g \cos \beta$, produces a hydrostatic pressure field. So, meniscus shape is determined by equation (3.6) with g replaced by $g \cos \beta$. This combination of rectilinear flow and a static meniscus represents the edge of a liquid layer on the inclined surface of a slide coater (Chapter 11). The flow-rate distribution near the edge is affected by the contact angle through the meniscus shape.

Stationary wetting lines can exist when there is flow, as in this example. In such cases, boundary condition (3.3) for a static contact angle still applies, even when meniscus shape is not determined by the Young–Laplace equation because of hydrodynamic stresses.

3.3 DYNAMIC MENISCI AND WETTING LINES

Liquid displaces air from a solid surface in a coating process. Inevitably, there is a wetting line that moves with respect to the solid.

In the flow of liquid onto the solid, viscous stresses and dynamic pressure generally influence meniscus shape. The meniscus shape and flow

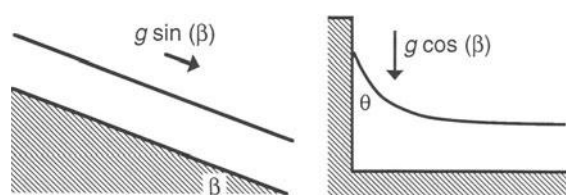


Figure 3.6 The edge of a layer in fully developed flow on an inclined plane.

field are coupled, and surface tension acting in a curved meniscus supports a net stress normal to the meniscus.

3.3.1 DYNAMIC WETTING LINES

Ablett (1923) was the first to find that the contact angle changes with the speed of the wetting line relative to the solid. The contact angle observed experimentally at a moving wetting line is called the dynamic contact angle, θ_D . It usually increases steadily with speed and ultimately approaches its maximum possible value of 180°. Except for extremely low speeds and special cases, the dynamic contact angle differs appreciably from its static advancing or receding values. Unfortunately, there is no dependable way of predicting the dynamic contact angle in flows where it has not been measured. In addition, some of the

factors influencing the dynamic contact angle are not well studied.

The methods used to measure θ_D are similar to those used to measure the static contact angle. In many experiments, θ_D is measured directly through low-power optics. However, if the flow is so weak (small Ca and We) that the meniscus is essentially a static meniscus, then θ_D can also be inferred by fitting a solution of the Young–Laplace equation to the observed profile, and mathematically extrapolating the solution to intersect the surface of the solid.

Examples of dynamic contact angles are shown in the photographs reproduced in Figs 3.7 and 3.8. Figure 3.7 shows a vertical tape entering a pool of liquid. Figure 3.8 shows a liquid curtain impinging on a horizontal tape (see Section 11.3). Through such observations, the contact angle can be determined at a distance of, at best, about

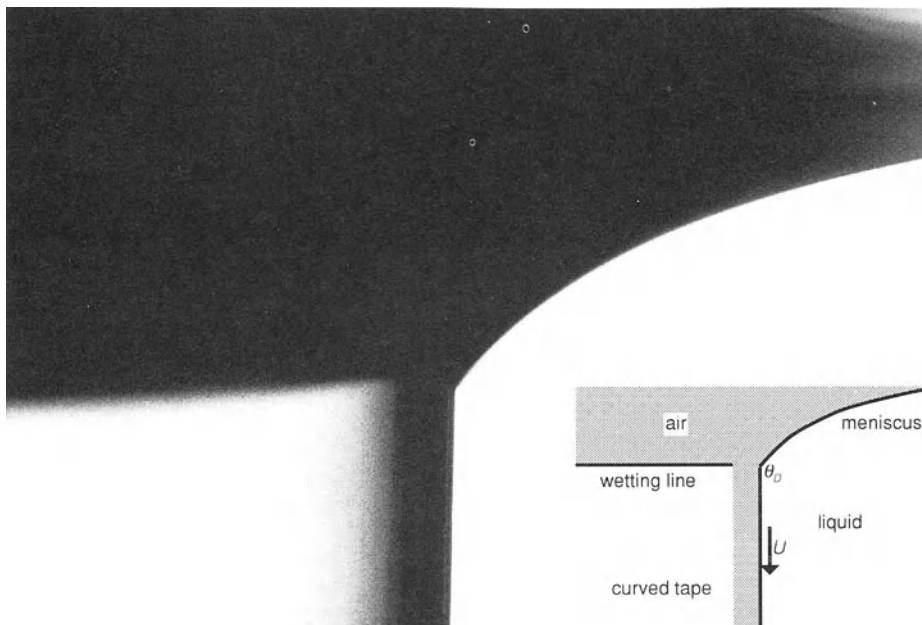


Figure 3.7 Photograph of a poly(ethylene terephthalate) tape entering a pool of aqueous glycerol (viscosity 77 mPa s and surface tension 63 mN m⁻¹). The tape is bent into an arc for a clear view of the meniscus profile near the wetting line; a portion of the smooth wetting line is visible. At the speed of 0.05 m s⁻¹, the dynamic contact angle is about 143°. The air appears dark due to total internal reflection at the interface.

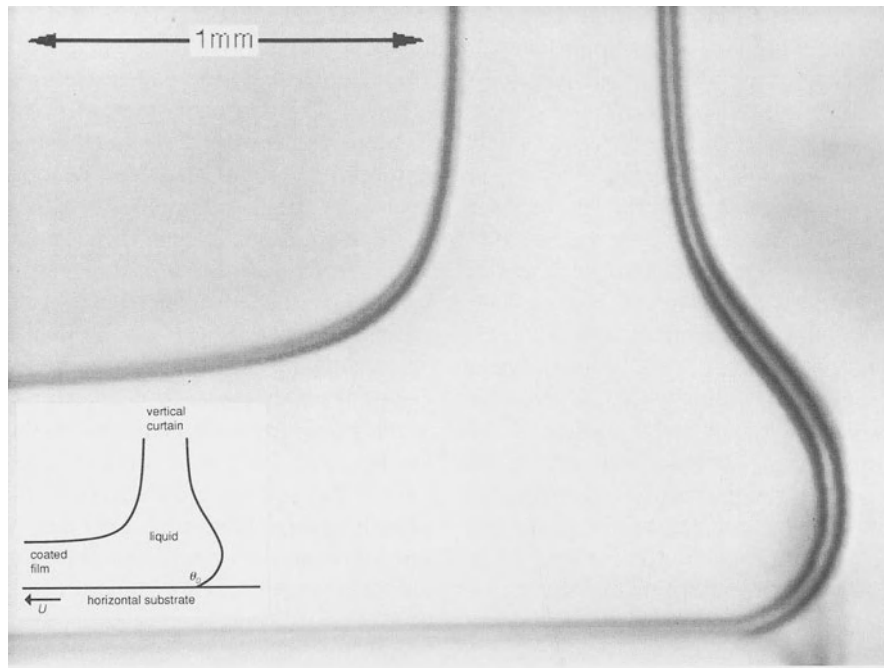


Figure 3.8 Photograph by A. Clarke of the impingement of a curtain of 15% aqueous gelatin on a moving tape (nominal viscosity 63 mPa s). The curtain height is 3 cm, and the volumetric flow rate is $4.3 \text{ cm}^3 \text{ s}^{-1}$ per cm of curtain width. At the speed of 0.83 m s^{-1} , the dynamic contact angle is about 156° .

0.01 mm from the solid. Little information is available at smaller distances. In this chapter, it is this measured or apparent contact angle that is referred to as the dynamic contact angle.

The dynamic contact angle is not a material property and does not have the fundamental significance and general applicability of the static contact angle. From the practical point of view, the angle is mainly important because dynamic wetting failure occurs as its value approaches 180° (Section 3.4). Mathematically, the dynamic contact angle is required as a boundary condition for modeling problems in capillary hydrodynamics, just as the static contact angle is required for modeling problems in capillary hydrostatics; the curvature term of equation (3.1) appears in the hydrodynamic equations.

Contact-angle variation with speed is usually attributed to one or both of two general mechanisms. An upset of the thermodynamic equilibrium expressed by Young's equation may

result in a changing contact angle. In that case, the contact angle is determined by some molecular rate process. This mechanism would seem to be operating, for example, in cases where the dynamic contact angle increases with speed from the static contact angle and then levels out over some higher range of speeds. The second general mechanism is hydrodynamic shaping of the meniscus. This mechanism would seem to be operating in cases where the dynamic contact angle depends on some macroscopic flow variable, such as flow rate. Hydrodynamic shaping of the meniscus is most likely at high capillary and Weber numbers where the influence of capillarity becomes weak. Kistler (1983) computed flow fields in the (singular) limit of infinite capillary number. Here, the meniscus-curvature term is lost from the equations of hydrodynamics, and no contact-angle boundary condition is needed to compute the macroscopic flow; rather, the dynamic contact angle is computed together with

the flow field. Capillary forces are important very near the wetting line, but the macroscopic flow is unaffected because the flow of information is toward the wetting line. Ostensibly, hydrodynamics should not affect the dynamic contact angle at small capillary number. However, it will be seen that the high stresses expected near the wetting line provide a roundabout way for hydrodynamics to influence θ_D at capillary numbers significantly below unity.

Beyond the uncertainty surrounding the dynamic contact angle, prospects for modeling are further clouded by a singularity that arises at the wetting line when the equations and boundary conditions of classical hydrodynamics are solved. The hydrodynamic problem posed in the customary manner does not produce a physically acceptable solution (Huh and Scriven 1971; Dussan V. and Davis 1974). Stresses are unbounded near the wetting line, and the force exerted by the fluids on the solid is also unbounded. The origin of the singularity is a discontinuity in velocity at the wetting line. In the frame of reference in which the wetting line is stationary, the limiting velocity as the wetting line is approached along the meniscus is zero, but because of the no-slip boundary condition, the limiting velocity as the wetting line is approached along the solid is the velocity of the solid.

Despite much attention, the best way to cope mathematically with dynamic wetting lines has not been settled. The solution can be truncated at a distance from the wetting line that is small compared with the macroscopic scale of the flow but large enough to be observationally accessible. The dynamic contact angle must then be determined by experiment. Alternatively, the solution can be truncated on the molecular scale, where the continuum description breaks down (Voinov 1976). When this is tried, it is found that hydrodynamic forces cause the meniscus to bend on a submicroscopic scale. In consequence, a contact angle differing from the observed contact angle needs to be specified at the cut-off point. Inevitably, this microscopic contact angle, θ_w , is observationally inaccessible, and the problem of the unknown contact angle on the macroscopic

scale becomes the problem of the unknown contact angle on the submicroscopic scale. Nonetheless, hydrodynamic bending of the meniscus on a submicroscopic scale provides a possible hydrodynamic mechanism for the change of the dynamic contact angle with speed that can operate at capillary numbers significantly less than unity.

The force singularity can also be dealt with by modifying the flow equations and boundary conditions to alleviate the singularity and continuing the solution up to the wetting line. A popular modification is to relax the no-slip boundary condition of classical hydrodynamics at the solid surface to eliminate the velocity discontinuity (Huh and Scriven 1971; Huh and Mason 1977; Dussan V. 1979). Very near the wetting line, the speed of the liquid adjacent to the solid is assumed to differ from that of the solid so that the limiting velocity as the wetting line is approached along the solid is zero. The force exerted on the solid is then finite, although stresses in the liquid are still unbounded. So far, however, no specific slip model has been established, and the physical validity of this approach remains unproven. The hydrodynamic model, with or without slip, predicts significant bending of the meniscus on the submicroscopic scale, and a submicroscopic contact angle θ_w differing from the dynamic contact angle is required.

It is sometimes assumed that the submicroscopic contact angle needed in hydrodynamic models is the advancing static contact angle. However, because of hysteresis, the static angle itself may not have significance at the submicroscopic level. Furthermore, because of the risk that a dynamic wetting line is not close to thermodynamic equilibrium, the possibility that θ_w depends upon speed must also be considered.

When the air or liquid extends to a thin film having a thickness of the order of 1 μm or less, as is the case when the dynamic contact angle is near 0° or 180°, long-range molecular forces must be taken into account. Teletzke, Davis and Scriven (1988) modified the hydrodynamic equations by including these effects as disjoining pressures. This modification does not resolve the

problems at the dynamic wetting line, but disjoining pressures evidently do affect meniscus shape over submicroscopic distances from the surface of the solid. de Gennes, Hua and Levinson (1990) applied the modified equations to a dynamic wetting line for a small dynamic contact angle. They concluded that van der Waals forces determine the cut-off for the classical hydrodynamic model. Inclusion of long-range molecular forces allowed the solution to be continued to a distance from the wetting line of the order of molecular size, at which scale the continuum description must break down. de Gennes, Hua and Levinson argued that slip can be expected *only* at the molecular scale.

A difficulty inherent in extending the hydrodynamic solution to the wetting line or to molecular distances from the wetting line is that the scale over which the meniscus bends is very small compared with the scale of the macroscopic flow. This disparity complicates the solution of flow problems. However, the macroscopic solution can be required to conform to the asymptotic behavior of the flow as the wetting line is approached, if that can be determined. A classical mathematical device is to use matched asymptotic expansions to exploit the small parameter that is the ratio of the submicroscopic length scale to the macroscopic length scale. Alternatively, if the problem is solved by large-scale numerical analysis, then substantial grid refinement is necessary near the wetting line (for example, Huh and Mason 1977; Tilton 1988).

In addressing a coating flow problem, a central question is the importance of the dynamic contact angle to the issue at hand. If the dependence of the response of interest on the dynamic contact angle is weak, then it may be sufficient to truncate the solution away from the wetting line and apply a reasonable dynamic contact angle. In high-speed coating flows, the dynamic angle is always well over 100°. Experimental measurements can perhaps supply values where greater precision matters. For many problems this is enough. If the contact angle is central to the issue at hand, as for dynamic wetting failure (Section 3.4), then modeling is probably not an option, and an

empirical or at least semi-empirical approach must be taken.

3.3.2 EXAMPLES OF FLOW WITH A DYNAMIC WETTING LINE

Three applications follow that illustrate how the dynamic-contact-angle boundary condition can affect flows. In the first example, the contact angle drives the flow; in the second, it determines the pressure to apply to a coating bead; in the third, it determines the migration of the wetting line as speed changes.

3.3.2.1 Meniscus advancing in a capillary tube

When the capillary tube of Fig. 3.3 is first touched to the liquid (time $t = 0$), the meniscus begins moving up the capillary toward its equilibrium position. If the capillary and Weber numbers are small, then the flow does not affect meniscus shape, which is a spherical cap as previously discussed. This type of flow problem was considered by Washburn (1921). For the case of wetting, the pressure in the liquid at the meniscus is $2\sigma \cos(\theta_D)/R_C$ below atmospheric pressure. The pressure at the level of the pool is atmospheric, and consequently there is a negative pressure gradient that drives the liquid up the capillary. With L the distance of the meniscus along the capillary, this pressure gradient is $-2\sigma \cos(\theta_D)/R_C L$. If inertial effects are negligible, the pressure gradient and the volumetric flow rate are those for Poiseuille flow, except within about a tube diameter of the meniscus. The volumetric flow rate, in turn, determines the rate of meniscus advance, dL/dt , through a mass balance

$$\frac{8\mu}{R_C^2} \frac{dL}{dt} = \frac{2\sigma \cos(\theta_D)}{R_C L} - \rho g \sin \alpha \quad (3.11)$$

For mathematical simplicity, wetting line speed is presumed so slow that the dynamic contact angle does not change much from the static advancing contact angle. Because θ_D increases with speed and $\cos(\theta_D)$ decreases, this simplification overpredicts meniscus speed in the more

likely case that θ_D does increase significantly. Eventually, the meniscus reaches the equilibrium position L_∞ given by equation (3.5). The solution to the differential equation is

$$t = \frac{8\mu L_\infty}{\rho g R_C^2 \sin \beta} \left\{ -\frac{L}{L_\infty} - \ln \left(1 - \frac{L}{L_\infty} \right) \right\} \quad (3.12)$$

At small times, or at all times for the special case of a horizontal capillary,

$$L \approx \sqrt{\frac{R_C \sigma \cos(\theta_A) t}{2\mu}}, \quad t \rightarrow 0 \quad (3.13)$$

and hence the common observation that $L \propto \sqrt{t}$. On the other hand, at large times the meniscus approaches its equilibrium position exponentially

$$\frac{L}{L_\infty} \approx 1 - \exp \left(-\frac{\rho g R_C^2 \sin \beta}{8\mu L_\infty} t \right), \quad t \rightarrow \infty \quad (3.14)$$

In each case, surface tension drives the flow via the dynamic-contact-angle boundary condition.

3.3.2.2 Wetting meniscus of a coating bead

In many coating methods, the applicator is spaced a small distance H_G from the substrate. The liquid bridge spanning this gap is sometimes called a coating bead. The bead has two menisci: one forms the coated film, and the other wets the moving solid surface. The slide hopper bead coating method (Section 11.2) is shown schematically in Fig. 3.9. The upper, film-forming meniscus of the bead is curved such that the pressure in the bead, P_B , is below atmospheric pressure. Application to the lower, wetting meniscus of a pressure P_S that is below atmospheric and of the same magnitude as P_B permits thinner films to be coated at speeds higher than would otherwise be possible (Beguin 1954).

Under conditions of small capillary, Weber and Bond numbers, the wetting meniscus is a circular arc of radius R . Ruschak (1976) modeled the bead under these circumstances. A dynamic contact angle θ_D applies at the moving solid surface. The wetting meniscus contacts the

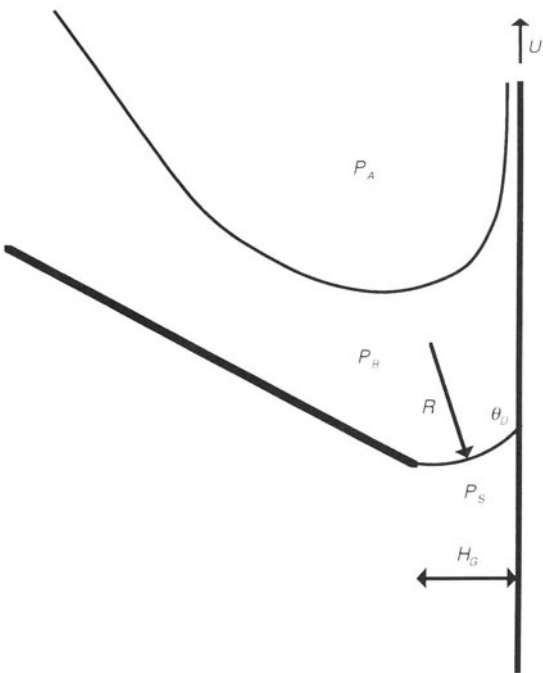


Figure 3.9 Slide-hopper bead coating.

applicator at a static wetting line that is presumed to be pinned at an edge. To a first approximation, the shape of the film-forming meniscus and hence P_B are determined by speed, coating thickness, and the properties of the liquid. The capability for setting P_S to subatmospheric pressure becomes essential to attaining equilibrium as P_B falls. Such is the case, for example, as thinner films are formed.

The configurations for the wetting meniscus can be determined with reference to the circles of Figs. 3.10a and b. The dynamic wetting line is point 1; point 1 in Fig. 3.10b is 180° from point 1 in Fig. 3.10a. The dynamic contact angle indicates the side of the meniscus that is the liquid; hence P_B is less than P_S in Fig. 3.10a and greater than P_S in Fig. 3.10b. Points 2a and 2b meet the gap requirement and are possible locations for the pinned wetting line. The largest possible gap occurs when points 2a and 2b coincide with point 3. Figure 3.10a shows that the gap can range from 0 to a maximum of

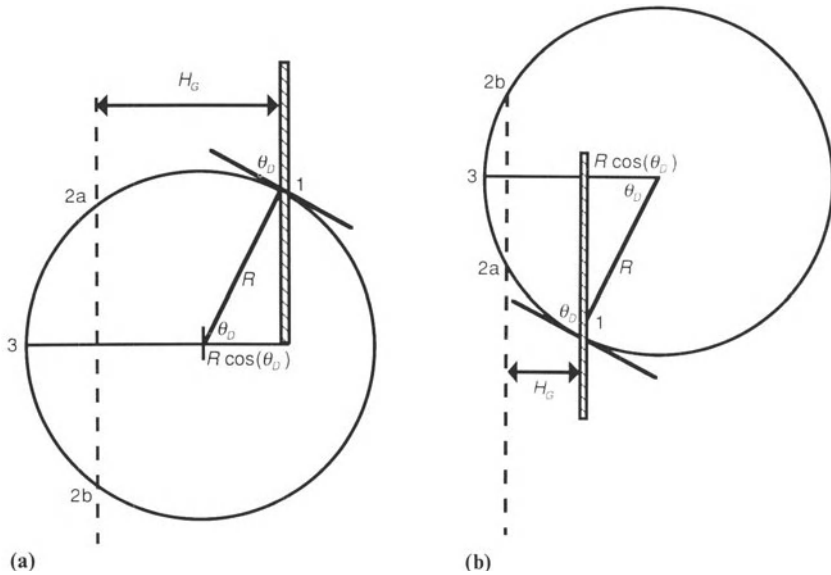


Figure 3.10 Possible configurations for the circular wetting meniscus of a coating bead.

$R + R \cos(\theta_D)$ for $P_s > P_B$, and Fig. 3.10b from 0 to $R - R \cos(\theta_D)$ for $P_s < P_B$. Thus,

$$0 \leq \frac{H_G}{R} \leq 1 + \cos(\theta_D) \quad (P_s > P_B) \quad (3.15)$$

$$0 \leq \frac{H_G}{R} \leq 1 - \cos(\theta_D) \quad (P_s < P_B) \quad (3.16)$$

Although these inequalities were derived with R fixed and H_G varying, they hold also for H_G fixed and R varying.

An inequality for the pressure drop across the wetting meniscus follows by substituting into equations (3.15) and (3.16) the relationship between pressure drop and curvature, equation (3.1).

$$-1 - \cos(\theta_D) \leq \frac{(P_B - P_s)H_G}{\sigma} \leq 1 - \cos(\theta_D) \quad (3.17)$$

If this relation is violated, a circular wetting meniscus is not possible, and a failure mode such as bead breakup occurs. For a specified dynamic contact angle, a range of pressure drops is possible because the wetting meniscus can adopt different curvatures. The application of suction

allows a broader range of bead pressures, and hence coating conditions, to be consistent with the configurations available to the wetting meniscus. The versatility of the wetting meniscus also provides important process latitude, as otherwise P_s would have to be set at precisely one value. Small gaps are necessary in bead coating because, as H_G increases, the latitude for P_s to vary around P_B becomes smaller and approaches zero. Evidently, the capability to adjust P_s to a value less than P_B is particularly important for dynamic contact angles near 180° that are typical of high-speed coating. Without suction ($P_s = P_A$), $P_B - P_A$ is negative, but the configurations available for the wetting meniscus limit P_B to values just slightly below atmospheric pressure. Indeed, in the limit as θ_D approaches 180° , no values for P_B are possible without suction, and the method fails.

Setting P_s below atmospheric pressure can also shift to higher speeds the onset of dynamic wetting failure (Section 3.4), which occurs as θ_D approaches 180° . In bead coating, the extent by which P_s can be reduced for this purpose is limited, as equation (3.17) makes plain.

3.3.2.3 Tape entering a pool

Frequently, dynamic contact angles are measured by plunging a tape vertically into a pool of liquid (Fig. 3.11). Usually, air entrainment occurs for capillary numbers above a critical value of order 0.1. With capillary and Weber numbers smaller than unity, the meniscus has roughly the Young–Laplace shape given by equation (3.9). The meniscus shape under dynamic conditions depends upon the dynamic contact angle just as

the meniscus shape under static conditions depends upon the static contact angle. When the tape is at rest, the wetting line is above the surface of the pool if the liquid wets the web ($\theta_A < 90^\circ$). As tape speed increases, the dynamic contact angle increases, and the wetting-line position moves downward. For example, the meniscus is essentially flat and horizontal when the dynamic contact angle is 90° . Wetting-line position and the dynamic contact angle are related by

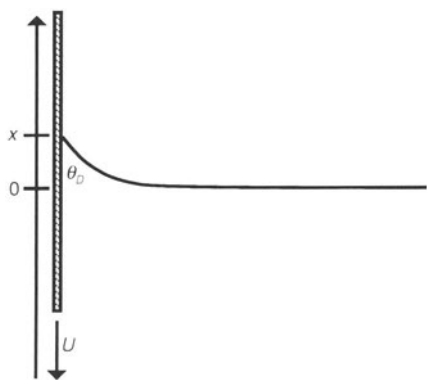


Figure 3.11 The meniscus for a tape entering a pool vertically.

$$\tan(\theta_D) = \frac{1 - \frac{x^2}{2}}{x \sqrt{\left(1 - \frac{x^2}{4}\right)}}, \quad \sqrt{2} > x > -\sqrt{2}, \quad x \neq 0 \quad (3.18)$$

As x passes through zero, θ_D passes through 90° . Equation (3.18) is plotted in Fig. 3.12. The main effect of the motion of the tape is to increase the dynamic contact angle, which in turn changes the shape of the static meniscus describing the pool surface through the contact-angle boundary condition. As the capillary number is small, the viscous drag of the tape on the liquid is not directly responsible for the migration of the wetting line.

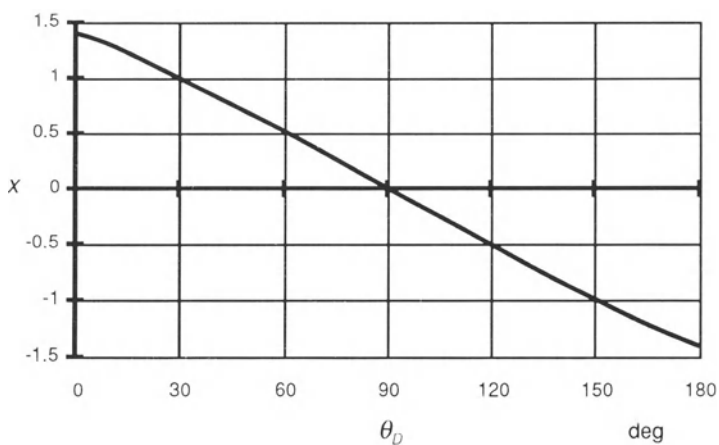


Figure 3.12 Wetting-line position versus dynamic contact angle for a tape entering a pool vertically, as predicted by equation (3.18).

3.3.3 THEORIES FOR THE DYNAMIC CONTACT ANGLE

There is, as yet, no complete and experimentally verified theory for the dynamic contact angle. Two different approaches to the problem are outlined here. According to the first, the motion of the wetting line disturbs the thermodynamic equilibrium that gives rise to the static contact angle. Dynamic wetting is viewed as a molecular-rate process, and the dynamic contact angle is considered to be the actual contact angle. The second approach is hydrodynamic, and the dependence of the dynamic contact angle on speed is attributed entirely, or at least in part, to hydrodynamic bending of the meniscus so close to the wetting line as not to be visible. In this case, the dynamic contact angle differs from the actual contact angle on the submicroscopic scale.

3.3.3.1 Molecular-kinetic theory

The molecular-kinetic theory of dynamic wetting is based upon the methods developed by Eyring and others (Glasstone, Laidler and Eyring 1941). The theory views wetting-line movement statistically as a stress-modified rate process composed of individual molecular displacements (Cherry and Holmes 1969; Blake and Haynes 1969; Blake 1993). In the simplest case, the velocity dependence of the contact angle is due to the disturbance of adsorption equilibria at the wetting line. The driving force that alters the energy barriers to molecular displacements, so that the wetting line can move, may have components arising from both surface tension and viscous shear stress.

According to Blake and Haynes, surface tension provides the primary driving force for wetting-line motion: specifically, $\sigma[\cos(\theta_E) - \cos(\theta_D)]$. This is equivalent to $\sigma_{SA} - \sigma_{SL} - \sigma \cos(\theta_D)$. If $\theta_D > \theta_E$, then the state of equilibrium described by Young's equation is not possible, and the wetting line moves. Although molecular interactions between the liquid and solid provide a major barrier to wetting line movement, the retarding influence of the viscosities of the advancing and retreating

fluids on the motion of molecules (Cherry and Holmes, 1969) can also be taken into account, and a nonhydrodynamic effect of viscosity on the contact angle then results. The final expression relating the wetting line speed U to the dynamic contact angle is

$$U = \frac{2K_S L_M h_p}{\mu v} \sinh\left(\frac{\sigma}{2NkT} [\cos(\theta_E) - \cos(\theta_D)]\right) \quad (3.19)$$

Here K_S is the frequency of molecular displacements at a stationary wetting line, L_M the length of an individual displacement, h_p the Planck constant, v the molecular flow volume, N the number of adsorption sites per unit area, k the Boltzmann constant, and T the absolute temperature. An estimate for L_M is $1/\sqrt{N}$. Hence, there are effectively just two parameters, K_S and N , that are determined by fitting experimental data. For small angles,

$$\theta_D^2 - \theta_E^2 \approx Ca \left(\frac{vNkT}{K_S L_M h_p} \right) \quad (3.20)$$

that is, $U \propto \theta_D^2$.

3.3.3.2 Hydrodynamic theory

A second approach, first investigated by Hansen and Toong (1971), is to account for much or all of the change in the dynamic contact angle through hydrodynamic bending of the meniscus at distances so close to the wetting line as not to be visible. Voinov (1976) developed the mathematics of this approach for a liquid displacing air. He considered conditions for which the slope of the meniscus changes slowly with distance from the solid. The flow field local to a point on the interface can then be approximated by flow in a wedge with an angle determined by the solid surface and the local meniscus slope. An integration of these wedge flows yields the meniscus shape. Voinov avoids the wetting line singularity by truncating the solution at molecular dimensions. He acknowledged but did not treat situations where long-range molecular forces must be taken into account.

Voinov's primary result is

$$\chi(\theta) - \chi(\theta_w) = Ca \ln(Y/Y_w) \quad (3.21)$$

where Y is the distance from the solid of a point on the meniscus and Y_w the value of θ at Y at which the solution is truncated, θ the angle through the liquid that the tangent to the meniscus makes with the solid, and θ_w the value of θ at $Y = Y_w$. The function $\chi(\theta)$ is defined by

$$\chi(\theta) = \frac{1}{2} \int_0^\theta [\hat{\theta}/\sin(\hat{\theta}) - \cos(\hat{\theta})] d\hat{\theta} \quad (3.22)$$

For $\theta < 3\pi/4$, the integrand may be approximated by $2\theta^2/3$, and equation (3.21) becomes

$$\theta^3 - \theta_w^3 = 9 Ca \ln(Y/Y_w), \quad \theta < 3\pi/4 \quad (3.23)$$

Voinov recognized that the angle near the wall, θ_w , may depend upon speed.

To estimate θ_D , suitable values for Y and Y_w are required. With $Y_w = 10^{-7}$ cm, the order of molecular size, and $Y = 10^{-3}$ cm, the approximate distance from the wetting line at which a contact angle can be measured, $\ln(Y/Y_w)$ is estimated to be on the order of 10. Later it will be seen that this rough estimate is in agreement with values obtained by fitting experimental data.

More often in hydrodynamic models, the force singularity at the wetting line is eliminated by permitting local slip. Dussan V. (1976), Huh and Mason (1977), Hocking and Rivers (1982) and others have developed this method. Cox (1986) treated both fluids as viscous and appears to have obtained the most general results. For the purpose of eliminating the force singularity, slip is permitted over a distance L_s from the wetting line that is small compared with the macroscopic scale of the flow L . The capillary number is presumed small, so that away from the wetting line the meniscus has a shape given by the Young–Laplace equation. The angle determined by extrapolating this static meniscus to the solid is the dynamic contact angle.

Cox used the method of matched asymptotic expansions to take advantage of the two small parameters, the capillary number and the ratio L_s/L . At distances from the wetting line of order

L_s (inner region), slip is important. The flow domain is wedge shaped, with an included angle equal to the submicroscopic contact angle θ_w . As distance from the wetting line increases, the flow comes to resemble that for no slip at the solid. To lowest order, the only information communicated outward from this region is the submicroscopic contact angle.

At distances from the wetting line of order $L \exp(-1/Ca)$, hydrodynamic bending of the meniscus takes place. This intermediate region connects the inner and outer regions and in effect converts the submicroscopic contact angle into the dynamic contact angle. In this region, the no-slip condition is appropriate at the solid. To lowest order in capillary number, the apparent contact angle is given by

$$\chi(\theta_D) - \chi(\theta_w) = Ca \ln(L/L_s) \quad (3.24)$$

where, for the case in which the displaced fluid is inviscid, $\chi(\theta)$ is given by equation (3.22); otherwise, the complete expression given by Cox must be used. For liquid displacing air, equation (3.22) applies except as θ_D nears 180° , in which case the viscosity of the air becomes important. For small and moderate values of θ_D , equation (3.23) applies with $\ln(Y/Y_w)$ replaced by $\ln(L/L_s)$. This linear variation of θ_D^3 with Ca was also arrived at by Tanner (1979) and de Gennes (1985). Kalliadasis and Chang (1994) considered the case of perfect wetting, where a precursor film advances faster than the meniscus. For a thick precursor film, they determined that $\theta = 7.48 Ca^{1/3}$. They also obtained a small correction, arising from disjoining pressure, for thin precursor films and very small capillary numbers.

Interpreted literally, the term $\ln(L/L_s)$ implies that the dynamic contact angle depends upon the outer (macroscopic) geometry. The term is basically an adjustable parameter because a precise value cannot be assigned. There is no proven model for the slip region, but the basic result, equation (3.24), depends neither on the particular form of the slip boundary condition (Dussan V. 1976) nor indeed on the model for the inner region, and so is likely to be true

regardless of the physics on the submicroscopic scale. This insensitivity to the inner-region model arises because only the submicroscopic contact angle is communicated outward to the intermediate region. So, although the inner region is explicitly taken into account in slip models, what is gained by continuing the solution to the wetting line over Voinov's truncated solution seems minimal.

Indeed, Dussan V., Rame and Garoff (1991) proposed a form of the hydrodynamic theory for the intermediate region, common to both the inner and outer regions, that is not expressed in terms of a slip length and a macroscopic length scale. Instead, they introduced the slope of the interface at some small distance from the wetting line within the intermediate region, θ_i . This angle might depend upon speed, but otherwise would be a material property of the system. A universal form for the variation of interface slope in the intermediate region supplies an asymptotic boundary condition for the interface slope θ , for use in solving the flow in the outer region:

$$\chi(\theta) - \chi(\theta_i) \approx Ca \ln\left(\frac{R}{R_i}\right) \quad (3.25)$$

Here, R is the distance of a point on the interface from the wetting line, and R_i is a value of R in the intermediate region where $\theta = \theta_i$. The intermediate and outer solutions can be combined to form a composite solution, and the value of R_i is chosen such that the outer solution has no significant effect on the composite solution at that location. It is an advantage that θ_i depends only upon material properties and perhaps speed, but the angle is submicroscopic and must be inferred. A comparison of equations (3.25) and (3.21) shows that the end result is substantially the same as Voinov's.

Petrov and Petrov (1992) allowed the submicroscopic contact angle in Cox's hydrodynamic theory to vary with speed according to the molecular-kinetic theory. This gave them three adjustable parameters. In this manner they were able to improve the fit between theory and certain experimental data.

3.3.4 EXPERIMENTAL DATA FOR DYNAMIC CONTACT ANGLES

Plentiful experimental data are available for the dynamic angle at small capillary numbers for the case where the displaced fluid is air. At extremely low speeds, the dynamic contact angle may remain equal to the advancing static angle (Schwartz and Tejada 1972; Johnson, Dettre and Brandreth 1977), but in many systems the dynamic contact angle begins to increase from its static value by speeds as low as $10 \mu\text{m/s}$. After this initial rise, the dynamic angle may become sensibly constant over some higher range of speeds, as found by Ablett (1923), Elliott and Riddiford (1967), and Cain *et al.* (1983). In all cases, however, further increases in speed eventually result in the dynamic contact angle approaching 180° .

Inverarity (1969a,b) measured dynamic contact angles for glycerol/water solutions on E-glass filaments. Data for 95% glycerol are shown in Fig. 3.13. The curve for the molecular-kinetic theory represents the data well. The curve for the hydrodynamic theory does not represent the data as well, and the combined theory does not improve the fit over molecular-kinetic theory alone. In this case, molecular-kinetic theory can adequately represent the data.

Hoffman (1975) measured apparent contact angles in glass capillary tubes for liquids ranging in viscosity from 0.96 to 2430 Pa s . He found that his data for liquids with zero contact angles, plotted as angle versus capillary number, fell on a single curve $Ca = F(\theta_D)$. His data for liquids with nonzero contact angles also fell on this curve if a shift factor was used: $Ca = F(\theta_D) - F(\theta_A)$. Hoffman's data are shown in Fig. 3.14.

Cox (1986) applied his theory to Hoffman's experimental results and concluded that if $\theta_W = \theta_A$, then $F(\theta) = \chi(\theta)/\ln(L/L_s)$. Hoffman's shift factor for producing a master curve appears naturally in Cox's theory. By fitting Hoffman's data, Cox determined that $\ln(L/L_s) = 9.21$. The resulting curve represents the data well and is plotted in Fig. 3.14. On the other hand, Jiang, Oh and Slattery (1979) determined an empirical equation

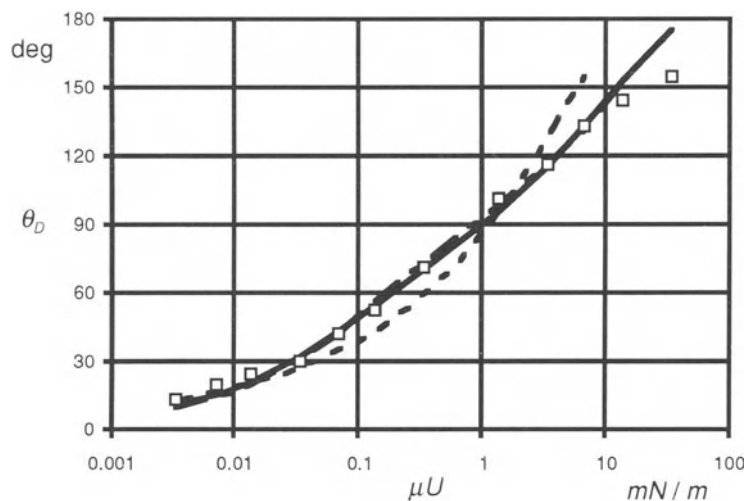


Figure 3.13 Data of Inverarity plotted as θ_D versus μU for E-glass filaments entering a pool of aqueous glycerol. Viscosity, 410 mPa s; surface tension, 65 mN/m. —— molecular-kinetic theory with $N = 2.5 \times 10^{14} \text{ cm}^{-2}$ and $K_s = 8.8 \times 10^9 \text{ s}^{-1}$; - - - hydrodynamic theory with $\ln(L/L_s) = 2.8$; —— combined theory.

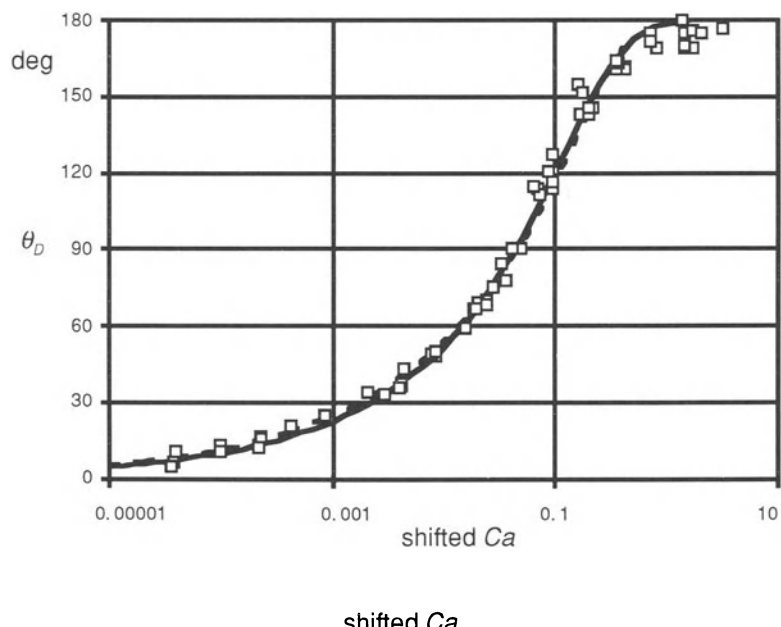


Figure 3.14 Data of Hoffman plotted as θ_D versus shifted Ca for liquids advancing in a capillary. - - - hydrodynamic theory with $\ln(L/L_s) = 9.21$; —— empirical equation (3.26).

which fits the data equally well:

$$\frac{\cos(\theta_A) - \cos(\theta_D)}{\cos(\theta_A) + 1} = \tanh(4.96 Ca^{0.702}) \quad (3.26)$$

This curve is also shown in Fig. 3.14. Note that a contact angle of 180° is reached only asymptotically as capillary number is increased.

Molecular-kinetic theory can fit Hoffman's data if the liquids are considered singly. This is necessary because the molecular flow volumes are not precisely known. Fig. 3.15 shows Hoffman's data for Brookfield standard viscosity oil. The curve for molecular-kinetic theory does not represent the data as effectively as hydrodynamic theory, but the curve for the combined theory represents the data as well as hydrodynamic theory alone, with the change in θ_w attributed to molecular-kinetic theory accounting for about 80% of the change in θ_D .

There are other empirical correlations for the dynamic contact angle besides those of Hoffman, and Jiang, Oh and Slattery. Bracke, De Voeght

and Joos (1989), using their data for solid strips dipped into a pool at capillary numbers greater than about 0.002, determined

$$\frac{\cos(\theta_A) - \cos(\theta_D)}{\cos(\theta_A) + 1} = 2 Ca^{0.5} \quad (3.27)$$

Their liquids were aqueous glycerol, aqueous ethylene-glycol, and corn oil; their solids were poly(ethylene) and poly(ethylene terephthalate). Seebergh and Berg (1992) found nearly the same result for strips of low-density and high-density poly(ethylene) dipped into silicone oil:

$$\frac{\cos(\theta_A) - \cos(\theta_D)}{\cos(\theta_A) + 1} = 2.24 Ca^{0.54} \quad (3.28)$$

Capillary numbers ranged between about 0.001 and 0.02.

There are also data for the dynamic contact angle suggesting that more than one mechanism is at work and that Hoffman's correlation is not universally applicable. Blake (1993) reported an extensive set of data (further augmented here)

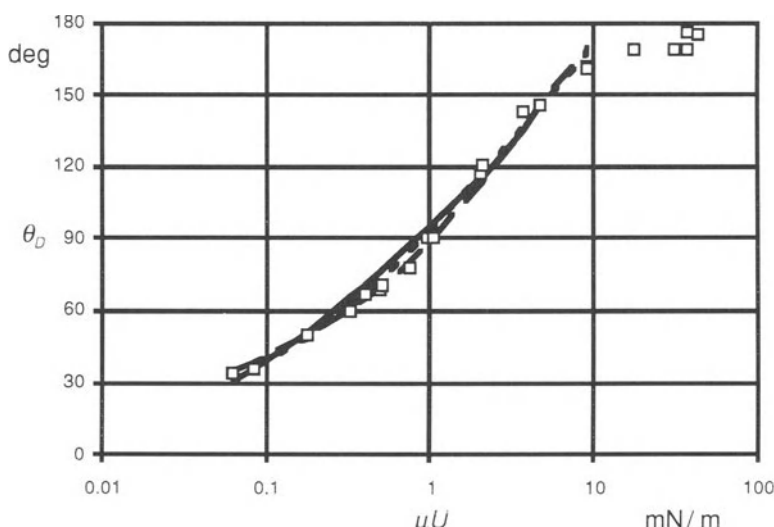


Figure 3.15 Data of Hoffman plotted as θ_D versus μU for Brookfield Standard Viscosity Fluid advancing in a capillary. Viscosity, 98.8 Pa s; surface tension, 21.7 mN/m; static contact angle, 0°. — hydrodynamic theory with $\ln(L/L_s) = 8.68$; - - - combined theory with $N = 1.2 \times 10^{14} \text{ cm}^{-2}$, $K_s = 1.6 \times 10^{11} \text{ s}^{-1}$, and $\ln(L/L_s) = 4.3$; —— molecular-kinetic theory with $N = 1.3 \times 10^{14} \text{ cm}^{-2}$ and $K_s = 9.2 \times 10^{10} \text{ s}^{-1}$.

for smooth poly(ethylene terephthalate) tape drawn vertically into a pool of aqueous glycerol. Viscosities ranged from 1 to 670 mPa s; the range of speeds was correspondingly broad. Data for five viscosities are shown in Fig. 3.16. Plotted in this way, the data make plain the major influence of viscosity on the dynamic contact angle. The complete set of data is plotted as dynamic contact angle versus capillary number in Fig. 3.17. The data collapse to a single curve at capillary numbers above about 0.005, except at contact angles near 180°. At lower capillary numbers, the data diverge systematically, even though the advancing contact angles differ by only a few degrees. This divergence is evidence that Hoffman's correlation is not universal. In Fig. 3.18, some of Blake's and Hoffman's data are plotted together. The data have been shifted in capillary number by Hoffman's method. Although there are substantial differences between the experiments in material properties and geometry, the data correspond to some significant extent, particularly

at dynamic contact angles in the vicinity of 130°. Nevertheless, Hoffman's data tail off to higher capillary numbers as the contact angle approaches 180°, and Blake's data do not correlate with capillary number as the dynamic angle approaches the static contact angle but lie systematically above Hoffman's results.

The fact that Hoffman's correlation does not fit Blake's data at low capillary numbers is shown more clearly in Fig. 3.19 where Blake's results for 0.67 and 0.10 Pa s aqueous glycerol are plotted with those for two of Hoffman's liquids, 11.2 Pa s Santicizer 405, and 109.3 Pa s Admex 760. Although the advancing static contact angles of the liquids are nearly the same (Hoffman's static contact angles are presumed to be advancing) and the data are in agreement at capillary numbers above about 0.01, the data diverge rapidly at smaller capillary numbers. Specifically, the data for aqueous glycerol approach the static contact angle at a capillary number about two orders of magnitude smaller than for Santicizer 405.

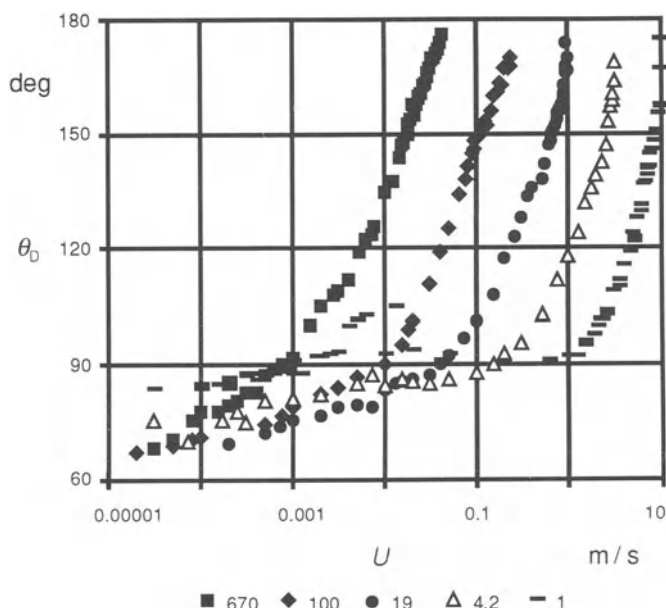


Figure 3.16 Data of Blake plotted as θ_D versus U for poly(ethylene terephthalate) tape vertically entering a pool of aqueous glycerol. The numbers in the legend indicate viscosities in mPa s.

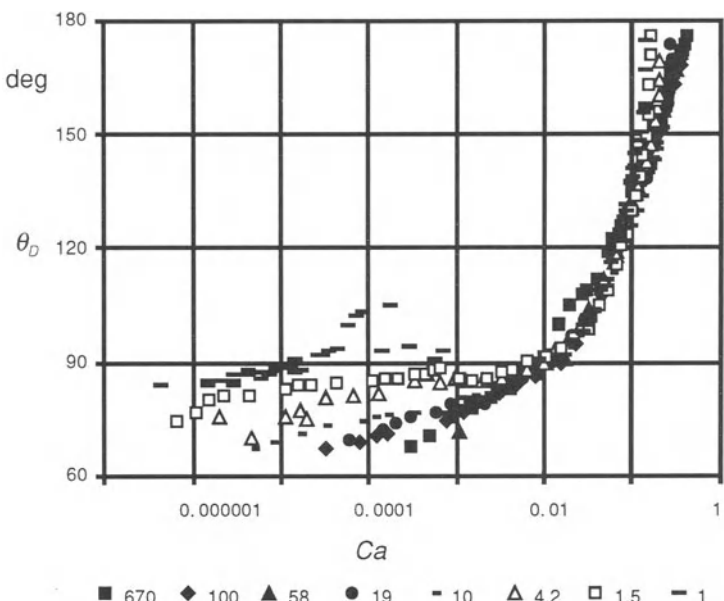


Figure 3.17 Data of Blake plotted as θ_D versus Ca for poly(ethylene terephthalate) tape entering a pool of aqueous glycerol. The numbers in the legend indicate viscosities in mPa.s.

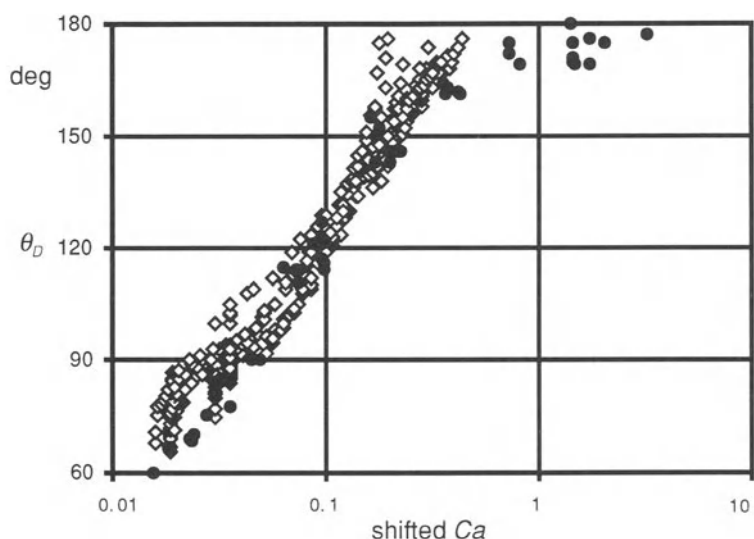


Figure 3.18 Data of Blake plotted as θ_D versus Ca for poly(ethylene terephthalate) tape entering a pool of aqueous glycerol (light symbols); the data of Hoffman for a meniscus advancing in a capillary tube (dark symbols).

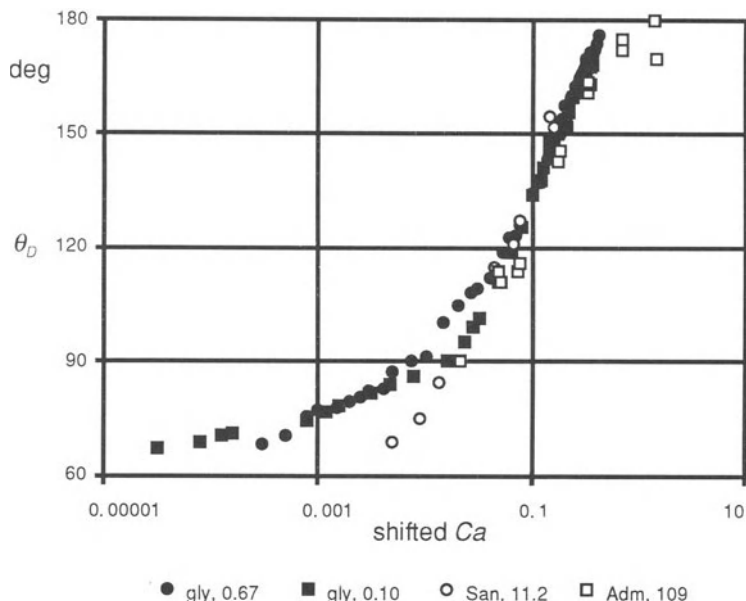


Figure 3.19 Data of Blake plotted as θ_D versus Ca for poly(ethylene terephthalate) tape entering a pool of aqueous glycerol (dark symbols), and data of Hoffman for liquid advancing in a capillary tube (light symbols). All liquids have about the same static contact angle. The numbers in the legend give the viscosities in Pa s.

The data for the lowest viscosities in Fig. 3.17 show rapid changes in slope that could imply a change in mechanism. In particular, the data for water (viscosity 1 mPa s) show a region where the contact angle falls as speed increases. The effect is even more evident for water on gelatin-subbed (having a thin subbing layer of dried gelatin) poly(ethylene terephthalate) tape, as shown in Fig. 3.20. Observational evidence supporting a change in mechanism is that the wetting line exhibits 'stick-slip' behavior in the region where the contact angle falls: the wetting line appears to advance irregularly and to catch and release in a way that is suggestive of fluctuations between two states.

The data for 10 mPa s aqueous glycerol on poly(ethylene terephthalate) tape are plotted again in Fig. 3.21. Neither hydrodynamic theory nor molecular-kinetic theory can describe the entire range of the data. Also shown is a curve for Petrov's combined theory. The combined theory gives a smooth curve that can reasonably fit the data in Fig. 3.21, but cannot cope with

the more irregular behavior of the data for water shown in Figs 3.17 and 3.20. Blake (1993) postulated a change in wetting kinetics to account for the apparent break in the slope of the data and suggested that molecular-kinetic theory could therefore be applied separately to the data above and below the break. Both high-speed and low-speed fits of molecular-kinetic theory are shown in Fig. 3.21. The values of the parameters for each curve indicate that the surface of the solid contains a low density of adsorption sites that interact strongly with the liquid, together with a higher density of more weakly interacting sites. At low wetting speeds, the strong interactions dominate the wetting process, but despite long relaxation times for each molecular displacement, a more or less equilibrium solid–liquid interface is expected to remain after the passage of the wetting line. On the other hand, at high wetting speeds, the strongly interacting molecules are unable to relax within the available time interval, and a nonequilibrium absorbed layer is entrained. The wetting process is then controlled by the

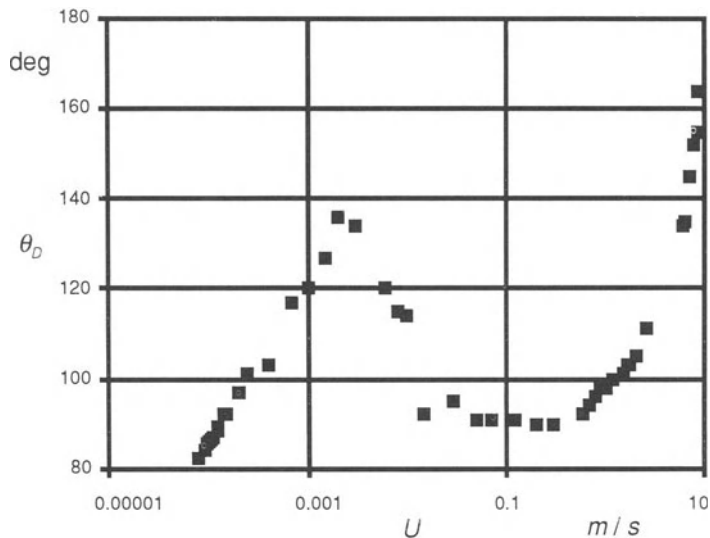


Figure 3.20 Data of Blake plotted as θ_D versus U for gelatin-subbed poly(ethylene terephthalate) tape vertically entering a pool of water.

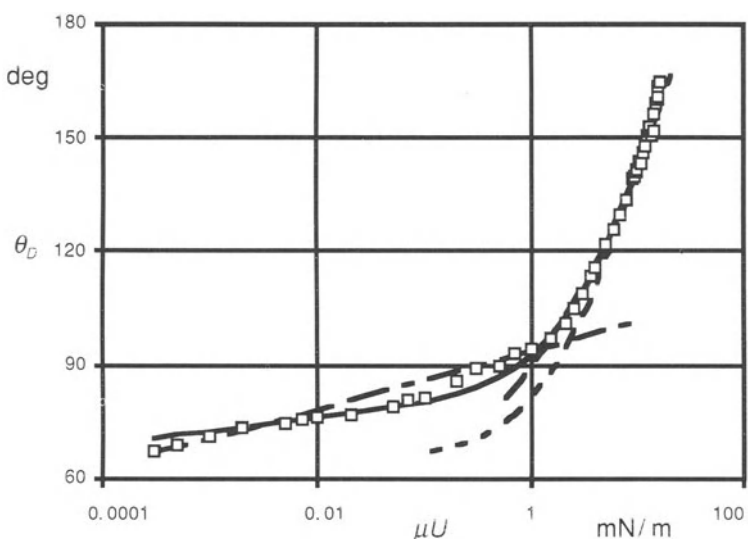


Figure 3.21 Data of Blake plotted as θ_D versus μU for poly(ethylene terephthalate) tape entering a pool of aqueous glycerol. Viscosity, 10 mPa s; surface tension, 65 mN/m; static contact angle, 64.5°. —— molecular-kinetic theory for low speeds with $N = 4.7 \times 10^{13} \text{ cm}^{-2}$ and $K_S = 9.0 \times 10^6 \text{ s}^{-1}$; ——— molecular-kinetic theory for high speeds with $N = 2.9 \times 10^{14} \text{ cm}^{-2}$ and $K_S = 3.4 \times 10^{10} \text{ s}^{-1}$; - - - hydrodynamic theory with $\ln(L/L_S) = 6.46$; — combined theory with $\ln(L/L_S) = 7.5$, $N = 2.0 \times 10^{13} \text{ cm}^{-2}$ and $K_S = 1.3 \times 10^5 \text{ s}^{-1}$.

weaker interactions, and the locus of molecular displacement effectively shifts from the surface of the solid to the plane immediately above the absorbed layer, where the influence of the solid is reduced. At intermediate speeds, the unsteady transition between these two planes gives rise to the observed stick-slip behavior.

The notion that there is more than one mechanism for the effect of wetting speed on the dynamic contact angle is well rooted in the literature. Schwartz and Tejada (1972) found an apparently discontinuous change in slope with speed in their data and concluded that there were at least two mechanisms in operation. The lower speed data could be represented by molecular-kinetic theory, whereas the higher speed data could be fitted to an expression of the form $\tan(\theta_D)$ proportional to Ca raised to a power. Similarly, Seebergh and Berg (1992) offered different correlations for data at capillary numbers below about 10^{-5} and above 10^{-3} . Hoffman (1975) suggested that changes in interfacial forces accounted for any low-speed variations in the contact angle that lay outside his correlation.

A small degree of surface roughness, up to at least $1\text{ }\mu\text{m}$, appears to have little effect on the dynamic angle (Schwartz and Tejada 1972). However, Seebergh and Berg (1992) associated degrees of surface roughness so light as to be unmeasurable by mechanical profilometry with unsteady, stick-slip motion of the wetting line. Cain *et al.* (1983) also reported that a surface roughed to a fraction of a micron caused the wetting line to be serpentine at rates of advance of about $10\text{ }\mu\text{m/s}$. Jansons (1985, 1986) modeled the effect of random roughness on the moving wetting line at small capillary number by considering successive pinning and release events at individual asperities. According to the theory, the motion of the wetting line can appear uniform at a distance from the wetting line which is large compared with the scale of the roughness, and the dynamic contact angle is predicted to be larger than the microscopic contact angle.

The degree of sensitivity of the dynamic contact angle to flow geometry is fundamentally and practically important. Jiang, Oh and Slattery

(1979) compared Hoffman's data for a capillary tube with some data of Schwartz and Tejada for a wire entering a pool and found reasonable agreement for cases where inertial effects were negligible and gravitational effects modest. They suggested that the contact angle may be independent of macroscopic geometry under restricted circumstances. There are other observations and results that support this hypothesis. The above comparison between Hoffman's data and Blake's suggests some degree of invariance to flow geometry. Burley and Jolly (1984) found in plunging-tape experiments that the dynamic contact angle was not affected by the angle with respect to the vertical that the tape entered the pool. Bracke, De Voeght and Joos (1989) applied their contact-angle data for plunging strips to predict successfully the rate of spreading of drops and the unsteady advance of the wetting line following the initial contact of a strip with the surface of a pool. On the other hand, Ngan and Dussan V. (1989) measured contact angles for low-capillary-number displacement between parallel plates spaced 0.1 to 1.2 mm apart and found that the apparent contact angle depended on the gap between the plates.

Virtually no dynamic contact angle data are available for non-Newtonian liquids, despite their prevalence in industrial coating processes. The effect of viscosity for Newtonian liquids and the expected high shear rates near the wetting line suggest the importance of shear-thinning behavior. Elastic properties need to be considered as well.

Although the origins of the dynamic contact angle are not clear, this review of theory and experimental results allows a few tentative conclusions to be drawn. At low capillary and Weber numbers, the dynamic contact angle has some degree of invariance to macroscopic geometry. The mechanism or mechanisms that cause the static and dynamic contact angles to differ operate locally at submicroscopic distances from the wetting line. Some portion of the difference between the dynamic and static contact angles is likely to be due to hydrodynamic bending of the interface on the submicroscopic

scale, particularly at capillary numbers above about 0.001. Hydrodynamic theory is well developed, and certain experimental data appear to correlate with the capillary number. Although there may be systems for which hydrodynamic bending is the only mechanism, there clearly are other systems whose behavior at low capillary numbers cannot be explained by hydrodynamic bending alone. For these systems, the submicroscopic contact angle appears to depend upon speed, and the variation is not always smooth. Thermodynamic equilibrium does not prevail at the wetting line, and molecular-kinetic theory provides a nonhydrodynamic mechanism for the difference between the dynamic and static contact angles. In general both mechanisms may operate together, but so far there is no definitive way to sort out the relative contributions.

All considered, it is still necessary to conduct experiments to obtain the dynamic contact angle for particular material systems and geometries. Some invariance to geometry is likely at small capillary and Weber numbers and moderate Bond numbers, but the degree of invariance and the precise parameter ranges are not established. In practical coating flows, the capillary and Weber numbers are commonly not small, in which case the macroscopic hydrodynamics will affect the dynamic contact angle. Under these conditions, the dynamic contact angle cannot be expected to be invariant to flow geometry.

3.4 DYNAMIC WETTING FAILURE

In the context of coating, the most important phenomenon associated with the dynamic contact angle is dynamic wetting failure. At sufficiently high speeds, the wetting line segments, and a thin film of air intrudes between the liquid and the solid. The flow becomes unsteady and three-dimensional, and air bubbles may be entrained into the liquid. Dynamic wetting failure is observed to occur when the dynamic contact angle approaches 180°. The term ‘air entrainment’ is most appropriate when visible air bubbles are produced.

3.4.1 EXPERIMENTAL OBSERVATIONS

The development of dynamic wetting failure for the well studied case of a tape entering a pool is typical. The wetting line becomes unsteady and breaks up into straight-line segments, and an air film forms. Each segment of the wetting line is inclined from the horizontal at an angle that increases steadily with speed. At any instant, the wetting line has the appearance of sawteeth (Perry 1967; Burley and Kennedy 1976; Blake and Ruschak 1979; Burley 1992), and air bubbles may be formed at the downstream vertices of the sawteeth and carried into the liquid. The scale of the sawteeth depends upon fluid properties and flow geometry and can be large enough to be readily visible or small enough to require magnified viewing.

The case where only one sawtooth, having one vertex, forms is special but particularly instructive. The photograph reproduced in Fig. 3.22 shows such a case for a tape plunging into aqueous glycerol. Fig. 3.23 is a schematic drawing of the air film. The wetting line consists of two slanted but steady straight-line segments in the shape of a ‘V.’ The vertex may be several centimeters downstream of the pool surface, and over this distance the liquid is separated from the substrate by a thin, triangular-shaped layer of air contained within the ‘V.’ As speed increases, the angle of inclination of the segments with respect to the horizontal increases. For polyester tape plunging into a pool of 100 mPa s aqueous glycerol, Blake and Ruschak (1979) showed that the angle of inclination increases such that the component of substrate speed normal to each segment remains constant. They termed this speed the maximum speed of wetting. Initially, no visible air bubbles are produced, but as the speed of the tape and the inclination of the wetting line segments increase, air bubbles begin to be entrained from the vertex. At still higher speeds, an air tube may form and persist for a significant distance downstream before breaking up.

Perry (1967) was the first to examine air entrainment in liquid/solid systems in detail. He found that he could influence the air film by

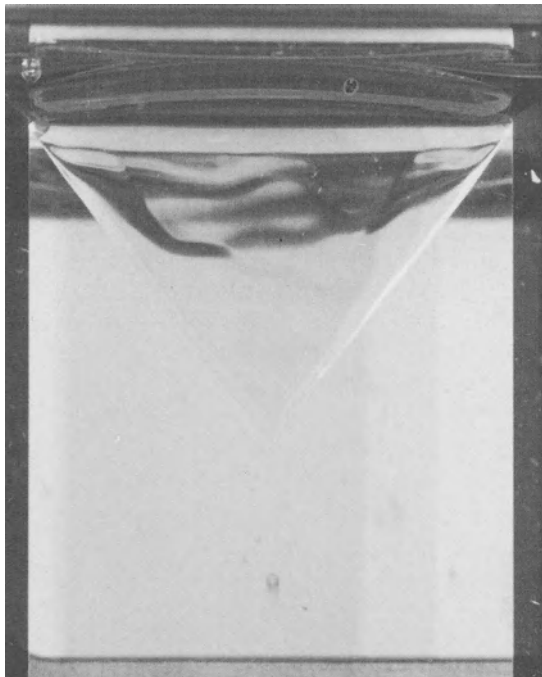


Figure 3.22 Photograph of gelatin-subbed, 35 mm wide poly(ethylene terephthalate) tape entering a pool of aqueous glycerol (nominal viscosity, 50 mPa s; surface tension, 62 mN/m). An air film, triangular in shape, separates the liquid and the tape. The segments of the wetting line are inclined at about 51° from horizontal. The tape is transparent, so wetting lines on both sides are visible. The tape speed is 0.585 m/s, and the dynamic contact angle reaches 180° at 0.39 m/s.

making changes in the macroscopic geometry or flow field. For example, he could change or eliminate the air film by placing a solid object in proximity or by jetting the liquid toward the air film. The application of a slight suction to the three-phase zone in bead coating increases the air entrainment speed (Beguin 1954; Gutoff and Kendrick 1987). Similarly, application of an electric field attracts the liquid to the solid and increases the speed at which dynamic wetting failure occurs (Miller and Wheeler 1962).

Using an optical method, Perry estimated the thickness of the visible air film as about 0.9 μm . Miyamoto (1991) used curtain coating to coat 122 mPa s gelatin onto gelatin-subbed triacetyl-

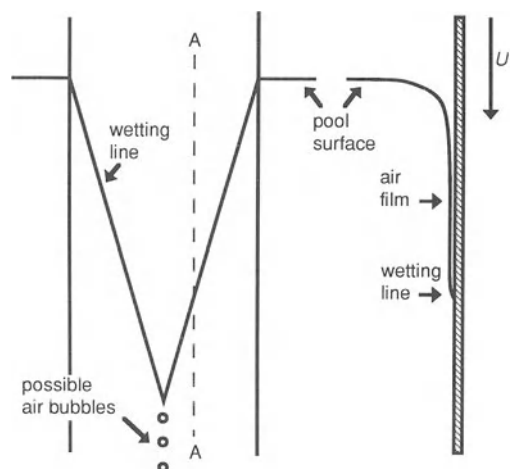


Figure 3.23 Schematic of a sawtooth wetting line and its associated air film for a tape vertically entering a pool.

cellulose tape and inspected the dried coatings by microscopy. For conditions where air bubbles appeared in the dried coating, Miyamoto estimated from the number and size of the bubbles an average air-film thickness in the range of 0.05 to 0.8 μm , with thickness increasing with speed. Below a certain speed no air bubbles were found, and the estimate is zero. However, Miyamoto did find craters in the dried coating at the lower speeds, which he postulated were created by air bubbles that had dissolved. He established experimentally that micron-sized bubbles dissolve in seconds and concluded that some air is entrained below the speed at which air bubbles appear in the dried coating. However, it is not clear how this interpretation can be reconciled with observations that the onset of both a sawtooth wetting line and the entrainment of air bubbles appear to be sudden.

Mues, Hens and Boij (1989) applied laser-Doppler velocimetry to bead coating at a speed about two-thirds of that for the obvious onset of air entrainment. They inferred that a thin air film extends a distance on the order of 100 μm downstream of the apparent wetting line. They did not determine whether bubbles were created in the coating.

Some correlations for the onset of dynamic wetting failure in experiments are available from the literature. The speed at which the dynamic contact angle reaches 180° , that for the onset of the sawtooth wetting line, or that for visible air entrainment may be reported. In the following correlations with dimensional parameters, speed is given in m/s, viscosity in mPa s, and surface tension in mN/m. Perry (1967) found that the air-entrainment speed for magnetic recording tape plunging into a pool of aqueous glycerol is inversely proportional to viscosity raised to a power:

$$U = \frac{3.5}{\mu^{0.8}} \quad 20 < \mu < 300, \theta_A = 70^\circ \quad (3.29)$$

$$U = \frac{6.6}{\mu^{0.73}} \quad 20 < \mu < 300, \theta_A = 20^\circ \quad (3.30)$$

The tape with a 20° advancing contact angle entrained air at a higher speed than that with a 70° contact angle. Increased surface tension also raised the air-entrainment speed. Burley and Jolly (1984) determined the following relationship for plunging tapes of cellophane, Melinex polyester,

and polypropylene:

$$U = 0.395 \left(\frac{\sigma}{\mu} \right)^{0.77} \quad 0.2 < \frac{\sigma}{\mu} < 3.2 \text{ m/s} \quad (3.31)$$

For a 180° dynamic contact angle, Gutoff and Kendrick (1987) found that the expression

$$U = \frac{5.1}{\mu^{0.67}} \quad 1 < \mu < 1000, \quad 22 < \sigma < 72 \quad (3.32)$$

holds for various liquids on gelatin-subbed polyester tape. Similarly, the data of Blake (1993) for poly(ethylene terephthalate) tape entering a pool of aqueous glycerol can be represented as

$$U = \frac{10.7}{\mu^{0.827}} \quad 1 < \mu < 670, \quad \sigma \approx 65 \quad (3.33)$$

The data and the fitted correlation are shown in Fig. 3.24. Virtually identical results, not shown, were obtained on gelatin-subbed poly(ethylene terephthalate).

Bracke, De Voeght and Joos (1989) obtained from the empirical equation (3.27)

$$Ca = 0.25 \quad (3.34)$$

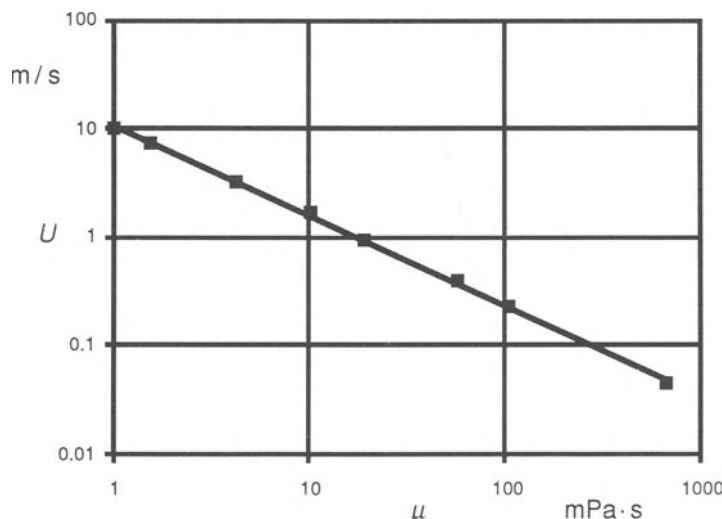


Figure 3.24 Data of Blake plotted as U versus μ for the onset of air entrainment for poly(ethylene terephthalate) tape entering a pool of aqueous glycerol. The solid line is equation (3.33).

However, constant capillary number is clearly not a precise criterion.

Finally, Wilkinson (1975) obtained data for the onset of air entrainment for a scraped cylinder rotating into a pool; presumably the cylinder surface was damp as it entered the pool. The liquids were aqueous glycerol and mixtures of hydrocarbon oils. The data can be represented by

$$Ca = 0.64\mu^{0.13} \quad \text{or} \quad U = 0.64 \frac{\sigma}{\mu^{0.87}}$$

$$29 < \mu < 288, \quad 30 < \sigma < 74 \quad (3.35)$$

So, different experimenters using different materials arrived at similar results. The inverse dependence of speed on viscosity is well established; a direct dependence on surface tension is probable but less firm. If the above expressions are evaluated for a viscosity of 10 mPa s and a surface tension of 65 mN/m, the results are 0.55 m/s from equation (3.29); 1.1, (3.30); 1.7, (3.31); 1.1, (3.32); 1.6, (3.33); 1.6, (3.34) and 5.6, (3.35). The speed from the scraped cylinder data stands out as high; otherwise, there is a variation of about a factor of three that might be attributable to the range of materials used.

At first glance, it may appear that surface roughness should always decrease the air entrainment speed, as the wetting line must move a greater distance across a rough surface than across a flat one of equivalent macroscopic dimensions. With a rough surface, the local speed of the wetting line must exceed the overall wetting speed for at least part of the time, hence air entrainment may be prematurely triggered. Theoretical studies of wetting such as those of Jansons (1985, 1986) and Joanny and Robbins (1990) indicate that the unsteady pinning and release of the wetting line as it moves across a rough or otherwise heterogeneous surface leads to energy dissipation in the vicinity of the wetting line above that expected on a smooth surface. As a result, the dynamic contact angle is expected to increase and the speed of dynamic wetting failure decrease.

On the other hand, trapping of air within surface cavities and hollows of very rough or

fibrous materials could lead to the formation of a composite liquid/solid–liquid/air interface. Small pockets of air might not be detected. Furthermore, they might reduce the net drag of the solid surface and so could increase the speed for the onset of visible air-entrainment. A related effect has been observed experimentally by Menchaca-Rocha (1992), who found that the mobility of mercury drops sliding across roughened glass plates increased with roughness due to the formation of a composite mercury/glass–mercury/air interface that reduced solid/liquid contact.

Overall, it does not seem possible to make generalized predictions on the effects of roughness. Once again, experimentation is necessary.

Buonopane, Gutoff and Rimore (1986) measured the effects of surface properties on air-entrainment speed in a plunging-tape experiment. The properties of the solid changed the air-entrainment speed by about a factor of 10. They concluded that speed increased with root-mean-square roughness, but that surface wettability had relatively little effect. These conclusions have yet to be confirmed, and our own experience leads us to doubt their generality.

In practice, liquids are frequently non-Newtonian. Shear thinning is likely to result in reduced viscosity near the wetting line and increased speed. We have found, for example, that the onset of air entrainment for poly(ethylene terephthalate) tape plunging into 21 mPa s aqueous gelatin, a modestly shear-thinning solution with a surface tension of 48 mN/m, occurs at 2.8 m/s. For a Newtonian liquid, equation (3.31) predicts 0.75 m/s, (3.32) 0.66, and (3.33) 0.86; all of these are well below the actual value.

A basic limitation of plunging tape and fiber experiments is that hydrodynamic forces are never more than comparable with capillary effects. Kistler (1983) and Blake, Clarke and Ruschak (1994) investigated stronger hydrodynamic effects on dynamic wetting failure using curtain coating (Chapter 11c). Kistler reported experiments for aqueous glycerol on a scraped cylinder. He found that the air entrainment speed at first increases with flow rate, reaches a maximum, and then decreases. That is, there is an optimum flow rate

that maximizes speed. Thus, air entrainment can depend significantly upon a flow parameter.

Blake, Clarke and Ruschak coated aqueous solutions of gelatin and other polymers onto dry base and found the same qualitative trend but much higher speeds for a given low-shear viscosity. They achieved conditions where the Weber number based on final film thickness was of order unity or larger and viscous and inertial effects were of comparable importance. They found that coating speed at the onset of air entrainment varied by over two orders of magnitude as flow rate, impingement angle, and impingement speed were changed. Flow visualization established that the speed maximized over flow rate corresponds to a wetting line position directly beneath the curtain. For aqueous gelatin the maximum speed can be represented as

$$U = \frac{8.12 V_n^{0.81}}{\mu^{0.19}} \quad (3.36)$$

in which μ is the low-shear viscosity and V_n the impingement speed normal to the solid in m/s. The value of the exponent of viscosity in equation (3.36) is much less than the 0.7–0.8 found in plunging tape experiments, but the hydrodynamic regime differs. Also, the shear-thinning nature of aqueous gelatin probably accounts for at least part of the difference. Because of high shear rates near the wetting line, the apparent viscosity is significantly reduced below its low-shear value.

We have found that the air-entrainment speed for 63 mPa s aqueous gelatin in a plunging tape experiment is about 1.8 m/s. For an impingement speed normal to the same tape of 2 m/s in curtain coating, the maximum air entrainment speed is about 6.5 m/s. In this latter case, the Weber number is close to 10, and the Bond number based on final film thickness is much less than unity. These conditions lie well beyond those achievable in the traditional flows by which dynamic wetting has been studied.

Blake, Clarke and Ruschak (1994) also found that for flow rates exceeding the optimum, air entrainment may be subject to hysteresis. In such cases, the speed at which air entrainment begins

as speed is increased can be substantially higher than the speed at which it ceases as speed is decreased. The effect can be as large as a few meters per second. Flow visualization shows that air-film formation in this situation is accompanied by major changes in the macroscopic flow field.

To illustrate the effects of macroscopic hydrodynamics on air entrainment, data from a coating experiment on a scraped cylinder are shown in Fig. 3.25. Aqueous glycerol solutions with viscosities 23 and 60 mPa s were delivered through a vertical pipette spaced 0.064 cm above the surface of the cylinder. The outside diameter of the nozzle was 0.29 cm and the inside diameter 0.13 cm. The experiment was performed by fixing the flow rate and increasing speed until an air film formed. Speed was then decreased until the air film disappeared. A hysteresis loop was found. Within the loop, an air film might or might not be observed, depending upon how the point was approached. The measured speeds were also inconstant, and the data points plotted are averages of three or four observations. When an air film formed, the liquid formed drops around the tip of the pipette. The speed for air-film formation was markedly affected by the flow rate, with speed increasing with flow rate. Speed also increased as viscosity decreased. Wilkinson's correlation, equation (3.35), predicts air entrainment at 2.7 m/s for 23 mPa s viscosity and 1.2 m/s for 60 mPa s viscosity. These values are roughly the results obtained at the highest flow rates.

3.4.2 THEORIES FOR DYNAMIC WETTING FAILURE

Dynamic wetting failure can be considered from two perspectives: how an air film forms between the liquid and the solid as speed increases, and, once formed, how the film vanishes as speed decreases. If there is hysteresis, then the speed for film formation is higher than the speed for film disappearance.

Perry (1967, p. 103) applied the film-formation theory of Landau and Levich, and Deryagin (see Ruschak 1985 for a review) to an air film in the plunging-tape geometry. This gives, to lowest

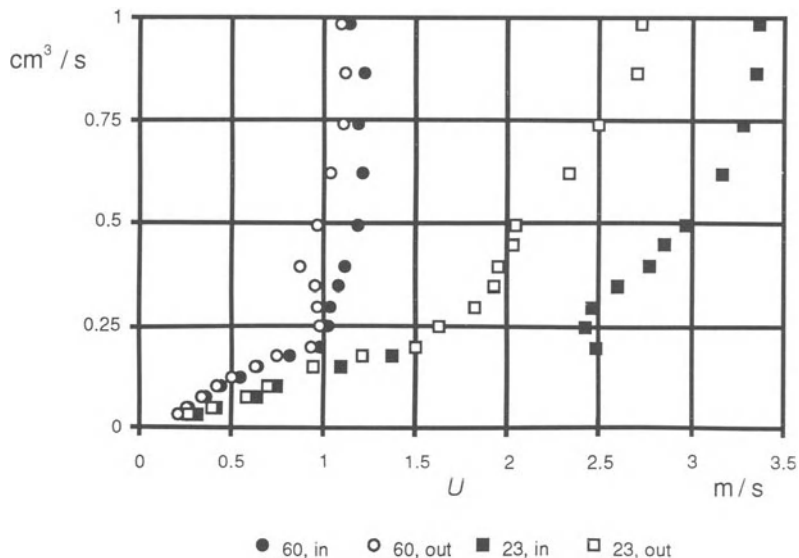


Figure 3.25 Data of Ruschak plotted as volumetric flow rate versus U for aqueous glycerol coated onto a scraped cylinder from a pipette. Dark symbols represent the speed at which air entrainment began as speed increased, and light symbols the speed at which air entrainment ceased as speed decreased. The numbers in the legend indicate viscosities in mPa s.

order,

$$H_A^\infty = 1.34R \left(\frac{\mu_A U}{\sigma} \right)^{2/3} \quad (3.37)$$

where H_A^∞ is the thickness of the air film, μ_A the viscosity of air, and $R = L_\sigma/\sqrt{2}$ the radius of curvature at the solid surface of the static meniscus that approximately describes the surface of the pool for a dynamic contact angle of 180° (see equations (3.6) and (3.18)). An evident shortcoming of equation (3.37) is that it predicts an air-film thickness regardless of how low the speed. Another weakness is that the prediction does not depend upon the viscosity of the liquid. Perry compared his experimental estimate for the thickness of the air film, $0.9 \mu\text{m}$, with the molecular mean free path for air, $0.09 \mu\text{m}$, and concluded that the air film is in slip flow. However, he did not take explicit account of this in his theory.

Teletzke, Davis and Scriven (1988) included the disjoining pressure of the air film and the viscosity of the liquid in their model. The flow

is a liquid displacing air from a narrow slit. Away from the walls, the meniscus is a cylindrical cap. They examined what happens as capillary number based on air viscosity decreases. At high capillary number, the film is so thick that disjoining pressure is negligible. On the other hand, for a sufficiently thin air film, disjoining pressure is expected to be negative and increasing toward zero with increasing film thickness. Hence, disjoining pressure promotes thinning of the air film, and there is no residual film below a critical capillary number. The critical capillary number based on the viscosity of air for a slit of order 1 mm in width is about 10^{-7} , which implies a minimum speed of order 0.001 m/s for the existence of an air film. When the film is thick, the circular meniscus appears tangent to the walls, but for small film thicknesses the meniscus appears to intersect the walls; that is, there is a dynamic contact angle of less than 180° . Bending of the meniscus by disjoining pressure occurs at sub-microscopic distances from the walls.

To account for the possible existence of an air

film at speeds far below that for the onset of visible air films in experiments, Teletzke, Davis and Scriven suggested that air is first entrained as a film too thin to be seen by visible light. Disjoining pressure causes such a thin film to be unstable; relatively thin regions tend to grow thinner, and the film breaks up into microbubbles that quickly dissolve in the liquid. The experimental results of Miyamoto (1991) and Mues, Hens and Boij (1989) qualitatively support the theory. Nevertheless, it is not clear that the theory is in accord with experimental results. The thinnest, visible air film is on the order of $1\text{ }\mu\text{m}$ thick; for a slit about 1 mm wide, the corresponding capillary number based on the viscosity of air is on the order of $10^{-5}\text{--}10^{-4}$, which implies speeds on the order of 0.1 m/s. This estimated speed seems much too low in light of the experimental data presented previously. At speeds far below that required for a visible air film, the dynamic contact angle is well below 180° , so the analysis of Teletzke, Scriven and Davis cannot apply at these speeds. Additionally, the theory predicts a weak effect of viscosity, whereas experiments show a major effect.

Theories of the dynamic contact angle can also

be used to predict dynamic wetting failure. Cox (1986) applied his hydrodynamic theory to predict air-film formation. There are no solutions to his hydrodynamic problem beyond the speed at which a dynamic angle of 180° is reached, and he postulated air-film formation at this point. A 180° contact angle corresponds to the following condition:

$$Ca = \frac{\frac{\pi}{6} \ln\left(\frac{4\mu}{3\pi\mu_A}\right) - \chi(\theta_w)}{\ln(L/L_s)} \quad (3.38)$$

Accordingly, the critical capillary number increases slowly with the viscosity of the liquid, although dimensional speed falls. If all else remains constant, the critical capillary number also increases as the submicroscopic contact angle decreases. Applying this expression to Blake's (1993) data for a tape plunging into aqueous glycerol gives the result shown in Fig. 3.26. The value 10.8 was used for $\ln(L/L_s)$. The theory also fits reasonably well Wilkinson's (1975) data for a scraped cylinder, but with $\ln(L/L_s)$ set to 3.45. This smaller value could reflect the presence of a liquid film remaining on the solid surface. Cox's theory accounts for

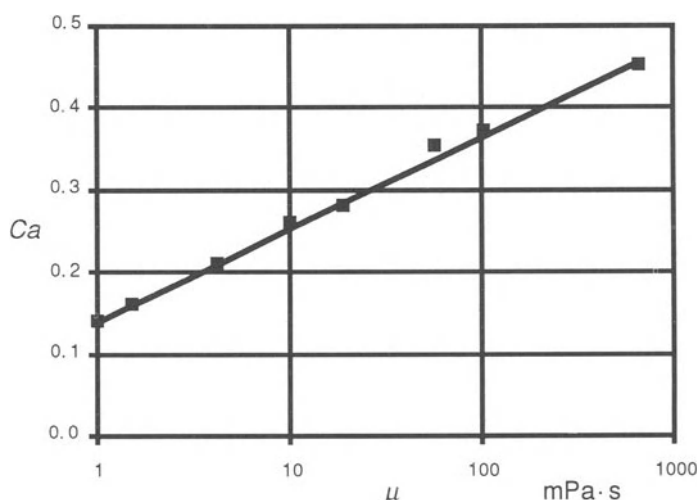


Figure 3.26 Data of Blake plotted as Ca versus μ for the onset of air entrainment for poly(ethylene terephthalate) tape entering a pool of aqueous glycerol. The solid line is equation (3.38).

the strong effect of the viscosity of the liquid but does not directly address the air film.

Molecular-kinetic theory predicts dynamic wetting failure when the dynamic contact angle reaches 180° because the wetting line can advance no faster. The sawtooth wetting line consisting of slanted straight-line segments that advance normal to themselves at the maximum speed is a consistent outcome. However, the air film is not addressed, and speed predictions require that the parameters K_s , N and v be known in advance.

3.4.3 MODEL PROBLEM AND ESTIMATES FOR AN ENTRAINED AIR FILM

A model problem similar to that of Teletsky, Davis and Scriven (1988) is helpful in explaining and estimating the factors likely to affect an air film. In Fig. 3.27, a thin air film separates a solid surface moving at speed U and a layer of liquid of average depth L_D . A gage pressure P_B above the liquid presses on the air film. The ends of the meniscus are most simply considered as circular sections; this is justifiable if the capillary and Weber numbers are small. These circular sections are tangent to a connecting straight line running parallel to the substrate at a distance equal to the final air-film thickness, H_A^∞ . The air film can be so thin that disjoining pressure affects it. In the manner of Teletzke, Davis and Scriven (1988), disjoining pressure is included in the flow

equations as $-A/H_A^3$, where H_A is air-film thickness and A is a positive constant taken to be 10^{-21} J in the sample calculations. The speed at the liquid/air interface is simply considered to be a constant V , expected to be greater than zero but less than U . If the pressure in the vicinity of the upstream circular section is P_L , then the radius of curvature of this section is approximately $R = \sigma/P_L$.

The origin of the coordinate system is on the solid surface where the upstream circular section makes its closest approach (Fig. 3.27). The flow in the air film is modeled by the lubrication approximation to the full set of equations; basically, hydrodynamic forces are strongest where the air film is thinnest and the streamlines are nearly parallel. The lubrication approximation enables the thickness of the air film beneath the upstream circular section to be approximated by a parabola, $H_A = H_A^\infty + X^2/2R$, which is accurate where the film is thinnest. In the lubrication approximation, the X -component of the Navier–Stokes equation reduces to $\partial P/\partial X = \mu_A \partial^2 U_A / \partial Y^2$ and the Y -component to $\partial P/\partial Y = 0$; therefore P does not vary across the film and the velocity profile is parabolic:

$$U_A = \left[\frac{3}{H_A^2} (U + V) - \frac{6Q}{H_A^3} \right] Y^2 + \left[\frac{6Q}{H_A^2} - \frac{4U}{H_A} - \frac{2V}{H_A} \right] Y + U \quad (3.39)$$

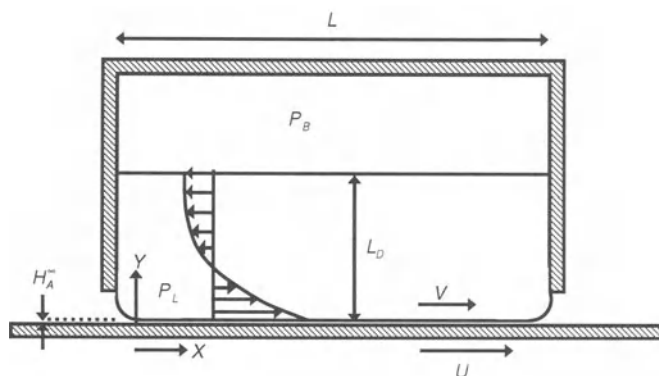


Figure 3.27 Model problem for an air film.

Here U_A is the X -component of velocity in the air, and Q is the volumetric flow rate per unit width of the air. From the velocity profile, the pressure gradient can be expressed as

$$\frac{\partial P}{\partial X} = \frac{12\mu_A}{H_A^3} \left[\frac{H_A}{2}(U + V) - Q \right] \quad (3.40)$$

In the fully developed air film, the pressure gradient is negligible and the velocity profile is nearly linear, so $Q = H_A^\infty(U + V)/2$. Equation (3.40) can be integrated with $P \rightarrow 0$, $X \rightarrow -\infty$, and the result evaluated at $X = 0$ to give the pressure developed in the air film:

$$P_L = \frac{3\pi\mu_A U(1+m)}{8(H_A^\infty)^{3/2}} \sqrt{2R} - \frac{A}{(H_A^\infty)^3} \quad (3.41)$$

Here, $m = V/U$, and the term on the far right represents the adjustment for disjoining pressure. Lubrication pressure tends to thicken the air film, but disjoining pressure tends to thin it. A large radius of curvature increases the lubrication pressure. The pressure changes by just a factor of two as the speed V at the meniscus ranges between 0 and U . Solving equation (3.41) for H_A^∞ gives

$$H_A^\infty = \left[\frac{3\pi\sqrt{2\sigma}\mu_A U(1+m)}{16P_L^{3/2}} + \sqrt{\left(\frac{3\pi\sqrt{2\sigma}\mu_A U(1+m)}{16P_L^{3/2}} \right)^2 - \frac{A}{P_L}} \right]^{2/3} \quad (3.42)$$

For the case $L \gg L_D$, the lubrication approximation can also be applied to the liquid layer. The velocity profile is again parabolic, and a pressure gradient $3\mu_V/L_D^2$ exists so that the net flow rate is zero. Because $H_A^\infty/L_D \ll 1$, the velocity profile in the air film is nearly linear, and equating shear stresses at the interface gives

$$m = \frac{1}{1 + 3\frac{H_A^\infty}{L_D} \frac{\mu}{\mu_A}} \quad (3.43)$$

The pressure gradient in the upper liquid layer causes the upper interface to be sloped, but in the special case where the layer thickness does not vary much, P_L can be estimated from the

gage pressure over the liquid and the hydrostatic pressure in the liquid as

$$P_L = P_B + \rho g L_D \quad (3.44)$$

Equations (3.42), (3.43) and (3.44) can be solved iteratively for H_A^∞ as a function of U .

Below a specific substrate speed there is no solution for H_A^∞ , as Teletzke, Davis and Scriven (1988) found. An air film exists only if the capillary number based on the viscosity of air is large enough that the term under the radical exceeds zero:

$$\frac{\mu_A U}{\sigma} > \frac{16}{3\pi(1+m)} \frac{P_L}{\sigma} \sqrt{\frac{A}{2\sigma}} \quad (3.45)$$

The air-film thickness at this critical capillary number is given by

$$H_A^\infty > \left(\frac{A}{P_L} \right)^{1/3} \quad (3.46)$$

For air films much thicker than this, the disjoining pressure term is negligible, and a result similar to Perry's is obtained:

$$H_A^\infty \approx \frac{\sigma}{P_L} \left[\frac{3\sqrt{2\pi}(1+m)}{8} \left(\frac{\mu_A U}{\sigma} \right) \right]^{2/3} \quad (3.47)$$

These concise results are qualitatively consistent with the complete calculations.

Sample calculations are shown in Fig. 3.28 for viscosity 10 mPa s, depth 0.2 cm (roughly representative of that in the plunging tape experiment), and surface tension 65 mN/m. The curves for increasing pressure loads P_L of 0, 100 and 1000 Pa show large speed increases. In plunging tape experiments, the speed for visible air entrainment is in the range of 0.55–1.7 m/s, depending upon the materials. The model predicts a very thin air film at speeds two or three orders of magnitude below this range, where the experimental dynamic contact angle is far below 180°. Moreover, the predicted speeds for an easily visible air film 1 μm thick are still too low. Accounting for Perry's observation that the air film is in slip flow would reduce the hydrodynamic pressure and increase speeds. However, the weak effect of the viscosity of the liquid, just a factor

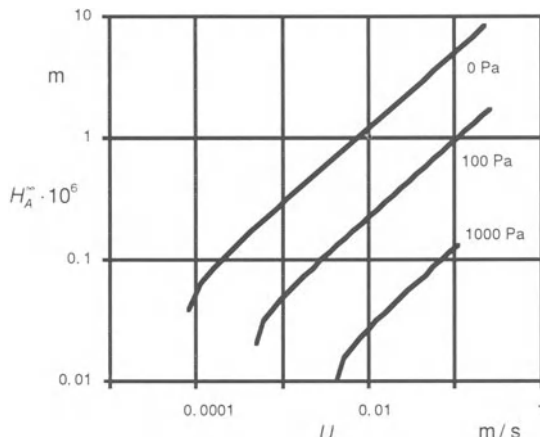


Figure 3.28 Plots of H_A versus U showing the effect of three pressure loads P_B on the thickness of an air film as predicted by equations (3.42), (3.43) and (3.44).

of two in speed, suggests a basic shortcoming in the model for the air film. The model does not explain dynamic wetting failure either qualitatively or quantitatively.

What appears to be wrong is viewing the appearance or disappearance of the air film as a gradual thickening or thinning with changing speed. Although solutions for two-dimensional air films can be obtained for speeds well below the observed onset of dynamic wetting failure, they are evidently unstable and are not realized in experiments. Observationally, dynamic wetting failure occurs at the maximum wetting speed where the dynamic contact angle is 180° . The wetting line adopts a sawtooth shape so that the component of the speed of the solid perpendicular to the wetting line does not exceed the maximum speed. The lengthened wetting line continues to wet the solid, except possibly at the downstream vertices. There is no visible air entrainment at the slanted wetting line segments bordering the air film. The air film grows or shrinks from its edges. A thick, visible air film can appear or disappear suddenly. So viewed, the air film is inherently a three-dimensional phenomenon not entirely explicable by two-dimensional models. The two-dimensional models probably describe

an existing air film away from its edges, but the existence of the film depends upon what takes place at its edges.

A complication is that the maximum speed of wetting depends in general upon the local flow field. The dynamics of the slanted segments of a wetting line are determined by the maximum speed of wetting there, the speed corresponding to a local dynamic contact angle of 180° (hence the strong viscosity dependence). If the flow field at the slanted wetting line is similar to the original two-dimensional flow, then the maximum speeds may be essentially the same and there may be little hysteresis. Such seems to be the case for a solid entering a pool. If the flow field at the slanted wetting line is markedly different from the original two-dimensional flow, then the maximum speeds may be much different; the onset of air entrainment may be catastrophic, and there may be large hysteresis. Such seems to be the case for curtain coating. Because the existence of the air film is linked to the maximum speed of wetting and hence the dynamic contact angle, the strong effect of the viscosity of the liquid found in experiments follows.

Finally, because the dynamic contact angle and maximum wetting speed generally depend on the macroscopic flow, the broad range of speeds at which a given liquid can undergo dynamic wetting failure also follows.

3.5 CONCLUDING REMARKS

Many opportunities remain for research on dynamic wetting and air entrainment. Although the subject has received much attention, no theory is as yet experimentally verified, generally accepted, and complete enough for general use in coating applications. On the experimental side, there is a clear need to study flows in addition to the plunging of solids into liquids and the displacement of air by liquid in capillary tubes. Air entrainment in other flows can occur at speeds much larger or smaller than that which would be expected from data on these flows. The effects of surface properties, including topography and electrical potential, need detailed examination.

Finally, non-Newtonian fluids are widespread in practice and need study.

The physics of dynamic wetting is key to high-speed coating processes. Because of the incomplete state of scientific study, most high-speed wetting problems have to be approached experimentally. Nonetheless, the qualitative and quantitative features of dynamic wetting and air entrainment reviewed in this chapter are useful in the design and interpretation of experiments.

REFERENCES

- Ablett, R. 1923. An investigation of the angle of contact between paraffin wax and water. *Phil. Mag.* **46**: 244–256.
- Adamson, A. W. 1982. *Physical Chemistry of Surfaces*. 4th edn. New York: Wiley.
- Beguin, A. E. 1954. Method of coating strip material. US Patent 2,681,234.
- Berg, J. C. ed. 1993. *Wettability*. Surfactant Science Series, Volume 49. New York: Marcel Dekker.
- Blake, T. D. 1993. Dynamic contact angles and wetting kinetics. In *Wettability*, Surfactant Science Series, Volume 49. ed. J. Berg. New York: Marcel Dekker.
- Blake, T. D., Clarke, A. and Ruschak, K. J. 1994. Hydrodynamic assist of dynamic wetting. *AIChE J.* **40**: 229–242.
- Blake, T. D. and Haynes, J. M. 1969. Kinetics of liquid/liquid displacement. *J. Colloid Interface Sci.* **30**(3): 421–423.
- Blake, T. D. and Haynes, J. M. 1973. Contact-angle hysteresis. *Progress in Surface and Membrane Science*. Volume 6. New York: Academic Press.
- Blake, T. D. and Ruschak, K. J. 1979. A maximum speed of wetting. *Nature*. **282**: 489–491.
- Bracke, M., De Voeght, F. and Joos, P. 1989. The kinetics of wetting: the dynamic contact angle. *Prog. Colloid Polym. Sci.* **79**: 142–149.
- Buonopane, R. A., Gutoff, E. B. and Rimore, M. M. T. 1986. Effect of plunging tape surface properties on air entrainment velocity. *AIChE J.* **32**: 682–683.
- Burley, R. 1992. Air entrainment and the limits of coatability. *JOCCA*. **5**: 192–202.
- Burley, R. and Jolly, R. P. S. 1984. Entrainment of air into liquids by a high-speed continuous solid surface. *Chem. Eng. Sci.* **39**(9): 1357–1372.
- Burley, R. and Kennedy, B. S. 1976. An experimental study of air entrainment at a solid/liquid/gas interface. *Chem. Eng. Sci.* **31**: 901–911.
- Cain, J. B., Francis, D. W., Venter, R. D. and Neumann, A. W. 1983. Dynamic contact angles on smooth and rough surfaces. *J. Colloid Interf. Sci.* **94**: 123–130.
- Cherry, B. W. and Holmes, C. M. 1969. Kinetics of wetting of surfaces by polymers. *J. Colloid Interface Sci.* **29**: 174.
- Cox, R. G. 1986. The dynamics of the spreading of liquids on a solid surface. Part 1. Viscous flow. *J. Fluid Mech.* **168**: 169–194.
- de Gennes, P. G. 1985. Wetting: statics and dynamics. *Rev. Modern Physics*. **57**(3): 827–863.
- de Gennes, P. G., Hua, X. and Levinson, P. 1990. Dynamics of wetting: local contact angles. *J. Fluid Mech.* **212**: 55–63.
- Dussan V., E. B. 1976. The moving contact line: the slip boundary condition. *J. Fluid Mech.* **77**: 665–684.
- Dussan V., E. B. 1979. On the spreading of liquids on solid surfaces: static and dynamic contact lines. *Ann. Rev. Fluid Mech.* **11**: 371–400.
- Dussan V., E. B. and Davis, S. H. 1974. On the motion of a fluid–fluid interface along a solid surface. *J. Fluid Mech.* **65**: 71–95.
- Dussan V., E. B., Rame, E. and Garoff, S. 1991. On identifying the appropriate boundary conditions at a moving contact line: an experimental investigation. *J. Fluid Mech.* **230**: 97–116.
- Elliott, G. E. P. and Riddiford, A. C. 1967. Dynamic contact angles. I. The effect of impressed motion. *J. Colloid Interface Sci.* **23**: 389–398.
- Glasstone, S., Laidler, K. J. and Eyring, H. J. 1941. *The Theory of Rate Processes*. New York: McGraw-Hill.
- Gutoff, E. B. and Kendrick, C. E. 1987. The flow limits of coatability on a slide coater. *AIChE J.* **33**: 141–145.
- Hansen, R. J. and Toong, T. Y. 1971. Dynamic contact angle and its relationship to forces of hydrodynamic origin. *J. Colloid Interface Sci.* **37**: 196–207.
- Hocking, L. M. and Rivers, A. D. 1982. The spreading of a drop by capillary action. *J. Fluid Mech.* **121**: 425–442.
- Hoffman, R. L. 1975. A study of the advancing interface. I. Interface shape in liquid–gas systems. *J. Colloid Interface Sci.* **50**(2): 228–241.
- Huh, C. and Mason, S. G. 1977. The steady movement of a liquid meniscus in a capillary tube. *J. Fluid Mech.* **81**: 401–419.
- Huh, C. and Scriven, L. E. 1971. Hydrodynamic model of steady movement of a solid/liquid/fluid contact line. *J. Colloid Interface Sci.* **35**(1): 85–101.
- Inverarity, G. 1969a. The wetting of glass fibres by liquids and polymers. PhD thesis, Univ. Manchester.
- Inverarity, G. 1969b. Dynamic wetting of glass fibre and polymer fibre. *Brit. Polymer J.* **1**: 245–251.
- Jansons, K. M. 1985. Moving contact lines on a

- two-dimensional rough surface. *J. Fluid Mech.* **154**: 1–28.
- Jansons, K. M. 1986. Moving contact lines at non-zero capillary number. *J. Fluid Mech.* **167**: 393–407.
- Jiang, T., Oh, S. and Slattery, J. C. 1979. Correlation for dynamic contact angle. *J. Colloid Interface Sci.* **69**(1): 74–77.
- Joanny, J. F. and Robbins, M. O. 1990. Motion of a contact line on a heterogeneous surface. *J. Chem. Phys.* **92**: 3206–3212.
- Johnson, R. E. and Dettre, R. H. 1993. Wetting of low-energy surfaces. In *Wettability*. Surfactant Science Series. Volume 49, ed. J. Berg. New York: Marcel Dekker.
- Johnson, R. E., Dettre, R. H. and Brandreth, D. A. 1977. Dynamic contact angles and contact angle hysteresis. *J. Colloid Interface Sci.* **62**(2): 205–212.
- Joos, F. M. 1992. Leveling of a liquid layer over a sorbing surface. AIChE Spring National Meeting, New Orleans, LA, pap. 49d.
- Kalliadasis, S. and Chang, H. 1994. Apparent dynamic contact angle of an advancing gas–liquid meniscus. *Phys. Fluids*. **6**: 12–23.
- Kistler, S. F. 1983. The fluid mechanics of curtain coating and related viscous free surface flows with contact lines. PhD thesis. Univ. Minnesota, Minneapolis.
- Levich, V. G. 1962. *Physicochemical Hydrodynamics*. Englewood Cliffs, N.J.: Prentice Hall.
- Menchaca-Rocha, A. 1992. The mobility of mercury drops on rough glass surfaces. *J. Colloid Interface Sci.* **149**: 472–480.
- Miller, Clarence, A. and Neogi, P. 1985. *Interfacial Phenomena*. New York: Marcel Dekker.
- Miller, F. D. and Wheeler, J. J. 1962. Coating high viscosity liquids. US Patent 3,206,323.
- Miyamoto, Kimiaki. 1991. On the mechanism of air entrainment. *Industrial Coating Research*. **1**: 71–88.
- Mues, W., Hens, J. and Boiy, L. 1989. Observation of a dynamic wetting process using laser-Doppler velocimetry. *AIChE J.* **35**(9): 1521–1526.
- Ngan, C. G. and Dussan V., E. B. 1989. On the dynamics of liquid spreading on solid surfaces. *J. Fluid Mech.* **209**: 191–226.
- Oliver, J. F., Huh, C. and Mason, S. G. 1977. Resistance to spreading of liquids by sharp edges. *J. Colloid Interface Sci.* **59**(3): 568–581.
- Perry, R. T. 1967. Fluid mechanics of entrainment through liquid–liquid and liquid–solid junctures. PhD thesis, University of Minnesota, Minneapolis.
- Petrov, P. G. and Petrov, J. G. 1992. A combined molecular–hydrodynamic approach to wetting kinetics. *Langmuir* **8**: 1762–1767.
- Ruschak, Kenneth J. 1976. Limiting flow in a pre-metered coating device. *Chem. Eng. Sci.* **31**: 1057–1060.
- Ruschak, Kenneth J. 1985. Coating flows. *Ann. Rev. Fluid Mech.* **17**: 65–89.
- Schrader, M. E. and Loeb, G. L. eds. 1992. *Modern Approaches to Wettability – Theory and Applications*. New York: Plenum Press.
- Schwartz, A. M. and Tejada, S. B. 1972. Studies of dynamic contact angles on solids. *J. Colloid Interface Sci.* **38**: 359–375.
- Seebergh, J. E. and Berg, J. C. 1992. Dynamic wetting in the low capillary number regime. *Chem. Eng. Sci.* **47**: 4455–4464.
- Tanner, L. H. 1979. The spreading of silicone oil drops on horizontal surfaces. *J. Phys. D: Appl. Phys.* **12**: 1473–1484.
- Teletzke, G. F., Davis, H. T. and Scriven, L. E. 1988. Wetting hydrodynamics. *Revue Phys. Appl.* **23**: 989–1007.
- Tilton, J. N. 1988. The steady motion of an interface between two viscous liquids in a capillary tube. *Chem. Eng. Sci.* **43**: 1371–1384.
- Voinov, O. V. 1976. Hydrodynamics of wetting. *Fluid Dynamics*. **11**: 714–721.
- Washburn, E. W. 1921. The dynamics of capillary flow. *Phys. Rev.* **17**: 273–283.
- Wilkinson, W. L. 1975. Entrainment of air by a solid surface entering a liquid/air interface. *Chem. Eng. Sci.* **30**: 1227–1230.

SURFACTANTS: STATIC AND DYNAMIC SURFACE TENSION

4

Yves-M. Tricot

4.1 INTRODUCTION

Surfactants – an acronym for surface-active agents – are versatile and ubiquitous chemicals. They are found in industrial areas related to detergents (Hancock 1984; Thayer 1993), pharmaceuticals (Tadros 1984; Attwood and Florence 1983), cosmetics (Ainsworth 1993), paints (Nylen and Sunderland 1965), pesticides (Wada *et al.* 1983; Tann, Berger and Berger 1992) and oil recovery (Neustalder 1984), to mention a few. Mother Nature used them, long before humans, as major building blocks of biological membranes, taking advantage of the so-called hydrophobic effect (Tanford 1980). This chapter focuses on applications of surfactants in liquid film coating processes, and in particular in coatings involving aqueous solutions, as encountered in the photographic industry.

The action of surfactants is a result of their partly hydrophilic and partly hydrophobic nature, which causes them to adsorb at interfaces separating media of different polarity. Water is particularly important, because of the strong hydrogen bonding which stabilizes water molecules in the bulk. Half of the stabilization energy is lost for the water molecules that must be at the interface. Additional energy is associated with the interface, which is observed as an interfacial tension. It is the energy required to create one unit of interfacial area (J/m^2) and is equivalent to a force acting along a boundary wetting line

(N/m). Unlike water, surfactant molecules require little energy to reside at the interface, because they are not well stabilized in the bulk. The hydrophilic part will orient towards the aqueous phase, while the hydrophobic part will orient towards the apolar phase. In the adsorption process, surfactant molecules replace high-energy surface water molecules, which reduces interfacial tension and decreases the free energy of the system. During the coating process, liquid films have to spread over solid surfaces or other liquid surfaces, an action generally called wetting. This will occur spontaneously if the new surface has a lower surface tension than the surface it covers. By reducing surface tension, surfactants therefore promote wetting.

Another critical parameter for liquid film coating is time. Coating is a dynamic process. The process of reduction of surface tension by surfactant adsorption is not instantaneous, but is generally diffusion-controlled. After sufficient adsorption time, the static or equilibrium surface tension will be reached. Determination of static surface tension is fairly easy (Section 4.4). Unfortunately, static surface tension is seldom reached during the most critical parts of a fast coating process and is of little use in predicting surfactant efficiency during coating. The dynamic or nonequilibrium surface tension is the relevant surface tension acting during fast processes. It is a recognized fact, and in coating practice surfactant

optimization is not made according to static surface tension data. However, the dynamic surface tension is not easy to measure and a workable wetting recipe is often empirically determined from practical coating trials. While coating tests cannot be completely eliminated, a more fundamental understanding of the dynamic wetting behavior reduces the risk of coating failure due to poor surfactant performance and could widen the coating window in particular towards higher speed.

The term 'dynamic surface tension' is not self-explanatory and requires further definition. For a particular interface, there is only one value for the static surface tension. It is a thermodynamic property which characterizes the equilibrium state of that interface at rest. However, the dynamic surface tension of the same interface, when placed under non-equilibrium conditions, can take a whole range of values. The highest value is generally that of the solvent (water), and the lowest will be equal to, and in some cases even lower than the static surface tension. All values in between are possible, depending on the time from creation of a fresh surface (surfactant adsorption time), or the rate of expansion or compression of the surface. The term dynamic surface tension for a particular solution of surfactant has only a clear meaning if one specifies under which dynamic process.

Methods for measuring dynamic surface tension abound but few of them are able to characterize surfaces at a time scale of relevance for coating processes (down to milliseconds or less). Some methods are designed to study surfaces' stretching or compression effects, others to study surfactant adsorption after fast surface creation with no or little subsequent area change. A typical geometry for the first case is an overflowing funnel and for the second case a flow coming out of a slit down an inclined plane. Both types are more complex than static surface tension measurement methods. Section 4.5 presents experimental results obtained with methods of the second type, chosen because they have been found to be the most reliable and practical to use. Examples of results obtained with a technique studying the

effect of surface expansion are presented in Chapter 11d.

The purpose of this chapter is to explain how surfactants can be better understood using a scientific experimental approach, as opposed to the commonly used empirical methods which consider surfactants as mysterious and unpredictable additives. The data presented here, measured using industrial (not purified) surfactants in aqueous and gelatin solutions, have not been previously published and were chosen because the media are of general interest. For practical applications, the most interesting results are obtained directly from actual coating solutions. An example of data taken from a real product is given, but with composition details withheld for proprietary reasons.

Dynamic surface tension methods can be applied to many types of liquids other than photographic coating solutions. However, one should not believe that they provide a miracle cure to solve all coating problems. Other important factors, such as bulk and surface rheology and flow characteristics, may cause coating failure. Contaminants may cause local coating defects, but have no effect on the measured dynamic surface tension, because it is not a local value. A systematic surfactant knowledge must be interactively combined with practical coating trials. Guidelines on how to use dynamic surface tension to determine wetting recipes with good chances of success are presented.

Unlike many other chapters in this book, this chapter is not about flow dynamics. Flow dynamics is treated in connection with surfactants in Chapter 11d, using literature values for parameters such as diffusion coefficient (diffusivity) and adsorption density to predict the effect of surfactants on the flow field. Using the methods described in this chapter, the required parameters could be experimentally determined in the solutions whose flow is simulated, and the calculated surface tensions could be compared with measured values. The two approaches are therefore complementary.

4.2 SURFACTANT PROPERTIES AND APPLICATIONS

4.2.1 BASIC SURFACTANT PROPERTIES

Surfactants exist in great variety. They all possess an hydrophobic (apolar) part and an hydrophilic (polar) one, but they can be distinguished according to the chemical structure of each of their parts. Based on the polar headgroup, one can find the following types of surfactants:

- anionic (permanent negative charge);
- cationic (permanent positive charge);
- non-ionic (only dipoles but no permanent charge);
- zwitterionic (simultaneous positive and negative charges);
- amphoteric (pH-dependent charge).

and the hydrophobic part can be:

- either hydrocarbon or fluorocarbon chain(s);
- single, double, multiple chains;
- linear or branched chain structure.

The degree of hydrophilic or hydrophobic character of surfactants has been described by the so-called HLB number (hydrophile–lipophile balance) (Griffin 1949). The HLB number is a predictor for the degree of solubility of a surfactant in a particular solvent or indicates its suitability for a particular type of application. HLB numbers lower than 10 indicate water-insoluble and above 12 water-soluble surfactants (Ross and Morrison 1988, Chapter IVA). Large collections of HLB numbers have been compiled by Becher (1985) and Becher and Griffin (1985).

Surfactants can also be characterized by their functions, which can be one or several of the following (non-exhaustive) list:

- wetting and spreading (on solid or liquid surfaces);
- emulsifying (insoluble solid, liquid or gaseous secondary phases);
- solubilizing (insoluble molecules);

- cleaning (through solubilizing and/or emulsifying);
- lubricating (solid surfaces).

Several of these functions overlap. For liquid film coating applications, the first three are the most important. Further general information about surfactants can be found in several extensive reviews and textbooks (Lucassen-Reynders 1981; Schick 1967; Rosen 1978; Ross and Morrison 1988).

Adsorption of surfactants at the air–water interface occurs because it lowers the free energy of the system. The adsorbed layer is in equilibrium with monomers in solution. However, when the surface becomes saturated, and more surfactant is added, it becomes more favorable to form surfactant aggregates in solution rather than to increase the adsorption density (Kahlweit, Busse and Jen 1991). These aggregates are called micelles and the concentration limit at which they start to form is called the critical micelle concentration (cmc). Micelles are more or less spherical structures with an aggregation number of the order of 100. The surfactant polar groups in a micelle are in direct contact with water, and form a shell that surrounds the core made of the hydrophobic part of the surfactants. The formation of micelles manifests itself by an abrupt change in a number of bulk parameters as the surfactant concentration is varied (conductivity, osmotic pressure, diffusivity, viscosity, etc.) and also by a plateau of surface tension (Ottewil 1984; Heimenz 1977). In a first approximation, the surfactant activity remains constant above the cmc, leading to a constant adsorption density and bulk monomer concentration. The excess of surfactants is absorbed in the form of micelles, which do not contribute significantly to the solution activity. The cmc and the size of the micelles depend strongly on the molecular properties of the surfactant, and on external parameters (ionic strength, pH, temperature, other solutes). Cmc's can vary by orders of magnitude. Many aggregates other than micelles can exist, depending on the molecular geometry of the surfactants and their concentration (Israelachvili, Marcelja and Horn 1980). Some typical structures are shown in Fig. 4.1.

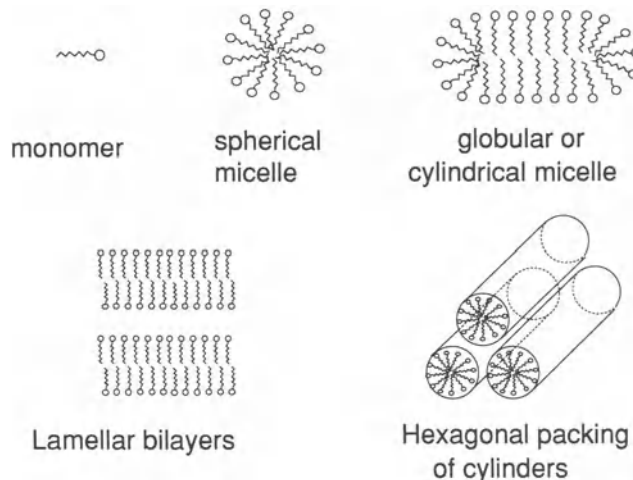


Figure 4.1 The most common surfactant aggregate structures.

Micelles are highly dynamic aggregates, with a half-life for micellar formation or breakdown of the order of 10^{-3} –1 s, while the residence time of monomers within micelles is of the order of 10^{-7} s (Aniansson *et al.* 1976; Okubo *et al.* 1979). This has important consequences for the interpretation of diffusion processes of hydrophobic solutes stabilized in micelles. A discussion of the various mathematical models which have been developed to describe micelles is presented in Chapter 11d.

4.2.2 SURFACTANT ACTIONS IN LIQUID FILM COATING

During the process of liquid film coating, surfaces are subjected to several disturbances. Surfactants respond to these disturbances by trying to restore adsorption equilibrium, through diffusion, convection and micellization processes. Figure 4.2 illustrates schematically how micelles, monomers and surface monolayers of surfactants interact.

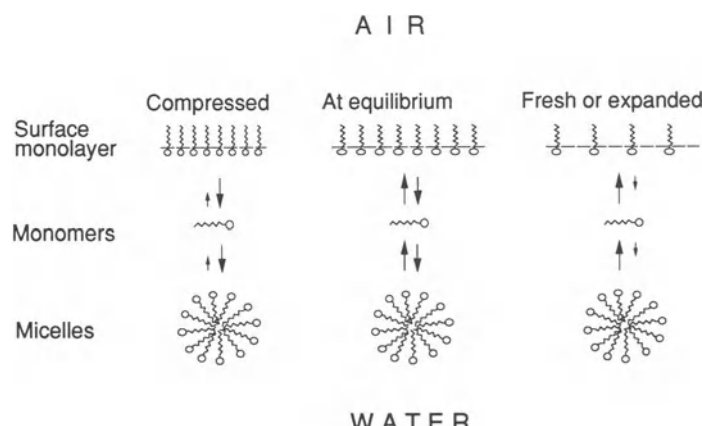


Figure 4.2 Dynamic response to a disturbed interface of surfactants at concentrations above the critical micelle concentration.

The micelles act as a reservoir of surfactant molecules which diffuses to or from the surface. Surface tension gradients induce the so-called Marangoni flows (Marangoni 1878; Ross and Morrison 1988, Chapter IVB). In this chapter, we will be concerned mostly with diffusion and adsorption processes. Theoretical concepts will be presented in Section 4.3.

When surfaces are created, stretched or compressed, the effective surface age, or residence time of a particular element of the flow at the liquid–air interface, can vary widely. Many coating processes use flow metering and guiding devices that produce laminar, multilayer flow exiting from parallel slits on an inclined plane and then transfer the liquid film on a moving web (see Chapter 11). Such devices are usually called hopper slides or cascades. Figure 4.3 illustrates a simplified coating situation and indicates the range of surface ages corresponding to various parts of the coating process. The residence time of the layer surface on the slide (up to a few seconds) is long enough for the surfactants to play an active and important role. Proper surfactant response will ensure stable interlayer wetting, proper wetting of the slide itself, and can guard against the formation of waves (Chapter 11d). During operation, the coating devices are positioned near a moving substrate that will

receive the liquid film. If placed within a few hundred microns of the substrate, one speaks of slide or cascade or meniscus coating (as is the case in Fig. 4.3), and if the liquid film is left to fall several centimeters before reaching the substrate, the technique is called curtain coating. Chapter 11 gives detailed descriptions. In the meniscus coating, the age that the back surface will reach can be very short (fractions of milliseconds) if the meniscus is held at or pinned to the edge of the coating device. When this is so, surfactants will usually have little impact because time is too short for adsorption to occur significantly. However, if the meniscus produces a heel or vortex (recirculation), surface ages can become rather long and surfactant effects will be important. Surfactants affect also edge quality and coating homogeneity after deposition on the substrate, until the layers have solidified and/or dried.

4.2.3 OTHER SURFACTANT ROLES

Using surfactants implies that they are present in the coating solutions before and after the coating process. Even during the process, surfactants can help control other defects than those related to macroscopic surface tension. Unfortunately, surfactants can also create unwanted

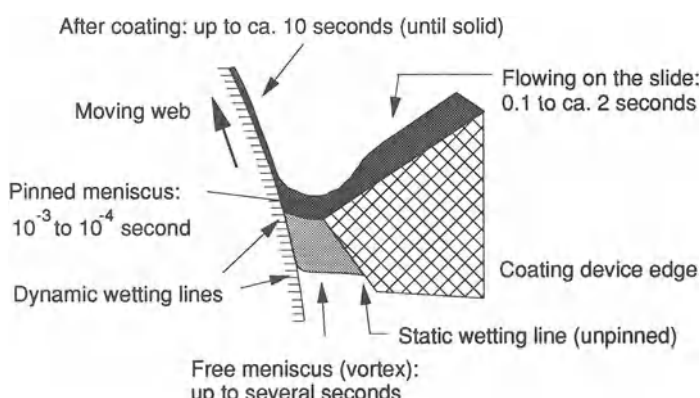


Figure 4.3 Surface age time scales in slide coating. Dark grey flow only: near optimum flow field, very short transit time at the back of the meniscus; dark + light grey flows together: free static wetting line and meniscus with recirculation or vortex (long transit times).

effects. These considerations are divided below into three categories.

4.2.3.1 Stability of coating solutions

A common problem with surfactants is the formation and stability of foam. While foam may be desirable in certain applications (cosmetic products, for instance), it is a nuisance for liquid film coating. Foam stability is high when the film surface elasticity, or excess surface tension due to non-equilibrium surfactant adsorption, is maintained for long periods of time (Ross and Morrison 1988, Chapter IVB; Abe and Matsumura 1983). The concept of surface elasticity is discussed further in Section 4.3. Fast-diffusing surfactants will quickly restore adsorption equilibrium and static surface tension, suppressing elastic energy and thus achieving low foam behavior. Some long-chain alcohols such as n-octanol have a similar effect and are used as effective defoaming agents. Even more powerful are non-volatile, very low surface tension substances made of perfluorinated hydrocarbons or silane polymers.

A completely different kind of problem can be caused by the solubilizing effect of surfactants on molecules adsorbed on suspended colloids. An example of this phenomenon is known in the photographic industry as ‘dye-stripping’, which is the removal of adsorbed sensitizing dyes from silver crystals (Diaz Garcia and Sanz-Medel 1986). This interaction later affects the properties of the finished product.

4.2.3.2 Control of coating defects

Surfactants must be able to avoid local defects caused by inhomogeneities in solution. These can be undissolved particles, hydrophobic oil droplets, insoluble molecules or even microscopic air bubbles. The solid substrate may be contaminated by hydrophobic impurities. All these defects can cause local de-wetting or ‘repellency’ spots (Gutoff 1992). The term ‘repellency’ refers to the phenomenon of liquid retraction from an hydrophobic zone. The driving force is the existence of surface tension gradients, which act as shear forces on

the adjoining liquids. Additionally, changes of temperature, composition or dynamic effects can all induce surface tension gradient-driven flows, generally called Marangoni flows (Marangoni 1878; Ross and Morrison 1988, Chapter IVB). Surfactants should be able to ‘outwet’ these hydrophobic spots. Unfortunately, as many industrial surfactants are of technical grade, they may bring oily impurities with them and produce hydrophobic spots which require other surfactants to fight them.

Surfactants can affect the response of coated films on ambient pressure fluctuations. It has been shown that some degree of surface elasticity is necessary to dampen waves produced by external disturbances (Ruschak 1987). To a degree, retaining some elasticity is incompatible with the fast diffusion required to fight potential repellency problems and avoid foam. A compromise may have to be found based on practical trials.

4.2.3.3 Interaction with other properties of the product

The surface properties of finished products can be strongly affected by surfactants. Some surfactants (often non-ionics) produce hydrophilic surfaces, which are easy to wet by processing liquids (like photographic developer) or by another coating solution when the product is manufactured in several steps. However, a very hydrophilic surface is also easy to contaminate by hydrophobic substances and may feel sticky. On the other hand, other surfactants (often anionics) tend to produce hydrophobic surfaces, which are more difficult to wet or re-wet, but are also more difficult to contaminate. The above trend is not necessarily general but was found for photographic products where the main component of the coating is gelatin (unpublished results).

In a liquid film coating process, the main role of surfactants is or at least should be to control the wetting behaviour of coating solutions. This is of course a matter of opinion, and there are situations where surfactants are also deliberately used to modify properties of the final products, not just to improve its manufacturability. However,

assigning too many roles to an additive such as a surfactant detracts from the robustness of the manufacturing process, and should be avoided whenever possible. Optimization of surfactant recipes is described in Section 4.5.6 based on their role of controlling dynamic surface tension. Surfactant optimization under different criteria has been reported elsewhere (Sturge 1977; Knox 1970).

4.2.4 SURFACTANT-RELATED PATENTS

A very large number of patents have been issued to describe the use and properties of many different types of surfactants. Virtually every surfactant on the market has been the object of one or several patents, some of them being still in effect. It is not within the scope of this chapter to review them. However, from reading patents about surfactants, it appears that it is difficult to assess the scientific reality of the advantages that certain types of surfactants are claimed to bring. In principle, patents exist for economic, not scientific reasons. It is probable that some claimed advantages are based on true and reproducible facts, but in other cases these advantages are probably exaggerated. In my opinion, there are no 'miracle surfactants', but many surfactants can be optimized to yield good results, based on simple physical principles describing surface tension and wetting, principles which have been known for nearly two centuries. Interestingly, a patent application has been issued, claiming the use of dynamic surface tension as one of the objects of the patent (Ishiwata *et al.* 1990). It was later withdrawn after publication of the search report. Such a claim was unjustified because there is nothing new in the desire to use dynamic surface tension as a critical parameter for optimizing coating. The idea goes back to Young's equation (Young 1805, see also Section 4.3), which quantifies how surface tension affects wetting. The only additional concept is that the relevant surface tension for the fast coating process is not the static surface tension, but the actual surface tension under the dynamic conditions, i.e. the dynamic surface tension. The concept

itself is rather trivial for anyone experienced in liquid film coating, but obtaining the relevant dynamic surface tension information is not. Demonstration of this concept has been reported (Valentini *et al.* 1991). The use of dynamic surface tension in optimizing surfactant recipe is further discussed in Section 4.7. Most methods for measuring dynamic surface tension are no longer patentable (although some patents had indeed covered such methods), because their use has been the object of scientific publications (see Section 4.4).

4.3 THEORETICAL TREATMENT

4.3.1 WETTING, SPREADING, ADHESION AND COHESION

Surface tension is a property defined by two immiscible phases. Wetting is a phenomenon (static or dynamic) involving three generally immiscible phases, usually a solid, a liquid and a gas. In all cases of interest in this chapter, wetting is the displacement of air by a liquid phase on the surface of a solid or another liquid phase. The boundary between the three phases is called the wetting line. Wetting is a complex subject which is treated in detail in Chapter 3. Below is a short review of the basic concepts related to wetting and spreading.

When a drop of liquid is placed on a solid surface, it can either spread completely (perfect wetting) or only partially, in which case the three-phase boundary defines a contact angle θ (Fig. 4.4). The relation between the three interfacial

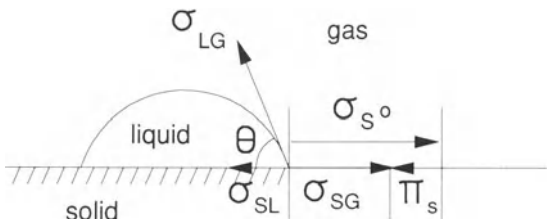


Figure 4.4 Vectorial representation of Young's equation (equation 4.1). See text for definition of symbols.

tensions and the contact angle is a force balance which has been proposed by Young (1805):

$$\sigma_{LG} \cos \theta = \sigma_{SG} - \sigma_{SL} \quad (4.1)$$

and

$$\sigma_{SG} = \sigma_{S0} - \pi_s \quad (4.2)$$

where σ is the interfacial tension and the indices S, L and G stand for solid, liquid and gas, respectively. σ_{S0} is the intrinsic interfacial tension of the pure solid and π_s is the two-dimensional film pressure exerted by the adsorbed gas on the solid. The contact angle can take in principle any value between 0° (perfect wetting) and 180° (no wetting). The film pressure π_s is usually negligible on apolar surfaces (hydrocarbons, PTFE). It is important for metals, which have high surface energies, causing strong water vapor adsorption.

When the liquid drop spreads completely, the contact angle θ is equal to 0°, $\cos \theta = 1$ and equation (4.1) becomes:

$$\sigma_{LG} \leq \sigma_{SG} - \sigma_{SL} \quad (4.3)$$

The difference between the two terms of equation (4.3) is the driving force of spreading, which is called the spreading coefficient, S :

$$S = \sigma_{SG} - \sigma_{SL} - \sigma_{LG} \quad (4.4)$$

S must be positive for spontaneous spreading. For spreading on solid surfaces, S is difficult to calculate because the solid–gas and solid–liquid interfacial tensions σ_{SG} and σ_{SL} are difficult to measure. However, if spreading of the liquid occurs on a second liquid, σ_{SG} in equation (4.4) should be substituted by σ_{L_2G} , the second liquid surface tension and σ_{SL} by $\sigma_{L_1L_2}$, the liquid–liquid interfacial tension, which are both directly accessible. An interesting example is benzene on water, for which S is initially positive and benzene spreads, when both liquids are pure, but becomes negative about a minute later, after each liquid saturates the other, causing retraction into droplets (Gutoff 1992, 129–130).

In a multilayer coating process, the top liquid layer must be able to spread over the layer just below. Aqueous layers cannot sustain interfacial tensions. Therefore, spontaneous spreading of

the top layer will occur (positive S in equation (4.4)) if its surface tension is lower than the surface tension of the layer below. Further requirements for multilayer coating stability are discussed in Section 4.5.6.

Important derived parameters are the work of adhesion and the work of cohesion (Blake 1984). The work of cohesion W_C of a liquid phase is the energy required to create two new interfaces of unit area:

$$W_C = 2\sigma_{LG} \quad (4.5)$$

Equation (4.5) is used in the ring detachment method for measuring static surface tension (Section 4.4). Similarly, the work of adhesion W_A is the work required to separate one unit area of a solid–liquid (or liquid–liquid) interface. For a solid–liquid interface, it is defined as:

$$W_A = \sigma_{SG} - \sigma_{SL} + \sigma_{LG} \quad (4.6)$$

and measures the attraction between the solid and the liquid phases. For two aqueous liquid phases, the interfacial tension is zero and W_A reduces to the sum of their surface tensions.

$$W_A = 2\sigma_{LG} \quad (4.7)$$

combined with equation (4.1), equation (4.6) gives:

$$W_A = \sigma_{LG}(1 + \cos \theta) \quad (4.8)$$

Equation (4.8) means that the condition for complete wetting ($\cos \theta = 1$) is $W_C = 2\sigma_{LG} \leq W_A$, or that the work of adhesion between the solid and liquid must be equal or superior to the work of cohesion of the liquid. If not, a finite contact angle will be formed. The difference between the work of cohesion and the work of adhesion is another definition of the spreading coefficient (equation (4.4)).

4.3.2 SURFACE TENSION COMPONENTS

On the molecular level, the attractive energy which needs to be overcome to create an interface can be of different types. The interfacial tension is decomposed into several components (Blake 1984; Hiemenz 1977):

$$\sigma = \sigma^d + \sigma^h + \sigma^m + \sigma^\pi + \sigma^i = \sigma^d + \sigma^{sp} \quad (4.9)$$

where the superscripts refer to dispersion forces (d), hydrogen bonds (h), metallic bonds (m), electron interactions (π) and ionic interactions (i). Only the dispersion forces (d) are common to all molecules. They arise from the interactions of fluctuating dipoles which exist even in non-polar molecules (London forces). All the other interactions can be referred to as specific forces (sp). The dispersion forces are also the only ones to operate across phase boundaries, as they are long-range and non-specific. Thus they are responsible for the work of adhesion W_A (equation (4.6)). From the studies of many non-polar substances, for which $\sigma_{LG} = \sigma^d$, it has been found experimentally that:

$$W_{A_{12}} = 2(\sigma_1^d \sigma_2^d)^{1/2} \quad (4.10)$$

where $W_{A_{12}}$ is the work of adhesion between liquids 1 and 2, and σ_1^d and σ_2^d are their respective dispersion component of surface tension. In water, the surface tension σ_w is composed of hydrogen bonds and dispersion forces, or:

$$\sigma_w = \sigma^h + \sigma^d \quad (4.11)$$

By measuring the interfacial tension σ_{WH} of water against pure hydrocarbon liquids, for which the surface tension σ_H is equal to its dispersion component σ_H^d , it is possible, by combining equation (4.6) with equation (4.10), to determine the dispersion component of the water surface tension σ_w^d :

$$\sigma_{WH} = \sigma_w + \sigma_H - 2(\sigma_w^d \sigma_H^d)^{1/2} \quad (4.12)$$

All quantities except σ_w^d are directly measurable, therefore equation (4.12) provides a means to evaluate this quantity. For water at 20°C, $\sigma_w = 72.5 \text{ mN/m}$ and $\sigma_w^d = 21.8 \text{ mN/m}$. A similar procedure can be applied to complex aqueous solutions, containing surfactants and/or colloids, to gain insight about the dispersion component in practical solutions, and about the surface free energy of solids (Janczuk *et al.* 1989).

4.3.3 STATIC SURFACE TENSION AND SURFACTANT ADSORPTION

The theoretical description of the relations between surface tension (static and dynamic) and surfactant

adsorption is a combination of thermodynamic relations, restricted to ideal systems, and empirical rules found to extend their application to practical cases. Detailed derivations and analyses can be found in several standard textbooks (see for instance Adamson 1967; Hiemenz 1977; Ross and Morrison 1988). Following is a short summary presenting the essential concepts relating surface tension and surfactant adsorption. Based on thermodynamic arguments, for an ideal, very dilute non-ionic surfactant, the variation of surface tension is related to surfactant adsorption according to the Gibbs equation:

$$\left(\frac{\partial \sigma}{\partial (\ln C)} \right)_{T,P} = -RT\Gamma \quad (4.13)$$

where σ is the surface tension, C the bulk concentration of the solute (surfactant), T the absolute temperature, P the pressure, R the universal gas constant, and Γ the surface concentration (or Gibbs's excess surface concentration) of the adsorbed surfactant. Equation (4.13) expresses the fact that surfactant adsorption reduces surface tension. The reduction of surface tension from the solvent value to the surface tension in the presence of adsorbed surfactant is called the spreading pressure π :

$$\pi = \sigma_s - \sigma \quad (4.14)$$

where σ_s is the surface tension of the solvent. At sufficiently low concentrations, the spreading pressure π becomes proportional to the surfactant concentration, or in other terms a surface tension isotherm would be linear (ideal behavior). For very surface-active solutes, the dilution required to reach ideality may be extreme and of little practical interest. Nevertheless, under such conditions an ideal surface equation of state can be derived from equations (4.13) and (4.14) (Ross and Morrison 1988):

$$\pi = \Gamma RT \quad \text{or} \quad \pi A = RT \quad (4.15)$$

where $A = 1/\Gamma$ is the molar surface area. For practical surfactant concentrations, equation (4.15) cannot be applied, but an empirical equation

(von Szyszkowski 1908), is often used:

$$\pi = \sigma_s - \sigma = RT \Gamma_\infty \ln(1 + C/a) \quad (4.16)$$

where Γ_∞ is the maximum excess surface concentration (or maximum adsorption density) and a an empirical constant. Below the critical micelle concentration (cmc), experimental plots of surface tension versus surfactant concentration can be very well fitted with equation (4.16) (see Section 4.5.3). Above the cmc, surface tension usually stays constant. Increase of surface tension is sometimes found above the cmc in the presence of impurities. The cmc is not always clearly defined, but can be seen sometimes as a broad transition region.

An adsorption isotherm can be derived from equations (4.13) and (4.16), as shown below. Equation (4.13) is rewritten as:

$$-\left(\frac{\partial\sigma}{\partial(C)}\right)_{T,P} = \frac{RT\Gamma}{C} \quad (4.17)$$

and taking the derivative of equation (4.16) yields:

$$-\left(\frac{\partial\sigma}{\partial(C)}\right)_{T,P} = \frac{RT\Gamma_\infty}{C+a} \quad (4.18)$$

Equating the right-hand terms in equations (4.17) and (4.18) and rearranging, gives:

$$\Gamma = \frac{\Gamma_\infty C}{a+C} \quad \text{or} \quad \frac{\Gamma}{\Gamma_\infty} = \frac{C}{a+C} = \frac{C/a}{1+C/a} \quad (4.19)$$

Equation (4.19) is known as the Langmuir adsorption isotherm, and the empirical constant a as the Langmuir constant. Because of its close relationship with equation (4.19), equation (4.16) is also called the Langmuir–von Szyszkowski equation.

By eliminating the surfactant concentration between equations (4.16) and (4.19), Frumkin (1925) obtained a new surface equation of state, relating the surface tension with the surfactant adsorption:

$$\sigma_s - \sigma = -RT\Gamma_\infty \ln\left(1 - \frac{\Gamma}{\Gamma_\infty}\right) \quad (4.20)$$

Equation (4.20) applies for both the static and dynamic surface tension. The area per surfactant

molecule is calculated from the adsorption density Γ (mol/m^2). Most surfactants occupy an area between 20 and 100 \AA^2 per molecule at saturation adsorption (when $\Gamma = \Gamma_\infty$). This area can vary considerably with the presence of other solutes that compete for the surface. The parameters Γ_∞ , a and σ_s are experimentally determined by a fit of the static surface tension versus surfactant concentration with equation (4.16) (see Section 4.5.3).

4.3.4 DIFFUSION AND DYNAMIC SURFACE TENSION

This section describes the action of diffusion as a mechanism trying to restore surfactant adsorption equilibrium after surface generation. Under conditions of diffusion-controlled adsorption (absence of adsorption barrier), the evolution of adsorption Γ with time is ruled by the Ward and Tordai equation (1946):

$$\Gamma = 2C_0\left(\frac{Dt}{\pi}\right)^{1/2} - 2\left(\frac{D}{\pi}\right)^{1/2} \int_0^{t^{1/2}} C_s(t-\tau) d\tau^{1/2} \quad (4.21)$$

where C_0 is the bulk concentration (far from the surface), C_s the subsurface concentration (concentration in equilibrium with the surface), D the diffusion coefficient (m^2/s), t the age of the surface (time), π the circle number π (not the surface pressure) and τ an auxiliary variable (s). The first term on the right-hand side of equation (4.21) represents the diffusion from the bulk to the subsurface. At the time of surface creation, the subsurface concentration and the adsorption density are nearly equal to zero. At very short surface ages, adsorption is still negligible and no significant back-diffusion takes place. A simple estimation of the diffusion coefficient (diffusivity) can be made from the initial stage of adsorption: a plot of Γ versus $t^{1/2}$ will be a straight line with a slope equal to $2C_0(D/\pi)^{1/2}$. When adsorption is significant, diffusion from the subsurface to the bulk (back-diffusion), represented by the second term (integral) of equation (4.21) cannot be neglected anymore. Evaluation of the integral term is complex and is usually approximated by iterative methods (van den Bogaert and Joos 1980).

Equation (4.21) is a rigorous description of truly diffusion-controlled adsorption. However, it has often been found easier and more convenient to use various approximations (van den Bogaert and Joos 1979). For surfactants following equation (4.16) (von Szyszkowski 1908) and for diffusion-controlled kinetics, Hansen (1960) has proposed approximations of equation (4.21) for short and long times. The short-time approximation is:

$$u = z + \left(1 - \frac{\pi}{4\bar{u}}\right)z^2 + \left(1 - \frac{2}{3\bar{u}} - \frac{\pi}{2\bar{u}} + \frac{\pi}{6\bar{u}^2}\right)z^3 \quad (4.22)$$

where

$$u = \frac{C_s}{a}; \bar{u} = \frac{C_0}{a} \quad \text{and} \quad z = \left(\frac{2C_0}{\Gamma_\infty}\right)\left(\frac{Dt}{\pi}\right)^{1/2}$$

and where C_s , C_0 , π and D have the same meaning as in equation (4.21). The parameters a and Γ_∞ are taken from the fit of the static surface tension data with equation (4.16). An initial value of the diffusion coefficient D is chosen and introduced in equation (4.22). The resulting values of the subsurface concentration C_s , as a function of the surface age t , are substituted to C in equation (4.16) (von Szyszkowski 1908) and yield a calculated curve of dynamic surface tension as a function of surface age. The calculated curve is then compared with the experimental data and the process is repeated with another value of the diffusion coefficient until a good fit is obtained. A diffusion coefficient for the short-time domain at a particular surfactant concentration is thus determined. The procedure is repeated for all measured surfactant concentrations.

The long-time approximation is:

$$\sigma = \sigma_{eq} + \frac{RT\Gamma_0^2}{C_0}\left(\frac{\pi}{kDt}\right)^{1/2} \quad (4.23)$$

where σ is the dynamic surface tension, σ_{eq} the equilibrium surface tension, Γ_0 the equilibrium adsorption density (different from Γ_∞) and k is a constant equal to 1 for anionic surfactants at low ionic strength, and equal to 4 for anionic surfactants at high ionic strength or for non-ionic surfactants at any ionic strength (Ross and

Morrison 1988). The equilibrium adsorption density Γ_0 is determined for each surfactant concentration by substituting Γ with Γ_0 and σ with σ_{eq} in equation (4.20) (Frumkin 1925). As for equation (4.22), values of the diffusion coefficient D are varied until a good fit with the experimental dynamic surface tension values is obtained.

Figure 4.5 shows the type of curves obtained from equations (4.22) and (4.23). Using two independent equations to simulate the short- and long-time domains of the experimental data offers more flexibility than equation (4.21). The best fit may lead to the determination of two different diffusion coefficients: one for the short-time and one for the long-time domain. Often with real surfactants, a concentration-dependent diffusion coefficient is found. Most industrial surfactants have indeed a complex diffusion behavior, as they are often mixtures of several surface-active compounds (see Section 4.5.1), and also because of the presence of micelles above the cmc. An extensive review of mathematical models and experimental data of surfactant adsorption and diffusion has been given by Chang and Franses (1994).

Discussion of other mechanisms affecting surface equilibrium, such as convection and surface area changes, can be found in Chapter 11d. These effects are of less significance for the dynamic

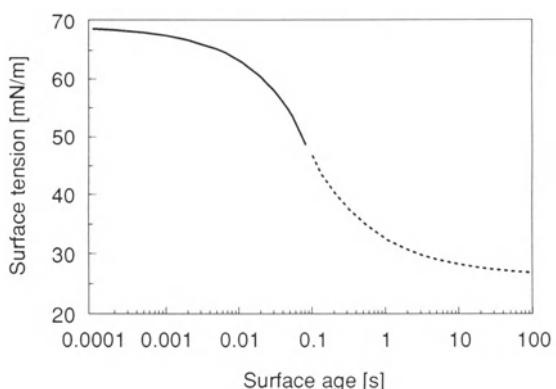


Figure 4.5 Combination of the short-time (solid line) and long-time (dashed line) Hansen approximations for simulation of dynamic surface tension.

surface tension methods used to produce the results presented in Section 4.5.

4.3.5 PARAMETRIC SIMULATION OF DYNAMIC SURFACE TENSION

It is possible to simulate the experimental dynamic surface tension values without any knowledge of the static surface tension, using a four-parameter equation (Hua and Rosen 1988):

$$\sigma = \sigma_M + \frac{\sigma_0 - \sigma_M}{1 + (t/t^*)^n} \quad (4.24)$$

where σ_M is the surface tension near to equilibrium (meso-equilibrium), σ_0 the surface tension extrapolated at zero surface age (not to be confused with σ_s , the surface tension of the solvent), t the surface age, t^* and n two characteristic constants. A typical curve produced by equation (4.24) is shown in Fig. 4.6. Its shape is very similar to that of the combined Hansen approximations, and excellent fits can easily be obtained (see Section 4.5.4). Regression is made using a linearized form of equation (4.24) (Hua and Rosen 1988). No molecular information can be derived from such a simulation. However, it is useful because static surface tension data are unnecessary and prediction of dynamic surface tension as a function of surface age and surfactant concentration can still be made. Equation (4.24) can also be applied

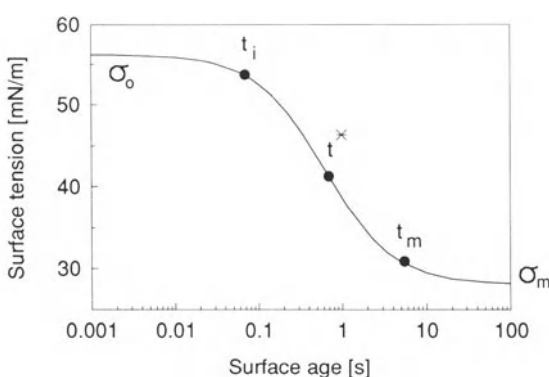


Figure 4.6 Typical curve of dynamic surface tension obtained using equation (4.24). The parameters are defined in the text.

to mixtures of surfactants or other complex solutions where static surface tension data do not follow equation (4.16).

4.3.6 SURFACE ELASTICITY AND SURFACE VISCOSITY

Many dynamic surface phenomena encountered in coating flows are due to the viscoelastic properties of surfaces. The surface elasticity is defined by (Gibbs 1961; Lucassen and Giles 1975; Lucassen-Reynders 1981):

$$E = \frac{d\sigma}{d \ln A} = A \frac{d\sigma}{dA} \quad (4.25)$$

where E is the dilational surface elasticity modulus, $d\sigma$ the surface tension increment corresponding to a relative molecular area change $d \ln A$ or dA/A . An equivalent definition relates E to the adsorption density:

$$E = - \frac{d\sigma}{d \ln \Gamma} = -\Gamma \frac{d\sigma}{d\Gamma} \quad (4.26)$$

Surface elasticity, measured isothermally from equilibrium surface pressure-molecular area curves, is called Gibbs elasticity. It is a thermodynamic property of the interface. Calculated values for the Gibbs surface elasticity can also be obtained as a function of parameters obtained from static surface tension data, as shown below. Differentiating equation (4.20) (Frumkin) with respect to the adsorption density Γ gives:

$$\frac{d(\sigma - \sigma_s)}{d\Gamma} = \frac{d\sigma}{d\Gamma} = RT\Gamma_\infty \frac{d \left[\ln \left(1 - \frac{\Gamma}{\Gamma_\infty} \right) \right]}{d\Gamma} \quad (4.27)$$

The logarithmic derivative term is rearranged as:

$$\begin{aligned} \frac{d \left(\ln \left(1 - \frac{\Gamma}{\Gamma_\infty} \right) \right)}{d\Gamma} &= \frac{1}{1 - \frac{\Gamma}{\Gamma_\infty}} \frac{d \left(1 - \frac{\Gamma}{\Gamma_\infty} \right)}{d\Gamma} \\ &= -\frac{1}{\Gamma_\infty - \Gamma} \end{aligned} \quad (4.28)$$

Combining equations (4.26), (4.27) and (4.28) yields:

$$E = RT\Gamma_\infty \frac{\Gamma}{\Gamma_\infty - \Gamma} \quad (4.29)$$

Finally, it is easily shown using equation (4.19) that $\Gamma/(\Gamma_\infty - \Gamma) = C/a$, and the elasticity is finally expressed as:

$$E = RT\Gamma_\infty(C/a) \quad (4.30)$$

Equation (4.30) has been used to describe the effect of elasticity in the stabilization of waves on a disturbed planar flow (Ruschak 1987). Surface elasticities measured under dynamic conditions are called Marangoni elasticities. As the surfaces are no longer isothermal under dynamic conditions, Marangoni elasticities are usually larger than Gibbs elasticities (Ross and Morrison 1988). In fact, there is a certain confusion in the literature, because what is called Marangoni elasticity is often a surface viscoelasticity. For instance, the dynamic surface tension response obtained after a jump of surface area of a surfactant solution, is an initial elastic response followed by a 'viscous' recovery to equilibrium surface tension. In this case, the mechanism of viscous dissipation of energy is surfactant diffusion and adsorption. Purely elastic behavior is characterized by a linear response to stress with no phase shift, as expressed in equation (4.25). However, under sinusoidal surface compression–dilatation cycles, the dynamic surface tension response was found to exhibit a phase shift with respect to the applied stress, which could reach up to 90° in the presence of micelles (Lucassen 1975). The 90° out-of-phase component of the surface tension response to surface area change is due to the surface dilational viscosity, defined as (Bergink-Martens *et al.* 1990):

$$\mu_s = \frac{\sigma - \sigma_{eq}}{d(\ln A)/dt} \quad (4.31)$$

where σ is the surface tension under surface expansion and σ_{eq} the surface tension of the surface at rest (equilibrium surface tension). The parameter μ_s ($N\text{s/m}$) is the two-dimensional equivalent of the three-dimensional bulk viscosity

μ ($\text{Pa s} = \text{N s/m}^2$). The surface dilational viscosity can only be determined from the surface under expansion or compression, unlike the Gibbs surface elasticity which is measurable from equilibrium experiments.

In oscillation experiments, the elasticity modulus is small at low frequencies, when the surface viscosity is dominant and dissipates most elastic energy, but at high frequencies the elasticity reaches a maximum limiting value which is generally higher than the Gibbs elasticity. At sufficiently high frequencies, diffusion can no longer contribute to energy dissipation and the surface becomes purely elastic. Wave dampening is optimum for a particular combination of viscous and elastic behavior, depending on the frequency of the perturbation (Ruschak 1987). Mathematical details of surface elasticity phenomena, and a recently developed measurement method based on an oscillating bubble, have been described by Lunkenheimer *et al.* (1990).

4.4 OVERVIEW OF SURFACE TENSION MEASUREMENT METHODS

4.4.1 THE WILHELMY PLATE

Proposed by Wilhelmy (1864), this is one of the simplest and most reliable methods used to measure surface tension. A clean, thin plate made of platinum, glass or even filter paper is placed vertically at the surface of the measured liquid. As the liquid wets the plate, the force F exerted by the meniscus on the plate is measured by a balance or a force transducer, and is expressed by:

$$F = p\sigma \cos \theta \quad (4.32)$$

where p is the perimeter of the plate, σ the surface tension and θ the contact angle of the liquid on the plate. If the plate is effectively clean, the contact angle is zero and the cosine term is equal to 1.

To avoid any buoyancy correction, the plate is positioned with its lower edge exactly at the average liquid level. The method can be calibrated with standard weights, independently of a reference liquid. It measures true static surface tension,

without any liquid motion. The reading is independent of the density of the liquid. In order to ensure zero contact angle, the plate must be thoroughly cleaned (platinum or glass) or replaced (filter paper) after each measurement.

The Wilhelmy plate technique is also applicable to dynamic surface tension measurements by placing the plate along a flowing liquid. A practical set-up is based on an inclined plane (van den Bogaert and Joos 1979). It will be described in more detail in Section 4.5.2.3.

4.4.2 THE DU NOUË RING

Named after du Nouë (1919), this method uses an horizontal ring instead of a vertical plate. The ring is normally made of platinum, to ensure good wetting, and easy cleaning through heating in a flame. Initially, the method consisted of measuring the force necessary to detach the ring from the liquid. The force to overcome is the cohesion of the liquid, equal to 2σ , as given in equation (4.5). The maximum force measured, equal to the weight of the meniscus held by the ring, is expressed as:

$$F = \sigma 4\pi R K \quad (4.33)$$

where R is the ring radius and K is a correction factor given by Harkins and Jordan (1930), which takes into account the small volume of liquid that remains attached to the ring and the difference between the ring radius and the actual radius of the meniscus in the rupture plane. The method is not as truly static as the Wilhelmy plate, as the meniscus is stretched – although as slowly as desired – during the measurement. Further refinements have been made to avoid the need for ring detachment and make the measurement automatic (Sucker *et al.* 1964). Specific details are given in Section 4.5.2.1.

4.4.3 THE CAPILLARY RISE

The capillary rise is based on the Laplace equation:

$$\Delta P = 2\sigma/R \quad (4.34)$$

where ΔP is the difference of pressure across a spherical interface of radius of curvature R . If the contact angle is smaller than 90°, the liquid will rise until the hydrostatic pressure just balances the Laplace pressure. At equilibrium:

$$\Delta P = \rho gh = 2\sigma \cos \theta / R \quad (4.35)$$

where ρ is the liquid density, g the gravity constant, h the meniscus height or capillary rise, σ the surface tension, θ the contact angle and R the radius of the glass tube. The method is used preferably when the contact angle is zero ($\cos \theta = 1$) because if a finite contact angle exists, its value is generally not known. The method is limited to liquids of low viscosity and the radius of the capillary tube must be precisely constant. Because of these limitations, this technique is used mostly for rough estimates of surface tension. It is not appropriate to measure even slow variations of surface tension.

4.4.4 THE OSCILLATING JET

The oscillating or vibrating jet has been originally described mathematically by Lord Rayleigh (Strutt 1897). It is applicable to the measurement of fresh surfaces, aged between *ca.* 3 to 50 ms. The measured liquid is ejected horizontally from an elliptical orifice. The differences of curvature in the elliptical section of the jet produce an internal pressure difference according to the Laplace equation:

$$\Delta P = 2\sigma(1/R_1 - 1/R_2) \quad (4.36)$$

where σ is the surface tension, R_1 is the small and R_2 the large radius of curvature in the elliptical section of the jet. The resulting flow causes the jet to oscillate between two extreme elliptical sections oriented at 90° to each other. When the flow is constant, this oscillation can be seen as a stationary wave. The dynamic surface tension can be calculated according to (Defay and Pétré 1971):

$$\sigma = \frac{4\rho V^*{}^2}{6a\lambda^2} \left(\frac{1 + (37/24)(b^2/a^2)}{1 + (5/3)(\pi R^2/\lambda^2)} \right) \Psi \quad (4.37)$$

where $\Psi = 1 + 2(\mu\lambda/\rho V^*)^{3/2} + 3(\mu\lambda/\rho V^*)^2$; μ is the liquid viscosity, ρ the density, V^* the volumetric flow rate, R the average radius of the capillary, $a = \sqrt{(R_1 R_2)}$ the radius of a circle of same area as the cross-section of the nozzle orifice, R_1 and R_2 are as defined in equation (4.36), $b = (R_2 - R_1)/2$ is the oscillation amplitude and λ the oscillation wavelength. For solutions of viscosity $\mu < 20 \text{ mPa s}$, the term Ψ is approximately unity.

As the liquid moves away from the orifice, the surface ages and the surface tension is reduced by adsorption of surfactants, which causes an increase of the wavelength of the oscillation. The age t of the surface can be calculated from the horizontal surface velocity V_s and the distance X from the nozzle orifice ($t = X/V_s$). The surface velocity is estimated from the flow rate ($V_s = V^*/(\pi a^2)$) or measured from the jet free-fall trajectory (see Section 4.5.2.2).

4.4.5 THE FALLING CURTAIN

The falling curtain technique is based on a thin sheet of liquid extruded from a slit and falling between two vertical guide wires. There are two basic possibilities: a symmetric curtain, where both sides of the curtain emerge vertically from the slit at the same time, or an asymmetric curtain where one surface is generated on an inclined plane before producing a falling curtain. The symmetric curtain has the advantage of simplicity, as both sides of the curtain have the same surface age. The asymmetric curtain is a better model for the curtain coating technique (see Chapter 11c), but is more difficult to interpret, since both sides of the curtain do not have the same surface age. Detailed mathematical descriptions of both methods have been reported (van Haverberg and Joos 1983; Balbaert, Bleys and Joos 1987).

The determination of the surface tension in the curtain is generally made by introducing a perturbation in the flow, causing the rupture of the film and the formation of a V-shaped edge, also called a Mach wave. The relation between the Mach angle α and the surface tension σ is

given by (Brown 1961):

$$\sigma = \frac{\rho H}{2} V^2 \sin^2 \alpha \quad (4.38)$$

where ρ is the liquid density, H is the film thickness and V is the velocity of the film at the point of rupture. For a symmetric curtain, the surface tension σ can be easily calculated from directly measurable quantities knowing that:

$$Q = H_0 V_0 = HV \quad \text{or} \quad H = \frac{Q}{V} \quad (4.39)$$

where Q is the flow rate per unit width, H_0 is the initial film thickness (slit width), V_0 is the initial velocity, while H and V are the same parameters at some distance X of the slit. According to Brown (1961), the velocity can be expressed as:

$$V^2 = V_0^2 + 2g[X - 0.5(\mu/\rho)^{(2/3)}] \quad (4.40)$$

where μ is the liquid viscosity. Combining equations (4.38), (4.39) and (4.40), the dynamic surface tension is expressed as:

$$\sigma = \frac{Q\rho}{2} \sin^2 \alpha \sqrt{\frac{Q^2}{H_0^2} + 2g[X - 0.5(\mu/\rho)^{(2/3)}]} \quad (4.41)$$

Equation (4.41) can be used as a rough approximation also for the asymmetrical curtain. However, Balbaert *et al.* (1987) have found that the Mach angle method applied to an asymmetrical curtain seems to measure only the lowest surface tension, and not the average between both sides of the curtain. Instead of the Mach angle, they used a technique based on generating, with a vibrator, capillary waves on the curtain and measuring the resulting wavelength by optical means. The method works, but is more delicate than the Mach angle technique. The mathematical treatment of the asymmetrical curtain is also more complex.

Another problem with the falling curtain technique is to relate the dynamic surface tension with a surface age. It is not trivial, as the surface is under expansion as the curtain is accelerated

by gravity. The detailed treatment of this problem can be found in the above reference.

4.4.6 THE MAXIMUM BUBBLE PRESSURE

When a gas is blown through a capillary tube into a liquid, bubbles are formed and escape when a critical pressure is reached. This 'maximum bubble pressure' is determined by the Laplace equation and is related to surface tension by (Garrett and Ward 1989):

$$\sigma = \left(\frac{\Delta P - \rho gh}{2} \right) R \quad (4.42)$$

where ΔP is the pressure difference, ρ the liquid density, g the gravity constant, h the hydrostatic height of liquid at the capillary tip and R the radius of the capillary. The method appears to work regardless of the orientation of the capillary, either pointing upwards (Garrett and Ward 1989), downwards (Bendure 1971; Hua and Rosen 1988) or sideways (Mysels 1989).

One advantage of this technique is its application to surface tension determination in remote places, for instance inside pipes along a production line. It can in principle measure dynamic effects over a wide range of surface ages, by simple variation of the bubble rate. The technique has been developed with automatic, computer-controlled operation and is highly suitable for routine analysis.

However, problems arise when one is interested in the details of the surface ages. The process is deceptively simple. In fact, a complex sequence of events is taking place during the formation and escape of the bubbles. The bubble growth period is a 'dead time', during which pressure drops. Pressure builds up while a fresh meniscus ages inside the capillary. When the pressure reaches the maximum Laplace pressure, the bubble starts to grow rapidly and irreversibly. According to Ward and Garrett (1989), the dead time is dependent of the measured dynamic surface tension as well as the capillary radius, thus complicating the estimation of true surface age.

The problem of determination of the true surface age may have been recently solved through the design of a new maximum bubble pressure instrument, developed by an Ukrainian research group (Fainerman 1992; Fainerman *et al.* 1994; Fainerman and Miller 1995) and available from the company Lauda. This instrument uses the transition between continuous jet and discrete bubble, as the flow rate is reduced, to determine the dead time in each experiment, combined with an acoustic or electric detection of the bubble detachment. The instrument was tested in our laboratory and found to work very well for aqueous surfactant solutions. Dynamic surface tension could be measured easily down to 5 ms or less of surface age. Some difficulties remained, however, in the presence of dispersed particles, caused by contamination of the small capillary walls. Further improvements in the quality of the capillary may be able to minimize the contamination tendency.

4.4.7 THE OVERFLOWING FUNNEL

The overflowing funnel is an apparently very simple and convenient method for measuring dynamic surface tension caused by a surface dilatation effect. The term 'apparently' is used because the interpretation of the technique is not simple and it shows an effect which cannot be related to a defined surface age. The method consists of feeding a liquid from underneath a vertical funnel and leaving it to overflow over the rim. The surface tension is measured with a Wilhelmy plate (or a du Nouy ring) usually at the center of the funnel (Joos and de Keyser 1980; Bergink-Martens *et al.* 1990). The surface is subjected to a relative expansion rate A_R^* :

$$A_R^* = \frac{1}{A} \frac{dA}{dt} = \frac{d(\ln A)}{dt} \quad (4.43)$$

where A is the surface area of the emerging liquid, equal to the area of the funnel exit. The increase of surface tension $\Delta\sigma$ can be related to physico-chemical parameters through a relation proposed by van Voorst Vader *et al.* (1964) (equation (4.44)).

$$\Delta\sigma = RT\Gamma_\infty \ln \left(\frac{2(1 + C_0/a)}{1 + C_0/a - K + \sqrt{(1 - C_0/a + K)^2 + 4C_0/a}} \right) \quad (4.44)$$

where C_0 is the surfactant concentration at equilibrium, a is the Langmuir constant and the parameter K is:

$$K = \frac{\Gamma_\infty}{a} \left(\frac{\pi A_R^*}{2D} \right)^{1/2} \quad (4.45)$$

The surface expansion rate A_R^* must be calculated independently of the change of surface tension, if one wants to determine the diffusion coefficient D by comparing the experimental data with the calculated values. The problem is complex, as elements of liquid are forming new surface areas not just from the center but from the entire funnel, with a defined velocity profile of the incoming liquid. The presence of surfactant causes surface tension gradients which can further complicate the analysis. Nevertheless, Joos and de Keyser (1980) have proposed a simple expression for the average surface expansion rate based on the volumetric flow rate dV/dt and the rise ΔH of the overflowing surface as compared to its position when the liquid is at rest:

$$Q = \frac{dV}{dt} = \Delta H \frac{dA}{dt} \quad (4.46)$$

and combining equation (4.46) with (4.43) gives:

$$A_R^* = \frac{Q}{A \Delta H} \quad (4.47)$$

Joos and de Keyser (1980) found that values of surface tension recalculated using equation (4.44) agreed well with their experimental data, taking independently determined values for Γ_∞ , a and D . On the other hand, Bergink-Martens *et al.* (1990) have analyzed in depth the problem of calculating the relative expansion rate $d \ln A/dt$ and found more complex expressions, even with an optimized geometry of the funnel. The reader is referred to the above paper for more details. The geometry is optimum when the conical part of the funnel has a small slope (1:10) and the axis of the funnel is exactly parallel to the gravity vector. The validity of Bergink-Martens *et al.*

analysis was confirmed by direct measurements of the radial surface velocity. Therefore, due care must be taken in interpreting the results obtained with the overflowing funnel. The type of overflowing funnel described in Chapter 11d has a non-ideal geometry, resulting in a very complex flow pattern which cannot be treated using the theory developed by Bergink-Martens *et al.* (1990).

4.4.8 THE SESSILE OR PENDANT DROP

The profile of a sessile ('sitting') drop resting on a plane or pendant ('hanging') drop is the result of the balance between surface tension and gravity forces. The shape of the drop has to be precisely measured and analyzed. Computer programs can now perform this task very accurately, and with ease in contrast to the use of the original tables from Bashforth and Adams (Rotenberg *et al.* 1983; López de Ramos, Redner and Cerro 1993). However, the method is still complex and tedious compared with the Wilhelmy plate or the du Nouÿ ring. It may be worthwhile when the greatest accuracy of surface tension is required. Interfacial tension can be measured and automatic operation of the technique is possible. Even highly viscous liquids can be measured. Slow dynamic (aging) effects can be studied. Pendant drops can be generated more quickly than sessile drops, so that faster dynamic effects can be followed. Pulsating techniques have been reported (Lunkenheimer *et al.* 1984). A general description of the method has been given by Patterson and Ross (1979) and Ambwani and Fort (1979).

4.4.9 OTHER METHODS

Many other methods have been developed to measure static and/or dynamic surface tension, or surface expansion. They are, for example, the maximum drop weight or volume, the maximum pull on a rod, the spinning drop, the plunging

tape, the wave propagation, the flowing bell, the flowing sheet, the vertical jet. The description of these techniques can be found in several reviews (Ross and Morrison 1988; Defay and Pétré 1971; Defay and Hommelen 1958).

4.5 EXAMPLES OF PRACTICAL APPLICATIONS

4.5.1 MEASURED INDUSTRIAL SURFACTANTS

Static and dynamic surface tension data of a number of industrial surfactants have been measured in our laboratory with the methods described in the next section. Our data have not been previously published. These products contain impurities to various degrees, but were chosen because they represent what is or could be used in reality. The detailed analysis of some of them is complex and will not be given here. The choice of the surfactants was based on their known use

or potential interest, and is intended to be neither exhaustive nor even representative of the very large number of available industrial surfactants. The names and main characteristics of the selected surfactants are listed in Table 4.1. The measurements were done in water at 40°C (deionized for dynamic studies, ultrapure, chromatographic grade for static ones) and in 4% gelatin at 40°C (inert cow bone type, medium viscosity and deionized).

Further information on the active chemicals is shown below. The molecular weight, when known, is an approximate value, due to the existence of a chain length distribution.

Triton 770 (70% anionic, 30% non-ionic):

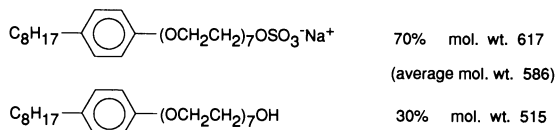


Table 4.1 List and main characteristics of various industrial surfactants

Surfactant	Type	Manufacturer	Approx. conc.† (%)	Solvent
Triton 770	Anionic*	Rohm & Haas	30	33% i-prop.†† 66% H ₂ O
Texapon K-12	Anionic	Henkel	100	—
Nekal BX	Anionic	BASF	100	—
Aerosol OT	Anionic	American Cyanamid	100	—
Empimin LSM30	Anionic	Albright & Wilson	30	H ₂ O
Fenopon CO-433	Anionic	GAF	35	H ₂ O
Niaproof #4	Anionic	Niacet Co.	27	25% EDG‡ 75% H ₂ O
Triton X-200	Anionic	Rohm & Haas	28	H ₂ O
Olin 10G	Non-ionic	Olin Co.	50	H ₂ O
Emcol 5130	Non-ionic	Witco	100	—
Igepal CA-720	Non-ionic	GAF	100	—
or Triton X-102	Non-ionic	Rohm & Haas	100	—
Lodyne S-103	Fluoro**	Ciba-Geigy	45	30% HEG‡‡ 70% H ₂ O
Fluorad FX-1002	Fluoro**	3M	25	H ₂ O

* contains also ca. 30% non-ionics

† '100' means no solvent, not 100% pure

‡ diethylene glycol monoethylether

** also anionic

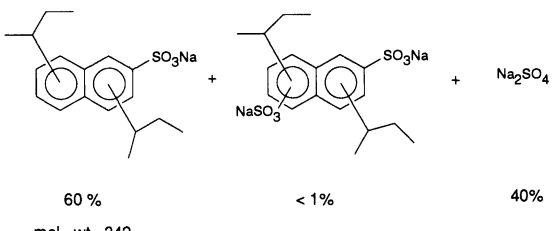
†† isopropanol

‡‡ hexylene glycol

Texapon K-12: Na-dodecyl sulfate (SDS), mol. weight 288.38.

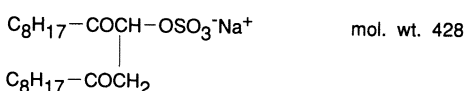
Emcol 5130 (non-ionic):

Nekal BX (anionic):

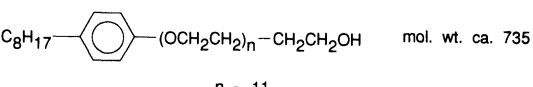


$\text{CH}_3 - (\text{CH}_2)_n - \overset{\text{O}}{\underset{ }{\text{C}}} - \text{N}(\text{CH}_2\text{CH}_2\text{OH})_2$	45 mol%	mol. wt. ca. 315
$n = 6, 8, 10, \underline{\underline{12}}, 14, 16, 18$		
- glycerine	15 mol%	
- diethanolamine	40 mol%	
- fatty acid mono- and diglycerides	(traces)	
- free fatty acids	(traces)	

Aerosol OT (anionic):



Igepal CA-720 or Triton X-102 (non-ionic):

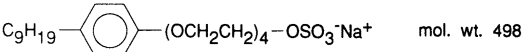


Empimin LSM30 (anionic):



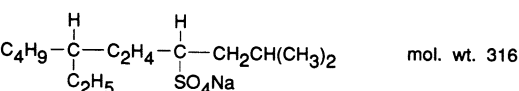
Lodyne S-103 (fluoro-anionic):
‘Fluoroalkyl sodium sulfonate’, estimated mol. wt.
ca. 700
(exact formula is proprietary information)

Fenopon CO-433 (anionic):



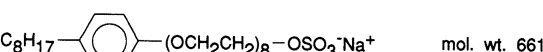
Fluorad FX-1002 (fluoro-anionic):
(average and approximate formula; exact formula
is proprietary information)

Niaproof #4 (anionic);



$$\text{CF}_3 - (\text{CF}_2)_6 - \overset{\text{O}}{\underset{||}{\text{C}}} - \text{O}^- \text{NH}_4^+ \quad \text{mol. wt. ca. 431}$$

Triton X-200 (anionic):



4.5.2 APPLIED MEASUREMENT METHODS

4.5.2.1 The du Nouÿ ring (static surface tension)

A Lauda TE1C automatic tensiometer, fitted with a platinum du Nouÿ ring attached to a force transducer (Hottinger Baldwin Messtechnik, range ± 5 g), was used. The instrument takes advantage of a special technique designed to avoid film rupture during measurement (Sucker *et al.* 1964). Consequently, the surface tension reading could be repeated several times until a constant value was reached, without need for ring cleaning. The accuracy of the surface tension values was better than 0.1 mN/m.

4.5.2.2 The oscillating jet (dynamic surface tension)

The oscillating jet technique was used to measure the dynamic surface tension of industrial surfactants in aqueous and gelatin solutions on the millisecond time scale. Jets were formed in front of a millimeter scale. A photograph of the entire continuous jet was taken. A bright lamp was placed above the jet, in such a way that each convex part of the jet would reflect the image of the lamp. This method was slightly less accurate than the optical front illumination method usually reported (Defay and Pétré 1971; Abe and Matsumura 1983), but was very simple and convenient. Typical photos (enlargements of the initial part of the jets) are shown in Fig. 4.7.

Precision elliptical nozzles were obtained from Ronda SA, Lausen, Switzerland, and were made by an electrocorrosion technique. The nozzle radii were $R_2 = 0.695$ mm and $R_1 = 0.515$ mm (low ellipticity, used for surfactants in deionized water) and $R_2 = 1.010$ mm and $R_1 = 0.325$ mm (high ellipticity, used for surfactants in 4% gelatin solutions). The high ellipticity, producing larger initial oscillation amplitudes, was necessary for gelatin solutions because of the dampening effect of viscosity.

The liquid jet was supplied by a pressurized container. The jet was free of vibrations or other instabilities that could have been produced by a pump. The flow rate was not measured, but the horizontal velocity was determined directly on the photograph of the jet by fitting its trajectory

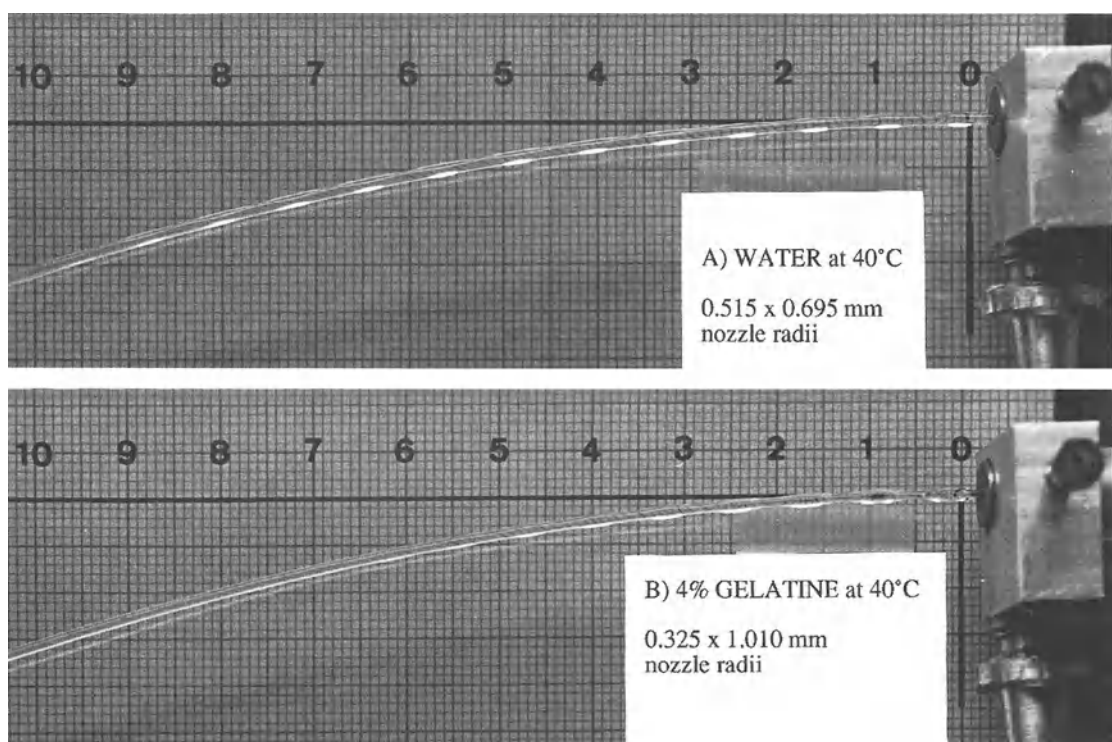


Figure 4.7 Typical photos (*ca.* 1/30 s) of the initial part of oscillating jets in the absence of surfactant. In the presence of surfactant (not shown), the oscillation length increases along the jet as surface tension decreases: (a) persistent oscillations due to the low viscosity of water at 40°C; (b) fast viscous dampening of the oscillations, despite stronger initial amplitude as in case (a). The numbers on the scale are cm; the horizontal velocity of the jets was *ca.* 2 m/s.

with the parabolic free-fall equation:

$$Y = a + bX + cX^2 \quad (4.48)$$

where Y and X are the vertical and horizontal coordinates, respectively, and a , b and c are the variable coefficients to find from a fit with the measured trajectory. The only interesting one is c , which relates to the horizontal velocity V_x as follows:

$$V_x = \sqrt{g/2c} \quad (4.49)$$

where g is the gravity constant. The uncertainty of V_x is estimated to be less than 1%.

Equation (4.37) (Section 4.4.4) can be modified by expressing the volumetric flow rate V^* as a function of the horizontal velocity $V_x = V^*/(\pi a^2) = V^*/(\pi R_2 R_1)$, the parameters a and b as a function of R_2 and R_1 , and by separating the variable flow parameters:

$$\sigma = \rho \left(\frac{V_x}{\lambda} \right)^2 \frac{2}{3} \pi^2 (\sqrt{R_2 R_1})^3 \times \left(\frac{1 + (37/24)(R_2 - R_1)^2/(4R_2 R_1)}{1 + (5/3)(\pi^2 R_2 R_1 / \lambda^2)} \right) \quad (4.50)$$

or

$$\sigma = \rho \left(\frac{V_x}{\lambda} \right)^2 K \quad (4.51)$$

where K contains all the geometric terms of equation (4.50), plus one term in λ^{-2} . However, the dependence of K on λ is weak. Variation of surface tension from 70 to 30 mN/m corresponds to an increase of the wavelength λ by ca. 50% and a variation of K of less than 5% for low viscosity aqueous solutions. K is in essence a 'nozzle constant'.

With aqueous solutions and the low ellipticity nozzle, direct calculations of the surface tension with equation (4.50) gave satisfactory values, within a few percents for pure water. The corresponding nozzle constant K was $1.27 \times 10^{-9} \text{ m}^3$. However, with data obtained measuring gelatin solutions with the high ellipticity nozzle, equation (4.50) yielded too high surface

tension values (up to 90 mN/m). The cause of the error may lie in the strong distortion caused to the jet by the high ellipticity, distortion which is assumed small in equation (4.50). In that case, a nozzle constant had to be determined in order to reconcile the surface tension of pure gelatin solutions with results from the inclined plane method described below (ca. 65 mN/m for short surface ages at 40°C). The nozzle constant value was, after adjustment, $1.15 \times 10^{-9} \text{ m}^3$.

4.5.2.3 The inclined plane (dynamic surface tension)

The inclined plane method is an application of the Wilhelmy plate method to a flowing liquid, with the plate oriented in the flow direction. It has the same advantages of simplicity, ease of operation and interpretation, and robustness as the Wilhelmy plate method. The inclined plane had a slope of ca. 14° versus horizontal, was 1 meter long, 10 cm wide, and was attached to a small two-slit liquid delivery device. The whole system was made of stainless steel and was temperature-controlled. The measured solution was circulated by a peristaltic pump, with a flow rate of ca. 3 cm³/s. Recently, the maximum flow rate was increased up to ca. 16 cm³/s. The set-up is represented in Fig. 4.8. Only the lower delivery slit was used. The Wilhelmy plate used for most of the reported results was 5 mm long, giving a time resolution of 30 to 50 ms for the 3 cm³/s flow rate. The time resolution was estimated as the time necessary for the flowing liquid to travel one plate length (see calculation of surface velocity below). The time resolution was recently improved to ca. 6 to 8 ms by using a shorter 2 mm Wilhelmy plate in conjunction with the higher flow rate. The plates, made of platinum, were cleaned by briefly heating to glowing red in a flame. Either of the plates was attached rigidly to a force transducer of ± 5 g capacity (Hottinger Baldwin Messtechnik) with the plate axis normal to the liquid surface. The slight drag force of the liquid had no influence on the 5 mm plate, and possibly a small effect on the 2 mm plate, which was taken into account by a correction factor. The accuracy

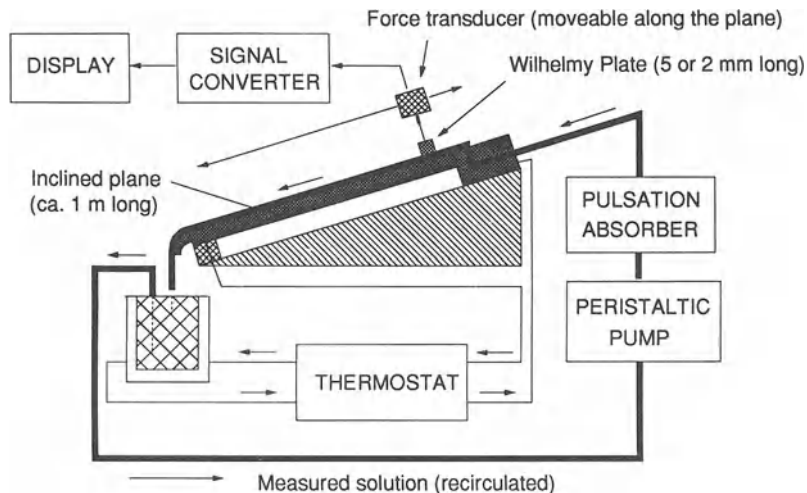


Figure 4.8 Experimental set-up for the inclined plane method of measuring dynamic surface tension.

of the dynamic surface tension measurement was *ca.* 0.5 to 1.0 mN/m for the 5 mm plate and *ca.* 1.0–1.5 mN/m for the 2 mm plate. Calibration was done by placing the transducer in a vertical position and suspending a standard weight to the plate, as for a static instrument.

The surface age t at different positions of the plane was calculated from the surface velocity V_s and the distance d from the slit exit (van den Bogaert and Joos 1979):

$$t = d/V_s \quad (4.52)$$

The surface velocity was measured experimentally by following surface tracers and compared with the theoretical surface velocity (Bird, Stewart and Lightfoot 1960):

$$V_s = \frac{3}{2} \left[\frac{Q^2 \rho g \sin \alpha}{3\mu} \right]^{1/3} \quad (4.53)$$

where Q is the flow rate per unit width, ρ the liquid density, g the gravity constant, α the inclined plane angle (14°) and μ the liquid viscosity. The experimental and theoretical values usually agreed to within 10%. For the sake of simplicity, we have assumed in reporting our results (see Section 4.5.4) that the surface velocity V_s was constant along the entire inclined plane. This is not strictly correct, in particular near the slit exit

where V_s starts at zero. More accurate models have been described (Rillaerts and Joos 1982; Ziller, Miller and Kretzschmar 1985; Wu and Whitaker 1986), but were not deemed necessary for the comparative purpose of our experiments.

Viscosity was measured using a Haake CV-100 viscometer, at shear rates between 0 and 1000 s^{-1} . All measured solutions were Newtonian.

4.5.3 STATIC SURFACE TENSION RESULTS

The static surface tension of solutions of all surfactants listed in Table 4.1 have been measured in deionized water and 4% gelatin at 40°C using the du Nouy ring technique. The data obtained below the critical micelle concentration were fitted with equation (4.16) (von Szyszkowski 1908) to determine the values of Γ_∞ and a . The results are summarized in Table 4.2.

The surface tension results are very different in water and in gelatin solutions. The main reason is that gelatin is itself already surface-active. The static surface tension of 4% gelatin with no surfactant was 42–45 mN/m, while the static surface tension of water (at 40°C) was 69.6 mN/m. Therefore, the range of accessible surface tension was much reduced in the gelatin solutions. Gelatin is known to form complexes with some

Table 4.2 Parameters derived from the static surface tension data of the measured surfactants in pure water and in 4% gelatin at 40°C

Surfactant	Max. ads. density $10^6 \times \Gamma_\infty$ (mol/m ²)		Area per molecule††		Langmuir constant $10^6 \times a$ (mol/dm ³)		$10^4 \times CMC$ (mol/dm ³)		Min. surface tension (mN/m)	
	Water	4% gel.	Water	4% gel.	Water	4% gel.	Water	4% gel.	Water	4% gel.
Triton 770*	5.57	2.35	30	70	2.22	16.3	0.50	2.83	26.2	27.2
Texapon K-12*	5.11	0.96	32	173	152	13.1	47.1	106	25.1	29.8
	3.98‡		41‡		297‡		63.1‡‡			
Nekal BX*	2.63	0.71	63	235	50.6	10.8	83.8	9.55	32.0	36.5
Aerosol OT*	2.45	1.41	67	117	11.0	6.97	58.6	4.33	26.5	30.6
	1.30§		126§		5.0§		31.6§			
Empimin										
LSM30*	3.16	0.93	53	177	16.2	35.0	14.2	9.74	32.5	35.1
Fenopon										
CO-433*	6.87	1.25	24	132	3.55	4.47	0.30	2.11	29.0	33.1
Niaproof #4*	3.28	0.87	51	191	119	40.2	226	1160	26.1	26.0
Triton X-200*	2.82	3.21	59	52	0.16	103.0	4.04	5.99	27.5	27.6
Olin 10G**	7.84	1.90	21	87	1.92	10.1	0.13	1.39	28.8	30.0
Emcol 5130**	11.40	2.72	15	61	3.68	11.3	0.14	0.99	26.4	26.9
Igepal CA-720**	5.17	1.79	32	92	4.67	15.8	0.44	1.90	30.5	31.1
Lodyne S-103†	28.40	1.64	6	101	7.81	0.49	0.08	2.32	18.7	19.0
Fluorad										
FX-1002†	7.78	3.72	21	45	2960	3510	336	358	19.0	19.5

* anionic (Triton 770 30% non-ionic)

‡ from Van den Bogaert and Joos (1980), no specified temperature (probably ambient)

** non-ionic

†† from Knox and Parshall (1970), no specified temperature (probably ambient)

†† at maximum adsorption density

§ from Chang and Franses (1992), data taken at 25°C

surfactants, in particular anionic ones. Knox and Parshall have studied the interaction of gelatin with Na-dodecylsulfate or SDS (1970) and Aerosol OT (1972). Interestingly, they found no interaction with Triton X-100, a non-ionic surfactant (presumably analogous to Triton X-102). The SDS or Aerosol OT surfactant-gelatin complexes appeared more surface-active than the monomeric surfactants. The structure of complexes between SDS and other types of polymers has been studied using low-angle neutron scattering by Cabane and Duplessix (1982, 1987). For other and more recent SDS-gelatin studies, see Griffith *et al.* (1996). Figures 4.9, 4.10 and 4.11 show examples of log (concentration) – surface tension curves for Niaproof #4 (anionic), Emcol 5130 (non-ionic) and Lodyne S-103 (fluoro-anionic surfactant) in water and 4% gelatin solutions.

Niaproof #4 is a Na-tetradecylsulfate, chemically similar to Na-dodecylsulfate except for a

highly branched hydrocarbon group (see Section 4.5.1), while SDS is normally a straight C₁₂ chain. This structural difference has a strong effect on the micelle formation tendency and probably also on the interaction with gelatin. A specific interaction between Niaproof #4 and gelatin cannot be demonstrated from Fig. 4.9. The only visible effect is a compression of the surface tension range due to the reduced surface tension of the gelatin solution. On the other hand, Emcol 5130 (Fig. 4.10), a non-ionic surfactant, seems to have a stronger interaction with gelatin than the anionic Niaproof #4, based on the distortion of the static surface tension curve. One should be cautious, therefore, in generalizing the finding of Knox and Parshall (1970) stating that non-ionic surfactants do not interact with gelatin. In the case of Emcol 5130, some interaction may also involve secondary components of the product (see Section 4.5.1).

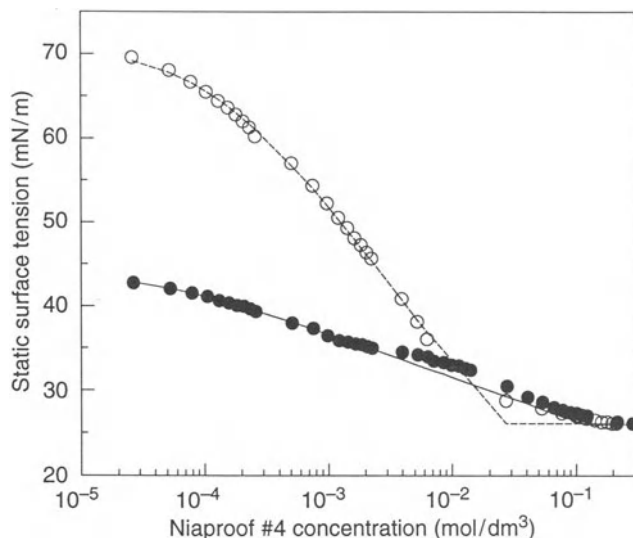


Figure 4.9 Static surface tension versus Niaproof #4 concentration. (○): in water at 40°C and (●): in 4% gelatin at 40°C. Lines: equation (4.16).

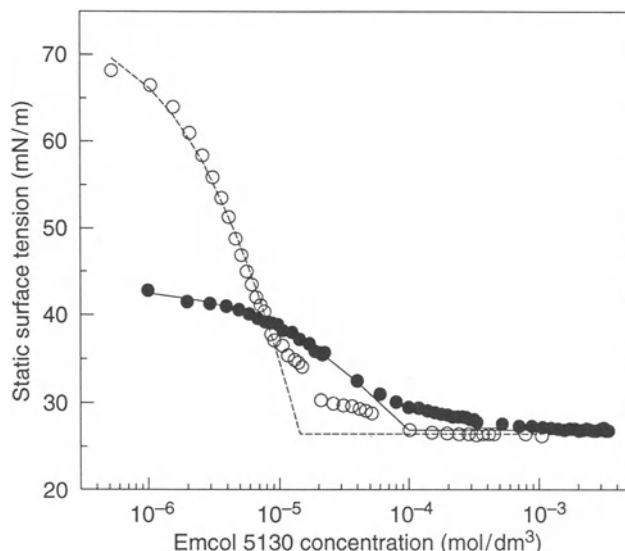


Figure 4.10 Static surface tension versus Emcol 5130 concentration. (○): in water at 40°C and (●): in 4% gelatin at 40°C. Lines: equation (4.16).

In the last example (Fig. 4.11), Texapon K-12 (SDS), an anionic surfactant, exhibits a very

curve in the presence of gelatin as compared with the curve in water, which is explained by the formation of complexes with gelatin. The

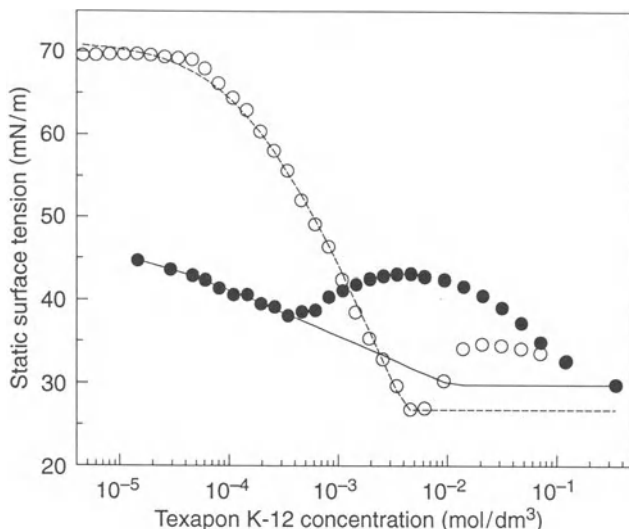


Figure 4.11 Static surface tension versus Texapon K-12 concentration. (○): in water at 40°C and (●): in 4% gelatin at 40°C. Lines: equation (4.16).

presence of a minimum in the static surface tension curve indicates the presence of impurities (possibly dodecanol). In Table 4.2, the cmc were determined from the fit of the initial part of the curves, at low surfactant concentration, with equation (4.16), using the regions of the curves that could give a precise fit. Then the curve was extrapolated down to the lowest measured surface tension. The concentration at which the fitted curve was equal to the lowest surface tension was taken as the cmc. Another choice could be to take the concentration at which the lowest surface tension is effectively reached. Some literature values of surface tension parameters were found for Na-decyldsulfate (equivalent to Texapon K-12) and Aerosol OT and are indicated in Table 4.2. The values are within 50% of each other, which is reasonable considering the differences of measurement temperatures and of sample purity. Because of the possibility of complex formation, the parameters found in the presence of gelatin may only be apparent values and have to be interpreted with caution. A probably real effect is, however, a lowering of the maximum adsorption density

Γ_∞ , explained by the presence of gelatin at the interface.

An increase of surface tension above the cmc region is a sign of surface active impurities. The surfactants other than Texapon K-12 which appear to contain such impurities are Fenopon CO-433 and Empimin LSM30, and, to a lesser degree, Triton X-200 and Igepal CA-720. Only Nekal BX has a sharp cmc transition followed by a constant surface tension at higher concentrations. Triton 770, Triton X-200, Olin 10G, Emcol 5130 and Lodyne S-103 have a poorly defined cmc region, indicating a broad distribution of chain length or a complex mixture of compounds. Fluorad FX-1002, although showing a rather well defined cmc transition in water, exhibits more complex behavior in gelatin, indicating an interaction of the surfactant with the gelatin molecules. Niaproof #4 hardly reaches a surface tension plateau up to 10^{-1} mol/dm³, indicating a lack of micelle formation, which could be the consequence of its bulky hydrocarbon group. Triton 770 reveals a simpler behavior in gelatin than in water, but this could also indicate some interaction with the gelatin molecules.

4.5.4 DYNAMIC SURFACE TENSION RESULTS

All the surfactants listed in Table 4.1 have been measured at several concentrations in water and 4% gelatin, both at 40°C, with the oscillating jet and the inclined plane methods. The concentrations were chosen to include what are considered practical concentrations in coating operations. An example of experimental results (Olin 10G in 4% gelatin) is shown in Fig. 4.12. The oscillating jet data points are in the range 5 to 30 ms of surface age, and the inclined plane data points in the range 60 ms to 4 s of surface age. These measurements were made before the inclined plane was modified to permit measurement at less than 10 ms of surface age (examples of newer data are given in Section 4.5.6). The combination of the two methods, oscillating jet and inclined plane, is useful because each technique can be used to confirm the other. The data in Fig. 4.12 show that the results of both methods are very consistent, and therefore reliable. A further check can be made by verifying that the dynamic

surface tension becomes equal to the static surface tension at long surface ages.

Without using any equation to fit the data, the experimental results already describe well the dynamic behavior of the surfactant (in the case of Fig. 4.12, Olin 10G). They also demonstrate that the gelatin solution without surfactant maintains a dynamic surface tension higher than 60 mN/m for several seconds, even though its static surface tension is 42 to 45 mN/m. Even more remarkable is the fact that all measured Olin 10G concentrations produce nearly the same static surface tension (limit of the curves in Fig. 4.12 at long surface ages). This proves clearly, at least in the case of Olin 10G, that measuring only static surface tension would miss most of the information and could not predict the dynamic behavior of a solution containing this surfactant.

A lot more can be extracted from the data if they can be fitted with suitable models. In Fig. 4.12, Olin 10G data in 4% gelatin follow rather well the models of equations (4.22) and (4.23),

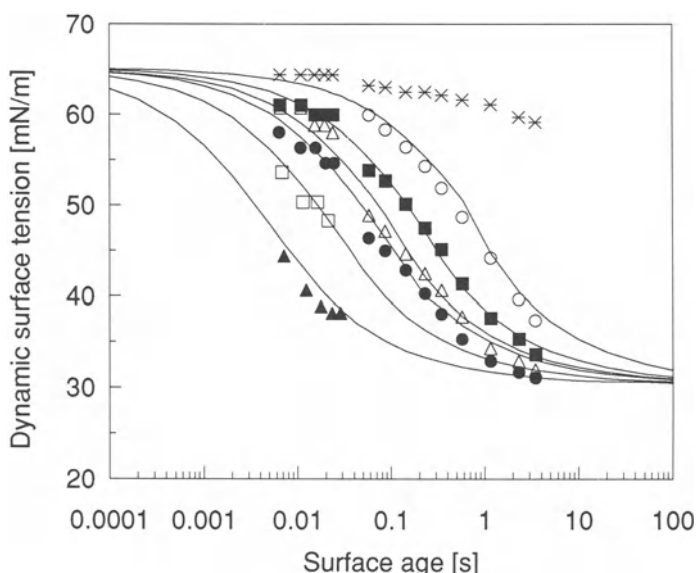


Figure 4.12 Dynamic surface tension of Olin 10G in 4% gelatin at 40°C. Lines: equations (4.22) and (4.23). (\times): no surfactant; (\circ): 2.00×10^{-4} mol/dm 3 ; (\blacksquare): 3.67×10^{-4} mol/dm 3 ; (\triangle): 5.24×10^{-4} mol/dm 3 ; (\bullet): 1.05×10^{-3} mol/dm 3 ; (\square): 2.10×10^{-3} mol/dm 3 ; (\blacktriangle): 5.24×10^{-3} mol/dm 3 .

which are based on diffusion-controlled adsorption. The diffusion coefficient of the surfactant can be extracted from these fits (see Figs 4.14 and 4.15), and the good quality of the fits indicates that the surfactant does not form complexes with gelatin and has no adsorption barrier. From a more practical point of view, the successful use of equations allows one to predict the dynamic surface tension as a function of surface age for intermediate concentrations of surfactant, using linear interpolation, for instance. To some extent, it allows one also to extrapolate the dynamic surface tension at shorter surface ages (also at longer surface ages, but it is less useful). The surface age scale in Fig. 4.12 extends to 0.1 ms, a surface age found in the pinned meniscus in slide coating (Fig. 4.3), which is not experimentally accessible. However, the extrapolated dynamic surface tension curves are plausible, considering the general quality of the fits. Based on the data in Fig. 4.12, it is possible to predict the dynamic surface tension of the measured solution at any surfactant concentrations and

surface ages within reasonable limits of extrapolation, without further measurement.

There are cases when equations (4.22) and (4.23) cannot fit the data in a satisfactory manner. This is shown, for instance, by the dashed lines in Fig. 4.13, for Empimin LSM30 in gelatin solution. The flexibility of the fits with equations (4.22) and (4.23) is limited, because the surface tension at zero surface age is determined by the solvent (69.6 mN/m for water at 40°C or 65 mN/m as the short-time dynamic surface tension of gelatin at 40°C without surfactant). In addition, the parameters derived from static surface tension data (Γ_∞ and a), which are used in equations (4.22) and (4.23), cannot be varied. The applicability of these parameters is doubtful in the presence of gelatin, as gelatin is much more surface-active at long surface ages (static situation) than at short surface ages. Therefore, equations (4.22) and (4.23) are not always able to fit the dynamic surface tension data, and even if they do, the diffusion coefficients derived in the presence of gelatin may only have apparent values. In the

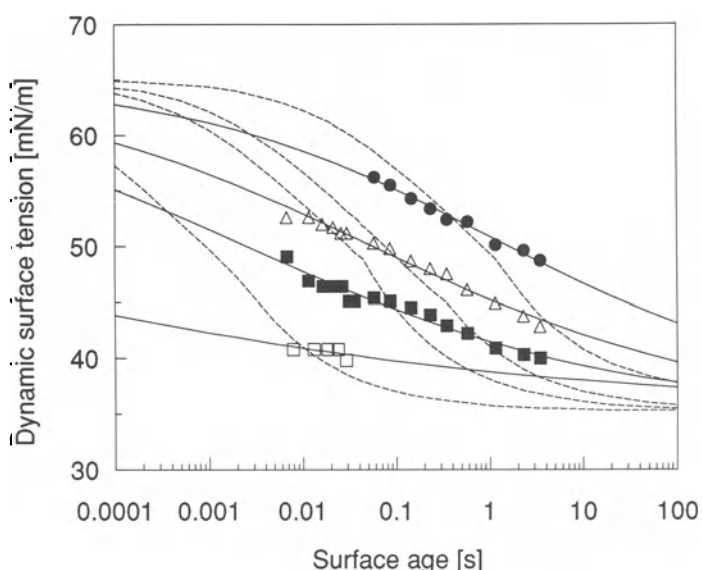


Figure 4.13 Dynamic surface tension of Empimin LSM30 in 4% gelatin at 40°C. Dashed lines: equation (4.22) and (4.23); solid lines: equation (4.24). (●): 5.79×10^{-4} mol/dm 3 ; (△): 1.45×10^{-3} mol/dm 3 ; (■): 2.90×10^{-3} mol/dm 3 ; (□): 1.45×10^{-2} mol/dm 3 .

case of Empimin LSM30, surfactant-gelatin complexes are probably formed, as is known for SDS and Aerosol OT, and/or its adsorption is not entirely diffusion-controlled. Chang and Frances (1992) have developed models taking into account concentration-dependent adsorption/desorption barriers. Surfactant-gelatin complexes would require new and more elaborate models.

More pragmatically, the parametric equation (4.24) can be used to obtain a better fit of the data (solid lines in Fig. 4.13). It does not give any molecular information about the surfactant, neither does it describe the mode of adsorption, but it still allows prediction of surface tension over a wide range of surface ages and surfactant concentrations (see Section 4.5.6). The extrapolated dynamic surface tensions at very small surface ages are, however, no longer realistic, because the parameter σ_0 is freely adjusted to obtain the best fit.

However, equation (4.24) did not always give very good fits of the data, probably because some surfactants produced more experimental errors than others. As an approximative guide, the fit quality of all measured surfactants with both types of equation has been rated 'good', 'fair' or

'poor' (even 'very poor' for Texapon K-12) and can be found in Table 4.3. 'Good' means that the derived parameters can accurately predict the data (although diffusion coefficients in gelatin should all be considered as apparent values), while 'poor' means that the given values should be taken with a pinch of salt. In general, it was easier to fit the data with the parametric equation (4.24) than with equations (4.22) and (4.23), for the reasons explained above.

A comparison of the short-time diffusion coefficients of the above surfactants is shown in Fig. 4.14, at three typical concentrations. The fits obtained with equations (4.22) and (4.23) for Texapon K-12 were so poor, even in water, that no diffusion coefficient could be reasonably estimated. In water, Na-dodecylsulfate or SDS (active substance of Texapon K-12) has been found to exhibit an adsorption barrier (Chang and Frances 1992), and SDS is known to interact strongly with gelatin (Knox and Parshall 1970 and 1972). In fact, it is unfortunate that this surfactant has been so popular as 'standard' anionic surfactant (see also van den Bogaert and Joos 1980; Weinheimer *et al.* 1981; Hempt *et al.* 1985; Chari and Hossain 1991) because it is one of the most peculiar as far as surface properties are concerned.

Table 4.3 Fit quality of the dynamic surface tension data with equations (4.22) and (4.23) (Hansen's approximations, diffusion model) and with equation (4.24) (parametric equation) of the measured surfactants

Surfactant	Equations (4.22) and (4.23)		Equation (4.24)	
	Water 40°C	4% gel. 40°C	Water 40°C	4% gel. 40°C
Triton 770	good	good	good	good
Texapon K-12	very poor	very poor	good	fair
Nekal BX	fair	good	fair	good
Aerosol OT	good	fair	fair	good
Empimin LSM30	poor	poor	fair	good
Fenopon CO-433	poor	good	good	good
Niaproof #4	fair	fair	fair	good
Triton X-200	fair	poor	good	good
Olin 10G	good	good	good	good
Emcol 5130	good	good	good	good
Igepal CA-720	good	fair	good	good
Lodyne S-103	good	good	good	good
Fluorad FX-1002	fair	poor	fair	fair

It can be seen in Fig. 4.14 that the diffusion coefficients are not concentration-independent. It is not surprising, considering that the surfactants are not pure substances, and that several of them form micelles in the range of concentrations indicated in Fig. 4.14. For similar reasons, the diffusion coefficient found for the long-time approximation was often different from the one found for the short-time approximation. However, the long-time domain is less critical for coating operations and detailed results are not given here. The surfactants have been ranked according to the value of the short-time diffusion coefficient found at 10^{-3} mol/dm³. Few diffusion coefficients for the above surfactants have been reported. The diffusion coefficient of a straight-chain isomer of Aerosol OT has been reported to be 9.6×10^{-10} m²/s from conductivity measurements and 2.7×10^{-10} m²/s from dynamic surface tension methods at 7.5×10^{-4} mol/dm³ (Serrien and Joos 1990). These values are reasonably close to the value of 12×10^{-10} m²/s shown in Fig. 4.14 at 6×10^{-4} mol/dm³ Aerosol OT. The diffusion coefficient of pure SDS is usually taken as 4×10^{-10} m²/s (see above references), but we cannot determine it from dynamic surface ten-

sion measurements using equations (4.22) and (4.23).

As mentioned previously, the presence of gelatin has a profound effect on the dynamic surface tension, either through the formation of surfactant–gelatin complexes, or simply through an increase of viscosity. The ratios of the diffusion coefficients (apparent values) found in gelatin and in water are reported in Fig. 4.15. The anionic surfactants, in particular Niaproof #4, Nekal BX and Aerosol OT, exhibit larger values in gelatin solutions than in pure water. Non-ionic surfactants show the opposite effect. Igepal CA-720, the fastest of the group at 10^{-3} mol/dm³ in water, is much slower in gelatin solutions. The fluorosurfactants, although anionic, behave like non-ionic surfactants towards gelatin.

The effects seen on the short-time diffusion coefficients are confirmed by the variations of the parameter t^* used in equation (4.24) (surface age at the inflection point of the curves). Figure 4.16 shows the t^* values of the series of surfactants in water and Fig. 4.17 the ratios of the values in water and in gelatin. The ratios were taken in the other direction, so that as for Fig. 4.15, a ratio larger than one would mean a faster action

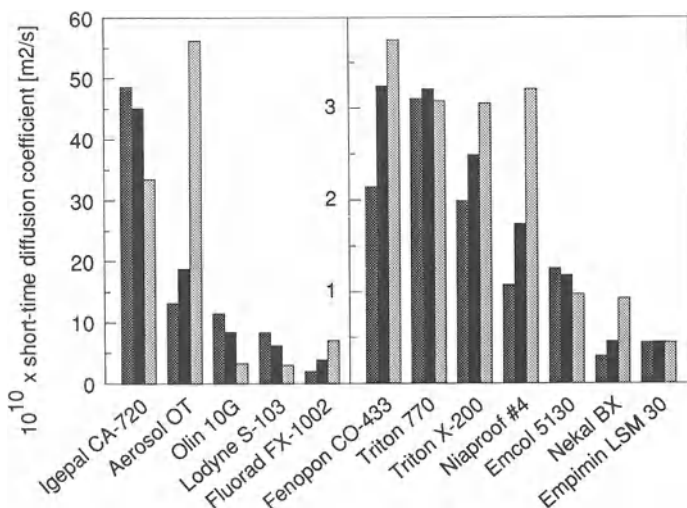


Figure 4.14 Short-time diffusion coefficients of surfactants in water at 40°C. (■): 6×10^{-4} mol/dm³; (■): 10^{-3} mol/dm³; (■): 3×10^{-3} mol/dm³. The surfactants are ranked according to the value found at 10^{-3} mol/dm³.

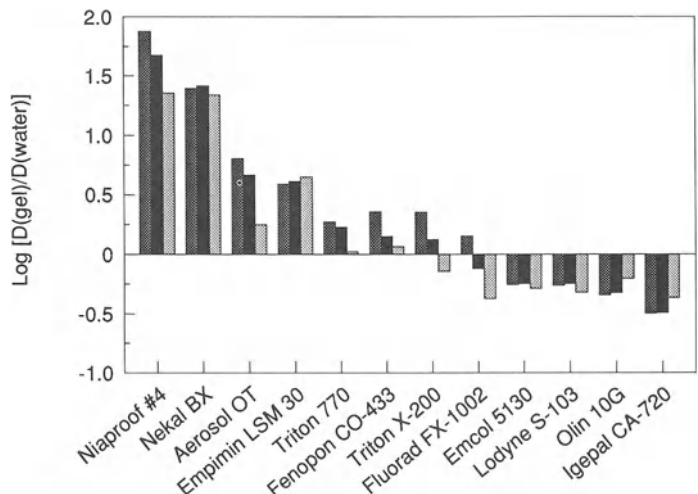


Figure 4.15 Ratios of the short-time diffusion coefficients of surfactants in 4% gelatin and in water. Positive log values mean faster diffusion in gelatin solution than in water. (■): $6 \times 10^{-4} \text{ mol}/\text{dm}^3$; (■): $10^{-3} \text{ mol}/\text{dm}^3$; (■): $3 \times 10^{-3} \text{ mol}/\text{dm}^3$.

in gelatin than in water. The trends are the same as for the diffusion coefficients, but the absolute values of the ratios are larger. The parameter t^* is expected to decrease at higher surfactant concentration as it measures the direct effectiveness of the solution to reduce surface tension and is not a theoretically concentration-independent parameter as the diffusion coefficient should be. The parameter t^* effectively decreases with increasing surfactant concentrations in all cases except for Texapon K-12 (SDS) in gelatin (not directly shown; can be seen from the combined Figs 4.16 and 4.17). Again, SDS exhibits a peculiar behavior in the form of a very strong concentration dependence in the parameter t^* .

4.5.5 SURFACTANT SELECTION CRITERIA

The basic properties of surfactants and their desired functions have already been discussed in Section 4.2. However, they appear under a new light when actual results of dynamic surface tension are known. Based on the presented experimental results, it is possible to select which type of surfactant would be appropriate for a particular purpose. Some criteria to be considered are:

1. the speed of action of the surfactant as a function of its concentration, which can be judged from the diffusion coefficients D and the characteristic times t^* ;
2. the lowest attainable surface tension, defining the wetting limit of the surfactant, its ability to spread on surfaces and ‘outwet’ hydrophobic particles, which can be seen from the static data;
3. the range of concentrations producing a change of static surface tension, determining the degree of control of the static surface tension by adjustment of the surfactant concentration, also seen in the static data;
4. the solubilizing power for hydrophobic molecules, which will determine the ability of the surfactant to stabilize insoluble substances in solution, and which will be efficient only above the cmc (static data).

The static surface tension data are therefore important, as three out of the four above criteria can be judged from them. However, the speed criteria is essential for fast coating operations and for this kind of application has at least as much weight as the three others combined. It would be rather arbitrary to establish a definitive

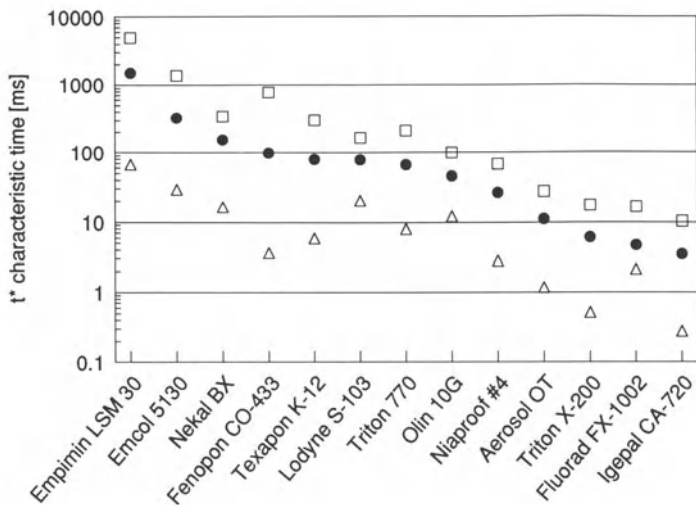


Figure 4.16 Comparison of the characteristic surface ages t^* of surfactants in water at 40°C. (□): $6 \times 10^{-4} \text{ mol}/\text{dm}^3$; (●): $10^{-3} \text{ mol}/\text{dm}^3$; (△): $3 \times 10^{-3} \text{ mol}/\text{dm}^3$.

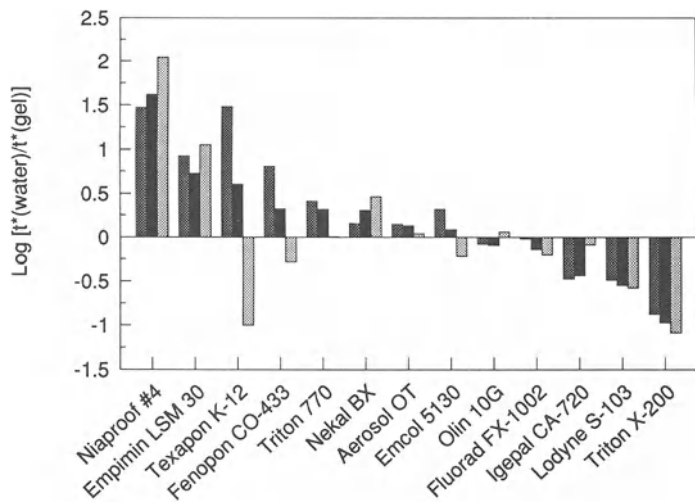


Figure 4.17 Ratios of the characteristic times t^* of surfactants in water and in 4% gelatin. Positive log values mean smaller t^* (faster surfactant) in gelatin solution than in water. (■): $6 \times 10^{-4} \text{ mol}/\text{dm}^3$; (▨): $10^{-3} \text{ mol}/\text{dm}^3$; (▨): $3 \times 10^{-3} \text{ mol}/\text{dm}^3$.

ranking of the surfactants whose experimental data are presented in the previous sections. Based on the present data, it should be fairly easy for the reader to make his or her own judgment. In

addition, the group of surfactants chosen in this chapter is very limited and finding a ‘best one’ among them would not mean a lot. If direct experimental data cannot be obtained from other

surfactants, some analogies could be made using the molecular structures shown in Section 4.5.1.

It is unlikely that one single surfactant will perform best for all the required criteria under one set of conditions. There is no 'perfect' surfactant. Therefore, usually two or more surfactants are used. Some of the best properties can be combined to match the criteria. However, using mixtures complicates the optimization process and the number of surfactants should be kept to a minimum.

If a surfactant is needed for testing flow simulation studies by numerical methods (see Chapter 11d), in particular when the effects of surfactant convection and diffusion on surface tension are to be taken into account, the best surfactant to use should be one that follows simple diffusion models, such as Olin 10G, or another non-ionic surfactant. It appears from the present data that several anionic surfactants behave in a more complex manner, in particular Na-dodecylsulfate (SDS).

4.5.6 SURFACTANT MULTILAYER RECIPE OPTIMIZATION

The transition from surface tension measurements to a successful coating formula is not an easy task. The reality of coating involves many interacting parameters and the applicability of the dynamic surface tension data must be proven by practical tests. A good illustration of this concept has been given by Valentini *et al.* (1991). These authors measured dynamic surface tensions using a maximum bubble pressure apparatus and correlated the data with the accessible coating window. The main message of their work confirmed that it is the dynamic, not the static surface tension which is the relevant parameter to measure. Similar conclusions have been reached by Hirt *et al.* (1990). In addition, Valentini *et al.* (1991) found that surface elasticity was stabilizing the flowing film against waves, confirming the work of Ruschak (1987).

Improvements from the work of Valentini *et al.* (1991) could be made in the area of dynamic surface tension measurements. These authors reported dynamic surface tension as a function

of the surfactant concentration for different bubble rates. As explained in Section 4.4.6, the bubble rate in the maximum bubble pressure apparatus does not give precise information of the effective surface age at which the dynamic surface tension is measured. The bubble rate is only a qualitative parameter which cannot be easily related to the physics of the process. The recent maximum bubble pressure instrument developed by Lauda (see Section 4.4.6) has the capability to determine the effective surface age, but it was not available to Valentini *et al.* (1991) and may still have difficulties measuring real coating solutions containing large amounts of dispersed colloids.

Dynamic surface tension measurements have been done in our lab with actual photographic solutions, using the inclined plane method in which the shortest accessible surface age has been recently reduced to *ca.* 10 ms. As an example, a three-layer package has been measured over a wide range of surfactant concentrations. This package, designed to be coated with the curtain-coating technique (see Chapter 11c), was plagued by curtain instabilities which were attributed to wrongly matched interlayer wetting properties. For proprietary reasons, details of the coating solutions and of the surfactants used are not given, but this information is not necessary for the purpose of the demonstration.

The aim of the work was to find a combination of surfactant concentrations for each layer (a surfactant recipe) which would result in stable interlayer wetting, in particular at the surface age time scale found in the curtain itself (*ca.* 10–100 ms). The general principle on which the optimization is based is directly derived from Young's equation (equation (4.1)): a liquid layer must have a surface tension as low or lower than the surface tension of the layer it is supposed to spread on. The point is that it must be true already when the surfaces are very fresh, down to the millisecond time scale. It means that when both layers are suddenly exposed to air, having both an initial surface tension close to the solvent value, the one that is supposed to spread on the other must be able to reduce its surface tension faster than the other. The top layer of a multilayer coating package is

always exposed to air, and to possible external disturbances. It is the most vulnerable layer. Therefore, this layer must be able to reduce its surface tension very shortly after it emerges from the slit of the coating device. The requirement for the surface tension or potential surface tension reduction speed of internal layers is not as critical, because these layers are generally not exposed to air and they do not sustain interfacial tension, provided they are miscible. However, a too large difference in surface tension between internal layers can have undesirable edge effects (Gutoff 1992). In practice, it is customary to maintain a similar or slightly increasing wetting tendency from the lower to the top layer in order to facilitate at start-up the formation of the multilayer package on a slide coater.

In the curtain coating operation, the back of the curtain is exposed to air during a significant time (*ca.* 50 to 100 ms). Therefore, the layer at the back of the curtain must be considered, at least temporarily, as a surface layer. In our example, there is only one internal layer (total three layers), and this layer must be easy to wet by the two others. For convenience, the layers

will be numbered from 1 to 3 starting at the back of the curtain. The necessary gradient of surface tension required to ensure stable wetting has not a definite value, but a few mN/m is generally considered sufficient (Gutoff 1992). On the other hand, a wrong gradient of the same order of magnitude can easily promote dewetting.

Knowing what surface tension relation is desired between the layers of the coating package, the optimization procedure using surface tension data is done as follows:

1. The static surface tension of the three solutions is measured as a function of the surfactant concentration (data not shown). This should match the long-time dynamic surface tension and gives a general picture of the accessible range of static surface tensions.
2. The dynamic surface tension of each solution is measured on the inclined plane as a function of surface age for several surfactant concentrations. Actual data for layer 1 are shown in Fig. 4.18. The accessible surface age range was 7 ms to 3 s, using the 2 mm-long Wilhelm plate and a flow rate of *ca.* 16 cm³/s.

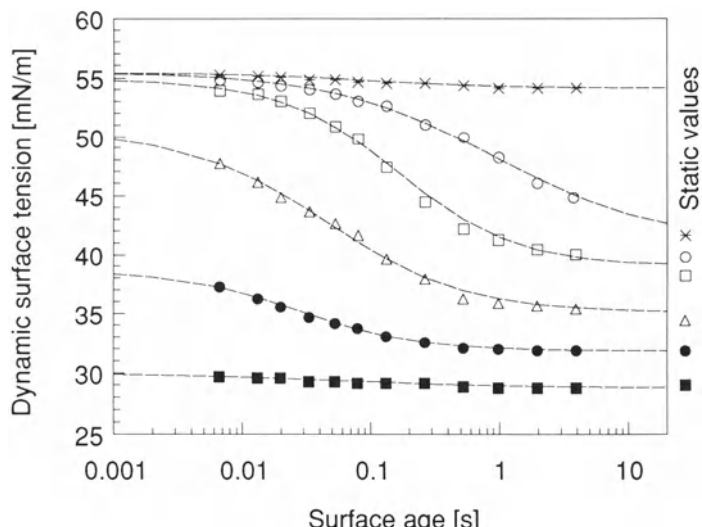


Figure 4.18 Dynamic surface tension for several surfactant concentrations of layer 1 in a three-layer package (inclined plane). (x): 0; (○): 2; (□): 5; (△): 10; (●): 20; (■): 50 (arbitrary units). The lines are fits with equation (4.24).

3. The experimental data are fitted with equation (4.24) and provide a set of the four parameters of equation (4.24) at each surfactant concentration. Then by using a simple computer worksheet, it is possible to determine these parameters as a function of the surfactant concentration only, anywhere within or near the measured concentration range. A simple and safe method consists of using linear interpolation. A graph showing the dynamic surface tension versus surface ages according to equation (4.24) can be generated from the four parameters and modified automatically every time a new surfactant concentration is entered.
4. A similar automatically generated curve can be established for each coating solution and combined in the same graph as the others. The combined graph will show automatically the relations between the dynamic surface tension versus surface ages of the three coating solutions together, and can be modified just by entering a new surfactant recipe. The surfactant concentrations are then empirically changed until the required criteria for the relative dynamic surface tensions of the three coated layers are satisfied.

The dynamic surface tensions curves corresponding to the current surfactant recipe, which was causing curtain instabilities, is shown in Fig. 4.19. It can be seen that the required wetting stability criteria were violated on both sides of the curtain. In particular, the layer 1 has a higher dynamic surface tension than layer 2 (internal layer) up to *ca.* 1 s of surface age. This situation could cause the internal layer to repel layer 1 if any particle could cause a temporary rupture of layer 1. The curtain layers are flowing along edge guides on each lateral end of the curtain. Layer 2 has more tendency to wet the edge guide than layer 1, because its surface tension is lower, and could have a tendency to repel layer 1 from the edge guide (Gutoff 1992). There is also a wrong gradient between layer 3 and layer 2, at least during the first second of surface aging. As a result, layer 3 may retract from the edge of the

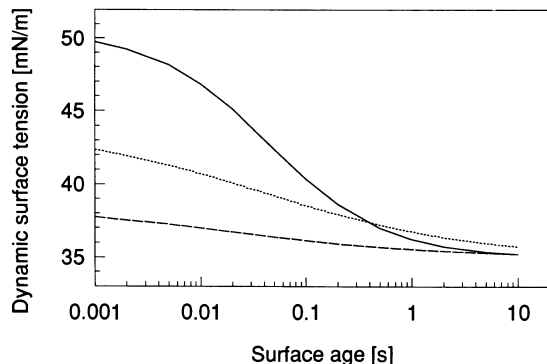


Figure 4.19 Recalculated dynamic surface tension (equation (4.24)) corresponding to an inadequate surfactant recipe: (—): layer 1 with conc. 10; (---): layer 2 with conc. 8; (·····): layer 3 with conc. 30 (arbitrary units).

coating and could be susceptible to repellency holes if hydrophobic particles reach its surface.

After trying a few other surfactant recipes, one finally arrives at the situation shown in Fig. 4.20. The internal layer (layer 2) has no more surfactant, causing its surface tension to remain above the surface tension of both outside layers of the curtain (layers 1 and 3). The amount of surfactant

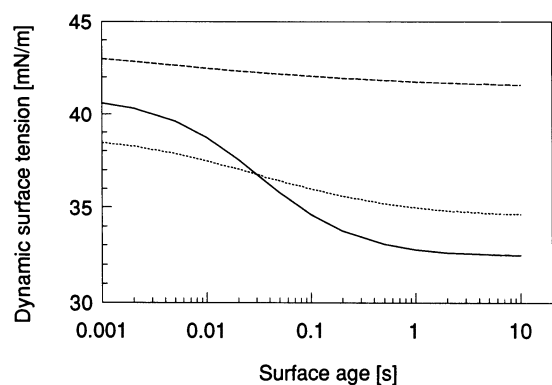


Figure 4.20 Recalculated dynamic surface tension (equation (4.24)) corresponding to an improved surfactant recipe. (—): layer 1 with conc. 18; (---): layer 2 with conc. 0; (·····): layer with conc. 100 (arbitrary units).

in layer 1 and especially in layer 3 has been increased to ensure quick surface tension reduction. The final surface tension for layer 3 is not very low, even with a relatively high surfactant concentration. If a lower surface tension is found necessary after practical test coatings, another surfactant should be used. Experiments on pilot coating machines have shown that the curtain stability responded as expected to the relative surface tension gradients between its layers.

The lower dynamic surface tension of layer 1 versus layer 2 could produce some difficulty for layer 2 to wet layer 1 in the slide flow region proceeding the curtain. However, the main wetting requirement for the slide flow stability is that the top layer (in this case layer 3) is able to wet the next layer (in this case layer 2), a requirement which is fulfilled in the above example. The dynamic surface tension relationship between internal layers is less critical, as discussed above.

4.6 SUMMARY AND CONCLUSIONS

This chapter has reviewed the basic aspects of surfactants, their applications to liquid film coating processes, and general concepts related to surfactants and wetting. The main focus of this work is the determination and use of static and dynamic surface tension. An overview of the major experimental methods able to determine static and/or dynamic surface tension have been given.

Two experimental techniques, the oscillating jet and the inclined plane methods, were used to characterize a group of industrial surfactants by their static and dynamic surface tensions. The measurements were made under conditions where the surfaces of the solutions were instantaneously created and not subjected to significant expansion afterwards. Industrial surfactants were chosen, despite their rather undefined purity, because they represent what is actually used by manufacturers involved with aqueous liquid films coating. It is apparent from the reported results that the studied surfactants differ very widely from each other. For instance, some are active

at very short surface ages and others are better at controlling near-equilibrium conditions.

Characterization of surfactants through their static and dynamic surface tension brings a detailed understanding of their behaviour in real processes. Dynamic surface tensions can be estimated at surface ages shorter than can actually be measured – down to the submillisecond time scale – by simulating experimental data with appropriate models. Practical coating tests and sometimes empirical corrections are still necessary, but fewer are needed and they can be made with greater confidence when the fundamental surfactant behavior is known. Surfactants can be qualified based on their effective static and dynamic properties and not on arbitrary characteristics.

This chapter has not directly considered dynamic flow situations, but focused on diffusion and adsorption processes near the interface. Therefore, the use of dimensionless numbers, very common in flow characterization, was not found useful. The experimental methods used, the oscillating jet and the inclined plane, have very simple flow characteristics which were not taken into account in discussing the results. The purpose of the work was to demonstrate how static and dynamic surface tension can be measured and used to optimize the dynamic wetting behavior of multiple layers in liquid film coating. When diffusion coefficients could be determined, their value can be used as input parameter in numerical flow studies which consider surfactants and the influence of their diffusion (Chapter 11d; Barthod 1993).

Despite the detailed information already gained from surface tension data, and the fact that it is a ‘mature’ science, one should not believe that there is nothing more to learn. In fact, we are only beginning to tackle more real and complex situations. For instance, a lot of current research activity is focused on surfactant interactions with other surfactants (Siddiqui and Franses, 1996), with latex particles (Bolze, Hörner and Ballauff, 1996), silica particles (Goloub *et al.* 1996), polymers (Holmberg and Sundelöf, 1996; De Oliveira, Tiera and Neumann, 1996) or liposomes (de la

Maza and Parra, 1996). There is a need to understand the behavior of surfactants in more and more complex systems. However, the kind of complexity encountered in actual coating solutions, such as in the photographic industry, will require direct and pragmatic experimentation for a long time still. Fundamental research should be balanced and completed with more applied investigations.

ACKNOWLEDGMENTS

The author gratefully thanks Professor P. Joos, University of Antwerpen, Belgium, Professor A. Prins, University of Wageningen, The Netherlands, and Dr R. Traber, Ciba-Geigy, Basel, Switzerland, for stimulating discussions and advice on selecting dynamic surface tension measuring methods; Ms S. Buser, Mr R. Carfagno, Mr M. Pasquier and particularly Mr L. Casarico, Ilford AG, for their essential contributions to the development of the methods and for obtaining experimental results; and Dr E. Kramp, Ilford AG, for initiating this work.

REFERENCES

- Abe, Y. and Matsumura, S. 1983. The relationship between defoaming power and dynamic surface tension of sodium dodecylbenzene sulfonate solutions with alcohols. *Tenside Detergents*, 218–224.
- Adamson, A. W. 1967. *Physical Chemistry of Surfaces*, 2nd edn. New York: Wiley.
- Ainsworth, S. J. 1993. Cosmetics, Product Report. *Chem. & Eng. News*. 26 April: 36–48.
- Ambwani, D. S. and Fort, Jr. T. 1979. Pendent drop technique for measuring liquid boundary tensions. *Surf. Colloid Sci.* **11**: 93–119.
- Aniansson, E. A. G., Wall, S. N., Almgren, M., Hoffmann, H., Kielmann, I., Ulbricht, W., Zana, R., Lang, J. and Tondre, C. 1976. *J. Phys. Chem.* **80**: 905.
- Attwood, D. and Florence, A. T. 1983. *Surfactant Systems, Their Chemistry, Pharmacy, and Biology*. New York: Chapman and Hall.
- Balbaert, I., Bleys, G. and Joos, P. 1987. Measurement of the dynamic surface tension in an asymmetric free-falling film. *J. Coll. Interf. Sci.* **115**: 362–371.
- Barthod, D. 1993. Contribution à l'étude de l'écoulement d'un rideau symétrique (avec ou sans tensio-actifs). PhD thesis, Ecole Centrale de Lyon, France.
- Becher, P. ed. 1985. *Encyclopedia of Emulsion Technology, Volume 2, Applications*. New York: Marcel Dekker.
- Becher, P. and Griffin, W. C. 1985. In *McCutcheon's Emulsifiers and Detergents*. McCutcheon Division, Glen Rock, NJ: MC Publishing.
- Bendure, R. L. 1971. Dynamic surface tension determination with the maximum bubble pressure method. *J. Coll. Interf. Sci.* **35**: 238–248.
- Bergink-Martens, D. J. M., Bos, H. J., Prins, A. and Schulte, B. C. 1990. Surface dilation and fluid-dynamical behavior of Newtonian liquids in an overflowing cylinder. I. Pure liquids. *J. Coll. Interf. Sci.* **138**: 1–9.
- Bird, R. B., Stewart, W. E. and Lightfoot, E. N. 1960. *Transport Phenomena*. New York: Wiley.
- Blake, T. D. 1984. Wetting. In *Surfactants*, ed. Th.F. Tadros, pp. 221–275. London: Academic Press.
- Van den Bogaert, R. and Joos, P. 1979. Dynamic surface tension of sodium myristate solutions. *J. Phys. Chem.* **83**: 2244–2248.
- Van den Bogaert, R. and Joos, P. 1980. Diffusion-controlled adsorption kinetics for a mixture of surface active agents at the solution–air interface. *J. Phys. Chem.* **84**: 190–194.
- Bolze, J., Hörner, K. D. and Ballauff, M. 1996. Adsorption of the nonionic surfactant Triton X-405 on polystyrene latex particles as monitored by small-angle X-ray scattering. *Langmuir*. **12**: 2906–2912.
- Brown, D. R. 1961. *J. Fluid Mech.* **10**: 297.
- Chang, C. H. and Franses, E. I. 1992. Modified Langmuir–Hinshelwood kinetics for dynamic adsorption of surfactants at the air/water interface. *Coll. and Surf.* **69**: 189–201.
- Chang, C. H. and Franses, E. I. 1994. Adsorption dynamics of surfactants at the air/water interface: a critical review of mathematical models, data and mechanisms. *Coll. and Surf.* **100**: 1–45.
- Chari, K. and Hossain, T. Z. 1991. Adsorption at the air/water interface from an aqueous solution of poly(vinylpyrrolidone) and sodium dodecyl sulfate. *J. Phys. Chem.* **95**: 3302–3305.
- Defay, R. and Hommelen, J. 1958. *Ind. Chim Belge*. **23**: 597.
- Defay, R. and Pétré, G. 1971. Dynamic surface tension. In *Surf. Coll. Sci.* 3, ed. E. Matijevic, pp. 27–81. New York: Marcel Dekker.
- Diaz Garcia, M. E. and Sanz-Medel, A. 1986. Dye-surfactant interactions: A review. *Talanta*. **33**: 255–264.
- Fainerman, V. B. 1992. Adsorption kinetics from concentrated micellar solutions of ionic surfactants at the water–air interface. *Coll. and Surf.* **62**: 333–347.
- Fainerman, V. B., Miller, R. and Joos, P. 1994. The

- measurement of dynamic surface tension by the maximum bubble pressure method. *Coll. Polym. Sci.* **272**: 731.
- Fainerman, V. B. and Miller, R. 1995. Dynamic surface tension measurements in the sub-millisecond range. *J. Coll. Interf. Sci.* **175**: 118–121.
- Frumkin, A. 1925. Die Kapillarkurve der höheren Fettsäuren und die Zustandsgleichung der Oberflächenschicht. *Z. Phys. Chem. Stoechiom. Verwandschaftsl.* **116**: 466–484.
- Garrett, P. R. and Ward, D. R. 1989. A reexamination of the measurement of dynamic surface tension using the maximum bubble pressure method. *J. Coll. Interf. Sci.* **132**: 475–490.
- Goloub, T. P., Koopal, L. K. and Bijsterbosch, B. H. 1996. Adsorption of cationic surfactants on silica. Surface charge effects. *Langmuir*. **12**: 3188–3194.
- Griffin, W. C. 1949. Classification of HLB values of non-ionic surfactants. *J. Soc. Cosmet. Chem.* **1**: 311–326.
- Griffith, P. C., Stilbs, P., Howe, A. M. and Cosgrove, T. 1996. A self-diffusion study of the complex formed by sodium dodecyl sulfate and gelatin in aqueous solutions. *Langmuir*. **12**: 2884–2893.
- Gutoff, E. B. 1992. Premetered coating. In *Modern Coating and Drying Technology*, eds E. Cohen and E. B. Gutoff, pp. 117–167. New York: VCH Publishers.
- Hancock, R. I. 1984. Macromolecular surfactants. In *Surfactants*, ed. ThF. Tadros, pp. 287–321. London: Academic Press.
- Hansen, R. S. 1960. The theory of diffusion-controlled adsorption kinetics with accompanying evaporation. *J. Phys. Chem.* **64**: 637.
- Harkins, W. D. and Jordan, H. F. 1930. *J. Am. Chem. Soc.* **52**: 1571.
- van Havenberg, J. and Joos, P. 1983. The dynamic surface tension in a free-falling film. *J. Coll. Interf. Sci.* **95**: 172–182.
- Hempt, C., Lunkenheimer, K. and Miller, R. 1985. On the experimental determination of the dilational elasticity and the exchange of matter of mixed gelatin surfactant adsorption layers. *Z. Phys. Chemie (Leipzig)*. **266**: 713–720.
- Hiemenz, P. C. 1977. *Principles of Colloid and Surface Chemistry*. New York: Dekker.
- Hirt, D. E., Prud'homme, R. K., Miller, B. and Rebenfeld, L. 1990. Dynamic surface tension of hydrocarbon and fluorocarbon surfactant solutions using the maximum bubble pressure method. *Coll. and Surf.* **44**: 101–117.
- Holmberg, C. and Sundelöf, L.-O. 1996. Temperature dependence of hydrodynamic properties and surfactant–polymer interaction in solution. The EHEC/SDS/water system. *Langmuir*. **12**: 883–889.
- Hua, X. Y. and Rosen, M. J. 1988. Dynamic surface tension of aqueous surfactant solutions I. Basic parameters. *J. Coll. Interf. Sci.* **124**: 652–659.
- Ishiwata, M., Kawame, N., Sakurai, T., Nakano, M., Tamazawa, K., Kimura, N., Saito, T. and Hada, G. 1990. Process for producing photographic materials. EU patent application 0 383 347.
- Israelachvili, J. N., Marcelja, S. and Horn, R. G. 1980. Physical principles of membrane organization. *Quart. Rev. Biophys.* **13**: 121–200.
- Janczuk, B., Bialopiotrowicz, T. and Wojcik, W. 1989. The components of surface tension of liquids and their usefulness in determination of surface free energy of solids. *J. Coll. Interf. Sci.* **127**: 59–66.
- Joos, P. and de Keyser, P. 1980. The overflowing funnel as a method for measuring surface dilational properties. *Levich Birthday Conference*, Madrid.
- Kalhweit, M., Busse, G. and Jen, J. 1991. Adsorption of amphiphiles at water/air interfaces. *J. Phys. Chem.* **95**: 5580–5586.
- Knox, W. J. 1970. Photographic surfactant compositions. US patent 3,514,213.
- Knox, W. J. and Parshall, T. O. 1970. The interaction of sodium dodecyl sulfate with gelatin. *J. Coll. Interf. Sci.* **33**: 16–23.
- Knox, W. J. and Parshall, T. O. 1972. The interaction of Aerosol OT with gelatin. *J. Coll. Interf. Sci.* **40**: 290–296.
- López de Ramos, A., Redner, R. A. and Cerro, R. L. 1993. Surface tension from pendant drop curvature. *Langmuir*. **9**: 3691–3694.
- Lucassen, J. 1975. Adsorption kinetics in micellar systems. *Disc. Faraday*. **59**: 76–87.
- Lucassen, J. and Giles, D. 1975. Dynamic surface properties of nonionic surfactant solutions. *J. Chem. Soc. Faraday Trans. I.* **71**: 217–232.
- Lucassen-Reynders, E. H. ed. 1981. *Anionic Surfactants*. New York: Marcel Dekker.
- Lunkenheimer, K., Hartenstein, C., Miller, R. and Wantke, K. -D. 1984. Investigations on the method of radially oscillating bubble. *Coll. and Surf.* **8**: 271–288.
- Lunkenheimer, K., Serrien, G. and Joos, P. 1990. The adsorption kinetics of octanol at the air/solution interface measured with the oscillating bubble and oscillating jet methods. *J. Coll. Interf. Sci.* **134**: 407–411.
- Marangoni, C. 1878. Difesa della teoria dell'elasticità superficiale dei liquidi: Plasticità superficiale. *Nuovo Cimento*. **3(3)**: 50–68, 97–123 and 193–211.
- De la Maza, A. and Parra, J. L. 1996. Interaction of

- equimolecular mixtures of nonionic/anionic surfactants with liposomes. *Langmuir*. **12**: 3393–3398.
- Mysels, K. 1989. Some limitations in the interpretations of the time dependence of surface tension measured by the maximum bubble pressure method. *Langmuir*. **5**: 442–447.
- Neustadler, E. L. 1984. Surfactants in enhanced oil recovery. In *Surfactants*, ed. Th.F. Tadros, pp. 277–285. London: Academic Press.
- Du Nouy, P. 1919. *Journal General Physiology*. **1**: 521. DIN-Blatt 53914.
- Nylen, P. and Sunderland, E. 1965. *Modern Surface Coatings*, pp. 650–660. London: John Wiley.
- Okubo, T., Kitano, H., Ishiwatari, T. and Isem, N. 1979. *Proc. Roy. Soc. A***366**: 81.
- De Oliveira, V. A., Tiera, M. J. and Neumann, M. G. 1996. Interaction of cationic surfactants with acrylic acid-ethyl methacrylate polymers. *Langmuir*. **12**: 607–612.
- Ottewil, R. H. 1984. Introduction. In *Surfactants*, ed. Th.F. Tadros, pp. 1–18. London: Academic Press.
- Patterson, R. E. and Ross, S. 1979. The pendent-drop method to determine surface or interfacial tension. *Surf. Sci.* **81**: 451–463.
- Rillaerts, E. and Joos, P. 1982. Rate of demicellization from the dynamic surface tension of micellar solution. *J. Phys. Chem.* **86**: 3471–3478.
- Rosen, M. J. 1978. *Surfactants and Interfacial Phenomena*. New York: Wiley.
- Ross, S. and Morrison, I. D. 1988. *Colloidal Systems and Interfaces*. New York: Wiley.
- Rotenberg, Y., Boruvka, L. and Neumann, A. W. 1983. Determination of surface tension and contact angle from the shapes of axisymmetric fluid interfaces. *J. Coll. Interf. Sci.* **93**: 169–183.
- Ruschak, K. J. 1987. Flow of a thin liquid layer due to ambient disturbance. *AIChE Journal*. 801–807.
- Schick, M. J. ed. 1967. *Nonionic Surfactants*. New York: Marcel Dekker.
- Serrien, G. and Joos, P. 1990. Dynamic surface properties of aqueous sodium dioctyl sulfosuccinate solutions. *J. Coll. Interf. Sci.* **139**: 149–159.
- Siddiqui, F. A. and Franses, E. I. 1996. Equilibrium adsorption and tension of binary surfactant mixtures at the air/water interface. *Langmuir*. **12**: 354–362.
- Strutt, J. W. (Lord Rayleigh) 1897. *Proc. Roy. Soc. 29*: 71.
- Sturge, J. M. 1977. *Neblette's Handbook of Photography and Reprography. Materials, Processes and Systems*. 7th edn. New York: van Nostrand Rheinhold.
- Sucker, Ch., Meskati, W. and Heusch, R. 1964. German patent 1 211 821, 10.10.64.
- von Szyszkowski, B. 1908. Experimental studies of the capillary properties of aqueous solutions of fatty acids. *Z. Phys. Chem., Stoechiom. Verwandschaftsl.* **64**: 385–414.
- Tadros, Th.F. 1984. Some applications of surfactants in biological systems. In *Surfactants*, ed. Th.F. Tadros, pp. 323–335. London: Academic Press.
- Tanford, C. 1980. *The Hydrophobic Effect: Formation of Micelles and Biological Membranes*, 2nd edn. New York: Wiley.
- Tann, R. S., Berger, P. D. and Berger, C. H. 1992. *Applications of Dynamic Surface Tension to Adjuvants and Emulsion Systems* (Conference on Pesticide Formulation and Application Systems, San Antonio, TX USA, November 1991). ASTM Special Technical Publication 1112, pp. 158–172. Philadelphia, USA: ASTM.
- Thayer, A. M. 1993. Soaps and detergents, Product Report. *Chem and Eng. News*. 25 January: 26–47.
- Valentini, J. E., Thomas, W. R., Sevenhuijsen, P., Jiang, T. S., Lee, H. O., Liu, Y. and Yen, S. C. 1991. Role of dynamic surface tension in slide coating. *Ind. Eng. Chem. Res.* **30**: 453–461.
- Van Voorst Vader, F., Erkelenz, Th.F. and van den Tempel, M. 1964. *Trans. Farad. Soc.* **60**: 1170.
- Wada, Y., Nakahara, T., Orrii, T., Okano, Y., Aya, M., Kasui, K., Kamochi, A., Yamada, Y., Katsumata, O., Sakawa, S. and Kurahashi, Y. 1983. In *Proc. 5th Int. Congress Pesticide Chem.* Volume 4. Oxford: Pergamon Press.
- Ward, A. F. H. and Tordai, L. 1946. Time-dependency of boundary tensions of solutions. I. The role of diffusion in time effects. *J. Phys. Chem.* **14**: 453–461.
- Wilhelmy, L. 1864. *Ann. Physik.* **1**: 521.
- Wu, A. and Whitaker, S. 1986. The recirculation zone at the entrance of a falling liquid film: consequences for the surfactant adsorption problem. *J. Coll. Interf. Sci.* **110**: 389–397.
- Young, T. 1805. An essay on the cohesion of fluids. *Phil. Trans. Royal Soc. (London)*. **95**: 65–87.
- Ziller, M., Miller, R. and Kretzschmar, G. 1985. A model of the adsorption kinetics for a flowing liquid layer of a surfactant solution. *Z. Phys. Chemie (Leipzig)*. **4**, 721–730.

COATING RHEOLOGY: COMPONENT INFLUENCE ON THE RHEOLOGICAL RESPONSE AND PERFORMANCE OF WATER-BORNE COATINGS IN ROLL APPLICATIONS

5

J. Edward Glass and Robert K. Prud'homme

5.1 INTRODUCTION

Even though much of the published coating-flow literature – including many chapters in this book – focuses on Newtonian liquids, most coating liquids in commercial applications are strongly non-Newtonian: the viscosity is not simply a constant, but depends on the deformation rates the liquid experiences; viscoelasticity gives rise to additional stresses that can significantly alter the local force balances in the flow; and, at sufficiently low deformation rates, coating liquids can exhibit solid-like yield behavior preventing flow altogether. In some instances, non-Newtonian characteristics of the formulation are adjusted for the specific purpose of enhancing coating process performance. In the pre-metered processes discussed in Chapters 11a–11c, for instance, small amounts of polymeric additives can enhance the stability and hence the operating latitude of the process. Another example comes from paints and varnishes, for which much research has been invested to achieve ease of flow during application yet resistance to sagging and other defects once the coating is applied. In many instances, on the other hand, the non-Newtonian behavior is

the result of major formulation components necessary to achieve the ultimate performance of the coated film, and can give rise to serious difficulties in applying uniform layers at acceptable speeds. A primary case in point is that of adhesives, for which the desired ‘tackiness’ in the final product is often associated with substantial viscoelasticity during processing.

The purpose of applied rheology in general is to understand and predict the response of non-Newtonian liquids to the complex flows in industrial processes from their response in much simpler flows that subject the test liquids to well-defined deformations and are amenable to laboratory instrumentation. The use of rheometry to determine material functions such as viscosity, normal stress coefficients, or dynamic moduli, is well documented in numerous texts (Walters 1980; Whorlow 1980; Schoff 1988). Also well established is the broader field of rheology which encompasses not only rheometric measurements, but also the development of so called constitutive equations that mathematically describe the material functions and associated non-Newtonian flow behavior; the explanation of these equations

in terms of the microstructure or molecular structure of the liquid; and the application of constitutive models to predict the flow in complex geometries and flow fields (e.g., Tanner (1985); Bird, Armstrong and Hassager (1987); Larson (1988)).

The specialized field of coating rheology, or the science of how non-Newtonian liquid behavior affects coating flow performance, is not as well developed, in spite of its industrial significance. A major difficulty arises from the extremely high and rapidly varying deformation rates found in most industrial coating processes (e.g., Schunk and Scriven (1990)). These deformations are difficult if not impossible to replicate in laboratory measurements with conventional rheometric equipment. Thus, the application of data from such measurements often requires considerable amounts of interpretation and speculation. Even if an apparent correlation between coating behavior observed in experiments and material functions measured on rheometers can be established, it does not unequivocally prove a cause-and-effect relationship. Constitutive theories and non-Newtonian fluid mechanics can in principle provide such a proof, but still face immense difficulties for realistic coating flows. They tax

beyond their limits the most advanced computational algorithms available to date (see Chapter 9). In fact, at least for viscoelastic liquids, there are virtually no publications that successfully predict coating flows and their stability from hydrodynamic principles and constitutive models.

Given the rather modest state-of-the-art of coating rheology in general, the present chapter does not attempt a broad review of the entire field but limits itself to reviewing basic rheological concepts and then describing in detail three particular studies for which some progress has been made in quantifying the interplay between formulation components, rheology, and ultimate performance during coating. The first is the application of architectural paints by means of a small porous mat roll at low speeds to wallboard, wood and stucco surfaces. House paints in which the lay-person is involved are typical examples. The second case is the coating of paper, ranging from low-cost newspaper to highly glossy corporate reports. Here, the substrate consists of flocculated cellulose fibers and is highly porous. Modern paper coaters rely on blades to apply the coating liquid and smooth the coated surface, as illustrated in Fig. 5.1. They can operate at

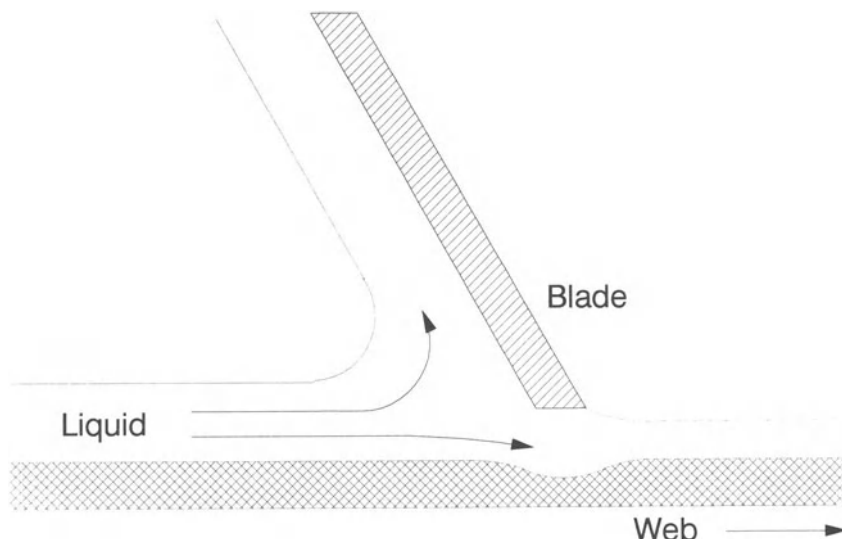


Figure 5.1 Schematic of a blade applicator for high-speed paper coating.

speeds in excess of 25 m/s, or 5000 ft/min (see Chapter 12d). The third case, finally, is that of protective coatings on metal substrates, used by a wide range of original equipment manufacturers for refrigerators, washing machines, automobiles, etc., and henceforth referred to as OEM coatings. Methods for applying OEM coatings include roll coating, as exemplified by the so-called Giordano coater shown in Fig. 5.2. OEM coatings on high-energy metal surfaces can exhibit unique defects different from those on other surfaces (Bierwagen 1975).

Illuminating the interplay of chemical components, rheological material properties, and performance during and after application of typical coating formulations is the primary focus in this chapter. Section 5.2 provides a brief introduction of the components and processes used to formulate coatings of the sort addressed in this chapter. After a brief review of basic rheological concepts, such as measurement techniques and material functions, Section 5.3 focuses on recounting various kinds of rheological behavior that are characteristic of common types of liquids in general and coating solutions in particular, and shows how some of that behavior can be interpreted in terms of the composition and microstructure of the coating system. Section 5.3 also selectively cites component influences on melt polymer rheology that have been identified

in the literature. Section 5.3 concludes with a brief review of some simple but useful rheological models (for an in-depth treatise of constitutive models, which constitute an entire field of study by themselves, see Larson 1988). Section 5.4 attempts to illuminate how the coating formulation and resulting rheology influence the success of the application step and the fate of the liquid film after application. The main focus is on architectural coatings, for which sufficient data is available to draw a fairly unified picture of the interplay of components, rheology, and performance during and after application. For formulations used in paper and OEM coatings, systematic rheological studies are not as common in the published literature, but the difficulties in the application of these coatings are nevertheless discussed in terms of the knowledge gained from the architectural area. Hot melts and adhesive coatings are not discussed in this chapter because the component influences on rheology and flow behavior in these systems are poorly identified in the published literature. Section 5.5 finally recapitulates the most significant formulation effects on the rheology of water-borne coating formulations.

5.2 FORMULATION CONCEPTS

There are two key ingredients in most coating formulations of the sort considered in this chapter:

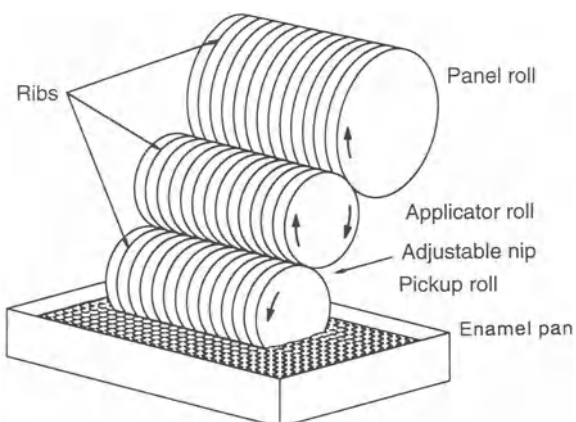


Figure 5.2 Schematic of 'Giordano' reverse-roll coater configuration (after Matsuda and Brendley, 1979).

the polymer that gives desired flow properties during application and mechanical integrity of the coated layer once it is solidified; and the pigment that provides color or opacity to the applied film, or merely serves as a cheap filler. Most architectural and paper coatings are latex based, i.e., the polymer is high in molecular weight and forms a dispersion of insoluble solid particles in water. The final film forms from the coalescence or fusion of the latex particles rather than chemical cross-linking. The films in OEM applications, in contrast, are cross-linked from dissolved or dispersed oligomers or resins to achieve hard and wear-resistant surfaces.

5.2.1 LATTICES IN ARCHITECTURAL AND PAPER COATINGS

Latices are prepared by an emulsion polymerization process that begins with an emulsion of monomer droplets of limited solubility in the aqueous phase (Odian 1993). A free-radical polymerization is started by a water-soluble initiator, and occurs in the presence of surfactant. The surfactant molecules aggregate into groups of generally spherical shapes called micelles (*c.f.* Chapter 4). In the polymerization of styrene, the 'stung' monomer enters the micelle to propagate the polymerization, which is relatively immune to termination as compared with solution polymerization. Vinyl acetate, a more hydrophilic monomer, on the other hand, does not participate significantly in micellar propagation. It polymerizes primarily in the aqueous phase and the polymer chains aggregate to form the latex particles. This sort of emulsion polymerization process is referred to as homonuclear. Methyl methacrylate, which is of intermediate hydrophilicity, polymerizes by both micellar and homonuclear propagation. In the final latex dispersion, surfactants play an important role in stabilizing the polymer particles. Typically, there is an excess of surfactant in the aqueous phase, particularly after the synthesis of small latex particles (100 nm).

For architectural coatings, methyl methacrylate, with its proven durability for exterior applications, is generally copolymerized with acrylic esters.

Acrylic esters lower the glass transition temperature of the latex particle and thereby facilitate particle coalescence in the film forming sequence. In coating formulations for less demanding interior applications, vinyl acetate copolymers with a low percentage of butyl acrylate are used. Styrene/butadiene latices were developed during World War II as a natural rubber substitute. Styrene is still used in many coating formulations, especially in the paper industry, but generally is no longer a primary monomer in architectural coatings because of its poor durability.

The stability of latices is well described by the Derjaguin, Landau, Verwey and Overbeck (DLVO) theory, as is documented in numerous textbooks (e.g., Napper (1983); or Sato and Ruch (1980)). For latices with small particles in the range of 100 nm or so in aqueous phases containing low salinity levels, electrostatic stabilization by anionic surfactants is not sufficient (Ottewill 1982). To provide high and low temperature stability as well as mechanical stability to such latices, 1–4 wt.% methacrylic acid is included in the latex synthesis. With a proper balance of hydrophilicity and glass transition temperature of the acrylate ester, the methacrylic acid units can be positioned at the methacrylate particle/water interface in a two stage emulsion synthesis (Karunasena and Glass 1989). In alkaline media, these surface segments stabilize the particle. Methacrylic surface acid stabilization is used in vinyl acetate latices for paper coatings, but not in vinyl acetate latices for architectural coatings. In the latter, water sensitivity of the final film is important (Ma *et al.* 1993), and stability of large latex particles is achieved by chemically grafting water-soluble polymer to the growing chain, which places nonionic surface segments on the latex surface (Craig 1986). With the high chain transfer rate and reactivity of the hydrophilic vinyl acetate monomer, grafting of the polymer segments leads to a broad particle size distribution that is beneficial in lowering the viscosity at lower shear rates. Section 5.4.2 discusses in detail the influence on rheology of grafted polymer segments for a 600 nm vinyl acetate latex coating stabilized by hydorxyethyl cellulose (HEC) segments, and

a 100 nm methyl methacrylate latex with methacrylic acid surface segments.

In architectural coatings, there is an even approach to using both polymer and pigment particles. The percentage of the latex binder is varied to produce a level of film quality that fits a given market need and cost point. The 'hiding' pigment that provides opacity is titanium dioxide, which is optimal based on its refractive index difference with air and the polymer binder. Its concentration in reference to the latex is close to 21% by volume, which is the minimum amount needed in an architectural coating for optimum opacity. Titanium dioxide pigment is seldom used in higher amounts because it is one of the most costly components in the formulation. However, other low-cost 'extender' pigments such as calcium carbonate, silicas and clays are often added to paint formulations because a number of coating properties (i.e., tendency for blistering, corrosion resistance, opacity) improve with increasing pigment volume concentration. Clays and other inorganic disperse phases can also be added – or substituted for more costly latex particles in poorer quality coatings – to achieve higher formulation viscosities without the need for additional, water soluble thickener polymers.

Past the so-called critical pigment volume concentration (CPVC), the amount of polymer binder is insufficient to form a continuous film. As a result, numerous coating properties exhibit abrupt changes as the particle concentration is increased past the CPVC, as was identified early in the development of latex coatings (e.g., Bierwagen and Hay (1975)). It was also realized early on that higher CPVCs could be obtained in lower cost architectural paints if a small particle size latex was used (Schaller 1968). In coatings with high particle volume concentrations (PVC), a small 100 nm latex is typically employed in an attempt to maintain a continuous film.

Paper coatings are low-cost formulations that serve market needs entirely different from those of architectural coatings. They are applied at very high speeds (sometimes in excess of 25 m/s, or 5000 ft/min) on highly porous cellulose-fiber substrates. The dominant disperse phases in

paper coatings typically include a kaolinite clay and calcium carbonate, with particle sizes of about 100 nm and 400–600 nm respectively (Garey 1977). The content of latex binder and TiO₂ pigment is often very small to minimize cost (e.g., Lundberg *et al.* (1990)). The latex has traditionally been a styrene/butadiene copolymer, but vinyl acetate latices have captured part of the market over the last decade. Small particle latices (100 nm) are used almost exclusively in paper coatings to maximize the amount of clay that can be used (Schaller 1968). In some paper coating formulations, the latex and/or the TiO₂ pigment are omitted altogether.

5.2.2 DISPERSE POLYMER SYSTEMS IN OEM COATINGS

In conventional high-solids OEM coatings, an oligomer is applied as a 60–80% solution (by weight) in organic solvents and is cross-linked after application to achieve the desired mechanical properties. Environmental factors and political legislation, however, are forcing the transition of OEM coatings from the high-solids approach in organic solvents to water-borne systems.

One approach to drastically reducing organic solvent emissions is to employ so-called 'water-reducible' resins whose solutions in a water-miscible organic solvent can be diluted with water to form acceptably stable dispersions of polymer aggregates swollen by solvent and water. There is indeed a close analogy between a 'water-reducible' acrylic and an acrylic latex, the main difference being that hydroxyethyl methacrylate is used in the synthesis of the OEM resin to provide cross-linking sites with multi-functional melamine or isocyanate groups after application. The low molecular weight resin is first prepared in a water-miscible solvent, and is diluted with water before being applied (Lambourne 1987). In OEM acrylic resins, methacrylic or acrylic acids are often included to provide electrosteric stabilization to the newly formed disperse phase when the organic, water-miscible solvent is diluted with water. In both the latex and in the OEM dispersions, the amount of oligometric acid buried

within the polymer particle is *ca.* 25% by weight (Richards 1977; Ma 1992), and in both binder systems the acids are incorporated into the chain by a chain-growth mechanism. In a chain-growth polymerization, several methacrylic acid monomers may add to a propagating radical. This permits the acid groups to be incorporated in sequence runs that, on neutralization, will provide greater stability to the particle than an individual acid unit.

In the synthesis of water-reducible polyester and polyurethane dispersions, acid groups are incorporated into the chain by a step-growth mechanism (Odian 1993) prior to water dilution of the organic solvent–resin solution (Lambourne 1987). The acid groups, incorporated by the reaction of the terminal hydroxyl in dimethylol-propionic acid with the terminal carboxylic acid units of a diacid, can enter the polyester chains only as individual units. These isolated units cannot sequence in the manner observed for acrylic resins prepared by a chain growth mechanism, and the percent of the individual acid units buried in the disperse has not been determined. Section 5.4.4 examines the influence of individual components on rheology and performance during application for ‘water-reducible’ acrylic and polyurethane dispersions.

In OEM coatings, pigments are typically not used. The disperse polymer phase is not a classical latex but is rather unstable, making pigmentation with TiO_2 or other extender fillers difficult.

5.3 RHEOLOGICAL CONCEPTS

5.3.1 STRESS AND STRAIN IN RHEOMETRIC FLOWS

As indicated in the Introduction (Section 5.1), most rheological measurements are performed in so-called rheometric flows that subject the test liquid to a very simple deformation, often uniform in space. The purpose is to isolate specific ‘material functions’ of the tested liquid, such as the viscosity, normal stress coefficients, or dynamic moduli as a function of shear rate, frequency of

the test, or time since inception of flow, as explained in more detail below. Material functions provide invaluable information about the structure and flow-induced changes in the structure of non-Newtonian liquids. They are useful to classify liquids. They are furthermore important to construct or select appropriate mathematical models, called ‘constitutive equations’, that describe relationships between imposed deformation and resulting stresses (e.g., Larson (1988)), and to determine adjustable constants in such models.

The definition of stress requires the specification of the direction of the force and the orientation of the surface upon which the force acts. Similarly, the rate of deformation, or velocity gradient, requires specification of the direction of the velocity and the direction in which the velocity varies. Figure 5.3 illustrates five flow fields that are extensively used in rheological measurements, namely steady shear, transient shear, uniaxial extension, biaxial extension, and oscillatory shear.

5.3.1.1 Steady shear flows

In the flow illustrated in Fig. 5.3a, a fluid between two plates is sheared as the top plate moves with velocity U_x in the x -direction while the bottom plate is at rest. The velocity gradient, or shear rate, $\dot{\gamma}_{yx} = dv_x/dy \equiv \dot{\gamma}$, is given by U_x/δ where δ is the distance separating the plates. The shearing action of the flow generates stresses that act parallel to the direction of shear, i.e., shear stresses

$$\tau_{yx} \quad (5.1)$$

and stresses that act perpendicular to the direction of shear, i.e., normal stresses. The latter include the stress induced by the fluid motion as well as the isotropic hydrostatic pressure. It is customary to eliminate the isotropic part by taking the difference between normal stresses, and these differences,

$$\tau_{xx} - \tau_{yy} = N_1 \quad (5.2)$$

$$\tau_{yy} - \tau_{zz} = N_2 \quad (5.3)$$

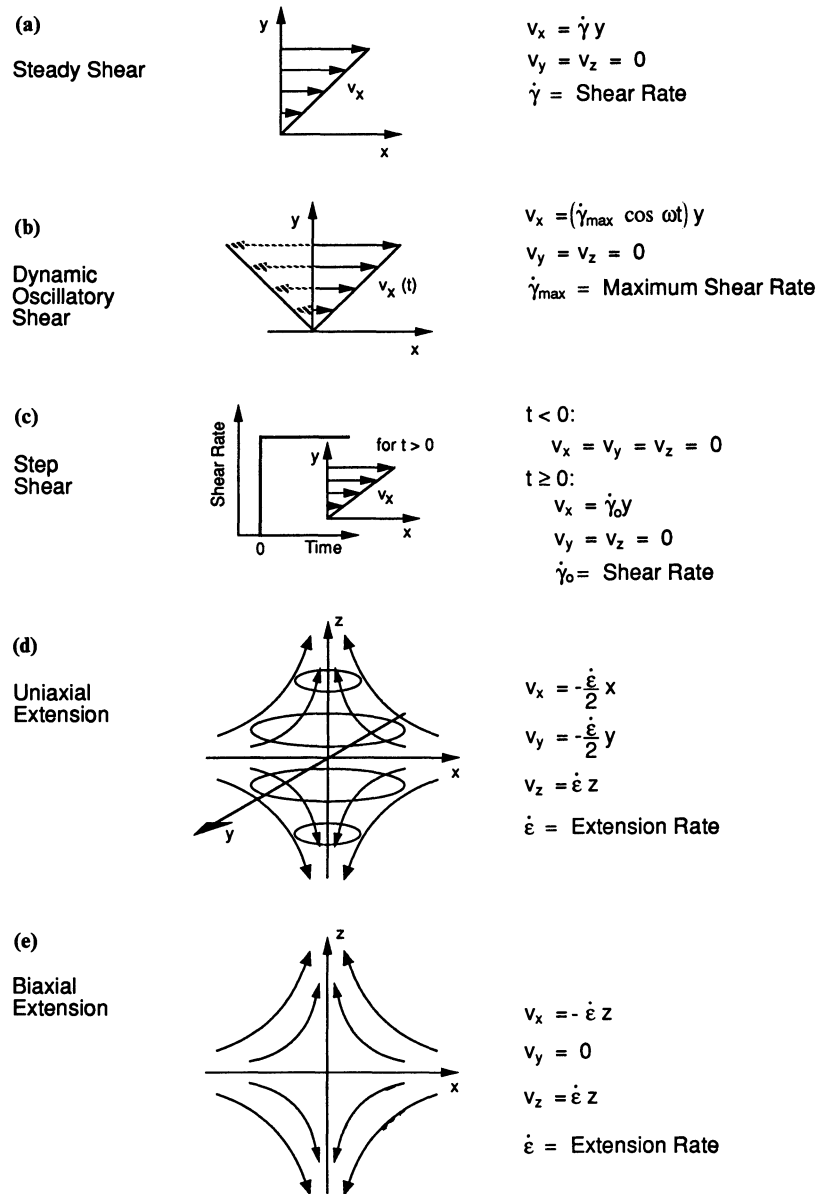


Figure 5.3 Common flow fields used to define material functions in rheological measurements.

are in fact measured in experiments. N_1 and N_2 are referred to as the primary and secondary normal stress differences. The relationships between the stresses and the velocity gradient, $\dot{\gamma}$,

define the material functions for steady shear flow, namely the viscosity η :

$$\tau_{yx} = -\eta \dot{\gamma} \quad (5.4)$$

and the primary and secondary normal stress coefficients, Ψ_1 and Ψ_2 :

$$\tau_{xx} - \tau_{yy} = -\Psi_1 \dot{\gamma}^2 \quad (5.5)$$

$$\tau_{yy} - \tau_{zz} = -\Psi_2 \dot{\gamma}^2 \quad (5.6)$$

The material functions η , Ψ_1 and Ψ_2 , generally vary with shear rate. The normal stress coefficients are defined in terms of the square of the velocity gradient because the stress difference must be an even power of shear rate; that is, changing the direction of the shear, which makes $\dot{\gamma}$ negative, does not change the direction or sign of the normal stress, whereas changing the direction of the velocity gradient does change the direction of the shear stress.

5.3.1.2 Extensional and compressive flows

Fig. 5.3d depicts a flow that either converges or diverges with respect to the z -axis. Such flows are produced by uniaxial stretching of a filament as in the case of fiber spinning (extension), or by biaxial stretching of a sheet as in the case of inflating a balloon (compression in the z -direction). The measurable material responses are the tensile normal stresses. As for the normal stresses in shear flow, the difference in stress is used in order to eliminate isotropic pressure terms, viz.,

$$\tau_{zz} - \tau_{xx} \quad (5.7)$$

The uniaxial elongational viscosity, η_e , is defined as the proportionality factor between this normal stress difference and the velocity gradient, $\dot{\epsilon} = dv_z/dz$:

$$\tau_{zz} - \tau_{xx} = -\eta_e \dot{\epsilon} \quad (5.8)$$

In general, η_e is a function of $\dot{\epsilon}$, the extension rate.

In planar extension, illustrated in Fig. 5.3e, the material is being stretched in the z -direction. This deformation arises when a sheet of material is pulled in one direction. The planar elongation viscosity is, as above, defined via the tensile stress difference:

$$\tau_{zz} - \tau_{xx} = -\eta_p \dot{\epsilon} \quad (5.9)$$

As in (5.8), the velocity gradient, or extension rate, is $\dot{\epsilon} = dv_z/dz$, but $dv_y/dy = 0$ and $dv_x/dx =$

$-dv_z/dz$, whereas in uniaxial extension $dv_y/dy = -1/2(dv_z/dz)$ and $dv_x/dx = -1/2(dv_z/dz)$.

5.3.1.3 Dynamic oscillatory flows

In oscillatory shear measurements, often also referred to as dynamic mechanical measurements, a sinusoidally varying shear field is imposed on a fluid and the amplitude of the resulting shear stress and the phase angle between the imposed shear and the measured stress is detected. The test is particularly simple to interpret and is said to be in the 'linear viscoelastic' regime if the stress is linearly proportional to the imposed strain and the stress response is also sinusoidal and involves only the first harmonic and no higher harmonics in frequency (in experimental work, the validity of these conditions must, of course, be verified).

In the test shown in Fig. 5.3b, the imposed oscillatory velocity field is

$$v_x = [\dot{\gamma}_{\max} \cos(\omega t)]y \quad (5.10)$$

where ω is the frequency, $\dot{\gamma}_{\max}$ is the maximum velocity gradient, and the maximum value of the strain is given by $\gamma_{\max} = \dot{\gamma}_{\max}/\omega$. The resulting stress also oscillates and goes through a maximum value, τ_{\max} , with some phase shift, ϕ , from the imposed shear.

$$\tau_{yx} = \tau_{\max} \cos(\omega t - \phi) \quad (5.11)$$

This oscillatory stress response can be decomposed into two terms, one in-phase with the velocity and one 90° out-of-phase. These, in turn, can be expressed in terms of the maximum velocity gradient.

$$\tau_{yx} = -\eta' \dot{\gamma}_{\max} \cos(\omega t) - \eta'' \dot{\gamma}_{\max} \sin(\omega t) \quad (5.12)$$

where

$$\tau_{\max} \cos \phi \equiv \eta' \dot{\gamma}_{\max}$$

$$\text{and } \tau_{\max} \sin \phi \equiv \eta'' \dot{\gamma}_{\max} \quad (5.13)$$

These expressions define the two dynamic viscosity coefficients, η' and η'' . A complex viscosity η^* can be defined as

$$\eta^* = \eta' - i\eta'' \quad (5.14)$$

which is the ratio of shear stress to shear rate, viz., $\eta^* = \tau_{yx}(t)/\dot{\gamma}_{yx}(t)$. At low frequencies, η' approaches the viscosity measured in steady shear as the shear rate approaches zero, and is usually given the name ‘dynamic viscosity’. Alternately, coefficients can be defined in terms of the maximum strain instead of the strain rate.

$$\tau_{yx} = -G' \gamma_{\max} \cos(\omega t) - G'' \gamma_{\max} \sin(\omega t) \quad (5.15)$$

where

$$\begin{aligned} \tau_{\max} \cos \phi &\equiv G' \gamma_{\max} \\ \text{and } \tau_{\max} \sin \phi &\equiv G'' \gamma_{\max} \end{aligned} \quad (5.16)$$

This defines the two material functions G' and G'' , referred to as the storage and loss moduli, respectively. It is customary to write

$$G^* = G' + iG'' \quad (5.17)$$

where G^* is called the complex modulus. The term ‘complex modulus’ is sometimes also used to refer to the magnitude of G^* , i.e.,

$$|G^*| = \sqrt{G'^2 + G''^2} \quad (5.18)$$

This is the case in the early literature on coating rheology where, in a somewhat arbitrary choice, $|G^*|$ was selected to project the importance of elastic effects and, at the same time, minimize data redundancy. This choice is adopted for much of Section 5.4 in this chapter. The modulus and viscosity coefficients are related via

$$G' = \omega \eta'' \quad (5.19)$$

$$G'' = \omega \eta' \quad (5.20)$$

G' , which is proportional to the stress in phase with strain, provides information about the recoverable elasticity of a material. An ideal elastic rubber band subjected to an oscillatory test, for instance, would have all of its stress in phase with strain or displacement. G'' , in contrast, is proportional to stress that is out of phase with displacement but in phase with rate-of-displacement or shear-rate. It accounts for the dissipative losses in the material. For a purely viscous liquid, of course, all of the stress would be out of phase with displacement.

The linear viscoelastic dynamic moduli, G' and G'' , are functions of frequency. They have proven

to be sensitive probes of the molecular structure of polymer solutions and gels, and a large body of literature exists on this subject (Ferry 1980). As an illustrative example, Fig. 5.4 shows the dynamic moduli of a polymer solution during gelation (Clark, Wellinghoff and Miller 1983). The material begins as a liquid solution in Fig. 5.4a and ends as a solid gel in Fig. 5.4d. For a polymer solution at low frequency, elastic stresses relax sufficiently rapidly and viscous stresses dominate. As a result, the loss modulus, G'' , is higher than the storage modulus, G' . Both decrease with decreasing frequency, but G' decreases more quickly. For a gel, in contrast, the stress cannot relax and G' therefore is independent of frequency. Also, because the gel is highly elastic, the storage modulus is higher than the loss modulus.

5.3.1.4 Transient flows

Fig. 5.3c shows an experiment in which the shear rate is stepped instantaneously from one value to another and the response in shear stress is monitored with time. The resulting material function is then the ‘stress growth function’:

$$\tau_{xy}(t) = \bar{\eta}^+ (\dot{\gamma}_{0,i}, t) \dot{\gamma}_0 \quad (5.21)$$

which describes the growth from an initial shear rate $\dot{\gamma}_{0,i}$ to the final shear rate $\dot{\gamma}_0$. Most commonly, the initial shear rate is zero.

In an alternative transient test, the step strain experiment, an instantaneous strain is applied to the material and the decay in the stress is monitored with time. This defines the shear modulus, $G(t)$, for an applied shear strain of magnitude γ_0 :

$$\tau_{xy}(t) = G(t) \gamma_0 \quad (5.22)$$

or the Young’s modulus, $E(t)$ for an elongational strain of magnitude ε_0

$$\tau_{xx}(t) - \tau_{yy}(t) = E(t) \varepsilon_0 \quad (5.23)$$

A more complicated transient deformation test that provides qualitative information about time-dependent fluid rheology ramps the shear rate continuously from zero to a higher value over a prescribed time period, and monitors the

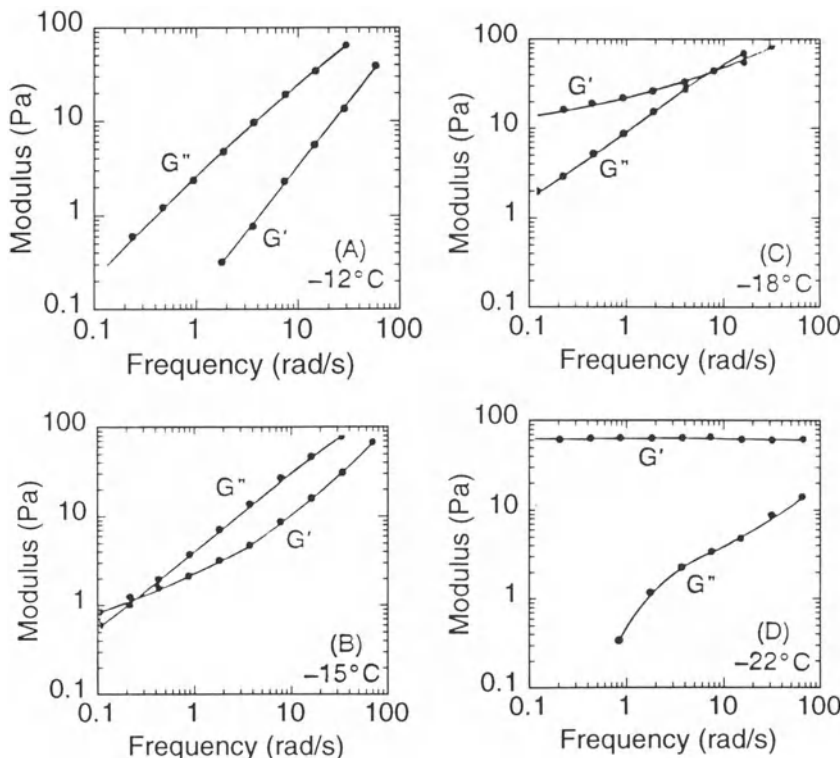


Figure 5.4 Dynamic moduli versus frequency during gelation upon cooling of polystyrene in carbon disulfide (after Clark, Wellinghoff and Miller, 1983).

resulting shear stress. This sort of test is sensitive to the kinetics of structure evolution, which can be important in aggregated colloidal dispersions. If the structures in the material are broken apart by shear and cannot reform during the time of the shear rate ramp, the stresses during the decreasing shear rate ramp are lower than the stresses during the increasing leg. The region between the stress and shear rate curves in the increasing and decreasing ramps is known as the ‘thixotropic loop’. It is typically difficult to interpret the measured data quantitatively because the response is a complex convolution of the kinetics of shear induced structure breakdown and the kinetics of aggregation. Nevertheless, thixotropic loops often provide useful ‘fingerprints’ of complicated coating materials such as paints and other pigmented dispersions.

Not only shear, but also extensional rheological

tests can be performed in a transient mode. Indeed, because of the difficulties involved in realizing purely extensional steady-state flows in laboratory tests, transient extensional flows are very important in rheometric practice. For the sudden start-up of extensional flow, the transient stress is described by the elongational stress growth function $\bar{\eta}_e^+$, in the coating rheology literature often referred to as dynamic uniaxial extensional viscosity, or DUEV.

5.3.1.5 Other flow configurations used in rheometry

Although the material functions are strictly defined for the simple flows just described, it is often most convenient to measure material properties in alternate experimental configurations that approximate the ideal flow geometries. Table 5.1

Table 5.1 Experimental geometries for measuring fluid rheology

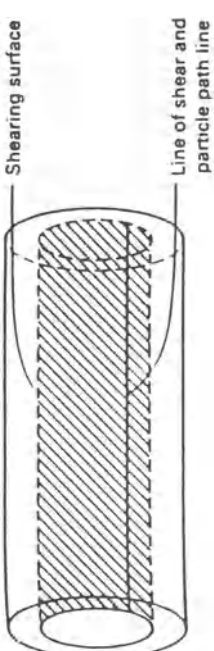
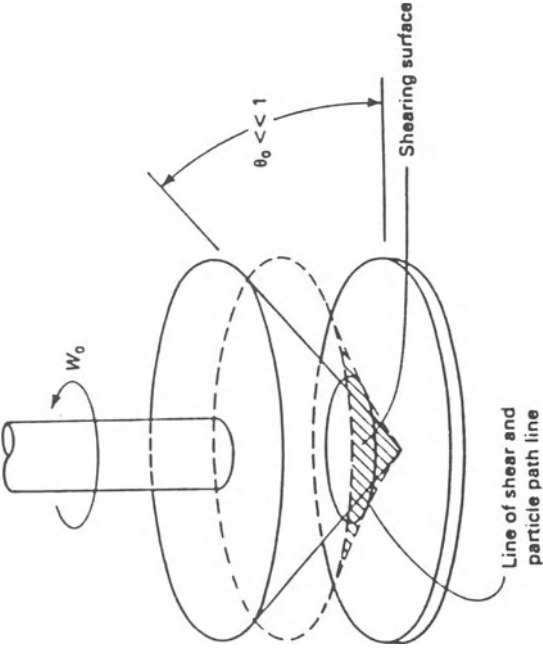
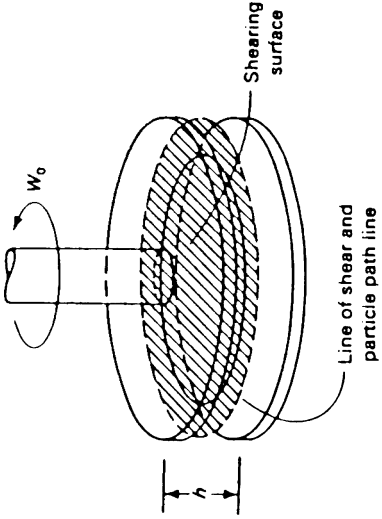
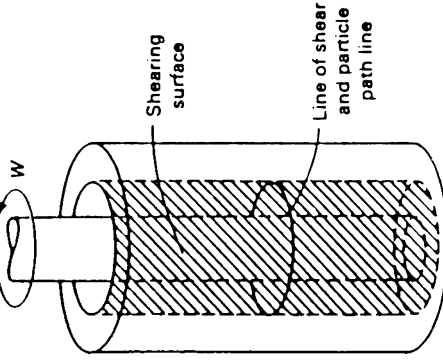
Experimental geometry	Measured quantities	Material function determination
Flow in a tube (capillary viscometer)	Q = volume rate of flow ΔP = pressure drop through tube R = tube radius L = tube length	$\eta(\dot{\gamma}_R) = \frac{\tau_R}{Q/\pi R^3} \left[3 + \frac{d \ln(Q/\pi R^3)}{d \ln \tau_R} \right]$ $\dot{\gamma}_R = \frac{1}{\tau_R^2} \frac{d(\tau_R^3 Q/\pi R^3)}{d \tau_R}$ $\tau_R = \frac{\Delta P R}{2L}$
	Shearing surface Line of shear and particle path line	R = radius of circular plate θ_0 = angle between cone and plate W_0 = angular velocity of cone T = torque on plate F = force required to keep tip of cone in contact with plate
		$\eta(\dot{\gamma}) = \frac{3T}{2\pi R^3 \dot{\gamma}}$ $\Psi_1(\dot{\gamma}) = \frac{2F}{\pi R^2 \dot{\gamma}^2}$ $\dot{\gamma} = \frac{W_0}{\theta_0}$

Table 5.1 Continued

Experimental geometry	Measured quantities	Material function determination
Torsional flow between parallel plates	$R = \text{radius of disks}$ $h = \text{separation of disks}$ $W_0 = \text{angular velocity of upper disk}$ $T = \text{torque required to rotate upper disk}$ $F = \text{force required to keep separation of disks constant}$	$\eta(\dot{\gamma}_R) = \frac{T/2\pi R^3}{\dot{\gamma}_R^2} \left[3 + \frac{d \ln(T/2\pi R^3)}{d \ln \dot{\gamma}_R} \right]$ $\Psi_1(\dot{\gamma}_R) - \Psi_2(\dot{\gamma}_R)$ $= \frac{F/\pi R^2}{\dot{\gamma}_R^2} \left[2 + \frac{d \ln(F/\pi R^2)}{d \ln \dot{\gamma}_R} \right]$ $\dot{\gamma}_R = \frac{W_0 R}{h}$
	 <p>Shearing surface Line of shear and particle path line</p>	$\eta(\dot{\gamma}) = \frac{T(R_2 - R_1)}{2\pi R_1^3 W}$ <p>$R_1, R_2 = \text{radii of inner and outer cylinders}$ $H = \text{height of cylinders}$ $W = \text{angular velocity of inner cylinder}$ $T = \text{torque on inner cylinder}$</p>  <p>Shearing surface Line of shear and particle path line</p>

gives several examples of configurations from which material functions can be determined for low viscosity fluids (see also Bird, Armstrong and Hassager (1987)).

In industry, unfortunately, many other ‘viscometers’ are in use that involve very complicated flow fields and hence cannot produce absolute viscosity data or other material functions needed for research and development purposes. In the US paint industry, the most notorious among such devices is the Stormer viscometer in which a shaft with two rectangular paddles is immersed in the paint and rotated at 200 rpm (for details, see ASTM Test Method D 562-81; and also Van Wazer (1963)). The force required to maintain this rate of rotation is measured with weights added to a platform that hangs from the end of a chord which, via a pulley and simple gear, drives the paddle. That force, in turn, is converted into so-called ‘Krebs Units’ (KUs) with an arbitrary conversion scale. Even though the value of this sort of measurement is quite dubious, the Stormer instrument is entrenched in the paint industry and very commonly used to test flow properties of paints. It is mentioned here because much of the literature cited below makes reference to data in Krebs Units (see Section 5.4).

5.3.2 EXAMPLES OF NON-NEWTONIAN MATERIAL BEHAVIOR

As rheology is frequently used as a probe of molecular structure and material interactions, it is helpful to have a general idea of what the material functions look like for commonly encountered fluids.

Low molecular weight fluids and resins generally are Newtonian, that is, they have a constant viscosity, independent of shear rate. They also generate no elastic normal stresses. The viscosity of polymer melts, filled polymers, polymer solutions and dispersions, on the other hand, is not constant but decreases with increasing shear rate, and the elastic normal stresses can be considerable. Dispersions of solid particles in nonpolymeric media may also exhibit shear-thinning viscosities (Wildemuth and Williams

1985), exactly like the polymeric counterparts; but they exhibit virtually no normal stresses.

For dispersions with either Newtonian or polymeric continuous phases, viscosity increases with increasing volume fraction up to a critical volume fraction above which the viscosity diverges to extremely large values and the material ceases to flow. This critical volume fraction is about 63% for noninteracting, monodisperse spheres, and increases to about 80% for a broad distribution of sphere sizes. It is markedly lower, however, for particles with long aspect ratios, such as chopped glass fibers. The limiting values for volume fraction are, of course, intimately linked to the closest packing densities inherent to the particles. Figure 5.5 illustrates the rise of the viscosity at high shear rates with increasing particle volume fraction for polymer latex particles of different sizes (Krieger 1972). The viscosity plotted is a relative viscosity made dimensionless with the viscosity η_0 of the suspending liquid. Figure 5.5 shows that, when the volume fraction of the particles is corrected to account for the increase in particle volume due to the adsorbed surfactant layer, the data points for the different particle sizes fall on the same master curve. This example makes plain that caution is in order when interpreting rheological data for chemically complex systems, a point reiterated in Section 5.4 below.

For particles that are strongly interacting, the critical volume fraction at which the viscosity rises sharply is also markedly lower than that expected from simple volume calculations. This is typically the case for particles smaller than 1000 nm for which surface forces can become dominant. The effect of particle surface interactions is illustrated for a polystyrene calcium carbonate system in Fig. 5.6. Decreasing particle size from 1700 to 70 nm at the same volume fraction of particles (30%) results in a ten-fold increase in viscosity (Suetsugu and White 1983). Additional information on filled melt rheology and particle orientation for non-spherical particles can be found in a review by Khan and Prud'homme (1987).

Polymer melts and other viscoelastic fluids

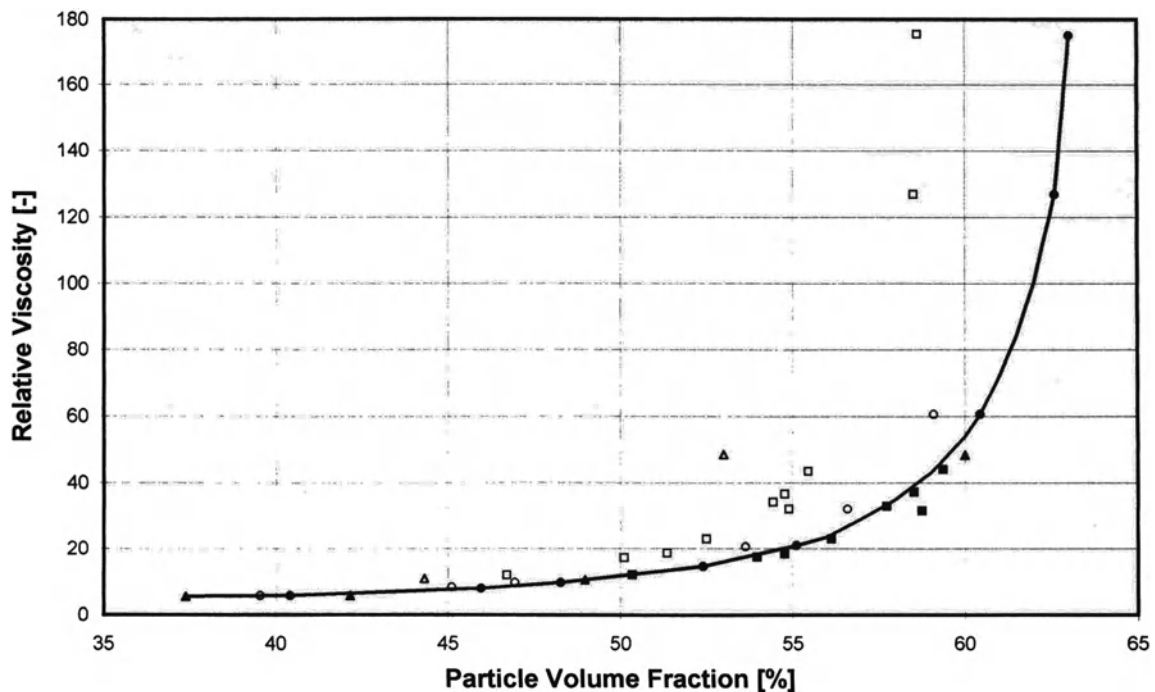


Figure 5.5 High-shear viscosity of latex dispersions versus nominal polymer volume fraction (open symbols) and effective particle volume fraction with adsorbed surfactant layer (closed symbols): ▲ 0.2 μm particle diameter; ■ 0.66 μm ; ● 1.1 μm (adopted from Krieger, 1972).

display elongational viscosities that strongly depend on strain rates. Figure 5.7 shows representative data of time-dependent or dynamic uniaxial extensional viscosity (DUEV) for fibers of two types of polystyrene melt at several constant elongation rates (Meissner 1985). The elongational viscosity increases with time initially, may reach a constant asymptotic value that is equal to three times the zero shear viscosity, and then may increase until the fiber breaks. The onset of the final rise in viscosity depends on the elongation rate, occurring earlier at higher rates. This so-called ‘strain hardening’ is a key mechanism in stabilizing the stretching of polymer fibers and is therefore very desirable in polymer melt spinning. On the other hand, it can be very detrimental to successful application of coating formulations, as discussed in Section 5.4.2 of this chapter. In dilute aqueous solutions, added fibers

with a large aspect ratio have also been observed to impart a dramatic increase in the dynamic uniaxial elongational viscosity, as illustrated in Fig. 5.8 (Weinberger and Goddard 1974).

Steady-state elongational viscosity measurements free of significant shear viscosity contributions are difficult to obtain, and hence are only qualitative in nature.

The relationship between the elongational viscosity of a liquid and its shear viscosity depends on the mechanisms by which the flow-induced microstructure transmits stresses. For Newtonian fluids, there are no extra flow-induced mechanisms, and the elongational viscosity is simply three times the shear viscosity. The rigid rods reported in Fig. 5.8, on the other hand, tend to align with the extensional flow and then transmit stress in the axial direction more efficiently than in the transverse direction, causing the

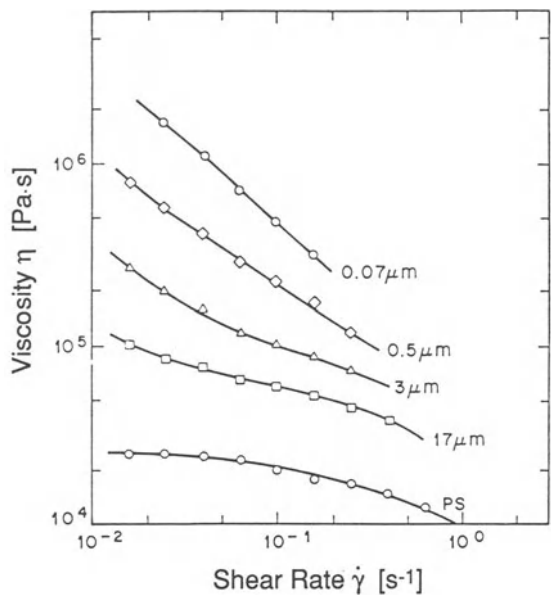


Figure 5.6 Viscosity versus shear rate for polystyrene melts with CaCO_3 fillers of various particle sizes labeled in the figure (after Suettsugu and White, 1983). The filler loading is constant at 30% by volume.

elongational viscosity to become much higher than the shear viscosity. For very high molecular weight linear polymer molecules in solution, or melts of the sort characterized in Fig. 5.7, the molecular chains undergo a conformational change at high elongational strain from random coils to highly stretched configurations. It is this change that results in the rise in elongational viscosity which, in turn, correlates with spatter and filament growth discussed for paint systems in Section 5.4.2. For colloidal or dispersed phase systems such as emulsions, the elongational viscosity is roughly equal to three times the shear viscosity over the entire shear rate range and, thus, shows thinning with increasing deformation rate just as the shear viscosity does (see, for example, Anklam, Warr and Prud'homme (1994)).

Dynamic oscillatory measurements are sensitive probes of molecular structure and interactions in melts and solutions. Figures 5.9 and 5.10 display the frequency dependence of the storage and loss moduli, G' and G'' respectively, for several types of polymeric materials (adapted from Ferry 1980). The materials are designated

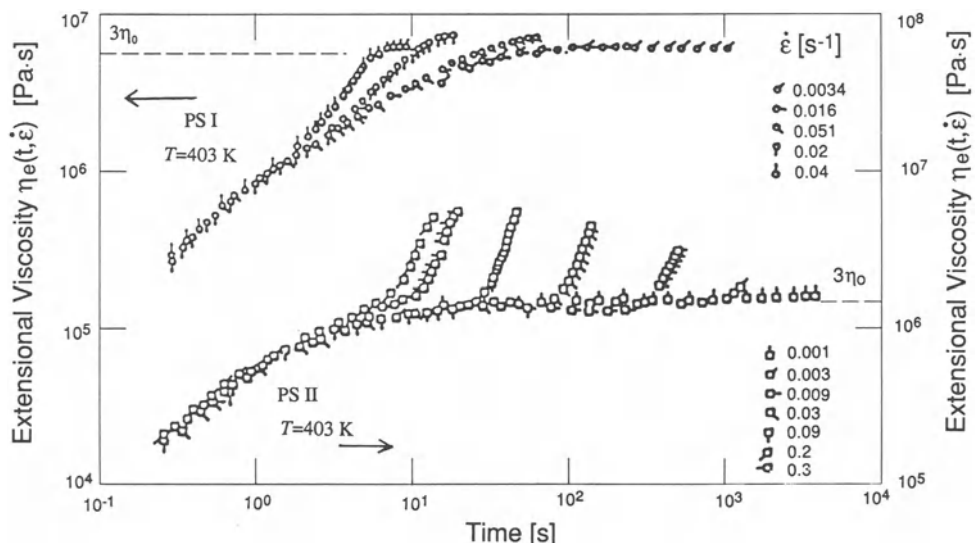


Figure 5.7 Elongational viscosity versus time for polystyrene melts at various constant elongation rates shown on the figure (after Meissner, 1985). The samples had a narrow molecular weight distribution, with average molecular weights of $M_w = 7.4 \times 10^4$ (PS I) and $M_w = 3.9 \times 10^4$ (PS II).

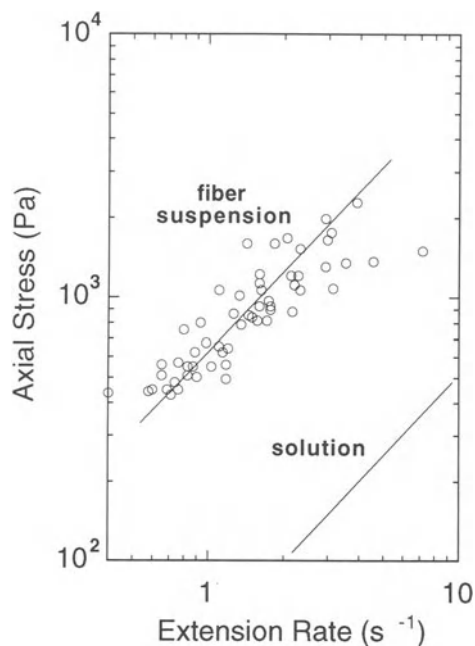


Figure 5.8 Axial stress versus extension rate for 200 µm long glass fibers with an aspect ratio of 1/57 suspended at 1.3 vol.% in 'Indopol' (Weinberger and Goddard, 1974). The lower solid line is the calculated axial stress for a pure 'Indopol' solution based on shear viscosity measurements.

in the figure by Roman numerals (complete details on the materials can be found in the original citation):

- Material I is representative of dilute polymer solutions. The data are for polystyrene with narrow molecular weight distribution around 860 000 M_w and dissolved in a chlorinated biphenyl at 25°C (the data are taken at several temperatures and then normalized to 25°C via time/temperature superposition as described by Ferry (1980)).
- Material II is prototypical for a low molecular weight, amorphous polymer. The data are for a 10 500 M_w poly(vinyl acetate) at 75°C.
- Material III is a typical high molecular weight, amorphous polymer. The data are for polystyrene at 100°C, with 600 000 M_w and a narrow molecular weight distribution.

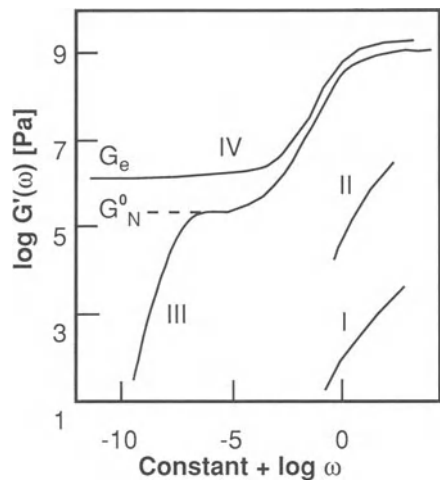


Figure 5.9 Storage modulus G' versus frequency ω for several classes of materials (after Ferry, 1980). The materials are identified in the text.

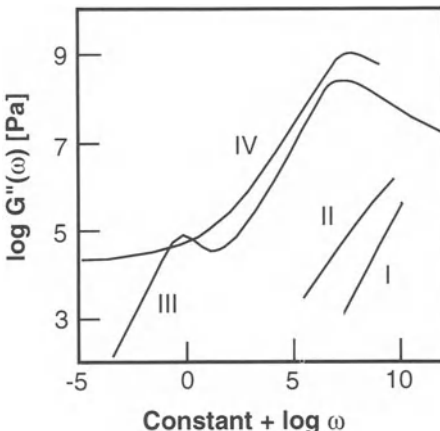


Figure 5.10 Loss modulus G'' versus frequency ω for several classes of materials (after Ferry, 1980). The materials are identified in the text.

- Material IV is a lightly cross-linked amorphous polymer. The data are for a lightly vulcanized Hevea rubber with an equilibrium modulus of E = 7.10⁵ Pa at 25°C.

For both the dilute polymer solution (material I) and the low molecular weight polymer (material II), the stresses decrease, or relax, with decreasing

frequency or increasing time. The elastic stresses, measured by G' , relax more quickly than the viscous stresses, indicated by G'' . In the limit of low frequencies, the loss modulus G'' plotted against frequency attains a constant slope of +1 on a log-log plot. In this region, $G''/\omega = \eta_0$, i.e., the zero-shear viscosity η_0 is given by the loss modulus divided by frequency (cf. equation (5.20)).

For the high molecular weight polymer (material III), the storage modulus exhibits a plateau toward high frequencies. The plateau is commonly referred to as the ‘glassy’ regime because the frequency imposed on the material is faster than the natural relaxation processes of the polymer chains and the material behaves like an amorphous, or glass-like, solid. Another plateau in the storage modulus, G_N^0 , appears at a lower frequency. It corresponds to a ‘pseudo network’ made up of temporary chain entanglements that do not have sufficient time to relax during the time of an oscillation at frequency ω . In this intermediate frequency range, the material behaves like a cross-linked rubber. Finally, toward lower frequencies, the moduli drop because the stresses can relax during the time scale of the imposed, slow oscillation. The zero shear viscosity is $\eta_0 = G''/\omega$ in this regime.

For the cross-linked rubber (material IV), the moduli approach the same glassy plateau at high frequencies as for polymers without cross-links. At these frequencies, the mechanical properties of the polymer are not affected by the constraints of the chemical cross-links because the spacing between cross-links is longer than the lengths of the polymer chain that can relax over the time-scale of an oscillation. In contrast to materials II and III, however, the ‘rubbery’ plateau for material IV at G_e extends over the entire low frequency range because the cross-links prevent elastic stresses from relaxing no matter how slow a deformation is applied. The loss modulus, G'' , decreases with decreasing frequency, and is two orders of magnitude below G' .

When a steady shear rate is imposed on a sample that is initially at rest (i.e., a step shear rate experiment), the stresses of polymeric materials rise with time and ultimately reach a steady shear

viscosity characteristic of that shear rate. At high shear rates, however, the viscosity can overshoot the equilibrium viscosity, as Fig. 5.11 illustrates for a 2 wt.% solution polyisobutylene in primol (Huppler *et al.* 1987). The maximum in the stress value occurs at increasingly shorter times as the shear rate increases. Indeed, experiments suggest that the maximum occurs at a constant value of strain (i.e., shear rate times the time that rate is applied). The demarcation between shear rates that are mild enough so as to allow monotonic behavior and shear rates that produce overshoot is given by the dimensionless Weissenberg number (see, for example, Bird, Armstrong and Hassager (1987)):

$$Wi = \lambda \cdot \dot{\gamma} \quad (5.24)$$

Here, λ is the characteristic relaxation time of the molecular structures within the liquid, and $\dot{\gamma}$ is the shear rate imparted externally on the liquid. For $Wi > 1$, the imposed deformation is faster than the material-internal relaxation, and non-linear effects such as stress overshoot are observed. Similarly, the onset of shear thinning in steady shear viscosity is governed by the Weissenberg number, i.e., shear thinning is observed for $Wi > 1$. The concept of characteristic relaxation times versus flow time scales is essential, and arises repeatedly in rheology.

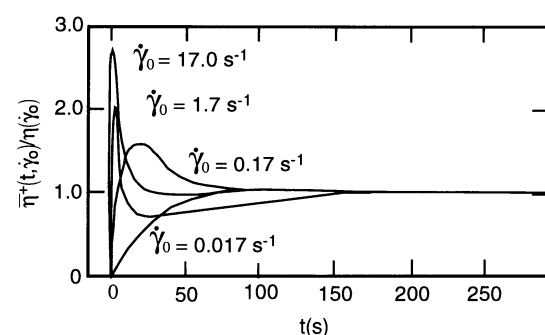


Figure 5.11 Shear stress growth function $\bar{\eta}^+(t; \dot{\gamma}_0)$, normalized by the equilibrium viscosity $\eta(\dot{\gamma}_0)$ at the given shear rate $\dot{\gamma}_0$, versus time t (after Huppler *et al.*, 1987). The data are for a 2.0% by weight polyisobutylene solution in primol.

5.3.3 CONSTITUTIVE MODELS OF RHEOLOGICAL BEHAVIOR

The simplest rheological equation of state is that of a Newtonian fluid for which only one material function – the viscosity η – is needed to characterize the liquid in any rheometric flow, and predict the flow behavior in any other laminar flow. This equation is

$$\tau = -\eta \dot{\gamma} \quad (5.25)$$

where $\dot{\gamma}$ is the rate-of-deformation tensor defined by

$$\dot{\gamma} = \nabla \mathbf{v} + (\nabla \mathbf{v})^T \quad (5.26)$$

where $\nabla \mathbf{v}$, in turn, is the velocity gradient tensor and the superscript T denotes its transpose (see also Chapter 2). The components of $\dot{\gamma}$ are

$$\dot{\gamma}_{ij} = \frac{\partial v_i}{\partial x_j} + \frac{\partial v_j}{\partial x_i} \quad (5.27)$$

where v_i are the Cartesian components of the velocity vector \mathbf{v} and x_i are the components of the position vector \mathbf{x} . For the shear flow given in Fig. 5.3a, for instance, the shear stress is

$$\tau_{xy} = -\eta \dot{\gamma}_{xy} = -\eta \frac{\partial v_x}{\partial y} \quad (5.28)$$

For non-Newtonian liquids, the Newtonian model (5.25) may be generalized by allowing the viscosity to become a function of shear rate. In such generalized Newtonian fluid models, the viscosity is made a function of the square root of the second invariant of the rate of deformation tensor because continuum mechanics arguments show that the viscosity can depend only on certain combinations of the rate of deformation tensor called invariants. Of the three independent combinations that can be formed, the second invariant is chosen because the first invariant is equal to zero for an incompressible fluid and the third invariant is equal to zero in a shear flow. The second invariant is defined by

$$II = \sum_i \sum_j \dot{\gamma}_{ij} \dot{\gamma}_{ji} \quad (5.29)$$

Instead of II directly, the viscosity is made a function of the square root of $1/2$ II, which is

the magnitude of the rate of deformation tensor and is given by:

$$\dot{\gamma}_{ij} = \sqrt{\frac{1}{2} \sum_i \sum_j \dot{\gamma}_{ij} \dot{\gamma}_{ji}} = \sqrt{\frac{1}{2} II} \quad (5.30)$$

For shear flow, the magnitude of the rate of deformation tensor is just equal to the velocity gradient or shear rate.

Generalized Newtonian fluid models work well for describing steady shear flows of polymeric fluids, but not transient or elongational flows. They are also inadequate for shear flows when elastic normal stresses are to be predicted (see, for instance, Chapter 10).

One of the most popular generalized Newtonian fluid models is the power-law model:

$$\eta = K \dot{\gamma}_{xy}^{(n-1)} = -\frac{\tau_{xy}}{\dot{\gamma}_{xy}} \quad (5.31)$$

which has two adjustable parameters, n and K . This model describes the viscosity versus shear rate curve on a log–log plot as a straight line. It is attractive because it is manageable in the direct mathematical solution of many simple flow problems. Also it adequately describes the high-shear-rate viscosity behavior of polymer solutions under realistic process conditions and requires only two parameters. The power-law model fails, however, to capture the constant, low-shear-rate viscosity observed at low flow rates (discussed in the preceding Section 5.2), or the limiting high-shear viscosity often seen at high processing speeds. Other models with more parameters must be chosen to account for these viscosity limits (see, for instance, Bird, Armstrong and Hassager (1987)). Very successful among these is the Carreau model

$$\frac{\eta - \eta_\infty}{\eta_0 - \eta_\infty} = [1 + (\lambda \dot{\gamma}_{xy})^2]^{\frac{n-1}{2}} \quad (5.32)$$

Here, η_0 and η_∞ are the low- and high-shear viscosities respectively, λ is a time constant that measures the characteristic shear rate at which the viscosity begins to drop off, and n is the power-law index as in (5.31).

Very concentrated filled melts, emulsions, foams, dispersions and gels display an additional non-Newtonian behavior toward low deformation rates, namely solid-like yield. A true yield stress implies the material will not flow until some minimum stress is achieved. In many liquid systems there may be very slow flow at low shear stresses; however, over the time scale of practical importance, the material can be treated as if it does not yield. This can be called an 'apparent' yield behavior. Models describing the shear stress versus the shear rate for materials with apparent yield stress have been reviewed by Prud'homme *et al.* (1983), and also Bird, Armstrong and Hassager (1987). Two popular and common models among these are the Bingham model,

$$\tau_{xy} = \tau_0 + \eta_p \dot{\gamma}_{xy} \quad \text{for } \tau_{xy} > \tau_0 \quad (5.33a)$$

$$\dot{\gamma}_{xy} = 0 \quad \text{for } \tau_{xy} \leq \tau_0 \quad (5.33b)$$

and the Casson Model,

$$\sqrt{\tau_{xy}} = \sqrt{\tau_0} + \sqrt{\eta_p} \sqrt{\dot{\gamma}_{xy}} \quad \text{for } \tau_{xy} > \tau_0 \quad (5.34a)$$

$$\dot{\gamma}_{xy} = 0 \quad \text{for } \tau_{xy} \leq \tau_0 \quad (5.34b)$$

In both, τ_0 is the apparent yield stress, and η_p is the plastic viscosity.

For liquids that exhibit viscoelastic behavior, polymer rheologists have constructed an impressive array of constitutive models. Most of these models have their origin in polymer melt processing where elastic effects often are quite large. To describe the flow of a viscoelastic fluid, constitutive models must account for both viscous and elastic behavior. The simplest model is the Maxwell model, which results from the superposition of the equations for a Newtonian fluid and a Hookean solid. For a shear flow, the Maxwell model can simply be written as:

$$\tau_{xy} + \frac{\eta}{G} \frac{d\tau_{xy}}{dt} = -\eta \dot{\gamma}_{xy} \quad (5.35)$$

Here, η is the viscosity as above and G is the elastic shear modulus. The ratio η/G is a time constant, often called the 'relaxation time', λ . Alternatively, equation (5.35) can be written in

integral form

$$\tau_{xy} = - \int_{-\infty}^t \left[\frac{\eta}{\lambda} e^{-\frac{(t-t')}{\lambda}} \right] \dot{\gamma}_{xy}(t') dt' \quad (5.36)$$

where the quantity in brackets is the relaxation modulus, $G(t)$, for the Maxwell fluid. The integral form of the Maxwell model can, furthermore, be written in terms of strain, γ_{xy} , rather than rate of strain, $\dot{\gamma}_{xy}$,

$$\tau_{xy} = \int_{-\infty}^t \left[\frac{\eta}{G} e^{-\frac{(t-t')}{\lambda}} \right] \gamma_{xy}(t') dt' \quad (5.37)$$

where the term in brackets is called the memory function, m , for the Maxwell fluid.

The Maxwell model, with its single time constant and single viscosity parameter (or modulus parameter) can qualitatively reproduce the creep behavior of 'ideal' viscoelastic fluids; however, it cannot qualitatively reproduce the linear viscoelastic behavior for real materials which, because of their composition, most often have a range of relaxation times and associated modulus parameters. To account for this, the Maxwell model can be generalized by replacing the relaxation modulus by a sum of contributions:

$$\tau_{xy} = \int_{-\infty}^t \sum_i \left[\frac{\eta^i}{G^i} e^{-\frac{(t-t')}{\lambda_i}} \right] \gamma_{xy}(t') dt' \quad (5.38)$$

Fig. 5.12 shows an example of the fitting of modulus data for a low density polyethylene melt with a generalized Maxwell model with ten time constants, λ_i , and ten modulus constants, G_i (Laun 1978). The agreement between the experimental data with the fitted moduli is excellent. However, even with the complexity that arises from multiple relaxation modes, the Maxwell model is still insufficient to predict shear thinning that is characteristic of most viscoelastic liquids, or stress overshoot as illustrated in Fig. 5.11 above. To account for these and many other aspects of viscoelastic flow behavior, more sophisticated constitutive models are needed (see Larson (1988), for an in-depth treatise).

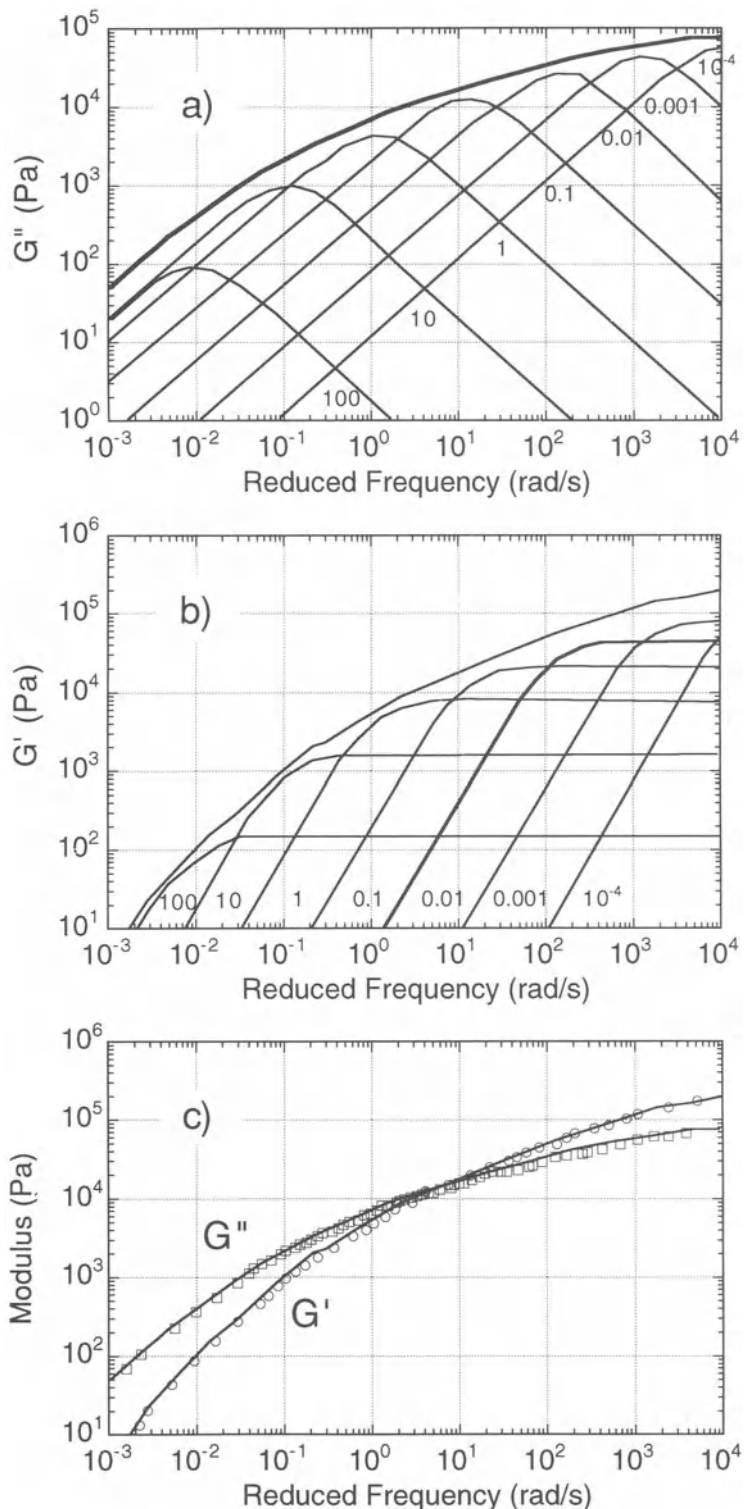


Figure 5.12 Fitting the modulus of a low-density polyethylene melt with a generalized Maxwell model with 10 time constants, λ_i , and 10 modulus constants, G_i (after Laun, 1978): (a) and (b) individual G' and G'' contributions from the terms comprising the Maxwell elements; (c) comparison of fitted model to experimental data.

5.4 INTERPLAY AMONG COMPONENTS, RHEOLOGY AND APPLICATION PERFORMANCE

5.4.1 ROLL COATING APPLICATIONS – A BRIEF OVERVIEW

For many if not most commercial paints and protective coatings, application by roll is the method of choice. For that reason, this section focuses primarily on roll applications. The principles involved in the application of coatings by brushes, blades, or spray share some similarities with those of roll application, but are not discussed in detail here.

For Newtonian liquids, the laminar flow in the nip region of a roll applicator generates pressure variations that are largely responsible for the amount of coating material that flows through the narrow nip passage, and also for the stability of the film split where the coated film separates from the material that remains on the roll. Numerous early investigators, interested primarily in printing ink applications, recognized the importance of the pressure variations in controlling coating thickness (e.g., Gaskell (1950), or Miller and Myers (1958)). They also identified various regimes of film-split instabilities, viewing the coating process from the interior of a coating roll. In particular, they noted that, when the product of velocity and viscosity exceeded a critical value, a regime of regularly spaced air cavities that are separated by ‘ribs’ is superseded by a regime in which the ribs break up into filaments (Miller and Myers 1958; Myers and Hoffman 1961). In total, four characteristic flow regions were identified early on in roll application processes: (1) a recirculating bead of liquid, often referred to as ‘bank’, at the inlet to the nip between the two rolls, with widely fluctuating shear rates, sometimes turbulent flow, and often ejection of material; (2) a nip region with laminar lubrication-type flow and varying shear rates; (3) a film-split region where ribs form due to an instability mechanism akin to ventilated cavitation in hydrodynamic lubrication and often grow into very thin, lamellar liquid sheets with low shear

rates and radial or extensional flows from cavity centers; and (4) a filamentation region where the lamellar liquid sheets progress into filaments extended in air between the two roll surfaces, with high localized shear at their roots and highly extensional flow normal to the roll applicator elsewhere. They dissipate into little droplets causing what is commonly referred to as ‘misting’.

Building on these early investigations, a wealth of experimental information has been amassed on roll coating processes, and numerous rigorous and comprehensive hydrodynamic analyses have been performed to explain the experimental findings (see Chapters 12a and 12c for a complete review). In fact, roll coating is one of the most thoroughly investigated and best understood coating application processes. Still, from the point of view of coating rheology, many unresolved issues remain. In particular, much of the academic and published work on roll coating has been confined to Newtonian fluids, yet small amounts of elasticity can drastically affect ribbing and filamentation. In addition, hydrodynamic stability analyses, as difficult and sophisticated as they may be, predict only the critical parameters at the onset of ribbing but, in their most commonly used, linearized form cannot describe the fate of ribs at flow conditions past the initial onset of the instability or their break-up into filaments and ensuing misting.

Even though ribbing can be interpreted as a form of cavitation, as suggested in the early literature cited above, its initial onset is triggered by a purely hydrodynamic instability of the two-dimensional, translationally symmetric film split meniscus between the substrate and the applicator roll to three-dimensional disturbances, as explained in detail in Chapter 12a. In fact, ribbing is very similar to the phenomenon of viscous fingering (Saffman and Taylor 1958), which occurs when a low-viscosity fluid, such as air, displaces a high-viscosity liquid from a confined flow channel between parallel walls (in roll coating, an observer sitting on the substrate or moving with the applicator roll sees air penetrate into the liquid coating bead in the nip region). Both the ribbing instability between

coating rolls and the viscous fingering instability between parallel plates are driven by the pressure gradients generated by viscous flow, and are stabilized by surface tension (see Chapter 12a). For Newtonian liquids, the onset of these instabilities is therefore governed by the capillary number, viz., $Ca = \eta U / \sigma$, where U is the application speed and σ is surface tension. The ribbing instability is further stabilized by the divergence of the flow channel between the applicator roll and the substrate (e.g., Ruschak (1985); Hakim *et al.* (1988)). Thus, the ratio H_0/R between the closest gap between the roll and substrate, H_0 , and the roll radius, R , becomes an additional parameter controlling the onset of ribbing. Mill and South (1967); see also Mill (1967), for instance, found

$$Ca = 10.3(H_0/R)^{0.75} \quad (5.39)$$

to provide a good fit for their own data for printing inks. Figures 12a.11 in Chapter 12a summarizes many other data for mostly Newtonian liquids. For non-Newtonian liquids, even small amounts of elasticity can drastically reduce the critical capillary number at the onset of ribbing. Bauman, Sullivan and Middleman (1982), for example, found that 10 ppm of a high-molecular-weight polyacrylamide added to a 90/10% mixture of glycerin/water reduced the critical capillary number by a factor of two to five while no normal stress was detectable. At 100 ppm, normal stresses could be measured and the reduction in capillary number was ten to thirty fold. For all practical purposes, roll applications for viscoelastic liquids – and even Newtonian liquids – operate well past the onset of ribbing.

As the capillary number is raised past the initial onset of ribbing, the ribs grow rapidly in amplitude to form lamellar liquid sheets, and their number per unit length increases. Mill and South (1967) noted that, when $\eta U / \sigma$ exceeds about 2.4, the rib frequency becomes independent of the capillary number and dependent solely on H_0/R . In contrast to the viscous fingering between parallel plates, where the unstable air pockets grow into irregular shapes and eventually combine

into one large ‘rib’, the three-dimensional flow state in roll coating is stabilized by the diverging geometry of the flow channel, allowing perfectly regularly spaced, large-amplitude ribs to exist over some parameter ranges (see Fig. 5.13). Eventually, these three-dimensional flow states become unstable themselves, giving way to transient, semi-chaotic flow states (e.g. Rabaud, Michelland and Couder (1990)). These phenomena are presumably strongly affected by elastic effects, but, unfortunately, no data exists in the published literature for well-characterized systems.

For elastic liquids, the ribs often also break up into fibers spanning the air space between the applicator roll and the substrate: see Fig. 5.13.

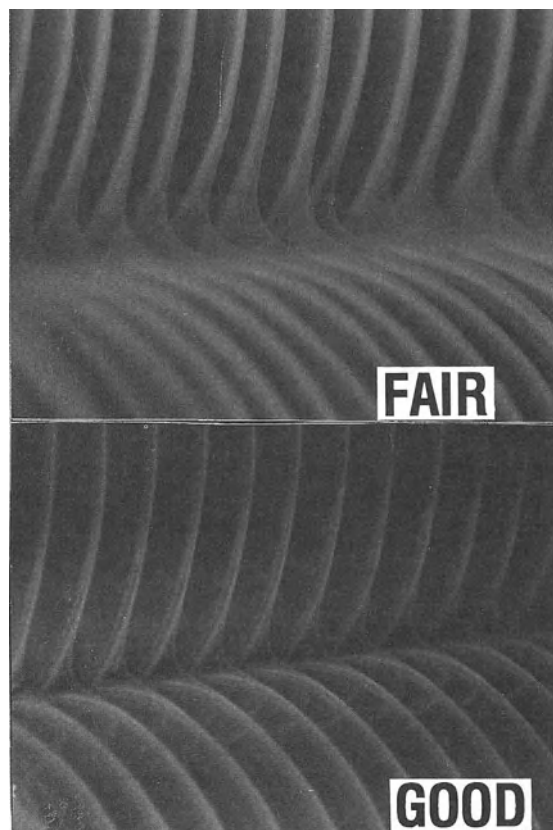


Figure 5.13 Comparison of ribbing in two industrial OEM coatings: (a) little misting; (b) significant misting (Soules, Fernando and Glass, 1988).

Raleigh instabilities, in turn, promote the break-up of the fibers into spatter droplets, often referred to as 'misting'. Elastic effects can delay the surface tension induced break-up and, in fact, aggravate misting problems. Soules, Fernando and Glass (1988), for example, investigated the performance of two commercial OEM acrylic dispersions in a Giordano roll coater of the sort described by Matsuda and Brendley (1979). Although their study was not adequate in detail and the coating compositions they used were proprietary, their data provide sufficient indication that the differences in ribbing and misting at high roll velocities are related to the dynamic uniaxial elongational viscosities, as might be expected. An

example of very poor roll coating performance with extreme filamentation is shown in Fig. 5.14 for an architectural latex paint that was purchased at a chain store (Glass 1978a). Massouda (1985) found calculated viscoelastic axial stresses to correlate well with spatter severity for eight commercial latex paints, and thereby provided additional evidence that elongational effects are key in controlling filamentation and misting.

All coating formulations (architectural, paper, and OEM) are applied at high deformation rates, which tend to break up aggregates, followed by 'flow-out' or leveling of surface imperfections at very low deformation rates. To simulate this in rheometric equipment, a steady high shear rate

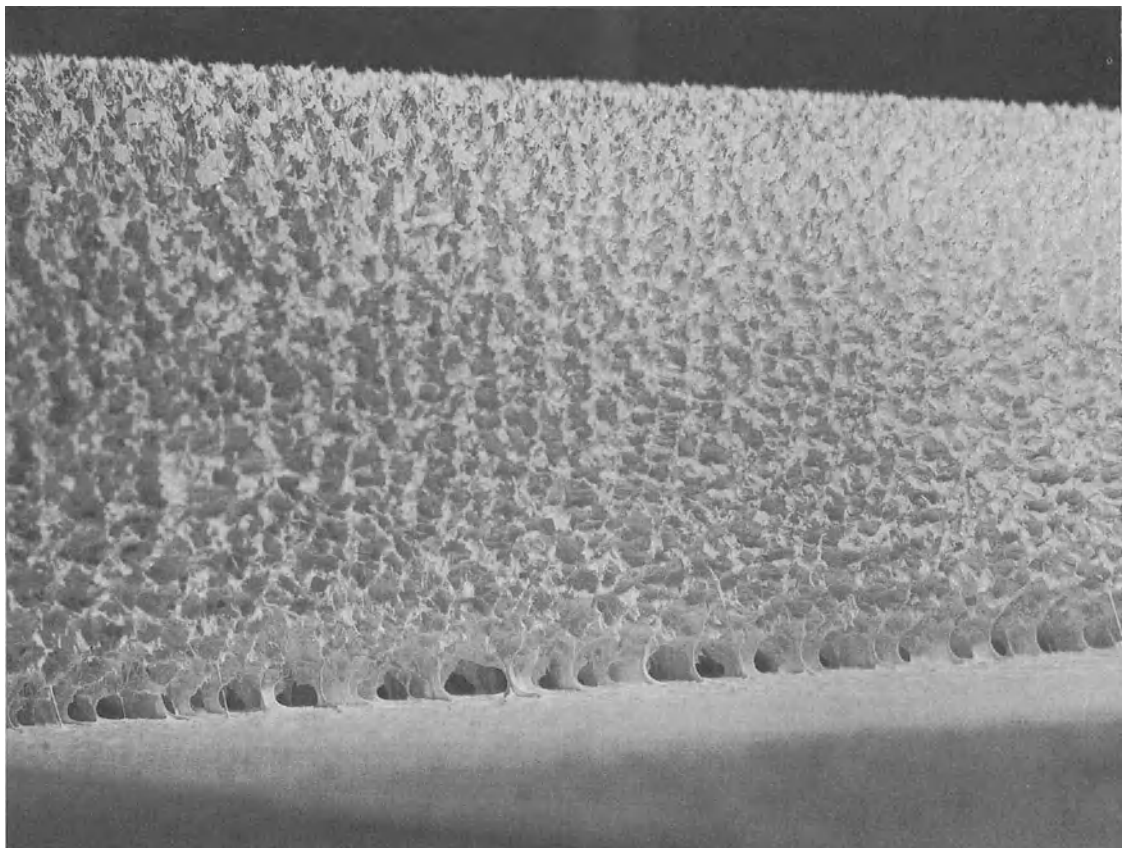


Figure 5.14 Example of ribbing, filamentation and fiber growth in mat-roll application of a commercial architectural coating at about 37 ft/s (Glass, 1978a).

is applied and then dropped rapidly to a low deformation rate, typically in an oscillatory mode, for instance in a cone-and-plate configuration. The cone angle in such experiments must be small to ensure a low deformation response during oscillation. This limits the shear rate that can be achieved under steady shear to about 3000 s^{-1} , which is much less than the shear rate in real applications. Nonetheless, valuable information can be extracted from such ‘simulated’ coating rheology measurements. Figure 5.15 gives an example. It shows the dynamic viscosity response of a formulation thickened with a maleic acid/methyl vinyl ether copolymer to a shear rate of 2750 s^{-1} imposed from an initial rest state (Glass 1975). The behavior is similar to that illustrated in Fig. 5.10 yet, to our knowledge, the data in Fig. 5.15 are the only data of this type reported for complicated non-Newtonian coating systems. The formulation chosen in Fig. 5.15 exhibited the greatest stress overshoot of all those studied by Glass (1975); curiously, however, the oscillatory response of this formulation did

not change with time. The stress overshoot of formulations that did vary with time in oscillatory studies were less than that of the formulation reported in Fig. 5.15. Clearly, stress overshoot of coating formulations in particular, and dynamic rheological studies attempting to simulate rapidly varying deformation histories in coating application steps in general, need to be investigated more systematically.

5.4.2 ARCHITECTURAL LATEX COATINGS

Among the coatings considered in this chapter, water-borne latex coatings for architectural applications have seen the greatest change in component compositions over the last three decades, and resulting improvements in coatings quality have been considerable. At first, the changes focused on the latex itself. The goal was to use small latex particles for better binding of pigments and fillers (Schaller 1968). The viscosities of small-particle latex dispersions, however, were high at low shear rates and prevented applied

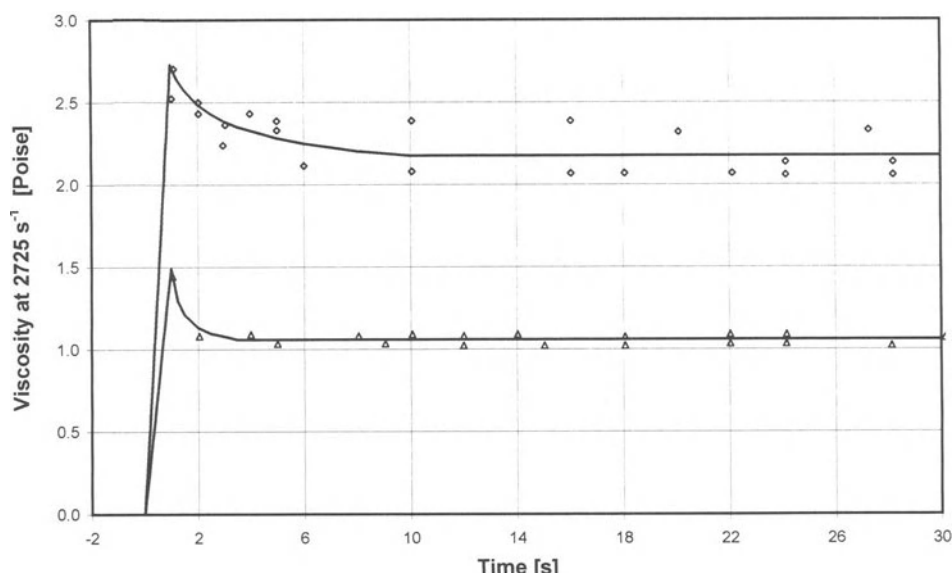


Figure 5.15 Transient viscosity response of interior coating formulations to a sudden shear rate of 2750 s^{-1} (after Glass, 1975). The formulations are thickened with a methyl vinyl ether/maleic acid copolymer to 81 Krebs Units (triangles) and 92 Krebs Units (diamonds) as measured with a Stormer instrument (*cf.* Section 5.3.1).

coatings from leveling out evenly. The high viscosities were attributed to inter-particle bridging via thickener molecules (Kreider 1964), but comprehensive attempts to quantify such mechanisms were not made. The size of a hydroxyethyl cellulose (HEC) thickener molecule of 410 000 molecular weight is about 120 nm and thus comparable to a 100 nm latex particle. However, the number of thickener molecules in a paint with 90 Krebs Units (see Section 5.3.1.5 for a discussion of this empirical viscosity measure) is too low to account for bridging of a significant number of latex particles. More recently, the industry moved toward bimodal particle size distributions, often achieved by intentional blending of latices with different particle sizes, which permitted formulation at higher volume percent solids (Chong, Christiansen and Baer 1971). The industry also moved to the synthesis of latices with larger particle sizes that provide multimodal distributions when the water-miscibility of the monomer is high as, for instance, for vinyl acetate.

The influence of individual components on the rheology and application performance of water-borne latex coatings is summarized in Table 5.2, and is discussed in more detail in the subsections that follow.

5.4.2.1 Influence of components on viscosities at high shear rates

Achieving high viscosities at high shear rates (viz., $\dot{\gamma} > 10^4 \text{ s}^{-1}$) is one of the goals in architectural

coating formulation. Higher viscosities provide a thicker film during application, which indirectly leads to improved leveling, or ‘flow-out’, as leveling is commonly referred to in paint-industry jargon. The effect of film thickness on leveling can be inferred from the modified Orchard equation (Smith, Orchard and Rhuid-Tutt 1961; Orchard 1962; see also Chapter 6 in this volume):

$$t_{1/2} \sim \log[\eta_0/(\sigma H^3)] \quad (5.33)$$

Here, $t_{1/2}$ is the half life for an amplitude decrease in surface irregularity, η_0 is the low-shear-rate viscosity of the fluid, σ is the surface tension, and H is the applied film thickness. In equation (5.33), only the variables that can be influenced by formulation components are listed. In architectural latex formulations, there is an excess of surfactant from the emulsion polymerization process (Section 5.2) and, therefore, surface tension is not a key variable in influencing coating ‘flow-out’ (it is, however, in high-solid solvent formulations applied without surfactants to high energy surfaces).

The median particle size and the particle size distribution of the disperse phases do not have much of a direct influence on high-shear-rate viscosity. However, increased viscosities at high shear rates can arise from nonionic water-soluble polymers that are grafted to the polymer chains during the emulsion polymerization process in order to stabilize larger latex particles (Craig 1986).

Adding water-soluble thickeners to a latex formulation also raises the viscosity at high shear

Table 5.2 Overview of effect of major formulation components on the rheology and application performance of water-borne latex coatings

Component	Viscosities at high shear rates $\dot{\gamma} \geq 10^4 \text{ s}^{-1}$		Viscosities at low shear rates $\dot{\gamma} < 10 \text{ s}^{-1}$		Spatter
	no	yes	yes	no	
Conventional thickener:					
Chemical structure	no		yes		yes
Molecular weight	yes		no		yes
Latex median particle size:					
Monodisperse	no		yes		no
Bimodal	no		yes		no
Protective colloid surface segments	yes		—		—

rates. However, even to someone familiar with the structure–rheology relationships in polymer solutions, the changes imparted by thickener additions to latex paints may seem difficult to understand. A major difficulty centers around the Stormer instrument, which is deeply entrenched in the paint industry yet, at best, reflects a viscosity at an intermediate shear rate of about 50 to 100 s^{-1} . With this ‘intermediate viscosity’ in Krebs Units fixed and dictated, the formulator has to live with whatever the components produce for viscosities at high or low shear rates. For example, Fig. 5.16 shows the effect on steady-shear viscosity at two shear rates (1800 and 14000 s^{-1}) of varying the total amount of hydroxyethyl cellulose thickener while holding different formulations at the same ‘intermediate viscosity’ (89 Krebs Units) by blending thickeners of different molecular weight (Glass 1975). Evidently, the use of lower molecular weight thickeners can provide higher viscosities at high shear rates than are observed with higher molecular weight thickeners but, in Fig. 5.16 the latter are, of course, used in smaller amounts to keep the Stormer ‘viscosity’

constant. Differences in chemical structure of the thickener can lead to different degrees of association at low shear rates, as is discussed below. At high shear rates, however, such associations are disrupted and, thus, thickeners affect high-shear viscosities not by their chemical structure, but primarily by their molecular weight which sets their hydrodynamic volume (Arney and Glass 1976).

5.4.2.2 Influence of components on viscosities at low shear rates

In the traditional coatings literature, the viscosity at low shear rates is discussed more frequently than the viscosity at high shear rates. This bias stems from paint applications on vertical surfaces where it is important that the applied coating does not sag under gravitational forces yet has a viscosity low enough to permit ‘flow-out’ of surface irregularities that arise during application. Equation (5.33) above highlights the importance of the viscosity at low shear rates, η_0 , for ‘flow-out’ or leveling of a coating.

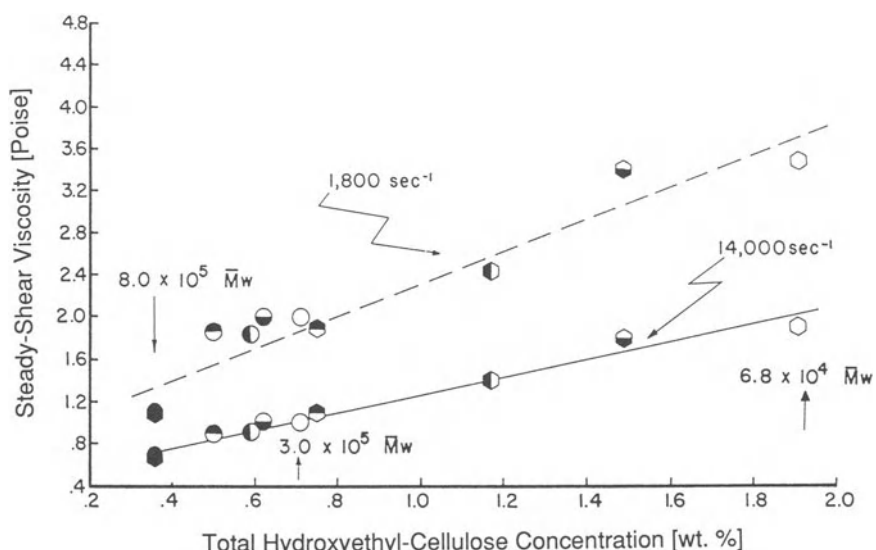


Figure 5.16 Steady-state viscosity of architectural latex coatings as a function of hydroxyethyl cellulose thickener content at a fixed intermediate ‘viscosity’ of 89 Krebs Units (Glass, 1975). The values of M_w marked by the arrows in the figure give the average molecular weight of the particular thickener used in blending with the highest molecular weight thickener.

In contrast to the viscosities at high shear rates, viscosities at low rates are affected by the latex size: they increase with decreasing median particle sizes below 150 nm. Figure 5.17 illustrates this effect for several model latices based on a variety of hard (i.e., high glass-transition temperature T_g) and soft (i.e., low T_g) methacrylate, acrylate and styrene compositions (Karunasena, Brown and Glass 1989). The synthesis of small latices requires an excess of surfactant. This excess plus oligometric surface acid salts stabilize the latex and, at the same time, prevent adsorption of cellulose-ether thickeners onto the latex. The surface stabilizers themselves, however, form hydration layers which can significantly increase the effective volume fraction of disperse phases (Krieger 1972, Nielsen 1977), and thereby drive the viscosity of smaller latices closer to the sharp rise seen in Fig. 5.5 (Karunasena and Glass 1992). The size effect is due to specific material interactions in real-world dispersions, and cannot be explained with the standard model approach for normalizing viscosities of different particle size latices (Krieger 1972).

Water-soluble thickeners, such as hydroxyethyl

cellulose (HEC), of course, also contribute to the viscosity at low and moderate shear rate. They do so through both their size and their amount. The volume fraction of the thickener must be added to the total volume fraction of solids, and thereby again moves the viscosity to higher values and closer to the sharp rise in Fig. 5.5. Table 5.3 summarizes the calculated relative volume fractions for a comparative set of coating formulations investigated by Lundberg *et al.* (1991). The size of the hydroxyethyl thickener was calculated from the root mean square end-to-end distance of the random polymer coil, R_c . Figure 5.18 shows how the corresponding, measured viscosities rise with increasing amounts of thickener added. Clearly, the rise is more sharp and the viscosities are higher for the small latex dispersions.

Figure 5.19 illustrates thickener effects on viscosity for another formulation study (Glass 1978c) in which an existing vinyl acetate/butyl acrylate latex dispersion was split into different batches, and hydroxyethyl cellulose (HEC) thickeners of different molecular weights as well as two other water-soluble polymers, namely

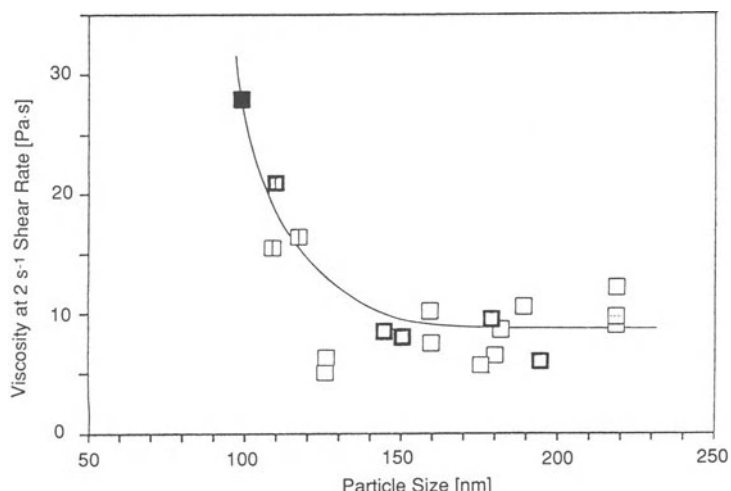
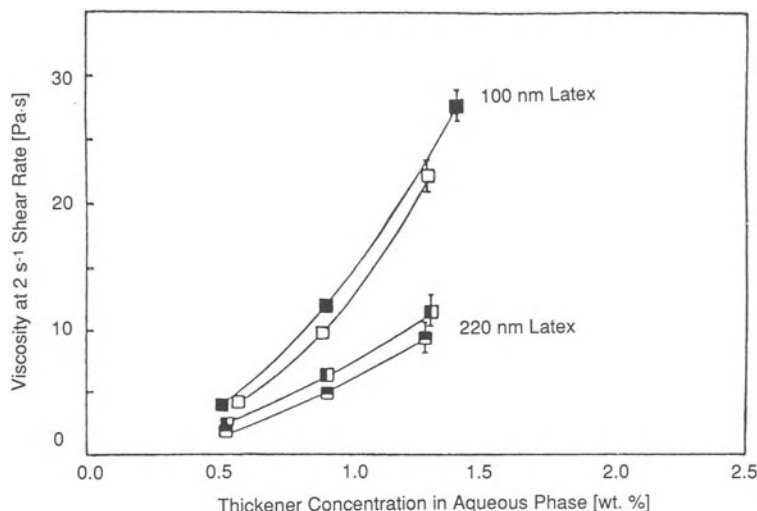


Figure 5.17 Effect of median particle size on viscosity at low shear rate (2 s^{-1}) for latex paint at total volume fraction of TiO_2 pigment and latex of 0.32, and a volume fraction of pigment as compared to latex particles of 0.21 (Karunasena, Brown and Glass, 1989; for complete descriptions of the formulations, refer to the original paper).

Table 5.3 Contributions of hydration layer and hydroxyethyl cellulose diameter to total effective volume fraction of latex dispersions at a nominal volume fraction of 0.32 (after Lundberg *et al.* (1991))

Latex size (nm)	Effective volume fraction with hydration layer	Wt.% HEC in aqueous phase	Estimated HEC volume fraction ($\sqrt{r^2} = 23$ nm)	Total effective volume fraction
100	0.42	0.50	0.15	0.57
		0.90	0.27	0.69
		1.41	0.42	0.84
220	0.36	0.51	0.15	0.51
		0.89	0.26	0.62
		1.33	0.39	0.75

**Figure 5.18** Effect of median particle size on viscosity at low shear rate (2 s^{-1}) as a function of hydroxyethyl cellulose concentration for model latex dispersions (Lundberg *et al.*, 1991).

poly(ethylene oxide) and an acrylic acid/acrylate ester copolymer, were added to each batch to achieve the same elevated viscosity as measured by a Stormer viscometer (127 Krebs Units). Table 5.4 lists the amounts of thickener added. Figure 5.19 shows that, toward low shear rates, the viscosity measured with a 'Rheometrics' cone/plate rheometer is higher for the dispersion containing a lower amount of higher molecular weight HEC, and that dispersion is more shear thinning than the dispersions containing higher amounts of the lower molecular weight hydroxyethyl cellulose

thickeners. On the other hand, when the highest and lowest molecular weight hydroxyethyl cellulose thickeners are employed in a realistic coating formulation of lower viscosity (about 90 Krebs Units), the latex dispersions not only have the same nominal 'formulation viscosity' (around 50 to 100 s^{-1} is the shear rate that may approximate the deformation rate in the Stormer viscometer), but the viscosities match remarkably well over the entire range of low shear rates, as shown in Fig. 5.20. Viscosity measurements in similar studies of a simplified formulation

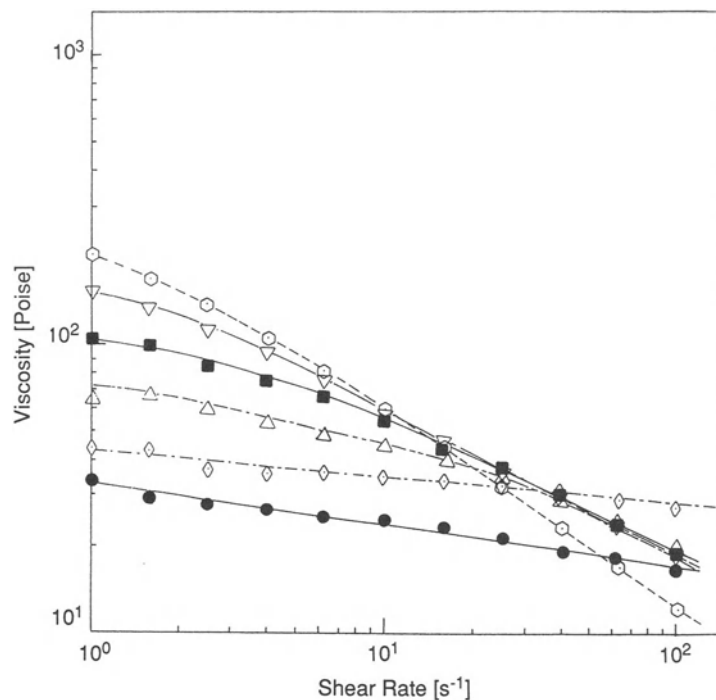


Figure 5.19 Steady-state viscosity as a function of shear rate for aqueous vinyl/acrylic latex dispersions (0.32 volume fraction) thickened to 127 Krebs Units with water-soluble polymers (Glass, 1978c). Filled squares: poly(ethylene oxide); closed circles: acrylic acid/ethyl acrylate copolymer; open circle: hydroxyethyl cellulose (HEC), $M_w = 800\,000$; open inverted triangles: HEC, $M_w = 650\,000$; open triangles: HEC, $M_w = 300\,000$; open diamonds: HEC, $M_w = 70\,000$.

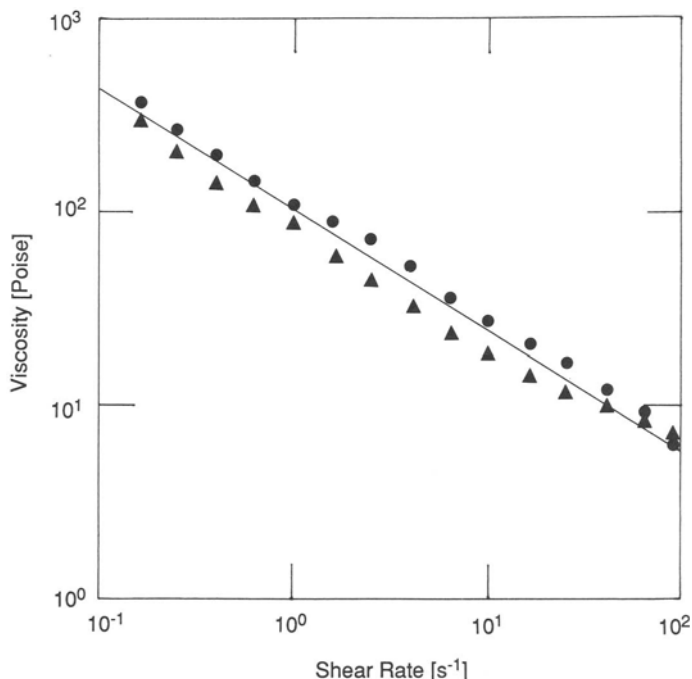
containing only thickener and TiO_2 pigment indicate that the pigment is flocculated (Lundberg and Glass 1992a). The formulations examined in Figs 5.19 and 5.20 contain many more ingredients such as calcium carbonate, silicas, etc. but the independence of the low-shear-rate viscosity on the molecular weight of the thickener is probably also related to aggregate structures.

The chemical structure of water-soluble polymer thickeners can also have a dramatic influence on viscosities at low shear rates. This effect is attributed to associations that arise from hydrogen bonding, which can lead to crystallinity or macromolecular superaggregation (e.g. Klenin *et al.* (1973)). Figure 5.21 documents a formulation study with *ca.* 700 nm vinyl acetate latex that was synthesized in the presence of hydroxyethyl

cellulose without surfactant (Glass 1975). As a result of this synthesis, the latex had a broad particle size distribution, and was stabilized with grafted hydroxyethyl cellulose fragments. The only surfactant present in the formulations came with the subsequent addition of TiO_2 pigment. Poly(vinyl alcohols) with different residual acetate contents were then used to thicken the formulations. Poly(vinyl alcohols) with 99% alcohol units are known to be difficult to solubilize in water at ambient temperatures, and solutions obtained at higher temperatures will readily precipitate under shear at lower temperatures. With increasing acetate content, up to 25 mol.%, the copolymers are easier to solubilize and remain soluble in aqueous solution under deformation. The acetate units serve to inhibit inter-

Table 5.4 Solution properties of aqueous vinyl acetate/acrylic latices with different thickeners (after Glass (1978c))

<i>Thickener</i>	<i>Type</i>	<i>M_w</i>	<i>Conc.</i> (wt.%)	<i>Latex</i> <i>conc.</i> (wt.%)	<i>Stormer</i> <i>viscosity of</i> <i>mixture</i> (KU)	<i>Power law</i> <i>coefficient n</i> <i>between 2.5 and</i> <i>25 s⁻¹</i>
Hydroxyethyl cellulose		80×10^4	1.9	2.6	127	0.30
Hydroxyethyl cellulose		65×10^4	2.0	2.6	128	0.54
Hydroxyethyl cellulose		30×10^4	5.5	2.6	128	0.75
Hydroxyethyl cellulose		7×10^4	14.0	2.6	126	0.97
Poly(ethylene oxide)		50×10^4	6.9	2.6	126	0.64
Acrylic acid/acrylate ester copolymer		unkwn.	23.3	2.9	127	0.93

**Figure 5.20** Steady-state viscosity as a function of shear rate for interior architectural coatings thickened to comparable intermediate viscosities with hydroxyethyl cellulose of high and low molecular weight (data from Glass, 1978b). Triangles: $M_w = 15 \times 10^5$, 94 Krebs Units; circles: $M_w = 3 \times 10^5$, 89 Krebs Units.

and intra-hydrogen bonding that facilitate super-molecular order in poly(vinyl alcohols) with high hydroxyl content (Klenin *et al.* 1973). Figure 5.21 shows the influence of the chemical structure of

the thickener on the response of the coating formulation after shearing as measured by the transient rise of the complex modulus, $|G^*|$ (see equations (5.17) and (5.18) and associated dis-

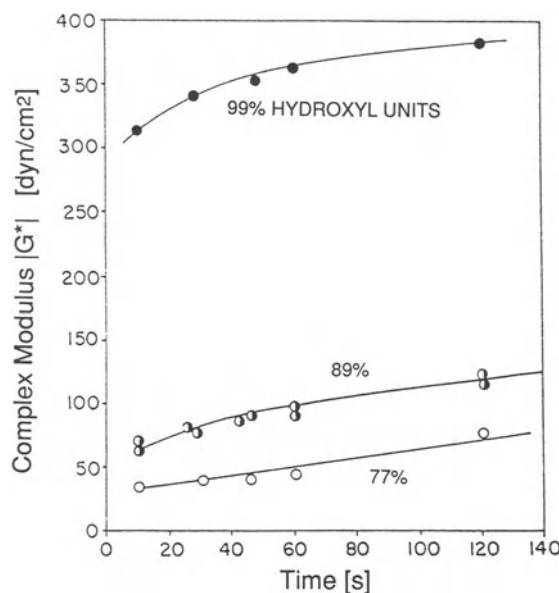


Figure 5.21 Time-dependent recovery of complex modulus $|G^*|$ (at 28 μm amplitude of the oscillatory measurement after steady-state shearing) of interior latex coatings thickened with alcohol/vinyl acetate copolymers with different degree of hydroxyl content (Glass, 1975).

cussion nearby). Clearly, with more hydrophobic groups, the $|G^*|$ values are lower and, as a result, much improved leveling of the coating was observed (see Glass 1975, for further details). A similar change in rheological response has been observed for cellulose ether in both aqueous solutions and complete coating formulations as the ratio of hydrophobic to hydrophilic groups (viz., methoxyl, oxyethylene and carboxyl) was varied (Glass 1976).

5.4.2.3 Influence of components on elastic response and leveling

As the example in Fig. 5.21 illustrates, oscillatory measurements of elastic rheological properties have proven to be sensitive probes of the structure of polymer solutions and gels in general, and of coatings in particular. For the latter, the ability to 'flow out', or self-level, strongly depends on

the structure formation right after the coating is applied. Indeed, in one of the earliest examinations of coating behavior with oscillatory rheometry (Glass 1975), the second dynamic viscosity coefficient, η'' , and the storage modulus, G' , were noted to be primary variables that increased after coating application. An earlier theoretical publication predicted that the poor leveling characteristics of coated films ought to be related to the elasticity of the coating formulation (Bierman 1968).

Another example illustrating the build-up of elastic rheological properties from structure formation is provided by the formulation study discussed already in reference to Fig. 5.16, which compared latex paints with the same Stormer 'viscosity' but with hydroxyethyl thickeners of different molecular weight (Glass 1975). The data in Fig. 5.22 show how the complex viscosity $|\eta^*|$, the dynamic viscosity η' , and the storage modulus G' increase with time after shear application for three formulations. Two were formulated with different molecular weights and concentrations of hydroxyethyl cellulose thickener to achieve the same intermediate formulation viscosity (90 Krebs Units as measured on a Stormer instrument). Despite substantial formulation differences, the elastic rheological responses of these two formulations are close, within experimental error – consistent with the findings from another study with hydroxyethyl cellulose reported in Fig. 5.20. The intermediate data set in Fig. 5.22 is for a formulation with a lower amount of high-molecular-weight hydroxyethyl cellulose, and its $G'(t)$ is markedly lower. Its viscosity in Krebs Units is also lower.

The elastic rheological response of coating formulations quite often proves to be very 'system specific', as is exemplified by a formulation study in which two different latices were thickened by three different types of thickeners (Glass 1978d). In Figs 5.23 and 5.24, the open symbols denote coating formulations with a 560 nm vinyl acetate latex, which is representative of a modern latex with moderate viscosity at low shear rates; and the closed symbols denote coatings containing a 117 nm acrylic latex, which is representative of

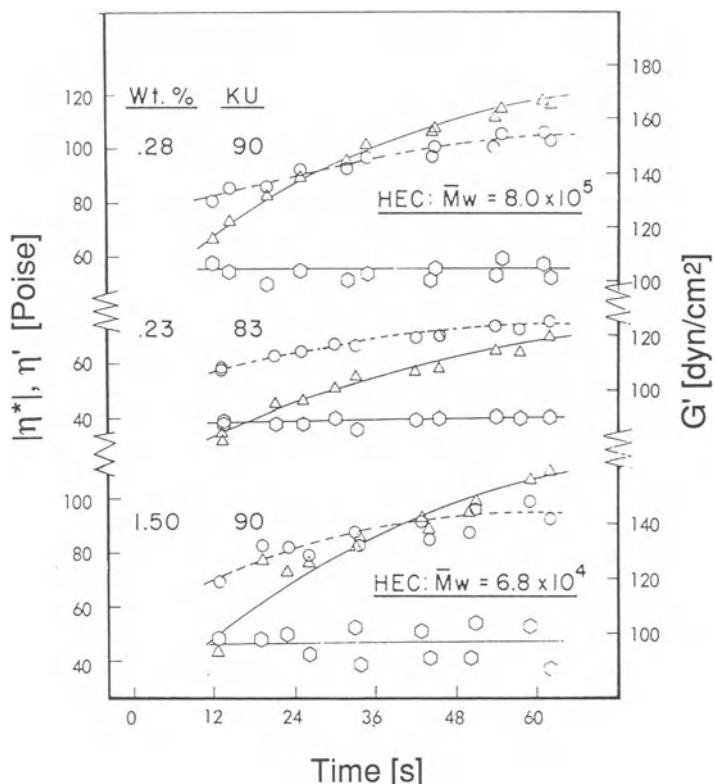


Figure 5.22 Time-dependent build-up of complex viscosity $|\eta^*|$ (circles), dynamic viscosity η' (hexagons) and storage modulus G' (triangles) of latex coatings thickened with hydroxyethyl cellulose. The molecular weight of the thickeners, the amount of thickener and the resulting viscosity in Krebs Units (KU) as measured by a Stormer instrument are given in the figure (Glass, 1975).

early, small particle latices which tended to exhibit high viscosities at low shear rates. The thickeners include a modified acrylic acid copolymer, hydroxyethyl cellulose (HEC) and an acrylic acid/ethyl acrylate copolymer (the effect on viscosity versus shear rate of the latter two thickeners in a latex dispersion is illustrated in Fig. 5.19 above). With the modified acrylic acid copolymer thickener, which is highly cross-linked, both latex formulations exhibit a high complex modulus, $|G^*|$ (Fig. 5.23), and the normal stress difference, N_1 , of the small acrylic latex also is high (Fig. 5.24). Neither $|G^*|$ or N_1 , however, exhibit a dependence on time or shear rate respectively. This suggests that the thickener

dominates the rheological response. For the HEC thickened paints, in contrast, $|G^*|$ and N_1 exhibit a time and shear rate dependence, with values of $|G^*|$ that are notably higher for the smaller 117 nm latex formulation than for the 560 nm latex. Considerably lower $|G^*|$ values are obtained for either latex with the low molecular weight acrylic acid/ethyl acrylate copolymer thickener, which is more hydrophylic than HEC. The $|G^*|$ values are particularly low for the 560 nm latex. These findings suggest that, in the HEC formulation, both the thickener and the latex contribute to rheology, whereas in the linear acid copolymer, the rheological reponse is dominated by the latex. Figure 5.25 shows that

the amount of leveling of the six formulations investigated in Figs 5.23 and 5.24 correlates quite closely with the measured $|G^*|$ values (Glass

1978d). The coatings were applied with a rake-like 'draw-down bar' and the profiles of the dried films were measured with a surface profilometer (Dodge 1972); the S -values on the charts denote sag ratings that are inversely related to the ability of a non-uniform coating to level out after application.

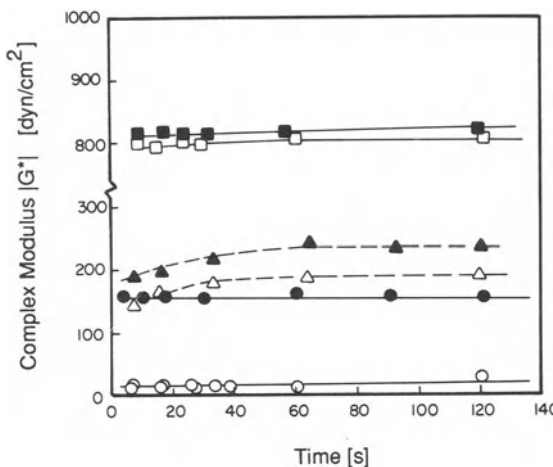


Figure 5.23 Time dependent recovery of complex modulus $|G^*|$ at $\pm 28 \mu\text{m}$ strain amplitude for large-particle latex with bimodal size distribution (open symbols) and latex with small monodisperse particles (closed symbols), both thickened to 90 Krebs Units with an acrylic acid/ethyl acrylate copolymer (circles), hydroxyethyl cellulose (triangles), or a modified acrylic acid copolymer (squares) (Glass, 1978d).

5.4.2.4 Influence of components on elongational viscosity and roll spatter

Contrary to what might be expected, dynamic measurements of shear elastic formulation properties are not good indicators of the susceptibility of coating formulations to misting or spattering in roll applications. The tendency for spattering appears to be more closely correlated with measurements of dynamic uniaxial extensional viscosity.

Figure 5.26 illustrates the dynamics of the film split in roll applications for the 117 nm all-acrylic latex coating formulations discussed in connection with Figs 5.23 and 5.24 above (Glass 1978c). The formulation with the acrylic acid/ethyl acrylate copolymer thickener (Fig. 5.26b) exhibits significant fiber elongation and resultant spatter, even though its $|G^*$ and N_1 responses are rather low.

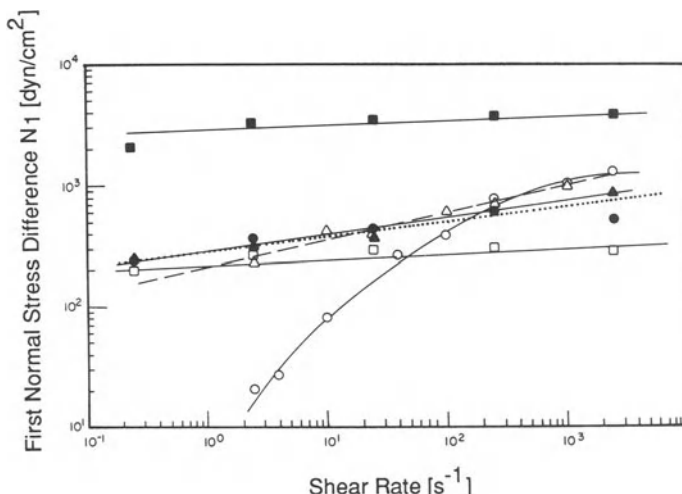


Figure 5.24 Shear-rate dependence of first normal stress difference for the same latex paints as in Fig. 5.23 (Glass, 1978d).

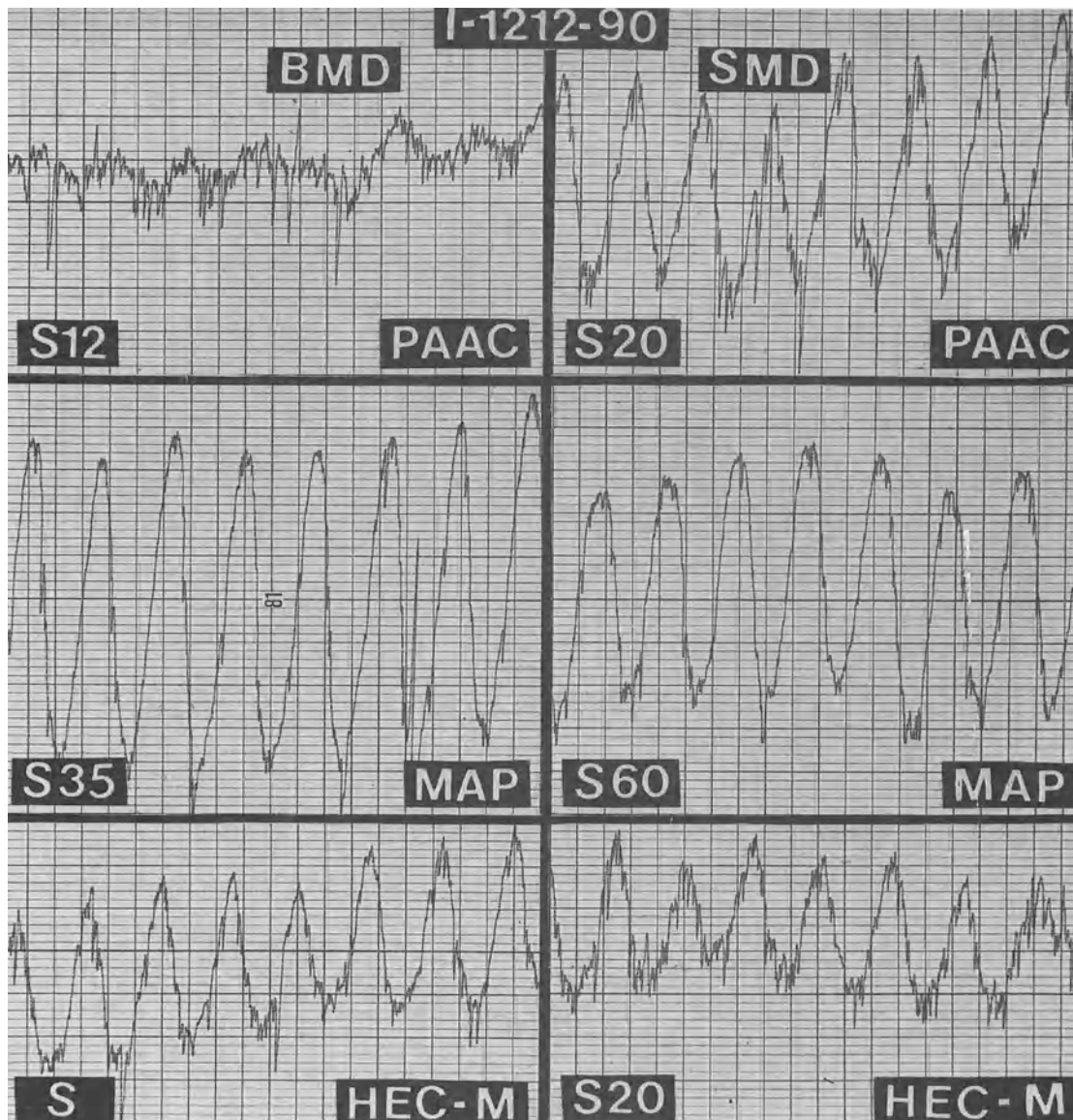


Figure 5.25 Profiles of dried films after leveling of the latex paints characterized in Figs 5.23 and 5.24 (Glass, 1978d). Left column ('BMD'): large-particle latex with bimodal size distribution; right column ('SMD'): latex with small monodisperse particles; first row ('PAAC'): acrylic acid/ethyl acrylate copolymer thickener; second row ('MAP'): modified acrylic acid copolymer; third row ('HEC-M'): hydroxyethyl cellulose (the label 1-1212-90 refers to a particular paint formulation standard).

On the other hand, its dynamic uniaxial elongational viscosity as measured by the spinning-fiber technique is very high, as Fig. 5.27 shows. The

low $|G^*|$ and N_1 values are consistent, however, with the good 'flow-out' of surface striations after applications seen for that formulation (*cf.* Fig. 5.25

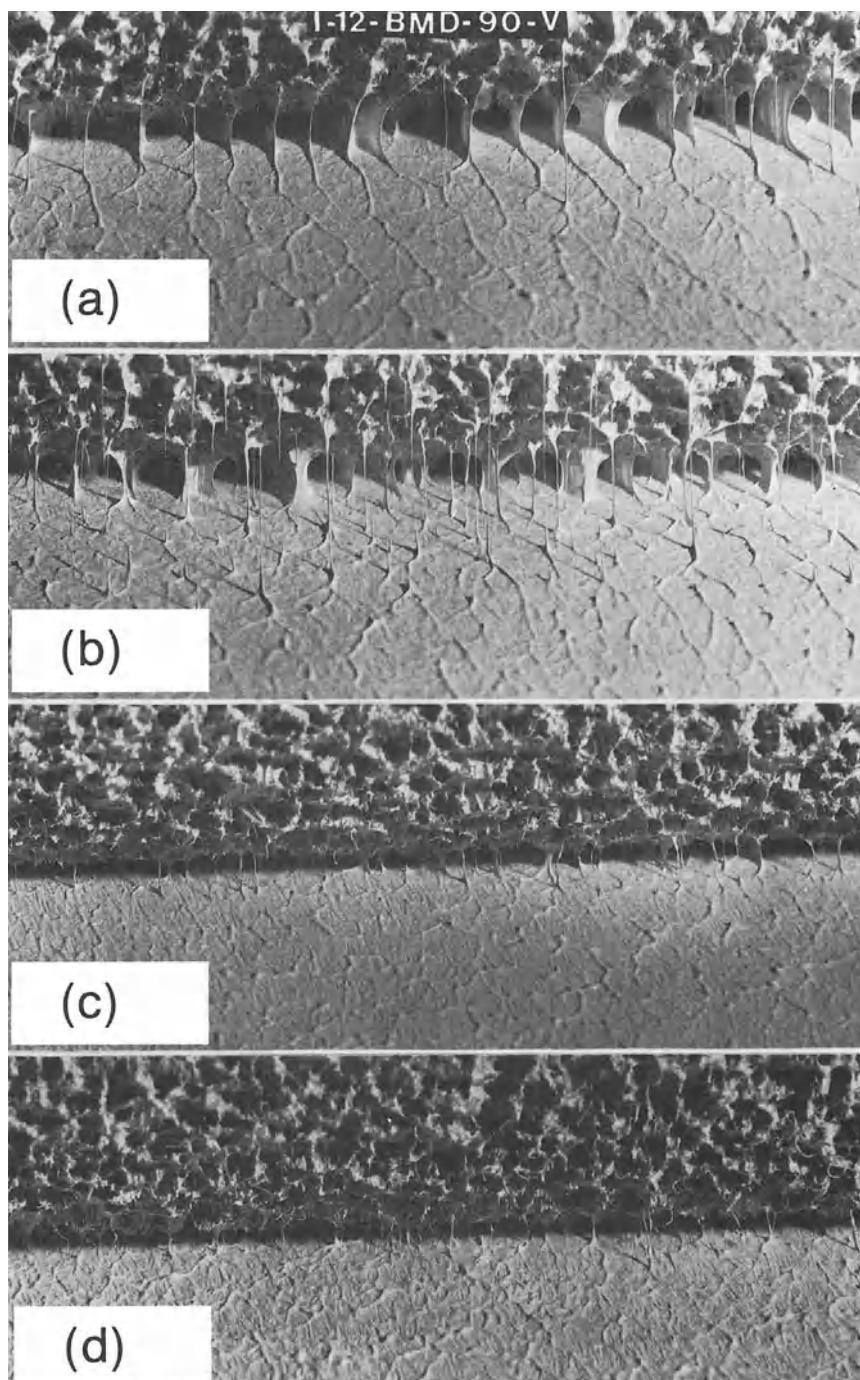


Figure 5.26 Instantaneous film-split patterns of interior paints formulated at 90 Krebs Units, and thickened with hydroxyethyl cellulose of high (a) and low molecular weight (c), acrylic acid/ethyl acrylate copolymer (b), and modified acrylic acid copolymer (d) thickeners (Glass, 1978c).

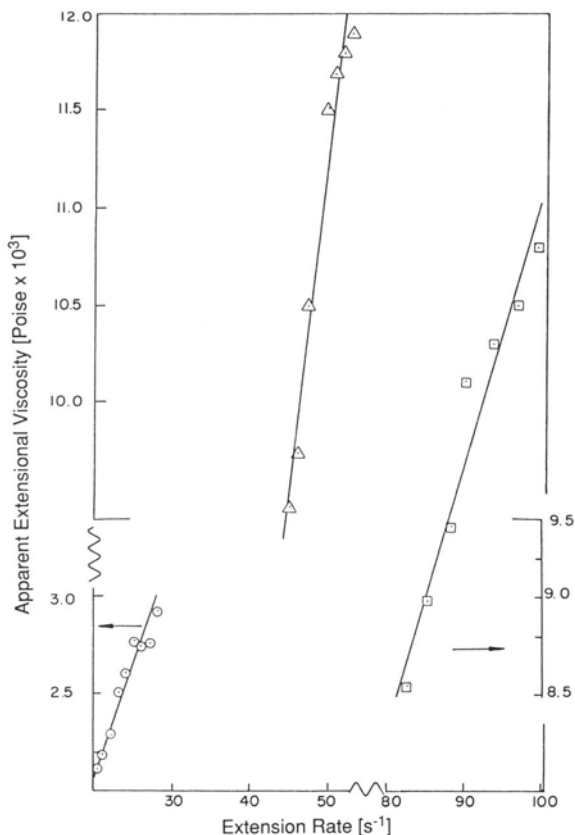


Figure 5.27 Apparent uniaxial elongational viscosity as a function of extension rate for vinyl/acrylic latex paints at 120 Krebs Units containing different thickeners: \circ acrylic acid/ethyl acrylate copolymer of unknown molecular weight; \triangle acrylamide/acrylic acid copolymer, $M_w = 6 \times 10^6$; \square poly(ethylene oxide), $M_w = 4 \times 10^6$ (Glass, 1978c).

above). The formulation with the modified acrylic acid copolymer follows exactly opposite trends: it did not support fiber growth at all and its elongational viscosity was too low to even be quantified (Glass 1978c, d); and, as expected from the high $|G^*|$ and N_1 values noted in Figs 5.23 and 5.24, the coating showed little evidence of ‘flow-out’ of surface striations (Fig. 5.25). The dynamic uniaxial elongational viscosities of hydroxyethyl cellulose (HEC) solutions are

proportional to the molecular weight of the thickener (Soules, Fernando and Glass 1988). Consistent with this finding, the low-molecular-weight HEC system exhibited substantially less filamentation and spatter than the high-molecular-weight system (compare Fig. 5.26c with 5.26a).

The relationship between decreasing molecular weight of the thickener and decreasing dynamic uniaxial elongational viscosity of a latex paint appears to be universal for a wide range of formulations. Figure 5.28 illustrates elongational

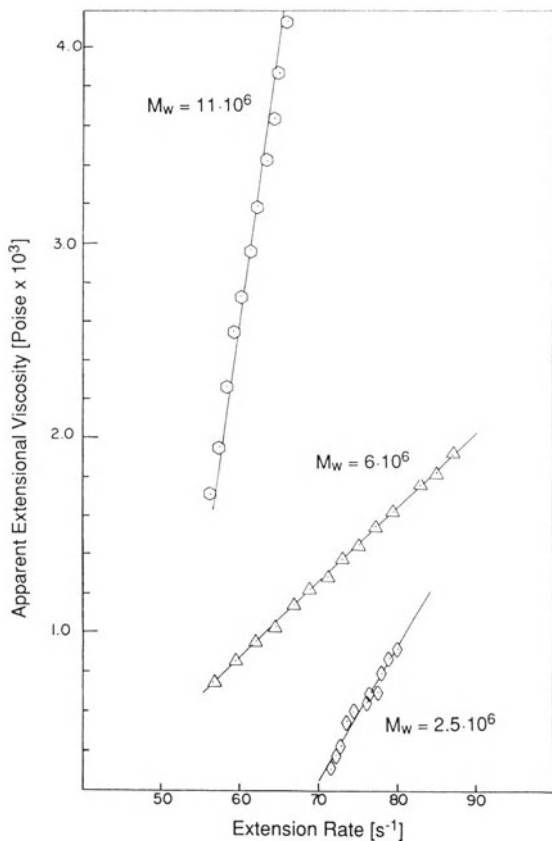


Figure 5.28 Apparent uniaxial elongational viscosity as a function of extension rate for vinyl/acrylic latex paints at 120 Krebs Units with acrylamide/acrylic acid copolymer thickeners of different molecular weights (after Glass, 1978c).

viscosities for another case study with acrylamide/acrylic acid copolymers (Glass 1978c). In this case also, high molecular weights led to stable fiber growth (Glass 1978c). The dependence of filamentation and spatter on molecular weight is even more dramatic for poly(ethylene oxide) thickeners, as Fig. 5.29 shows. The sequence of high-speed photographs in Fig. 5.30 reveals that, for the high-molecular-weight poly(ethylene oxide) system, large spatter drops result from the breakage at two points and subsequent 'snap-back' of a filament.

5.4.2.5 Recent trends in surfactant modified, water-soluble polymers

Cellulose ethers have dominated the water-borne thickener market for architectural coatings from their first commercialization in the 1960s until the early 1980s. During the last decade, however, surfactant modification of water-soluble polymers has produced a new generation of thickeners (Glass 1984). Hydrophobic modification of alkali swellable emulsions and hydroxyethyl cellulose have produced thickeners that have gained acceptance due, in part, to the lower spatter and misting they provide for certain market segments. The most dominant of these new thickeners has become the hydrophobically-modified, ethoxylated urethane (HEUR) family which, to date, has proven to be the only class of thickeners whose viscosity is enhanced by nonionic surfactants at low polymer concentrations (Lundberg, Glass and Eley 1989). These water-soluble polymers follow general surfactant behavior. With increasing size of the hydrophobic group, the thickening efficiency of the polymer increases (Brown and Glass 1989), and the solutions exhibit an increasing storage modulus, G' .

In the HEUR family, where structural features can be controlled, the optimum spacing between terminal hydrophobic groups is approximately 500 oxyethylene units (Kaczmarek and Glass 1993). The size of the alkyl units of the diisocyanate is an important complement to the terminal hydrophobe in promoting an 'effective terminal hydrophobe size' for viscosity enhancement, but in internal placements (i.e., as coupling units for 6000 molecular weight oxyethylene chains) these units do not contribute to solution viscosities (Kaczmarek and Glass 1992). Broadening of molecular weight distributions, as observed in classical step-growth polymerizations, diminishes the viscosifying properties of HEUR thickeners (May, Kaczmarek and Glass 1993). In coating formulations, the associative thicker may also interact with the latex and pigment but competes in this interaction with a variety of surfactants present.

If the surface of TiO_2 is pretreated with an

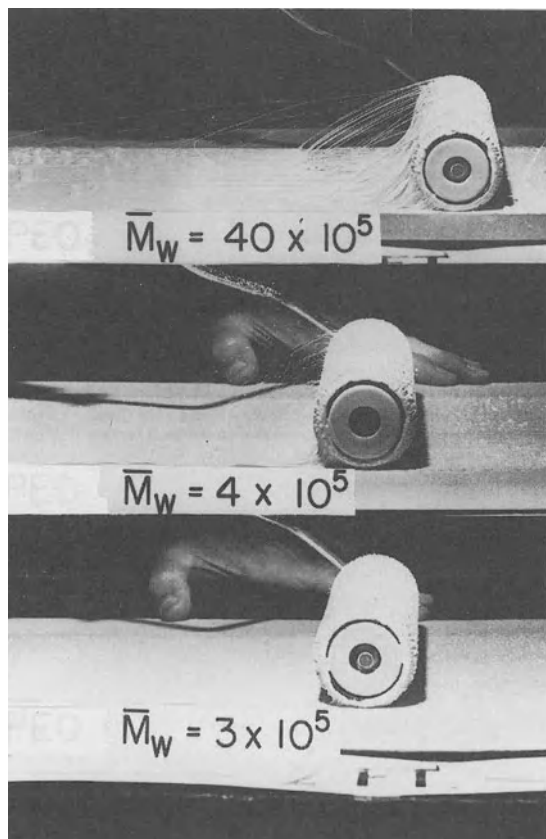


Figure 5.29 Effect of molecular weight of poly(ethylene oxide) thickeners on filamentation in roller application at 2 ft/s of a latex paint at 120 Krebs Units (Glass, 1978c).

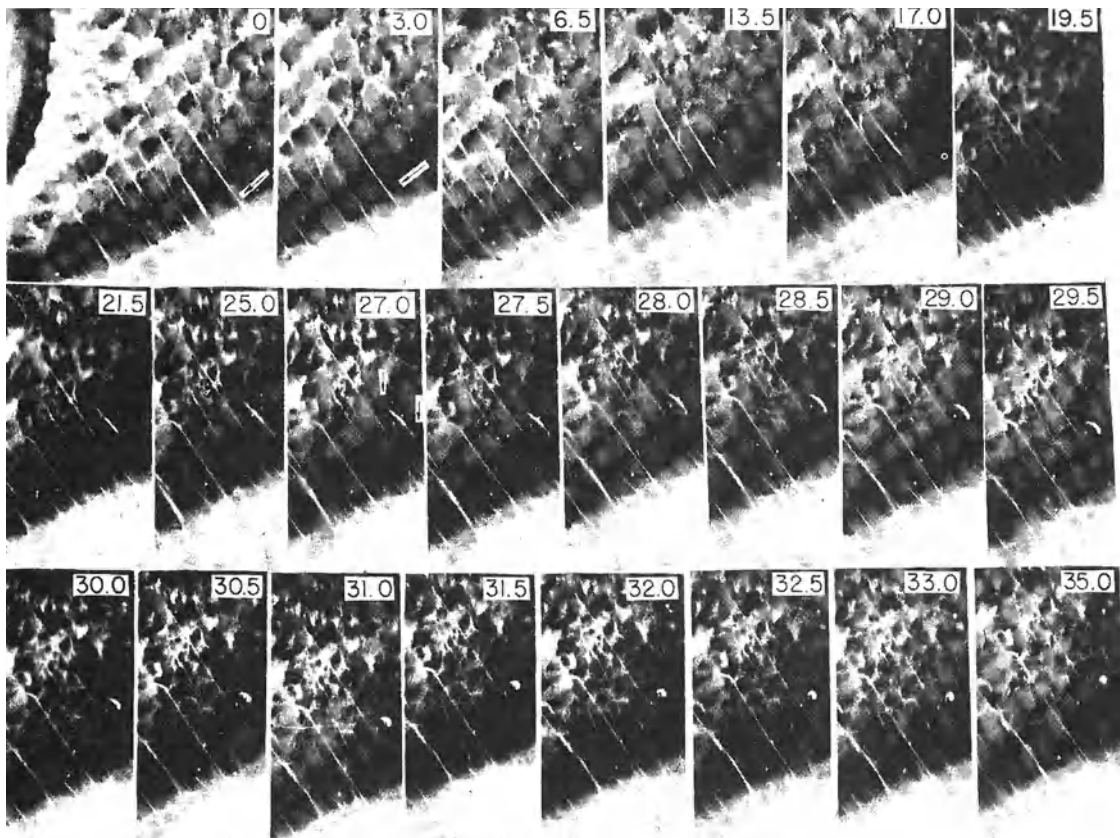


Figure 5.30 High-speed flow visualization at 2000 frames/s of film split in roller application at 37 ft/s of latex paint thickened with poly(ethylene oxide) at $M_w = 40 \times 10^5$ (Glass, 1978c). The time intervals given in the figure are in milliseconds.

oligometric polyacid that contains hydrophobic entities and acts as a dispersant, HEUR thickeners will ‘adsorb’ on the pigment through hydrophobic interactions with the dispersant (Lundberg and Glass 1992b), even in the presence of other surfactants in the formulation (Kaczmarek, Glass and Buchacek 1993). The impact of this interaction on the viscosity of the coating formulation is minimal, but the interaction stabilizes the pigment and tends to promote higher gloss in the applied film. The interaction of associative thickeners with latices could provide a higher dispersion viscosity via an increased effective volume fraction of particles in the system. However, this contri-

bution is difficult to quantify because of the many equilibria with the different types of surfactants that are present in coating formulations and because of the variability in surface stabilizers and the median size of the latex. For that reason, a comprehensive study of such interactions has not been reported to date. Associative thickeners in the HEUR family have been shown to contribute to the viscosity at high shear rates in much the same manner as observed with hydroxyethyl cellulose thickeners: the more thickener added the higher the viscosity. For HEUR thickeners, this effect arises from a reduction in the number, spacing (Kaczmarek and Glass 1993) and size

of terminal hydrophobes (Howard *et al.* 1991; Brown and Glass 1989). The high-shear viscosity obtained by blending different HEUR thickeners is not linear with concentration, but blends of high-molecular-weight hydrophobe-modified hydroxyethyl cellulose and an HEUR thickener provide linear relationships (Anwari and Schwab 1989).

5.4.3 PAPER COATINGS

Even though the latex content in paper coatings is typically quite small (*cf.* Section 5.2.1), the latex appears to have a significant influence on the formulation's 'runnability' (Barber and Bartel 1976), a loosely defined term that reflects a shear-thickening behavior under deformation, sometimes also referred to as dilatancy. The dilatant behavior of monodisperse, well characterized latices without steric stabilizers has been described by Hoffman (1972, 1974). In paper coatings, the latex is stabilized by oligomeric methacrylic surface segments, and both types of latices used in paper coatings, styrene/butadiene copolymers and vinyl acetates, have been described as superior in runnability. However, neither latex has been studied by state-of-the-art rheometers with acceptable geometries, alone or conjunction with the clays used in paper coatings to probe for specific latex–clay interactions.

The clay is usually the primary component in paper coatings and finely dispersed clays such as kaolinite, montmorillonite or attapulgite are notably shear thinning and often also give rise to substantial elastic responses (Lundberg *et al.* 1990). This is illustrated in Fig. 5.31 by the low-frequency oscillatory response of a latex coating containing attapulgite (Glass 1975). Prior to and within 30 s of the oscillatory test, the formulation was subjected to an intermediate shear rate to break up loose aggregates and reach an equilibrium viscosity. The deformation was then dropped into a low-amplitude oscillatory mode. The immediate, substantial low frequency response of the storage modulus reveals the dominance of elasticity in formulations with high clay content.

In practical paper coating applications, a primary problem arises from the need to increase the solids content of the formulation in order to cope with dryer capacity limitations when production rates are raised. An increase in solids content increases the viscosity which, in turn, can give rise to considerable difficulties in the blade application step, such as 'weeping', spraying or blade 'whispering' (see Chapter 12d for an in-depth discussion).

Low-molecular-weight water-soluble polymers, such as starch or carboxymethyl cellulose, are usually added to paper coating formulations. They decrease the rate of drying immediately after application while at the same time raising the viscosity, which retards penetration of the coating into the porous cellulose fiber substrate. The addition of low-molecular weight thickener polymers contributes minimally to the elongational viscosity of the formulation. However, the elastic response of paper formulations that results from the interaction of clays with starch or carboxymethyl cellulose could be considerable and warrants further, detailed study (*e.g.*, Preston, McGenity and Husband (1993)). Hydrophobically-modified, alkali-swellable emulsion (HASE) thickeners have achieved some success in paper coatings (Roper *et al.* 1995). These thickeners bring about viscosity increases without a notable increase in the elastic component of the solution (Tarn and Glass 1992). They may also reduce the electro-viscous response of the clays, in part by adsorbing onto the clays and thereby stabilizing them from flocculation into a 'house-of-cards' arrangement (Heinle, Shah and Glass 1986). This latter effect is under further investigation (Tarn 1995).

5.4.4 OEM COATINGS

Even though the composition of water-reducible acrylic resins is similar to that of latices used in paper or architectural coatings (*cf.* Section 5.2.2), their response to dilution with water is unusual. 'Water-reducible' dispersions are water-swollen during dilution, giving rise to an abnormal viscosity maximum as illustrated in Fig. 5.32

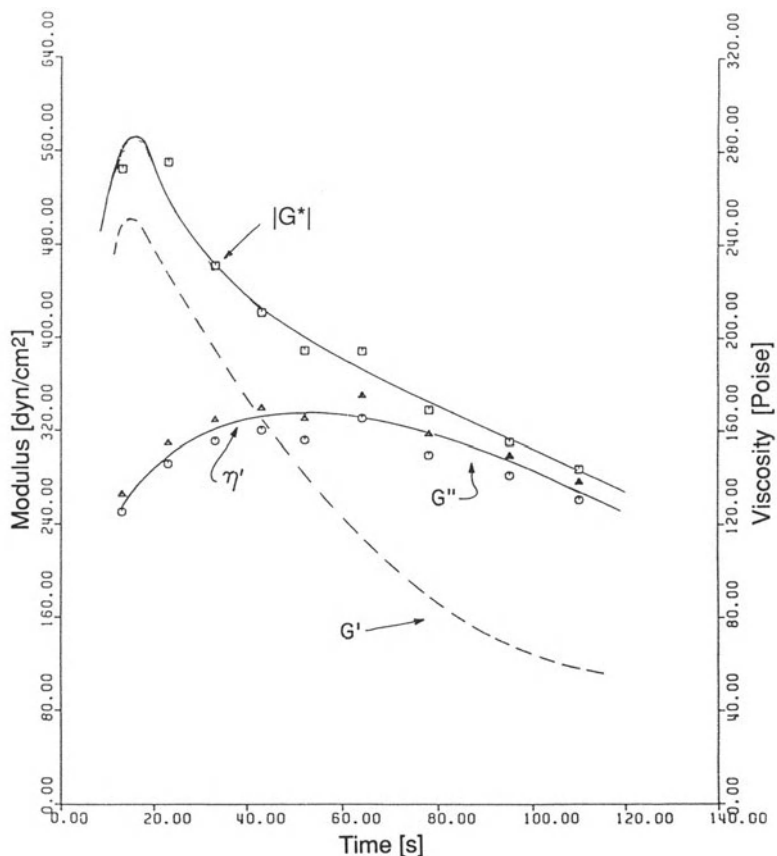


Figure 5.31 Time dependence, after shearing, of complex modulus, loss modulus and storage modulus of an architectural coating thickened with attapulgite clay at 2.6% by weight (Glass, 1975).

(Richards 1977). Such a maximum is not evident upon dilution of latex dispersions, or dilution of solvent-based resins used in coatings with oligomer synthesis. Figure 5.33 shows that the molecular weight of the resin and its acrylic acid content influence the magnitude of the maximum (Richards 1977). In the vicinity of the maximum the dispersions are shear thinning, but detailed rheological studies of such systems have not been reported. The molecular weight of the disperse phase influences the misting behavior during roll application to metal substrates but, again, there are no comprehensive rheological studies published, for either clear or pigmented formulations.

Polyurethane-based aqueous dispersions, or PURADs, exhibit phase separation when

thickened with nonadsorbing hydroxyethyl cellulose. This so-called syneresis increases with increasing particle size. The latex size effect suggests depletion flocculation of a poorly stabilized dispersion as a mechanism. When aqueous polyurethane dispersions are thickened with hydrophobically-modified, ethoxylated urethane (HEUR) thickeners, on the other hand, phase separation is not observed. Commercial HEUR thickeners that exhibit high loss modulus responses with conventional latices (Lundberg *et al.* 1991) exhibit high storage modulus responses with aqueous polyurethane dispersions: see Fig. 5.34 (Kaczmarski, Fernando and Glass 1993). To elucidate the mechanism responsible for this difference, model systems without the high

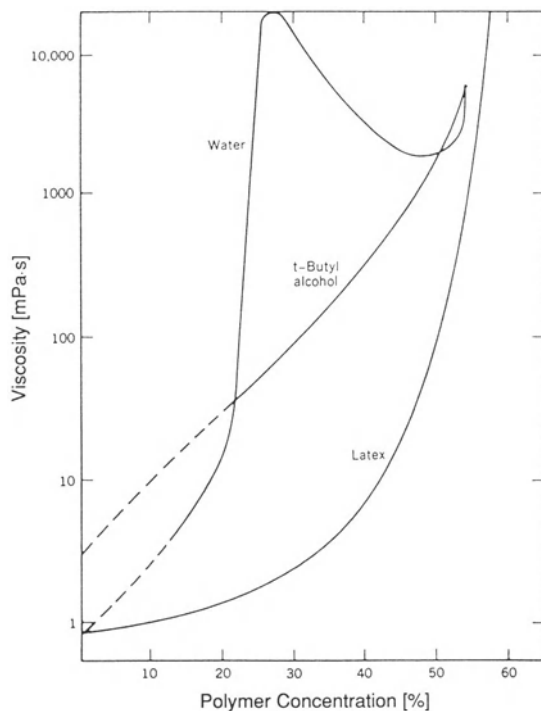


Figure 5.32 Viscosity dependence on polymer concentration for a latex and for water and t-butyl alcohol solutions of a 10/90 acrylic acid/butyl methacrylate copolymer with 75% effective neutralization with dimethylaminoethanol (Richards, 1977).

cosolvent contents typical of commercial polyurethane dispersions are under investigation (Chen 1997).

5.5 CONCLUDING REMARKS

As the case studies in this chapter illustrate, establishing the interplay among formulation components, rheological behavior and ultimate coating application performance requires judicious selection of the chemical constituents and detailed study of possible associations between the constituents; careful selection of the appropriate material functions and comprehensive and sometimes tedious rheological measurements of these material functions; and systematic application testing in either actual coating configurations or

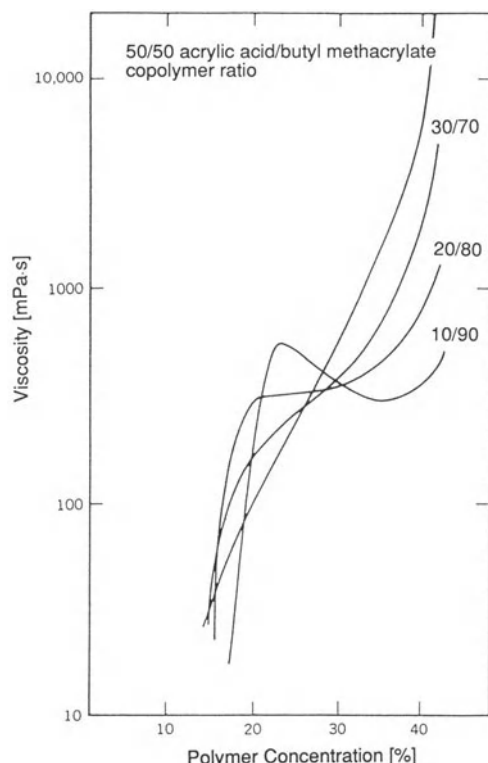


Figure 5.33 Viscosity dependence on polymer concentration for dilutions in water of acrylic acid/butyl methacrylate with different copolymer ratios and 75% effective neutralization with dimethylaminoethanol (Richards, 1977).

simpler model flows that mimic essential features of the application flow of interest. As this chapter also makes plain, the connections between formulation, rheology and flow behavior can be very subtle and material specific and, hence, it is very difficult if not impossible to extract very general and broad conclusions from most investigations in coating rheology. Nevertheless, with sufficient diligence and effort invested into a particular case study, conclusions and insights of some general validity typically emerge, as is the case for the water-borne latex coatings featured in detail in this chapter.

In the rheology of water-borne latex coatings, the median particle size of the latex plays an

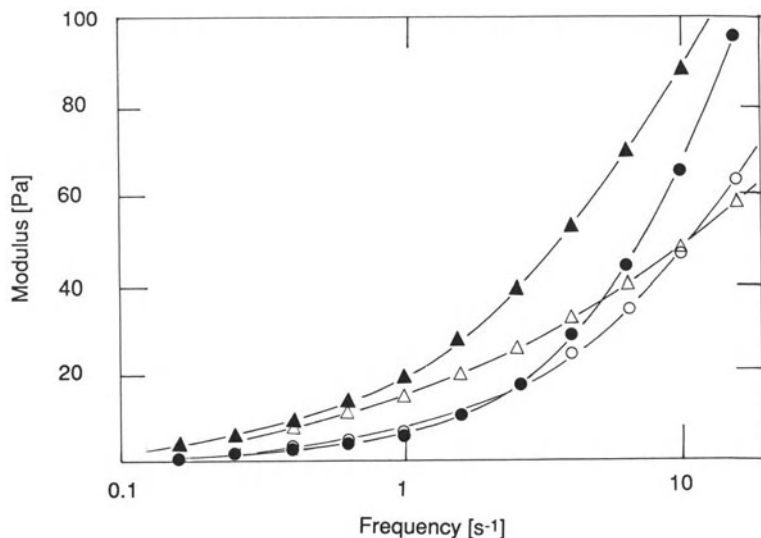


Figure 5.34 Storage modulus G' (circles) and loss modulus G'' (triangles) as a function of frequency for 20 wt% polyurethane-based aqueous dispersions (PURAD) with 0.6 wt% hydrophobe-modified ethoxylated urethane (HEUR) thickeners (after Kaczmarski, Fernando and Glass, 1993). Closed symbols: HEUR thickener with dicyclohexylmethane disocyanate end groups; open symbols: HEUR thickener with hexamethylene diisocyanate end groups.

important role, similar to the influence of the size of the disperse phase on the rheological response of polymer melts. The viscosity increases with decreasing size of the disperse phase and influences phenomena associated with shear deformations (i.e. leveling and thickness of applied film). Water-soluble polymer thickeners may play a subordinate role in the rheological behavior of coating formulations containing larger particle size latices, yet the thickener may dominate the rheology if there are chemical associations among its macromolecular chains. Chemical associations predominantly influence the viscosities at low shear rate and thus affect the leveling or ‘flow-out’ behavior of applied coatings. Raising the viscosity at high shear rates ($> 10^4 \text{ s}^{-1}$) increases the coated film thickness and, hence, the hiding power of the applied film. Through their influence on film thickness, high-shear-viscosities also affect the leveling of the coating after application. The size and particle size distribution of the latex do not have much of an effect at high shear rates,

but the amount of thickeners used to achieve an ‘intermediate formulation viscosity’ can have a dramatic effect at high shear rates. Higher viscosities at high shear rates are achieved by using lower-molecular-weight conventional thickeners which allow greater amounts to be added to the formulation. Among a new class of surfactant-modified thickeners, higher viscosities can be achieved with a thickener of a given molecular weight by decreasing the size of the terminal hydrophobic group. Surfactant-modified polymers thicken through hydrophobic associations, and can also be used to lower the viscosity of coating formulations containing small-particle latices, because the latter contains an excess surfactant.

In roll coating applications, the onset of ribbing and the ensuing spatter and misting behavior are influenced by the dynamic uniaxial elongational viscosity (DUEV) of the coating formulation, but not the elastic functions associated with shear deformations. This rheological response is deter-

mined primarily by the chemical composition and molecular weight of the thickener. Surfactant-modified, water-soluble polymers are an effective way to lower the DUEV of coating formulations and thereby minimize spatter and misting during roll application. The viscosities at low and high shear rates and the DUEV of surfactant-modified, water-soluble polymers are influenced by the amount of surfactant present in the formulation. Surfactant-modified, water-soluble polymers are also observed to inhibit the depletion flocculation of step-growth aqueous dispersions.

REFERENCES

- Anklam, M. R., Warr, G. G. and Prud'homme, R. K. 1994. The use of opposed nozzles configuration in the measurements of the extensional rheological properties of emulsions. *J. Rheology*. **38**: 797–810.
- Anwari, F. M. and Schwab, F. G. 1989. Optimizing latex paint rheology with associative thickeners. Chapter 23 in *Polymers in Aqueous Media: Performance through Association*, ed. J. E. Glass, Advances in Chemistry Series, Volume 223, pp. 527–542. Washington DC: American Chemical Society.
- Arney, W. C. and Glass, J. E. 1976. The role played by water-soluble polymers in paint performance. Part III: molecular weight and concentration effects in mixed thickener studies. *J. Oil Col. Chem. Assoc.* **59**: 372–378.
- Barber, E. J. and Bartel, D. G. 1976. Soluble polymers in air knife coating. *Tappi*. **59**(6): 123–126.
- Bauman, T., Sullivan, T. and Middleman, S. 1982. Ribbing instability in coating flows: effect of polymer additives. *Chem. Eng. Commun.* **14**: 35–46.
- Bierman, M. 1968. Das Fließen ebener Schichten inkompressibler viskoelastischer Flüssigkeiten mit einer in Ablaufrichtung infinitesimal gestörten Oberfläche. *Rheol. Acta*. **7**: 138–165.
- Bierwagen, G. P. 1975. Surface dynamics of defect formation in paint films. *Prog. Org. Coatings*. **3**: 101–113.
- Bierwagen, G. P. and Hay, T. K. 1975. The reduced pigment volume concentration as an important parameter in interpreting and predicting the properties of organic coatings. *Prog. Org. Coatings*. **3**: 281–303.
- Bird, R. B., Armstrong, R. C. and Hassager, O. 1987. *Dynamics of Polymeric Liquids – Volume 1: Fluid Mechanics* 2nd edn. New York: Wiley-Interscience.
- Brown, R. G. and Glass, J. E. 1989. Application of a viscosity model to the onset of viscosity enhancement in solutions of linear HM W-SP's. *Proc. Am. Chem. Soc. Div. Polym. Mater.: Sci. Eng.* **61**: 634–638.
- Chen, M. 1997. Synthesis and adsorption behavior of model pigment dispersants. PhD thesis (in preparation), North Dakota State University, Fargo, North Dakota.
- Chong, J. S., Christiansen, E. B. and Baer, A. D. 1971. Rheology of concentrated suspensions. *J. Appl. Polym. Sci.* **15**: 2007–2021.
- Clark, J., Wellinghoff, S. T. and Miller, W. G. 1983. Rheological properties of polystyrene-carbon disulfide gels. *ACS Polym. Preprints*. **24**: 86–87.
- Craig, D. H. 1986. Grafting reactions of (hydroxyethyl)cellulose during emulsion polymerization of vinyl monomers. Chapter 18 in *Water-Soluble Polymers: Beauty with Performance*, ed. J. E. Glass, Advances in Chemistry Series, Volume 213, pp. 351–368. Washington, DC: American Chemical Society.
- Dodge, J. S. 1972. Quantitative measures of leveling. *J. Paint Technol.* **44**(564): 72–78.
- Ferry, J. D. 1980. *Viscoelastic Properties of Polymers*, 3rd edn. New York: Wiley.
- Garey, C. L. 1977. *Physical Chemistry of Pigments in Paper Coating*. Atlanta, GA: TAPPI Press.
- Gaskell, R. E. 1950. The calendering of plastic materials. *J. Appl. Mech. (Trans. ASME)*. **17**: 334–336.
- Glass, J. E. 1975. The role played by water-soluble polymers in paint performance. *J. Oil Col. Chem. Assoc.* **58**: 169–177.
- Glass, J. E. 1976. The role played by water-soluble polymers in paint performance. Part II: Chemical modeling studies. *J. Oil Col. Chem. Assoc.* **59**: 86–94.
- Glass, J. E. 1978a. Dynamics of roll spatter and tracking. Part I: Commercial latex trade paints. *J. Coatings Technol.* **50**(640): 53–60.
- Glass, J. E. 1978b. Dynamics of roll spatter and tracking. Part II: Formulation effects in experimental paints. *J. Coatings Technol.* **50**(640): 61–68.
- Glass, J. E. 1978c. Dynamics of roll spatter and tracking. Part III: Importance of extensional viscosities. *J. Coatings Technol.* **50**(641): 56–71.
- Glass, J. E. 1978d. Dynamics of roll spatter and tracking. Part IV: Importance of G^* recovery and N_1 in tracking. *J. Coatings Technol.* **50**(641): 72–78.
- Glass, J. E. 1984. Perspectives in thicker development for water-borne coatings. *Amer. Paint J.* August 6th issue, pp. 45–47.
- Greener, J., Sullivan, T., Turner, B. and Middleman, S. 1980. Ribbing instability of a two-roll coater: Newtonian fluids. *Chem. Eng. Commun.* **5**: 73–83.
- Hakim, V., Rabaud, M., Thomé, H. and Couder, Y.

1988. Directional growth in viscous fingering. In *New Trends in Nonlinear Dynamics and Pattern Forming Phenomena: The Geometry of Nonequilibrium*, Proceedings of the NATO Advanced Research Workshop, Cargese, eds P. Coullet and P. Huerre.
- Heinle, S. A., Shah, S. and Glass, J. E. 1986. Influence of water-soluble polymers on the filtration control of bentonite muds. Chapter 11 in *Water-Soluble Polymers: Beauty with Performance*, ed. J. E. Glass, Advances in Chemistry Series, Volume 213, pp. 183–196. Washington DC: American Chemical Society.
- Hoffman, R. L. 1972. Discontinuous behavior in concentrated suspensions. *Trans. Soc. Rheol.* **16**: 155–173.
- Hoffman, R. L. 1974. Discontinuous and dilatant behavior in concentrated suspensions. II. Theory and experimental tests. *J. Colloid Interface Sci.* **46**: 491–506.
- Howard, P. R., Leasure, E. L., Rosier, S. T. and Schaller, E. J. 1991. Systems approach to rheology control. Chapter 12 in *Polymers as Rheology Modifiers*, eds J. E. Glass and D. N. Schulz, ACS Symposium Series, Volume 462, pp. 207–221. Washington, DC: American Chemical Society.
- Huppler, J. D., Macdonald, I. F., Ashare, E., Spriggs, T. W., Bird, R. B. and Holmes, L. A. 1987. Rheological properties of three solutions. Part II. Relaxation and growth of shear and normal stresses. *Trans. Soc. Rheol.* **11**: 181–204.
- Kaczmarski, J. P., Fernando, R. H. and Glass, J. E. 1993. Interactions of HEUR associative thickeners with waterborne polyurethanes. *J. Coatings Technol.* **65**(818): 39–46.
- Kaczmarski, J. P. and Glass, J. E. 1992. Structure property relationships in HEUR associative thickeners: influence of the diisocyanate coupler on aqueous solution rheology. *Proc. Am. Chem. Soc. Div. Polym. Mater.: Sci. Eng.* **67**: 282–283.
- Kaczmarski, J. P. and Glass, J. E. 1993. Synthesis and solution properties of hydrophobically modified ethoxylated urethanes with variable oxyethylene spacer lengths. *Macromolecules* **26**: 5149–5156.
- Kaczmarski, J. P., Glass, J. E. and Buchacek, R. J. 1993. Development of SEC technique for analysis of competitive adsorption of surfactant, HEUR associative thickeners and oligometric carboxylate dispersants on titanium dioxide. *Proc. Am. Chem. Soc. Div. Polym. Mater.: Sci. Eng.* **69**: 199–200.
- Karunasena, A., Brown, R. G. and Glass, J. E. 1989. Hydrophobically modified ethoxylated urethane architecture – importance for aqueous- and dispersed-phase properties. Chapter 26 in *Polymers in Aqueous Media: Performance through Association*, ed. J. E. Glass, Advances in Chemistry Series, Volume 223, pp. 495–525. Washington, DC: American Chemical Society.
- Karunasena, A. and Glass, J. E. 1989. Interactions in associative thickener/220 nm methyl methacrylate latex dispersion. *Prog. Org. Coatings* **17**: 301–320.
- Karunasena, A. and Glass, J. E. 1992. The effect of latex particle size on the rheology of thickened dispersions. *Prog. Org. Coatings* **21**: 53–67.
- Khan, S. A. and Prud'homme, R. K. 1987. Melt rheology of filled thermoplastics. *Rev. Chem. Eng.* **4**: 205–270.
- Klenin, V. J., Klenina, O. V., Kolnibolotchuk, N. K. and Frenkel, S. Ya. 1973. Structural levels of supermolecular organization in aqueous solutions of poly(vinyl alcohol). *J. Polym. Sci.: Polym. Sympos.* **42**: 931–942.
- Kreider, R. W. 1964. Factors controlling latex paint rheology and their measurement. *Official Digest – J. Paint Technol. Eng. (Federation of the Societies for Paint Technology)*. **36**(478): 1244–1260.
- Krieger, I. M. 1972. Rheology of monodisperse latices. *Adv. Colloid Interface Sci.* **3**: 111–136.
- Lambourne, R. 1987. *Paint and Surface Coatings: Theory and Practice*. Chichester, England: Ellis Horwood.
- Larson, R. G. 1988. *Constitutive Equations for Polymer Melts and Solutions*. Boston: Butterworths.
- Laun, H. M. 1978. Description of the non-linear shear behavior of a low density polyethylene melt by means of an experimentally determined strain dependent memory function. *Rheol. Acta* **17**: 1–15.
- Lundberg, D. J., Alahapperuna, K., Fernando, R. H. and Glass, J. E. 1990. Viscoelastic behavior in paper coating formulations containing associative thickeners. *Proc. TAPPI Coatings Conference* (Boston, May 1990), pp. 479–489. Atlanta, GA: TAPPI Press.
- Lundberg, D. J. and Glass, J. E. 1992a. Pigment stabilization through mixed associative thickener interactions. *J. Coatings Technol.* **64**(807): 53–61.
- Lundberg, D. J. and Glass, J. E. 1992b. Titanium dioxide ‘association’ with HEUR thickeners through model dispersant interactions. *Proc. Am. Chem. Soc. Div. Polym. Mater.: Sci. Eng.* **66**: 21–22.
- Lundberg, D. J., Glass, J. E. and Eley, R. R. 1989. Model-HEUR/surfactant/model latex matrix rheology studies. *Proc. Am. Chem. Soc. Div. Polym. Mater.: Sci. Eng.* **61**: 533–538.
- Lundberg, D. J., Ma, Z., Alahapperuna, K. and Glass, J. E. 1991. Surfactant influences on hydrophobically modified thickener rheology. Chapter 14 in *Polymers as Rheology Modifiers*, eds J. E. Glass and D. N.

- Schulz, ACS Symposium Series, Volume 462, pp. 234–253. Washington DC: American Chemical Society.
- Ma, Z. 1992. Associative thickener disperse systems. PhD thesis, North Dakota State University, Fargo, North Dakota.
- Ma, Z., Lundberg, D. J., Roberts, S. and Glass, J. E. 1993. Phase behaviors and film properties of dispersions and coatings containing associative and conventional thickeners. *J. Appl. Polym. Sci.* **49**: 1509–1527.
- Massouda, D. F. 1985. Analysis and prediction of roll-spatter from latex paints. *J. Coatings Technol.* **57**(722): 27–36.
- Matsuda, T. and Brendley, W. H. 1979. Transfer and leveling processes and rheological design in water-borne reverse-roll coating systems. *J. Coatings Technol.* **51**(658): 46–60.
- May, R., Kaczmarski, J. P. and Glass, J. E. 1993. Influence of molecular weight distributions of associative thickener on solution rheology. *Macromolecules*. **29**: 4745–4753.
- Meissner, J. 1985. Experimental aspects in polymer melt elongational rheometry. *Chem. Eng. Commun.* **33**: 159–180.
- Mill, C. C. 1967. The behavior of liquids on rotating rollers. *J. Oil Col. Chem. Assoc.* **50**: 396–406.
- Mill, C. C. and South, G. R. 1967. Formation of ribs on rotating rollers. *J. Fluid Mech.* **28**: 523–529.
- Miller, J. C. and Myers, R. R. 1958. A photographic study of liquid flow in a roll nip. *Trans. Soc. Rheol.* **2**: 77–93.
- Myers, R. R. and Hoffman, R. R. 1961. The distribution of pressure in the roll application of Newtonian fluids. *Trans. Soc. Rheol.* **5**: 317–328.
- Napper, D. N. 1983. *Polymer Stabilization and Dispersion Stability*. New York: Academic Press.
- Nielsen, L. E. 1977. *Polymer Rheology*. New York: Marcel Dekker.
- Odian, G. 1993. *Principles of Polymerization*. New York: John Wiley & Sons.
- Orchard, S. E. 1962. On surface leveling in viscous liquids and gels. *Appl. Sci. Res.* **A11**: 451–464.
- Ottewill, R. H. 1982. The stability and instability of polymer latices. Chapter 1 in *Emulsion Polymerization*, ed. I. Piirma, pp. 1–49. New York: Academic Press.
- Preston, D. J., McGenity, P. M. and Husband, J. C. 1993. The use of rheological techniques in the study of interactions between components of paper coating colours. In *Thin Film Coating*, ed. H. Benkreira, pp. 23–33. Cambridge: The Royal Society of Chemistry.
- Prud'homme, R. K., Uhl, J. T., Poinsatte, J. P. and Halverson, F. 1983. Rheological monitoring of the formation of polyacrylamide/chromium (III) gels. *Soc. Petrol. Eng. J.* **23**(5): 804–808.
- Rabaud, M., Michelland, S. and Couder, Y. 1990. Dynamical regimes of directional viscous fingering: spatiotemporal chaos and wave propagation. *Phys. Rev. Lett.* **64**: 184–187.
- Richards, B. M. 1977. Viscosity of water reducible acrylic copolymers. MS thesis, North Dakota State University, Fargo, North Dakota.
- Roper, J., Chonde, Y., Salminen, P. and Pollok, M. 1995. Determining the rheological and water retention properties of various thickeners for paper coatings. *Proc. Am. Chem. Soc. Div. Polym. Mater.: Sci. Eng.* **73**: 52–53.
- Ruschak, K. J. 1985. Coating flows. *Ann. Rev. Fluid Mech.* **17**: 65–89.
- Saffman, P. G. and Taylor, G. I. 1958. The penetration of a fluid into a porous medium or Hele-Shaw cell containing a more viscous liquid. *Proc. Royal Soc. Lond. A.* **245**: 312–329.
- Sato, T. and Ruch, R. 1980. *Stabilization of Colloidal Dispersions by Polymer Adsorption*. New York and Basel: Marcel Dekker.
- Schaller, E. J. 1968. Critical pigment volume concentration of emulsion based paints. *J. Paint Technol.* **40**(525): 433–438.
- Schoff, C. K. 1988. Rheological measurements. In *Encyclopedia of Polymer Science and Engineering*, Volume 14, 2nd edn., eds H. F. Mark *et al.*, pp. 454–451. New York: Wiley.
- Schunk, P. R. and Scriven, L. E. 1990. Constitutive equation for modeling mixed extension and shear in polymer solution processing. *J. Rheol.* **34**: 1085–1119.
- Smith, N. D. P., Orchard, S. E. and Rhind-Tutt, A. J. 1961. The physics of brushmarks. *J. Oil Col. Chem. Assoc.* **44**: 618–633.
- Soules, D. A., Fernando, R. H. and Glass, J. E. 1988. Dynamic uniaxial extensional viscosity (DUEV) effects in roll application. I. Rib and web growth in commercial coatings. *J. Rheol.* **32**: 181–198.
- Suetsugu, Y. and White, J. L. 1983. The influence of particle size and surface coating of calcium carbonate on the rheological properties of its suspensions in molten polystyrene. *J. Appl. Polym. Sci.* **28**: 1481–1501.
- Tanner, R. I. 1985. *Engineering Rheology*. Oxford: Clarendon Press.
- Tarng, M.-R. 1995. Interactions of water-soluble polymers with surfactants and disperse systems. PhD thesis, North Dakota State University, Fargo, North Dakota.
- Tarng, M.-R. and Glass, J. E. 1992. The role of

- surfactant in HASE thickener rheology. *Proc. Am. Chem. Soc. Div. Polym. Mater.: Sci. Eng.* **67**: 280–281.
- Van Wazer, J. R. 1963. *Viscosity and Flow Measurements*. New York: Inter Science Publishers.
- Walters, K. 1980. *Rheometry*. New York: Wiley.
- Weinberger, C. B. and Goddard, J. D. 1974. Extensional flow behavior of polymer solutions and particle suspensions in a spinning motion. *Int. J. Multiphase Flow*. **1**: 465–486.
- Whorlow, R. W. 1980. *Rheological Techniques*. New York: Wiley.
- Wildemuth, C. R. and Williams, M. C. 1985. A new interpretation of viscosity and yield stress in dense slurries: coal and other irregular particles. *Rheol. Acta*. **24**: 75–91.

THE FATE OF THIN LIQUID FILMS AFTER COATING

6

Haroon S. Kheshgi

6.1 INTRODUCTION

The fate of liquid films is determined by their state following application, and their environment. In most coating operations the region of film application is spatially separated from that following application. Exceptions do exist in operations such as spin coating where application, leveling, and drying all occur simultaneously as is described in Chapter 14. Phenomena of importance after application are caused by a largely different set of mechanisms than do those of importance in coating application, which is the primary emphasis of this book. During application, the liquid is often severely deformed through a complex geometry and the resulting fluid mechanics often requires sophisticated computational methods to analyze. After application liquid films are usually, and often desirably, of uniform thickness – a simple geometry; the film, however, is composed of material of increasingly complex properties as the film is set and dried.

During the transition of a recently applied film to a ‘dry’ solid film, the film may undergo a wealth of experiences as illustrated in Fig. 6.1. Irregularities in film thickness originated during application or by ambient disturbances can heal by capillary leveling, if there is time before the film becomes too viscous or undergoes transition to a solid. Alternatively, large amplitude irregularities in film thickness can lead to film rupture

and to dry patch formation, if the liquid does not wet the underlying substrate. Films containing solvents must be dried. Drying can lead to

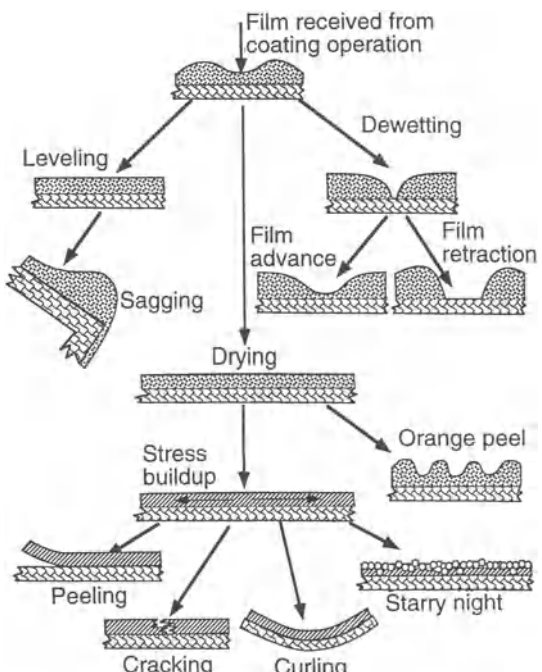


Figure 6.1 Phenomena that films undergo after coating application.

composition variation with depth into the film. Drying also leads to liquid/solid transition. Once solid, the film may still continue to dry, and shrink, leading to stress build-up within the film which is the cause of a variety of coating defects.

Experiences are governed by a diverse group of physical mechanisms. Fluid mechanics is crucial in healing of nonuniform films or breaking of unstable ones. Diffusion and phase behavior in complex media, chemical kinetics in reacting films, and boundary layer theory define phenomena during drying and setting. Mechanical properties as a function of evolving composition and temperature are needed to analyze stress build-up and relaxation in solidifying films, in order to predict the final state of stress in the film which, if severe enough, leads to modes of film failure such as peeling, cracking or curling (see Fig. 6.1). Understanding all of these phenomena becomes a challenge when we realize that the evolving film is a complex media, e.g., a polymeric film or a film of suspended solids undergoing liquid to solid transition.

Many defects arrive after coating application as the ultimate result of coating formulation and the way in which the coated film is treated after coating. While it is beyond the scope of this chapter to examine the entire catalogue of specific defects, many of which are still not understood or even well defined, the phenomena which are thought to cause the majority of defects will be addressed. It is hoped that applying understanding of these phenomena to specific defect problems will lead to ways of removing them by optimal choice of coating formulation and post-application environment. Formulation could be altered for example by addition of solvent, plasticizer (non-volatile solvent), surfactants or treatment of the coating substrate. Environment could be altered by changing temperature, residence time, overlying gas flow or solvent vapor pressure. This wide range of choices offers both the opportunity to arrive at favorable coating properties, or those that are not so favorable, such as defects. It remains the challenge of the coating engineer to make these choices with proper consideration of the many phenomena

which occur simultaneously in coatings after application.

This chapter first addresses leveling of films of uneven thickness by capillary pressure – the normal resultant of surface tension in a curved interface. Surface leveling is an essential and beneficial phenomenon in, for example, most paint coating operations where uneven films are applied. The leveling of nonuniformities in simple Newtonian liquid films is a well understood phenomenon; however, in practice the effects of gravity, film rheology, curved solid substrate shape and variations in surface tension brings us to the current state of research. In the following section the phenomenon of film dewetting is considered. Local thin or dry regions sometimes form in otherwise uniform films. These defects go by the names of pinholes or craters and can limit how thin one can coat. A connection is sought between the long-range intermolecular forces which constitute the effect of disjoining pressure (see Chapter 2) and this phenomenon. Next, the phenomena important in film drying are considered. Drying technologies (see, for example, Cohen (1992a and b)) speed drying by application of heat and mixing of the gas overlying the film. However, diffusion limitation or unwanted phase separation in the film, or film disturbance by gas flow or by surface tension gradients can present operability limits on the maximum rate of drying. Finally, once the film has passed through the sometimes-ambiguous transition from liquid to solid, it can still shrink by further drying. Shrinkage in a solid film leads to the build-up of stress which can result in the defects shown in Fig. 6.1. And while the effects of film stress are reduced in practice by altering film formulation or drying/curing conditions, the theory for doing so is still in its infancy.

6.2 SURFACE LEVELING: HEALING OF FILM IRREGULARITIES

Coating operations often leave films of irregular thickness as illustrated in Fig. 6.2. Instabilities in the coating operation such as brushmarks in

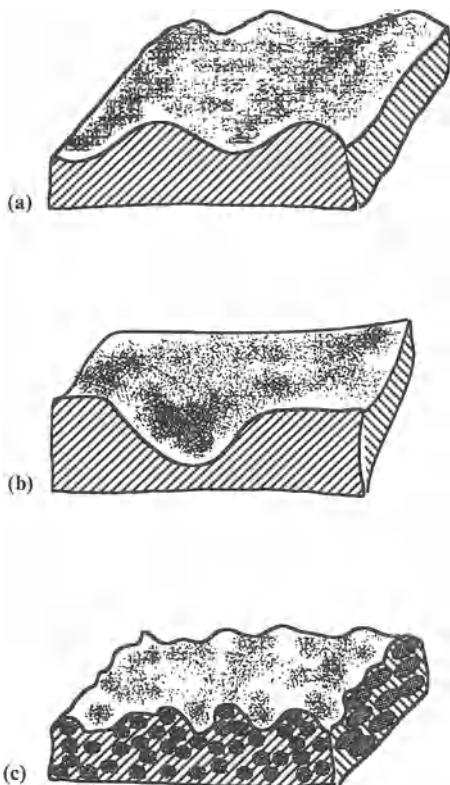


Figure 6.2 Sources of film irregularities: (a) coating applicator instability: ribbing; (b) local disturbances: impact of surfactant aerosol particle; and (c) irregularities inherent to the coating method: powder coating.

painted films (Smith, Orchard and Rhind-Tutt 1961), or ribbing instabilities in roll (Pearson 1960; Pitts and Greiller 1961; Coyle 1984) or slot (Bixler 1982) coated films lead to nearly-sinusoidal two-dimensional variations in film thickness. Defects caused by scratching, edge effects, bubbles, particulates, electrostatic forces, or surface tension gradients can leave localized irregularities in film thickness of large amplitude (Hansen and Pierce 1974; Gutoff 1993). The inherent nature of the coating operation produces a film of irregular film thickness in, for example, powder coating (Spitz 1973; Anshus 1973; de Lange 1984), or gravure coating (Munter 1990).

Uniformity of the final coated product, nonethe-

less, is often a critical aspect of film quality. To achieve a uniform film thickness, the surface smoothing effect of capillarity may be required to heal film irregularities. There is, however, limited time between coating application and the point at which the film is immobilized by, for example, drying; therefore, the leveling rate of an irregular surface is crucial. While films often have complex rheological behavior and may be nonhomogeneous, it is instructive to first consider the ideal case of leveling of a Newtonian liquid film.

Horizontal films of liquid that wet the underlying solid are absolutely stable: any disturbance decays to leave ultimately a quiescent flat film. There are two mechanisms that can act. Capillarity straightens a curved free surface. Gravity levels an inclined free surface. Either or both set disturbed liquid films in motion. Once in motion, inertia tends to maintain the momentum of liquid in motion while viscous stresses tend to distribute the momentum uniformly over the entire mass and to transmit it to the rigid horizontal surface on which the film sits. How disturbances evolve depends on which of these forces dominates the situation.

Disturbances of infinitesimal amplitude in Newtonian liquid decay exponentially to leave a flat, quiescent film provided the viscosity is high, the film thickness h is small or the horizontal length scale of the disturbance is great compared with the film thickness. The evolution of a disturbance of infinitesimal amplitude, i.e. $\varepsilon \equiv a/h_0 \rightarrow 0$ where a is the amplitude and h_0 is the undisturbed film thickness, which is chosen as the unit of film thickness measure, is identical to the evolution of the sum of the Fourier components of the disturbance. It has long been known (e.g. Lamb (1945)) that the exponential decay of a sinusoidal disturbance is exact in the asymptotic limit of infinitesimal amplitude ($\varepsilon \rightarrow 0$) and small Reynolds number ($Re \rightarrow 0$). The Reynolds number $Re \equiv \rho h_0^4 \sigma / 3\mu^2 l^3$ where $3\mu l^4/\sigma h_0^3$ is the unit of time measure t_0 , ρ is density and μ is viscosity, $2\pi l$ is the wavelength of the sinusoidal disturbance as seen in Fig. 6.3, and l is chosen as the unit of film length measure. The evolution of two-dimensional disturbances

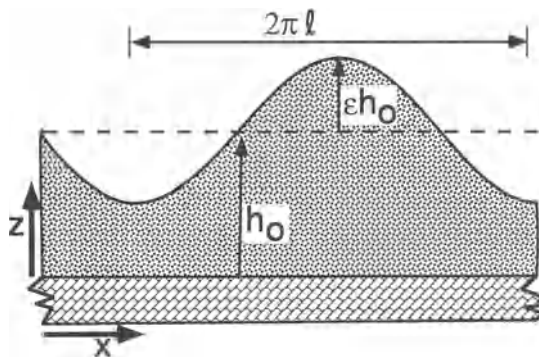


Figure 6.3 Sinusoidal film irregularity.

considered here is (Orchard 1962):

$$H(X, T) = 1 + \varepsilon \sin(X) \exp\left[-\frac{3}{2}\left(\frac{\tanh(\alpha) - \alpha \operatorname{sech}^2(\alpha)}{1 + \alpha^2 \operatorname{sech}^2(\alpha)}\right)\left(\frac{1 + Bo/\alpha^2}{\alpha^3}\right)T\right] \quad (6.1)$$

where the wavenumber $\alpha \equiv h_0/l$, and the Bond number $Bo \equiv h_0^2 g \rho / \sigma$ is the ratio of gravitational force to capillary force, σ is the surface tension of the film free surface, g is the acceleration of gravity, $H \equiv h/h_0$, $X \equiv x/l$, and $T \equiv t/t_0$. Anshus (1973) has since extended (6.1) to predict the evolution of three-dimensional, doubly-sinusoidal disturbances.

When the effects of liquid inertia become sizable in relation to viscous stresses, the evolution of small disturbances changes. Not always does a disturbance decay exponentially: it may instead overshoot the flat rest state to eventually approach periodically a flat film. In the asymptotic limit of infinitesimal amplitude ($\varepsilon \rightarrow 0$) and vanishing viscous stress ($Re \rightarrow \infty$), a solution has again long been known (Lamb 1945; Whitham 1974):

$$H(X, T) = 1 + \varepsilon \sin(X) \cos\left\{\left[\frac{\tanh(\alpha)}{\alpha} \frac{1 + Bo/\alpha^2}{\alpha Re}\right]^{1/2} T\right\} \quad (6.2)$$

In this asymptotic limit liquid disturbed

sinusoidally oscillates without loss of amplitude: it executes a standing wave. Liquids, however, are not inviscid fluids; damped standing waves are observed (cf. Lamb 1945; Batchelor 1967). The theory for decay of infinitesimal disturbances for intermediate values of Reynolds number was given by Wehausen and Laitone (1960; see also Kheshgi 1989). Kheshgi (1989) shows that inertial effects are negligible for $\alpha Re \ll 1$, which is true for essentially all coated films.

In horizontal films the leveling effect of capillarity dominates that of gravity when $Bo \ll \alpha^2$ which is the case for irregularities of length less than the capillary length – i.e. $l \ll (\sigma/\rho g)^{1/2}$. In this instance (6.1) can be approximated by

$$H(X, T) = 1 + \varepsilon \sin(X) \exp\left[-\frac{3}{2\alpha^3} \frac{\tanh(\alpha) - \alpha \operatorname{sech}^2(\alpha)}{1 + \alpha^2 \operatorname{sech}^2(\alpha)} T\right] \quad (6.3)$$

In the limit of long irregularity length compared with film thickness, $\alpha \ll 1$, (6.3) can be further simplified to

$$H(X, T) = 1 + \varepsilon \sin(X) \exp(-T) \quad (6.4)$$

Although this equation gives only the evolution of a sinusoidal disturbance, the decay of a small amplitude irregularity of arbitrary shape can be represented as the linear superposition of a series of Fourier components. Since the decay time t_0 of the Fourier components is proportional to the fourth power of the component wavelength (when α is small), the longest wavelength component is the most persistent.

To get a feel for the time required for healing of disturbances by surface leveling, consider the following example. A typical (Cohen 1992a) slide coating operation could have a coating speed of 3 m/s, viscosity $\mu = 50$ cp, surface tension $\sigma = 50$ dynes/cm, and film thickness $h_0 = 100 \mu\text{m}$. The time scale for capillary-driven leveling of a long-wavelength irregularity in film thickness is $t_0 \equiv 3\mu l^4/\sigma h_0^3$. If the characteristic length of the disturbance $l = 0.5 \text{ mm}$ ($\alpha = 0.2$) – which may be produced by a local disturbance such as a scratch or crater – then the exponential decay time $t_0 = 0.08 \text{ s}$; one decay time will expire after the

coating has translated only 0.2 m. If the characteristic length of the disturbance $l = 4$ mm ($\alpha = 0.025$) – which may be produced by flow maldistribution in the coating head, edge effects, or a long wavelength ribbing instability (Coyle 1992) – then the exponential decay time $t_0 = 768$ s; one decay time would require 2.3 kilometers of travel before setting of the coating. Only short wavelength disturbances can be healed by surface leveling when coatings are rapidly dried, as is often a requirement for high speed coating operations.

Most detrimental to coated film quality are irregularities of large amplitude ($\varepsilon \gg 0$) and such irregularities are often of long wavelengths ($\alpha \ll 1$). Kheshgi and Scriven (1988) show that irregularities level significantly slower than predicted by linear theory, if the amplitude is sufficiently large. When $\alpha \ll 1$, the evolution of a finite-amplitude two-dimensional irregularity can be predicted by the film profile equation (Orchard 1962)

$$\frac{\partial H}{\partial T} = -\frac{\partial}{\partial X} \left(H^3 \frac{\partial^3 H}{\partial X^3} \right) \quad (6.5)$$

The evolution of initially sinusoidal (two-dimensional) irregularities was calculated (Kheshgi 1984; Kheshgi and Scriven 1988) by numerical solution of (6.5), and examples are shown in Fig. 6.4. Evident is the distortion of the irregularity for the larger amplitude disturbance in Fig. 6.4b. The shallow region of the film rises much slower than the thickest region falls. Soon after leveling proceeds there is even a slight thinning of the film at its shallowest point and an increase in surface inclination.

The rate at which the shallowest regions of film are flooded is, for instance, of prime importance for smoothing brushmarks, because thin paint films often do not optically hide the underlying surface. Figure 6.5 (Kheshgi 1984; Kheshgi and Scriven 1988) shows the decay time $T_{1/2}$ required for the shallowest region of film to rise halfway to the mean film thickness, l , predicted by solution of (6.5). While brushmarks are predominantly of moderate wavelength (Orchard 1962), i.e. $\alpha = 0(1)$, the long-wavelength approxi-

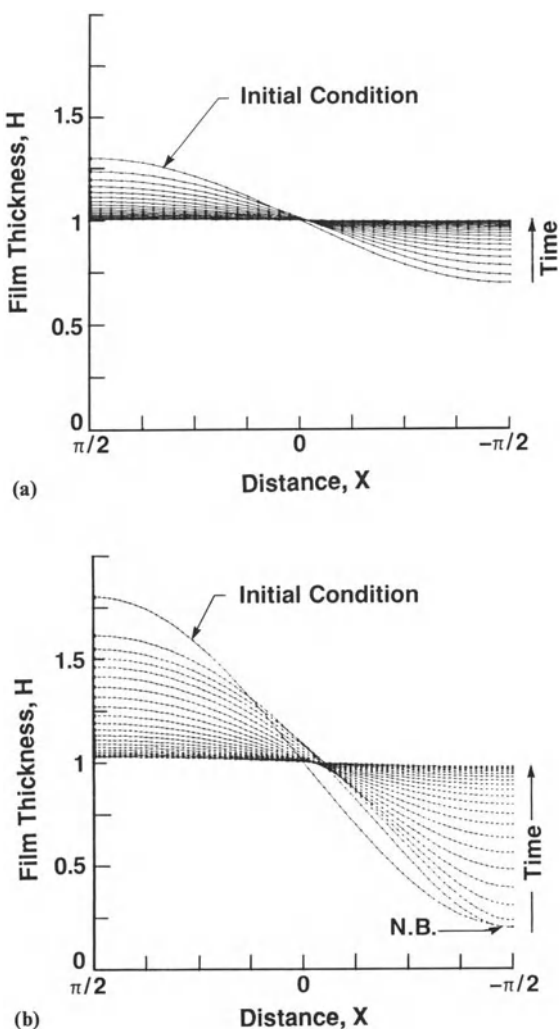


Figure 6.4 Capillary-driven surface leveling of a sinusoidally shaped disturbance. Free surface profiles predicted by finite difference solution of film profile equation (6.5) shown at time increments of 0.2. (a) $\varepsilon = 0.3$, (b) $\varepsilon = 0.8$ (Kheshgi and Scriven, 1988).

mation leads qualitatively to the right behavior as confirmed by finite element solution of the full Navier–Stokes system (Kheshgi and Scriven 1988). Linear theory for long wavelength irregularities given by (6.4) predicts $T_{1/2} = \ln(2)$. As is evident in Fig. 6.5, the time required to raise the shallowest portion of film increases as the

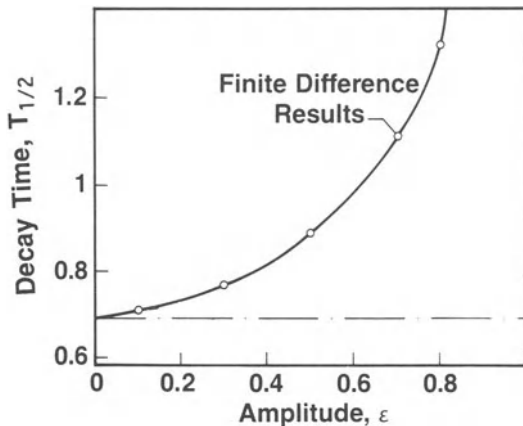


Figure 6.5 Decay time required for thinnest portion of disturbed film to rise half way to the mean film thickness $H = 1$.

amplitude ε becomes greater, and appears to become unbounded as $\varepsilon \rightarrow 1$ ($a \rightarrow h_0$). While the initial rate of film leveling of irregularities is sensitive to its amplitude, the final rate of leveling will eventually approach that of linear theory. Therefore, if we consider the time required to level an irregularity to an amplitude of one fifth (instead of one half) its initial amplitude, as did Orchard (1962), then the effect of amplitude on leveling rate does not appear significant until the amplitude of the irregularity becomes greater than about 80% of the mean film thickness ($\varepsilon > 0.8$).

While leveling of a coating (especially paints), is a desired effect, unwanted are effects such as capillary straightening of the free surface above a substrate of complex geometry or sagging of wet films due to gravity.

When a uniform film is coated on an irregular surface, the effect of capillary leveling is to squeeze liquid from the convex regions of the surface to the concave regions. This causes thinning of the coating above local asperities common in sandpaper or edges common in painting, and thickening in depressions or corners (see Kornum and Nielsen (1980)); all of these are usually detrimental effects to be avoided. The spin coating of an uneven substrate is considered in Chapter 14.

The effect of gravity on a horizontal film with a solid substrate below is to speed leveling as is evident in (6.1). However, if the film is inclined or inverted, then the effect of gravity is to increase the size of disturbances. Formulators of coatings have long been active in trying to formulate coatings so that they will level without sagging as is evidenced by the review by Quach (1973). Many types of non-Newtonian and/or time-dependent behavior have been proposed to accomplish this: yield-stress liquids, viscoelastic liquids, thixotropic liquids and viscosity increase by evaporation of solvent. Although a theoretical justification for these approaches has not been developed, the goal is clear: to formulate a non-Newtonian or time-dependent behavior that allows surface leveling but does not permit other detrimental effects. For example, a coating may be formulated so that it has a yield stress small enough to allow capillary driven leveling of large-amplitude, short-wavelength disturbances, but large enough to prevent gravity effects. And estimates, based on the theory of capillary leveling, of the magnitude of stress during capillary leveling (Orchard 1962) can be used to guide design of such yield-stress fluids.

In practice, coated films are rarely homogeneous Newtonian liquids which solidify abruptly upon drying, but rather complex fluids exhibiting viscoelasticity, surface tension gradients, complex geometry and depth dependent properties. These complications have been included in analyses to illustrate the phenomena which are possible, however analysis of specific applications requires individual consideration.

Keunings and Bousfield (1987) show that viscoelastic effects can significantly retard capillary leveling. It is not clear, however, what rheology would result in enhanced leveling as opposed to sagging as Quach (1973) suggests. Viscoelastic effects may well retard gravity effects less than capillary leveling.

Schwartz and Eley (1992a) found a wide variety of effects caused by surface tension gradients induced by variations in surface concentrations of surfactants. Lowering surface tension with a surfactant will, by itself, lead to a slower rate of

surface leveling as indicated by the unit of time measure $t_0 \equiv 3\mu l^4/\sigma h^3$. In addition, the elastic effect of slowly diffusing surfactant can further delay leveling; the corollary was shown (Ruschak 1987) that uniform films better resist disturbance by fluctuations in the overlying ambient gas pressure if surfactant is present. During drying the presence of volatile surfactants can have larger effects as is discussed later in this chapter.

Often coatings are not homogeneous. Joos and Jacobmeyer (1992) analyze the leveling of an initially two layer coating with a solvent rich surface layer on top of a soluble polymer base layer. In the situation they study, diffusion of the polymer into the solvent rich film leads to a growing (or swelling) immobile or high viscosity polymer base which limits leveling to a thinning solvent rich film. Bousfield (1991) analyzes the leveling of a liquid/solid slurry layer on a porous substrate, a common situation in the paper coating industry. He finds that absorption of the liquid into the porous substrate has a more rapid effect on raising film viscosity than does drying in such situations. Removal of the liquid leads to solid behavior and termination of leveling.

A good example of the analysis of the trade-offs between leveling effects and those of defect growth is given by de Lange's (1984) analysis of the leveling of powder coatings. Such coatings are applied as a solid coating. Heating melts the coating, allowing the particles to coalesce and irregularities to consequently level. Thermosetting leads back to a solid film. Low viscosity or high surface tension speed the leveling phenomenon. And leveling must be complete (with some tolerance) before solidification occurs, in order to give an acceptable product. This leads to operability bounds as shown in Fig. 6.6. Viscosity and surface tension can be adjusted with additives. However, low viscosity enhances capillary-driven flow away from corners, edges or asperities and gravity-driven flow which may take the form of sagging of the film. And high surface tension can lead to the formation of pinholes, which are discussed in the next section of this chapter, due to either enhanced surface tension gradients or

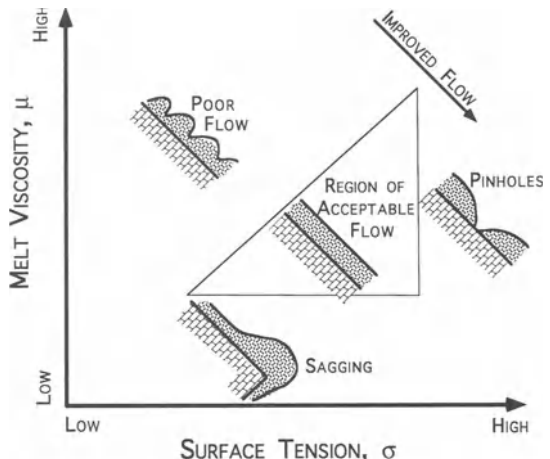


Figure 6.6 Operability diagram for leveling of powder coating which illustrates the conclusions of de Lange (1984).

to a high contact angle with the substrate which often are consequences of high surface tension.

6.3 DEWETTING: NUCLEATION AND GROWTH OF DRY REGIONS

It is common to see the edges of a nonwetting liquid film retract soon after the film is created by coating a solid or by causing bulk liquid to drain away from a solid. Retraction continues until the liquid has drawn up into small beads or larger patches. At the contact line of these, the apparent contact angle varies to some extent about a characteristic value that should be called the recently receded contact angle (*cf.* Huh and Scriven (1971)). It is not uncommon to see such a liquid film also rupture spontaneously at places distant from its original edges, the rupture creating an apparently dry patch with a brand new edge, which retracts in the same fashion as that on the outer limits of the film (*cf.* Padday (1971)). In these ways a nonwetting film tends to dewet.

Retraction and rupture/retraction can be seen in a water film spread on a waxed automobile, in a water film left by draining of a sink basin, in a paint film applied to an ill-prepared surface, and in many other everyday situations. These

phenomena can also be seen on occasion in carefully coated liquid films that are meant to be not only continuous but also precisely uniform, as in the manufacture of photographic film, photoresist, optical coatings and similar products. The phenomena are then greatly undesired, of course. Here it is hypothesized that there are three stages which lead to and can limit the formation of a new dry patch.

Dewetting of a solid surface covered by a film of nonwetting liquid either proceeds from a pre-existing dry patch or edge, or initiates from some film-thinning disturbance that continues to grow until the film ruptures. Local thinning can be caused by evaporation; by electrostatic forces; by drainage due to gravity or capillary-driven flow, especially from sharp protuberances; or by surface tension gradients, such as are caused by surface-active substances delivered by particles falling on or already in the film. Once a nonwetting film has been sufficiently thinned, long-range intermolecular forces can accelerate thinning until rupture. Rupture can be followed by film retraction and growth of a dry patch or to film advance and healing of the rupture.

A liquid film spread over a solid surface may be a wetting film or a nonwetting one, depending on the nature of the long-range interactions between molecules of the liquid and solid. The consequences of these interactions collectively can be modeled by disjoining pressure in the wetting case, and by its negative, conjoining pressure, in the nonwetting case as reviewed in Chapter 2. They are appreciable effects only in submicroscopically thin liquid films. However, sufficiently near a contact line where the surface of a liquid film, a liquid/gas interface, appears to intersect a solid surface, the thickness of the liquid diminishes to submicroscopic scale and these effects of stress anisotropy and solid–liquid interaction are active. So it is that the apparent contact angle at the contact line between liquid, gas and solid is an index to whether the liquid is wetting or nonwetting (Frenkel 1946; Mohanty 1981). When the apparent contact angle, measured through the liquid, is zero, the liquid is said to wet the solid, for usually it will spread sponta-

neously to cover ever more of a smooth solid surface. The term nonwetting is applied to those cases in which the apparent contact angle is greater than zero. (Sometimes ‘nonwetting’ is reversed for cases where the angle is greater than some arbitrarily chosen nonzero value, but that is not the usage in this chapter).

6.3.1 FILM-THINNING DISTURBANCES

Liquid films delivered in coating operations are usually of average thickness great enough, e.g. more than 1 µm, that the film rupturing effect of conjoining force is not appreciable if the film is uniform. For assumed models of conjoining force, it has been estimated (Scheludko 1967; Sharma and Ruckenstein 1986) that film rupture by conjoining pressure proceeds at an appreciable rate only in films thinner than 0.1 µm. In careful experiments, Padday (1971), however, observed that films of average thickness, shown in Table 6.1, of about 500 µm to dewet. (Note that the contact angles and critical film thicknesses in Table 6.1 are significantly larger than those found in most coatings). His observation can be explained: if a film that is on average stable to infinitesimal amplitude disturbances is thinned by some disturbance until its thickness is small enough, conjoining forces can rupture the film: see Fig. 6.7. For this explanation to be true, film thinning disturbances would have to be responsible for thinning the film by more than a factor of ten.

Film-thinning disturbances trigger the conjoining-driven rupture of nonwetting films. Numerous are the external sources of disturbances. One is film thinning by gravity-driven and capillarity-driven drainage, an obvious mechanism. A second is film-thinning by surface tension gradients, which may be common and the most dangerous source in coating operations.

From a solid substrate that is locally elevated, gravity drains and thins liquid films. From solids which are locally convex, capillary pressure squeezes thin liquid films and makes them ever thinner (the difficulty encountered when trying to paint a convex corner is a testament to this

Table 6.1 Observed thickness h_c for film rupture and equilibrium contact angle θ for several polar and nonpolar solid/liquid systems

Solid/liquid system	Contact angle θ †	Critical thickness h_c
Teflon/benzene	45°	160 μm *
Teflon/1-decene	33°	260 μm *
Teflon/1-tetradecene	45°	270 μm *
Teflon/1-octadecene	50°	270 μm *
Parafin/water	65° ‡‡	310 μm *
Polymethylene metacrylate/water	70–80°	393 μm **
Polyethylene/water	94°	420 μm **
Teflon/water	110°	510 μm *
Teflon/ethylene glycol	92°	560 μm *
Teflon/water	110°	787 μm **

† Contact angles estimated by Sharma and Ruckenstein (1989).

‡‡ Receding contact angle.

* Critical thickness measured by Padday (1971).

** Critical thickness measured by Doughman, Holly and Dohmlan (1971).

fact). However, film drainage from blunt surfaces is so slow that it is rarely the sole film-thinning mechanism leading to a dewetting occurrence; other film-thinning mechanisms intrude. But from a sharp object, film drainage is rapid. For example, the film covering a pinpoint rising up out of a body of liquid drains quite quickly because of the high curvature at the tip. Thus,

asperity of a surface to be coated can cause dewetting; coating of sandpaper provides a familiar example.

The surface of a small gas bubble attached to a solid substrate is also sharp, i.e. it has a small radius of curvature, and is a common source of coating defects (Gutoff 1993). Kheshgi and Scriven (1991) present photographs which illustrate bubbles' role in nucleation of dry patches. In coating operations considerable care is often obligatory to remove gas bubbles from a liquid before it is coated; one of several reasons for this is to avoid nucleation sites for dewetting.

If surface tension is reduced locally by some agency, the accompanying surface-tension gradients can flow that can thin a liquid film: see Fig. 6.8. If film thinning continues until the effect of conjoining forces become profound, thinning can continue ever more rapidly and the liquid film can rupture.

Surface-tension gradients arise from sources often present in coating operations. Locally high temperature lowers surface tension in the vicinity and results in surface-tension-gradient-driven thinning (shown vividly in the National Committee for Fluid Mechanics Films movie coordinated by Trefethen 1972). Suractant concentration gradients can incite flow instabilities driven by surface tension gradients. This is a common problem as reviewed by Scriven and Sternling (1960) and recognized by, among others, Hansen and Pierce (1974) in certain coatings

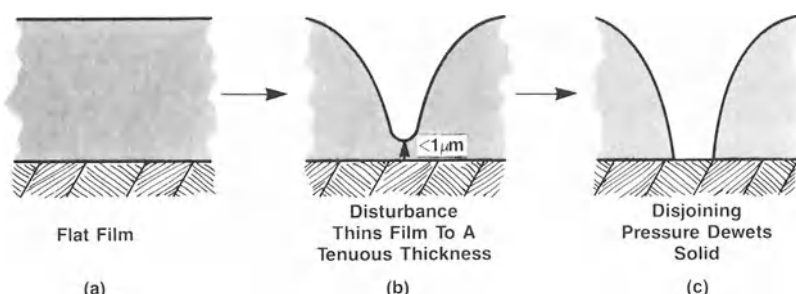


Figure 6.7 A flat coated film of nonwetting liquid: (a) usually greater than 1 μm thick can dewet if a disturbance thins the film; (b) to the extent (ordinarily less than 1 μm) that the effect of conjoining force is to dewet; (c) the solid substrate.

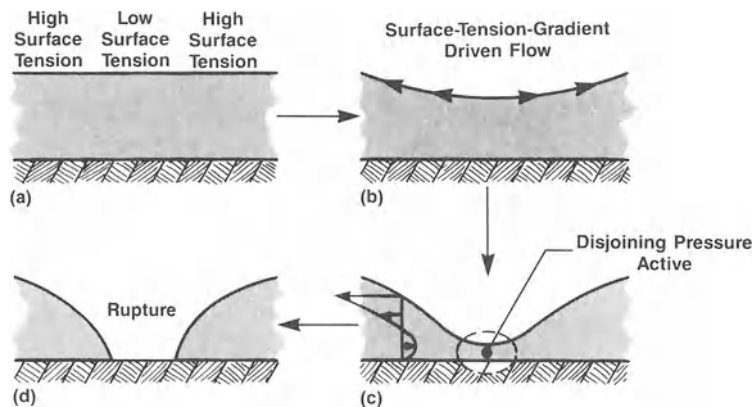


Figure 6.8 Surface-tension-gradient-driven flow draws liquid from regions of locally low tension (a–b). Film thinning might continue until conjoining forces become appreciable (c), and rupture the film (d).

during drying processes where solvent concentration, which affects surface tension, decreases and does so nonuniformly. Surface tension can also be lowered locally by surfactant impurities arriving at the free surface from within the film, or from the gas above.

Dewetting occurrences triggered by the last of these causes of surface tension gradients, namely airborne surfactant particles is ubiquitous to all but the most carefully isolated films. Kheshgi and Scriven (1983) easily observed, with the aid of moiré topography, local depressions (compare with Hahn (1971)) which formed when unseen particles lit on a wetting film. Such depressions can lead to the coating defect called craters, discussed by Hahn (1971), should the film set before the depression heals. Particles of or containing surface-active material can dewet a nonwetting film, as demonstrated in experiments by Kheshgi and Scriven (1991) and Gaver and Grotberg (1992) where surfactant was intentionally placed on a film. However, surfactant-bearing particles are more often unnoticed microscopic dust motes, droplets, or even dandruff or lint that fall on the film. Precision coating facilities are sometimes placed in clean rooms to, in part, reduce the likelihood of dewetting; there are reports that this practice is becoming more prevalent in industrial manufacturing.

6.3.2 FILM RUPTURE

If a nonwetting film is sufficiently thinned, then conjoining pressure will rupture it; a dry patch is nucleated. For this to occur, a nonwetting liquid film must have been created on a solid substrate. In order to resolve the mechanisms of film rupture, conjoining forces are considered here. These act on an invisible (submicron) scale to make a film nonwetting. Also considered are the hydrodynamic forces of pressure gradient and viscous shear that are activated in the process of dewetting. Computational solution of the equations of film motion augmented with conjoining forces gives prediction of whether or not an externally-generated, initial disturbance leads to rupture; and if it does, how much time elapsed before the film ruptures.

The equilibrium chemical potential, or partial molar (or mass) free energy, of material in a thin liquid film differs from that in bulk liquid. This difference in chemical potential is referred to as the disjoining potential or, as Deryagin (1955) expressed it, as the disjoining pressure Π . When the difference Π is negative, it is referred to here as conjoining pressure, for it is conjoining force which tends to make liquid conjoin into beads, or drops, and hence dewet the solid in which the film lies.

The origins of conjoining pressure are the long-range intermolecular forces that are always present between neutral molecules (e.g., dispersion, and multipolar electrostatic forces) and are often stronger between charged molecules (i.e., ionic-electrostatic forces which are quite important, for instance, when electrostatic double layers are present), and short-range or structural interactions (e.g., hydrogen bonding and so-called solvation forces); Derjagin (1989) and Teletzke, Scriven and Davis (1987) give details. In a flat or nearly flat film, i.e. a flat film altered by disturbances of length l that is great in comparison with the mean film thickness h_0 , conjoining (or disjoining) pressure beneath the liquid–gas interface (the gas lying above) can be approximated as a function of film thickness h (see, for example, Mohanty (1981); Teletzke, Scriven and Davis (1987))

$$\Pi(h) = \sum_{i=1}^{\infty} a_i/(h)^i \quad (6.6)$$

The coefficients a_i are determined by the particular forces that contribute to conjoining pressure; these forces are specific to each solid–liquid–gas combination. The disjoining (conjoining) pressure profiles, i.e. the thickness dependencies, of different contributing forces are listed by, among others, Mohanty (1981) and Teletzke, Scriven and Davis (1987). Conjoining pressure depends sensitively on thickness and ordinarily affects films no greater than $1\text{ }\mu\text{m}$ thick; if electrostatic contributions are absent the conjoining pressure may be inconsequential until the film thins to a thickness of only a few score of nanometers.

Conjoining pressure influences the stability of thin films. When disjoining pressure decreases monotonically as film thickness increases, i.e. $d\Pi/dh < 0$, it tends to level any disturbance to a liquid film; a disjoining pressure profile like that in Fig. 6.9a is of a wetting film. However, when disjoining pressure is negative and so an increasing function of film thickness, i.e. $d\Pi/dh > 0$, it tends to unlevel, i.e. to reinforce any disturbance and make unstable a flat liquid film; a conjoining pressure profile like that shown in Fig. 6.9b is of a nonwetting film. Conjoining

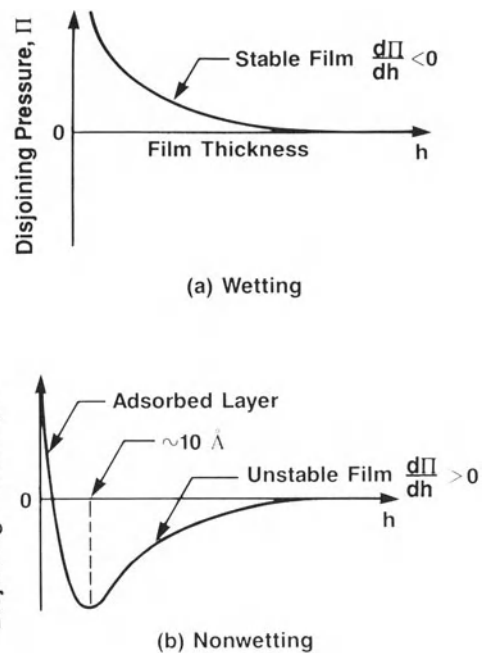


Figure 6.9 Disjoining pressure profiles of (a) a wetting liquid film, and (b) a nonwetting liquid film.

pressure does not alone determine the time-evolution of a disturbance; hydrodynamic forces, viz. capillary pressure, gravity, and viscous stresses, influence the behavior.

To estimate the time evolution of translationally symmetric, long disturbances of horizontal liquid films with a gas above and a flat solid surface beneath, it is appropriate to adopt the film profile equation employed by Teletzke (1983; see also Teletzke, Scriven and Davis (1987); Williams and Davis (1982); Sharma and Ruckenstein (1986); and Kheshgi and Scriven (1991):

$$\frac{\partial H}{\partial T} = \frac{\partial}{\partial X} \left\{ H^3 \frac{\partial}{\partial X} \left[-\frac{\partial^2 H}{\partial X^2} + \frac{Bo}{\alpha^2} H - \left(\frac{\mu l^4}{\sigma h_0^4} \right) \Pi \right] \right\} \quad (6.7)$$

The x -coordinate runs along the solid–liquid interface. Film viscosity is presumed not to depend on film thickness; this presumption may not be warranted in films thinner than about

5–10 molecules, at which thickness the structural contribution to disjoining pressure (*cf.* Fig. 6.9b) might influence nonequilibrium momentum transfer.

Solution of film profile equation (6.7) leads to predictions (Williams and Davis 1982; Kheshgi and Scriven 1991; Yiantios and Higgins 1991) of the time required for film rupture, given an initial irregularity in film thickness $h(x)$ at time $t = 0$. Results show that the time required for rupture is short if the film thickness is less than a critical thickness which is somewhat less than 1 µm depending on the model for conjoining pressure.

Experimental confirmation of this mechanism for film rupture is confounded by the difficulty in producing thin films, monitoring and modeling film thinning disturbances, and modeling conjoining pressure and its effects. For example, Jensen and Grotberg (1992) attempted to analyze the observed dewetting initiated by surfactant, and continued by rupture dominated by conjoining pressure; their theoretical analysis, however, led to the disconcerting result that the surfactants considered do not thin the film sufficiently to lead to rupture, contrary to observations. There has been recent improvement of measurement, modeling and analysis of the effects of conjoining pressure. For example, ellipsometry has been used to measure (Gupta and Sharma 1992a) and aid in developing models for disjoining/conjoining pressure (Gupta and Sharma 1992b). However, even fundamental predictions like that of contact angle from a measured conjoining pressure profile have not been made quantitatively. Recently Hocking (1993) proposed a new approach to calculating contact angle which includes the effect of finite inclination of the free surface with respect to the solid substrate (as opposed to just the film thickness as is the case in (6.7)), although it has not been used actually to predict measured contact angles. To complicate the situation further, for some solid/liquid systems ‘dewetting’ will leave behind a thin film instead of a dry surface due to short-range interactions (see Brochard-Wyart *et al.* (1991)); and this complication may be enhanced by the presence of surfactants. These

learnings notwithstanding, it remains a challenge to predict the nucleation of a dry patch quantitatively, beginning from a uniform film.

6.3.3 GROWTH OF HEALING OF DRY PATCHES

Once a rupture is formed, energy arguments of the sort used in fluid statics determine whether the hole will grow or shrink. Surface tension perpendicular to the contact line – which tends to expand the size of the hole – competes with tension parallel to the contact line. The rate of growth, however, depends on film viscosity and this rate, like that of surface leveling, must be viewed relative to the time increment designed for film setting.

Pinholes or dry patches in an otherwise continuous film may either grow in size with the film retracting, or shrink with size and eventually heal should there be sufficient time. If the fluid properties are not changing in time, the growth or shrinkage of the dry patch can be determined by fluid static considerations.

This is a familiar observation in for example a sink where dry patches in thick films or puddles of water on a horizontal surface can be seen to either grow or heal. If the film is thick enough, the effect of gravity (in thick horizontal films) dominates the effect of surface tension to advance the contact line and heal the dry patch. Lamb (1945) and then Taylor and Michael (1973) found that the critical film thickness where this occurs is

$$h_1 = 2 \left(\frac{\sigma}{\rho g} \right)^{1/2} \sin\left(\frac{\theta}{2}\right) \quad (6.8)$$

where σ is the surface tension, g the acceleration of gravity, θ the equilibrium contact angle and ρ is the liquid density. For films greater than this critical film thickness, the continuous film will always have lower free energy than a film with a hole of any size. In thick films, long-range intermolecular forces do not have an appreciable contribution to the energy of the film except at the free surface and contact line. If the film is

thinner than the critical thickness h_1 , then dry patches will grow from a pre-existing hole in the film, if the hole is of sufficient size. In fact, the fate of a hole of radius r_h (see Fig. 6.10) was shown to be a function of static considerations, and properties such as advancing and receding contact angle, gravity, density, and surface tension, and not dynamical properties such as viscosity. For a hole of radius r_h with contact angle θ , there is but some film thickness, h_e , which yields an equilibrium solution to the Young–Laplace equation for hydro-capillary statics. This equilibrium represents a balance between surface tension perpendicular to the contact line, which tends to expand the size of the hole, and the effect of surface tension parallel to the contact line plus gravity (which is negligible for thin films), which tends to close the hole. An important imperfection of this theory comes from the fact that in real systems there is a difference between the recently advanced and receded contact angle, which lead to a range in film thicknesses (or alternatively, hole sizes) over which the hole will be an equilibrium solution. The equilibrium hole radius r_e (or range of radii if there is contact angle hysteresis) increases monotonically with film thickness until at $h = h_1$, $r_e \rightarrow \infty$. Sharma and Ruckenstein (1990) calculate the ratio of equilibrium film thickness to hole radius, h_e/r_h , as a function of contact angle θ and the ratio of hole radius to capillary length, $\Gamma \equiv r_h/(\sigma/\rho g)^{1/2}$. For most coatings the effects of gravity is small, which means that both $\Gamma \ll 1$ and $h \ll h_1$. If the gravity is neglected, Sharma and Ruckenstein (1990) find that a good approximation for h_e/r_h is

$$\frac{h_e}{r_h} = (1 - \cos \theta) \quad (6.9)$$

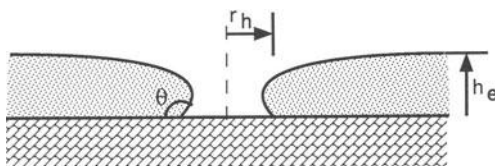


Figure 6.10 Small rupture (hole) in a liquid film.

Note that as θ approaches zero, h_e/r_h also goes to zero. So for a film of thickness h with an initial hole of radius r , if $h/r_h > h_e/r_h$ then the hole will shrink and if $h/r_h < h_e/r_h$ then the hole will grow. The metastable equilibrium state is a maximum in free energy of the system, so to make a hole of radius r_e in an otherwise continuous film of thickness h_e , energy must be added. Sharma and Ruckenstein (1990) argue that it is more likely that holes significantly larger than r_e , for a given film thickness h , form initially because it requires less energy to form the hole, yet they do not address what are the mechanisms for hole formation.

It is interesting to note that there is a correlation between the thickness h_c at which holes form in liquid films, and the equilibrium contact angle shown in Table 6.1. Of course, contact angle is one effect of conjoining pressure (Mohanty 1981) and so the magnitude of conjoining pressure is also apparently related to the critical film thickness h_c ; and so the frequency and size of film ruptures may be greater when the contact angle is greater. According to the theory based on fluid statics, the unstable equilibrium film thickness h_e is related to contact angle by (6.9). Sharma and Ruckenstein (1989) observe that if initial hole size is constant the measurements shown in Table 6.1 can be explained by fluid statics. The initial hole size in coating situations is, however, most often caused by dynamic effects, as is the growth rate of an unstable hole. In a coating, pinholes may be an important defect even if the static contact angle is near zero if there is not enough time for a hole formed by a disturbance to heal. Alternatively, significant dewetting may not occur in a nonwetting film if there is not time for either disturbances to form holes or for holes to grow. Adachi and Marukawa (1992) found the time t_h required for holes to become visible on a rotating roll after a point where the wetted roll is scraped by a knife coater to be

$$t_h = (1500) U^{-1/2} h_0^{2/3} \mu^{1/6} \sigma^{-1/12} g^{-1/4} \rho^{-1/12} \quad (6.10)$$

where U is the roll speed. This is evidence that

dynamics is critical in the rupture and growth of dry patches in contrast to Sharma and Ruckenstein's (1989) observation.

Once a large hole in a thin nonwetting film is formed, the contact line recedes at velocity, v , building up a thick rim of liquid which originally resided over the area of the hole which is evident in photographs shown by Kheshgi and Scriven (1991). Redon, Brochard-Wyart and Rondelez (1991) observed that the contact line of large holes retracts at a constant velocity

$$v \propto \frac{\sigma}{\mu} \theta^3 \quad (6.11)$$

and is independent of film thickness.

The mechanism for film thinning, rupture and contact line retraction is now clear. If a liquid made nonwetting by conjoining forces is thin enough, those forces can rupture the liquid, as demonstrated by the theory of dewetting hydrodynamics. Continuously coated liquid films are ordinarily too thick for conjoining to break them, unless some disturbance thins the film to a thickness of less than 1 μm . If after a film is formed it is thinned by evaporation or by some local film thinning disturbance, then conjoining forces can rupture the film. Examples of film-thinning disturbances were shown by Kheshgi and Scriven (1991) to lead to dry patch formation in nonwetting films: drainage driven by gravity and capillary pressure gradient thins liquid above an underlying gas bubble, and film thinning driven by surface tension gradients caused by airborne surface-active particles impinging on the film. To decrease the likelihood of dewetting, sources of film-thinning disturbances should be removed in order to reduce the number of nucleation sites where dewetting can occur; in addition, the solid or liquid can be treated or altered to lessen the strength of conjoining pressure (contact angle) so that thinner films are stable.

6.4 FILM DRYING

While coatings of concern in this book are applied as liquids, the final coated product is

nearly always a solid film. Films are often solidified by drying, removal of solvent by vaporization at the gas/liquid interface or sorption of the solvent by the substrate. The rate of drying in coating operations can be limited by the mass transfer into the overlying gas, volatility of the solvent, contamination of the liquid/gas interface, or diffusion through the liquid. Film dryers can be designed in response to these phenomena by providing heat, resistance time and enhanced gas-side mass transfer. An overview of drying devices can be found in Cohen (1992b).

6.4.1 GAS-SIDE MASS TRANSFER RESISTANCE

The maximum evaporation rate in a vacuum is given by the Langmuir–Knudsen equation:

$$G = p_e \left(\frac{M}{2\pi R\theta} \right)^{1/2} \quad (6.12)$$

where G is the mass flux, p_e is the equilibrium solvent vapor pressure, R is the gas constant, M is the molecular weight of the solvent and θ is the surface temperature of the liquid film (Knudsen 1946). The kinetic theory of gas diffusion originates from the same line of thought.

At finite rates of vaporization, however, solvent molecules leaving the interface have a chance to collide with others, reducing the actual evaporation rate to (Palmer 1976)

$$G = B p_e \left(\frac{M}{2\pi R\theta} \right)^{1/2} \quad (6.13)$$

In a vacuum the accommodation coefficient, B , is somewhat less than one (Cong and Bird 1978; Kaplon, Kawala and Skoczyłas 1986).

However, most relevant drying situations are not operated in a vacuum, but at near atmospheric pressure. Moreover, in many cases condensation of solvent vapor (e.g. water) in the overlying gas can occur at a rate proportional to the ambient partial pressure, p_a , modifying the mass flux to

$$G = B(p_e - p_a) \left(\frac{M}{2\pi R\theta} \right)^{1/2} \quad (6.14)$$

Near atmospheric pressure the accommodation

coefficient, B , in this formulation must account for diffusion through the overlying gas and is much less than one. Although some have opted to use this formulation for mass flux from the surface (e.g., Bierwagon (1979); Burelbach, Bankoff and Davis (1988)), the more prevalent formulation uses a mass transfer coefficient k which represents the mass flux by

$$G = \frac{k}{p_0} (p_e - p_a) \quad (6.15)$$

where p_0 is a reference pressure.

Drying is often enhanced by agitating the overlying gas and thereby increasing the mass transfer coefficient. The mass transfer coefficient, k , can be approximated by well-known correlations for analogous flows as seen in dryers (Bird, Stewart and Lightfoot 1960). Often gas jets are used to enhance mass transfer, and Martin (1977) gives both theoretical and empirical correlations for common geometries. For example, the correlation for k that Martin finds for a square of hexagonal array of round jets impinging on a flat surface is given by

$$Sh = Sc^{0.42} Re_g^{2/3} F(h_n/d_n, l_n/d_n) \quad (6.16)$$

Here the Sherwood number $Sh \equiv k d_n / D_g$ where d_n is the diameter of the nozzle exit and D_g is the diffusivity of the solvent vapor through the gas. The Schmidt number $Sc \equiv v_g / D_g$ where v_g is the kinematic viscosity of the gas. The gas Reynolds number $Re_g \equiv w_n d_n / v_g$ where w_n is the mean exit gas velocity from the nozzle. The height of the nozzle exits above the surface is h_n , and the distance between neighboring nozzles is l_n . The function F of nozzle geometry is given by Martin (1977). When details of the drying rate dependence on gas flow are needed, the fluid mechanics and mass transfer in the gas phase can be accounted for as is done for a spin coating process by Bornside and Brown (1992).

Drying is not an isothermal process. As the equilibrium solvent vapor pressure, p_e , is often a sensitive function of temperature, film temperature can change the rate of evaporation as given by (6.15). Evaporative cooling of the film slows

drying and must be accounted for when it is an appreciable effect. Drying rate can be increased by heating the surrounding gas, or directly heating the film, thereby increasing the equilibrium vapor pressure of the solvent. While high vaporization rate leads to shorter required residence time for drying, it also can make concentration gradients through the film more severe. For this reason, it is beneficial in some cases to slow down drying.

One source of disturbances to coatings is agitation by motion of the overlying gas. These disturbances often take the form of Dryer Bands which are stripes of film thickness or property variation aligned with the direction of coating translation, or Mottle which is an irregular pattern of variation (see Cohen (1992b)). Analysis (Ruschak 1987) shows that the amplitude variation is dependent on the pattern and intensity of gas motion, coating viscosity and surface tension, gravity and the effects of surfactants (if present). One obvious cure to these defects is to reduce gas agitation in the initial stages of drying until the coating is sufficiently dried or cooled so that its viscosity (or yield-stress) is high enough to resist disturbances.

6.4.2 DIFFUSION LIMITED TRANSPORT WITHIN THE FILM

If removal of solvent at either the liquid/gas or the liquid/substrate interface exceeds the rate of diffusion of the solvent through the liquid to the interface, then the interface will be depleted of solvent and concentration gradients within the film will develop. In polymer solutions, especially, diffusivity decreases markedly with removal of solvent. With continued removal of solvent, transition to a solid state can lead to even smaller coefficients of diffusion of the solvent through the solid and may lock solvent or impurities in the core of the film. In extreme cases 'skinning' can occur, where a solid forms at the interface while the film core remains liquid. At the interface between the gas and the liquid film, surfactants which may be contaminants can also form a solid 'skin' and limit diffusion of solvent from the

underlying liquid to the gas phase, however this phenomenon has yet to receive attention.

Diffusive resistance in films has been analyzed by application of Fick's law of diffusion, conservation of mass and constitutive equations for diffusivity in the material being considered. For a multi-component mixture, conservation of mass dictates that the variation of mass concentration of component i , ρ_i , with time and the one space dimension z perpendicular to the film substrate is given by

$$\frac{\partial \rho_i}{\partial t} = - \frac{\partial g_i}{\partial z} \quad (6.17)$$

where $g_i(z, t)$ is the mass flux of component i in the z -direction. If we assume constant partial specific volume and no flux through the substrate located at $z = 0$, then the fluxes g_i can be attributed solely to diffusion by

$$g_i = - \sum_{j=1}^{n-1} \left(D_{ij} \frac{\partial \rho_j}{\partial z} \right) \quad (6.18)$$

where D_{ij} s are the diffusion coefficients for the n -component system. The movement of the gas/liquid interface due to shrinkage of the film can be accounted for by a coordinate transformation as shown by Vrentas, Duda and Ling (1985). At the gas/liquid interface the boundary condition is that the mass flux is equal to that given by (6.15)

Diffusivity in polymer films can be modeled by the free-volume theory of polymer solvent diffusion laid out by Duda *et al.* (1982); (see also Vrentas and Duda (1979)), although simpler empirical models abound (e.g., Okazaki *et al.* (1974); Blandin *et al.* (1987); Ng and Ross (1991)). Vrentas, Duda and Ling (1985) found, in a study of ternary diffusion in polymer films, that a formulation including a second less-volatile solvent can be used to promote removal of the first solvent, which may be deemed an impurity in the final product. This may be advantageous compared with devolatilization by increasing temperature, since this may lead to degradation of the polymer. Non-isothermal effects in drying

of binary and ternary solutions containing polymer have been studied by Yapel (1988).

In slurry coatings Whithan and Perera (1992); (see also Bierwagen (1979)) find that below a critical moisture content, ϕ_{crit} , the drying rate starts to fall rapidly. They find that this occurs at roughly the liquid content consistent with the maximum packing fraction derived from rheological studies. Drying rate can be explained with a model where diffusivity decreases significantly when the moisture content falls below ϕ_{crit} . A detailed analysis of diffusion for this system, however, remains to be carried out.

Surface tension gradients set up during drying cause flow – and disturbance of film thickness – when there is a gradient of concentration or temperature tangent to the film base. In cases where there is only a gradient normal to the film base there remains potential for the so-called Marangoni instability which manifests itself by forming a hexagonal pattern of roll cells (Pearson 1958; Scriven and Sternling 1960; Anand and Karam 1969). This instability is the cause for well known defects that lead to pigment flocculation, pigment segregation and lack of gloss in paint coatings (Hansen and Pierce 1973, 1974). The instability is expected (Pearson 1958; Scriven and Sternling 1960; Anand and Karam 1969; Kornum and Nielsen 1980) at Thompson or Marangoni's number

$$N_{TH} \equiv \frac{\partial \theta}{\partial z} \frac{\partial \sigma}{\partial \theta} \frac{h^2}{\kappa \mu}$$

greater than a critical value. Here, θ is temperature (or concentration) and κ is the thermal (or molecular) diffusion coefficient.

6.4.3 PHASE TRANSITION

Phase behavior of a multi-component film undergoing drying can impact product quality. Examples have been studied in films containing three components: polymer, solvent and a non-solvent which may serve the purpose of a plasticizer.

In the 'phase inversion' method of membrane

production, phase separation leads to useful properties of the membrane, while in a protective coating, for example, phase separation may lead to a permeable coating which would be of poor quality. Consider the ternary phase diagram shown in Fig. 6.11. This type of phase diagram can be generated from experimental measurements or using a modified Flory-Huggins theory as discussed by Yilmaz and McHugh (1986). What is seen in Fig. 6.11 is that there is a large two phase region bounded by the binodal curve for high concentrations of non-solvent component. Between the binodal and spinodal curve the liquid is metastable and phase separation is slow – time delayed phase separation is important to membrane quality (Tsay and McHugh 1990). In the phase inversion process a film of solvent/polymer is submerged in a bath of non-solvent in order to induce phase separation which gives the membrane beneficial qualities. Phases separation can also lead, however, to various defects. Diffusion during phase separation has yet to receive serious attention with regards to coating.

Diffusion limitation during drying of films

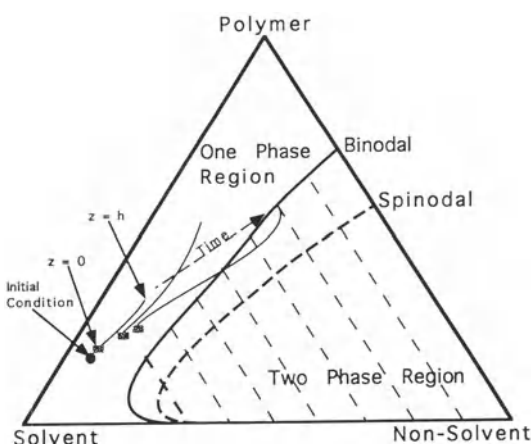


Figure 6.11 Illustrative ternary phase diagram showing a single- and two-phase region. Also shown is the time evolution of film concentration from an initially uniform concentration to depth dependent concentrations.

containing plasticizer, solvent and polymer leads to variation in composition with depth in a drying film, as shown with respect to a phase diagram in Fig. 6.11. If the time-dependent concentration of the film were uniform with depth – no diffusion limitation – the ratio of plasticizer to polymer would remain equal to the initial ratio. However, with diffusion limitation, counter-diffusion of the solvent and plasticizer will, in most cases, lead to an increase in the ratio within the film and a decrease at the free surface (see Adachi and Scriven 1992)). Significant concentration gradients in the film may lead to conditions with the potential of phase separation depicted in Fig. 6.11. While higher plasticizer concentration near the solid substrate may be preferred, because the softening effect of the plasticizer may be of great use near the substrate where stress build-up is greatest and may lead to delamination (peeling), there is also a danger of phase separation.

6.5 STRESS BUILDUP

A liquid film once solidified can evolve to have significant stress buildup. Stress, if beyond some critical value, can lead to stress related defects such as crazing, cracking, curling or peeling. An obvious mechanism for stress buildup is from shrinking of a solid film due to removal (drying) of solvent. Other mechanisms for stress buildup such as phase transitions, phase separations, reactions or temperature changes may well exist, but have not been studied in detail in the context of liquid film coatings.

The buildup of stress leading to defects occurs nonuniformly through the film. Stress is concentrated at inhomogeneities such as cracks or interfaces (at the substrate or within the film between phases) as discussed by Tam, Stolarski and Scriven (1992). Before delving into the complexities of stress buildup, it is instructive to review the theory for homogeneous stress buildup in drying films.

Stress in ordinary (e.g. Newtonian) liquids is nonzero (aside from the isotropic stress which is pressure) only during deformation (a nonzero

rate of strain). This is not the case in, for example, viscoelastic or yield-stress liquids, elastic or plastic solids, and suspensions of solids where stress can exist without concurrent strain. In these materials, stress buildup can be determined by past deformation due, for instance, to drying. The point at which a film goes through a transition from liquid to solid state is often not well defined in practice, although it was a useful approximation in analyses of Croll (1979) and Bierwagon (1979) which will now be recounted.

Croll (1979) found that liquid polymer films (both polyisobutyl methacrylate and polystyrene) underwent a glass transition to an amorphous solid as solvent (toluene) is removed by drying. The transition was detected by measuring the glass transition temperature by a differential scanning calorimeter as a function of solvent volume fraction ϕ . Croll (1979) found the solvent volume fraction to be very nearly proportional to the solvent concentration. Once the glass transition occurs, we should expect the physical properties of the solid to depend rather strongly on solvent concentration. In addition, diffusion will likely limit drying in the solid due to low values of diffusivity. Plasticizers (non-volatile solvents) are sometimes added to allow a final uniform solvent concentration that is sufficient to maintain flexibility in the product and can allow drying of volatile impurities (Vrentas, Duda and Ling 1985), e.g., another solvent.

Bierwagon (1979) considered drying of latex paint films which are suspensions of latex polymer particles in water. As water is removed the polymer coalesces leading to increased elasticity and solid behavior. Bierwagon (1979) modeled this transition to occur when enough solvent was removed so that the particles were close packed. At this point diffusion of the solvent slows, hindering drying of the film. Similar behavior was seen in slurry coatings by Whithan and Perera (1992) who measured rheological behavior and drying rates, and compared these with idealized predictions of the solvent fractions at which the particles would have their densest packing; they found that rheology was correlated with diffusional resistance but not well correlated

with idealized predictions based, for example, on packing of spheres.

Once a transition to solid occurs, further drying causes film shrinkage and stress buildup. Consider a film drying slowly enough that there is little diffusional resistance within the film, so that the volume fraction of solvent ϕ is independent of position. With either type of liquid/solid transition mentioned above, there is a transition solvent volume fraction ϕ_t . It is interesting to note that for the liquid/glass transition the transition solvent volume fraction ϕ_t can be altered by changing (or programming) drying temperature. Removal of solvent reducing the volume fraction below ϕ_t leads to stress buildup.

The extent the solid film shrinks from its volume V_t at the liquid/solid transition to its final volume V_f is related to the volume fraction of solvent by

$$\frac{V_f}{V_t} = \left(\frac{1 - \phi_t}{1 - \phi_f} \right) \quad (6.19)$$

where ϕ_f is the final solvent volume fraction. In a film that adheres to the substrate, this film is fixed in the $x-y$ plane tangent to the film and can only shrink in the direction, z , normal to the film. And so the film is stretched in the $x-y$ plane and compressed in the z -direction giving the strain tensor

$$\gamma = \begin{bmatrix} \gamma_{xx} & 0 & 0 \\ 0 & \gamma_{yy} & 0 \\ 0 & 0 & \gamma_{zz} \end{bmatrix} \quad (6.20)$$

where

$$\begin{aligned} \gamma_{xx} = \gamma_{yy} &= -\frac{1}{2}\gamma_{zz} = \left(\frac{V_f}{V_t} \right)^{1/3} \\ -1 &\simeq -\frac{1}{3} \left(1 - \frac{V_f}{V_t} \right) = -\frac{1}{3} \left(\frac{\phi_t - \phi_f}{1 - \phi_f} \right) \end{aligned} \quad (6.21)$$

The approximation is made for a small extent of shrinkage.

If the material is approximated to be a Hookean

(elastic) solid, then the stress tangent to the film is

$$\begin{aligned}\tau_{xx} &= -\tau_{yy} = -\frac{E \gamma_{xx}}{1-v} \\ &= \frac{1}{3} \left(\frac{E}{1-v} \right) \left(\frac{\phi_t - \phi_f}{1-\phi_f} \right) \quad (6.22)\end{aligned}$$

where E is the Young's modulus and v is the Poisson's ratio. And so if the mechanical properties in the film E and v can be measured, then (6.22) gives an estimate of the stress in the film. It is interesting to note that the residual internal stress does not depend on the thickness of the coating or on the initial concentration of solvent. Estimates of homogeneous stress buildup in films, such as that given by (6.22), can be used to form a criteria for the occurrence of stress related defects.

Diffusion limited drying leads to inhomogeneous distributions of solvent and nonuniform stress buildup. Solidification of the surface prior to the core of the film is responsible, for instance, for a coating defect where the solid skin becomes wrinkled while the film core solidifies leading to nonuniform film thickness. The mechanical properties and the diffusivity vary widely with depth even in the finished product. While this can degrade product quality, this could alternatively be tailored, for instance, to give flexibility near the substrate to give better adhesion, while having a hardened film surface (low solvent fraction near the free surface).

Drying of suspensions of solid particles leads to nonuniform stress buildup due to nonuniform mechanical properties and, if drying is diffusion limited, nonuniform diffusivity. Christodoulou and Lightfoot (1992) examined the consequences of these phenomena in the context of the defect, common in production of graphic arts photographic films, known as 'starry night'. As shown in Fig. 6.1, the defect is caused by internal stresses built up in the upper layer of the coating which push solid particles (matting agent) into the lower coating containing silver halide particles leading to holes or thin spots in the silver halide coating (see, e.g., Gutoff (1993)). Christodoulou and Lightfoot (1992) modeled the nonuniform drying of the film around particles, the nonuniform

stresses that build up, and the motion of the particles in order to understand this defect.

Stress buildup can lead to a variety of defects as shown in Fig. 6.1. Even if stress builds up uniformly in an ideal film, stress will be concentrated at imperfections or boundaries of a film. The defects which occur relieve stress locally. Bierwagon (1979) related stress in films to a critical stress for cracking in order to predict 'mudcracking' in paint films, and found the critical stress does decrease with increasing film thickness. Croll (1979) noted that in drying of polymer films there was a critical stress at which point crazing occurred.

6.6 SUMMARY

Phenomena which occur after coating application often limit coating speed, restrict formulation and affect product quality.

Healing of irregularities in film thickness born during coating application is required in many coating situations such as painting operations. Capillary straightening of liquid surfaces or interfaces can make uniform films on flat substrates. Healing of irregularities requires time and a film of not-too-high viscosity. While the effects of capillary pressure can straighten irregularities of short length quickly, irregularities that span a long extent of coating heal slowly. So healing of irregularities requires a time period after coating before the coating has set and film viscosity or yield stress has risen. However, the action of gravity on inclined or inverted substrates, or capillarity on curved substrates can lead to growth or formation of film irregularities in time. And so formulation of coatings to allow healing of nonuniformly applied films, yet resist subsequent disturbance, is often critical especially for paints.

Liquid films are vulnerable to rupture and film retraction, leading to holes in coatings and dry patches on coated substrates. The mechanism for film thinning, rupture and contact line retraction is now clear. If a liquid film made nonwetting by conjoining forces is thin enough, those forces can rupture the liquid film, as demonstrated by the theory of dewetting

hydrodynamics. However, a quantitative prediction of dewetting has not been successfully made from models of the physical mechanisms: film thinning, conjoining forces and film retraction. Nevertheless, the qualitative description suggests actions. To decrease likelihood of dewetting, sources of film-thinning disturbances should be removed in order to reduce the number of nucleation sites where dewetting can occur; in addition, the solid or liquid can be treated or altered to lessen the strength of conjoining pressure (contact angle) so that thinner films are stable.

Curing and drying of coatings can be rate limiting and defects can occur during this process. Drying is limited by evaporation of solvent from the surface of the film, and diffusion of solvent in the film. Evaporation is often decreased by agitation of the overlying gas and heating of the film. Excessive gas agitation can lead to disturbance of once uniform liquid films. Diffusion limitation can lead to severe gradients of concentration with depth into the coating. This can lead to (Marangoni) instability driven by surface tension gradients, or unwanted phase separation. Control of the rate of drying through dryer conditions, and diffusivity of the components in the coating through coating formulation holds promise for increasing drying rate and reducing the occurrence of defects.

Film rheology changes significantly as the coating is dried. The film usually changes from liquid to solid phase well before the coating is dry. Buildup of stress in the coating can lead to defects such as cracking or peeling. Limiting stress buildup by changing coating formulation or drying conditions, while not fully understood, has long been practiced in the paint coating industry. Translation of this know-how to relatively newer coating applications along with heightened theoretical understanding is an area of future research.

REFERENCES

- Adachi, A. and Scriven, L. E. 1992. Migration of solute during drying. Paper No. 46h. *AICHE, 1992 Spring National Meeting*, New Orleans, March 29–April 2.

- Adachi, K. and Marukawa, T. 1992. The critical film thickness for formation of a pinhole and its growth time. Paper No. 48b. *AICHE, 1992 Spring National Meeting*, New Orleans, March 29–April 2.
- Anand, J. N. and Karam, H. J. 1969. Surface deformation of thin coatings caused by evaporative convection, III. *J. Coll. and Interface Sci.* **31**: 208–215.
- Anshus, B. E. 1973. The leveling process in polymer powder painting – a three-dimensional approach. *A. Chem. Soc. Div. Org. Coating Plastics Chem.* **33**(2): 493–501.
- Batchelor, G. K. 1967. *An Introduction to Fluid Dynamics*. Cambridge: Cambridge University Press.
- Bierwagon, G. P. 1979. Film formation and mudcracking in latex coatings. *J. Coatings Technology*. **51**(658): 163–170.
- Bird, R. B., Stewart, W. E. and Lightfoot, E. N. 1960. *Transport Phenomena*. John Wiley: New York.
- Bixler, N. E. 1982. Stability of coating flows. PhD thesis, University of Minnesota, Minneapolis.
- Blandin, H. P., David, J. C., Vergnaud, J. M., Illien, J. P. and Malizewicz, M. 1987. Modeling the drying process of coatings with various layers. *J. Coatings Technology*. **59**: 27–32.
- Bornside, D. E. and Brown, R. A. 1992. The effects of forced convection in the overlying gas on the rate of mass transfer from the thinning liquid film on a spinning wafer during spin coating. Paper No. 39b. *AICHE, 1992 Spring National Meeting*, New Orleans, March 29–April 2.
- Bousfield, D. W. 1991. A model to predict the leveling of coating defects. *Tappi J.* 163–170.
- Brochard-Wyart, F., di Meglio, J.-M., Quere, D. and de Gennes, P.-G. 1991. Spreading on nonvolatile liquids in a continuous picture. *Langmuir*. 335–338.
- Burelbach, J. P., Bankoff, S. G. and Davis, S. H. 1988. Nonlinear stability of evaporating/condensing liquid films. *J. Fluid Mech.* **195**: 463–94.
- Christodoulou, K. N. and Lightfoot, E. J. 1992. Stress induced defects in the drying of thin films. Paper No. 46c. *AICHE, 1992 Spring National Meeting*, New Orleans, March 29–April 2.
- Cohen, E. D. 1992a. Choosing the coating method. In *Modern Coating and Drying Technology*, eds E. D. Cohen and E. B. Gutoff, pp. 1–22. VCH Publishers: New York.
- Cohen, E. D. 1992b. Thin film drying. In *Modern Coating and Drying Technology*, eds E. D. Cohen and E. B. Gutoff, pp. 266–298. VCH Publishers: New York.
- Cong, T. T. and Bird, G. A. 1978. One-dimensional

- outgassing problem. *Physics of Fluids*. **21**: 327–333.
- Coyle, D. J. 1984. The fluid mechanics of roll coating – steady flows, stability and rheology. PhD thesis, University of Minnesota, Minneapolis.
- Croll, S. G. 1979. The origin of residual internal stress in solvent-cast thermoplastic coatings. *J. Applied Polymer Science*. **23**: 847–58.
- de Lange, P. G. 1984. Film formation and rheology of powder coatings. *J. Coatings Technology*. **56**: 23–33.
- Deryagin, B. V. 1955. The definition and magnitude of disjoining pressure and its role in the statics and dynamics of thin fluid films. *Kolloid Zhurnal*. **17**: 205–214.
- Deryagin, B. V. 1955. *Theory and Stability of Colloids and Thin Films*. New York: Plenum.
- Doughman, D. J., Holly, F. J. and Dohlman, C. H. 1971. Preliminary studies on the stability of aqueous films on solids. Presented at the ARVO Spring Meeting, Sarasota, Florida.
- Duda, J. L., Vrentas, J. S., Ju, S. T. and Liu H. T. 1982. Prediction of diffusion coefficients for polymer-solvent systems. *AIChE J.* **28**: 279–285.
- Frenkel, J. 1946. *Kinetic Theory of Liquids*. Oxford: Oxford University Press.
- Gaver, D. P. and Grotberg, J. B. 1992. Droplet spreading on a thin viscous film. *J. Fluid Mech.* **235**: 399–414.
- Gupta, A. and Sharma, M. M. 1992a. Stability of films on solid surfaces I. ellipsometric measurement of disjoining isotherms for aqueous films bounded by glass and mercury. *J. Colloid and Interface Sci.* **149**: 392–406.
- Gupta, A. and Sharma, M. M. 1992b. Stability of films on solid surfaces II. a model for aqueous bounded by dissimilar charge regulating surfaces. *J. Colloid and Interface Sci.* **149**: 407–424.
- Gutoff, E. B. 1993. Avoid coating and drying defects. *Chem. Eng. Prog.* **89**: 49–55.
- Hahn, F. J. 1971. Cratering and related problems. *J. of Paint Tech.* **43**: 58–67.
- Hansen, C. M. and Pierce, P. E. 1973. Cellular convection in polymer coatings – an assessment. *Ind. Eng. Chem. Prod. Res. Develop.* **12**: 67–70.
- Hansen, C. M. and Pierce, P. E. 1974. Surface effects in coatings processes. *Ind. Eng. Chem. Prod. Res. Develop.* **13**: 218–225.
- Hocking, L. M. 1993. The influence of intermolecular forces on thin fluid layers. *Phys Fluids A*. **5**: 793–799.
- Huh, C. and Scriven, L. E. 1971. Hydrodynamic model of steady movement of a solid/liquid/fluid contact line. *J. Coll. Interf. Sci.* **35**: 85–101.
- Jensen, O. E. and Grotberg, J. B. 1992. Insoluble surfactant spreading on a thin viscous film: shock evolution and film rupture. *J. Fluid Mech.* **240**: 259–288.
- Joos, F. M. and Jacobmeyer, R. L. 1992. Levelling of a liquid layer over a sorbing surface. Paper No. 49d. AIChE, 1992 Spring National Meeting, New Orleans, March 29–April 2.
- Kaplon, J., Kawala, Z. and Skoczylas, A. 1986. Evaporation rate of a liquid from the surface of a rotating disc in high vacuum. *Chem. Eng. Sci.* **41**: 519–522.
- Keunings, R. and Bousfield, D. W. 1987. Analysis of surface tension driven leveling in viscoelastic films. *J. Non-Newt. Fluid Mech.* **22**: 219–33.
- Kheshgi, H. S. 1984. The motion of viscous liquid films. PhD thesis, University of Minnesota, Minneapolis.
- Kheshgi, H. S. 1989. Profile equations for film flows at moderate Reynolds numbers. *AIChE J.* **35**: 1719–1727.
- Kheshgi, H. S. and Scriven, L. E. 1983. Measurement of liquid film profiles by moiré topography. *Chem. Eng. Sci.* **38**: 525–34.
- Kheshgi, H. S. and Scriven, L. E. 1988. The evolution of disturbances in horizontal films. *Chem. Eng. Sci.* **43**: 793–801.
- Kheshgi, H. S. and Scriven, L. E. 1991. Dewetting: nucleation and growth of dry regions. *Chem. Eng. Sci.* **46**: 519–26.
- Knudsen, M. 1946. *The Kinetic Theory of Gases*. Methuen, London.
- Kornum, L. O. and Nielsen, H. K. R. 1980. Surface defects in drying paint films. *Progress in Organic Coatings*. **8**: 275–324.
- Lamb, H. 1945. *Hydrodynamics*. Dover, New York.
- Martin, H. 1977. Heat and mass transfer between impinging gas jets and solid surfaces. In *Advances in Heat Transfer*. eds J. P. Harnett and T. F. Irving Jr. New York, Academic Press, **13**: 1–60.
- Mohanty, K.K. 1981. Fluids in porous media: two-phase distribution and flow. PhD thesis, University of Minnesota, Minneapolis.
- Munter, J. D. 1990. Attenuation of cell patterns for gravure coating. Paper No. 51f. AIChE, 1990 Spring National Meeting, Orlando, Florida, March 19–22.
- Ng, K. C. and Ross, D. S. 1991. Diffusion in swelling gelatin. *J. of Imaging Science*. **35**: 356–361.
- Okazaki, M., Shioda, K., Masuda, K. and Toei, R. 1974. Drying mechanism of coated film of polymer solution. *J. of Chem. Eng. Japan*. **7**: 99–105.
- Orchard, S. E. 1962. On surface levelling in viscous liquids and gels. *Appl. Sci. Res.* **11**: 451–464.
- Padday, J. F. 1971. Cohesive properties of thin films

- of liquids adhering to a solid surface. In *Special Discussion Faraday Soc. on 'Thin Liquid Films and Boundary Layers'*, pp. 64–74. London: Academic Press.
- Palmer, H. J. 1976. The hydrodynamic stability of rapidly evaporating liquids at reduced pressure. *J. Fluid Mech.* **75**: 487–511.
- Pearson, J. R. A. 1958. On convection cells induced by surface tension. *J. Fluid Mech.* **4**: 489–500.
- Pearson, J. R. A. 1960. The instability of uniform viscous flow under rollers and spreaders. *J. Fluid Mech.* **7**: 481–500.
- Pitts, E. and Greiller, J. 1961. The flow of thin liquid films between rollers. *J. Fluid Mech.* **11**: 33–50.
- Quach, A. 1973. Polymer coatings. Physics and mechanics of leveling. *Ind. Eng. Chem. Prod. Res. Develop.* **12**(2): 110–116.
- Redon, C., Brochard-Wyart, F. and Rondelez, F. 1991. Dynamics of dewetting. *Phys. Rev. Letters.* **66**(6): 715–18.
- Ruschak, K. J. 1987. Flow of a thin liquid layer due to ambient disturbances. *AIChE J.* **33**: 801–807.
- Schwartz, L. W. and Eley, R. R. 1992a. Numerical simulation of post-application flows, including flows arising from surface tension gradients. Paper No. 48i. AIChE, 1992 Spring National Meeting, New Orleans, March 29–April 2.
- Schwartz, L. W. and Eley, R. R. 1992b. Coating flows on complex surfaces. Paper No. GI4. 1992 APS Fluid Dynamics Division Meeting, Tallahassee, November 22–24.
- Scriven, L. E. and Sternling, C. V. 1960. The Marangoni effects. *Nature.* **187**: 186–188.
- Sharma, A. and Ruckenstein, E. 1986. An analytical nonlinear theory of thin film rupture and its application to wetting films. *J. Coll. Interf. Sci.* **113**: 456–479.
- Sharma, A. and Ruckenstein, E. 1989. Dewetting of solids by the formation of holes in macroscopic liquid films. *J. Coll. Interf. Sci.* **133**: 358–368.
- Sharma, A. and Ruckenstein, E. 1990. Energetic criteria for the breakup of liquid films on nonwetting solid surfaces. *J. Coll. Interf. Sci.* **137**: 433–445.
- Sheludko, A. 1967. Thin liquid films. *Advances in Colloid and Interface Science.* **1**: 391–464.
- Smith, N. D. P., Orchard, S. E. and Rhind-Tutt, A. J. 1961. The physics of brushmarks. *J. Oil Colour Chemist's Assoc.* **44**: 618–633.
- Spitz, G. T. 1973. Leveling in powder coatings. *Amer. Chem. Soc. Div. Org. Coating Plastics Chem.* **33**: 502–507.
- Tam, S., Stolarski, H. K. and Scriven, L. E. 1992. How to analyze defect-related stresses in drying films. Paper No. 48f. AIChE, 1992 Spring National Meeting, New Orleans, March 29–April 2.
- Taylor, G. I. and Michael, D. H. 1973. On making holes in a sheet of fluid. *J. Fluid Mech.* **58**: 625–639.
- Teletzke, G. F. 1983. Thin liquid films: molecular theory and hydrodynamic implications. PhD thesis, University of Minnesota, Minneapolis.
- Teletzke, G. F., Scriven, L. E. and Davis, H. T. 1987. How liquids spread on solids. *Chem. Eng. Commun.* **55**: 41–81.
- Trefethen, L. M. 1972. Surface tension in fluid mechanics. *Illustrated Experiments in Fluid Mechanics.* ed. A. H. Shapiro, MIT Press, Cambridge, MA.
- Tsay, C. S. and McHugh, A. J. 1990. Mass transfer modeling of asymmetric membrane formation by phase inversion. *J. Polymer Science.* **B28**: 1327–1365.
- Vrentas, J. S. and Duda, J. L. 1979. Molecular diffusion in polymer solutions. *AIChE J.* **25**: 1–24.
- Vrentas, J. S., Duda, J. L. and Ling, H.-C. 1985. Enhancement of impurity removal from polymer films. *J. Applied Polymer Science.* **30**: 4499–4516.
- Wehausen, J. V. and Laitone, E. V. 1960. Surface waves. *Handbuch der Physik.* ed. S. Flugge, **9**: 446–778.
- Whitham, G. B. 1974. *Linear and Nonlinear Waves.* John Wiley, New York.
- Whitman, P. K. and Perera, W. 1992. Prediction of coating thickness and drying rate for forced air dried slurry coatings. Paper No. 46i. AIChE, 1992 Spring National Meeting, New Orleans, March 29–April 2.
- Williams, M. B. and Davis, S. H. 1982. Nonlinear theory of film rupture. *J. Coll. Interf. Sci.* **90**: 220–228.
- Yaple, A. 1988. A physical model of the drying of coated films. MS thesis, University of Minnesota, Minneapolis.
- Yiantios, S. G. and Higgins, B. G. 1991. Rupture of thin films: nonlinear stability analysis. *J. Coll. Interf. Sci.* **147**: 341–350.
- Yilmaz, L. and McHugh, A. J. 1986. Analysis of nonsolvent-solvent-polymer phase diagrams and their relevance to membrane formation modeling. *J. Appl. Polymer Sci.* **31**: 997–1018.

NOTATION

- a* amplitude of irregularity
- a_i* coefficients in (6.6)
- B* accommodation coefficient
- Bo* Bond number, $h_0^2 \rho g / \sigma$
- D_g* binary diffusion coefficient of solvent vapor through gas

D_{ij}	multicomponent diffusion coefficient for component pair $i-j$	t_0	unit of time measure, $3l^3\mu/\sigma h_0^3$
d_n	nozzle diameter	$T_{1/2}$	dimensionless time for sinusoidal disturbance to level to half its initial amplitude
E	Young's modulus	u	liquid velocity in x -direction
F	function of nozzle geometry	U	roll speed
g	acceleration of gravity	v	contact line speed
G	mass flux	V_f	final film volume
G_i	mass flux of component i	V_t	final volume at liquid/solid transition
h	film thickness	w_n	mean exit gas velocity
H	dimensionless film thickness, h/h_0	x, y	spatial coordinate along and normal to the solid/liquid interface
h_c	film thickness below which spontaneous formation of holes is observed	X	dimensionless x -coordinate, x/x_0
h_e	equilibrium film thickness for a hole of radius r_h	z	spatial coordinate perpendicular to the solid/liquid interface
h_l	film thickness above which gravity prevents formation of holes		
h_n	distance between nozzle exit and surface		
h_0	mean film thickness and unit of film thickness measure		
k	mass transfer coefficient	α	wave number of irregularity, h_0/ℓ
l	characteristic length scale parallel to substrate	γ	strain tensor
l_n	distance between neighboring nozzles	Γ	capillary length, $r_h/(\sigma/\rho g)^{1/2}$
M	molecular weight	ε	dimensionless amplitude, a/h_0
N_{TH}	Thompson number	θ	contact angle
p_a	ambient partial vapor pressure	Θ	temperature
p_e	equilibrium solvent vapor pressure	κ	thermal (or molecular) diffusion coefficient
p_0	reference pressure	μ	liquid viscosity
R	gas constant	ν	Poisson's ratio
r_e	equilibrium hole radius for a film of thickness h	ν_g	gas kinematic viscosity
r_h	hole radius	Π	disjoining potential
Re	film leveling Reynolds number, $\rho h_0^4 \sigma / 3 \mu^2 l^3$	ρ	liquid density
Re_g	gas Reynolds number, $w_n d_n / v_g$	ρ_i	mass concentration of component i
Sc	Schmidt number, v_g / D_g	σ	surface tension
Sh	Sherwood number, $k d_n / D_g$	τ_{xx}	xx component of the stress tensor
t	time	ϕ	solvent volume fraction
T	dimensionless time, t/t_0	ϕ_{crit}	critical moisture content for a suspension of particles
t_h	time for hole to become visible	ϕ_f	final solvent volume fraction
		ϕ_t	solvent volume fraction at liquid/solid transition

Greek letters

PART TWO

**METHODS OF INVESTIGATING
COATING PROCESSES**

Peter M. Schweizer

7.1 INTRODUCTION – VALUE OF EXPERIMENTAL METHODS

Experiments – operations carried out under controlled conditions in order to discover an unknown effect or law, to test or establish a hypothesis, or to illustrate a known law – as defined in Webster's dictionary, are the basis of scientific knowledge and hence, their value is paramount. In the beginning of science, there were only experiments. Later, experimental observations combined with human ingenuity led to the formation of theoretical models. Finally, mathematical tools have been developed to solve the theoretical models for arbitrary and complex applications. Today, most branches of science are characterized by the fact that some aspects are well known and can accurately be modeled, but other aspects need yet to be investigated and clarified. This is also true for coating technology. It was recognized long ago that science advances most effectively, if experiments and the development of theories and analyses are carried out in concert. Macosko and Scriven (1984) have called this balanced concept the 'three-legged stool', and Savage *et al.* (1992) have named it the 'tripartite approach.'

A coated product that can be marketed – a photographic film or a floppy disk – for example, is the result of a manufacturing process acting on and interacting with a coating solution. Typically, the coating solution is composed of various chemical components and/or emulsions and dispersions, e.g. light sensitive emulsions for

photographic materials, metallic dispersions for magnetic recording media, polymers, surfactants and cross-linking agents. The manufacturing process comprises sub-process or unit operations like film formation, dynamic wetting, solidification, drying, etc. A product with desired and well specified properties can only be manufactured if the performance of the relevant unit operations and the actions and interactions of the chemical components among themselves and in conjunction with the unit operations are understood and controlled. Photographic films and papers, for example, consist of several layers each of which contains a variety of chemical components that affect photographic and physical aspects of the final product. In modern manufacturing operations these layers are coated simultaneously and it is therefore not surprising that there exist no theoretical models that can completely describe the performance of such complex systems, much less accurately predict the properties of the coated product. Consequently, experiments are a crucial part of product development activities. For many branches of the coating industry, the following classes of experiments are typical:

- studying the effects of single solution components on the product performance;
- studying the effects of component interactions in single- or multi-layer films;
- studying unit operations of the coating process, e.g. film formation, film flow on an inclined plane, dynamic wetting, etc;

- studying product manufacturability in terms of capacity (maximum coating speed) and yield (various coating defects), i.e. determining the coating window;
- optimizing product and process performance with respect to quality and manufacturability criteria;
- scaling-up from pilot to production operation;
- testing of raw materials.

If experiments are essential, so are the methods and methodologies used to carry them out. The subject of this chapter is to discuss experimental methods and methodologies that are relevant for studying coating flows and their limits with respect to the uniformity of the coated film. While the methods presented will focus on laboratory applications, the methodologies, which guarantee an effective use of the methods, can also be applied to computer experiments with ease.

Section 7.2 presents not only tools and instruments (including pilot coating machines and sensors to measure various parameters), but also methods to gather data effectively (experimental design plans) and evaluate them (quantification of film thickness uniformity). Section 7.3 focuses on applications with regard to film thickness, surface topography, fluid velocity and flow visualization. Section 7.4 is a picture album, showing visualizations of various flow fields of slide coating. The purpose of the photographs is to compare characteristic features of the flow fields as a result of variations in operating and geometrical parameters. Finally, Section 7.5 is an outlook, offering thoughts on the direction of future developments of experimental methods, that may help to advance the understanding of coating processes further.

Obviously, there exists a very large number of experimental methods that have been or could be applied toward studying coating flows. It is not the purpose of this chapter, however, to present all these methods nor to compile a complete list of references. Instead, only a few techniques suitable to investigate a broad variety of important coating flow aspects have been selected. Along the same line, selected equipment

manufacturers or software vendors are cited throughout the chapter. The author has either had personal experience with these methods, instruments, or software packages, or they have generally been accepted by industrial and academic coating engineers. No intention exists to particularly endorse those manufacturers or vendors that are cited in the chapter, nor to discriminate against those that are not listed.

If the discussion in this chapter occasionally appears to be biased toward coating processes and experimental methods predominantly used in the manufacturing of photographic products, it is because the author had over 15 years of experience in this sector of industry. However, with a bit of imagination on the part of the reader, many of the methods can equally well be applied to other types of coating processes in other segments of the coating industry.

Further references to experimental methods can be found throughout this book, particularly in Chapter 3 on wetting, Chapter 4 on surfactants, and Chapter 5 on coating rheology.

7.2 TOOLS, INSTRUMENTS AND METHODS

The purpose of experiments is to generate knowledge in the form of ‘know-how’ or, preferably, ‘know-why.’ In most industrial companies, the research and development environment in which such experiments are carried out is controlled by an associated business unit. This implies the need for effective and efficient experimental work in order to contribute to the financial success of the business unit. While effectiveness (doing the right thing) is expressed by long-term and short-term strategic and action plans, efficiency (doing things right) is determined by the tools, methods, methodologies and skills that are available to carry out experiments.

Experimental skills can be learned in school, but above all, they are acquired through hands-on work in the laboratory. Apart from a broad knowledge of tools and techniques, experience combined with theoretical understanding of the area of interest are the basis for good experimental work. Equally important are personal qualities of

the experimentalist such as resourcefulness, perseverance, love of detail, etc. As far as equipment and instruments are concerned, they often require considerable capital investments. To spend the money wisely, it is therefore important to know the goals of the experiments and the most effective way of reaching those goals.

7.2.1 PILOT COATING EQUIPMENT

In most cases, it is not economical to perform experiments on production machines. Instead, a set of pilot coating machines is necessary. The number and types of machines can be deducted from the activities (such as those listed in Section 7.1) that need to be performed in a particular environment. Generally, pilot coating machines should meet the following requirements:

- adequate solution preparation facilities and delivery systems, see for example Schweizer (1992);
- more capabilities in terms of speed and variation of geometrical parameters than the production machine;
- multiple coating modes, e.g. extrusion, bead, curtain, various roll configurations;
- single- and/or multi-layer;
- narrow coating width;
- light and/or dark operation (for coating light-sensitive products);
- setting (gelatinization), curing and drying facilities, if samples are needed.

An overview of pilot coating machines suitable

for process and product development in the photographic industry has been published by Gellrich *et al.* (1991). According to our own experience, two types of pilot machines have proven themselves extremely valuable for setting up flow visualization experiments, and for investigating the fluid mechanics and physical principles of various coating flows.

The first one is a simple table-top rig, consisting of a (scraped) coating roller and some means of delivering the fluid to the coating point. Geometrical flexibility is the key feature as demonstrated in Fig. 7.1, where three exemplary configurations are shown.

The fluid, often a water-glycerin or a polymer solution at room temperature, is recirculated by a suitable means, for example a gear pump, or a pressurized solution supply vessel. There is no web involved, so no coating samples can be obtained, nor can the effects of dynamic wetting as they exist in production coating operations be studied precisely. In spite of these deficiencies, the setup is a good general learning tool, and it is perfect for flow visualization experiments. Moreover, qualitative features of flow fields such as shapes and locations of free surfaces can be investigated, and conditions for the onset of various vortices or flow instabilities such as ribbing can be determined quantitatively. Even the dependence of the onset of air entrainment (dynamic wetting) upon relevant process parameters can be studied, at least qualitatively. Last but not least, investment and operating costs are low.

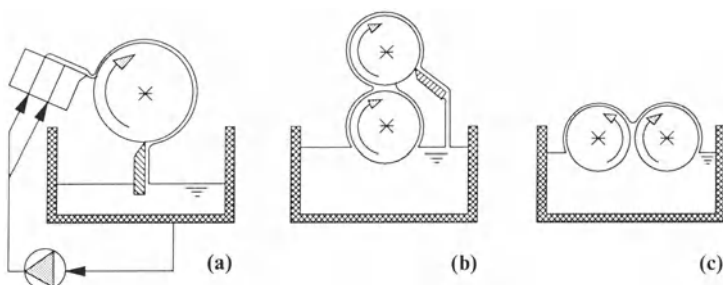


Figure 7.1 Schematic configurations for table-top pilot coating rigs: (a) slide coating; (b) forward roll coating; (c) film splitting.

The second type is a narrow-width coating machine with web transport. It can be operated either continuously or in a loop mode, see schematic layout in Fig. 7.2 as designed in principle by M. Gueggi and M. Pasquier, senior mechanical engineers at Ilford AG. In the continuous mode, the coated liquid is neither set nor dried but scraped off the web prior to winding. Dynamic wetting can be studied, and boundaries of coating windows can be determined exactly. In the loop mode, an air box is activated which sequentially supplies cold air for chilling/setting and warm air for drying. With adequate mechanical design and process control, the setting and drying steps of a production machine having multiple dryer sections can be simulated. If need be, a curing/cross-linking step can be added or mounted in place of the chilling/setting and/or drying steps, depending on the particular products that are being investigated. Coating samples can be obtained, and hence the machine is suitable for studying edge effects, splice coatability, start-ups and defects such as cross bars, lines, diffuse streaks, mottle, repellencies, etc.

Apart from edge effects, which are confined to about 1 cm on each side, successful coating flows are essentially two-dimensional. This is true for many coating modes such as slot, extrusion, slide, curtain, roll, blade and dip spin coating. In practice, however, the aforementioned coating flows are often characterized by unwanted three-dimensional features related to instabilities or

other defects, not only along the lateral edges of the flow, but also in the supposedly two-dimensional inner region. In addition, coating modes such as gravure, wire rod and spray coating feature free surfaces with highly three-dimensional structures, at least immediately after the application point and before the spreading, coalescing and leveling processes are completed. The dimensions (wave length) of these structures are typically small compared with the coating width. In any case, the coating width of a pilot machine can be minimized in order to minimize investment and operating costs. The maximum coating width can be estimated from the requirement that 'a few' typical repeats of relevant cross-web disturbances must be included; for most applications, 10 to 30 cm are sufficient. On a 30 cm wide machine operated in the closed loop mode, additional savings may be possible by coating two subsequent 10 cm stripes side by side on the same web loop.

Coating equipment is worth nothing without the proper coating fluid. In a pilot environment, the preferred fluids often have test or model character in that they contain none, or only a partial number, of chemical additives found in final products, but they are able to simulate real coating solutions in terms of their rheological behavior or other characteristic responses, for example with respect to the addition of surfactants.

One of the simplest model fluids is an aqueous glycerin solution. It shows Newtonian flow

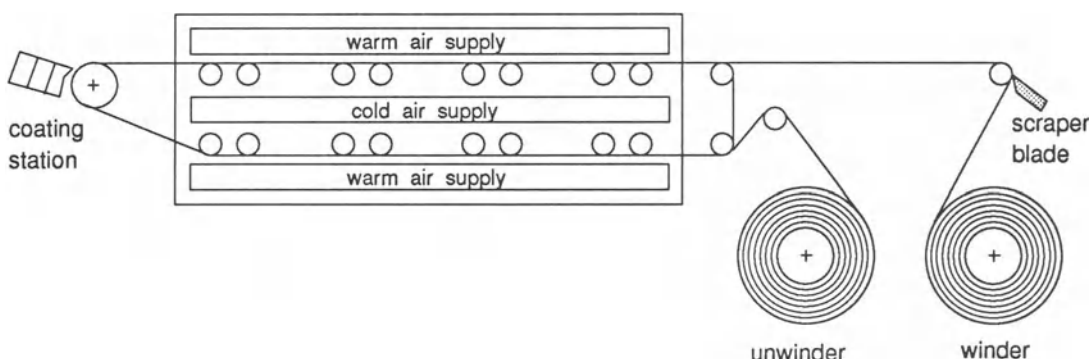


Figure 7.2 Schematic diagram of multipurpose pilot coating machine: continuous and closed-loop coating modes.

behavior up to shear rates of at least 10^4 s^{-1} , it is clean, transparent, odorless, and its viscosity can easily be adjusted between one and several hundred mPas by changing the glycerin concentration. At high concentrations, viscosity control becomes more difficult, because, owing to the hygroscopic nature of glycerin, fluctuations of the relative humidity in the surrounding air may alter the solution concentration and hence its viscosity. Glycerin solutions do not gel or cure, which is why they are not suitable for studies where samples of the coated film are needed. However, they can be worked with at room temperature, which makes them very attractive for investigations on pilot coating rigs such as those shown in Fig. 7.1. Glycerin solutions are well suited for flow visualization experiments (see Section 7.3.4), and, at least qualitatively, for studying issues of flow stability, e.g., determination of the onset of ribbing lines (see Chapters 11a, 11b, 12a), or the phenomenon of air entrainment.

If samples of the coated film are needed for further evaluation of the coating uniformity, or if the real coating solutions exhibit non-Newtonian flow behavior, then a polymer solution with setting or curing properties is more appropriate as test fluid. Gelatin solutions, for example, have proven useful. Much like glycerin solutions, they are clean, transparent, odorless, and their viscosity can be adjusted over a wide range simply by changing the gelatin concentration. To prevent unwanted setting and gelling, the operating temperature has to be kept above ambient, at about 40°C . The rheological behavior of gelatin solutions can be characterized with a Carreau-type constitutive equation (Chapter 5; Bird, Armstrong and Hassager 1977). The low shear rate viscosity and the time constant that indicates the transition between Newtonian and power law behavior are functions of the gelatin concentration (Blake, Clarke and Ruschak 1994). In contrast, the power law index seems to be independent of the concentration.

The value of the power law index, and other rheological characteristics of gelatin or other polymeric solutions, such as the level of elasticity, can be altered by adding small amounts of a

different polymer component, for example, latices, surfactants and thickening agents such as polysaccharides or sulfonated polystyroles. Typically, the best type and the optimum concentration of a polymer additive needed to simulate a real coating solution is found by trial and error. This matching process relies on accurate measurement of fluid properties both for the test and the real coating solutions. Suitable methods for measuring static and dynamic surface tensions as well as rheological properties are described in detail in Chapters 4 and 5, respectively, as well as in the book by Makosko (1994).

7.2.2 SENSORS

The purpose of sensors is to measure the degree of uniformity of the coated film, and to quantify relevant parameters of coating flows such as fluid velocities, pressures and temperatures. Here, the word 'sensor' refers to instruments and methods suitable for assessing film thickness, surface topography, fluid velocities and other features revealed by flow visualization. Several sensors will be described in detail in Section 7.3.

Sensors capable of reading relevant parameters of coating flows must work in contactless modes so as to not disturb the flow. Depending on the parameter of interest, they must be able to capture a two-dimensional area of the coating, or they must be focused on a point. Moreover, they are in motion relative to the flow or the web, either in a parallel or perpendicular direction. Some features are best detected on-line during the coating process, while others are more easily measured off-line from a test sample. On-line measurements can be done at the wet end of the coating machine (immediately after the application of the liquid layer), or at the dry end (after the drying or curing process). Regardless of the measurement system used, they all must meet very stringent requirements on resolution, particularly in the vertical direction, because typical wet film thicknesses are on the order of 10 to 1000 μm or less, and dry film thicknesses are one to two orders of magnitude smaller. In addition, film thickness variations must be kept below 1%

in many applications to ensure acceptable product uniformity, for example photographic films and papers with typical coating widths between 1 and 2 meters.

As will be shown below, most sensors and instruments suitable for coating flow research use radiant energy, which – ideally – emits from a uniform source, impinges on the coating, is altered by desirable or undesirable features (defects) in the coating, and is received either in transmission or reflection by a detector. In practice, measurement systems are found whose wavelengths of the radiant energy cover a wide range of the electromagnetic spectrum, including beta radiation, x-rays, micro waves, ultraviolet, visible and infrared light. Not all types of radiation are equally suited to detect all types of features, because of diffraction limited focusing constraints and consequent problems with spatial resolution. An important class of sensors working in the visible wavelength range are cameras combined with appropriate illumination, see Section 7.3.4.

The state of successful coating flows is not only two-dimensional but also steady. In reality, however, transient situations exist such as start-up or inception of a defect. In recent years, these transients have caught the interest of coating engineers, because their fundamental understanding contributes to yield increases. Consequently, there is a need for suitable sensors that can either freeze a rapidly changing situation, or resolve it in sufficiently small time intervals. Flash lights and stroboscopes are examples of the former category, while the latter one includes traditional silver halide high-speed photography and modern high-speed video cameras, see Section 7.3.4.

7.2.3 EXPERIMENTAL DESIGN METHODS

Any manager of research and development activities, be it in an industrial company or at a university, has the responsibility to assure that such activities are carried out efficiently and generate a maximum ‘return on investment.’ In this context, ‘return’ means specific results and

increased knowledge about the subject matter at hand, and ‘investment’ refers to time as well as human and material resources spent on such activities.

Work efficiency is determined by many factors. They include employing a R&D staff with adequate formal education and/or professional experience, making available properly designed and well equipped experimental pilot machines, and offering access to powerful computer hard- and software. Another factor we particularly would like to point out is called the method of statistical experimental design (SED). This subject was developed several decades ago, and it is extensively described in the literature. Selective examples of textbooks are Draper and Smith (1966), Montgomery (1984), and Deming and Morgan (1986). Software packages that have proven themselves useful for PC applications include ECHIP and Statgraphics for design and evaluation of experiments, and SAS for data analysis. Addresses of these software houses are included in the list of references.

Deming and Morgan (1986) have stated that ‘statistical treatment is no substitute for good data, and good data comes from a well designed set of experiments.’ Experimental design is a powerful tool to determine the number and placing of experimental conditions to obtain the desired information with a minimum of expenditure of resources.

Even though the method of SED has been proven useful time and time again, we have observed that not every engineer or scientist is readily willing to work with it. There are many reasons which explain this reluctance. Sometimes, the relatively large number of experiments requested at the beginning of an investigation may be a deterrent, because it is hoped that the desired information can be obtained with much less effort, i.e. varying just one or two parameters and hoping that the so-determined optimum is not only of local but global nature (home run syndrome). Sometimes, a problem may be viewed with too narrow a perspective, thereby missing important parameters which would have been necessary to obtain a complete understanding of

the problem. This oversight may then make the problem look small enough so as to not resort to a SED but rather hope for a ‘home run.’ Reluctance may also come from the fact that a successful application of experimental design requires thinking before experimenting, because questions like ‘will the desired information help to solve the problem?’ and ‘can the desired information be quantified?’ must be answered positively.

On the other hand, the benefits of experimental design are significant. As mentioned above, the method has the highest return on investment of any alternative approach, which is substantiated, for example, by the ease of fitting an empirical or stochastic model (usually a mathematical equation) to the data. This ease is based on the optimal placing of experimental conditions. The expression ‘stochastic’ points to a residual term in the model which allows to account for uncertainty. The term ‘empirical’ describes models in which the transformation between the dependent and the independent variables is not known or cannot be presumed. The process of model building itself is empirical, for there are no recipes to tell which model is best. Experience has shown that nature is often well approximated, if the mathematical equation takes the form of a polynomial or power-law function. Another promising approach is graphical data analysis by comparing the experimental curve with a variety of generic curves that can be found in mathematical handbooks (Abramowitz and Stegun 1965, Daniel and Wood 1971).

Proper statistical data treatment and model building is important because it not only allows one to correctly identify important parameters and interactions between parameters, but also to test the goodness of the model by performing an analysis of variance (ANOVA). Furthermore, replication of experiments, which is requested in most experimental design plans, provides the basis for estimating the magnitude of imprecision in the experimental process. Finally, statistical data treatment and model building is a perfect way of condensing the desired information into a user-friendly tool for further applications such

as sensitivity analysis of the desired result with respect to variation of relevant process parameters.

For complex problems, the number of experiments needed to obtain the desired information can quickly increase. For a full-factorial design where all independent parameters are varied simultaneously over several levels (Montgomery 1984), the number of experiments is equal to the number of parameter levels raised to the power of number of parameters. One way of reducing the experimental efforts is using dimensionless numbers. According to the Π -theorem, or Buckingham theorem (Buckingham 1914, Grassmann 1971), any process or system that can be described by a functional relationship among q parameters, whose units may be given in terms of u fundamental units (i.e. length, mass, time, temperature, electrical charge, etc.), may also be written as a function of $(q-u)$ dimensionless groups. Dimensionless representations have the additional advantages of being independent of units, and of indicating the ratios of forces that act on a particular process or system. On the other hand, they are less transparent for practical applications because the latter are always described by dimensional parameters.

Another way of reducing the experimental efforts is applying a sequence of screening and optimizing. During screening, a coarse experimental design plan is carried out to identify relevant parameters and discard irrelevant ones. Subsequently, an optimum is sought by performing a second, finer experimental design plan with only the relevant parameters.

Many different experimental design plans have been developed, each of which is characterized by particular advantages and disadvantages. In contrast to the so called one-parameter method (one parameter is varied systematically while all other parameters are held constant), methods of the class called factorial experiments vary all parameters simultaneously over several levels. Names of well known plans include simplex design, star design, central composite design, full factorial design, fractional factorial design, Box–Behnken design, etc. The

reader is referred to the references for detailed descriptions and optimum choice for a particular application.

Traditionally, statistical experimental design methods refer to experiments performed in the laboratory. This restriction is unnecessary, because the same methods could very well be applied to experiments carried out on a computer using an established mechanistic model. To date, however, the one-parameter method has been preferred in most publications where coating flows have been examined theoretically by using numerical methods to solve the momentum and continuity equations. While this approach allows one to visualize and explain physical principles, results, often obtained with considerable computational effort, remain of limited practical use, because they are still presented in a form that does not allow interpolation for conditions not specifically treated in the study. This is particularly true for complex multidimensional systems, even if highly developed techniques for tracking desired flow states at reduced computational efforts are used, for example multiparameter continuation combined with critical point tracking (Yeckel and Scriven 1992).

Obviously, we are convinced of the benefits of statistical experimental design methods. However, it is not a fool-proof tool that will automatically solve all existing problems. Instead, as with any other tool, it must be applied wisely and when appropriate. In particular, the application of SED is not a free pass to neglect thinking. Rather, it is necessary to state clearly the problem at hand and to develop the objectives of the experiments. Appropriate application of the methodology refers mainly to that class of experiments where the basic process is well established and the goal is to find optimum operating conditions for the process. This is in contrast with another class of experiments where the main interest is focused on identifying, verifying or visualizing certain physical mechanisms. Here, as in still other situations, for example those that incorporate hysteresis due to multiple flow states (Kistler 1983), the application of SED is more difficult, if not inappropriate.

7.2.4 QUANTIFICATION OF COATING UNIFORMITY

Most experiments are more meaningful, if the desired information – often some aspect of film thickness uniformity – can be quantified in an objective and reproducible manner. In fact, quantification of dependent variables is a requirement for proper evaluation of statistical experimental designs. In reality, however, the uniformity of coated products is often assessed by visually comparing a sample against a set of standards. Typically, there are standard sets for various types of coating defects, mottle for example, whereby each sample of the standard is assigned a numerical value, indicating a different level of the defect. Quality assessment of this kind is often performed by individuals and can be somewhat subjective.

The situation described above is rooted in the early years of coating technology because there was nothing else available then. Today, in the age of highly developed sensor technologies, coating quality can be measured objectively and represented in terms of amplitude and frequency or wavelength, in terms of statistical parameters, or in other desirable ways. Usually, the uniformity of the coated film is captured by an optical sensor, and the desired quality information is extracted by way of image processing and/or suitable data analysis and treatment.

It is often advantageous or necessary to amplify coating defects for better evaluation, either before detection by using, for example, the moiré technique (see Section 7.3.2), or after detection via digital image processing such as algorithms for contrast enhancement, etc. If coating processes are studied with model fluids, dyes and color filters have proven themselves very useful. Coating defects can be made more visible, if their color corresponds to the most sensitive wavelength of the detector.

The uniformity of colored layers in simultaneously coated multi-layer color photographic materials can be assessed in detail by looking at a sample through an appropriate set of color filters. Unfortunately, experience has shown that

defect patterns of individual color channels, as they are seen by electronic sensors and expressed in units of optical density, do not necessarily agree with the superimposed defect patterns of all color channels together, as seen through the eyes of the quality inspector. This discrepancy prevents optimum feedback from Quality Control to the Process Development Department, which in turn may slow down the process of eliminating coating defects. The discrepancy can be reduced, if the optical density variations per color channel of a defective coating are translated into coordinates of a colorimetric system, for example the chromaticity diagram as developed by the International Commission on Illumination, C.I.E. (Williamson and Cummins 1983).

Often, quality attributes of coated materials are judged by subjective perception of customers. The method called multidimensional scaling (MDS) is a suitable tool to quantify objectively such quality assessments (Torgerson 1958, Lyne and Parush 1983). MDS is a statistically based metric scaling technique which permits the identification, separation and quantification of the factors used by people to judge image quality. Numerical values of these quality factors can be related to image analysis measurements and other known parameters that distinguish the test samples. The test procedure requires a controlled environment with regard to illumination and sample preparation. The judges are asked to compare pairs of test samples, and to indicate with a check mark on a continuous scale (from 'exactly alike' to 'completely different') the degree of difference seen, as well as to indicate with a check mark on another scale (from 'prefer A' to 'prefer B') the preference between samples A and B. The judges are not instructed as to which factors should be used in making their assessment of difference and preference.

There are many roads that lead to the quantification of coating uniformity. Early attempts by the author involved two-dimensional CCD cameras for on-line capture of coating quality, mottle for example, and sophisticated image analysis hardware in combination with various image analysis algorithms to manipulate,

enhance and evaluate film thickness nonuniformity. While this elaborate and expensive approach may be necessary in some applications, it seems, in retrospect, exaggerated for many cases because success can only be achieved with large and long-term deployment of resources.

A simpler but quite successful approach is the use of Fourier analysis for treating one- or two-dimensional data on film thickness uniformity. While this technique is limited to signals that contain some kind of periodicity, or that can be converted to periodic signals, it is still very useful because there is a host of coating defects that satisfy this requirement, such as lateral cross profile, bands of diffuse longitudinal streaks, mottle, ribbing lines, cross bars, etc. Here, periodic coating nonuniformities are first captured by a suitable sensor, e.g., a CCD array. Next, the discrete (sampled) signal is subjected to a fast Fourier transformation (FFT) to represent coating uniformity in terms of amplitude and spatial frequency or wavelength. Today, FFT is readily available as part of various software packages for personal computers, for example MathCAD or LabWindows. Moreover, an introduction to Fourier analysis can be found in the book by Lynn (1983).

If a coating defect with a characteristic and dominant frequency is the subject of the investigation, it can be isolated by multiplying the spectral information with a low-pass, high-pass or band-pass filter. The cut-off frequencies of the filter are determined either by analyzing the frequency spectrum, by measuring the wavelength of the defect on the coated sample, or by trial and error. The resulting information may be examined in the frequency domain, or it may be transferred back into the original parameter space.

The power of this technique is demonstrated by the following example provided by Rossier (1992). A narrow stripe (*ca.* 3 cm wide, *ca.* 1.3 m long) of a full-width sample of a color photographic film was uniformly exposed and processed. Then, the optical density in each of the three color channels cyan, magenta, and yellow was measured at discrete points spaced apart by about 0.5 cm.

These raw signals represent the widthwise density distribution; an example is shown for the cyan channel in Fig. 7.3. Subjecting this signal to a Fourier transformation, multiplying the resulting spectrum with a low-pass filter (whereby only defects with a wavelength of once or twice the web width can pass), and performing an inverse Fourier transformation on the filtered signal, allows one to extract a long-wavelength cross profile which comprises a symmetrical and an asymmetrical component, see Fig. 7.4. If the low-pass filter is replaced by a band-pass filter, in this case allowing nonuniformities with a wavelength between 2 and 10 cm to pass, a defect called ‘bands of diffuse longitudinal streaks’ can be visualized, see Fig. 7.5. Here, diffuse refers to the edges of the streaks, indicating not a sudden but a gradual change in film thickness.

The challenge of quantifying coating uniformity lies in reducing the available data, and in representing the degree of coating imperfection with as few parameters as possible. In what follows, a model is developed for deterministic

signals to express the coating uniformity with a single parameter called quality index.

Consider a generally periodic signal obtained from a single scan across the coated web containing bands of diffuse streaks as shown in Fig. 7.5. In Fig. 7.6, a similar signal is depicted schematically; it can be characterized by four parameters, namely the mean value B (DC-component), the deviation A from the mean value (AC-component), the length λ indicating the size of the deviation, and the length C measuring the distance between adjacent deviations. Here, W is the width of the final product format.

A model relating these parameters to the coating uniformity can now be constructed by considering that the visual perception of an imperfection increases with

- increasing ‘visibility’ of the imperfection, i.e. the ratio of deviation to mean value, A/B ;
- increasing contrast of the imperfection, i.e. the spatial rate of change of the signal (slope of curve), represented in a simple way by the ratio A/λ ;

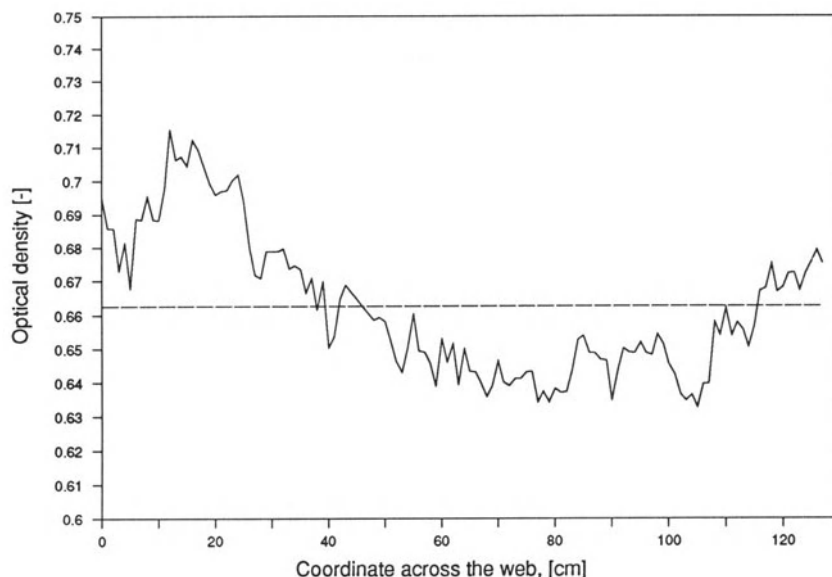


Figure 7.3 Unprocessed signal of optical density distribution on a full-width sample. Horizontal line = mean density value. From Rossier (1992).

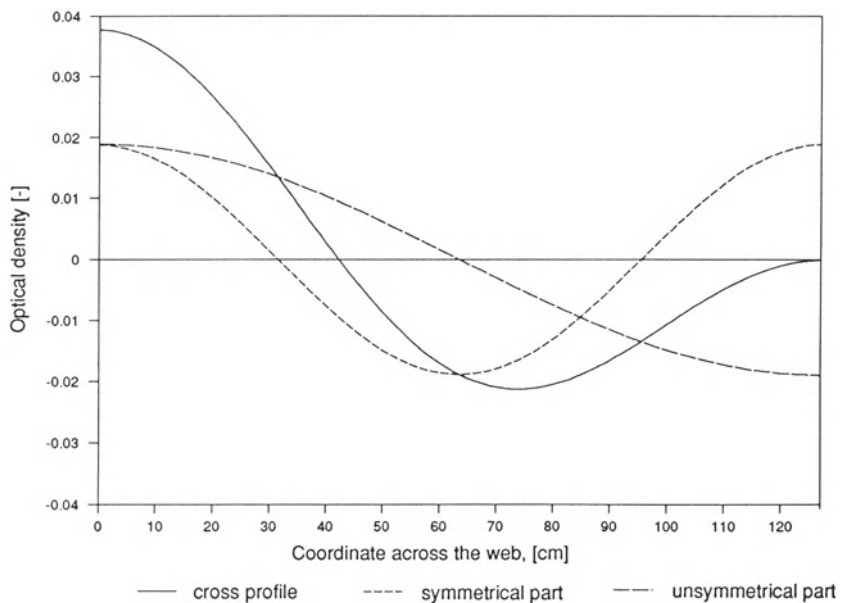


Figure 7.4 Low-pass filtered signal from Fig. 7.3, showing the densitometric cross profile, and its symmetrical and asymmetrical components. From Rossier (1992).

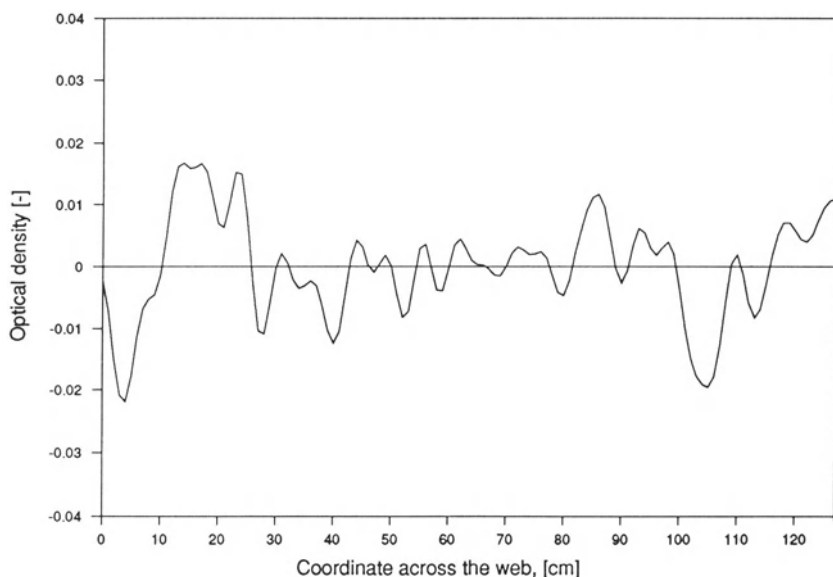


Figure 7.5 Band-pass filtered signal from Fig. 7.3, showing a defect called 'diffuse longitudinal streaks'. From Rossier (1992).

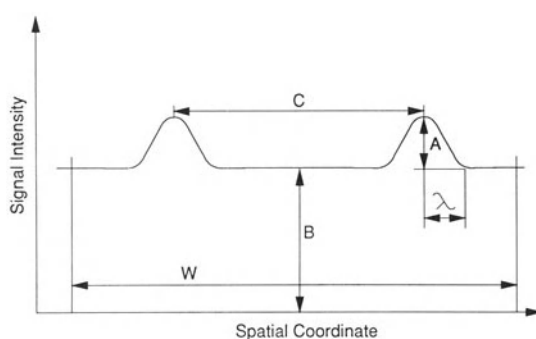


Figure 7.6 Schematic signal of a nonuniform film thickness profile.

- increasing number of imperfections, i.e. the ratio of format width to spacing of the imperfections W/C .

The quality index, QI , is the product of these three factors

$$QI = \frac{A}{B} \frac{A}{\lambda} \frac{W}{C} = \frac{A^2 W}{B \lambda C} \quad (7.1)$$

The smaller the quality index, the better is the coating uniformity. The parameters in equation (7.1) are obtained from appropriate signal processing, for example by computing the mean value and the standard deviation of the signal to get A and B , and by performing a Fourier analysis (FFT) to get λ and C .

A set of eight test samples has been constructed by superposing stripes of transparent optical filter sheets having different optical densities and widths to form rectangular wave trains with varying A , B , C and λ . The ranking of these samples by a group of test persons was in good agreement with the ranking as computed by equation (7.1).

If the raw signal of the coating uniformity is not deterministic but contains a large stochastic component, the above described approach for quantification does not work, because even though several measurement traces from the same sample would result in several different (deterministic) signals, their mean value of the deviation from uniformity is zero. Such signals must be charac-

terized statistically, for example by computing the ratio of standard deviation to signal average. This parameter corresponds to the first term in equation (7.1); it is a special case for which the quality index can only be computed without distinct frequency information. For the signal in Fig. 7.5, the parameter takes the value of $0.008315/0.663 = 0.013$.

A more informative way of characterizing stochastic signals is using amplitude and frequency information extracted from the power spectrum of the signal, because power spectral information does not zero-out for stochastic signals (Shulman 1970).

Examples of this approach, which was developed to quantify the severity of mottle, are shown in Figs 7.7 and 7.8 (Rast 1989). Here, mottle is a sensitometric defect found in photographic products coated on uneven paper support. Mottle has characteristic wavelengths ranging from 1 to 10 mm; it is thought to be caused by liquid leveling after coating due to an egg-carton-like surface topology of the paper. Even though mottle is an area-wide defect, it appears to be isotropic, at least in some cases, i.e. its spectral response does not strongly depend on the direction of measurement across the web.

In Fig. 7.7, the optical density information of a mottle pattern in the cyan channel of a color paper as captured by a one-dimensional CCD camera and treated by a FFT is presented in the frequency domain in terms of the logarithm of the amplitude A , and the square root of the wave number σ . σ is defined as $1/\lambda$, with λ being the characteristic wavelength of the disturbance in millimeters. The lack of a dominant frequency peak is apparent, indicating the stochastic nature of the signal. Nevertheless, the mottle pattern can be characterized and quantified by two parameters, namely the extrapolated amplitude A_0 at wave number $\sigma=0$ ($\lambda=\infty$), and the wave number $\sigma_{1/2}$ corresponding to an amplitude of $A_0/2$.

A_0 and $\sigma_{1/2}$ are extracted from the spectrum by approximating the curve with a suitable analytical expression. In the example at hand, equation (7.2) is a best fit for mottle application; it has

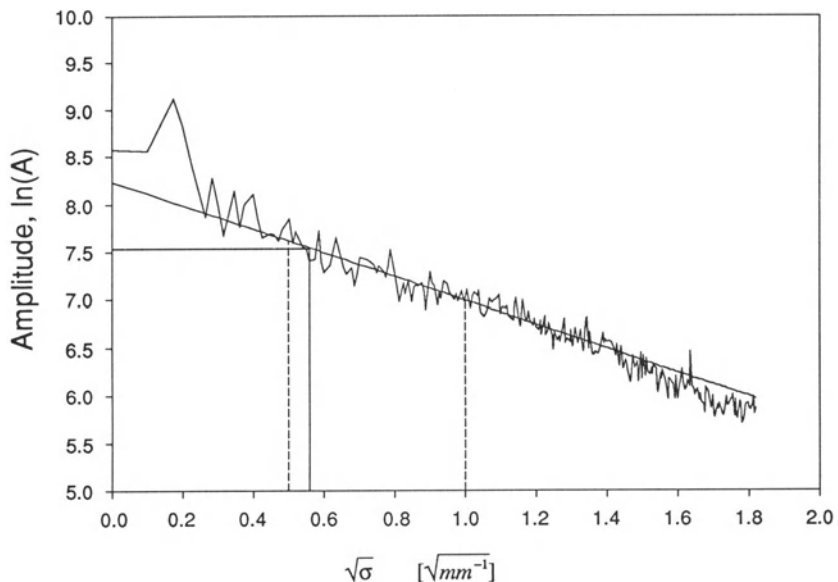


Figure 7.7 Frequency spectrum of a coating defect called mottle. $A_0 = 3728.2$, $\sigma_{1/2} = 0.312$. From Rast (1989).

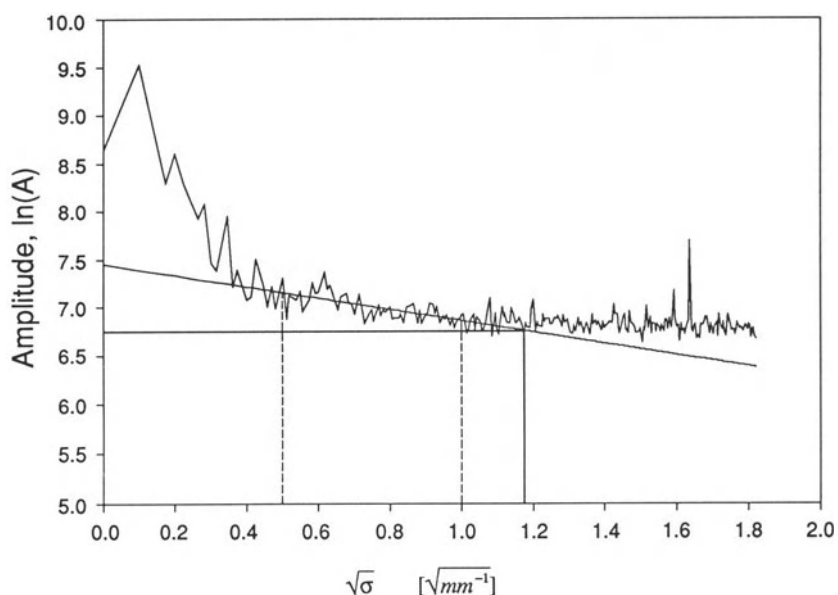


Figure 7.8 Frequency spectrum of a coating defect called mottle. $A_0 = 1716.4$, $\sigma_{1/2} = 1.395$. From Rast (1989).

been found by trial and error, and it is shown as solid lines in Figs 7.7 and 7.8. To evaluate A_0 and $\sigma_{1/2}$, only that portion of the spectrum in terms of wavenumber is used that is relevant for the defect under consideration; here, $0.25 \text{ mm}^{-1} < \sigma < 1.0 \text{ mm}^{-1}$, corresponding to $1 \text{ mm} < \lambda < 4 \text{ mm}$.

$$A(\sigma) = A_0 2^{-(\sigma/\sigma_{1/2})^{0.5}} \quad (7.2)$$

As shown in Fig. 7.8 for the yellow channel of a different type of color paper, the parameters A_0 and $\sigma_{1/2}$ have changed compared with Fig. 7.7, because process and product related parameters such as viscosity, density, surface tension, coating speed and layer thickness are different.

Once the product uniformity has been quantified, quality criteria or threshold levels must be specified to separate acceptable from unacceptable uniformity. This task is dependent on the particular application, for example format size, and whether the product is transparent or opaque in the case of photographic products. This task is also rather difficult because, beyond the parameters contained in equations (7.1) or (7.2), such criteria must account for the sensitivity of the customer's eyes to spatial frequencies (Campbell and Robson 1968) and spectral wavelengths of nonuniformities (Cornsweet 1970; Kueppers 1973). In practice, however, acceptability thresholds are often set subjectively against a particular reference or 'standard' sample. Objective measures can then be defined from measurements on the standard.

7.3 APPLICATIONS

7.3.1 FILM THICKNESS

There is an abundance of scientific literature describing film thickness measurement methods. The material that follows, however, focuses only on a few techniques that have proven themselves useful for fundamental coating flow studies and for routine quality surveillance of production coating processes.

An important class of non-contacting measurement devices utilizes a point source that emits radiation of a particular frequency range in the electromagnetic spectrum, and a detector that

measures the loss of energy due to selective absorption by the coated film. For transparent films, the energy absorption is described by Lambert's law, which states that equal paths in the same absorbing medium absorb equal fractions of the light that enters them (Longhurst 1973).

$$I_t = I_0 e^{(-KH)} \quad (7.3)$$

where I_0 is the incident energy, I_t is the transmitted energy, H is the coating thickness, and K is the absorption coefficient. If the absorbing substance is a solution, then its absorption coefficient is directly proportional to the solution concentration. This statement is called Beer's law; it is valid, if the absorbing power of a molecule is not affected by the proximity of its neighbours (Longhurst 1973).

Depending on the frequency or wavelength of the emitted energy, different measurement methods are distinguished. Infrared absorption, microwave absorption, and x-ray fluorescence belong to this class of measurement technique; they are described in more detail in the following sections.

7.3.1.1 Infrared absorption

This measuring technique is concerned with wavelengths λ from the near (0.7 to 3.5 μm) and mid (up to 20 μm) infrared spectrum. Infrared energy is produced by any hot or incandescent object; hence, simple low-watt halogen bulbs are sufficient and often used as energy source.

When infrared radiation is passed through a film or coating, some of it is selectively absorbed (Hindle 1984). This loss of energy is due to the vibrational excitation of particular molecules present in the material. Furthermore, the loss of energy is characterized in the electromagnetic spectrum by an absorption band whose mean wavelength is indicative of the absorbing molecule, and whose depth is proportional to the loss of energy and hence to the film thickness. In Fig. 7.9, the absorption spectrum of a polyethylene film is shown. The spectral curve contains a trough (band of maximum absorption or minimum transmission) with a maximum depression at a wavelength of 2.32 μm . Examples of absorption

peaks for other hydrocarbon groups include polyester at $3.4\text{ }\mu\text{m}$ and polystyrene at $2.1\text{ }\mu\text{m}$. Wet films of aqueous coatings, or equivalently, the water content of a coated film can be gauged by using the absorption band of the -OH hydroxyl radical at $1.94\text{ }\mu\text{m}$. As the absorption is selective in all cases, the components of the air, including moisture, do not significantly affect the radiation at these wavelengths.

Once the absorption band of a particular molecule is known, it can be isolated with an optical reference filter (narrow band-pass filter), which means that only a narrow portion of the spectrum around the absorbed wavelength is considered. In Fig. 7.9, the interference filter is schematically indicated by a hatched spike at $\lambda=2.32\text{ }\mu\text{m}$. Using a second interference filter placed outside the absorption band (second hatched spike near $\lambda=2.2\text{ }\mu\text{m}$ in Fig. 7.9) provides a means of determining what would have been the incident light level I_0 at the absorbing wave-length. By applying equation (7.3) to both locations of the interference filters, it can be derived that the film thickness is proportional to the logarithm of the ratio of the detected transmitted energy at these two wavelengths according to

$$H = \frac{1}{K_2 - K_1} \ln\left(\frac{I_{t1}}{I_{t2}}\right) \quad (7.4)$$

The proportionality factor, the inverse of the

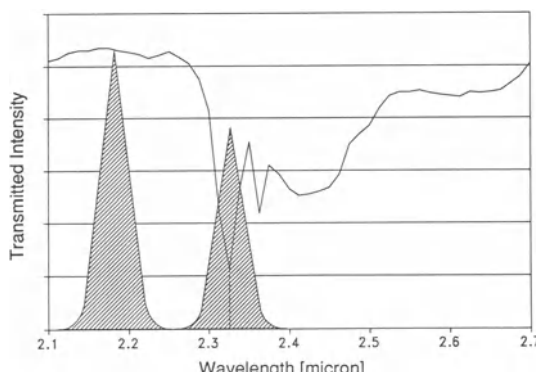


Figure 7.9 Infrared adsorption spectrum of a $50\text{ }\mu\text{m}$ thick polyethylene film. From Hindle (1984).

difference of absorption at the two wavelengths, must be determined via calibration.

The infrared method has been highly developed by equipment manufacturers, for example Moisture Systems Corporation, or Infrared Engineering Limited. It is possible to measure a great variety of coatings on metal, paper or plastic substrates. Moreover, problems associated with interference fringes on very thin and flat films, with light scattering due to pigments and fillers, and with measuring the thickness of a coating whose absorption band is very close to or even overlapping with the one of the substrate, have been solved (Hindle 1984; Edgar and Stay 1985). However, some critical issues remain that warrant a cautious use of the method; they include coatings on highly reflective substrates, and influence of the measurement signal by lateral gloss variation in scanned applications. Moreover, variations in the moisture trapped within the substrate can mask subtle changes due to nonuniformities in the coating.

Characteristic specifications of the infrared method are listed in Table 7.1 together with similar data for other measurement methods. The compilation of the table caused some difficulties as there is no consistent way by which manufacturers specify the performance of their equipment. Furthermore, most manufacturers offer several equipment classes, each of which covers a different range of application. Finally, in most cases, the optimum attainable performance depends on the particular application and should be discussed with a qualified specialist. Hence, the numbers indicated in the table are not absolute but rather 'ball park' figures. The term 'accuracy' indicated in the table as $\pm\%$ is a measure for the vertical resolution of the measurement system relative to its range of application.

7.3.1.2 Microwave absorption

Microwaves, covering wavelengths between 1 cm and 1 m in the electromagnetic spectrum, have long been used to determine the relative moisture content of materials. In early applications, that property could only be obtained by additional

Table 7.1 Performance comparison between film thickness measurement methods

Method	Range (μm)	Accuracy $\pm\%$	Sampling time (s)	Sampling area (mm)	Scan velocity (cm/s)
Infrared	2–150	>0.5	>0.2	\varnothing 10	<4.2
Microwave	1000	>1	>1	\varnothing 5–10	—
X-ray fluorescence	depends on several factors	1–10	>5–100	\varnothing 30	<7.5
Capacitance gauge	<500	>0.1	>0.001	\varnothing 5	<3

densitometric measurements, because, in the lower frequency range around 1 GHz, the electrical properties of many materials are influenced by ionic conductivity and other effects. However, the need for such extra efforts was eliminated by operating microwave guides above about 10 GHz (Meyer and Schilz 1980).

In later applications, the use of microwaves for measuring the thickness of liquid films has also been considered (Roy *et al.* 1986; Hurley, Kaufman and Roy 1990). Instruments are typically operated either in the attenuation mode or in the phase mode. In the attenuation mode, the amount of microwave power absorbed by a material is proportional to its water content. On the other hand, the phase mode depends on the measurement of the propagation velocity of electromagnetic waves through a material. The waves experience a larger phase delay per unit length of travel in a structure containing material with a high dielectric constant, such as water, than in the same structure with a low dielectric value.

The response of microwave guide systems as a function of the film thickness is slightly nonlinear, and a calibration procedure is required prior to use. Performance specifications are listed in Table 7.1. Compared with other methods, microwave absorption is not suitable to measure very thin films. COMPUR Electronic GmbH is a vendor of microwave moisture meters.

7.3.1.3 X-ray fluorescence

X-ray fluorescence (XRF) is primarily a spectrometric technique where, in a shielded envi-

ronment, the sample is irradiated with a low-level radioactive source (x-rays). An x-ray photon ejects an electron from the inner shell of an atom and an outer shell electron drops to fill the vacancy. The difference in orbital energy causes the outer electron to fluoresce and emit an x-ray during the transition (Asoma Instruments 1992). The energy (wavelength) emitted by the electron depends on the type of transition which has been made, i.e. it is indicative of the type of atom that has been excited. Once the equipment has been calibrated, coating thickness is determined by measuring the x-ray intensity of excited atoms; this procedure is known as the x-ray emission method. The relation between intensity and thickness is typically nonlinear, although it can be linearized for thin coatings, Fig. 7.10. As the

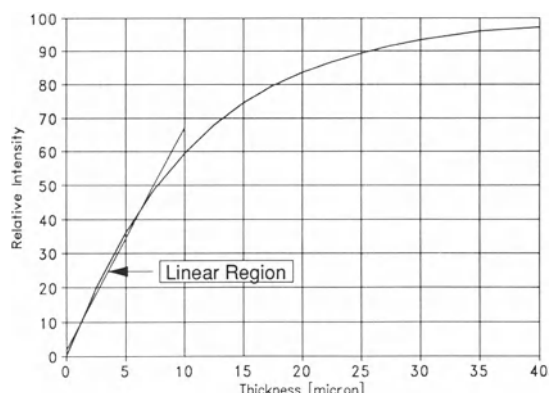


Figure 7.10 Zinc coating on aluminum. Intensity of zinc coating x-rays relative to the intensity of an infinitely thick zinc coating versus the thickness of the coating. From Asoma (1992).

incident x-rays are absorbed by the coating they can only penetrate a certain distance into the film. Hence, the application of this method is limited by a maximum film thickness, defined by the American Society for Testing and Materials (ASTM A-754) to be $3/\mu_e$, with μ_e being the mass absorption coefficient of the coating for the detected x-rays.

XRF is capable of detecting a great number of atoms ranging from aluminum to uranium. For example, the method has been used to detect Ag in photographic films, Fe in coating of magnetic recording media, Si and Ti in paper, etc. However, several x-ray sources are needed to cover the entire range, which necessitates a proper adaptation of the source to a particular measurement application. The level of radioactivity of the source is normally low enough so that no special licence to process or operate is required.

If the coating does not contain any elements detectable by XRF, its thickness can still be determined by exciting suitable atoms in the substrate and measuring the absorption and attenuation of the resulting x-rays by the coating (x-ray absorption attenuation method). Now the method can be described by the Beer–Lambert

law (equations 7.3 and 7.4), and a typical response curve is shown in Fig. 7.11 (Asoma Instruments 1992). If both the coating and the substrate contain no detectable elements, an excitable backing specimen may be added, and the absorption of the x-ray by the substrate and the coating can be recorded. However, this approach is only reliable if the thickness variations in the substrate are minimum.

Asoma Instruments is a vendor of XRF equipment. Typical performance characteristics are presented in Table 7.1. To achieve good accuracy, reliable standards for calibration are necessary, preferably similar to actual coatings. Surface cleanliness and flatness influence the attainable accuracy. One drawback to this method is the relatively long sample times necessary to acquire accurate mean values. Consequently, the sample rate is low, which will greatly reduce the maximum scan coverage, if the measuring head is scanned across a traveling web.

7.3.1.4 Capacitance gauging

The electrical capacitance, C , of a parallel plate capacitor is given by

$$C = \epsilon_0 \epsilon_r \frac{A}{D} \quad (7.5)$$

where ϵ_0 is the permittivity of the free space or the dielectric constant of the vacuum ($\epsilon_0 = 0.885 \times 10^{-11} \text{ A s/V m}$), ϵ_r is the dielectric constant of the medium between the plates (for example paper: $\epsilon_r \approx 4.0$, Mylar polyester: $\epsilon_r \approx 3.1$), A is the plate area and D is the distance between the plates. Capacitance varies with the distance between two conductive plates, thus this electrical principle can be used for contactless displacement gauging between a flat plate sensor and a grounded target plate, or for measuring the thickness of a nonconductive film by moving the film between the sensor and the grounded metallic backplane. In the latter case, the capacitance changes according to material thickness, which is proportional to the dielectric constant. After scaling for the dielectric constant of the film, the signal

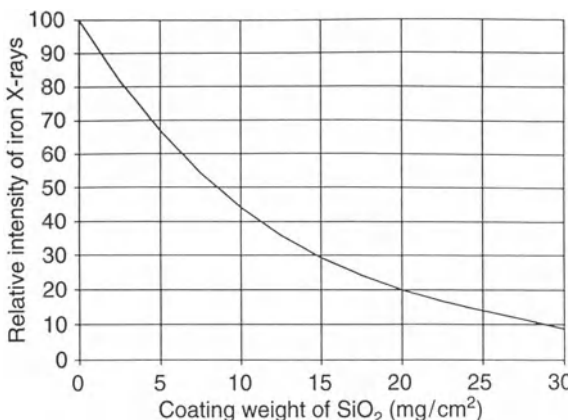


Figure 7.11 XRF response of a substrate as a function of the thickness of a film containing no elements detectable by XRF. Example: Intensity of iron x-rays as a function of the coating weight of a SiO_2 film. From Asoma Instruments (1992).

can be converted into a thickness value (McRae 1988; Ayers 1993).

All other parameters being equivalent, the signal output from a capacitance gauge is proportional to its sensor area. This means that the signal-to-noise ratio, the signal stability, and the vertical resolution improve with larger sensors, at the expense of reduced spatial resolution in the film plane. A possibility to improve spatial resolution without reducing the sensor size is to use a rectangular 'stripe' sensor instead of the usual round sensor. However, as spatial resolution worsens in the orthogonal direction, this option is sensible only in certain applications. A high vertical resolution can only be obtained, if the sensor surfaces are placed closely together, typically just a few hundred microns. This fact may render the application of the technique critical, if the film thickness must be measured on an unsupported (fluttering) web. Performance specifications for capacitance gauges are listed in Table 7.1. An example of a supplier of such instruments is Lion Precision Corporation.

Applications of capacitance probes to measure film thickness of coating flows have been shown to be accurate and convenient, particularly in pilot coating rigs with stainless steel coating rolls of relatively large diameters, such as those shown in Fig. 7.1. Examples of experimental data of such investigations can be found in Spiers, Subbaraman and Wilkinson (1974), and Tharmalingam and Wilkinson (1978).

Capacitance gauges are also used to measure the uniformity of thin gaps and slots as they exist in extrusion dies and coating hoppers or between pairs of cylinders in roll coating operations. Here, the probe is shaped like a button and mounted in a thin shim for support. Capacitec is a supplier of such instruments. Gaps as narrow as 300 µm can be measured with a probe diameter of 4 mm and a claimed vertical resolution of 1 µm. Reliable measurements depend on a tight fit of the probe in the gap; this in turn makes the delicate probe susceptible to mechanical damage, if the probe has to be inserted deep into the gap and pulled across the width of the gap (coating width). In practice, a compromise between ease of measure-

ment and accuracy of the obtained results should be sought.

7.3.2 SURFACE TOPOGRAPHY

Surface topography describes the configuration of a surface including its relief and the position of characteristic features. Topography does not provide any information about what happens below the surface. In contrast, film thickness measures the distance between the surface and an interface located below the surface. In general, film thickness cannot be inferred from knowledge of the topography. To illustrate this situation, consider a process where a liquid film is coated onto an uneven substrate characterized by a sinusoidal waviness. Assuming conformal coating, then, immediately after coating, the film thickness will be uniform throughout, but the topography of the free surface will show the same nonuniformity as the substrate. As time proceeds, the liquid film will level due to gravity and surface tension forces until a new equilibrium state is reached. Now, topographical information will show a perfectly flat surface, while the film thickness profile is nonuniform according to the sinusoidal waviness of the substrate.

7.3.2.1 Profilometry

Instruments that probe the film surface in a raster-like fashion by way of mechanical or optical sensors are called profilometers. Film thickness must be inferred by calculating the difference between the coated sample and the uncoated reference surface. As this is a rather cumbersome process, profilometers are typically not used for film thickness measurements but for the assessment of surface topography. Tactile sensors (similar to the pick-up needle of a record player) make physical contact with the test surface, hence, they are not suitable for measuring liquid films. Moreover, their measurement rate is relatively low compared with optical sensors, two of which are worth mentioning and are described in more detail below (Blum *et al.* 1990).

The triangulation method utilizes a laser beam

that is focused onto the test surface and viewed at a fixed angle by a position-sensitive detector. When the target moves in the direction of the incident beam, the light spot moves accordingly on the detector, which can be converted into a displacement of the test surface relative to the detector. The method is characterized by high sampling rates (up to 40 kHz), high vertical and lateral resolutions (0.5 µm and 100 µm, respectively), a large measurement range (10 mm), and a moderate working distance (3 to 5 cm). Best results are achieved on mat or rough surfaces that are opaque. A drawback leading to measurement errors is attributed to the fact that the incident light beam may partly penetrate into the test surface, if the latter consists of an optically transparent material such as a polymer film. In this case, the light seen by the detector no longer originates from the test surface, but from some unknown location beyond the surface. A supplier of laser displacement meters based on the triangulation principle is KEYENCE Corporation.

In the auto-focus method, a laser beam is focused onto the test surface so that the distance between the focusing lens and the surface is held constant by a dynamic control mechanism. The reflected beam is imaged via a prism onto a differential photodiode such that both diodes are illuminated equally, if the distance between surface and focusing lens exactly corresponds to the focal length of the lens. If the surface is slightly displaced, then the two photodiodes are no longer illuminated equally, and the control mechanism becomes active in order to re-establish a focused beam. Compared with the triangulation method, the auto-focus method has lower sampling rates (1 kHz), better vertical and lateral resolutions (<0.01 µm and 1 µm, respectively), a smaller measurement range (<1 mm), and a smaller working distance (2 mm). Measurement uncertainties related to light penetration on transparent surfaces are much less of a problem than with the triangulation method, due to the highly focused incident laser beam (Breitmeier 1993). A supplier of auto-focus profilometers is UBM Messtechnik GmbH.

A method for determining highly curved surface profiles of the upper meniscus in slide bead coating has recently been presented by Ikin (1992). In this 'bead profile tracker', a wire electrode of 75 µm diameter is mounted on a *x*- and *y*-translator driven by stepper motors. The probe is slowly lowered toward the liquid surface, and upon contact, the electrical circuit switches the *y*-translator to up-stroke. The wire must be lifted far enough to shed the drop which clings to the probe due to capillary action. After each vertical cycle, the probe is displaced horizontally by the *x*-translator to its next measurement point. The surface profile is recorded by memorizing the *y*-position on the downstroke at the point of initial electrical contact. The method also allows for correction for the wire radius, depending on whether the wire is leading or trailing the free liquid surface. Bead profiles obtained in this fashion have successfully been used as initial guesses for finite element calculations of the bead flow field. Moreover, the technique can be extended to plotting three-dimensional effects, for example ribbing lines. A similar setup was published by Campanella and Cerro (1984) who used a micrometer to measure the film thickness on a partly submerged rotating cylinder. Here, a high impedance meter provided visual indication that the micrometer tip had touched either the liquid film or the metallic surface of the roll.

7.3.2.2 Moiré technique

Contactless measurement of the area-wide topography of a surface can be achieved with interference techniques. Classic optical interferometry requires a coherent laser light source and a vibration-free environment. The measurement range of application is on the order of 10 µm, and the resolution is as high as nanometers. These characteristics render the method unsuitable for studying liquid film coatings.

In contrast, the moiré technique, which is also called mechanical interferometry, does not require coherent light. Its measurement range (depth of topography) extends over five orders of magnitude

from about $10\text{ }\mu\text{m}$ to more than 1 meter with a depth resolution of better than $10\text{ }\mu\text{m}$, and the characteristic dimension of the object may be between centimeter and meter.

The development of surface topography by moiré technique started in the 1960s (Nishijima and Oster 1964; Theocaris 1967; Meadows, Johnson and Allen 1970) with considerable efforts in medical applications for contouring human backs (Takasaki 1970, 1979). More recently, Kheshgi and Scriven (1983, 1991) have described how the method can successfully be applied to coating flows. In particular, they have investigated the leveling of a horizontal film as a function of time, the growth of surface waves in a film flowing down an inclined plane, deformations in a liquid curtain due to ambient disturbances, and the local thinning of a liquid film due to surface tension gradients as a result of a surface-active contamination.

The author of this paper has successfully used the moiré technique as an optical amplifier to facilitate the determination of the inception point of 'ribbing lines' in slide coating. As described in Chapter 11b, ribbing is a flow instability that

leads to a periodic deformation of the film surface. Instability is obtained by changing one of the process parameters, for example increasing the coating speed, beyond a critical value, while all other parameters are held constant. However, the growth of the amplitude of the deformation after the inception is relatively weak, making it difficult to determine exactly the onset of the instability without the help of an optical amplifier.

In optical interferometry, a fringe pattern of bright and dark areas is produced by superposing two coherent light beams, i.e. beams that have the same wavelength and a constant phase relation. With moiré, similar fringe patterns are generated by superposing two mechanical grids or optical gratings. The line spacing of the grating should be large enough to avoid blurring of the image through diffraction effects (i.e. grating pitch less than about 40 lines/mm). If the spacing of the two gratings is even, then the spacing of the resulting fringe pattern is also even, Fig. 7.12a. However, if one of the gratings is distorted, so will be the fringe pattern, Fig. 7.12b.

With respect to coating flows, deformations of liquid surfaces can be used to distort one of the

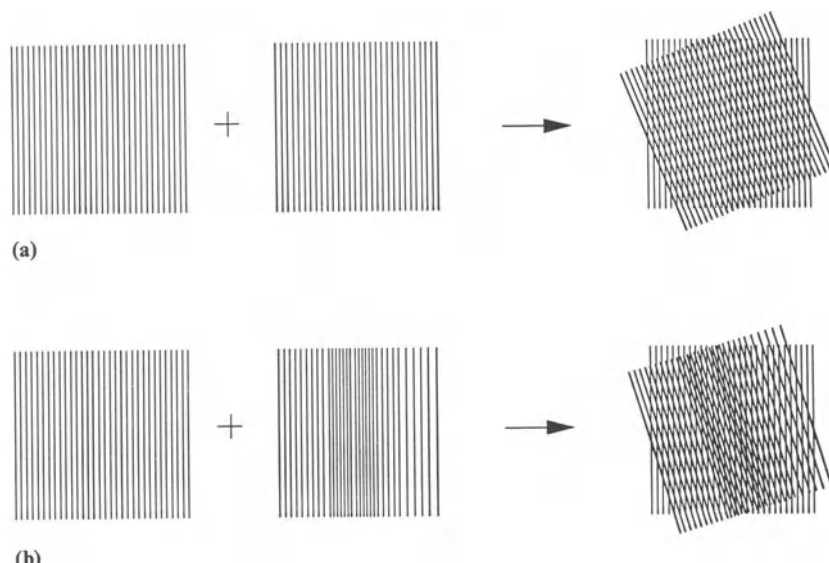
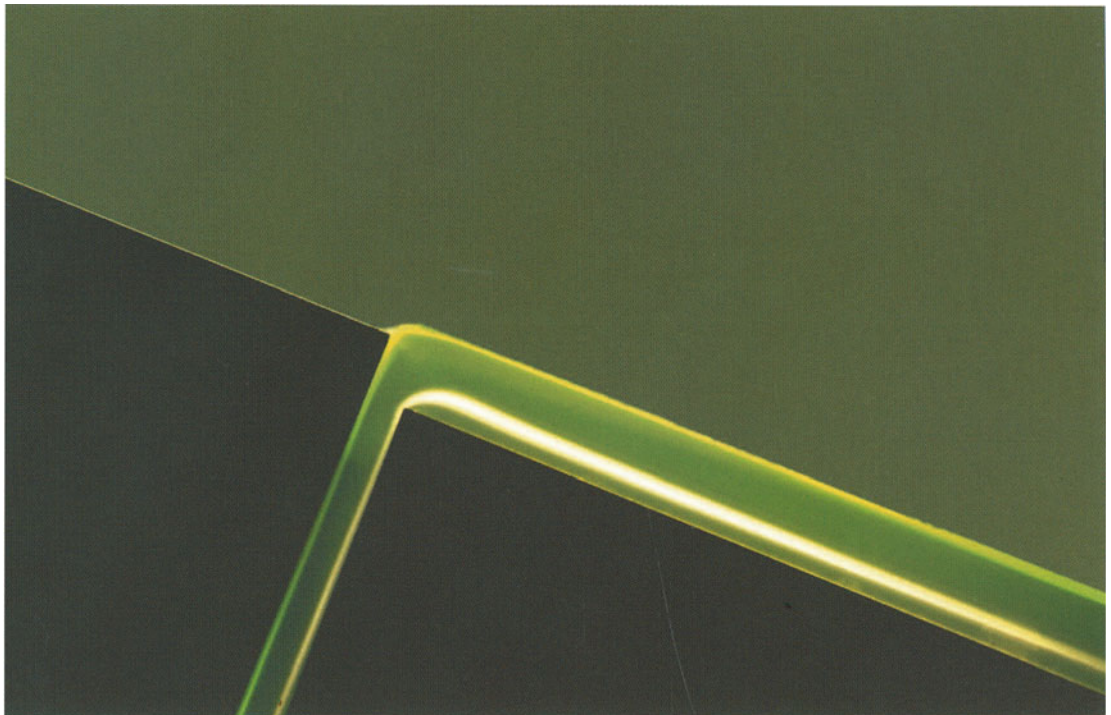
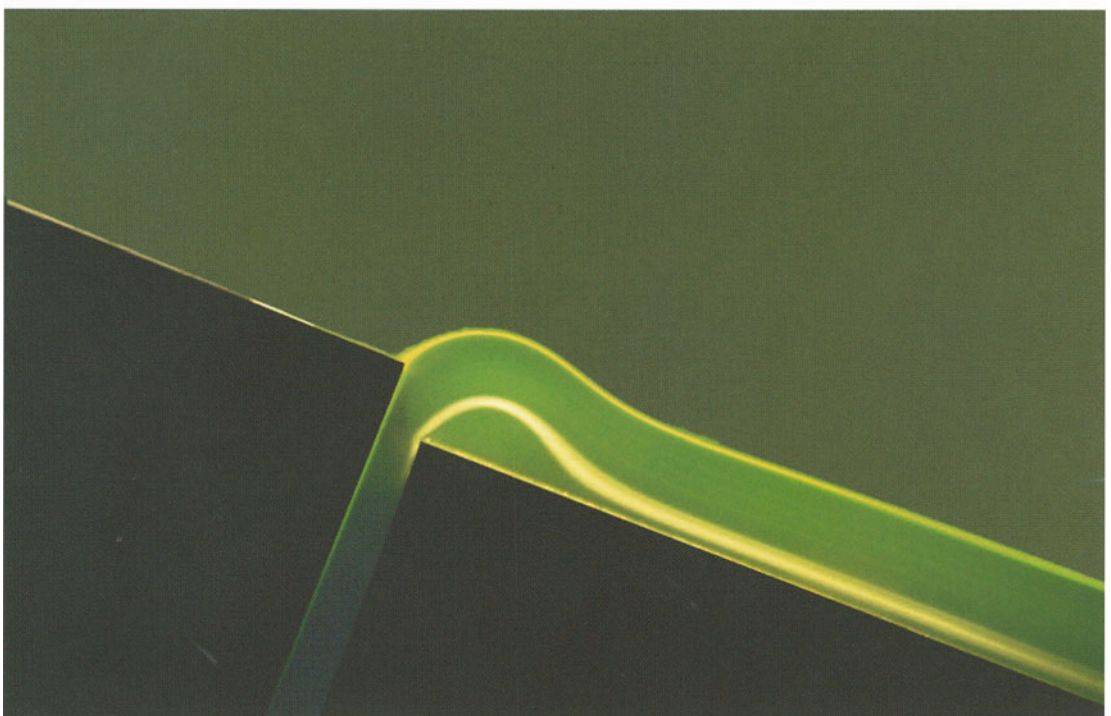


Figure 7.12 Formation of moiré patterns: (a) evenly spaced fringes by superposing two uniform grids; (b) unevenly spaced fringes by superposing an uniform and a disturbed grid.

ALBUM OF COATING FLOWS



(a)

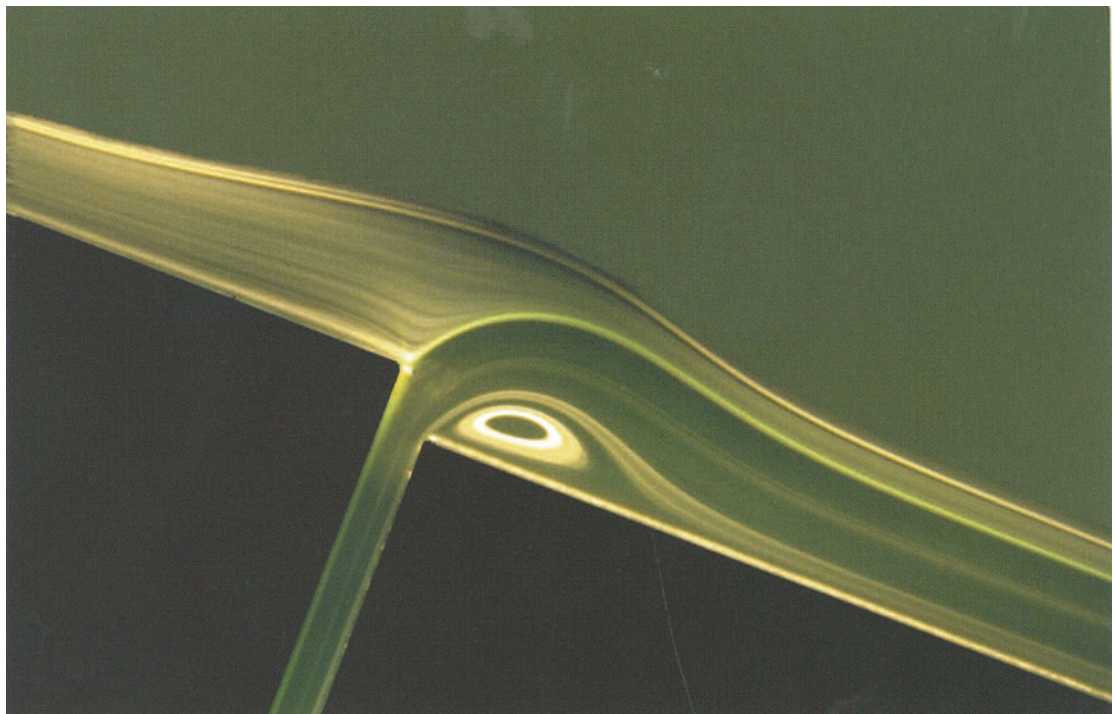


(b)

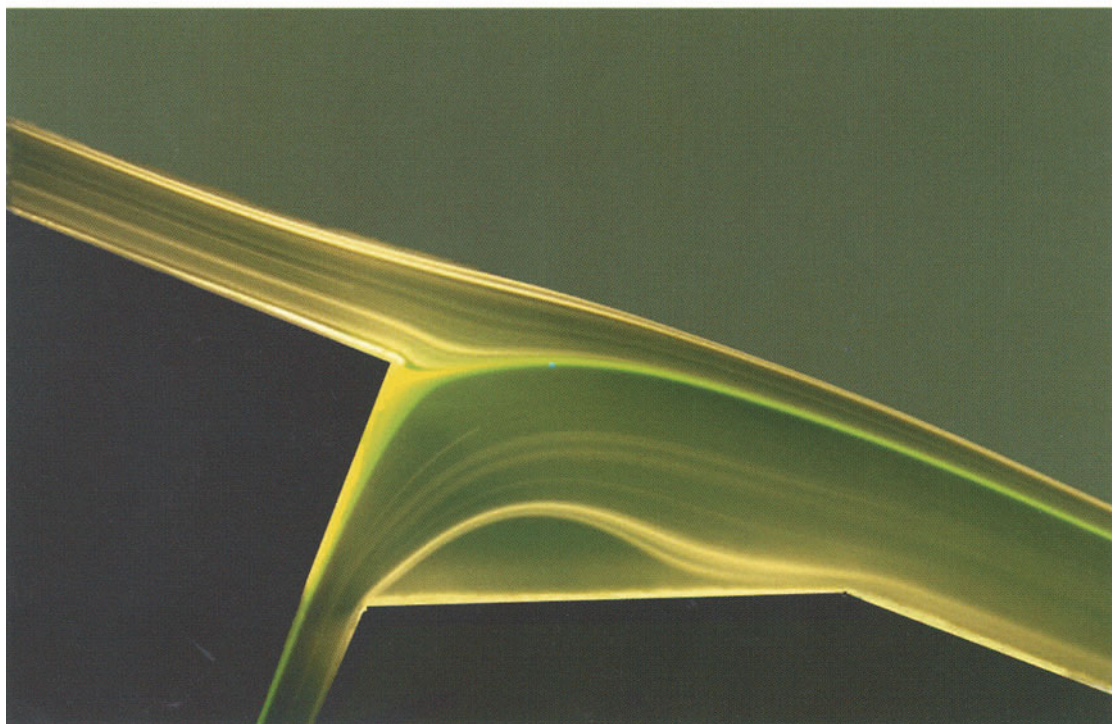


(c)

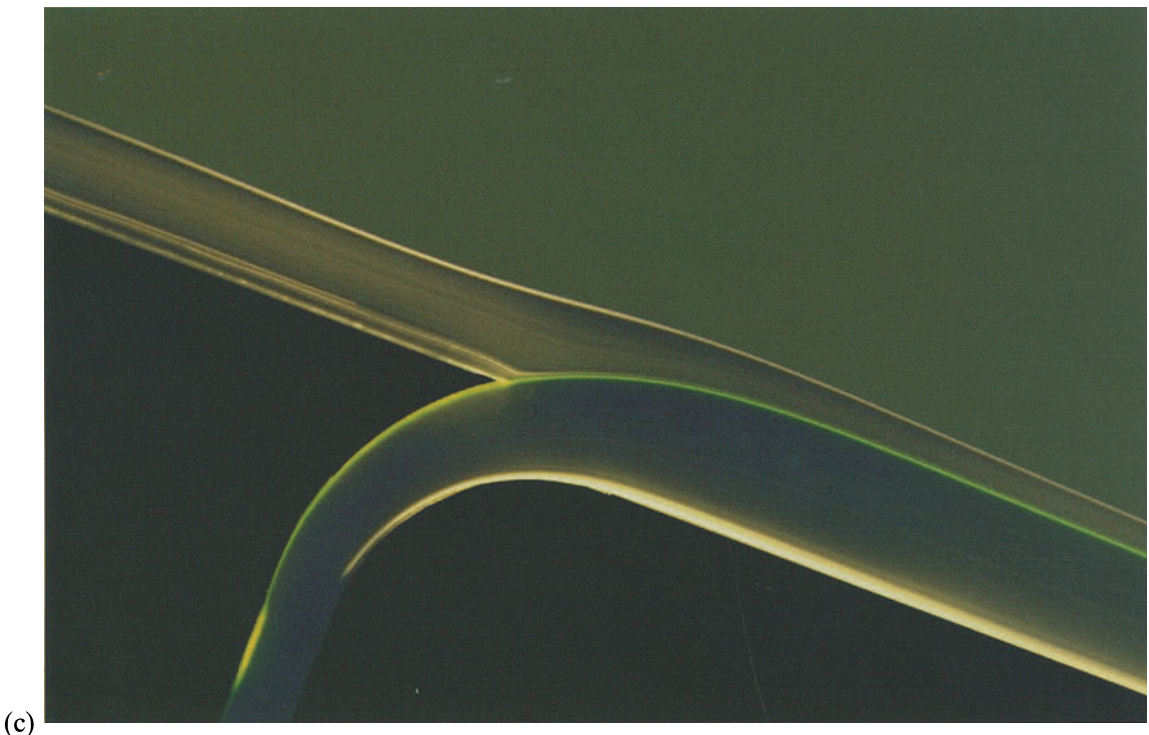
Fig. 7.20 Visualization of a liquid layer exiting from a slot onto an inclined plane: effect of the flow rate on the presence of vortices and the position of the static wetting line. Flow parameters are listed in Table 7.2.



(a)

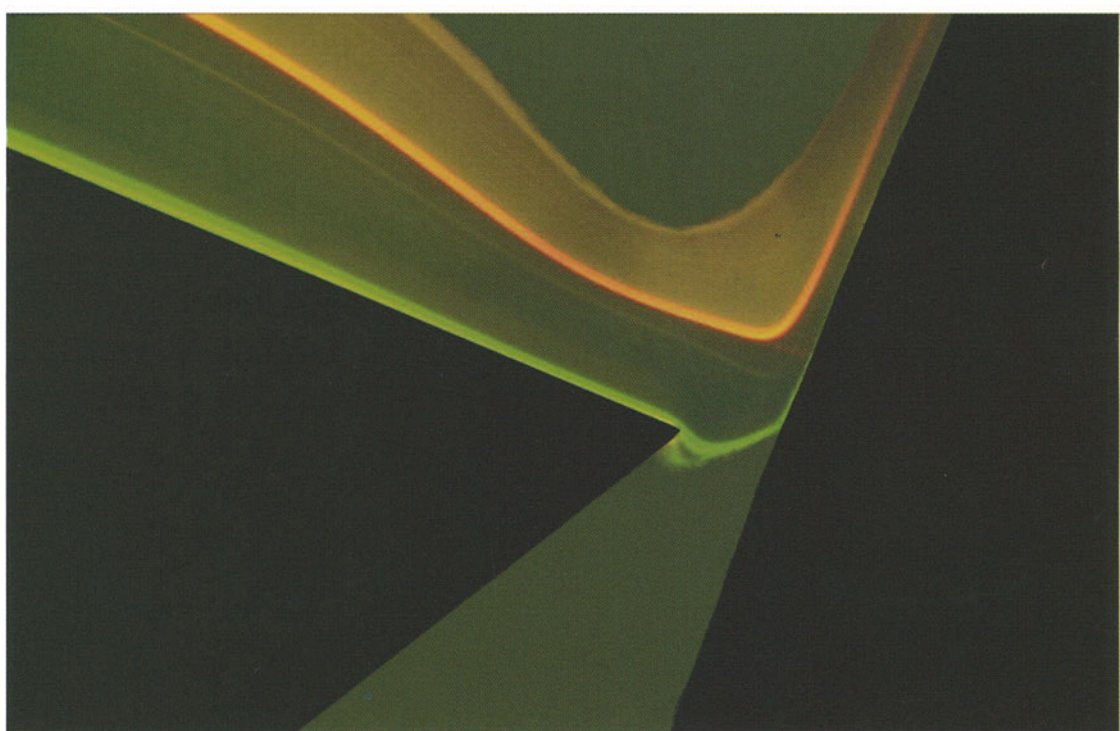
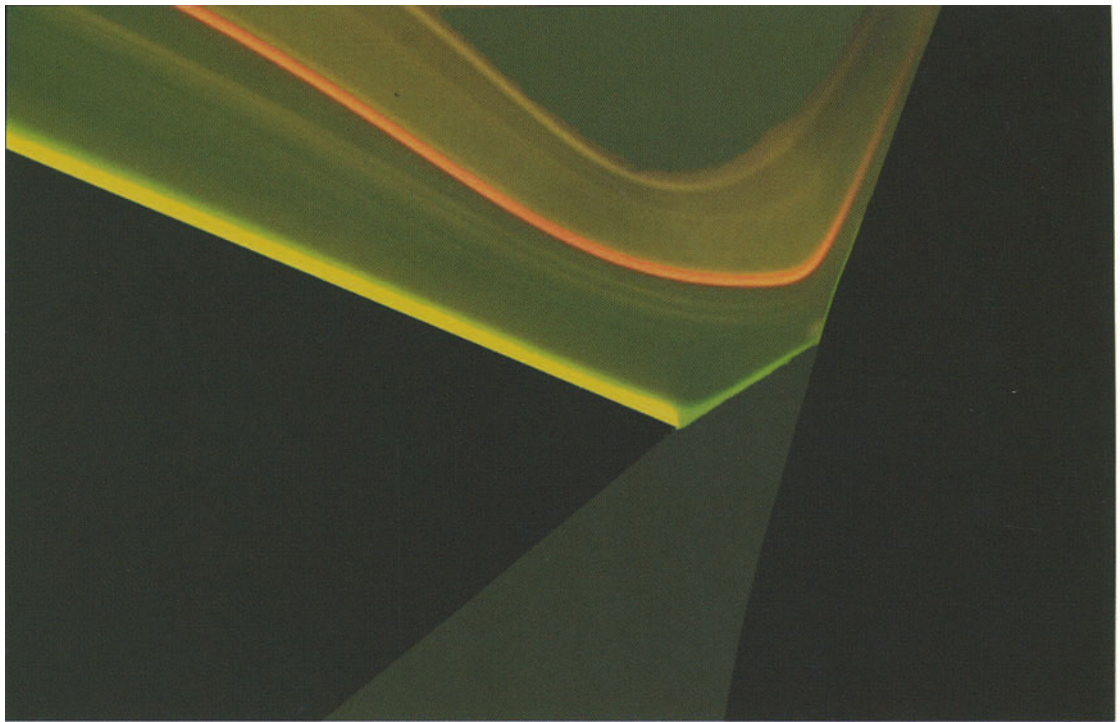


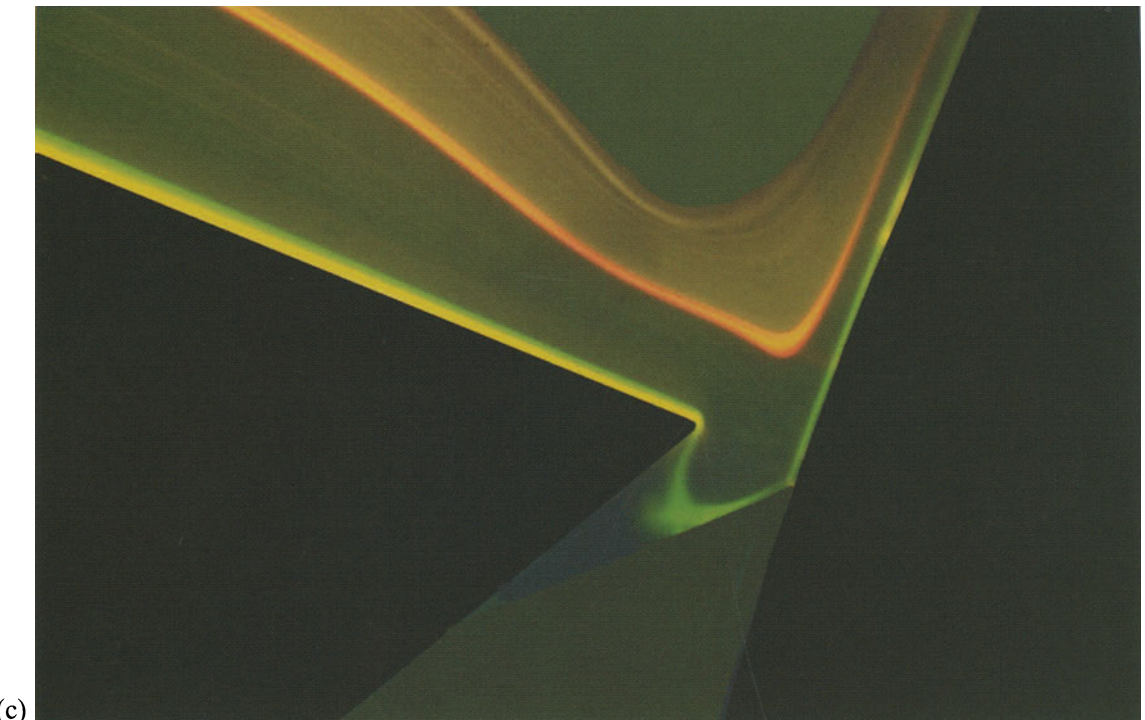
(b)



(c)

Fig. 7.21 Visualization of a liquid layer exiting from a slot and merging with another layer on an inclined plane: effect of the geometry of the downstream corner on the presence of vortices. Flow parameters are listed in Table 7.2.





(c)

Fig. 7.22 Visualization of the bead (liquid bridge) in slide coating: effect of the pressure difference across the bead on the positions of the static and dynamic wetting lines. Flow parameters are listed in Table 7.2.

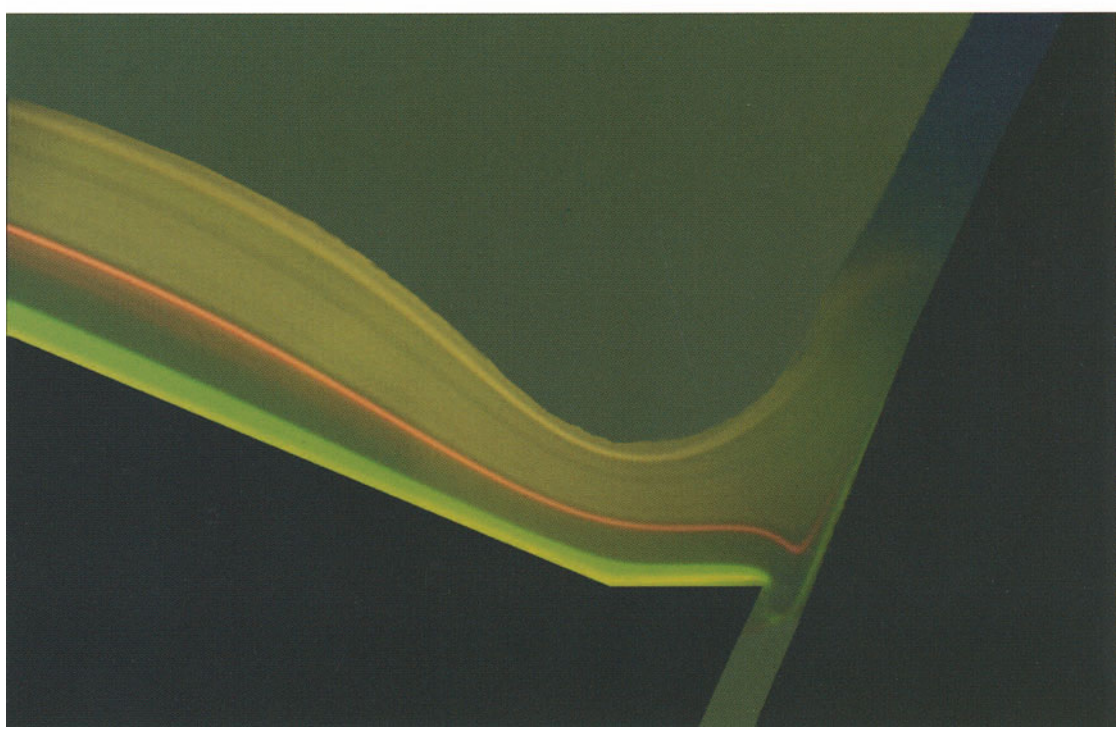
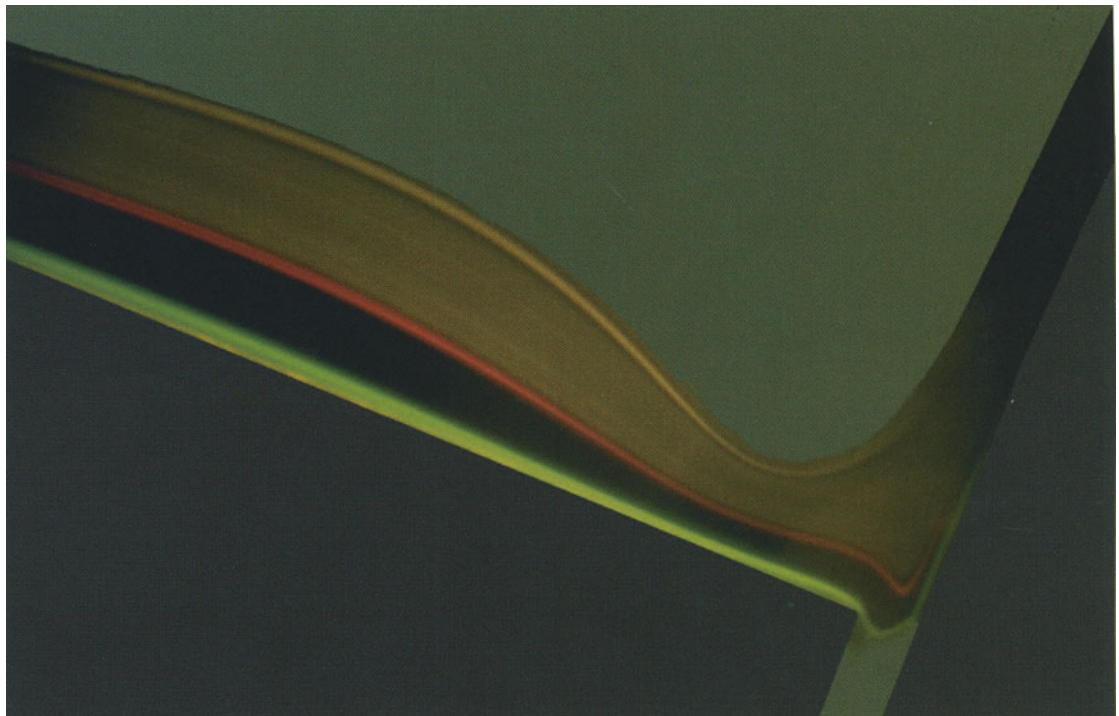
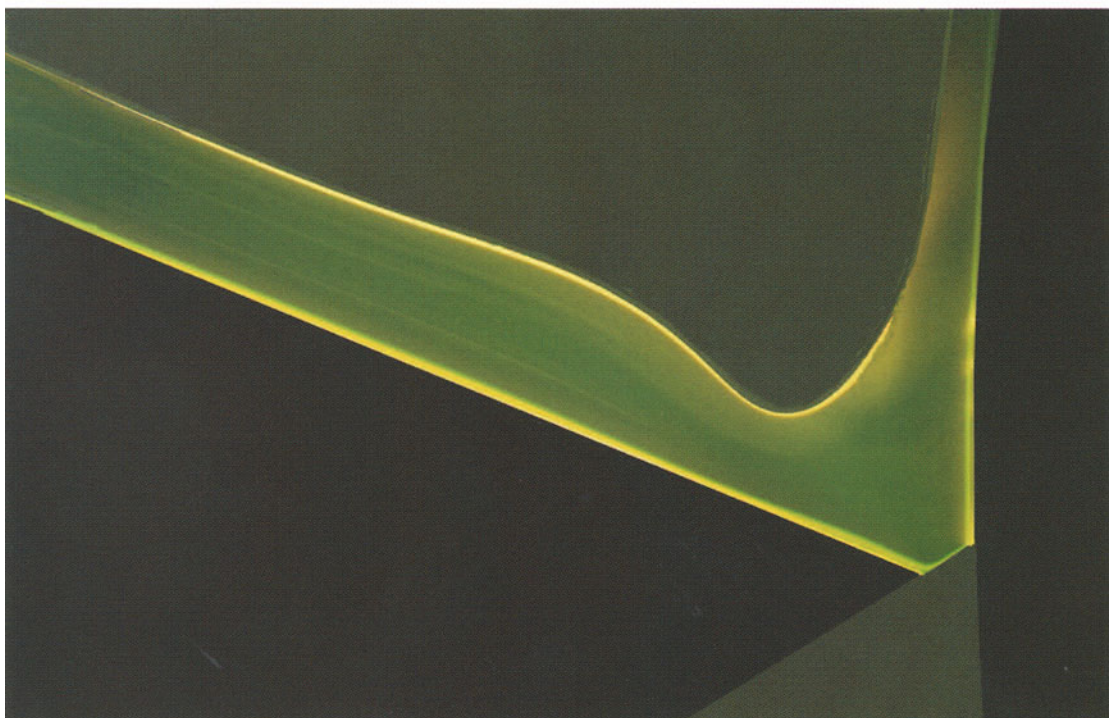
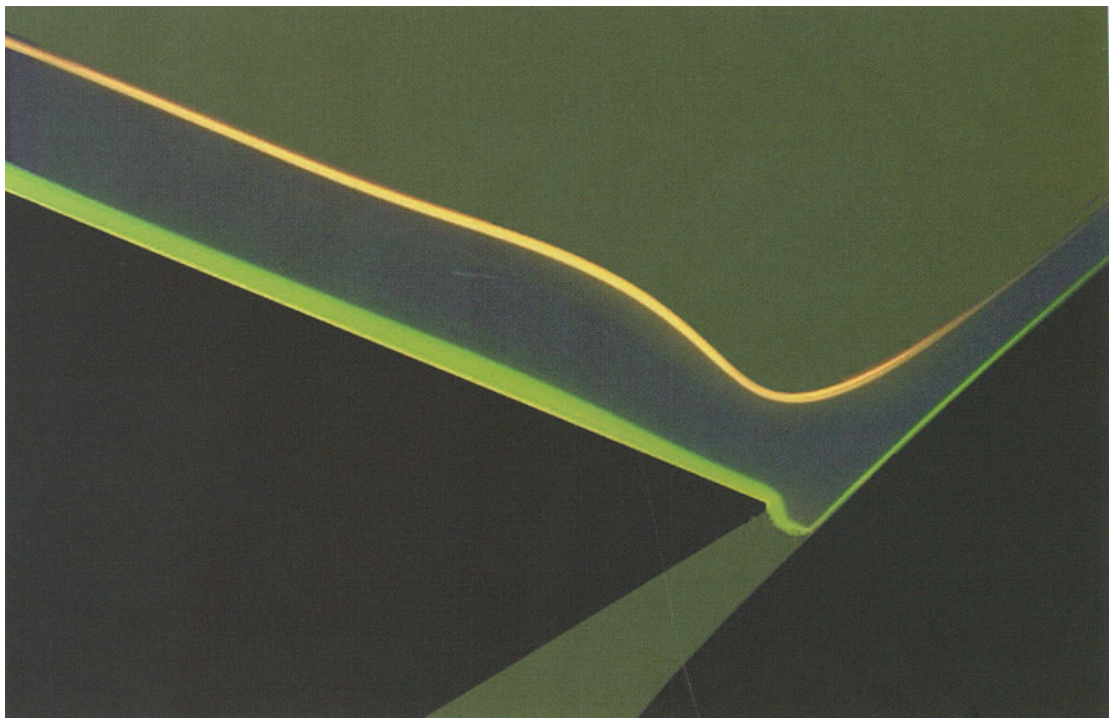




Fig. 7.23 Visualization of the bead (liquid bridge) in slide coating: effect of the lip geometry on the flow field of the bead. Flow parameters are listed in Table 7.2.



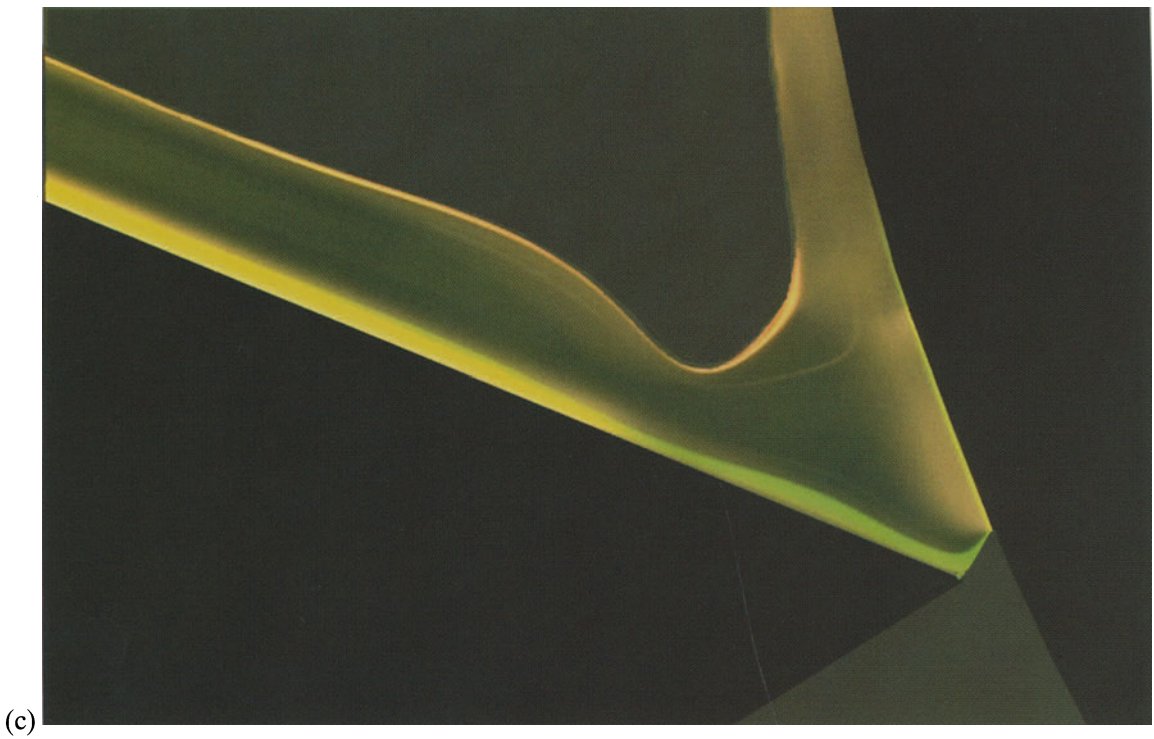


Fig. 7.24 Visualization of the bead (liquid bridge) in slide coating: effect of the application angle on the flow field of the bead. Flow parameters are listed in Table 7.2.

gratings, which then is superposed with an undistorted reference grating to generate the fringe pattern that contains the desired information about the surface topography.

Moiré topography can be set up according to different optical arrangements, which are called oblique shadow method, reflected image method, and refracted image method. Selection criteria for a particular application include the light source (collimated or diffuse), the characteristics of the surface to be tested (diffusely reflecting, specularly reflecting, or transparent), the relative positions of the illuminating and receiving optics (reflection or transmission mode), the sensitivity to movement of the surface to be tested, and the type of information to be extracted. Details and characteristic features of each method are described by Kheshgi and Scriven (1983).

Here, the optical lay-out of the oblique shadow method is presented as an example and schematically depicted in Fig. 7.13 (Meadows, Johnson and Allen 1970).

A non-collimated light source is used to illuminate the grating, which is casting a shadow on the specimen surface. If the specimen surface is distorted, the shadow will be as well. Moiré fringes are obtained by superposing the shadow with the reference grating. The sensitivity of the method, i.e. the height difference ΔZ between two points on the surface corresponding to two

adjacent equidistant fringes (vertical resolution) has been calculated by Meadows, Johnson and Allen (1970); the result in approximate form is given by equation (7.6):

$$\Delta Z = \frac{pH}{D} \quad (7.6)$$

Thus, the difference in height between two points that are separated by n fringes is obtained by multiplying the right-hand side of equation (7.6) by n . The sensitivity of the method can be tuned by changing either the line spacing of the illuminated grating, p , the distance between the illuminated grid and the observer, H (which is assumed to be equal to the distance between the grid and the light source), or the distance, D , by which the source and the observer are separated. With $D = 200$ mm, $H = 50$ mm, and $p = 0.05$ mm, for example, a resolution of $12.5\text{ }\mu\text{m}$ is obtained.

The evaluation and quantitative interpretation of moiré fringe patterns that contain information about the surface topography is not an easy task. An example can be found in Kheshgi and Scriven (1983). They measured the leveling (temporal evolution of the surface topography) of a wavy liquid film, and they derived a mathematical reconstruction of that film surface from the moiré fringe pattern that was generated by the refracted image method. Their analysis involves an integration which, in practice, may be rather cumbersome to carry out. Today, more convenient methods are commercially available. Breuckmann, for example, offers a system in which the fringe pattern is captured by a CCD camera and fed into a computer for image analysis. The surface topography is extracted by way of sophisticated algorithms based on the phase shift method (Breuckmann and Thieme 1985), and displayed either as colored contour plot or as three-dimensional mesh. This added convenience has a price of several thousand dollars, however.

In summary, the moiré technique is a useful method for generating two-dimensional topographical information of deformed liquid surfaces. Its theoretical maximum resolution of about

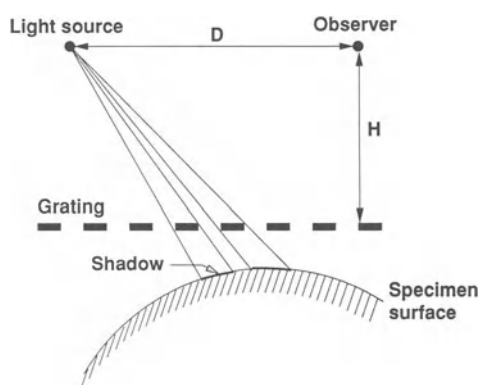


Figure 7.13 Moiré technique: schematic diagram of the optical configuration for the oblique shadow method.

1 µm is adequate for most coating flow applications. Practical resolutions, however, may not be quite as good due to physical limitations in setting up an optimum optical arrangement as in the case of detecting the onset of ribbing lines in the nip of a forward roll coating process. Quantitative information about surface topography is either difficult to obtain or at a relatively high price for image analysis equipment. The last argument points the value of the moiré technique toward qualitative visualization of deformed liquid surfaces.

7.3.2.3 Laser scanners

Laser scanners are powerful electro-optical systems that measure surface or interface deformations resulting from discrete disturbances. Their main purposes include:

- on-line monitoring of the quality of a coated film (uniformity of surface topography);
- triggering an alarm in case of an event (excessive deviation from product uniformity). Owing to the fast response time, this feature not only reduces coating waste, but it also provides a means for identifying and subsequently elim-

inating problems of the coating process, for example leaky pipe fittings that lead to air bubbles in the coating solution;

- memorizing events in terms of size and position on the web in order to facilitate the elimination of defects in a later process step;
- identifying 100% defect-free master rolls (the term 'master roll' refers to uncut, coated rolls, as they come off the coating machine);
- serving as a research tool for studying particular coating defects such as ribbing lines and their temporal decay (leveling) after the coating point as a function of relevant process parameters (Ikin 1992).

A variety of laser scanner schemes exist, and they are well described in the literature (Beiser 1974; Pietzsch, Müller and Feige 1988). In essence, they comprise emitting optics, receiving optics, and a computer for data processing and evaluation. In a typical commercially available system, the heart of the emitting optics is a laser whose beam is reflected off a fast rotating multifaceted mirror wheel (typically eight faces), which causes the beam to scan across the web, Fig. 7.14. Scan rates of up to 3 kHz result in very high linear scan velocities of several km/s. The wavelength

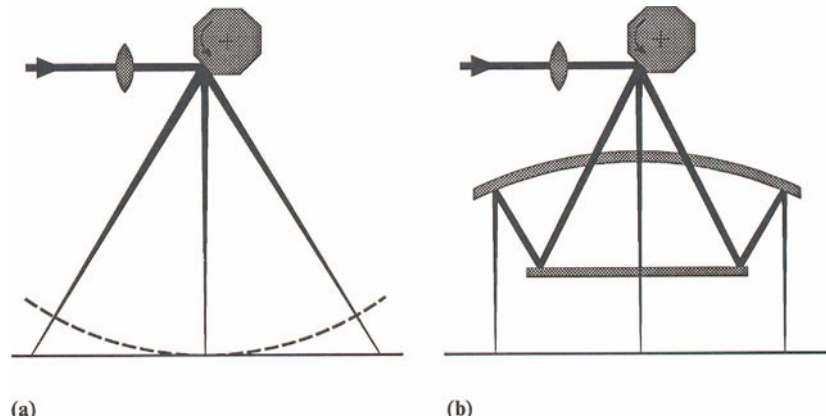


Figure 7.14 Emitting optics of a laser scanner system: (a) simple optical arrangement with rotating multifaceted mirror wheel; (b) telecentric beam path resulting in perpendicular intersection between beam and web. From Pietzsch, Müller and Feige (1988).

of the laser light may be chosen between 442 nm (blue) and 830 nm (infrared) to optimize product compatibility for a particular application.

In a simple optical arrangement as described in Fig. 7.14a, the incident laser beam would intersect the web at an angle that varies with lateral position, hence resulting in unequal interpretation of coating defects across the web. To overcome this difficulty, Sick (1972) has patented the so called telecentric beam path which guarantees a perpendicular intersection between the incident beam and the web at any position across the web, Fig. 7.14b. The size of the scanning laser spot (spatial resolution) is small and may even be varied in sophisticated systems. Typically, it has the shape of an ellipse with a cross-sectional area of less than 1 mm². Despite this small size, the high scan frequencies allow for 100% scan coverage even for high coating speeds of up to 3 m/s.

The receiving optics can be arranged in either reflection or transmission mode, depending on the particular application. Furthermore, they can be classified according to their receiving aperture with respect to the scan and down-web direction, and according to the receiving angle of the detector, i.e. bright field or dark field (Pietzsch, Müller and Feige 1988). These different characteristic features of the receiving system can be used to distinguish between different types of defects, for the extent of scatter (distribution of the scattered laser light in terms of intensity and angle) depends on the nature and structure of the surface deformation on the web. Typically, the ability of a laser scanner system not only to recognize but also unequivocally differentiate between various surface defects depends on the particular application and must be established by trial and error.

The so called light-guide rod collector (Sick 1979) is a plexiglass bar that spans across the entire web. The laser beam enters the bar, is reflected off a metalized mirror raster and, by way of total internal reflection, is guided onto a photomultiplier which produces an electrical current that is proportional to the amount of incident light, Fig. 7.15a. This receiver is char-

acterized by a large (*ca.* $\pm 15^\circ$) aperture in scan direction and by a small (*ca.* $\pm 5^\circ$) aperture in down-web direction.

In another optical arrangement, the laser beam from the web is focused onto the point-like detector by way of a lens or a combination of cylindrical lenses and cylindrical mirrors (parabolic mirror collector), Fig. 7.15b. This system features a very small (*ca.* $\pm 1^\circ$) aperture in both scan and down-web direction which, in combination with dark- and bright-field apertures, allows the detection of defects which produce very small beam deflections such as longitudinal lines.

A bright-field detector receives predominantly specularly reflected light and light from strongly scattering surfaces. Defect-free coating surfaces will lead to high detector signals while any surface defect will lower the signal amplitude. Dark-field detectors, on the other hand, have a small plate in their center that blocks off all specularly reflected light and hence gives a low output signal for defect-free surfaces. However, weakly scattering surfaces or surface defects causing only slight deflections of the specularly reflected beam will lead to high detector signals. The latter is often the case with sharp longitudinal lines or streaks.

Laser scanner systems are, above all, good at detecting surface deformations such as scratches, impressions, creases, wrinkles, fibers, air bubbles, inclusions, repellencies, ribbing lines, etc. Detection of high-frequency cross lines and longitudinal lines, particularly if they are located at an interior interface of a multilayer film, is more difficult. Detection of a particular defect is facilitated by selecting the optimum aperture and detector type which, in most cases, is arrived at by trial and error. Defect classification is achieved by real-time data processing using algorithms which examine 'fingerprints' of defects, for example size, aspect ratio, orientation of major axes, edge contrast, signal amplitude, rate of repetition, and other parameters (Pietzsch, Müller and Feige 1988; Pietzsch and Müller 1988). Once a defect is identified, it is displayed on a screen by its specific mark, a letter for example. The temporal evolution of this display represents the defect map of the coated web.

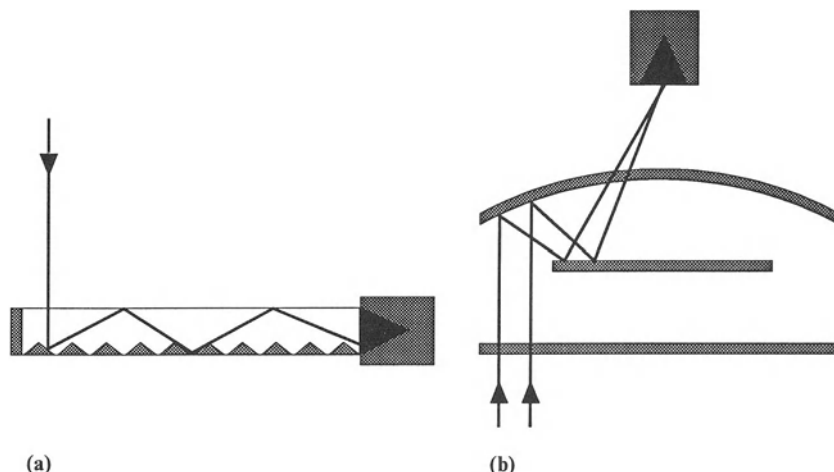


Figure 7.15 Receiving optics of a laser scanner system: (a) light-guide rod collector; (b) parabolic mirror collector. From Pietzsch, Müller and Feige (1988).

Suppliers of laser scanner equipment are, for example, Rheinmetall Sick Optical Inspection Systems GmbH and Intec Corporation.

While laser scanners are sophisticated, powerful, and very useful instruments for coating process surveillance, they require not only substantial investment funds (several hundred thousand dollars for a coating width of 1.5 m), but, more importantly, a strong commitment from engineers and operating personnel to obtain an optimum scanner performance for a particular application. The task of translating, with any degree of certainty, the scanner signals into English expressions describing familiar defects like bubbles, comets, fibers, is not trivial but can be accomplished successfully with sufficient effort and dedication.

The long-term purpose of a laser scanner system should be to put itself out of business. This operating philosophy is based on the fact that a laser scanner is really an element in an on-line feed back quality control loop, and as such it detects coating defects after the fact. A more desirable operating mode is prevention of defects. Hence, the scanner could be used as an instrument toward that goal by using defect indications to spur the investigation and subsequent

elimination of the defect cause. In some instances, this approach requires shutting down the coating line to facilitate the search of the defect cause. Such action, in turn, calls for production managers who can withstand the pressure of short-term profit maximization at the benefit of sustainable process and product development on the basis of prevention and ‘quality designed into the product.’

The scenario described above is of course an ideal and difficult-to-reach goal. In the meantime, therefore, the use of laser scanners is justified for ‘inspecting quality into the product’ by identifying and eliminating defects after the coating process in order to guarantee the delivery of defect-free master rolls to customers.

7.3.3 FLUID VELOCITY MEASUREMENTS

Experimental determination of fluid velocities has long been a challenge for fluids engineers, and, judging from the small number of publications, the task has been particularly challenging in the area of coating flows. Explanations for this situation include the small characteristic dimensions of, and the presence of free liquid surfaces in coating flow fields. In addition,

determination of fluid velocities today can be accomplished with relatively little effort compared with experimental approaches, by using commercial software packages for computational fluid mechanics, see also Chapter 9. Finally, the exact knowledge of the entire velocity field of a coating flow may be of limited value for solving practical problems. In spite of the above reservations, velocity information is needed, for example, to determine velocity gradients, which in turn are indicative of the degree of non-Newtonian flow behavior of most polymeric fluids (see also Chapter 5). Moreover, fluid velocities are essential for estimating the magnitude of the transport of surfactant molecules by convection relative to diffusion, in order to characterize the effects of surfactants added to the coating solution (see also Chapter 11d). As shown by the examples below, there are other instances where the determination of fluid velocities is useful. Whether it is advantageous to acquire such velocity information experimentally or by way of computer calculations depends on the particular application.

One of the most elegant experimental measurement techniques is called Laser-Doppler Anemometry, LDA. It is an electro-optical system, characterized, among others, by the following features: nonintrusive, instantaneous velocity, high spatial and temporal resolution, high

accuracy, linear relationship between measured signal and fluid velocity, direction sensitive, free of calibration, wide velocity range (order 10^{-3} to 10^{+2} m/s), simultaneous measurement of three velocity components, relatively expensive, ‘not so easy to use.’

In a LDA system whose optical components are arranged according to the dual beam or fringe mode, two laser beams are focused and intersected by a focusing lens to form the so called measuring volume which has the shape of an ellipsoid, see schematic diagram in Fig. 7.16. As a result of the coherent laser light, a fringe pattern of light and dark areas is produced in the measuring volume. A small particle flowing through the measuring volume will scatter light whose frequency, v (Doppler frequency), is proportional to its velocity and indirectly proportional to the spacing ΔX of the light fringes. The latter is completely determined by the wavelength λ_0 of the laser light in the vacuum, the refractive index, n , of the fluid, and the half angle, Φ , of the intersecting laser beams, equation (7.7).

$$\Delta X = \frac{\lambda_0}{2n \sin(\Phi)} \quad (7.7)$$

LDA is an indirect measurement system, inferring fluid velocities by measuring particle velocities under the assumption of no slip. According to the above explanations, the particle

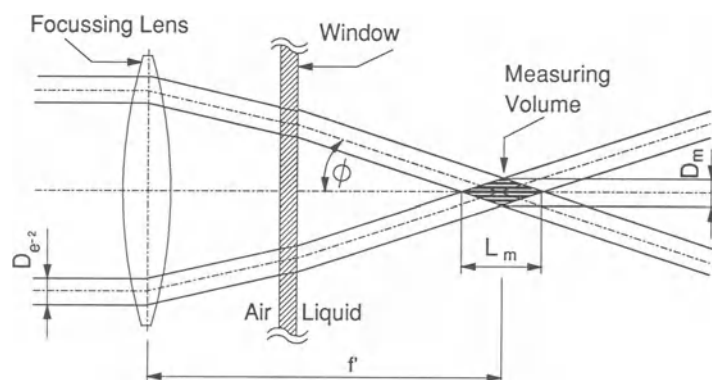


Figure 7.16 Laser-Doppler Anemometer: formation of interference fringes in the measuring volume by focusing and intersecting two laser beams in the test fluid.

velocity V , is given by

$$V = \frac{v\lambda_0}{2n \sin(\Phi)} \quad (7.8)$$

The components of a LDA system include a laser source, illuminating optics to produce the measuring volume, receiving optics to collect the scattered light which contains the velocity information, a light detector and a signal processor which is either of a counter or a tracker type. A transparent window in the confinement of the flow system is needed as an entry gate for the laser beams, if the fluid to be measured is a liquid, see Fig. 7.16. Many optical configurations are possible with the illuminating and receiving optics on the same or opposite sides of the test section. Modern systems use fiber optics components to enhance flexibility and versatility. A comprehensive book describing all aspects of LDA was written by Durst, Melling and Whitelaw (1976).

When applying LDA to coating flows, the dimensions of the measuring volume are of principal concern. Owing to the Gaussian intensity distribution of laser beams, their diameter, and hence the boundaries of the measuring volume, are usually defined by the point where the intensity has a value of e^{-1} or e^{-2} of the center intensity. As shown in Fig. 7.16 and derived by Durst, Melling and Whitelaw (1976), the diameter D_m and the length L_m of the effective measuring volume can be calculated by equation (7.9). The term 'effective' refers to the measuring volume as seen by the photodetector through a small aperture (pinhole), placed in front of the detector. The effective diameter is smaller than the real diameter of the intersection region in order to ensure that the outer region of the fringe pattern, with its poor signal quality, does not contribute to the measurement.

$$D_m = \frac{4\lambda_0 f'}{\pi n D_{e^{-2}} \cos(\Phi)} \quad L_m = \frac{4\lambda_0 f'}{\pi n D_{e^{-2}} \sin(\Phi)} \quad (7.9)$$

Here, f' is the effective focal length of the focusing lens in the test fluid, and $D_{e^{-2}}$ is the diameter of the incident beam at the focusing lens.

Small values for L_m are favored by a small wavelength of the incident light, by thick incident beams (use of beam expanders), and by large intersection angles. Argon-ion lasers are advantageous compared with He-Ne lasers owing to the emitted light in the blue (476.5 nm) or green (514.5 nm) range as opposed to the red light at 632.8 nm. Typically, argon-ion lasers are more powerful, but also more expensive. Large intersection angles are not easy to realize, because they require a lens with a large diameter and a short focal length. High quality lenses of SLR or TV cameras with a focal length of 50 mm and small f -numbers, preferably below 1.0, have proven themselves successful for measurements in film and slot flows (Oldengarm, van Krieken and van der Klooster 1975; Schweizer and Widmer 1981). The effective size of the measuring volume used for extracting velocity information can be additionally decreased via electronic means by suppressing low-amplitude portions of the Doppler signal. On the other hand, the measuring volume may be enlarged due to lens imperfections (Mues, Hens and Boij 1989). In summary, the size of the measuring volume in a practical application is associated with some degree of uncertainty.

The small diameters of the incident laser beams in the measuring volume that are necessary to achieve a high spatial resolution of the LDA system lead to alignment problems of the optical components. The task of perfectly crossing two narrow beams in space becomes important, and it is crucial to guarantee parallel interference fringes. To overcome these difficulties, Oldengarm, van Krieken and van der Klooster (1975) propose an optical arrangement in which a rotating radial diffraction grating is used as beam splitter and frequency shifter, instead of the usual prism and acusto-optical cell, respectively.

Practical LDA experience of the author includes the examination of the fluid mechanics of a mechanically agitated thin film evaporator (Schweizer and Widmer 1981). In this apparatus, a liquid film flows down along the inside wall of a vertical cylinder. In addition, the liquid film is agitated by several blades that form a rotor, whose axis is coincident with the axis of the

cylinder. The tip of each blade is slightly submerged in the liquid film, so that a puddle, or so called 'bow wave', is formed in front of each blade. The turbulence associated with the flow field in the bow wave is responsible for the enhanced heat and mass transfer rates typical for this type of evaporator. This flow field in the vicinity of the blade tip is not unlike blade coating, except that the blade is in motion and the substrate is at rest.

In another LDA study by the author, velocity profiles in the metering slot of a coating die were measured as a function of the cross-web coordinate, in an attempt to test theoretical predictions of outflow profiles for non-Newtonian liquids. The die was 43.2 cm wide, and the length of the metering slot was 4.0 cm; its width was adjustable between 508 and 1016 μm . The metering slot was formed by the honed metal surface of the die plate on the one side, and by a 6 mm thick glass plate of optical flatness on the other side. A dual beam backscatter mode was chosen as optical arrangement, and the resulting length, L_m , of the measuring volume according to equation 7.9 was 59.7 μm , using a He–Ne laser with beam expander and a Canon SLR lens with a focal length of 50 mm.

For a Newtonian fluid (water–glycerin solution), the parabolic velocity profile in a 660 μm metering slot could be measured perfectly over about 75% of the slot width. However, in the vicinity of the metal wall, excessive signal noise due to reflections of the incident laser beams made it impossible to extract velocity information. More interestingly, rheological and inertial effects on the uniformity of the lateral velocity profile for Newtonian and shear thinning fluids (power law index as low as 0.51) could be demonstrated. Unfortunately, the validity of all results was jeopardized by a great amount of uncertainty in slot width, owing to a substantial deflection of the glass plate due to fluid pressure in the slot. As can easily be shown for Newtonian fluids, relative variations in velocity are directly proportional to the negative value of relative variations in slot height.

Mues, Hens and Boiy (1989) have measured fluid velocities in the vicinity of the dynamic contact line in a slide coating process. The optical arrangement is described by Oldengarm, van

Krieken and van der Klooster (1975), and the spatial resolution was claimed to be much less than 40 μm . Some of the experimental results regarding fluid velocities in the web direction were unexpected at first. They could only be explained by postulating a thin entrained air film located just downstream of the apparent dynamic wetting line and extending along the web to the position of the real contact line. The dimensions of the air film depended on operating conditions and have been estimated to be of order 100 μm (length) and 10 μm (thickness), see also Chapters 3 and 11b for cross reference.

These findings are of great significance, because they shed further light on dynamic wetting, a process for which correct physio-chemical mechanisms have yet to be established and proven. However, the interpretation of some of the results by Mues, Hens and Boiy is made difficult by the fact that they used an instrument with a spatial resolution of order 10 μm to study a phenomenon on a molecular scale. Moreover, one of the incident laser beams is deflected by the liquid–air interface of the lower meniscus of the coating bead. As the exact shape and location of this liquid–air interface depend on operating conditions and are not known in general, so is the location of the measuring volume. Hence, velocity information is associated with uncertainty related to spatial uncertainty of the measuring volume. It is this very feature which makes the application of LDA questionable for coating flow studies, particularly if the laser beams enter the liquid through a curved interface of unknown shape and location. As a consequence, the notion of an entrained air film located downstream of the dynamic wetting line, as is postulated by Mues, Hens and Boiy (1989), remains a conjecture, for the available experimental data do not qualify as unequivocal proof.

There are alternative techniques to determine fluid velocities experimentally. One is the hydrogen bubble flow visualization method described in Section 7.3.4. If the voltage applied to the electrode wire that produces the hydrogen bubbles is pulsed at regular temporal intervals, then combined time streak markers are obtained (Schraub

et al. 1965). Ikin (1992) was able to extract velocity information from hydrogen bubble streak lines taken in the bead flow field of slide coating by using a chopper wheel to modulate the illuminating light beam.

Another approach is Particle Image Velocimetry (PIV), which allows the simultaneous nonintrusive measurement of flow motion at all points in a stroboscopically illuminated region (single instant in time). As in laser-Doppler anemometry, fluid velocity is inferred by measuring the velocity of light scattering particles which are assumed to follow the flow path lines. PIV is an optical technique which involves flow illumination and photography followed by particle identification and tracking based on image processing algorithms. The power of PIV lies in its ability to collect large amounts of flow data in a short time. However, the large data quantity leads to the main drawback of the method, namely the long processing times required for image analysis. Overview articles and reports of recent developments in this area include those by Adrian (1991) and Buchhave (1992) who described methods for processing PIV images and discussed practical limitations of PIV with respect to measurable velocities, obtainable accuracy, and spatial resolution, Grant and Liu (1990) who presented a novel method for resolving the directional ambiguity which is common to all particle tracking techniques, and Hassan, Blanchat and Seeley (1992) who developed multi-frame tracking and cross-correlation algorithms to determine fluid velocities. With regard to coating flows, Gaskell *et al.* (1992) have applied a computer particle tracking system to extract velocity information from the starved bead of a roll coating process, and Clarke (1995) has used the method to obtain flow functions such as the rate of strain and vorticity for the flow field of an impinging liquid curtain.

In summary, measuring fluid velocities of coating flows is possible, but not without considerable effort and investment, either in the field of electro-optics, or by developing suitable algorithms for electronic image processing. Depending on a particular problem at hand, we

therefore recommend, first, the thorough justification of the gathering of velocity information and, secondly, the consideration of computational methods as an alternative for generating such information, given the advanced level and the availability of commercial codes for computational fluid mechanics; see also Chapter 9 on Computational Methods. Still another option is the use of flow visualization techniques as described below, if qualitative velocity information in the form of streamline patterns is sufficient.

7.3.4 IMAGING

Picture taking is a widely used tool in coating technology, particularly when related to research and development activities. The main attraction lies in its communication power by capturing qualitative features of coating flow fields and of coated films. Flow visualization in the visible wavelength range is a popular application of imaging in coating technology, see Section 7.3.5. Imaging in the near infrared range (*ca.* 0.7–3.0 µm) allows one to ‘see in the dark.’ This feature is sometimes used in the photographic industry for process surveillance. Video cameras whose peak sensitivity is in that wavelength range can be used, for example, to control the curtain coating process by displaying to the operator in the bright control room if the curtain is still attached to the edge guides. Imaging in the mid and far infrared ranges (3–5 µm and 8–14 µm) is called thermal imaging. It produces temperature maps of the objects in the picture. Thermal imaging may be helpful in processes where the fluids are coated at temperatures above ambient. With adequate optics (wide angle lens), a temperature profile across the coated web can be produced which, if not flat, may be indicative of lateral film thickness nonuniformities owing to the temperature sensitivity of the viscosity of many coating fluids.

The choice of hardware in terms of cameras and lenses is virtually unlimited. In terms of light sensitive sensors, traditional silver-halide films are still the medium with the highest spatial resolution. The lack of immediate display can be

waved by using instant films, but at the expense of lower spatial resolution and of poorer picture quality compared with the traditional films. Electronic sensors such as video tubes and one- or two-dimensional CCD-arrays (charge-coupled device) offer the convenience of instant display, but the spatial resolution does not quite match the one of silver-halide films. For many applications in coating flows, however, the resolution of electronic sensors and instant films is sufficient.

Owing to the small characteristic dimensions of coating flows, imaging, and in particular flow visualization, is often supported by optical aids. Combining a camera with a low-power microscope is necessary when displaying cross-sections of film flows (see Section 7.3.5). The use of an endoscope has been reported by Ikin (1992), for example, who looked at the lower meniscus in slide coating, and monitored positions of the static and dynamic wetting lines as a function of relevant process parameters.

Still photography as well as conventional movie and video techniques may not be appropriate if unsteady or transient flows are viewed, for example the start-up of a coating process, the passage of a splice, the onset of air entrainment, the impingement of droplets in spray coating, etc. Instead, high-speed photography is called for in order to resolve the characteristic time scale of such flows. While traditional high-speed imaging is a powerful method of observation, setting up a proper system requires consideration of factors such as velocity of the phenomenon being studied, resolving power of the photographic system, magnification, total recording time, type of camera (stationary or moving film, slit or mirror scanning, shutter design, etc.), synchronization between phenomenon and recording, illumination (continuous, pulsed, or laser light source), etc. Picture taking rates of 10^4 to 10^7 frames per second are standard, which is more than adequate for visualizing phenomena in coating processes, because their characteristic velocities are relatively low, typically on the order of meter per second. Relevant aspects of high-speed photography are reviewed in detail by, for example, Dubovik (1981).

In contrast, high-speed video systems are simpler in terms of hardware, and therefore easier to use, but picture taking rates and resolution are lower compared with traditional silver-halide systems. The EktaPro Intensified Imager Model SI (Eastman Kodak Company 1993), for example, can record images at rates between 30 and 12 000 frames per second. With 192×239 pixels the resolution of the sensor is relatively low, but with 3200 ISO at 5500 K its light sensitivity is extremely high.

An application of high-speed photography has been published by Aidun, Veverka and Scriven (1992) who investigated and visualized the details of the dynamic wetting line instability which, so they argue, is a prerequisite for air entrainment in coating processes. The authors used a 16 mm silver-halide camera, equipped with a rotary prism and continuous film feed, and capable of recording up to 11 000 frames per second (fps). However, with 4 kW of installed illumination the maximum picture rate was limited to only 240 fps when using a 400 ISO film. Nevertheless, the temporal resolution was judged sufficient relative to the maximum coating speed of 0.45 m/s (rotating roller partly immersed in a pool of liquid), and far superior to the resolution of standard video systems which were also tried unsuccessfully because of inadequate frame rates (30 fps).

In another application, Branston *et al.* (1994) visualized the formation of deposits in blade coating of paper known as 'weeping.' The term refers to a localized bleeding of coating fluid past the blade tip and into wet deposits called 'weeps' that grow on the otherwise dry tip zone of the outer surface of the blade. An EktaPro 1000 video system (Eastman Kodak Company) was combined with a long working distance microscope to take pictures at a rate of 1000 fps. This set-up allowed the authors to resolve details of the inception, oscillation, growth, partial solidification and detachment of 'weeps' at coating speeds of up to 15.2 m/s.

In flow visualization, the illumination of tracers – be they bubbles or flakes – is best achieved with a light sheet that originates from a cylindrical and parallel beam, and that is shaped and

focused by a spherical and a cylindrical lens in sequence. A bulb, e.g. xenon, with an output power of about 150 W is sufficient as light source. However, if the light sheet is formed by way of slit apertures, most of the available light is blocked off, and tracer illuminations may no longer be adequate. The use of light fibers is more convenient in terms of handling than a set of lenses, but due to its strong divergence the light beam exiting from the fiber bundle is impossible to focus into a concise sheet, resulting again in loss of light. Laser beams fanned into a sheet by a cylindrical lens have not proven useful, because the Gaussian intensity distribution remains in the sheet and leads to a highly uneven light intensity in the flow field of interest. An interesting alternative with an even intensity distribution is offered by Dantec. A laser beam is reflected off a scanning mirror, thereby creating a pseudo light sheet. Scanning frequency and divergence angle can be controlled, and the laser light reaches the mirror through optical fibers.

Continuous lighting may be inappropriate when viewing unsteady or transient flows. Here, single or multiple flash illumination (stroboscope) is an option, possibly in conjunction with high-speed photography in order to either 'freeze' the flow or resolve its characteristic time scale.

Typically, continuous high-speed photography needs very high levels of illumination (several kilowatts), particularly when combined with magnifying optics. The associated heating effects must be shielded from the experiments to avoid unwanted modification of process parameters, for example change of viscosity due to increasing fluid temperature.

An instrument called a laserstrobe (Oxford Lasers Inc. 1992) may be able to overcome many of the problems associated with lighting. Its main features include single pulse for still photography (pulse duration as short as 30 ns), high-frequency stroboscopic action for high speed photography (flash rate of up to 32 kHz), auto synchronization for compatibility with high speed camera or video systems, laser light available at 511 nm (green) and 578 nm (yellow), no emission of infrared light, hence minimum thermal effects,

and light transmission by optical fibers for easy access to tight spaces. In an application cited by Oxford Lasers Inc., the laserstrobe was used to illuminate the flow in the nip between a pair of rotating rollers.

Taking an image is often only the first step in a process toward understanding the data that has been acquired on the image. Another important step in this process is data or image processing. The purpose of image processing is to generate knowledge by extracting quantitative information from large data sets or 'fuzzy' pictures. Image processing requires the data to be available in digital form, which can be achieved by using digital cameras, e.g. CCD arrays, or by scanning positive or negative images. Classical image processing techniques make use of a variety of algorithms, many of which have been developed for applications such as pattern recognition in aerial images. The algorithms include intensity distributions, averaging, edge detection, edge enhancement, low pass and high pass filters, convolution, fast Fourier transformation (FFT), inverse FFT, etc. Nowadays, most algorithms are available on affordable software packages that even run on personal computers. Moreover, the algorithms are readily adapted to processing images of fluid flows (Hesselink 1988; Hesselink, Helman and Ning 1992). A general but practical introduction to image processing may be found in the book by Russ (1992).

With regard to coating processes, image processing may be used to enhance the visibility or the form of distinctive patterns of subtle defects on the coated web, such as mottle. Digital image processing of a different kind is presented in Section 7.4. Flow visualization pictures from the slide coating process have been 'cleaned' from undesired reflections that could not be avoided during the experiment. The purpose of such a cleaning action is to remove information from the picture that strictly lays outside of the fluid flow cross-section, but that is strong enough to excessively distract the attention of the viewer. Moreover, equipment contours that are not visible on the original photo can be redrawn. The result is a clear picture with a uniform

background, and with a focus on the unaltered cross-section of a fluid flow whose boundaries are distinctly visible.

Recent developments in image processing have led to real-time imaging. Here, pictures of a process are captured by way of machine vision at rates that are comparable to temporal changes of important process features. The pictures are immediately (real time) evaluated in order to provide a feed-back signal for the control loop of the process (Batchelor and Waltz 1993). The above described situation, where cameras are used to survey the flow of a falling curtain along its edge guides, is an example of process control with real-time imaging, if the picture evaluation results in an alarm as soon as the curtain detaches from the edge guide.

7.3.5 FLOW VISUALIZATION

Coating flows are highly two-dimensional flow fields, characterized by two free surfaces with curved menisci, by one or more interfaces in multi-layer systems, by static and dynamic contact lines, and, depending on operating conditions, by vortices or areas of flow separation. The scale of the flows is small, typically on the order of 100 µm. The purpose of experimental flow visualization as discussed below is to

- highlight, by way of suitable tracers, characteristic flow features in the plane of interest, such as free surfaces, interfaces, streamlines, stagnation points, separating streamlines, and solid surfaces like rollers, substrates, or inclined planes;
- show how these features change as a function of relevant process parameters;
- determine the onset of flow separation or flow instabilities;
- provide realistic boundary and initial conditions for studies in computational fluid mechanics.

The first attempts of experimentally visualizing coating flows were published in the late 1970s and early 1980s. They succeeded in displaying

the complicated and curved free surfaces and menisci, but they were not able to resolve details of the flow interior. An overview of these studies is given by Schweizer (1988). At about the same time, Scriven and his students at the University of Minnesota began visualizing coating flows by way of computer simulations, see for example Saito and Scriven (1981), Kobayashi, Saito and Scriven (1982), Coyle, Macosko and Scriven (1982), and Kistler and Scriven (1983) for an overview of the early works. The publication of these theoretical results helped to open the way for industrial companies to demonstrate experimental visualization methods which, as seen in retrospect, they had developed years ago. The first quality pictures featuring streamline patterns, shapes and locations of free surfaces, static and dynamic contact angles, and vortices of two liquid films merging on an inclined plane, and of the flow field of the 'bead' of the slide coating process appeared in print in 1988 (Schweizer). Since then, the method has been improved and applied to many other coating methods by numerous authors, for example Sartor (1990) who studied slot coating, Scriven and Suszynski (1990) who visualized various premetered and selfmetered coating methods, Chen and Scriven (1992) who compared flow visualization of multilayer slide coating with results obtained from theoretical modeling, or Ogawa and Kashiwabara (1992) and Blake, Clarke and Ruschak (1994) who presented pictures of curtain coating, or Clarke (1996) who showed video footage of three different vortices in the flow field of an impinging curtain.

The method of choice for visualizing coating flows is called optical sectioning, because it introduces tracers in only one plane, namely the plane of interest which contains the desired information. The major advantage of this technique is its ability to produce concise pictures, revealing flow details down to micron scales, if adequate illumination and magnification are used.

Optical access into the flow is gained through a window which is mounted such that it coincides with the side confinement of the flowing liquid film, Fig. 7.17. As the flow fields of interest are

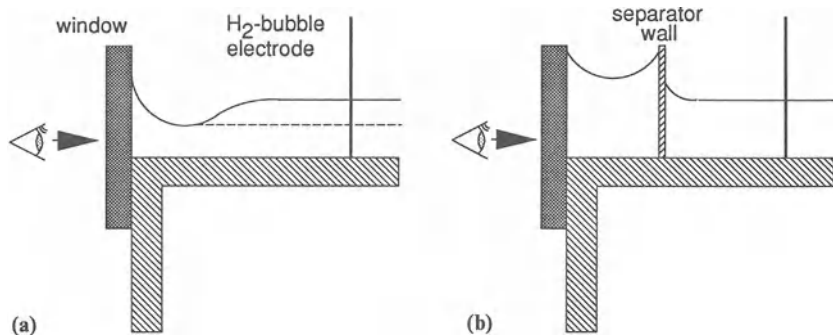


Figure 7.17 Flow visualization: optical access into the liquid film and onto the plane of interest through a side window: (a) three-dimensional edge disturbances due to capillary effects along the side window; (b) displacement of edge effects by way of a separator wall and feeding extra liquid along the window.

characterized by curved, free surfaces of unknown shape and location, it is practically impossible to match the shape of the flow with the shape of the side window exactly. Consequently, edge effects due to capillary effects will develop in the form of curved free surfaces and possibly curved interfaces in multilayer films, Fig. 7.17a. Therefore, the plane of observation must be placed sufficiently far away from the window to guarantee truly two-dimensional results. A distance of at least 2 cm has proven adequate for a wide range of flow conditions.

If the disturbed film surface near the edge penetrates below the equilibrium film thickness, then the upper part of the flow field may not be visible due to optical distortions (lens effects), Fig. 7.17a. Ikin (1992) has overcome this problem by mounting a separator wall between the side window and the plane of interest and by feeding extra liquid into this channel, resulting in a locally larger film thickness, Fig. 7.17b. The separator wall runs parallel to the side window and extends to a position just upstream of the flow field to be visualized. Downstream of the separator wall, the two liquid streams merge in such a way that the edge disturbance is still above the field of view, and the leveling of the two uneven film thicknesses does not yet affect the flow field of interest.

The most convenient tracers are hydrogen

bubbles generated by electrolysis of aqueous solutions, because they are highly visible, if properly illuminated, and because they do not contaminate the liquid, which is particularly important in closed-loop systems with recirculation. Thin platinum wires are used as electrodes from which the hydrogen bubbles detach to form the streamlines of the flow. Several quantitative requirements for a successful application of this technique have been described in the literature (Clutter and Smith 1961; Schweizer 1988). They concern the maximum wire diameter needed to guarantee a negligible disturbance effect of the electrode, the resulting diameter of the hydrogen bubbles necessary to limit the departure of the bubbles from the true streamlines due to buoyancy effects, and the electrical conductivity of the liquid required to provide adequate bubble production rates with inexpensive DC power supplies.

Other interesting tracers are very thin dye streams injected through small holes located along the solid walls of the flow and in the plane of interest (Schweizer 1988). Dye streams are suitable for visualizing interfaces in multilayer films, and solid surfaces of coating equipment, or, when the liquid detaches from the coating equipment, the free surface of the meniscus that starts at a static wetting line and ends at the dynamic wetting line. Since the latter streamline

continues to highlight the substrate surface, it also serves as a tool to measure static and apparent dynamic contact angles.

Depending on the flow field that needs to be visualized, or a particular detail thereof, there are numerous ways for mounting wire electrodes and for placing ports for dye filaments, see Fig. 7.18 for an overview. The main wire extending through the entire liquid film may be sandwiched between two plates of a multilayer coating die or 'hopper', as it is also called (Schweizer 1988), whereby the sandwich structure provides not only electrical insulation between the inclined plane and the wire, but also contains zinc shims which serve as slave electrodes for cathodic corrosion protection, Fig. 7.18a. An alternative for visualizing film flows is to lower the wire electrode into a small hole in the solid surface (Ikin 1992). If the surface is metallic, the hole may be drilled into an insulating material such as epoxy resin, which fills out a larger cavity in the vicinity of the wire electrode, Fig. 7.18b. Streamlines of internal flows such as slot flow in extrusion hoppers can be highlighted by pulling the wire through two holes located in line but on opposite sides of the slot confining walls (Sartor 1990), Fig. 7.18d. Visualizing free liquid surfaces is achieved by using additional wire electrodes mounted such that their tip just touches the free surface (Schweizer 1988; Blake, Clarke and Ruschak 1994). Owing to the high current density at the wire tip, the bubble production rate is also high, resulting in a concise bubble stream which, owing to buoyancy forces, tends to stay in the free surface as it progresses through the flow field, Fig. 7.18f.

Vortices, be they attached to solid or free surfaces, are divided from the main flow by the so called separating streamline, which starts and ends at stagnation points located on the surface. Visualizing internal streamlines of vortices is difficult because, in theory, there is no mass penetration, and hence no bubble penetration across the separating streamline, if the flow is laminar. In practice, it has proven useful to discharge hydrogen bubbles from the tip of an additional wire electrode which is temporarily

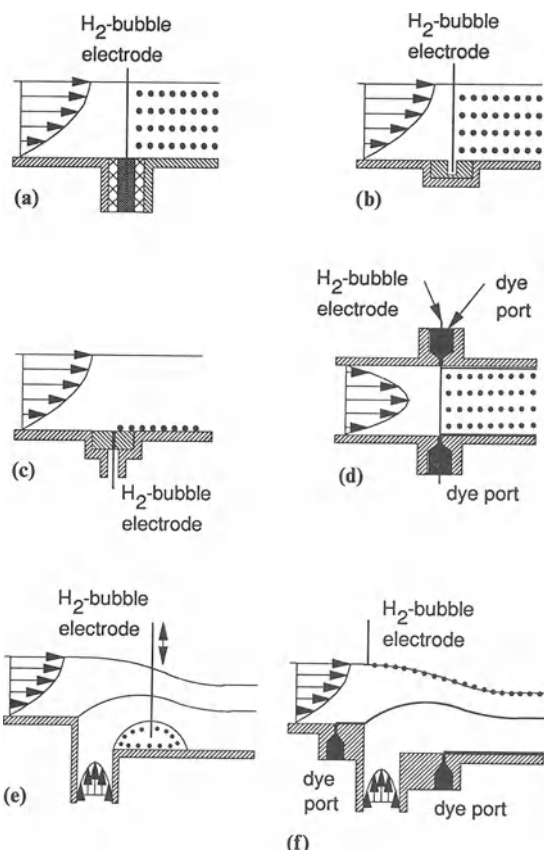


Figure 7.18 Flow visualization: generation of streamlines by way of (a) and (b) electrolysis along wire; (c) and (e) electrolysis at wire tip; (d) electrolysis along wire and injection of dye streams; (f) electrolysis at wire tip and injection of dye streams.

lowered into the vortex (Schweizer 1988), Fig. 7.18e. After withdrawal of the wire, the bubbles remain inside the vortex long enough to capture the flow patterns on film. For certain operating conditions, however, the flow inside the vortex is three-dimensional with a strong helical component, leading to an immediate drainage of the injected bubbles from the plane of observation, and making it impossible to visualize the local streamline pattern.

Flow features near the exit of slot flows, such as the bead of an extrusion coater, can be

visualized by physically combining the hydrogen bubble and dye injection methods, and in particular by injecting dye through the same holes that hold the electrode wire, Fig. 7.18d. While this is convenient from a hardware point of view, our own experience has shown that the sharpness of the dye filament downstream of the injection port decreases considerably due to the wire which acts as a disturbance. It is recommended to separate the dye ports and the electrode wire by a large enough distance so as to allow the decay of local disturbances (Sartor 1990).

Another possibility to point out contours of solid surfaces is to cast the electrode wire into the solid, possibly using an insulating epoxy resin, such that its tip is flush with the surface, Fig. 7.18c. Depending on the flow orientation with respect to gravity, this latter approach may lead to distorted stream line patterns because of unfavorable ratios between bubble rise velocity and film velocity, owing to the parabolic velocity profile near the solid wall.

Adding a small amount of fluorescent dye to the coating solution makes the liquid glow when illuminated, which helps to separate it optically from the surrounding solid or gas phases. This in turn is also a means of highlighting contours of film flows.

A different class of tracers are solid particles or flakes dispersed in the bulk of the coating solution. While this technique does not allow one to visualize flow cross-sections clearly, it may still give satisfactory results, particularly in situations where the above described methods are difficult to apply. Examples include Gaskell *et al.* (1992), who have produced illustrative pictures of recirculating flows in the nip of a meniscus roll coater, and Schweizer and Scriven (1983), who visualized the onset of Görtler-type vortices in curved film flows.

The unaided eye cannot resolve enough detail in the small-scale flow field of coating flows; hence, magnification is essential. A mono zoom microscope, e.g. Bausch & Lomb, is the instrument of choice, because it offers advantages such as ease of handling, large and variable working distance, flexible but sufficient magnification (7

to 1 zoom ratio), small depth of field, convenient focusing mechanism and camera adapters for silver halide or electronic imaging. A viable alternative with similar features but less comfort is to combine a low power ($5 \times$ to $20 \times$) microscope objective with a bellows and a camera. Higher magnification to resolve a particular detail of the flow field, for example the vicinity of a contact line, can be obtained by mounting an additional lens in front of the objective lens of the mono zoom. At the same time, however, the working distance decreases by the same factor as the magnification increases. In any case, the total magnification achievable with any type of optical system depends on the final viewing medium, for example a television screen or a photographic print. Typical magnification factors are on the order of 10 to 100.

While optical sectioning as described above is a powerful visualization technique and an efficient learning and communication tool, it is not without limitations. One major difficulty is related to visualizing multilayer films whose layers have different physical and optical properties. Differences in indices of refraction lead to unequal path lengths of the light, which explains why streamline patterns of multilayer films cannot be focused onto the same image plane in the camera, owing to the typically very small depth of focus of microscopes. Matching indices of refraction by adding salt to one of the fluids is a possibility. However, the approach is very tedious and renders the viscosity of that fluid a dependent variable. Adjusting the positions of the bubble wires in the different fluid layers to compensate for differences in optical path lengths is an attractive option.

Often, the flow visualization method is installed on an inexpensive table-top apparatus, where the liquid is not coated onto a dry substrate but onto a scraped roll, see Fig. 7.1. Therefore, any results influenced by dynamic wetting are burdened with uncertainty and must be used with caution.

The need for transparent fluids makes the method unsuitable for most practical coating solutions. It is therefore important to at least match rheological properties between model

liquids and real coating solutions by adding appropriate polymeric additives. It may also be advantageous to abandon the optical sectioning technique and to resort to alternative visualization methods such as the one described by Ikin (1992) who used an endoscope and a transparent hollow coating roll to observe the positions of the static and dynamic contact lines of the lower meniscus in slide coating.

To close this chapter, attention is directed to well known general references about flow visualization methods, including Merzkirch (1974), and several volumes of the Proceedings of the International Symposium on Flow Visualization, for example Véret (1987).

7.4 ALBUM OF COATING FLOWS

The capabilities of the optical sectioning method are demonstrated in a small ‘album of coating flows’, see Figs 7.20 to 7.24 (between pages 228 and 229). The flow fields are taken from the slide bead coating process; they show the slot exit flow including the position of the static wetting line (circle A in Fig. 7.19), the merging of two layers on the inclined hopper slide (circle B in Fig. 7.19), and the coating bead, i.e. the transfer of the liquid film from the hopper slide onto the moving

substrate (dynamic wetting, circle C in Fig. 7.19). The emphasis of the picture sequences is on showing the effects of changing geometrical or operating parameters.

The experimental setup was similar to the one schematically depicted in Fig. 7.1a. The surface to be coated was constantly cleaned by a rubber squeegee; it was dry to the touch, but not clean on a molecular scale. The slide angle, β , was held constant at 23°, the radius, R , of the coating roll was 53 mm, the slot height, H , was 500 μm , and the step height, F , (the off-set between adjacent hopper elements) was 1 mm. In all cases, the coating fluid was an aqueous glycerin solution. In two-layer experiments, both layers contained the same liquid to avoid differences in refractive indices. Interfaces were made visible by injecting a thin filament of green (sodium fluorescein, Kodak # 136 7499) and/or red (sulforhodamine B, Kodak # 136 7366) dye, or by generating hydrogen bubbles off the tip of a platinum wire with a diameter of 0.1 mm. Additional geometrical details are defined in Fig. 7.19. α is the application angle with respect to horizontal, γ is the lip angle, δ is the angle of the lip land with respect to the slide surface, Θ is the upstream angle of the chamfer at the slot exit, H_G is the coating gap, L_1 is the length of the lip land, L_2 is the length

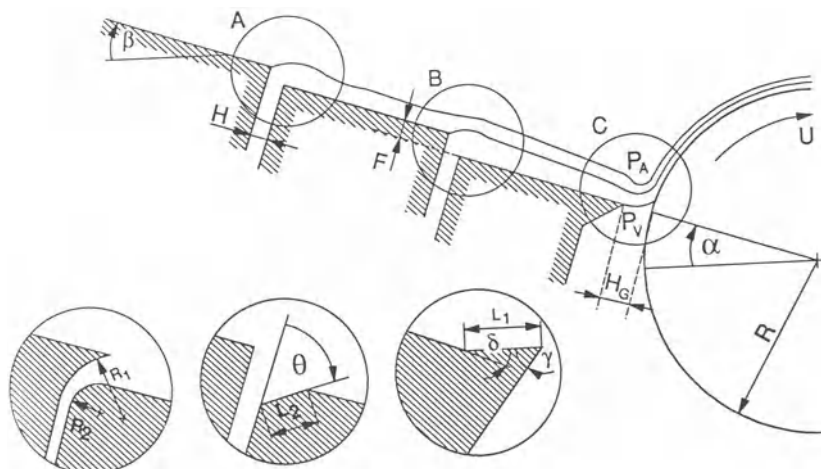


Figure 7.19 Schematic diagram of the slide coating process; forming, merging and coating of liquid films.

of the chamfer at the slot exit, R_1 is the upstream radius of the curved diffusor, R_2 is the downstream radius of the curved diffusor, μ is the viscosity, ρ is the density, σ is the surface tension, $\Delta P = P_A - P_V$ is the pressure difference across the coating bead (vacuum), Q_1 and Q_2 are the volumetric flow rates per unit width of the lower and upper layers, respectively and U is the coating speed. All relevant parameter values for each photograph are listed in Table 7.2.

In spite of considerable efforts devoted to the experimental work in the laboratory, the raw photographs did not turn out perfectly. Many of them were plagued by excessive reflections that distracted the attention of the viewer from the essential information in the picture. In other photographs, details of the equipment contour (e.g. lip shape, coating roll) were not clearly visible. To improve the appearance of the various flow fields, the photographs have been digitized (Kodak Photo CD System) and manipulated with the help of a software package called Adobe Photoshop. Image processing was restricted to removing unwanted reflections outside of the flow cross-section, and to enhancing equipment contours. At no time was the content of the flow field altered.

In Fig. 7.20a, liquid is flowing upwards in the

uppermost slot of a multilayer slide hopper. The flow boundary along the right slot wall appears as a white line; it has been visualized with a stream of hydrogen bubbles according to Fig. 7.18c. The opposite flow boundary in the slot is marked with a green line (injection of fluorescent dye, see Fig. 18d). At the slot exit, the liquid is turning to the right around a 90° corner, and it continues to flow as a gravity driven film down the inclined hopper slide. Here, the white line from the slot indicates the location of the slide plane, while the green line coincides with the free film surface. The upstream hopper plate is offset by a small distance with respect to the downstream plate so as to form a step in the slide surface. Finally, the flow rate, and the corresponding momentum of the slot flow, is low enough that the liquid is able to turn around the corner without separating on the downstream side. More importantly, the resulting film thickness on the slide is on the order of the step height, so that the static wetting line appears to be pinned to the upstream corner.

In Fig. 7.20b, the flow rate has been increased enough to cause flow separation after the downstream corner. Starting at the slot exit, the white line follows the path of the separating streamline, thereby outlining the shape and

Table 7.2 Parameter values for flow visualization photographs

Photo #	α (deg)	γ (deg)	δ (deg)	θ (deg)	R_1 (mm)	R_2 (mm)	L_1 (mm)	L_2 (mm)	H_G (μm)	μ (mPa s)	ρ (kg/m^3)	σ (mN/m)	ΔP (Pa)	Q_1 (cm^2/s)	Q_2 (cm^2/s)	U (m/s)
7.20a	—	—	—	0	—	—	—	—	16.0	1171	68.3	—	1.24	—	—	
7.20b	—	—	—	0	—	—	—	—	16.0	1171	68.3	—	3.30	—	—	
7.20c	—	—	—	0	—	—	—	—	28.0	1187	67.4	—	3.03	—	—	
7.21a	—	—	—	0	—	—	—	—	18.0	1175	68.1	—	3.06	1.19	—	
7.21b	—	—	—	67	—	—	—	5.9	—	18.0	1175	68.1	—	3.06	1.19	—
7.21c	—	—	—	0	2.5	3.5	—	—	18.0	1175	68.1	—	3.06	1.19	—	
7.22a	23	60	0	—	—	—	0.0	—	508	33.0	1191	67.1	0	1.22	1.56	0.28
7.22b	23	60	0	—	—	—	0.0	—	508	33.0	1191	67.1	49	1.22	1.56	0.28
7.22c	23	60	0	—	—	—	0.0	—	508	33.0	1191	67.1	196	1.22	1.56	0.28
7.23a	23	67	23	—	—	—	1.0	—	254	13.7	1165	68.6	0	0.56	1.96	0.83
7.23b	23	90	0	—	—	—	0.0	—	254	13.7	1165	68.6	0	0.56	1.96	0.83
7.23c	23	135	-45	—	—	—	1.41	—	254	13.7	1165	68.6	0	0.56	1.96	0.83
7.24a	46	53	0	—	—	—	0.0	—	508	24.7	1184	67.6	0	3.49	—	0.78
7.24b	0	53	0	—	—	—	0.0	—	508	24.7	1184	67.6	0	3.49	—	0.78
7.24c	-23	53	0	—	—	—	0.0	—	508	24.7	1184	67.6	0	3.49	—	0.78

location of the resulting vortex. Here, the streamline pattern inside the vortex is not visualized. As a consequence of the increased flow rate, the free film surface above the slot exit is bulging out, but the static wetting line is still pinned to the corner. Experiments have shown that excessive bulging leads to a metastable flow that will rearrange into a different stable state, if sufficiently disturbed. The result is evident in Fig. 7.20c, where, upon tapping on the hopper, the static wetting line has moved several slot heights upstream along the upstream hopper plate, thereby forming a wedge of liquid that is separated from the exiting slot flow. The flow pattern inside the wedge is similar to the classical corner flow described by Moffatt (1964) and Taneda (1979), in that the wedge is filled with a series of vortices, driven by the outer flow, and rotating in alternate directions. The size and rotational strength of the vortices decrease rapidly in the upstream direction, so that only the streamlines of the first vortex can be visualized (Fig. 7.18e).

In Fig. 7.21a, liquid is exiting from a slot in the same way as described in Fig. 7.20a. In addition, a second liquid layer, generated further upstream on the slide, is merging with the exiting liquid to form a two-layer film downstream of the slot. The lower white line marks the downstream slot boundary and the slide surface. The green line follows the upstream slot boundary and continues as the interface between the two liquid layers. The upper white line is generated by hydrogen bubbles according to Fig. 7.18f and is indicative of the free film surface. As in Fig. 7.20b, the flow rate of the slot flow is too high, resulting in a large vortex downstream of the exit. Attempts to facilitate the change in flow direction and to prevent the onset of separation by cutting of the sharp 90° corner are shown in Fig. 7.21b. Obviously, this measure is not effective, because, with all other parameters held constant, separation cannot be prevented. In fact, the size of the vortex has only marginally decreased. In contrast, Fig. 7.21c shows a slot exit design involving a 'curved diffusor.' Here, the change in flow direction is forced upon the liquid by the

upstream hopper plate, and flow separation is completely suppressed. An eddy, located further downstream on the slide, will only appear if the flow rate of the slot flow is considerably increased.

The flow field of the 'coating bead', i.e. the liquid bridge between the end of the hopper slide and the moving web, is shown in Fig. 7.22a. Two layers are being coated, whereby the green, red and white streamlines depict the slide surface, the layer interface and the free film surface, respectively. These streamlines have been visualized according to Fig. 7.18f. In addition, the upper layer appears bright, because hydrogen bubbles have been released according to Fig. 7.18b. In contrast, the cross-section of the lower layer is dark, as no bubbles have been generated intentionally. The purpose of the picture sequence in Fig. 7.22 is to show the effect of the pressure difference (vacuum) across the liquid bridge on the location of the lower meniscus and the dynamic wetting line. In Fig. 7.22a, the pressure difference across the bead is zero. The lower meniscus (shown as the continuation of the green streamline) is pinned to the tip of the hopper slide (lip), its shape is straight, and the dynamic wetting line is located more than one gap width above the corner of the lip. The apparent dynamic contact angle is about 143°.

Increasing the vacuum to 49 Pa (Fig. 7.22b) and 196 Pa (Fig. 7.22c) causes the dynamic wetting line to move upstream along the web surface. At first, the static wetting line remains pinned to the lip corner. However, as the separating angle between the slide surface and the lower meniscus continues to increase, critical conditions will eventually be reached where the so called Gibbs inequality (Gibbs 1906; Kistler 1983) is violated. At that point, the static wetting line migrates downstream along the underside of the lip. As the lip angle in this example is only 60°, and as the bead flow field is illuminated from above the hopper slide, the lip itself is casting a shadow over the flow field near the static wetting line, rendering it invisible. Therefore, the green streamline in Figs 7.22b and 7.22c is only indicative of the position and shape of the lower meniscus near the dynamic wetting line but not near the

static contact line. Additional flow visualization experiments have revealed that for many operating conditions, particularly for small lip angles, the liquid near the static wetting line is separated from the main flow, and a wedge, filled with a series of vortices, is formed, much like the one shown in Fig. 7.20c.

For the parameter sequence in Fig. 7.22, the apparent dynamic contact angle decreases from 143° to 134° and to 133° as the vacuum is increased from zero to 49 Pa and to 196 Pa.

The effect of the lip shape on the flow field of the bead is shown in Fig. 7.23 for a two-layer film. The sequence of geometrical changes starts with a ‘normal’ 90° corner (Fig. 7.23a), continues with an upswept or ‘ski jump’ lip (Fig. 7.23b), and ends with a downswung or chamfered lip (Fig. 7.23c). Process conditions such as flow rate, viscosity and substrate speed have been chosen such that the characteristic dimension of the bead flow field, e.g., the minimum film thickness on the slide, is comparable to the characteristic dimension of the lip geometry, e.g., the length of the lip land. This is a prerequisite for the lip geometry to have a significant effect on the flow field. The effects manifest themselves in different locations for the minimum film thickness on the slide and the dynamic wetting line on the substrate, in different radii of curvature of the upper meniscus, and in different amounts of ‘back flow’ (flow opposite to the web motion near the dynamic wetting line), as is clearly visualized by the red streamline marking the interface between the two layers. According to several patents (Jackson 1976; Isayama and Takehara 1979; Choinski 1981), upswept lip geometries are favorable to postpone the onset of ribbing lines to higher coating speeds, see also Chapter 11b.

If, on the other hand, the flow rate is increased compared with the conditions in Fig. 7.23, the liquid volume in the bead, and hence its characteristic dimension, will grow to such an extent that the details of the lip geometry will no longer have a significant effect on the flow field.

The last picture sequence depicts the effect of the application angle on the bead flow field for a single-layer film. In Fig. 7.24a, the application

angle is 46° positive, meaning that the application point is in the upper quadrant of the coating roll (the application angle is measured against a horizontal line through the center of the coating roll). In Fig. 7.24b, the application angle is zero, i.e. the tip of the hopper lip is level with the center of the coating roll. Finally, in Fig. 7.24c, the application angle is 23° negative, moving the application point well into the lower quadrant of the coating roll.

Similar to Fig. 7.23, the magnitude and location of the minimum film thickness on the slide and the radius of curvature of the upper meniscus are greatly affected by this geometrical parameter. In fact, the impingement angle as determined by the local feature of the lip geometry in Fig. 7.23b is 113° and equal to the impingement angle in Fig. 7.24a; furthermore, the impingement angles in Figs 7.23c and 7.24c are also similar (both <90°). Thus, it appears that desired features of the bead flow field may be obtained in two ways, either by varying the characteristic dimension of the lip geometry (if it matches the characteristic dimension of the bead flow field), or by varying the application angle. Unfortunately, neither way is convenient or cheap, if a particular feature should be maintained for several coating applications with greatly differing process parameters such as flow rate, viscosity and substrate speed.

7.5 OUTLOOK

Today, the ‘tripartite’ or ‘three-legged stool’ approach is well established in both industrial and academic coating flow research, and experimental methods are recognized as valuable tools to advance the fundamental understanding of coating processes. Nevertheless, there still is room for improving various aspects of these methods.

To this day, the process of dynamic wetting, for example, is not fully understood. Clearly, the reason is a lack of clear insight into what happens at the three-phase contact line. The challenge, therefore, is to develop a visualization technique that is able to resolve the wetting process on at least a sub-micron scale. Attempts of the author

in this direction were not successful. The goal was to investigate dynamic wetting of the slide coating process by using the maximum magnification of a standard stereo-zoom microscope. Failure was mainly due to insufficient lighting, the inability to keep the wetting line in the viewing field of the microscope because of slight spatial fluctuations of the contact line position, and the lack of suitable tracers in the liquid/air interface that approaches the wetting line.

Another aspect offering room for improvement does not concern specific experimental methods, but their application in general. In a highly competitive industrial environment, resources can be deployed meaningfully, and the return on experimental work can be maximized, if experimental techniques are consistently combined with statistical experimental design methods as appropriate.

Finally, the major role of experimentation is to reveal the fundamental and elemental behavior of the physical world in general and of coating processes in particular, in order to guide the development of individual terms in theoretical models (Churchill 1992). Experimental data, however, are recognized as being subject to uncertainty and imprecision arising from incomplete definition and control of the environment in which the experiments are conducted (for example, the variation of physical properties with temperature), and also from measurement errors. Consequently, care must be taken to increase the reliability of experimental results, if the important role of experimentation is to be carried out successfully.

ACKNOWLEDGMENTS

I am grateful to Jacques Rast, manager of Production Technology, and Pierre-André Rossier, research engineer, both at ILFORD AG in Fribourg, Switzerland, for their informative input and for providing illustrative examples about the Quantification of Film Thickness Uniformity. I am grateful to René Sudan, technician at ILFORD AG, for setting up the experimental flow visualization rig and for carrying out much of the

experimental work. His commitment and resourcefulness led to the development of several new features of the visualization technique. I am also indebted to René Sudan, and Rita Hofmann, research physical chemist at ILFORD AG, for offering their time to improve the flow visualization pictures with digital image processing techniques.

REFERENCES

- Abramowitz, M. and Stegun, I. A. 1965. *Handbook of Mathematical Functions*. New York: Dover Publishing.
- Adobe Systems Incorporated. 1585 Charleston Road, PO Box 7900, Mountain View, CA 94039-7900, USA.
- Adrian, R. J. 1991. Particle-imaging techniques for experimental fluid mechanics. *Ann Rev. Fluid Mechanics*. **23**.
- Aidun, C. K., Veverka, P. J. and Scriven, L. E. 1992. Interfacial instability and excessive air entrainment. Paper 49a read at *6th International Coating Process Science and Technology Symposium*, AIChE Spring National Meeting, 29 March–2 April 1992, New Orleans, LA.
- Asoma Instruments, 1992. *X-ray Fluorescence—Application Summary for Coating Weight Measurement*. 11675 Jollyville Road, Austin, TX 78759, USA.
- Ayers, J. 1993. *Capacitive Dimensional Measurement—Theory and Application*. Technical Report, Lion Precision Corporation, 563 Shoreview Park Road, St Paul, MN 55126-7014.
- Batchelor, B. G. and Waltz, F. 1993. *Interactive Image Processing for Machine Vision*. New York: Springer Verlag.
- Bausch & Lomb, MonoZoom-7 Optical System, Bausch & Lomb Inc., Optical Systems Division, PO Box 450, Rochester NY 14692-0450.
- Beiser, L. 1974. Laser scanning systems. In *Laser Applications, Volume 2*, ed. Monte Ross, pp. 53–160. New York: Academic Press.
- Bird, R. B., Armstrong, R. C. and Hassager, O. 1977. *Dynamics of Polymeric Liquids, Volume 1: Fluid Mechanics*. New York: Wiley.
- Blake, T. D., Clarke, A. and Ruschak, K. J. 1994. Hydrodynamic assist of dynamic wetting. *AIChE Journal*. **40**(2): 229–242.
- Blum, G., Daams, H. J., Flegel, H. et al. 1990. Rascher Zugriff, wirkungsvolle Lenkung; optoelektronische Messverfahren zur fertigungsintegrierten Qualitäts-sicherung. *Technische Rundschau*. **50**(82): 22–33.
- Branston, R. E., Clark, P. C., Errico, M., Scriven, L. E., Sheehan, J. G., Suszynski, W. J., Takamura, K.

- and Vodniek, J. L. 1994. Weeping in blade coating, Part I: High-speed video and still macro-photography. *TAPPI Journal*. 77(1): 131–138.
- Breitmeier, U. 1993. Schnell abtasten: optische und taktile Oberflächenprofilometrie. *Kontrolle*. (October): 38–42.
- Breuckmann GmbH, Industrielle Bildverarbeitung und Automation, Kunkelgasse 1, D-7758 Meersburg, Germany.
- Breuckmann, B. and Thieme, W. 1985. Computer analysis of holographic interferograms using phase shift method. *Applied Optics*. 24: 2145–2149.
- Buchhave, P. 1992. Particle image velocimetry – status and trends. *Experimental Thermal and Fluid Science*. 5: 586–604.
- Buckingham, E. 1914. *Physic. Rev.* 4: 345–376.
- Campanella, O. H. and Cerro, R. L. 1984. Viscous flow on the outside of a horizontal rotating cylinder: The roll coating regime with a single fluid. *Chem. Engng. Sci.* 39(10): 1443–1449.
- Campbell, F. W. and Robson, J. G. 1968. Application of Fourier analysis to the visibility of gratings. *J. Physiology*. 197: 551–566.
- Capacitec, PO Box 819, 87 Fitchburg Road, Ayer, MA 01432, USA.
- Chen, K. S. A. and Scriven, L. E. 1992. Multilayer slide coating: flow visualization and theoretical modeling. Paper 4li read at 6th International Coating Process Science and Technology Symposium, AIChE Spring National Meeting, 29 March–2 April 1992, New Orleans, LA.
- Choinski, E. J. 1981. Method and apparatus for coating web. US Patent 4,283,443, August 11, 1981, Polaroid Corporation.
- Churchill, S. W. 1992. The role of analysis in the rate processes. *Ind. Eng. Chem. Res.* 31(3): 643–658.
- Clarke, A. 1995. The application of particle tracking velocimetry and flow visualization to curtain coating. *Chem. Eng. Sci.* 50(15): 2397–2407.
- Clarke, A. 1996. Recirculating flows in curtain coating. Proceedings of the First European Coating Symposium on the Mechanics of Thin Film Coatings, eds P. H. Gaskell, M. D. Savage and J. L. Summers, pp. 32–41. Singapore: World Scientific Publishing.
- Clutter, D. W. and Smith, A. M. O. 1961. Flow visualization by electrolysis of water. *Aerospace Engineering* 1: 24–76.
- COMPUR Electronic GmbH, D-8000 Munich, Germany.
- Cornsweet, T. N. 1970. *Visual Perception*. New York: Academic Press.
- Coyle, D. J., Macosko, C. W. and Scriven, L. E. 1982. Computer simulation of nip flow in roll coating. In *Computer Applications in Applied Polymer Science*, ed. T. Provder, pp. 251–264. ACS Symposium Series 197, Washington: American Chemical Society.
- Daniel, C. and Wood, F. S. 1971. *Fitting Equations to Data*. New York: Wiley.
- Dantec Publication No. 9002E, Dantec Elektronik, Tonsbakken 16-18, DK-2740 Skovlunde, Denmark.
- Deming, S. and Morgan, S. 1986. *Fundamentals of Experimental Design*, Short Course of the American Chemical Society, Department of Educational Materials, 1155 16th Street N.W., Washington, DC 20036.
- Draper, N. R. and Smith, H. 1966. *Applied Regression Analysis*. New York: Wiley.
- Dubovik, A. 1981. *The Photographic Recording of High-Speed Processes*. New York: Wiley.
- Durst, F., Melling, A. and Whitelaw, J. H. 1976. *Principles and Practice of Laser-Doppler Anemometry*. London: Academic Press.
- Eastman Kodak Company. 1993. Motion Analysis Systems Division, 11633 Sorrento Valley Road, San Diego, CA 92121-1097.
- ECHIP Inc., 7460 Lancaster Pike, Suite 6, Hockessin, DE 19707.
- Edgar, R. F. and Stay, B. J. 1985. Techniques for suppressing optical interference errors in infrared film gauging. *Infrared Technology and Applications*, SPIE 590: 316–320.
- Gaskell, P. H., Malone, B., Savage, M. D. and Thompson, H. M. 1992. Flow visualization study of meniscus roll coating. Paper 41j read at 6th International Coating Process Science and Technology Symposium, AIChE Spring National Meeting, 29 March–2 April 1992, New Orleans, LA.
- Gellrich, P., Schliephake, R., Matter, G. and Sturm, W. 1991. Versuchsbegiessanlagen für Fotofilme und Fotopapier. *Coating*. 3: 76–81.
- Gibbs, J. W. 1906. *The Scientific Papers of J. W. Gibbs, Volume I: Thermodynamics*. pp. 314–331. New York: Longmans, Green and Co.
- Grant, I. and Liu, A. 1990. Directional ambiguity resolution in particle image velocimetry by pulse tagging. *Experiments in Fluids*. 10: 71–76.
- Grassmann, P. 1971. *Physical Principles of Chemical Engineering, Volume 12*, International Series of Monographs in Chemical Engineering. General editor: P. V. Danckwerts. Oxford: Pergamon Press.
- Hassan, Y. A., Blanchat, T. K. and Seeley Jr., C. H. 1992. PIV flow visualization using particle tracking techniques. *Meas. Sci. Technol.* 3: 633–642.
- Hesselink, L. 1988. Digital image processing in flow

- visualization. *Annual Review of Fluid Mechanics*. **20**: 421–485.
- Hesselink, L., Helman, J. and Ning, P. 1992. Quantitative image processing in fluid mechanics. *Experimental Thermal and Fluid Science*. **5**: 605–616.
- Hindle, P. H. 1984. Thickness measurement – the infrared method. *Paper Technology and Industry*. **25**(5).
- Hurley, R. B., Kaufman, I. and Roy, R. P. 1990. Noncontacting microstrip monitor for liquid film thickness. *Rev. Sci. Instrum.* **61**(9): 2462–2465.
- Ikin, J. B. 1992. Flow visualization studies of a slide bead coating process. Paper 41c read at *6th International Coating Process Science and Technology Symposium*, AIChE Spring National Meeting, 29 March–2 April 1992, New Orleans, LA.
- Infrared Engineering Limited, Galliford Road, The Causeway, Maldon, Essex, CM9 7XD, England.
- Intec Corporation, 1 Trefoil Drive, Trumbull, CT 06611, USA.
- Isayama, S. and Takehara, N. 1979. Web coating. UK Patent Application 2037 622 A, filing date December 11, 1979. Fuji Photo Film Co.
- Jackson, B. W. 1976. Apparatus for coating a web. US Patent 3,993,019, November 23, 1976. Eastman Kodak Company.
- KEYENCE Corporation, 2-13, Aketa-cho, Takatsuki, Osaka 569, Japan.
- Kistler, S. F. 1983. The fluid mechanics of curtain coating and related viscous free surface flows with contact lines. PhD thesis, University of Minnesota. Available from University Microfilms International, Ann Arbor, MI.
- Kistler, S. F. and Scriven, L. E. 1983. Coating flows. In *Computational Analysis of Polymers*, ed. J. Pearson and S. Richardson, pp. 243–299. New York: Applied Science Publishers.
- Kheshgi, H. S. and Scriven, L. E. 1983. Measurement of liquid film profiles by moiré topography. *Chem. Eng. Sci.* **38**(4): 525–534.
- Kheshgi, H. S. and Scriven, L. E. 1991. Dewetting: nucleation and growth of dry regions. *Chem. Eng. Sci.* **46**(2): 519–526.
- Kobayashi, C., Saito, H. and Scriven, L. E. 1982. Study of slide coating by finite element method. Paper 45e read at *AIChE Spring National Meeting*, 28 February–3 March 1982, Orlando, FL.
- Kueppers, H. 1973. *Color: origin, systems, uses*. London: Van Nostrand Reinhold.
- LabWindows 1991. Version 2.1. National Instruments Corporation, 6504 Bridge Point Parkway, Austin, TX 78730-5039.
- Lion Precision Corporation, 563 Shoreview Park Road, St Paul, MN 55126-7014.
- Longhurst, R. S. 1973. *Geometrical and physical optics*. 3rd edn. New York: Longman.
- Lyne, M. Bruce and Parush, A. 1983. A survey of offset and letterpress newsprint print quality. *J. Pulp and Paper Science, Trans. of the Technical Section*. **9**(5): 1–7.
- Lynn, P. A. 1983. *An Introduction to the Analysis and Processing of Signals*. New York: Macmillan Press.
- Makosko, C. W. 1994. *Rheology – Principles, Measurements and Applications*. New York: VCH Publishers.
- Macosko, C. W. and Scriven, L. E. 1984. *Coating flows and coating rheology research: A review for interested researchers and companies*. Department of Chemical Engineering and Materials Science, University of Minnesota, Minneapolis, Minnesota, September 20–21, 1984.
- MathCAD. Version 2.0. MathSoft Inc., 1 Kendall Square, Cambridge, MA 02139.
- McRae, D. J. 1988. Using capacitive sensing for noncontact dimensional gauging. *Sensors*. October: 13–20.
- Meadows, D. M., Johnson, W. O. and Allen, J. B. 1970. Generation of surface contours by moiré patterns. *Applied Optics*. **9**(4): 942–947.
- Merzkirch, W. 1974. *Flow Visualization*. New York: Academic Press.
- Meyer, W. and Schilz, W. 1980. A microwave method for density independent determination of the moisture content of solids. *J. Physics D: Applied Physics*. **13**: 1823–1830.
- Moffatt, H. K. 1964. Viscous and resistive eddies near a sharp corner. *J. Fluid Mechanics*. **18**: 1–18.
- Moisture Systems Corporation, 117 South Street, Hopkinton MA 01748, USA.
- Montgomery, Douglas, C. 1984. *Design and analysis of experiments*. New York: Wiley.
- Mues, W., Hens, J. and Boij, L. 1989. Observation of a dynamic wetting process using laser-Doppler velocimetry. *AIChE Journal*. **35**(9): 1521–1526.
- Nishijima, Y. and Oster, G. 1963. Moiré patterns: their application to refractive index and refractive index gradient measurements. *J. Optical Society of America*. **54**(1): 1–5.
- Ogawa, S. and Kashiwabara, Y. 1992. Theoretical and experimental study of curtain coating flow. Paper 41b read at *6th International Coating Process Science and Technology Symposium*, AIChE Spring National Meeting, 29 March–2 April 1992, New Orleans, LA.
- Oldengarm, J., van Krieken, A. H. and van der Klooster, H. W. 1975. Velocity profile measurements in a liquid film flow using the laser Doppler technique. *J. Physics E: Scientific Instruments*. **8**: 203–205.

- Oxford Lasers Inc. 1992. Data sheet on laserstrobe. 33 Nagog Park, PO Box 2620, Acton, MA 01720-6620.
- Pietzsch, K. and Müller, P. 1988. Automatic surface inspection with laser scanners for quality control in the production of steel strip. *World Steel and Metalworking*. **9**: 240.
- Pietzsch, K., Müller, P. and Feige, C. 1988. Lückenlose Oberflächenprüfung mit Laserscannern. *Metall Oberfläche*. **42**(8): 373–378.
- Rast, J. 1989. Spectral analysis of mottle. Unpublished Technical Report. ILFORD AG, Fribourg, Switzerland.
- Rheinmetall Sick Optical Inspection Systems GmbH, Machtlfingerstrasse 21, D-8000 Munich, Germany.
- Rossier, P. A. 1992. Quantification of cross-profiles and other coating defects. Unpublished Technical Report. ILFORD AG, Fribourg, Switzerland.
- Roy, R. P., Ku, J., Kaufman, I. and Shukla, J. 1986. Microwave method for measurement of liquid film thickness in gas-liquid flow. *Rev. Sci. Instrum.* **57**(5): 952–956.
- Russ, J. C. 1992. *The Image Processing Handbook*. Boca Raton: CRC Press.
- Saito, H. and Scriven, L. E. 1981. Study of coating flows by the finite element method. *J. Comp. Physics*. **42**: 53.
- Sartor, Luigi. 1990. Slot coating: Fluid mechanics and die design. PhD thesis, University of Minnesota.
- SAS. 1987. SAS system for elementary statistical analysis. Version 6. SAS Institute Inc., Box 8000, SAS Circle, Cary, NC 27512–8000.
- Savage, M. D., Gaskell, P. H., Malone, B. and Thompson, H. M. 1992. The relevance of lubrication theory to roll coating. Paper 39e read at 6th International Coating Process Science and Technology Symposium, AIChE Spring National Meeting, 29 March–2 April 1992, New Orleans, LA.
- Schraub, F. A., Kline, S. J., Henry, J., Runstadler Jr., P. W. and Littell, A. 1965. Use of hydrogen bubbles for quantitative determination of time-dependent velocity fields in low-speed water flows. *J. Basic Engineering, Transactions of the ASME*. **6**: 429–444.
- Schweizer, P. M. 1988. Visualization of coating flows. *J. Fluid Mechanics*. **193**: 285–302.
- Schweizer, P. M. 1992. Fluid handling and preparation. In *Modern Coating and Drying Technology*, eds Edward D. Cohen and Edgar B. Gutoff, pp. 23–61. New York: VCH Publishers.
- Schweizer, P. M. and Scriven, L. E. 1983. Evidence of Görtler-type vortices in curved film flows. *Physics of Fluids*. **26**(3): 619–623.
- Schweizer, P. M. and Widmer, F. 1981. Die Verweilzeit mittel- und hochviskoser Flüssigkeiten im Dünn-schichtapparat. *Verfahrenstechnik*. **15**(1): 29–33.
- Scriven, L. E. and Suszynski, W. J. 1990. Visualizing coating flows builds process understanding. *Chem. Engng. Progress*. **9**: 24–29.
- Shulman, A. R. 1970. *Optical data processing*. New York: Wiley.
- Sick, E. 1972. Vorrichtung zum photoelektrischen Abtasten durchlaufenden Gutes. Patentschrift der Bundesrepublik Deutschland, DE 1 422 235. Ausgabetag October 26, 1972. Erwin Sick GmbH Optik-Elektronik.
- Sick, E. 1979. Lichtleitstab. Patentschrift der Bundesrepublik Deutschland, DE 27 00 027. Ausgabetag September 20, 1979. Erwin Sick GmbH Optik-Elektronik.
- Spiers, R. P., Subbaraman, C. V. and Wilkinson, W. L. 1974. *Chem. Engng. Sci.* **29**: 389.
- Statgraphics STSC Inc., 2115 East Jefferson Street, Rockville, MD 20852.
- Takasaki, H. 1970. Moiré topography. *Applied Optics*. **9**(6): 1467–1472.
- Takasaki, H. 1979. The development and the present status of moiré topography. *Optica Acta*. **26**(8): 1009–1019.
- Taneda, S. 1979. Visualization of separating Stokes flows. *J. Phys. Soc. Japan*. **46**(6): 1935–1942.
- Tharmalingam, S. and Wilkinson, W. L. 1978. The coating of Newtonian liquids onto a rotating roll. *Chem. Engng. Sci.* **33**: 1481–87.
- Theocaris, P. S. 1967. Moiré topography of curved surfaces. *Experimental Mechanics*. **7**(7): 289–296.
- Torgerson, W. S. 1958. *Theory and Methods of Scaling*. New York: Wiley.
- UBM Messtechnik GmbH, Ottostrasse 2, D-7505 Ettlingen, Germany.
- Véret, C. 1987. Flow Visualization IV, *Proceedings of the Fourth International Symposium on Flow Visualization*, August 26–29, 1986, Paris. Washington: Hemisphere Publishing Corporation, and Berlin: Springer Verlag.
- Williamson, S. J. and Cummins, H. Z. 1983. *Light and Color in Nature and Art*. New York: Wiley.
- Yeckel, A. and Scriven, L. E. 1992. Multiparameter continuation methods for tracking desired flow states. Paper read at *Supercomputing '92 Conference of the IEEE/ACM*, 16–20 November 1992, Minneapolis, Minnesota.

ASYMPTOTIC METHODS FOR THE MATHEMATICAL ANALYSIS OF COATING FLOWS

8

Marc K. Smith

8.1 INTRODUCTION

As we have seen in Part One of this book, coating a solid surface with a liquid film is a very complex physical process. The behavior of the liquid film is influenced in very important and fundamental ways by the physics associated with surface tension and interfacial phenomena, the wetting of the solid by the liquid, fluid rheology, surfactants, and the heat and mass transfer and chemical reactions involved in the drying and curing of the film. One of the tasks of a coating engineer or scientist is to incorporate these physical effects into a predictive mathematical model of the coating process. Complete and accurate mathematical models and accurate numerical computations for simple coating processes are available today. However, this is not the case for the mathematical models of the more complicated coating processes. These complex models may contain many dependent variables and have large sets of nonlinear differential equations and boundary conditions. They may be posed on a very complicated geometry. For some effects, such as wetting and fluid rheology, the fidelity and accuracy of the mathematical models are still debated. These and other difficulties put the solution of such complex models out of the range of our mathematical capabilities and may severely strain our current numerical methods. In addition,

the uncertainties in the physics of some portions of these models bring into question whether accurate predictions are indeed possible.

In spite of this difficulty, there has been significant progress in the understanding of coating flows because many of the important and interesting questions that needed to be answered allowed for great simplifications in the mathematical models. Many of these more successful coating flows are strongly two-dimensional, and so we may confine our attention to a two-dimensional version of the mathematical model. The characteristic length scale associated with the motion of the liquid in most coating flows is very small, and so the Reynolds number is small. Thus, the flow is laminar and all of the questions and concerns associated with the modeling and calculation of a turbulent flow in the liquid do not appear. Finally, all of the possible complexities that could appear in a coating flow may not all appear in any one coating flow, or at least not all in the same area of interest. Thus, some of the complex effects described above can quite often be ignored in a calculation designed to answer a question concerning one particular region of the flow field. For example, the liquid being coated in a particular process may not display any significant non-Newtonian effects in the region of interest.

In this chapter, we consider simple two-dimensional coating flows composed of an incompressible, Newtonian liquid, and in which heat and mass transfer effects are negligible. The mathematical model for such a flow is composed of the Navier–Stokes equations, the incompressible continuity equation, and the appropriate stress and kinematic boundary conditions on any solid or free surface in the system. Modern numerical codes of the sort described in Chapter 9 have been developed to the point where the accurate solution of these model equations in many different coating flow geometries is fairly routine. However, such simulations have their own limitations. It is often just as difficult for an engineer with a numerical code to understand the dominant physical interactions simulated by the computations as it is for an engineer looking at the actual physical coating process itself. Certainly, the computations will provide megabytes of data and detailed pictures of the relevant flow fields and variables, some of which may be difficult or impossible to measure. But the precise interplay of the forces that govern the behavior of the flow is sometimes difficult to determine, both numerically and experimentally. It is here that a mathematical analysis can contribute most effectively to the understanding of coating flows.

Exact solutions of the full form of the mathematical model for coating flows are very rare. This is due to the complicated geometry of the flows, the nonlinearities of the differential equations and boundary conditions, and the presence of a free surface or of liquid–liquid interfaces whose locations are unknown. In wetting problems, there is the additional complexity of a moving contact line whose location is also unknown (see Chapter 3 for a discussion of this contact-line problem). To make progress with a mathematical analysis of a coating flow in the midst of all this complexity, some simplification of the model is necessary. One way to do this is to exploit the presence of a small parameter in the model. For example, in some coating flows the thickness of the film is less than one millimeter. If this corresponds to a small Reynolds number for the flow, then we can justifiably neglect the nonlinear

acceleration terms in the momentum equations. This low-Reynolds number flow or Stokes' flow is somewhat simpler to handle.

Another way to produce mathematical results is to look in those regions of the model where the flow and the geometry are particularly simple. For instance, the rectilinear flow of a liquid film down an inclined plane has an exact solution, because the parallel flow eliminates the nonlinear acceleration terms and the difficulties associated with the unknown free surface. Such a simple flow is found in the slide coating, dip coating and curtain coating processes for example. It may also be the case that the length scale of the longitudinal flow variations in a liquid film is much larger than the thickness of the film. In such a case, the flow may be considered as almost one-dimensional. This type of simplification is the basis of lubrication theory, which is used so extensively in coating flows and tribological problems. One of the results obtained from an analysis of a thin liquid film using lubrication theory is a differential equation for the shape of the free surface. In fact, modern numerical algorithms have used such results to construct the appropriate boundary conditions that match a two-dimensional flow region to a one-dimensional flow region (see Chapter 9 for examples of this technique).

The simplifications described above are at the heart of a collection of mathematical techniques known as asymptotic methods. These techniques exploit the smallness or largeness of some of the parameters in a problem in order to reduce the original equations to a simpler set of equations. The terms in these simpler equations reflect the fundamental balance of forces in the problem as measured by the small or large parameters. The result of the analysis is an approximation to the exact solution with an error that is well characterized. The purpose of this chapter is to acquaint the reader with the basics of asymptotic analysis and to show how such techniques can be used to understand essential aspects of various coating flows.

As a matter of perspective, we note that there are many other techniques besides asymptotic

methods that can be used to develop simplified theories or to approximate the solutions of differential equations. One of the simplest techniques, as we discussed above, is the removal of any small terms from the governing equations. Two prominent examples of this method, lubrication theory and boundary-layer theory, show that it can produce very useful mathematical models. The danger of this technique is that the *ad hoc* nature of the process could lead to inconsistencies in the removal of the small terms. There is also no way to estimate the errors associated with the process. Luckily, many of these simplified theories, such as lubrication theory for example, can be developed in a systematic and consistent manner using the ideas of asymptotic analysis, as we will see below.

Galerkin's method and the various forms of the method of weighted residuals are also popular ways to find approximate solutions to differential equations. These methods begin by writing the solution of the problem in terms of a finite series of well-known basis functions with unknown coefficients. The coefficients are determined so that the series satisfies the governing equations in some sense, where the 'sense' being used is what defines the particular method. When a large number of terms are used in the series, the coefficients are determined numerically. For example, the finite-element method discussed in Chapter 9 is based on Galerkin's method.

Galerkin and weighted-residual methods are useful in terms of deriving approximate mathematical theories when only a small number of coefficients are used. For example, in some transient problems with one spatial dimension the method of weighted residuals produces a small set of coupled ordinary differential equations for the time-dependent coefficients that works well in terms of describing the response of the original system. The work of Joo and Davis (1992), which is discussed in Section 8.6.1 below, contains an example of this approach.

The integral method is another easy and effective approximation technique that is often used in problems involving boundary layers or thin liquid films. In this method, the governing

equations are first integrated over the thickness of the layer. The resulting integrals are then evaluated using simple approximations or correlations for the dependent variables. The result is a differential equation that describes the thickness of the layer as a function of the remaining independent coordinates. This method is very useful if the response of the system is fairly insensitive to the details of the solution across the thickness of the layer. As an example, the momentum integral equation used in the study of boundary-layer flows is derived using this technique. The derivation is discussed in most elementary fluid mechanics textbooks.

The methods discussed above are very useful when they work and have led to significant advances in the study of various fluid flows. However, in the remainder of this chapter we will confine ourselves to the study and use of asymptotic methods. This reflects the opinion of the author that the techniques are some of the more powerful and rigorous of the approximation methods at our disposal.

In the next section, we present a brief discussion of four different asymptotic methods. This will not be an extensive tutorial on these methods, but rather a look at the kinds of problems that are amenable to such analysis and the kinds of approximation that result. In the remainder of this chapter, we examine four different coating processes and show how asymptotic methods are used to describe essential flow characteristics in these systems. First, we analyze knife coating using standard lubrication theory, which exploits the quasi-one-dimensional flow of the liquid under the knife. Next, we use forward roll coating to show how the standard lubrication theory fails because of the difficulty in determining the correct boundary conditions for the flow near the free surface of the film that appears in the nip of the rolls. We then describe how this failure is resolved by using a slowly varying domain perturbation method together with singular perturbation techniques to recover lubrication theory at leading order and to derive the appropriate boundary conditions for this flow. The next problem we consider is that of a liquid

film rising from or falling into a static liquid bath. This model is relevant to the dip coating process and also to certain areas of roll coating. Here, domain perturbation techniques lead to nonlinear equations that can predict the shape of the free surface of the film. Finally, we consider the flow of a liquid film on an inclined plane, which occurs in some regions of slide and curtain coating. The vital question of the stability of the free surface and of the interfaces in a multilayered film is addressed using regular perturbation and domain perturbation techniques. These four case studies highlight the current usage of these asymptotic methods and the advantages they can bring to the understanding of coating flows.

8.2 ASYMPTOTIC METHODS

When faced with a complex physical system, scientists and engineers often resort to simplifications of the mathematical model in order to produce an approximation that could be useful. Successful simplifications are based on a good physical understanding of the system and a knowledge of the relative sizes of the forces, fluxes, velocities, etc. in the problem. These simplifications can be done on an informal basis by noting the dominant terms in the governing equations and neglecting the smaller ones. The resulting simplified theory is then supplemented with appropriate boundary conditions and solved. The model is a success if it agrees with the relevant physical experiments.

The reduction of a complex mathematical model to one that displays just the dominant physical effects of interest to the engineer is the very simplest kind of asymptotic analysis. The problem with this approach is that some of the simplifications and/or boundary conditions are entirely *ad hoc* in nature. Even if they were constructed from sound physical reasoning, they may lack a clear mathematical justification. One result of this is that any agreement between the results of such a model and an experiment may be entirely fortuitous. The model may not lead to any fundamental insights into the physics of the process and it may not be useful in determining

if similar simplifications would be successful in other systems. Another problem with such an informal method is that there is no way to systematically refine the mathematical results or to determine the error associated with the analysis.

We can remove these difficulties by formalizing the simplification process described above. This can be done using several well-defined techniques known collectively as asymptotic methods or perturbation methods. The basis of each technique is to start with the dimensionless governing equations, and then to exploit the relative sizes of the dimensionless parameters in a certain way. In the following four subsections, four asymptotic methods are described. Each method is applied to a simple heat transfer problem in order to show how it is used, to demonstrate its fundamental characteristics, and to show how it isolates the fundamental physics involved in the model. Heat transfer problems were chosen for these examples because they are relatively simple and they lend themselves to clear interpretations in terms of the physics they represent. The details of the mathematics used in each perturbation method is not described in great depth. For that, please refer to the many good books on this subject, some of which are the standard references of Nayfeh (1973) and Van Dyke (1975), and the more recent book by Hinch (1991).

8.2.1 THE REGULAR PERTURBATION METHOD

Consider the differential equation

$$\phi_{xx} + \phi_x + \epsilon\phi = 0, \quad \phi(0) = 0, \quad \phi(1) = 1 \quad (8.1)$$

where the letter x subscript denotes a derivative with respect to x and $|\epsilon| \ll 1$ is a small parameter. This equation can be interpreted in terms of a one-dimensional heat transfer problem with a dimensionless temperature given by $\phi(x)$. The domain of the problem is a layer of liquid of unit thickness and the independent coordinate x measures the dimensionless distance through the layer. The first term represents conduction through the layer, the second a uniform downward convection, and the third a small amount of heat

generation proportional to the local temperature and of magnitude ε . Ignoring the fact that we can solve this equation exactly, we use the regular perturbation method to find an approximation to the solution.

First, we expand the function ϕ in a power series in ε as follows

$$\phi = \phi_0 + \varepsilon\phi_1 + \dots$$

This is substituted into the differential equation and then terms of the same power of ε are collected and set equal to zero (see Nayfeh (1973) pp. 2–4 for more details). The result is a sequence of differential equations that determines each of the ϕ_i -terms in the expansion. If the mathematical solution of the original differential equation is difficult or impossible, then one would hope that each problem in this sequence is easily solved. For the differential equation (8.1) above, the approximation to the solution is

$$\begin{aligned} \phi = & \frac{1 - e^{-x}}{1 - e^{-1}} + \varepsilon \left\{ \left(\frac{1 + e^{-1}}{1 - e^{-1}} \right) \left(\frac{1 - e^{-x}}{1 - e^{-1}} \right) \right. \\ & \left. - x \left(\frac{1 + e^{-x}}{1 - e^{-1}} \right) \right\} + \dots \quad (8.2) \end{aligned}$$

This approximation is compared with the exact solution for $\varepsilon = 0.5$ and $\varepsilon = 0.8$ in Fig. 8.1. Note that even though these values of ε are not small, the approximate solution compares quite well to the exact solution. The difference in the exact solution for these two values of ε is not noticeable on the graph. The error in the approximation is uniformly small over the entire domain of interest and it approaches zero uniformly as ε becomes smaller. This kind of behavior in the error is a characteristic of a regular perturbation problem.

8.2.2 THE SINGULAR PERTURBATION METHOD

Now consider equation (8.1) above, but with the small parameter in front of the first term in the equation,

$$\varepsilon\phi_{xx} + \phi_x + \phi = 0, \quad \phi(0) = 0, \quad \phi(1) = 1 \quad (8.3)$$

where $|\varepsilon| \ll 1$. In terms of our interpretation of

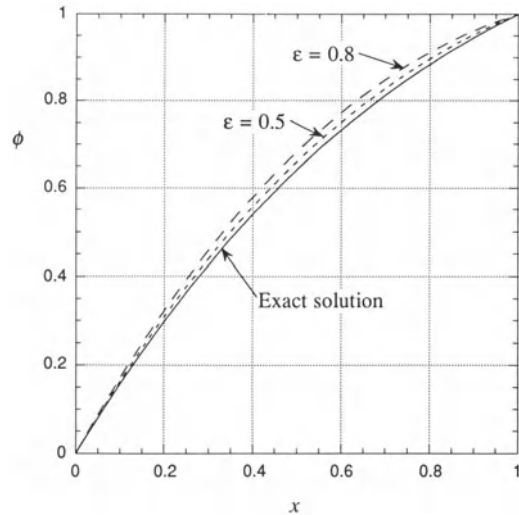


Figure 8.1 A comparison of the results of a regular perturbation analysis of equation (8.1) for two values of ε . The solid line is the exact solution and the broken lines are the perturbation approximation (8.2).

this equation as a heat transfer problem, we might assume that conduction through the layer is very small, and that the primary balance is between the uniform downward convection and the internal heat generation. Following this assumption, we apply the regular perturbation method as described above and obtain the following approximation,

$$\phi = e^{1-x} \{1 + \varepsilon(1-x)\} + \dots$$

This approximation, known as the outer expansion, satisfies the boundary condition at $x = 1$, but it does not satisfy the boundary condition at $x = 0$. The reason is that when we set $\varepsilon = 0$ in the original differential equation, it is reduced from a second-order to a first-order differential equation. Thus, the outer expansion can only legitimately satisfy one of the original boundary conditions. This reduction of order is a signal that we are faced with a singular perturbation problem.

The regular perturbation method failed because we implicitly assumed that the term $\varepsilon\phi_{xx}$ representing heat diffusion is uniformly small in

the whole interval as we let $\varepsilon \rightarrow 0$, and this is not true. There is a small region near the point $x = 0$, known as the inner or boundary-layer region, where this second-derivative term becomes very large and the regular perturbation approximation breaks down. In this boundary-layer region, heat diffusion is balanced by the downward convection of heat, and heat generation has only a small effect. The region outside the boundary-layer region is called the outer region and the dominant balance here is between heat generation and convection. Heat diffusion is small in the outer region.

The perturbation analysis is modified to correct this problem by making what is known as a stretching formulation of the x -variable in order to look locally within the boundary layer near $x = 0$. The transformation is simply $\tilde{x} = x/\varepsilon^m$, and the power of ε is determined in this case by balancing the second-derivative term with the first-derivative term in the differential equation to obtain $m = 1$. The solution of the resulting second-order differential equation is then approximated using the regular perturbation method to obtain the inner expansion. The two constants that arise are determined from the boundary condition at $x = 0$ and by matching to the outer expansion for large values of \tilde{x} . The inner and outer expansions are then combined to form what is known as a composite expansion, which is uniformly close to the exact solution over the entire domain. See Nayfeh (1973) pp. 110–22 for more details of this procedure. For this problem, the composite expansion is

$$\begin{aligned}\phi &= e^{1-x}\{1 + \varepsilon(1-x)\} \\ &\quad - e^{1-x/\varepsilon}\{1 + x + \varepsilon\} + \dots\end{aligned}\quad (8.4)$$

This approximation is compared to the exact solution for three different values of ε in Fig. 8.2. Here, we clearly see the development of the boundary layer as ε gets small.

8.2.3 THE DOMAIN PERTURBATION METHOD – SMALL DEFORMATION

One form of a domain perturbation problem arises when the boundary of a region of interest

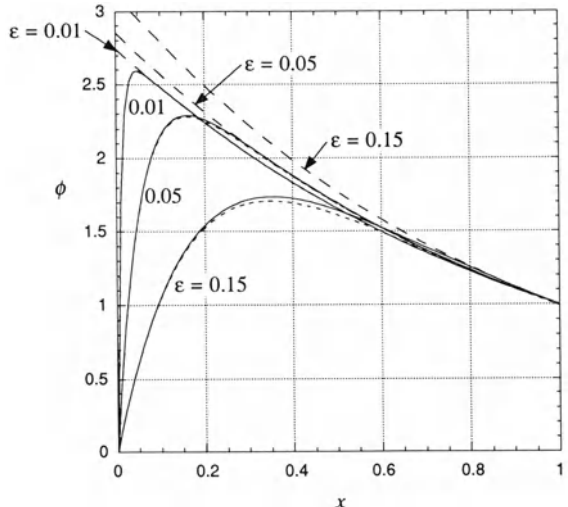


Figure 8.2 A comparison of the results of a singular perturbation analysis of equation (8.3) for three different values of ε . The solid lines are the exact solution, the short-dash lines are the perturbation approximation (8.4), and the long-dash lines are the two-term outer expansion.

is just slightly deformed away from some regular shape that is easy to deal with. For example, consider the following two-dimensional heat conduction problem for the dimensionless temperature $\phi(x, y)$ as a function of the Cartesian coordinates x and y ,

$$\nabla^2 \phi = 0, \quad \phi(x, 0) = 0, \quad \phi(x, h(x)) = 1 \quad (8.5)$$

and let ϕ and h be periodic in the x -direction.

This boundary-value problem describes heat conduction in a layer of some material with a planar surface held at a fixed temperature and an upper surface located at $y = h(x)$ held at a higher temperature. The numerical solution of this problem is quite routine these days, but mathematical solutions can be found only for some specific forms of the upper surface. The simplest case is the planar upper surface $h = 1$, and the solution is just one-dimensional heat conduction with a linear temperature profile $\phi = y$.

Now, consider an upper surface that is a small perturbation of a plane as described by $h(x) = 1 + \varepsilon h_1(x)$, where $|\varepsilon| \ll 1$ and $|h_1| \leq 1$. In

general, to approximate the solutions for this class of small-deformation, domain perturbation problems we first expand the boundary condition on the perturbed surface in a Taylor series about the unperturbed surface. In the present example, we expand the upper boundary condition about the plane $y = 1$ to obtain

$$\begin{aligned}\phi(x, h) &= \phi(x, 1) + \phi_y(x, 1)\varepsilon h_1 \\ &\quad + \phi_{yy}(x, 1)\varepsilon^2 h_1^2/2 + \dots = 1\end{aligned}$$

where letter subscripts denote partial differentiation. Next, we use the regular perturbation method, expand ϕ in a power series in ε , substitute it into equation (8.5) and the above boundary condition, group terms of like powers of ε , and solve the resulting sequence of boundary-value problems. For the specific case of $h_1 = \cos(\alpha x)$, where the wave number α is an arbitrary constant, the resultant asymptotic approximation is

$$\phi = y - \varepsilon \cos(\alpha x) \sinh(\alpha, y)/\sinh(\alpha) + \dots \quad (8.6)$$

The first or leading-order term of this approximation represents pure one-dimensional heat conduction. The second term is the first-order correction for the slightly deformed upper surface. We show the isotherms corresponding to this approximation in Fig. 8.3 for $\alpha = 2\pi$ and $\varepsilon = 0.1$.

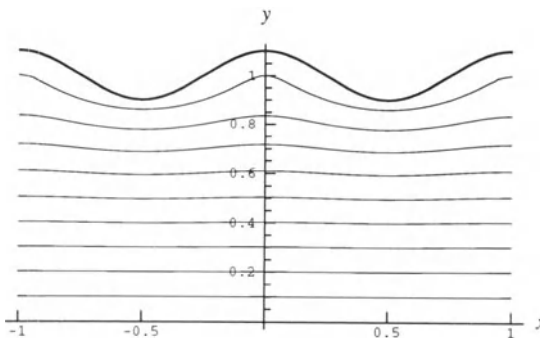


Figure 8.3 The isotherms computed from the perturbation approximation (8.6) for a small-amplitude domain perturbation analysis of heat conduction through a slab of material given by equation (8.5). The amplitude of the surface displacement is $\varepsilon = 0.1$. The darker line is the upper surface of the slab.

Note that the deformation of the isotherms is localized near the upper surface because of the somewhat large value of α .

The first two terms in the expansion of the boundary condition on the upper surface represent the linearization of the upper boundary condition about $h = 1$. Thus, the two terms shown in the approximation (8.6) represent the solution to the original problem linearized about $h = 1$. This kind of linearization is used to study the stability of solutions and to obtain boundary conditions for some initial-value and boundary-value problems. Specific examples of the use of this kind of linearization are discussed in Sections 8.5 and 8.6 below.

8.2.4 THE DOMAIN PERTURBATION METHOD – SLOWLY VARYING DEFORMATION

Another kind of domain perturbation problem occurs when the position of the boundary varies very slowly in some direction. Consider the heat conduction problem (8.5) above with the upper surface given by $y = h(\tilde{x})$, where $\tilde{x} = \varepsilon x$ and $|\varepsilon| \ll 1$. We impose no further restrictions on the magnitude of h except that it be physically realizable, i.e., $h > 0$. The dependence of h on the variable \tilde{x} together with the smallness of the parameter ε means that the upper-surface position changes very slowly in the x -direction. Given this gradual variation, we might expect that locally, the solution looks like pure one-dimensional heat conduction through a layer of constant thickness h . This result is obtained in a more formal way when we rescale the x -variable in the differential equation in order to introduce the variable \tilde{x} , and then use the regular perturbation method. We let $\partial/\partial x = \varepsilon\partial/\partial\tilde{x}$ and obtain the boundary-value problem

$$\varepsilon^2 \phi_{\tilde{x}\tilde{x}} + \phi_{yy} = 0, \quad \phi(\tilde{x}, 0) = 0, \quad \phi(\tilde{x}, h) = 1 \quad (8.7)$$

with ϕ and h periodic in the \tilde{x} -direction. Here, letter subscripts denote partial differentiation.

The solution of this problem is approximated using a regular perturbation expansion of ϕ in terms of powers of ε^2 . At leading order, we obtain

$$\phi_{0yy} = 0, \quad \phi_0(\tilde{x}, 0) = 0, \quad \phi_0(\tilde{x}, h) = 1$$

The solution is $\phi_0 = y/h$, which is the pure one-dimensional heat conduction solution we expected.

The problem at the next order is

$$\phi_{1,yy} = -\phi_{0,xx}, \quad \phi_1(\tilde{x}, 0) = 0, \quad \phi_1(\tilde{x}, h) = 0$$

Physically, this problem is heat conduction and variable heat generation inside a layer of uniform thickness h , in which the boundaries are held at the same temperature. The heat generation effect, represented by the term $\phi_{0,xx}$, is actually an asymptotic model for the lateral conduction of heat in the x -direction due to the slow variation in the thickness of the layer.

The two-term approximation to the solution of the original problem (8.7) is

$$\phi = y/h + \varepsilon^2 \{ (2h_x^2 - hh_{xx})/h^3 \} (h^2 y - y^3)/6 + \dots \quad (8.8)$$

The isotherms for the specific case of $h = 1 + \Delta \cos(\varepsilon x)$, with $\Delta = 1/2$ and $\varepsilon = \pi/3$ are shown in Fig. 8.4. The large value of ε was chosen to accentuate the first-order correction of the isotherms in this figure. Note, however, that even for this value of ε the mean layer thickness to surface wavelength ratio is $1/6$, which implies slowly varying upper surface position. The dashed isotherms correspond to the linear leading-order temperature field. The solid isotherms contain the first-order effects of the surface deformation. We see that these isotherms are lowered with

respect to the linear temperature field under crests of the upper surface. This effect is due to the lateral conduction of heat from each side of the crest on the upper surface toward the center of the crest. This increases the temperature under the crests and lowers the isotherms.

The slowly varying domain perturbation method is very important in the study of film flows and coating flows because the length scale for variations in the film thickness is often much larger than the mean thickness of the film. In fact, this is the main assumption used in the theory of lubrication. We study this theory and how it is used in two important coating flows in the next two sections.

8.3 KNIFE COATING AND LUBRICATION THEORY

We begin our examination of asymptotic methods for the analysis of coating flows by introducing a method that is not, in the strict sense, asymptotic. This method is standard lubrication theory, and it is a set of simplifying assumptions that has been used successfully to describe many thin-film coating problems. In this section, we apply the theory to knife coating and briefly discuss its success and some key results. In the following section, we apply the same theory to roll coating and show how it fails to describe the response of the system adequately. Once we see this failure,

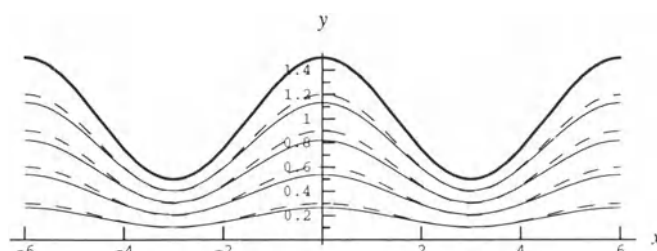


Figure 8.4 The isotherms for a slowly varying domain perturbation analysis of heat conduction through a slab of material given by equation (8.7). The solid lines are the isotherms computed from the perturbation approximation (8.8). The dashed lines are the leading-order isotherms representing pure one-dimensional heat conduction. The amplitude of the surface displacement is $\Delta = 1/2$ and the wave number is $\varepsilon = \pi/3$. This wavenumber gives a mean thickness-to-wavelength ratio of $1/6$. The darker line is the upper surface of the slab.

we use formal asymptotic methods to derive lubrication theory, to demonstrate why it fails, and to show how it can be repaired to produce accurate results. There are of course many other coating flows in which lubrication theory can be applied, such as flexible-blade coating, membrane coating, squeeze-roll coating and slot-fed knife coating. See Chapters 11a and 12 for further discussions of these other systems.

For simplicity, we consider the simple knife-coating geometry shown in Fig. 8.5. The end of the knife and the coating substrate form a thin converging passage through which the coating liquid flows. The flow is driven by the lower substrate as it moves to the right relative to the knife at the speed U^* , and it forms a thin liquid film on the moving substrate downstream from the knife as shown in the figure. We assume that the liquid is Newtonian with viscosity μ and is incompressible and that the flow is two-dimensional. We use a Cartesian coordinate system fixed to the knife with the origin at the lower substrate, the X -axis along the plane of the lower substrate, and the Y -axis normal to this substrate. The surface of the knife tip is inclined at a very small angle with respect to the plane of the moving substrate.

The governing equations for the flow under the knife are the Navier–Stokes equations and the continuity equation together with the appropriate boundary conditions on the solid surfaces, at the inlet to the flow passage and in the film downstream from the knife. The flows near the inlet and at the outlet to the passage are fully two-dimensional and difficult to determine.

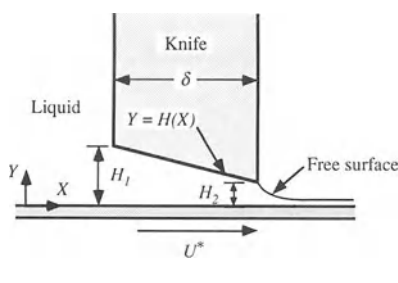


Figure 8.5 A schematic of the knife coating process.

However, away from the ends of the passage the flow under the knife will be nearly parallel if the angle between the knife tip and the lower substrate is small. These nearly parallel solid surfaces form a flow passage that has a slowly varying thickness H in the flow direction. In this situation, we can assume that variations in the flow in the X -direction are small compared with variations in the Y -direction. We also expect that the velocity in the X -direction is much larger than the velocity in the Y -direction. Finally, we neglect the body force oriented in the Y -direction as we anticipate that the hydrostatic pressure it produces will be much smaller than the viscous lubrication pressure in the thin liquid film under the knife.

The governing equations for the flow under the knife but away from the ends reduce to the following set of equations when the small terms described above are neglected:

$$0 = -P_x + \mu U_{YY} \quad (8.9a)$$

$$0 = -P_y \quad (8.9b)$$

$$U_x + V_y = 0 \quad (8.9c)$$

$$U = U^*, V = 0 \quad \text{on } Y = 0 \quad (8.9d)$$

$$U = 0, V = 0 \quad \text{on } Y = H(X) \quad (8.9e)$$

where letter subscripts denote partial differentiation. The set of assumptions used to obtain these equations is known as lubrication theory. The first two equations (8.9a, b) are the momentum equations for a laminar, parallel flow in a channel with no gravity. These equations are viewed to hold locally at any point in the flow passage under the knife. The continuity equation (8.9c) connects the small variations of the longitudinal velocity due to the slowly changing thickness of the flow passage with the small normal velocity.

The normal momentum equation (8.9b) says that the pressure is constant across the height of the passage. This allows one to integrate the longitudinal momentum equation (8.9a) to find the parabolic longitudinal velocity

$$U = \frac{1}{2\mu} P_x (Y^2 - HY) + U^*(1 - Y/H) \quad (8.10)$$

The continuity equation is now integrated

across the height of the passage. The second integral in this equation is zero because of the no-slip boundary conditions on the two solid surfaces. When the first term is integrated and the no-slip boundary condition is applied we obtain

$$Q_x = 0, Q = \int_0^H U dY \quad (8.11)$$

Here, Q is the net flow rate in the passage. The integrated continuity equation (8.11) says that the flow rate is constant along the length of the passage. This fact can also be deduced from a simple control-volume, conservation of mass analysis for this flow.

Integrating the longitudinal velocity (8.10) across the thickness of the passage gives

$$Q = -\frac{H^3}{12\mu} P_x + \frac{1}{2} U^* H \quad (8.12)$$

Substituting this into the global mass conservation equation (8.11) yields

$$(H^3 P_x)_x = 6\mu U^* H_x \quad (8.13)$$

This equation is called the Reynolds equation. It was first devised by Reynolds (1886) for the more general case of longitudinal motion of the lower boundary, longitudinal and normal motion of the upper boundary, and both longitudinal and transverse variations in the thickness of the liquid film. This equation is also discussed by Lamb ([1932] 1945, Sec. 330a).

The Reynolds equation (8.13) is a second-order differential equation for the pressure variation under the knife. Integrating this requires a specification for the shape of the knife tip. In our example of Fig. 8.5, the knife tip is a straight line. Furthermore, we need two boundary conditions on the pressure. If the inlet and the outlet to the flow passage are completely immersed in liquid, then the appropriate boundary condition is zero pressure (atmospheric) at each end. There is a small hydrostatic pressure at these ends to consider, but any observed pressure is negligible compared with the large lubrication pressure that is seen under the knife. As we neglected the

gravitational body force in the flow under the knife for this very reason, we also neglect it at the two ends. We can now integrate the differential equation (8.13) to obtain the pressure under the knife

$$P(H) = \frac{6\mu U^* \delta}{(H_1^2 - H_2^2)} \frac{(H_1 - H)(H - H_2)}{H^2} \quad (8.14)$$

where H_1 and H_2 are the thicknesses of the inlet and the outlet to the flow passage under the knife respectively and δ is the thickness of the knife in the flow direction.

This pressure can be integrated to give the net upward force on the knife due to the flow beneath it

$$F = \frac{6\mu U^* \delta^2}{(H_1 - H_2)^2} \left\{ \ln\left(\frac{H_1}{H_2}\right) - \frac{2(H_1 - H_2)}{(H_1 + H_2)} \right\} \quad (8.15)$$

Substituting the pressure (8.14) into the flow rate given by equation (8.12) yields a simple expression for the flow rate beneath the knife

$$Q = \frac{U^* H_1 H_2}{H_1 + H_2} \quad (8.16)$$

And finally, the thickness H_∞ of the liquid film far downstream from the knife is determined from the mass-balance relation $Q = U^* H_\infty$. It is

$$H_\infty = \frac{H_1 H_2}{H_1 + H_2} \quad (8.17)$$

The standard lubrication theory just described is in fact a simple form of a slowly varying domain perturbation analysis, which we demonstrate in the next section. The theory is very successful in predicting the flow rate under the knife when applied to the knife coating of a viscous liquid with no significant viscoelastic effects. The success of the method lies in the fact that the flow and the pressure under the knife are well-characterized by the quasi-one-dimensional flow away from the ends of the flow passage. Near the inlet and the outlet to the passage the flow is two-dimensional and the lubrication approximation fails, but the failure is local. A full two-dimensional calculation of the

flow under the knife would produce a pressure field that is only slightly different from that computed with lubrication theory and the differences would be localized near the inlet and the outlet regions of the flow passage. These differences would not significantly influence the flow rate under the knife (provided the gap thickness and the knife-tip angle remain small) and the difference in the computed normal force on the knife would also be small. The simple boundary conditions for the pressure at the ends of the flow passage used in this lubrication theory do an adequate job in modeling the effect of the two-dimensional flow in the end regions on the quasi-one-dimensional flow under the knife but away from the ends. In the next section, we describe an analysis in which similar simplified boundary conditions are not so successful, and we discuss the reasons for this failure.

8.4 FORWARD ROLL COATING

8.4.1 AN AD HOC LUBRICATION ANALYSIS

A schematic of the symmetric, forward roll-coating process is shown in Fig. 8.6. The two rolls have equal diameters and rotate in opposite directions with the same surface speed U^* . The rotation of the rolls drags a liquid through the gap between the rolls from the left to the right. On the right side, the liquid splits apart to form

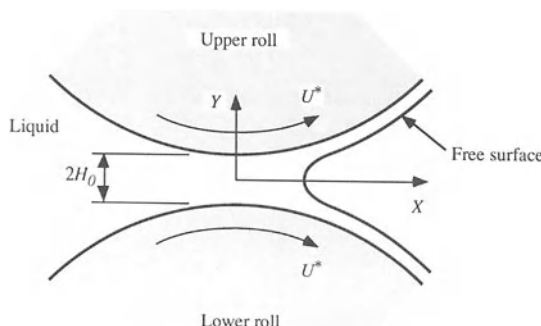


Figure 8.6 A schematic of the forward roll coating process.

a free surface bounding two liquid films of equal thickness attached to the two rolls. Far to the right of the film-splitting point, each liquid film is in rigid-body rotation with its respective roll.

We will write down the full set of governing equations and boundary conditions for this flow in the next subsection, but for now we note that the curved geometry and the free surface make this a very difficult problem. The first steps toward a mathematical understanding of this process were made using the simplifications of lubrication theory. In many industrial roll-coating processes the roll radius is very large compared with the gap between the rolls. The gap close to the nip of the rolls (the point of minimum gap width) actually looks like a channel with a slowly varying thickness and so in this region lubrication theory is valid. The difficulty with this approach is the proper treatment of the free surface that appears at the film-splitting point. It is not clear that lubrication theory is valid in describing the flow near this free surface, but at a minimum the location of the film-splitting point must be close to the nip to be inside the region where lubrication theory is valid. In this subsection, we describe the lubrication model for the flow in the nip of the rolls and discuss two sets of *ad hoc* boundary conditions that have been used to model the flow near the film-splitting point. We contrast the results of each model and then discuss the reasons for their failure.

The Cartesian coordinate system we use has its X -axis directed along the symmetry plane of the two rolls, the Y -axis is normal to this plane, and the origin is at the nip of the two rolls as shown in Fig. 8.6. The half-gap thickness is $H(X)$. The governing equations for the flow are simplified using lubrication theory to produce the same lubrication equations found in the previous problem of knife coating, i.e., equations (8.9a–c) together with the no-slip boundary condition on the rolls. The solution of these equations yields the horizontal velocity

$$U = \frac{1}{2\mu} P_x(Y^2 - H^2) + U^* \quad (8.18)$$

and the following differential equation for the pressure

$$P_x = 3\mu \left(\frac{U^*}{H^2} - \frac{Q}{H^3} \right)$$

where $Q = \int_0^H U dY$ is one half of the flow rate through the nip.

We can integrate this pressure equation once we have an expression describing the surface of the roll in the nip region. To within the approximation used in the lubrication theory, the required expression is the parabola

$$H = H_0 \left(1 + \frac{X^2}{2H_0 R} \right) \quad (8.19)$$

where R is the radius of the roll and H_0 is the minimum gap half-width. The spatial transformation $\tan^2 \theta = X^2/2H_0 R$ applied to the gap half-width (8.19) yields $H = H_0 \sec^2 \theta$. After substituting this into the differential equation for the pressure and writing the result in dimensionless form, we obtain

$$p_\theta = 3\sqrt{2}(\cos^2 \theta - q \cos^4 \theta). \quad (8.20)$$

Here, the dimensionless volume flux q scales with $U^* H_0$, the pressure scale is $\mu U^*/H_0 \epsilon$, and $\epsilon = \sqrt{(H_0/R)}$ is a small parameter measuring the variation in the thickness of the gap.

The pressure boundary condition to the left of the nip (the inlet side) is the same as in knife coating. We assume that the space next to the rolls is fully immersed in liquid and ignore the small hydrostatic pressure that is present compared with the large lubrication pressure between the rolls. Thus, the pressure goes to zero as $x \rightarrow -\infty$, or in terms of θ , $p(-\pi/2) = 0$. With this boundary condition, we integrate equation (8.20) to obtain the pressure in the gap

$$\begin{aligned} p(\theta) = 3\sqrt{2} & \left\{ \frac{1}{2} \left(\theta + \frac{\pi}{2} \right) + \frac{1}{4} \sin 2\theta \right. \\ & \left. - q \left[\frac{3}{8} \left(\theta + \frac{\pi}{2} \right) + \frac{1}{4} \sin 2\theta + \frac{1}{32} \sin 4\theta \right] \right\} \end{aligned} \quad (8.21)$$

To the right of the nip, we can only reasonably expect lubrication theory to hold up to the film-splitting point, and maybe not even that far, because of the two-dimensional nature of the flow in this region. The location of the film-splitting point $\theta = \theta_m$ and the flow rate through the gap q are both unknown. They are determined by posing two boundary conditions for the pressure at the film-splitting point. A variety of different pairs of boundary conditions have been proposed, usually based on *ad hoc*, physical arguments about the nature of the flow field near this point. These boundary conditions have been discussed by Savage (1977), Dowson and Taylor (1979), Ruschak (1985), and Coyle, Macosko and Scriven (1986). As it turns out, none of these *ad hoc* pairs of boundary conditions have lead to very accurate results from the lubrication analysis of roll coating. To highlight this difficulty, we describe two cases: the Swift–Steiber conditions and the Hopkins flow-separation conditions.

The Swift–Steiber boundary conditions are

$$P(X_m) = 0, \quad \frac{dP}{dX}(X_m) = 0 \quad (8.22a,b)$$

where X_m is the horizontal position of the film-splitting point. These conditions were originally proposed for a roll-coating process composed of a single roll on a stationary flat plate (see Fig. 8.6 and replace the horizontal symmetry plane with a rigid flat plate). The liquid film separates from the flat plate to the right of the nip forming an air cavity between the liquid film and the rigid plate. The pressure and the pressure gradient inside the air cavity are zero. If we assume that these conditions hold inside the liquid film at the film-splitting point, we obtain the boundary conditions (8.22). For the single-roll/flat-plate problem, a zero pressure gradient in the liquid implies that the horizontal velocity profile is linear at the film-splitting point, which seems reasonable. However, in forward roll coating a zero pressure gradient at the film-splitting point implies that the horizontal velocity is uniform, as shown by equation (8.18). This is because the mid-plane symmetry condition is one of no shear

stress rather than a rigid plane with no slip. A uniform horizontal velocity is not expected to be a very good approximation to the flow field at the film-splitting point and so one should not expect very good results with the Swift–Steiber conditions.

The second of the Swift–Steiber conditions leads to an equation for the flow rate $q = \sec^2 \theta_m$, and the first applied to equation (8.21) together with this value of q produces a nonlinear equation for the location of the film-splitting point. This is easily solved numerically to obtain $\theta_m = 0.443554$ and $q = 1.22575$.

The Hopkins flow-separation conditions are based on the idea that the film-splitting point is a true flow-separation point. Therefore, the horizontal velocity, the tangential shear stress and the pressure are all zero at this point, which is located on the mid-plane $Y = 0$ and horizontally at the position $X = X_m$. These conditions are

$$U(X_m, 0) = 0, \frac{\partial U}{\partial Y}(X_m, 0) = 0, P(X_m) = 0 \quad (8.23a-c)$$

In the roll-coating problem, symmetry ensures a zero shear stress on the mid-plane. The zero-velocity condition together with the horizontal velocity (8.18) imply that the pressure gradient at the film-splitting point is

$$\frac{\partial P}{\partial X}(X_m) = \frac{2\mu U^*}{H^2(X_m)} \quad (8.23d)$$

This pressure-gradient condition leads to the flow rate $q = \sec^2(\theta_m)/3$. The zero-pressure condition applied to equation (8.21) together with this value of q produces a nonlinear equation for the location of the film-splitting point. The numerical solution of this equation yields $\theta_m = 1.04017$ and $q = 1.30152$.

The pressure distributions between the rolls as a function of θ/π for these two *ad hoc* models are shown in Fig. 8.7. Comparing these with the distributions obtained with a more accurate asymptotic method described in the next subsection shows that the separation model is at least qualitatively correct, while the Swift–Steiber

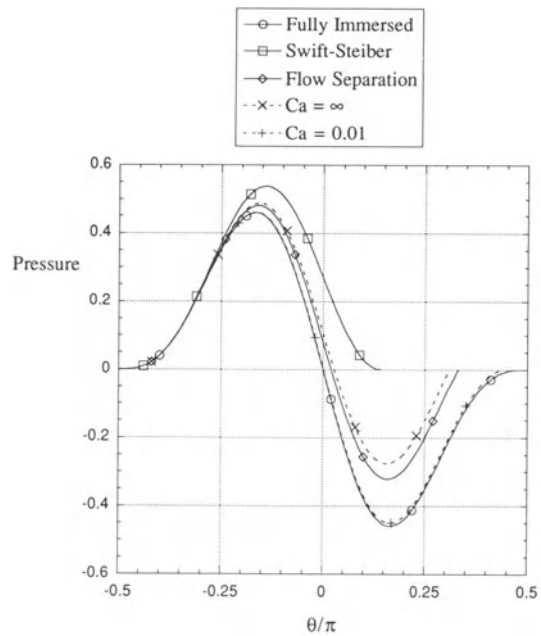


Figure 8.7 The liquid pressure in the nip of the forward roll coating process for different models. The solid lines are based on three different *ad hoc* models for the downstream pressure boundary conditions: \square , Swift–Steiber; \diamond , Hopkins flow separation; \circ , fully immersed. The dashed lines are based on the results of an asymptotic solution of the flow in this process. Numerical values for the flow rate were obtained from the results of Ruschak (1982): $+$, $Ca = 0.01$; \times , $Ca = \infty$.

model misses the negative pressures to the right of the nip. As a point of reference, the pressure distribution when the right side of the nip is fully immersed in the liquid is also plotted in Fig. 8.7. For this case, $q = 4/3$.

One deficiency of both of these *ad hoc* models is that the surface tension of the free surface is not included. The experiments of Taylor (1963) showed that the surface tension is an important parameter that influences the flow rate through the nip of the rolls. The necessary modification is to replace the zero-pressure boundary condition with a capillary pressure boundary condition at the film-splitting point $P(X_m) = -\sigma/R_m(X_m)$. Here, σ is the surface tension of the free surface and $R_m(X_m)$ is the mean curvature of the free

surface at the film-splitting point (defined as positive when the free surface is oriented as in Fig. 8.6). The difficulty with this new condition is that the radius of curvature of the free surface is unknown and so an approximation is needed for the free-surface shape. One approximation that has been used is to assume a local shape for the free surface at the film-splitting point, such as a parabola or a circular arc, connect it to the geometry of the thin films on the two rolls, and then use the resultant free-surface shape to compute the radius of curvature at the film-splitting point. This approximation is extremely *ad hoc* and we should expect the accuracy of the modified models to be fairly crude. In fact, Coyle, Macosko and Scriven (1986) showed that the separation model with the capillary pressure boundary condition incorrectly predicts the trends for the flow rate through the gap and the location of the film-splitting point as a function of the capillary number $Ca = \mu U^*/\sigma$.

The reason for the failure of these *ad hoc* models to describe the roll-coating process accurately is that the two-dimensional flow at the film-splitting point is a controlling influence on the behavior of the system as a whole. The *ad hoc* models attempt to reduce the entire effect of this two-dimensional flow into a pair of effective pressure boundary conditions using just simple physical assumptions and qualitative reasoning about the flow. The zero-pressure boundary condition is adequate as shown in the next subsection, but the pressure-gradient and the capillary-pressure boundary conditions that have been used do not contain enough information about the intricate behavior of the two-dimensional flow to model its effects adequately on either the lubrication flow between the rolls or on the location of the film-splitting point. For instance, when the capillary number is small enough a pair of small recirculation cells exists near the free surface in the film-splitting region and the size of these cells depends strongly on the capillary number. While lubrication theory can model an infinitely long recirculation cell, it cannot adequately represent the effect of these small two-dimensional recirculation cells. The *ad hoc*

boundary conditions used with the lubrication flow fail to compensate for this defect.

As the location of the film-splitting point used in the lubrication analysis is intimately dependent on the two-dimensional flow in the film-splitting region, we should have been suspicious of any simple attempt to construct an effective boundary condition. This kind of intimate dependence between two-dimensional flow effects and a lubrication flow variable is a signal that an *ad hoc* model may not be adequate.

In contrast, lubrication theory does work well in describing knife coating. The reason for this is that we only needed to specify the zero-pressure boundary condition at the inlet and outlet points to the flow passage under the knife. This condition does an adequate job in communicating the effect of the two-dimensional flows in these regions to the lubrication flow under the knife. (In the next subsection, we show that this condition also has a clear mathematical justification). In addition, the locations of the inlet and outlet points are fixed, and so there is no intimate dependence between the two-dimensional flows near these points and the locations used in the lubrication analysis. Thus, we do not receive the signal of potential difficulty that we received in the case of roll coating.

Another pitfall in using these *ad hoc* boundary conditions is seen in the work of Savage (1982). He analyzed the film-splitting problem in asymmetric roll coating, in which two rolls of different diameters are used. Savage assumed that the stagnation streamline separating the flow going onto the upper and lower rolls also separated two recirculation cells that were both attached to the free surface. However, numerical calculations by Coyle, Macosko and Scriven (1986) for asymmetric roll coating showed that this picture of the flow field is completely wrong. The dividing streamline for the flow lies below both of the recirculation cells, and only one of these cells is attached to the free surface. Even though the asymmetry in this numerical model was provided by the different surface speeds of two equally sized rolls, one would expect the same kind of behavior for equal speeds and differently sized

rolls as in the problem of Savage. The lesson here is that *ad hoc* models of this kind may inadvertently miss many of the important features of the flow field because the original assumptions used to construct the models don't allow such features to develop. If these features turn out to be major determining factors in the flow, then the *ad hoc* model will never faithfully reproduce the observed behavior of the system.

So, if the *ad hoc* models used in the lubrication analysis of roll coating are not accurate enough, how does one proceed with the analysis? One way is to do a complete numerical simulation of the process. Following this path, we would incur all of the computational expenses involved with the large number of elements or nodes needed to produce accurate results. In addition, we would lose the simple representation of the flow given by lubrication theory that is accurate away from the film-splitting point. An alternative approach is to use a slowly varying domain perturbation analysis coupled with a singular perturbation analysis. The slowly varying domain perturbation analysis provides a good approximation to the quasi-one-dimensional flow near the nip (we actually recover lubrication theory to leading order). The singular perturbation analysis isolates the flow in the two-dimensional region near the film-splitting point from the lubrication flow near the nip. Then as we described in Section 8.2.2, these two flow fields are connected through a well-defined matching process. An asymptotic analysis of this kind for symmetric, forward roll coating was first done by Ruschak (1982), and the extension to asymmetric roll coating was presented by Coyle, Macosko and Scriven (1986). The former analysis is described next. For more information on roll coating, see Chapter 12a.

8.4.2 A SINGULAR PERTURBATION ANALYSIS

The geometry of symmetric forward roll coating is shown in Fig. 8.6. The liquid is isothermal, incompressible and Newtonian with constant density ρ and viscosity μ . The flow is steady and the governing equations are the Navier–Stokes

equations and continuity. Gravity is ignored. Standard boundary conditions on the solid surface of the roll and on the free surface of the liquid are used. As the flow is symmetric, we consider only the flow in the upper half of the system.

The parameter $\varepsilon = \sqrt{(H_0/R)}$, where H_0 is the half-gap thickness at the nip and R is the radius of the rolls, is a measure of the slope of the upper-roll surface near the nip. It is typically small in roll coating, say $\varepsilon < 0.1$. Such small values of ε imply that the gap thickness between the rolls near the nip changes very slowly as one moves through the nip. Thus, we may analyze this problem using the slowly varying domain perturbation method.

The appropriate scales for this analysis are the standard lubrication scales. Vertical distances are scaled with the minimum half-gap thickness at the nip H_0 , and horizontal distances are scaled with the much larger length scale H_0/ε . This horizontal length scale comes from forcing the horizontal variation of the roll surface to appear at leading order in the equation for the surface of the roll. Horizontal velocities are scaled with the surface speed of the roll U^* and vertical velocities are scaled with εU^* . This velocity scale is derived from balancing the two terms in the continuity equation and it is a reflection of the small vertical velocities that are expected in the nip. Finally, the pressure is scaled on a large viscous pressure scale $\mu U^*/\varepsilon H_0$ in order to balance the pressure gradient and the viscous terms in the horizontal momentum equation near the nip.

The resulting dimensionless equations of motion are

$$\varepsilon Re \{uu_x + vu_y\} = -p_x + \varepsilon^2 u_{xx} + u_{yy} \quad (8.24a)$$

$$\varepsilon^3 Re \{uv_x + vv_y\} = -p_y + \varepsilon^4 v_{xx} + \varepsilon^2 v_{yy} \quad (8.24b)$$

$$u_x + v_y = 0 \quad (8.24c)$$

Here, $Re = \rho U^* H_0 / \mu$ and letter subscripts denote partial differentiation.

The equation for the upper-roll surface $y = h(x)$ is

$$h(x) = 1 + \varepsilon^{-2} - \varepsilon^{-2} \sqrt{(1 - \varepsilon^2 x^2)} \quad (8.24d)$$

The no-slip boundary condition on the upper-roll surface is

$$(u, \varepsilon v) = (1, \varepsilon h_x)/(1 + \varepsilon^2 h_x^2)^{1/2} = \mathbf{t}_r \quad (8.24e)$$

where \mathbf{t}_r is the unit tangent vector to the surface of the roll.

Symmetry conditions are imposed on the mid-plane $y = 0$,

$$u_y = 0, \quad v = 0. \quad (8.24f, g)$$

The free surface of the liquid film is described by the function $y = \eta(x)$. The tip of this free surface, called the film-splitting point, is located at the point $x = x_m$. Thus, we require

$$\eta(x_m) = 0, \quad \eta_x(x_m) \rightarrow \infty \quad (8.24h, i)$$

The boundary conditions imposed on the free surface are the normal- and tangential-stress balances and the kinematic condition,

$$\begin{aligned} -p + 2\varepsilon^2 \{v_y - \eta_x(u_y + \varepsilon^2 v_x) + \varepsilon^2 \eta_x^2 u_x\} N^{-2} \\ = -\varepsilon Ca^{-1} \kappa \\ (u_y + \varepsilon^2 v_x)(1 - \varepsilon^2 \eta_x^2) + 2\varepsilon^2 \eta_x(v_y - u_x) = 0 \\ v = u\eta_x \end{aligned} \quad (8.24j-l)$$

where $N = (1 + \varepsilon^2 \eta_x^2)^{1/2}$, the curvature of the free surface is $\kappa = -\varepsilon^2 \eta_{xx} N^{-3}$, and the capillary number is $Ca = \mu U^*/\sigma$.

Far to the right of the film-splitting point, the liquid film is in rigid-body rotation with the roll

$$(u, \varepsilon v) = (1 + \varepsilon^2 r) \mathbf{t}_r \text{ for } 0 \leq r \leq h_\infty \quad (8.24m)$$

$$h_\infty = \varepsilon^{-2} \{[(1 + \varepsilon^2 - \varepsilon^2 \eta)^2 + \varepsilon^2 x^2]^{1/2} - 1\} \quad (8.24n)$$

Here, r is a radial coordinate measured from the surface of the roll and h_∞ is the final thickness of the film on the roll. In this rigid-rotation region, the free surface of the liquid is a circular arc concentric with the roll. Its slope is

$$\eta_x = x(1 + \varepsilon^2 - \varepsilon^2 \eta)^{-1} \quad (8.24o)$$

Finally, far to the left of the nip as x approaches the radius of the rolls, we only need to specify

the condition that the pressure in the liquid falls to atmospheric

$$p \rightarrow 0 \text{ as } x \rightarrow -\varepsilon^{-1} \quad (8.24p)$$

This is appropriate because we have ignored gravity and have assumed that the region to the left of the nip is fully immersed in liquid.

As the parameter ε is very small, consider the limit of the horizontal momentum equation (8.24a) as $\varepsilon \rightarrow 0$. The disappearance of the viscous term u_{xx} in this limit signals that we have a singular perturbation problem as discussed in Section 8.2.2. We should expect the existence of an inner region, or internal layer, of small horizontal extent in which this viscous term is important. Given our physical understanding of roll coating, it is reasonable to suppose that the inner region contains the film-splitting point. Thus, the asymptotic analysis of the flow between the rolls starts with an application of the regular perturbation method to equations (8.24) to find the equations for the leading-order approximation to the flow in the outer nip region. Then a stretching transformation at the film-splitting point is applied to equations (8.24) to determine the governing equations for the inner film-splitting region. A second application of the regular perturbation method on these stretched equations is used to determine the equations for the leading-order approximation to this inner flow. A second outer region is the rigid-rotation of the liquid far to the right of the film-splitting point. The flow field here is known exactly. Matching these three flows leads to the appropriate boundary conditions that allow us to compute fully the flows to leading order in both the inner film-splitting region and the outer nip region. In particular, matching the pressure in the outer nip region with that in the film-splitting region yields the asymptotic boundary conditions for the pressure that replaces those in the *ad hoc* models used in previous lubrication analyses of roll coating. From these flow solutions, a final composite approximation that is uniformly valid everywhere can be constructed if desired. To begin the regular perturbation analysis of the outer nip region, we expand the dependent

variables in terms of the small parameter ε as follows

$$u = u_0 + \varepsilon u_1 + \dots \quad v = v_0 + \varepsilon v_1 + \dots \quad \text{and}$$

$$p = p_0 + \varepsilon p_1 + \dots$$

We substitute these expressions into the governing equations (8.24) and obtain the usual sequence of boundary value problems.

The leading-order equation set is

$$0 = -p_{0x} + u_{0yy} \quad (8.25a)$$

$$0 = -p_{0y} \quad (8.25b)$$

$$u_{0x} + v_{0y} = 0 \quad (8.25c)$$

$$h(x) = 1 + x^2/2 \quad (8.25d)$$

$$u_0 = 1, v_0 = h_x, \text{ on } y = h \quad (8.25e,f)$$

$$u_{0y} = 0, v_0 = 0, \text{ on } y = 0 \quad (8.25g,h)$$

$$p_0 \rightarrow 0 \text{ as } x \rightarrow -\infty \quad (8.25i)$$

Note that equations (8.25a–c) are identical to the scaled form of equations (8.9a–c), which were the result of standard lubrication theory applied to knife coating. The boundary conditions posed on the upper and lower surfaces are different, but these result from the different coating models being examined, and not from the asymptotic method used to obtain them. This equivalence demonstrates that standard lubrication theory is obtained as the leading-order problem from a slowly varying domain perturbation analysis. One estimate of the range of validity of the theory is given by the asymptotic condition that the next term in the series is small, i.e., $|\varepsilon| \ll 1$.

The solution of equations (8.25) was presented above during our discussion of standard lubrication theory applied to the flow through the nip of the rolls. The pressure field is given by equation (8.21). The flow rate q in this equation is as yet unknown.

We could continue with this method and proceed to the next-order problem and to higher orders if desired. This would bring in small corrections to the flow and pressure fields due to the effects of inertia, other viscous effects, and a more accurate representation of the roll surface.

Indeed, it is precisely the next higher correction that allows us to estimate the error associated with the approximation at any given order and to develop the parameter bounds that establish the domain of validity of the approximation. The boundary value problems produced in this way would resemble the leading-order problem, but they would have additional forcing terms formed from the solutions to the lower-order problems. For example, the horizontal momentum equation at the next order is

$$-p_{1x} + u_{1yy} = Re \{u_0 u_{0x} + v_0 u_{0y}\}$$

The terms on the right-hand-side of this equation are forcing functions that represent the convective acceleration of the liquid at the leading-order velocity. Inertia was neglected at leading order and so these terms force another purely viscous flow that corrects the leading-order flow for this deficiency. As one might expect, carrying this procedure to higher orders can quickly become very cumbersome. Fortunately, symbolic manipulation software can be used to remove some of the drudgery and the potential for error in this procedure.

Rather than continue with the analysis of the outer nip region, we now consider the inner region that exists near the film-splitting point $x = x_m$. The appropriate stretching transformation for the x -coordinate in this region is $\tilde{x} = (x - x_m)/\varepsilon$. Physically, the new variable \tilde{x} is a horizontal coordinate scaled with the length scale H_0 , which is the same scaling used for the vertical coordinate. In addition, we define new inner dependent variables as follows

$$\begin{aligned} \tilde{u}(\tilde{x}, y) &= u(x, y), \quad \tilde{v}(\tilde{x}, y) = \varepsilon v(x, y), \quad \text{and} \\ \tilde{p}(\tilde{x}, y) &= \varepsilon^{-1} p(x, y) \end{aligned} \quad (8.26)$$

The new vertical velocity has effectively been scaled on the surface velocity of the roll U^* , the same scale used for the horizontal velocity. The new pressure variable is equivalent to using the viscous pressure scale $\mu U^*/H_0$ instead of the large lubrication pressure scale used in the outer nip region. Both of these scales are the more reasonable ones to use when we consider that

the flow near the film-splitting point is two-dimensional and bounded by a free surface.

After performing this transformation and rescaling, the governing equations become the following,

$$Re\{\tilde{u}\tilde{u}_{\tilde{x}} + \tilde{v}\tilde{u}_y\} = -\tilde{p}_{\tilde{x}} + \tilde{u}_{\tilde{x}\tilde{x}} + \tilde{u}_{yy} \quad (8.27a)$$

$$Re\{\tilde{u}\tilde{v}_{\tilde{x}} + \tilde{v}\tilde{v}_y\} = -\tilde{p}_y + \tilde{v}_{\tilde{x}\tilde{x}} + \tilde{v}_{yy} \quad (8.27b)$$

$$\tilde{u}_{\tilde{x}} + \tilde{v}_y = 0 \quad (8.27c)$$

The equation for the upper-roll surface, now defined as $y = \tilde{h}(\tilde{x})$ is

$$\tilde{h} = 1 + \varepsilon^{-2} - \varepsilon^{-2}\sqrt{1 - \varepsilon^2(x_m + \varepsilon\tilde{x})^2} \quad (8.27d)$$

The no-slip boundary condition on the upper-roll surface is

$$(\tilde{u}, \tilde{v}) = (1, \tilde{h}_{\tilde{x}})/(1 + \tilde{h}_{\tilde{x}}^2)^{1/2} = \tilde{\mathbf{t}}_r \quad (8.27e)$$

where $\tilde{\mathbf{t}}_r$ is the tangent vector to the upper-roll surface.

The symmetry conditions on the plane $y = 0$ are

$$\tilde{u}_y = 0, \tilde{v} = 0 \quad (8.27f, g)$$

The free surface of the liquid film is described by the function $y = \tilde{\eta}(\tilde{x})$. The film-splitting point is located at $\tilde{x} = 0$ and we require that

$$\tilde{\eta}(0) = 0, \tilde{\eta}_{\tilde{x}}(0) \rightarrow \infty \quad (8.27h, i)$$

The boundary conditions imposed on the free surface are

$$\begin{aligned} -\tilde{p} + 2\{\tilde{v}_y - \tilde{\eta}_{\tilde{x}}(\tilde{u}_y + \tilde{v}_{\tilde{x}}) + \tilde{\eta}_{\tilde{x}}^2 \tilde{u}_{\tilde{x}}\} \tilde{N}^{-2} &= -Ca^{-1} \tilde{\kappa} \\ (\tilde{u}_y + \tilde{v}_{\tilde{x}})(1 - \tilde{\eta}_{\tilde{x}}^2) + 2\tilde{\eta}_{\tilde{x}}(\tilde{v}_y - \tilde{u}_{\tilde{x}}) &= 0 \\ \tilde{v} &= \tilde{u}\tilde{\eta}_{\tilde{x}} \end{aligned} \quad (8.27j-l)$$

where $\tilde{N} = (1 + \tilde{\eta}_{\tilde{x}}^2)^{1/2}$ and the curvature of the free surface is $\tilde{\kappa} = -\tilde{\eta}_{\tilde{x}\tilde{x}}\tilde{N}^{-3}$.

Far to the right of the film-splitting point, the rigid-body rotation of the liquid film with the roll is given by

$$(\tilde{u}, \tilde{v}) = (1 + \varepsilon^2 r)\tilde{\mathbf{t}}_r \text{ for } 0 \leq r \leq h_{\infty} \quad (8.27m)$$

$$\begin{aligned} h_{\infty} &= \varepsilon^{-2}\{[(1 + \varepsilon^2 - \varepsilon^2\tilde{\eta}) \\ &\quad + \varepsilon^2(x_m + \varepsilon\tilde{x})^2]^{1/2} - 1\} \end{aligned} \quad (8.27n)$$

The slope of the free surface of the liquid in this region is

$$\tilde{\eta}_{\tilde{x}} = \varepsilon(x_m + \varepsilon\tilde{x})(1 + \varepsilon^2 - \varepsilon^2\tilde{\eta})^{-1} \quad (8.27o)$$

We use the regular perturbation method to approximate the solution of this inner problem. The dependent variables are expanded as follows

$$\tilde{u} = \tilde{u}_0 + \varepsilon\tilde{u}_1 + \dots, \tilde{v} = \tilde{v}_0 + \varepsilon\tilde{v}_1 + \dots,$$

$$\tilde{p} = \tilde{p}_0 + \varepsilon\tilde{p}_1 + \dots \text{ and}$$

$$\tilde{\eta} = \tilde{\eta}_0 + \varepsilon\tilde{\eta}_1 + \dots$$

The resulting leader-order problem is

$$\begin{aligned} Re\{\tilde{u}_0\tilde{u}_{0\tilde{x}} + \tilde{v}_0\tilde{u}_{0yy}\} &= -\tilde{p}_{0\tilde{x}} + \tilde{u}_{0\tilde{x}\tilde{x}} + \tilde{u}_{0yy} \\ \end{aligned} \quad (8.28a)$$

$$\begin{aligned} Re\{\tilde{u}_0\tilde{v}_{0\tilde{x}} + \tilde{v}_0\tilde{v}_{0y}\} &= -\tilde{p}_{0y} + \tilde{v}_{0\tilde{x}\tilde{x}} + \tilde{v}_{0yy} \\ \end{aligned} \quad (8.28b)$$

$$\tilde{u}_{0\tilde{x}} + \tilde{v}_{0y} = 0 \quad (8.28c)$$

The upper-roll surface is the horizontal plane

$$y = \tilde{h}_m = 1 + x_m^2/2 \quad (8.28d)$$

The no-slip boundary condition on the upper-roll surface is

$$(\tilde{u}_0, \tilde{v}_0) = (1, 0) \text{ on } y = \tilde{h}_m \quad (8.28e)$$

Symmetry conditions on the mid-plane are

$$\tilde{u}_{0y} = 0, \tilde{v}_0 = 0 \text{ on } y = 0 \quad (8.28f, g)$$

The conditions at the film-splitting point are

$$\tilde{\eta}_0(0) = 0, \tilde{\eta}_{0\tilde{x}}(0) \rightarrow \infty \quad (8.28h, i)$$

The free-surface boundary conditions are

$$\begin{aligned} -\tilde{p}_0 + 2\{\tilde{v}_{0y} - \tilde{\eta}_{0\tilde{x}}(\tilde{u}_{0y} + \tilde{v}_{0\tilde{x}}) + \tilde{\eta}_{0\tilde{x}}^2 \tilde{u}_{0\tilde{x}}\} \tilde{N}_0^{-2} &= -Ca^{-1} \tilde{\kappa}_0 \\ \end{aligned}$$

$$\begin{aligned} (\tilde{u}_{0y} + \tilde{v}_{0\tilde{x}})(1 - \tilde{\eta}_{0\tilde{x}}^2) + 2\tilde{\eta}_{0\tilde{x}}(\tilde{v}_{0y} - \tilde{u}_{0\tilde{x}}) &= 0 \\ \tilde{v}_0 &= \tilde{u}_0 \tilde{\eta}_{0\tilde{x}} \end{aligned} \quad (8.28j-l)$$

where $\tilde{N}_0 = (1 + \tilde{\eta}_{0\tilde{x}}^2)^{1/2}$ and the curvature of the free surface is $\tilde{\kappa}_0 = -\tilde{\eta}_{0\tilde{x}\tilde{x}}\tilde{N}_0^{-3}$.

In a standard singular perturbation problem, the leading-order equations for the inner problem

are solved exactly in terms of several unknown constants. These constants are then determined by matching the inner expansion to the outer expansion. However, the leading-order equations (8.28) are the full Navier–Stokes equations posed on a domain with an unknown free surface and cannot be solved exactly. To solve these leading-order equations numerically, we need the appropriate boundary conditions for the inlet and outlet to the flow domain. These conditions are found by doing the asymptotic matching now.

The matching conditions to leading-order are very simple. For a given inner flow variable $\tilde{u}(\tilde{x})$ and an outer-flow variable $u(x)$, we must have $\tilde{u}(\tilde{x} \rightarrow \infty) = u(x \rightarrow x_{m+})$ for matching to the right and $\tilde{u}(\tilde{x} \rightarrow -\infty) = u(x \rightarrow x_{m-})$ for matching to the left. The reader should be warned that these conditions are appropriate only for a leading-order match. If higher-order corrections are desired, then a generalized matching procedure is needed as described by Van Dyke (1975), Nayfeh (1973) or Hinch (1991).

The inner flow at the film-splitting point has simplified somewhat because the upper-roll surface is now a flat, horizontal plane as shown by equation (8.28d). This occurs because the flow passage in physical variables has a very small slope (as we said above, this small slope is the basis for analyzing this flow using the slowly-varying domain perturbation method). If we just look at a small region near the film-splitting point, the small slope is imperceptible and the upper-roll surface appears to be flat and horizontal. Far to the right of the film-splitting point the liquid film is in rigid-body translation with the upper roll and the free surface of the liquid is parallel to the upper-roll surface. Thus, the appropriate matching condition for the inner problem is the rigid-body translation of a uniform film on the moving horizontal flat surface,

$$\left. \begin{aligned} (\tilde{u}_0, \tilde{v}_0) &= (1, 0) \text{ for } \tilde{\eta}_0 \leq y \leq \tilde{h}_m \\ \tilde{\eta}_0 &= \tilde{h}_m - h_\infty, \quad \tilde{\eta}_{0x} = 0 \end{aligned} \right\} \text{ as } \tilde{x} \rightarrow \infty \quad (8.28m-o)$$

To the left of the film-splitting point, the inner flow must match to the locally parallel, lubrication

flow of the outer nip region. Simplifying the inner-flow equations for a parallel flow as $\tilde{x} \rightarrow -\infty$ yields

$$0 = -\tilde{p}_{0x} + \tilde{u}_{0yy}, \quad 0 = -\tilde{p}_{0y}, \\ \tilde{u}_0(\tilde{h}_m) = 1, \quad \tilde{u}_{0y}(0) = 0$$

The solution is $\tilde{u}_0 = \frac{1}{2}\tilde{p}_{0x}(y^2 - \tilde{h}_m^2) + 1$, where \tilde{p}_{0x} is a constant. This constant can be determined in terms of the half-flow rate through the nip, $\tilde{q}_0 = \int_0^{\tilde{h}_m} \tilde{u}_0 dy$. We find that $\tilde{p}_{0x} = 3\{\tilde{h}_m - \tilde{q}_0\}/\tilde{h}_m^3$. Thus, the matching condition for the flow to the left of the film-splitting point is

$$\tilde{u}_0 = 1 - \frac{3\{\tilde{h}_m - \tilde{q}_0\}}{2\tilde{h}_m} \left(1 - \frac{y^2}{\tilde{h}_m^2}\right), \text{ for } \\ 0 \leq y \leq \tilde{h}_m, \text{ as } \tilde{x} \rightarrow -\infty \quad (8.28p)$$

Also note that the flow rate leaving the film-splitting region on the right must be the same as the flow rate entering the region on the left. This implies the dimensionless relation $h_\infty = \tilde{q}_0$.

We now have a fully-posed, leading-order flow problem in the inner region. Because of how the boundary of the upper roll has simplified, the flow looks like that of a liquid past a large two-dimensional bubble in a parallel channel of width $2\tilde{H}_m$, as shown in Fig. 8.8. Here we have used a moving reference frame fixed to the bubble (the free surface of the liquid film) and the upper and lower solid surfaces (the rolls) are moving past the bubble at the dimensional surface speed

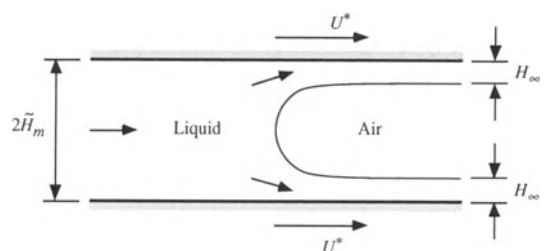


Figure 8.8 The simplified inner problem near the film-splitting point in forward roll coating.

*U**. For simplicity, we rescale the y -variable used in equations (8.28) so that the channel has a dimensionless width of two. In doing so, the matching condition for the flow to the left of the film-splitting point becomes

$$\tilde{u}_0 = 1 - \frac{3}{2}(1 - \tilde{q}_s)(1 - y^2), \text{ for } 0 \leq y \leq 1, \text{ as } \tilde{x} \rightarrow -\infty, \quad (8.29)$$

where $\tilde{q}_s = \tilde{q}_0/\tilde{h}_m$ is one-half of the flow rate through this rescaled channel.

The leading-order inner-flow problem (8.28) is now solved numerically using one of a variety of different techniques, some of which are described in Chapter 9. The results of such a computation include the velocity field, the pressure field, and the shape of the free surface (see Coyle, Macosko and Scriven 1986). However, the only result needed to complete the asymptotic analysis of the flow in the outer nip region is the flow rate. For a channel scaled to a unit half width the half-flow rate is $\tilde{q}_s = \tilde{q}_s(Ca, Re)$ and so the half-flow rate through the inner region is $\tilde{q}_0 = \tilde{q}_s \tilde{h}_m$.

To complete the asymptotic analysis of this flow the pressure and the flow rate in the outer nip region and the inner film-splitting region are matched. The pressure in the inner region is $p_{\text{inner}}(\tilde{x}) = \varepsilon \tilde{p}_0 + O(\varepsilon^2)$ and the pressure in the outer region is $p_{\text{outer}}(x) = p_0 + O(\varepsilon)$, where the inner and outer pressures have been scaled the same. The different orders of the leading-order terms in these expressions are a result of the different scalings originally used in each region. The appropriate matching condition to the left for the pressure is $p_{\text{inner}}(\tilde{x} \rightarrow -\infty) = p_{\text{outer}}(x \rightarrow x_m^-)$. The result to leading order is $p_0(x = x_m) = 0$ or $p_0(\theta_m) = 0$. The relation between the variable θ and the half-gap thickness near the nip as defined below equation (8.19) shows that $\tilde{h}_m = \sec^2 \theta_m$. So, matching the flow rates through the outer nip and the inner film-splitting region is simply $q = \tilde{q}_0 = \tilde{q}_s \tilde{h}_m = \tilde{q}_s \sec^2 \theta_m$.

The two matching conditions $p_0(\theta_m) = 0$ and $q = \tilde{q}_s \sec^2 \theta_m$ together with the leading-order

pressure distribution in the outer nip region given by equation (8.21) produce the following equation for the location of the film-splitting point θ_m .

$$\begin{aligned} & \frac{1}{2}\left(\theta_m + \frac{\pi}{2}\right) + \frac{1}{4}\sin 2\theta_m - \tilde{q}_s \\ & \times \sec^2 \theta_m \left[\frac{3}{8}\left(\theta_m + \frac{\pi}{2}\right) + \frac{1}{4}\sin 2\theta_m + \frac{1}{32}\sin 4\theta_m \right] \\ & = 0 \quad (8.30) \end{aligned}$$

Given $\tilde{q}_s = \tilde{q}_s(Ca, Re)$ from the numerical solution of the inner region, equation (8.30) is solved using a simple root-finding routine. Once θ_m is known, the half-flow rate through the nip is easily calculated from the equation $q = \tilde{q}_s \sec^2 \theta_m$.

Some specific results from solving equation (8.30) were obtained using the data for \tilde{q}_s presented by Ruschak (1982) for $Re = 0$. For $Ca = \infty$, $\tilde{q}_s = 0.41$ and we find $\theta_m = 0.972$ and $q = 1.29$. For $Ca = 0.01$, $\tilde{q}_s = 0.052$ and we find $\theta_m = 1.372$ and $q = 1.33$. These results show that the flow rate is fairly insensitive to the capillary number over the range of 0.01 to infinity and that the film-splitting point moves away from the nip as the capillary number decreases (or as surface tension increases). The pressure distributions in the nip for these two capillary numbers are shown in Fig. 8.7. Further results and discussions of roll-coating flows are found in Chapter 12a.

A final note on the *ad hoc* boundary conditions used with the standard lubrication analysis discussed in Section 8.4.1 is in order. Both the Swift–Steiber model and the Hopkins flow-separation model use the same zero-pressure boundary condition. We now see that this condition has a firm mathematical justification as it was derived using the asymptotic matching process described just above. The pressure-gradient boundary conditions used in these two models lead to an expression for the flow rate through the nip in the form $q = \tilde{q}_s \sec^2 \theta_m$, where $\tilde{q}_s = 1$ in the Swift–Steiber model and $\tilde{q}_s = 1/3$ in the Hopkins flow-separation model. Equation (8.30) shows that the parameter \tilde{q}_s , which physically is

the flow rate in the scaled inner film-splitting region, is the only parameter controlling the location of the film-splitting point. As \tilde{q}_s is determined completely by the solution to the leading-order, inner problem, we see that the dynamics of the flow in the film-splitting region is a major controlling factor for the flow in the roll-coating process as a whole. Comparing the values of \tilde{q}_s from the *ad hoc* models with the results of Ruschak (1982) shows that the *ad hoc* boundary conditions do not approximate the behavior of the flow in this inner region very well at all. Even including the effect of surface tension into the *ad hoc* models does not improve the situation as shown by Coyle, Macosko and Scriven (1986). It is not surprising then that the *ad hoc* lubrication models are ineffective.

We have seen in this section a very successful application of the singular perturbation method. The strength of this method is that it can isolate and describe a flow that occurs over a very small length scale compared with the length scale of the main flow. This characteristic is usually, but not always, signaled by a small parameter in front of a highest-order derivative in the governing differential equations for the flow. Boundary-layer or interior-layer flow problems of this kind are difficult for numerical analysis precisely because of this disparity in length scales. The singular perturbation method we have described has also been used successfully in many other problems. It has been used to describe the viscous bending of the free surface that occurs very near to a moving contact line (see Chapter 3 for a discussion of this dynamic wetting problem). It has resolved the controversy regarding the inclusion of gravity in the analysis of the dip coating process (see the discussion at the end of Section 8.5). And of course, the singular perturbation method has been extremely useful in fluid mechanics problems such as the high-Reynolds-number boundary-layer flow over a solid surface (this is important in the short-dwell coater described in Chapter 12d), the low-Reynolds number flow past a sphere, Ekman-layer flow on a rotating plane, etc. Van Dyke (1975) discusses a number of these problems in greater detail.

8.5 RISING OR FALLING FILM FLOW – A DOMAIN PERTURBATION ANALYSIS

A liquid film rising from or falling into a liquid bath is a common occurrence in many film coating processes. In dip coating, the rising film formed on a solid substrate that is dipped into a liquid bath and then withdrawn is the desired liquid coating. Falling films occur in roll coating where the roll enters the liquid bath. In this section, we analyze rising and falling films according to the geometries shown in Fig. 8.9. For the sake of simplicity, we confine ourselves to a vertical surface or wall moving upward or downward with respect to a large container of liquid with the speed U^* . Two length scales are immediately apparent: the thickness of the liquid

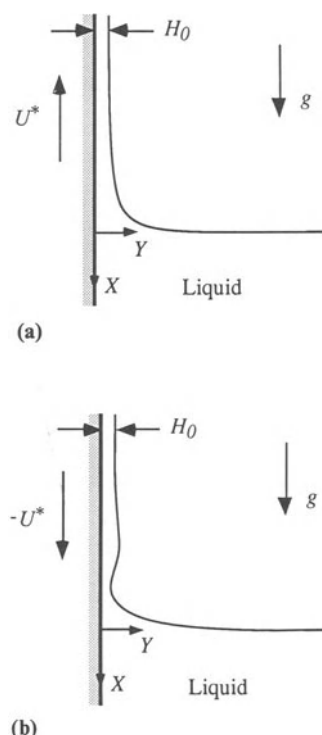


Figure 8.9 A schematic of the rising and falling film problems: (a) a monotonic film rising from a liquid bath; (b) a film falling into a liquid bath with surface waves.

film far above the bath H_0 and the width of the container. We assume that the container is large enough so that the free surface becomes flat far from the moving surface, but before the container wall. Therefore, the width of the container is not a relevant length scale for this analysis. If there was no film on the vertical surface and it was motionless, the liquid bath itself would be static and the free-surface shape would be governed by the equation of capillary statics. The force balance between surface tension and gravity represented by this equation gives rise to yet another length scale called the capillary length $L_\sigma = (\sigma/\rho g)^{1/2}$. We are particularly interested in rising or falling liquid films in which $H_0 \ll L_\sigma$. For such thin films, we expect that the flow in the film will have only a local effect on the shape of the free surface near where the film enters or leaves the liquid bath. The free-surface shape near the bath should be close to that computed by capillary statics. For the film above the bath, it has been observed that the free-surface shape changes very slowly along the direction of the moving wall. The analysis of a thin-film flow of this kind is done using the slowly varying domain perturbation technique. This is described next.

The governing equations for the rising or falling film flows shown in Fig. 8.9 are normalized with the following scales. All lengths are scaled on the capillary length L_σ as the primary region of interest is governed by this length scale. The velocity scale is $U_s = \rho g H_0^2 / \mu$. This represents a balance between the vertical component of gravity and the viscous shear in a film of thickness H_0 and it is a measure of the velocity entering the region of interest. Time is scaled on a convective scale based on this velocity and the capillary length, $t_s = L_\sigma / U_s$. Pressure is scaled on the capillary pressure $P_s = \sigma / L_\sigma$. Finally, the volume-flux scale is $Q_s = U_s L_\sigma$. With these scalings, the governing equations and boundary conditions become:

$$\varepsilon Re \{u_t + uu_x + vu_y\} = -p_x + 1 + \varepsilon^2(u_{xx} + u_{yy}) \quad (8.31a)$$

$$\varepsilon Re \{v_t + uv_x + vv_y\} = -p_y + \varepsilon^2(v_{xx} + v_{yy}) \quad (8.31b)$$

$$u_x + v_y = 0 \quad (8.31c)$$

$$u(x,0) = -N, v(x,0) = 0 \quad (8.31d,e)$$

$$\begin{aligned} -p + 2\varepsilon^2 \{v_y - h_x(u_y + v_x) + h_x^2 u_x\} N^{-2} &= -\kappa \\ (u_y + v_x)(1 - h_x^2) + 2h_x(v_y - u_x) &= 0 \\ h_t + q_x &= 0 \end{aligned} \quad (8.31f-h)$$

$$\text{on } y = h(x,t) \quad (8.31f-h)$$

Here, $N = (1 + h_x^2)^{1/2}$ and the curvature of the free surface is $\kappa = -h_{xx}N^{-3}$. The three parameters in these equations are the Reynolds number $Re = \rho^2 g H_0^3 / \mu^2$, the upward wall speed $N = \mu U^* / \rho g H_0^2$, and the film thickness $\varepsilon = H_0 / L_\sigma$.

We wish to solve this problem for the case $\varepsilon \ll 1$ and $O(1)$ values of the Reynolds number and the wall speed. When $\varepsilon = 0$, we see that all of the highest-order derivatives in equations (8.31) disappear. As we saw in Section 8.2.2, this is a signal of a singular perturbation problem. We should expect different length scales in both the x - and y -directions for the flow in the liquid film near the point where it either enters or leaves the bath, and that both of these scales will be smaller than the capillary length L_σ .

To find an approximation for the flow in the outer bath region, we ignore the boundary conditions near the moving wall as this is where we expect the rapid variations in velocity to occur. The equations describing the leading-order behavior in the outer bath region away from the moving wall are obtained by letting $\varepsilon = 0$ in equations (8.31). The result is

$$0 = -p_x + 1, 0 = -p_y, p(x,h) = \kappa,$$

which reduce to one differential equation for the curvature of the free surface, the equation of capillary statics

$$\kappa_x = 1 \quad (8.32)$$

To all higher orders the result is zero velocity and pressure (remember that we do not impose the wall boundary conditions on the outer problem). Thus, the solution of equation (8.32) is the complete and exact solution of this outer problem. This equation is most easily integrated

in arc length coordinates along the free surface. From this formulation, one integration gives the relation $c_m = \kappa^2 + 2 \sin \phi$, where ϕ is the angle between the tangent to the free surface and the x -axis and c_m is a constant that parameterizes the solution. This parameterization was presented by Ruschak (1978). For a horizontal free surface far from the moving wall, $c_m = 2$.

The inner region near the moving wall has two domains of interest. There is one boundary layer on the wall beneath the free surface of the bath that generates a weak recirculation flow in the main part of the bath. It allows the liquid to satisfy the no-slip conditions on the moving wall and the recirculating flow conforms to the static-bath, free-surface shape governed by equation (8.32). We are not concerned with this flow. The second inner region is the rising or falling film on the moving wall above the free surface of the bath. We will focus on this second region and develop an equation for the free-surface profile of the film that will match to the free-surface shape in the nearly static bath.

To examine the film-flow region next to the moving wall, we stretch the y -coordinate with the transformation $\tilde{y} = y/\varepsilon$ and $\tilde{h} = h/\varepsilon$, where the tilded quantities are order one. This is equivalent to changing the scalings for these variables from the capillary length L_σ to the thickness of the film far above the bath H_0 . The stretching transformation must also include a rescaling of some of the other variables in this flow. The appropriate scalings are determined by considering the physical forces of interest in the film. The free surface in both rising and falling films is almost parallel to the vertical wall far above the bath, but then it curves away from the wall to form the free surface of the bath. The curvature of the free surface near the bath gives rise to a capillary pressure gradient in the film such that the lowest pressure occurs near the point where the free surface curves away from the wall. This pressure gradient accelerates the flow in this region and could possibly thin the film. We wish to retain the effect of this capillary pressure gradient at leading order in the flow equations. To make $\kappa_x = (-h_{xx}N^{-3})_x$ of order

one given our scaling $\tilde{h} = h/\varepsilon$, we must rescale the x -coordinate as $\tilde{x} = x/\varepsilon^{1/3}$. This is equivalent to the length scale $l = (\sigma H_0/\rho g)^{1/3}$ used by Wilson and Jones (1983).

The scale for the velocity in the longitudinal direction remains the same as before. With this scale and the new scalings for the independent variables, the horizontal velocity component must be rescaled as $\tilde{v} = v/\varepsilon^{2/3}$ in order to balance the two terms in the continuity equation. The effect of the capillary pressure gradient is felt in the longitudinal momentum equation through the pressure-gradient term. To ensure that this term balances the viscous term and gravity, we must rescale pressure as $\tilde{p} = p/\varepsilon^{1/3}$. The volume flux in the film should scale according to the film thickness, and so $\tilde{q} = q/\varepsilon$. Finally, the time scale is adjusted to represent the convective time based on the new x -length scale, $\tilde{t} = t/\varepsilon^{1/3}$.

The complete stretching transformation yields the following form of the governing equations and boundary conditions

$$\begin{aligned} \varepsilon^{2/3} Re \{ u_{\tilde{t}} + uu_{\tilde{x}} + \tilde{v}u_{\tilde{y}} \} \\ = -\tilde{p}_{\tilde{x}} + 1 + \varepsilon^{4/3} u_{\tilde{x}\tilde{x}} + u_{\tilde{y}\tilde{y}} \end{aligned} \quad (8.33a)$$

$$\begin{aligned} \varepsilon^2 Re \{ \tilde{v}_{\tilde{t}} + u\tilde{v}_{\tilde{x}} + \tilde{v}\tilde{v}_{\tilde{y}} \} \\ = -\tilde{p}_{\tilde{y}} + \varepsilon^{8/3} \tilde{v}_{\tilde{x}\tilde{x}} + \varepsilon^{4/3} \tilde{v}_{\tilde{y}\tilde{y}} \end{aligned} \quad (8.33b)$$

$$u_{\tilde{x}} + \tilde{v}_{\tilde{y}} = 0 \quad (8.33c)$$

$$u(\tilde{x}, 0) = -N, \quad \tilde{v}(\tilde{x}, 0) = 0 \quad (8.33d, e)$$

$$\left. \begin{aligned} & -\tilde{p} + 2\varepsilon^{4/3} \{ \tilde{v}_{\tilde{y}} - \tilde{h}_{\tilde{x}}(u_{\tilde{y}} + \varepsilon^{4/3} \tilde{v}_{\tilde{x}}) + \varepsilon^{4/3} \tilde{h}_{\tilde{x}}^2 u_{\tilde{x}} \} \tilde{N}^{-2} \\ & = -\tilde{\kappa} \\ & (u_{\tilde{y}} + \varepsilon^{4/3} \tilde{v}_{\tilde{x}})(1 - \varepsilon^{4/3} \tilde{h}_{\tilde{x}}^2) + 2\varepsilon^{4/3} \tilde{h}_{\tilde{x}}(\tilde{v}_{\tilde{y}} - u_{\tilde{x}}) \\ & = 0 \\ & \tilde{h}_{\tilde{t}} + \tilde{q}_{\tilde{x}} = 0 \end{aligned} \right\} \quad (8.33f-h)$$

Here, $\tilde{N} = (1 + \varepsilon^{4/3} \tilde{h}_{\tilde{x}}^2)^{1/2}$ and the curvature of the free surface is $\tilde{\kappa} = -\tilde{h}_{\tilde{x}\tilde{x}} \tilde{N}^{-3}$.

In equations (8.33), the ratio of the x -length scale to the y -length scale is $\varepsilon^{-2/3}$, which is very large as $\varepsilon \rightarrow 0$. This means that for any dependent variable, such as the free-surface position, the length scale for variations in the x -direction is

much larger than the length scale in the y -direction. Thus, the scales used above are the appropriate ones to use in setting up this problem for a slowly varying domain perturbation analysis. The end result of such an analysis on this problem is a differential equation for the free-surface position \tilde{h} . We derive this equation by expanding the dependent variables in an appropriate power series in ε as follows,

$$u = u_0 + \varepsilon^{2/3} u_1 + \dots, \quad \tilde{v} = v_0 + \varepsilon^{2/3} v_1 + \dots \quad (8.34a,b)$$

$$\tilde{p} = p_0 + \varepsilon^{2/3} p_1 + \dots, \quad \tilde{q} = q_0 + \varepsilon^{2/3} q_1 + \dots \quad (8.34c,d)$$

We now substitute the expansions (8.34) into the equations of motion (8.33) and expand the result. The leading-order equations from this expansion are

$$0 = -p_{0x} + 1 + u_{0yy}, \quad 0 = -p_{0y}, \quad u_{0x} + v_{0y} = 0 \quad (8.35a-c)$$

$$u_0(0) = -N, \quad v_0(0) = 0 \quad (8.35d,e)$$

$$p_0(\tilde{h}) = \tilde{\kappa}, \quad u_{0y}(\tilde{h}) = 0. \quad (8.35f,g)$$

This is standard lubrication theory for the flow in the thin film (see equations (8.9) and (8.25) for comparison). The pressure is constant across the thickness of the film and is determined by the local curvature of the free surface. The longitudinal velocity is determined as a locally parallel shear flow driven by the capillary pressure gradient and gravity. There is no slip on the moving wall and no tangential stress on the free surface. Note that we have kept the entire curvature term in the normal-stress boundary condition (8.35f) even though it contains some small terms that could be formally neglected at this order. In doing so, we follow Wilson (1982), Wilson and Jones (1983), Kheshgi (1989), and Kheshgi, Kistler and Scriven (1992). There is no difficulty in keeping this full curvature expression, and it leads to a uniform approximation for the free-surface profile as we will see below.

The solution of this leading-order problem is

$$u_0 = F(\tilde{h}\tilde{y} - \tilde{y}^2/2) - N \quad (8.36a)$$

$$v_0 = -F_{\tilde{x}}(\tilde{h}\tilde{y}^2/2 - \tilde{y}^3/6) - F\tilde{h}_{\tilde{x}}\tilde{y}^2/2 \quad (8.36b)$$

$$p_0 = \tilde{\kappa}, \quad q_0 = F\tilde{h}^3/3 - N\tilde{h} \quad (8.36c,d)$$

$$F = 1 - \tilde{\kappa}_{\tilde{x}} \quad (8.36e)$$

From the next order in the expansion, we obtain

$$Re\{u_{0\tilde{t}} + u_0 u_{0\tilde{x}} + v_0 u_{0\tilde{y}}\} = -p_{1\tilde{x}} + u_{1\tilde{y}\tilde{y}},$$

$$0 = -p_{1\tilde{y}}, \quad u_{1\tilde{x}} + v_{1\tilde{y}} = 0 \quad (8.37a-c)$$

$$u_1(0) = 0, \quad v_1(0) = 0 \quad (8.37d,e)$$

$$p_1(\tilde{h}) = 0, \quad u_{1\tilde{y}}(\tilde{h}) = 0 \quad (8.37f,g)$$

Here, the normal-stress boundary condition (8.37f) represents zero pressure on the free surface of the film. All of the small terms that would have normally appeared here when the curvature is expanded are missing because they were included to leading order. The result of this boundary condition and the horizontal momentum equation (8.37b) is that the pressure in the layer at this order is zero. The longitudinal velocity in the film is a parallel shear flow with no-slip at the rigid wall and no tangential stress on the free surface. The flow is driven solely by the inertia of the leading-order flow field. The horizontal velocity in the film is just that required to satisfy continuity.

The solution of the flow field at this order is easily obtained using symbolic manipulation software, or with somewhat more difficulty, by hand. Of direct interest to the remainder of this analysis is the longitudinal flow rate

$$q_1 = Re\left\{-\frac{2}{15}F_{\tilde{t}}\tilde{h}^5 - \frac{37}{840}FF_{\tilde{x}}\tilde{h}^7 - \frac{5}{24}F\tilde{h}^4\tilde{h}_{\tilde{t}} - \frac{3}{40}F^2\tilde{h}^6\tilde{h}_{\tilde{x}} + \frac{2}{15}F_{\tilde{x}}\tilde{h}^5N + \frac{5}{24}F\tilde{h}^4\tilde{h}_{\tilde{x}}N\right\}. \quad (8.38)$$

With equations (8.36d) and (8.38), we now have an expression for the flow rate in the film to two orders in ε , i.e., $\tilde{q} = q_0 + \varepsilon^{2/3}q_1$. Inserting this into the kinematic condition for the free surface $\tilde{h}_{\tilde{t}} = -\tilde{q}_{\tilde{x}}$ produces an evolution equation for the free-surface position. This equation can be used

to study the transient motion of the film profile as well as its stability.

In the remainder of this section, we confine ourselves to the study of steady rising or falling film flows. For this case, the evolution equation reduces to $\tilde{q}_{\tilde{x}} = 0$ and so the flow rate in the film is constant, a result in keeping with a simple mass balance argument in the film. The constant is evaluated by noting that far above the free surface of the bath the film is parallel to the vertical moving wall. This means that $\tilde{h} = 1$, $\tilde{\kappa} = 0$, $F = 1$, and $\tilde{q} = 1/3 - N$. The expression $\tilde{q} = q_0 + \varepsilon^{2/3} q_1 = 1/3 - N$ leads to the following film profile equation

$$\begin{aligned} -\tilde{\kappa}_{\tilde{x}} + 1 - \frac{1}{\tilde{h}^3} + 3N\left(\frac{1}{\tilde{h}^3} - \frac{1}{\tilde{h}^2}\right) \\ + \varepsilon^{2/3} Re \left\{ -\frac{37}{280} FF_{\tilde{x}} \tilde{h}^4 - \frac{9}{40} F^2 \tilde{h}^3 \tilde{h}_{\tilde{x}} \right. \\ \left. + \frac{2}{5} F_{\tilde{x}} \tilde{h}^2 N + \frac{5}{8} F \tilde{h} \tilde{h}_{\tilde{x}} N \right\} = 0 \end{aligned} \quad (8.39a)$$

where again

$$F = 1 - \tilde{\kappa}_{\tilde{x}} \quad \text{and} \quad \tilde{\kappa} = -\tilde{h}_{\tilde{x}\tilde{x}}(1 + \varepsilon^{4/3} \tilde{h}_{\tilde{x}}^2)^{-3/2} \quad (8.39b,c)$$

Equation (8.39a) is a fourth-order, nonlinear ordinary differential equation describing the profile of the film above the bath. It is solved subject to the boundary conditions for a uniform film far above the surface of the bath, and the solution is matched as \tilde{h} gets large to the shape of the static open bath given by equation (8.32). Once the film profile equation is solved, we can use the result to compute the pressure and velocity fields within the film. To match these quantities to those within the bath, we would need to compute the flow in the bath driven by the moving wall and by the film (if it is falling). This calculation is simplified to some degree as the analysis of equations (8.31) for the flow in the outer bath region indicated that these flows do not influence the shape of the free surface of the bath to leading order, i.e., the free-surface shape

always looks like that of a static bath. However, our main goal in this section is to obtain a uniformly valid representation of the free-surface shape from the horizontal surface of the bath to the uniform film on the vertical wall far above the bath. The matching of the flow fields in the film and in the bath is not necessary for this purpose, and so we do not attempt it.

The matching of the film profile given by equation (8.39a) with the shape of the static open bath occurs as the film thickness increases. Consider the inertialess film profile equation generated by ignoring the inertial terms in equation (8.39a), i.e., set $Re = 0$. In the limit of $\tilde{h} \rightarrow \infty$, this inertialess film profile equation reduces to $\tilde{\kappa}_{\tilde{x}} = \kappa_x = 1$, which is exactly the equation for the free surface of a static bath. Thus, the matching of the thin-film inner region to the static-bath outer region occurs automatically because we retained the small terms in the expression for the curvature that would have ordinarily been neglected to leading order in a standard asymptotic analysis of this film flow. The solution of the inertialess form of equation (8.39a) yields a composite approximation to the free-surface position that is uniformly valid over the entire domain of interest. This conclusion does not hold, however, when the inertial terms are included. To properly incorporate inertial effects into the film profile equation, equation (8.39a) must be modified. The problem introduced by the inertial terms is best illustrated by considering the boundary conditions needed to solve the film profile equation (8.39a).

Two of the four necessary boundary conditions are posed far above the surface of the bath where the film is uniform. These are $\tilde{h} = 1$ and $\tilde{h}_{\tilde{x}} = 0$ for $\tilde{x} \rightarrow -\infty$. As the film profile equation was constructed to enable an automatic matching to the free surface of the static bath, the remaining two boundary conditions are posed far from the moving wall where the film merges with the flat, horizontal free surface of the static, open bath. These boundary conditions are $\tilde{h}_{\tilde{x}} \rightarrow \infty$ and $\tilde{h}_{\tilde{x}\tilde{x}} = 0$ as $\tilde{h} \rightarrow \infty$. The numerical solution of the film profile equation (8.39a) with these boundary conditions uses the shooting method. We start

far above the bath where the film is flat and integrate this equation toward the bath as an initial value problem. During the integration, we simultaneously compute the parameter $c_m = \kappa^2 + 2 \sin \phi$. Recall that c_m was the sole parameter characterizing the free-surface shape in a static bath as given by equation (8.32). As \tilde{h} gets large and the film profile matches to a static-bath, free-surface shape, c_m should approach a constant. Varying the initial conditions, and for a rising film the film thickness parameter ε , will yield the appropriate set of conditions that correspond to the open bath configuration $c_m = 2$.

There are several difficulties with this numerical integration. The first one is in identifying the four initial conditions for the film far above the bath. One attempt is to use the conditions for a vertical uniform film, i.e., $\tilde{h} = 1$, $\tilde{h}_{\tilde{x}} = 0$, $\tilde{h}_{\tilde{x}\tilde{x}} = 0$ and $\tilde{h}_{\tilde{x}\tilde{x}\tilde{x}} = 0$ for $\tilde{x} \rightarrow -\infty$. However, a uniform film is also an exact solution of equation (8.39a) and using these initial conditions in the numerical integration will produce the solution $\tilde{h} = 1$. To overcome this difficulty, we use a small-amplitude domain perturbation in the region far above the bath. We define a small perturbation to the free surface $\tilde{h} = 1 + h_1$, where $|h_1| \ll 1$, substitute this into the film profile equation (8.39a), and then linearize the equation for small h_1 . The resulting ordinary differential equation is

$$h_{1\tilde{x}\tilde{x}\tilde{x}} + 3(1 - N)$$

$$\begin{aligned} & h_1 + \varepsilon^{2/3} Re \left(-\frac{37}{280} + \frac{2}{5} N \right) h_{1\tilde{x}\tilde{x}\tilde{x}} \\ & + \varepsilon^{2/3} Re \left(-\frac{9}{40} + \frac{5}{8} N \right) h_{1\tilde{x}} = 0 \end{aligned} \quad (8.40a)$$

The solutions of this equation have the exponential form $h_1 = \exp(m\tilde{x})$, where m is a characteristic exponent. Substituting this form for h_1 into equation (8.40a) produces a fourth-order characteristic equation for m ,

$$\begin{aligned} & m^3 + 3(1 - N) + \varepsilon^{2/3} Re \left(-\frac{37}{280} + \frac{2}{5} N \right) m^4 \\ & + \varepsilon^{2/3} Re \left(-\frac{9}{40} + \frac{5}{8} N \right) m = 0 \end{aligned} \quad (8.40b)$$

Of the four roots of this equation, the one with

the largest real part is the dominant root. The exponential with this root will grow the fastest (or decay the slowest) as we move down the film toward the bath. Thus, it governs the behavior of the small-amplitude perturbation of the film far above the surface of the bath. We write the film profile using this dominant exponential in the form $\tilde{h} = 1 + \Delta \text{Real}\{\exp(m_d \tilde{x})\}$, where Δ is a small amplitude parameter and m_d is the dominant root and we ignore the other three roots. With this film profile and its first three derivatives, we now have the four required initial conditions for the film in terms of only one unknown constant Δ . The film profile equation (8.39a) is then integrated from some fixed initial point $\tilde{x}_{-\infty}$ far above the surface of the bath. The constant Δ , and for a rising film the film thickness parameter ε , is varied until the solution matches to the open bath configuration.

The roots of the characteristic equation (8.40b) are easily approximated if we treat $\varepsilon^{2/3} Re$ as a small parameter. The first three roots of this equation are close to the three cube roots of $3(N - 1)$. The character of these roots change with the wall speed. For films with $N < 1$, there is one negative real root and a complex conjugate pair with positive real parts. For films with $N > 1$, there is one positive real root and a complex conjugate pair with negative real parts. The fourth root of the characteristic equation is a singular root because the small parameter $\varepsilon^{2/3} Re$ multiplies the m^4 term. We use the singular perturbation method to obtain the following leading-order approximation of this root

$$m \approx \left(\frac{37}{280} - \frac{2}{5} N \right)^{-1} (\varepsilon^{2/3} Re)^{-1} \quad (8.41)$$

For small values of $\varepsilon^{2/3} Re$ and $N > 37/112 = 0.33036$, the singular root is very large and negative. One of the three cube roots of $3(N - 1)$ has the larger real part and so it would be the dominant root. Thus, the singular root has little effect on the linear behavior of the film far above the bath.

For small values of $\varepsilon^{2/3} Re$ and $N < 37/112$, the singular root from the characteristic equation is very large and positive. It is now the dominant root, and it describes a rapid exponential increase in the film thickness as we approach the bath. However, the fact that this root is proportional to $\varepsilon^{-2/3}$ implies that the \tilde{x} -variable should be rescaled by this same amount. The original stretching transformation of the governing equations (8.31) for the inner film region used the transformation $\tilde{x} = x/\varepsilon^{1/3}$. An additional $\varepsilon^{-2/3}$ scaling means that we should have used the transformation $\tilde{x} = x/\varepsilon$. This is the same scaling used for the y -variable, and physically it represents the film thickness far above the surface of the bath. After this new stretching transformation for the inner film region is completed (this also includes new scales for the pressure and the y -component of velocity), we find that the leading-order approximation to the governing equations are the full, two-dimensional Navier–Stokes equations and the complete free-surface boundary conditions. There is no simplification!

The implication of this result is that the film profile equation (8.39a) breaks down on either a physical or a mathematical level when $N < 37/112$ owing to the appearance of the positive singular root. A physical breakdown means that the equation no longer describes the physics of the flow in the proper way. This often happens in an asymptotic analysis. From the scaling argument described above, we may suspect that the film connects with the bath through a two-dimensional flow region that scales with the film thickness H_0 in both directions. This kind of flow violates the original scalings used in the asymptotic development of the film profile equation. A slowly varying, lubrication-like film flow above the bath could possibly be matched to this two-dimensional flow, or it may not even exist. Within this two-dimensional flow region, inertia should also be important as the singular root is derived from the inertial terms in the film profile equation. To verify this conjecture, a two-dimensional calculation of a falling film with inertia is needed.

Hansen (1987) considered a falling film on a moving wall formulated as a two-dimensional Stokes flow in the liquid. His results indicated that the film is well-described by lubrication theory. A falling film with inertia on a stationary wall was investigated by Ruschak (1978). He computed the film flow based on lubrication-type equations, and his results indicated that inertia behaved as a small perturbation to the flow. We conclude from these two studies that the physical breakdown of the film profile equation described above probably does not occur.

The only remaining explanation for the breakdown of the film profile equation is now mathematical, and this is found through an examination of how the singular root was generated. Recall that the film profile equation (8.39a) is essentially an equation for a constant flow rate in the film,

$$1/3 - N = \tilde{q} = q_0 + \varepsilon^{2/3} q_1 + \dots$$

The flow rate \tilde{q} is approximated with an asymptotic expansion in terms of the free-surface shape function \tilde{h} . For this expansion to be asymptotically valid, the second term should be much smaller than the first. We found the first three roots of the characteristic equation (8.40b) as regular perturbation expansions that are close to the cube roots of $3(N - 1)$. When the linearized free-surface shape based on these roots is substituted back into the film profile equation, the equation $q_0 = 1/3 - N$ is satisfied to leading order. The remaining small terms from this equation balance with the small terms generated from the second term of the expansion $\varepsilon^{2/3} q_1$. Thus, the expansion for the flow rate \tilde{q} based on these roots is a valid asymptotic expansion. When the linearized free-surface shape based on the singular root is substituted back into the film profile equation, the leading-order balance is between the first term q_0 and the second term $\varepsilon^{2/3} q_1$. Such a balance destroys the underlying asymptotic structure of the expansion. This balance also destroys the automatic matching of the film profile to the static bath shape that was seen to leading order. On a more physical level, balancing the two terms q_0 and $\varepsilon^{2/3} q_1$ means that we are

attempting to balance inertia with the capillary pressure gradient and the viscous stresses to leading order. The film profile equation breaks down because this balance can only be made in the context of a two-dimensional flow, as shown by the scaling argument above. This balance does not work for the lubrication-type flow that is examined in a slowly varying domain perturbation analysis.

The singular root from the characteristic equation (8.40b) is now recognized as a spurious root. It has no physical implications for this film flow because it is a mathematical artifact produced by violating the asymptotic structure of the film profile equation. We should just ignore it. Once this is done, the three remaining roots from the characteristic equation (8.40b), which are close to the cube roots of $3(N - 1)$, control the entire linear response of the film. For $N > 1$, the positive real root is dominant and we should see a monotonic increase in the thickness of the film as we move towards the bath. For $N < 1$, the complex conjugate pair of roots with positive real parts are the dominant roots and we should expect to see an oscillation of the free surface with an increasing amplitude as we move toward the bath. This kind of wave-like structure has been observed in falling films in the experiments of Cook and Clark (1973). Such observations lend further support to this mathematical explanation for the breakdown of the film profile equation.

Ignoring the spurious root in the initial conditions for the integration of the film profile equation is easy enough. However, this root must also be ignored in the differential equation itself. If we integrated the film profile equation (8.39a) with the appropriate initial conditions, we would eventually see the spurious solution contaminate the entire numerical solution when the spurious root is positive, i.e., for $N < 37/112$. As we move toward the bath, we would see a rapid increase in the film thickness, and we would probably not be able to match to any static bath configuration for large values of \tilde{h} . This behavior, of course, is entirely unphysical.

Kheshgi (1989) developed an alternative film

profile equation in which the effect of this spurious solution is removed. Using the slowly varying, domain perturbation technique, he derived a film profile equation that is equivalent to equation (8.39a) when his different scalings are taken into account. He then developed an alternative form of this equation using the idea that the basic force balance in the film is between the capillary pressure gradient and the viscous shear stresses, and that inertia should always act as a small perturbation to the flow. As a first approximation then, he ignored inertia and enforced the leading-order flow rate condition $q_0 = 1/3 - N$ to produce the inertialess film profile equation

$$-\tilde{\kappa}_{\tilde{x}} + 1 = F = \frac{1}{\tilde{h}^3} - 3N\left(\frac{1}{\tilde{h}^3} - \frac{1}{\tilde{h}^2}\right) \quad (8.42)$$

Substituting the expression for F from the right-hand side of equation (8.42) into the inertial terms of equation (8.39a) yields the alternative equation

$$\begin{aligned} -\tilde{\kappa}_{\tilde{x}} + 1 - \frac{1}{\tilde{h}^3} + 3N\left(\frac{1}{\tilde{h}^3} - \frac{1}{\tilde{h}^2}\right) \\ + \varepsilon^{2/3} Re \frac{2}{35} \left\{ \frac{3}{\tilde{h}^3} + N\left(\frac{1}{\tilde{h}^2} - \frac{18}{\tilde{h}^3}\right) \right. \\ \left. + 3N^2\left(\frac{9}{\tilde{h}^3} - \frac{1}{\tilde{h}^2} - \frac{1}{\tilde{h}}\right)\right\} \tilde{h}_{\tilde{x}} = 0 \end{aligned} \quad (8.43)$$

This film profile equation is an asymptotically consistent, third-order differential equation describing the shape of both rising and falling films. It is asymptotically consistent because the substitution (8.42) for F converts the fourth-derivative term in the film profile equation (8.39a) into a first-derivative term. This is clearly seen if we linearize the alternative film profile equation (8.43) about $\tilde{h} = 1$ to obtain

$$\begin{aligned} h_{1\tilde{x}\tilde{x}\tilde{x}} + 3(1 - N)h_1 \\ + \varepsilon^{2/3} Re \frac{6}{5} \left(\frac{1}{7} - \frac{17}{21}N + N^2 \right) h_{1\tilde{x}} \\ = 0 \end{aligned} \quad (8.44a)$$

The corresponding characteristic equation is

$$m^3 + 3(1 - N) + \varepsilon^{2/3} Re \frac{6}{5} \left(\frac{1}{7} - \frac{17}{21} N + N^2 \right) m = 0 \quad (8.44b)$$

Here the fourth-derivative term in the linearized perturbation equation and the fourth-order term in the characteristic polynomial do not appear as they do in the original equations (8.40).

One can also show that in the limit of $\tilde{h} \rightarrow \infty$, the full film profile equation (8.43) reduces to the equation for a static bath $\tilde{\kappa}_x = \kappa_x = 1$. Thus, the solution of this film profile equation matches automatically to the shape of a static bath. This solution represents a composite approximation for the film profile that includes the effects of capillary pressure, viscosity and inertia.

Kheshgi (1989) linearized both the original and the alternate film profile equations about a uniform film thickness, found the corresponding characteristic equations and then computed the roots for a rising film with no gravity. The dominant root governing the behavior of the film was compared with the exact results of Higgins (1982) who computed the root by linearizing the full Navier-Stokes equations. The alternative equation (8.43) produced more accurate results for the rising-film problem over a wider range of Reynolds numbers than did the original film profile equation (8.39a). In this comparison, the spurious root did not affect the results because it is never the dominant root for a rising film. Based on this success, Kheshgi, Kistler and Scriven (1992) used the alternative film profile equation (8.43) to compute the film profiles for both rising and falling film flows. They showed how the film profile is affected by changes in the bath configuration, i.e., changes in the parameter c_m that parameterizes the free-surface shape of a static bath. Their results for the open bath configuration followed the expected behavior discussed above.

Landau and Levich (1942) did the classical derivation of a film profile equation for the rising-film problem in order to obtain the final thickness of the film on the moving wall far above

the open bath. Their approach, as described by Levich (1962), was to apply standard lubrication theory to the slow, steady-state motion in a rising film. In terms of the slowly varying domain perturbation analysis described above, their results are the leading-order approximation for the flow in the film given by equations (8.36). The only difference is that they used the asymptotically correct leading-order form of the surface curvature $\tilde{\kappa} \approx -\tilde{h}_{xx}$, while in the present analysis, the small terms in the curvature were retained in order to produce a uniformly valid differential equation. Equation (8.36d) for the flow rate in the film with this modification of the curvature and written in dimensional form is

$$Q = -U^*H + (\rho g + \sigma H_{xxx})H^3/3\mu$$

This result is equivalent to the film profile equation given by Levich (1962, equation (133.12)). (Recall that a positive U^* is a velocity in the $-X$ -direction, which is the negative of the velocity defined by Levich).

To solve this third-order differential equation, four boundary conditions are needed because the final film thickness is also unknown. Three of these conditions correspond to a flat uniform film far above the bath. The fourth condition is obtained by explicitly matching the shape of the thin film on the vertical, moving wall to the shape of the static free surface in the open bath. This must be done because of the simple curvature term employed in the analysis. Levich (1962) did this matching by first computing the static free-surface shape of an open bath in which the free surface was tangent to the vertical wall at its point of contact (the liquid film on the wall is so thin that its thickness was ignored). Then, he ignored gravity in the film profile equation and matched the curvature of the thin film for large values of thickness to the curvature of the static free surface at its point of contact with the moving wall. With these four boundary conditions, he was able to compute the thickness of the film on the moving wall far above the bath.

The matching condition employed by Landau and Levich (1942) works well when gravity is ignored in the thin film. In this case, it is an

example of the simple leading-order asymptotic matching that was used in the roll-coating problem of Section 8.4. However, the matching condition does not work at all when gravity is included in the thin film because the curvature of the film as the thickness gets large does not approach a constant. This difficulty was resolved using a formal singular perturbation analysis by Ruschak (1976) and more completely by Wilson (1982) who obtained a two-term approximation for the final thickness of a rising film in terms of the small capillary number, $Ca = \mu U^*/\sigma$.

Other workers have considered falling films in various special limits or approximations. Wilson and Jones (1983) considered a falling film with no inertia and used a singular perturbation analysis to compute a series of waves that appears on the free surface of the film as it approaches the bath. Ruschak (1978) examined a falling film with inertia. In his analysis, he removed small terms from the governing equations by assuming a lubrication-like flow in the film above the bath. He then approximated the longitudinal velocity in the film with a second-order polynomial, developed the corresponding horizontal velocity, and integrated the longitudinal momentum equation to obtain a nonlinear equation for the free-surface position. He solved this equation numerically and found waves on the free surface of the film above the bath. Hansen (1987) considered a falling film on a wall that was either stationary or moving downward into the bath. He assumed a pure Stokes flow in the film and used a boundary integral method to compute the shape of the free surface. He also found waves in the free surface of the film above the bath. In addition, for a stationary wall and low values of the surface tension, he saw a depression in the free surface of the bath near the wall such that the free surface there was actually lower than the free surface of the bath far from the wall. The depression deepened for a moving wall as the speed of the wall into the bath increased until a kink appeared on the free surface. At this point, the calculation was stopped because of a loss in accuracy. Further discussion of various dip-coating analyses and results can

be found in the review by Ruschak (1985) and in Chapter 13.

Finally, we mention that the slowly varying domain perturbation method is not the only way to derive useful film profile equations. A number of other techniques are available. One method is just to neglect small terms from the governing equations to obtain an approximate set of differential equations. A second method is to integrate the longitudinal momentum equation across the film and to approximate the longitudinal velocity with a simple expression or perhaps a correlation of some kind. The work of Ruschak (1978) described above uses both of these techniques. These methods are discussed in slightly more detail in the introduction to this chapter. Higgins *et al.* (1977) and Higgins and Scriven (1979) have also discussed these two methods and compared them with asymptotic methods within the specific context of their use in deriving film profile equations.

8.6 THE STABILITY OF INCLINED LIQUID FILM FLOWS

Consider a uniform liquid film flowing steadily on a solid substrate under the action of gravity. This situation occurs in the dip coating process far above the free surface of the liquid bath, in some portions of the flow domain in slide coating, and in other coating flow processes. In these situations, the steadiness of the film flow is an important factor to consider. An instability of the flow would lead to wave-like motions in the free surface of the film that could in turn produce unacceptable nonuniformities in the thickness of the final coating. Thus, it is important to consider the stability of the associated coating flows during the design of any quality coating process. The first, and probably the easiest, analysis that should be done is a linear stability analysis.

A linear stability analysis of any flow is based on a technique somewhat akin to the regular perturbation method. The small parameter in this case is the amplitude of a disturbance to the

flow under consideration, such as the falling film in the above coating processes. Usually this flow field, called the basic-state flow, is known as an exact solution of the governing equations. The mathematical details of the stability analysis are simpler if this is the case, but a numerically determined basic-state flow can also be used (see Chapter 9 for examples of this kind of analysis). Once the basic state is known, the method develops a set of disturbance equations that are linearized and solved. The solution of these equations characterizes the temporal and spatial behavior of a disturbance to the basic state and provides information on when the amplitude of a disturbance is expected to grow or decay in either time or space.

The stability analysis has one additional complication in a free-surface flow that is not seen in flows with just rigid boundaries. The free-surface position in these flows is a dependent variable and must be determined as part of the solution. However, as the free-surface position of the basic-state flow is known, we can use a small-amplitude, domain perturbation analysis to determine the perturbations to the system, including those to the free surface.

In the next two subsections, we apply these asymptotic techniques to single- and multi-layered, falling film flows. The techniques are discussed first, and then the results are discussed in terms of the underlying physical processes reflected in the analysis. For a more complete discussion of the techniques of linear and nonlinear stability theory, see the standard texts by Drazin and Reid (1981), Joseph (1976), and Chandrasekhar ([1961] 1981). Further examples of stability problems in various coating flows are discussed in Chapters 9, 11b and 11d.

8.6.1 A SINGLE LIQUID LAYER FLOWING DOWN AN INCLINED PLANE

Consider a single liquid layer flowing down a smooth rigid plane inclined at the angle β with respect to the horizontal as shown in Fig. 8.10. We use a Cartesian coordinate system fixed to

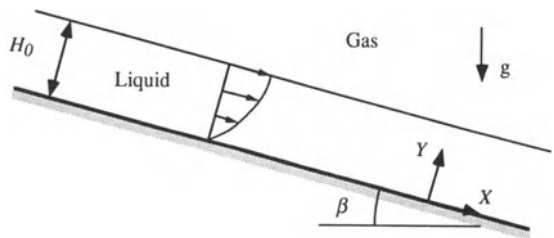


Figure 8.10 A schematic of a single liquid layer flowing down a rigid inclined plane.

the inclined plane with the X -axis embedded in the plane and aligned in the flow direction and with the Y -axis normal to the plane. All lengths are scaled using the undisturbed thickness of the film H_0 , the velocity scale is based on a balance between the longitudinal body force and the viscous shear stress $U_s = \rho g H_0^2 \sin(\beta)/\mu$, time is scaled on the convective scale $t_s = H_0/U_s$, and pressure is based on the viscous scale $P_s = \mu U_s / H_0$. The governing equations and boundary conditions become

$$Re\{u_t + uu_x + vu_y\} = -p_x + 1 + u_{xx} + u_{yy} \quad (8.45a)$$

$$Re\{v_t + uv_x + vv_y\} = -p_y - \cot(\beta) + v_{xx} + v_{yy} \quad (8.45b)$$

$$u_x + v_y = 0 \quad (8.45c)$$

$$u(x,0) = 0, \quad v(x,0) = 0 \quad (8.45d,e)$$

$$\left. \begin{aligned} -p + 2\{v_y - h_x(u_y + v_x) + h_x^2 u_x\} N^{-2} &= -Ca^{-1}\kappa \\ (u_y + v_x)(1 - h_x^2) + 2h_x(v_y - u_x) &= 0 \\ v &= h_t + uh_x \end{aligned} \right\}$$

$$\text{on } y = h(x,t) \quad (8.45f-h)$$

Here $N = (1 + h_x^2)^{1/2}$ and the curvature of the free surface is $\kappa = -h_{xx}N^{-3}$. The two parameters are the Reynolds number $Re = \rho^2 g H_0^3 \sin(\beta)/\mu^2$ and the capillary number $Ca = \rho g H_0^2 \sin(\beta)/\sigma$.

The basic-state flow is an exact solution of these equations in the form of a uniform, parallel

film flow. This solution, marked by an overbar, is

$$\bar{u} = y - y^2/2, \bar{v} = 0, \bar{p} = \cot(\beta)(1 - y), \bar{h} = 1 \quad (8.46a-d)$$

The stability of this basic-state flow is examined by assuming that there exists some disturbance to the system, and then writing all of the flow variables in terms of the basic state and this disturbance. For example, the longitudinal velocity is written as $u = \bar{u} + u'$, where primes denote the disturbance quantities. These disturbance quantities are substituted into the original governing equations, which are then simplified. The result is a set of nonlinear disturbance equations

$$\begin{aligned} Re\{u'_t + \bar{u}u'_x + u'u'_x + v'\bar{u}_y + v'u'_y\} \\ = -p'_x + u'_{xx} + u'_{yy} \end{aligned} \quad (8.47a)$$

$$Re\{v'_t + \bar{u}v'_x + u'v'_x + v'v'_y\} = -p'_y + v'_{xx} + v'_{yy} \quad (8.47b)$$

$$u'_x + v'_y = 0 \quad (8.47c)$$

$$u'(x,0) = 0, v'(x,0) = 0 \quad (8.47d,e)$$

$$\left. \begin{aligned} & -\bar{p} - p' + 2\{v'_y - h'_x(\bar{u}_y + u'_y + v'_x)\} \\ & + (h'_x)^2 u'_x \} \hat{N}^{-2} = -Ca^{-1} \kappa' \\ & (\bar{u}_y + u'_y + v'_x)[1 - (h'_x)^2] \\ & + 2h'_x(v'_y - u'_x) = 0 \\ & v' = h'_t + \bar{u}h'_x + u'h'_x \\ & \text{on } y = h(x,t) \end{aligned} \right\} \quad (8.47f-h)$$

Here, $\hat{N} = [1 + (h'_x)^2]^{1/2}$ and the curvature of the free surface is $\kappa' = -h'_{xx}\hat{N}^{-3}$.

Given the appropriate initial conditions, these equations describe the temporal spatial development of the disturbance in the layer. However, they are just as difficult to solve as the original set of governing equations and so it appears that we have gained nothing at this point. We make further progress by assuming that the amplitude of the disturbance is small compared with the basic state. Thus, we let $u', v' \ll \bar{u}, p' \ll \bar{p}$, and $h' \ll \bar{h} = 1$. We now neglect all terms in the

governing equations that are products of two or more disturbance quantities and obtain a linearized set of equations. In effect, we expand the disturbance quantities in a regular perturbation expansion in terms of a small parameter measuring the amplitude, and then only consider the leading-order problem. The difficulty in applying boundary conditions on the unknown free-surface position is resolved by using the small-amplitude domain perturbation method and linearizing the result. This method allows us to write the free-surface boundary conditions in terms of linear conditions evaluated at the basic-state free-surface position, which is known. The resulting set of linear partial differential equations and boundary conditions is

$$Re\{u'_t + \bar{u}u'_x + \bar{u}_y v'\} = -p'_x + u'_{xx} + u'_{yy} \quad (8.48a)$$

$$Re\{v'_t + \bar{u}v'_x\} = -p'_y + v'_{xx} + v'_{yy} \quad (8.48b)$$

$$u'_x + v'_y = 0 \quad (8.48c)$$

$$u'(x,0) = 0, v'(x,0) = 0 \quad (8.48d,e)$$

$$\left. \begin{aligned} & -p' + 2v'_y = \bar{p}_y h' + Ca^{-1} h'_{xx} \\ & u'_y + v'_x = -\bar{u}_{yy} h' \\ & v' = h'_t + \bar{u}h'_x \end{aligned} \right\} \quad \text{on } y = 1 \quad (8.48f-h)$$

To solve these linear partial differential disturbance equations, we note that the nonconstant coefficients in the equations (which are all basic-state quantities) depend only on the y -coordinate. Therefore, the general form of the solution contains exponentials in the x - and t -variables. (This is motivated by recalling that the general form of the solution of a linear ordinary equation with constant coefficients in the independent variable x is $\exp(mx)$, where m is a constant.) On a physical level, this means that an arbitrary disturbance in the film can be written as the sum of an infinite number of small amplitude traveling waves of arbitrary wavelength and frequency. The amplitude of these waves may grow or decay in time or space. This kind of structure and the linearity of the equations

allows us to break up the disturbance into its individual components and to solve the disturbance equations for only a single traveling wave. This kind of analysis is called the method of normal modes (see Drazin and Reid 1981; Joseph 1976). For example, we write the longitudinal velocity in the form

$$u' = \text{Real}\{\hat{u}(y)\exp[i\alpha(x - ct)]\} \quad (8.49)$$

Here, α is the real-valued wave number of the disturbance and $c = c_r + i c_i$ is a complex number. The phase speed of the disturbance wave is the real part c_r and αc_i is the exponential growth rate of the disturbance. The complex function $\hat{u}(y)$ is the depth-dependent amplitude of the disturbance wave. The normal-mode form just described is designed to examine the temporal stability of a traveling disturbance wave because the complex number c in front of the time variable allows the wave to grow or decay in time. We can also write the normal-mode form to allow bounded oscillations in time and growth or decay in the x -direction by letting αc be real and α be complex. These spatial instabilities are described in more detail in Drazin and Reid (1981).

Substituting the temporal form of the solution for the dependent variables (8.49) into the linear disturbance equations (8.48) yields the normal-mode form of the disturbance equations

$$\text{Re}\{i\alpha(\bar{u} - c)\hat{u} + \bar{u}_y\hat{v}\} = -i\alpha\hat{p} - \alpha^2\hat{u} + D^2\hat{u} \quad (8.50a)$$

$$i\alpha\text{Re}(\bar{u} - c)\hat{v} = -D\hat{p} - \alpha^2\hat{v} + D^2\hat{v} \quad (8.50b)$$

$$i\alpha\hat{u} + D\hat{v} = 0 \quad (8.50c)$$

$$\hat{u}(0) = 0, \hat{v}(0) = 0 \quad (8.50d,e)$$

$$\left. \begin{aligned} -\hat{p} + 2D\hat{v} &= \bar{p}_y\hat{h} - \alpha^2 Ca^{-1}\hat{h} \\ D\hat{u} + i\alpha\hat{v} &= -\bar{u}_{yy}\hat{h} \\ \hat{v} &= i\alpha(\bar{u} - c)\hat{h} \end{aligned} \right\} \text{on } y = 1 \quad (8.50f-h)$$

Here, we use the operator $D^n = d^n/dy^n$. The letter subscripts on the basic-state quantities also represent derivatives with respect to y .

This system of disturbance equations is often written in terms of a disturbance stream function,

which in normal-mode form is $\Psi = \text{Real}\{\phi(y)\exp[i\alpha(x - ct)]\}$. From the standard definition of the stream function we write the velocity components as $\hat{u} = D\phi$ and $\hat{v} = -i\alpha\phi$. The pressure is eliminated in the two momentum equations (8.50a,b) by differentiating (8.50a) and then combining the two equations, the pressure in the normal-mode free-surface boundary condition (8.50f) is eliminated by using the momentum equation (8.50a), and the free-surface disturbance, \hat{h} , is written in terms of the function, ϕ , by using the kinematic boundary condition (8.50h). The final result is

$$(D^2 - \alpha^2)^2\phi - i\alpha\text{Re}\{(\bar{u} - c)(D^2 - \alpha^2)\phi - \bar{u}_{yy}\phi\} = 0 \quad (8.51a)$$

$$\phi(0) = D\phi(0) = 0 \quad (8.51b,c)$$

$$D^2\phi(1) + \left\{ -\frac{\bar{u}_{yy}(1)}{(\bar{u}(1) - c)} + \alpha^2 \right\} \phi(1) = 0 \quad (8.51d)$$

$$\begin{aligned} D^3\phi(1) - \{i\alpha\text{Re}[\bar{u}(1) - c] + 3\alpha^2\}D\phi(1) \\ + \left\{ \frac{i\alpha[\cot(\beta) + \alpha^2 Ca^{-1}]}{(\bar{u}(1) - c)} \right\} \phi(1) = 0 \end{aligned} \quad (8.51e)$$

Equation (8.51a) is known as the Orr–Sommerfeld equation.

In either form, the disturbance equations (8.50) or (8.51) are a fourth-order system of linear ordinary differential equations with non-constant coefficients that constitute an eigenvalue problem for the complex eigenvalue c . The eigenvalues depend on the four parameters α , Re , β and Ca . Numerical codes today can easily integrate these equations and compute the eigenvalues. One major difficulty occurs when αRe is large. In this case, the differential equations become stiff and increased grid resolution or special techniques such as orthonormalization are needed to deal with the situation. Spectral methods provide an accurate and effective way to solve these disturbance equations. They are described by Canuto *et al.* (1988, Section 6.4) in the framework of the Orr–Sommerfeld problem. These methods can

provide the complete eigenvalue spectrum of a truncated system, which is very useful in determining the most dangerous eigenvalue as defined below. The paper by Scott and Watts (1977) describes a special-purpose code called SUPORT that uses the shooting method and orthonormalization to solve stiff two-point boundary value problems. (The current version of this public domain code, BVSUP, is a member of the SLATEC library maintained on the World Wide Web with the URL <http://gams.nist.gov/>.) An eigenvalue for the above disturbance equations is computed by combining the BVSUP code (or its equivalent) for the integration of the equations with a root-finding routine supplied by the user. The result is an accurate calculation of an eigenvalue given a good enough initial guess. However, the fact that only one eigenvalue is computed at a time is a serious disadvantage. One must be careful to determine if the most dangerous eigenvalue has indeed been found.

The stability characteristics of the system are defined by the behavior of the most dangerous eigenvalue. This eigenvalue is the one with the largest imaginary part. It corresponds to the disturbance mode that grows the fastest or decays the slowest. For fixed values of the parameters β and Ca , the computations described above are used to find this eigenvalue as a function of the wave number and the Reynolds number in the form $c_r = c_r(\alpha, Re)$ for the real part and $c_i = c_i(\alpha, Re)$ for the imaginary part. The neutral curve for the system is determined by finding the locus of points for which $c_i(\alpha, Re) = 0$. A schematic of one such curve is shown in Fig. 8.11. This curve divides the (α, Re) -plane into the shaded region above the curve where c_i is positive (unstable modes) and the region below the curve where c_i is negative (stable modes). The minimum of this neutral curve (α_c, Re_c) is called the critical point or onset point of the instability. For $Re < Re_c$, all possible disturbances decay in time and so the system is stable. For $Re > Re_c$, disturbances within a finite range of wavenumbers will grow in amplitude and so the system is unstable. The Reynolds number Re_c characterizes the onset of instability in the system to a

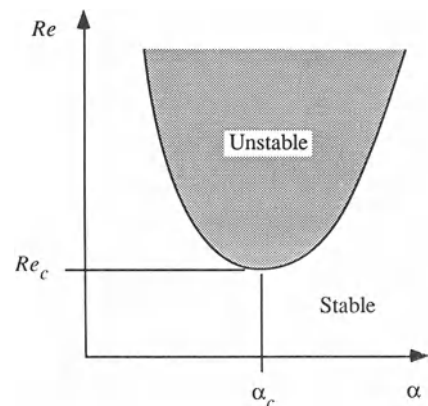


Figure 8.11 A schematic of a neutral curve for a two-dimensional fluid flow.

disturbance with the wave number α_c and with the phase speed $c_{rc} = c_r(\alpha_c, Re_c)$.

The stability calculation for an inclined falling film shows that the film is susceptible to two different types or modes of instability. The first is a shear-flow instability similar to that seen in a parallel flow inside a two-dimensional channel. There is only a small deflection of the free surface of the film for this mode. A detailed numerical analysis of this instability was presented by Floryan, Davis and Kelly (1987) for the angles of inclination $0.5^\circ < \beta < 4^\circ$. The critical conditions are affected by changes in the surface tension and the angle of inclination of the film, but roughly the critical Reynolds number is on the order of 7400 or larger, the wavelength of the critical disturbance is from two to six times the mean film thickness, and the phase speed of the critical disturbance is from 16 to 26% of the free-surface speed of the film in the base state. These rough ranges also seem to hold for $\beta > 4^\circ$. The mechanism for the instability lies in the inertial Reynolds-stress term $Re \bar{u}_y v'$ found in the longitudinal momentum equation (8.48a). This term describes how energy is fed into the disturbance through the motion of high-momentum liquid from the upper part of the film downward into the low-momentum region of the film near the wall.

The second mode of instability seen in an inclined film flow takes the form of a free-surface deflection or wave. A defining feature of this instability is that the wavelength of the critical disturbance is much larger than the film thickness. In fact, Yih (1963) showed that the wavelength of the critical disturbance is infinite in an infinitely long liquid layer. In a finite coating device, disturbances of large, but not infinite, wavelength compared with the thickness of the liquid layer have been observed. For this reason, the mode is called a long-wave instability. Numerical computations by Floryan, Davis and Kelly (1987) and De Bruin (1974) have shown that the critical Reynolds number for the long-wave instability is less than the critical Reynolds number for the shear-flow instability when $\beta > 0.5'$. This means that for these angles of inclination the long-wave mode is unstable while the shear-flow mode is stable. Thus, long waves are the more dangerous mode for $\beta > 0.5'$. As angles of inclination greater than half a minute occur in typical coating processes, the long-wave instability is of particular importance to coating engineers. Numerical integration of the linear disturbance equations has been used to find the neutral curves and the critical conditions that completely characterize this instability, as discussed by Floryan, Davis and Kelly (1987) and De Bruin (1974).

Rather than proceeding numerically, the long-wavelength character of the observed disturbances allows us to look for simple approximate forms of the critical conditions using the regular perturbation method. This method was first used on the inclined-film-flow problem by Yih (1963). We first expand the dependent variables in terms of the small wave number α . These expansions are

$$\hat{u} = u_0 + \alpha u_1 + \alpha^2 u_2 + \dots \quad (8.52a)$$

$$\hat{v} = \alpha v_1 + \alpha^2 v_2 + \dots \quad (8.52b)$$

$$\hat{p} = p_0 + \alpha p_1 + \alpha^2 p_2 + \dots \quad (8.52c)$$

$$c = c_0 + \alpha c_1 + \alpha^2 c_2 + \dots \quad (8.52d)$$

As equations (8.50) represent an eigenvalue problem for c and the solution is known only to within a multiplicative constant, we do not

expand the free-surface variable \hat{h} . Instead we normalize the solution by choosing $\hat{h} = 1$.

The expansions (8.52) are substituted into the disturbance equations (8.50) and a sequence of flow problems are produced. The leading-order flow problem is

$$D^2 u_0 = 0, \quad u_0(0) = 0, \quad Du_0(1) = 1 \quad (8.53a-c)$$

$$Dp_0 = 0, \quad p_0(1) = \cot(\beta) \quad (8.53d,e)$$

The first-order flow problem is

$$Dv_1 + iu_0 = 0, \quad v_1(0) = 0, \quad c_0 = \bar{u}(1) + iv_1(1) \quad (8.54a-c)$$

$$D^2 u_1 = ip_0 + iRe(\bar{u} - c_0)u_0 \\ + Re\bar{u}_y v_1, \quad u_1(0) = 0, \quad Du_1(1) = 0 \quad (8.54d-f)$$

The necessary equations from the second-order flow problem are

$$Dv_2 + iu_1 = 0, \quad v_2(0) = 0, \quad c_1 = iv_2(1) \quad (8.55a-c)$$

After solving these three flow problems for the velocity field, equations (8.54c) and (8.55c) are used to determine the eigenvalue. The result is

$$c = 1 + \alpha i \left\{ -\frac{1}{3}\cot(\beta) + \frac{2}{15}Re \right\} + \dots \quad (8.56)$$

The critical Reynolds number is found by setting the imaginary part of this eigenvalue to zero,

$$Re_c = 5 \cot(\beta)/2 \quad (8.57)$$

To verify that the Reynolds number given by equation (8.57) is indeed the critical value, we should continue with the perturbation procedure and compute the two-term expansion for the Reynolds number. It has the form $Re_c = 5 \cot(\beta)/2 + \alpha^2 R_2$, where $R_2 = R_2(\cot(\beta), Ca^{-1})$. Benney (1966) found R_2 using a different asymptotic procedure. His result shows that R_2 is positive for $\beta > 4.1'$ and $Ca^{-1} = 0$ (zero surface tension). This verifies that for this parameter range, the minimum of the neutral curve for the long-wave instability is given by equation (8.57) and it

occurs at $\alpha = 0$. For $\beta < 4.1'$, R_2 is negative and there is a local maximum at $\alpha = 0$. Most probably, there is also a local minimum very close to this point, although this has never been examined in such fine detail. The numerical calculations of the disturbance equations (8.51) by Floryan, Davis and Kelly (1987) suggest that the critical Reynolds number is given by (8.57) for $\beta > 0.5'$. However, these calculations did not consider wavenumbers small enough to observe the behavior suggested by Benney's result (J. M. Floryan, personal communication, June 1994).

The critical Reynolds number (8.57) is not very large except when β is very small. In fact, $Re_c = 0$ for a film flow down a vertical wall. Thus, a vertical film flow is always unstable to a long-wavelength disturbance. We also note that the critical Reynolds number does not depend on the capillary number to this order of the approximation because the long wavelength of the disturbance implies an extremely small curvature of the free surface. Surface tension appears in the next term of the expansion for the critical Reynolds number. The phase speed determined from the eigenvalue (8.56) shows that the disturbance wave travels at about twice the free-surface speed of the film in the base state.

Aside from these closed-form results for the critical Reynolds number and the eigenvalue c , the use of the regular perturbation method in the inclined film-flow problem allows us to interpret the motion of the unstable mode in the film in terms of readily identifiable forces and accelerations. A detailed discussion of this kind was presented by Smith (1990). We present a more concise version next.

Consider a thin liquid film flowing down a rigid inclined plane as shown in Fig. 8.12. The basic-state flow in the film is a parallel shear flow driven by the longitudinal component of the gravitational body force. Now consider a long-wavelength disturbance to the free surface of this film. The disturbance equations (8.53a–c) indicate that the leading-order longitudinal flow perturbation behaves like a parallel shear flow, but one driven by a perturbation shear stress on the free surface. This shear stress, given by $-\bar{u}_{yy}(1)\hat{h}$ from

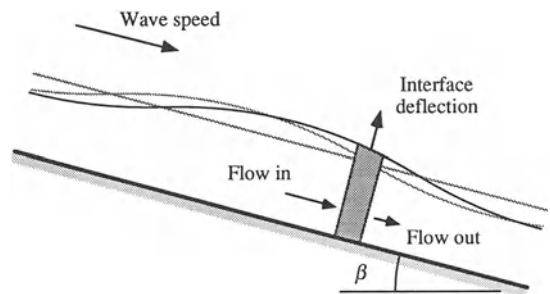


Figure 8.12 A schematic of the motion in a disturbed liquid film. The upper straight gray line is the undisturbed free-surface position. The upper solid line is the disturbed free-surface position. The leading-order longitudinal flow rate in the film is proportional to the deflection of the free surface. The upper wavy gray line is proportional to the longitudinal flow rate in the film. It is phase shifted to the left due to inertial effects in the flow. The gray box in the layer is a control volume showing the interfacial deflection at leading order.

the normal-mode form of the disturbance tangential-stress boundary condition (8.50g), exactly cancels the shear stress in the basic-state flow at the disturbed location of the free surface. Taken together the basic state and the leading-order flow perturbation form an almost parallel shear flow in the thin film in which the free surface is subjected to a small amplitude, long-wavelength disturbance. When the free surface is deflected upward by this disturbance, the increased longitudinal body force on the liquid in the film increases the longitudinal velocity in direct proportion to the magnitude of the deflection. Thus, the velocity disturbance u_0 is exactly in phase with the free-surface deformation.

A small elemental control volume in the film located to the right of a disturbance crest is shown in gray in Fig. 8.12. The flow rate entering the left side of this control volume is larger than the flow rate exiting from the right side, because the flow rate increases with the deflection of the free surface. Conservation of mass within the control volume implies that the free surface of the film is deflected upwards. The same argument applied to a control volume to the left of the

disturbance crest shows that the free surface there is deflected downwards. The net result of these motions is that the disturbance moves to the right as a wave with a phase speed faster than the liquid velocity in the film. Thus, the leading-order longitudinal velocity perturbation in the film controls the phase speed of the long-wavelength disturbance.

The leading-order pressure perturbation governed by the disturbance equations (8.53d,e) is simply the extra hydrostatic pressure in the layer due to the normal component of gravity. When the free surface is deflected upwards, the extra liquid above the mean position of the free surface increases the hydrostatic pressure underneath the disturbance crest. This pressure perturbation is exactly in phase with the free-surface deformation.

The instability of a long-wavelength disturbance to the film is a direct result of the longitudinal flow perturbation given by equations (8.54d–f). These disturbance equations describe this flow as a parallel shear flow driven by the leading-order pressure field and the inertial effects of the leading-order shear flow. The p_0 -term represents the pressure gradient established by the variation along the layer of the leading-order pressure disturbance. This pressure disturbance is greatest under a free-surface crest and lowest under a trough. The resulting pressure gradient pushes liquid away from the crest and towards the troughs. The result is a leveling of the free surface; a stabilizing effect measured by the $-\cot(\beta)/3$ term in the growth rate (8.56).

The three terms proportional to the Reynolds number in the longitudinal disturbance equation (8.54d) represent the effects of inertia associated with the leading-order flow field. The effect of the unsteady term $-iRe_{\text{c}_0}u_0$ is seen by considering the motion in the film under a crest of the free-surface disturbance wave. As the crest approaches a fixed point in the film from the left, we observe an increase in the film thickness and to leading order an increase in the longitudinal velocity because these two quantities are exactly in phase. However, the inertia of the liquid prevents it from accelerating fast enough to follow the free-surface deflection exactly and so

we actually see a small reduction in the longitudinal velocity compared with the leading-order value on the right side of the crest. As the left side of the crest passes the fixed point, the free-surface deflection decreases and the flow decelerates. Inertia resists this motion and we see a small increase in the longitudinal velocity on the right side of the crest. The net effect is a phase lag between the free-surface deflection and the longitudinal velocity, as shown in Fig. 8.12.

The effect of this phase lag on the deflection of the free surface is seen with another control-volume analysis. The control volume includes all of the liquid underneath a disturbance crest and between the two node points. The inertial phase lag in the film flow slows the longitudinal velocity of the liquid at the front node point and speeds up the velocity at the rear node point creating a net volume flow into the control volume. The result of this volume flow is an increase in the free-surface deflection, which then causes an increase in the phase lag of the longitudinal velocity, which then further increases the net volume flow underneath a disturbance crest, and so on. Here, the unsteadiness of the flow and the inertia of the liquid have combined to form a destabilizing feedback mechanism.

The advection of inertia exerts a similar influence on the flow in the film. The term $iRe\bar{u}u_0$ in the disturbance equation (8.54d) represents the effect of longitudinal advection. Consider the flow field at a particular instant in time. On the right side of a disturbance crest, the liquid is being advected longitudinally from a region of higher velocity at the crest to a region of lower velocity at the trough of the disturbance. The inertia of the liquid resists this deceleration resulting in a small increase in the longitudinal velocity of the liquid to the right of the crest. The opposite effect is seen on the left side of the crest causing a small decrease in the longitudinal velocity. The net effect is to advance the phase between the free-surface deflection and the longitudinal velocity in the film. Applying the previous control-volume analysis to this case, we see that this phase advance has a stabilizing effect on the film.

The term $Re\bar{u}_y v_1$ in the disturbance equation (8.54d) represents the effect of advection by the flow normal to the film. On the right side of a disturbance crest, the normal velocity of the liquid in the film is towards the free surface. This motion advects liquid with a small longitudinal, basic-state velocity from near the solid surface towards the faster-moving liquid near the free surface. The inertia of the liquid resists this acceleration causing a small decrease in the longitudinal velocity of the liquid to the right of the crest. Similarly, the liquid to the left of the crest increases its velocity. As we saw for the unsteady term, this is equivalent to a phase lag between the free-surface deflection and the longitudinal velocity. The effect is destabilizing to the flow in film.

The contribution of each of these inertial effects to the imaginary part of the eigenvalue (8.56) is $25Re/120$ for the unsteady effect, $-11Re/120$ for longitudinal advection, and $2Re/120$ for normal advection. The unsteady inertial effect is the dominant one and it is destabilizing according to the mechanism described above. The flow driven by these inertial effects competes with the stabilizing flow produced by the longitudinal variation of the hydrostatic pressure in the film, which is measured by $\cot(\beta)/3$. If the Reynolds number is large enough, the inertial effects win, the film is unstable and the free-surface disturbance wave grows in amplitude.

The linear instability of a single Newtonian liquid layer flowing down an inclined plane is now well understood. One deficiency of this theory is that it is linear and so it only describes the initial development of a disturbance. The stability theory for long-wavelength disturbances has two additional deficiencies. At the critical point, the most dangerous mode has an infinite wavelength and such a disturbance cannot exist in any finite system. Secondly, when the Reynolds number is above the critical point the maximum growth rate occurs for nonzero wave numbers. We must compute additional terms in the expansion for the growth rate in order to estimate this maximum, and even then the estimate may

not be very accurate if it occurs at a wave number that is not small enough. If this second deficiency occurs, the results violate the original asymptotic assumption that the wavelength of the disturbance is large and so the theory may not be applicable to the problem at all.

The first two of the deficiencies noted above are removed by incorporating nonlinear effects into the stability theory for an inclined film flow. One of the first of such investigations was Lin (1969) who did a weakly nonlinear asymptotic analysis on the full Navier–Stokes equations. The method he used is based on the fact that for a Reynolds number just above the critical value there are two very different time scales in the problem. The first time scale is based on the characteristic speed of the basic-state film flow. The second time scale is much smaller and is based on the growth rate of the unstable disturbance. Lin used these two time scales in a regular perturbation analysis and computed several terms in the expansions to obtain a nonlinear equation for the amplitude of a disturbance wave. Gjevik (1970) also did a weakly nonlinear analysis, but his results were based on the fully nonlinear evolution equation for the shape of the free surface that was first obtained by Benney (1966). This equation was derived using the slowly-varying domain perturbation method in the same way as our development of the film profile equation in the first part of Section 8.5. From this equation, Gjevik obtained a nonlinear amplitude equation for a small disturbance near the critical point. The more recent work of Chang (1989) considered a higher-order form of Benney's nonlinear evolution equation for the free surface. He analyzed this equation near the critical point using modern ideas of bifurcation theory. All of this nonlinear work showed that a linearly unstable long-wavelength disturbance on the liquid film can grow and equilibrate to a finite-amplitude wave of permanent form. This behavior has also been seen in the fully nonlinear, numerical calculations of Joo, Davis and Bankoff (1991). Three-dimensional numerical calculations for the flow in the film have been done by Joo and Davis (1992).

This work showed that the two-dimensional finite-amplitude wave of permanent form is itself unstable to a three-dimensional disturbance of long enough wavelength. The film evolves to an irregular three-dimensional pattern that does not equilibrate to a pattern of permanent form, at least to within the extent of this calculation.

Additional work on liquid film flows has examined how additional physical and geometrical effects influence the instability. A heated film that includes the effects of thermocapillarity and evaporation has been studied both linearly and nonlinearly in the long-wave limit by Joo, Davis and Bankoff (1991). Evaporation may lead to the rupture of the film and to the breaking of surface waves. Thermocapillary forces may promote significant local thinning of the film, enhance wave breaking and accelerate the rupture process brought about by evaporation. The effect of inertia for larger Reynolds numbers in the film flow has been studied by Prokopiou, Cheng and Chang (1991) using an integral technique to develop the evolution equation and to study its nonlinear behavior. This work has shown that inertia causes the disturbances in the liquid film to rapidly evolve into finite-amplitude solitary waves. A thin-film evolution equation for the flow on the outside of a circular cylinder with strong surface tension effects has been derived by Frenkel (1993). A numerical study of this equation for an axi-symmetric liquid film coating a vertical fiber has been done by Kerchman and Frenkel (1994) and Kalliadasis and Chang (1994). This work showed that if the film thickness is large enough the film will evolve to form a drop on the fiber, although the mechanism through which this is achieved is different in each of these papers. This result should be of direct interest to coating engineers involved in the coating of wires and fibers.

The effect of equipment vibration on the growth of surface waves propagating on a liquid film has been studied by Weinstein, Baumlin and Servant (1993). The geometry they considered was a single liquid layer flowing down an inclined solid wall from an upstream entrance port. They showed mathematically that in-plane oscillations

of the solid wall do not affect wave propagation in the uniform-flow region of the film. However, their experiments showed that the surface waves on the liquid film had the same frequency as the wall oscillations, and that they evolved according to a linear, spatial stability theory. The conclusion they made was that the wall oscillations forced the development of the surface waves in the entrance region to the flow where the liquid is introduced onto the inclined wall. Once formed, these waves propagate through the uniform-film region without any further interaction with the oscillating wall.

In the coating of polymers and adhesives, the non-Newtonian nature of the liquids is an important consideration. Shaqfeh, Larson and Fredrickson (1989) considered the linear stability of a film flow composed of an Oldroyd-B liquid flowing down an inclined plane. They formulated the stability problem in terms of a spatial instability and solved the linear disturbance equations numerically. This work showed that the viscoelastic nature of the liquid does reduce the critical Reynolds number, as seen in earlier studies. However, for Reynolds numbers greater than about 7, viscoelastic effects actually reduce the maximum growth rate in the system. This implies that the viscoelastic destabilization of the film may not be observable.

The pure viscoelastic mode of instability seen in a film with no inertial effects (zero Reynolds number) has a growth rate an order of magnitude smaller than that of the inertial instability. This suggests that a pure viscoelastic instability may never be observed in an actual coating device because there may not be enough time for a disturbance to grow to a discernible size. The review article by Larson (1992) contains a further discussion of the work on the instability of viscoelastic liquids in single-layer and multi-layered film flows.

Lastly, the study of surfactants and how they alter the stability characteristics of a liquid film flow is of direct interest to coating engineers. Surfactants affect the inertial instability in the layer directly and they introduce new instability mechanisms of their own. The effects of surfactants

on the flows found in coating processes are discussed in detail in Chapter 11d.

8.6.2 A MULTI-LAYERED LIQUID FILM FLOWING DOWN AN INCLINED PLANE

The production of photographic film involves the simultaneous application of many different liquid layers onto a substrate. One process that can accomplish this task is slide coating (see Chapter 11b). The flows occurring in this process are very complex, but in several regions there is a rectilinear flow of a multi-layered liquid film on a rigid, inclined plane surface. As the uniformity of the final coating depends to some degree on the stability of the flow in these regions, the question of the stability of multi-layered film flows must be addressed.

A linear stability analysis of N liquid layers flowing down a rigid, inclined plane is the same in principle as that of a single liquid layer. The mathematical model is formulated by writing the Navier–Stokes and continuity equations for each individual layer. The boundary conditions for the rigid plane and for the free surface of the film are the same as in the single-layer case. At the interface between any two adjacent layers, we pose a total of five continuity conditions. In the following, we present only these interfacial continuity conditions as they are the major difference between the single-layer and the multi-layered film flow models.

Let the interface between layer i and layer $i+1$ be given by $y = \eta^{(i)}(x, t)$. For each of the $N-1$ interfaces, we impose the condition of continuity of velocity across the interface

$$u^{(i)} = u^{(i+1)}, \quad v^{(i)} = v^{(i+1)} \quad (8.58a, b)$$

where the superscript (i) refers to the individual liquid layers. We also impose the normal- and tangential-stress balances

$$\begin{aligned} -p^{(i)} + 2\lambda_\eta^{(i)}\{v_y^{(i)} - \eta_x^{(i)}(u_y^{(i)} + v_x^{(i)}) \\ + (\eta_x^{(i)})^2 u_x^{(i)}\}(N^{(i)})^{-2} \\ = -p^{(i+1)} + 2\lambda_\eta^{(i+1)}\{v_y^{(i+1)} - \eta_x^{(i)}(u_y^{(i+1)} \\ + v_x^{(i+1)}) + (\eta_x^{(i)})^2 u_x^{(i+1)}\}(N^{(i)})^{-2} - (Ca^{(i)})^{-1} \kappa^{(i)} \end{aligned} \quad (8.58c)$$

$$\begin{aligned} & \lambda_\eta^{(i)}\{(u_y^{(i)} + v_x^{(i)})[1 - (\eta_x^{(i)})^2] + 2\eta_x^{(i)}(v_y^{(i)} - u_x^{(i)})\} \\ & = \lambda_\eta^{(i+1)}\{(u_y^{(i+1)} + v_x^{(i+1)})[1 - (\eta_x^{(i)})^2] \\ & \quad + 2\eta_x^{(i)}(v_y^{(i+1)} - u_x^{(i+1)})\} \end{aligned} \quad (8.58d)$$

Here, for each interface we have $N^{(i)} = \{1 + (\eta_x^{(i)})^2\}^{1/2}$, the curvature $\kappa^{(i)} = -\eta_{xx}^{(i)}(N^{(i)})^{-3}$, and the capillary number $Ca^{(i)} = \mu_s U_s/\sigma^{(i)}$, for which μ_s and U_s are a reference viscosity and velocity respectively and $\sigma^{(i)}$ is the surface tension of the i -th interface. The dynamic viscosity ratio for each layer is $\lambda_\eta^{(i)} = \mu^{(i)}/\mu_s$, where $\mu^{(i)}$ is the dynamic viscosity of the i -th layer. Finally, we pose a kinematic condition for the motion of this interface

$$v^{(i)} = \eta_t^{(i)} + u^{(i)}\eta_x^{(i)} \quad (5.58e)$$

Given this set of governing equations and boundary conditions, one proceeds just as in the case of a single-layer film flow. A basic state of steady, rectilinear motion is found, it is disturbed by an infinitesimal, normal-mode perturbation, and a set of linear disturbance equations is derived. These equations are solved either numerically for arbitrary wave numbers, or approximately in the limit of small wave numbers using the regular perturbation method. There are no mathematical problems associated with this analysis, but there are practical difficulties. For N liquid layers, the normal-mode stability equations form a system of $4N$ ordinary differential equations. This increases the complexity of the numerical solution and the algebra associated with the perturbation technique.

We expect the same types of behavior in a multi-layered film flow as we saw in the single-layer film flow. There is still a shear mode of instability that occurs for large values of the Reynolds number. For lower Reynolds numbers, there is a separate mode of instability associated with each of the $N-1$ interfaces and one with the free surface. The motion in each liquid layer and the mechanism of the instability for the long-wave interfacial and free-surface modes can be described as we did for the single-layer film flow. However, this description is more complex for the multi-layered film because the motion of the interfaces and the free surface are all coupled

together. This increases the difficulty of describing the force balances at work in the unstable motion of the film.

A number of authors have examined the linear stability of a multi-layered film flow down an inclined plane. The effect of density stratification in two inclined liquid layers with different thicknesses was studied by Kao (1965a, 1965b) using long-wave asymptotics. He showed that the free-surface mode is more stable when the upper liquid is lighter than the lower liquid. This effect is more pronounced as the upper layer gets thicker. When the upper liquid is heavier than the lower liquid, the free-surface mode is more unstable, but the effect does not depend all that much on the relative thicknesses of the two layers. The interfacial mode that appears in the two-layer system is always stable when the upper liquid is the heavier liquid. When the lower liquid is the heavier liquid but the two densities are not too different, the interfacial mode is always unstable. In this case, the free-surface mode could be stable if the Reynolds number is smaller than the critical value, and so the film flow would be dominated by the instability of the interfacial mode. If the lower liquid is much heavier than the upper liquid, the interfacial mode is stable for Reynolds numbers less than some critical value. If the upper layer is thin enough, the critical Reynolds number for the free-surface mode is less than the one for the interfacial mode and the instability of the free-surface mode dominates the system.

The effect of density and viscosity stratification and of different layer thicknesses in a two-layer inclined film flow was studied by Kao (1968) in the long-wave limit. A two-layer flow in which the liquids had different thicknesses and viscosities but the same density was examined more recently by Chen (1993), who did numerical computations for all wavenumbers. His results showed that the stratification does not alter the character of the free-surface mode. It is still a long-wave instability with a critical Reynolds number above which the mode is unstable. However, the character of the interfacial mode reacts strongly to the viscosity stratification. Consider the case in which the less

viscous liquid is next to the wall. When the Reynolds number is zero so that inertia is not important and there is no surface tension the interfacial mode is always unstable. The unstable disturbances have a long-wave character when the upper-layer thickness is more than about twice the thickness of the lower layer. When the upper layer is thinner than this, the unstable disturbances have a short-wave character. Increasing the surface tension of the free surface and of the interface stabilizes these short waves. If the surface tension of the interface is large enough the short-wave instability is completely eliminated, as expected. Adding inertia to the system stabilizes the long-wavelength disturbances so that they are completely stable for large enough Reynolds numbers. Short waves are destabilized by inertia but stabilized by surface tension. For this case when the less viscous liquid is next to the wall, it is not possible to have both the interfacial mode and the free-surface mode stable at the same time.

When the more viscous liquid is next to the wall and inertia is negligible, the interfacial mode is always stable to long waves and neutrally stable to very short waves. Any amount of inertia in the system destabilizes all of the disturbances. Thus, long waves are stable for Reynolds numbers less than a critical value, and short waves are always unstable. Adding enough surface tension to the interface completely stabilizes the short waves so that all disturbances are stable for Reynolds numbers less than a critical value. The critical wave number in this case is nonzero and may not be small.

A three-layer inclined film flow was considered by Akhtaruzzaman, Wang and Lin (1978), Wang, Seaborg and Lin (1978), and Weinstein and Kurz (1991). These authors gave results for the effects of density and viscosity stratification and varying layer thicknesses. In contrast to the single-layer and the two-layer problems, the instability of a three-layer film flow can arise both at leading order and at first order in the expansions for the growth rate.

The complex rheology of modern coating liquids has prompted investigators to examine

non-Newtonian liquids in multilayered film flows. Weinstein (1990) considered a two-layer inclined film flow with shear-thinning liquids using the Carreau constitutive relation for the viscosities. He showed that the free-surface mode of instability behaves as if it sees some kind of an average viscosity in the film except at very small disturbance frequencies. This is expected given the mechanism for this mode of instability as discussed above in the context of a single-layer film flow. In contrast, the interfacial mode depends strongly on the local viscosities near the interface. It is possible to either stabilize or destabilize this interfacial mode through alterations of the rheology of the two shear thinning liquids in the film. See the review by Larson (1992) for a more complete discussion of the instabilities seen in multilayered inclined film flows of viscoelastic liquids.

8.7 CONCLUSION

Asymptotic methods are powerful tools that can be used to obtain approximate solutions to fluid-flow problems of direct interest to coating engineers. These methods should be considered whenever a small parameter exists in the problem, or when there are two or more length or time scales for the flow, one of which is much smaller than the others. An asymptotic method is successful when it generates a simplified problem that is solvable, either mathematically or numerically. The resulting approximation to the exact solution is useful because it displays the primary balance among the dominant forces in the problem. Asymptotic approximations can also be used to augment numerical computations by simulating boundary conditions at infinity, and by representing the flow field in critical regions that would have otherwise forced an expensive increase in the resolution of the numerical method.

Besides the examples discussed in this chapter, asymptotic methods have been used in many other coating flow problems. Hsu *et al.* (1985) studied a coating process in which a knife was placed upon a large rotating roll. They used regular perturbation techniques to examine the

influence of a small amount of inertia in the liquid and the small curvature of the roll on the loading of the knife. The singular perturbation method has been used successfully in computing the viscous bending of the free surface that occurs very near to a moving contact line (see Chapter 3 for a discussion of this dynamic wetting problem). Domain perturbation and asymptotic techniques have been used to study the spreading of a droplet on a solid surface by Hocking (1983) and to study the effects of insoluble surfactants in dip coating by Park (1991). And of course, linear stability theory has been applied to many coating flows of interest (see Chapters 9, 11b, 11d, and 12a for some more examples).

Lubrication theory is probably one of the oldest methods of approximation used in fluid mechanics. It is often employed to study the flow in thin liquid films in which the thickness of the film varies slowly in the flow direction. In these situations, the flow in the film is quasi-one-dimensional. The original formulation of lubrication theory by Reynolds (1886) was nothing more than a simplification of the momentum equations based on the quasi-one-dimensional nature of the flow. We have seen in this chapter that lubrication theory can be formally derived as the leading-order problem in a slowly varying domain perturbation analysis of the flow in a thin liquid film.

Standard lubrication theory is very successful in the knife coating of a viscous liquid with no significant viscoelastic effects. The most important characteristics of the system, the flow and the pressure in the gap beneath the knife and the normal lifting force on the knife, are all computed easily and accurately. The obvious deficiency of the theory is that the two-dimensional flows in the small inlet and outlet regions to the gap under the knife are not well characterized. However, asymptotic techniques show that the effect of these flows on the lubrication flow through the gap takes the form of two zero-pressure boundary conditions imposed at the ends of the flow passage. These boundary conditions successfully replace a more detailed knowledge of the two-dimensional flows in the inlet and outlet regions

of the gap. This implies that the details of these flows are relatively unimportant to the overall behavior of the system.

The application of standard lubrication theory to roll coating is not so successful. The flow in the region of the nip of two large rolls is quasi-one-dimensional and it is accurately described by the Reynolds equation. However, it is not clear how to formulate the boundary conditions for the lubrication flow at the film-splitting point. Not only is the flow in this region two dimensional, but the location of this region is also unknown. Various *ad hoc* boundary conditions based on a number of different physical arguments have been proposed and used to create lubrication models for roll coating. None of these models accurately predict the location of the film-splitting point or the flow rate past the rolls as a function of the capillary number. In hindsight, one should have expected such difficulties because the two-dimensional flow near the film-splitting point is a critical influence on the location of this point. It would be surprising if these *ad hoc* boundary conditions actually did contain enough information about this flow to allow accurate predictions.

The asymptotic resolution to this dilemma is the realization that roll coating must be solved as a singular perturbation problem. The two-dimensional flow at the film-splitting point is the inner or interior-layer problem, and it is found using numerical methods. The quasi-one-dimensional flow in the nip region of the rolls is an outer flow, and it is described using lubrication theory. The rigid-body rotation of the film after the film-splitting point is a second outer flow, but with an exact solution. The flows in these three regions are matched together to form a uniformly valid approximation to the flow over the entire domain. One interesting feature of the inner problem is that the matching to the outer flows must be done first in order to supply the appropriate boundary conditions for the numerical calculation of the two-dimensional flow in the film-splitting region. One set of results from this analysis is a pair of effective boundary conditions for the outer lubrication flow in the nip region that are applied at the film-splitting point. One

of these is the simple zero-pressure condition. The other specifies the flow rate through the nip region and it depends on an accurate calculation of the flow in the inner region about the film-splitting point. The *ad hoc* boundary conditions used above do not approximate this flow-rate condition very well and so the results of the *ad hoc* models are unacceptable.

Rising and falling liquid films appear in dip coating and in other coating processes where a wetted roll or surface moves into or out of a nearly static liquid bath. The free surface of the liquid film far enough above the surface of the bath is parallel to the underlying moving surface, and it is of interest to determine how the thickness of the film varies as it joins to the surface of the bath. For thin liquid films, these variations in the film thickness typically occur over a length scale that is much larger than the average film thickness. Thus, the film profile can be computed using a slowly varying domain perturbation technique. The result of such an analysis is a third-order, asymptotically-consistent, nonlinear differential equation describing the profile of the film. Because some of the normally neglected small terms in the curvature of the free surface were kept during the development of this equation, its solution is a uniformly valid approximation of the film thickness from far above the bath all the way to and including the free surface of the static bath itself. The numerical solution of this equation does a good job in describing the film profile for both rising and falling liquid films. This calculation shows that when the upward velocity of the underlying surface is larger than some critical value, the film profile will join to the static bath in a smooth monotonic way. When the upward velocity is less than this critical value, the profile develops a series of waves as it joins to the bath. This wave-like structure occurs for all falling films (a falling film has a net flow rate into the bath), and even for some rising films.

The last problem considered in this chapter was the linear stability analysis of one or more liquid layers flowing down a rigid inclined plane. Linear stability theory is essentially the leading-

order problem from a regular perturbation analysis based on the small amplitude of a disturbance to a known basic state. The normal difficulty associated with the unknown position of the interfaces of the liquid layers is removed in this stability analysis by using the small-amplitude domain perturbation technique. The interfacial boundary conditions are then applied at the known basic-state positions and the small deviation of the interfaces from these positions become additional dependent variables in the problem.

The linear stability of a single liquid layer flowing down an inclined plane was discussed in detail. The appropriate linear disturbance equations have been solved numerically for arbitrary wave numbers. The results show that there is a shear-mode of instability occurring for large values of the Reynolds number, and a long-wave mode that appears for relatively small values of the Reynolds number except when the inclined plane is almost horizontal. Thus, in most coating flow applications, the long-wave mode would occur before the shear mode. The long-wave mode was then examined using a regular perturbation expansion of the disturbance equations for small wavenumbers. There are two advantages of such an analysis over a numerical calculation of the disturbance equations. First, it yields algebraic expressions for the stability characteristics of the layer that are easily computed. Secondly, the mechanism of the instability can be clearly described by examining the force and mass balances represented by the governing equations at each order in the expansion. Current research on single-layer inclined film flows involves the study of the nonlinear response of the film and the influence of additional effects of interest to coating engineers and others, such as heating, surfactants and non-Newtonian rheology.

The linear stability analysis of a multilayered film flow is not fundamentally different from that of a single liquid layer. The same linear analysis and small-amplitude domain perturbation techniques are used. The problem gets more complicated of course, both in terms of its analysis and in terms of its response, as more layers are added

to the film. In a multilayered film flow, there is a separate long-wave mode of instability for the free surface and for each of the interfaces in the film. The property stratification occurring among the different liquid layers influences the free-surface mode to some degree, but the essential character of this mode is still the same as in the single-layer film flow. However, this same stratification is the ultimate cause of the interfacial modes of instability. Each interfacial mode is influenced very strongly by the fluid property discontinuities occurring at that interface. Some specific examples of this complex phenomena for a two-layer film flow with density and viscosity stratification were discussed.

The coating flows discussed in this chapter were chosen to display how asymptotic techniques can be used to provide accurate approximations and useful information about a flow without resorting to full numerical calculations. These techniques can also provide boundary conditions for a numerical computation on those surfaces where the flow must join to another flow that is well-characterized mathematically. The most critical part of these asymptotic analyses is the scaling of the governing equations. It is here that the dominant balances and the required small parameters are introduced into the problem. Once this is done, the actual application of the asymptotic method is more or less routine. The art of scaling is where the physical insight of the coating engineer into the nature of the coating flow under investigation enters the analysis. This is where the engineer will have the greatest influence on both the success and the utility of the analysis.

ACKNOWLEDGMENTS

I would like to thank the editors Stephan F. Kistler and Peter M. Schweizer, and also Haroon S. Kheshgi for their careful editorial work on this chapter. The chapter is better because of it. I would also like to thank my colleagues Stephen H. Davis, Prateen V. Desai and Cyrus K. Aidun for their useful comments on a draft of this chapter.

REFERENCES

- Akhtaruzzaman, A. F. M., Wang, C. K. and Lin, S. P. 1978. Wave motion in multilayered liquid films. *J. Appl. Mech.* **45**: 25–31.
- Benney, D. J. 1966. Long waves on liquid films. *J. Math. Phys.* **45**: 150–155.
- Canuto, C., Hussaini, M. Y., Quarteroni, A. and Zang, T. A. 1988. *Spectral Methods in Fluid Dynamics*. New York: Springer-Verlag.
- Chandrasekhar, S. [1961] 1981. *Hydrodynamic and Hydromagnetic Stability*. Reprint. New York: Dover Publications.
- Chang, H.-C. 1989. Onset of nonlinear waves on falling films. *Phys. Fluids A* **1**: 1314–1327.
- Chen, K. 1993. Wave formation in the gravity-driven low-Reynolds number flow of two liquid films down an inclined plane. *Phys. Fluids A* **5**: 3038–3048.
- Cook, R. A. and Clark, R. H. 1973. An analysis of the stagnant band on falling liquid films. *Ind. Eng. Chem. Fundam.* **12**: 106–114.
- Coyle, D. J., Macosko, C. W. and Scriven, L. E. 1986. Film-splitting flows in forward roll coating. *J. Fluid Mech.* **171**: 183–207.
- De Bruin, G. J. 1974. Stability of a layer of liquid flowing down an inclined plane. *J. Eng. Math.* **8**: 259–270.
- Dowson, D. and Taylor, C. M. 1979. Cavitation in bearings. *Ann. Rev. Fluid Mech.* **11**: 35–66.
- Drazin, P. G. and Reid, W. H. 1981. *Hydrodynamic Stability*. Cambridge: Cambridge University Press.
- Floryan, J. M., Davis, S. H. and Kelly, R. E. 1987. Instabilities of a liquid film flowing down a slightly inclined plane. *Phys. Fluids* **30**: 983–989.
- Frenkel, A. L. 1993. On evolution equations for thin films flowing down solid surfaces. *Phys. Fluids A* **5**: 2342–2347.
- Gjevik, B. 1970. Occurrence of finite-amplitude surface waves on falling liquid films. *Phys. Fluids* **13**: 1918–1925.
- Hansen, E. B. 1987. Stokes flow down a wall into an infinite pool. *J. Fluid Mech.* **178**: 243–256.
- Higgins, B. G. 1982. Downstream development of two-dimensional viscopillary film flow. *Ind. Eng. Chem. Fundam.* **21**: 168–173.
- Higgins, B. G. and Scriven, L. E. 1979. Interfacial shape and evolution equations for liquid films and other viscopillary flows. *Ind. Eng. Chem. Fundam.* **18**: 208–215.
- Higgins, B. G., Silliman, W. J., Brown, R. A. and Scriven, L. E. 1977. Theory of meniscus shape in film flows. A synthesis. *Ind. Eng. Chem. Fundam.* **16**: 393–400.
- Hinch, E. J. 1991. *Perturbation Methods*. Cambridge: Cambridge University Press.
- Hocking, L. M. 1983. The spreading of a thin drop by gravity and capillarity. *Q. J. Mech. Appl. Math.* **36**: 55–69.
- Hsu, T. C., Malone, M., Laurence, R. L. and Middleman, S. 1985. Separating forces in blade coating of viscous and viscoelastic liquids. *J. Non-Newtonian Fluid Mech.* **18**: 273–294.
- Joo, S. W. and Davis, S. H. 1992. Instabilities of three-dimensional viscous falling films. *J. Fluid Mech.* **242**: 529–547.
- Joo, S. W., Davis, S. H. and Bankoff, S. G. 1991. Long-wave instabilities of heated falling films: two-dimensional theory of uniform layers. *J. Fluid Mech.* **230**: 117–146.
- Joseph, D. D. 1976. *Stability of Fluid Motions*. Berlin: Springer Verlag.
- Kalliadasis, S. and Chang, H. -C. 1994. Drop formation during coating of vertical fibers. *J. Fluid Mech.* **261**: 135–168.
- Kao, T. W. 1965a. Stability of two-layer viscous stratified flow down an inclined plane. *Phys. Fluids* **8**: 812–820.
- Kao, T. W. 1965b. Role of the interface in the stability of stratified flow down an inclined plane. *Phys. Fluids* **8**: 2190–2194.
- Kao, T. W. 1968. Role of viscosity stratification in the stability of two-layer flow down an incline. *J. Fluid Mech.* **33**: 561–572.
- Kerchman, V. I. and Frenkel, A. L. 1994. Interactions of coherent structures in a film flow: Simulations of a highly nonlinear evolution equation. *Theoret. Comput. Fluid Dynamics* **6**: 235–254.
- Kheshgi, H. S. 1989. Profile equations for film flows at moderate Reynolds numbers. *AIChE J.* **35**: 1719–1727.
- Kheshgi, H. S., Kistler, S. F. and Scriven, L. E. 1992. Rising and falling film flows: viewed from a first-order approximation. *Chem. Eng. Sci.* **47**: 683–694.
- Lamb, H. [1932] 1945. *Hydrodynamics*. Reprint. New York: Dover Publications.
- Landau, L. D. and Levich, V. G. 1942. Dragging of a liquid by a moving plate. *Acta Physicochimica URSS.* **17**: 42–54.
- Larson, R. G. 1992. Instabilities in viscoelastic flows. *Rheol. Acta.* **31**: 213–263.
- Levich, V. G. 1962. *Physicochemical Hydrodynamics*. Englewood Cliffs, NJ: Prentice-Hall.
- Lin, S. P. 1969. Finite-amplitude stability of a parallel flow with a free surface. *J. Fluid Mech.* **36**: 113–126.
- Nayfeh, A. H. 1973. *Perturbation Methods*. New York: John Wiley.

- Park, C.-W. 1991. Effects of insoluble surfactants on dip coating. *J. Colloid Interface Sci.* **146**: 382–394.
- Prokopiou, T., Cheng, M. and Chang, H.-C. 1991. Long waves on inclined films at high Reynolds number. *J. Fluid Mech.* **222**: 665–691.
- Reynolds, O. 1886. On the theory of lubrication and its application to Mr. Beauchamp Tower's experiments, including an experimental determination of the viscosity of olive oil. *Phil. Trans. Roy. Soc. London.* **177**: 157–234.
- Ruschak, K. J. 1976. Limiting flow in a pre-metered coating device. *Chem. Eng. Sci.* **31**: 1057–1060.
- Ruschak, K. J. 1978. Flow of a falling film into a pool. *AICHE J.* **24**: 705–709.
- Ruschak, K. J. 1982. Boundary conditions at a liquid/air interface in lubrication flows. *J. Fluid Mech.* **119**: 107–120.
- Ruschak, K. J. 1985. Coating flows. *Ann. Rev. Fluid Mech.* **17**: 65–89.
- Savage, M. D. 1977. Cavitation in lubrication. Part 1. On boundary conditions and cavity-fluid interfaces. *J. Fluid Mech.* **80**: 743–755.
- Savage, M. D. 1982. Mathematical models for coating processes. *J. Fluid Mech.* **117**: 443–455.
- Scott, M. R. and Watts, H. A. 1977. SUPORT – A computer code for two-point boundary-value problems via orthonormalization. *SIAM J. Num. Analy.* **14**: 40–70.
- Shaqfeh, E. S. G., Larson, R. G. and Fredrickson, G. H. 1989. The stability of gravity driven viscoelastic film-flow at low to moderate Reynolds number. *J. Non-Newtonian Fluid Mech.* **31**: 87–113.
- Smith, M. K. 1990. The mechanism for the long-wave instability in thin liquid films. *J. Fluid Mech.* **217**: 469–485.
- Taylor, G. I. 1963. Cavitation of a viscous fluid in narrow passages. *J. Fluid Mech.* **16**: 595–619.
- Van Dyke, M. 1975. *Perturbation Methods in Fluid Mechanics*. Stanford, CA: The Parabolic Press.
- Wang, C. K., Seaborg, J. J. and Lin, S. P. 1978. Instability of multi-layered liquid films. *Phys. Fluids.* **21**: 1669–1673.
- Weinstein, S. J. 1990. Wave propagation in the flow of shear-thinning fluids down an incline. *AICHE J.* **36**: 1873–1889.
- Weinstein, S. J., Baumlin, J.-M. and Servant, J. 1993. The propagation of surface waves in flow down an oscillating inclined plane. *AICHE J.* **39**: 1113–1123.
- Weinstein, S. J. and Kurz, M. R. 1991. Long-wavelength instabilities in three-layer flow down an incline. *Phys. Fluids A.* **3**: 2680–2687.
- Wilson, S. D. R. 1982. The drag-out problem in film coating theory. *J. Eng. Math.* **16**: 209–221.
- Wilson, S. D. R. and Jones, A. F. 1983. The entry of a falling film into a pool and the air-entrainment problem. *J. Fluid Mech.* **128**: 219–230.
- Yih, C.-S. 1963. Stability of liquid flow down an inclined plane. *Phys. Fluids.* **6**: 321–334.

ADVANCES IN COMPUTATIONAL METHODS FOR FREE-SURFACE FLOWS

9

*Kostas N. Christodoulou, Stephan F. Kistler and
P. Randall Schunk*

9.1 INTRODUCTION

As in many areas of science and technology, computational mathematics performed on high-speed, large-memory computers has become an essential ingredient of modern coating process research and development. Traditionally, most advances in the manufacture of imaging films, magnetic storage and many other precision coatings have been based on extensive experimentation. A predominantly empirical approach was sufficient to achieve a remarkable level of technological perfection. Nowadays, however, rapidly intensifying competitive pressures demand ever increasing coating speeds, thinner and more uniform coatings (often multilayered), reduced defect levels and diminished waste. Further refinements in coating technology become increasingly intricate and put a premium on analyzing the physical mechanisms that determine success or failure of a coating process. Imperfections in a coated layer may arise from a wide variety of mechanisms, including inhomogeneities or foreign matter in the coating solutions, disturbances induced by equipment vibration or uncontrolled air flow, various wetting phenomena, and also flow instabilities that grow in the coating device but partially decay further downstream. Complete coating failure, on the other hand, almost exclusively arises from

catastrophic hydrodynamic instabilities. It is often aggravated by edge effects, and might be triggered by large transients of the sort encountered during start-up or splice passage. Catastrophic coating failure may also stem from the inability of the coating liquid to displace sufficient air previously in contact with the dry substrate.

In the quest to identify the mechanisms by which defects form or coating processes fail, scientifically designed experiments are indispensable, for they are the ultimate test for any hypothesis or theory (*cf.* Chapter 7). Experiments alone, however, often fail to elucidate fully cause-and-effect relationships. They can also be very costly. Conventional methods of mathematical analysis can furnish valuable insights into essential mechanisms, but are usually restricted to idealized flow configurations and limited parameter ranges (*cf.* Chapter 8). Practically relevant analyses of realistic coating processes often require advanced numerical methods that solve the full set of Navier–Stokes equations and associated boundary conditions for complicated free-surface flows. State-of-the-art computer-aided analysis can explain many hydrodynamic mechanisms that control the outcome of coating processes; suggest design of process and product for improved coatability; visualize details of the flow field that are inaccessible to the experimentalist due to

geometric constraints or non-transparent liquids; evaluate many more configurations than could realistically be tested in experiments, thereby saving cost and time; allow systematic optimization, thereby further narrowing the choice of prototypes that need to be built; and permit exploration of parameter ranges that may be inaccessible with existing pilot equipment.

The objective of the present chapter is to give a comprehensive overview of computational methods suitable for the analysis of viscous free-surface flow of the sort found in industrial coating processes. The chapter focuses on four key challenges in computational flow mechanics which, by and large, have been met with algorithms available today. The first is to identify and calculate possible film-forming flows that produce uniform coatings. The second is to assess the stability of the predicted flows to small disturbances in order to establish parameter windows of successful coater operation. The third challenge is to compute the sensitivity of stable flow states to small upsets in order to identify parameter ranges within the coating window in which coating performance will be optimal. And the fourth is to predict how fast or whether at all the desired flow states recover from large upsets of the sort induced during start-up or splice passage. A further challenge is to predict whether the calculated flows displace sufficient amounts of the air previously in contact with the substrate. This challenge remains unanswered to date because of incomplete understanding of the wetting physics. Another challenge is to make sure that successful operation of a steady, uniform coating flow is not fouled by the inability of the edge regions to survive satisfactorily at the desired conditions; this also has received insufficient attention to date. Last but not least, a final challenge is to extend computational coating-flow models to include mechanisms other than those accounted for by the standard Navier–Stokes system, namely viscoelastic stresses from non-Newtonian behavior, surface-tension gradients due to surfactants and/or mass transfer, and elastic deformations of solid members confining the flow.

Computational methods that seek to address

the challenges listed above face serious mathematical difficulties. Several are inherent in solving the Navier–Stokes system, even on fixed domains: the incompressibility constraint couples the velocity components among themselves and with pressure, thereby precluding the use of purely explicit time-marching procedures; the viscous term has a broad eigenvalue spectrum that makes the equation system stiff, and hence adds to the need for implicit treatment; the advection term makes the equations nonlinear; additional nonlinearities – and even changes in type of the governing equations – arise when the coating liquid is non-Newtonian. Further difficulties arise from the free surfaces of liquid against air, interfaces between immiscible liquids, as well as deformable boundaries such as tensioned webs, flexible blades, or rubber rolls. The location of all these features is unknown *a priori*, making the equation system severely nonlinear, even when inertia is negligible, the liquid is Newtonian, and the deformable materials are Hookean solids. In addition, their shape is rarely a small perturbation from a configuration that fits a standard coordinate system. In fact, coating flow geometries can undergo dramatic variations as flow parameters vary or time evolves, including formation of cusp-like corners in the interface and even changes in topology. Additional difficulties, both physical and mathematical, stem from static contact lines where the free surfaces separate from solid coating devices, and dynamic wetting lines where the coating liquid appears to advance over a previously dry substrate. Contact angle hysteresis and sharp edges can inhibit the migration of static contact lines, and thereby allow multiple steady flow states. Conventional continuum theory breaks down altogether at dynamic contact lines. *Ad hoc* boundary conditions are frequently used to substitute for a refined physical model of the wetting dynamics, but compromise the predictive capabilities of even the most sophisticated coating-flow models advanced to date. Further complications arise from the extremely wide ranges in deformation rates encountered in coating flows, especially close to the apparent singularities associated

with contact lines. They tax the capabilities of the best rheological instruments available to date, and are sure to put to test the most sophisticated constitutive models and algorithms for viscoelastic flows. Polymeric and surface-active additives that are commonly employed as coating aids present further challenges in computational analyses, for they can give rise to steep, boundary-layer-like concentration gradients. In addition, their equilibrium and transport properties are often unknown.

To date, no algorithm has been advanced that successfully copes, in a robust manner, with all the difficulties inherent in coating-flow analysis. Thus many problems posed by practicing coating engineers are still far from routine solution. Nonetheless, significant advances in computational mathematics and computer hardware have made accessible to rigorous theory many practically relevant coating flows which, ten or even five

years ago, were locked away from analysis – especially their stability to small transitory disturbances, their operability in the space of parameters, and their sensitivity to ongoing disturbances. Many of the advances have relied on finite-element techniques (Strang and Fix 1973). The governing equations are discretized on boundary-confining meshes that adapt to changes in flow geometry independently of the underlying liquid flow. Such a mesh movement strategy accurately tracks irregular flow domains in both steady-state free-boundary problems and transient moving-boundary problems. Together with finite-element discretization, boundary-conforming meshes also simplify considerably the imposition of free-surface boundary conditions. The strategy is sometimes called arbitrary Lagrangian–Eulerian (ALE) because the mesh is neither tied to a fixed Eulerian frame of reference, as in one special class of numerical

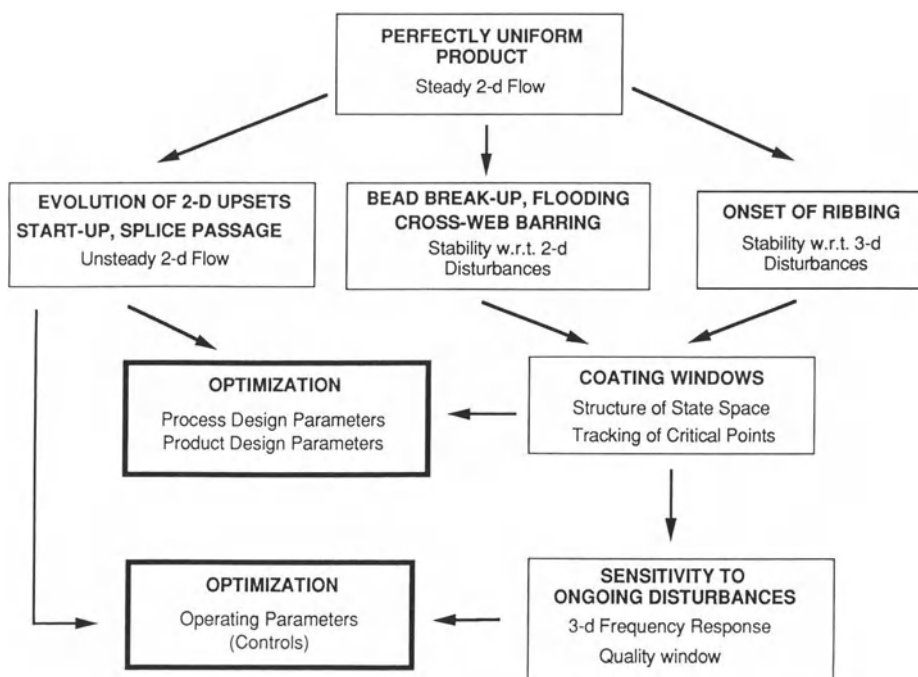


Figure 9.1 Overview of finite-element analysis of coating flows.

methods for free-surface flow analysis (*cf.* Section 9.4.1), nor does the mesh movement follow the fluid motion or the Lagrangian frame of reference associated with it, as in another class of methods (*cf.* Section 9.4.2).

ALE-type finite-element methods are the main emphasis of the present chapter. Section 9.2 describes all the basic steps that make up a modern finite-element algorithm for coating flows (for an overview, see Fig. 9.1). An earlier review by Kistler and Scriven (1983) summarized the state-of-the-art as it stood more than ten years ago, focusing on robust ‘spine’ parameterization of free surfaces and interfaces. That review also discussed the efficient coupling of flow and free-boundary computations via Newton’s method. The present review provides an update, testifying to the considerable progress that has been made since. Section 9.2.1 briefly recounts the governing equations and boundary conditions, and then describes their finite-element discretization by numerically stable combinations of the approximation spaces. Section 9.2.2 reviews generalized algebraic and elliptic mesh generation schemes that endow state-of-the-art finite-element algorithms with the flexibility to accommodate complicated free-surface flow geometries and automatically adapt to significant changes in flow geometry. Section 9.2.3 revisits the advantages of linearizing the resulting set of discretized equations by Newton-like methods. It also comments on the effectiveness of recently developed iterative matrix solvers for the resulting system of sparse linear equations. Section 9.2.4 discusses computational strategies for initial start-up when no prior solution is available, and continuation in one or several parameters for advancing from the very first start-up solution to realistic solutions that are of practical interest. Systematic continuation may also lead to the discovery of limit and bifurcation points which can provide preliminary insights into the stability of the computed solution branches. Altogether, Sections 9.2.1 through 9.2.4 describe the tools necessary to meet the first challenge in computational coating flow mechanics – the calculation of steady flows that yield uniform coatings. In

most precision coating configurations, the desired coating flows are uniform across the width of the coater except for unavoidable edge regions. For that reason, Sections 9.2.1 through 9.2.4 focus primarily on two-dimensional flows. Most of the computational techniques presented, however, can be generalized to three-dimensional flows – at least in principle – and selected comments are interjected on how to do so.

The second challenge – a full stability analysis of steady, two-dimensional flows – is also within the reach of available, albeit more sophisticated finite-element methods. Section 9.2.5 describes methods that predict the growth or decay of two-dimensional disturbances as a flow parameter varies. The methods can detect the onset of instabilities that produce cross-web patterns on coated layers, such as coating bead break-up, ‘barring’ or ‘chatter’, and bead flooding. Section 9.2.6 reviews methods that monitor the fate of three-dimensional disturbances as a coating condition is varied and cross-web wavelength is scanned. These methods can predict the onset of instabilities such as ribbing, bead break-up into rivulets and diagonal chatter or ‘chevrons’. In both types of analysis, the main problem boils down to solving a large, sparse, generalized and singular eigenproblem for at least the leading eigenvalues and corresponding modes that dominate flow stability. Section 9.2.7 explains methods that accurately compute a critical point detected by linear stability analysis (*i.e.*, the critical parameter and critical state for two-dimensional disturbances and, in addition, the critical disturbance wavenumber for three-dimensional disturbances), and systematically trace its path (*i.e.*, critical boundary) as a second parameter varies in order to map out the operability diagram of the process. The same section also presents a novel extension of Abbott’s (1978) method for accurately computing the critical conditions at which the flow loses translational invariance to the ribbing instability. Operability analysis is useful to determine optimal process designs that give maximum operating latitude.

The third challenge – investigating the sensitivity of two-dimensional coating flows to omnipresent

disturbances within the window of stable coater operation – can be addressed with computer-aided methods of frequency response analysis. Section 9.2.8 describes such methods for ongoing two-dimensional disturbances; they are rather straightforward extensions of steady-state finite-element methods. Section 9.2.8 also introduces a recent extension that handles three-dimensional disturbances of a single cross-web wavenumber. Sensitivity analysis is a powerful tool to identify the subregion of optimal coating operating conditions within the coating window in which steady-states are the least sensitive to disturbances and therefore produce the highest-quality coating.

The fourth challenge – tracking the consequences of large-amplitude transients – necessitates fully nonlinear time-dependent analysis. Section 9.2.9 recounts methods of fully implicit time-integration. It also briefly comments on alternative formulations with semi-implicit integration. Apart from finding the most efficient method for solving the stiff differential/algebraic system, the key issues are choosing self-consistent initial conditions and designing appropriate error estimates for step size control. Transient analysis has the potential to follow the evolution of growing disturbances to a final defect, and is needed to simulate start-up, ‘skip-out’ and splice passage. To date, however, none of these problems has been tackled satisfactorily, largely because ALE-type finite-element approaches have great difficulty in tracing very large deformations.

Section 9.3 takes up special topics in the physics of coating flows that are not always included in standard algorithms, namely the elusive physics of dynamic wetting (Section 9.3.1), the computational challenges of non-Newtonian behavior (Section 9.3.2), the care needed to account for the impact of surface-active and volatile additives accurately (Section 9.3.3), and the complexities inherent in elastohydrodynamic computations (Section 9.3.4).

Section 9.4 reviews alternative schemes for free-surface flow computations, most developed in contexts quite different from coating and many suitable only for transient calculations. Indeed, fully transient analysis of free-surface flows that

undergo extremely large distortions – including changes of topology as may be associated with the break-up of a liquid layer or jet into rivulets or droplets – is the forte of fully explicit free-surface computations on fixed Eulerian grids (Section 9.4.1), and also Lagrangian rezoning methods, especially what are called free-Lagrangian techniques (Section 9.4.2). Such algorithms may be of particular value when only limited *a priori* knowledge of the free-surface flow configuration is available and intelligent design of a boundary-conforming mesh is impossible. It is tempting, furthermore, to invoke various transient algorithms to perform *ad hoc* stability analyses of coating flows. Such analyses must be performed with care, however, because the computed predictions depend strongly on the initial state from which integration in time is started. Moreover, transient analyses fail altogether to elucidate the structure of nonlinear solution spaces.

Apart from methods that offer a true alternative, other methods for computational free-surface flow analysis more closely resemble boundary-confining finite-element methods for base-flow analysis. Among these are finite-difference methods combined with mapping to a rectangular domain (Section 9.4.3a) and spectral-element methods (Section 9.4.3b). While the former offer no compelling advantage, the latter share many of the hallmarks of finite-element methods yet may provide improved accuracy. Boundary-element methods would also be very attractive for coating-flow analysis, especially of three-dimensional situations, if it were not for their inability to cope effectively with flow-internal nonlinearities (Section 9.4.4).

9.2 FINITE-ELEMENT METHODS

9.2.1 COATING FLOWS AND THEIR DISCRETIZATION

9.2.1.1 Governing equations and boundary conditions

Chapter 2 provides a comprehensive introduction to the hydrodynamics that govern viscous

free-surface flows of the sort encountered in coating operations. Figure 9.2 recounts the governing equations in the dimensionless form most frequently used in finite-element simulations of coating flows, exemplified here for the case of two-dimensional slide-coating flow of two Newtonian liquid layers A and B of viscosities μ_A and μ_B , densities ρ_A and ρ_B , and surface tension σ (for an in-depth discussion of slide coating, refer to Chapter 11b): (9.1) is the momentum equation, (9.2) the Newtonian constitutive relation and (9.3) the continuity equation; (9.4) and (9.5) are the kinematic condition and traction balance at free surfaces; (9.6) is the condition of no slip at solid surfaces (away from contact lines); (9.7) is

Navier's slip boundary condition near the apparent dynamic contact line (which can be replaced by a discontinuous velocity field, see Section 9.3.1); (9.8) specifies the angle of contact of the liquid/air interface with the moving substrate surface; (9.9) is Gibbs' complementarity condition at the static wetting line where the liquid/air interface meets with the stationary die wall and $\theta \equiv \cos^{-1}(\mathbf{n} \cdot \mathbf{n}_s)$; and (9.10) is the condition of stress continuity at the interface (approximated here as a mathematical surface) between miscible layers, A and B.

In the equations listed in Fig. 9.2, \mathbf{u} is the velocity measured in units of U , a characteristic velocity, such as web speed; length is measured in units of L , a characteristic length such as gap

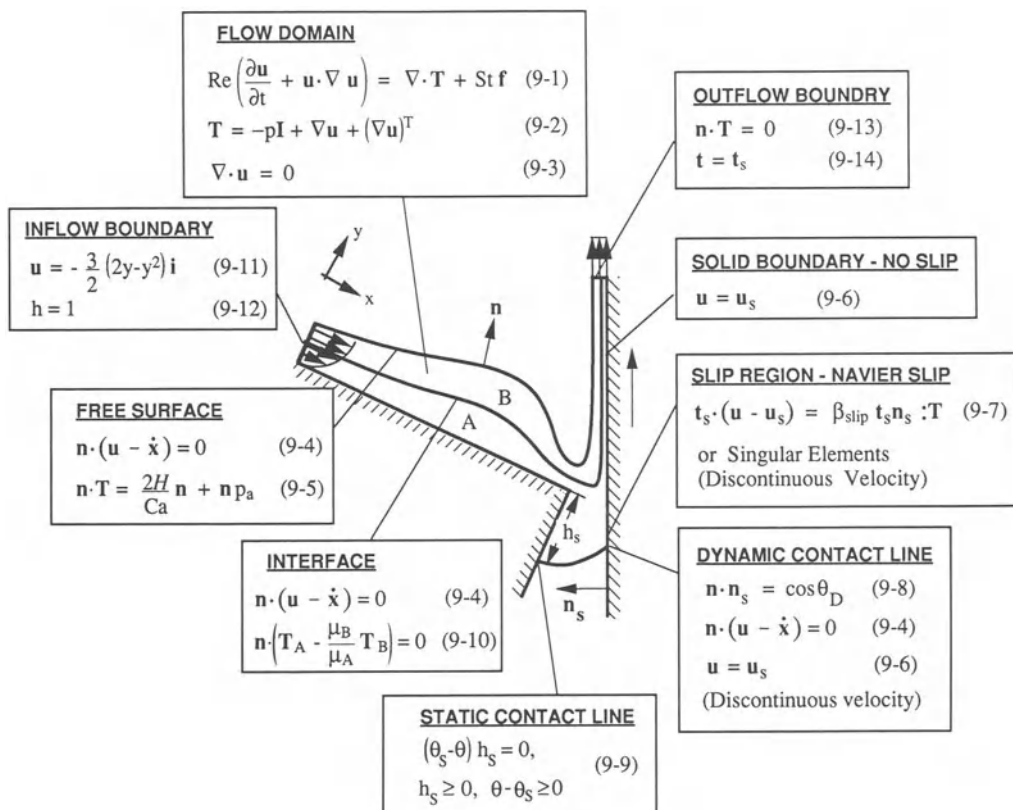


Figure 9.2 Governing equations and boundary conditions for free-surface flow in two-layer slide coating.

clearance or, as in Fig. 9.2, the thickness H_0 of the film on the inclined slide; time in units of L/U ; \mathbf{i} and \mathbf{j} are the unit vectors in the x and y directions; \mathbf{f} is the unit vector in the direction of gravity; \mathbf{T} the stress tensor and p the pressure, both measured in units of $\mu U/L$; \mathbf{I} the unit dyadic; $Re \equiv \rho Q/\mu$ the Reynolds number; $Ca \equiv \mu U/\sigma$ the capillary number; $St \equiv gL^2\rho/\mu U$ the Stokes number, where g is the force of gravity per unit mass and Q is the volumetric flow rate per unit width in the cross-web direction; \mathbf{u}_s the dimensionless velocity at solid boundaries; \mathbf{n} the local unit normal to the boundary; H the mean curvature of the interface; \mathbf{n}_s and \mathbf{t}_s the unit normal and tangent to the solid surface; θ_s the static contact angle; h_s the dimensionless wetted distance from the corner to the contact line; θ_D the dynamic contact angle; and β_{slip} the dimensionless slip coefficient. β_{slip} , θ_D and θ_s can be regarded as empirical parameters that have to be inferred from experiments (see Section 9.3.1, and also Chapter 3).

Because computational resources are finite, there is a need to truncate the computational domain upstream and downstream of the region of main interest, the so-called flow forming zone. Artificial boundary conditions must then be imposed at the resulting inflow and outflow boundaries. To limit the influence of these conditions, the boundaries are most often placed sufficiently far upstream and downstream of flow forming zones, where the flow relaxes to almost fully developed film or channel flow. In Fig. 9.2, for example, equation (9.11) specifies the two components of velocity and (9.12) the free surface location at the inflow boundary. At the outflow boundary, a natural condition of the form (9.13) results in zero traction if the flow is indeed fully developed where the condition is imposed (the effect of gravity is assumed negligible here); and (9.14) specifies the slope of the free surface. Most commonly, at inflow boundaries, the free surface location and either all velocity components or the tangential velocity component and the normal traction are specified. At outflow boundaries, preferably the slope of the free surface and either the traction in both directions or the tangential

velocity component and the normal traction are imposed. Prescribing the normal velocity component is also feasible, but can result in spurious wiggles unless the normal component at the inflow is not fixed at the same time.

To shrink the length of the computational domain further where a grid needs to be deployed and the full Navier–Stokes system is solved, improved inflow and outflow conditions can be constructed from approximate descriptions of the capillary hydrodynamics, such as the lubrication approximation or the Young–Laplace equation (*cf.* Chapters 2 and 8), or more rigorous perturbation expansions (Chapter 8). Such approximations quite often reduce the governing equations (9.1)–(9.6) into a single nonlinear ordinary differential equation for the film thickness profile (e.g., Christodoulou and Scriven (1989)). If the approximations apply throughout the flow domain, this equation can be solved numerically for the film thickness (e.g., Ruschak (1978)). More often, however, this equation is linearized and then integrated once to provide boundary conditions of the third kind (Robin) (e.g., Bixler (1982); Christodoulou and Scriven (1989)). A third alternative is to match the nonlinear equation for the film profile in upstream or downstream flow regimes to the full Navier–Stokes system for the flow forming zone, and solve the two equation sets simultaneously (e.g., Kistler and Scriven (1983); Kistler (1984)). Malamataris and Papanastasiou (1991) advocate imposing the traction $\mathbf{n} \cdot \mathbf{T}$ and free surface slope at outflow boundaries as calculated from the discretized yet still unknown flow field and free surface profile. This so called ‘free boundary condition’ amounts to imposing no boundary condition at all. It yields well-posed problems for hyperbolic problems in which disturbances and even discontinuities propagate downstream without any upstream influence. It also looks promising for elliptic problems in which the entire equilibrium solution depends on the boundary conditions on all the boundaries. For the latter, however, the ramifications and possible limitations of the ‘free boundary condition’ need to be studied further.

9.2.1.2 Finite-element discretization

In flow regions of viscous free surface flows where the flow domain fits no standard coordinate system, the finite-element method is the technique of choice for finding steady and transient solutions of the system (9.1)–(9.14). The main idea is to approximate the unknown flow field (i.e., velocity, pressure, flow geometry, etc.) in terms of a collection of particularly simple, polynomial basis functions. These are nonzero on only a few subdomains of the flow domain, in contrast to the traditional functions of mathematical physics, which span the entire domain. The partial differential or integral equations are converted into ordinary or algebraic equations for the coefficients of the basis functions by forming their weighted residuals. In the Galerkin method the weighting or test functions are the same as the basis functions. Although this choice is optimal for linear second-order elliptic problems, other choices such as Petrov–Galerkin methods may be better for hyperbolic and convection dominated problems (e.g., Brooks and Hughes (1982)).

As in the solution of the Navier–Stokes equations on fixed domains, finite-element analysis of free-surface flows can start from several different formulations of the equations depending on the treatment of the incompressibility constraint (*cf.* Gresho (1991)): the primitive-variable or velocity–pressure (u – P) formulation, which has been used almost exclusively for free-surface flows; the penalty function formulation, which is very attractive because it allows elimination of the pressure unknowns and thereby significantly reduces the dimension of the discretized equation set; the pressure Poisson equation formulation (PPE), which is gaining popularity because it allows semi-implicit time integration; and the streamfunction–vorticity (Ψ – ω) formulation, which is very popular in finite-difference algorithms of the sort described in Section 9.4.3, but rarely used with the finite-element method, especially for free surface problems. The first three formulations are described in detail in what follows. For the Ψ – ω formulation, the interested reader is referred to Gresho (1991).

Primitive variable formulation (u – P)

In the u – P formulation, the system of equations (9.1) and (9.3) with boundary conditions (9.4)–(9.14) (see Fig. 9.2) is discretized as is, using a so called mixed interpolation. Velocity, pressure, and position are expanded in terms of simple polynomial basis functions $\phi^i(\xi, \eta)$, $\psi^k(\xi, \eta)$ and $\phi^l(\xi, \eta)$ which are constructed on a standard element, for instance a square with local ξ and η coordinates in the ranges $-1 \leq \xi \leq 1$ and $-1 \leq \eta \leq 1$:

$$\mathbf{u} = \sum_i \mathbf{u}_i(t) \phi^i(\xi, \eta), \quad (9.15a)$$

$$p = \sum_k p_k(t) \psi^k(\xi, \eta), \quad (9.15b)$$

$$\mathbf{x} = \sum_l \mathbf{x}_l(t) \phi^l(\xi, \eta) \quad (9.15c)$$

Equation (9.15) is written here for two-dimensional flows; for three-dimensional flows, the expansions are of the same form but the basis functions $\phi^i(\xi, \eta, \zeta)$, $\psi^k(\xi, \eta, \zeta)$ and $\phi^l(\xi, \eta, \zeta)$ depend on a third coordinate ζ . In both cases, the basis functions are defined only locally (i.e., within each element) and need only have limited continuity between elements. The coefficients \mathbf{u}_i , p_k and \mathbf{x}_l are the unknowns. With the exception of those variables for which the basis functions are discontinuous at inter-element boundaries, the coefficients represent nodal values of the flow field and the flow geometry. They are time dependent in transient analyses and constant in steady-state analyses.

In finite-element solutions of the Navier–Stokes equations for free-surface flow problems, as for fixed boundary problems, not every combination of basis functions for velocity and pressure gives stable results. The key requirement is that the interpolations satisfy the so called LBB condition, a compatibility condition named after Ladyzhenskaya (1963), Babuska (1971) and Brezzi (1974). It ensures that the discrete pressure field is not polluted by nonphysical oscillations – so called spurious pressure modes – and the discretized system of equations is stable, i.e., its

solution converges with mesh refinement. Commonly used combinations are nine-node biquadratics for ψ^i and four-node bilinears or linear discontinuous functions for ψ^k (see Huyakorn *et al.* (1978)). Finding stable combinations for viscoelastic flows, with or without free surfaces, is still an area of active research (see Section 9.3.2).

Equal-order interpolation is most commonly used for nodal position and velocity, as in equation (9.15c). The mapping of each element of the boundary-conforming mesh in the physical domain onto the standard domain (ξ, η) on a fixed rectangular grid – provided by equation (9.15c) – is then called iso-parametric. For interior nodes away from free surfaces, sub-parametric mapping with lower-order basis functions is also possible. In fact, it is advantageous in conjunction with elliptic mesh generation (Christodoulou and Scriven (1992); see also Section 9.2.2).

In transient problems, the mesh usually deforms at each time step to follow the motion of free boundaries in an arbitrary Lagrangian–Eulerian manner that preserves the topology of the initial mesh configuration yet is independent of the underlying liquid flow (see also Section 9.4.2). Essential to the formulation of the discretized transient problem is proper accounting for the relative motion between the deforming grid and the flow. It is readily taken care of via the iso- or sub-parametric mapping (9.15c) (see Lynch (1982)). Time derivatives $\partial/\partial t$ at a fixed Eulerian location are transformed to time derivatives at fixed (iso)-parametric coordinates, denoted by an over-dot:

$$\dot{\mathbf{u}}/\partial t = \dot{\mathbf{u}} - \dot{\mathbf{x}} \cdot \nabla \mathbf{u} \quad (9.16)$$

Here, $\dot{\mathbf{x}}$ is the mesh velocity. The term $\dot{\mathbf{x}} \cdot \nabla \mathbf{u}$ is, of course, the same as the extra term that arises in so called arbitrary Lagrangian–Eulerian methods – which recently have received much ‘hype’ in the context of free-surface flow computations (see Section 9.4.3).

The governing equations (9.1), (9.3) and (9.4) are transformed into a discretized system of ordinary differential equations by multiplying with the appropriate basis functions, integrating over the computational domain, and applying

the divergence theorem to the momentum equation:

$$\mathbf{R}_i^M \equiv \int_A \{ \mathbf{T} \cdot \nabla \phi^i + [Re(\dot{\mathbf{u}} + (\mathbf{u} - \dot{\mathbf{x}}) \cdot \nabla \mathbf{u}) - Stf] \phi^i \} dA - \int_{\partial A} \mathbf{n} \cdot \mathbf{T} \phi^i ds \quad (9.17)$$

$$R_k^C \equiv \int_A \psi^k \nabla \cdot \mathbf{u} dA = 0 \quad (9.18)$$

$$\mathbf{R}_m^K \equiv \int_{\partial A_f} \mathbf{n} \cdot (\mathbf{u} - \dot{\mathbf{x}}) \phi^m ds = 0 \quad (9.19)$$

Here M, C and K denote momentum, continuity and kinematic residuals; A denotes the computational domain, ∂A its entire boundary, and ∂A_f all free-surface boundaries. Introducing the expansions (9.15) into the integrals (9.17)–(9.19) turns the latter into a system of algebraic and ordinary differential equations – or just algebraic equations in the case of steady state calculations – for the unknown coefficients in the basis function expansions. The integrals (9.17)–(9.19) are sometimes referred to as the weak form because the original set of governing equations and boundary conditions is satisfied only in an average, integral sense rather than being exactly valid at every point in the domain.

Imposition of boundary conditions: Essential boundary conditions (BC), usually at solid or inflow boundaries, are imposed by replacing the corresponding weighted residual equations (9.17) or (9.19) with the desired velocity or free-surface specifications. Natural boundary conditions, usually at free surfaces and outflow boundaries, are imposed through the boundary integral $\int_{\partial A} \mathbf{n} \cdot \mathbf{T} \phi^i ds$ in (9.17). For example, the stress boundary condition at the free surface is imposed by substituting the right-hand side of (9.5) into the traction boundary integral of (9.17) and applying the surface divergence theorem (Ruschak 1980). For two-dimensional (2D) problems,

equation (9.17) becomes:

$$\begin{aligned} \mathbf{R}_i^M = & \int_A [(Re \mathbf{u} \cdot \nabla \mathbf{u} - St \mathbf{f}) \phi^i \\ & + \nabla \phi^i \cdot \mathbf{T}] dA + \frac{1}{Ca} \int_{\partial A_f} \mathbf{t} \frac{d\phi^i}{ds} ds \\ & - \frac{1}{Ca} (\phi^i \mathbf{t}_1 - \phi^i \mathbf{t}_0) \end{aligned} \quad (9.20)$$

The end-point terms in (9.20) are ‘shell forces’ due to surface tension. Their directions \mathbf{t}_0 and \mathbf{t}_1 have to be specified at inflow and outflow boundaries, and also at contact lines. Specifying a contact angle in the weak form (9.20) rather than through an essential condition works well at static separation lines that are free to migrate along a solid, but is problematic at dynamic wetting lines (see Christodoulou and Scriven (1989)).

In three-dimensional (3D) problems, the boundary integral of the traction on free surfaces ∂A_f in equation (9.17) is a surface integral:

$$\begin{aligned} \int_{\partial A_f} \mathbf{n} \cdot \mathbf{T} \phi^i dA = & \frac{1}{Ca} \int_{\partial A_f} (\nabla_{II} \cdot \mathbf{e}\mathbf{n}) \mathbf{n} \phi^i dA \\ & + \int_{\partial A_f} \mathbf{n} p_a \phi^i dA \end{aligned} \quad (9.21)$$

Application of the surface divergence theorem (Weatherburn 1927, p. 123) to the first term on the right-hand side of (9.21) lowers the order of spatial derivatives (Ruschak 1983), so that

$$\int_{\partial A_f} \phi^i (\nabla \cdot \mathbf{n}) \mathbf{n} dA = \int_{\partial A_f} \nabla_{II} \phi^i dA - \oint_C \phi^i \mathbf{m} ds \quad (9.22)$$

Here s is the arclength along C , the curve bounding ∂A_f , and \mathbf{m} is the unit tangent to the free surface ∂A_f along C that is normal to C . As in the two-dimensional case, equation (9.22) is substituted into (9.21), and (9.21) in turn into (9.17).

The system (9.17)–(9.19) – the formulation of choice when full Newton iteration is used (see Section 9.2.3 below) – singles out the kinematic BC as the ‘distinguished equation’ of change for the free-boundary location (other choices are

possible, as mentioned in Section 9.2.3). The kinematic condition is a hyperbolic equation and, hence, a Galerkin weighted residual of the form (9.19) can be unstable. However, in a system of partial differential equations, it is the type of the entire system and not the type of the individual equations that determines the numerical treatment required. Indeed, difficulties with the Galerkin formulation of the kinematic condition mostly arise at high capillary numbers, and are especially likely close to static and dynamic contact lines where spurious wiggles can totally destroy the solution. Kistler and Palmquist (1990) advocated an alternative formulation to (9.19) that insists explicitly on the net mass flux between neighboring nodes being zero. Where applicable, this approach completely eliminates wiggles. Soulaïmani *et al.* (1991) made use of a Petrov–Galerkin method to eliminate spurious free-surface wiggles. Likewise, Wambersie and Crochet (1992) tried to fight the wiggles with a streamline-upwinding/Petrov–Galerkin formulation (Brooks and Hughes 1982) for the kinematic BC.

System (9.17)–(9.19) is closed by suitable mesh generation equations to be introduced in Section 9.2.2 below (e.g., equation (9.27)). These equations determine the location of interior mesh nodes as well as the distribution of nodes along the boundary. The position of the boundary in the direction of its normal is, of course, determined by a distinguished equation that captures the physics of the problem, such as equation (9.19), or a parametric equation for the (solid) boundary shape.

Integrals in (9.17)–(9.19) and the mesh generation equations are usually evaluated by Gaussian quadrature. The final result is a system of differential and algebraic equations of index two (Petzold 1982); see also Section 9.2.9),

$$\mathbf{R}(t, \mathbf{y}, \dot{\mathbf{y}}) = \mathbf{0} \quad (9.23)$$

where $\mathbf{y} \equiv [u_i, v_i, p_j, x_l, y_l]^T$ is the vector of time-dependent coefficients, and $\dot{\mathbf{y}} \equiv dy/dt$ the vector of their time derivatives. Section 9.2.3 addresses methods for finding steady state solutions of the system (9.23); Section 9.2.9 discusses time stepping methods.

Penalty function formulation

In the penalty function formulation the equation

$$p = \lambda \nabla \cdot \mathbf{u} \quad (9.24)$$

replaces the continuity equation (e.g., Bercovier and Engelman (1980), Kheshgi and Scriven (1985)). Here λ is a large, empirically chosen number and p is an approximate pressure which approaches the exact pressure in the limit $\lambda \rightarrow \infty$. Exact incompressibility $\nabla \cdot \mathbf{u} = 0$ is only enforced in that limit. The penalty parameter must be chosen carefully: too small a value of λ results in inaccurate results; too high a value causes matrix conditioning problems. Kheshgi and Scriven (1985) suggested varying λ locally with element size to reduce rounding error, and were the first to tackle successfully free-surface flows with the penalty method. The most successful variant of the penalty method, though, is the Uzawa algorithm (see Fortin and Glowinski (1983)) which by-passes the difficulties of specifying a variable penalty parameter altogether. As an application of the augmented Lagrangian method, the algorithm includes iterative correction steps that ensure the continuity equation is satisfied to computer precision regardless of the value of the penalty parameter λ . Fortin and Fortin (1985) extended Uzawa's algorithm from Stokes' flow to the full Navier–Stokes system.

When equation (9.24) is used to eliminate pressure from the momentum equation before discretization, reduced (i.e. lower order) integration must be applied to the λ -dependent terms in the Jacobian matrix. Otherwise, the trivial solution (i.e. $\mathbf{u} = \mathbf{0}$) may be computed as λ becomes large. Reduced integration effectively lowers the order of pressure interpolation but does not satisfy the LBB condition. It is therefore subject to parasitic ‘pressure modes.’ In an alternative and preferable formulation, called the consistent or discrete penalty method, the Galerkin weighted residuals of the momentum equation (9.1) and penalty-continuity equation (9.24) are formed as usual, respecting the requirements on velocity and pressure interpolation – and therefore satisfying the LBB condition. The basis functions of choice

for pressure are discontinuous at inter-element boundaries so that (9.24), weighted with the pressure basis functions on each element, gives rise to algebraic equations that can be solved as an independent set. In this way, the discrete continuity and momentum equations are solved sequentially rather than simultaneously (see, for example, Kheshgi and Scriven (1985)).

Pressure Poisson equation (PPE) formulation

In the PPE formulation, an elliptic equation is derived for pressure by taking the divergence of the momentum equation (9.1) and using the time derivative of the continuity equation (9.3) to eliminate the divergence of the acceleration:

$$\nabla^2 p = St \nabla \cdot \mathbf{f} - \nabla \cdot (\mathbf{u} \cdot \nabla \mathbf{u}) \quad (9.25)$$

Equation (9.25) can replace the continuity equation to form, together with (9.1), a system that is equivalent to (9.1) and (9.3). The new system has index one (Petzold (1982), see also Section 9.2.9) and, hence, is easier to solve than (9.1) and (9.3). For the pressure Poisson equation (9.25) to be free of spurious solutions, however, the incompressibility condition must be satisfied on the domain and its boundary. The main advantage of the PPE formulation, however, is that it allows the separation of the velocity calculation from the pressure calculation and therefore makes possible the use of semi-implicit methods (Gresho 1991). The typical semi-implicit method uses an explicit treatment of the advection terms and an implicit one for the viscous term. The objective is to reduce the intense coupling between the two terms and thereby permit the sequential solution of smaller and linear systems for the individual velocity components, usually by iterative methods. Pressure, of course, is an inherently implicit variable and is obtained by solving the pressure Poisson equation (9.25). A long-standing controversy about the correct boundary condition for the pressure in (9.25) was resolved by Gresho and Sani (1987). That condition is the Neuman condition that results from forming the component of the momentum equation normal to the boundary.

In practice, the so called consistent pressure Poisson equation (CPPE) is preferred over direct discretization of equation (9.25) (Gresho 1991; Gresho and Sani 1987). This slightly different form is obtained from the discretized momentum equation and the time derivative of the discretized continuity equation. It ensures that the discrete velocity field is incompressible at the boundaries and the normal accelerations are zero at the walls, and allows the use of discontinuous pressure basis functions that satisfy the LBB condition (*cf.* discrete penalty method, above). Care must also be taken when using PPE formulations to ensure they satisfy the solvability conditions of the original $u-P$ formulation. Otherwise, spurious solutions can be obtained (Gresho 1991). For a recent application of the CPPE formulation to three-dimensional free-surface flow problems at high capillary numbers, see Wambersie and Crochet (1992).

9.2.2 FREE BOUNDARY PARAMETERIZATION AND MESH GENERATION

Most numerical methods for computational fluid dynamics discretize the governing equations on a mesh (grid) of nodes (points). Finite-element methods organize the nodes in a large number of small subdomains, or elements. For an accurate solution of free-surface problems like coating flows, so-called boundary-conforming meshes that deform in response to changes in free-boundary shape are particularly well suited. Element boundaries coincide with free surfaces and/or interfaces, and hence become computational entities that expressly and accurately track the position and shape of the free boundaries. In addition, curvilinear coordinate systems defined on the boundary-conforming elements greatly simplify the application of boundary conditions and the solution of the hosted set of partial equations. By mapping the curvilinear coordinates on a fixed rectangular grid, all computation can in effect be performed on rectangular coordinates regardless of the shape or movement of the physical boundaries.

The task of generating boundary-conforming

meshes for free surface flows can be divided into two steps. The first step is to parameterize the location of the nodes that reside on the free or moving boundaries; and the second is to calculate values of the nodal coordinates in the interior of the computational flow domain from the values at the boundaries. The goal is to keep in check the discretization errors in the solution of the hosted physical problem. Finite-element size is of course of main concern – especially in regions where increased resolution is demanded by the physics of the flow – but subdomain angles grossly deviating from orthogonality and rapid local changes of subdomain size can also cause significant discretization errors. There are two ways to generate meshes of acceptable orthogonality and smoothness: algebraic mesh generation, which interpolates the location of interior nodes from the boundary nodes with the aid of algebraic blending functions (Smith 1982; Thompson, Warsi and Mastin 1985); and differential (elliptic) mesh generation, which computes the mesh points by solving a system of partial differential equations for the mapping from the rectangular computational domain to the deformed physical domain.

9.2.2.1 Algebraic mesh generation

The simplest form of algebraic mesh generation for free-surface flows is based on one-dimensional parameterization of the physical coordinates of the boundary nodes. The earliest finite-element schemes for two-dimensional flows relied on a one-dimensional representation that simply saves the interface position as a discrete set of heights above the axis in a standard coordinate system, most often a Cartesian one, i.e., $y_i = h(x_i)$ (Nickell, Tanner and Caswell 1974; Zienkiewicz 1977; Frederiksen and Watt 1981). To handle highly curved menisci, Saito and Scriven (1981) and later Ungar and Brown (1985) combined Cartesian and polar representations. A more flexible one-dimensional free-boundary representation came with Ruschak's (1980) generator-line method in which the free surface is parameterized by its distance along straight lines from fixed boundary points (supports). The position of the boundary

supports and the orientation of the lines was arbitrary but had to be prescribed *a priori*. In the similar, but more flexible method of spines (Kistler and Scriven 1983, 1984), the boundary supports (base points) and line directions are not necessarily fixed but can be made to follow predicted, salient features of a free surface flow. The method of spines, originally developed for two-dimensional flows, has been generalized to handle three-dimensional coating flows (e.g., Katagiri (1992)) and extrusion flows (e.g., Karagiannis, Hrymak and Vlachopoulos (1988); Legat and Marchal (1992); Wambersie and Crochet (1992)).

In conjunction with one-dimensional free-surface parameterization, algebraic mesh generation typically relies on interpolation of the domain-internal nodal positions along a single direction, namely that of coordinate or generator lines which form two opposing element boundaries. Most often, simple algebraic proportions (e.g., Nickell, Tanner and Caswell (1974); Ruschak (1980); Kistler and Scriven (1983); Karagiannis, Hrymak and Vlachopoulos (1988)) or explicit algebraic mapping functions (e.g., Ettouney and Brown (1983); Ungar, Ramprasad and Brown (1988)) are used to place the nodes. In the so-called streamlined finite-element method, two element boundaries still consist of generator lines, but the other two are made to form streamlines (Papanastasiou, Macosko and Scriven 1985). This method is most useful for viscoelastic flows, especially those governed by integral constitutive equations (Papanastasiou, Scriven and Macosko 1987), but cannot be applied to flows with recirculation. The method is also well-suited for three-dimensional extrusion problems (e.g., Yokoi and Scriven (1989); Ellwood, Papanastasiou and Wilkes (1992)). Legat and Marchal (1992) devised an alternative scheme for three-dimensional extrusion problems that constrains only free-surface nodes to move along prescribed directions; the interior remeshing relies on a generalized but still linear algebraic rule to relate the interior node displacement via the Euclidian spacing to that of the boundary.

One-dimensional free-surface parameterization

and associated unidirectional algebraic mesh generation are computationally efficient, and have been widely used in solving coating flow problems. The methodology, however, is easily applied only for strip-like domains such as those encountered in extrusion, thin-film flows, and simple bead-coating flows like curtain or slide coating. Non-strip-like domains require tedious patching of several boundary representations, and may necessitate multidirectional algebraic interpolation. Even for strip-like domains, simple algebraic generator lines require some *a priori* knowledge of the solution and a large number of input data. For large deformations, moreover, they are prone to yield excessive mesh distortions, intersect within the flow domain, or cause multivalued free-surface representation (e.g., Christodoulou and Scriven (1989)). To avoid such problems, skillful user interaction is often needed as time evolves or parameters vary during a simulation.

Kistler and Palmquist (1990) advanced a generalized algebraic mesh generation scheme that liberates free-boundary parameterization from the limitations inherent to generator lines and, hence, can tackle two-dimensional free-surface flows of great complexity and track large deformations with much less user interaction than earlier algebraic schemes. The scheme permits the flow region of interest to be divided into quadrilateral subregions or macro-elements of arbitrary connectivity. The edges of each macro-element can be made into ‘free boundaries’ – some physical boundaries such as free surfaces, interfaces, deformable elastic members, etc., and others merely auxiliary internal boundaries. The position of the nodes along these edges is parameterized by their two Cartesian coordinates. One is determined from a ‘distinguished’ boundary condition as in conventional, one-dimensional free-boundary parameterization schemes. The other is calculated from an additional, user-selected or adaptive constraint that controls the spacing between boundary nodes. Key to the flexibility and adaptability of the method are the extra conditions that control the position of the vertices of the macro-elements. These conditions can be

chosen so as to make the mesh automatically follow essential features of the flow. They can even be designed so as to allow algebraic mesh generation to replicate many essential characteristics of elliptic mesh generation. Figure 9.3 illustrates, for the case of heel formation in curtain coating (see also Chapter 11c), the ability of the generalized algebraic scheme to track dramatic changes in flow geometry. Figure 9.4 demonstrates the same capability for the formation of a rolling inflow bank in forward kiss coating (see also Chapters 12a and 12c), which involves not only free surfaces but also deformable substrates. Figure 9.3, however, also reveals some of the shortcomings of algebraic mesh generation – and most other deforming mesh schemes – namely the need to deploy a mesh with a predetermined structure based on some *a priori* knowledge of the flow geometry, the necessity to change some mesh control parameters as

significant changes in flow geometry occur, and the ultimate failure of a mesh with a given topology to follow extreme distortions in flow geometry.

In the version presented by Kistler and Palmquist (1990), the generalized algebraic procedure was restricted to at most two free boundaries along opposing edges of each macro-element, and relied on unidirectional interpolation to distribute internal nodes between those two boundaries. However, the procedure can readily be augmented to accommodate four free boundaries per macro-element and to employ multi-directional algebraic interpolation. A widely used form of the latter is the so called transfinite interpolation (Gordon and Hall 1973). It applies a unidirectional interpolation in each direction and then adds a correction term for the corners. When the coefficients in algebraic blending functions are made to depend not only on the

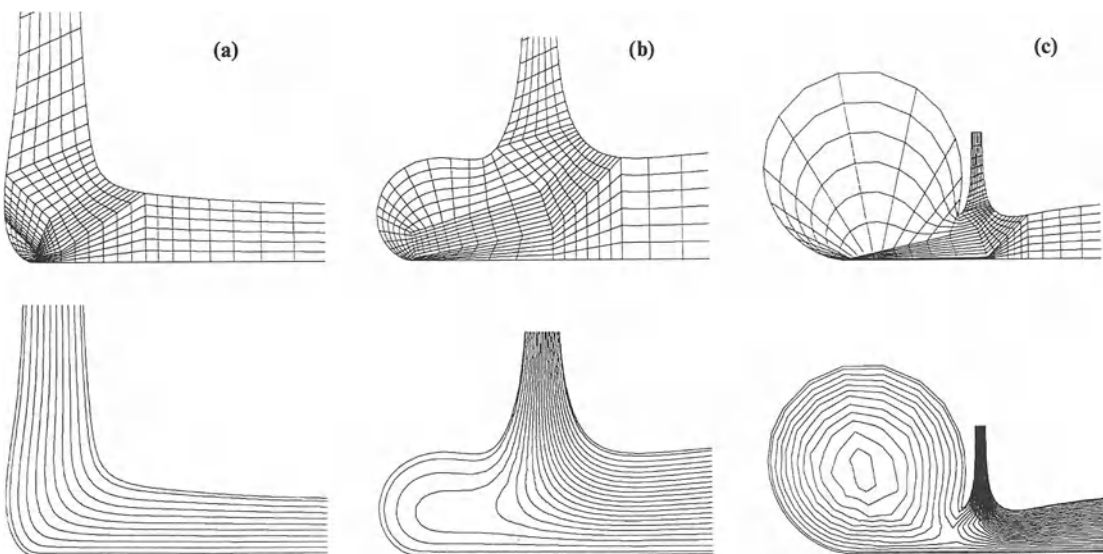


Figure 9.3 Finite-element meshes and associated flow fields for impingement flow in curtain coating, generated by the algebraic technique of Kistler and Palmquist (1990): (a) $U/V = 1.0$, where U is the coating speed and V is the vertical impingement speed; (b) $U/V = 0.25$; (c) $U/V = 0.15$ ($Re \equiv \rho Q/\mu = 2.5$, where ρ is the liquid density, Q the volumetric flow rate per unit coating width, and μ the liquid viscosity; $Ca \equiv \mu V/\sigma = 10$, where σ is the surface tension; note that the three sets of figures are not drawn to the same scale).

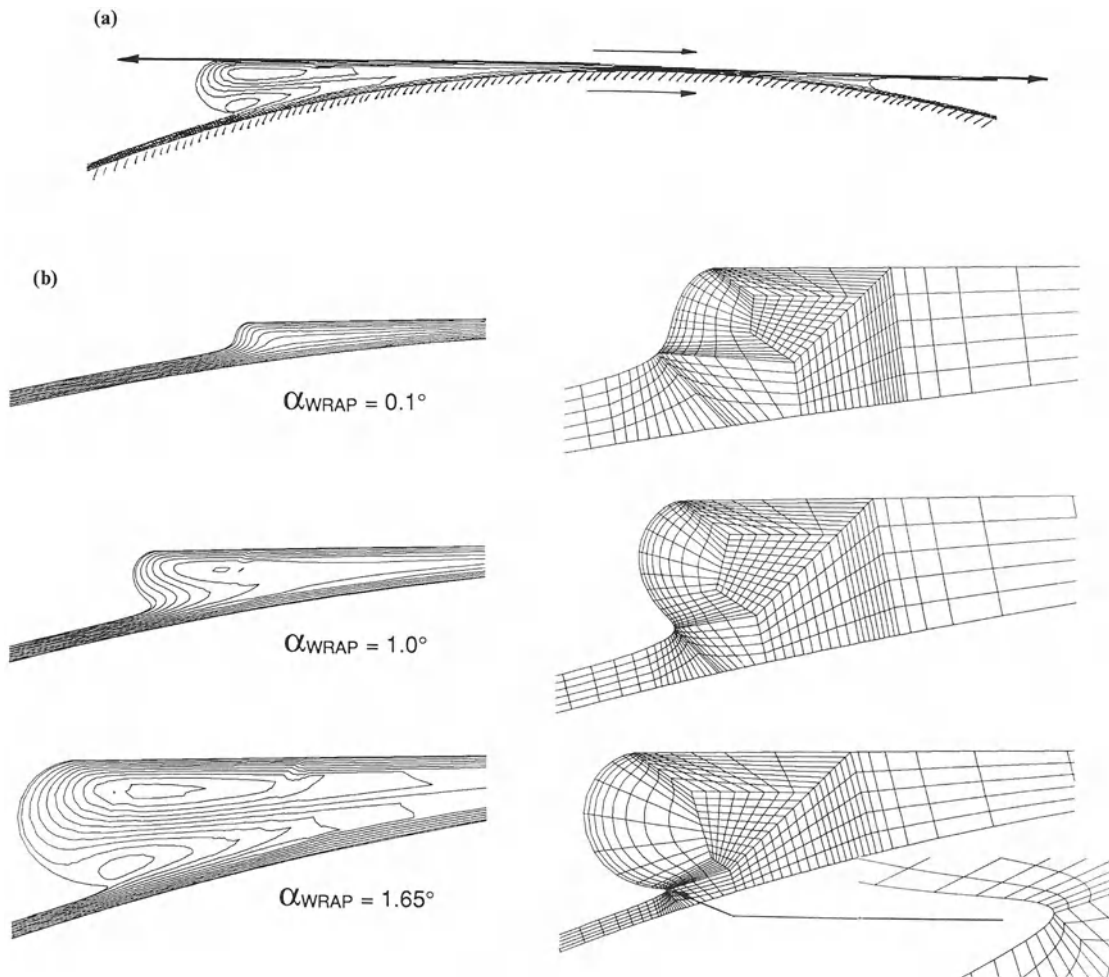


Figure 9.4 Finite-element meshes and associated flow fields for the inlet zone of forward kiss coating, generated by the algebraic technique of Kistler and Palmquist (1990): (a) overview of flow configuration; (b) details of the inlet zone as a function of the angle of wrap of the tensioned web around the coating roller (for purposes of clarity, the mesh plots on the right-hand side are not drawn to scale). $Re \equiv \rho Q / \mu = \rho U H_0 / \mu = 3.0$, $Ca \equiv \mu U / \sigma = 10$, $H_0 / R = 0.006$, $E \delta^3 / [12(1 - v^2) \mu U H_0^2] = 1.11$, $T / \mu U = 20000$, where H_0 is the coming film thickness, R is the roller radius, E is Young's modulus, δ is the substrate thickness, v is Poisson's ratio, and T is the tension in the substrate per unit width.

physical coordinates of the boundaries but also their derivatives, algebraic mesh generation can even ensure orthogonality of the elements at the boundaries (e.g., Smith (1982)). To date, however, no applications of such methods to free-boundary problems have been reported.

9.2.2.2 Elliptic mesh generation

Differential elliptic mesh generation locates the mesh points by solving a system of partial differential equations for the mapping from the computational to the physical domain. Compared

with algebraic techniques, it is usually more expensive but it provides inherent smoothness of the mesh, less danger of singularity and automatic local control of mesh properties.

A variety of elliptic mesh generation methods have been reviewed by Thompson and co-workers (1982, 1985) who focused on two-dimensional flows – like the discussion that follows here. The simplest method locates two-dimensional meshes by solving a pair of Laplace equations for the ξ and η coordinates, $\nabla^2 \xi = 0$ and $\nabla^2 \eta = 0$ (Winslow 1967). This system satisfies an extremum principle in the physical space and, hence, precludes overlapping coordinate lines. Other methods solve a Poisson system $\nabla^2 \xi = P(\xi, \eta)$ and $\nabla^2 \eta = Q(\xi, \eta)$, where P and Q are specified spacing control functions (e.g., Thompson, Thomas and Mastin (1974); Thomas and Middlecoff (1980); Thomas (1982)). Applications to water-wave problems have been reported by Shanks and Thompson (1977), Haussling (1982), Aston and Thomas (1982), and to mold-filling flows by Subbiah, Trafford and Gücéri (1989). A disadvantage of the Poisson-generated meshes is lack of control of orthogonality in the interior, particularly when the physical region is curved or patched. Orthogonal meshes, generated by stretching of conformal ones (e.g., Potter and Tuttle (1973); Eiseman (1982); Ryskin and Leal (1983)), overcome this difficulty but are not suitable for highly distorted domains. Behrens *et al.* (1987) generated meshes for mold filling flows by using the system $\nabla_{\xi,\eta}^2 x = 0$ and $\nabla_{\xi,\eta}^2 y = 0$. This and related systems do not satisfy any extremum principles in the physical space and, therefore, pose the danger of coordinate lines overlapping in general configurations (see Thompson, Warsi and Mastin (1985), p. 205).

Mesh generation can be viewed as an optimization (variational) problem for the mapping that minimizes the discretization error in the numerical solution of the physical problem. The discretization error is generally formidable to evaluate, however. The usual approach is to employ simple error indicators tailored after the error in the first spatial derivative of a dependent

variable. The most widely accepted of such error indicators quantify the smoothness, orthogonality and concentration of the mesh. Brackbill and Saltzman (1982a, 1982b) proposed the functional

$$\begin{aligned} & \iint [(\nabla \xi)^2 + (\nabla \eta)^2] dx dy \\ & \quad \text{smoothness} \\ & + \lambda_0 \iint [\nabla \xi \cdot \nabla \eta]^2 J^3 dx dy \\ & \quad \text{orthogonality} \\ & + \lambda_w \iint w J dx dy \quad (9.26) \\ & \quad \text{node spacing} \end{aligned}$$

Here $J \equiv x_\xi y_\eta - x_\eta y_\xi$ is the Jacobian of the mapping from the physical to the computational domain. The mesh results from solving a pair of second-order, quasi-linear partial differential equations that are the Euler equations of the problem of minimization of (9.26). The three functionals in (9.26), however, are dimensionally inhomogeneous and, as a consequence, the Euler equations can change type and become ill-posed. This was pointed out by Kreis, Thamnes and Hassan (1986), who addressed the problem by rescaling the weights λ_0 and λ_w . Christodoulou and Scriven (1992) chose an orthogonality functional that scales with smoothness and has the same functional form as in the discretization error (Thompson, Warsi and Mastin 1985). The resulting mesh generating system is

$$\begin{aligned} & \nabla \cdot \{(\sqrt{[(x_\xi^2 + y_\xi^2)/(x_\eta^2 + y_\eta^2)]} + \varepsilon_s) \nabla \xi\} \\ & - \frac{\varepsilon_1}{J} \frac{\partial}{\partial \xi} \ln [(x_\xi^2 + y_\xi^2) f(\xi)] = 0 \\ & \quad (9.27) \end{aligned}$$

$$\begin{aligned} & \nabla \cdot \{(\sqrt{[(x_\eta^2 + y_\eta^2)/(x_\xi^2 + y_\xi^2)]} + \varepsilon_s) \nabla \eta\} \\ & - \frac{\varepsilon_2}{J} \frac{\partial}{\partial \eta} \ln [(x_\eta^2 + y_\eta^2) g(\eta)] = 0 \end{aligned}$$

Here $f(\xi)$ and $g(\eta)$ are manually set stretching functions that control the concentration of nodal

points and ε_1 and ε_2 are their weights; ε_s weighs the smoothness of the mesh. The most important advantage of the system (9.27) over Brackbill and Saltzman's equation (9.26) is that the resulting meshes are nearly orthogonal, even for patched domains of the sort often needed for coating flow simulations.

With sub-parametric mapping in the interior of the mesh, i.e. straight-sided elements, elliptic mesh generation is only about 10% more expensive than spine parameterization, as was first demonstrated by Christodoulou and Scriven (1992). As an added bonus, the nonlinearity of the Jacobian of the mapping from the physical to the computational domain is less severe, and with it the nonlinearity of the weighted residuals (9.17) and (9.18), resulting in improved accuracy of the numerical integration. Sub-parametric mapping can equally well be applied to algebraic mesh generation for improved accuracy, but there is no cost advantage because the number of nodal position unknowns remains the same. Sub-parametric mapping is an example of a more general and attractive two-level strategy: a coarse elliptically generated mesh of macro-elements with well-controlled orthogonality; and a finer mesh within each macro-element, efficiently generated with algebraic techniques (see also Morice (1983)).

Figure 9.5a illustrates sequences of steady states of slide-coating flow, with meshes generated by Christodoulou and Scriven's (1992) method. Figure 9.5b illustrates how a single mesh topology can successfully capture either liquid bridges that pin at the sharp die edge or ones that wet the underside of the die lip. By virtue of the degrees of freedom of every node in the mesh, elliptic mesh generation is particularly well-suited for design and shape optimization problems.

Tsiveriotis and Brown (1992, 1993) adopted Christodoulou and Scriven's (1992) method to highly deformed interfaces in solidification problems, but failed to generate suitable grids because of a sign error in the control parameters ε_1 and ε_2 which, for small ε_s , resulted in an ill-posed system. They still managed to get solutions by discarding the concentration terms

and replacing the η -equation with a Poisson equation. The resulting method, called the mixed-mapping method (MMM), is similar to the two-step procedure of Visbal and Knight (1982). Because the generating system is anisotropic, its application to more complex geometries with free surfaces that conform to both coordinate directions is difficult. A more general modification was proposed by de Santos (1991), who employed a concentration functional based on equidistribution of a weight function in each coordinate direction. According to the experience of one of us (KNC), de Santos' method shares a disadvantage with other methods based on Laplace's equations in that it cannot achieve the desired distribution close to highly curved boundaries (Thompson, Warsi and Mastin 1985, p. 192).

Elliptic mesh generation can be refined to become adaptive, i.e. automatically to place nodal points where accurate resolving of the flow is most important. With (9.27), adaptive meshes can be generated by making the control functions $f(\xi)$ and $g(\eta)$ depend on critical features, such as directional derivatives of the flow field or curvature of free surfaces. An alternative is to add to the mesh generating system a concentration functional (e.g., Brackbill and Saltzman (1982a, 1982b); Demkowicz and Oden (1986); de Santos (1991)). Saeger, Davis and Scriven (1990) proposed a generalization of (9.27) to three dimensions and applied it to generate finite-element meshes of three-dimensional elemental structures for self-assembling surfactant systems. Contrary to the two-dimensional case, orthogonality in three dimensions is a strong constraint (no infinity of solutions). For that reason, the system of Saeger, Davis and Scriven (1990) had to make compromises between smoothness, orthogonality and adaptivity. Adaptivity functions based on estimates of the solution curvature proved to be more robust than functions relying on magnitudes of the raw (i.e. unweighted) residuals. Attempts by one of us (KNC) to apply similar adaptive-mesh strategies to coating flows were encouraging only for problems without singularities. More research is needed to identify effective indicators of solution

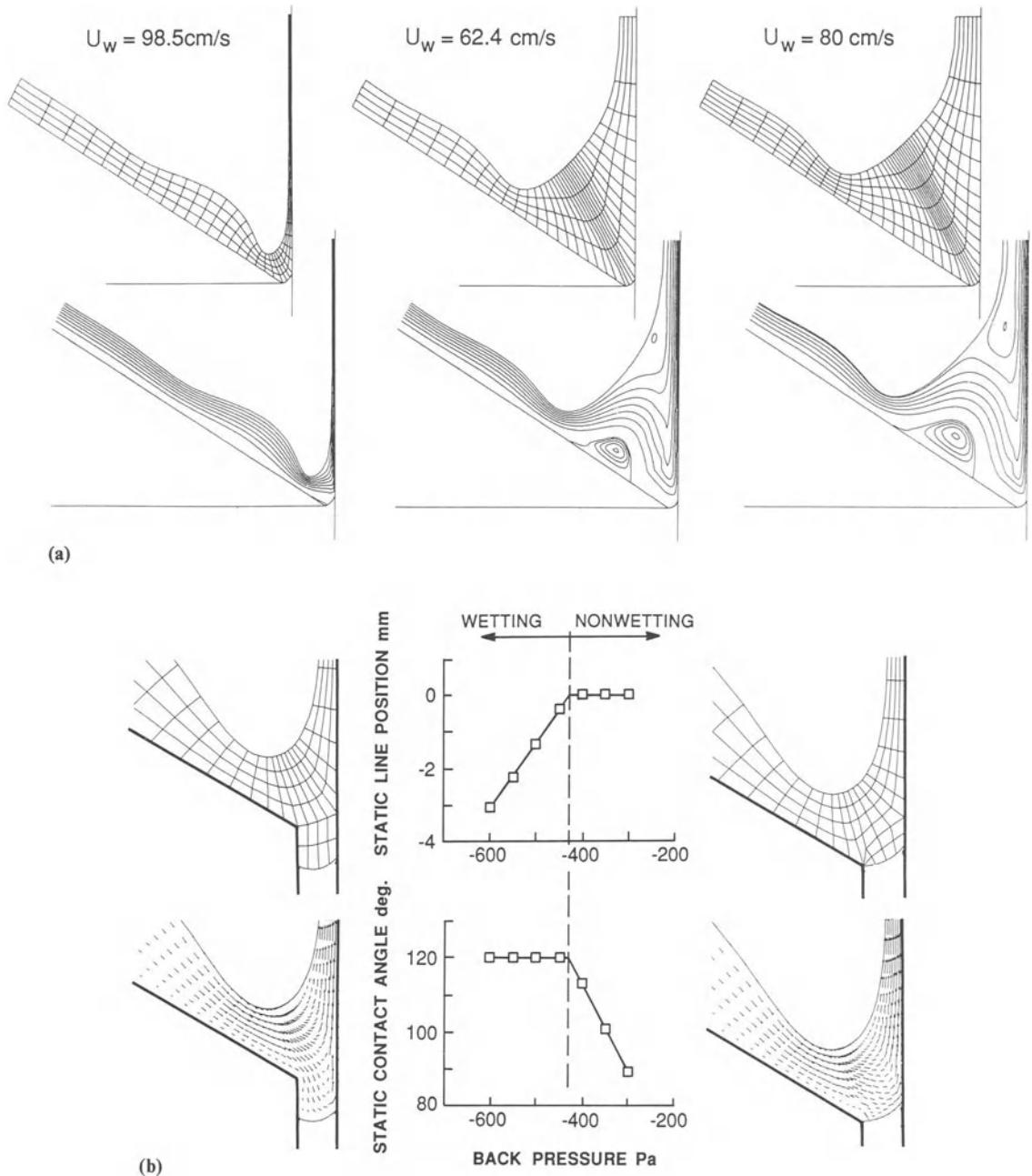


Figure 9.5 Finite-element meshes and associated flow fields for slide-coating, generated by the elliptic technique of Christodoulou and Scriven (1992). (a) Sequence of steady states for different web speeds (pressure difference $\Delta P = -161 \text{ Pa}$, coating gap $H_{\text{GAP}} = 0.347 \text{ mm}$, liquid viscosity $\mu = 8.717 \text{ mPa s}$, liquid density $\rho = 1130 \text{ kg/m}^3$, surface tension $\sigma = 70.1 \text{ mN/m}$, imposed dynamic contact angle $\theta_D = 160^\circ$, slide inclination 30°); the last state is past a turning point – see Fig. 9.7. (b) Lip wetting versus non-wetting states (same parameters as in (a), except that $U_w = 1.67 \text{ m/s}$ and the pressure difference ΔP varies).

error in patched meshes, especially when static or dynamic contact lines are part of the flow.

Unfortunately, elliptic mesh generation in its current form places restrictions on grid structure. In fact, both algebraic and elliptic mesh motion strategies require structured meshes on some level, with unstructured aspects arising only in the domain decomposition, e.g., into macro-elements, as in the Kistler and Palmquist (1990) scheme. As for the elliptic mesh generation approach, once the conceptual hurdle is made to placing mesh points onto the reference domain without restricting the grid structure to lie upon constant coordinate surfaces, unstructured grids can probably be accommodated. Sackinger *et al.* (1996) have recently proposed a natural follow-on that removes all restrictions on grid structure, and hence can take advantage of automatic mesh generators. Their approach is to employ the differential equations governing the displacements of an elastic solid deforming in a Lagrangian fashion. The distinguished conditions (e.g., the kinematic boundary condition, equation (9.19)) are apportioned to boundary loads on the pseudo-solid and are satisfied when the solid reaches static equilibrium. Sackinger *et al.* have demonstrated the pseudo-solid mesh motion technique for several coating problems and have found that unstructured grids allow for efficient refinement around static and dynamic contact lines and greatly reduced user-interaction time. Essentially, for the particular case of a reversible elastic deformation, the pseudo-solid approach is equivalent to using elliptic mesh generation equations to perform a mapping with the condition of minimizing a strain energy functional.

Trial method

In two-dimensional viscous free-surface flows like coating flows, the traction condition (9.5) and the kinematic boundary condition (9.4) furnish three scalar boundary conditions, one more than would be required to solve the Navier–Stokes equations on a fixed domain. The third boundary condition – sometimes referred to as the distinguished condition – is necessary to determine the unknown position of the free surface. That is, if one of the free boundary conditions is neglected, the governing system can be solved on a fixed domain. This is the principle of the trial method, common in the earliest finite-element schemes for viscous free-surface flows (e.g., Nickell, Tanner and Caswell (1974)).

The trial method assigns, at each iteration step, a fixed shape to the free surface and computes the flow field, ignoring the distinguished boundary condition. Next, that boundary condition, along with the current estimate of the flow field, is used to update the free surface location, and the cycle is repeated to convergence. The key advantages of this method – a special case of fixed point iteration (also known as Picard iteration, successive substitution, or functional iteration: see Isaacson and Keller (1966) and Ortega and Rheinboldt (1970)) – are its simplicity and, compared with the methods discussed below, its large radius of convergence. Its main drawback is the slow, linear rate of convergence inherent in fixed-point iteration. Worse, the method may fail to converge altogether depending on the choice of the boundary condition used to update the free surface and the value of the capillary number. Silliman and Scriven (1980) showed that at low capillary numbers the normal-stress scheme converges whereas the kinematic scheme does not, and conversely at high capillary numbers. At intermediate capillary numbers, i.e. $Ca = O(1)$, which are quite often of most practical interest, there is a range where both schemes converge but do so slowly and sometimes only with the aid of artful under-relaxation. Wambersie and Crochet (1992) recently applied the trial method to three-dimensional extrusion flows, extending the

9.2.3 STEADY-STATE SOLUTIONS

9.2.3.1 Iteration procedures

The discretized system of equations (9.17)–(9.19) combined with, for instance, the mesh generation equations (9.27) is severely nonlinear. Finding steady-state solutions therefore requires iteration.

decoupling algorithm of Gresho and Chan (1990) and relying on a pseudo-transient approach to reach the desired steady state. They only considered cases with $Ca \geq O(1)$ and chose the kinematic equation as the distinguished condition. This choice is consistent with Silliman's findings and, as expected, their method converges.

Newton's method

The tedious iteration between the flow-field calculation and free-surface update can be avoided by simultaneously solving all the equations, including equations for the position of the nodes on the free surface and, if applicable, additional nodes in the interior. Newton's method (e.g., Isaacson and Keller (1966); Ortega and Rheinboldt (1970)) linearizes the complete equation set (9.23) around the current estimate of the solution, \mathbf{y}^k , to yield

$$\frac{\partial \mathbf{R}}{\partial \mathbf{y}}(\mathbf{y}^k) \Delta \mathbf{y} = -\mathbf{R}(\mathbf{y}^k) \quad (9.28)$$

and adds the solution $\Delta \mathbf{y} = [\mathbf{y}^{k+1} - \mathbf{y}^k]$ of the resulting linear system to the current estimate \mathbf{y}^k in order to provide an updated estimate of the flow field, including the position of the free surface(s). The iteration is repeated until convergence. The structure of the Jacobian matrix $\partial \mathbf{R} / \partial \mathbf{y}$, with many of its entries related to free surface unknowns, has been described in detail by Kistler and Scriven (1984). Their description is readily generalized to elliptic mesh generation schemes (Christodoulou and Scriven 1992).

In contrast to the trial method, Newton's method has superb convergence properties. In fact, it converges quadratically and, hence, requires only four or five iterations in most cases, the number being independent of the flow parameters (Ruschak 1980; Saito and Scriven 1981). Besides, the Jacobian $\partial \mathbf{R} / \partial \mathbf{y}$ of the converged solution contains invaluable information for parameter continuation (Section 9.2.4), stability analysis to transient disturbances (Section 9.2.5), direct tracking of critical points (Section 9.2.7), and sensitivity analysis to ongoing disturbances (Section 9.2.8).

The main disadvantage of full Newton iteration is that the Jacobian matrix as well as its decomposition into an upper and lower triangular matrix needed for Gauss elimination (so called LU-decomposition; see Section 9.2.3.2 below) must be recomputed at every iteration. The computational cost can be reduced considerably, however, by quasi-Newton methods (Engelman and Sani 1983). For simple algebraic mesh generation schemes, another disadvantage of Newton's method and its modified versions is that the variations of the residuals with respect to all free surface degrees of freedom involve integrals that span a large portion of the domain. This non-local structure drastically increases the band-width of the Jacobian matrix and, thereby, precludes the use of standard finite-element codes, in which an equation associated with a nodal point receives contributions only from neighboring elements. A further difficulty in applying Newton's method arises from the complicated manner by which the free-surface unknowns enter the discretized equations (see Kistler and Scriven (1984)). In fact, computing and coding the variations with respect to free boundary unknowns analytically can be a tedious programming challenge. Even small errors in a single entry to the Jacobian matrix can severely hamper the overall rate of convergence. For the same reason, on the other hand, the rate of convergence becomes a useful test of the correctness of the code that computes the residual and Jacobian entries.

There are three alternatives to analytically deriving and manually programming the Jacobian matrix. The first is to compute its entries by numerical differentiation of the finite-element residuals. Caution is in order, however, in estimating a suitable step size so as to manage properly the trade-off between approximation error and round-off error. The second alternative is to calculate the analytical Jacobian by using a symbolic manipulator such as MACSYMA (Pavelle and Wang 1985). The resulting computer code can be made efficient by optimizing compilers that recognize and remember repeatedly occurring sub-expressions. The third alternative is to leave

the differentiation to a preprocessor or compiler that uses the newly arising techniques of automatic differentiation (e.g., Griewank and Corliss (1992)).

Total linearization method (TLM)

In contrast to Newton's method, which linearizes the discretized equation set, the TLM linearizes the continuous weak form before discretization – as first done by Dupret (1982) – and then simplifies the linearized form by means of the free-surface boundary conditions (see Kruyt *et al.* (1988) for details). As a result, the influence of the unknown position of the free surface(s) is confined to boundary integrals, and hence the TLM is readily incorporated into standard finite-element codes for fixed domains. To do so, the distance of the next approximation of a free surface from the current one is made an additional unknown function, and is expanded into one-dimensional finite-element basis functions. The distance is usually measured along the normal to the current estimate of a free surface, although other definitions can be used, for instance spines. In principle, the TLM is much easier to implement than Newton's method while retaining a super-linear rate of convergence. However, only limited evidence for its effectiveness is available to date (Kruyt *et al.* 1988; Cuvelier and Schulkes 1990). In particular, its advantages in conjunction with elliptic mesh generators are not clear; and its applicability to stability analysis has not been explored.

9.2.3.2 Solution of linear equations

All the solution algorithms introduced above produce one or more matrix equations of the form $\mathbf{Ax} = \mathbf{b}$ that have to be solved at each iteration. The matrix \mathbf{A} is usually large (5 to 50 thousand or more), sparse, banded and unsymmetric.

Direct matrix solvers

In most conventional algorithms, a direct method is used to find the solution in three distinct steps:

- (1) Gauss elimination with or without pivoting to generate the LU factorization of \mathbf{A} , where \mathbf{L} is a lower triangular and \mathbf{U} an upper triangular matrix;
- (2) forward reduction of the vector \mathbf{b} , i.e. solution of the system $\mathbf{Lz} = \mathbf{b}$, which can be performed at the same time as the LU factorization;
- and (3) back-substitution, i.e. solution of $\mathbf{Ux} = \mathbf{z}$.

As \mathbf{A} is sparse, a reduced storage mode such as the skyline method (see Hasbani and Engelman (1979)) can be used. The main drawback of this method is that no pivoting can be performed. This limits accuracy and stability, especially close to singular points of the nonlinear system.

A class of more robust and widely used Gauss-elimination methods for the solution of sparse linear systems resulting from finite-element discretization is that of frontal solvers, first applied to unsymmetric matrices by Hood (1976, 1977). Frontal solvers rely on the fact that Gauss elimination of a variable can commence immediately after its last appearance during the process of assembling the discretized equations, i.e. before assembly of all the residuals and Jacobian entries is complete. LU factorization can thus be confined to a small subset of equations associated with nodes on a 'front' that propagates through the mesh as Gauss elimination proceeds. For enhanced stability, the frontal method can be combined with full, partial or threshold pivoting among a set of fully assembled equations that are carried along with the front. Reid (1981) reviewed such algorithms, including element reordering methods to minimize front width and sub-structuring techniques leading to multi-frontal algorithms. More recent work has focused on enhancing performance on specific computer architectures, e.g. Duff (1984), Duff, Erisman and Reid (1986) and Benner (private communications 1984, 1985). Habashi, Nguyen and Bhat (1991) suggested that frontal-like methods optimized for vector-parallel processing on CRAY supercomputers are superior to other sparse-matrix solution algorithms.

Quite often, there is a need to augment the system of partial differential equations with one or more global (or dense) constraint equations. A prominent example comes from pseudo-arc-length continuation (see Section 9.2.4 below).

Global equations destroy the bandedness of the coefficient matrix, making standard sparse techniques inapplicable. Thomas and Brown (1987) proposed a modification of the frontal solver to cope with added global constraints in finite-element equation systems. In our experience, a much simpler yet equally efficient alternative is to assign the global constraints to an extraneous node that belongs to every element in the mesh. The global constraint equations become complete only after the assembly of the last element in the mesh and are therefore carried in the front throughout the elimination.

The number of operations required for the most efficient direct solution of a banded linear system increases as the square of the bandwidth and as a linear function of the number of equations. The resulting computational cost is tolerable for most two-dimensional flows, and direct solvers have been found adequate for such applications. However, the cost usually becomes unacceptably high for realistic 3D problems with their inherently much larger bandwidths. Increasing user demands for fully 3D simulations has stimulated a resurgent search for methods whose computational expense grows at a slower rate than direct solution. Currently emerging iterative techniques may be able to deliver the needed break-through.

Iterative matrix solvers

The key idea behind iterative solvers is to compute a sequence of approximate solutions by means of simple and hence computationally efficient matrix operations, starting from an initial guess and ultimately converging to the exact solution (for a fairly recent review, see Engelman and Hasbani (1990)). The main advantage is that the computational expense is independent of the matrix bandwidth. Moreover, many implementations require only the product of the coefficient matrix and a vector, rather than the coefficient matrix itself. The main drawback of iterative methods, on the other hand, is the strong dependence of their performance on

properties of the coefficient matrix (e.g., symmetry, positive definiteness, sparseness).

For symmetric coefficient matrices, successful iterative techniques are well established. Most popular is the conjugate gradient (CG) method, actually a semi-iterative method. It is based on minimization of a certain error norm and is closely related to the Lanczos method for tri-diagonalizing a matrix. An attractive feature of the CG method is that it requires no estimation of parameters. The conjugate residual method (CR) is quite similar, differing mainly in the error functional used.

For unsymmetric systems, the most successful class of iterative methods is that of preconditioned polynomial iterative methods, with two important subclasses: Chebychev-like methods and conjugate-gradient-like methods. Chebychev methods (Manteuffel 1977) rely on minimax polynomials and require *a priori* or adaptive estimates of the eigenvalue spectrum of the coefficient matrix. Moreover, their iteration parameters are independent of the initial guess and so there is no benefit from a good initial guess. Chebychev methods are not suitable when the spectrum of the coefficient matrix includes the origin. Conjugate-gradient-like methods generalize the CG method to unsymmetric matrices. The most popular class uses projection methods onto special Krylov sub-spaces. The most noteworthy among these, in turn, are conjugate gradient squared techniques (Sonneveld 1989) and the stabilized bi-conjugate gradient methods (Van der Vorst 1992), which are similar to CG but use different residual norms; and generalized minimum residual techniques (Saad and Schulz 1986), which create an orthogonal sub-space of specified size with Gram–Schmidt orthogonalization. The last are often considered to be the most robust, but Howard, Connolley and Rollet (1990) found that, for flow problems, bi-conjugate gradient and conjugate-gradient squared methods work better.

Preconditioning, i.e. pre-multiplying the matrix equation by a conditioning matrix, is often essential to achieving tolerable convergence rates with iterative matrix solvers. The intent is to

reduce the condition number (or the spread of the spectrum) of the resulting linear system. The preconditioning matrix should be sparse, easy to compute, and easy to invert. Commonly used strategies include incomplete factorization methods based on classical matrix splitting such as Jacobi (diagonal scaling), Gauss–Seidel or successive overrelaxation (SOR), and incomplete LU decompositions (see Jackson and Robinson (1985)). Multigrid methods (see Brandt (1977) and Sonneveld, Weissling and de Zeeuw (1985)) may also be viewed as a special form of preconditioning.

With the exception of a few isolated cases (e.g., Einset and Jensen (1992); Carey, Wang and Joubert (1989); Howard, Connolley and Rollet (1990)), even the most robust iterative methods perform poorly at the core of Newton or Picard procedures for solving fully coupled Navier–Stokes problems. In particular, the matrix systems resulting from the mixed velocity–pressure (\mathbf{u} – P) formulation are indefinite and poorly conditioned (Engelman and Hasbani 1990), often causing convergence that is erratic and distressingly slow. Achieving robust convergence properties for general Navier–Stokes problems remains one of the outstanding challenges in numerical analysis.

At present, the key to successful application of iterative methods to incompressible Navier–Stokes problems comes from highly specialized matrix preconditioners that depend on detailed knowledge of the matrix structure (e.g., Einset and Jensen (1992)). Resorting to transient analysis is another way to overcome poor performance of iterative solvers (see for example Mittal and Tezduyar (1992); Strigberger *et al.* (1993)). The idea is to take advantage of iterative solvers thriving on a good initial guess – which transient analysis with small enough a time increment delivers at each time step. Also, the smaller the time step the more diagonally dominant the matrix system, because the time derivatives occur on or near the diagonals. For this strategy to be effective, of course, one has to avoid solving the continuity equation which lacks time derivatives, for instance by solving the pressure Poisson equation (PPE) instead (see Section 9.2.1). This

is the basis of a noteworthy finite-element solution technique called the segregated solver approach (e.g., Haroutunian, Engelman and Hasbani (1993)), which first treats the convective terms explicitly to make the equations linear, then uses the consistent PPE formulation to decouple pressure from velocity, and finally solves the pressure equation and each individual component of the momentum equations separately and successively by iterative techniques.

9.2.4 INITIALIZATION AND PARAMETER CONTINUATION PROCEDURES – SOLUTION FAMILIES

9.2.4.1 Standard continuation

Newton's method and its variants are currently preferred for computing coating flows. Their superior rate of convergence, however, can only be realized in a small neighborhood of an isolated solution, called the basin of attraction. The boundary of the basin of attraction has a very complex structure and is often of fractal dimension (Peitgen and Pruefer 1984). Outside the basin, usually characterized by the radius of its inscribing (hyper)-circle called the radius of convergence, the iteration diverges or oscillates indefinitely. For that reason, Newton-like methods are preferably used in combination with a continuation technique which produces an initial estimate from one or more known solutions at nearby parameter sets.

The most popular continuation technique is first-order or Euler–Newton continuation (Keller 1977). Given a solution $\mathbf{y}_0 \equiv \mathbf{y}(P_0)$ of the governing equations at a parameter value P_0 , an approximation of the solution at a nearby parameter value $P_0 + \delta P$ is predicted along the tangent vector to the solution branch at \mathbf{y}_0 from

$$\mathbf{y}_0(P_0 + \delta P) = \mathbf{y}(P_0) + \frac{\partial \mathbf{y}}{\partial P} \delta P \quad (9.29)$$

The derivative $\partial \mathbf{y} / \partial P$ is calculated from the solution of the linear system

$$\frac{\partial \mathbf{R}}{\partial \mathbf{y}}(\mathbf{y}(P_0), P_0) \frac{\partial \mathbf{y}}{\partial P} = -\frac{\partial \mathbf{R}}{\partial P} \quad (9.30)$$

Here $\partial\mathbf{R}/\partial\mathbf{y}(\mathbf{y}(P_0), P_0)$ is the Jacobian matrix at \mathbf{y}_0 , whose LU decomposition is already available from the preceding Newton iteration. Therefore, the additional cost of continuation amounts only to one re-solution (i.e. solution of two triangular systems) with the different right-hand side $-\partial\mathbf{R}/\partial P$.

Another popular continuation technique, applicable when converged solutions at more than one point along a solution branch are available, uses an interpolation polynomial through these points to produce a good estimate for the solution at a new point (e.g., Jackson and Winters (1984)). Usually only two or three previous points are used because higher-order interpolation polynomials tend to become oscillatory and eventually unstable. Sophisticated methods for selecting the parameter step-size along the solution branch have been proposed by Heijer and Rheinboldt (1981) and Rheinboldt and Burkardt (1983), for example. Often, however, simple heuristic strategies suffice, for instance doubling or halving the step size depending on the convergence history (e.g., Jackson (1987)). Similar techniques can be used to adjust the time-step size in integration of the transient equations, with additional controls for the time truncation error (see Section 9.2.9).

9.2.4.2 Continuation around singular points

Newton's method is guaranteed to converge provided that the initial guess for \mathbf{y} is sufficiently close to the solution and the Jacobian matrix is nonsingular. Convergence becomes difficult or impossible, however, close to points where the Jacobian matrix becomes singular. Prime examples are turning points where a solution branch turns back on itself, or bifurcation points where one solution branch meets with another; see Fig. 9.6. So called Hopf points that mark the onset of spontaneous oscillations usually cause no convergence problems because the Jacobian is nonsingular there.

First-order continuation can still be used to step over bifurcation points (Keller 1977) but fails at turning points. Quadratic or higher order

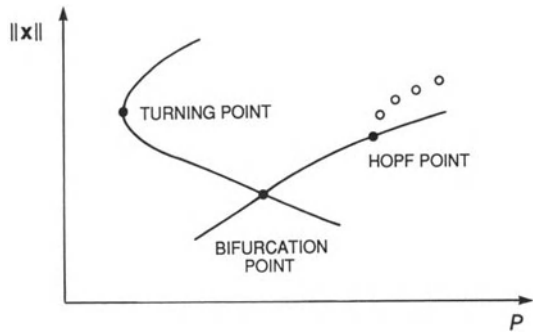


Figure 9.6 Schematic of turning points and bifurcation points, which are singular points of a two-dimensional free surface flow; and Hopf bifurcation points which are regular, or non-singular ($\|\mathbf{x}\|$ denotes a norm of the solution, such as arc-length or another variable that changes monotonically in the vicinity of the critical point; P is the bifurcation parameter; the circles past the Hopf point, or rather their distance from the steady-state branch, designate the amplitude of the bifurcating, time-dependent solution).

interpolation allows stepping around turning points (e.g., Jackson and Winters (1984)), but the singularity of the Jacobian continues to hamper convergence. A more robust procedure is to introduce a new parameter which increases monotonically, such as the arc-length s along the solution family, defined by

$$(\mathbf{y} - \mathbf{y}_0) \cdot (\mathbf{y} - \mathbf{y}_0) + (P - P_0)^2 = (s - s_0)^2 \quad (9.31)$$

More commonly, a 'pseudo-arc-length', defined by a linearized version of (9.31), is used (see Keller (1977) for details). Equation (9.31) or its linearized version is added to the original equation set and the augmented system is solved for (\mathbf{y}, P) , with s serving as the continuation parameter. The Jacobian of the augmented system is nonsingular at simple turning points (Keller 1977), but remains singular at simple bifurcation points. Arc-length continuation can still be used to step over the latter, but special techniques may be necessary to ensure convergence and to switch branches reliably (Keller 1977).

Abbott (1978) suggested choosing as pseudo-arc-length a component of the solution vector, preferably the one that locally changes the fastest along the solution branch. This amounts to switching the parameter for a component of the solution vector. Such parameter switching can be invaluable not only for stepping over turning points, but also for getting a first solution when the parameter range for which a two-dimensional steady state exists is unknown (e.g., vacuum range in slot coating). It is also useful when static contact lines of coating flows approach sharp corners, where Gibbs' condition (9.9) applies (pinning the contact line to a sharp edge by introducing a geometrical or sometimes compositional discontinuity is a common practice in industry for achieving a uniform line across the width of a coating die). Because Gibbs' condition is a 'unilateral constraint', it has discontinuous derivatives with respect to the contact line location and hence causes convergence difficulties for the Newton iteration. Abbott's continuation method eliminates the difficulties by fixing the contact line at a given location and computing the required vacuum, for instance.

9.2.4.3 Initialization

Continuation methods are useful when a solution at a nearby point is known. When solving a new problem, however, such an initial solution is usually not available. To get a very first solution, one can sometimes simplify the problem into one whose solution is known or easy to find, and then apply a continuation technique to proceed to the sought first solution of the original (i.e. not simplified) problem. During the course of such 'strategic start-up continuation', flow parameters, boundary conditions and even the geometry of the solid boundaries can be varied. Christodoulou and Scriven (1989), for example, managed to obtain a converged solution of slide-coating flow starting from a known solution of curtain-coating flow (Kistler and Scriven 1983). An alternative is to solve for the creeping flow (zero Reynolds number) with the free boundaries temporarily fixed and the kinematic

and no-shear stress conditions applied at free surfaces. The resulting solution is often a good enough initial estimate for the free-surface flow, especially when under-relaxation is used for the first few Newton steps. Another alternative is to start from an *ad hoc* initial guess but to precede Newton iteration by a few steps of successive substitution which, for a proper choice of the distinguished boundary condition at free surfaces, usually has a larger radius of convergence.

9.2.5 LINEAR STABILITY ANALYSIS WITH RESPECT TO 2D DISTURBANCES

Steady, 2D states of coating flows are often unstable to 2D and 3D disturbances over wide ranges of their characteristic parameters. Some of the disturbed flow fields are steady, others are periodic, others may be chaotic in time, and most result in unacceptable nonuniformities. For practical applications, predicting the limits of the operating parameters past which the flow is unstable is therefore an essential ingredient of a comprehensive coating-flow analysis.

Even though a fully transient analysis of the complete system of nonlinear equations may be needed to investigate stability to all types of disturbances (see Section 9.2.9), an asymptotic analysis with respect to infinitesimally small, two-dimensional disturbances is sufficient to predict the critical parameters at the onset of many coating flow instabilities. Like conventional procedures of linear stability analysis in hydrodynamics (e.g., Drazin and Reid (1981); and also Chapter 8), finite-element stability analysis decomposes the disturbances into their normal modes. Two-dimensional disturbances of velocity, pressure, and free surface position can be represented by the same set of basis functions as the steady base flow, $\phi^i(\xi, \eta)$, $\psi^k(\xi, \eta)$, $\phi^l(\xi, \eta)$ (*cf.* equation (9.15)), and exponentials in time:

$$\begin{aligned} \mathbf{u}(\xi, \eta, t) &= \sum_i [\mathbf{u}_i^0 + \varepsilon \mathbf{u}'_i \exp(\lambda t)] \phi^i(\xi, \eta) \\ p(\xi, \eta, t) &= \sum_k [p_k^0 + \varepsilon p'_k \exp(\lambda t)] \psi^k(\xi, \eta) \\ \mathbf{x}(\xi, \eta, t) &= \sum_l [\mathbf{x}_l^0 + \varepsilon \mathbf{x}'_l \exp(\lambda t)] \phi^l(\xi, \eta) \end{aligned} \quad (9.32)$$

Here \mathbf{u}_i^0 , p_k^0 , \mathbf{x}_i^0 , are nodal coefficients that describe the undisturbed steady state; \mathbf{u}'_i , p'_k , \mathbf{x}'_i , are nodal parameters that describe the disturbance mode; ε is the amplitude of the disturbance; and $\lambda = \lambda_r + i\lambda_i$ is the complex growth rate whose real part determines whether a disturbance decays, in which case λ_r is negative, or grows, in which case λ_r is positive. The imaginary part λ_i is the temporal frequency of the disturbance.

To derive the discretized stability problem, the representations of the disturbed fields (9.32) are inserted into the weighted residuals (9.17)–(9.19), and also the weighted residuals of the mesh generation equations, e.g., equation (9.27), when the elliptic technique is used. The resulting expressions are then linearized with respect to ε . These steps are complicated because the nodal velocities \mathbf{u} , pressures p and coordinates \mathbf{x} all depend on ε . The end result is a large, sparse, unsymmetric generalized eigenproblem of the form

$$\mathbf{J}\Phi = \lambda \mathbf{M}\Phi \quad (9.33)$$

The elements of the Jacobian matrix $\mathbf{J} \equiv \partial \mathbf{R} / \partial \mathbf{y}$ ($\mathbf{y}_0, \dot{\mathbf{y}} = \mathbf{0}$), already defined at (9.28), measure the sensitivity of the residuals of the Navier–Stokes equations and boundary conditions to changes in the nodal unknowns (i.e., velocities, pressures, positions). The elements of the mass matrix $\mathbf{M} \equiv -\partial \mathbf{R} / \partial \dot{\mathbf{y}}$ ($\mathbf{y}_0, \dot{\mathbf{y}} = \mathbf{0}$) measure the sensitivity of the same residuals to changes in the time derivatives of the nodal unknowns (liquid accelerations, velocities of nodal points). Solutions of (9.33) are eigenvectors Φ , which represent possible modes of instability, and eigenvalues λ , which are their corresponding complex growth rates.

Finding solutions of (9.33) is challenging for several reasons. First, the eigenproblem is unsymmetric. Therefore, eigenvalues and eigenvectors may be complex. Second, the size of the full eigenproblem rules out computing all eigenvalues. Only the most dangerous (or leading) eigenvalues, i.e. the ones of algebraically largest real parts, should be sought. Most existing methods for partially solving such problems find eigenvalues of smallest modulus and not the most dangerous ones. And third, the mass matrix \mathbf{M}

is singular because the continuity residuals and essential boundary conditions do not involve time derivatives of the nodal unknowns. The singularity of \mathbf{M} gives rise to ‘infinite’ eigenvalues that correspond to unbounded speeds of propagation of sound waves in an incompressible medium. There are as many of them as equations with no time derivatives, and all should be eliminated before the most dangerous ones can be computed.

Christodoulou and Scriven (1988) advanced a method that successfully addresses all three challenges and efficiently computes leading eigenvalues and their eigenvectors. The method is based on Arnoldi’s algorithm with Schur–Wielandt deflation, developed by Saad (1989). In contrast to the simple power method (e.g., Wilkinson (1965)) and the subspace iteration method (Stewart 1978) – which rely on the same iterative principle as Arnoldi’s method but discard all previous estimates of the eigenvectors except the very last one – Arnoldi’s algorithm uses the results from all previous iterations to form the best approximation of the desired eigenvectors. The result is an enormous speed up of the rate of convergence of the modes corresponding to the eigenvalues in the outer part of the spectrum (Saad 1980).

To eliminate the infinite eigenvalues mentioned above, Christodoulou and Scriven (1988) used a few steps of ‘rational acceleration’, a scheme that filters out the corresponding modes from the initial vectors (cf. Goldhirsch, Orszag and Maulik (1987)). The idea is to perform a few steps of inverse iteration on the initial vector, much like initializing the time integration of differential-algebraic systems by a few steps of backward-differences (e.g., Kheshgi and Scriven (1984); see also Section 9.2.9). Inverse iteration requires the LU-decomposition of the Jacobian matrix or of a linear combination of the Jacobian and mass matrices. To extract the most dangerous eigenvalues, Christodoulou and Scriven (1988) used approximately exponential preconditioning by rational transformation. This transforms the eigenproblem to one whose eigenvalues are the exponentials of the original eigenproblem, and

thereby maps leading eigenvalues to ones of largest modulus, which are then easily calculated by the Arnoldi algorithm.

When the imaginary part of the most dangerous mode is large compared with the modulus of the second leading modes, convergence of the method outlined above is slow. Christodoulou and Scriven (1988) found that once a crude approximation to the leading mode has been found in such cases of slow convergence, the complex shift approach of Parlett and Saad (1985) can resolve the leading mode efficiently. Used by itself, the complex shift approach carries the danger of missing the leading mode, especially in cases of frequent mode overtaking. The same is true for Natarajan's (1992) multiple shift-and-invert, restarted Arnoldi algorithm which employs automatic shift selection.

Christodoulou and Scriven (1988) applied their algorithm to analyze the stability of slide coating flows to disturbances that leave the flow uniform in the cross-web direction. Instabilities usually arise at turning points, where solutions of the steady-state equation set cease to exist, or at Hopf bifurcation points, where the flow begins to oscillate spontaneously. Figure 9.7, taken from Christodoulou (1990), illustrates the most dangerous part of the eigenvalue spectrum for a slide coating flow at selected states along a parameter family with varying web speed. More generally, the main findings of Christodoulou and Scriven (1988) are: at low web speeds and/or high flow rates a turning point marks the onset of bead flooding; at insufficient pressure differences ('vacuum') a Hopf point marks onset of spontaneous bead oscillations; and at large gap clearances a Hopf point is followed very closely by a turning point. Static liquid bridges, in contrast, break at a single turning point (Higgins 1980).

In another illustrative example, Anturkar, Papanastasiou and Wilkes (1991) applied Christodoulou and Scriven's (1988) algorithm to calculate the stability of 2D coextrusion flows of viscoelastic liquids through long converging dies and compared critical values of the flow-rate ratio between two layers with those predicted by a simplified Orr–Sommerfeld-type analysis. They found good agreement in all cases except when

interfacial tension is zero and the power law indices of the two layers are equal. In such cases, leading eigenmodes exist at high wavenumbers that cannot be resolved by the Arnoldi method.

9.2.6 LINEAR STABILITY ANALYSIS WITH RESPECT TO 3D DISTURBANCES – ONSET OF RIBBING

Even if a steady flow is immune to 2D disturbances, it can be unstable to 3D disturbances that break the translational symmetry and make the flow nonuniform in the third, transverse direction. The most prominent three-dimensional coating-flow instability is ribbing, a set of evenly spaced, stationary free-surface waves in the cross-web direction that results in a corduroy-type pattern in the down-web direction. It often arises in thin liquid layers applied by brushing, spreading, or rolling (for a recent review, see Coyle (1992) and also Chapter 12a). Ribbing is also common in various pre-metered bead coating devices (for details, see Chapters 11a and 11b), which can also suffer from many other three-dimensional instabilities, including rivulets (break-up of the film flow into individual strands or 'streamers'), diagonal chatter (or 'chevrons') and even air entrainment (for the last, see also Chapter 3).

To predict fully 3D flow states with finite amplitudes in free-surface elevation, 3D flow models are needed. At present, such models still tax the most advanced algorithms available. To predict the onset of instabilities that break the translational symmetry of 2D flow, however, linear stability analysis by the Galerkin/finite-element method is again sufficient. The methodology follows standard procedures of stability analysis, relying on Fourier expansions in the third dimension to describe 3D disturbances (e.g., Davey (1962); DiPrima and Rogers (1969); Meyer (1969)). Bixler (1982) and Ruschak (1983) were the first to show that, with such expansions, analysis of stability to 3D disturbances can be performed on the same 2D mesh as analysis of the base flow that is uniform in the transverse (cross-web) direction.

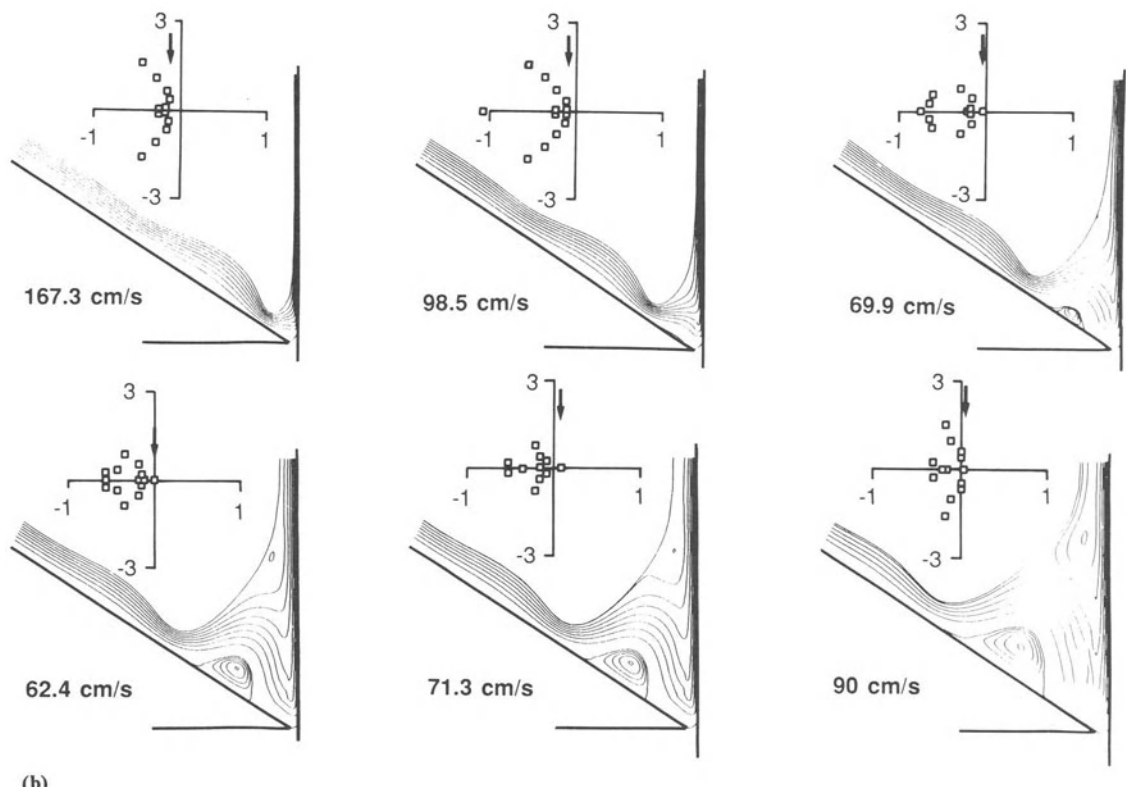
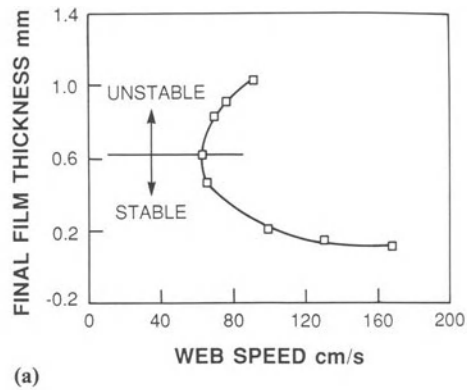


Figure 9.7 Evolution of final film thickness (a) and associated flow field together with leading part of eigenvalue spectrum (b) for slide coating along a parameter family of varying web speed at a constant flow rate of $1.93 \text{ cm}^2/\text{s}$. Past the turning point at 62.4 cm/s , the family turns back toward larger values of web speed (pressure difference $\Delta P = 161 \text{ Pa}$, coating gap $H_{\text{GAP}} = 0.347 \text{ mm}$, liquid viscosity $\mu = 8.717 \text{ mPa s}$, liquid density $\rho = 1130 \text{ kg/m}^3$, surface tension $\sigma = 70.1 \text{ mN/m}$, static contact angle $\theta_0 = 60^\circ$, imposed dynamic contact angle $\theta_D = 160^\circ$, slide inclination 30° ; from Christodoulou (1990)).

The key idea is to represent 3D disturbances by 2D finite-element basis functions multiplied by Fourier basis functions of wavenumber N in the cross-web direction, i.e.

$$\begin{aligned} \mathbf{u}(\xi, \eta, \zeta, t) &= \sum_i [\mathbf{u}_i^0 + \varepsilon \mathbf{u}'_i \cdot \mathbf{D}(N\zeta) \exp(\lambda t)] \phi^i(\xi, \eta) \\ p(\xi, \eta, \zeta, t) &= \sum_k [p_k^0 + \varepsilon p'_k \cos(N\zeta) \exp(\lambda t)] \psi^k(\xi, \eta) \\ x(\xi, \eta, \zeta, t) &= \sum_l [x_l^0 + \varepsilon x'_l \cos(N\zeta) \exp(\lambda t)] \phi^l(\xi, \eta) \\ y(\xi, \eta, \zeta, t) &= \sum_l [y_l^0 + \varepsilon y'_l \cos(N\zeta) \exp(\lambda t)] \phi^l(\xi, \eta) \\ z(\xi, \eta, \zeta, t) &= \zeta \end{aligned} \quad (9.34)$$

where $\mathbf{D} \equiv [(\mathbf{ii} + \mathbf{jj}) \cos(N\zeta) + \mathbf{kk} \sin(N\zeta)]$. All other quantities are defined as in (9.32).

Ruschak (1983) adopted a computational domain of infinitesimal thickness in the cross-web (z) direction. For weighting functions, he employed the 2D ones used in solving for the base flow. To reduce the order of derivatives in the capillary term of the boundary traction integral at the free surfaces, Ruschak applied the surface divergence theorem (Weatherburn (1927), p. 123; recently rediscovered by Ho and Patera (1991)). Bixler (1982), in contrast, chose a computational domain consisting of the 2D flow domain extended over one wavelength in the cross-web direction. He constructed weighting functions of the form $\phi^i(\xi, \eta) \mathbf{D}$ for the momentum equations (9.1), $\psi^k(\xi, \eta) \cos(N\zeta)$ for the continuity equation (9.3), and $\phi^l(\xi, \eta) \cos(N\zeta)$ for the kinematic condition (9.4). At free surfaces, Bixler applied the tensor form of the surface divergence theorem (9.22) to the capillary term of the boundary traction integral, which again reduced the order of derivatives.

In either Bixler's or Ruschak's approach, the disturbed fields (9.34) are then inserted into the weighted residuals (9.17)–(9.19) and the resulting expressions are linearized with respect to ε (in more modern algorithms with elliptic mesh generation, the same procedure is applied to the weighted residuals of equation (9.27)). Christodoulou (1990) showed that both Bixler's and Ruschak's approaches result in the same large,

generalized, unsymmetric eigenproblem for the finite-element coefficients of the normal modes, Φ , and the corresponding eigenvalues, λ :

$$\mathbf{J}_{3D}\Phi = \lambda \mathbf{M}_{3D}\Phi \quad (9.35)$$

with $\mathbf{J}_{3D} \equiv \partial \mathbf{R} / \partial \mathbf{y} (\mathbf{y}_0, \dot{\mathbf{y}} = \mathbf{0}; N)$ and $\mathbf{M}_{3D} \equiv -\partial \mathbf{R} / \partial \dot{\mathbf{y}} (\mathbf{y}_0, \dot{\mathbf{y}} = \mathbf{0}; N)$. The main difference from 2D stability is that here the Jacobian and mass matrices are functions of the disturbance wavenumber N , and so are consequently the calculated eigenvectors and eigenvalues. The most dangerous disturbances must therefore be found by calculating growth rates over a wide range of wavenumbers. As wavenumber is raised, the growth rate of the most dangerous mode may pass through a maximum but, eventually, it will decrease because capillarity dampens the growth of short waves. The search for the maximum growth rate must be repeated at different values of a flow parameter of particular interest. The onset of a 3D instability is signalled by the maximum in the growth rate versus wavenumber reaching zero.

As in the two-dimensional case, solving (9.35) for the eigenvalues λ and corresponding three-dimensional modes Φ is a major computational challenge. Ruschak (1983), and later Coyle, Macosko and Scriven (1990), took an elegant short-cut by omitting the time derivative terms in the momentum equation. This procedure statically condenses the large eigenproblem to one of much smaller dimension, equal to the number of kinematic residual equations. The latter can be solved with standard subroutines available in various software libraries. However, in the resulting approximation, the computed growth rates are correct only for non-oscillatory instabilities at vanishingly small Reynolds numbers. Bixler (1982), in contrast, solved the full eigenproblem (9.35) without simplifications by using inverse subspace iteration (Stewart 1978). Christodoulou (1990) calculated the most dangerous modes and their growth rates by the deflated Arnoldi algorithm of Section 9.2.5 without making any approximations either.

To date, most published applications of 3D finite-element stability analysis have been aimed

at predicting the onset of ribbing. Quite some time ago, approximate lubrication-flow analyses of simple configurations such as wedge spreaders (Pearson 1960), forward roll coating (Pitts and Greiller 1961) and journal bearings (Savage 1977a, 1977b) had made plain that the adverse pressure gradient under the meniscus is the root cause of the instability (see also Chapter 12a). Quantitative predictions of the onset of ribbing, however, were compromised by uncertainties in the lubrication approximation, the most serious being the arbitrariness of the boundary conditions imposed near the meniscus, where the flow is generally far from rectilinear. Bixler (1982), who applied full finite-element stability theory to a liquid film emerging from a diverging coating knife, was the first to compute the onset of ribbing without any *ad hoc* assumptions. Unfortunately, because of an elusive error in the derivation of the stability matrices of the 3D flow, Bixler – and Coyle (1984) after him for the case of ribbing in forward roll coating – overestimated the critical capillary number by about 20%. Ruschak (1983) carefully tested his finite-element stability method against standard results on the stability of a stagnant liquid layer and Hele–Shaw flow. In spite of the success of his algorithm, he later showed that the much simpler lubrication-flow theory can accurately predict the onset of ribbing in slowly diverging flow sections if it is complemented with accurate boundary conditions obtained from steady, two-dimensional finite-element analysis of the ‘inner’ meniscus region (Ruschak 1985). Coyle, Macosko and Scriven (1990) successfully compared their finite-element predictions of the onset of ribbing between counter-rotating rolls with experimental data as well as Ruschak’s (1985) theory. Christodoulou (1990) validated his algorithm against Ruschak’s (1983) results for a stagnant layer and Hele–Shaw flow at zero Reynolds number. He then proceeded to show that, towards higher Reynolds numbers, the discrepancy between his exact analysis and Ruschak’s (1983) quasi-static condensation method increases. At high Reynolds numbers $Re = O(10)$, the approach used by Ruschak (1983) and Coyle, Macosko and Scriven (1990) may fail altogether.

For forward roll coating, for instance, it misses several complex modes that become more unstable than the ribbing mode.

Christodoulou (1990) applied his method also to slide coating. He predicted that ribbing sets in when the sub-ambient pressure (‘vacuum’) applied under the liquid bridge is reduced, coating speed is decreased, or flow rate is diminished. Increasing gap clearance stabilizes the flow with respect to ribbing when the lower meniscus pins at the die edge, but destabilizes the flow when the liquid wets the lip underside and the lower meniscus takes a position past the edge. In contrast to lubrication-type flows under spreaders and between rollers, the effect of surface tension is small and non-monotonic in the parameter ranges examined, and the physical mechanisms responsible for ribbing in slide coating are still not fully understood (see also Chapter 11b).

Using the same method, Do and Christodoulou (1992) computed the stability of curtain coating flow (see also Chapter 11c, which discusses curtain coating in detail). They found that 2D liquid curtains are linearly stable to both 2D and 3D disturbances, with the 2D ones being the most dangerous. As Weber number (i.e. the ratio of inertial forces to capillary forces) was reduced below $We < 2$ – where, according to earlier publications, a falling liquid curtain is unstable (e.g., Lin (1981)) – the most dangerous growth rate approached zero but never became positive. Further reductions in flow rate caused the lower part of the curtain to be pulled by the web while the growth rate started decreasing. In a recent Orr–Sommerfeld-type analysis, Lin, Lian and Creighton (1990) also found that a liquid curtain is stable to 2D varicose and sinuous disturbances of either the temporally or spatially growing type, thereby disproving Lin’s earlier result (1981) that was incorrectly based on Gaster’s (1962) transformation. Recently, Finnicum, Weinstein and Ruschak (1993) reported observations of stable liquid curtains in a wide range of flow conditions, including $We < 2$. They attributed the observed stability at low We to nonlinear effects that may stabilize disturbances after they grow to a finite amplitude. According to the analyses by Lin,

Lian and Creighton (1990) and Do and Christodoulou (1992), however, it is the occasionally observed instability for $We < 2$ (low flow rates) rather than stability that arises from nonlinear effects (i.e. large amplitude disturbances such as those caused by bubbles).

9.2.7 OPERABILITY ANALYSIS TO 2D AND 3D DISTURBANCES – COATING WINDOW

As a consequence of the nonlinearity of the governing system, at a given set of parameters, a coating flow may have no steady state, one steady state, or multiple steady states. As parameters are varied, multiplicity and stability of states change at certain parameter values – usually called critical points. In designing and operating coating systems, it is important to know how many steady states exist at a given set of parameters, whether these states are stable to disturbances, and how they are connected in the space of parameters. This, in turn, puts a premium at devising computational schemes that automatically locate critical points in order to construct operability diagrams efficiently, which are invaluable in technological applications.

With continuation and linear stability analysis, critical points can be located approximately. Constructing operability windows that are of practical interest, though, requires locating critical points in one parameter more accurately and tracking their paths as other parameters are varied. An efficient means to do so is to augment the steady-state equations with an additional equation set that uniquely characterizes the critical point, and to solve the augmented set with a Newton-like method that simultaneously finds the critical parameter value and the critical flow state. Such critical point tracking algorithms have been reviewed by Melhem and Rheinboldt (1982), and also by Schwetlick (1984) who focused on constrained optimization problems.

9.2.7.1 2D disturbances

To locate turning points, the steady-state equations can be augmented with one of the following

conditions (Melhem and Rheinboldt 1982): (1) the tangent vector to the solution branch is perpendicular to the parameter axis; (2) the Jacobian has a zero eigenvalue; (3) the Jacobian has a nonzero right null-vector; (4) the Jacobian has a nonzero left null-vector; or (5) the determinant of the Jacobian vanishes. For Hopf bifurcation points, the extra condition is the existence of a purely imaginary eigenvalue. The additional equation set for turning point tracking is of approximately equal dimension as the original problem, and for Hopf-point tracking the set is twice as large. Efficient critical point tracking algorithms avoid solving linear systems twice or three times as large as the steady-state set – as they would arise from direct application of Newton's method – by taking advantage of the block structure of the augmented system. One Newton iteration for finding turning points reduces then to solving two linear systems of the same dimension as the steady-state equation set, and only twice that dimension for Hopf bifurcation points. Altogether the cost of computing a critical point is only a few times that of computing a steady state.

Continuation methods can be applied to the augmented system in order to track paths of critical states, and to step over bifurcations, points of isola birth and cusps. The last are simple turning points of the augmented system itself and are especially important for the dynamic response of the system. Examples of applications to flow problems with fixed boundaries have been given by Cliffe (1983), Cliffe and Spence (1984), Winters, Cliffe and Jackson (1987) and Jackson (1987). Ungar and Brown (1982) used Abbott's (1978) method to compute turning points and bifurcations of a rotating cylinder, a capillary statics problem. Christodoulou (1990) tried Abbott's as well as Poenisch and Schwetlick's (1981) algorithms to follow turning points of 2D slide coating flow, and uncovered a wealth of structure in the parameter space. He also proposed an extension of Abbott's methods for computing Hopf points that is easier to implement in existing finite-element codes than a method proposed by Jepson (1981).

9.2.7.2 3D disturbances

When a coating flow loses stability to 3D disturbances before it becomes unstable to 2D ones – as at the onset of the ribbing instability (see Section 9.2.6) – computing the corresponding symmetry-breaking bifurcation points and tracing out their paths in parameter space is more important than computing and tracking turning or Hopf bifurcation points of the 2D flow states.

Cliffe (1983) was the first to consider extended systems for the direct computation of bifurcation points at which stability of translationally invariant flow states is lost. Werner and Spence (1984) proposed more efficient systems that capitalize on the symmetry of the underlying steady flow. Applications have focused on the axisymmetric Taylor flow between concentric rotating cylinders and the onset of Bénard convection in a liquid layer heated from below (e.g., Cliffe (1983); Cliffe and Spence (1984); and Winters, Cliffe and Jackson (1987)). In these cases, however, the bifurcating flows are still 2D (or axisymmetric) and the methods used are not directly applicable to the ribbing instability. Christodoulou, Scofield and Scriven (1990) proposed a system for tracing paths of ‘pitchfork’ bifurcations that break the translational invariance of a 2D flow. Their augmented system consists of the equations for the 2D steady flow, the eigenvalue problem of the linear stability analysis to 3D disturbances (with a 2D mesh and a single Fourier mode in the cross-web direction, see Section 9.2.6), and the condition that the maximum growth rate at the most dangerous wavenumber vanishes:

$$\begin{aligned} \mathbf{R}(\mathbf{y}, P) &= \mathbf{0} \\ (\mathbf{J}_{3D} - \lambda \mathbf{M}_{3D}) \Phi &= \mathbf{0} \\ \Phi_r \equiv \mathbf{e}_r^T \cdot \Phi &= 1 \\ d\lambda/dN &= 0 \\ \lambda &= 0 \end{aligned} \quad (9.36)$$

Here, the eigenvector is normalized with $\mathbf{e}_r \equiv [0, \dots, 1]^T$, the unit vector whose r th entry is unity and all others are zero; the distinguished index r is chosen so that at the last computed

state Φ_x is the greatest among all the entries of Φ . Solution of the system (9.36) gives the critical state \mathbf{y} , critical parameter value P , nullvector Φ , and critical disturbance wavenumber N . Christodoulou, Scofield and Scriven (1990) used a rather inefficient extension of Abbott’s method that required eight LU decompositions and several back-solutions per Newton iteration. An algorithm similar to Poenisch and Schwetlick’s (1981) would require only two LU decompositions per iteration but is more difficult to implement.

Christodoulou, Scofield and Scriven (1990) applied their method to predict the maximum allowable pressure difference across a slide coating bead without ribbing. They found that this upper vacuum limit increases with web-to-slide angle in the range between 0° and 90° and has a maximum at 90° or above, depending on the final coated film thickness. These trends corroborate experimental measurements by Burkett, Conaghan and Hirshburg (1984). Christodoulou, Scofield and Scriven (1990) also examined the effect of water redistribution between the layers of two-layer slide coating, keeping the total amount of water and thus the dryer load constant, and found that viscosity stratification raises the upper vacuum limit. Francis *et al.* (1990) applied the same method to slot coating flow and found that the upper vacuum limit increases with die-to-web angle at the downstream meniscus.

To date, quantitative comparisons between theoretical predictions for the onset of ribbing and experiments have been published only for roll coating (*cf.* Chapter 12a). For slide coating, unpublished work of one of us (KNC) suggests that computed values of the upper vacuum limit agree with experiments to within 20–30%, even when dynamic and static contact angles are taken to be constant. The lower vacuum limit, in contrast, is highly sensitive to the contact angles imposed as boundary conditions and reliable predictions cannot be made unless accurately measured angles are available – or much needed theories are advanced for predicting contact angles from first principles (see also Section 9.3.1).

9.2.8 SENSITIVITY ANALYSIS TO 2D AND 3D DISTURBANCES – QUALITY WINDOW

Even if a coating flow is stable so that transitory disturbances damp out with time, it can be measurably sensitive to ongoing disturbances coming from mechanical vibrations, pump pulsations, speed variations, inhomogeneities in the web surface, etc. Such sensitivity is of practical significance because it translates directly into coating quality and, hence, ought to be predicted as part of a complete analysis. Tracking the effect of large-amplitude disturbances requires transient analysis of the full nonlinear equation set (Section 9.2.9). Such analysis can be quite costly, especially when sensitivity to a wide range of disturbances and frequencies needs to be studied. For small-amplitude disturbances, transient analysis of the linearized equations set is adequate and more efficient than the nonlinear transient analysis (Kaneko and Scriven 1988), but shares some of its major shortcomings. The most attractive and efficient method is frequency-response analysis, quite similar to the analysis of small-signal response of nonlinear electrical systems.

9.2.8.1 2D disturbances

In the finite-element based frequency-response analysis of Van Abbenyen, Christodoulou and Scriven (1989) (see also Christodoulou (1990)), small disturbances of a particular parameter, usually one entering a boundary condition, are decomposed into their Fourier spectrum, and so are the resulting perturbations of the coating flow. The responses of velocities, pressures and nodal positions are discretized by the same set of basis functions as is used to represent the steady 2D flow. The Navier–Stokes system governing the perturbed transient system reduces to a linear system of complex algebraic equations of the form:

$$(\mathbf{J} + i\omega \mathbf{M}) \mathbf{z} = -\mathbf{F} \quad (9.37)$$

Here \mathbf{J} and \mathbf{M} are the Jacobian and mass matrices of the linear stability analysis, already defined at (9.33); ω is the frequency of the external

disturbance; $\mathbf{F} \equiv \partial \mathbf{R} / \partial P(\mathbf{y}_0, \dot{\mathbf{y}} = \mathbf{0})$ is the sensitivity vector of the weighted residuals with respect to the parameter P that is forced to oscillate; and \mathbf{z} is the complex nodal response vector. Sensitivity at each frequency ω is then computed as the magnitude of the response compared with the magnitude of the disturbance. To avoid complex arithmetic, for which frontal solvers are not commonly available, the real and imaginary parts of (9.37) can be separated – at the expense of doubling the dimension of the linear system. Reordering the equations in pairs of real and imaginary parts minimizes the bandwidth, only doubling it from steady-state analysis.

Van Abbenyen, Christodoulou and Scriven (1989) demonstrated the utility of their method for slide coating. For parameter disturbances up to 20% of their steady-state values, frequency-response predictions, expressed as an amplitude ratio, compared well with solutions of the fully nonlinear transient system, as obtained earlier by Katagiri and Scriven (1986). The cost of the linear frequency response analysis, however, was about two orders of magnitude lower than that of the transient analysis. Both approaches detected the same two resonant frequencies, one associated with the upper free surface and the other with the lower one. Frequency-response analysis also uncovered an important interfacial mode in two-layer flow and showed that forcing different parameters excites distinct eigenmodes of the base flow. Finally, the analysis made clear that the susceptibility to forced disturbances strongly depends on whether the lower meniscus remains pinned at the corner or not (see also Chapter 11b).

Van Abbenyen *et al.* (1990) and Bussmann, Hoffmann and Beck (1992) attempted to verify computed frequency responses with experiments, also for slide coating. Agreement with experiments was acceptable only if the vacuum imposed in the model was adjusted to ensure the computed and measured dynamic contact lengths matched. The disagreement between theoretical and experimental frequency response at identical vacuum levels was attributed by these authors to uncertainties in modeling dynamic wetting, unknown liquid rheology at the high deformation rates

close to contact lines, and surface-tension gradient effects ignored in the model.

9.2.8.2 3D disturbances

As transitory disturbances can be nonuniform in the cross-web direction, so can ongoing and steady disturbances. Examples include spot-like inhomogeneities on a web surface, cross-web variations of the pressure difference ('vacuum') imposed over a coating bead, and damaged surfaces and edges (scratches and nicks) of coating dies – which all can result in unacceptable spot- or streak-like defects. The method of frequency response analysis can be extended to predict cross-web flow and film-thickness variations in addition to ones in the machine direction. To describe the perturbations, Hackler *et al.* (1992) combined Fourier expansions in both time and cross-web coordinate with finite-element basis functions in the two space coordinates of the underlying uniform flow. As in linear stability analysis to 3D disturbances (Section 9.2.6), only a single (representative) Fourier mode was used in the transverse direction. The Navier–Stokes system was thereby transformed into a set of linear algebraic equations similar to (9.34) but now depending on two parameters, the disturbance frequency ω and the cross-web wavenumber N :

$$(\mathbf{J}_{3D} + i\omega \mathbf{M}_{3D})\mathbf{z} = -\mathbf{F}_{3D} \quad (9.38)$$

Here \mathbf{J}_{3D} and \mathbf{M}_{3D} are the Jacobian and mass matrices already defined at (9.32); $\mathbf{F}_{3D} \equiv \partial \mathbf{R}_{3D} / \partial P (\mathbf{y}_0, \dot{\mathbf{y}} = \mathbf{0})$ is the sensitivity factor of the weighted residuals of the 3D equation set with respect to the parameter P that is forced into oscillation; and \mathbf{z} is the discretized response vector which, here, depends on both ω and N . Hackler *et al.* (1992) computed the maximum amplitude ratio of the response to the forced disturbance by direct search in the (ω, N) space. Their results for slide coating show that 3D disturbances can be amplified even when 2D ones are strongly damped, especially close to the onset of ribbing.

The combination of linear stability analysis, direct tracking of critical points, and frequency response analysis is a comprehensive strategy for

systematic coating-flow analysis. It is useful not only to predict coating windows, but also to assess the sensitivity to disturbances of every steady state within a coating window and therefrom delineate a quality window where resulting film-thickness uniformity is acceptable.

As an example, Fig. 9.8 (taken from Hackler *et al.* (1992)) shows a computed coating window for a single-layer slide coating, complemented with contours of sensitivity to two different disturbances in imposed pressure difference ('vacuum'): one is a steady, 3D disturbance (Fig. 9.8a); the other is 2D but oscillatory (Fig. 9.8b). These disturbances correspond to two peaks identified beforehand in the 3D response surface of the amplitude ratio as a function of frequency and wavenumber. Figure 9.8 illustrates that, contrary to a belief widely held among practitioners, parameter regions of least sensitivity to disturbances – and therefore best product quality – do not necessarily coincide with regions of maximum coating latitude, defined as the difference between upper and lower 'vacuum' limits (the lower limit, usually arising from air entrainment or bead breakup, is taken here to be zero because experiments suggests it is typically well below the upper limit and accurate theoretical predictions are still difficult for reasons indicated above). Figure 9.8 also makes evident that the region of least sensitivity to one disturbance can be quite different from that to another. Hackler *et al.* (1992) concluded that, to maximize the benefit from computational sensitivity analysis, the prevalent ambient disturbances ought to be identified and measured in experiments first.

9.2.9 TRANSIENT ANALYSIS

Time-dependent analysis of the full, nonlinear equation set (9.23) is indispensable to study the large-amplitude transients associated with start-up, splice passage and termination of coating. Time-dependent analysis is also useful to investigate the fate of liquid films after coating (see Chapter 6), such as the leveling of nonuniformities resulting from moderate (i.e. non-catastrophic) instabilities in the coating bead, the local break-up

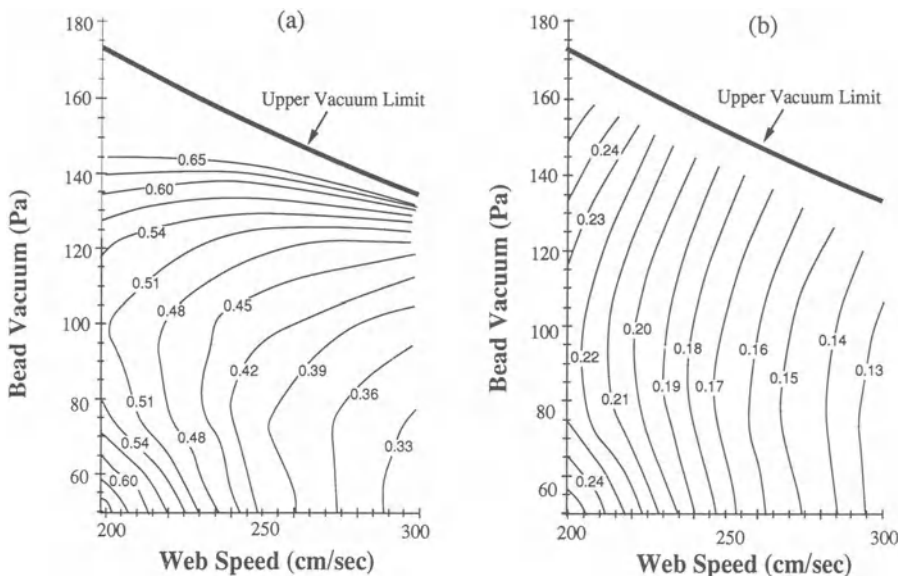


Figure 9.8 Coating window of single-layer slide coating, showing ‘upper vacuum limit’ as well as contours of sensitivity to perturbations in the imposed pressure difference (‘vacuum’): (a) steady perturbation ($\omega = 0$) and wavenumber $N = 30/\text{cm}$; (b) two-dimensional perturbation with $\omega = 45 \text{ Hz}$ and $N = 0$ (from Hackler *et al.* (1992)).

and de-wetting of coated films due to contaminants or defects and, of course, drying and solidification. A complete time-dependent analysis can also be a ‘poor man’s’ way of performing stability and sensitivity analysis. In fact, such analysis may be the only way to predict and track the complete flow breakdown that results from catastrophic instabilities. Transient analysis, combined with iterative solution of the matrix problem at each time step, can furthermore be a pragmatic, yet successful approach to tackling large, three-dimensional free-surface flow problems (Ho and Patera 1990; Wambersie and Crochet 1992).

Algorithms for integrating the nonlinear differential and algebraic equation system (9.23) in time must cope with the fact that the time derivatives $\dot{\mathbf{y}}$ enter the system implicitly, although usually linearly. In the $u-P$ formulation, the time derivatives cannot be solved for explicitly – and implicit schemes are therefore mandated – because the algebraic constraints of continuity (9.3), mesh generation such as (9.27), and various essential

boundary conditions make the mass matrix $\partial\mathbf{R}/\partial\dot{\mathbf{y}}$ singular, and the linkage between velocity and time derivatives renders ‘mass-lumping’ questionable (Engleman and Sani 1983).

Differential/algebraic equation systems (DAES) like (9.23) can be quite different from ordinary differential equation systems (ODES) and numerical methods for solving ODES do not always work for DAES (Petzold 1982). DAES are classified according to the degree of singularity of the mass matrix $\partial\mathbf{R}/\partial\dot{\mathbf{y}}$. The minimum number of times that all or part of the constraints of a DAES must be differentiated with respect to time in order to obtain an ODES is called the index of the DAES. The index has important implications for the numerical solution of the system, which encounters serious difficulties when the index is two or higher with regard to: (1) finding initial conditions that satisfy not only the algebraic equation subset, but also the hidden algebraic constraints, i.e. constraints that would come up during the reduction to a differential system; (2)

developing stable integration algorithms; and (3) developing estimates of the time-truncation error.

The Navier–Stokes system discretized with the u - P formulation has index two (Petzold 1982). In free surface problems, the nodal position unknowns appear explicitly in the mesh generation equations, e.g. (9.27), as do their time derivatives in the kinematic condition (9.4). As only one time-differentiation yields time derivatives of all nodal position unknowns, the index (two) of the Navier–Stokes system is not affected by the presence of free surfaces.

Christodoulou and Scriven (1992) successfully employed the differential-algebraic solver DASSL by Petzold (1982), thereby demonstrating that sufficiently sophisticated package solvers can provide an easy yet effective means to perform the integration in time of (9.23). Most finite-element codes for viscous free-surface flow analysis, however, incorporate a finite-difference discretization in time as integral part of the algorithm (Frederiksen and Watts (1981), early on pioneered a finite-element discretization of both time and space which, more recently, is gaining popularity again: see, for example, Mittal and Tezduyar (1992)). State-of-the-art algorithms use predictor–corrector schemes, many with a second-order Adams–Bashforth rule as predictor and a second-order unconditionally stable trapezoid rule as corrector (Gresho, Lee and Sani 1980; Engelman and Sani 1983; Kheshgi and Scriven 1984). Simpler schemes employ first-order extrapolation and implicit Euler correction (Keunings 1986). A typical algorithm recurrently executes five essential steps. First, the predictor extrapolates the flow field, free boundaries and internal node locations, the time derivatives being known from the preceding time steps. Second, the finite-element method reduces the partial differential equations to a set of ordinary differential equations. Third, the corrector discretizes the set in time and reduces it to a nonlinear system of algebraic equations. Fourth, Newton’s method solves the system simultaneously for the displacement of the free boundaries and internal mesh nodes together with the flow field. And fifth, the time

derivatives for the next predictor step are evaluated. Depending on the predictor and corrector used, special procedures may be needed for the first few time steps. The Adams–Bashforth/trapezoid-rule integration, for instance, is best initiated with three or four backward-difference steps to generate the time ‘history’ needed for the second-order scheme and to ensure the initial trajectory is devoid of spurious transients that can result from inappropriate initial data for the index-two system (e.g., Gresho, Lee and Sani (1980); Kheshgi and Scriven (1984)). Another key to efficient time integration is automated time-step size control that sets each step so as to keep the local time truncation error within a user-specified tolerance (Gresho, Lee and Sani 1980; Engelman and Sani 1983; Kheshgi and Scriven 1984). With the predictor/corrector scheme and automated time-step control, Newton’s method often requires only one iteration per time step for convergence. In addition, the Jacobian may not have to be reformed every time step, analogously to quasi-Newton methods in steady-state analysis (*cf.* Section 9.2.3). As an added boon from judicious time-step limitation, the matrix systems become more and more diagonally dominant, even in fully implicit schemes, and thereby maximize the effectiveness of iterative solvers (e.g., Liou and Tezduyar (1991); see also Section 9.2.3).

Finite-element algorithms with fully implicit time integration have been applied to a wide variety of free-surface flow problems, including large-amplitude waves traveling down inclined plates (Kheshgi and Scriven 1984); leveling and de-wetting phenomena (Kheshgi and Scriven (1988); see also Chapter 6 in this volume); the response of coating beads to step changes in coating conditions (Kheshgi and Scriven 1984; Katagiri and Scriven 1986); frequency response of coating beads to externally imposed forced disturbances (Katagiri and Scriven (1986); see also Section 9.2.8, and Chapters 11b and 11c); periodic oscillatory flow states that ensue past a Hopf bifurcation point as predicted independently by linear stability analysis (Katagiri and Scriven 1986; Christodoulou and Scriven 1988); and the catastrophic transient response of a coating bead

to small parameter changes near a limit point (Christodoulou and Scriven 1992). In spite of these successful applications, the capabilities and limitations of implicit finite-element algorithms have not been fully explored. Arche-types of transient coating phenomena such as start-up or splice passage, for instance, remain formidable computational challenges that have not been satisfactorily tackled. Frederiksen and Watts (1981) investigated the inception of dip coating from a pool with their space-time finite-element formulation, but their results are based on coarse meshes and must be considered preliminary.

To enhance the efficiency of time-dependent free-surface flow analysis, especially for 3D cases, semi-implicit methods can offer some distinct advantages (Ho and Patera 1990; Wambersie and Crochet 1992). Most of these methods are based on the pressure Poisson equation (PPE) formulation introduced in Section 9.2.1 (see equation (9.25)). For free-surface flow problems, the PPE formulation is usually combined with Picard iteration (e.g., Wambersie and Crochet (1992)). De-coupling free-surface and flow-field calculations avoids any extra complications from the presence of free surfaces.

As another alternative, Krylov subspace projection methods ought to be extended to transient viscous free surface flows, for they hold significant promise for improved efficiency. Until recently these methods were used only for linear stability analysis (see Section 9.2.5), but now they are gaining popularity for the calculation of steady and also transient states of fixed boundary flows (see Edwards *et al.* (1994)). The key idea is to project the discretized transient system on Krylov sub-spaces that are constructed by the Arnoldi process from evaluations of the Navier–Stokes residual and Jacobian without inversion of the viscous operator. Incompressibility is handled via the PPE formulation in the vein of semi-implicit schemes. Nonlinearities result in an integral equation which is solved by functional iteration. The final result is a small system that is efficiently solved through exact exponentiation, or so called ‘exponential propagation’, of the coefficient matrix.

9.2.10 INVERSE PROBLEMS – PROCESS AND PRODUCT DESIGN AND OPTIMIZATION

A coating system consists of coating hardware (process) and a coated film on a substrate (product). Traditionally, process and product design are pursued in two independent stages. The goal of process design is typically to determine the hardware parameters for best coatability of a range of predetermined products. The goal of product design is to determine the physical parameters (rheology, surface properties, etc.) of a new product for best product performance and coatability in a given process, the latter quite often even playing a secondary role. Computational analysis of coating flows is usually fitted in as a tool for understanding the complex interplay of the forces that control the process and predicting process effects on product quality. Such a subdivision of the global process and product optimization problem is prone to result in suboptimal solutions.

The real challenge is to design the whole flow system to satisfy certain quality, productivity or cost constraints (see also Chapter 15 in this volume). This goal can only be achieved by solving ‘inverse problems’ – which are more difficult than direct problems because they are often ill-posed and thus require regularization techniques.

Design and analysis of coating processes gives rise to three kinds of inverse problems. The first, and simplest, is to predict a control or design parameter so that the corresponding flow satisfies a given condition. An example is the problem of finding the maximum pressure difference ('vacuum') applied across a coating bead that leaves the static contact line pinned at a die tip. Pinning the contact line there is often advantageous as it precludes thickness variations resulting from contact lines that are not straight across the width of the die, and may also minimize the susceptibility of the coating bead to external disturbances (see Section 9.2.8). A single control or design parameter can be found by augmenting the governing equation set with a global (or local) constraint which provides the

additional equation necessary to calculate the unknown parameter value. This procedure is exactly Abbott's (1978) method of continuation (see Section 9.2.4).

The second inverse problem is that of die shape optimization to achieve desirable characteristics of the global flow field. Examples of shapes that are readily amenable to this sort of optimization include the cross-sections of distribution cavities to achieve a uniform flow profile across the width of the coater (see Chapters 10 and 15), or the shapes of extrusion slots that result in extrudates of a given shape or thickness profile (e.g., Yokoi and Scriven (1989); Wambersie and Crochet (1992)). In these cases, the governing systems need to be augmented by several equations that result from the discretization of the differential equation that expresses the desirable flow condition.

The third, and most difficult, inverse problem is to identify a single flow or geometrical parameter that results in optimal coatability, as quantified for example by widest operability latitude for changes in 'vacuum' or lowest sensitivity to disturbances. To accomplish this, a nonlinear eigenvalue problem and additional constraints have to be solved together with the original governing system, as described in Section 9.2.7. A yet more difficult case arises when not a single parameter but the shape of an entire piece of hardware needs to be optimized, as for example the shape of a coating lip in a slide coater that ensures widest latitude in 'vacuum'. The sought after shape must then be parameterized as an unknown free boundary much in the same way as a free surface. Again, the extra equations required for determining its location arise from the optimality condition. Application of such optimization to coating flows appears to not have been reported to date. Well-established techniques for optimization of solid structures (e.g., Chung (1985); Haftka and Grandhi (1986); Kikuchi *et al.* (1986)) could possibly be adopted, but may have to be advanced considerably to handle the complicated solution spaces of coating flows. Some optimization problems may be nonconvex, producing non-smooth and often

'fractal' solutions with infinitely detailed structure. Special regularization techniques may be required to impart desired smoothness to the solution of convex optimization problems (e.g. Chung (1985)).

9.3 SPECIAL TOPICS

9.3.1 CONTACT LINES

An essential element of industrial coating processes is continuous film formation at a static contact line where the free surface of the coated layer separates from a solid coating device; static wetting often also influences or controls the position of the upstream meniscus of a coating bead (see, for example, Chapters 11a and 11b in this volume). When a contact line is free to migrate along a solid surface, its position is set by the static contact angle θ_s . For the purpose of macroscopic flow computations, θ_s can be considered a material property (see Chapters 2 and 3). At a sharp corner, the contact line has a propensity to remain pinned. The critical condition for either advance or retreat is Gibbs' inequality condition (see Chapter 3) which can be written as a set of complementary conditions of the form (9.9) (Christodoulou and Scriven 1992), as listed in Fig. 9.2. Most published, computational analyses of coating flows force a static contact line to be either pinned or free to migrate *a priori*, and require cumbersome remeshing procedures to accommodate transitions from one wetting configuration to another (see, for instance, Kistler and Scriven (1994)). Christodoulou and Scriven (1992), in contrast, devised an elegant scheme that imposes the conditions (9.9) as a unilateral solver constraint and deploys several collapsed finite elements at the sharp corner automatically to accommodate solutions in which the meniscus advances past the corner (see Fig. 9.5b). Evidence published to date indicates that Gibbs' inequality applies in the presence of flow as it does under static conditions (Kistler and Scriven 1994), but further comparisons between computed predictions and experiments are needed to establish unequivocally under what conditions successful contact line pinning is independent of the

surrounding flow. In addition, care must be taken to account properly for the well-known contact angle hysteresis that afflicts static wetting on nonideal surfaces encountered in most coating devices (see Chapter 3). Hysteresis in static wetting line position may also arise from purely hydrodynamic effects, i.e. multiplicity of steady-state solutions (e.g., Kistler and Scriven (1994)). The latter can be predicted with suitable computational procedures, outlined in Section 9.2.4 and 9.2.7.

A special case arises at static separation lines of interfaces between two miscible fluids in multilayer coating. Because miscible fluids interdiffuse, an inter-layer forms that has no interfacial tension and, hence, a contact-angle boundary condition is inappropriate to locate the separation line. Scanlan (1990) enforced continuity in pressure across the interface where it intersects the solid as an additional condition to complete the equation set. Attempts to impose continuity of total stress have been less successful because deformation rates are very small near the separation line (Dheur and Crochet 1987; Scanlan 1990). A contact angle condition and an extrapolation of the interface to the solid surface have also been tried (Dheur and Crochet 1987), but both are *ad hoc* procedures that lack a physical basis. Away from the immediate proximity of the stagnation line, nonetheless, computed solutions appear to be insensitive to the particular boundary condition chosen (Dheur and Crochet 1987).

Another central mechanism in coating flows that requires particular attention in computer-aided analysis is dynamic wetting, the process by which the coating liquid displaces most of the air previously in contact with the substrate (for comprehensive reviews, see Chapter 3, and also Kistler (1993)). Assuming that the liquid/gas interface meets the solid surface at a wetting line where the advancing liquid completely displaces the receding air, conventional hydrodynamic continuum theory predicts a multivalued velocity that gives rise to a well-known, unphysical force singularity. In addition, when surface tension effects are significant, hydrodynamic theory requires that a contact angle be specified as a

boundary condition at the putative wetting line – even though apparent dynamic contact angles observed in experiments vary with coating conditions and, in complete theories, ought to be predicted variables. Worse yet, even if the proper value of the local contact angle were known, the singularity at the wetting line is so severe that the boundary condition for the angle cannot be satisfied in rigorous mathematical treatments.

To cope with the difficulties in modeling dynamic wetting, five distinct procedures have been adopted in finite-element codes for coating flows. The first restricts the analysis to conventional continuum theory at macroscopic length scales. It removes the multivalued velocity at the wetting line by *ad hoc* boundary conditions that allow perfect slip at the line (i.e., the liquid velocity at the wetting line is the same as that of the line) and partial slip nearby, and prescribes a contact angle that is supposed to represent an apparent dynamic contact angle of the sort observed in experiments, possibly taken from an empirical correlation. This approach is by far the most common and permits computed predictions of realistic coating configurations (e.g., Christodoulou and Scriven (1989)). However, the approach defeats a major purpose of performing computer-aided analysis, for it presupposes one of the most important aspects of the coating flow dynamics. The imposed angle can significantly affect the predicted flow state as well as its sensitivity and stability. Moreover, imposing an apparent dynamic contact angle can be more subtle than is commonly appreciated. When the mesh is refined to yield converged macroscopic solutions that are consistent with the local slip-flow problem posed, the angle of meniscus inclination at ‘visible’ distances from the solid may be different from that imposed at the putative wetting line (see Tilton (1988) for a case in point). The assumption of perfect slip at the wetting line leads to another disconcerting feature in computed coating-flow solutions, namely abrupt liquid deceleration immediately upstream of the wetting line. It is most likely unphysical and particularly consequential in simulations that seek to account for

the transport and influence of surface-active materials (Schunk (1989); see also Section 9.3.3 and Chapter 11d).

The second approach overcomes the need to specify perfect slip at the putative wetting line by exploiting the weak form of the Galerkin weighted residual equations which – in an *ad hoc* manner – can accommodate multi-valued velocities at dynamic wetting lines without catastrophic consequences for the flow nearby. The first attempt allowed multiple unknowns at the same node (Kistler 1984). More refined schemes collapse several nodes onto the same point (Schunk 1989; Christodoulou and Scriven 1990), a standard procedure in fracture mechanics to capture the stress singularity at crack tips (Bathe 1982). To accurately reproduce the multivalued velocity field and associated $1/r$ singularity in rate of strain at dynamic wetting lines, at least two elements ought to be collapsed, one at each side of the wetting line, and the pressure basis function must be modified to explicitly account for the $1/r$ pressure singularity (Christodoulou and Scriven 1990). Computed predictions suggest that the velocity along the free surface retains a nonzero value of 80–90% of the web speed down to the wetting line, in good agreement with the analytical ‘outer’ solution of Moffat (1964) and also experimental measurements (Mües, Hens and Boiy 1989). The dynamic contact angle, however, remains an empirical input parameter. Moreover, the use of collapsed elements to simulate a ‘rolling motion’ at a dynamic wetting line remains an *ad hoc* procedure, for it does not yield solutions that converge with systematic mesh refinement.

The third approach adheres to the use of standard, *ad hoc* boundary conditions at a putative contact line, i.e. prescribed contact angle and local slip flow, but imposes a sub-microscopic static angle rather than a macroscopic apparent one, uses a dimensionless slip length well below 0.001, and systematically refines the mesh to permit a local analysis that attributes dynamic variations in an apparent contact angle to viscous bending of the meniscus at length scales invisible by the naked eye or a low-power microscope (Lowndes 1980; Zhou and Sheng 1990; Kistler

and Zvan 1991); for an extended summary, see also Kistler (1993). Computed values of apparent contact angles (Zhou and Sheng 1990; Kistler and Zvan 1991) corroborate results from asymptotic theory (Voinov 1976; Cox 1986). Results from both types of analysis, in turn, agree with selected experimental data – at least up to $Ca \leq O(0.1)$ (Kistler 1993). Computed velocity fields for slide coating at $Ca \leq 0.16$ (Kistler and Zvan 1991) furthermore agree with laser-Doppler-velocimetry data for the acceleration of liquid toward the dynamic wetting line (Mües, Hens and Boiy 1989), even though the finite-element model insists on perfect slip at the line. Above $Ca \geq O(0.1)$, however, where many industrial coating processes operate, systematic deviations set in between computed and measured apparent dynamic contact angles. Thus, single-phase hydrodynamic theories with *ad hoc* assumptions at the wetting line cannot be relied upon to predict the impact of the macroscopic flow configuration (see also Chapter 3).

The fourth approach attempts to predict the impact of the macroscopic flow on apparent dynamic wetting behavior by restricting the analysis to high capillary numbers. In the limit $Ca \gg 1$, the interface cannot transmit the influence to the local wetting physics upstream, and apparent dynamic contact angles θ_D become dependent variables that can be computed without specifying a boundary condition for a local contact angle (Kistler 1984). Predicted flow conditions for curtain coating at which θ_D comes close to 180° , for example, agree qualitatively with those measured at the onset of catastrophic air entrainment (Kistler 1984); for further details, see also Chapter 11c. Nevertheless, the practical relevance of this limiting regime needs to be explored further.

The fifth approach seeks to resolve the submicroscopic physics of dynamic wetting. It incorporates a refined model for the local air displacement mechanism right into a macroscopic coating-flow computation, and thereby attempts to provide realistic boundary conditions for the macroscopic flow. In high-speed coating, entrainment and subsequent collapse of a thin layer

of air is a plausible mechanism (Miyamoto 1992); for more details, see also Chapters 3 and 11c. In steady-state flow calculations, it is easiest to ignore the likely collapse of the air film and restrict the simulation to steady, two-dimensional two-phase flow under the influence of Van der Waals and possibly electrostatic forces between a liquid and a smooth solid as well as compressibility and slip flow in a thin air layer. For slide coating, a preliminary analysis of this sort produced free-surface shapes which, at macroscopic length scales, appear to resemble those in realistic flows (Christodoulou and Scriven 1984). A complete analysis, however, would have to address stability and maybe three-dimensional surface topography. These are formidable challenges which, to date, have precluded quantitative predictions of apparent contact angles or critical air-entrainment velocities that agree with experimental data.

9.3.2 NON-NEWTONIAN LIQUID BEHAVIOR

Although much of the published literature on coating flows focuses on simple, Newtonian liquids, most liquids coated in industrial practice come in the form of particle suspensions, polymer solutions, polymer melts or other nonideal mixtures that exhibit significant non-Newtonian behavior. Moreover, even liquids that appear to be Newtonian when tested in conventional rheological equipment may exhibit nonlinear material responses when subjected to the very intense and highly localized shear, extension and mixed deformations that are characteristic of most coating flows. In slide and other bead coating devices, for example, shear rates easily reach 10^5 s^{-1} , and extension rates 10^4 s^{-1} (see, for example, Schunk and Scriven (1990)). Even in the comparatively slow dip coating process, surface tension gradients can induce shear rates in excess of 1000 s^{-1} (*cf.* Chapter 13).

Non-Newtonian liquid behavior can drastically alter the success or failure of a coating process, as is well established through experimental observation (see Chapters 5 and 12a for specific examples). However, designing suitable consti-

tutive models and incorporating them into realistic computer simulations remains one of the most prominent unresolved issues in computational coating-flow mechanics.

Almost all non-Newtonian coating formulations experience a reduction in viscosity with increasing shear rate, and most numerical studies of non-Newtonian coating flows have been limited to generalized Newtonian models for viscosity as a function of the second invariant of the rate of deformation tensor (*cf.* Chapters 2 and 5). The most useful example is perhaps the well-known Carreau equation (Bird, Armstrong and Hassager 1987) which adequately describes shear-dominated processing flows of suspensions and polymer solutions (Bird 1976). For liquids that exhibit solid-like behavior at very low deformation rates, a Bingham-type yield model may have to be used instead (Bird, Armstrong and Hassager 1987), or may be combined with the Carreau model at higher deformation rates (Nelson, Kistler and Olmsted 1990). The classical power-law model, which is a degenerate case of the Carreau equation, may sometimes be sufficient to capture the essence of shear-thinning viscosity behavior. It can cause difficulties, though, in flows with stagnant zones because the viscosity diverges where the shear rate vanishes. Contrary to a widely held belief (Coyle, Macosko and Scriven 1987; Pranckh and Scriven 1990), however, even the more sophisticated Carreau model and its relatives can run into serious if not catastrophic computational difficulties when naïvely solved with Newton's method (Tanner and Milthorpe 1983): in regions of low deformation rates, not viscosity but its higher-order derivatives with respect to deformation rate diverge – in violation of one of the necessary conditions for Newton's method to converge (*cf.* Dahlquist and Björk (1974)). A much more slowly converging successive substitution of a pseudo-Newtonian viscosity or other specialized iteration procedures are often the only recourse (Engelman 1982; Gartling and Phan-Thien 1984; Karagiannis *et al.* 1989), especially for small power-law indices or vastly different high- and low-shear viscosities. For liquids with a distinct yield point and associated

discontinuous material behavior, added computational complexities arise from the need to track yield surfaces, another form of free boundaries whose position is unknown *a priori* (Gartling and Phan-Thien 1984; Beris *et al.* 1985). In conventional finite-element algorithms, these complexities can be avoided in an *ad hoc* manner by replacing rigid plastic regions with a liquid of finite, but very high viscosity below a preset threshold in deformation rate (Bercovier and Engelman 1980), or by the use of a modified Bingham-type constitutive relation that approximates the transition from yielded to unyielded regions in a continuous manner (Papanastasiou 1987).

Many coating formulations, especially solutions including high-molecular-weight additives, exhibit a viscosity that not only falls as the rate of shear increases but also rises as the rate of extension increases. Viscosity rise in steady-state extension can be represented by an analogous Carreau equation (Fuller *et al.* 1987). Schunk and Scriven (1990) incorporated into a simulation of slide coating a constitutive equation that is a linear combination of a Carreau equation for shear thinning with the same type of equation for extension thickening. Their work suggests that such an inelastic constitutive equation may be able to account for certain extensional, elastic-like effects in dilute polymer solutions and other mildly viscoelastic coating formulations (*cf.* Hyun and Ballman (1978)), but quantitative verification of this conjecture is still outstanding.

For many coating liquids with measurable elasticity, realistic flow simulations will probably require complete viscoelastic constitutive models, which come in either differential or integral form (see, for example, Bird, Armstrong and Hassager (1987)). In spite of significant progress over the last decade, reviewed not too long ago by Crochet (1989) and Keunings (1989, 1991), incorporating viscoelastic models into computational fluid mechanics algorithms necessitates highly-specialized computational procedures that are still far from routine, even in the absence of free surfaces. Computational difficulties arise primarily from excessive approximation errors due to (1)

the formation of thin stress boundary layers; (2) non-integrable stress singularities from either physical features in the flow domain or the mathematical nature of the constitutive equation; (3) incompatibility of stress and velocity interpolants (failure to satisfy the LBB condition); and (4) the hyperbolic character of the governing equations and boundary conditions that are not compatible with the characteristics of the governing equations. These errors can lead to spurious bifurcations and turning points in the solution space, and also an artificial change of type of the discretized system that leads to a loss of the evolutionary character and Hadamard (short wave) instabilities (Crochet 1989; Joseph 1990; Keunings 1991). The difficulties become increasingly apparent – and challenging – as the natural relaxation time of the liquid rises in comparison to the characteristic time of the flow (the ratio between the two time scales is commonly referred to as the Deborah number; *cf.* Chapter 5). For integral constitutive equations, the difficulties are compounded by the need to trace the deformation history throughout the flow domain, which becomes especially involved for flows with recirculations.

Several recently developed algorithms are able to cope with at least some of these difficulties. One group of algorithms for differential viscoelastic models relies on a 4×4 sub-element interpolation of stress and non-consistent stream-line upwinding of the convective term of the upper-convective stress derivative (Marchal and Crochet 1987; Crochet and Legat 1992). Even though effective and successfully extended to free-surface flow problems (e.g., Dheur and Crochet (1989)), this scheme alters the constitutive equation by introducing artificial diffusivity and accuracy is limited to first order. In an alternative approach, King *et al.* (1988) were the first to directly address the issue of change of type by using an ‘explicitly elliptic’ form of the momentum equations (EEME) designed to maintain its elliptic character independently of the Deborah number (Rao and Finlayson (1991) suggested that the EEME form may not always prevent the catastrophic change of type and resulting loss of evolutionary character).

The EEME formulation was restricted to the upper convected Maxwell model, and is not easily extended to other differential models for viscoelasticity. The simplest way of regularizing the momentum equation to be strictly elliptic for a wide variety of differential constitutive models is to add the effect of a solvent viscosity. The method of choice for incorporating this effect into a computational algorithm, in turn, appears to be the so-called elastic-viscous split stress (EVSS) formulation of Rajagopalan and co-workers (1990, 1992). It divides the deviatoric stress into its elastic and viscous parts and thereby assures a dominant, explicitly elliptic operator on velocity in the momentum equations, even without added solvent effect. The EVSS formulation is also readily adopted to free surface flows (Rajagopalan *et al.* 1992). For special flow geometries amenable to spectral or pseudo-spectral expansions, a third approach capitalizes on the rapid convergence with increasing node number of such expansions to produce highly accurate and numerically stable predictions of viscoelastic flows (e.g., Pilitsis and Beris (1989)). In conjunction with domain decomposition into several large subdomains, spectral collocation methods can mimic the geometric flexibility of conventional finite-element methods while maintaining the superior accuracy so advantageous for viscoelastic flow computations (Souvaliotis and Beris 1992). To date, however, this approach has not been applied to viscoelastic free-surface flow. A fourth approach, finally, seeks to take advantage of the increased realism of integral constitutive models in describing complex rheological behavior, and thereby minimize computational difficulties (e.g., Papanastasiou, Scriven and Macosko (1987); Luo and Tanner (1988); Luo and Mitsoulis (1990)). The limitation to flows without recirculation of early algorithms with their streamlined elements (Papanastasiou, Scriven and Macosko 1987) can be overcome by decoupling the velocity and pressure calculation from the stress calculation in a Picard iteration scheme (e.g., Luo and Mitsoulis (1990); Rajagopalan, Armstrong and Brown (1993)). Contrary to the belief held by the early proponents, however, algorithms relying

on integral constitutive models are still susceptible to convergence difficulties and can be quite costly to execute. Hence, they do not necessarily offer a clear-cut advantage except for liquids that require a spectrum of relaxation times (Rajagopalan, Armstrong and Brown 1993).

For viscoelastic free-surface flows, currently available algorithms are most robust for ‘smooth’ flow configurations free of singularities such as wetting lines or even sharp corners. Examples most pertinent to industrial coating operations include rimming flow of a film in a rotating tube (Rajagopalan *et al.* 1992), flow and stability of a film down an incline (Salamon, Armstrong and Brown, 1992), and leveling of films after coating (Keunings 1986). As for viscoelastic free-surface flows with static contact lines, solutions to the die-swell flow of liquid emanating from a slot, tube, or other cross-section are abundant in the published literature (see Crochet (1989) and Keunings (1989) for extensive references). Unless obtained with one of the recent, numerically stable algorithms mentioned above, however, these solutions may not hold up to a test of convergence with mesh refinement. Worse yet, unless care is taken to ensure that the singular stress fields resulting from a particular constitutive model are consistent with the function spaces that can be represented by the finite-element approximation, the published solutions suffer from additional numerical artifacts, including spurious limit points (e.g., Rosenberg and Keunings (1991), Coates, Armstrong and Brown (1992)). For these reasons, computing viscoelastic coating flows with static contact lines is still at the forefront of current research. Viscoelastic flows with dynamic wetting lines – which involve singularities that are even more severe (see Section 9.3.1 and also Chapter 3) – have yet to be tackled in a satisfactory manner.

9.3.3 SURFACTANT SOLUTIONS – CONVECTIVE DIFFUSION EFFECTS

Coating solutions, especially aqueous systems such as photographic gelatins or pressure-sensitive adhesives, often contain a wide variety of surface

active components, commonly called surfactants. Small amounts of these materials usually serve as wetting agents, solubilizers, sensitizers, color formers and many other formulation purposes. Quite often, they are also added to enhance stability of the coating process (for further details, see Chapters 4 and 11d). Surfactants influence the coating flow dynamics by concentrating and adsorbing at liquid/gas interfaces, where they reduce capillary pressure by depressing surface tension and create interfacial shear stresses by inducing surface-tension gradients.

Accurate computational analysis of coating flows affected by surfactants requires not only a modified version of the interfacial traction condition (9.5) to include the dynamic surface tension effects, but also interfacial species balances and a bulk/interface equilibrium model to account for surfactant adsorption and transport along interfaces as well as changes in concentration due to interface expansion or contraction. It furthermore requires bulk transport equations to describe convection and diffusion of both monomer and aggregated micelle species, and kinetic models to account for the interchange of surfactant monomer between the bulk and micelles of various sizes. Chapter 11d, in conjunction with Chapter 4, lays out in detail all the requisite equations and boundary conditions. Fortunately, these equations can be solved together with the Navier–Stokes system by augmented standard finite-element techniques of the sort described in Section 9.2 above.

Apart from a much increased size of the computational problem, the main challenge added by surfactant effects arises from the extremely thin boundary layers in concentration that can develop next to free surfaces. Refining the discretization near free surfaces to equal level for all the unknowns is highly inefficient because solute diffusivities are much smaller than the kinematic viscosity of the liquid and, hence, concentration boundary layers are drastically thinner than momentum boundary layers. To avoid squandering computational work on unwarranted resolution of broad boundary layers in the flow field, Schunk (1989) devised a two-level

discretization technique to fit a finite-element mesh that is highly refined near free surfaces and responsible for resolving the convective diffusion field of the various species into a coarse mesh that suffices for the rest of the flow field. From a rigorous theory of affine deformation, Schunk derived a finite deformation dyadic and used it to compute deformations of the fine mesh in terms of those of the coarse mesh, the latter being tracked as part of the free-surface flow problem as described in Section 9.2.2. Interpolation of the velocity field onto the fine mesh and projection of the concentration fields onto the coarse mesh are readily accomplished via the finite-element basis function representation of the physical domain (i.e. the parametric mapping (9.15c)) and the dependent variables. With properly designed interpolation and projection, the efficiency of Newton's method can be retained for solving the free-surface flow and concentration field simultaneously in a few iterations. Several case studies in Chapters 11d and 13 attest to the power and effectiveness of the two-level discretization technique for complex free-surface flows that are strongly influenced by surfactant effects – and also solvent evaporation/condensation. Accurate predictions of the latter may require accounting of the coupled flow and species transport in both phases and the complete set of interfacial boundary conditions, as discussed in detail in Chapter 13.

9.3.4 ELASTOHYDRODYNAMICS COATING SYSTEMS

Quite a few industrial coating processes employ deformable members such as rubber covered rolls, flexible blades, inflated membranes and tensioned webs to control the coated film thickness in a self-metered configuration, or to lessen the sensitivity of the process to the mechanical precision of the coating machine (for further details, see Chapter 12c). The nonlinear mechanics that govern the deformation of many of these members and the elastohydrodynamic coupling between solid deformation and liquid flow add considerable complexity to the numerical simulation of coating processes.

To predict the effect of deformable roll covers – quite often made of elastomeric rubber – a further challenge is to come up with constitutive models and mechanical theories that accurately describe not only the resilience of the material to local indentation but also the deformations at one place on the roll surface due to loads acting at other places. The simplest models account only for purely elastic roll deformations, but systematic deviations from experimental data cast doubts on whether such models accurately capture physical reality (for a critical review see Coyle (1992) and also Chapter 12c). Models that have been tried in roll coating simulations include a one-dimensional Hookean model which amounts to a continuous distribution of linear springs (Coyle 1988; Carvalho and Scriven 1993); a neo-Hookean spring model, also one-dimensional but nonlinear to describe rubber and other elastomers better (Carvalho and Scriven 1993); a one-dimensional integral approximation for plane strain of a semi-infinite slab of Hookean material, which amounts to a two-dimensional and volume-conserving model (Carvalho and Scriven 1993); and a fully two-dimensional finite-element description of large plane strain of a curved layer of either Hookean or neo-Hookean material (Coyle 1990, 1992). These models were all solved together with Reynolds' equation for lubrication flow (see equation 12c.2)). With the exception of the integral representation for two-dimensional plane strain, however, the deformable-roll models are also readily incorporated into algorithms for fully two-dimensional free-surface flows, especially algorithms with elliptic or generalized algebraic mesh generation schemes to accommodate the additional free boundaries at the rubber–liquid interface(s), and Newton's method to cope with the nonlinearities from the elastohydrodynamic coupling. The computational challenge is considerably more formidable for finite-strain analysis of nonlinear viscoelastic solid materials, which may be necessary to describe adequately elastomeric roll-cover materials used in practice. Bapat and Batra (1984) performed such an analysis for the dry contact between a deformable and a rigid roll. Coyle (1990) attempted

to compute viscoelastic roll deformation coupled with lubrication flow, but ran into serious and as yet unresolved convergence difficulties.

Computations of coating flows with flexible blades, inflated membranes or tensioned webs are considerably more straightforward, provided the flexible members are thin compared with their radius of curvature and their deformation is not altered by creep or other not strictly elastic behavior. In that case, cylindrical shell theory applies (for full details, see Pranckh and Scriven (1990a, b, 1989)). It yields a set of differential equations that describe the position, curvature, and tension along deformable members (e.g. equations (12c.12) and (12c.13) in Chapter 12c). Pranckh and Scriven (1990a, b) recommend Galerkin/finite-element techniques to discretize these equations and thereby furnish the distinguished free-boundary equations in finite-element algorithms of the sort described in this chapter. Spurious oscillations, however, tend to arise when first-order equations such as (12c.12a) are approximated by Galerkin weighted residuals (as they do for the kinematic boundary condition, as mentioned in Section 9.2.1 above). Here, in the experience of one of us (SFK), simple centered differences provide a ready remedy. Special procedures, described in detail by Pranckh and Scriven (1989), are also needed at points where one deformable member separates from another, as does the trailing blade from the inflated membrane in membrane coating.

9.4 OTHER METHODS

9.4.1 ALTERNATIVE FREE-SURFACE PARAMETERIZATION AND MESH-GENERATION SCHEMES: FIXED-GRID ALGORITHMS AND FRONT TRACKING

Deforming-mesh algorithms of the sort described in Section 9.2 accurately resolve the position and shape of free boundaries. Hence, they are well-suited to predict steady, two-dimensional flows that make up many successful coating operations, and to assess sensitivity and stability of these flows to small two- and three-dimensional disturbances. With the algorithms published to

date, however, the topology of the flow field must be largely known *a priori*. Automated parameter-continuation or time-stepping procedures can follow only moderate variations in free boundary location. Large alterations in flow geometry require cumbersome remeshing procedures, and changes in domain connectivity – as might occur during start-up or break-up of a coating bead, for instance – are very difficult if not impossible to track. Similarly, generally applicable extensions to three dimensions of conventional algorithms are far from trivial to program and costly to execute.

Significant changes in flow topology, especially break-up or merging of fluid bodies, are more readily followed with so called fixed-grid algorithms that keep track of the position of irregularly shaped, moving interfaces on a fixed, rectangular grid that covers both regions occupied by fluid and regions filled with air or another immiscible fluid (for extended reviews, see Hirt and Nichols (1981); Hyman (1984); Oran and Boris (1987); and Floryan and Rasmussen (1989)). As far back as the early 1960s, free-surface flows of remarkable complexity have been simulated with finite-difference algorithms that solve the time-dependent Navier–Stokes equations on grids fixed in an Eulerian frame of reference (e.g., Harlow and Amsden (1971)).

Fixed-grid algorithms are typically quite simple. Many make use of explicit iterative schemes to update the discretized variables at each time step. Nevertheless, fixed-grid methods face several challenges for viscous free-surface flow analysis. The key challenge is to devise a scheme that monitors the position of the interfaces, and to design an algorithm that advances the interfaces as time progresses without spurious numerical diffusion. A second major challenge is the precise reconstruction of the local slope and curvature of the interface. And a closely related, third challenge is the accuracy with which the interfacial traction boundary condition (9.5) is satisfied.

9.4.1.1 Front capturing

In so called front capturing methods, the transition in fluid properties across moving fronts is

embedded as a steep gradient into the solution of the governing equations. No additional computational tool is introduced to identify the position of the fronts. Conventional front-capturing methods have been used with great success to locate shocks in compressible flows (e.g., Boris (1989)), for instance. In their simplest form, however, they are less well suited to follow material interfaces.

More recent, novel front capturing methods, on the other hand, show great promise for accurate representation of material interfaces, and should be tried for coating flow analysis. One such method defines the interfaces as a level set $\Psi = 0$ of a function that is advected according to a generalized Hamilton–Jacobi equation, viz. $\partial\Psi/\partial t + f|\nabla\Psi| = 0$, where f is the propagation speed normal to the interface (Osher and Sethian 1988). Simulations of complicated crystalline shapes in dendritic solidification (Sethian and Strain 1992) attest to the ability of the method to describe accurately intricate interfacial geometries. Level-set interface capturing would seem to be particularly attractive for capillary flows because it permits computing the local curvature without the need to reconstruct the interface (Osher and Sethian 1988). To date, however, Rayleigh–Taylor and Kelvin–Helmholz instabilities in compressible gas dynamics (Mulder, Osher and Sethian 1992) are the only free-surface flows to which the method has been applied.

9.4.1.2 Implicit volume tracking

Most common among fixed-grid algorithms are those that rely on interface tracking, i.e. they introduce additional computational devices to locate, on the fixed grid, interfaces between immiscible fluids. The earliest schemes employed implicit volume tracking via some marker quantity which monitors the interior motion of the fluids of interest rather than the interfaces. The position of the interfaces is not stored explicitly, but is reconstructed cell-by-cell whenever needed.

A prime example is the classical marker-and-cell (MAC) finite-difference method (Harlow and Welch 1965). It traces distinct fluids with

mass-less particles that are advected passively with the computed flow field. Some recent finite-element implementations do the same (e.g., Matsushiro *et al.* (1990)). The particles participate in the dynamics only in determining the position of the interface, which must be identified in cells that contain tracers of both fluids. The original particle-in-cell (PIC) method (Harlow 1964; Amsden 1966), in contrast, treats the particles as Lagrangian mass points. It is therefore a Lagrangian technique (see Section 9.4.2 below), even though it accounts for momentum and energy at cell centers of a fixed Eulerian grid.

More recent volume tracking schemes abandon the computationally costly marker particles in favor of a volume-fraction function which is taken to be $F = 1$ in cells occupied by the fluid of primary interest, $F = 0$ in cells outside or in another fluid, and $0 < F < 1$ in cells that contain the interface. In early implementations, such as the simple-line interface calculation (SLIC) algorithm of Noh and Woodward (1976), the fraction-of-cell-volume function is transported directly from cell to cell with a judiciously designed donor-acceptor scheme that maintains F as a step function as the computations advance in time. More recent implementations, the most prominent being the volume-of-fluid (VOF) method of Hirt and Nichols (1981), advect the function F with the flow – and hence the interface – by solving an auxiliary evolutionary equation, viz., $\partial F/\partial t + \mathbf{v} \cdot \nabla F = 0$. The interface is reconstructed from $F = 0.5$. To avoid spurious diffusion of F that would result from standard finite-difference discretization, a donor-acceptor flux approximation is again essential (Hirt and Nichols 1981). A related volume tracking scheme, based on the degree of filling around each vertex in a triangular mesh, is key in modern fixed-mesh finite-element simulations of injection molding (e.g., Wang and Lee (1989)). Other volume tracking schemes related to the VOF method employ a pseudo-concentration function ϕ that fills the empty regions with a second, fictitious fluid of negligible density (as first suggested by Nichols and Hirt (1975)) or viscosity (e.g., Thompson (1986)). Like the VOF method, such schemes

track the evolution of $\phi(x, y, t)$ by solving an auxiliary advection equation. Pseudo-concentration functions on fixed finite-element meshes are gaining popularity in mold-filling simulations (e.g., Dhatt, Gao and Ben Cheikh (1990); Reddy and Reddy (1991)), but have not been applied to visco-capillary flows of the sort found in coating processes.

Perhaps the biggest problem with implicit volume tracking is the need repeatedly to reconstruct the local position, slope and curvature of the interface. Numerous interface reconstruction schemes have been devised for a wide variety of applications (e.g., Noh and Woodward (1976); Chorin (1980); Hirt and Nichols (1981); Youngs (1982); Barr and Ashurst (1984); Sethian (1984); Chorin (1985); Liang (1991); Fatemi and Kistler (1992)). However, a robust and reliably accurate scheme for visco-capillary free-surface flows of the sort encountered in coating processes has not been advanced to date (Fatemi and Kistler 1992).

Many implicit volume-tracking algorithms furthermore rely on questionable *ad hoc* approximations of the dynamics near the interfaces, which makes them even less reliable for visco-capillary flows. The earliest algorithms merely set the pressure to its ambient value at the center of cells adjacent to the free surface, and forced the velocities at fictitious nodes outside the fluid to be equal to those inside (e.g., Harlow and Welch (1965)). Subsequent improvements sought to impose the pressure condition at the actual free-surface location (Chan and Street 1970; Nichols and Hirt 1971), account for normal stress contributions (Hirt and Shannon 1968; Nichols and Hirt 1971; Pracht 1971; Hill, Shook, and Esmail 1981) as well as capillary pressure due to a curved interface (Daly 1967; Nichols, Hirt, and Hotchkiss 1980, 1985; Liang 1991), and enforce a shear-free interface separately (Nichols and Hirt 1971). Boundary conditions for the total normal traction, however, still entered the equation set via a modified pressure in boundary cells. Sicilian and Hirt (1984) tried to impose the traction boundary condition by setting all velocity derivatives that involve discretized velocity

components outside the liquid to zero. It is unclear, however, how this *ad hoc* procedure can capture the impact of normal viscous stresses when they are important. Fatemi and Kistler (1992) more recently solved for the pressure in the boundary cells, treating the traction condition as a boundary condition for the discretized momentum equations rather than imposing it separately. They validated their formulation for an oscillating liquid cylinder in the limit controlled by capillarity, and for a viscous sheet in purely extensional flow in the limit dominated by normal viscous stresses.

Most early applications of fixed-grid algorithms with implicit volume tracking were aimed at simulating large-scale free-surface flows dominated by inertia, such as sloshing in tanks, breaking waves, splashing of low-viscosity drops, etc. For such flows, accurate resolution of the local interfacial shape is not as critical as for small-scale flows that are dominated by capillarity. Besides, explicit time-stepping procedures are ideally suited to simulate flows at elevated Reynolds numbers. Nevertheless, attempts have been published to apply conventional fixed-grid techniques with explicit time-stepping and implicit volume tracking to flows at low and moderate values of Re – some of interest in the context of coating. Hirt and Shannon (1968) used the teapot effect (*cf.* Chapter 11c) as a test case to validate their improved treatment of the normal stress boundary condition in a MAC algorithm, but failed to account for surface tension which plays a central role in controlling the deflection of a freely falling liquid sheet where it is being formed (Kistler and Scriven 1994). Harlow and Amsden (1971) also showed a computed prediction of the teapot effect, but did not comment on the details of the free-surface boundary conditions. Hill, Shook and Esmail (1981) employed a MAC-type algorithm to simulate viscous die swell for $4.2 < Re < 92.3$, and obtained surprisingly good agreement with experiments and standard finite-element predictions even though the swelling extended over less than one grid size. Golafshani (1988) successfully compared computed results for a highly viscous fluid draining from a

rectangular box with experimental observations. To overcome the problem of excessively small time steps demanded by explicit techniques for viscous flows, he modified the SOLA-VOF method of Hirt and Nichols (1981) to account for viscous stresses in an implicit manner as Pracht (1971) had done much earlier for the MAC method. Hirt *et al.* (1990) applied the commercial SOLA-VOF code FLOW-3D to analyze planar spin casting of metal melts, a process which resembles extrusion coating even though it occurs at $Re = O(1000)$ and involves solidification. McKibben and Aidun (1991), evidently unaware of the work by Hill, Shook and Esmail (1981), computed solutions of a two-dimensional jet emanating from a slot in an attempt to demonstrate that fixed-grid finite-difference codes with VOF-type volume tracking can yield predictions that compare favorably with results from finite-element algorithms of the sort expounded in Section 9.2. Like Hill and his co-workers, however, McKibben and Aidun excluded capillary pressure effects and considered only a single value of $Re = 300$ for which the jet contracts rather than swells as it does when viscous effects dominate. Miura and Aidun (1992) applied several versions of a VOF algorithm to simulate how pressure variations induced by flow instabilities in the pond of a short-dwell blade coater affect the uniformity of the coated film. They did not address the accuracy of their results, however. Fatemi and Kistler (1992) modeled the impingement region in curtain coating at $Ca = 1$ and $4 < Re < 10$ with their modified SOLA-VOF algorithm, and obtained good agreement with predictions from a conventional finite-element code (Kistler and Scriven 1983), especially for the interfacial shape and dynamic wetting line position.

Altogther, the simplicity of implicit volume tracking is very attractive, but algorithms currently available are not refined enough to routinely predict coating flows with accuracy comparable to that of state-of-the-art finite-element codes (Section 9.2). The crux remains the limited capability of implicit volume tracking to capture the details of the interfacial shape and to account for the full set of traction conditions. The

consequences of these shortcomings can be particularly grave in the vicinity of apparent singularities such as static separation lines, dynamic wetting lines, or sharply curved interfaces. Improving interface resolution via grid refinement is typically not a viable alternative with explicit time-stepping procedures because the largest step for which the algorithm is stable is dictated by the smallest grid spacing.

9.4.1.3 Explicit interface tracking

Many of the inherent difficulties of implicit volume tracking can be overcome by explicit interface tracking, which introduces computational elements that expressly describe the position and shape of interfaces, and store their values at each time step. Saving the position of an interface as a discrete set of heights above a reference line (Chan and Street 1970; Hirt, Nichols and Romero 1975) or plane (Nichols and Hirt 1973) is the most obvious choice but may, of course, become multivalued. More powerful procedures track the interface by an ordered chain of marker points (Daly 1967; Chan and Street 1970; Nichols and Hirt 1971; Glimm and McBryan 1985; Glimm *et al.* 1986, 1988) or line segments (Miyata 1986), and rely on arc-length to parameterize the local shape of the interface (Hyman 1984). Interfacial marker points are typically advected in a Lagrangian manner with the flow, and hence may have to be added or deleted in regions where they deplete or accumulate (Nichols and Hirt 1971; Glimm and McBryan 1985; Glimm *et al.* 1986, 1988). Between the points, the interface is approximated by interpolants, quite often simple straight-line segments (Nichols and Hirt 1971; Glimm and McBryan 1985; Glimm *et al.* 1986, 1988), but sometimes also more elaborate piecewise polynomials (Hyman 1984).

While conventional explicit interface tracking methods discretize the governing equations on a fixed finite-difference grid, Hyman (1984) described a local grid-adjustment procedure that moves each mesh point within one half spacing from the interface to the nearest horizontal or vertical location where the interface intersects a

grid line, and approximates the interface by the new cell edges or diagonals on a locally mildly distorted grid. Glimm and co-workers (Glimm and McBryan 1985; Glimm *et al.* 1986, 1988) advanced and refined a similar scheme in which an irregular, triangular finite-element mesh near the interface connects a lower-dimensional moving interface grid with an otherwise fixed rectangular mesh. Because the marker points along the interface advance with the fluid, Glimm's method can be classified as mixed Eulerian–Lagrangian (*cf.* Section 9.4.2). Similar schemes that blend local, deforming meshes near free boundaries with global, fixed finite-element meshes in the remainder of the computational domain have also been advocated by Couñot and Crochet (1986) and Tabata and Morishta (1989) for finite-element algorithms to solve mold filling problems. Applications of Glimm's method include compressible flows of stratified fluids (Chern *et al.* 1986) and saturation fronts advancing in porous media (Daripa *et al.* 1988). Viscous free-surface flows with surface tension have, regrettably, not been tackled to date. Fromm (1981, 1986), however, successfully analyzed several visco-capillary flows with a related algorithm that combines a fixed finite-difference grid with local surface coordinates to improve the resolution of the dynamics near the interface.

In comparison to implicit volume tracking, explicit interface tracking greatly improves the accuracy of the local interface representation, permitting sub-cell resolution if marker points are packed more densely than the fixed grid (the accuracy of the underlying dynamics is, of course, still limited by the cell size of the fixed grid). Advanced methods of explicit interface tracking (Glimm *et al.* 1988; Unverdi and Tryggvason 1992) – and also front capturing of the sort introduced in Section 9.4.1.1 (Osher and Sethian 1988) – improve furthermore the treatment of entangling interfaces and associated changes in topology. In particular, they are less likely to cause spurious entrapment of gas pockets within the liquid or breaking away of stray particles from the liquid, which both tend to plague conventional volume tracking schemes. For viscous

free-surface flows, moreover, explicit interface tracking algorithms with local grid adjustment are capable of incorporating the interfacial traction boundary condition without *ad hoc* approximations. Hence, they ought to match the accuracy of conventional finite-element formulations or other special-purpose methods, such as boundary-integral techniques, and deserve a more systematic evaluation for coating-flow analysis.

Unverdi and Tryggvason (1992) advanced a promising hybrid between explicit interface tracking and implicit front capturing that may also be attractive for coating flow calculations. Their algorithm relies on a special unstructured surface grid to monitor the kinematics of the interfaces through a fixed grid that is used to compute the fluid dynamics. The transition from one set of density and viscosity values to the other extends over a finite thickness of the order of one cell size of the fixed grid. The tracked interface transports the jump in fluid properties, which is approximated from the solution of Poisson-type equations, and thereby avoids spurious diffusion and interface oscillations, difficulties frequently encountered with conventional volume tracking algorithms. The algorithm implicitly accounts for the interfacial traction condition (9.5), yet permits the flow field to be advanced through the fixed Eulerian grid by a conventional, MAC-type finite-difference scheme without any special consideration for the interface – except for interfacial tension. The latter is incorporated as a body force distributed onto the fixed grid in a manner first proposed by Peskin (1977) to treat elastic boundaries in fixed-grid flow computations. Brackbill, Kothe and Zemach (1992) very recently proposed a similar ‘pseudo-continuum’ method to implement capillary pressure in fixed-grid algorithms which, in effect, mimics the molecular origin of surface tension.

In summary, sophisticated techniques for computing the motion of interfaces – such as the level-set technique (Osher and Sethian 1988) or hybrid interface tracking/front capturing schemes (Unverdi and Tryggvason 1992) – endow fixed-grid algorithms with the potential to predict reliably and accurately complicated coating flows that

are of practical interest, and should be advanced for that purpose. While such algorithms may offer no apparent advantage for the types of analysis performed so well by standard finite-element methods, they may make amenable to analysis coating flows which at present are difficult if not impossible to solve. Such flows include fully three-dimensional flows, flows for which there is limited *a priori* knowledge of feasibility, and flows in which the topology changes dramatically as, for instance, during start-up or catastrophic failure of a coating process.

9.4.2 ALTERNATIVE FORMULATIONS: LAGRANGIAN AND RELATED METHODS

9.4.2.1 Strictly Lagrangian methods

In an alternative class of numerical methods for simulating free-surface flows, the governing equations are formulated in their Lagrangian form and computational entities are employed that move with material points in the flow. Conventional finite-difference grids and finite-element meshes, as well as particle and vortex methods have been used to discretize the governing equations (see Donea (1983); Leonard (1985); Monaghan (1985); Oran and Boris (1987) and Floryan and Rasmussen (1989) for comprehensive reviews). Because the computational cells or particles always follow the same fluid material, Lagrangian methods are ideally suited for free-surface flows. The position of interfaces is tracked in a ‘natural’ manner without the need for explicit parameterization, and interfacial boundary conditions are readily imposed. Lagrangian methods are also particularly attractive for flows that are dominated by convection. In a frame of reference tied to the material, convective terms are absent and, hence, the methods avoid the spurious diffusion that typically arises from convective transport across grid boundaries in Eulerian algorithms. Unfortunately, Lagrangian methods have several drawbacks that have limited their application to viscous free-surface flows.

A major drawback arises from the topological restrictions inherent in Lagrangian grids. The

earliest schemes relied on strictly Lagrangian grids that retain a fixed connectivity structure and follow specific material elements throughout the computation (e.g., Hirt, Cook and Butler (1970)). Such grids become easily distorted, especially in flows with recirculations or large shear deformations, and are prone to yield large discretization errors. To avoid disastrous grid distortions, several strategies have been developed. The most common is remeshing, often also referred to as rezoning, which transforms the discretized variables on a distorted grid onto a more regular grid with the same connectivity structure. In continuous rezoning, the grid is adjusted in small increments after each time step (e.g., Hirt, Amsden and Cook (1974)); in general rezoning, larger grid adjustments occur intermittently after many time steps (e.g., Bach and Hassager (1985); Addessio *et al.* (1986); Rama-swamy (1990); Shopov, Minev and Bazhlekov (1992)). Unfortunately, rezoning adds much complexity and computational cost to the algorithms. In addition, rezoning requires interpolation of the discretized variables between two grids. It thereby reintroduces the spurious numerical diffusion in convection-dominated flows that Lagrangian methods seek to avoid in the first place. Nevertheless, a considerable amount of research has greatly improved the efficiency and accuracy of rezoning schemes (e.g., Margolin and Nichols (1983); Dukowicz (1984); Ramshaw (1985); Addessio *et al.* (1986); and Huh, Golay and Manno (1986)).

Perhaps the most robust counter to grid distortion problems in Lagrangian free-surface flow computations comes from methods that rely on grid reconnection, often also referred to as free-Lagrangian methods. These methods allow grid points to acquire new neighbors and thereby alter the mesh topology as the algorithm steps through time. Earlier schemes delete, add and reconnect grid points as the need arises (e.g., Crowley (1971); Fritts and Boris (1979); Crowley (1985); see also Fritts, Crowley and Trease (1985)). Current state-of-the-art schemes (e.g., Fritts, Crowley and Trease (1985); Fyfe, Oran and Fritts (1988); Muttin *et al.* (1991)) often make use of

completely unstructured Voronoi–Delaunay tessellations of the sort first proposed by Dukowicz (1981).

Most published applications of Lagrangian methods for free-surface flows focused on compressible and incompressible flows that are dominated by inertia (see Oran and Boris (1987); Floryan and Rasmussen (1989)). In the very first application of a strictly Lagrangian method, for instance, Hirt, Cook and Butler (1970) employed a finite-difference technique to analyze the Rayleigh–Taylor instability and sloshing in tanks, accounting for surface tension via an excess pressure applied along free surface segments. Lagrangian methods have also been applied to visco-capillary free-surface flows of the sort found in coating processes. In the most pertinent application, Bach and Hassager (1985) advanced a Lagrangian finite-element scheme with general rezoning to solve for the flow field and free surface shape in slide coating. The scheme retained the viscous and pressure terms in their Eulerian form and evaluated them iteratively at each time step, but treated the material/mesh coordinates as dependent variables as conventional Lagrangian schemes do. The results seem to agree with those from conventional finite-element analysis (Kistler and Scriven 1983). Bach and Villadsen (1984) had earlier used a similar scheme to analyze the wave motion in falling liquid films. Fyfe and collaborators (1988) successfully analyzed the effects of surface tension on viscous drop oscillations and capillary waves with a free-Lagrangian finite-difference algorithm. Muttin *et al.* (1991) simulated the filling stage of a die-casting process with a free-Lagrangian finite-element scheme. And Shopov and Bazhlekov (1991) used a Lagrangian finite-element algorithm with rezoning to solve several transient wetting problems.

All in all, Lagrangian methods have the potential to accurately predict realistic coating flows. Because of their inherent ability to track material fronts, Lagrangian methods are particularly well suited to simulate the start-up of coating processes, especially when automated grid reconnection schemes accommodate drastic changes in flow

topology. On the other hand, Lagrangian formulations by necessity produce initial-value problems. Hence, they are less attractive when the primary interest lies in steady-state solutions that are so fundamental in systematic coating flow analyses. The futility of Lagrangian methods is most severe when the steady states feature eddies of enclosed recirculations. From the applications published to date, it remains unclear how the computational burden from costly rezoning or reconnecting and subsequent interpolation schemes stacks up against the cost of conventional finite-element algorithms with deforming meshes. It is also unclear how to handle rapid mass transport across phase boundaries, which are no longer material surfaces (see Chapter 13 in this volume).

9.4.2.2 Arbitrary Lagrangian–Eulerian methods

To combine the advantages of accurate interface tracking and minimal mesh distortion that result from purely Lagrangian and Eulerian descriptions respectively, hybrid Lagrangian–Eulerian algorithms have been developed that let the mesh/grid points move independently of the kinematics of the coincident flow and formulate the governing equations in a frame-of-reference tied to the moving grid/mesh points. The grid/mesh movement is typically arbitrary and user-prescribed, falling between the two extremes of strictly Lagrangian formulations in which the grid is embedded in the fluid and moves with it, and purely Eulerian formulations in which the grid remains fixed in a laboratory frame. Such hybrid techniques, commonly referred to as arbitrary Lagrangian-Eulerian (ALE), began nearly twenty years ago as an outgrowth of Lagrangian finite-difference techniques with continuous rezoning (Hirt, Amsden and Cook 1974; Amsden, Ruppel and Hirt 1980). The latter are, in effect, ALE algorithms themselves, so can be Lagrangian algorithms with general rezoning (e.g., Wang and McLay (1986); Ramaswamy (1990)). More recently, numerous finite-element based ALE algorithms have been advanced (e.g., Belytschko (1980);

Hughes, Liu and Zimmerman (1981); Donea (1983); Huerta and Liu (1988); Hayes, Dannelongue and Tanguy (1991); Hurez, Tanguy and Bertrand (1991); Soulaimani *et al.* (1991); Tezduyar and co-workers (1992)) that seek to resolve moving interfaces accurately while maintaining acceptable element shapes, even for large deformations of the flow domain.

Even though many authors derive their ALE formulations for completely arbitrary referential kinematics (e.g., Hughes, Liu and Zimmerman (1981); Huerta and Liu (1988); Soulaimani *et al.* (1991)) and establish comprehensive strategies for mesh movement (e.g., Donea (1983); Huerta and Liu (1988)), most sample computations published along with the elaborate theories restrict the Lagrangian motion to free-surface nodes and move the internal modes with simple *ad hoc* procedures. The so called deforming-spatial-domain/space-time procedure of Tezduyar and co-workers (1992), which makes use of a space-time finite-element discretization but otherwise is closely related to conventional ALE algorithms, also confines the Lagrangian motion to nodes on the moving boundaries, often in the direction normal to the boundary. Similarly, most ALE algorithms for simulating materials processing flows (e.g., Hayes, Dannelongue and Tanguy (1991); Ahmed and Alexandrou (1992)) limit the Lagrangian description to the normal component of the velocity at the interface nodes; the other nodes are held fixed, but are updated after each time step with an unstructured remeshing scheme (Hayes, Dannelongue and Tanguy 1991) or a simple elliptic mesh-generation scheme (Ahmed and Alexandrou 1992). Hurez and collaborators (1990, 1991) use a time-stepping iterative strategy based on the kinematic boundary condition to compute steady-state free surface flows; they invoke an ALE-type description to account for the displacement of inner-mesh nodes that is needed to avoid severe element distortions near the free surface. Frank and Lazarus (1964) a long time ago proposed a technique akin to the ALE concept in which the coordinate system is Eulerian in one direction and Lagrangian in the other. This technique, in turn, is similar to what is

known as the streamlined finite-element method (Papanastasiou, Macsoko and Scriven 1985) in which the mesh deforms normal to material lines.

As may have become apparent from the foregoing discussion, many ALE algorithms are quite analogous to ‘standard’ finite-element algorithms that accommodate changes in free-boundary position with deforming meshes, as described in Section 9.2.2. Curiously, researchers devising ‘generalized’ ALE algorithms have uncovered the analogy only recently (e.g., Soulaïmani *et al.* (1991)). The reason may be that, for steady-state algorithms with either algebraic or elliptic mesh generation, the analogy may be subtle, for these algorithms solve what may be called free-boundary problems, whereas ALE algorithms most often seek to analyze transient moving-boundary problems. However, transient algorithms with deforming meshes are in essence ALE methods; the mesh moves with the flow normal to the interface, yet is adjusted independently of the flow kinematics otherwise. In fact, the additional term that arises from the transformation of the governing equations into a moving frame of reference (Hughes, Liu and Zimmerman 1981; Huerta and Liu 1988; Soulaïmani *et al.* 1991) is equivalent to the extra term that arises from the time-dependent isoparametric mapping (9.16) in conventional finite-element algorithms (see Lynch (1982) and Khesghi and Scriven (1984)). When the Lagrangian description is restricted to a single, Cartesian direction that is nearly normal to the interface, and a simple algebraic procedure is deployed to adjust the mesh underneath – as is so often the case (e.g., Hughes, Liu and Zimmerman (1981); Huerta and Liu (1988); Soulaïmani *et al.* (1991)) – the much touted ALE approach boils down to nothing more than a classical Monge representation of the sort used in the earliest finite-element methods for free-surface flows (see Nickell, Tanner and Caswell 1974).

The earliest applications of ALE algorithms for free-surface flows addressed fluid/structure problems (e.g., Belytschko (1980); Donea (1983)). More recently, however, free-surface flows have been tackled that are of interest in conjunction with

coating processes, such as wave propagation on liquid layers (e.g., Hughes, Liu and Zimmerman (1981); Ramaswamy (1990); Tezduyar *et al.* (1992)), die swell with static separation lines (e.g., Hurez, Tanguy and Bertrand (1991)), or mold filling flows with dynamic wetting (e.g., Wang and McLay (1986); Hayes, Dannelongue and Tanguy (1991); Ahmed and Alexandrou (1992)). Hurez and Tanguy (1990) solved for a coating flow proper, namely dip coating of Newtonian and Bingham fluids.

Even though they are potentially quite powerful, ALE-type algorithms share many similarities with conventional time-dependent finite-element algorithms for viscous free-surface flows, and it remains unclear what their distinct advantages are for coating flow analysis. The robustness of ALE algorithms hinges entirely on the ability of the user to construct an automated rezoning scheme that maintains the regularity and orthogonality of the computational mesh yet allows significant distortions of the fluid boundaries. For complicated flow geometries, this task is no less formidable than the design of deforming-mesh schemes in conventional formulations (see Section 9.2.2). Nevertheless, the ability of certain ALE algorithms to rely on completely unstructured meshes (e.g. Sackinger, Schunk and Rao (1996)) deserves further examination, especially for simulating start-up and break-up of coating beads.

9.4.2.3 Other Lagrangian methods

For the sake of completeness, this section briefly mentions two additional Lagrangian methods which are intriguing but, at present, have no practical use for coating flow analysis. Particle methods simulate fluid flow with discrete particles whose interactions are designed to mimic, in a collective statistical average, continuum behavior. While older algorithms – such as the classical particle-in-cell (PIC) method (Harlow 1964; Amsden 1966), see also Section 9.4.1 – rely on a fixed Eulerian grid to account for macroscopic dynamic variables, more recent versions abandon the mesh concept altogether and use particle differencing schemes to simulate mathematical operators and Simpson’s rule to perform inte-

grations (Monaghan 1985). Particle methods readily track different materials, even for large distortions. However, they are prone to suffer from statistical fluctuations, fail to accurately describe the interfacial shape, and remain unproven for incompressible viscous flows (see Monaghan (1985) for a comprehensive review).

Vortex methods follow the evolution of localized vorticity fields in incompressible high-Reynolds-number flows with a large set of discrete parcels of vorticity (see Leonard (1985) for an excellent overview). These methods are capable of very precisely tracking moving boundaries with interfacial tension (e.g., Tryggvason (1988)). Unfortunately, however, vortex methods cannot be made accurate for the viscous flow regime typically encountered in coating processes.

9.4.3 ALTERNATIVE DISCRETIZATIONS: FINITE-DIFFERENCES AND SPECTRAL-ELEMENTS

9.4.3.1 Finite-difference and finite-volume methods

Even though finite-element techniques have several distinct advantages for coating-flow analysis, as outlined in Section 9.1 and documented in Section 9.2, finite differences and finite volumes can also be used to discretize the governing equations. Indeed, finite differences are standard in most fixed-grid algorithms (see Section 9.4.1), and are preferred in many Lagrangian and ALE codes (see Section 9.4.2). In the last decade, several finite-difference and finite-volume formulations have also been advanced that seek to emulate essential aspects of standard finite-element formulations, in particular the use of grids that deform in response to changes in free-surface location. Some insist that the curvilinear grid be orthogonal (e.g., Dutta and Ryan (1982); Ryskin and Leal (1984); Dandy and Leal (1989)). Others employ nearly orthogonal, boundary-fitted grids generated with elliptic methods (e.g., Esmail and Markov (1989); Liu, Yu and Chen (1991)), as first introduced by Thompson and co-workers (1974, 1982), or rely on simple algebraic coordinate stretching (e.g., Christov and Volkov (1984); Loh

and Rasmussen (1987); Shokoohi and Elrod (1987); Ahn and Ryan (1991)). Most formulations map the deformed flow domain onto a rectangular computational domain, modify the governing equations to account for the mapping and, in steady-state computations, update the free-boundary location by a Picard-type scheme in which the mapping is recomputed after each iteration step. Dandy and Leal (1989) abandoned this inefficient successive approximation scheme in favor of Newton's method. They also adopted advanced techniques for computer-aided analysis of nonlinear systems to track solution families with arc-length continuation (*cf.* Section 9.2.4) and thereby demonstrated that, in many ways, finite-difference methods for viscous free-surface flows can be made to match the capabilities of finite-element methods.

Still, published applications of finite-difference algorithms with mapping of a deforming grid onto a fixed rectangular grid have been restricted to flow geometries that deviate only moderately from standard shapes, such as a circle or rectangular strip. The most prominent case studies include rising bubbles (Christov and Volkov 1984; Ryskin and Leal 1984; Dandy and Leal 1989), die swell (Dutta and Ryan 1982; Ahn and Ryan 1991; Liu, Yu and Chen 1991), break-up of a jet (Shokoohi and Elrod 1987), and flow in cavities with a free surface driven by one of the vertical walls moving downward (Loh and Rasmussen 1987; Esmail and Markov 1989). Durst *et al.* (1991) applied a finite-volume scheme to analyze the flow in slot coating (for specific results, see Chapter 11a).

Evidently, finite-difference or finite-volume methods can be furbished to the point where they predict practically relevant coating flows. No clear-cut advantages are apparent, however, over well-established finite-element methods. A distinct disadvantage of finite-difference methods arises from the need to impose boundary conditions at the free surfaces explicitly, which requires tedious programming. In addition, incorporating the coordinate transformations into the governing equations is more complicated than the iso-parametric or sub-parametric map-

ping which finite-element basis functions provide in a straightforward manner.

9.4.3.2 Spectral-element methods

The spectral-element method seeks to combine the geometric flexibility of finite elements with the potential for improved accuracy that arises from the rapid convergence of delocalized spectral expansions (Patera 1984; Maday and Patera 1989). The method divides the computational domain into a few subdomains, or spectral elements, each supporting a tensor product of polynomial basis functions of high degree (typically 5 to 15) to approximate the flow variables. As in finite-element methods, iso-parametric mapping conveniently describes the shape of distorted spectral elements that are needed to accommodate complex flow geometries, and a variational formulation together with Gauss-type quadrature generates a discretized equation set. To apply the spectral-element method to viscous free-surface flows, Ho and Patera (1990) introduced an ALE-type description that tracks the evolution of the free-surface with a mesh whose motion is tied to the fluid velocity normal to the free surface. They also advanced an iterative solution scheme that is implicit in the treatment of the pressure and viscous elliptic components of the Navier–Stokes equations, yet explicit in the treatment of the convective operators and the coupling of all the operators with the time-dependent flow geometry (see also Section 9.2.9).

Ho and Patera (1990) focused their analysis on the stability of falling liquid films in two dimensions. Later, they extended their algorithm to fully three-dimensional free-surface flows (Ho and Patera 1991), and illustrated its capabilities with a transient analysis of the stability of an initially axisymmetric film. Johnson *et al.* (1991) applied a commercial version of the algorithm (NEKTON) to verify an integral film-flow model for the growth of unduloids in an annular film lining a cylindrical tube. Recently, the software package has been applied to a variety of coating flows, producing results that compare favorably with earlier finite-element predictions (Grald *et al.* 1994).

Spectral-element algorithms are potentially quite powerful for the analysis of realistic coating flows. They may be particularly attractive for three-dimensional flows with inherent periodicity in at least one direction (see, for example, Fig. 12a.12 in Chapter 12). However, in spite of the advertised efficiency of preconditioned conjugate-gradient iterative schemes (Ho and Patera 1991), the cost-effectiveness of high-order spectral basis function remains to be verified by direct comparison with low-order finite-element polynomials, especially for three-dimensional flows. A potential problem with spectral-elements is their inherent inability to capture local singularities without spurious influences on a large part of the computational domain. This difficulty, especially critical at wetting lines, can apparently be overcome by confining the size of spectral element that includes the singularity to a small neighborhood of the singularity (Grald *et al.* 1994). However, no expedient exists for steep gradients in the flow field internal to the domain at unknown locations.

9.4.4 BOUNDARY INTEGRAL TECHNIQUES

Discretization of the entire flow-domain of interest can be avoided altogether for potential flows (Longuet-Higgins and Cokelet 1976) and creeping flows (Youngren and Acrivos 1976). In these limiting regimes, the governing equations are linear and their fundamental singular solutions – which, for Stokes flow, were first derived by Ladyzhenskaya (1963) – can be used to reduce a general n -dimensional problem to one or several $(n - 1)$ -dimensional integral equations. A solution to a particular flow problem results when the integral equations are combined with the boundary conditions and solved by a finite-element or other standard collocation technique. This approach, known as the boundary-element method, requires discretized values of the unknowns, such as velocity or traction forces, along the boundaries. At any point within the flow domain, the flow variables can be calculated by quadrature in a post-processing step. Even though the method necessitates nontrivial integral evaluations and leads to dense coefficient matrices, it

has the potential of reducing the computational cost because of the comparatively small size of the resulting matrix system.

Boundary-element methods are particularly well suited for free-surface flows, for the boundary discretization readily tracks large interface distortions without loss of accuracy. The interfacial velocity is calculated directly and the traction condition, including capillary pressure, is easily incorporated into the integral equations (Tanzosh, Manga and Stone 1992). Most algorithms for steady-state computations avoid the nonlinearity associated with the free surface by successive substitution, relying on the kinematic boundary condition (e.g., Tran-Cong and Phan-Thien (1988)), the normal-stress condition (e.g., Kelmanson (1983); Lu and Chang (1988)), or even the shear-stress condition (Yuan and Ingham 1991) to update the shape of the boundary. As in conventional finite-element algorithms, each distinguished condition has its own, limited range of convergence. Pozrikidis (1988) was the first to solve the distinguished boundary condition simultaneously with the integral equation(s), using Newton's method. Boundary-element algorithms for transient free-surface flows typically employ an iterative procedure that calculates the surface velocities for a temporarily fixed shape and advances the surface in time via the kinematic boundary condition (e.g., Lee and Leal (1982); Geller, Lee and Leal (1986)). Yiantios and Higgins (1989) attempted to incorporate the kinematic boundary condition into a fully implicit scheme using Newton's method.

Boundary-element methods have been applied to a wide variety of viscous free-surface flow problems. Among the most frequently studied ones are the deformation of drops and bubbles (for a comprehensive overview, see Tanzosh, Manga and Stone (1992)) and two- and three-dimensional extrusion flows (e.g., Bush and Tanner (1983); Kelmanson (1983); Tran-Cong and Phan-Thien (1988)). Case studies relevant to coating processes have been rather limited, addressing the effect of isolated and periodic corrugations on the two-dimensional film flow down an inclined slide (Pozrikidis 1988; Hansen 1991); the three-

dimensional film-flow disturbance generated by an isolated, small particle arrested on an inclined slide (Pozrikidis and Thoroddsen 1991); the profile of a film formed with a slot coater (Yuan and Ingham 1991); dip coating, especially the extremely slow and delicate application of Langmuir–Blodgett films (see Chapter 13); and the plunging of a liquid film into a pool as may be found in certain roll-coating configurations (Hansen 1987; Geonaga and Higgins 1990).

In spite of its many attractive features, the boundary-element method is rarely applied to realistic coating flows. The primary reason is the method's ineffectiveness in dealing with nonlinearities within the flow domain. Bush and Tanner (1983), for instance, attempted to account for inertia effects via a modified body-force term, but their iterative procedure failed at Reynolds numbers larger than 10. Viscoelastic effects in two- and three-dimensional extrusion problems have been handled in a similar manner (Bush, Milthorpe and Tanner 1984; Tran-Cong and Phan-Thien 1988). Treating nonlinear effects via an effective body force requires domain-internal discretizations which defeat the main purpose of using a boundary-integral technique. The main forte of the boundary-element method remains therefore its ability to accurately resolve intricate interfacial shapes in creeping flows while economically concentrating the computational effort where it is most needed. For coating processes, the method is probably most applicable to local analysis of small-scale flow features around particles and bubbles (e.g., Geller, Lee and Leal (1986); Pozrikidis and Thoroddsen (1991)), wetting lines (e.g., Goodwin and Homsy (1991)), apparent singularities in the interface (Geonaga and Higgins 1990) or the like – possibly matched to conventional finite-element analyses of the large-scale flows surrounding the local feature.

9.5 RETROSPECTIVE AND OUTLOOK

To date, the most comprehensive computational analyses of coating flows – and of viscous free-surface flows in general – rely on sophisticated Galerkin/finite-element methods, applied on

moving boundary conforming grids. The last 10 to 15 years have seen several significant advances in the capabilities of these methods. Novel elliptic mesh generation techniques and even some generalized algebraic schemes are sufficiently flexible for discretizing very complicated coating-flow configurations. Once set up for a particular flow, the resulting meshes are quite robust for tracking significant changes in position and shape of the free boundaries with minimal user interference. In combination with Saad's (1989) iterative Arnoldi algorithm, specialized preconditioning techniques are efficient for computing the few most dangerous modes of the generalized unsymmetric eigenproblem to which linear, finite-element based stability analysis reduces. Critical-point-tracking locates turning and bifurcation points at which the stability of the computed flow changes without the need for trial and error procedures and at a computational cost only a few times higher than that of calculating a simple steady operating state. Methods of computer-aided sensitivity analysis very effectively and systematically probe the frequency response of stable coating flows to small-amplitude, oscillatory disturbances that are invariably omnipresent in practical coating operations. And state-of-the-art time integrators for systems of differential-algebraic equations are available (e.g., DASSL, DASPK), should the transient response of a viscous free-surface flow to large disturbances be of interest.

Altogether, advanced finite-element methods can predict much of what a coating engineer is interested in: they reveal a wealth of detail and insight into the physical mechanisms that control the two-dimensional flow in successful coater operation; they assess the stability of the computed flow states, including modes that produce oscillatory and three-dimensional flow states; they systematically map out stability limits that delineate operability windows; and they quantify susceptibility of successful coating flows to external disturbances and thereby identify quality windows.

Unfortunately, many of the advanced methods are highly specialized to a limited class of coating flows (e.g., photographic precision coating) and are accessible only to a selected few experts,

mostly those who have developed the codes. To become more generally applicable and more accessible to non-expert users, the methods ought to be improved in several directions. For instance, automated mesh generation algorithms are needed that decide on an optimal sub-division of the flow domain into a few quadrilateral macro-elements and, if necessary, adjust their topology during a simulation; handle the complex data structures that describe the connectivity between macro-elements and between finite elements in complex flow geometries; refine the tessellation in regions of steepest and most rapidly changing gradients; and extend all these capabilities to three-dimensional flows with free and unknown boundaries. Much work would also have to be done to provide robust algorithms for stability, operability and sensitivity analysis that are applicable to a wide range of coating configurations. More research is also needed in finding consistent initial conditions for transient systems of index two and higher that are usually encountered in fluid mechanics and control theory; and in more accurately estimating and controlling time discretization errors. Finally, coating flow computations should be more cleverly combined with sophisticated optimization methods.

Existing finite-element methods for coating-flow analysis should also be improved in their computational efficiency. Even though still under development, iterative matrix methods hold great promise to speed up the solution of the large linear systems of equations that result from Newton's methods in steady-state and transient analyses, preconditioning techniques so useful for linear stability analysis, and critical point tracking and sensitivity analyses which further augment the size of the system. Speed-up of the solution process is especially needed for analysis of 3D flows of realistic size, or 2D flows susceptible to 3D instabilities, and would also be crucial for achieving real-time integration in transient analysis for on-line process control purposes. For the latter, the benefits of semi-implicit time integration should also be investigated more systematically.

For certain coating-flow problems, finite-element techniques on deforming meshes may

not even be the best choice. Free-surface flows that undergo dramatic variations in free boundary shape or changes in topology are much easier handled by fixed-grid methods or free Lagrangian methods. These methods are also very attractive when little is known *a priori* about the flow geometry. Both methods have seen considerable advances in the last 10–15 years, and should be revisited for coating flow simulations. Spectral-element techniques may also offer advantages, especially for 3D periodic flows and deserve consideration as well.

Currently available methods for computational coating-flow analysis fall furthermore short in their ability to account satisfactorily for essential physical mechanisms. Most importantly, no computational technique advanced to date reliably predicts the important high-speed coating limit that arises from excessive air-entrainment, or the dynamic contact angles observed at lower speeds. This shortcoming, however, is not as much computational as it stems from the lack of a well-developed theory of the sub-microscopic air displacement process that constitutes dynamic wetting. Computing coating flows of highly non-Newtonian liquids also remains a formidable challenge, in spite of considerable progress in modeling viscoelastic flows in general. This precludes an accurate analysis of many industrially relevant coating systems. Species transport and interfacial mass transfer, electrostatic forces, magnetic forces, or even long-range fluid–solid interaction forces are more readily included in coating flow simulations, but are not as commonly accounted for as they probably should be.

Finally, extending coating process simulations to predict essential characteristics of the final coated product remains largely uncharted territory. Chapter 13 in this volume leads the way for the special case of sol-gel systems that are dominated by evaporation of volatile solvents, but much work remains to be done to compute particle migration and orientation in coating and drying; diffusion, phase behavior, chemical reactions and stress build-up during drying and/or cure of the films; and many other phenomena that may influence not only physical properties such as

micro-structure, porosity, or surface texture but, more importantly, ultimate performance of the coating in its intended function.

REFERENCES

- Abbott, J. P. 1978. An efficient algorithm for the determination of certain bifurcation points. *J. Comput. Appl. Math.* **4**: 19–27.
- Addessio, F. L., Carroll, D. E., Dukowicz, J. K., Harlow, F. H., Johnson, J. N., Kashiwa, B. A., Maltrud, M. E. and Ruppel, H. M. 1986. CAVEAT: a computer code for fluid dynamics problems with large distortion and internal slip. *Los Alamos National Laboratory Report*: LA-10613-MS.
- Ahmed, A. and Alexandrou, A. N. 1992. Compression molding using a generalized Eulerian–Lagrangian formulation with automatic remeshing. *Adv. Polym. Technol.* **11**: 203–211.
- Ahn, Y. C. and Ryan, M. E. 1991. A finite-difference analysis of the extrudate swell problem. *Int. J. Numer. Meth. Fluids.* **13**: 1289–1310.
- Amsden, A. A. 1966. The particle-in-cell method for the calculation of the dynamics of compressible fluids. *Los Alamos Scientific Laboratory Report*. LA-3466.
- Amsden, A. A., Ruppel, H. M. and Hirt, C. W. 1980. SALE: A simplified ALE computer program for fluid flow at all speeds. *Los Alamos Scientific Laboratory Report*. LA-8095.
- Anturkar, N. R., Papanastasiou, T. C. and Wilkes, J. O. 1991. Stability of coextrusion through converging dies. *J. Non-Newt. Fluid Mech.* **41**: 1–25.
- Aston, B. M. and Thomas, J. W. 1982. An implicit scheme for water wave problems. *Appl. Math. Comput.* **10-11**: 809–818.
- Babuska, B. 1971. Error bounds for finite element method. *Numer. Meth.* **16**: 322–333.
- Bach, P. and Hassager, O. 1985. An algorithm for the use of the Lagrangian specification in Newtonian fluid mechanics and applications to free-surface flow. *J. Fluid Mech.* **152**: 173–190.
- Bach, P. and Villadsen, J. 1984. Simulation of the vertical flow of a thin, wavy film using a finite-element method. *Int. J. Heat Mass Trans.* **37**: 815–827.
- Bapat, C. N. and Batra, R. C. 1984. Finite plane strain deformation of nonlinear viscoelastic rubber-covered rolls. *Int. J. Numer. Meth. Eng.* **20**: 1911–1927.
- Barr, P. K. and Ashurst, W. T. 1984. An interface scheme for turbulent flame propagation. *Sandia National Laboratories Report*. 82-8773.
- Bathe, K.-J. 1982. *Finite Element Procedures in*

- Engineering Analysis*. Englewood Cliffs, NJ: Prentice Hall.
- Behrens, R. A., Crochet, M. J., Denson, C. D. and Metzner, A. B. 1987. Transient free-surface flows: motion of a fluid advancing in a tube. *AICHE J.* **33**: 1178–1186.
- Belytschko, T., Kennedy, J. M. and Schoeberle, D. F. 1980. Quasi-Eulerian finite-element formulation for fluid-structure interaction. *ASME J. Pressure Vessel Technol.* **102**: 62–69.
- Bercovier, M. and Engelman, M. S. 1980. A finite element method for incompressible non-Newtonian flow. *J. Comput. Phys.* **36**: 313–326.
- Beris, A. N., Tsamopoulos, J. A., Armstrong, R. C. and Brown, R. A. 1985. Creeping motion of a sphere through a Bingham plastic. *J. Fluid Mech.* **158**: 219–244.
- Bird, R. B. 1976. Useful non-Newtonian models. *Ann. Rev. Fluid Mech.* **8**: 13–26.
- Bird, R. B., Armstrong, R. C. and Hassager, O. 1987. *Dynamics of Polymeric Liquids – Volume 1: Fluid Dynamics*, 2nd edn. New York: Wiley.
- Bixler, N. E. 1982. Stability of coating flow. PhD thesis, University of Minnesota, Minneapolis.
- Boris, J. P. 1989. New directions in computational fluid dynamics. *Ann. Rev. Fluid Mech.* **21**: 345–385.
- Brackbill, J. U., Kothe, D. B. and Zemach, C. 1992. A continuum method for modeling surface tension. *J. Comput. Phys.* **100**: 335–354.
- Brackbill, J. U. and Saltzman, J. S. 1982a. Adaptive zoning for singular problems in two dimensions. *J. Comput. Phys.* **46**: 342–368.
- Brackbill, J. U. and Saltzman, J. S. 1982b. Applications and generalizations of variational methods for generating adaptive meshes. *Appl. Math. Comput.* **10-11**: 865–884.
- Brandt, A. 1977. Multi-level adaptive solutions to boundary-value problems. *Math. Comput.* **31**: 333–390.
- Brezzi, F. 1974. On the existence, uniqueness and approximation of saddle point problems arising with Lagrange multipliers. *RAIRO, Serie Rouge. 8 R-2*: 129–151.
- Brooks, A. N. and Hughes, T. J. R. 1982. Streamline upwind Petrov–Galerkin formulations for convection dominated flows with particular emphasis on the incompressible Navier–Stokes equations. *Comput. Meth. Appl. Mech. Eng.* **32**: 199–259.
- Burket, R. S., Conaghan, B. F. and Hirshburg, R. I. 1984. Coating method. US Patent 4,443,504.
- Bush, M. B., Milthorpe, J. F. and Tanner, R. I. 1984. Finite element and boundary element methods for extrusion computations. *J. Non-Newt. Fluid Mech.* **16**: 37–51.
- Bush, M. B. and Tanner, R. I. 1983. Numerical solution of viscous flows using integral equation methods. *Int. J. Numer. Meth. Fluids.* **3**: 71–92.
- Bussmann, H., Hoffmann, H. and Beck, D. 1992. Frequency response in slide coaters: FE calculations and measurements. Paper read at *AICHE Spring National Meeting*, New Orleans, LA, March 29–April 2.
- Carey, G. F., Wang, K. C. and Joubert, W. D. 1989. Performance of iterative methods for Newtonian and generalized Newtonian flows. *Int. J. Numer. Meth. Fluids.* **9**: 127–150.
- Carvalho, M. S. and Scriven, L. E. 1993. Effect of deformable roll cover on roll coating. In *Proc. 1993 TAPPI Polymers, Laminations and Coatings Conference*, Chicago, IL, August 29–September 2, Book 2, pp. 451–460. Atlanta, GA: TAPPI.
- Chan, R. K.-C. and Street, R. L. 1970. A computer study of finite-amplitude water waves. *J. Comput. Phys.* **6**: 68–94.
- Chern, I.-L., Glimm, J., McBryan, O., Plohr, B. and Yaniv, S. 1986. Front tracking for gas dynamics. *J. Comput. Phys.* **62**: 83–110.
- Chorin, A. J. 1980. Flame advection and propagation algorithms. *J. Comput. Phys.* **35**: 1–11.
- Chorin, A. J. 1985. Curvature and solidification. *J. Comput. Phys.* **58**: 472–490.
- Christodoulou, K. N. 1990. Computational physics of slide coating. PhD thesis, University of Minnesota, Minneapolis.
- Christodoulou, K. N., Scofield, D. F. and Scriven, L. E. 1990. Stability of multilayer coating flows to three-dimensional disturbances. Paper read at *AICHE Spring National Meeting*, Orlando, FL, March 18–22.
- Christodoulou, K. N. and Scriven, L. E. 1984. The physics of slide coating, dynamic wetting, and air entrainment. Paper read at *AICHE Annual Meeting*, San Francisco, CA, November 25–30.
- Christodoulou, K. N. and Scriven, L. E. 1988. Finding leading modes of a viscous free surface flow: an asymmetric generalized eigenproblem. *J. Sci. Comput.* **3**: 355–406.
- Christodoulou, K. N. and Scriven, L. E. 1989. The fluid mechanics of slide coating. *J. Fluid Mech.* **208**: 321–354.
- Christodoulou, K. N. and Scriven, L. E. 1990. Singular elements at dynamic wetting lines (unpublished).
- Christodoulou, K. N. and Scriven, L. E. 1992. Discretization of free surface flows and other moving boundary problems. *J. Comput. Phys.* **99**: 39–55.
- Christov, C. I. and Volkov, P. K. 1984. Numerical

- investigation of the steady viscous flow past a stationary deformable bubble. *J. Fluid Mech.* **158**: 341–364.
- Chung, K. Y. 1985. Shape optimization and free boundary problems with grid adaptation. PhD thesis, University of Michigan.
- Cliffe, K. A. 1983. Numerical calculations of two-cell and single-cell Taylor flows. *J. Fluid Mech.* **135**: 219–233.
- Cliffe, K. A. and Spence, A. 1984. The calculation of high-order singularities in the finite Taylor problem. In *Numerical Methods for Bifurcation Problems*, Intl. Series Numer. Math., Vol. 70, ed. T. Kuepper, H. D. Mittelmann and H. Weber, pp. 129–144. Basel, and Boston, MA: Birkhaeuser.
- Coates, P. J., Armstrong, R. C. and Brown, R. A. 1992. Calculation of steady-state viscoelastic flow through axisymmetric contractions with the EEME formulation. *J. Non-Newt. Fluid Mech.* **42**: 141–188.
- Couinot, A. and Crochet, M. J. 1986. Finite-elements for the numerical simulation of injection molding. In *Proc. 2nd Intl. Conf. Numerical Methods in Industrial Forming Processes: NUMIFORM 86*. Gothenburg, Sweden, August 25–29, pp. 165–170. Rotterdam, Netherlands, and Boston, MA: A. A. Balkema.
- Cox, R. G. 1986. The dynamics of the spreading of liquids on a solid surface. Part 1. Viscous flow. *J. Fluid Mech.* **168**: 169.
- Coyle, D. J. 1984. The fluid mechanics of roll coating: steady flows, stability, and rheology. PhD thesis, University of Minnesota, Minneapolis.
- Coyle, D. J. 1988. Forward roll coating with deformable rolls: a simple one-dimensional elastohydrodynamic model. *Chem. Eng. Sci.* **43**: 2673–2684.
- Coyle, D. J. 1990. Nonlinear theory of squeeze-roll coating. Paper read at *AICHE Spring National Meeting*, Orlando, FL, March 19–22.
- Coyle, D. J. 1992. Roll coating. In *Modern Coating and Drying Technology*, eds E. D. Cohen and E. B. Gutoff, pp. 63–116. Weinheim, Germany: VCH Publishers.
- Coyle, D. J., Macosko, C. W. and Scriven, L. E. 1987. Film-splitting flows of shear-thinning liquids in forward roll coating. *AICHE J.* **33**: 741–746.
- Coyle, D. J., Macosko, C. W. and Scriven, L. E. 1990. Stability of film splitting between counter-rotating cylinders. *J. Fluid Mech.* **216**: 437–458.
- Crochet, M. J. 1989. Numerical simulation of viscoelastic flow: a review. *Rubber Chem. Technol.* **62**: 426–455.
- Crochet, M. J. and Legat, V. 1992. The consistent streamline-upwind/Petrov–Galerkin method for viscoelastic flow revisited. *J. Non-Newt. Fluid Mech.* **42**: 283–299.
- Crowley, W. P. 1971. FLAG: a free-Lagrange method for numerically simulating hydrodynamic flows in two dimensions. *Lecture Notes in Physics*. **8**: 37–43.
- Crowley, W. P. 1985. Free-Lagrange methods for compressible hydrodynamics in two space dimensions. *Lecture Notes in Physics*. **238**: 1–21.
- Cuvelier, C. and Schulkes, R. M. S. 1990. Some numerical methods for the computation of capillary free boundaries governed by the Navier–Stokes equations. *SIAM Review*. **32**: 355–423.
- Dahlquist, G. and Björk, A. 1974. *Numerical Methods*. Englewood Cliffs: Prentice Hall.
- Daly, B. J. 1967. Numerical study of two fluid Rayleigh–Taylor instability. *Phys. Fluids*. **10**: 297–307.
- Dandy, D. S. and Leal, L. G. 1989. A Newton's scheme for solving free-surface flow problems. *Int. J. Numer. Meth. Fluids*. **9**: 1469–1486.
- Daripa, P., Glimm, J., Lindquist, B., Maesumi, M. and McBryan, O. 1988. On the simulation of heterogeneous petroleum reservoirs. In *Numerical Simulation of Oil Recovery*, ed. E. M. Wheeler, pp. 89–100. New York: Springer.
- Davey, A. 1962. The growth of Taylor vortices in flow between rotating cylinders. *J. Fluid Mech.* **14**: 336–368.
- de Santos, J. M. 1991. Two-phase co-current downflow through constricted passages. PhD thesis, University of Minnesota, Minneapolis.
- Demkowicz, L. and Oden, J. T. 1986. On a mesh optimization method based on a minimization of interpolation error. *Int. J. Eng. Sci.* **24**: 55–68.
- Dhatt, G., Gao, D. M. and Ben Cheikh, A. 1990. A finite-element simulation of metal flow in molds. *Int. J. Numer. Meth. Eng.* **30**: 821–831.
- Dheur, J. and Crochet, M. J. 1987. Newtonian stratified flow through a sudden expansion. *Rheol. Acta*. **26**: 401–413.
- Dheur, J. and Crochet, M. J. 1989. Stratified flows of Newtonian and viscoelastic fluids. *J. Non-Newt. Fluid Mech.* **32**: 1–18.
- DiPrima, R. C. and Rogers, E. H. 1969. Computing problems in nonlinear hydrodynamic stability. *Phys. Fluids Suppl. II*: 165–170.
- Do, D. V. and Christodoulou, K. N. 1992. Multilayer curtain coating flows: stability and sensitivity to small 3-D disturbances. Paper read at *AICHE Spring National Meeting*, New Orleans, LA, March 29–April 2.
- Donea, J. 1983. Arbitrary Lagrangian–Eulerian finite

- element methods. In *Computational Methods for Transient Analysis*, eds T. Belytschko and T. R. J. Hughes, pp. 473–516. Amsterdam: North-Holland.
- Drazin, P. G. and Reed, W. H. 1981. *Hydrodynamic Stability*. New York: Cambridge University Press.
- Duff, I. S. 1984. Design features of a frontal code for solving sparse unsymmetric linear systems out-of-core. *SIAM J. Sci. Stat. Comput.* **5**: 270–280.
- Duff, I. S., Erisman, A. M. and Reid, J. K. 1986. *Direct Methods for Sparse Matrices*. New York: Oxford University Press.
- Dukowicz, J. 1981. Lagrangian fluid dynamics using Voronoi–Delaunay mesh. In *Numerical Methods for Coupled Problems*, eds E. Hinton, P. Bettes and R. W. Lewis, pp. 82–104. Swansea, UK: Pineridge Press.
- Dukowicz, J. 1984. Conservative rezoning (remapping) for general quadrilateral meshes. *J. Comput. Phys.* **54**: 411–424.
- Dupret, F. 1982. A method for the computation of viscous flow by finite elements with free boundaries and surface tension. In *Finite Element Flow Analysis, Proc. 4th Int. Symp. FEM Flow Problems, Tokyo, 26–29 July 1982*, ed. T. Kawai, pp. 495–502. Tokyo: University of Tokyo Press.
- Durst, F., Haas, R., Peric, M., Scheurer, G. and Wagner, H.-G. 1991. Numerische Simulation zweidimensionaler Schlitzdüsenströmungen bei der Fliesserbeschichtung. *Coating*, **2/91**: 52–54, **3/91**: 90–92, **7/91**: 259–263, and **10/91**: 360–366.
- Dutta, A. and Ryan, M. E. 1982. Dynamics of a creeping Newtonian jet with gravity and surface tension – a finite difference technique for solving steady free-surface flows using orthogonal curvilinear coordinates. *AICHE J.* **28**: 220–232.
- Edwards, W. S., Tuckerman, L. S., Friesner, R. A. and Sorensen, D. C. 1994. Krylov methods for the incompressible Navier–Stokes equations. *J. Comput. Phys.* **110**: 82–102.
- Einset, E. and Jensen, K. F. 1992. A finite element solution of three-dimensional mixed convection gas flows in horizontal channels using preconditioned iterative matrix methods. *Int. J. Numer. Meth. Fluids*, **14**: 817–841.
- Eiseman, P. R. 1982. Orthogonal grid generation. *Appl. Math. Comput.* **10–11**: 193–233.
- Ellwood, K. R. J., Papanastasiou, T. C. and Wilkes, J. O. 1992. Three-dimensional streamlined finite elements – design of extrusion dies. *Int. J. Numer. Meth. Fluids*, **14**: 13–24.
- Engelman, M. S. 1982. Quasi-Newton methods in fluid dynamics. In *The Mathematics of Finite Element Applications, Vol. IV*, ed. J. R. Whiteman, pp. 479–487. London: Academic Press.
- Engelman, M. S. and Hasbani, I. 1990. Matrix-free solution algorithms in a finite-element context. *Fluid Dynamics International Technical Report* 88-1.
- Engelman, M. S. and Sani, R. L. 1983. Finite element simulation of incompressible fluid flows with a free/moving surface. In *Numerical Methods in Laminar and Turbulent Flow (Proc. 3rd Int. Conf. Seattle, WA)*, eds C. Taylor, J. A. Johnson and W. R. Smith, pp. 47–74. Swansea, UK: Pineridge Press.
- Esmail, M. N. and Markov, V. V. 1989. Numerical simulation of dynamic contact angles. *Trans. Math. Inst. Acad. Sci. USSR (English Trans.)* **186**: 203–208.
- Ettouney, H. M. and Brown, R. A. 1983. Finite-element methods for steady solidification problems. *J. Comput. Phys.* **49**: 118–150.
- Fatemi, E. A. and Kistler, S. F. 1992. Finite-difference discretization of viscous free-surface flows. Paper read at *AICHE Spring National Meeting*, New Orleans, LA, March 29–April 2.
- Finnicum, D. S., Weinstein, S. J. and Ruschak, K. J. 1993. The effect of applied pressure on the shape of a two-dimensional liquid curtain falling under the influence of gravity. *J. Fluid Mech.* **255**: 647–665.
- Floryan, J. M. and Rasmussen, H. 1989. Numerical methods for viscous flows with free/moving boundaries. *Applied Mechanics Reviews*, **42**: 323–341.
- Fortin, M. and Fortin, A. 1985. A generalisation of Uzawa's algorithm for the solution of the Navier–Stokes equations. *Comm. Appl. Numer. Meth.* **1**: 205–210.
- Fortin, M. and Glowinski, R. 1983. *The Augmented Lagrangian Method*. Amsterdam: North-Holland.
- Francis, D. C., Christodoulou, K. N., Scofield, D. F. and Lang, C. 1990. Fundamental studies of slot coating. Paper read at *AICHE Spring National Meeting*, Orlando, FL, March 18–22.
- Frank, R. M. and Lazarus, R. B. 1964. Mixed Eulerian–Lagrangian methods. *Methods in Computational Physics*, **3**: 117–179.
- Frederiksen, C. S. and Watts, A. M. 1981. Finite-element method for time-dependent incompressible free surface flow. *J. Comput. Phys.* **39**: 282–304.
- Fritts, M. J. and Boris, J. P. 1979. The Lagrangian solution of transient problems in hydrodynamics. *J. Comput. Phys.* **31**: 173–215.
- Fritts, M. J., Crowley, W. P. and Trease, H. E. (eds). 1985. *The Free Lagrange Method*. Lecture Notes in Physics, Volume 238. New York: Springer Verlag.
- Fromm, J. 1981. Finite-difference computation of the capillary jet free surface problem. *Lecture Notes in Physics*, **141**: 188–193.
- Fromm, J. 1986. Free-surface calculation of capillary spreading. *Lecture Notes in Physics*, **264**: 283–289.

- Fuller, G. G., Cathey, C. A., Hubbard, B. and Zebrowski, B. B. 1987. Extensional viscosity measurements for low-viscosity fluids. *J. Rheol.* **31**: 235–249.
- Fyfe, D. E., Oran, E. S. and Fritts, M. J. 1988. Surface tension and viscosity with Lagrangian hydrodynamics on a triangular mesh. *J. Comput. Phys.* **76**: 349–384.
- Gartling, D. K. and Phan-Thien, N. 1984. A numerical simulation of a plastic fluid in a parallel-plate plastometer. *J. non-Newt. Fluid Mech.* **14**: 347–360.
- Gaster, M. 1962. A note on the relation between temporally-increasing and spatially-increasing disturbances in hydrodynamic stability. *J. Fluid. Mech.* **14**: 222–224.
- Geller, A. S., Lee, S. H. and Leal, L. G. 1986. The creeping motion of a spherical particle normal to a deformable interface. *J. Fluid Mech.* **169**: 27–69.
- Glimm, J., Grove, J., Lindquist, B., McBryan, O. A. and Tryggvason, G. 1988. The bifurcation of tracked scalar waves. *SIAM J. Sci. Stat. Comput.* **9**: 61–79.
- Glimm, J. and McBryan, O. A. 1985. A computational model for interfaces. *Adv. Appl. Math.* **6**: 422–435.
- Glimm, J., McBryan, O., Menikoff, R. and Sharp, D. H. 1986. Front tracking applied to Rayleigh-Taylor instability. *SIAM J. Sci. Stat. Comput.* **7**: 230–251.
- Goenaga, A. and Higgins, B. G. 1990. Analysis of free surface flow problems by the boundary element method. Paper read at *AICHE Spring National Meeting*, Orlando, FL, March 18–22.
- Golafshani, M. 1988. A simple numerical technique for transient creep flows with free surface. *Int. J. Numer. Meth. Fluids.* **8**: 897–912.
- Goldhirsch, I., Orszag, S. A. and Maulik, B. K. 1987. An efficient method for computing leading eigenvalues of large asymmetric matrices. *J. Sci. Comput.* **2**: 33–58.
- Goodwin, R. and Homsy, G. M. 1991. Viscous flow down a slope in the vicinity of a contact line. *Phys. Fluids A – Fluid Dynamics* **3**: 515–528.
- Gordon, W. J. and Hall, C. A. 1973. Construction of curvilinear coordinate systems and applications to mesh generation. *Int. J. Numer. Meth. Eng.* **7**: 461–477.
- Grald, E. W., Chakrabarti, M., Subbiah, S. and Gephart, J. 1994. The spectral element method and its application to modeling coating flows. Paper read at *AICHE Spring National Meeting*, Atlanta, GA, April 17–21.
- Gresho, P. M. 1991. Some current CFD issues relevant to the incompressible Navier–Stokes equations. *Comput. Meth. Appl. Mech. Eng.* **87**: 201–252.
- Gresho, P. M. and Chan, S. T. 1990. On the theory of semi-implicit projection methods for viscous incompressible flow and its implementation via a finite-element method that also introduces a nearly consistent mass matrix. Part 2: Implementation. *Int. J. Numer. Meth. Fluids.* **11**: 621–660.
- Gresho, P. M., Lee, R. L. and Sani, R. L. 1980. On the time-dependent solution of the incompressible Navier–Stokes equations in two and three dimensions. In *Recent Advances in Numerical Methods in Fluids*, eds C. Taylor and K. Morgan, pp. 27–75. Swansea, UK: Pineridge Press.
- Gresho, P. M. and Sani, R. L. 1987. On pressure boundary conditions for the incompressible Navier–Stokes equations. *Int. J. Numer. Meth. Fluids.* **7**: 1111–1145.
- Griewank, A. and Corliss, G. F. 1992. *Automatic Differentiation of Algorithms*. Philadelphia: SIAM.
- Habashi, W. G., Nguyen, V.-N. and Bhat, M. V. 1991. Efficient direct solvers for large-scale computational fluid dynamics problems. *Comput. Meth. Appl. Mech. Eng.* **87**: 253–265.
- Hackler, M. A., Christodoulou, K. N., Hirschburg, R. I. and Lightfoot, E. J. 1992. Frequency response of coating flows to small three-dimensional disturbances by supercomputer-aided analysis. Paper read at *AICHE Spring National Meeting*, New Orleans, LA, March 29–April 2.
- Haftka, T. and Grandhi, R. V. 1986. Structural shape optimization – a survey. *Comput. Meth. Appl. Mech. Eng.* **57**: 91–106.
- Hansen, E. B. 1987. Stokes flow down a wall into an infinite pool. *J. Fluid Mech.* **178**: 243–256.
- Hansen, E. B. 1991. Stokes flow of a fluid layer over an obstacle on a tilted plane. *Math. Comput. Modeling.* **15**: 185–193.
- Harlow, F. 1964. The particle-in-cell computing method for fluid dynamics. *Methods in Computational Physics.* **3**: 313–343.
- Harlow, F. H. and Amsden, A. A. 1971. Numerical fluid dynamics. In *Fluid Dynamics, Los Alamos Scientific Laboratory Report* LA-4700.
- Harlow, F. H. and Welch, J. E. 1965. Numerical calculation of time-dependent viscous incompressible flow of fluid with free surface. *Phys. Fluids.* **8**: 2182–2189.
- Haroutunian, V., Engelman, M. S. and Hasbani, I. 1993. Segregated finite element algorithms for the numerical solution of large-scale incompressible flow problems. *Int. J. Numer. Meth. Fluids.* **17**: 323–348.
- Hasbani, Y. and Engelman, M. 1979. Out-of-core solution of linear equations with non-symmetric coefficient matrix. *Comput. Fluids.* **7**: 13–31.
- Haussling, H. J. 1982. Solution of nonlinear water wave problems using boundary-fitted coordinate systems. *Appl. Math. Comput.* **10–11**: 385–407.

- Hayes, R. E., Dannelongue, H. H. and Tanguy, P. A. 1991. Numerical simulation of mold filling in reaction injection molding. *Polym. Eng. Sci.* **31**: 842–848.
- Heijer, C. D. and Rheinboldt, W. C. 1981. On steplength algorithms for a class of continuation methods. *SIAM J. Numer. Anal.* **18**: 925–948.
- Higgins, B. G. 1980. Capillary hydrodynamics and coating beads. PhD thesis, University of Minnesota, Minneapolis.
- Hill, G. A., Shook, C. A. and Esmail, M. N. 1981. Finite-difference simulation of die-swell for a Newtonian fluid. *Canad. J. Chem. Eng.* **58**: 100–108.
- Hirt, C. W., Amsden, A. A. and Cook, J. L. 1974. An arbitrary Lagrangian-Eulerian computing method for all flow speeds. *J. Comput. Phys.* **14**: 227–253.
- Hirt, C. W., Cook, J. L. and Butler, T. D. 1970. A Lagrangian method for calculating the dynamics of an incompressible fluid with free surface. *J. Comput. Phys.* **5**: 103–124.
- Hirt, C. W., Korzekwa, D. R., Rollet, A. D. and Wilde, P. 1990. Planar flow casting: modeling and understanding. *Flow Science (Flow Science Inc., Los Alamos, NM) Report FSI-90-00-4*.
- Hirt, C. W. and Nichols, B. D. 1981. Volume of fluid (VOF) method for the dynamics of free boundaries. *J. Comput. Phys.* **39**: 210–225.
- Hirt, C. W., Nichols, B. D. and Romero, N. C. 1975. SOLA – a numerical solution algorithm for transient flows. *Los Alamos Scientific Laboratory Report LA-5852*.
- Hirt, C. W. and Shannon, J. P. 1968. Free-surface stress conditions for incompressible flow calculations. *J. Comput. Phys.* **2**: 403–411.
- Ho, L.-W. and Patera, A. T. 1990. A Legendre spectral element method for simulation of unsteady incompressible free-surface flows. *Comput. Meth. Appl. Mech. Eng.* **80**: 355–366.
- Ho, L.-W. and Patera, A. T. 1991. Variational formulation of three-dimensional free-surface flows. Natural imposition of surface tension boundary conditions. *Int. J. Numer. Meth. Fluids* **13**: 691–698.
- Hood, P. 1976. Frontal solution program for unsymmetric matrices. *Int. J. Numer. Meth. Eng.* **10**: 379–399.
- Hood, P. 1977. Correction. *Int. J. Numer. Meth. Eng.* **11**: 1055.
- Howard, D., Connolley, W. M. and Rollet, J. S. 1990. Unsymmetric conjugate gradient methods and sparse direct methods in finite element flow simulations. *Int. J. Numer. Meth. Fluids* **10**: 925–945.
- Huerta, A. and Liu, W. K. 1988. Viscous flows with large free surface motion. *Comput. Meth. Appl. Mech. Eng.* **69**: 277–324.
- Hughes, T. J. R., Liu, W. K. and Zimmerman, T. K. 1981. Lagrangian-Eulerian finite-element formulation for incompressible viscous flows. *Comput. Meth. Appl. Mech. Eng.* **29**: 329–349.
- Huh, K. Y., Golay, M. W. and Manno, V. P. 1986. A method for reduction of numerical diffusion in the donor treatment of convection. *J. Comput. Phys.* **63**: 201–221.
- Hurez, P. and Tanguy, P. A. 1990. Finite element analysis of dip coating with Bingham fluids. *Polym. Eng. Sci.* **30**: 1125–1132.
- Hurez, P., Tanguy, P. A. and Bertrand, F. H. 1991. A finite element analysis of die swell with pseudoplastic and viscoplastic fluids. *Comput. Meth. Appl. Mech. Eng.* **86**: 97–103.
- Huyakorn, P. S., Taylor, C., Lee, R. L. and Gresho, P. M. 1978. A comparison of various mixed interpolation finite elements in the velocity-pressure formulation of the Navier–Stokes equations. *Comput. Fluids* **6**: 25–35.
- Hyman, J. M. 1984. Numerical methods for tracking interfaces. *Physica* **12D**: 396–407.
- Hyun, J. C. and Ballman, R. L. 1978. Isothermal melt spinning – Lagrangian and Eulerian viewpoints. *J. Rheol.* **22**: 349–380.
- Isaacson, E. and Keller, H. B. 1966. *Analysis of Numerical Methods*. New York: Wiley.
- Jackson, C. P. 1987. A finite-element study of the onset of vortex shedding in flow past variously shaped bodies. *J. Fluid Mech.* **182**: 23–45.
- Jackson, C. P. and Robinson, P. C. 1985. A numerical study of various algorithms related to the preconditioned conjugate gradient method. *Int. J. Numer. Meth. Eng.* **21**: 1315–1338.
- Jackson, C. P. and Winters, K. H. 1984. A finite-element study of the Bénard problem using parameter-stepping and bifurcation search. *Int. J. Numer. Meth. Fluids* **4**: 127–145.
- Johnson, M., Kamm, R. D., Ho, L.-W., Shapiro, A. and Pedley, T. J. 1991. The nonlinear growth of surface-tension-driven instabilities of a thin annular film. *J. Fluid. Mech.* **233**: 141–156.
- Joseph, D. D. 1990. *Fluid Dynamics of Viscoelastic Liquid*. New York: Springer.
- Kaneko, N. and Scriven, L. E. 1988. Transient analysis of a curtain coating flow. Paper read at *AICHE Spring National Meeting*, New Orleans, LA, March 6–10.
- Karagiannis, A., Hrymak, A. N. and Vlachopoulos, J. 1988. Three-dimensional extrudate swell of creeping Newtonian jets. *AICHE J.* **34**: 2088–2094.
- Karagiannis, A., Mavridis, H., Hrymak, A. N. and Vlachopoulos, J. 1989. A finite element convergence

- study for shear-thinning flow problems. *Int. J. Numer. Meth. Fluids* **8**: 121–133.
- Katagiri, Y. 1992. Analysis of edge effects in curtain coating. Paper read at *AICHE Spring National Meeting*, New Orleans, LA, March 29–April 2.
- Katagiri, Y. and Scriven, L. E. 1986. Supercomputer-aided analysis of transient response of a coating operation. Paper read at *AICHE Annual Meeting*, Miami Beach, FL, November 2–7.
- Keller, H. B. 1977. Numerical solution of bifurcation and nonlinear eigenvalue problems. In *Applications of Bifurcation Theory*, ed. P. H. Rabinowitz, pp. 45–52. New York: Academic Press.
- Kelmann, M. A. 1983. Boundary integral equation solution of viscous flows with free surfaces. *J. Eng. Math.* **17**: 329–343.
- Keunings, R. 1986. An algorithm for the simulation of transient viscoelastic flows with free boundaries. *J. Comput. Phys.* **62**: 199–220.
- Keunings, R. 1989. Simulation of viscoelastic flow. In *Fundamentals of Computer Modeling for Polymer Processing*, ed. C. L. Tucker, pp. 403–469. Munich: Hanser.
- Keunings, R. 1991. Progress and challenges in computational rheology. *Rheol. Acta* **29**: 556–570.
- Kheshgi, H. S. and Scriven, L. E. 1984. Penalty finite-element analysis of unsteady free-surface flows. In *Finite Elements in Fluids*, Volume 5, eds R. H. Gallagher, J. T. Oden, O. C. Zienkiewicz, T. Kawai and M. Kawahara, pp. 393–434. New York: John Wiley.
- Kheshgi, H. S. and Scriven, L. E. 1985. Variable penalty method for finite element analysis of incompressible flow. *Int. J. Numer. Meth. Fluids* **5**: 785–803.
- Kheshgi, H. S. and Scriven, L. E. 1988. The evolution of disturbances in horizontal films. *Chem. Eng. Sci.* **43**: 793–801.
- Kikuchi, N., Chung, K. Y., Torigaki, T. and Taylor, J. E. 1986. Adaptive finite element methods for shape optimization of linearly elastic structures. *Comput. Meth. Appl. Mech. Eng.* **57**: 67–89.
- King, R. C., Apelian, M. N., Armstrong, R. C. and Brown, R. A. 1988. Numerically stable finite element techniques for viscoelastic calculations in smooth and singular geometries. *J. Non-Newt. Fluid Mech.* **29**: 147–216.
- Kistler, S. F. 1984. The fluid mechanics of curtain coating and other related viscous free surface flows with contact lines. PhD thesis, University of Minnesota, Minneapolis.
- Kistler, S. F. 1993. The hydrodynamics of wetting. In *Wettability*, ed. J. C. Berg, pp. 311–429. New York: Marcel Dekker.
- Kistler, S. F. and Palmquist, K. E. 1990. A simple, algebraic finite-element discretization of free surface flows. Paper read at *AICHE Spring National Meeting*, Orlando, FL, March 18–22.
- Kistler, S. F. and Scriven, L. E. 1983. Coating flows. In *Computational Analysis of Polymer Processing*, eds J. R. A. Pearson, and S. M. Richardson, pp. 243–299. London and New York: Applied Science Publishers.
- Kistler, S. F. and Scriven, L. E. 1984. Coating flow theory by finite-element and asymptotic analysis of the Navier–Stokes system. *Int. J. Numer. Meth. Fluids.* **4**: 207–229.
- Kistler, S. F. and Scriven, L. E. 1994. The teapot effect: sheet forming flows with deflection, wetting, and hysteresis. *J. Fluid Mech.* **263**: 19–62.
- Kistler, S. F. and Zvan, G. 1991. Hydrodynamic models of forced wetting in coating flows. Paper read at *44th IS&T Conference*, St Paul, MN, May 12–17.
- Kreis, R. I., Thames, F. C. and Hassan, H. A. 1986. Application of a variational method for generating adaptive grids. *AIAA J.* **24**: 404–410.
- Kruyt, N. P., Cuvelier, C., Segal, A. and van der Zanden, J. 1988. A total linearization method for solving viscous free boundary flow problems by the finite element method. *Int. J. Numer. Meth. Fluids.* **8**: 351–363.
- Ladyzhenskaya, O. A. 1963. *The Mathematical Theory of Viscous Incompressible Flow*. New York: Gordon and Breach.
- Lee, S. H. and Leal, L. G. 1982. The motion of a sphere in the presence of a deformable interface. II. A numerical study of the translation of a sphere normal to an interface. *J. Colloid Interface Sci.* **87**: 81–106.
- Legat, V. and Marchal, J.-M. 1992. Prediction of three-dimensional general shape extrudates by an implicit iterative scheme. *Int. J. Numer. Meth. Fluids.* **14**: 609–625.
- Leonard, A. 1985. Computing three-dimensional incompressible flows with vortex elements. *Ann. Rev. Fluid Mech.* **17**: 523–559.
- Liang, P. Y. 1991. Numerical method for calculation of surface tension flows in arbitrary grids. *AIAA J.* **29**: 161–167.
- Lin, S. P., Lian, Z. W. and Creighton, B. J. 1990. Absolute and convective instability of a liquid sheet. *J. Fluid Mech.* **220**: 673–689.
- Lin, S. P. and Roberts, G. 1981. Waves in a viscous liquid curtain. *J. Fluid Mech.* **112**: 443–458.
- Liou, J. and Tezduyar, T. E. 1991. Computation of compressible and incompressible flows with the

- clustered element-by-element technique. In *Domain decomposition methods for partial differential equations*, eds R. Glowinski *et al.*, pp. 140–150. Philadelphia, PA: SIAM.
- Liu, J.-J., Yu, T.-A. and Cheng, S.-H. 1991. Finite-difference solution of a Newtonian jet swell problem. *Int. J. Numer. Meth. Fluids.* **12**: 125–142.
- Loh, C. Y. and Rasmussen, H. 1987. A numerical procedure for viscous free surface flows. *Appl. Numer. Math.* **3**: 479–495.
- Longuet-Higgins, M. S. and Cokelet, E. D. 1976. The formation of steep surface waves on water. Part 1: a numerical method of computation. *Proc. Roy. Soc. Lond., Ser. A.* **350**: 1–26.
- Lowndes, J. 1980. The numerical simulation of the steady movement of a fluid meniscus in a capillary tube. *J. Fluid Mech.* **101**: 631–646.
- Lu, W. Q. and Chang, H. C. 1988. An extension of the biharmonic boundary integral method to free-surface flow in channels. *J. Comput. Phys.* **77**: 340–360.
- Luo, X.-L. and Mitsoulis, E. 1990. An efficient algorithm for strain history tracking in finite-element computations of non-Newtonian fluids with integral constitutive equations. *Int. J. Numer. Meth. Fluids.* **11**: 1015–1031.
- Luo, X.-L. and Tanner, R. I. 1988. Finite-element simulation of long and short circular die experiments using integral models. *Int. J. Numer. Meth. Eng.* **25**: 9–22.
- Lynch, D. R. 1982. Unified approach to simulation on deforming elements with application to phase change problems. *J. Comput. Phys.* **47**: 387–411.
- Maday, Y. and Patera, A. T. 1989. Spectral element methods for the Navier–Stokes equations. In *State-of-the-art Surveys in Computational Mechanics*, eds J. T. Oden, and A. K. Noor. New York: ASME.
- Malamataris, N. T. and Papanastasiou, T. C. 1991. Unsteady free surface flows on truncated domains. *Ind. Eng. Chem. Res.* **30**: 2211–2219.
- (Manteuffel, T. A. 1977. The Tchebychev iteration for non-symmetric linear systems. *Numer. Math.* **28**: 307–327.)
- Marchal, M. and Crochet, M. J. 1987. A new mixed finite-element method for calculating viscoelastic flow. *J. Non-Newt. Fluid Mech.* **26**: 77–114.
- Margolin, L. G. and Nichols, B. D. 1983. Momentum control volumes for finite-difference codes. In *Numerical Methods in Laminar and Turbulent Flows (Proc. 3rd Intl. Conf., Seattle, WA)*, eds C. Taylor, J. A. Johnson and W. R. Smith, pp. 411–421. Swansea, UK: Pineridge Press.
- Matsuhiro, I., Shiojima, T., Shimazaki, Y. and Daijui, H. 1990. Numerical analysis of polymer injection moulding process using finite element method with marker particles. *Int. J. Numer. Meth. Eng.* **30**: 1569–1575.
- McKibben, J. F. and Aidun, C. K. 1991. Computational visualization of three-dimensional free surface flows. In *Proc. TAPPI Engineering Conference (Nashville, TN, Sept. 30–Oct. 3)*, Book 2, pp. 711–718. Atlanta, GA: TAPPI Press.
- Melhem, R. G. and Rheinboldt, W. C. 1982. A comparison of methods of determining turning points of nonlinear equations. *Computing.* **29**: 201–226.
- Meyer, K. A. 1969. Three dimensional study of flow between concentric rotating cylinders. *Phys. Fluids. Suppl. II*: 155–165.
- Mittal, S. and Tezduyar, T. E. 1992. Space-time finite element computations of incompressible flows involving oscillating cylinders. *Int. J. Numer. Meth. Fluids.* **15**: 1073–1118.
- Miura, H. and Aidun, C. K. 1992. Pressure fluctuations and coat-weight nonuniformities in blade coating. In *Proc. 1992 TAPPI Coating Conference*, pp. 193–216. Atlanta: TAPPI Press.
- Miyamoto, K. 1992. On the mechanism of air entrainment. *Ind. Coating Res.* **1**: 71–88.
- Miyata, H. 1986. Finite-difference simulation of breaking waves. *J. Comput. Phys.* **65**: 179–214.
- Moffat, H. K. 1964. Viscous and resistive eddies near a sharp corner. *J. Fluid Mech.* **18**: 1–18.
- Monaghan, J. J. 1985. Particle methods for hydrodynamics. *Comput. Phys. Rep.* **3**: 71–124.
- Morice, P. 1983. Numerical generation of boundary-fitted coordinate systems with optimal control of orthogonality. In *Advances in Grid Generation (Proc. ASME Applied Mechanics, Bioengineering, and Fluids Engineering Conference, Houston)*, FED-Vol. 5, eds K. N. Ghia and U. Ghia, pp. 71–78. New York: ASME.
- Mües, W., Hens, J. and Boij, L. 1989. Observation of dynamic wetting process with laser-Doppler velocimetry. *AIChE J.* **35**: 1521–1526.
- Mulder, W., Osher, S. and Sethian, J. A. 1992. Computing interface motion in compressible gas dynamics. *J. Comput. Phys.* **100**: 209–228.
- Muttin, F., Coupez, T., Bellet, M. and Chenot, J. L. 1991. Newtonian fluid computations in Lagrangian variables with a remeshing technique. Application to the filling stage of the diecasting process. In *Proc. 1st Intl. Conf. Computational Modelling of Free and Moving Boundary Problems (Southampton, England, July 2–4)*, eds L. C. Wrobel and C. A. Brebbia, pp. 207–221. Southampton, England: Computational Mechanics Publications.

- Natarajan, R. 1992. An Arnoldi-based iterative scheme for nonsymmetric matrix pencils arising in finite element stability problems. *J. Comput. Phys.* **100**: 128–142.
- Nelson, N. K., Kistler, S. F. and Olmsted, R. D. 1990. A generalized viscous model for the steady shear rheology of magnetic dispersions. Paper read at *62nd Annual Meeting of the Society of Rheology*, Santa Fe, NM, October 21–25.
- Nichols, B. D. and Hirt, C. W. 1971. Improved free surface boundary conditions for numerical incompressible-flow calculations. *J. Comput. Phys.* **8**: 434–448.
- Nichols, B. D. and Hirt, C. W. 1973. Calculating three-dimensional free surface flows in the vicinity of submerged and exposed structures. *J. Comput. Phys.* **12**: 234–246.
- Nichols, B. D. and Hirt, C. W. 1975. Methods for calculating multi-dimensional transient free surface flows past bodies. In *Proc. First Intl. Conf. Numer. Methods Ship Hydrodynamics*, Gaithersburg, Maryland, pp. 253–277.
- Nichols, B. D., Hirt, C. W. and Hotchkiss, R. S. 1980. SOLA-VOF – a solution algorithm for transient fluid flow with multiple free boundaries. *Los Alamos Scientific Laboratory Report LA-8355*.
- Nickell, R. E., Tanner, R. I. and Caswell, B. 1974. The solution of viscous incompressible jet and free surface flows using finite-element methods. *J. Fluid Mech.* **65**: 189–206.
- Noh, W. F. and Woodward, P. 1976. SLIC (simple line interface calculation). *Lecture Notes in Physics*. **59**: 330–340.
- Oran, E. S. and Boris, J. P. 1987. *Numerical Simulation of Reactive Flow*. New York: Elsevier.
- Ortega, J. M. and Rheinboldt, W. C. 1970. *Iterative Solution of Nonlinear Equations in Several Variables*. New York: Academic Press.
- Osher, S. and Sethian, J. A. 1988. Fronts propagating with curvature-dependent speed: algorithms based on Hamiltonian–Jacobi formulation. *J. Comput. Phys.* **79**: 12–49.
- Papanastasiou, T. C. 1987. Flows of material with yield. *J. Rheol.* **31**: 385–404.
- Papanastasiou, T. C., Macosko, C. W. and Scriven, L. E. 1985. Streamlined finite-elements and transit times. In *Finite Elements in Fluids*, Vol. 6, eds R. H. Gallagher, G. F. Carey, J. T. Oden and O. C. Zienkiewicz, pp. 263–278. New York: Wiley.
- Papanastasiou, T. C., Scriven, L. E. and Macosko, C. W. 1987. A finite element method for liquid with memory. *J. Non-Newt. Fluid Mech.* **22**: 271–288.
- Parlett, B. and Saad, Y. 1985. Complex shift and invert strategies for real matrices. *Yale University, Computer Science Dept. Tech. Report* YALEU/DCS-RR-424.
- Patera, A. T. 1984. A spectral element method for fluid flow: laminar flow in a channel expansion. *J. Comput. Phys.* **54**: 468–488.
- Pavelle, R. and Wang, P. S. 1985. MACSYMA from F to G. *J. Symbol. Comput.* **1**: 69–100.
- Pearson, J. R. A. 1960. The instability of uniform viscous flow under rollers and spreaders. *J. Fluid Mech.* **7**: 481–500.
- Petigen, H. and Pruefer, M. 1984. Global aspects of Newton's method for nonlinear boundary value problems. In *Numerical Methods for Bifurcation Problems*, Intl. Series Numer. Math., Vol. 70, eds T. Kuepper, H. D. Mittelmann and H. Weber, pp. 352–368. Basel: Birkhauser.
- Peskin, C. S. 1977. Numerical analysis of blood flow in the heart. *J. Comput. Phys.* **25**: 220–252.
- Petzold, L. R. 1982. A description of DASSL: A differential/algebraic system solver. *Sandia National Laboratory Report* SAND82-8637.
- Petzold, L. R. 1982. Differential/algebraic equations are not ODE's. *SIAM J. Sci. Stat. Comput.* **3**: 367–384.
- Pilitsis, S. and Beris, A. N. 1989. Calculation of steady-state viscoelastic flow in an undulating tube. *J. Non-Newt. Fluid Mech.* **31**: 231–287.
- Pitts, E. and Greiller, J. 1961. The flow of thin liquid films between rollers. *J. Fluid Mech.* **11**: 33–50.
- Poenisch, G. D. and Schwetlick, H. H. 1981. Computing turning points of curves implicitly defined by nonlinear equations depending on a parameter. *Computing*. **26**: 107–121.
- Potter, D. E. and Tuttle, G. H. 1973. The construction of discrete orthogonal coordinates. *J. Comput. Phys.* **13**: 483–501.
- Pozrikidis, C. 1988. The flow of a liquid film along a periodic wall. *J. Fluid Mech.* **188**: 275–300.
- Pozrikidis, C. and Thoroddsen, S. T. 1991. The deformation of a liquid film flowing down an inclined plane wall over a small particle arrested on the wall. *Phys. Fluids A – Fluid Dynamics*. **3**: 2546–2558.
- Pracht, W. E. 1971. A numerical method for calculating transient creep flows. *J. Comput. Phys.* **7**: 46–60.
- Pranckh, F. R. and Scriven, L. E. 1989. Elastohydrodynamics of membrane coating. *University of Minnesota Supercomputer Institute Report* UMSI 89/83.
- Pranckh, F. R. and Scriven, L. E. 1990a. The elastohydrodynamics of blade coating. *AICHE J.* **36**: 587–597.
- Pranckh, F. R. and Scriven, L. E. 1990b. The physics

- of blade coating of a deformable substrate. *TAPPI J.* **73**(1): 163–173.
- Rajagopalan, D., Armstrong, R. C. and Brown, R. A. 1990. Finite element methods for calculation of steady, viscoelastic flow using constitutive equations with a Newtonian viscosity. *J. Non-Newt. Fluid Mech.* **36**: 159–192.
- Rajagopalan, D., Armstrong, R. C. and Brown, R. A. 1993. Comparison of computational efficiency of flow simulations with multimode constitutive equations: integral and differential models. *J. Non-Newt. Fluid Mech.* **46**: 243–273.
- Rajagopalan, D., Philips, R. J., Armstrong, R. C. and Brown, R. A. 1992. The influence of viscoelasticity on the existence of steady solutions in two-dimensional rimming flow. *J. Fluid Mech.* **235**: 611–642.
- Ramaswamy, B. 1990. Numerical simulation of unsteady viscous free-surface flow. *J. Comput. Phys.* **90**: 396–430.
- Ramshaw, J. D. 1985. Conservative rezoning algorithm for generalized two-dimensional meshes. *J. Comput. Phys.* **59**: 193–199.
- Rao, R. R. and Finlayson, B. A. 1991. Adaptive refinement of a viscoelastic flow problem with the explicitly elliptic momentum equation. *J. Non-Newt. Fluid Mech.* **38**: 223–246.
- Reddy, M. P. and Reddy, J. N. 1991. Finite element simulation of mold filling processes. In *Advances in Finite Deformation Problems in Materials Processing and Structures*, AMD-Vol. 125, pp. 65–74. New York: ASME.
- Reid, J. K. 1981. Frontal methods for solving finite-element systems of linear equations. In *Sparse Matrices and their Uses*, ed. I. S. Duff, pp. 275–281. New York: Academic Press.
- Rheinboldt, W. C. and Burkardt, J. V. 1983. A locally parametrized continuation process. *ACM Trans. Math. Software*. **9**: 215–235.
- Rosenberg, J. and Keunings, R. 1991. Numerical integration of differential viscoelastic models. *J. Non-Newt. Fluid Mech.* **39**: 269–290.
- Ruschak, K. J. 1978. Flow of a falling film into a pool. *AICHE J.* **24**: 705–709.
- Ruschak, K. J. 1980. A method for incorporating free boundaries with surface tension in finite element fluid flow simulators. *Int. J. Numer. Meth. Eng.* **15**: 639–648.
- Ruschak, K. J. 1983. A three-dimensional linear stability analysis for two-dimensional free boundary flows by the finite element method. *Comput. Fluids*. **11**: 391–401.
- Ruschak, K. J. 1985. Coating flows. *Ann. Rev. Fluid Mech.* **17**: 65–89.
- Ryskin, G. and Leal, L. G. 1983. Orthogonal mapping. *J. Comput. Phys.* **50**: 71–100.
- Ryskin, G. and Leal, L. G. 1984. Numerical solution of free-boundary problems in fluid mechanics. Part 1. The finite-difference technique. *J. Fluid Mech.* **148**: 1–17.
- Saad, Y. 1980. Variations on Arnoldi's method for computing eigenelements of large unsymmetric matrices. *Linear Algeb. Appl.* **34**: 269–295.
- Saad, Y. 1989. Numerical solution of large nonsymmetric eigenvalue problems. *Comput. Phys. Commun.* **53**: 71–90.
- Saad, Y. and Schultz, M. 1986. GMRES: a generalized minimal residual algorithm for solving nonsymmetric linear systems. *SIAM J. Sci. Stat. Comput.* **7**: 856–869.
- Sackinger, P. A., Schunk, P. R. and Rao, R. R. 1996. A Newton–Raphson pseudo-solid domain mapping technique for free and moving boundary problems: a finite element implementation. *J. Comp. Phys.*, **125**: 83–103.
- Saeger, R. B., Davis, H. T. and Scriven, L. E. 1990. Adaptive elliptic grid generation for 3-D elemental structures. *Univ. of Minnesota Supercomputer Institute Report UMSI 90/73*.
- Saito, H. and Scriven, L. E. 1981. Study of a coating flow by the finite element method. *J. Comput. Phys.* **42**: 53–76.
- Salamon, T. R., Armstrong, R. C. and Brown, R. A. 1992. Modification of inertial film instability by viscoelasticity. In *Theoretical and Applied Rheology (Proc. XIth Intl. Congr. Rheology, Brussels, Belgium, August 17–21, 1992)*, eds P. Moldenaers and R. Keunings, pp. 213–215. Amsterdam: Elsevier.
- Savage, M. D. 1977a. Cavitation in lubrication. Part 1. On boundary conditions and cavity–fluid interfaces. *J. Fluid Mech.* **80**: 743–755.
- Savage, M. D. 1977b. Cavitation in lubrication. Part 2. Analysis of wavy interfaces. *J. Fluid Mech.* **80**: 757–767.
- Scanlan, D. J. 1990. Two-slot coater analysis: inner layer separation issues in two-layer coating. MS thesis, University of Minnesota, Minneapolis.
- Schunk, P. R. 1989. Surfactant and polymer effects in coating and related flows. PhD thesis, University of Minnesota, Minneapolis.
- Schunk, P. R. and Scriven, L. E. 1990. Constitutive equation for modeling mixed extension and shear in polymer solution processing. *J. Rheol.* **34**: 1085–1119.
- Schwetlick, H. 1984. Algorithms for finite-dimensional turning point problems from viewpoint to relationships with constrained optimization methods. In

- Numerical Methods for Bifurcation Problems*, Intl. Series Numer. Math., Vol. 70, eds T. Kuepper, H. D. Mittelmann and H. Weber, pp. 459–479. Basel: Birkhaeuser.
- Sethian, J. 1984. Turbulent combustion in open and closed vessels. *J. Comput. Phys.* **54**: 425–456.
- Sethian, J. A. and Strain, J. 1992. Crystal growth and dendritic solidification. *J. Comput. Phys.* **98**: 231–253.
- Shanks, S. P. and Thompson, J. F. 1977. Numerical solution of the Navier–Stokes equations for 2D hydrofoils in or below a free surface. In *Proc. 2nd Intl. Conf. Numerical Ship Hydrodynamics*, pp. 202–220. Berkeley: Univ. of Calif. Extension Publ.
- Shokoohi, F. and Elrod, H. G. 1987. Numerical investigation of the disintegration of liquid jets. *J. Comput. Phys.* **71**: 324–341.
- Shopov, P. J. and Bazhlekov, I. B. 1991. Numerical method for viscous hydrodynamic problems with dynamic contact lines. *Comput. Meth. Appl. Mech. Eng.* **91**: 1157–1174.
- Shopov, P. J., Minev, P. D. and Bazhlekov, I. B. 1992. Numerical method for unsteady viscous hydrodynamical problems with free boundaries. *Int. J. Numer. Meth. Fluids.* **14**: 681–705.
- Sicilian, J. M. and Hirt, C. W. 1984. HYDR-3D: a solution algorithm for transient 3D flows. *Flow Science (Flow Science Inc., Los Alamos, NM) Report FSI-81-00-1*.
- Silliman, W. J. and Scriven, L. E. 1980. Separating flow near a static contact line: slip at a wall and shape of a free surface. *J. Comput. Phys.* **34**: 287–313.
- Smith, R. E. 1982. Algebraic grid generation. *Appl. Math. Comput.* **10–11**: 137–170.
- Sonneveld, P. 1989. CGS: a fast, Lanczos-type solver for nonsymmetric linear systems. *SIAM J. Sci. Stat. Comput.* **10**: 36–52.
- Sonneveld, P., Wesseling, P. and de Zeeuw, P. M. 1985. Multigrid and conjugate gradient methods as convergence acceleration techniques. In *Multigrid Methods for Integral and Differential Equations*, eds D. J. Paddon and H. Holstein, pp. 117–167. Oxford: Clarendon Press.
- Soulaïmani, A., Fortin, M., Dhatt, G. and Quellet, Y. 1991. Finite element simulation of two- and three-dimensional free-surface flows. *Comput. Meth. Appl. Mech. Eng.* **86**: 265–296.
- Souvaliotis, A. and Beris, A. N. 1992. Application of domain decomposition spectral collocation methods in viscoelastic flows through model porous media. *J. Rheol.* **36**: 1417–1453.
- Stewart, G. W. 1978. SRRIT – a FORTRAN subroutine to calculate the dominant invariant subspaces of a real matrix. *University of Maryland Computer Science Center (College Park) Technical Report TR-514*, ONR-N00014-76-C-0391.
- Strang, G. and Fix, G. 1973. *An Analysis of the Finite Element Method*. Englewood Cliffs, NJ: Prentice Hall.
- Strigberger, J., Baruzzi, G., Habashi, W. and Fortin, M. 1993. Some special purpose preconditioners for conjugate gradient-like methods applied to CFD. *Int. J. Numer. Meth. Fluids.* **16**: 581–596.
- Subbiah, S., Trafford, D. L. and Güceri, S. I. 1989. Non-isothermal flow of polymers into two-dimensional, thin cavity molds: a numerical grid-generation approach. *Int. J. Heat Mass Transfer.* **32**: 415–434.
- Tabata, M. and Morishita, A. 1989. Fractional step finite element scheme for free boundary problems. *Theor. Appl. Mech.* **39**: 251–257.
- Tanner, R. I. and Milthorpe, J. F. 1983. Numerical simulation of the flow of fluid with yield stresses. In *Numerical Methods in Laminar and Turbulent Flow (Proc. 3rd Intl. Conf.)*, eds C. Taylor, J. A. Johnson and W. R. Smith, pp. 680–690. Swansea: Pineridge Press.
- Tanzosh, J., Manga, M. and Stone, H. A. 1992. Boundary integral methods for viscous free-boundary problems: deformation of single and multiple fluid–fluid interfaces. In *Proc. 7th Intl. Conf. Boundary Element Technology*, Vol. VII, eds C. A. Brebbia and M. S. Ingber, pp. 19–39. Southampton, England: Computational Mechanics Publications.
- Tezduyar, T. E., Behr, M. and Liou, J. 1992. A new strategy for finite-element computations involving moving boundaries and interfaces – the deforming-spatial-domain/space-time procedure: I. The concept and the preliminary numerical tests. *Comput. Meth. Appl. Mech. Eng.* **94**: 339–351.
- Tezduyar, T. E., Behr, M., Mittal, S. and Liou, J. 1992. A new strategy for finite-element computations involving moving boundaries and interfaces – the deforming-spatial-domain/space-time procedure: II. Computation of free-surface flows, two-liquid flows and flows with drifting cylinders. *Comput. Meth. Appl. Mech. Eng.* **94**: 353–371.
- Thomas, P. D. 1982. Composite three-dimensional grids generated by elliptic systems. *AIAA J.* **20**: 1195–1202.
- Thomas, P. D. and Brown, R. A. 1987. LU decomposition of matrices with augmented dense constraints. *Int. J. Numer. Meth. Eng.* **24**: 1451–1459.
- Thomas, P. D. and Middlecoff, J. F. 1980. Direct control of the grid point distribution in meshes generated by elliptic equations. *AIAA J.* **18**: 652–656.

- Thompson, E. G. 1986. Use of pseudo-concentrations to follow creeping viscous flow during transient analysis. *Int. J. Numer. Meth. Fluids.* **6**: 749–761.
- Thompson, J. F., Thomas, F. C. and Mastin, C. W. 1974. Automatic numerical generation of body-fitted curvilinear coordinate system for field containing any number of arbitrary two-dimensional bodies. *J. Comput. Phys.* **15**: 299–319.
- Thompson, J. F., Warsi, U. A. and Mastin, C. W. 1982. Boundary-fitted coordinate systems for numerical solution of partial differential equations – a review. *J. Comput. Phys.* **47**: 1–108.
- Thompson, J. F., Warsi, Z. U. A. and Mastin, W. C. 1985. *Numerical Grid Generation*. New York: Elsevier.
- Tilton, J. N. 1988. The steady motion of an interface between two viscous liquids in a capillary tube. *Chem. Eng. Sci.* **43**: 1371–1384.
- Torrey, M. D., Cloutman, L. D., Mjolsness, R. C. and Hirt, C. W. 1985. NASA-VOF2D: A computer program for incompressible flows with free surfaces. *Los Alamos National Laboratory Report*. LA-10612-MS.
- Tran-Cong, T. and Phan-Tien, N. 1988a. Three-dimensional study of extrusion processes by boundary element method. I. An implementation of high-order elements and some Newtonian results. *Rheol. Acta.* **27**: 21–30.
- Tran-Cong, T. and Phan-Thien, N. 1988b. Three-dimensional study of extrusion processes by boundary element method. II. Extrusion of a viscoelastic fluid. *Rheol. Acta.* **27**: 639–648.
- Tryggvason, G. 1988. Numerical simulation of the Rayleigh-Taylor instability. *J. Comput. Phys.* **75**: 253–282.
- Tsiveriotis, K. and Brown, R. A. 1992. Boundary-conforming mapping applied to computations of highly deformed solidification interfaces. *Int. J. Numer. Meth. Fluids.* **14**: 981–1003.
- Tsiveriotis, K. and Brown, R. A. 1993. Solution of free-boundary problems using finite-element/Newton methods and locally refined grids: application to analysis of solidification microstructure. *Int. J. Numer. Meth. Fluids.* **16**: 827–843.
- Ungar, L. H. and Brown, R. A. 1982. The dependence of the shape and stability of rotating captive drops on multiple parameters. *Philos. Trans. Roy. Soc. Lond. A* **306**: 457–480.
- Ungar, L. H. and Brown, R. A. 1985. Cellular interface morphologies in directional solidification. IV. The formation of deep cells. *Phys. Rev. B.* **31**: 5931–5940.
- Ungar, L. H., Ramprasad, N. and Brown, R. A. 1988. Finite element methods for unsteady solidification problems arising in prediction of morphological structure. *J. Sci. Comput.* **3**: 77–108.
- Unverdi, S. O. and Tryggvason, G. 1992. A front-tracking method for viscous, incompressible, multi-fluid flows. *J. Comput. Phys.* **100**: 25–37.
- Van Abbenen, W., Christodoulou, K. N. and Scriven, L. E. 1989. Frequency response of a coating flow: predictions for slide coating. *University of Minnesota Supercomputer Center Report* UMSI 89/40.
- Van Abbenen, W., Goetmaeckers, B., Van de Vijver, H., Bussmann, H. and Beck, D. 1990. Experimental verification of the calculated frequency response of a multilayer slide-coating operation. Paper read at *AICHE Spring National Meeting*, Orlando, FL, March 19–22.
- Van der Vorst, H. A. 1992. Bi-CGSTAB: a fast and smoothly converging variant of Bi-CG for the solution of nonsymmetric linear systems. *SIAM J. Sci. Stat. Comput.* **13**: 631–644.
- Visbal, M. and Knight, D. 1982. Generation of orthogonal and nearly orthogonal coordinates with grid control near boundaries. *AIAA J.* **20**: 305–306.
- Voinov, O. V. 1976. Hydrodynamics of wetting. *Fluid Dynamics.* **11**: 714–721.
- Wambersie, D. and Crochet, M. J. 1992. Transient finite element method for calculating steady state three-dimensional free surface flows. *Int. J. Numer. Meth. Fluids.* **14**: 343–360.
- Wang, H. P. and Lee, H. S. 1989. Numerical techniques for free and moving boundary problems. In *Fundamentals of Computer Modeling for Polymer Processing*, ed. C. L. Tucker, pp. 369–401. Munich, Vienna and New York: Hanser Publishers.
- Wang, H. P. and McLay, R. T. 1986. Automatic remeshing scheme for modeling hot forming process. *J. Fluid Eng. (ASME)* **108**: 465–469.
- Weatherburn, C. E. 1927. *Differential Geometry of Three Dimensions*. London: Cambridge Univ. Press.
- Werner, B. and Spence, A. 1984. The computation of symmetry-breaking bifurcation points. *SIAM J. Numer. Anal.* **2**: 388–399.
- Wilkinson, J. H. 1965. *The Algebraic Eigenvalue Problem*. Oxford: Clarendon Press.
- Winslow, A. M. 1967. Numerical solution of the quasilinear Poisson equation in a nonuniform triangle mesh. *J. Comput. Phys.* **2**: 149–172.
- Winters, K. H., Cliffe, K. A. and Jackson, C. P. 1987. The prediction of instabilities using bifurcation theory. In *Numerical Methods for Transient and Coupled Problems*, eds R. W. Lewis, E. Hinton, P. Bettess and B. A. Schrefler, pp. 179–198. New York: Wiley.
- Yiantios, S. G. and Higgins, B. G. 1989.

- Rayleigh–Taylor instability in thin viscous films. *Phys. Fluids A – Fluid Dynamics.* **1**: 1484–1501.
- Yokoi, T. and Scriven, L. E. 1989. Profile extrusion analyzed and die shape designed by Galerkin's method with streamline-adapted basis functions. *University of Minnesota Supercomputer Institute Report UMSI 89/65*.
- Youngren, G. K. and Acrivos, A. 1976. On the shape of a gas bubble in a viscous extensional flow. *J. Fluid Mech.* **76**: 433–442.
- Youngs, D. L. 1982. Time-dependent multi-material flow with large fluid distortion. In *Numerical Methods for Fluid Mechanics*, eds K. W. Morton and M. J. Baines, pp. 273–285. New York: Academic Press.
- Yuan, Y. and Ingham, D. B. 1991. Numerical solution of viscous flows with a free surface. In *Computational Modeling of Free and Moving Boundary Problems (Proc. 1st Intl. Conf.)*, eds L. C. Wrobel and C. A. Brebbia, pp. 325–339. Southampton, UK: Computational Mechanics Publ.
- Zhou, M.-Y. and Sheng, P. 1990. Dynamics of immiscible-fluid displacement in a capillary tube. *Phys. Rev. Lett.* **64**: 882–885.
- Zienkiewicz, O. C. 1977. *The Finite Element Method*. London: McGraw-Hill.

PART THREE

**THEORY AND PRACTICE OF COATING
PROCESSES**

ANALYSIS AND DESIGN OF INTERNAL COATING DIE CAVITIES

10

Robert B. Secor

10.1 INTRODUCTION

The purpose of the internal cavities of coating dies of all types is to distribute the coating liquid in a manner which in conjunction with the rest of the coating process produces a liquid film with uniform dimensions and properties. Whereas the constancy of feed rate and take-away speed play the biggest role in the down-web uniformity of the final film, the liquid passages internal and external to the coating die have the biggest impact on the cross-web uniformity of the coated liquid. Although cross-web nonuniformities in the liquid passages external to the coating die can drastically affect the final coating uniformity, the focus of this chapter is the influence on the cross-web uniformity of the passages internal to the coating die.

The distribution chambers of most coating dies have a common general shape. They consist of a cavity (also referred to as a distribution chamber or channel) that is oriented substantially in the cross-web direction which is connected to a slot (or slit or land) on one side, (see Fig. 10.1). The combination of the cavity and slot is referred to as the distribution manifold. Two particular types are often distinguished: the T-manifold and the coathanger manifold. The T-manifold, (also referred to as an ‘infinite cavity’ manifold), has a uniform cross-section across the width of the die. The coathanger manifold features decreasing slot length and cavity size with cross-web distance

from the feed location. Two coathanger manifolds, linearly tapered and curvilinearly tapered are often distinguished. The linearly tapered coathanger manifold is sometimes referred to as a fishtail manifold. The cross-sectional shape of the manifold cavities also come in various shapes, (see Fig. 10.2). Circular shapes are very popular for analysis but not so common in practice. More common are the teardrop, triangular, and rectangular shapes.

Often coating dies are equipped with adjustment mechanisms for tuning the cross-web flow uniformity produced by the die manifold. Figure 10.3 shows the two most common mechanisms: the flexible die lip and the choker bar (sometimes referred to as a straining bar or restrictor bar). The flexible die lip features a weakened die lip with a mechanism for locally moving the lip and thus changing the slot gap near the die exit. Traditionally, the die lips are flexed mechanically with a number of bolts evenly spaced across the width of the coating die (*cf.* Kasamatsu (1987); Iguchi *et al.* (1987)). Alternatively, the movement of the die lip can be accomplished by thermal expansion (Lowey 1960; Nissel 1976; Anthony *et al.* 1988), piezoelectric or magnetostrictive translation (Reifenhauser *et al.* 1986; Erckmann 1988). The choker bar is a separate member in the die cavity that can be flexed to change the slot gap locally usually a distance upstream of the die exit. When either flexible lip or choker

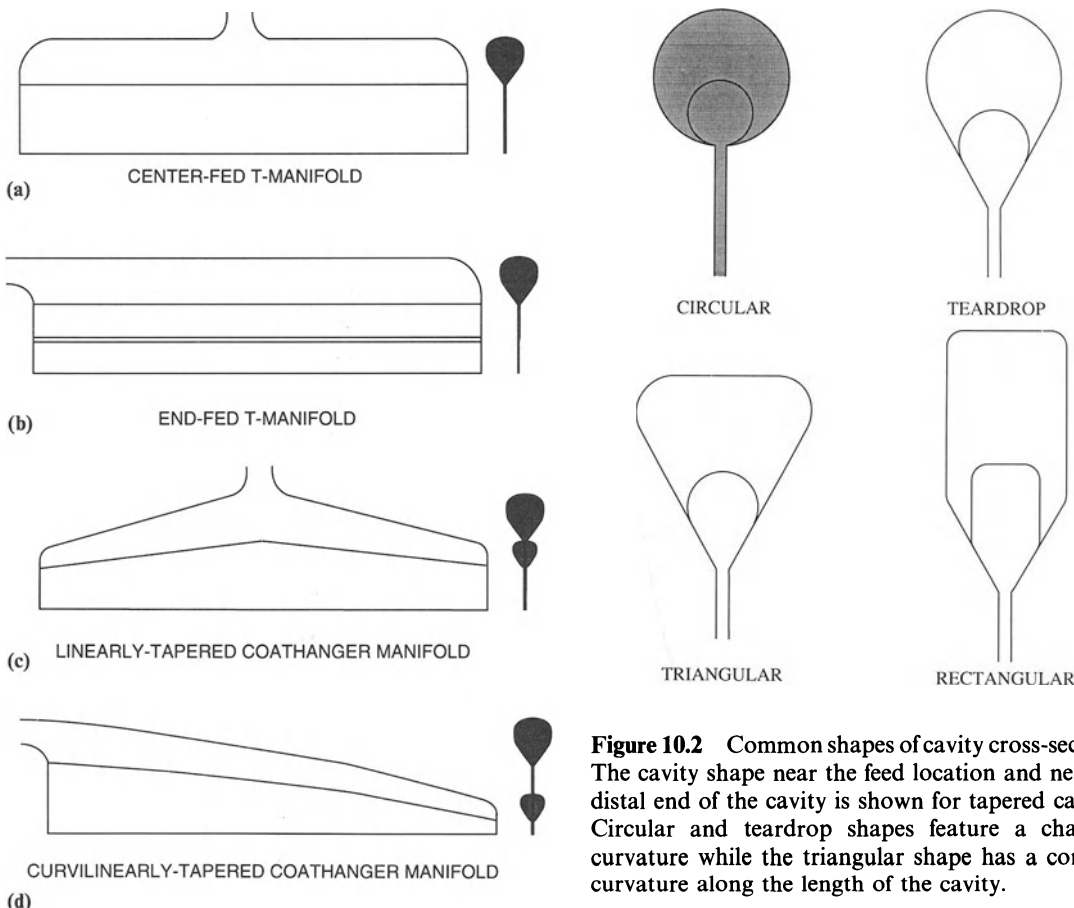


Figure 10.1 Examples of common coating die manifold shapes including: (a) a center-fed T-manifold with a single-stage slot; (b) an end-fed T-manifold with a multi-stage slot; (c) a center-fed linearly tapered coathanger manifold, and (d) an end-fed curvilinearly tapered manifold. The cross-sectional views on the right-hand side show the variation in manifold cross-section from feed location to distal end.

bar adjustment is used on a coating die, the role of the distribution manifold is different from that in a die without means of uniformity adjustment. If there is no means of adjustment, the distribution provided by the die manifold is what will be ultimately observed, and thus, must be quite uniform. If flexible lips or choker bars are present, however, the distribution provided by the die manifold does not need to be so uniform. It only needs to be sufficiently uniform that the

Figure 10.2 Common shapes of cavity cross-sections. The cavity shape near the feed location and near the distal end of the cavity is shown for tapered cavities. Circular and teardrop shapes feature a changing curvature while the triangular shape has a constant curvature along the length of the cavity.

flow can be evenly distributed within the range of adjustment of the flexible lip or the choker bar. Nevertheless, it is usually wise to design the die manifold for as uniform a distribution as possible as highly contorted flexible die lips or choker bars can produce cross-web flow and material property differences.

Public literature on the flow analysis of die manifolds falls into several broad categories. The majority use a combination of a one-dimensional flow model of viscous effects in the cavity and the slot to determine flow uniformity. In chronological order, these are:

Carley (1954) Newtonian and power-law liquids in T-manifolds;

Pearson (1964) effects of temperature variations and die distortion;

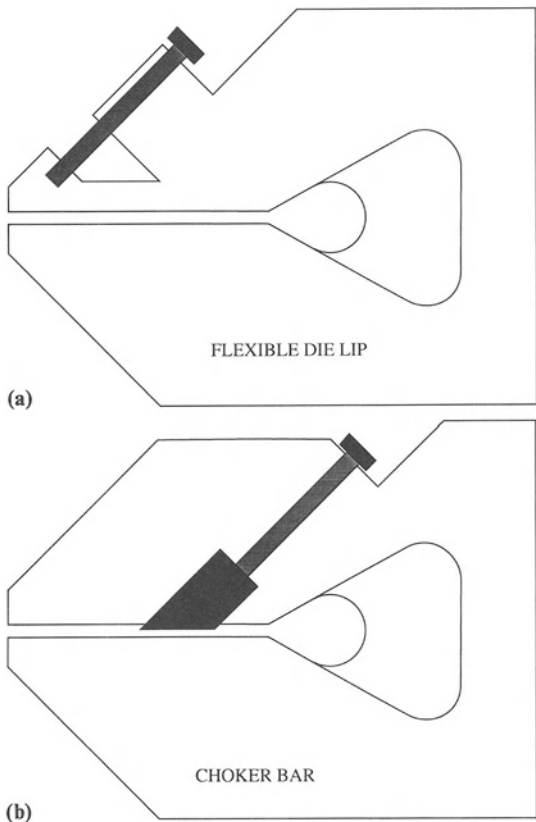


Figure 10.3 Adjustment mechanisms for coating dies:
(a) flexible die lips and (b) choker bar.

- McKelvey and Ito (1971) multi-stage slots and tapered cavities in T-manifolds;
- Procter (1972) coathanger manifolds and optimal cavity tapering for fishtail dies;
- Klein and Klein (1973) effect of flow rate on uniformity for non-power-law liquids in fishtail manifolds;
- Chung and Lohkamp (1976) related size of the cavity with the angle of the tapered slot length;
- Matsubara (1981) shapes of curvilinearly tapered coathanger manifolds in terms of the power-law index of the liquid and residence time distribution;
- Booy (1982) electrical resistance network analogy for manifold flow analysis;
- Winter and Fritz (1986) flow uniformity and residence time distribution in circular and rectangular cavities;

Liu and Hong (1988) flow uniformity and residence time distribution in coathanger manifolds with non-circular cavities.

In addition, a number of papers (Miller 1972; Huang and Yu 1973; Liu 1983; Liu and Hong 1988) specifically address the problem of using one-dimensional cavity flow models for the noncircular shapes often encountered. Of these, Liu and Hong (1988) incorporated a $1\frac{1}{2}$ -dimensional model (one velocity component varying in two dimensions) for the flow through the cavity. Papers that address two- or three-dimensional flow models in the slot include:

- Tadmor, Broyer and Gutfinger (1974) developed flow analysis network (FAN) method for two-dimensional slot flow of Newtonian and non-Newtonian liquids;
- Vergnes and Agassant (1986) two-dimensional flow and thermal analysis of coathanger manifolds;
- Sartor (1990) two-dimensional slot flow analysis mostly for Newtonian liquids;
- Vlcek *et al.* (1990) two-dimensional flow and thermal analysis with the control volume method;
- Vrahopoulou (1991) two-dimensional slot flow of Newtonian liquids with the boundary integral method;
- Wang (1991) three-dimensional finite element analysis of a coathanger manifold.

Specific discussions about the thermal analysis of manifold analysis can be found in Winter (1975) and Vergnes *et al.* (1984).

Fairly comprehensive discussions of manifold analysis can be found in the following:

- Leonard (1985b) general analysis of the effects of viscous, inertial and gravitational effects in T-die manifolds;
- Sartor (1990) analysis of viscous and inertial effects in coathanger dies;
- Michaeli (1992) general analysis of effects encountered in polymer processing.

The intent of this chapter is first to review the analysis in the public literature of the different

flow regimes and then describe how it can be best used by coating engineers to design and use coating die manifolds.

10.2 ANALYSIS OF INTERNAL DIE FLOWS

The analysis of the flow in the internal passages of coating die manifolds will be divided according to the four flow sections: (1) feeding of the cavity, (2) flow through the cavity, (3) flow through the cavity-slot transition, and (4) flow through the slot region. The flow in the immediate vicinity of the slot exit is the subject of other chapters. Figure 10.4 schematically shows these regions. In the discussion, attention will be paid to the relationship between the geometry of the die cavities, the rheological characteristics of the liquid, and the pressure and flow distribution that results.

10.2.1 CAVITY FEED

Coating die cavities can be fed in a number of different ways. Center-fed cavities, end-fed cavities, and cavities with multiple feed locations are possible. Ordinarily, the method of feeding the manifold cavity has little effect on the final flow uniformity but there are exceptions. The exceptions occur when the flow in the feed section is such that the process of feeding the cavity significantly disrupts the pressure distribution in the cavity. For low viscosity liquids, inertial forces in the flow of the feed section can disrupt the pressure

distribution in the cavity and the final flow uniformity as a result. Although no specific analysis of this appears in the published literature, analyses of an analogous situation, a liquid jet impinging on a flat plate, can be found in many fluids mechanics textbooks (e.g., Whitaker (1981) pp. 254–258; Batchelor (1967) pp. 392–396). In this situation the ratio of the force exerting on the plate to the cross-sectional area of the impinging jet is related to the kinetic energy arriving in the jet,

$$\frac{F_{\text{plate}}}{A} = \rho V^2 \quad (10.1)$$

Here ρ is the liquid density and V is the average velocity of the impinging jet. If this force to area ratio is analogous to the pressure disruption caused by inertial forces in the feed section of coating die manifolds then flow disruption can be expected when the kinetic energy of the feedstream (the right-hand side of (10.1)) is significant in comparison with the pressure in the manifold cavity.

The method of feeding high viscosity and viscoelastic coating liquids into cavities can also disrupt the ultimate uniformity. Stafford (1971) discloses that extrusion of a three-layer film from a center-fed manifold will yield an uneven distribution of the center layer whereas no disruption occurs in an end-fed manifold. According to Cloeren (1993), ‘flow divergence’ in a center-fed cavity leads to a disruption in the

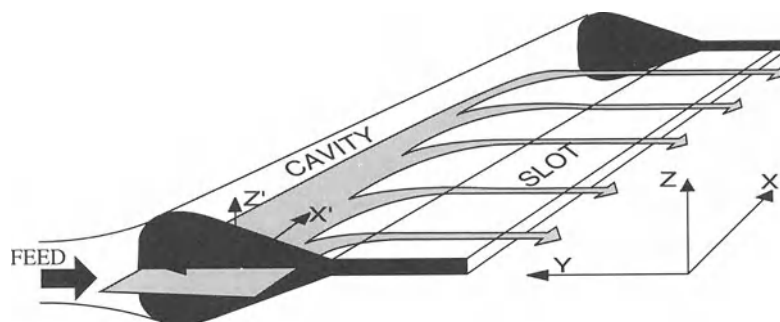


Figure 10.4 Schematic diagram of the general flow pattern in a coating die manifold.

uniformity of both multilayer and single layer films. The ‘flow divergence’ results from the ‘... division of the (feed)stream into substreams that flow in generally opposite directions to both ends of the manifold.’ Apparently, the response of melts and other viscoelastic liquids to the stretching (or extensional) flow that occurs as the feedstream splits in a center-fed cavity disrupts the pressure distribution in the manifold cavity and ultimately the flow uniformity (Secor 1995). End-fed cavities have no flow split (or ‘flow divergence’), and hence, have no resulting uniformity disruption.

Figure 10.5 shows an example of the flow nonuniformity caused by the flow split in a center-fed cavity. The upper graph shows the measured flow distribution for a center-fed T-manifold, while the lower graph shows the distribution when the same T-manifold is fed from the end. As will be discussed later, a relatively high flow is expected opposite the feed location in a T-manifold from viscous forces alone, but the nonuniformity would be expected to be higher in the end-fed manifold. Note that in this case the flow split causes a dramatically higher nonuniformity in the center-fed cavity.

10.2.2 CAVITY FLOW

After the feed section, the coating liquid flows mainly down the axis of the cavity with a small portion leaking into the slot. Ordinarily, the cross-section of the manifold cavity is a simply connected area, but there are exceptions. Michaeli (1992, pp. 205–206) shows a manifold cavity with a rotating screw inside, while Hiraki *et al.* (1989) describe a rotating rotor in the manifold cavity. Both are exceptional cases of attempts to increase the movement of the liquid in the cavity. In the cavity flow analysis here, only simply connected cavity cross-sections will be considered. Figure 10.2 shows a number of the common shapes.

Because the flow in the manifold cavity is mainly down its axis, the interplay of the different forces is captured by a balance of momentum in the direction of the cavity axis (Huang and Yu 1973). As the axis of manifold cavity may be angled slightly to the slot exit and also possibly

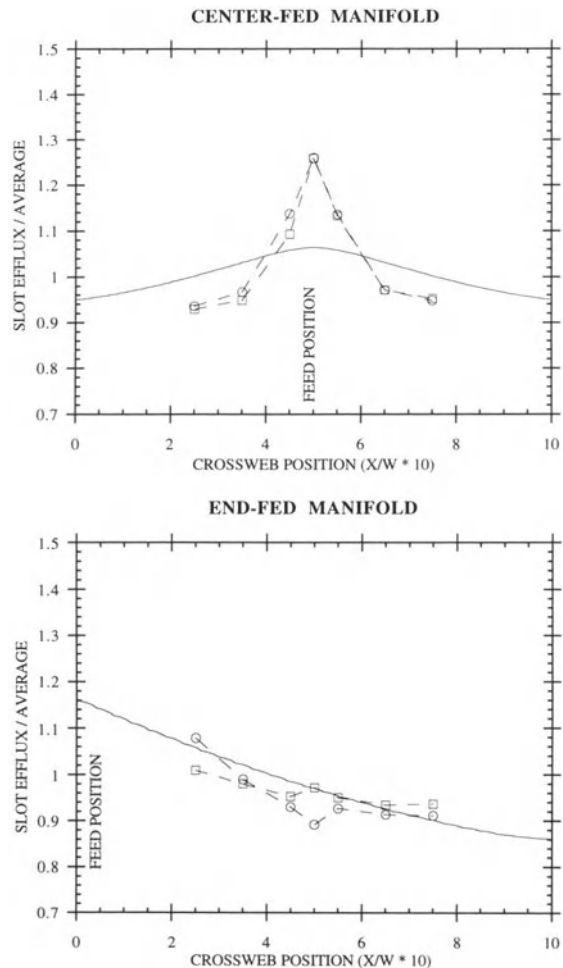


Figure 10.5 Example of the flow nonuniformity caused by the flow split in a center-fed cavity. The symbols represent experimental data points whereas the solid lines represent model predictions which ignore any influence of the method of feeding the cavity.

curved, a (X', Y', Z') Cartesian coordinate system is employed where the X' -axis locally points down the cavity axis. The X' -axis is parallel to the slot exit in T-manifolds, angled to the slot exit in linearly tapered coathanger manifolds, and curved in curvilinearly tapered coathanger manifolds. The use of this coordinate system is equivalent to ‘unrolling’ the curvature, if any, of

the manifold cavity. The momentum conservation equation for steady flow of liquid in the nonconservative form is

$$\rho \left[\frac{\partial U^2}{\partial X'} + \frac{\partial(UV)}{\partial Y'} + \frac{\partial(UW)}{\partial Z'} \right] = \frac{\partial \tau_{XX'}}{\partial X'} + \frac{\partial \tau_{XY'}}{\partial Y'} + \frac{\partial \tau_{XZ'}}{\partial Z'} - \frac{\partial P}{\partial X'} + \rho G_{X'} \quad (10.2)$$

where (U, V, W) are Cartesian components of the liquid velocity vector \mathbf{V} , τ is the stress tensor, P the hydrodynamic pressure, ρ the liquid density and $G_{X'}$ the X' -component of the gravitational force vector. The variation of the hydrodynamic pressure down the axis of the manifold cavity is of primary interest here because it is mostly this that influences the subsequent flow in the slot. As the flow in the cavity is mainly down the cavity axis, the pressure is nearly uniform across any cavity cross-section. Thus, integration over the cross-sectional area, A , of the cavity yields the following for the cavity pressure:

$$\begin{aligned} \frac{dP}{dX'} = & -\frac{\rho}{A} \int_A \frac{\partial U^2}{\partial X'} dA - \frac{\rho}{A} \int_{S_{\text{slot}}} V_N U dS \\ & + \frac{1}{A} \int_A \frac{\partial \tau_{XX'}}{\partial X'} dA \\ & + \frac{1}{A} \int_S \tau_{NX'} dS + \rho G_{X'} \end{aligned} \quad (10.3)$$

Here the subscript N refers to the direction normal to the perimeter of the manifold cavity but in the $Y'Z'$ -plane.

The first term in (10.3) represents the main contribution of inertial forces to the cavity momentum balance. For convenience, it can be rewritten in terms of an inertial shape factor, α , (Huang and Yu 1973; Leonard 1985b),

$$\begin{aligned} \rho \int_A \frac{\partial U^2}{\partial X'} dA &= \rho \frac{d}{dX} \int_A U^2 dA - \rho \int_{S_{\text{slot}}} \\ U^2 \tan \theta dS &\approx \rho \frac{d}{dX'} \int_A U^2 dA \\ &= \rho \frac{d}{dX'} \left(\alpha \frac{Q^2}{A} \right) \end{aligned} \quad (10.4)$$

$$\alpha \equiv \frac{A}{Q^2} \int_A U^2 dA, \quad Q \equiv \int_A U dA \quad (10.5)$$

Here the angle θ is the inclination of the cavity wall to the axis of the cavity. Because the liquid adheres to the walls of the manifold cavity, the second terms in (10.3) and (10.4) contain nonzero contributions only where the liquid exits the cavity and enters the slot. Because the liquid leaves the cavity substantially perpendicular to the main axis of the cavity, these terms are small in magnitude and can be entirely neglected.

The third term on the right side of (10.3) represents the role of normal stresses in the cavity momentum balance. The normal stresses can be viscous or elastic stresses due to extensional flows or elastic stresses resulting from the shear flow in the die cavity. The penultimate term in (10.3) accounts for the shear stresses acting on the perimeter of the cavity cross-section. Because the liquid ordinarily adheres to the cavity there, these stresses are viscous in nature, even for elastic liquids. They constitute the pressure drop in the cavity when inertial, gravitational and elastic forces are absent,

$$\frac{dP_{\text{vis}}}{dX'} = \frac{1}{A} \int_S \tau_{NX'} dS \quad (10.6)$$

With these modifications, the cavity momentum balance in its final form is as follows:

$$\begin{aligned} \frac{dP}{dX'} = & \frac{dP_{\text{vis}}}{dX'} - \frac{\rho d}{AdX'} \left(\alpha \frac{Q^2}{A} \right) \\ & + \frac{1}{A} \int_A \frac{\partial \tau_{XX'}}{\partial X'} dA + \rho G_{X'} \end{aligned} \quad (10.7)$$

It stipulates that the change in the hydrodynamic pressure down the cavity results from a combination of viscous losses, inertial accelerations, normal stresses and gravitational forces. Because most of the reports in the literature are targeted toward relatively high viscosity melt processing, often only viscous losses are included in the cavity momentum balance. Leonard (1985a, 1985b), Lee and Liu (1989) and Sartor (1990) are exceptions that include non-viscous forces such as inertia and gravitational forces following the

analysis by Huang and Yu (1973). Sartor (1990) included normal stresses from the extension of Newtonian liquids in his cavity momentum balance, even though they are extremely small as shown in (10.37) below. There have been no accounts in the literature of elastic effects in the manifold cavity momentum balance.

Practical application of the cavity momentum balance requires evaluation of the integrals in (10.5) and (10.6) in order to determine the inertial shape factor and the viscous pressure drop. For simplicity's sake, most analyses assume the manifold cavity cross-section is circular even though most common shapes are very noncircular. Miller (1972) proposed determining the viscous pressure drop in terms of the average wall shear stress, $\bar{\tau}$ which was postulated to depend only on an average shear rate, $\bar{\gamma}$,

$$\frac{dP_{\text{vis}}}{dX'} = \frac{1}{A} \int_S \tau_{NX'} dS = \frac{\bar{\tau}(\bar{\gamma})}{R_h}, \quad \bar{\gamma} \equiv \frac{Q\lambda}{8R_h A} \quad (10.8)$$

R_h , the hydraulic radius (*cf.* Whitaker (1981) p. 159), is the ratio of the area to the perimeter of the cavity cross-section and λ is a shape factor which is different for different cavity shapes. The functional dependence of the average wall shear stress on the average shear rate is presumed to be independent of cavity shape. Liu (1983) finds that different shape factors are required depending on the shear-thinning behavior of the liquid viscosity and tabulates values according to the power-law index of the liquid.

Coating engineers encounter two principal problems with this procedure. The first is that although the shape factors are tabulated according to power-law index, common liquids encountered in industrial situations exhibit a variety of viscosity behavior that is not represented by the power-law viscosity function (Chung and Lohkamp 1976). For solutions and polymeric liquids, the Carreau–Yasuda viscosity model (*cf.* Bird *et al.* (1987)),

$$\eta(\dot{\gamma}) = \eta_\infty + (\eta_0 - \eta_\infty) [1 + (\lambda\dot{\gamma})^a]^{\frac{n-1}{a}} \quad (10.9)$$

exhibits sufficient flexibility to capture almost all the observed variations in viscosity behavior

with shear rate. For dispersions and other more complicated materials, the Bingham–Carreau–Yasuda representation is sometimes required (Nelson, Kistler and Olmsted 1990),

$$\eta(\dot{\gamma}) = \eta_\infty + \left(\eta_0 - \eta_\infty + \tau_Y \frac{1 - e^{-F\dot{\gamma}}}{\dot{\gamma}} \right) \frac{[1 + (\lambda\dot{\gamma})^a]^{\frac{n-1}{a}}}{(10.10)}$$

Figure 10.6 compares the viscosity behavior of two liquids to that of a power-law liquid. Whereas the power-law liquid has a constant slope, both material A and material B show significant changes in their slope. Material A is representative of many shear-thinning materials that are best represented by the Carreau–Yasuda model. Material B is representative of more complicated materials that are best represented by the Bingham–Carreau–Yasuda model. In either the case of the five parameter Carreau–Yasuda model or the seven parameter Bingham–Carreau–Yasuda model, the number of parameters required to specify the viscosity behavior accurately precludes the efficient use of tabulated values for manifold flow analysis.

The second principal problem is the accuracy achieved if values for the shape factor can be found. Liu and Hong (1988) assessed the accuracy of Miller's procedure by using two numerical methods to discretize the cross-section of the manifold cavity and compute the velocity field $U(Y', Z')$ according to

$$\frac{\partial P_{\text{vis}}}{\partial X'} = \frac{\partial \tau_{XY'}}{\partial Y'} + \frac{\partial \tau_{XZ'}}{\partial Z'} \quad (10.11)$$

They concluded that for very non-Newtonian liquids, Miller's shape factor procedure is very inaccurate. As a consequence, the most efficient method for computing the viscous pressure drop in the cavity momentum balance with sufficient accuracy is apparently the $1\frac{1}{2}$ -dimensional (one velocity component varying in two dimensions) modeling procedure of Liu and Hong. The flow rate and inertial shape factor in (10.5) can then be computed by suitable integration of the velocity field.

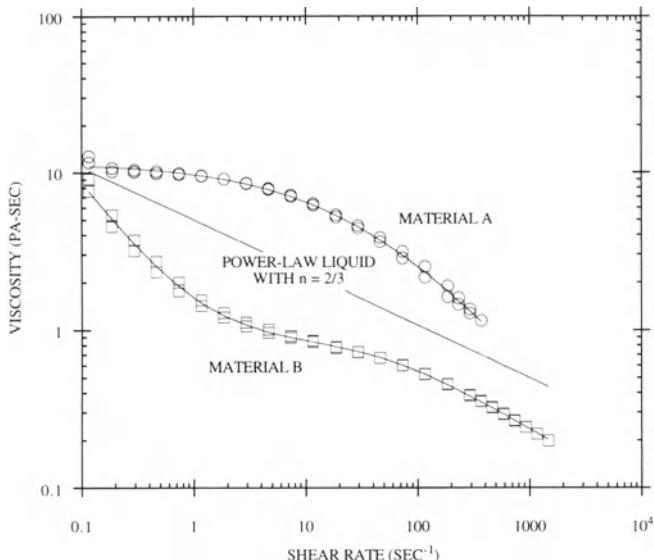


Figure 10.6 Comparison of the viscosity behavior of two materials to that of a power-law liquid. Material A shows a general shear-thinning behavior while material B shows yield stress behavior in addition to shear-thinning.

10.2.3 SLOT FLOW

The flow of the coating liquid in the slot portion of coating dies is nearly rectilinear by virtue of the large aspect ratio of most coating die slots. Typically, the length of the slot is 10 to 100 times larger than the height. The width of the die slot may in addition be 10 to 100 times the length of the slot. As a result, the analysis of the flow in the slot of the die is amenable to the lubrication approximation which applies under the following conditions (*cf.* Cameron (1981));

$$\left(\frac{H}{L}\right)^2 \ll 1, \quad Re \left(\frac{H}{L}\right)^2 \ll 1 \quad (10.12)$$

Here H and L are the characteristic thickness and length of the slot flow channel and Re is the Reynolds number.

Most analyses of the slot flow assume that the flow is unidirectional from slot inlet to outlet. Recent work has shown that this assumption can lead to erroneous results (Sartor 1990; Vrahopoulou 1991). But even these researches were restricted to Newtonian or power-law viscosity models. Apparently, it was not generally realized that the FAN method developed by

Tadmor *et al.* (1974) was capable of modeling two-dimensional slot flow of liquids of arbitrary viscosity. Here, a more general treatment is shown with its relationship to the governing equations of the FAN method.

Conservation of mass in the two-dimensional lubrication approximation results from the integration of the continuity equation over the thickness of the slot channel, see Fig. 10.7

$$\int_{H_B(X,Y)}^{H_A(X,Y)} \nabla \cdot \mathbf{V} dZ = \nabla_{II} \cdot \mathbf{Q}_S = 0, \quad \mathbf{Q}_S \equiv \int_{H_B}^{H_A} \mathbf{V}_{II}(X, Y) dZ \quad (10.13)$$

The subscripts A and B refer to the upper and lower surfaces of the slot channel and the subscript II refers to the plane of the flow channel,

$$\nabla_{II} \equiv \mathbf{I} \frac{\partial}{\partial X} + \mathbf{J} \frac{\partial}{\partial Y}, \quad \mathbf{V}_{II} \equiv \mathbf{I} U + \mathbf{J} V \quad (10.14)$$

The (X, Y, Z) Cartesian coordinate system used here has the X -axis parallel to the slot exit as shown in Fig. 10.4. The unit vectors \mathbf{I} and \mathbf{J} point in the X - and Y -directions respectively.

Conservation of momentum in the lubrication

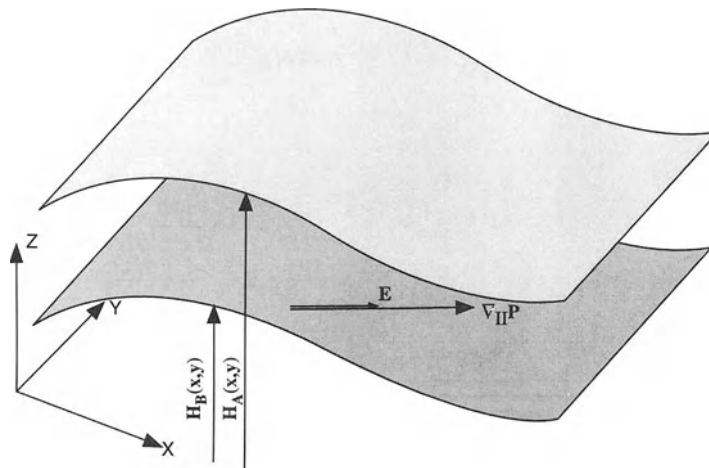


Figure 10.7 Diagram of the lubrication approximation geometry.

approximation stipulates that the liquid pressure is constant across the thickness of the flow channel. The pressure gradient in the plane of the flow channel varies in response to the shear stresses in the plane of the flow,

$$\nabla_{\text{II}} P = \frac{\partial \tau_{\text{II}Z}}{\partial Z} \quad \text{or} \quad \tau_{\text{II}Z} = \nabla_{\text{II}} P Z + \tau_0, \\ \tau_0 = \tau_{\text{II}Z}(Z = 0) \quad (10.15)$$

Because the flow is parallel to the direction of the pressure gradient, it is convenient to resolve this equation into a component parallel to the direction of the pressure gradient,

$$|\nabla_{\text{II}} P| Z = \mathbf{E} \cdot (\tau_{\text{II}Z} - \tau_0), \quad \mathbf{E} \equiv \frac{\nabla_{\text{II}} P}{|\nabla_{\text{II}} P|} \quad (10.16)$$

The boundary conditions for the surfaces of the flow channel are sensibly no slip between the liquid and its solid boundaries. For the present purpose, it is convenient to express this in integral form,

$$0 = \int_{H_B}^{H_A} \frac{\partial \mathbf{V}_{\text{II}}}{\partial Z} dZ \quad (10.17)$$

Because the lubrication flow is nearly rectilinear, only the dominant velocity gradients appear in the constitutive relation for shear-sensitive liquids

in the lubrication approximation,

$$\tau_{\text{II}Z} = \eta \left(\frac{\partial \mathbf{V}_{\text{II}}}{\partial Z} \right) \frac{\partial \mathbf{V}_{\text{II}}}{\partial Z} \quad (10.18)$$

In the lubrication flow of Newtonian liquids, the viscosity is constant throughout the flow channel and the solution of the governing equations (10.16), (10.17) and (10.18) is straightforward. In the case of shear-sensitive liquids, the viscosity varies throughout the channel and, thus, it is convenient to transform the integration variable in the governing equations from the coordinate Z to stress. Rearrangement of equation (10.13) using integration by parts followed by transformation of the integration variable yields the following:

$$\begin{aligned} \mathbf{Q}_S &= - \int_{H_B}^{H_A} Z \frac{\partial \mathbf{V}_{\text{II}}}{\partial Z} dZ \\ &= - \frac{1}{|\nabla_{\text{II}} P|^2} \int_{E_{\text{II}Z}}^{E_{\text{II}Z}} \mathbf{E} \cdot (\tau_{\text{II}Z} - \tau_0) \frac{\partial \mathbf{V}_{\text{II}}}{\partial Z} \mathbf{E} \cdot d\tau_{\text{II}Z} \end{aligned} \quad (10.19)$$

With the application of the no-slip boundary conditions (10.17), further transformation of the integration variable from stress to velocity gradient, and some manipulation, (10.19) is reduced to an

expression for the flow rate in terms of the velocity gradient at the bounding surfaces,

$$\begin{aligned} \mathbf{Q}_s &= -\frac{(H_A - H_B)^2}{4} L_A \mathbf{E} \\ &\left[1 - \frac{1}{\eta^2(|L_A|) L_A^3} \int_0^{|L_A|} \eta^2(|L|) L^2 dL \right] \quad (10.20) \\ L_A &\equiv \mathbf{E} \cdot \frac{\partial \mathbf{V}_{II}}{\partial Z} (Z = H_A) = -\mathbf{E} \cdot \frac{\partial \mathbf{V}_{II}}{\partial Z} (Z = H_B) \end{aligned}$$

(10.21)

L_A , the velocity gradient at the upper surface, is determined by applying (10.15) at the upper and lower surfaces,

$$|\nabla_{II} P| (H_A - H_B) = 2 \eta (|L_A|) L_A \quad (10.22)$$

The combination of (10.22), (10.20) and the conservation of mass principle, (10.13) serve to determine the pressure and flow rate distribution in the slot channel of a die manifold. This combination is general in that any viscosity model can be incorporated. The only requirement is that the integral in (10.20) has to be evaluated either analytically or numerically.

The FAN method starts with the solution to the two-dimensional lubrication flow of a Newtonian liquid with no-slip boundary conditions on each boundary,

$$\mathbf{Q}_s = -\frac{(H_A - H_B)^3}{12 \mu} \nabla_{II} P \quad (10.23)$$

For shear-thinning liquids, the Newtonian viscosity μ is replaced by an equivalent viscosity defined in terms of the wall shear stress, τ_w ,

$$\mu_{\text{equivalent}} = \frac{\tau_w^3}{3 \int_0^{\tau_w} \tau \dot{\gamma} d\tau} \quad (10.24)$$

The combination of (10.23) and (10.24) is equivalent to (10.19) in foregoing development. In either case, efficient and accurate two-dimensional lubrication flow analyses of liquids with arbitrary viscosity functions in the slots of die manifolds are possible.

10.2.4 CAVITY–SLOT TRANSITION

The cavity flow and the slot flow described in the preceding two sections are joined by a transitional flow between them. Liquid leaves the cavity on one side and enters the manifold slot. Conservation of mass dictates that whatever liquid leaves the cavity must enter the slot,

$$\frac{dQ}{dX'} = N_{II} \cdot \mathbf{Q}_s \quad (10.25)$$

Here N_{II} is the unit normal vector in the plane of and pointing outward from the manifold slot.

The balance of momentum over the transitional flow serves to relate the pressure at the beginning of the slot to the pressure in the cavity. All literature reports of manifold models assume that the cavity pressure is identical to the pressure at the head of the slot. In reality these pressures will differ by an entrance pressure loss which characterizes the viscous losses, inertial forces, extensional viscosity effects and elastic effects in the cavity–slot transitional flow,

$$P_{\text{cavity}} = \Delta P_{\text{ent}} + P_{\text{slot}} \quad (10.26)$$

A related flow, the contraction flow, has been studied extensively and the roles of the different forces delineated, (Boger 1987; Binding 1988; White, Gotsis and Baird 1987; Binding 1991). For Newtonian liquids in a circular contraction, Boger (1987) reports the following for the role of inertial forces and viscous losses in the entrance pressure loss:

$$\frac{\Delta P_{\text{ent}}}{2 \tau_w} = 0.0725 Re + 0.69 \quad (10.27)$$

The Reynolds number and wall shear stress are those based on the smallest tube in the contraction flow. A similar expression is also reported for shear-thinning liquids. Although the entrance pressure loss in the planar contraction flow that occurs in die manifolds would be expected to be somewhat different, a few points from the circular contraction flow entrance pressure loss are noteworthy. Because the viscous contribution to the dimensionless entrance pressure loss in (10.27) is on the order of unity, the viscous loss is not

expected to be significant as long as the slot has a relatively large aspect ratio, (e.g., $L/H > 10$). Likewise, the inertial contribution to the entrance pressure loss is only significant when the Reynolds number (based on the slot flow) is large.

Contraction flow analyses also yield information about the viscoelastic effects in the cavity–slot transitional flow. In abrupt contractions, elastic liquids often show vortices just upstream of the contraction. The vortices are more pronounced in circular contractions than planar ones and can be eliminated by a sufficient tapering of the entry flow geometry (White, Gotsis and Baird 1987). The size of the vortices and likewise the size of the entrance pressure loss is largest for liquids that exhibit large extensional viscosities (Luo and Mitsoulis 1990). Binding (1988) provides an accounting of the extensional viscosity effects on the entrance pressure loss based on considerations of the energy dissipation in the contraction flow. The entrance pressure loss in a planar contraction for a liquid which shows power-law viscosity behavior in both extension and shear is

$$\frac{\Delta P_{\text{ent}}}{\tau_w} = \frac{2\left(2 + \frac{1}{n}\right)}{3\left(3 + \frac{2}{n}\right)\left(4 + \frac{3}{n}\right)} (1 - \beta^2) Re + \frac{(1+t)^2}{2t^2(1+n)} \frac{\dot{\gamma}_w}{\dot{\varepsilon}_{\max}} \left(1 - \beta^{2t\frac{n+1}{t+1}}\right) \quad (10.28)$$

Here n and t are the power-law indices of the shear and extensional viscosity and β is the inverse of the contraction ratio. The first term represents the inertial contribution to the entrance pressure loss while the second, which contains the ratio of maximum shear rate to extension rate in the flow, characterizes the viscous and extensional viscosity effects.

10.2.5 MANIFOLD ANALYSIS

The combination of mass and momentum conservation equations for the cavity flow, the slot flow and the transitional flow described in the last three sections comprise a model for

analysis of flow in coating dies. They provide the means of determining expected cross-web flow distribution in a coating die manifold given the manifold geometry, the material properties of the coating liquid and the throughput rate of liquid through the manifold.

For example, Fig. 10.8 shows the resulting cross-web uniformity computed for a T-manifold compared with experimental data. The flow uniformity was computed with a combined model of $1\frac{1}{2}$ -dimensional cavity flow, two-dimensional lubrication flow in the slot, and no entrance pressure loss in the transitional flow. The gap in the slot of this manifold varied in the cross-web direction as is shown in Fig. 10.8. As will be discussed later, a high flow would ordinarily be expected opposite the location of the cavity feed. Although the T-manifold is fed at a location which corresponds to the left side of the figure, due to the nonuniform slot gap the slot efflux is highest on the right. This example serves to illustrate the sensitivity of manifold flow to small changes in the slot gap. According to (10.23) the flow in the slot is proportional to the cube of the gap for Newtonian liquids. For shear-thinning liquids the sensitivity is higher. As a result, small gap variations can lead to large flow nonuniformities.

10.2.6 DIMENSIONAL ANALYSIS

In order to assess the regimes better where the different forces (i.e. inertial, gravitational and elastic) play an integral role, dimensional analysis is employed. Here we follow closely the procedure used by Leonard (1985b) for dimensional analysis of T-manifolds with some modifications.

The drop in pressure due to the flow through the slot of the manifold scales according to

$$P^* = \frac{2L\eta_s \dot{\gamma}_s}{H}, \quad \eta_s \equiv \eta(\dot{\gamma}_s), \quad \dot{\gamma}_s \equiv \frac{6Q_0}{WH^2} \quad (10.29)$$

where L is the length of the slot, H the gap in the slot channel, W the width of the die, and Q_0 the volumetric flow rate of liquid entering the die. The ratio of the viscous pressure drop in the

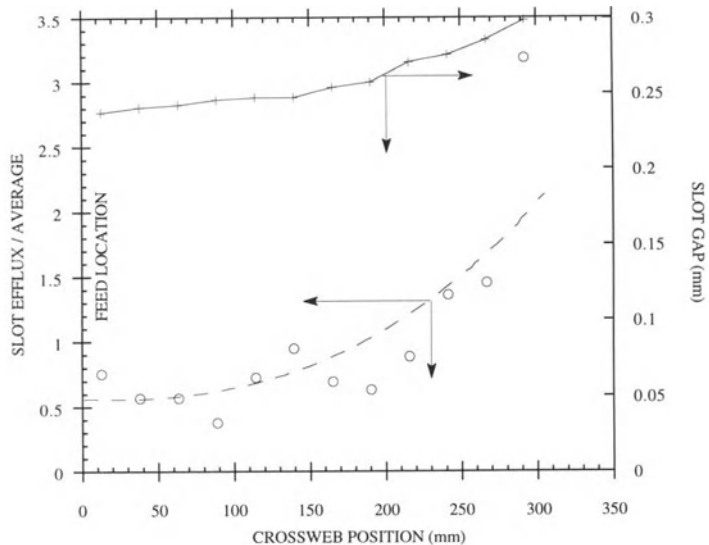


Figure 10.8 Comparison of the flow uniformity predicted for a T-manifold with experimental data. The coating liquid has a viscosity described by (10.10) with $\eta_0 = 1.365 \text{ Pa s}$, $n = 0.0532$, $\lambda = 0.0556 \text{ s}$, $a = 2$, $\eta_\infty = 0.0057 \text{ Pa s}$, $\tau_y = 5.96 \text{ Pa}$ and $F = 511$.

manifold cavity to the pressure drop in the die slot comprises the viscous number, Nv ,

$$Nv = \frac{W\eta_c \dot{\gamma}_c}{R_h P^*}, \quad \eta_c \equiv \eta(\dot{\gamma}_c), \quad \dot{\gamma}_c \equiv \frac{2Q_0}{AR_h} \quad (10.30)$$

Here R_h is the hydraulic radius of the cavity cross-section and serves as the characteristic length scale of flow in the manifold cavity. A is the cross-sectional area of the manifold cavity. Note that as long as the viscosity behavior in the slot and in the cavity are similar, Nv and hence the relative flow resistance in the cavity and the slot is independent of the throughput rate through the die. This is not the case if inertial forces are significant as measured by the momentum number, Nm . It is the ratio of the inertial pressure gradient in the cavity to the slot pressure drop,

$$Nm = \frac{\rho Q_0^2}{A^2 P^*} \quad (10.31)$$

The ratio of the momentum to viscous numbers reflects the relative importance of inertial and

viscous forces in the cavity and is closely associated to the Reynolds number in the manifold cavity,

$$\frac{Nm}{Nv} = \frac{Re}{8(W/R_h)} \quad (10.32)$$

The influence of gravitational forces on the manifold flow is contained in the gravity number which is the ratio of the gravitational force in the cavity to viscous forces in the slot,

$$Ng = \frac{\rho G_x W}{P^*} \quad (10.33)$$

The ratio of the gravity to viscous numbers reflects the role of gravitational forces in the manifold cavity and is closely related to the cavity Stokes number,

$$\frac{Ng}{Nv} = \frac{St}{32} \quad (10.34)$$

The viscoelasticity of the coating liquid would sensibly affect the manifold flow through three sources: (1) the ‘memory’ of viscoelastic liquids; (2) elastic normal stresses from shear flow, and

(3) normal stresses from extensional flows. Ordinarily the viscoelastic memory of coating liquids would be expected to influence the manifold flow when the Deborah number, which is the ratio of the characteristic memory time of the liquid to the characteristic time scale of the flow, becomes large. But the majority of the distribution characteristics of a coating die manifold are determined by flow conditions at or very near the walls of the manifold. At the manifold walls, the coating liquid is stationary or moving very slowly, and hence, experiences the flow near the wall for a very long time. As a result, the viscoelastic memory plays an insignificant role in the manifold flow distribution.

Elastic normal stresses from shear flows may influence the manifold flow in both the cavity and the slot. Based on the cavity momentum balance (10.7), normal stresses in the cavity are expected to influence flow distribution in accordance with the normal stress number,

$$Nns = \frac{\Psi_{1c} \dot{\gamma}_c^2}{P^*} \quad (10.35)$$

where Ψ_{1c} is the first normal stress coefficient evaluated at the characteristic cavity shear rate. The ratio of the normal stress number to the viscous number represents the relative importance of normal stress and viscous effects in the cavity flow and is proportional to the stress ratio,

$$\frac{Nns}{Nv} = \frac{SR}{(W/R_h)}, \quad SR \equiv \frac{\Psi_1 \dot{\gamma}}{\eta} \quad (10.36)$$

As it is rare for coating liquids to have stress ratios greater than ten (Bird, Armstrong and Hassager 1987) and because the aspect ratio of industrial manifold cavities are often quite large, normal stress effects are not expected to be significant in manifold flows.

Normal stresses derived from extensional flows may affect the manifold flow in both the cavity and the cavity–slot transition. In the cavity, their influence is represented by the extension number,

$$Nex = \frac{\eta_{ext} Q_0}{AWP^*}, \quad \frac{Nex}{Nv} = \frac{\eta_{ext}}{\eta_c} \frac{R_h^2}{2W^2} \quad (10.37)$$

Here η_{ext} is the extensional viscosity in the cavity

flow. The ratio of extensional to viscous effects in the cavity is represented by the ratio of extension to viscous numbers which is proportional to the ratio of extensional to shear viscosity in the cavity. Here again, the appearance of the cavity aspect ratio in the scaling of the extensional effects diminishes their importance. In the cavity–slot transition, however, the extensional properties of the coating liquid are likely to have a bigger influence. Because extensional effects can lead to large entrance pressure losses in the flow into the slot according to (10.26), they can have a large impact on the hydrodynamic pressure in the manifold cavity. However, the extensional effects will have a smaller impact on the flow distribution of the manifold. Because the cavity momentum balance (10.7) contains only pressure gradients, only the cross-web gradient of the entrance pressure loss will affect the flow distribution of the die manifold. That is, if a manifold yields a uniform distribution without entrance pressure losses, it will also yield a uniform distribution with entrance pressure losses included. Furthermore, if a manifold has a nonuniform distribution without entrance pressure losses, the distribution will be more uniform when entrance pressure losses are included. This applies equally to entrance pressure losses from inertial forces and extensional viscosity effects.

In addition to the viscous, inertial, gravitational and viscoelastic forces described above, the flow distribution of die manifolds can be affected by elastic deformation of the coating die itself. This is characterized by analogy with the deflection of a cantilevered beam that has a load that linearly decreases from the support to the free end (*cf.* Blodgett (1966)). The ratio of the maximum die deflection to the slot gap comprises the deflection number,

$$N_d \equiv \frac{\delta}{H} = \frac{P^* L^4}{30 EI H} = \frac{2\eta_s Q_0 L^5}{5 EI W^4} \quad (10.38)$$

Here E is the elastic modulus of the coating die material and I is the moment of inertia of the die cross-section. For small values of the deflection number (approximately $N_d < 0.01$) the manifold

flow distribution is unaffected by the elastic deformation of the die, but at large deflection numbers (approximately $N_d > 0.1$) the effect is significant.

10.2.7 THERMAL ANALYSIS

In the preceding discussion, it has been implicitly assumed that the coating die and the liquid maintain a constant temperature. Occasionally, temperature gradients are used as a means of changing the cross-web uniformity or incidentally introduced when the die manifold is used to remove or add heat from a liquid stream before coating. Less common is the generation of temperature gradients due to viscous dissipation in the manifold flow.

Variations in temperature influence the manifold flow through the temperature dependence of the liquid viscosity. For polymeric materials, the temperature dependence is often represented in terms of a temperature shift factor, a_T (*cf.* Bird, Armstrong and Hassager (1987)),

$$\eta(\dot{\gamma}, T) = a_T(T)\eta_{\text{ref}}(a_T\dot{\gamma}) \quad (10.39)$$

where η_{ref} is a reference viscosity at the reference temperature, T_{ref} . Two functional forms of the temperature shift factor are commonly used: (1) the Arrhenius form:

$$a_T(T) = \exp\left[\frac{\Delta H}{R}\left(\frac{1}{T} - \frac{1}{T_{\text{ref}}}\right)\right] \quad (10.40)$$

and (2) the WLF equation:

$$\log a_T = \frac{-C_1(T - T_{\text{ref}})}{C_2 + T - T_{\text{ref}}} \quad (10.41)$$

Characterization of temperature fields in flow systems can be found in several sources (Winter 1975; Pearson 1985; Bird, Armstrong and Hassager 1987). The salient points are recounted here with reference to the flow through coating die manifolds. If the coating liquid is fed to the manifold with a homogeneous temperature that is equal to that of the die body, then the only temperature gradients present would sensibly be those that arise from viscous dissipation in the flow. The

Nahme number (or Nahme–Griffith number) indicates when viscous dissipation can be expected to influence the flow,

$$Na \equiv \frac{\eta^* V^2}{k} \left| \frac{1}{\eta} \frac{d\eta}{dT} \right| \quad (10.42)$$

The characteristic viscosity, velocity, and thermal conductivity are denoted by η^* , V and k . Large Nahme numbers (i.e. $Na > 1$) indicate a strong influence of viscous dissipation on the flow while a small Nahme number represents negligible influence. Except for very high speed coating of very viscous liquids (e.g. $\eta^* > 10^3$ Pa s, $V > 1$ m/s), viscous dissipation ordinarily does not play a significant role in manifold flows.

Whether produced by viscous dissipation or introduced by temperature differences between coating die and liquid feed, temperature fields in manifold flows are governed by the interplay between thermal convection with the flow and thermal conduction mostly perpendicular to the flow. The Graetz number, which is closely related to the thermal *Pé* number, measures the relative importance of thermal convection to conduction and provides a measure of the degree of thermal development,

$$Gz \equiv \frac{VH^{*2}}{\alpha L^*} = P\acute{e} \frac{H}{L} \quad (10.43)$$

Here H^* is a characteristic dimension for conduction, L^* is a characteristic length in the flow direction, α is the thermal diffusivity and V is a characteristic velocity. Large Graetz numbers are indicative of convection-dominated temperature field which is still in the infantile stages of development. Typical Graetz numbers for manifold flows range from 10 to 10^4 . The ratio of the Graetz number in a manifold cavity to that in the slot is approximately equal to the aspect ratio of the slot

$$\frac{Gz_{\text{cavity}}}{Gz_{\text{slot}}} \approx \frac{L_{\text{slot}}}{H_{\text{slot}}} \quad (10.44)$$

Thus, thermal conduction plays a bigger role in the slot flow than it does in the cavity flow and

thermal manipulation of the die slot would have a larger impact on the flow uniformity.

Because of the complexity of the developing temperature field in manifold flows there have been relatively few analyses in the public literature. Vergnes *et al.* (1984) investigated the effects of temperature gradients in a coathanger die manifold but considered only a mean temperature across the depth of the cavity and slot. Nordberg and Winter (1990) used a similar approach in analyzing multilayer slot flows. Consideration of only a mean temperature across the depth of the manifold channels is a little disquieting because the temperature in the vicinity of the walls of the manifold should influence the flow more than the temperatures elsewhere. Equation (10.20) shows that the viscosity (and hence, the temperature) in the regions of highest shear rate (i.e. in the vicinity of the solid boundaries) has a much greater influence on the slot flow than the viscosity elsewhere. As a result, the actual influence of the temperature field on the flow uniformity might be lost by a mean temperature approximation.

Bird, Armstrong and Hassager (1987, pp. 211–215) show a solution to the temperature field in the flow through channels that might be quite useful in conjunction with manifold flow models. The solution is valid for the initial stages of thermal development, small viscous dissipation effects, and assumes a linear velocity profile in the vicinity of the channel wall. The resulting temperature field is

$$\frac{T - T_{\text{wall}}}{T_{\text{initial}} - T_{\text{wall}}} = \frac{1}{\Gamma(\frac{4}{3})} \int_0^x \exp[-\bar{\chi}^3] d\bar{\chi},$$

$$\chi \equiv y \left(\frac{\gamma_{\text{wall}}}{9\alpha x} \right)^{1/3} \quad (10.45)$$

where $\Gamma()$ is the gamma function, y is the distance from the walls of the channel and x is the distance in the flow direction.

10.3 DESIGN CONSIDERATIONS

The goal of a manifold design is to define a manifold geometry that will produce a uniform

cross-web distribution of coating liquid. The uniformity of the distribution is measured in terms of the uniformity index (Leonard 1985b):

$$UI \equiv \frac{(-\mathbf{J} \cdot \mathbf{Q}_s)_{\max} - (-\mathbf{J} \cdot \mathbf{Q}_s)_{\min}}{Q_0/W} \quad (10.46)$$

which is the ratio of the difference between the maximum and the minimum efflux from the manifold slot to the average slot efflux. A uniform distribution and hence, a small uniformity index, results from all flow paths through the manifold have substantially the same resistance to flow. A number of different strategies may be undertaken depending on the final application of the coating die. The discussion of these considerations begins with the characteristics of two limiting cases, the T-manifold and coathanger designs.

10.3.1 T-MANIFOLD DESIGN – NO GRAVITY, INERTIA EFFECT

The T-manifold (or infinite cavity) design strives for equal flow resistance through the die manifold by incorporating a uniform slot of high flow resistance with a uniform cavity of low flow resistance. In the limiting case of zero flow resistance in the cavity, a cavity of ‘infinite’ size, the degree of uniformity is determined only by the uniformity of the slot gap and length. For relatively high viscosity liquids ($Nm \ll 1, Ng \ll 1$), the flow uniformity from a T-manifold depends only on the viscous number, Nv , which is the ratio of viscous losses in the cavity to those in the slot. Leonard (1985b) has presented an approximate equation for the uniformity index for power-law liquids in this situation,

$$UI = \sqrt{Nv} n^{0.3909(1 - \sqrt{n}) - 1.527}$$

$$\tanh\left(\frac{\sqrt{Nv}}{2}\right) \quad (10.47)$$

Here n is the power-law index of the power-law viscosity function and Nv is defined according to (10.30). Figure 10.9 is a graphical representation of (10.47) and shows the values of the viscous number required for acceptable uniformity. Note

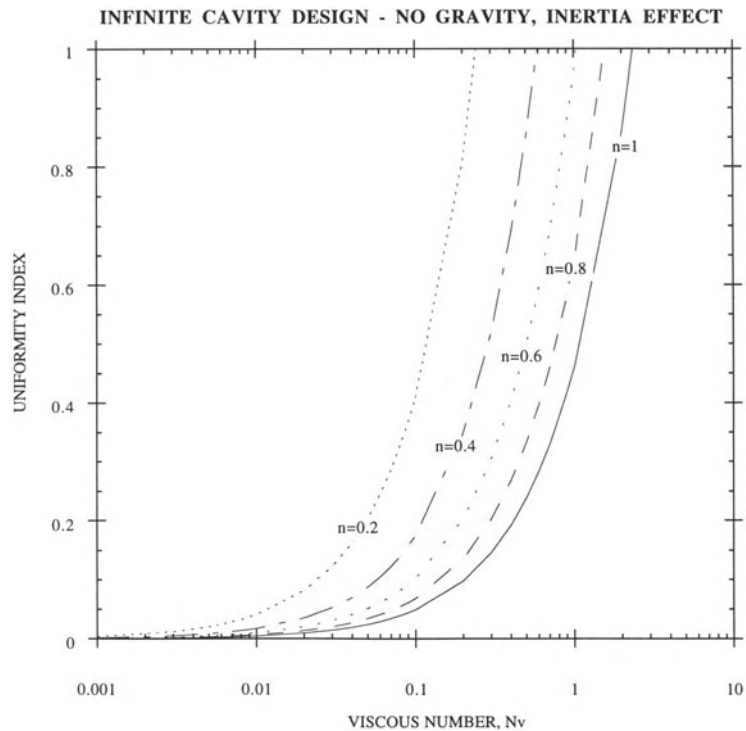


Figure 10.9 The cross-web uniformity of power-law liquids in infinite cavity manifolds according to equation (10.47). Gravitational and inertial effects are neglected in this case.

that for small viscous numbers ($Nv < 0.1$), a uniform distribution is predicted regardless of the power-law index, that is, regardless of the shear-thinning behavior of the liquid. It is this characteristic that in many cases makes the T-manifold design an attractive choice. It has substantial ability to produce uniform flow distributions with a wide variety of liquids.

Another implication of equation (10.47) and Fig. 10.9 is that the uniformity is dependent on the throughput through the die only through the viscous number, Nv . For the special case of power-law liquids, the viscous number is entirely independent of flow rate. As a result, the uniformity of a power-law liquid is a constant for all flow rates. Figure 10.10 shows an example of this for a power-law liquid with a power-law index equal to 2/3. Also shown is the expected uniformity from a liquid with the viscosity behavior of

material A in Fig. 10.6. Note the large differences in flow uniformity that result from a relatively small departure from power-law viscosity behavior.

It is noteworthy that the analysis performed by Leonard (1985b) on which equation (10.47) is based does not include the possibility of entrance pressure losses in the cavity–slot transitional flow. Highly elastic liquids are likely to have large extensional viscosities, and hence, large entrance pressure losses. As a result, equation (10.47) represents an upper bound for the uniformity index as the presence of entrance pressure losses would improve the uniformity by providing an added flow resistance in the cavity–slot transition.

T-manifolds have the disadvantage that for high viscosity liquids extraordinarily high cavity pressures or very large cavities may be required to achieve reasonable uniformity. Rearrangement

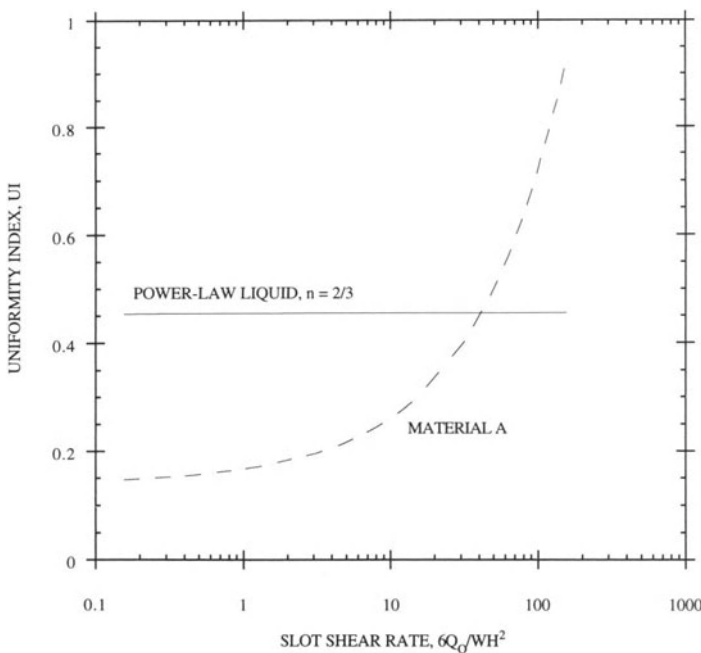


Figure 10.10 The variation of the cross-web uniformity with flow rate in a power-law liquid and one with the viscosity behavior of material A in Fig. 10.6. The viscous number, Nv , is 0.39 for the power-law liquid and varies from 0.17 to 0.52 over the flow rate range for material A.

of (10.30) expresses the scale of the cavity pressure in terms of the viscous number:

$$P^* = \frac{1}{Nv} \frac{W}{R_h} \eta_c \dot{\gamma}_c \quad (10.48)$$

In order to maintain flow uniformity (i.e. maintain a small Nv number) while increasing viscosity, either the cavity pressure will increase or the cavity size must increase to limit the pressure increase. Large cavity pressures in turn require very bulky coating dies to resist deflection of the coating die. The die size required is gauged from the die cross-section moment of inertia needed to keep the deflection number defined in (10.38) small. Large cavities diminish the ability of the die to resist deflection from hydrodynamic pressure and increase the residence time of the liquid in the manifold. Large residence times may cause thermal degradation problems or other detrimental effects if the coating liquid is reactive.

Matsubara (1980) analyzed the distribution of average residence time in a T-manifold with a circular cavity cross-section. This distribution of residence times is that which arises from the different flow paths the liquid takes through the manifold and not the distribution that arises from the roughly parabolic velocity profile through the channels of the manifold. The residence time distribution, $t(X)$, calculated as the length of the flow path divided by the average velocity through it, is

$$\begin{aligned} \left(\frac{t(X)}{HWL} \right) &= 1 + \frac{\pi R^2}{HL} \ln \left[\frac{W}{W-X} \right] \\ &\quad + \frac{\pi R^2 E}{2 HWL} \end{aligned} \quad (10.49)$$

where E is the length of the entrance tube that feeds the manifold cavity. Liquid exiting from the slot opposite the feed location of the cavity has

the shortest residence time whereas liquid that travels through the distal end of the cavity has the longest. The breadth of the residence time distribution is clearly influenced by the size of the cavity and the slot.

10.3.2 T-MANIFOLD DESIGN – GRAVITY, INERTIA EFFECTS

When gravitational and inertial effects are negligible in the T-manifold (i.e. $Nm \ll 1, Ng \ll 1$), the flow exiting from the slot is always highest adjacent to the cavity feed location. The presence of gravitational and/or inertial effects can change this slot efflux from a maximum to a minimum. Acrivos, Babcock and Pigford (1959) describe the essential physical mechanisms for the inertial effects.

Both Leonard (1985b) and Sartor (1990) report that for Newtonian liquids, the T-manifold flow distribution can be made perfectly uniform by matching the momentum and viscous forces. Under this condition, the viscous losses in the cavity flow are exactly offset by the inertial forces. When the momentum number is much less than the viscous number, the slot efflux is still highest adjacent to the feed location. As the momentum number approaches and then exceeds the viscous number, the slot efflux becomes lowest adjacent to the feed location. Figure 10.11 shows an example of this effect.

For shear-thinning liquids, in particular, liquids with power-law viscosities, Leonard (1985b) reports that a perfect flow distribution is not possible, but a minimum occurs as the momentum number is increased in relation to the viscous number. The location of the minimum is shifted to higher ratios of the momentum and viscous numbers with lower power-law indices.

It is also noteworthy to add here that since the analysis by Leonard (1985b) ignores entrance pressure losses in the cavity–slot transition, the predictions of the uniformity index may be over-estimated. An entrance pressure loss due to inertial forces will increase the flow resistance in relation to the local flow rate, and hence, increase the uniformity of the flow distribution.

Gravitational effects can affect the flow uniformity of a T-manifold design in much the same way as inertial effects when the cavity axis is not aligned horizontally. Leonard (1985b) shows the minimum uniformity index for several power-law liquids appearing between values of 0.5 and 1 for ratio of the gravity number to viscous number. Negative values of the gravity number always decrease the flow uniformity of the T-manifold.

10.3.3 COATHANGER DESIGN

An alternative to the T-manifold is the coathanger manifold design. This design matches the flow resistance in the cavity and the slot so that each path through the die has equal resistance. Pearson (1964) describes a coathanger design that tailors the flow resistance in the slot using the slot gap. McKelvey and Ito (1971) and Cloeren (1993) use a multistage slot in which the gaps in the individual stages and the total length of the slot are constant across the width of the manifold. The length of the individual stages have a cross-web variance that changes the slot flow resistance. A more common approach is to use a single-stage slot whose length varies in the cross-web direction. That is, the slot length is longer near the feedport and shorter at the distal end of the die so that lower slot flow resistance at the end is exactly balanced by the resistance from the flow through the manifold cavity. The difference between the slot length at the feedport and the slot length at the end of the die is referred to as the slot length taper. The amount of taper required in the slot length is given approximately by setting the viscous number equal to one in (10.30),

$$L_{\text{taper}} = \frac{WH}{2R_h} \frac{\eta_c \dot{\gamma}_c}{\eta_s \dot{\gamma}_s} \quad (10.50)$$

Thus larger taper in the slot length is required for more shear-thinning liquids, wider dies, smaller cavities and larger slot gaps.

In addition to the taper in the slot, the cavity cross-section usually decreases in size from the

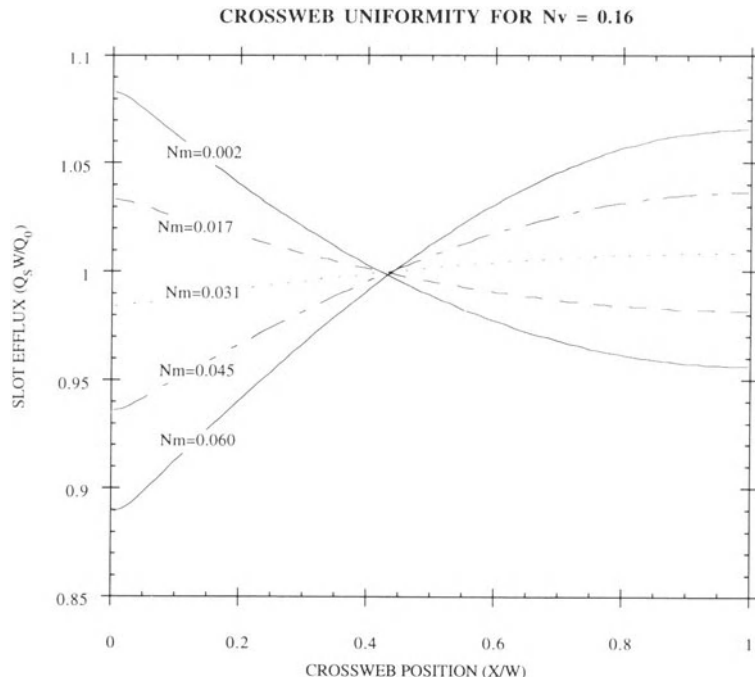


Figure 10.11 An example of the cross-web uniformity change due to inertial effects. The cavity feed location is at $X = 0$.

feed location to the distal end in order to reduce the liquid residence time. Whereas a circular cavity of constant size is easily fabricated, a circular cavity of decreasing radius is difficult to machine. It is much easier to fabricate a noncircular cavity (such as the triangular cavity in Fig. 10.2) using a constant-radius machine tool (Chung and Lohkamp 1976). The size of the cavity is varied by changing the depth of the machine tool cut.

Two types of coathanger manifolds are often distinguished: (1) the linearly tapered coathanger (or fishtail manifold) and (2) the curvilinearly tapered coathanger. The linearly tapered coathanger often, but not always, has a linear taper in both the slot length and the cavity size. Traditionally, the linearly tapered coathanger has been preferred because of its ease of manufacture with acceptable resulting flow uniformity (Michaeli 1992). The advent of computer-controlled fabrication machinery, however, has made

the curvilinearly tapered coathanger manifold as simple to fabricate as the linearly tapered coathanger. In addition, because uniformity requirements have generally increased, the superior resulting flow uniformity obtained from the curvilinearly tapered coathanger manifold makes it the preferred choice.

A number of prescriptions are available for designing the appropriate tapers in the slot length and cavity size in coathanger manifolds. Most are derived under the tenuous assumption that the slot flow is everywhere parallel to the machine direction (opposed to the direction of the Y-axis in Fig. 10.4). Under this flow condition, equality of flow resistance for each flow path is specified mathematically as a relation between the slot and cavity pressure gradients and the slope of the slot length taper:

$$\left[\frac{dP}{dY} \right]_{\text{slot}} = - \left[\frac{dP}{dX'} \right]_{\text{cavity}} \frac{1}{\sin \phi} \quad (10.51)$$

The angle ϕ characterizes the slot length taper,

$$\frac{dL}{dX} = -\tan \phi \quad (10.52)$$

Procter (1972) reports that the optimal uniformity from a linearly tapered coathanger is obtained when the cavity radius (or equivalent radius) at the feed location is 1.5 times bigger than that at the distal end. Chung and Lohkamp (1976), Tadmor and Gogos (1979, pp. 545–551), and Matsubara (1983) report that for perfect uniformity in a coathanger with a linearly tapered slot length, the cavity radius (or equivalent radius) should have the following form:

$$R(X) = R_0 \left[1 - \frac{X}{W} \right]^{\frac{n}{3n+1}},$$

$$R_0 = \left[\frac{H^{2n+1}}{\sin \phi} \left(\frac{(3n+1)W}{(2n+1)2\pi} \right)^n \right]^{\frac{1}{3n+1}} \quad (10.53)$$

where n is the power-law index of the liquid. Figure 10.12 shows the cavity radius taper according to (10.53). Here and everywhere in this discussion the cavity is fed at $X = 0$ and the distal end of the cavity is at $X = W$. Also shown is a curve for an infinite power-law index which corresponds to the cavity radius specified by (10.54). Note that especially for shear-thinning liquids the taper is almost linear over most of

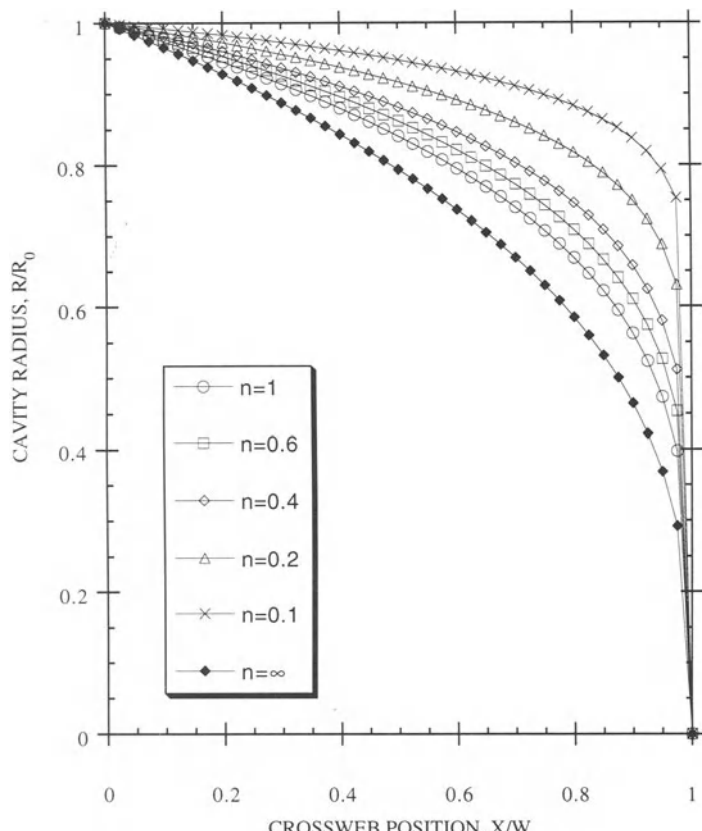


Figure 10.12 The taper in the cavity radius (or equivalent radius) for coathanger manifolds according to equation (10.53). The power-law index of the liquid is given by n . The curve for an infinite power-law index corresponds to the cavity radius profile dictated by equation (10.54).

the manifold width. In addition, the cavity radius ratio of 1.5 proposed by Procter (1972) is approximately obeyed by (10.53) over a relatively large range of power-law indices.

Obviously, there are a multitude of possible coathanger designs that produce uniform cross-web flow distribution. Other criteria may be invoked to limit the design choices. Matsubara (1979) showed that a uniform residence time distribution is obtained when cavity radius (or equivalent radius) has the following profile:

$$R(X) = R_0 \left[1 - \frac{X}{W} \right]^{1/3},$$

$$R_0 = \left[\frac{H^2 W}{\pi} \left(\frac{3n+1}{2(2n+1)} \right)^{\frac{n}{n+1}} \right]^{1/3} \quad (10.54)$$

The corresponding slot length profile has a more complicated functional form,

$$\frac{L(X)}{W} = \frac{3}{2} \beta \left[\left(1 - \frac{X}{W} \right)^{1/3} \times \sqrt{\left(1 - \frac{X}{W} \right)^{2/3} - \beta^2} \right. \\ \left. + \beta^2 \ln \left\{ \frac{(1-X/W)^{1/3} + \sqrt{(1-X/W)^{2/3} - \beta^2}}{\beta} \right\} \right] \quad (10.55)$$

where the parameter β is the ratio of the area of the largest cavity cross-section to that of the slot exit:

$$\beta \equiv \frac{\pi R_0^2}{HW} = \left(\frac{\pi H}{W} \right)^{1/3} \left[\frac{3n+1}{2(2n+1)} \right]^{\frac{2n}{3n+3}} \quad (10.56)$$

Figure 10.13 shows the slot length profile specified by (10.55) for various values of the area ratio β . The maximum slot length, L_0 , is proportional to the manifold width,

$$\frac{L_0}{W} = \frac{3}{2} \beta \left[\sqrt{1 - \beta^2} + \beta^2 \ln \left(\frac{1 + \sqrt{1 - \beta^2}}{\beta} \right) \right] \quad (10.57)$$

The slot length decreases to zero at the cross-web position $X = W(1 - \beta^3)$ where the cavity is

perpendicular to the cross-web direction. Figure 10.14 shows the relationship between the maximum slot length to the aspect ratio of the slot exit. Note that a slot with large aspect ratio is required to maintain a relatively short slot length in the uniform residence time coathanger manifold design.

In cases where a uniform residence time distribution is not essential, Matsubara (1981) has parameterized the cavity and slot profiles in terms of a ratio of average residence times, M , which is the ratio of residence time of liquid that traverses the entire length of the cavity and exits the slot at $X = W$ to that of liquid which exits the slot at $X = 0$. The cavity and slot profiles in (10.54) and (10.55) represent a residence time ratio, M , equal to unity and the profiles for other values of the residence time ratio have similar forms:

$$R_0(M) = M^{1/(3n+3)} R_0^{(M=1)},$$

$$L(X, M, \beta) = L^{(M=1)} \left(X, \frac{\beta}{M} \right) \quad (10.58)$$

A larger cavity than that specified by (10.54) subjects liquid travelling through the cavity to a larger residence time than that which exits adjacent to the cavity feed location. The corresponding decrease in the required slot length taper is obtained by replacing β in (10.55) or (10.57) with β/M . Figure 10.15 shows how the maximum cavity radius and slot length vary with power-law index and residence time ratio.

Coincidentally, the cavity defined by (10.54) or (10.58) has a uniform wall shear rate and shear stress along its length. The wall shear rate in the slot is also uniform across the manifold width and is related to the cavity shear rate in the following manner;

$$\frac{\dot{\gamma}_{\text{slot}}}{\dot{\gamma}_{\text{cavity}}} = \left[\frac{2(2n+1)}{3n+1} M \right]^{1/(n+1)} \quad (10.59)$$

The slot shear rate is ordinarily larger than the cavity shear rate and the difference increases with increasing shear-thinning (i.e., lower power-law index) or increasing residence time ratio. Equality of cavity and slot wall shear rates necessitates a

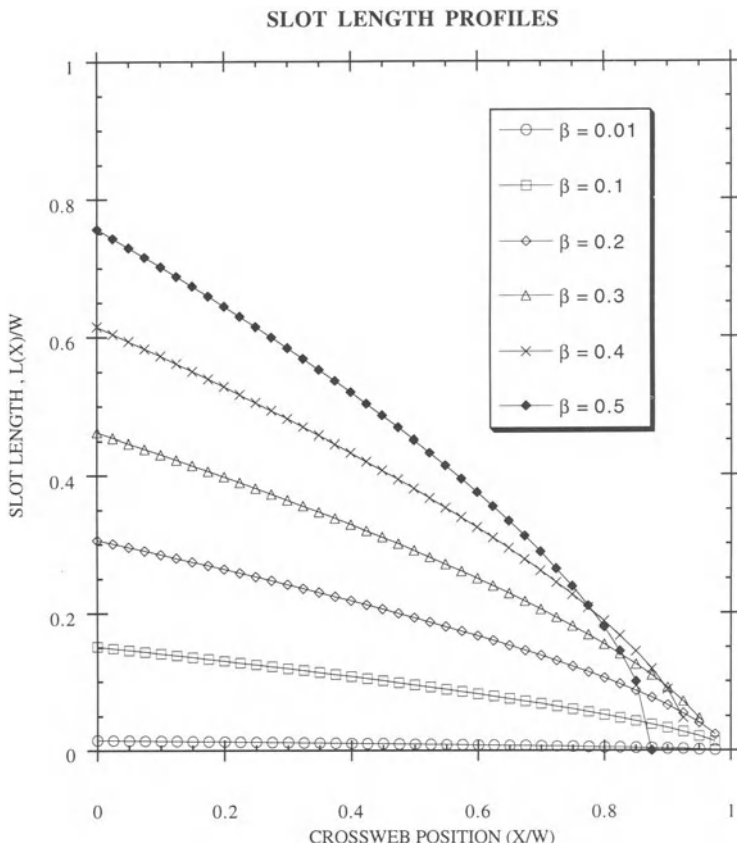


Figure 10.13 The slot length taper for a coathanger manifold with a uniform residence time distribution according to equation (10.55). The ratio of the maximum cavity cross-sectional area to that of the slot exit is given by the parameter β .

design with a residence time ratio less than unity (Charbonneau 1991),

$$M = \frac{3n + 1}{2(2n + 1)} \quad (10.60)$$

In this case, liquid that traverses the cavity and exits at $X = W$ has the shortest residence time.

Winter and Fritz (1986) proposed that rectangular cavities be used to produce material-independent manifold designs by matching the cavity and slot wall shear rates. In cavities with a constant aspect ratio, equality of cavity and slot shear rates is achieved with the following

profiles of the height and width of the cavity;

$$H_c(X) = \left[\frac{H^2 W}{a f_p} \right]^{1/3} \left[1 - \frac{X}{W} \right]^{1/3},$$

$$W_c(X) = a H_c(X) \quad (10.61)$$

a is the aspect ratio of the cavity and f_p is the shape factor which characterizes the effects of the finite aspect ratio of the rectangular cavity (cf. Middleman (1977) pp. 90–92). The corresponding slot length profile is the same as that given by (10.55) with the following substitution for the parameter β :

$$\beta = \left[\frac{a H f_p}{W} \right]^{1/3} = \frac{H}{H_c(X=0)} \quad (10.62)$$

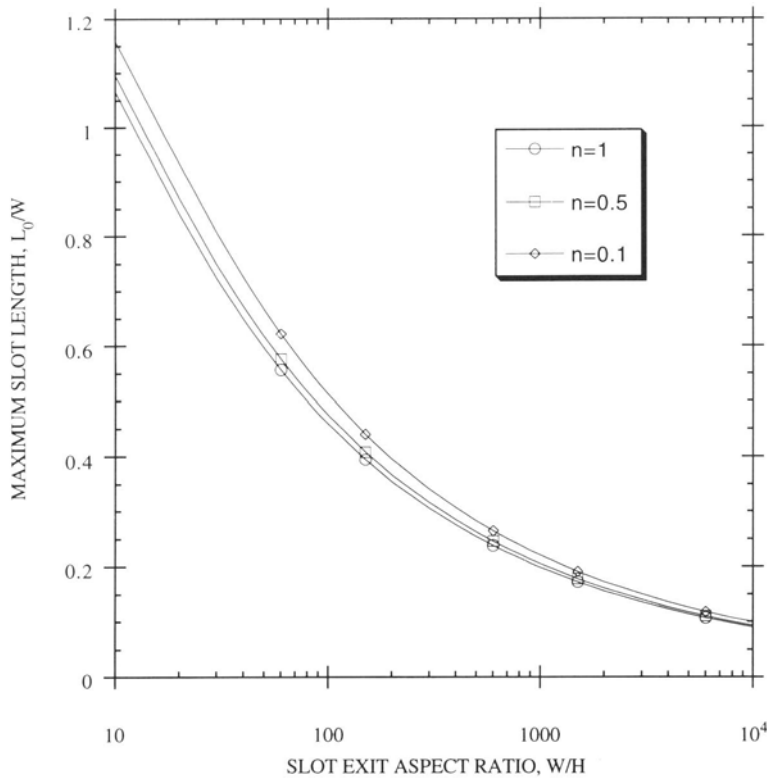


Figure 10.14 The slot length taper for a coathanger manifold with a uniform residence time distribution according to equations (10.56) and (10.57).

The shear-thinning nature of the liquid (i.e. the power-law index) enters into this manifold design only through the shape factor, f_p , which depends on both the aspect ratio of the cavity cross-section and the power-law index of the liquid. Winter and Fritz (1986) point out that for large aspect ratio cavities, the shape factor, and thus the manifold design, is independent of power-law index and equal to unity. In addition, uniformity of residence time is achieved if the shape factor is equal to unity. Unfortunately, a large aspect ratio cavity also requires either a long slot length taper or a very small slot gap. For example, if the cavity aspect ratio is equal to 10 and the manifold width is 1 m, a slot gap of 2.5 mm requires a slot length taper of 494 mm and a slot gap of 29 μm is required to shorten the slot length

taper to 100 mm. Reducing the aspect ratio of the cavity reduces the slot length taper, but it also increases the sensitivity of the design to the power-law index of the liquid through the shape factor. Uniformity of residence time is also sacrificed by reducing the cavity aspect ratio.

So it is that a material-independent coathanger manifold design that provides uniform flow and residence time distribution is possible with the use of large aspect ratio rectangular cavities. Unfortunately, the application of this design is often not practical for the wide coating dies commonly encountered. Either very long slot length tapers or very narrow slot gaps are required. Long slot tapers often produce unacceptable elastic deformation of the coating die as portrayed by the deflection number in (10.38).

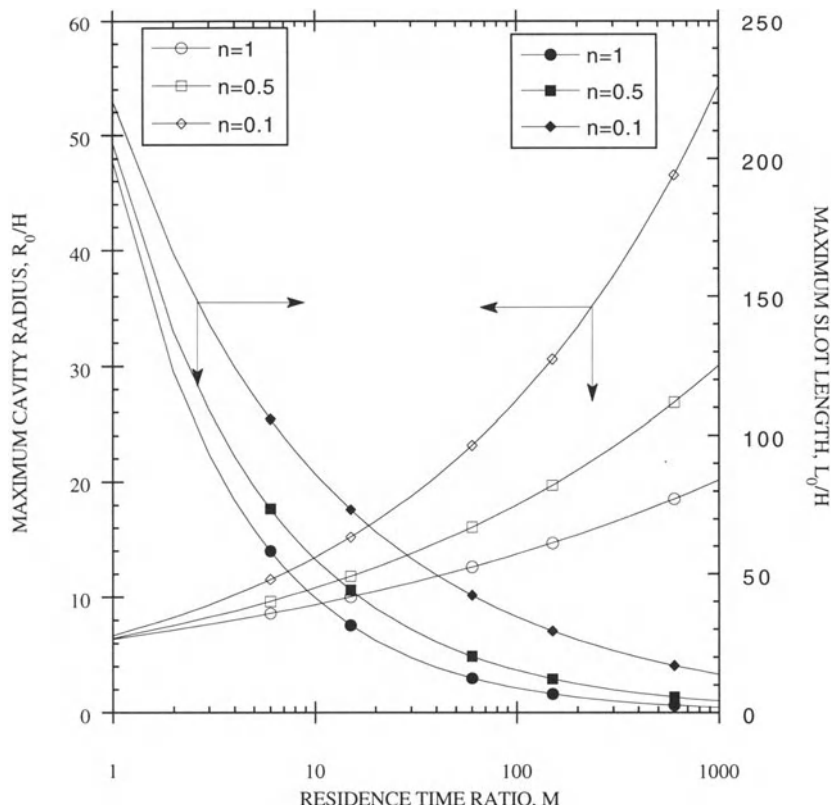


Figure 10.15 The variation of the coathanger manifold design with residence time ratio and shear-thinning behavior (power-law index) of the liquid according to equation (10.58). The aspect ratio of the slot exit is held constant and equal to 1000.

Owing to the sensitivity of the flow distribution to slot gap variations (see Fig. 10.8), narrow slot gaps require prohibitive gap uniformity. The coathanger manifolds described by Matsubara (1979, 1981) provide flow uniformity with varying degrees of residence time uniformity, but are dependent on the shear-thinning nature of the coating liquid. For many nonreacting coating liquids, uniformity of residence time in the manifold is not as desirable as insensitivity to the shear-thinning nature of the liquid. But note that according to (10.59), uniformity of residence time also decreases the shear rate disparity between the cavity and the slot which reduces the sensitivity of the manifold design to material changes (see

Fig. 10.15). Thus, coathanger manifold designs which increase the uniformity of residence time also increase the applicability of the design to materials of varying shear-thinning behaviour. This is contrary to the widely-held belief expressed by Lippert (1991) that 'Larger flow channels are less sensitive to rate and viscosity changes than small channels.' Figure 10.15 suggests that sensitivity to changes in shear-thinning behavior is decreased in coathanger manifold designs by reducing the size of the cavity. Sartor (1990) showed that increasing the size of the cavities and slots in T-manifold designs reduces the sensitivity to rate and viscosity changes. He also showed that uniformly increasing the slot length

decreases the sensitivity of coathanger manifold designs. However, it is still not clear whether sensitivity is better diminished by uniformly increasing the slot length or increasing the slot length taper and thereby reducing the shear rate disparity between the slot and the cavity.

Caution is well-advised in the use of the aforementioned coathanger cavity and slot profiles. These coathanger designs account only for viscous effects while ignoring the influence of inertia and gravitational forces. In addition, very simplified models for the cavity and slot flow were used to produce the coathanger manifold designs and the liquid was assumed to follow the power-law viscosity model. Although the general features and trends may be correct, the details of the coathanger designs are likely to be inaccurate. More accurate coathanger manifold designs can be obtained with the combination of $1\frac{1}{2}$ -dimensional cavity flow and two-dimensional slot flow models described in the previous sections. Inertia and gravitational effects can be incorporated into coathanger designs computed with these models, the accuracy of the cavity and slot flow representation is much improved, and a wide variety of liquid viscosity behavior can be incorporated. Sartor (1990) details a procedure that can be used to compute slot length profiles for coathanger manifold designs in conjunction with a two-dimensional slot flow model. The length of the slot at numerous cross-web positions is treated as a variable whose value is determined by requiring the slot efflux to be uniformly distributed. It is interesting to note that the slot length profiles computed by Sartor (1990) have a shape that is very different from that in (10.55) near the distal end of the cavity. The length of the slot tends to approach the end of the cavity substantially perpendicular to the machine direction while the profiles from (10.55) shown in Fig. 10.13 tend to be more parallel to the machine direction.

10.3.4 SECONDARY CAVITIES

Another option in the design of flow distribution manifolds is the inclusion of additional cavities

in the slot region of the manifold. Secondary cavities provide another chance for flow across the die if a nonuniform distribution resulted from the flow out of the original cavity. Leonard (1985a) modeled secondary cavities with a procedure very similar to the analysis of primary cavities. He reported that there was not a clear optimum secondary cavity position and that the utility of adding secondary cavities depended on the viscous number and the shear-thinning behavior of the liquid. For large viscous numbers and very shear-thinning liquids, it was more beneficial to enlarge the primary cavity than it was to add a secondary one. For small viscous numbers and Newtonian liquids, the opposite was true.

Sartor (1990) analyzed secondary cavities through the lubrication approximation applied to the slot flow. He found a clear optimal location for the secondary cavity at the midpoint of the slot. An optimum size of the secondary cavity was also indicated which was half the cross-sectional area of the primary cavity. In addition, Sartor (1990) analyzed secondary cavities through an electrical resistor analogy to viscous flow based on the work of Booy (1982). The optimal secondary cavity location was still at the mid-point of the slot, but the optimum size was with the secondary cavities slightly smaller than the primary one.

The shape of the secondary cavity can also have a significant impact on the resulting flow field. Lee, Wen and Liu (1990) observed closed recirculations on the upstream side of a secondary cavity with glycerine/water solutions. When an aqueous polyacrylamide solution was observed, the closed recirculations appeared on the downstream side of the secondary cavity. In both cases, reducing the entry or exit angle of the secondary cavity eliminated the eddy.

From the coating engineer's viewpoint, the discussion of the utility and optimal design of secondary cavities is probably moot. Improvements in the design and fabrication of the primary cavity and slot have greatly reduced the need for secondary cavities. In addition, Lee, Wen and Liu (1990) have vividly demonstrated

potential problems that secondary cavities can create. As a result, it is often advantageous to eliminate secondary cavities.

10.3.5 MULTILAYER MANIFOLD DESIGN

When the coating liquid to be distributed by the die manifold is a multilayer package of a number of different materials, different design considerations may need to be considered. In some multilayer coextrusion dies, the layers are combined externally and the manifold considerations are essentially identical to single layer dies. It is when the layers are combined internally through feedblock systems or common lands that significant changes occur. Michaeli (1992) provides a good description of the various externally and internally combined manifold systems. Cloeren (1979, 1980) also describes die manifolds for internally combining different layers.

One of the principal concerns in combining layers in the die manifold is whether or not the layer interfaces will remain smooth and stable. Schrenk *et al.* (1978), Han and Shetty (1978) and Butler (1992) describe interfacial instabilities in polymeric melt systems which produce distorted interfaces. All indicate that the layer interfaces become unstable when the interfacial shear stress exceeds a critical value. Schrenk *et al.* (1978) report that the interfaces remain smooth and stable until the final die land where the interfacial shear stresses are presumably the highest. The interfacial shear stress can be reduced (and the instability potentially eliminated) by increasing the thickness or decreasing the viscosity of the layer adjacent to the die walls, reducing the throughput rate, or increasing the slot gap of the manifold. Kim and Han (1991) addressed interfacial instability in compatible polymeric systems from the viewpoint of the interdiffusion and the subsequent adhesive bond strength that develops after the interface is formed. High interfacial shear stresses inhibit diffusion through molecular orientation in the vicinity of the interface. Weak adhesive strength and presumably high susceptibility to interfacial instability result. In addition to interfacial shear stress, the contact time for

interdiffusion is an important consideration from this viewpoint.

Two-layer coextrusion flow in a slot of incompatible polymers was analyzed both theoretically (Su and Khomami 1992) and experimentally (Wilson and Khomami 1992). The theoretical analyses depict a rather complicated situation in which the interfacial stability is influenced by inertial, viscous and elastic forces, as well as the thickness ratio of the layers. Interfacial shear stress does not appear in this picture. Generally, the studies show that the interface is stable if the more viscous layer is thick and unstable if the more viscous layer is thin. There is a critical layer thickness ratio, r_c :

$$r_c = \frac{h_{\text{more viscous}}}{h_{\text{less viscous}}} = \sqrt{\left(\frac{\eta_{\text{more viscous}}}{\eta_{\text{less viscous}}} \right)} \quad (10.63)$$

defined in terms of the viscosity ratio of the layers. If the layer thickness ratio is greater than r_c , then the elasticity of the liquids has a stabilizing effect. Below this critical thickness ratio, stability can be enhanced by decreasing the elasticity of the more viscous layer and increasing the elasticity of the less viscous one. Inertia generally destabilizes the interface while the effect of any interfacial tension is stabilizing. If the slot has a converging cross-section, the extensional stresses developed in the converging flow have essentially the same effect as increasing the elasticity of the layers. The wavelength of the most dangerous mode of the interfacial instability scales with the thickness of the more viscous layer:

$$\lambda \approx 2\pi h_{\text{more viscous}} \quad (10.64)$$

Whether the interfacial instability of multilayer flows is controlled by interfacial shear stress or a more complicated combination of viscous, elastic and inertial forces, the use of stability criteria in die manifold design requires knowledge of the flow conditions in the individual layers and near the interfaces. A number of researchers (Sornberger, Vergnes and Agassant 1986a, 1986b; Nordberg and Winter 1988, 1990; Puissant *et al.* 1992) have developed flow models with this objective in mind. The models feature approximate

one- and two-dimensional representations of multilayer flow in slots that provide information about the interface locations and conditions. The common practice of adjusting layer viscosity by changing its incoming temperature necessitates the inclusion of thermal effects in the flow models with the accompanying difficulties discussed above.

Another concern in the design of multilayer die manifolds is the tendency of low viscosity liquids to encapsulate those of higher viscosity. In the manifold flow of wide dies, this results in a preferential flow of the lower viscosity liquids towards ends of the manifold (Butler 1992). Cloeren (1993) states that manifold cavities of rectangular cross-section are superior to those of circular shape for distributing multilayer flows. It may be that encapsulation may be responsible for some of the rationale.

10.3.6 OTHER CONSIDERATIONS

There are a number of other considerations that may impact the design of a coating die manifold. These include the effects of elastic deformation of the die, temperature nonuniformities and implications of reactive liquids. Charbonneaux (1991) points out that die designs for reactive thermosetting materials should maintain the shear stress at the walls of the cavity and slot above a critical value to avoid plugging of the die glue to gel formation. Schweizer (1992) also reports that removal of bubbles and contaminants from the walls of the die manifold is facilitated by maintaining the wall shear stress above a critical value which depends on the contaminant size and its interfacial properties. The coathanger designs described in (10.58) and (10.61) are well suited for this task as they maintain a constant shear stress along the length of the cavity. T-manifold designs do not fulfill this requirement and are likely to plug near the ends of the cavity. However, Sartor (1990) notes that even in T-manifolds the wall shear stress can be increased by drawing a recycle liquid stream from the distal end of the cavity.

Although increasing the wall shear stress may be beneficial in preventing plugging due to

gelation of thermosetting liquids, it would be detrimental if the coating liquid is a dispersion susceptible to shear-induced coagulation. The rate of coagulation in the absence of repulsive forces is proportional to the shear rate (Russel, Saville and Schowalter 1989). Thus, in order to minimize the total coagulation during the flow through the die manifold, both shear rate (or wall shear stress) and residence time should be kept small.

As was mentioned in previous sections, the slot efflux varies according to, at least, the cube of the slot gap. For shear-thinning liquids the dependence of flow on the slot gap is higher. As a result, maintaining uniformity of the slot gap across the width of the coating die manifold is a high priority. Machining tolerances and elastic deformation of the die due to the hydrodynamic pressure from the liquid flow through the manifold are common causes of gap nonuniformities. The deflection number defined in (10.38) can be used to gauge when elastic die deflections can be expected to be excessive. In addition, the deflection number shows that the parameters which have the largest influence on the deflection of the die are the length and gap of the slot. Shorter slot lengths and larger slot gaps will decrease the amount of deflection.

The slot efflux also varies in proportion to the reciprocal of the liquid viscosity. Maintaining uniform viscosity through temperature uniformity across the width of the manifold is also a priority. Equation (10.39) describes the expected viscosity variation due to temperature differences. Temperature nonuniformities may arise from variations in the liquid feed, differences between the temperatures of the liquid feed and the die, or temperature variations in the die itself.

Proper design of coating dies to insure minimal elastic die deflection and sufficient heat transfer to control the temperature uniformity is a subject that largely falls outside the scope of this writing. A number of the significant mechanical design considerations as summarized by Michaeli (1992) are as follows: (1) the number of parts should be kept to a minimum; (2) sealing surfaces should be small and flat; (3) a few, large die bolts are

better than many, small die bolts to hold the die together; (4) the die dimensions must be sufficient to keep elastic deformations acceptable; (5) the flow channel surface should be polished to a surface roughness less than $0.2 \mu\text{m}$, and (6) the die material should be selected based on corrosion resistance, machinability, toughness, surface hardness and thermal conductivity.

10.4 SUMMARY

The flow distribution that results from the flow through internal cavities of a coating die is a result of the interplay between the manifold geometry and the viscous, inertial, gravitational, and elastic forces in the coating liquid. In some cases, the elastic deformation of the die itself plays an important role. In the manifold cavity flow, the dominant forces are viscous losses, inertia and gravity. In the slot flow, viscous forces dominate. In the cavity-slot transitional flow, inertial forces as well as elastic forces in the form of extensional viscosity are the key components. A detailed understanding of the effect of each requires the simultaneous solution of the combined mass and momentum conservation principles in all three regions.

A rudimentary understanding of the role of each of the forces is gained from a set of dimensionless numbers. The viscous, momentum, and gravity numbers reflect the importance of the viscous, inertial and gravitational forces in the manifold cavity to the viscous forces in the slot. The importance of elastic forces in the form of normal stresses either from shear or extensional flow in the cavity is captured in the normal stress and extension numbers. Finally, the characterization of elastic deformation of the die due to hydrodynamic forces in the liquid flow is captured in the deflection number.

The design strategies of coating die manifolds vary depending on the intended die application. T-manifold cavity designs are suited for distributing a variety of liquids of varying material properties, but may result in excessive liquid residence time or excessive die deformation due to high cavity pressures. Coathanger designs

feature better uniformity of residence time and lower cavity pressures, but the flow uniformity tends to be more sensitive to liquid material properties. Detailed understanding of the best design strategy for a particular application requires analysis of the interplay between the various fluid mechanical forces. This is provided by the solution of the appropriate mass and momentum conservation principles. In addition, mechanical considerations such as elastic deflection due to hydrodynamic pressure in the manifold cavity and appropriate heat transfer for temperature uniformity are also important considerations.

Overall, the science of die manifold design and analysis is fairly well-developed. Exceptions, which should be the focus of future research, include understanding of the effects of temperature nonuniformities, design of the best cavity ends and design of manifolds for multilayer flows.

REFERENCES

- Acrivos, A., Babcock, B. D. and Pigford, R. L. 1959. Flow distribution in manifolds. *Chemical Engineering Science*. **10**: 112–124.
- Anthony, J. D., Jr., Leffew, K. W. and Trentacosta, J. D. 1988. Thickness control system for an extrusion coating apparatus. US Patent 4,765,941.
- Batchelor, G. K. 1967. *An Introduction to Fluid Dynamics*. Cambridge: Cambridge University Press.
- Binding, B. M. 1988. An approximate analysis for contraction and converging flows. *J. Non-Newt. Fluid Mech.* **27**: 173–189.
- Binding, B. M. 1991. Further considerations of axisymmetric contraction flows. *J. Non-Newt. Fluid Mech.* **41**: 27–42.
- Bird, R. B., Armstrong, R. C. and Hassager, O. 1987. *Dynamics of Polymeric Liquids*. New York: John Wiley.
- Blodgett, O. W. 1966. *Design of Welded Structures*. Cleveland, Ohio: James F. Lincoln Arc Welding Foundation.
- Boger, D. V. 1987. Viscoelastic flows through contractions. *Ann. Rev. Fluid Mech.* **19**: 157–182.
- Booy, M. L. 1982. A network flow analysis of extrusion dies and other flow systems. *Polymer Eng. Sci.* **22**(7): 432–437.
- Butler, T. I. 1992. Effects of flow instability in coextruded films. *TAPPI Journal*, September: 205–211.

- Cameron, A. 1981. *Basic Lubrication Theory*. Chichester, West Sussex, England: Ellis Horwood.
- Carley, J. F. 1954. Flow of melts in 'crosshead'-slit dies; criteria for die design. *J. Appl. Phys.* **9**: 1118–1123.
- Charboneaux, T. G. 1991. Design of sheet dies for minimum residence time distribution: a review. *Polym.-Plast. Technol. Eng.* **30**(7): 665–684.
- Chung, C. I. and Lohkamp, D. T. 1976. Designing coat-hanger dies by power-law approximation. *Modern Plastics*. March: 52–55.
- Cloeren, P. F. 1979. Method for forming multi-layer laminates. US Patent 4,152,387.
- Cloeren, P. F. 1980. Variable thickness extrusion die. US Patent 4,197,069.
- Cloeren, P. F. 1993. End feed extrusion. US Patent 5,234,649.
- Erckmann, B. 1988. Shaping tool for an extruder or calibrator for thermoplastic material. US Patent 4,721,447.
- Han, C. D. and Shetty, R. 1978. Studies on multilayer film coextrusion II. Interfacial instability in flat film coextrusion. *Polymer Eng. Sci.* **18**(3): 180–186.
- Hiraki, Y., Tanaka, Y. and Noda, S. 1989. Coating method. US Patent 4,828,779.
- Huang, J. C. P. and Yu, H. S. 1973. Pressure distributions in porous ducts of arbitrary cross section. *J. Fluids Eng. Trans. ASME*. **95**: 342–348.
- Iguchi, K., Nitta, S., Wada, H. and Sano, T. 1987. T-dies adapted for extrusion molding. US Patent 4,704,083.
- Kasamatsu, T. 1987. Film-forming T die for low viscosity resin. US Patent 4,708,629.
- Kim, J. K. and Han, C. D. 1991. Polymer-polymer interdiffusion during coextrusion. *Polymer Eng. Sci.* **31**(4): 258–269.
- Klein, I. and Klein, R. 1973. Computer modelling of coat hanger dies may be cheaper for the long run. *SPE Journal*. **29**: 33–37.
- Lee, K. and Liu, T. 1989. Design and analysis of a dual-cavity coat-hanger die. *Polymer Eng. Sci.* **29**(15): 1066–1075.
- Lee, K., Wen, S. and Liu, T. 1990. Vortex formation in a dual-cavity coat-hanger die. *Polymer Eng. Sci.* **30**(19): 1220–1227.
- Leonard, W. K. 1985a. Effects of secondary cavities, inertia and gravity on extrusion dies. *ANTEC '85*, pp. 144–148.
- Leonard, W. K. 1985b. Inertia and gravitational effects in extrusion dies for non-Newtonian fluids. *Polymer Eng. Sci.* **25**(9): 570–576.
- Lippert, H. G. 1991. Slot die coating for low viscosity fluids. In *Coatings Technology Handbook*, ed. D. Satas. New York: Marcel Dekker.
- Liu, T. 1983. Fully developed flow of power law fluids in ducts. *Ind. Eng. Chem. Fundam.* **23**: 183.
- Liu, T. and Hong, C. 1988. The pressure drop/flow rate equation for non-Newtonian flow in channels or irregular cross-section. *Polymer Eng. Sci.* **28**(23): 1559–1564.
- Lowey, R. E., Jr. 1960. Plastic extrusion die. US Patent 2,938,231.
- Luo, X.-L. and Mitsoulis, E. 1990. A numerical study of the effect of elongational viscosity on vortex growth in contraction flows of polyethylene melts. *J. Rheology*. **34**(3): 309–342.
- Matsubara, Y. 1979. Geometry design of a coat-hanger die with uniform flow rate and residence time across the die width. *Polymer Eng. Sci.* **19**(3): 169–172.
- Matsubara, Y. 1980. Residence time distribution of polymer melt in the T-die. *Polymer Eng. Sci.* **20**(3): 212–214.
- Matsubara, Y. 1981. Coat hanger die. US Patent 4,285,655.
- Matsubara, Y. 1983. Residence time distribution of polymer melts in the linearly tapered coat-hanger die. *Polymer Eng. Sci.* **23**(1): 17–19.
- McKelvey, J. M. and Ito, K. 1971. Uniformity of flow from sheeting dies. *Polymer Eng. Sci.* **11**(3): 258–263.
- Michaeli, W. 1992. *Extrusion Dies for Plastics and Rubber*. New York: Oxford University Press.
- Middleman, S. 1977. *Fundamentals of Polymer Processing*. New York: McGraw-Hill.
- Miller, C. 1972. Predicting non-Newtonian flow behavior in ducts of unusual cross section. *Ind. Eng. Chem. Fundam.* **11**(4): 524–528.
- Nelson, N. K., Kistler, S. F. and Olmsted, R. D. 1990. A generalized viscous model for the steady shear rheology of magnetic dispersions. Paper read at *62nd Annual Society of Rheology meeting*, 21–25 October 1990, Santa Fe, New Mexico.
- Nissel, F. R. 1976. Thickness control system for an extrusion die. US Patent 3,940,221.
- Nordberg III, M. E. and Winter, H. H. 1988. Fully developed multilayer polymer flows in slits and annuli. *Polymer Eng. Sci.* **28**(7): 444–452.
- Nordberg III, M. E. and Winter, H. H. 1990. A simple model of nonisothermal coextrusion. *Polymer Eng. Sci.* **30**(7): 408–415.
- Pearson, J. R. A. 1964. Non-Newtonian flow and die design. *Trans. J. Plastics Institute*. **32**(99): 239–244.
- Pearson, J. R. A. 1985. *Mechanics of Polymer Processing*. New York: Elsevier Science Publishing Co.
- Procter, B. 1972. Flow analysis in extrusion dies. *SPE Journal*. **28**: 34–41.
- Puissant, S., Vergnes, B., Demay, Y. and Agassant, J. F. 1992. A general non-isothermal model for one-

- dimensional multilayer coextrusion flows. *Polymer Eng. Sci.* **32**(3): 213–220.
- Reifenhäuser, H., Beisemann, H., Reitemeyer, P. and Grabowski, R. 1986. Extruder or calibrating die. US Patent 4,594,063.
- Russel, W. B., Saville, D. A. and Schowalter, W. R. 1989. *Colloidal Dispersions*. New York: Press Syndicate of the University of Cambridge.
- Sartor, L. 1990. Slot coating: fluid mechanics and die design. PhD thesis, University of Minnesota.
- Schrenk, W. J., Bradley, N. L., Alfrey, Jr., T. and Maack, H. 1978. Interfacial flow instability in multilayer coextrusion. *Polymer Eng. Sci.* **18**(8): 620–623.
- Schweizer, P. F. 1992. Fluid handling and preparation. In *Modern Coating and Drying Technology*, eds E. D. Cohen and E. B. Gutoff. New York: VCH Publishers.
- Secor, R. B. 1995. Viscoelastic effects in die manifold flows. Paper read at 67th Annual Society of Rheology meeting, 8–12 October 1995, Sacramento, CA.
- Sornberger, G., Vergnes, B. and Agassant, J. F. 1986a. Two directional coextrusion flow of two molten polymers in flat dies. *Polymer Eng. Sci.* **26**(7): 455–461.
- Sornberger, G., Vergnes, B. and Agassant, J. F. 1986b. Coextrusion flow of two molten polymers between parallel plates: non-isothermal computation and experimental study. *Polymer Eng. Sci.* **26**(10): 682–689.
- Stafford, L. O. 1971. Apparatus for casting multi-layer composite film. US Patent 3,583,032.
- Su, Y. and Khomami, B. 1992. Interfacial stability of multilayer viscoelastic fluids in slit and converging channel die geometries. *J. Rheology*. **36**(2): 357–387.
- Tadmor, Z., Broyer, E. and Gutfinger, C. 1974. Flow Analysis Network (FAN) – a method for solving flow problems in polymer processing. *Polymer Eng. Sci.* **14**(9): 660–665.
- Tadmor, Z. and Gogos, C. G. 1979. *Principles of Polymer Processing*. New York: John Wiley.
- Vergnes, B. and Agassant, J. F. 1986. Die flow computations: A method to solve industrial problems in polymer processing. *Advances in Polymer Technology*. **6**(4): 441–455.
- Vergnes, B., Saillard, P. and Agassant, J. F. 1984. Non-isothermal flow of a molten polymer in a coat-hanger die. *Polymer Eng. Sci.* **24**(12): 980–987.
- Vlcek, J., Mailvaganam, G. N., VLachopoulos, J. and Perdikoulias, J. 1990. Computer simulation and experiments of flow distribution in flat sheet dies. *Advances in Polymer Technology*. **10**(4): 309–322.
- Vrahopoulou, E. P. 1991. A model for fluid flow in dies. *Chem. Eng. Sci.* **46**(2): 629–636.
- Wang, Y. 1991. Extrusion of rubber compounds and highly filled thermoplastics through coathanger dies. *Intern. Polymer Processing*. **6**(4): 311–317.
- Whitaker, S. 1981. *Introduction to Fluid Mechanics*. Malabar, Florida: Robert E. Krieger Publishing Company.
- White, S. A., Gotsis, A. D. and Baird, D. G. 1987. Review of the entry flow problem: experimental and numerical. *J. Non-Newt. Fluid Mech.* **24**: 121–160.
- Wilson, G. M. and Khomami, B. 1992. An experimental investigation of interfacial instabilities in multilayer flow of viscoelastic fluids. Part I. Incompatible polymer systems. *J. Non-Newt. Fluid Mech.* **45**: 355–384.
- Winter, H. H. 1975. Temperature fields in extruder dies with circular, annular, or slit cross-section. *Polymer Eng. Sci.* **15**(2): 84–89.
- Winter, H. H. and Fritz, H. G. 1986. Design of dies for the extrusion of sheets and annular parisons: the distribution problem. *Polymer Eng. Sci.* **26**(8): 543–553.

Franz Durst and Hans-Günter Wagner

11a.1 INTRODUCTION

Chapter 11 presents pre-metered coating methods for which all the liquid fed into the coating die by a metering device, e.g., a displacement pump, is deposited on the substrate. Therefore, the average wet film thickness H_∞ is predetermined for a given feed flow rate V^* , coating width in the cross-web direction, W , and substrate speed, U , and is independent of rheological properties of the coating liquid.

The purpose of this chapter is an explanation of the physical background of slot coating as a basis for understanding the advantages, the drawbacks and the limits of coatability. It is shown how information on these limits is obtained and how it is used to predict coating windows. Internal and external design go hand in hand for a stable coating process and aspects of the external design are the topic of this chapter.

As the terms slot and extrusion coating suggest, in this process (Figs 11a.1 and 11a.2), the coating liquid is forced through a coating die on to the substrate. Within the coating die, a distribution system, consisting of a distribution chamber and a feed slot, provides a uniform liquid flow rate over the coating width W , as explained in detail in Chapter 10. The feed slot separates the downstream and upstream die lips. The domain bounded by the die lips and the substrate is the coating gap; the width of this domain is known as the gap clearance, H_G . The hydrodynamic process of formation of the coated layer occurs within the liquid bridge (also called the coating

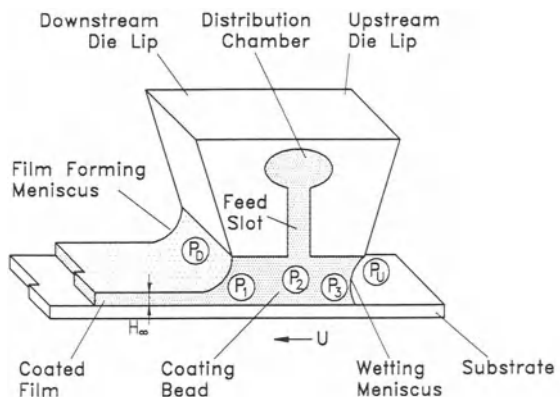


Figure 11a.1 Slot coating.

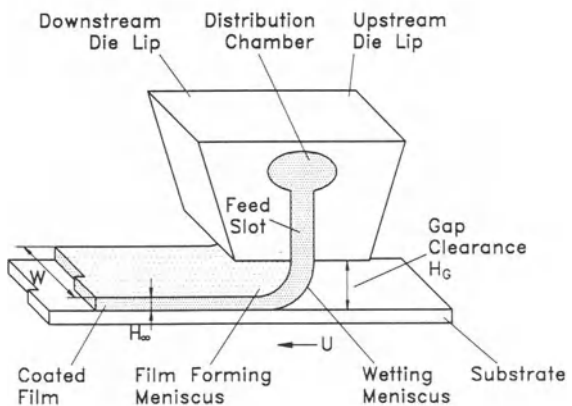


Figure 11a.2 Extrusion coating.

bead) between the coating die and the moving substrate. Depending on the forces acting on the liquid, different shapes of the liquid bridge can be observed. The two-dimensional representation of the bead shows two free surfaces: the film forming meniscus is located downstream of the feed slot and forms the wet film surface; the wetting meniscus is upstream of the feed slot and wets the substrate.

In the following we distinguish between slot coating and extrusion coating operation. In slot coating operation, viscous and capillary forces are dominant. The gap clearance is small, from less than twice up to more than ten times the final wet film thickness. The coating gap under the downstream die lip is filled by the liquid and the upstream coating gap can be partially or completely filled. In extrusion coating operation, the liquid bridge has the shape of a short liquid curtain. The die lips are usually not wetted by the coating liquid, as shown in Fig. 11a.2. The gap clearance can be more than 100 times the wet film thickness. Stable bridging of the coating gap is possible owing to the rheological properties of the coating liquid, e.g. viscoelasticity, or to external forces, such as magnetic fields which can accelerate magnetic liquids in the liquid curtain and increase the liquid inertia (Ankenbrand, Herrmann and Wilke 1969) and electrostatic force fields which can assist in positioning the coating bead (Nadeau 1960; Miller and Wheeler 1965).

We shall concentrate on slot coating operation and provide additional references on extrusion coating operation as appropriate. Flow processes in extrusion coating, e.g. 'heel formation' and the 'teapot' effect, are very similar to those in curtain coating, which are explained in Chapter 11c, but because the gap clearance is small, acceleration of the coating liquid by gravitational forces, which is typical of curtain coating, is negligible. Increasing the gap clearance in extrusion coating, when the direction of the falling liquid curtain coincides with the earth's gravitational vector, will lead to a curtain coating operation.

Flow processes similar to those within the coating gap under the upstream lip can be

observed in slide coating, which is described in Chapter 11b. In knife coating, which is discussed in Chapter 12a, the flow is similar to that within the coating gap under the downstream die lip.

The control of the wet film thickness by an independent metering device is of advantage in many applications, in particular for high precision coating. However, the wet film thickness cannot be chosen arbitrarily, because for all coating processes there exists a parameter space of stable operating conditions outside the limits of which coating defects occur. In slot coating, flow instabilities can be found which lead to typical variations of the coating thicknesses as shown in Fig. 11a.3. The boundary of successful operating conditions is reached when these instabilities exceed the tolerable limit of product quality. The coating window includes the parameter space of liquid properties, operating conditions and die geometry, within which defect-free coatings can be produced.

Slot and extrusion coating are very versatile operations for coating single layers on to a web. With a single external design, a very wide range of applications with the viscosity of the coating liquids varying between less than 1 mPa s and several thousand Pa s can be handled. Coating liquids with even higher viscosity are applied with extrusion coaters. The web velocities can be less than 0.1 m/s or exceed 10 m/s. The minimum wet film thickness is in the order of 10 µm with an achievable variation of less than $\pm 2.5\%$. Some examples of materials coated with slot coaters are photosensitive materials, e.g., photoresist, magnetic suspensions, wax, inks, hot melt adhesives, silicon, rubber and foams (Aurin 1985; Campbell 1980; Lippert 1987). Low viscosity melts of alloys, metals and organic materials can also be applied (Carpenter and Steen 1990). In highly viscous melts of plastics and adhesives, viscoelastic effects will dominate and these are typically extrusion coated. Slot coaters can be used for the simultaneous application of multiple layers, and many patents describe multilayer slot coating. However, multilayer slot coating is not very common in industrial applications.

First we give a selected overview on equipment

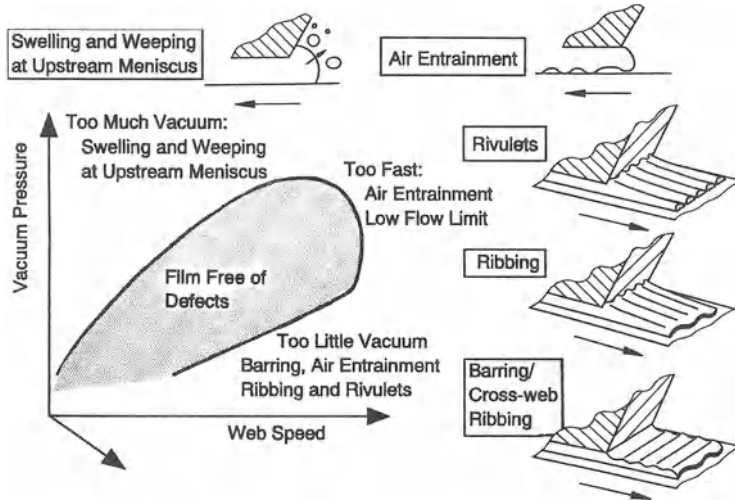


Figure 11a.3 Coating window and flow instabilities.

used for slot coating in Section 11a.2. In Section 11a.3 the physics of slot coating is explained and Section 11a.4 focuses on stable operating conditions. The influence of small disturbances on the stability of the coating flow is discussed in Section 11a.5. Section 11a.6 provides information on practical issues of slot coating and a summary in Section 11a.7 closes this chapter.

11a.2 DESCRIPTION OF EQUIPMENT

The basic elements of slot and extrusion coating processes are shown in Fig. 11a.4. The coating liquid is pumped from the liquid preparation to the coating die. The pulsation damper reduces oscillations induced by the feed system, which can cause flow instabilities. The filter system keeps back impurities and large particles to prevent coating defects such as streaks. Details on liquid preparation and transport to the coating die were given in an overview on fluid handling by Schweizer (1992).

The center piece is the coating die. Many different die designs are shown in the patent literature, publications and brochures from die manufacturers. The external design, in particular the shape, the inclination of the die lips and the

positioning of the coating die relative to the substrate, is varied to find an ideal design for any application. Fig. 11a.5 shows different geometries of the coating die. The lip geometry influences the liquid flow and the pressure distribution in the coating gap. In the case of highly viscous coating liquids, the pressure within the coating bead can become substantial. The maximum pressure can be reduced by inclined

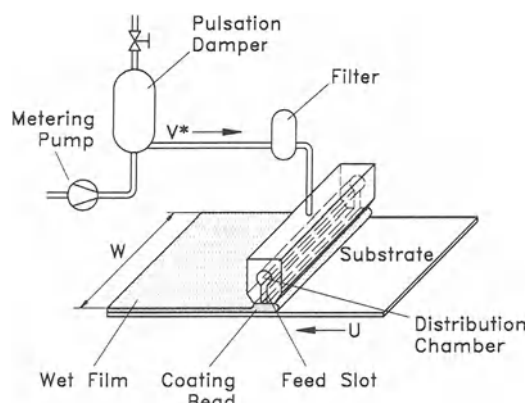


Figure 11a.4 Basic elements of slot and extrusion coating.

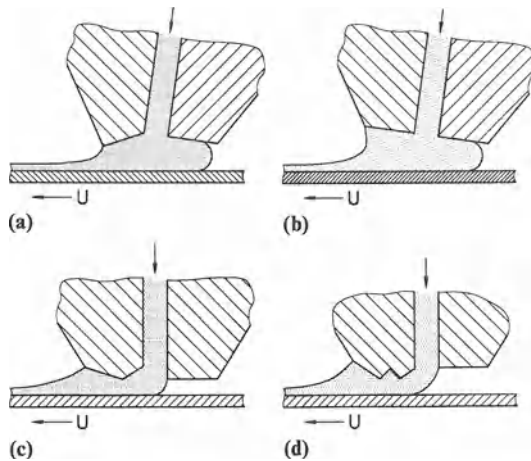


Figure 11a.5 Various die designs of slot coater.

lips (O'Brien 1984) as indicated in Figs 11a.5a and 5b, or by special lip designs as shown by Kageyama and Yoshida (1986), Figs 11a.5c and 5d, which create sinusoidal pressure variations within the coating bead. A high manufacturing quality of the die and the application roll is necessary as the gap clearance can be very small. Die lips are in general planar, mainly owing to ease of manufacturing. The deviations in flatness of the die lips and roundness of the coating roller should be less than $\pm 1\text{ }\mu\text{m}$ for gap clearances less than $50\text{ }\mu\text{m}$. According to Fahrni and Zimmermann (1978), the curvature of the edges should be less than $50\text{ }\mu\text{m}$ where the meniscus should pin.

Beguin's (1954) suggestion to apply a pressure difference between the upstream and downstream menisci was a very important contribution to increasing the coating speed in an operation mode where the gap clearance is greater than twice the wet film thickness. It has revolutionized an entire industry. The necessary pressure difference, which can reach values of 3000 Pa , can be achieved with the help of a vacuum box located at the upstream meniscus. An example is given in Fig. 11a.6c (Woodworth, Winkler and Jackson 1982). The same effect is produced by a box which creates an over-pressure at the

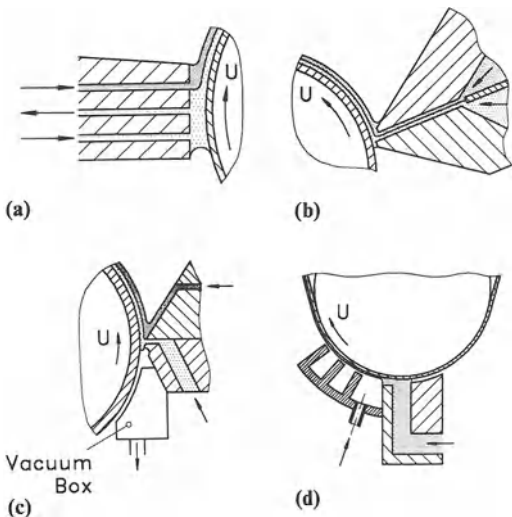


Figure 11a.6 Devices for the pressure control and multilayer slot coating.

downstream meniscus as indicated in Fig. 11a.6d (Browatzki *et al.* 1975). This device has to be designed very carefully as the air flow, which is necessary to sustain the over-pressure, can have a damaging influence on surface uniformity of low-viscosity wet films. A further method to apply the pressure difference was shown by Cameron, Alfred and Hills (1968), where the pressure of the coating liquid under the upstream lip can be controlled by circulating the liquid as shown in Fig. 11a.6a. Similar stabilizing effects on the coating bead can be obtained by an electrostatic assist or by a magnetic assist in the case of a magnetic fluid.

Several examples of the many patents on multilayer slot coating are shown in Figs 11a.6a–6c and 11a.7b. The liquid layers can be combined within the feed slot as Fig. 11a.6b demonstrates (Russel 1956; Jackson 1976) or within the coating gap (Cameron, Alfred and Hills 1986), see Figs 11a.6a and 11a.7b. Combinations of slide and slot coating principles were proposed as indicated in Fig. 11a.6c by Russel (1956) and Jackson (1976).

In general, the web will be supported by a rigid or rubber-covered roll, see Figs 11a.6a–6d, or by a flat surface. It is also possible to push

the coating head towards a tensioned web. The coating liquid should act as a lubricating layer and prevent the contact of web and coating die as shown in Fig. 11a.7a (Tanaka and Noda 1988). Such elasto-hydrodynamic coating processes are described in Chapter 12d. Slot coaters can be used to coat both surfaces of the web simultaneously as shown in Fig. 11a.7b (Ishiwata and Nagai 1970), and in this way one coating operation provides the support for the other.

Many commercially available slot coaters have

mechanisms for modifying the clearance of the feed slot to provide the desired fluid distribution in the cross-web direction. The control of the cross-web flow uniformity is a topic of internal design. Nevertheless, variations of the clearance of the feed slot have to be considered as they can change the flow field within the coating bead.

Owing to the narrow coating gap in slot coating, great care has to be taken in properly positioning the coating die relative to the application roll. Exact repeatability of the positioning is required. The support must allow an in and out movement of the die normal to the surface of the roll, with two adjustments. First, a coarse in/out adjustment with a movement over a distance up to 200 mm provides fast access for cleaning of the die lips and prevents damage while a splice of the substrate passes the coating station. Second, a fine in/out adjustment for perfect alignment provides independent adjustment of the gap clearance at both ends of the die, monitored by micrometer gauges. Two concepts are used for further fine adjustment of the coating gap, namely a straight movement normal to the in/out system and an adjustment of the angle of attack of the die lips. A favorable center of the angle of attack movement is the downstream edge of the downstream die lip where the film forming meniscus pins.

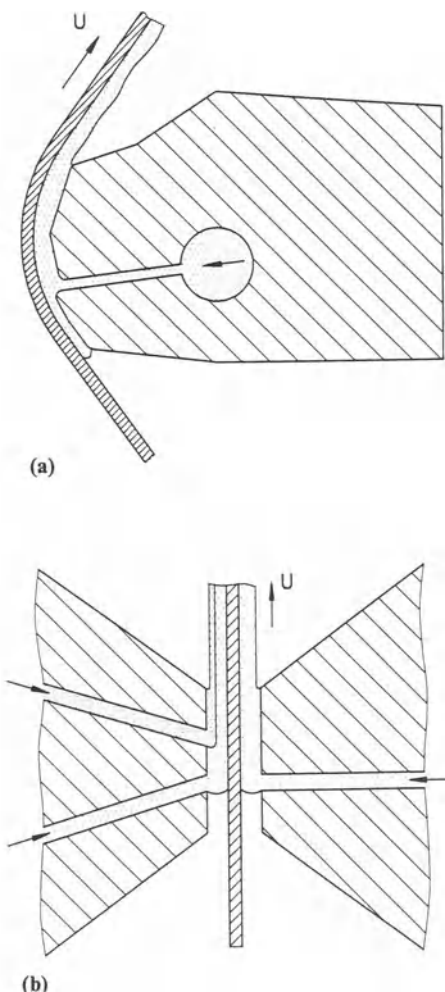


Figure 11a.7 Tensioned web slot coating.

11a.3 SUCCESSFUL STEADY STATE OPERATION: FORCES, PRINCIPLES

11a.3.1 QUALITATIVE DESCRIPTION OF THE FLOW

To maintain a stable coating process, the interaction of inertial, viscous, capillary and external forces acting on the coating bead must be properly managed. Various parameters which determine the position and shape of the coating bead and the flow processes within it are listed below.

Fluid and material properties

- The wetting behavior of the coating fluid on the web and the coating die. The static and

dynamic contact angles, θ and ν , of the fluid with the die lips and the substrate, respectively, are shown in Fig. 11a.8. Detailed information on the complexity of the wetting behavior and contact angles is given in Chapter 3.

- The rheological properties of the coating fluid, which very often show non-Newtonian behavior. The Newtonian viscosity is μ .
- The surface tension, σ , of the coating fluid.
- The density, ρ , of the coating fluid.
- Properties of the substrate, e.g. deformability, dewatering of the coating fluid or electrostatic surface charges.

- External forces, e.g. direction of gravity, electric or magnetic fields.
- Gas pressure at the upstream and downstream menisci, P_U and P_D , respectively.

The dimensionless numbers of relevance for the slot coating process are in general the Reynolds number, Re , the capillary number, Ca , the Bond number, Bo , and the dimensionless pressures, p_i :

$$\begin{aligned} Re &= \frac{\rho U H_\infty}{\mu}; \quad Ca = \frac{\mu U}{\sigma}; \\ Bo &= \frac{\rho g H_\infty^2}{\sigma}; \quad p_i = \frac{H_\infty P_i}{\delta} \end{aligned} \quad (11a.1)$$

Geometric parameters

- Design variables of the coating die, which define shape, dimensions, inclination and position of the die lips and feed slot.
- Design variables, which define shape of the web, gap clearance and radius of the application roll.

These clarify the importance of the various forces. Chapter 8 provides useful information on these dimensionless quantities. All geometric values are made dimensionless by the wet film thickness, H_∞ .

In nearly all practical applications of slot coating, the Bond number is much smaller than unity, implying that the influence of gravity is negligible and the coating die can be operated in any position relative to the gravity field. The capillary number is often greater than unity at high coating speeds and hence the effect of capillary forces on the coating flow is minor. Fig.

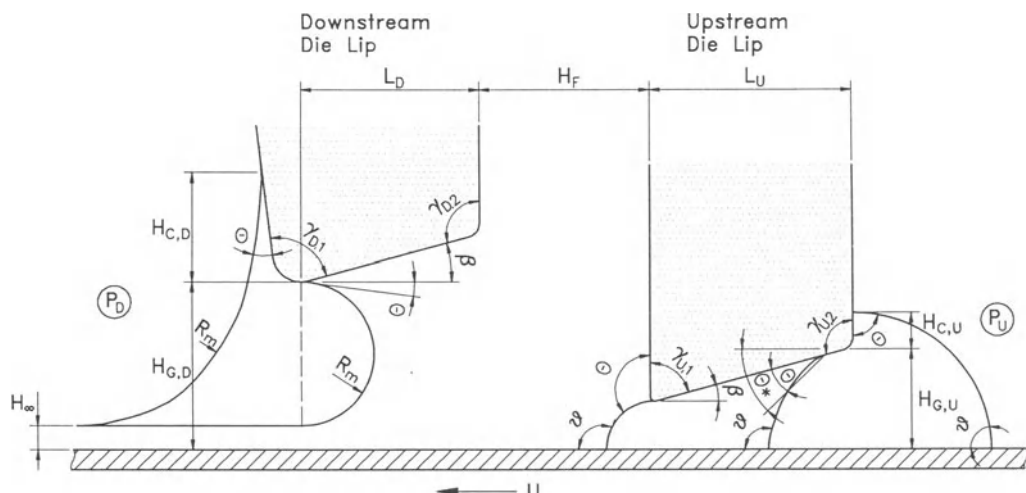


Figure 11a.8 Geometric parameters of slot coater.

11a.8 sketches the coating bead and shows the geometric parameters used.

A qualitative description of the change in the coating bead due to variations of the feed flow rate is shown in Fig. 11a.9. The speed of the substrate is constant. If the flow rate is too low, the liquid forced out of the feed slot cannot maintain a stable liquid bridge across the web and single drops or rivulets will form on the web, as shown in Figs 11a.9a and 9b. The pulling action of the moving web on the liquid is stronger than the stabilizing effects of liquid inertia and capillary forces. Disturbances, present in any coating process and propagating faster than the fluid velocity, lead to a rupture of the liquid bridge. Therefore, the liquid forms several bridges in the cross-web direction, each being stable owing to the higher flow rate within it. A detailed treatment of the stability of curtains is given in Chapter 11c. Increasing the flow rate will lead to a stable situation. In extrusion coating, a coating bead will form as indicated in Fig. 11a.2. The cohesive strength of the liquid or external magnetic or electrostatic forces compensate for the viscous force exerted by the pulling action of the web. In slot coating, the coating liquid will fill the gap under the downstream lip, the free surface of the wet film is formed at the downstream edge of the lip and the wetting meniscus bridges the gap at the exit of the feed

slot, see Fig. 11.9c. The capillary pressure drop across the free surfaces and the pressure drop caused by friction at the die lip are in equilibrium with the pressure drop caused by the viscous forces of the moving substrate. Increasing the flow rate further increases the pressure drop within the downstream coating gap. Hence the pressure level at the feed slot increases. The liquid is pushed into the upstream coating gap against the direction of the web motion. The wetting meniscus moves into the rear gap and the upstream die lip will be wetted as indicated in Figs 11a.9d and 9e. Figure 11a.9f shows the coating bead when the limit of stable coating conditions is reached after a further increase in the flow rate. The pressure drop within the downstream coating gap also increases. The pressure at the feed slot is so high that it cannot be reduced sufficiently by the viscous forces within the upstream coating gap. The capillary forces at the upstream meniscus cannot compensate for the pressure difference between the liquid and the gas. The upstream meniscus swells and liquid wets the upstream die shoulder of the upstream die lip. The wetting meniscus can no longer bridge the gap and the coating liquid spills on to the web. If the downstream meniscus does not pin at the edge of the downstream die lip, the film-forming meniscus climbs up the die shoulder.

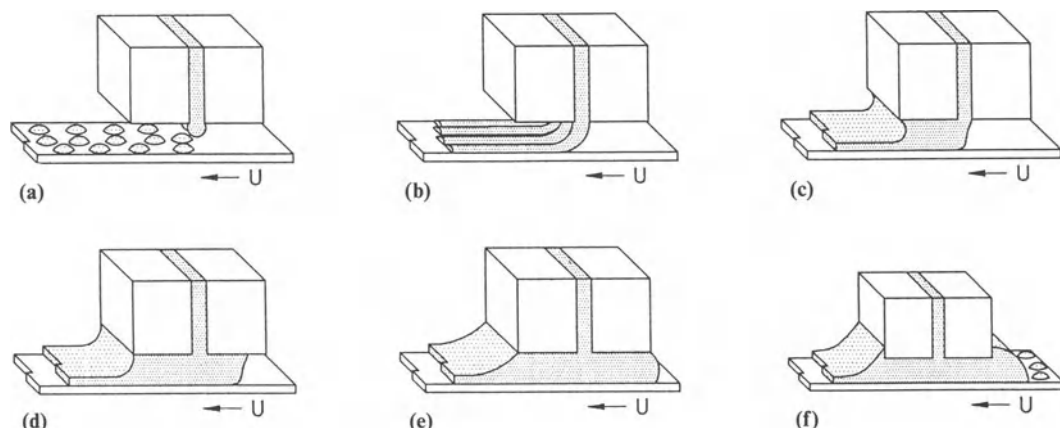


Figure 11a.9 Influence of the flow rate on the shape of the coating bead. The flow rate is increased from (a) to (f).

11a.3.2 ANALYTICAL DESCRIPTION OF SLOT COATING

The qualitative picture of the interplay of forces within the coating bead can be quantified by analytical expressions. In this section these expressions will be used to explain the pressure distribution, the location of the menisci and the occurrence of recirculation zones in a slot coater, whereas the analysis of the same equations provides invaluable information about the operability of a slot coater presented in Section 11a.4. The flow processes within the coating bead are divided into zones with different flow regimes. The flow within the first zone at the film-forming meniscus rearranges from the flow within the coating gap into the fluid at rest within the wet film. The pressure difference, ΔP_{D1} , between the pressure within the fluid, p_1 , and the gas pressure, p_D , is the capillary pressure. Figure 11a.1 indicates the location of the relevant pressures. The flow processes within the downstream coating gap, the second zone, are caused by the drag of the moving substrate and possibly by a driving pressure gradient. The pressure gradient is given by the pressure difference, ΔP_{12} , between the pressure at the film forming zone, p_1 , and the pressure at the feed slot, p_2 . At the feed slot the fluid turns and viscous shear, normal stresses and sometimes inertia determine the flow processes. If the upstream coating gap is filled, then a further zone exists, within which a pressure gradient driven flow opposes the drag flow of the web so that the net flow rate within the zone is zero. The driving gradient is the pressure difference, Δp_{23} , between the pressure at the feed slot, p_2 , and the pressure at the upstream meniscus. At the wetting meniscus, the last zone, the fluid flowing against the direction of the web has to turn at the free surface and is then accelerated by the web in the direction of the web. The capillary pressure at the upstream meniscus is the pressure difference, Δp_{3U} , between the pressure within the fluid, p_3 , and the gas pressure, p_U . The so called equilibrium state requires that the pressure differences across the zones balance the pressure difference, Δp_{DU} , of the gas pressure, p_D and p_U , at the downstream and upstream menisci. The pressure balance is given by:

$$\Delta p_{DU} = \Delta p_{D1} + \Delta p_{12} + \Delta p_{23} + \Delta p_{3U} \quad (11a.2)$$

Ruschak (1976) analyzed the limiting flow conditions within the coating bead of a slot coater when capillary forces are dominant and Higgins and Scriven (1980) extended this work to include viscous and capillary forces. In the following, their considerations are used to determine the parameters which influence the free surfaces and the flow of a Newtonian liquid within the coating bead in such a way that a stable and steady coating process is possible.

It is assumed that the Bond number is much smaller than unity and inertial effects are negligible. The free surfaces will then be influenced only by capillarity and viscosity. If the capillary number Ca is small, no dynamic forces are present and the capillary pressure at the free surfaces can be calculated as for a static drop. The wetting and film forming menisci are curved and their shape can be approximated in the simplest form as cylinders. The curvature of the surfaces induces a capillary pressure, which is calculated from the Young–Laplace equation. This is explained in Chapter 2.

The capillary pressure has to equal the pressure difference, Δp_{3U} , between the pressure within the fluid, p_3 , and the gas pressure, p_U , at the wetting meniscus. The curvature of the free surface can be calculated from geometrical considerations for given static and dynamic contact angles θ and v , respectively. The actual value of these contact angles is strongly related to the history of wetting, as discussed in Chapter 3. The position of the wetting meniscus depends on the pressure distribution in the coating bead. All possible shapes of the wetting meniscus are given by the following equation:

$$\Delta p_{3U} = \frac{\cos \theta^* + \cos v}{h_{G,U}} \quad (11a.3)$$

The angle θ^* , included by the free surface and the horizontal at the static contact line, is indicated in Fig. 11a.8, where $\theta^* = \theta + \beta$ within the

upstream coating gap. The resulting pressure difference is positive when the meniscus is curved into the coating bead and negative when the meniscus bulges out.

An equation for the pressure difference, Δp_{D1} , at the film forming meniscus can be derived by the method of matched expansions (Wilson 1982). The resulting equation is valid for small capillary numbers ($Ca \ll 1$). The influence of inertia is neglected ($Re \ll 1$) and the terms of the first-order approximation do not reflect the influence of gravity ($Bo \ll 1$). For capillary numbers greater than unity viscous forces will dominate within the coating bead and the pressure difference, Δp_{D1} , can be set to zero:

$$\Delta p_{D1} = \begin{cases} 1.3376 \cdot Ca^{2/3} - 0.1551 \cdot Ca; & Ca \ll 1 \\ 0 & ; Ca > 1 \end{cases} \quad (11a.4)$$

The flow processes within the downstream and upstream coating gap are influenced by the geometry of the coating gap. If the gap clearance is small compared with the length of the die lips, then the flow is one-dimensional and the influence of inlet and boundary effects on the pressure difference can be neglected. The flow can be expressed by the Reynolds lubrication approximation as a superposition of Couette and Poiseuille flows. Details on the lubrication approximation are given in Chapter 8. The net flow rate within the downstream gap is equal to the premetered flow of the coating liquid. The viscous pressure drop is

$$\Delta p_{12} = Ca \cdot 6 \cdot l_D (D2_D - 2 \cdot D3_D) \quad (11a.5)$$

The contributions of Couette and Poiseuille flows under the upstream die lip are identical and the net flow rate is zero. The pressure drop follows as

$$\Delta p_{23} = Ca \cdot 6 \cdot l_U \cdot D2_U \quad (11a.6)$$

The terms $D2$ and $D3$ take into account the variable clearance of the coating gap, $h_i(x)$, as

shown in Fig. 11a.8.

$$\begin{aligned} D2_i &= \frac{1}{l_i} \int_0^{l_i} \frac{1}{h_i^2(x)} dx; \\ D3_i &= \frac{1}{l_i} \int_0^{l_i} \frac{1}{h_i^3(x)} dx \end{aligned} \quad (11a.7)$$

The influence of the flow at the feed slot and the contributions from the areas where the flow is not fully one dimensional can be neglected if the length of the die lips is sufficiently greater than the gap clearance. The numerical calculation presented in the following section demonstrates that it takes less than one gap clearance in the flow direction to reach the fully developed flow condition.

In the limiting case of small capillary numbers, the pressure differences Δp_{12} and Δp_{23} are negligible in comparison with the pressure differences at the menisci. The slot coater operates in the capillary mode. The pressure difference at the upstream meniscus is always positive. Hence, if the gas pressure difference between upstream and downstream menisci is zero, then the surface of the wetting meniscus must curve into the coating bead to satisfy equation (11a.2). Reducing the gas pressure at the wetting meniscus by a vacuum box has a pulling action on the wetting meniscus and it may bulge out.

A common situation in slot coating is the second limiting case, where the capillary numbers are much greater than unity. The slot coater operates in the viscous mode and the contributions of the pressure differences at the menisci are negligible. The pressure difference Δp_{23} within the upstream coating gap is always positive and independent of the flow rate. It increases with increasing web speed, increasing viscosity and decreasing gap clearance. If the pressure difference Δp_{DU} is zero, then equation (11a.2) can only be satisfied if the pressure difference Δp_{12} within the downstream coating bead is negative. From equation (11a.5), it can be concluded that the pressure gradient in the flow direction is always negative if the gap clearance is less than twice the wet film thickness. It might be assumed now that a sufficiently high pressure difference in the

gas pressures at the free surfaces allows arbitrarily high values of the gap clearance. However, that is not true, as there exists a 'low flow limit', which is explained in Section 11a.4.

In many applications, viscous and capillary forces have to be considered and operating conditions are possible where a positive pressure difference Δp_{12} within the downstream coating gap occurs. The border between positive and negative pressure differences within the downstream coating gap is the pure Couette flow condition, where the gap clearance is twice the wet film thickness and no pressure gradient exists. If the dimensionless gap clearance is greater than 2, then the Poiseuille flow opposes the Couette flow and the pressure in the flow direction increases.

The onset of recirculating flow within the downstream coating gap is given by a velocity profile which has a zero velocity gradient in the wall normal direction at the wall of the die lip. By superposing the velocity profiles of Couette and Poiseuille flows, the velocity gradients of which at the wall are of the same magnitude with opposite sign, it can be deduced that there is no recirculating flow under the downstream die lip if the gap clearance is smaller than three times the wet film thickness. If the gap clearance is greater than this a recirculation zone can be found.

These equations reflect the physics of slot coating well and provide a very good qualitative picture. One might wonder why the effects of the gas boundary layer at the wetting meniscus have not been included in the balance of forces. The maximum pressure which can be exerted on the wetting meniscus by the gas flow is the stagnation pressure, which is calculated as

$$P = \frac{\rho}{2} U^2 \quad (11a.8)$$

This pressure is 65 Pa at a very high web speed of 10 m/s and reduces to 16.25 Pa at a high web speed of 5 m/s. The density ρ of the gas is 1.3 kg/m³. The capillary pressure at the wetting meniscus of a fluid with a surface tension of 0.03 N/m and at a very high gap clearance of

300 μm can reach values of up to 200 Pa, and at a gap clearance of 100 μm it is up to 600 Pa. It is therefore reasonable to neglect the influence of the gas boundary in the balance of forces.

A similar analytical approach can be used for the design of coaters for axisymmetric substrates such as cables, wires and fibers. Analytical expressions for the axisymmetrical case were presented by Lange *et al.* (1991). The extension to the case of two-layer slot coating was described by Scanlan and Scriven (1990) and Cohen and Scriven (1992). The resulting equation system provides information on the existence of recirculation zones and the position of the interface between the two coating liquids, which is an important issue in this type of coating operation.

Secor (1991) and Strenger and Secor (1991) included the influence of the viscoelastic behavior of the coating liquid in the simplified equations. They considered the flow within the downstream coating gap, which is operated at less than twice the wet film thickness. They found that the elastic stress counteracts the negative pressure gradient in the flow direction at high shear rates, which increases the possibility of ribbing instability.

11a.3.3 NUMERICAL SIMULATIONS OF SLOT COATING

The analytical description of the flow within slot coaters has its limits and numerical calculations are a powerful tool for simulating the flow processes of slot coating. Chapter 9 elaborates on the details of numerical simulations. Detailed information on flow processes within regions which are experimentally accessible only with great difficulty were provided, for example, by Sartor (1990) and Durst *et al.* (1988, 1991). Velocities, pressure, shape and location of the menisci and size and location of recirculation zones within the coating bead can be predicted. Such programs are further useful for studying the influence of parameter variations on the coating flow and its stability. In principle, all acting forces, properties of the fluid and the wetting behavior of the coater materials can be included in these calculations. However, all

calculations published in the literature contain some simplifications. Major shortcomings are the treatment of the wetting behavior and simulations of three-dimensional flows with free surfaces, which are still difficult and laborious.

Figure 11a.10 depicts a numerical grid employed in the calculations, profiles of the velocity component parallel to the web and a streamline plot of the coating bead. The flow within the downstream and upstream coating gap is one-dimensional and fully developed, as shown by the unchanged velocity profiles and the parallel streamlines. At the entrance and exit zones of the coating gap the fluid needs only about one gap clearance to assume the fully developed state. The arrows point to the stagnation points, where the fluid is at rest, which indicate the end-points of a streamline which separates the recirculation zone from the main flow.

Figure 11a.11 shows various geometries of the coating gap under the same flow conditions. The upstream meniscus is free to move along the

upstream die lip. The size of the coating bead is determined by the pressure drop within the upstream and downstream coating gap. Increasing the upstream gap clearance reduces the pressure drop and the wetted length of the upstream die lip increases. Within the coating bead the distribution of the streamlines changes according to the gap clearance.

The pressure distribution within the coating bead is given by Fig. 11a.12 for four of the slot configurations. The pressure at the end of the calculation domain in the downstream direction is identical to the ambient pressure at the downstream free surface ($p = 0$). The pressure decreases in the upstream direction owing to the curvature of the free meniscus. Within the downstream coating gap the pressure gradient is constant, which indicates the fully developed flow regime. Across the exit of the feed slot the pressure is nearly constant, although there are strong changes in the flow direction. Within the upstream coating gap the pressure gradient is

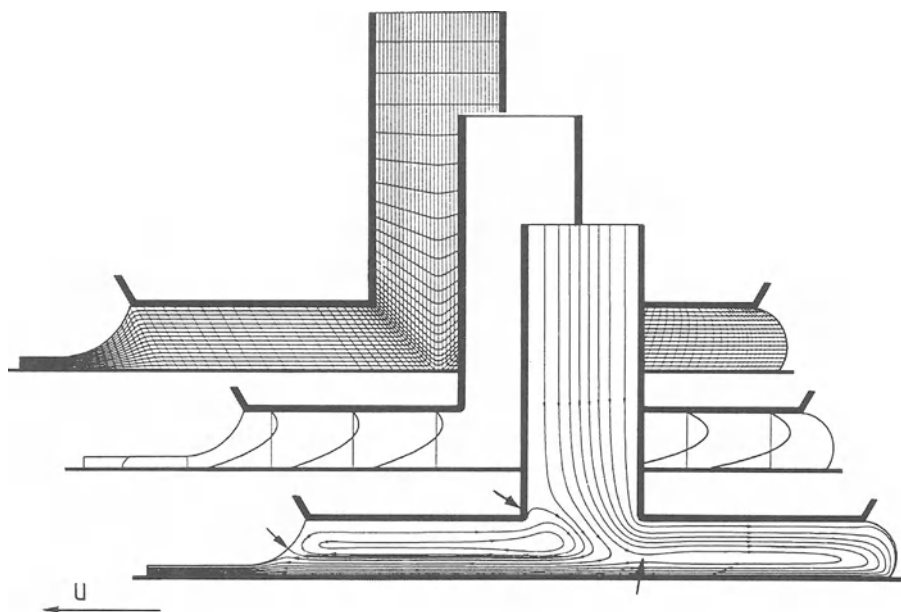


Figure 11a.10 Numerical simulation of slot coating: numerical grid, velocities and streamlines. $Re = 9.3$, $Ca = 0.05$, $\Delta p_{DU} = 1.6$, $\theta = \text{pinned}$, $\nu = 110^\circ$, $h_{G,D} = h_{G,U} = 5$, $h_F = 10$, $l_D = l_U = 20$.

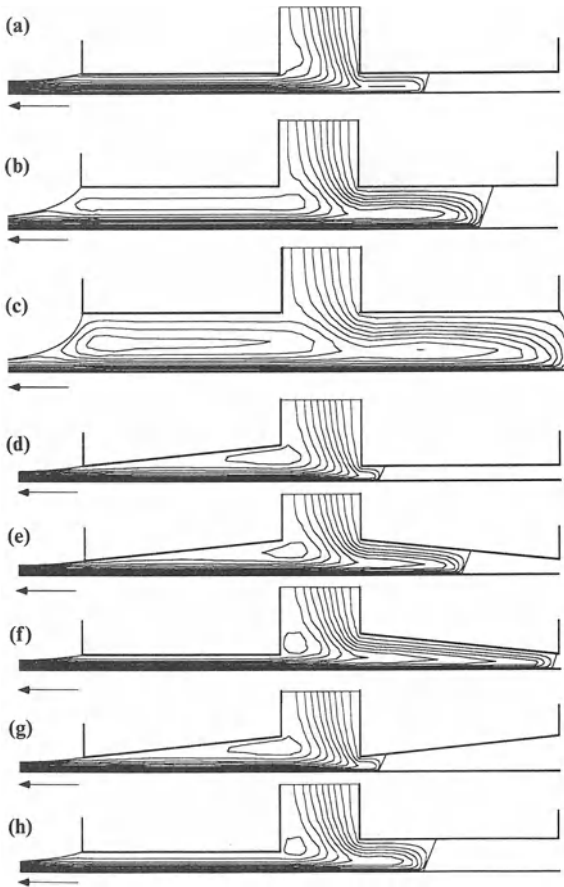


Figure 11a.11 Numerical simulation of slot coating: various die designs. $Re = 10$, $Ca = 0.05$, $I_D = I_U = 25$, $h_F = 10$, $\theta = 60^\circ$, $v = 110^\circ$, $\Delta p_{UD} = 10$. (a) $h_{G,D} = h_{G,U} = 1.75$; (b) $h_{G,D} = h_{G,U} = 5$; (c) $h_{G,D} = h_{G,U} = 7.5$; (d) $h_{G,D} = h_{G,U} = 1.75$, $\beta_D = 6^\circ$; (e) $h_{G,D} = 1.75$, $h_{G,U} = 4.37$, $\beta_D = 6^\circ$, $\beta_U = -6^\circ$; (f) $h_{G,D} = 1.75$, $h_{G,U} = 4.37$, $\beta_U = -6^\circ$; (g) $h_{G,D} = h_{G,U} = 1.75$, $\beta_D = \beta_U = 6^\circ$; (h) $h_{G,D} = 2.5$, $h_{G,U} = 4$.

again constant. The upstream meniscus has to take a position where the vacuum pressure applied at the free surface of the upstream meniscus is in equilibrium with the capillary pressure of the free surface and the pressure within the coating bead.

Different vacuum levels change the location of the upstream meniscus as shown in Fig. 11a.13.

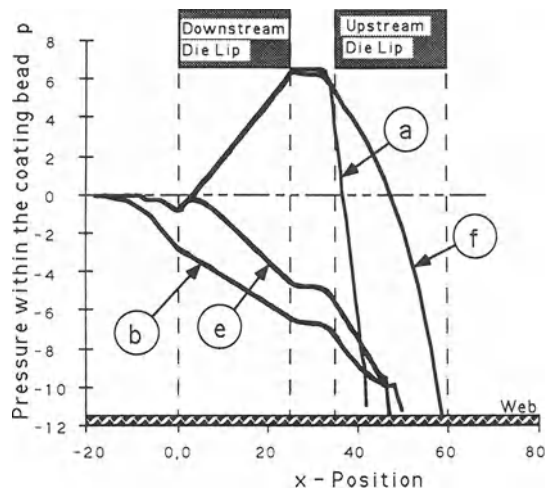


Figure 11a.12 Pressure profiles within the coating bead; for parameters see caption to Fig. 11a.11.

Without vacuum the upstream meniscus is located close to the feed slot. The coating liquid is pulled further upstream by an increase in the vacuum. The meniscus will pin when the edge of the upstream die lip is reached and changes its curvature to compensate for the pressure difference. The limiting curve of the stable positions of the upstream meniscus can be determined with this kind of numerical simulation (Sartor 1990). The

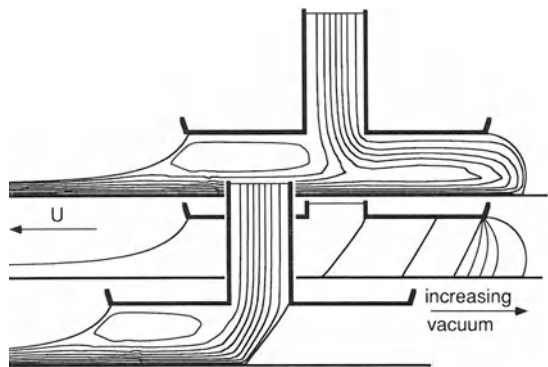


Figure 11a.13 Change in shape of the coating bead due to vacuum, Δp_{DU} increases from 3 to 9 in increments of 1. $Re = 10$, $Ca = 0.1$, $I_D = I_U = 10$, $h_{G,D} = h_{G,U} = h_F = 5$, $\theta = 60^\circ$, $v = 110^\circ$.

same method can be used to find the limiting positions of the downstream meniscus to determine the low flow limit, which is explained in Section 11a.4.

Figure 11a.14 shows the flow field at the exit of the feed slot where the upstream coating gap is filled by the coating liquid. The Reynolds number is constant and the clearance of the coating gap and the feed slot are varied. From analytical expressions in the previous section it could be deduced that recirculations within the downstream coating gap can only be observed if the dimensionless coating gap clearance is greater than 3. The numerical simulation in Fig. 11a.14 points out that if the dimensionless clearance, h_F , of the feed slot is smaller than the dimensionless clearance, h_G , of the coating gap, then additional vortices will appear at the die lips upstream and downstream of the feed slot even at clearances of the coating gap $h_G < 3$. These vortices are caused by the high momentum of the coating liquid exiting the feed slot. The flow processes are similar to a jet emanating from a nozzle. If the clearance of the feed slot is greater than about twice the clearance of the coating gap, then the mean momentum of the liquid exiting the feed slot is too small to

displace the liquid flowing within the coating gap. A vortex will form within the feed slot which blocks the exit of the latter and provides a higher momentum to the liquid leaving the feed slot. This vortex will be completely within the feed slot if the clearance of the coating gap is $h_G < 2$. For higher values of h_G the vortex will intrude into the coating gap and combine with the recirculation zone within the downstream coating gap. The geometric configurations which are believed to be optimum show no additional regions of recirculating liquid.

There is still a definite need to improve the numerical predictions. More powerful computer programs are needed which can handle efficiently complex three-dimensional coating flows. A drawback of numerical simulations is that often realistic boundary conditions, e.g. contact angles, are unknown, and values have to be assumed. Sensitivity studies are required to determine the influence of the specific boundary condition on the flow processes. Nevertheless, the accuracy of the calculations provided so far is sufficient in most cases for engineering purposes and provides a deeper understanding of the physics underlying thin film coating processes.

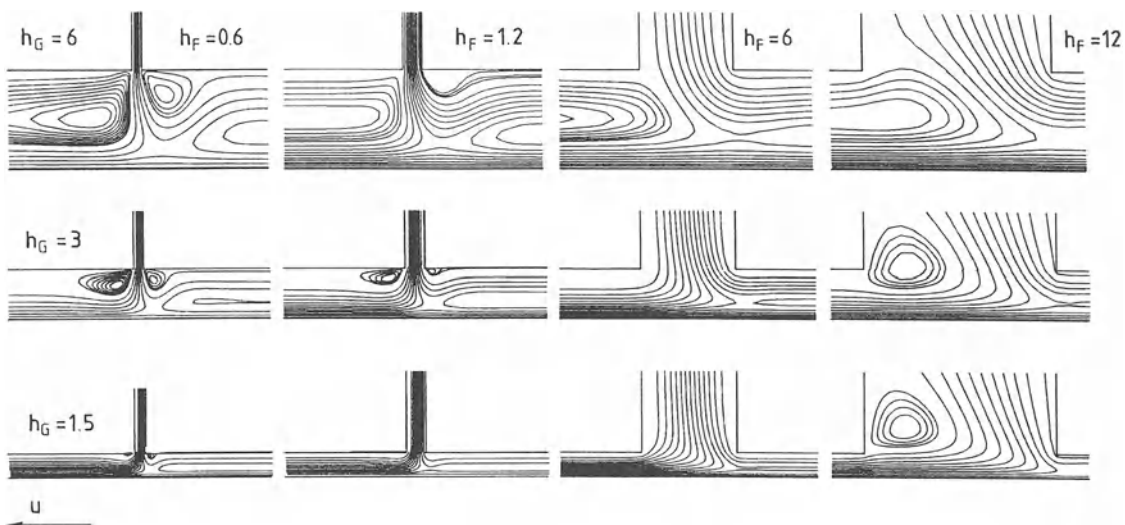


Figure 11a.14 Flow processes within the coating bead at the feed slot. $Re = 10$.

11a.3.4 EXPERIMENTAL STUDIES OF SLOT AND EXTRUSION COATING

The easiest way to obtain information on the coating process is by visual observation of the film quality, i.e. the occurrence of undesired surface structures. As an indirect method, it provides information only on the effects of the flow processes within the coating bead. The experimental methods utilized to study the flow within the coating bead range from these simple investigations to very sophisticated and time consuming flow visualization experiments (Sartor 1990). The benefits of sophisticated experimental investigations and suitable experimental methods are discussed in Chapter 7.

Durst *et al.* (1988) monitored the coating bead of a slot coater in side view with a video camera. They used a scaled-up slot coater to provide easy optical access to the coating bead. Fluids of higher viscosity permitted operating conditions similar to those of the real size slot coater, where the coating gap is very narrow. The flow was visualized with aluminum flakes as tracers, and dynamic shape changes of the coating bead due to variations of the web speed, flow rate and gap clearance were recorded. The qualitative comparison of the flow processes with numerical simulations showed good agreement, even though the capillary numbers differed between the scaled-up experiment and the computations of the real-size slot coater. Grader (1985) investigated the flow processes within the upstream coating gap. He monitored the movement of the wetting meniscus within the gap, and found good agreement between experimental data and numerical simulation.

An example of flow visualization of extrusion coating is given in Fig. 11a.15. Gilbert and Eckel (1992) looked into the shape change of the liquid bridge of a magnetic fluid within the force field of a permanent magnet. Fig. 11a.15a shows the flow when the magnet is positioned underneath the web immediately below the exit of the feed slot. The shape of the liquid bridge is similar to that for curtain coating presented in Chapter 11c. The permanent magnet accelerates the fluid

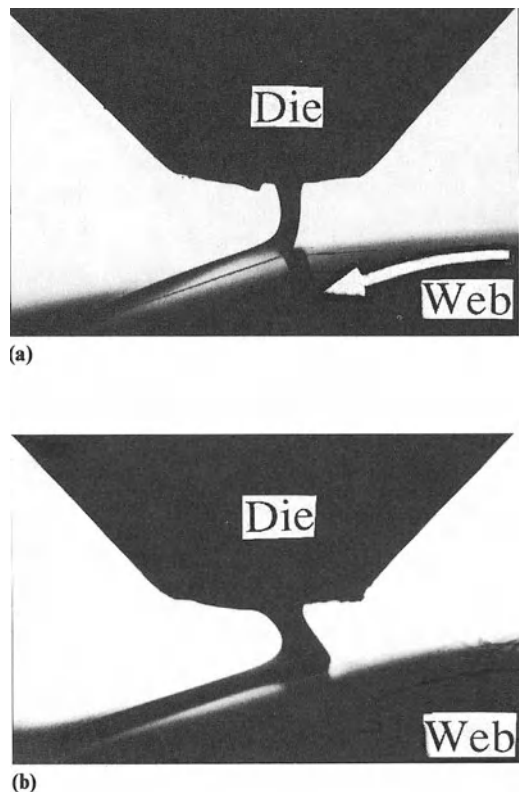


Figure 11a.15 Flow visualization of extrusion coating in the presence of magnetic forces (Gilbert and Eckel, 1992). $Re = 0.5$, $Ca = 3.3$, $St_{mag} = 2$. (a) Magnet is opposite to die, (b) magnet is upstream of die.

in the direction normal to the web and assists in positioning the wetting line. The pulling action of the magnetic force is demonstrated in Fig. 11a.15b, where the magnet is positioned further upstream. A 'heel' is formed as the magnetic fluid is pulled in a direction opposite to the web motion.

Colored dyes and hydrogen bubbles were used to visualize the flow patterns in slot coating (Sartor 1990) and in two-layer slot coating (Cohen, Suszynski and Scriven 1992). The experiments reveal interesting information on eddy motions and yielded vortex maps as shown in Fig. 11a.16. The figures indicate the different flow processes with recirculation zones within the coating bead. Flow structures which can be found in single-layer slot coating are given by combinations of the

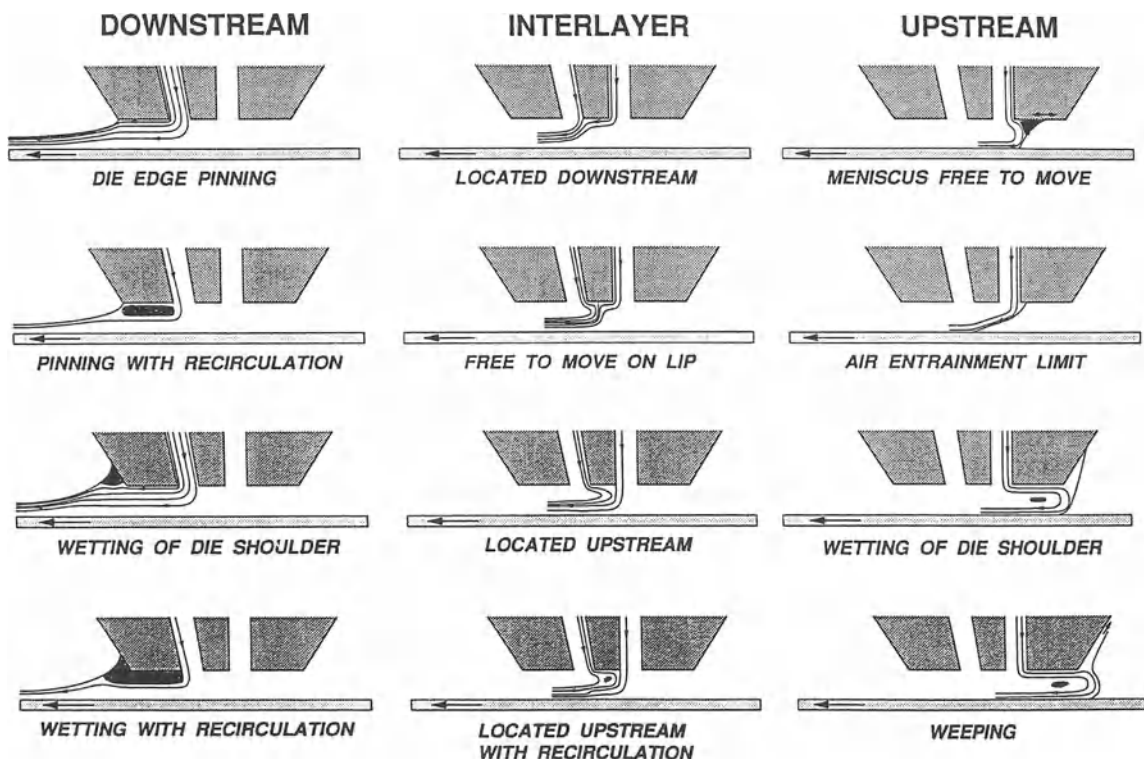


Figure 11a.16 Microvortex map of two-layer slot coating (Cohen, Suszynski and Scriven, 1992).

flow charts in the left- and right-hand columns of Fig. 11a.16. Flow processes in two-layer slot coating are given by combinations of flow charts in the left-hand, middle, and right-hand columns. The various combinations show how complex flow conditions can exist within the coating bead. It is of practical interest to know the optimum flow conditions and flows with no vortices are desired. These are depicted by the figures in the topmost row. The flow charts show that there are several admissible locations of the interface between the two layers. In general, mixing of the two layers has to be avoided and therefore stable positioning of the separation line at corners is desired.

Many coating fluids show a non-Newtonian rheological behavior; viscoelastic fluids in particular can be difficult to handle. Strenger and Secor (1991) found that in slot coating viscoelastic

effects change the pressure field within the coating gap. Owing to this, the ribbing instability occurs and shrinks the size of the coating window dramatically. Tanaka and Yasui (1992) investigated the influence of viscoelasticity in slot and extrusion coating. They observed that in extrusion coating the spacing between the thickness variations of the liquid layer is increased by increasing the shear rate within the feed slot and is decreased by increasing the elongation rate within the liquid bridge. The minimum spacing of the variations was the clearance of the feed slot, h_F . The wetting meniscus in slot coating showed similar curvature variations in the cross-web direction. By increasing the shear rate within the feed slot, the spacing increased. The spacing decreased by a combination of smaller curvature variations when the meniscus moved further upstream within the upstream coating gap. All

these effects were amplified by increasing the viscoelasticity of the fluid.

The complexity of the flow studies may require specially designed coating equipment with glass and Plexiglas rollers, through which flow visualization and optical velocity measurements can be performed. Steps in that direction were taken by Cohen, Suszinski and Scriven (1992).

11a.4 STABLE COATING OPERATIONS

Successful coating requires that the operating parameters lie within the parameter space of stable coating conditions. This area of study, two-dimensional flow processes is called the coating or operability window. The operating conditions have to be chosen in such a way that fluctuations in the operating parameters, which are present in any process, will not cause the operating point to leave the stable operation area. It is useful to define a further and more restrictive quality window, which is limited by operating parameters where the quality standard of the specific product is not achieved owing to undesired eddies, potentially nonuniform wetting lines or high sensitivity to external disturbances.

The theoretical description of the flow with asymptotic approximation equations presented in Section 11a.3 is useful for efficient calculation of coating windows. This analysis is restricted, as it allows one only to exclude the parameter space where the coating flow is unstable and stable coating conditions definitely cannot be achieved. This does not necessarily imply that within the predicted coating window any stable coating condition exists. In this section, the limiting parameters of the coating window are determined using equations (11a.1) to (11a.7) and the inequalities contained in these equations are discussed with respect to static equilibrium conditions at the menisci.

A stable static equilibrium condition at the meniscus of the free surfaces requires that the capillary pressure compensates the pressure difference at the meniscus (Δp_{D1} and Δp_{3D}) and that any change in this pressure difference leads to a new stable equilibrium by changing the

curvature of the free surface, which opposes the change in the pressure difference across the meniscus.

The limiting values of the curvature at the downstream meniscus are derived from the following considerations. The minimum value of r_m at the downstream meniscus is determined by the smallest radius of curvature which can bridge the coating gap for a given static wetting angle θ . The smallest radius is found for a static wetting angle of zero. There exists no limit for the maximum value of the radius r_m . The stability condition can be fulfilled for all values of θ as long as the meniscus is not pinned at the downstream edge of the die lip and there is no restriction on the height, h_C , of the wetting line climbing up the die shoulder (see Fig. 11a.8 for details). The limiting cases at the film forming meniscus can therefore be given by

$$\frac{h_{G,D} - 1}{1 + \cos \theta^*} \leq r_m \leq \frac{h_{G,D} - 1 + h_C}{1 - \sin \theta^*}; \quad 0 \leq \theta^* < \frac{\pi}{2} \quad (11a.9)$$

$$\frac{h_{G,D} - 1}{1 + \cos \theta^*} \leq r_m \leq \infty; \quad \frac{\pi}{2} \leq \theta^* < \pi$$

If the wetting line climbs up the downstream die shoulder, then flow situations will be observed as depicted in Fig. 11a.16, where a vortex forms at the static wetting line of the downstream meniscus. This is an undesired flow situation as the wetting line which is not pinned may no longer be straight and this increases the possibility of a nonuniform wet film in the cross-web direction.

At the upstream meniscus the same static stability consideration as for the film forming meniscus can be made. The radius of curvature of the upstream meniscus is given by

$$r_m = \frac{h_{G,U} + h_C}{\cos \theta^* + \cos \nu} \quad (11a.10)$$

The wetting line, as shown in Fig. 11a.8, may climb up the die shoulder by an amount h_C . Three cases of the meniscus location are distinguished, as follows.

At the **downstream edge** of the upstream die lip, the static contact angle can take the following

values:

$$\theta - \pi + \beta + \gamma_1 < \theta^* < \theta + \beta \quad (11a.11)$$

Stability requires that a positive pressure change is compensated by a decrease in the radius of curvature and this is equivalent to an increase in the angle θ^* . The minimum value of θ is zero. The value of θ^* can increase and the meniscus will be pinned at the edge until $\theta^* = \theta + \pi - \gamma_1$. If θ^* becomes larger, then the meniscus will climb up the die shoulder. Stable conditions are possible for values of θ^* between 0 and π and $h_c = 0$.

Within the coating gap, the angle θ^* can take on only one value, which is given by $\theta^* = \theta + \beta$. If the die lips are inclined, stable conditions can be achieved for

$$\begin{aligned} \beta < 0 \quad \text{and} \quad 0 \leq \theta^* < \frac{\pi}{2} \\ \beta > 0 \quad \text{and} \quad \frac{\pi}{2} < \theta^* \leq \pi \end{aligned} \quad (11a.12)$$

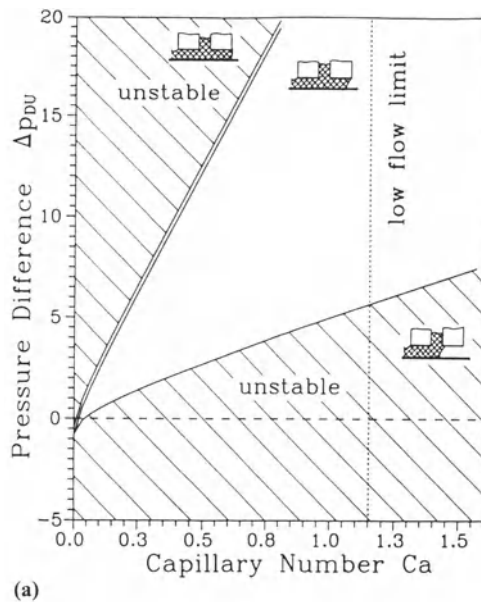
If the inclination angle β of the die lip is zero, no stable position exists within the coating gap. The wetting meniscus moves freely within the gap and has to jump to an edge of the die lip in order to find a new stable position when the pressure difference changes. In reality, viscous forces within the coating bead will compensate for the pressure fluctuations and stabilize the position of the wetting meniscus. A positive pressure difference, Δp_{3U} , fluctuation increases the wetting length under the die lip and the shape of the meniscus is unchanged. A negative value of Δp_{3U} decreases the wetting length.

At the **upstream edge**, the angle θ^* can take the values

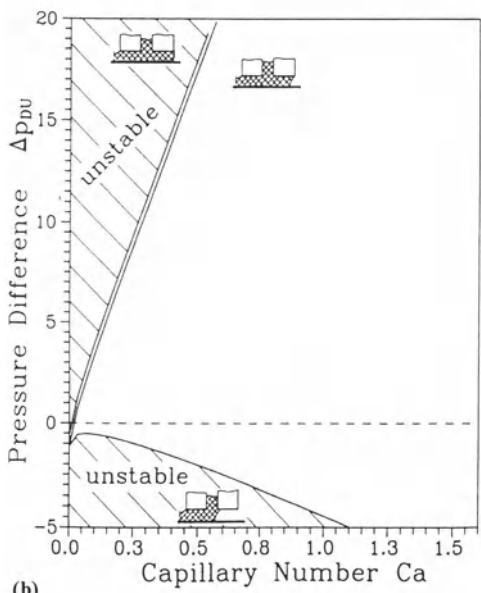
$$\theta + \beta < \theta^* < \theta + \beta + \pi - \gamma_2 \quad (11a.13)$$

and stable conditions are possible only for values of θ^* between zero and π and $h_c = 0$.

Figure 11a.17 shows two typical examples of coating windows with vacuum at the upstream meniscus calculated from the inequalities contained in equations (11a.1) to (11a.7) and equations (11a.9) to (11a.13). The abscissa gives the coating speed expressed by the capillary number. The



(a)



(b)

Figure 11a.17 Coating windows: influence of gap clearance. $l_D = l_U = 20$, v = equation 11a.16. (a) $h_{G,D} = h_{G,U} = 2.5$; (b) $h_{G,D} = h_{G,U} = 1.75$.

ordinate shows the difference between upstream and downstream gas pressures. The static wetting angle, θ , is zero and the dynamic wetting angle, v , is calculated from equation (11a.14) (Guthoff and Kendric 1982):

$$v = 541 \cdot U^{0.22} \cdot \sigma^{0.11} \cdot \mu^{0.18} \quad (11a.14)$$

The values are to be input in the dimensions of kg, m and s. Three limiting conditions are calculated for each capillary number. They are distinguished by the location of the upstream meniscus. The lowest line in the graph represents the flow where the upstream die lip is not wetted and the upstream meniscus pins at the edge of the die lip. This is also called the starving condition. The broken line shows the case where the upstream meniscus pins at the upstream edge and has its maximum value of curvature into the gap. The upper line shows the condition where the meniscus bulges out and assumes its maximum curvature. The pressure difference between the broken line and the upper line describes the influence of the capillary action at the upstream meniscus on the coating window. The difference between the broken line and minimum is the pressure drop due to viscous forces within the upstream coating gap. With increasing capillary number (web speed) the pressure drop within the upstream coating gap increases and therefore the height of the coating window increases.

Figure 11a.17b demonstrates an important characteristic of the operating behavior of a slot coater. If the coating gap is smaller than twice the wet film thickness, then the lowest curve showing the lower stability limit has a negative slope. No vacuum is necessary at all web speeds, whereas in Fig. 11a.17a vacuum is necessary if the capillary number Ca exceeds a certain value. With increasing web speed (Ca) the vacuum level necessary to maintain a stable coating condition increases. The size of the coating window, admissible pressure differences and range of coating speeds depicted in Fig. 11a.17b are much greater than those in Fig. 11a.17a.

Outside the domain bounded by the minimum and maximum pressure difference no stable coating conditions can be found. At the lower border of

the coating window periodic variation of the film thickness in the web direction can be observed. This kind of coating defect is also called barring and is caused by periodic changes of the location of the upstream menisci. In this manner, the volume of the coating bead fluctuates and, assuming a constant feed flow rate, the film thickness will change according to the volume variation.

At the lower or starving limit, the pressure drop within the coating bead due to viscous forces is too high to be balanced by the capillary forces of the menisci and ribbing of the wet film thickness occurs (cf. Ruschak (1985)). These periodic thickness variations in the cross-web direction are due to a nonuniform curvature of the menisci in the cross-web direction, by which the coating bead tries to compensate for the viscous pressure drop. These ribbing patterns will transform into rivulets, with uncoated streaks between them, if the pressure inequality increases.

At the upper border of the coating window, swelling and weeping of the meniscus can be found. If the limit point given by equation (11a.13) is exceeded, swelling of the meniscus occurs, which can lead to weeping, i.e. the discharge of coating liquid from the coating bead. This causes thickness variations in the cross-web direction as not all liquid supplied by the die is coated on to the web at the same time.

The dotted line in Fig. 11a.17a indicates a limit of stable operation, the low flow limit, which can be derived from equation (11a.3). Again it is assumed that the meniscus is of cylindrical shape. The maximum pressure difference Δp_{D1} is found for the smallest meniscus radius (compare equation (11a.9)) which bridges the minimum gap clearance of the downstream coating bead. For reasons of simplicity the second term equation (11a.3) is omitted and the static contact angle θ is set to zero. The capillary number, which indicates the low flow limit, follows as

$$Ca_{\max} = 0.65 \left(\frac{2}{h_{G,D} - 1} \right)^{3/2}; \quad Ca \ll 1 \quad (11a.15)$$

If Ca exceeds the critical limit, the meniscus will recede into the gap or break. At this limit

coating defects due to ribbing or rivulets can be found. With increasing Re , liquid inertia decreases the receding action and the limiting capillary number is raised by a certain amount, as shown in Fig. 11a.18. The marked points in Fig. 11a.18 are taken from numerical flow simulations of the downstream meniscus and show the limiting condition. The low flow limit exists only for values of $h_{G,D}$ greater than twice the wet film thickness.

In practical applications, defects caused by air-entrainment along the wetting line of the upstream meniscus will define a further coating speed limit. Equations to predict the onset of air-entrainment are given in Chapter 3.

The analytical expressions for the prediction of coating windows are very helpful for the selection of the optimum operation parameters. Figure 11a.19 gives an example which shows the admissible variations of the coating gap as a function of the coating speed for the coating of 20 μm thick wet film. At low coating speeds and in the case of a low viscosity coating liquid, high gap clearances can be selected. On the other hand, at high speeds and in the case of a highly

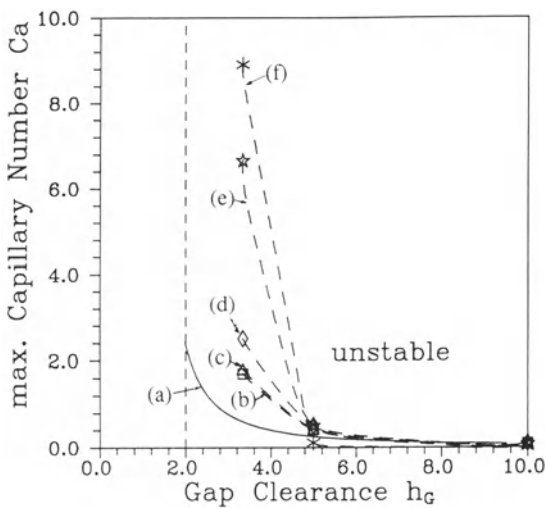


Figure 11a.18 Low flow limit: numerical and analytical data. (a) equation 11a.15; (b) $Re = 0.1$; (c) $Re = 1$; (d) $Re = 10$; (e) $Re = 100$; (f) $Re = 1000$.

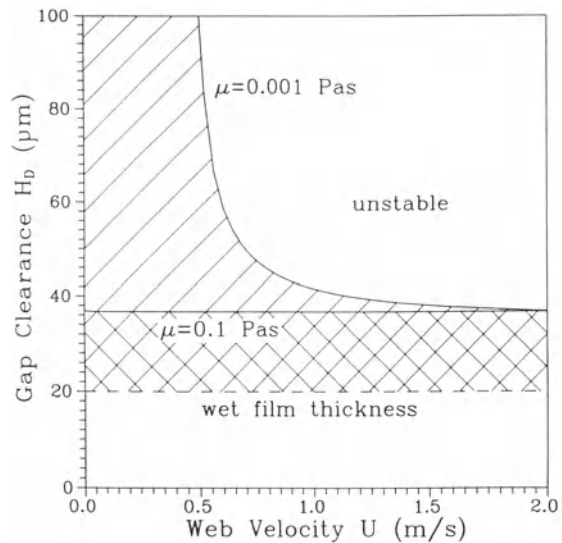


Figure 11a.19 Coating window: gap clearance versus coating speed. $L_D = L_U = 1 \text{ mm}$, $H_D = H_U$, $\sigma = 0.03 \text{ N/m}$.

viscous liquid, the gap clearance has to be less than twice the film thickness. With increasing viscosity and web speed, the capillary number increases. This implies that the influence of surface tension becomes negligible compared with the viscous forces and stable coating conditions can be achieved only for gap clearances less than twice the wet film thickness.

The analytical expressions can be compiled into a PC program which predicts operational windows for slot coaters (Lange and Wagner 1992). The influence of non-Newtonian rheology of the coating fluid can be approximated by using the viscosity of the current shear rate within the gap. Normal stress components can also be considered as was done by Secor (1991) and Strenger and Secor (1991). PC programs of this kind visualize the influence of parameter variations on the coating window and demonstrate that the following parameter changes decrease the size of the coating window:

- increasing viscosity of the coating fluid;
- decreasing surface tension of the coating fluid;

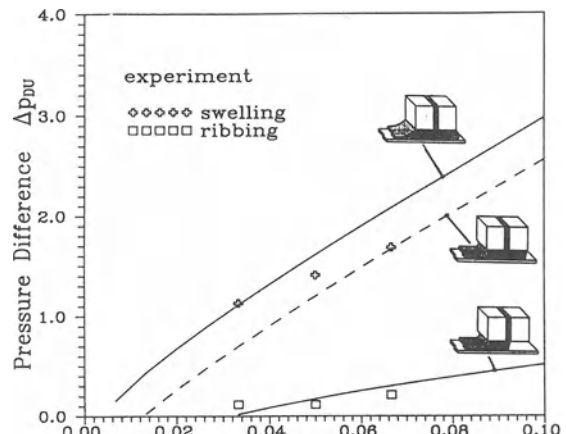
- increasing downstream lip length of the slot coater;
- increasing the coating gap;
- increasing web speed.

Comparison of experimental and predicted coating windows shows good agreement and this justifies the presented approach to obtain parameter combinations for stable conditions. Figure 11a.20 shows Sartor's experiments (1990) and in Fig. 11a.21 the authors' own experimental results are depicted, which were compared with predicted coating windows from equations (11a.1) to (11a.7) with the limiting conditions, equations (11a.9) to (11a.15), given above.

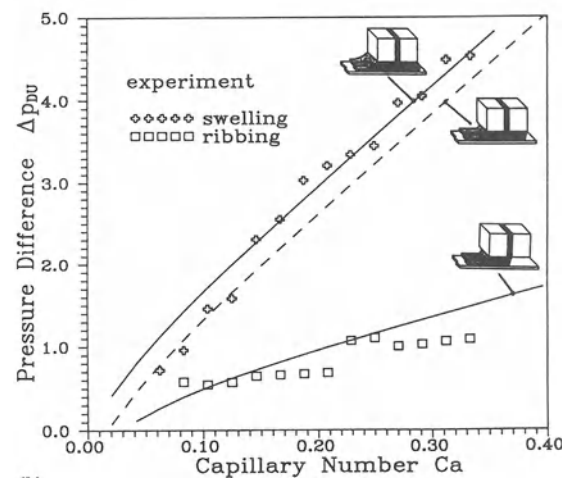
11a.5 SMALL DISTURBANCES AND FILM STABILITY

The considerations provided in the previous section do not permit any conclusions regarding the growth of disturbances with time. Linear and nonlinear stability analysis of the flow processes can provide such information. However, only a few linear stability analyses of flow processes of slot coaters could be found in the literature. It might be that the confined flow field of the slot coater which allows a relative easy and fairly reliable prediction of coating windows still satisfies the needs of industry. This situation contrasts with multilayer slide and curtain coating where this kind of analysis is common, as Chapters 11b and 11c show.

Using lubrication approximations, a stability analysis of the flow at the downstream meniscus under small disturbances will fail to predict the onset of instability, as was shown by Bixler and Scriven (1982). They used a finite element simulation instead to calculate the base flow in a two-dimensional flow domain and studied the influence of three-dimensional disturbances on the stability of their two-dimensional flow. The meniscus was not pinned and could move along the inclined die face. Bixler and Scriven (1982) could show for the limited parameter range of their study that the following will induce ribbing instability:



(a)



(b)

Figure 11a.20 Coating window: comparison of experiment with theoretical predictions (Sartor, 1990). (a) $l_D = l_U = 20.3$, $h_{G,D} = h_{G,U} = 3$, $\beta_D = 22.5^\circ$, $\nu = \text{equation 11a.16}$; (b) $l_D = l_U = 12$, $h_{G,D} = 2.5$, $h_{G,U} = 3.19$, $\nu = \text{equation 11a.16}$.

- increasing the capillary number;
- decreasing the flow rate;
- decreasing the channel divergence angle;
- decreasing the Reynolds number.

An analysis of the sensitivity of the upstream

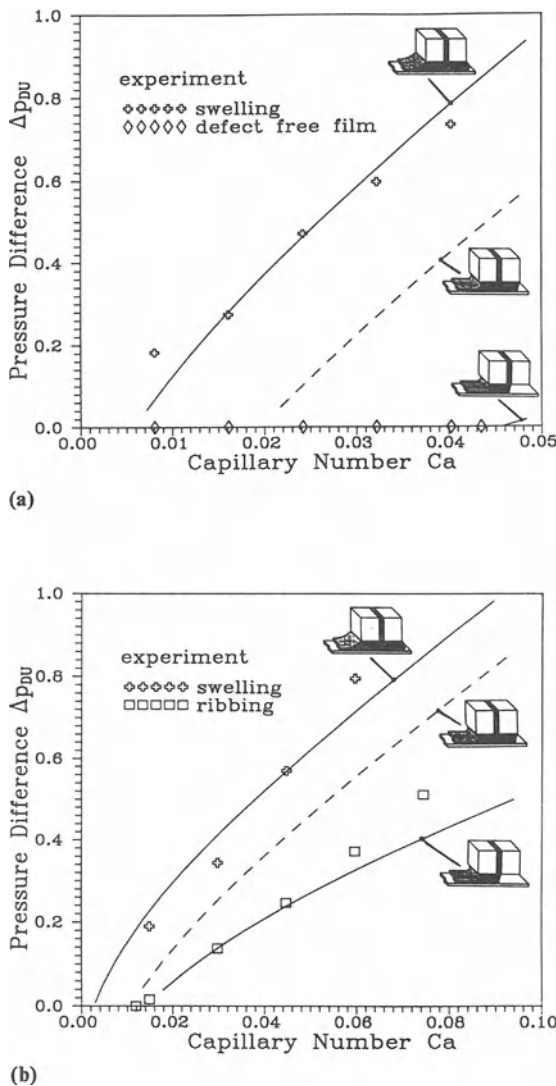


Figure 11a.21 Coating window: comparison of experiment with theoretical predictions. (a) $l_D = 14.8, h_{G,D} = 6.5, h_{G,U} = 2.8, v = \text{equation (11a.16)}$; (b) $l_D = l_U = 25, h_{G,D} = h_{G,U} = 6.25, v = \text{equation (11a.16)}$.

meniscus to three-dimensional disturbances was made by Higgins and Brown (1984). It confirmed the results of the static analysis given by equations (11a.10) to (11a.13).

Higgins and Scriven (1979) suggested predicting the dynamic behavior of the coating bead by a

global energy balance of the flow processes within the coating bead including the viscous forces. This balance leads to a nonlinear differential equation. Analytical solutions were presented for two limiting cases. At low capillary numbers capillary forces will dominate. The simplified equation reflects the coupling of the two menisci. This is not considered in equations (11a.1) to (11a.15) and instabilities will occur if

$$\frac{d}{dl_W} \left(\frac{1}{r_{m,D}} + \frac{1}{r_{m,U}} \right) > 0 \quad (11a.16)$$

where l_W denotes the wetted length of the upstream die lip and $r_{m,D}$ and $r_{m,U}$ are the radii of curvature of the downstream and upstream menisci, respectively. For the second limiting case purely viscous behavior can be assumed and a condition for the minimum wet film thickness is derived. It is expected that disturbances will be damped if

$$\frac{h_{G,U}(l_D + l_W)}{12l_D} < h \quad (11a.17)$$

No further predictions for the dynamic behavior of the coating bead and the growth rate of instabilities have been published even though the numerical methods are available today.

11a.6 GUIDE TO PRACTITIONERS, PROBLEMS IN PRACTICE

The proper design and positioning of the die are only one important part of the stable and reliable slot coating process. There exist many sources of disturbances which can amplify instabilities and create coating defects. All elements of the process need to be considered. In general, the gap clearance in slot coating is small and therefore very sensitive to vibrations. Even small amplitudes in the range of a few micrometers can create the barring defect. This variation of the wet film thickness in the downstream direction can be caused only by pulsations of the flow rate or changes of the web speed, e.g., due to stick and slip effects. Coating defects such as different wet film thicknesses in the cross-web direction, which are due to a misaligned coating gap, can be prevented by a high-precision system for posi-

tioning the die relative to the application roll. Special measures, e.g., automated control of gap clearance, can prevent damage of the die lips while a splice passes through.

The narrow gap clearance requires that much effort has to be put into preparation and delivery of the coating liquid. Experience shows that the coating liquid should be degassed and filtered to remove all contaminations, e.g., bubbles and particles. Cleaning of the web is also essential as dirt will accumulate at the die lips, creating streaks of uncoated web and in the worst case these accumulations will lead to a rupture of the web.

At small Bond numbers a slot coater can be operated in any position relative to earth's gravitational field. However a position should be chosen such that no bubbles are entrapped within the liquid distribution system. Bubbles transported by the liquid can stick to the edges of the die lips or block the coating gap. This leads to a wavy wet film surface in the cross-web direction, and streaks and uncoated areas may appear on the substrate.

The edges of the die lips should be very sharp, as mentioned in Section 11a.2, and the curvature should be uniform in the cross-web direction. Cleaning and handling requirements set limits to the radius of curvature. If the radius is too small the lips are difficult to handle and the edges are easily damaged. The angle γ_{D1} included between die lip and shoulder (see Fig. 11a.8) should be small (about 90°) to prevent the wetting of the die shoulder. If the wetting line does not pin at the edge, vortices can occur, as shown by Cohen, Suszinski and Scriven (1992), and the wetting line may become distorted, which can lead to wavy wet film surfaces.

Drying processes at the static wetting lines create depositions of non-volatile components which distort the wetting line so that wavy films occur. Especially if the coating liquid contains highly volatile solvents, encapsulation of the die can prevent the rapid evaporation of the solvents. For removing the sources of streaks, the coating gap can be cleaned with a soft, flat tool. In this way contaminants sticking to the die lip will be removed.

The methods for preventing air-entrainment in slot coating are similar to other coating operations. However, as the free surfaces exposed to the ambient gas are very small compared with other coating methods, degassing of the coating liquid can increase the potential of the coating liquid to dissolve bubbles entrained at the dynamic wetting line, and by this means the occurrence of defects due to air entrainment can be reduced (Miyamoto 1991).

The operating conditions should be chosen such that the pressure drop in the coating gap is much less than that in the feed slot. In this manner, the uniform distribution of the coating liquid is not influenced by the flow within the coating bead. Fixed die lips are preferred over adjustable ones. Nevertheless, for applications where the viscosity of the liquids coated with the same die differs widely, a uniform liquid distribution might be achieved only by changing the pressure drop within the feed slot in the cross-web direction. This can be done by automatic positioning systems, e.g. piezo positioners, which control the gap clearance of the feed slot in combination with an in-line measurement of the wet film thickness (Lippert 1987). A high pressure at the exit of the feed slot spreads the coating liquid in the cross-web direction. In some applications it is possible to block the coating gap by soft inserts at the edges to limit the coating width.

By blocking of the feed slot it is possible to reduce the coating width or coat stripes. Blocking the feed slot will change the liquid distribution and special care has to be taken not to damage the lips.

In the case of long die lips and application rolls of small diameter, the pressure level under the downstream die lip can become so small that dissolved gas and solvent will leave the coating liquid and bubbles will be created. Figure 11a.22 gives an example of pressure distributions within the coating gap. The die is translated horizontally, parallel to the x-axis. Even at ambient pressure at the downstream and upstream menisci, the pressure within the coating bead can decrease well below the ambient pressure. It can further

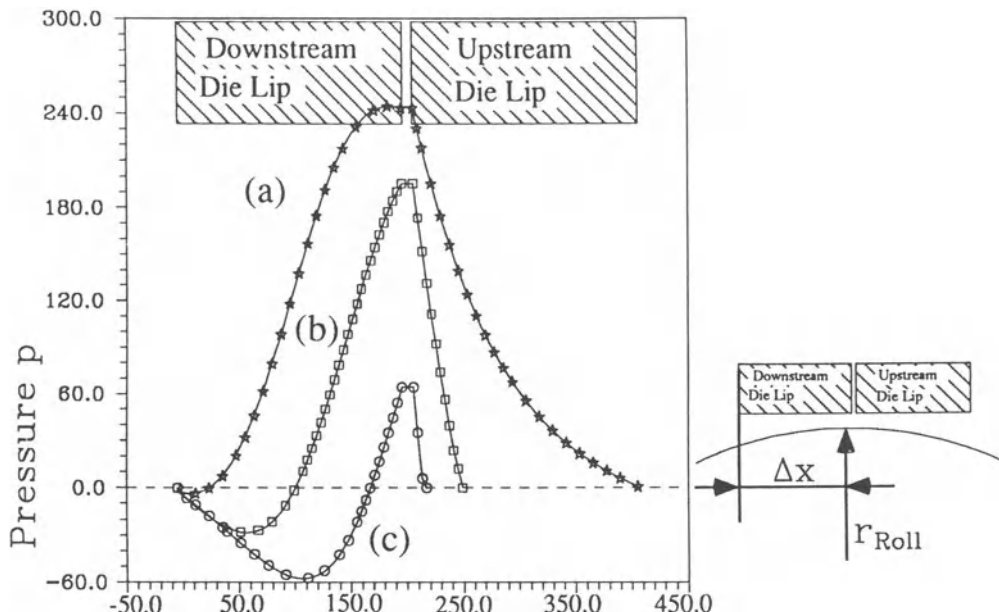


Figure 11a.22 Variable gap clearance: pressure profiles within the coating bead. $Re = 0.66$, $Ca = 2.78$, $l_D = l_U = 200$, $h_{G,\min} = 1.5$, $h_F = 5$, $r_{\text{roll}} = 8000$. (a) $\Delta x = 150$; (b) $\Delta x = 100$; (c) $\Delta x = 50$.

be seen in this configuration that the coating gap is diverging in the downstream direction and that the pressure increases in the downstream direction, which can enhance the ribbing instability.

It is commonly believed that a coating process without vortices is the most stable. Further reasons for avoiding vortices within the coating bead are that particles deposit at the walls in areas of low shear rate, namely vortices and recirculation zones, and change the flow field. Vortices promote separation processes and an uncontrollable residence time of the liquid, which endangers the stable operation of the process.

The asymptotic equations given in this chapter can be implemented into PC programs (Lange and Wagner 1992) which are useful for monitoring and controlling the instantaneous operating conditions. It is possible to indicate the actual point of operation within the coating window to assist the operating personnel. These coating windows can also be used to find a stable path for the start-up of the process. The risk of wetting

the downstream die shoulder during the start-up of the system is fairly high and starving conditions should be chosen.

11a.7 SUMMARY AND OUTLOOK

Slot coating is a very versatile operation which has a broad range of applications. It is premetered and therefore allows the control of the film thickness independent of liquid properties. High coating speeds can be achieved and very low- and high-viscosity coating liquids can be applied. The maximum gap clearance in slot coating is often very small, thereby requiring high precision of the die and the applicator roll and in their relative positioning. Dirt and dust particles can very easily create serious coating defects if the coating gap is narrow. Hence the goal has always been to coat at high speeds with a high gap clearance. Under certain conditions, the gap clearance can be increased at low and moderate

web speeds with a vacuum box located at the upstream meniscus. The flow within the coating bead is confined by the die lips and the web. Only a very small surface area of the coating liquid is exposed to the ambient gas during the process of layer formation. Therefore, even coating liquids with a high content of extremely volatile solvents can be applied with a small risk of defects by early evaporation of the solvent. Many patents describe multilayer slot coating processes; however, the number of industrial applications today is small compared with slide and curtain coating.

In extrusion coating the positioning and precision of roll and die are less sensitive to errors as the admissible gap clearance is much higher than in slot coating. The advantages of a higher gap clearance are obtained at the expense of greater disturbances by edge effects. The flow processes in extrusion coating are closely related to curtain coating.

The confined coating bead of a slot coater permits the description of the flow processes by approximate equations. These equations can be used to calculate coating windows, which are a valuable tool for designing and controlling slot coating processes. In the case of fluids with simple rheology, the predicted areas of stable coating conditions agree very well with experimental findings.

Steadily increasing requirements on product quality and optimization of the coating process will drive researchers to study the flow phenomena within the coating gap in more detail in order to obtain a better prediction of coating windows. Still, the influence of strongly viscoelastic coating liquids cannot be adequately simulated by numerical programs. The avoidance of undesired edge effects and three-dimensional flow structures will also draw more attention. Future research will concentrate even more on combined experimental and numerical studies, with a stronger emphasis on numerical simulations than today; experimental studies tend to be expensive and numerical simulation programs are becoming more and more powerful while simultaneously the cost of computing is decreasing.

REFERENCES

- Ankenbrand, F., Herrmann, K. and Wilke, W. 1969. Verfahren zum Auftragen magnetisierbarer bindemittelhaltiger Schichten auf einer Trägerfolie mit einem Extrudergießer. German Patent 1,907,212.
- Aurin, W. 1985. Hot melt pressure sensitive adhesive coating equipment. In *Proceedings of the 1985 Polymers, Laminations and Coating Conference*, pp. 43–49. Atlanta: TAPPI.
- Beguin, A. E. 1954. Method of coating strip material. US Patent 2,681,294.
- Bixler, N. E. 1982. Stability of a coating flow. PhD thesis, University of Minnesota, Minneapolis.
- Bixler, N. E. and Scriven, L. E. 1982. Stability of slot and knife coating by finite element analysis. Paper read at AIChE 1982 Spring National Meeting, at Orlando, FL.
- Browatzki, K., Maus, F., Platz, S. and Schweicher, W. 1975. Verfahren und Vorrichtung zum Begießen bandförmiger Unterlagen. German Patent 1,921,044.
- Cameron, E., Alfred, P. and Hills, R. 1968. High speed coating apparatus. US Patent 3,413,143.
- Campbell, D. P. 1980. Slot orifice coating in 1980. In *Proceedings of the Paper Synthetics Conference, Cincinnati, Ohio*, pp. 309–313, Atlanta: TAPPI.
- Carpenter, J. K. and Steen, P. H. 1990. Inertial effects in the fluid mechanics of planar-flow melt-spinning. Paper read at AIChE 1990 Spring National Meeting, at Orlando, FL.
- Cohen, D. and Scriven, L. E. 1992. Viscocapillary model of two-layer slot coater. Paper read at AIChE 1992 Spring National Meeting, at New Orleans, LA.
- Cohen, D., Suszinski, W. and Scriven, L. E. 1992. Flow visualization of two-layer slot coating. Paper read at AIChE 1992 Spring Meeting, at New Orleans, LA.
- Demirdzic, I., Durst, F., Perić, M. and Wagner, H.-G. 1990. A finite volume numerical method for free surface flow analysis. Paper read at AIChE 1990 Spring National Meeting, at Orlando, FL.
- Durst, F., Haas, R., Perić, M. and Scheurer, G. 1988. Computational study of the flow in slot coaters. Paper read at AIChE 1988 Spring National Meeting, at New Orleans, LA.
- Durst, F., Haas, R., Perić, M., Scheurer, G. and Wagner, H.-G. 1991. Numerische Simulation zweidimensionaler Schlitzdüsenströmungen bei der Fließbeschichtung. *Coating* 2/91, 3/91, 7/91, 10/91.
- Fahrni, F. and Zimmermann, A. 1978. Coating device. US Patent 4,109,611.
- Gilbert, N. and Eckel, A. 1992. Analysis of extrusion coating in the presence of external forces. Paper read at AIChE 1992 Spring National Meeting, at New Orleans, LA.

- Grader, L. 1985. *Untersuchungen zum Benetzungsprozeß, dargestellt am Beispiel der Beschichtung von Informationsaufzeichnungsmaterialien*. Dissertation, Technische Hochschule 'Carl Schorlemmer', Leuna-Merseburg, Germany.
- Guthoff, E. B. and Kendrik, C. E. 1982. Dynamic coating angles. *AICHE J.* **28**: pp. 456–466.
- Higgins, B. G. and Brown, R. A. 1984. Multiple equilibrium shapes of partially constrained menisci: a quasi-static mechanism for instability of a coating bead. *Chem. Eng. Sci.* **39**(9): 1339–1345.
- Higgins, B. G. and Scriven, L. E. 1979. Coating beads behave as nonlinear oscillators that have limited stability. Paper read at AIChE 72nd Annual Meeting, at San Francisco, CA.
- Higgins, B. G. and Scriven, L. E. 1980. Capillary pressure and viscous pressure drop set bounds on coating bead operability. *Chem. Eng. Sci.* **35**: 673–682.
- Ishiwata, M. and Nagai, Y. 1970. Überzugsverfahren und Überzugsvorrichtung. German Patent Application, 1,939,038.
- Jackson, B. W. 1976. US Patent, 3,996,885.
- Kageyama, T. and Yoshida, M. 1986. Extrusion coating apparatus. UK Patent 2,120,132.
- Lange, U., Durst, F., Raschillier, H. and Wagner, H.-G. 1991. Axisymmetric slot coater for cables, wires and fibers: Theoretical treatment and layout considerations. Paper read at IS&T 44th Annual Conference, St. Paul, MN.
- Lange, U. and Wagner, H.-G. 1992. DESC: A computer program for the design of slot coating devices. LSTM-Erlangen, University of Erlangen-Nürnberg, Germany.
- Lippert, H. G. 1987. Slot die coating – A technical update on recent techniques and design developments. In *1987 Polymers, Laminations and Coating Conference Book 1*. Atlanta: TAPPI.
- Miller, F. D. and Wheeler, J. J. 1965. Coating high viscosity liquids. US Patent 3,206,323.
- Miyamoto, K. 1991. On the mechanism of air entrainment. *Ind. Coating Res.* **1**: 71–88.
- Nadeau, G. F. 1960. Method of coating a liquid photographic emulsion on the surface of a support. US Patent 2,952,559.
- O'Brien, W. G. 1984. Beveled edge metered bead extrusion coating apparatus. US Patent 4,445,458.
- Ruschak, K. J. 1976. Limiting flow in a pre-metered coating device. *Chem. Eng. Sci.* **31**: 1057–1060.
- Ruschak, K. J. 1985. Coating flows. *Ann. Rev. Fluid Mech.* **17**: 65–89.
- Russel, T. A. 1956. Multiple coating apparatus. US Patents 2,761,417 and 2,761,418.
- Sartor, L. 1990. Slot coating: Fluid mechanics and die design. PhD thesis, University of Minnesota, Minneapolis.
- Scanlan, D. J. and Scriven, L. E. 1990. Two-slot coater analysis: Separation line issues in two-layer coating. Paper read at AIChE 1990 Spring National Meeting, at Orlando, FL.
- Schweizer, P. 1992. Fluid handling and preparation. In *Modern Coating and Drying Technology*, eds E. D. Cohen and E. B. Gutoff, pp. 23–62. New York: VCH Publishers.
- Secor, R. B. 1991. Process modeling of contact extrusion and coextrusion. *Tappi Journal*. Nov.: 168–174.
- Strenger, M. R. and Secor, R. B. 1991. Behavior of knife coaters: Operating bounds, thickness control, and stress characteristics. Paper read at IS&T 44th Annual Conference, St. Paul, MN.
- Tanaka, T. and Yasui, Y. 1992. Anomalous phenomenon in die coating with viscoelastic fluids. Paper read at AIChE 1992 Spring National Meeting, at New Orleans, LA.
- Tanaka, Y. and Noda, S. 1988. Beschichtungsvorrichtung. German Patent 3,144,655.
- Wilson, S. D. R. 1982. The drag-out problem in film coating theory. *J. Eng. Math.* **16**: 209–221.
- Woodworth, C. B., Winkler, D. E. and Jackson, B. W. 1982. German Patent 2,403,313.

NOTATION

Bo	Bond number
Ca	capillary number
$D2$	averaged square of inverse dimensionless gap clearance
$D3$	averaged third power of inverse dimensionless gap clearance
H_C	height of meniscus climbing up the die shoulder
H_F	clearance of feed slot
$h_{G,D}$	dimensionless clearance of downstream coating gap
$H_{G,D}$	downstream clearance of coating gap
$h_{G,U}$	dimensionless upstream clearance of coating gap
$H_{G,U}$	upstream clearance of coating gap
h_∞	dimensionless final wet thickness of coated film
H_∞	final wet thickness of coated film
L_D	length of downstream die lip

L_U	length of upstream die lip	θ	static wetting angle
p_i	dimensionless pressure at locations $i = D, U, 1, 2$ and 3	θ^*	static wetting angle measured between free surface and parallel to the web
P_i	pressure at locations $i = D, U, 1, 2$ and 3	μ	Newtonian viscosity
R	radius of application roll	ρ	density
Re	Reynolds number	σ	surface tension
R_m	mean radius of curvature	ν	dynamic wetting angle
U	coating/web speed		
V^*	feed flow rate		
W	width of coating in cross-web direction		
<i>Indices</i>			
<i>Greek letters</i>			
β	inclination angle of die lip	D	downstream
γ	angle included by two die lip faces	U	upstream
Δp_{ij}	dimensionless pressure difference between locations $i, j = D, U, 1, 2$ and 3	m	mean
		C	climbing
		G	gap
		F	feed

Jules Hens and Willy Van Abbenyen

11b.1 INTRODUCTION

In Chapter 11a a first premetered coating system – the slot coater – was discussed. An important limitation of the slot coater is the difficulty of building dies for coating more than two layers simultaneously. In the photographic industry the production of color films requires the superposition of many (up to twenty) layers; so it is not surprising that slide coating – allowing an unlimited number of premetered layers to be coated simultaneously – was invented and developed in the photographic industry (Mercier, Torpey and Russell 1956).

A slide coater (Fig. 11b.1) basically consists of a multilayer die with an inclined plane, placed

at a small distance (0.2 to 0.4 mm) from a moving web, supported by a backing roll. Coating liquids are fed through distribution cavities and slots, forming a multilayer stack on the incline without convective mixing. The liquids are bounded sideways by edge guides.

At the end of the inclined plane, the liquid bridges the narrow gap between coater and web, wets the web and gets entrained by it. The liquid puddle, extending from the coater to the web and bounded by an upper and a lower free surface is commonly called the bead. If the flow in this bead is stable, steady, uniform and without vortices, the slide coating operation is satisfactory.

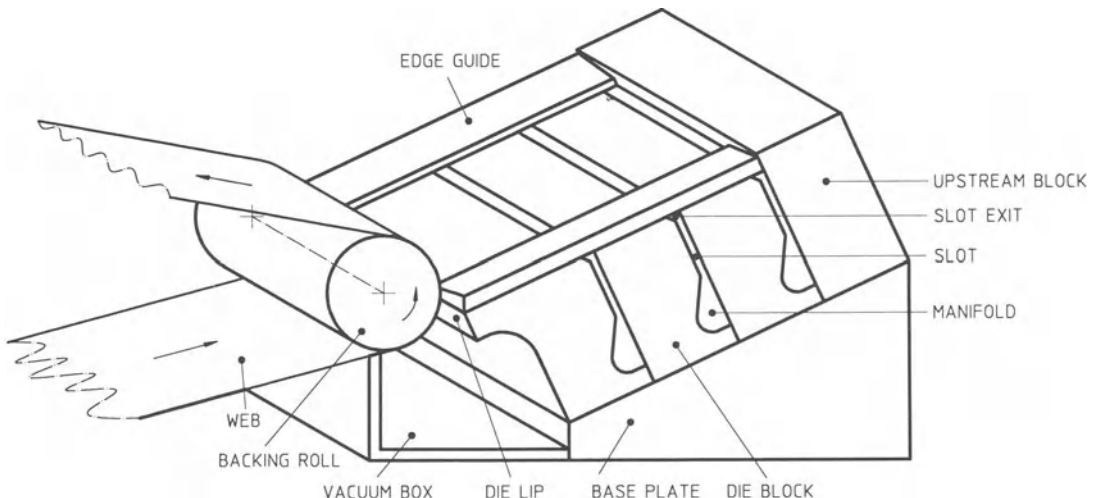


Figure 11b.1 Perspective view on a slide coater.

Generally a slightly sub-ambient pressure P_V is applied below the bead, at most 1000 Pa less than the ambient pressure P_A above. The difference $\Delta P = P_A - P_V$ is often referred to as the ‘bead vacuum’ or ‘backpressure’ (Beguin 1954). As will be shown, such a ‘bead vacuum’ is useful in order to broaden the operability window, i.e. the range of parameters within which a satisfactory coating can be made.

Alternatively the bead can be stabilized by means of an electrical potential difference (of the order of 1000 V) between the backing roll and the coating liquid (Nakai and Okada 1968).

Slide coating can be performed at web speeds ranging from very low (say 0.1 m/s) up to rather high (say 4 m/s). Typical viscosities in slide coating are between 0.5 mPa s and a few hundred mPa s. The total wet coated thickness is typically of the order of 100 µm; it can be substantially thicker, but it is difficult to coat thinner than about 20 µm. The total thickness, however, may be distributed over several layers, each of which can be as thin as a few microns.

It should be clear at this point that not every combination of the parameter values cited is possible; on the other hand, in special cases the parameter range attainable can even be extended. We shall explore the possibilities and the limitations of slide coating in more detail in the following sections.

In Section 11b.2 we shall discuss important details of slide coater geometry, such as slot exits, inclination angle, lip geometry, etc. In Section 11b.3 we shall attempt to give an insight into slide-coating flow, based upon principles of fluid mechanics, flow visualization experiments and numerical calculations. This will enable us to understand some of the limitations of slide coating. More limitations are covered in Section 11b.4. In Section 11b.5 we discuss how the quality of the coated product may be affected by external disturbances and in Section 11b.6 the main defects of slide coating will be reviewed. Finally in Section 11b.7 we summarize the advantages and drawbacks of slide coating.

The contents of this chapter are mainly based upon information from patents and scientific

publications, including PhD theses, although much information is also drawn from presentations at the coating symposia held every two years as part of the AIChE meetings.

11b.2 GEOMETRY OF A SLIDE COATER ARRANGEMENT

11b.2.1 DIE ASSEMBLY – NUMBER OF LAYERS

A slide die comprises a number of blocks, in principle one per layer, mounted on an inclined base plate. It is convenient to use rectangular blocks that are (nearly) identical, but they may also be designed individually according to the rheology and the flow rate of each specific layer (Paton 1968).

The number of layers that can be coated simultaneously is in principle unlimited. As early as 1977 an example with seven layers was described (Dittmann and Rozzi 1977); today, some films for color photography have twenty and it is desirable to manufacture such films in one pass at one coating station.

In practice, the stability of the multilayer flow on the inclined plane may become a problem upon increasing the length of the die by adding more blocks (see also Section 11b.4.3). In addition, the reliability of any system is severely decreased upon increasing the number of components. These and other potential problems have to be taken into consideration when deciding upon the number of layers to be coated simultaneously.

11b.2.2 SLOT EXIT

The coating solutions, making up the different layers, are uniformly distributed across the width of the die by a manifold/slot system, one for each layer; this topic is covered thoroughly in Chapter 10.

Additionally, the geometry of the slot exit (at which a newly formed layer joins the stack on the inclined plane) is crucial in slide coating (and in slide-fed curtain coating, see Chapter 11c). Some problems and some proposed solutions are discussed below and are illustrated in Fig. 11b.2.

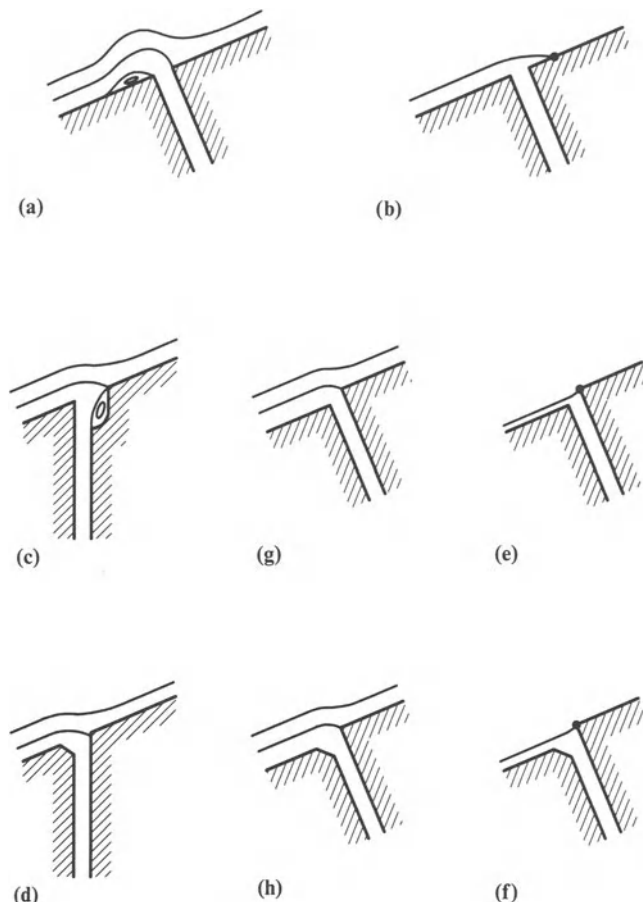


Figure 11b.2 Slot exit details.

In the most simple geometric arrangement the slot is formed by two rectangular blocks mounted in such a way that their top sides making up the slide are in one plane (Fig. 11b.2a). The fluid arriving from this slot flows underneath the other layer(s), but due to its momentum it is likely that separation will occur, giving rise to a vortex. This is undesirable, because in practice such a vortex is generally neither two-dimensional nor steady (see Schweizer (1988), see also Chapter 7), making the coating nonuniform. Furthermore a particle can become trapped in such a vortex and a sharp, prolonged nonuniformity (a streakline, Section 11b.6.1) will result. Additionally, in such a geometry

the top layer tends to flow back, wetting the upstream slide surface (Fig. 11b.2b). Unfortunately, there is little chance that the thus formed static wetting line is straight, resulting in ‘bandedness’, another nonuniformity across the web, but less sharp than streaklines (see also Section 11b.6.1).

The separation vortex can be avoided by increasing the width of the slot near the exit. Padday (1961) proposed the geometry shown in Fig. 11b.2c. Such a design has one serious drawback, however; a stagnant zone (with very slow recirculation) in the widened part of the slot creating the possibility that suspended particles settle causing streaklines. The same idea, however,

can be employed in other and better ways, e.g. by chamfering as in Fig. 11b.2d (Russell 1969; Ade 1976).

Backflow and upstream wetting at the uppermost slot can be avoided by elevating the upstream block (Fig. 11b.2e); Ade (1976) combined this with a chamfered downstream block (Fig. 11b.2f).

The same concept can be used for the other slots too (Figs 11b.2g and 2h). The step height should be chosen according to the flow parameters in such a way that the flow of the upper layers is nearly rectilinear. A drawback of such a ‘stepped’ geometry is the necessity for more complicated edge guides: designs based upon simple single plates cannot be used.

An optimal slot exit design is based upon the rheology and flow rates of the actual layers; visualization experiments and/or numerical simulations are indispensable (see Chapter 7 and also Kistler (1983), Scanlan (1990) and Berghezan (1991)).

11b.2.3 APPLICATION ANGLE α

Intuitively, it might seem logical to mount the die and the backing roll in such a way that the axis of the roll lies in the plane of the slide (Fig. 11b.3a: $\alpha = \beta$); in such a geometry the momentum of the arriving liquid will optimally assist the

wetting process (see also Sections 11b.3 and 11b.4.1).

Such a geometry is impossible, however, in coating machines in which the web is conveyed (nearly) vertically upwards into a chilling or drying zone. Furthermore, the web is preferably kept in contact with the backing roll over an angle of at least 5° to 10° beyond the coating position in order to make sure that web vibrations cannot perturb the coating bead. Hence the die is often mounted with its leading edge under the horizontal plane through the axis of the backing roll (Fig. 11b.3b: $\alpha < 0$).

Even when the web leaves the coating roll (nearly) horizontally, it is more convenient to have the die positioned as in Fig. 11b.3b, because of the start-up procedure. Indeed, immediately before the start of the coating operation, the liquid coming from the slide is not yet taken away by the web, and hence has to be evacuated somehow. With a geometry such as shown in Fig. 11b.3b everything flows into the vacuum box (see Section 11b.2.8), and can be drained easily; a design such as that shown in Fig. 11b.3a requires a starting plate or the like, as with curtain coating (see Chapter 11c). This extra complication probably explains why nearly all publications mention a geometry as shown in Fig. 11b.3b.

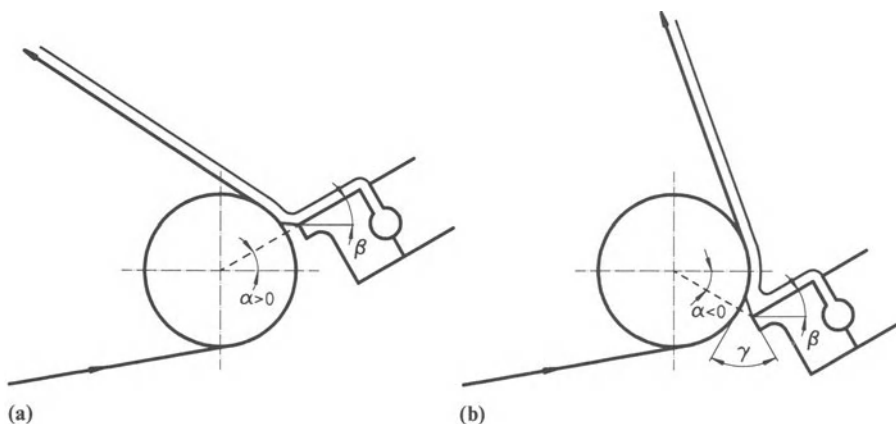


Figure 11b.3 The application angle α .

11b.2.4 SLIDE INCLINATION ANGLE β

It should be possible to find an optimal value for the inclination of the slide (the angle β with the horizontal plane) because both extremes ($\beta \approx 0^\circ$ and $\beta \approx 90^\circ$) have their own problems, as explained below.

The smaller the inclination, the thicker the layer on the slide H_s will be:

$$H_s = \left(\frac{3\mu Q}{\rho g \sin \beta} \right)^{1/3} \quad (11b.1)$$

where Q is the total flow rate per unit width, μ is the viscosity, ρ is the fluid density, and g is the gravitational acceleration.

This expression holds for the one layer case, but can easily be extended to a multilayer system. The momentum of the flow on the slide is proportional to the flow rate squared, divided by the thickness on the slide; so the momentum, which makes up the hydrodynamic assist of the wetting process (see Section 11b.4.1), tends to zero with decreasing inclination.

On the other hand, increasing the inclination makes a flow less stable, as the growth rate of waves on an inclined plane (see Section 11b.4.3.1) increases with $\sin \beta$ (Yih 1963; Kao 1968).

A steep incline positioned in such a way that the momentum optimally assists the wetting process has been described (Burket, Conaghan and Hirshburg 1984). The drawbacks of instability on the slide and start-up complication are, in our opinion, not worth the possible gain in maximum coating speed.

As far as we know, a complete study of the optimization of the inclination angle of a multilayer slide die has never been published. In most publications and studies an angle between 15° and 30° is mentioned. It is the authors' experience that in this range a few degrees are not crucial.

11b.2.5 LENGTH OF THE DIE

The length of the slide should be as small as possible, because waves, if present, may grow

exponentially with increasing slide length (see Section 11b.4.3). In practice, manufacturing issues impose a minimum length per block (of the order of 3 to 6 cm) to maintain mechanical stability. The larger the coating width, the more difficult it is to obtain a good die with a slide that is as short as possible.

11b.2.6 GAP WIDTH H_G

The die is placed in close proximity to the web, at a gap of between 0.1 and 0.5 mm, preferably between 0.2 and 0.4 mm. For completeness an alternative geometry should also be mentioned (Timson 1973; 1976) in which a gap as small as 25 μm can be obtained by using a pressure chamber instead of a backing roll, but this geometry does not appear to be widely used.

A small gap produces a coating bead which is less prone to disturbances (because the surface, on which e.g. pressure variations can act, is smaller) and hence the coating window (or more precisely the quality window, see Sections 11b.4.4 and 11b.5) is larger. From this point of view a gap of the order of 0.1 mm is preferred.

On the other hand, splices (and other web unevennesses) must pass the coating die. With too narrow a gap there is a serious risk of web rupture; and if the web does not break, but merely touches the die face, the static wetting line may become distorted, yielding streaklines (see Section 11b.6.1). When these types of problem occur, an increase of the gap width is recommended.

11b.2.7 DIE FACE

The detailed geometry of the die lip is important in view of the positioning of the static wetting line. It should be straight in order to obtain a uniform coating (a well known feature common to all die-coating operations). This can be achieved by 'pinning' the contact line at a sharp edge, according to Gibb's principle (see Chapters 3 and 9). Fahrni and Zimmermann (1977) defined a sharp edge at which a wetting line will pin as a physical edge with a radius of curvature of less

than 100 µm, preferably less than 50 µm. On the other hand of course, the sharper the edge, the greater the risk of damaging it, and of the operator getting injured when manipulating the die.

Whether the static contact line of the lower meniscus is pinned at the slide edge or wets the slide face lip depends upon both geometry and flow parameters. The larger the angle γ between the die face and the web (see Fig. 11b.3), the more the flow will tend to pin at the slide edge. Increasing web speed or viscosity or decreasing the gap width or the pressure difference over the bead also forces a ‘wetting’ contact line to move upward, and eventually pin at the edge.

Wetting should be avoided, not only because the contact line may become crooked, but also because of the possibility of recirculation in the lowermost part of the bead between die lip and web (see Section 11b.3.4). Furthermore, numerical calculations show that a pinned contact line is qualitatively advantageous, due to reduction of the sensitivity to disturbances (see Van Abbenyen, Christodoulou and Scriven (1988); see also Section 11b.5).

11b.2.8 VACUUM BOX

In order to create a pressure difference over the bead a so called vacuum box is built between the die and the backing roll. Precision labyrinth seals are mostly used to minimize the leakage of air (inevitable due to the moving web) into the vacuum box. Maintaining the pressure difference requires continuous evacuation of air out of the vacuum box. This should be done carefully and uniformly, because the coating quality can be impaired by fluctuations in the applied pressure difference, especially when a relatively large gap is used (see Section 11b.5).

Multiple chambers have been described (Krussig 1981), even with adjustable walls (Bassa 1984). In general, standing acoustic waves in the vacuum box should be avoided and noise sources (such as the fan generating the pressure difference) need to be damped carefully.

11b.3 SATISFACTORY STEADY STATE OPERATION

In slide coating different flow regions can be distinguished: the zone near the slot exit where the slide flow is formed, the flow on the slide itself, a transitional zone between slide and bead, the bead zone and another transitional zone in which the flow rearranges towards plug flow to be finally convected away by the web (see Fig. 11b.4, and examples of flow visualization in Chapter 7).

The forming flow at the slot exit delivering one fluid underneath the other(s), has been thoroughly studied by Kistler (1983) and Scanlan (1990), by numerically solving the Navier–Stokes equations.

On the slide the flow eventually reaches a one-dimensional steady state regime which can be easily calculated in the case of Newtonian liquids, the flow profile being a (multiple) parabola (Aktharuzzaman, Wang and Lin 1978). Other liquids yield a modified, yet always parabola-like profile on the inclined plane.

Where the slide flow ends (because the liquid eventually impinges on the web) the free surface transforms into a standing wave. This typical transitional flow pattern was first described by Ruschak (1978), further by Kheshgi, Kistler and Scriven (1992) and studied numerically in the case of slide coating by Kobayashi, Saito and Scriven (1982).

Higgins and Scriven (1979) showed that the flow in the transitional zone out of the bead exponentially rearranges into a plug flow, or more precisely a solid body translation with the web, at least if one disregards the effect of gravity.

Galehouse and Colt (1984) re-examined both the flow at the end of the slide and the flow leaving the bead, attempting to study the slide coater analytically. Christodoulou and Scriven (1989) used these analytical approximations as boundary conditions for their finite element calculations of the flow field in a slide coater.

We shall now focus on the flow in the bead region, which is really the heart of the slide coater. Here the liquid arriving from the incline

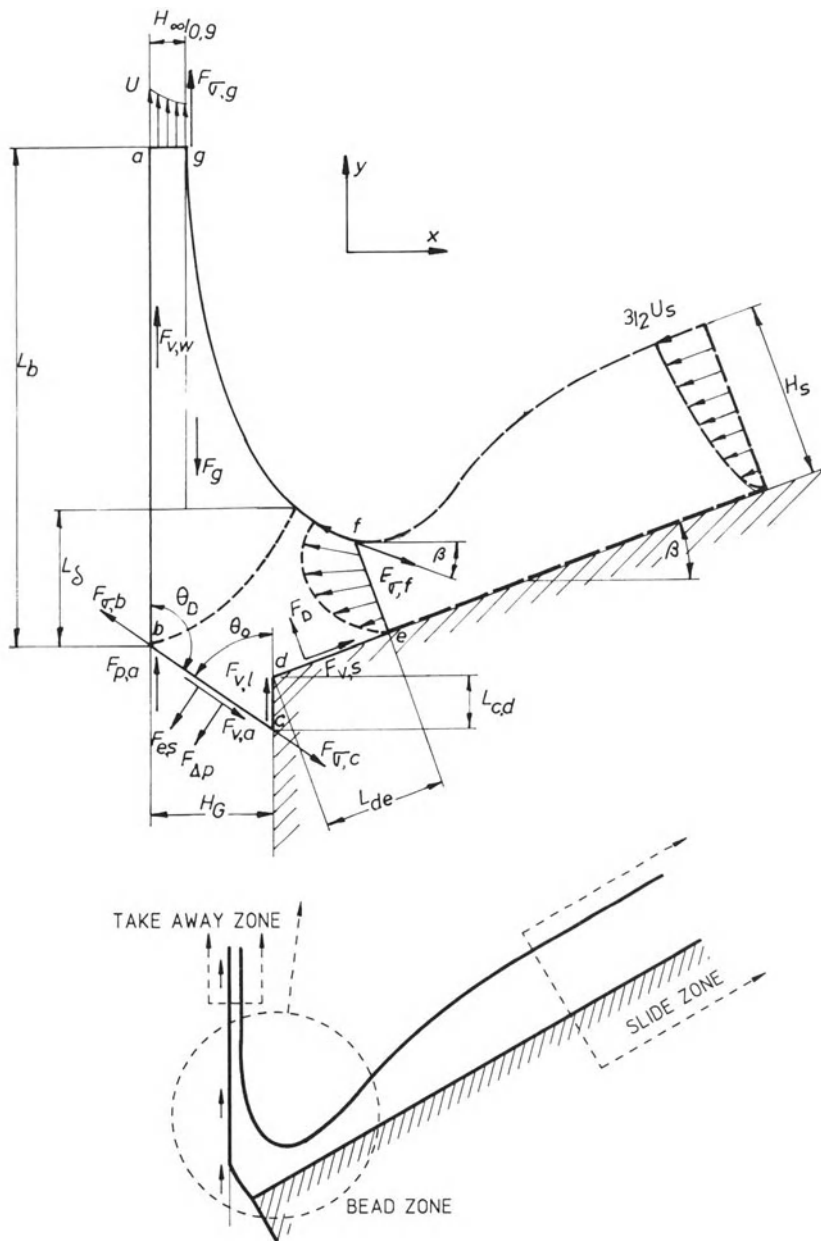


Figure 11b.4 Definition sketch of a slide coating bead: the control volume and the forces acting upon it.

is deflected, wets the moving web and becomes entrained by it. Two important processes take place in the bead. First, at the dynamic wetting

line the coating liquid displaces the air that previously adhered to the web. This is called the wetting of the web and it is the subject of Chapter 3.

We shall return to this subject in the next section (Section 11b.4.1). Secondly, the two free liquid–air interfaces allow the bead to change its geometry in such a way that the rate at which the liquid is entrained by the web exactly balances the rate at which liquid is delivered to the coater, making it possible to use satisfactorily a premetered coating system such as slide coating with a wide range of parameters.

Many years ago Levi, Cvetkov and Babcin (1966) investigated slide coating in the limiting case where capillary forces dominate over both viscous and inertial effects. They came to the conclusion that the determining phenomenon was the change in the mean radius of curvature R_m of the upper free surface. Hens and Boiy (1986) investigated the inertia-dominated regime and found that the contact length of the boundary layer was the determining parameter.

In the remainder of this section the geometrical adaptivity of the bead is discussed further. The flow in the bead is entirely two-dimensional (if satisfactory, otherwise it can be three-dimensional and/or unsteady – see below). It can be calculated numerically by means of finite element techniques as shown by a number of investigators (e.g., Beck and Muës (1988); Christodoulou and Scriven (1989); Schunk (1989); Chen (1992); see also Chapter 9).

However, here we want to emphasize the physics involved by using an analytical approach; unfortunately, an accurate quantitative analysis of this kind has not been published to this day. Therefore, we shall follow the, inevitably approximate, qualitative approach as proposed by Hens and Van Abbenen (1994): they estimated the different forces acting upon the coating bead, and developed an expression showing the order of magnitude of the dimension of the bead and the qualitative effect of different coating parameters on it; assuming that this dimension can vary between a lower and an upper bound, the approximate expression suggests how some of the limits of the operability range of a slide coater may be estimated.

This analysis is approximate, because some terms are only roughly estimated, and others are

neglected. In part these simplifications are physically clear or intuitively reasonable; others rely on results of flow visualization or numerical flow calculations; and some are only justified *a posteriori* because the results seem to correlate qualitatively with practical coating experience.

11b.3.1 VERTICAL MOMENTUM BALANCE – FORCES AT WORK

The liquid delivered to the bead is accelerated by the viscous action of the moving web, as described in classical boundary layer theory (Sakiadis 1961). Hens and Boiy (1986) found a good correlation between Sakiadis' boundary layer length L_s and the height L_b of the slide coating bead when inertia dominates. Here we shall also consider, or at least mention, capillary effects, gravity, pressure difference over the bead, electrostatic forces, incoming momentum, and effects of the air entrained by the web.

A given control volume (abcdefg) is defined (Fig. 11b.4) which corresponds to the bead region. It is bounded by the two free surfaces (bc) and (fg), the moving web (ab), the slide surface (de), an entrance section (ef) somewhere under the trough of the standing wave near the end of the incline, at a distance L_{de} from the edge (d) (how the point (e) is chosen will be explained later), and an exit section (ag) located where the mean velocity of the entrained liquid has reached 90% of the web speed U ; the layer thickness at this position is $H_\infty/0.9$, H_∞ denoting the final wet layer thickness. The distance between the exit section (ag) and the dynamic wetting line (b) we call the bead height L_b . For the sake of simplicity, we assume a vertically moving web, a vertical die lip face (cd), a Newtonian liquid with constant surface tension σ and the lower free surface located at (c) (at a small distance L_{cd} from the edge (d), with an apparent static contact angle θ_0 and an apparent dynamic contact angle θ_D as defined in Fig. 11b.4.

The rate of change of momentum in this control volume is brought about by the sum of all the external forces (both bulk and surface forces) acting upon the liquid. The horizontal

component of momentum plays a role in the wetting process, but is not considered here. The vertical component controls the entrainment of the liquid by the web. With velocities, momentum and forces taken to be positive in the upward direction, and with U_s denoting the mean velocity of the flow far upstream on the slide and ΔP the pressure difference over the bead, the terms of this vertical momentum balance (per unit width) can be estimated as follows.

Momentum leaving (ag) by convection

$$M_{\text{out}} \approx 0.9 \rho U^2 H_\infty \quad (11b.2)$$

Momentum entering (ef) by convection

The developed flow far upstream at the slide carries a momentum of

$$M_s = -(6/5) \sin(\beta) \rho (U_s)^2 H_s \quad (11b.3)$$

At the entrance section, chosen under the trough of the standing wave, the liquid is accelerated (by the pressure gradient caused by the curved meniscus, see also further) from U_s to a value usually not more than U , and consequently the film thickness is smaller than H_s , but not smaller than H_∞ . Hence we may estimate:

$$M_{\text{in}} \geq -(6/5) \sin(\beta) \rho U^2 H_\infty \quad (11b.4)$$

Drag force of the web (ab)

Sakiadis (1961) calculated the total viscous friction force over the boundary layer:

$$F_{v,sak} \approx 1.44 \mu U L_\delta / H_\infty \quad (11b.5)$$

Here, however, we not only consider the boundary layer length L_δ , but the bead height L_b , which also includes the zone in which the boundary layer reorganizes towards a plug flow. In this reorganization zone the viscous effect is less than in the zone where the boundary layer forms. Therefore it seems reasonable to estimate:

$$F_{v,w} \approx \mu U L_b / H_\infty \quad (11b.6)$$

Drag force of the die lip (cd)

$$F_{v,1} \approx \mu (\partial U / \partial x) L_{cd} \quad (11b.7)$$

Drag force of the slide (de)

$$F_{v,s} = \mu (\partial U / \partial y) L_{de} \quad (11b.8)$$

Drag force of the air (bc)

$$F_{v,a} \approx \mu_{\text{air}} (\partial U_{\text{air}} / \partial x) H_G \cot g(\theta_D) \quad (11b.9)$$

Dynamic pressure of air, entrained by the web, at (bc)

$$F_{p,a} \leq \rho_{\text{air}} U^2 H_G \quad (11b.10)$$

Surface tension at (g)

$$F_{\sigma,g} = \sigma \quad (11b.11)$$

Surface tension at (f)

We may choose the inflow section (ef) of our control in such a way that the free surface at the point (f) makes an angle $(-\beta)$ with the horizontal plane. The choice may seem arbitrary, but by doing so, the net effect of capillarity on the upstream part of the flow (on the incline) is vertically upward; it causes a decrease in pressure under the trough of the standing wave, and accelerates the flow; this effect has been taken into account by the momentum at the inflow section in equation (11b.4). The surface tension effect on the control volume in (f) then becomes:

$$F_{\sigma,f} = -\sin(\beta) \sigma \quad (11b.12)$$

Surface tension at (b)

$$F_{\sigma,b} = -\cos(\theta_D) \sigma \quad (11b.13)$$

Surface tension at (c)

$$F_{\sigma,c} = -\cos(\theta_0) \sigma \quad (11b.14)$$

Pressure difference over the bead

$$F_{\Delta P} = -H_G \Delta P \quad (11b.15)$$

Gravity

The weight of (unsupported) liquid can be estimated roughly as:

$$F_g \approx -\rho g L_b (H_\infty + H_G)/2 \quad (11b.16)$$

Reactive force of the die

$$F_D \sim L_{de} \cos(\beta) \quad (11b.17)$$

Electrostatic force F_{es}

This force is hard to quantify, but it is retained here in order to show its influence qualitatively.

11b.3.1.1 Approximations – simplifications

It is reasonable to suppose that the reactive force of the die F_D and its viscous force $F_{v,s}$ approximately balance out that part of the gravitational force F_g that is proportional to slide length (and that was not mentioned in equation (11b.16)). The dynamic pressure of the air $F_{p,a}$ can be neglected, because ρ_{air}/ρ_{liquid} is of the order of 10^{-3} . Furthermore, the capillary forces at the lower free surface $F_{\sigma,b}$ and $F_{\sigma,c}$ approximately cancel each other if the lower meniscus is not too strongly curved, a situation often encountered in practice (Faust 1975). We further neglect the viscous action $F_{v,l}$ of the die lip because L_{ed}/L_b has been assumed to be small. Hence $(\partial U/\partial x)$ is small because the flow rate downwards in the gap between the web and the die lip is small. This assumption is consistent with flow visualization and laser-Doppler measurements of satisfactory steady state flows. In the next sections, however, we shall also encounter cases where this simplification probably is not fully valid anymore; so caution is needed here. Furthermore, the viscous action $F_{v,a}$ of the air acting on the lower free surface is also neglected. This is certainly permissible as long as $\cot g(\theta_D)$ remains bounded, i.e. if $\theta_D <$ e.g. 160° , a situation commonly

met in satisfactory steady state slide coating. However, this restriction also implies that the limiting case where θ_D approaches 180° cannot be addressed (see Section 11b.4.1).

Finally, $\sin(\beta)$ is typically of the order of 0.5. Thus $M_{out} - M_{in}$ becomes:

$$M_{out} - M_{in} \approx 1.5\rho U^2 H_\infty \quad (11b.18)$$

With equations 11b.5 through 11b.18, the momentum balance then becomes:

$$\begin{aligned} 1.5\rho U^2 H_\infty &\approx \mu U L_b / H_\infty + 0.5\sigma - H_G \Delta P \\ &\quad - \rho g L_b (H_\infty + H_G)/2 - F_{es} \end{aligned} \quad (11b.19)$$

11b.3.2 THE BEAD HEIGHT L_b

From the approximate momentum balance (11b.19) we can derive an expression for the (dimensionless) bead height L_b/H_∞ :

$$\frac{L_b}{H_\infty} \approx \frac{1.5\rho U^2 H_\infty - 0.5\sigma + H_G \Delta P + F_{es}}{\mu U - \rho g H_\infty (H_G + H_\infty)/2} \quad (11b.20)$$

or

$$\frac{L_b}{H_\infty} = \frac{\left(\begin{array}{l} \text{inertia} - \text{capillary forces} \\ + \text{vacuum forces} \\ + \text{electrostatic forces} \end{array} \right)}{\text{viscous forces} - \text{gravity}} \quad (11b.21)$$

We can write (11b.20) in terms of dimensionless numbers as follows:

$$\frac{L_b}{H_\infty} \approx \frac{1.5 We - 0.5 + N_{\Delta P} + N_{es}}{Ca(1 - St^*)} \quad (11b.22)$$

where

$$We = \rho U^2 H_\infty / \sigma \quad (\text{Weber number}) \quad (11b.23)$$

$$N_{\Delta P} = H_G \Delta P / \sigma \quad (\text{dimensionless pressure number}) \quad (11b.24)$$

$$N_{es} = F_{es} / \sigma \quad (\text{dimensionless electrostatic force}) \quad (11b.25)$$

$$Ca = \mu U / \sigma \quad (\text{capillary number}) \quad (11b.26)$$

$$St^* = St(H_G + H_\infty)/2H_\infty \quad (\text{modified Stokes number}) \quad (11b.27)$$

$$St = \rho g H_\infty^2 / \mu U \quad (\text{Stokes number}) \quad (11b.28)$$

It is interesting to consider the limiting case studied by Hens and Boij (1986), for a Weber number that is very large ($We \gg 1$), indicating that capillary forces are small compared with inertial effects. In most cases St^* is much smaller than unity, and may be neglected. Further, assuming a case without pressure difference and electrostatic forces ($N_{\Delta P} = N_{es} = 0$), equation (11b.22) reduces to

$$L_b/H_\infty \approx 1.5 Re \quad (11b.29)$$

where

$$Re = We/Ca = \rho U H_\infty / \mu \quad (\text{Reynolds number}) \quad (11b.30)$$

and hence

$$H_\infty = 0.82(\mu L_b / \rho U)^{1/2} \quad (11b.31)$$

It should be no surprise that this relationship is close to the one given by Sakiadis (1961) using boundary layer theory, except that we find a coefficient of 0.82 instead of 1.616; this is because we deliberately defined our bead height longer than the boundary layer length, and because we took the incoming momentum into account. Hens and Boij found a coefficient of about 1.28.

In the following sections we shall study the cases in which, according to expression (11b.22), the bead height L_b tends to zero and to infinity, because intuitively it is clear that in practice there must be limits to L_b , and hence both very small and very large values of L_b are likely to set operability limits.

11b.3.3 SMALL VALUES OF L_b

It is clear that the previous analysis is meaningless when L_b becomes negative or zero. Let us assume therefore that satisfactory coating requires a

value of L_b above a lower critical value $L_{b,\min}$:

$$L_b > L_{b,\min} \quad (11b.32)$$

Neglecting gravity and electrostatic effects, we can rewrite (11b.22) as

$$L_b/H_\infty \approx (1.5 We + N_{\Delta P} - 0.5)/Ca \quad (11b.33)$$

With assumption (11b.32) this becomes:

$$1.5 Re + (N_{\Delta P} - 0.5)/Ca > L_{b,\min}/H_\infty \quad (11b.34)$$

or otherwise, from (11b.32) and (11b.20)

$$(1.5 \rho U^2 H_\infty^2 + (H_G \Delta P - 0.5 \sigma) H_\infty) / \mu U > L_{b,\min} \quad (11b.35)$$

Expression (11b.34) suggests that a minimum flowrate is needed for slide coating to be feasible.

An experimental study by Gutoff and Kendrick (1987) clearly shows the existence of such a ‘low flow limit of coatability’. This is the minimum layer thickness $H_{\infty,\min}$ that can be coated at a given speed. Eventually, at very small H_∞ values the bead becomes unstable and breaks up. This break-up is similar to the collapse of a liquid curtain at small We numbers (Brown 1961). Often this phenomenon starts at the edges; it may or may not stabilize: sometimes the bead completely collapses, but often a new stable but undesired flow can persist, with very thick edges due to necking-in, or reorganized into ‘rivulets’ (a steady regular pattern of wet ‘ropes’, separated by completely dry paths). The study of Gutoff and Kendrick (1987) shows that at higher viscosities the minimum layer thickness increases (Fig. 11b.5) and presents regression formulae for the experimentally determined limits.

The qualitative agreement between the low flow limit as described by Gutoff and Kendrick (1987) and inequality (11b.35) is illustrated in Fig. 11b.6, by plotting the ratio of the actual coating thickness H_∞ over the minimum thickness $H_{\infty,\min}$ as found experimentally by Gutoff and Kendrick (1987) versus the bead height L_b for a number of cases, described in Table 11b.1. The apparent correlation suggests that the lower coatability limit may correspond to small values of L_b . Expression (11b.35) then indicates how

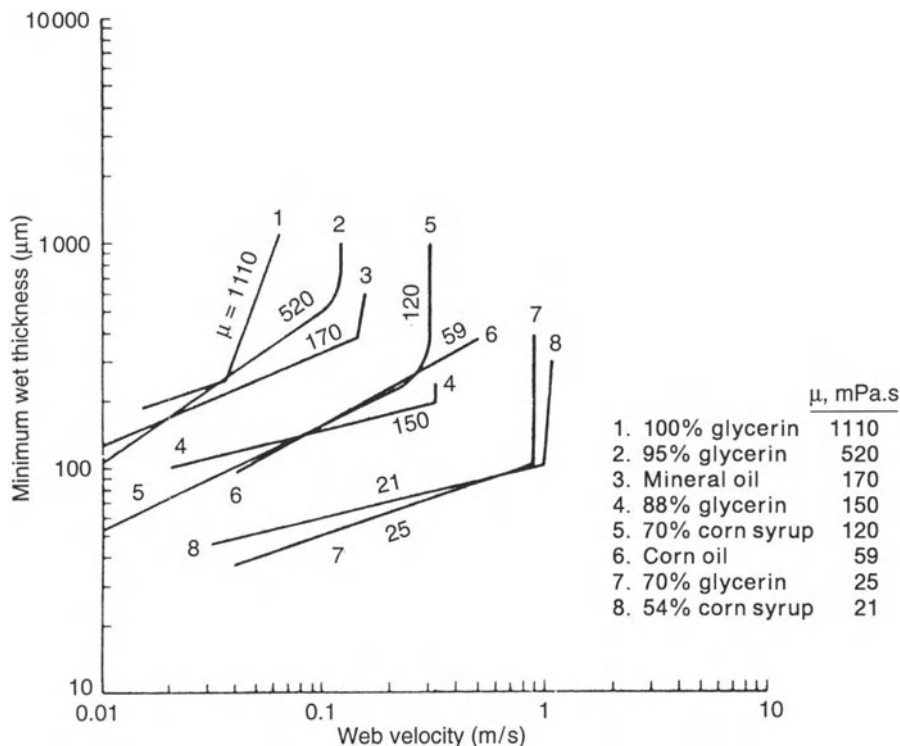


Figure 11b.5 Minimum wet thickness vs. web velocity for slide coating various Newtonian liquids – 500 Pa bead vacuum. From: ‘Low flow limits of coatability on a slide coater.’ E.B. Gutoff and C.E. Kendrick (1987) *AIChE J.* 33 (1): 141–145. (Reproduced by permission of the American Institute of Chemical Engineers © 1987 AIChE.)

this operability limit might be overcome by increasing the coating thickness H_∞ and/or decreasing the viscosity μ and the surface tension σ . Also the positive effect of a pressure difference on the bead may be observed.

Interestingly, a consequence of assumption (11b.35) is that $H_{\infty,\min}$ does not vary monotonically with the coating speed U . Indeed, if we rewrite (11b.32) with (11b.20) and then solve for H_∞ , we find the following relationships:

$$\text{at small } Re: H_{\infty,\min} \sim \mu U \quad (11b.36)$$

$$\text{at large } Re: H_{\infty,\min} \sim (\mu/U)^{1/2} \quad (11b.37)$$

At very low speed, $H_{\infty,\min}$ is found to be proportional to (μU) . At very high speed, however,

$H_{\infty,\min}$ varies with $(\mu/U)^{1/2}$: i.e., at low speed one has to coat more thickly in order to coat faster, whereas at high speed the minimum layer thickness decreases with increasing webspeed. This behavior was observed by Gutoff and Kendrick (1987), but only in the case of a polymeric liquid. With Newtonian liquids one cannot reach high enough coating speeds to detect this phenomenon, because of another defect (air entrainment, see Section 11b.4.1).

11b.3.4 LARGE VALUES OF L_b

In the last section we looked for a coatability limit due to a bead becoming too small. Analogously, we may suppose that for a satisfactory

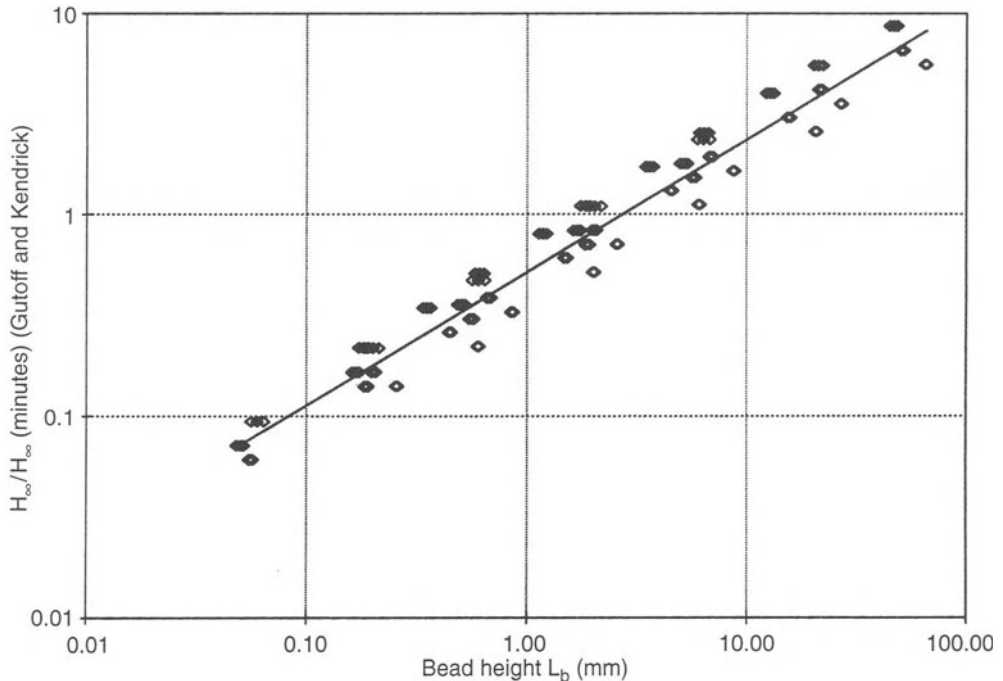


Figure 11b.6 Correlation between the bead height L_b calculated with (11b.20) and the ratio of layer thickness H_∞ over the minimum wet layer thickness $H_{\infty,\min}$ as found by Gutoff and Kendrick (1987) at 500 Pa bead vacuum.

coating a bead cannot be infinitely large either. Let us therefore assume that there is an upper critical value $L_{b,\max}$ in satisfactory slide coating:

$$L_b < L_{b,\max} \quad (11b.38)$$

Large values of L_b can, according to equation (11b.22), arise in three ways:

- (1) for $We \gg 1$ and $Ca \ll 1$, i.e. for $Re \gg 1$;
- (2) with very large values of $N_{\Delta P}$ and/or N_{es} , or
- (3) with $(1 - St^*)$ close to zero.

In the remainder of this section we shall treat these three cases in turn. For simplicity we neglect electrostatic forces, i.e. $N_{es} = 0$. For both cases (1) and (2) gravity can be neglected. Using (11b.33) assumption (11b.38) then becomes:

$$1.5 Re + (N_{\Delta P} - 0.5)/Ca < L_{b,\max}/H_\infty \quad (11b.39)$$

or otherwise, from (11b.38) and (11b.20)

$$(1.5 \rho U^2 H_\infty^2 + (H_G \Delta P - 0.5 \sigma) H_\infty)/\mu U < L_{b,\max} \quad (11b.40)$$

Expression (11b.39) suggests that for satisfactory slide coating there is a maximum Reynolds number for any given capillary number, or equivalently, that there is a minimum capillary number for any given Reynolds number. There is also an effect of the gap and the pressure difference over the bead, with the pressure force apparently reducing the useful parameter range.

We suggest that the defect arising at this supposed limit may be vortex formation. Indeed, flow visualizations (Schweizer 1988; Chen 1992) and finite element calculations (Christodoulou and Scriven 1989; Chen 1992) show that in certain coating conditions vortices may develop in the bead, as illustrated in Fig. 11b.7. As stated

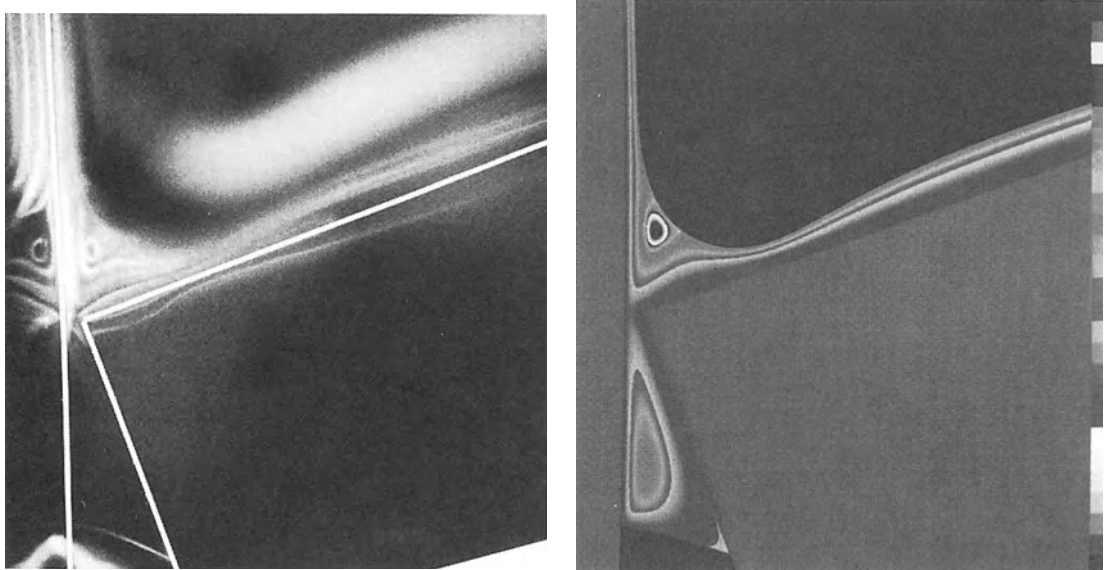


Figure 11b.7 Vortices in the bead of a two-layer slide coating. Left: visualized flow field; right: computed flow field. Parameter values: webspeed $U = 0.25 \text{ m/s}$; gapwidth $H_G = 250 \mu\text{m}$; vacuum $\Delta P = 257 \text{ Pa}$; slide inclination $\beta = 20^\circ$. Bottom layer: thickness $H_{\infty,B} = 90 \mu\text{m}$; viscosity $\mu_B = 15 \text{ mPa s}$; surface tension $\sigma_B = 69 \text{ mN/m}$; density $\rho_B = 1170 \text{ kg/m}^3$. Top layer: thickness $H_{\infty,T} = 91 \mu\text{m}$; viscosity $\mu_T = 15 \text{ mPa s}$; surface tension $\sigma_T = 69 \text{ mN/m}$; density $\rho_T = 1170 \text{ kg/m}^3$. From K. S. A. Chen: Studies of multilayer slide coating and related processes; PhD thesis, University of Minnesota (1992); available from University Microfilms International, Ann Arbor, MI 48106 USA.

above (see Section 11b.2.2) vortices are undesirable because they are neither steady nor two-dimensional and because particles and bubbles may get trapped, causing defects such as, e.g. streaklines (see Section 11b.6.1). In the next sections we shall discuss these vortices, and show some correlation with the bead height L_b .

11b.3.4.1 Case 1: Upper vortex

From his visualization experiments Schweizer (1988) deduced that a vortex near the upper free surface appears when the capillary number is smaller than Ca_{crit} , which is given by the expression:

$$Ca_{\text{crit}} = 0.5406 Po^{0.1441} \exp(0.8434 Re Po^{0.2170}) \quad (11b.41)$$

with Po being the property number, defined by Schweizer as

$$Po = g\mu^4/\rho\sigma^3 = Ca^3 St/Re^2 \quad (11b.42)$$

(It should be noted here that this definition deviates from the one used throughout this book, by the $(-1/3)$ th power). He used a constant slide inclination of 15° and found no significant influence of gap width or pressure difference on the upper vortex.

Chen (1992) deduced from his experiments that vortices occur when the drawdown ratio H_s/H_∞ (which is proportional to $St^{-1/3}$) becomes smaller than some limit, depending upon the capillary number. For small Ca , the maximum value of St decreases with decreasing Ca ; for large Ca , the upper limit of St becomes independent of Ca . It is remarkable that in this work no effect of the Reynolds number was reported, although the

existence of a maximum Reynolds number for the onset of a vortex near the upper free surface was clearly established by Schweizer (1988), see above, and also suggested by Christodoulou and Scriven (1989).

11b.3.4.2 Case 2: Lower vortex

A very large value of $N_{\Delta P}$ (resulting from a high pressure difference and/or a large gap) also leads to a large value of L_b . Intuitively it is clear that in such cases the bead will tend to fill the gap between the web and the die face. Severe wetting of the die will occur, and, apart from a possible crooked static contact line, another vortex may appear between the die lip and the web, as seen in visualizations and numerical calculations (Schweizer 1988; Chen 1992).

To the authors' knowledge no systematic study has been published about the vortex in the

lower part of the meniscus. Chen (1992) derived from his experiments a correlation between the Ca number and the critical pressure difference for die face wetting, but his expression does not include the gap width, although this parameter obviously plays an important role.

Correlations, comments and conclusion on vortices in the bead zone

In Fig. 11b.8 we plotted the ratio of the actual capillary number over the critical value Ca_{crit} (equation (11b.41)) versus the calculated bead height L_b , for the cases defined in Table 11b.1. The apparent correlation that is illustrated in this figure, and the qualitative agreement between expressions (11b.38 to 11b.40) and the published evidence on vortices makes the proposition tenable that in practice vortices are likely to occur when the bead height L_b exceeds some critical value.

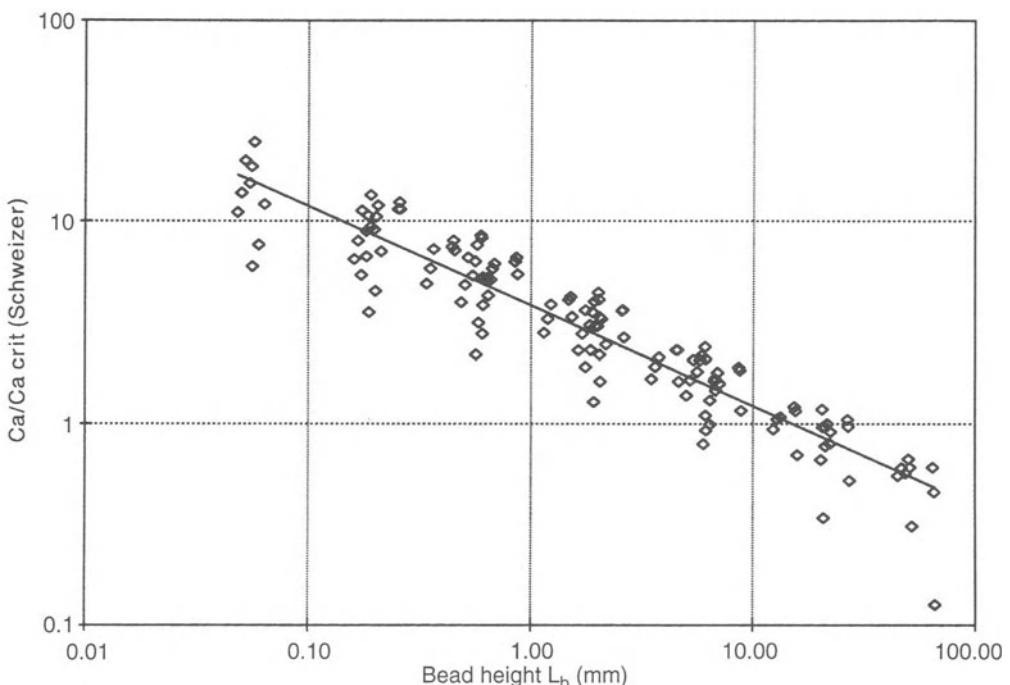


Figure 11b.8 Correlation between the bead height L_b calculated with (11b.20) and the ratio of the capillary number over the critical capillary number Ca_{crit} for the onset of an upper vortex, as found by Schweizer (1988).

Table 11b.1

Inclination angle, β (degrees)	30
Gap width, H_G (μm)	350
Pressure difference, ΔP (Pa)	500
Layer thickness, H_∞ (μm)	30–70–110
Viscosity, μ (mPa s)	1–3–10–30–100
Web speed, U (m/s)	1–2–3
Surface tension, σ (mN/m)	15–40–65

This is illustrated in Fig. 11b.9. Starting with a base case without vortices (Fig. 11b.9a) the value L_b is increased by varying U , H_∞ , μ , H_G and ΔP respectively, as specified in Table 11b.2. In each of these cases a vortex is observed.

Criterion (11b.38) seems to cover not only the vortex at the upper free surface, as predicted by Schweizer's correlation, but also the vortex formed between the die face and the web in the case of a large gap width or pressure difference. Expression (11b.40) indicates how this operability limit may be overcome by decreasing the coating thickness H_∞ , the gap width H_G and the pressure difference ΔP and/or increasing the web speed U , the viscosity μ and the surface tension σ .

Figure 11b.9 also illustrates that at least four types of vortices are possible, probably caused by different physical mechanisms.

An upper vortex (as in Fig. 11b.9b, 9c, 9d and 9e and in Fig. 11b.7) will appear when the liquid at the free surface decelerates towards a stagnation point and the flow reverses. Schweizer (1988)

argued that this occurs when the amount of liquid entrained by the viscous boundary layer equals the flow rate supplied from the slide before the boundary layer reaches the free surface. Beyond that point, the web will entrain more liquid, but this has to flow down again near the upper free surface in order to maintain the flow rate balance.

A lower vortex (as in Fig. 11b.9e and 9f and in Fig. 11b.7) forms when the gap between the web and the die lip is filled with liquid and the amount of liquid entrained by the viscous action of the web is smaller than that allowed by regular Couette–Poiseuille flow, resulting in a vortex that partially fills up the gap width. Such vortices are well known in slot coating (see Chapter 11a). It is intuitively clear that this will be the case when both L_b and the gap width H_G are large.

Vortices may also appear underneath the standing wave at the end of the slide (as weakly visible in Fig. 11b.9c). According to Schweizer (1988) this is due to the large adverse pressure gradient caused by the impingement on the web of the liquid arriving from the slide. Such vortices appear at high Weber numbers.

Finally, a weak vortex may form near a static contact line when the die lip is wetted (as noticeable in Figs 9d, 9e and 9f). This is a well known feature of flow in a sharp corner, as analyzed by Moffat (1964).

The mechanisms causing vortices have been elucidated more in general by Goenaga and Higgins (1992).

Table 11b.2

Figure	U (m/s)	H_∞ (μm)	μ (mPa s)	H_G (μm)	ΔP (Pa)	L_b (mm)	Ca/Ca_{crit}
9a	0.6	100	8	200	200	1.6	1.31
9b	0.2	100	8	200	200	1.8	0.53
9c	0.6	275	8	200	200	11.1	0.79
9d	0.6	100	5	200	200	2.6	1.05
9e	0.6	100	8	500	200	3.0	1.31
9f	0.6	100	8	200	500	2.9	1.31

Constant: Inclination angle β : 30°

Surface tension σ : 40 mN/m

Density: 1000 kg/m³.

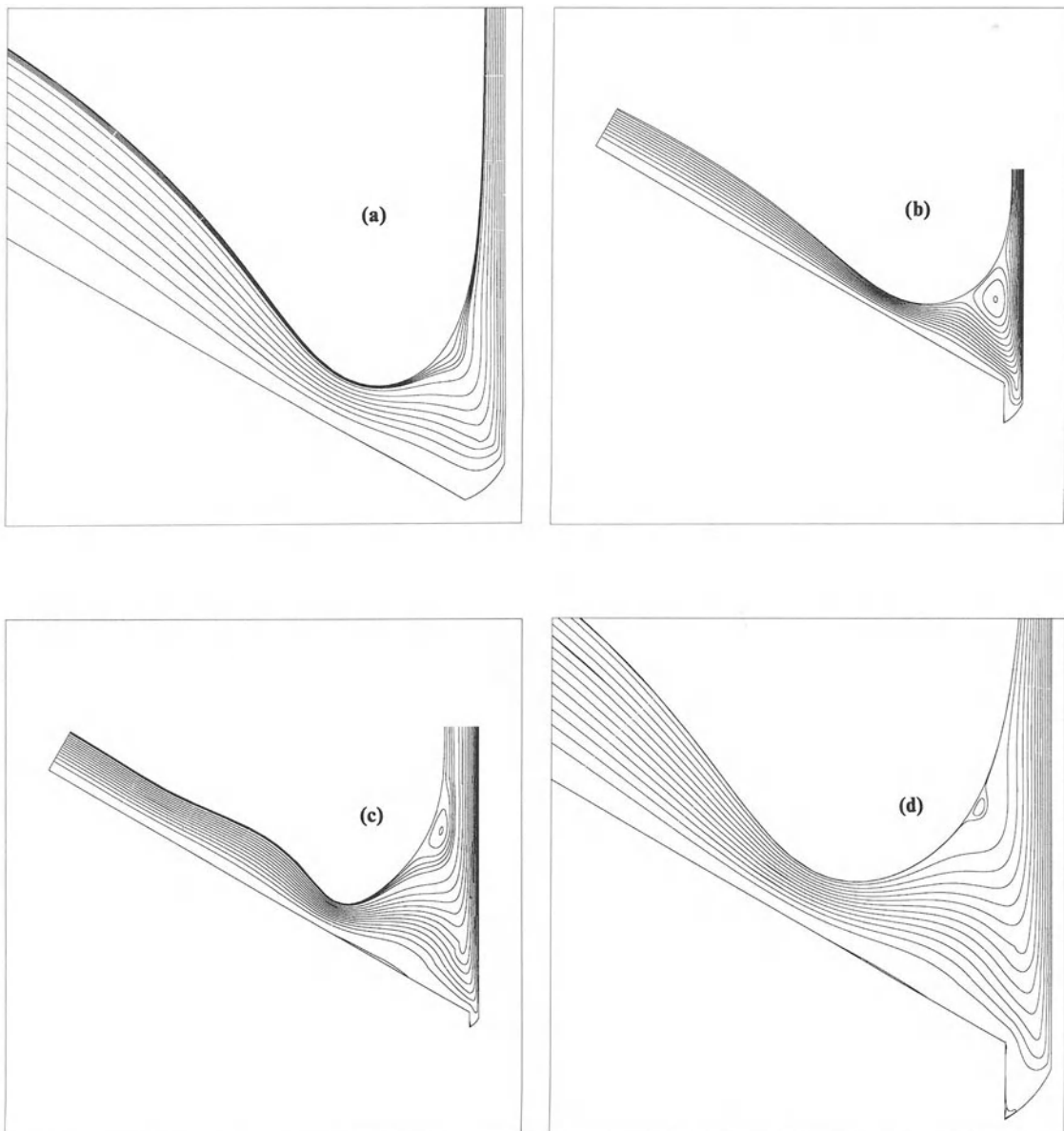


Figure 11b.9 Flow field (calculated by B. Goetmaeckers) for the parameter sets given in Table 11b.1. (a) is the base case, without vortices. (b)–(f) all have an increased bead height as compared with the base case, due to the change in one parameter; they all suffer from vortices.

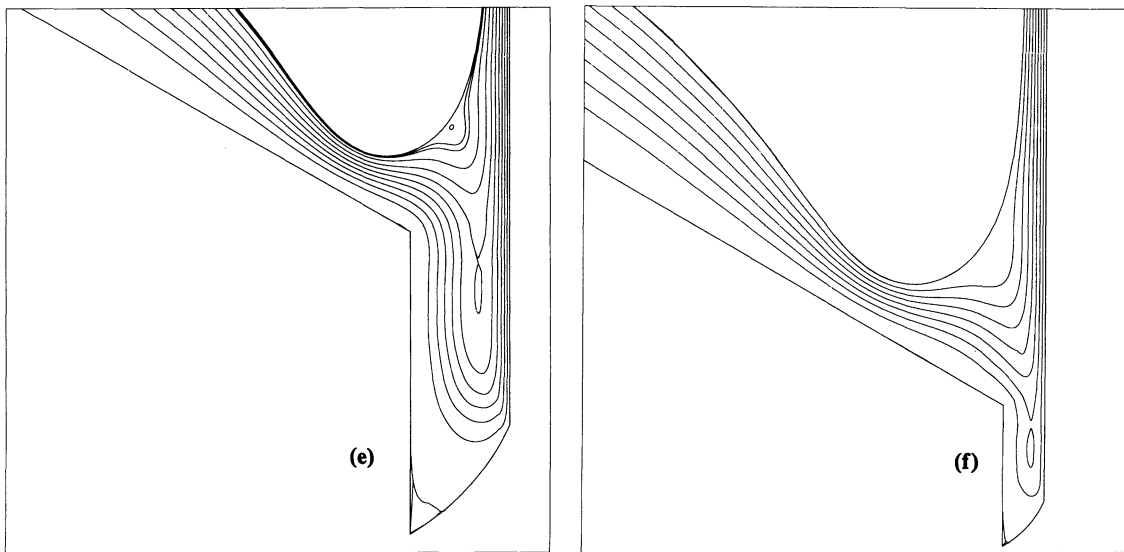


Figure 11b.9 *Continued.*

11b.3.4.3 Case 3: Bleeding

It is worth commenting, that formula (11b.22) allows L_b to become infinite, when the denominator of the expression tends to zero, i.e. when St^* approaches unity. Such a high value of St^* is, however, only reached with parameter settings seldom met in industrial coating practice. St^* is usually of the order of 10^{-2} or less. From (11b.24) and (11b.25) it can be immediately deduced that this limit will occur only when coating a very thick, very low viscosity layer at very low speed using a large gap.

Under such conditions it is physically impossible for the web to entrain all the liquid delivered by the slide. In coating experiments ‘bleeding’ (also known as ‘pull through’ or ‘weeping’) occurs: part of the liquid is not entrained by the web, but leaks into the vacuum box, or flows out of the bead at the edges. This results in a deposited layer that is much thinner than expected, far from uniform and of ill-defined thickness.

Again there is a qualitative correlation between an operability limit of slide coating and expressions (11b.22) and (11b.38). Not apparent from these

expressions, but intuitively obvious, is that ‘bleeding’ also occurs when the die lip is either very short or is sharply cut away.

11b.3.5 CONCLUSIONS ON THE BEAD HEIGHT – APPLICABILITY

In the previous sections qualitative correlations were noted between the vertical momentum balance and some operability limits of slide coating. We proposed that the lower coatability limit might be related to small values of the bead height L_b and that vortices are likely to occur when L_b is larger than some higher critical value. ‘Bleeding’ also appears to be observed at high values of L_b .

We therefore conclude that the bead height L_b is an important feature in slide coating, and that, in order to achieve a satisfactory coating, it should remain between some maximum and some minimum value: too large beads suffer from vortices or bleeding, too small beads become unstable and will break up.

In practice, the layer thickness H_∞ and the viscosity μ have the largest influence on L_b (see

(11b.20)). These are the most important parameters to control in slide coating. A liquid with very high viscosity cannot be coated very thinly because of bead break-up and an extremely low viscosity will give rise to vortices or ‘bleeding’ in the case of very large layer thicknesses.

It should be emphasized, however, that equation (11b.22) and the criteria (11b.32) and (11b.38) should not be considered as more than rules of thumb. They merely indicate the parameters that may influence the operation of the slide coater. Any specific flow can be analyzed much more precisely by flow visualization and/or by numerical simulation (as, for example, Fig. 11b.9/Table 11b.2, which also illustrates that values of L_b must be interpreted in a relative way).

11b.3.5.1 Multilayer coating

Relations (11b.1) to (11b.40) were derived for single layer coating. In practice, however, multilayer coating is much more important. When the liquid properties (ρ, μ) do not differ too much, approximate calculations can be performed by using some weighted viscosity as proposed by Chen (1992):

$$\mu^{-1} = \mu_B^{-1} Q_B/Q + \mu_T^{-1} Q_T/Q \quad (11b.43)$$

where

μ_B, μ_T ; Viscosity of the bottom and top layers respectively

Q_B, Q_T ; Flow rate of the bottom and top layers respectively

$$Q = Q_B + Q_T$$

When the differences in liquid characteristics are appreciable, analytical calculations become too crude and confusing and flow visualization and/or numerical calculations are the best approach. It is the authors' experience that the single layer analysis presented above can be useful in planning multilayer experiments and calculations and in interpreting the results. In general, multilayer coating with too large a bead height leads to vortices and with too small a bead height leads to break-up.

11b.3.5.2 Non-Newtonian fluids

Many of the liquids used in practice are not Newtonian. At the high shear rates ($> 10^5 \text{ s}^{-1}$) close to the dynamic wetting line (Muës, Hens and Boij 1989) many polymeric liquids display shear-thinning behavior as shown by Blake, Clarke and Ruschak (1992) for gelatin–water solutions. This makes the viscosity dependent forces more difficult to estimate, but analytical approximations can still be useful. When, however, viscoelasticity is involved, these approximations become useless, because elastic effects have not been taken into account and viscoelasticity effects can be important, as we shall briefly discuss in Section 11b.4.4.

11b.3.5.3 Surfactants

It is common practice to add surfactants to coating liquids (see also Chapters 4 and 11d). As a result tangential forces may develop at the free surfaces due to surface tension gradients caused by the expansion and compression of the free surfaces. Such gradients may not change the overall force balance, but they do influence the exact shape of the free surfaces (Schunk 1989) and may therefore affect the incidence of vortices.

Surfactant effects have not been taken into consideration in the overall force balance approach used in this chapter so we cannot even think of finding a correlation whatsoever in this way. Numerical simulation may be valuable in gaining an insight into their effect, but it is difficult to collect all the experimental data necessary for correct modeling of surfactant behavior. Experiments, including flow visualization, therefore remain indispensable to this day.

11b.4 LIMITS OF OPERABILITY

Our intention in the previous chapter was to elucidate the flow field of a slide coating bead for steady state two-dimensional flow with the liquid satisfactorily wetting the web. The low flow limit, the onset of vortices and

weeping/bleeding were discussed as limitations of satisfactory operation. However, other restrictions to satisfactory operation also exist.

If the air adhering to the arriving web cannot be removed and replaced by the liquid, chaotic two-phase flow results. This phenomenon is known as air entrainment, and although related to the low flow limit discussed in the previous section, it is really a different physical phenomenon. It will be covered in Section 11b.4.1. Coating flows can also rearrange spontaneously into a steady but three-dimensional pattern, known as ribbing (Section 11b.4.2). Finally, they can also oscillate spontaneously, producing a two-dimensional but unsteady (periodic) flow (Section 11b.4.3).

All these limitations together determine the so called operability window, being the range of parameters that permit satisfactory coating, i.e. steady two-dimensional coating without vortices. This is addressed in Section 11b.4.4. Moreover, it is desirable that small external disturbances do not give rise to unacceptably severe coating defects. The required coating quality will, of course, be dependent upon the specifications required by the user. The susceptibility to minor variations in coating conditions and the resulting quality window will be covered in Section 11b.5.

11b.4.1 AIR ENTRAINMENT AND LOW FLOW LIMIT

As mentioned above, wetting of the web, which is common to all coating systems, is one of the main functions of the bead. Wetting process failure delineates one of the operational limits of the slide coater. Plunging tape experiments (see Chapter 3) show that the wetting process fails when the dynamic contact angle θ_D reaches 180° and air entrained by the web is not displaced by the liquid. This occurs at a critical velocity U_{AE} . As the physics of the wetting process is still poorly understood, the critical velocity U_{AE} has been studied experimentally by several investigators (Burley and Kennedy 1976; Gutoff and Kendrick 1982; Bracke, De Voeght and Joos

Table 11b.3

	<i>a</i>	<i>b</i>
Burley and Kennedy (1976)	0.335	0.67
Gutoff and Kendrick (1982)	—	0.67
Bracke, De Voeght and Joos (1989)	1.0	1.0

1989). They all deduced a relationship of the form:

$$U_{AE} \sim \mu^{-b} \sigma^a \quad (11b.44)$$

Table 11b.3 gives the values of *a* and *b* disclosed by the different authors.

A dependency of U_{AE} on the viscosity is clearly established by all the authors. There is, however, no agreement between different investigators concerning the influence of surface tension on U_{AE} . The dependency on surface tension is, however, much less important because the σ -range used in practice is rather small (*ca.* 20 to 72 mN/m). Such a narrow range of σ makes it difficult to determine its dependence precisely, which could explain the lack of agreement between the different investigators (Kistler 1993). The influence of other parameters such as the surface properties of the web have been studied, but their influence is not clearly established.

The air entrainment limit in a slide coater is close to the air entrainment limit in a plunging tape geometry. Gutoff and Kendrick (1987) investigated U_{AE} in slide coating with Newtonian liquids whose viscosities ranged from 21 to 2110 mPa s. At layer thicknesses larger than approximately 100 µm the air-entrainment limits in both geometries are reported to be almost identical, and the limit in slide coating is hardly influenced by the pressure difference ΔP .

When coating thinner layers, however, the bead collapsed at much lower coating velocities (Fig. 11b.5). This phenomenon, known as low flow limit, has already been discussed in Section 11b.3.3. In this case a pressure difference over the bead allows substantially thinner layers to be coated. A possible physical explanation might be that the pressure difference, apart from increasing the bead height as mentioned before,

affects the position of the dynamic wetting line in such a way that more of the momentum of the liquid arriving from the slide becomes available to assist the dynamic wetting. (Schweizer 1993: personal communication). The momentum of the liquid impinging on the web is also significant in curtain coating (see Chapter 11c), where it is much more important than in slide coating (Van Abbenyen, Muës and Goetmaeckers 1992; Blake, Clarke and Ruschak 1992).

Electrostatic forces can also be used to assist the wetting of the web by the liquid and to increase the critical velocity U_{AE} (De Geest and Verkinderen 1967; Nakai and Okada 1968). This can be achieved by giving the substrate a surface charge, or by connecting the backing roll to a high voltage power supply. Feng and Scriven (1992) illustrated these effects by numerical modeling. Unfortunately, the obtaining of a perfectly homogeneous distribution of electrostatic charges appears to be difficult, as illustrated by the large amount of patents claiming improvements (e.g. Nakajima and Miyamoto (1993); Hartman (1989)). It may thus impair coating uniformity, making electrostatic assist unusable whenever high coating quality is required.

In multilayer coating U_{AE} is determined by the local viscosity of the layer that wets the web. The operability limits of slide coating can therefore be significantly widened by introducing an additional layer underneath the other layers. This layer, often called the carrier layer, should be relatively thin and should have a low viscosity, easily wet the web and yield high U_{AE} values (Dittman and Rozzi 1977). In this way liquid layers with high solid contents can be coated at high viscosities and at high speed without air entrainment problems. A low viscous liquid layer underneath can, however, endanger the stability of the multilayer flow on the inclined plane (see Chapter 8 and Section 11b.4.3.1). Therefore, Choinski (1978) recommended the use of a shear-thinning lowermost layer, having a high viscosity at the low shear rate on the inclined plane and a lower viscosity at the very high shear rate near the wetting line (Muës, Hens and Boij 1989). In this way, conflicting requirements for

stable flow on the slide and satisfactory high speed wetting can be met.

11b.4.2 RIBBING – A STEADY THREE-DIMENSIONAL FLOW

In Sections 11b.3 and 11b.4.1 we have already mentioned that the limit of coatability can be extended to thinner and more viscous layers by applying a small pressure difference over the bead (0 to 1000 Pa). However, at sufficiently high pressure differences a steady regular pattern of lengthwise streaklines, known as 'ribbing', is formed. Other names used to describe this defect include 'vacuum streaks', 'corduroy', 'rakelines' and 'phonography'. The wavelength of the ribs is typically a few millimeters. Although it is difficult to detect precisely the onset of ribbing, it is clear that, in practice, a maximum pressure difference limit exists in the operability window beyond which the ribbing pattern becomes unacceptable (Saito, Ishizuka and Fuchigami 1982).

When surfactants are present, extension and compression of the free surfaces causes local changes in the surface concentration (adsorption) of the surfactants. This effect is highly dependent upon the time scale. It is quantified by the surface elasticity, being defined as the derivative of the surface tension with respect to the relative change of the surface. Valentini *et al.* (1991, 1992) have studied the influence of surfactants on the ribbing phenomenon. Their work indicates that surface elasticity suppresses the onset of ribbing.

The influence of other coating parameters is not clearly documented in the literature on slide coating.

The spontaneous appearance of ribbing is not limited to slide coating; it is well known in roll coating, blade coating and other flows with free surfaces (see Chapters 11a and 12a). The flow, expected to be steady and two-dimensional, loses stability to three-dimensional disturbances and cross-web waves or ribs start growing. At some finite amplitude of the ribs the flow regains stability and becomes steady, but remains three-dimensional (Savage 1992).

Numerical simulation can predict whether or not ribbing will occur, as well as the wavelength that is likely to appear at the onset of ribbing. Such calculations were carried out and experimentally verified for roll coating by Coyle, Macosko and Scriven (1990). For slide coating the onset of ribbing was calculated by Christodoulou (1990), but experimental verification is not yet forthcoming.

The wavelength that can be calculated is the one that appears at the onset of ribbing. This wavelength may change as the flow parameters exceed their critical values at the onset of ribbing (Mill and South 1967). The amplitude of the ribs that appear in the steady state flow cannot yet be predicted to this day.

The exact cause of the instability in the case of slide coating is not yet completely clear. A Taylor–Görtler mechanism (basically centrifugal instability) was suggested, but immediately rejected again as unlikely (Schweizer and Scriven 1983). Hens and Boij (1986) contended that a higher pressure difference resulted in a greater adverse pressure gradient in the upper bead region due to capillarity, this in analogy with the adverse pressure gradient hypothesis put forward for the roll coating case (Coyle, Macosko and Scriven 1990). The most recent hypothesis (Christodoulou and Scriven 1989) attributes the 3-D instability to an adverse normal stress gradient in the bead.

Although none of these theories has been confirmed so far, there is evidence supporting the most recent one. Schunk (1989) reviewed the scarce data in the literature on the effect of polymeric additives and concluded that these are mostly destabilizing with respect to ribbing. He also calculated numerically a slide coating flow with extensional thickening fluid, which suggested that the adverse normal stress gradient increases due to the extensional thickening effect. This is not at variance with the hypothesis of Christodoulou and Scriven (1989), but it does not confirm it either: more evidence in support is required.

Special coater geometries with ‘upswept lips’ have been proposed, delivering the liquid from the slide with a velocity component in the direction of the movement of the web and

permitting the use of a higher pressure difference without the occurrence of ribbing (Isayama and Takehara 1980; Choinski 1981). According to the authors’ experience, however, the manufacture of such dies is complicated and they are hard for the operators to handle. Only in very special cases might the benefits balance the drawbacks.

11b.4.3 BARRING – A TWO-DIMENSIONAL BUT UNSTEADY FLOW

Barring (also called chatter, chatter marks or crosslines) is a coating defect caused by a two-dimensional but unsteady flow. Oscillations occur, either spontaneously or excited by external disturbances, resulting in a coated product showing periodic cross-web thickness undulations. Section 11b.5 deals with barring as a result of external disturbances such as mechanical vibrations or pressure difference variations and in Section 11b.6.2 we shall discuss the effect of periodic pointwise disturbances. In the remainder of this section we shall focus on spontaneously unsteady flow.

The instability may originate on the inclined plane, in a non-horizontal web section after coating or in the bead itself. The defect will have a different appearance depending on the location of the instability.

11b.4.3.1 Flow instabilities on the inclined plane

The flow of one or more layers on the inclined plane is prone to instabilities: an infinitesimal perturbation of the free surface profile may grow while traveling downwards. Wave speed and rate of damping or amplification can be calculated from the Orr–Sommerfeld equations, as described in Chapter 8. These equations describe an infinite number of wave modes, most of them fortunately highly damped. Nevertheless with N layers, N leading modes can be associated with the free surface and the interfaces. For each mode there can be a most amplified wavelength, eventually the most amplified wavelength of the dominating (i.e. most amplified) mode, if any, will be visible in the coated product.

Analytical solutions are available for the limiting case of long waves, i.e. with a wavelength much larger than the layer thickness on the slide. Both viscosity and density stratification can be destabilizing, as shown by Kao (1968) and Wang, Seaborg and Lin (1978). The effect of density is less important, however, because the possible jump in density at an interface is very much smaller than the possible jump in viscosity.

Weinstein (1990) extended the calculations to shear-thinning fluids, and showed that the surface mode is governed by some mean value of the viscosity, while for the interface modes the jump of the local viscosities at the interface matters. Weinstein and Kurz (1991) clearly showed that a three-layer case is destabilized by a middle layer that has a lower viscosity or lower density than the adjacent layers.

Smith (1990) elucidated the physical mechanisms that give rise to wave amplification on an inclined plane (see Chapter 8).

The long-wave condition, however, is not always met in slide coating and consequently numerical methods have to be used to solve the problem. Kobayashi (1992) investigated the behavior of multilayer flows down an inclined plane and calculated that an interface mode is always unstable, as soon as the viscosity of the adjacent layers becomes different.

In practice, however, it is perfectly possible to apply a number of layers, stratified in viscosity and density, with a very good coating quality. Consequently, slide flows that are theoretically unstable can be ‘practically stable’: if it takes a very long distance (compared with the length of the slide) for a small wave to grow up to a significant amplitude, the instability will not be reflected in the final product. Kobayashi (1992) therefore defined the growth length L_e as the length required for a perturbation to grow by a factor e . $L_{e,\min}$ is then the growth distance of the most amplified wavelength and an amplification factor A_{\max} relates $L_{e,\min}$ to the length L_s of the inclined plane:

$$A_{\max} = \exp(L_s/L_{e,\min}) \quad (11b.45)$$

Kobayashi (1992) determined empirically that

the coating unevenness became unacceptable beyond a threshold value. In his experiments with photographic material this threshold value A_{\max} was approximately 2000.

Figure 11b.10 shows the dimensionless growth distance $L_{e,\min}/H_{s,\text{bottom}}$ for a two-layer coating as a function of the viscosity ratio $m = \mu_{\text{top}}/\mu_{\text{bottom}}$, as obtained by solving the Orr-Sommerfeld equations numerically (Kobayashi 1992). The two modes, the surface mode with a characteristic wavelength of the order of 10 cm and the interface mode with a typical wavelength of the order of 1 to 10 mm, are represented. When m is close to unity, the surface mode dominates. When $m > 1.4$ or $m < 0.73$ the interface mode is the most dangerous one, the smallest value of $L_{e,\min}$ occurring when the top layer viscosity is substantially lower than the bottom layer viscosity. Generally, an interface mode is more problematical than a surface mode because there is no interfacial tension acting as a damping force (on the assumption that miscible fluids are concerned).

When more than two layers are involved, Kobayashi (1992) recommended viscosities decreasing from top to bottom with the viscosity ratio of adjacent layers as close to unit as possible: smaller than 2, preferably smaller than 1.5. This seems to be logical. When two layers have the same characteristics, they will act as a single layer and interfacial modes will be absent. In practice, however, it is perfectly possible to deviate from this rule of thumb, as illustrated by several publications (Dittmann and Rozzi 1977; Koepke *et al.* 1984), although according to Weinstein and Kurz (1991) one has to avoid a middle layer that has a lower viscosity or a lower density than the adjacent layers.

When dealing with fluids used in practice the situation becomes even more complicated, even for the very simple one-dimensional flow on an inclined plane. Surface elasticity (due to surfactants) for instance brings additional damping (Schunk 1989; Baumlin 1990; Gutoff 1993; see also Chapter 11d). Viscoelasticity is destabilizing at small Reynolds numbers and stabilizing at moderate Reynolds numbers magnifying both magnitude

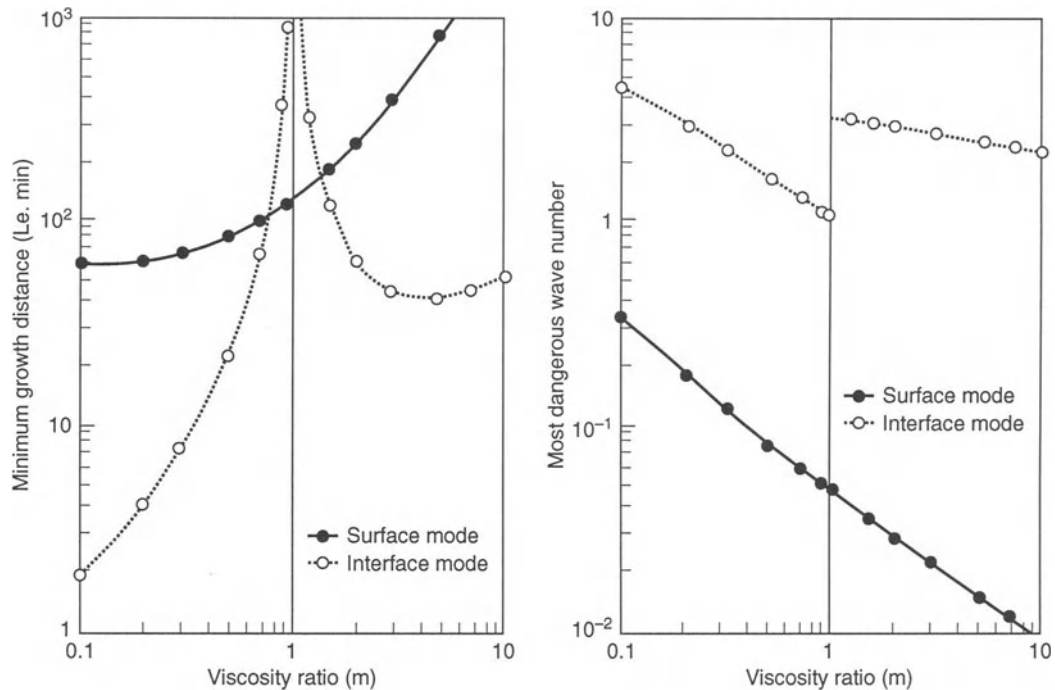


Figure 11b.10 Dimensionless growth length (left) and most dangerous wave number (right) of a two-layer flow on an inclined plane as a function of the viscosity ratio. From: Kobayashi, c. 1992. Stability analysis of film flow on an inclined plane. I. One layer, two layer flow. *Ind.Cat.Res.* 2: 65–88. (Reproduced by permission of the editor.)

and wavespeed of nonlinear waves (Salamon, Armstrong and Brown 1992). Furthermore, Van Abbenyen and Muës (1992) suggested that diffusion might play a destabilizing role by creating a watery layer between two layers of different chemical composition.

We conclude that, despite the study on an inclined plane by many authors, it is still, at least in multilayer coating, incompletely understood. Nevertheless the available theories are helpful and provide a reasonable approximation, some researchers indeed reporting qualitative agreement between experiment and prediction (Baumlin and Pasquet 1988; Kobayashi 1992).

11b.4.3.2 Non-horizontal web section

Flow in a non-horizontal web section after a coating station is similar to flow on an inclined

plane, only with the layer thickness being an order of magnitude smaller (100 µm rather than 1 mm). If the flow is unstable a wavy pattern results with typically a sub-millimeter wavelength. The waves are across the web, but not completely straight. This defect resembles the structure of a beach at low tide and is known as runback or sagging (see Chapter 6).

11b.4.3.3 Bead

In the previous sections we discussed instabilities giving rise to waves on the inclined plane and on the web, both fairly straight zones of the flow. It is also possible that the bead itself oscillates as a whole. The coated web then exhibits waviness with a fairly straight pattern of cross-web ‘bars’ with a wavelength of the order of centimeters.

Whether this oscillation occurs spontaneously or results from external perturbations is often difficult to determine in practice. When the defect occurs at once under manufacturing conditions, it is likely that an external disturbance will be the cause. Katagiri and Scriven (1986), however, predicted the existence of an oscillatory state. Katagiri (1988) experimentally confirmed his predictions and by applying linear stability analysis Christodoulou (1990) illustrated the physics involved (see also Chapter 9). He showed that an oscillatory state is characterized by a pair of complex conjugate eigenvalues with a vanishing real part, the corresponding eigenmode then being a periodic vibration that is neither damped nor amplified. Nearby states, with their leading eigenvalues having a small but negative real part, will be stable but very sensitive to external disturbances (see Section 11b.5).

Fruhner, Krägel and Kretzschmar (1989) showed that the bead is likely to start oscillating when the coated layer thickness H_∞ is small and the viscosity μ is large, i.e. near the low flow limit.

11b.4.4 OPERABILITY WINDOWS

The operability window is the region in the multidimensional parameter space in which a stable, steady, two-dimensional flow is possible. Depending on the requirements of the coated product, parts of the operability window may be unusable due to certain combinations of parameters producing a coating quality, which is too sensitive to external disturbances (see Section 11b.5). The rest of the operability window can be termed the quality window. In this region the flow is steady, stable, two-dimensional, free of vortices and sufficiently unresponsive to external disturbances from the surroundings.

In principle, one could represent the operability limits in a multidimensional space, e.g. in terms of the dimensionless numbers We (or Re), Ca , St^* , $N_{\Delta P}$ and N_{es} , suggested by equation (11b.22). Even when neglecting N_{es} , a four-dimensional space remains. A two-dimensional section representing Ca as a function of Re with St^* and $N_{\Delta P}$ as parameters, would probably look like Fig.

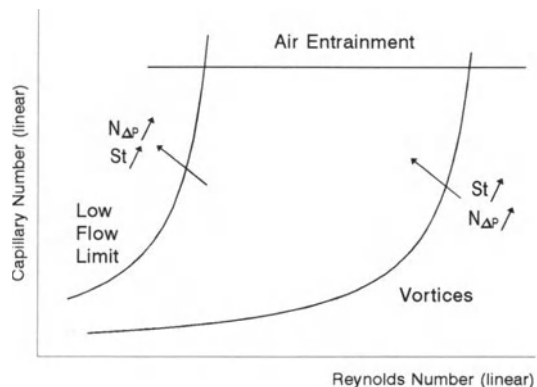


Figure 11b.11 Possible form of an operability window of slide coating in dimensionless representation.

11b.11. In such a diagram Schweizer (1988) represented his upper vortex correlation (11b.41), only using the property number Po (a function of Re , Ca and St , see (11b.42)) as a parameter. To the authors' knowledge, such dimensionless diagrams have not yet been published.

This may be due to the development and practical use of slide coating long before theoretical analyses were published, with practitioners preferring dimensional variables to dimensionless numbers.

The coating parameters include liquid properties such as ρ , σ and μ (or the rheology in general), geometrical parameters such as gap width H_G , application angle α , inclination of the slide β , length of the slide L_s , and process parameters such as web speed U , wet layer thickness H_∞ and pressure difference ΔP .

Most of these parameters cannot be chosen freely. For an existing coating station α , β and L_s are fixed. Possible variation in σ and ρ is very limited and the same is true for the coating gap H_G . Viscosity μ and wet layer thickness H_∞ can usually be varied, but within limits and not independently of each other (because the dry layer thickness is normally fixed, and viscosity depends upon concentration). Because for economical reasons one wants to coat as fast as possible, provided the quality remains acceptable, the degrees of freedom in viscosity and layer thickness are usually used to maximize the

coating speed and quality according to the principles discussed in Sections 11b.3 and 11b.4 so far. Hence only one parameter remains really free: the pressure difference over the bead ΔP .

There are, in practice two types of two-dimensional sections of the operability diagram in use. In the first H_∞ versus U and H_∞ versus μ diagrams are used to illustrate the practical implications of the physics of slide coating. They show the operability limits as described above, with air-entrainment at $U > U_{AE}$, low flow limit of coatability at small H_∞ and large μ , and the occurrence of vortices at very large H_∞ and small μ . Figure 11b.12 is a qualitative example. In practice, it is well known that slide coating is unsuitable for coating very thin layers or highly viscous liquids and certainly not for a combination of both. Equation (11b.35), despite its being a very rough approximation, gives an indication of why this is the case. It is equally well known that thick layers of low viscosity cannot be applied with great uniformity, due to the appearance of vortices, as discussed in Section 11b.3.4 and indicated by equation (11b.40).

In the second, ΔP versus U diagrams are used to determine the coatability range, the maximum and minimum allowable pressure difference with a given set of parameters indicating the proximity to the operating limits of coatability. This type of diagram seems to be very popular in practice, probably because it is also quite easy to obtain experimentally.

An example of what such a ΔP versus U diagram with constant values of H_∞ , μ and H_G might look like is represented in Fig. 11b.13. At high ΔP values, ribbing (see Section 11b.4.2) and bleeding (see Section 11b.3.4) delineate the coating window. In practice it is known that at low ΔP the sensitivity to disturbances increases, setting a limit to the quality window. At even lower ΔP values, the bead edges break loose and the bead will break up (low flow limit), either completely or in rivulet form.

This figure 11b.13 is typical for a gelatine–water coating, but these diagrams may be rather different when working with other fluids. The diagrams given by Chen (1992) were for glycerine, in which

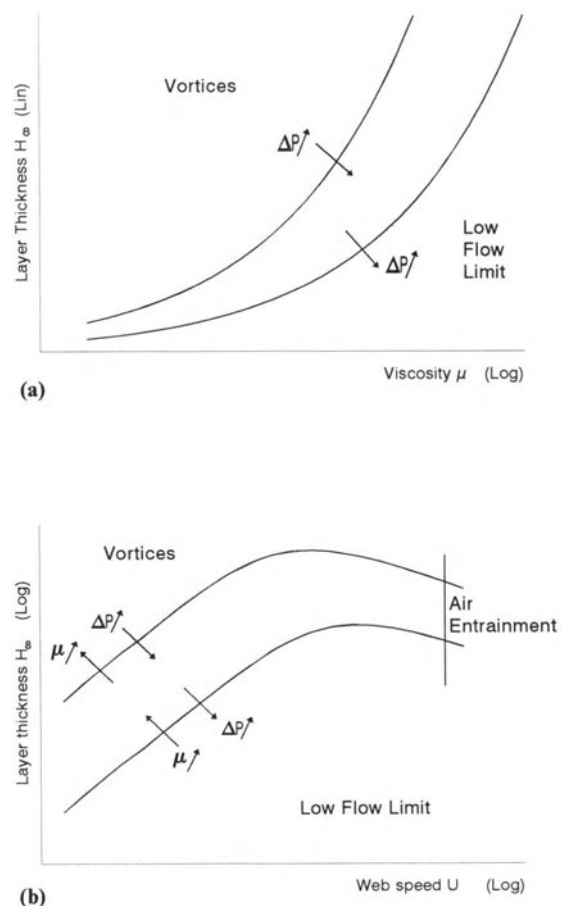


Figure 11b.12 Typical form of two coating windows of slide coating: (a) layer thickness H_∞ versus viscosity μ on a semilogarithmic scale; (b) layer thickness H_∞ versus web speed U on a logarithmic scale.

ribbing is deferred to much higher ΔP values. Gutoff and Kendrick (1987), on the other hand, showed that a polyvinyl alcohol solution can have a much larger ‘low flow limit of coatability’ than a ‘corresponding’ Newtonian liquid. It was also mentioned above that ribbing is promoted by viscoelasticity.

In general we conclude that it is usually wise, if not necessary, to check the operability window experimentally with the coating liquids that will be used in practice, because the rheology of the

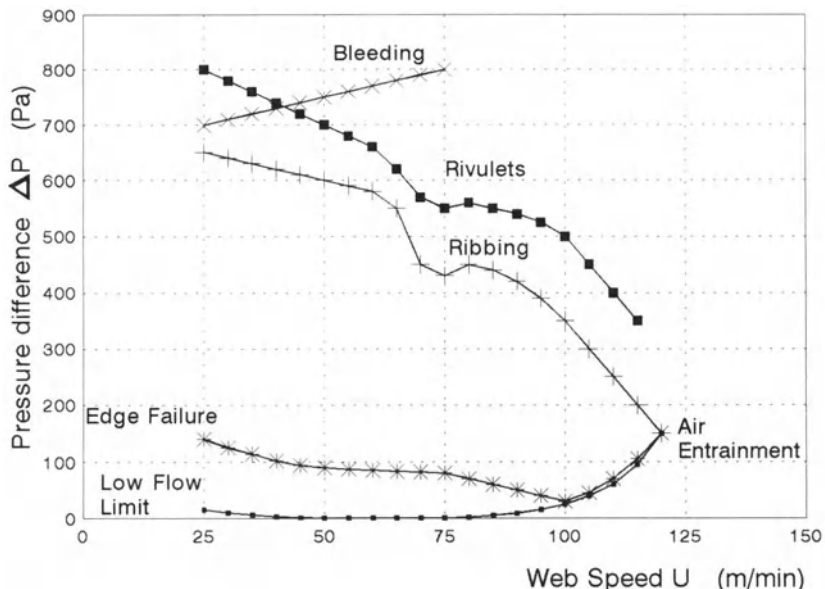


Figure 11b.13 Example of a practical coating window of a slide coater: pressure difference ΔP versus web speed U on a linear scale. Data are from 10% gelatin in water, viscosity 20 mPa s, surface tension 32 mN/m.

fluids used may considerably influence the coating flow.

11b.5 SENSITIVITY TO DISTURBANCES

It is obvious that, in order to be of any importance in practice, a coating flow has to be stable (or practically stable): a small disturbance may cause a defect, but the flow should recover to its original state when the disturbance is over (or the small disturbance may become amplified, but to such a minor extent that the quality of the final product remains within tolerances). Several unstable states cannot even be realized experimentally because any disturbance will eventually cause the bead to break up. Numerically, however, steady states, either stable or unstable, can be calculated. Eigenvalue calculations or transient behavior will reveal the (in)stability of the flow (Katagiri and Scriven 1986; Christodoulou 1990; see also Chapter 9).

In practice, only that part of the operability window can be used, in which small external disturbances, inevitably present in any industrial

process, do not produce a nonuniform product. Whatever the precautions taken, such disturbances cannot be avoided completely, just minimized.

There are many sources of external disturbances. The coating die may oscillate if it is not properly isolated from its environment, in which all kinds of mechanical vibrations can be present. The backing roll may have a certain runout. In both cases the gap width is not perfectly constant, but fluctuates periodically.

Acoustic noise, e.g. originating from the fan generating the pressure difference, is nothing but a periodic disturbance of the pressure difference across the bead, causing forced oscillations of the bead by exciting the lower free surface.

Web speed and flow rates usually are automatically controlled and maintained between very narrow limits, but small periodic fluctuations about the set-point can always occur.

Furthermore, air currents can disturb the flow on the inclined plane and in the bead and the web to be coated is also likely to have small variations in wettability that may influence the coating quality.

The degree of resulting nonuniformity depends upon engineering design parameters such as the mechanical robustness of the coating equipment, the quality of process control (determining the amplitude of the possible disturbances) and the susceptibility of the flow to small perturbations. To obtain the optimal coating quality in a given coating facility, one should choose the parameters of the flow in such a way that susceptibility to disturbances is minimized.

Several investigators have established that the flow in slide coating becomes extremely sensitive to disturbances near the low flow limit (Hackler *et al.* 1992; Fruhner, Krägel and Kretzschmar 1989). Indeed, at small L_b values, the liquid mass in the bead is relatively small, which may intuitively result in a greater susceptibility to disturbances such as vibrations of the die or the backing roll, variations in vacuum, unevenness of the web, fluctuations in the premetered flow rate, etc.

Neither theoretical analysis nor experimental study of the dynamic behavior of a flow is easy. Weinstein, Baumlin and Servant (1993) recently studied the effect of external perturbations on the flow on an (oscillating) inclined plane and showed both theoretically and experimentally that the entrance region is responsible for exciting the various wave frequencies which are observed downstream.

The dynamic behavior of a coating flow as a whole is even more complicated. There are several eigenfrequencies and the response to perturbations cannot be predicted without numerical calculations. Such calculations were first made by Katagiri and Scriven (1986) and later more efficiently by Van Abbenyen, Christodoulou and Scriven (1988), assuming that the disturbances were small enough for the response to remain linear, an assumption that was found to hold quite well for disturbances of web speed and pressure difference with amplitudes of up to 10%, as shown by comparison with nonlinear time-dependent calculations. Hackler *et al.* (1992) extended this type of calculation to three-dimensional periodic disturbances.

Van Abbenyen, Christodoulou and Scriven (1988) showed that the frequency response of a

multilayer slide flow (i.e. the transfer function between the periodic disturbance of some external parameter (e.g., flow rate) and the resulting variation in some flow characteristics (mostly the layer thickness at the exit of the bead) as a function of frequency) is strongly dependent upon the type of perturbation (Fig. 11b.14). In the two-layer slide-coating flow they modeled, web speed variations caused defects at low frequencies with a resonance peak at about 20 Hz, the flow field indicating that this resonance mode was associated with the upper free surface. Horizontal vibrations of the backing roll on the other hand were found to be particularly dangerous at very high frequencies, because the lower free surface seemed to show a resonance mode at several hundred hertz. They also found evidence of so-called 'exchange modes': the reflection, at certain distinct frequencies, of perturbations in the flow rate of one layer in thickness variations of another layer.

In our own experience, the shape of such calculated frequency responses is rather typical: amplitudes may change significantly and the peak frequencies may shift a bit as coating parameters (layer thicknesses, viscosities, web speed, pressure difference, etc.) are varied, but the appearance of the different response curves remains largely unchanged.

Remarkably, the dominant eigenfrequencies of the upper and the lower free surfaces can be estimated from a rather crude approximation. An undamped second-order system is known to have an eigenfrequency

$$\Omega_0 = (1/2\pi) * (k/m)^{1/2} \quad (11b.46)$$

where k is the stiffness or the spring constant, and m is the mass of the system. The mass of the coating bead per unit width is estimated to be

$$m \approx \rho L_b H_G \quad (11b.47)$$

A rough estimate of the spring constant k may be obtained from the ratio of the surface tension to the length over which it is active, which for the upper free surface is of the order of L_b and for the lower one is H_G . It can be easily verified that, for the coating flows used in practice, these

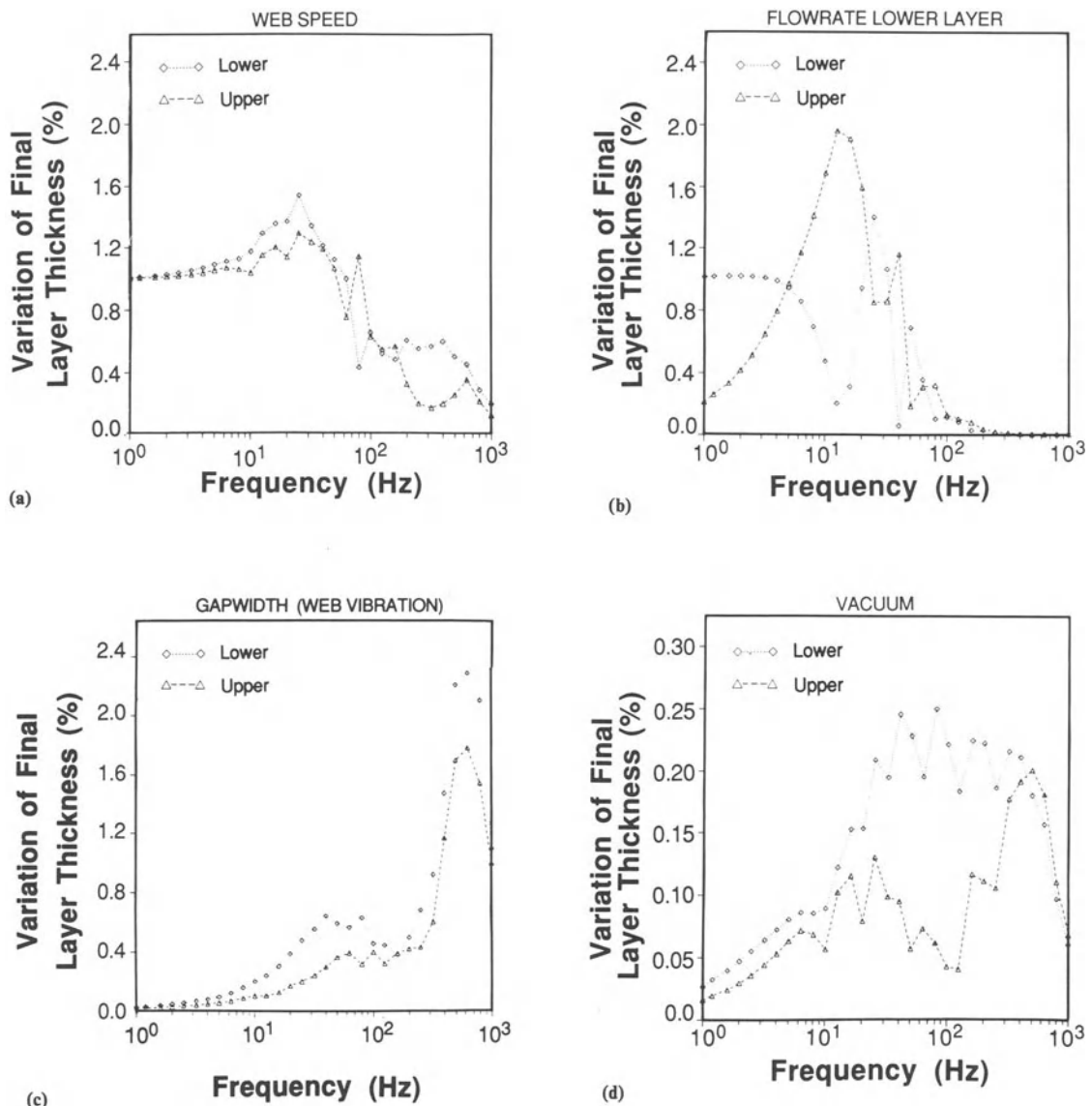


Figure 11b.14 Some frequency responses of a two-layer slide coater. (Amplitude $A\%$ means: 1% variation in the considered parameter causes $A\%$ variation in the thickness of the (upper or lower) layer). From: Van Abbenyen, W., Christodoulou, K. and Scriven, L. E. 1988. Frequency response of a coating flow: predictions for slide coating. University of Minnesota Supercomputer Institute, Report UMSI 89/54, March 1989.

approximations yield eigenfrequencies of the order of 10 to 50 Hz for the upper free surface, and of the order of 50 to 200 Hz for the lower one.

Slide coating experiments show only limited

agreement with numerically calculated frequency responses. The resonance frequencies do agree, but the amplitudes are not quantitatively correct (Katagiri 1988; 1990; Van Abbenyen *et al.* 1990;

Bussmann, Hofmann and Beck 1992). This is probably due to the complexity of this kind of experiment.

As yet frequency response calculations are not entirely verified, but may be helpful because frequency responses yield interesting dynamic information for the coating engineer. Such information, however, should be used with care: interpretation by an expert 'skilled in the art', as well as some experimental work remain indispensable.

11b.6 COATING DEFECTS IN SLIDE COATING

A coating defect always results from either unstable coating conditions or, when operating under stable conditions, by unwanted but identifiable external causes. The former type of defects have been dealt with in Sections 11b.3 and 11b.4, the latter will be addressed in this section. We shall successively consider lengthwise streaks, chatter, fat edges, spreading problems, blotchiness and point defects, which are probably the most frequently encountered defects in slide coating, but the list is by no means complete. A more complete survey of coating defects, not limited to slide coating, has been presented by Gutoff (1993).

11b.6.1 LENGTHWISE STREAKLINES AND 'BANDEDNESS'

Lengthwise streaklines, not appearing in a regular pattern, such as ribbing, but rather randomly, are the most encountered defects in slide coating. 'Bandedness' can be considered to be a weak, smoother form of streaklines. 'Real' streaklines can be very sharp, and disastrous for coating quality. They can be caused in many ways, the most important of which will be discussed below.

Particles can become trapped, somewhere on the inside of the die (Vrahopoulou 1992), at the exit of the slots on the inclined plane, or even at the die face lip or on the inclined plane (Pozrikides and Thoroddsen 1991). By correctly designing the coater geometry to avoid zones with stagnant

or slowly moving liquid (Russell 1969), deposition of particles can be prevented (see also Chapter 15, where this matter is discussed in the context of die design optimization). Furthermore, the liquids should be adequately filtered before coating.

Discontinuous three-phase contact lines (air–liquid–solid or liquid 1–liquid 2–solid) are another important cause of streaks. Pinning the free liquid surfaces or interfaces on a sharp edge (see Section 11b.2.7) is a way of ensuring that a contact line remains straight. Encapsulating the coating equipment in an enclosure filled with saturated gas (Ishiwata *et al.* 1980) has been proposed to avoid local drying, another source of streaks that is especially relevant when dealing with volatile liquids.

Scratches in the underlying layers may also show up as severe streaklines, even if the defect on the web before coating may seem insignificant, as in the case of a scratched 'subbing layer' (i.e. the very thin layer often applied to the base to promote adhesion).

Splices crossing the bead may disturb the static contact line at the die lip, particularly when this contact line is not pinned and the splice quality is poor. Furthermore, air may get trapped at the trailing edge of the splicing tape, preventing rewetting of the web surface. Steps can be taken to facilitate rewetting, e.g. temporarily increasing the pressure difference over the bead (Fowble 1975; Finnicum, Pegoni and Story 1991), locally roughening the web surface (Takagi *et al.* 1975), or hydrophobizing the tape zone (Bourns and McDonald 1969). Splicing the web at its backside (Verkinderen *et al.* 1979) prevents air getting trapped at the trailing edge of the splicing tape.

The problems related to the passage of splices can of course be avoided by a die withdrawal. Unfortunately the start-up of coating after interruption brings its own difficulties. Indeed, at the first contact between the multilayer liquid and the web, the layers are deposited upside down. Normally the flow reorganizes itself spontaneously in less than one second, but a thick zone is generally formed immediately downstream from the line where the liquid starts wetting the web. As the drier will generally be

incapable of handling such a thick coating, the result is a dirty machine and a sticky web at the winding station. The thick starting zone can be thinned by increasing the pressure difference over the bead, thereby reducing the thickening of the layer near the end of the slide when the die approaches the web during start-up (Johnson 1965). Local roughening of the web surface can also be advantageous (Takeda and Oyama 1976). An alternative start-up procedure relies on a combination of electrostatic assist, a temporarily narrower coating gap and deliberately altered flow rates of the different layers during start-up (Willemseens, Van Abbenyen and Criel 1989). Apart from patent literature, there is little work published on start-up in slide coating. Owing to the complexity of the process, scientific research has only recently been started (Fenoglio *et al.* 1990; Palmquist *et al.* 1992).

11b.6.2 CHATTER AND CHEVRONS

When a coating suffers from chatter, the cause is not immediately clear. Either there is hydrodynamic instability (barring, see Section 11b.4.3), in which case the problem can be solved by changing the coating parameters, or some external disturbance may induce the defect, which requires the identification of the disturbance and its elimination or at least minimization (see Section 11b.5). Externally induced chatter or crosslines can have many causes, which can be identified by measurements. The most common are mechanical vibrations (affecting the gap between the coating die and the backing roll) and pressure variations (affecting the upper or the lower free surface of the bead). Other causes of chatter are flow rate variations in one of the liquids and web speed fluctuations.

A particular form of chatter is called 'chevrons': thickness undulations that are not cross-web, but at a diagonal angle. The cause of this defect is a periodic disturbance that is not uniform over the width of the coating but rather located at one fixed point, often the edge of the coating meniscus. Such a disturbance initiates a wave traveling from the edge to the center of the web, while the

web is moving, resulting in thickness variations, at an angle with the web direction.

The sensitivity of the flow to disturbances is addressed in Section 11b.5. How such disturbances can be eliminated will not be discussed here. We just refer the reader to the article by Gutoff (1993), because this problem is common to several coating systems.

11b.6.3 FAT EDGES

Thick edges at both sides of the coating width occur in nearly all coating systems (see Chapter 3). The patent literature abounds in tips to minimize their effects once they have been formed.

In slide coating thick edges can already originate in the die (Vrahopoulou 1991). They can also arise on the inclined plane, when the edge guides are improperly designed, i.e. if their height differs from the thickness of the liquid layer on the slide, the liquid-air interface is curved and a pressure gradient along the interface arises. Under such conditions liquid gets transported sideways, creating a thinner and a thicker zone on the slide. Furthermore, the thinner zone may give rise to 'necking-in' of the coating bead ('edge failure'). The coating edges thus formed are, of course, extremely thick: up to twice the nominal layer thickness or even more. During the drying process, thick edges can develop due to locally lower surface tension as a result of faster evaporation there – provided that the liquid viscosity is still low enough to allow flow.

The formation of thick edges on the inclined plane can be prevented by edge guides with the height of the surfaces facing the liquid flowing down the incline equaling the thickness of the liquid layer (Barstow 1966). As slide coaters are generally used for many products with different layer thicknesses on the incline, it has been proposed to use edge guides with surfaces sloping from the inclined plane towards the outside (Koepke *et al.* 1982). Alternatively it is possible to avoid the thick edges in certain cases by choosing the width of all but the uppermost slot smaller than the desired coating width (Willemseens 1980).

11b.6.4 SPREADING PROBLEMS

Multilayer coating can be faulty due to surface tension effects. On the inclined plane the uppermost layer(s) should not neck in, but spread evenly over the underlying ones. To achieve this it is sufficient that the surface tension of the layers decreases from bottom to top by one or more mN/m per layer. This condition is not necessary, however, as only the uppermost layer (in contact with the air) has to have a lower surface tension than the other layers (Bacon and Fogg 1969; Do and Scriven 1991). It may be difficult, however, to start the coating or to recover from temporary defects when the surface tension is not properly stratified.

Defects due to spreading problems, such as craters, repellencies, compass, comets, fish eyes, etc. can also arise after coating. Such defects are also encountered in other coating systems and therefore will not be treated here. They have been discussed by Gutoff (1993) and by Do and Scriven (1991). For a discussion of spreading problems the reader is referred to Chapters 4 and 6.

11b.6.5 BLOTCHESS OR MOTTLE

Blotchiness or mottle is a coating defect which is exhibited as random thickness fluctuations without any regular pattern or direction. The most obvious cause of this defect is an uneven air flow over the coated layer before the coating is chilled or sufficiently dried down.

Mottle can, however, also be caused by inhomogeneous properties of the substrate, such as nonuniform surface energy or electrostatic charges, which affect the dynamic contact angle at the wetting line. Blotchiness is also observed in other coating systems, but a slide coater is particularly sensitive to it, as the relatively small bead height means that contact angle fluctuations can temporarily disrupt the balance between delivered and entrained flow rate. The reader is again referred to Gutoff (1993).

11b.6.6 POINT DEFECTS

Dust particles adhering either to the front side or to the back side of the web can disturb the

bead and cause defects, which can affect areas of the web surface that are larger than the particle dimensions. Indeed, at constant flow rate a thinner coated area must necessarily be followed by a thicker one, after the dust particle has left the bead (Do and Scriven 1991, 1992). When a particle sticks to the backing roll, the defect is repeated every time the particle deforms the bead zone.

Particles, gel slugs or bubbles in a coating solution can create unwanted defects, the size of which are much larger than the particles themselves, due to flow effects. Particularly in multilayer coating such defects can be devastating because the interface becomes disturbed and layers may become partly interchanged. Spreading phenomena can also occur, as explained in Section 11b.6.1.

Coating defects caused by particles cannot be eliminated by improving the coating technique. Steps must be taken to remove particles from the web and the backing roll (scraper, airknife, vacuum brush system, etc.) and from the coating solutions (filtering) before coating.

11b.7 CONCLUSIONS

Slide coating is a versatile method of premetering and assembling multiple layers and applying them simultaneously to a web, with an excellent uniformity and within an industrially interesting operability range. Some of these layers may even be so thin or so viscous that they cannot be coated separately.

In obtaining high quality products, with other (single layer) coating systems, the production speed is rather limited. Multilayer slide coating can meet the same or even higher quality standards at much higher speeds. In the next chapter it will be shown that curtain coating can reach even higher speeds with multilayers and comparable quality.

Blade coating and elastohydrodynamic systems can coat at much higher speeds, but with a limited uniformity.

To obtain a coated product with an excellent quality it is necessary, however, to design carefully the coating installation (control of vibrations,

noise, dust etc.) and to acquire a lot of operating skills (start-up, spreading, edges, streaklines, optimum pressure difference, etc.).

Drawbacks of slide coating are the rather large minimum wet layer thickness (not less than about 20 µm) and the relatively limited solid content (to achieve low thicknesses at high coating speeds), certainly when compared with roll or blade coating.

That multilayer slide coating is neither a mere curiosity nor an old and obsolete coating system is demonstrated by the continuous stream of patents disclosing small improvements and scientific articles aimed at explaining its operation.

REFERENCES

- Ade, F. 1976. Gleitflächenbeschichtungsvorrichtung, Deutsche Offenlegungsschrift 2521995; US Patent 4,041,897.
- Aktharuzzaman, A. F. M., Wang, C. K. and Lin, S. P. 1978. Wave motion in multilayered liquid films. *J. Applied Mech.* **45**: 25–31.
- Bacon, R. E. and Fogg, D. B. 1969. Method of making multilayer coatings containing a water resistant layer. US Patent 3,425,857.
- Barstow, F. C. 1966. Cascade coating apparatus for applying plural layers of coating material to a moving web, US Patent 3,289,632.
- Bassa, A. 1984. Layer casting apparatus. European Patent 0,119,850.
- Baumlin, J. M. 1990. Surfactant effects on surface waves of flowing liquid. Paper read at AIChE Spring Meeting, March 18–22, 1990, Orlando, FL, paper 19h.
- Baumlin, J. M. and Pasquet, A. 1988. Flow stability on an inclined plane: modeling and experimental results. Paper read at AIChE Spring Meeting, March 6–10, 1988, New Orleans, LA, paper 5b.
- Beck, D. and Muës, W. 1988. Analysis of flow field in slide coaters by FE-calculations and comparison with LD-measurements. Paper read at AIChE Spring Meeting, March 6–10, 1988, New Orleans, LA, paper 2b.
- Beguin, A. E. 1954. Method of coating strip material. US Patent 2,681,294.
- Berghezan, D. 1991. Simulation numérique d'écoulements en couches intervenant dans l'industrie photographique. PhD thesis, Université Catholique de Louvain-la-Neuve, Belgium.
- Blake, T. D., Clarke, A. and Ruschak, K. J. 1992. Hydrodynamic assist of dynamic wetting. Paper read at AIChE Spring Meeting, March 30–April 2, 1992, New Orleans, LA, paper 43c.
- Bourns, R. T. and McDonald, L. G. 1969. Verfahren zum kontinuierlichen Auftragen einer Schicht auf ein laufendes Band. Deutsche Offenlegungsschrift 1,805,734.
- Bracke, M., De Voeght, F. and Joos, P. 1989. The kinetics of wetting: the dynamic contact angle. *Progr. Colloid Polym. Sci.* **79**: 142–149.
- Brown, D. R. 1961. A study of the behavior of a thin sheet of moving liquid. *J. Fluid Mech.* **10**: 297–305.
- Burket, R. S., Conaghan, B. F. and Hirshburg, R. I. 1984. Coating method. US Patent 4,443,504.
- Burley, R. and Kennedy, B. S. 1976. An experimental study of air entrainment at a solid/liquid/gas interface. *Chem. Eng. Sci.* **31**: 901–911.
- Bussmann, H., Hofmann, H. and Beck, D. 1992. Frequency response in slide coaters: F. E. calculations and measurements. Paper read at AIChE Spring Meeting, March 30–April 2, 1992, New Orleans, LA, paper 43h.
- Chen, K. S. A. 1992. Studies of multilayer slide coating and related processes. PhD thesis, University of Minnesota, Minneapolis.
- Choinski, E. J. 1978. Method of multilayer coating. US Patent 4,113,903.
- Choinski, E. J. 1981. Method and apparatus for coating webs. US Patent 4,283,443.
- Christodoulou, K. N. 1990. Computational physics of slide-coating flow. PhD thesis, University of Minnesota, Minneapolis.
- Christodoulou, K. N. and Scriven, L. E. 1989. The fluid mechanics of slide coating. *J. Fluid Mech.* **208**: 321–354.
- Coyle, D. J., Macosko, C. W. and Scriven, L. E. 1990. Stability of symmetric film-splitting between counter-rotating cylinders. *J. Fluid Mech.* **216**: 437–458.
- De Geest, W. and Verkinderen, P. 1967. Improvements relating to the coating of webs with liquid compositions. GB Patent 1,061,431.
- Dittmann, D. A. and Rozzi, A. 1977. Method of multi-layer coating. US Patent 4,001,024.
- Do, D. V. and Scriven, L. E. 1991. Analysis of coating defects, especially those caused by particles and bubbles in slide coating. Paper read at IS&T 44th Annual Conference, May 12–17, 1991, St. Paul, MN.
- Do, D. V. and Scriven, L. E. 1992. Dynamics of particles and bubbles in coating flows. Paper read at AIChE Spring Meeting, March 30–April 2, 1992, New Orleans, LA, paper 40t.
- Fahrni, F. and Zimmermann, A. 1977. Beschichtungsvorrichtung. Deutsche Offenlegungsschrift 2,614,068.

- Faust, H. L. 1975. Menisci studies in bead coating. MS thesis, Drexel University.
- Feng, J. and Scriven, L. E. 1992. Electrostatic effects in continuous liquid coating. Paper read at AIChE Spring Meeting, March 30–April 2, 1992, New Orleans, LA, paper 38d.
- Fenoglio, A. et al. 1990. On the physics of establishing coherent coating beads and continuous liquid coatings. Paper read at AIChE Spring Meeting, March 18–22, 1990, Orlando, FL, paper 81n.
- Finnicum, D., Pegoni, J. and Story, T. 1991. Method and apparatus for use in bead coating a web with liquid composition. International Patent Application, Publication Number WO 91/014969.
- Fowble, W. F. 1975. Method of coating a spliced web. US Patent 3,916,043.
- Fruhner, H., Krägel, J. and Kretzschmar, G. 1989. Untersuchungen zur Stabilität der Flüssigkeitsbrücke beim Wultstbeschichtungsverfahren. *J. Inf. Rec. Mater.* **17**: 107–115.
- Galehouse, D. and Colt, J. 1984. Simplified analytical solutions of the free fluid surfaces associated with slide coating. Paper read at AIChE Winter Meeting, Atlanta, 1984, paper 16c.
- Goenaga, A. S. and Higgins, B. G. 1992. Mechanisms for flow reversal in coating operations. Paper read at AIChE Spring Meeting, March 30–April 2, 1992, New Orleans, LA, paper 49i.
- Gutoff, E. B. 1993. Avoid coating and drying defects. *Chem. Eng. Proc.* **93**(1): 49–55.
- Gutoff, E. B. and Kendrick, C. E. 1982. Dynamic contact angles. *AIChEJ.* **28**(3): 459–466.
- Gutoff, E. B. and Kendrick, C. E. 1987. Low flow limits of coatability on a slide coater. *AIChEJ.* **33**(1): 141–145.
- Hackler, M. A. et al. 1992. Frequency response of coating flows to small three-dimensional disturbances by supercomputer aided analysis. Paper read at AIChE Spring National Meeting, March 30–April 2, 1992, New Orleans, LA, paper 43d.
- Hartman, R. L. 1989. High speed curtain coating process and apparatus. International Patent Application, Publication Number WO 89/05477.
- Hens, J. and Boiy, L. 1986. Operation of the bead of a pre-metered coating device. *Chem. Eng. Sci.* **41**(7): 1827–1831.
- Hens, J. and Van Abbenyen, W. 1994. Explaining the limits of operability of slide coating. Paper read at AIChE Spring Meeting, April 17–21, 1994, Atlanta, GA, paper 7h.
- Higgins, B. G. and Scriven, L. E. 1979. Interfacial shape and evolution equations for liquid films and other visco-capillary flows. *Ind. Eng. Chem. Fundam.* **18**(3): 208.
- Isayama, S. and Takehara, N. 1980. Beschichtungsvorrichtung. Deutsche Offenlegungsschrift 2,951,515.
- Ishiwata, M. et al. 1980. Beschichtungsverfahren und Vorrichtung zur Durchführung dieses Verfahrens. Deutsche Offenlegungsschrift 2,948,962.
- Johnson, H. R. 1965. Method of coating strip material. US Patent 3,220,877.
- Kao, T. W. 1968. Role of viscosity stratification in the stability of two-layer flow down an incline. *J. Fluid Mech.* **33**: 561.
- Katagiri, Y. 1988. Natural oscillation in slide-coating flow. Paper read at AIChE Spring Meeting, March 6–10, 1988, New Orleans, LA, paper 2c.
- Katagiri, Y. 1990. Comparative study of unsteady behavior in slide and curtain coating. Paper read at AIChE Spring Meeting, March 18–22, 1990, Orlando, FL, paper 96c.
- Katagiri, Y. and Scriven, L. E. 1986. Supercomputer-aided analysis of transient response of a coating operation. Paper read at AIChE '86 Annual Meeting, November 2–7, 1986, Miami Beach, FL.
- Kheshgi, H. S., Kistler, S. F. and Scriven, L. E. 1992. Rising and falling film flows: viewed from a first-order approximation. *Chem. Eng. Sci.* **47**(3): 683–694.
- Kistler, S. F. 1983. The fluid mechanics of curtain coating and related viscous free surface flows with contact lines. PhD thesis, University of Minnesota, Minneapolis.
- Kistler, S. F. 1993. Personal communication.
- Kobayashi, C. 1992. Stability analysis of film flow on an inclined plane. I. One layer, two layer flow. *Ind. Coat. Res.* **2**: 65–88.
- Kobayashi, C., Saito, H. and Scriven, L. E. 1982. Study of slide coating by finite-element method. Paper read at AIChE Winter Meeting, Feb. 28–March 3, 1982, Orlando, FL, paper 45e.
- Koepke, G. et al. 1982. Randleisten an Gleitflächen von Kaskaden- und Vorhanggiessern. Deutsche Offenlegungsschrift 3,037,612.
- Koepke, G. et al. 1984. Verfahren zur Mehrfachbeschichtung von bewegten Gegenständen oder Bahnen. Deutsche Offenlegungsschrift 3,238,905 A1.
- Krussig, K. 1981. Vorrichtung zum begießen von Bahnen mit viskosen Gießlösungen. Deutsche Offenlegungsschrift 3,014,816.
- Levi, S. M., Cvetkov, G. M. and Babcin, A. I. 1966. Physical principles of the extrusion method for coating of photographic emulsions. *Uspechi Naoetch. Photogr.* (11): 74–84.
- Mercier, J. A., Torpey, W. A. and Russell, T. A. 1956. Multiple coating apparatus. US Patent 2,761,419.
- Mill, C. C. and South, G. R. 1967. Formation of ribs on rotating rolls. *J. Fluid Mech.* **28**(3): 523–528.

- Moffat, H. K. 1964. Viscous and resistive eddies near a sharp corner. *J. Fluid Mech.* **18**: 1–18.
- Muës, W., Hens, J. and Boiy, L. 1989. Observation of a dynamic wetting process using laser-Doppler velocimetry. *AIChEJ.* **35**(9): 1521–1526.
- Nakai, S. and Okada, T. 1968. Procédé d'enduction. French Patent 1,517,840.
- Nakajima, K. and Miyamoto, K. 1993. Coating method. European Patent 0,530,752 A1.
- Padday, J. F. 1961. Multiple coating apparatus. US Patent 3,005,440.
- Palmquist, K. *et al.* 1992. Visualization of a falling liquid film in air carried by a roller. Paper read at AIChE Spring Meeting, March 30–April 2, 1992, New Orleans, LA, paper 40hh.
- Paton, 1968. Kaskadenbeschichtungsvorrichtung. Deutsche Offenlegungsschrift 1,752,885.
- Pozrikides, C. and Thoroddsen, S. 1991. The deformation of a liquid film flowing down an inclined plane wall over a small particle arrested on the wall. *Phys. Fluids A.* **3**(11): 2546–2558.
- Ruschak, K. J. 1978. Flow of a falling film into a pool. *AIChEJ.* **24**(4): 705–709.
- Russell, T. A. 1969. Vorrichtung zum Zuführen flüssigen Beschichtungsmassen. Deutsche Offenlegungsschrift 1806887; US Patent 3,474,758.
- Saito, H., Ishizuka, S. and Fuchigami, S. 1982. Instability of the slide-coating flow. Paper read at AIChE Winter Meeting, Feb 28–March 3, 1982, Orlando, FL, paper 47c.
- Sakiadis, B. C. 1961. Boundary-layer behavior on continuous solid surfaces. *AIChEJ.* **7**(2): 21–25.
- Salamon, T. R., Armstrong, R. C. and Brown, R. A. 1992. Modification of inertial film instability by viscoelasticity. In *Theoretical and Applied Rheology*, eds P. Moldenaers and R. Keunings, Elsevier Science Publishers B.V. pp. 213–215.
- Savage, M. D. 1992. Meniscus instability and ribbing. *Industrial Coating Research.* **2**: 47–58.
- Scanlan, D. J. 1990. Two-slot coater analysis: Inner layer separation issues in two-layer coating. MS thesis, University of Minnesota, Minneapolis.
- Schunk, P. R. 1989. Surfactant and polymer additives in coating and related flows. PhD thesis, University of Minnesota, Minneapolis.
- Schweizer, P. M. 1988. Visualization of coating flows. *J. Fluid Mech.* **193**: 285–302.
- Schweizer, P. M. 1993. Personal communication.
- Schweizer, P. M. and Scriven, L. E. 1983. Evidence of Görtler-type vortices in curved films. *Phys. Fluids.* **26**(3): 619–623.
- Smith, M. K. 1990. The mechanism for the long-wave instability in thin liquid films. *J. Fluid Mech.* **217**: 469–485.
- Takagi, A. *et al.* 1975. Überzugsverfahren Deutsche Offenlegungsschrift 2,440,280; US Patent 4,024,302.
- Takeda, H. and Oyama, N. 1976. Coating method. US Patent 3,959,528.
- Timson, W. J. 1973. Coating apparatus. US Patent 3,749,053.
- Timson, W. J. 1976. Coating apparatus. US Patent 3,958,532.
- Valentini, J. *et al.* 1991. Role of dynamic surface tension in slide coating. *Ind. Eng. Chem. Res.* **30**(3): 453–461.
- Valentini, J. *et al.* 1996. Surface elastic effects in premetered coating techniques. *Ind. Eng. Chem. Res.* **35**: 434–449.
- Van Abbenyen, W., Christodoulou, K. and Scriven, L. E. 1988. Frequency response of a coating flow: Predictions for slide coating. Paper read at AIChE Spring Meeting, March 6–10, 1988, New Orleans, LA, paper 2d.
- Van Abbenyen, W. *et al.* 1990. Experimental verification of the calculated frequency response of a multilayer slide coating operation. Paper read at AIChE Spring Meeting, March 18–22, 1990, Orlando, FL, paper 96a.
- Van Abbenyen, W., Muës, W. and Goetmaeckers, B. 1992. Explaining limits of operability in curtain coating. Paper read at AIChE Spring Meeting, March 30–April 2, 1992, New Orleans, LA, paper 43a.
- Van Abbenyen, W. and Muës, W. 1992. Comments on 'Stability analysis of multilayer stratified flow on an inclined plane'. *Ind. Coat. Res.* **2**: 89–93.
- Verkinderen, P. A. *et al.* 1979. Method for the continuous coating of webs having spliced joints. European Patent 0,001,465.
- Vrahopoulou, E. P. 1991. A model for fluid flow in dies. *Chem. Eng. Sci.* **46**(2): 629–636.
- Vrahopoulou, E. P. 1992. Flow distortions around particles between parallel walls with application to streak formation in slide-coating methods. *Chem. Eng. Sci.* **47**(5): 1027–1037.
- Wang, C. K., Seaborg, J. J. and Lin, S. P. 1978. Instability of multi-layered liquid films. *Phys. Fluids.* **21**: 1669–1673.
- Weinstein, S. J. 1990. Wave propagation in the flow of shear-thinning fluids down an incline. *AIChEJ.* **36**(12): 1873–1889.
- Weinstein, S. J. and Kurz, M. R. 1991. Long-wavelength instabilities in three-layer flow down an incline. *Phys. Fluids.* **A3**(11): 2680–2687.
- Weinstein, S. J., Baumlin, J. M. and Servant, J. 1993. The propagation of surface waves in flow down an oscillating inclined plane. *AIChEJ.* **39**: 1113–1123.

- Willemse, K. S. 1980. Method and device for slide hopper multilayer coating. European Patent 0,018,029; GB Patent 7,913,627.

Willemse, K. S., Van Abbenen, W. N. and Criel, F. B. 1989. Coating method. European Patent 0,300,098.

Yih, C. 1963. Stability of liquid flow down an inclined plane. *Phys. Fluids*. **6**(3): 321.

Yoshida, K. and Ishiwata, M. 1970. Verfahren und Vorrichtung zum Regulieren der Beschichtungs- oder Überzugsdicke. Deutsche Offenlegungsschrift 1,929,176.

NOTATION

<i>a</i>	exponent (of surface tension) in correlation [—]
<i>A</i> _{max}	amplification factor of the most amplified wavelength [—]
<i>b</i>	exponent (of viscosity) in correlation [—]
<i>F</i> _D	reactive force of the die per unit width (kg/s^2)
<i>F</i> _{es}	electrostatic force per unit width (kg/s^2)
<i>F</i> _g	gravity force per unit width (kg/s^2)
<i>F</i> _{p,a}	dynamic pressure of air per unit width (kg/s^2)
<i>F</i> _{ΔP}	force of pressure difference over the bead per unit width (kg/s^2)
<i>F</i> _v	viscous friction force per unit width (kg/s^2)
<i>F</i> _{v,a}	drag force of the air per unit width (kg/s^2)
<i>F</i> _{v,l}	drag force of the die lip per unit width (kg/s^2)
<i>F</i> _{v,s}	drag force of the slide per unit width (kg/s^2)
<i>F</i> _{v,sak}	drag force of the boundary layer per unit width (kg/s^2)
<i>F</i> _{v,w}	drag force of the web per unit width (kg/s^2)
<i>F</i> _{σ,f}	surface tension force (in point f) per unit width (kg/s^2)
<i>g</i>	gravitational acceleration (m/s^2)
<i>H</i> _G	gap width (m)
<i>H</i> _s	layer thickness on the slide (m)
<i>H</i> _∞	eventual wet layer thickness on the web (m)
<i>H</i> _{∞,min}	minimum coating thickness (m)
<i>k</i>	stiffness of the bead per unit width (kg/ms^2)
<i>L</i> _b	bead height (m)
<i>L</i> _{b,max}	upper limit value of bead height (m)
<i>L</i> _{b,min}	lower limit value of bead height (m)
<i>L</i> _{cd} , <i>L</i> _{de}	length scales of control volume (m)
<i>L</i> _e	distance for a perturbation to grow by a factor e (m)
<i>L</i> _{e,min}	idem, for most amplified wave (m)
<i>L</i> _s	length of the inclined plane of a slide coater (m)
<i>L</i> _s	Sakiadis' boundary layer length (m)

m	mass of the system (the coating bead) per unit width (kg/m)
M	momentum per unit width (kg/s^2)
M_{in}	momentum entering the control volume by convection, per unit width (kg/s^2)
M_{out}	momentum leaving the control volume by convection, per unit width (kg/s^2)
M_s	momentum of the flow on the slide, per unit width (kg/s^2)
N	number of layers (—)
P_A	ambient pressure (kg/ms^2)
P_v	pressure under the bead (kg/ms^2)
Q	total flow rate per unit width (m^2/s)
Q_B, Q_T	flow rate of bottom, resp. top layer (m^2/s)
U	web speed (m/s)
U_{AE}	critical velocity for the onset of air entrainment (m/s)
U_s	mean velocity of the flow far upstream on the slide (m/s)
x	horizontal component
y	vertical component

Greek letters

α	application angle (degrees)
β	slide inclination angle (degrees)
γ	angle between die face and web (degrees)
ΔP	pressure difference over the bead (kg/ms^2)
μ	viscosity (kg/ms)
μ_B, μ_T	viscosity of bottom, resp. top layer (kg/ms)
ρ	density (kg/m^3)
ρ_{air}	density of the air (kg/m^3)
σ	surface tension (kg/s^2)
Θ_0	apparent static contact angle (degrees)
Θ_D	apparent dynamic contact angle (degrees)
Ω_0	eigenfrequency ($= (1/2\pi) * (k/m)^{1/2}$) (s^{-1})

Dimensionless numbers

Ca	capillary number ($= \mu U / \sigma$)
Ca_{crit}	critical capillary number for the onset of vortices
m	viscosity ratio ($= \mu_{\text{top}} / \mu_{\text{bottom}}$)
N_{es}	dimensionless electrostatic force ($= F_{es} / \sigma$)
$N_{\Delta P}$	dimensionless pressure number ($= H_G \Delta P / \sigma$)
Po	property number ($= g u^4 / \gamma \sigma^3$)
St	Stokes number ($= \rho g H_\infty^2 / \mu U$)
St^*	modified Stokes number ($= St(H_G + H_\infty) / 2H_\infty$)
We	Weber number ($= \rho U^2 H_\infty / \sigma$)

Kimiaki Miyamoto and Yoshinobu Katagiri

11c.1 INTRODUCTION

Curtain coating is one of the three most prominent pre-metered coating methods. The other two, slot coating and slide coating, are discussed in the preceding Chapters 11a and 11b. Even though curtain coating can be performed with coating dies similar to those used in slot or slide coating, it is quite different. The most distinguishing feature is a liquid sheet that falls freely over a considerable height before it impinges onto the substrate to be coated. Curtain coating has two outstanding advantages: it can apply thin liquid layers to irregular surfaces, and it can coat at very high speeds. The first capability is made possible by the large distance between the coating die and the moving surface, and also the impinging velocity of the falling liquids sheet which is usually much higher than the vertical velocity component of the substrate motion. Together, the two effects attenuate the consequences of up-and-down movement of the substrate. The second capability may be attributed to the localized pressure that results from the high impinging velocity. That pressure presumably squeezes out the air film that may be entrained between the liquid and the substrate, and thereby prevents shear-induced instability of the air/liquid interface which would otherwise cause catastrophic air entrainment. This and other operating limits are treated in full detail in Section 11c.5.

Although curtain coating is suitable and attractive for modern mass production, it poses some inherent difficulties, mostly related to the

freely falling liquid sheet. One difficulty arises from a lower limit in flow rate below which the falling liquid sheet suddenly breaks apart. Another difficulty stems from the susceptibility to disturbances of the unsupported liquid sheet which results in unevenness of the coated film. Technological measures for dealing with both difficulties are explained in Section 11c.6.

Recent applications of curtain coating include multilayer precision coating, such as that used in manufacturing of photographic film. A historical review, however, shows that the sophisticated technology of modern curtain coating evolved from much simpler origins. The first industrial use of the method can be found in a German patent by Taylor (1903) for a machine that manufactured chocolate candies. A falling curtain of molten chocolate emerged from a slit to coat candy cores in a uniform manner. Several decades later, curtain coating became important in the furniture industry. Up until the 1960s, in fact, curtain coating was used primarily for coating pieces and sheets because of its tolerance for irregular shapes and the possibility of recovering unused coating liquid by a collection system placed underneath the parts being conveyed through the falling curtain (e.g., Wandtke (1964)). Applications for continuous webs, such as aluminum foil and corrugated paperboard, became common in the 1960s because coating operations could be performed at speeds as high as, say, 8 m/s (Poirier 1966; Booth 1970). Cox (1968)

described two types of sheet-forming equipment. The first, shown in Fig. 11c.1, forms a free-falling sheet from an overflowing weir. The second type, illustrated in Fig. 11c.2, makes use of a slot-shaped orifice at the bottom of a pressurized coating head. Both types are limited to coating single layers.

The prototype of modern multilayer curtain coaters was invented by Hughes (1970). Figure 11c.3 shows an example of a particular embodiment with a multilayer slide-fed die. Hughes not only disclosed a device and method for multilayer precision coating, but also illustrated the wide range of curtain coating with fairly viscous liquids at high speeds. Hughes' invention furthermore includes specific configurations for air shields and edge guides. The detailed design of these parts is essential for demanding applications, especially multilayer precision coating of photographic and other imaging products. Further details on all the important parts of a multilayer curtain-coater die, including some of the latest innovations, are explained in Section 11c.2 below.

Section 11c.2 also introduces typical coating

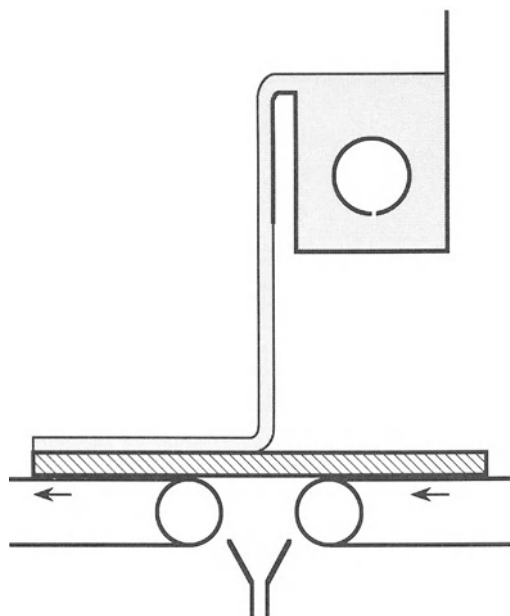


Figure 11c.1 Weir type curtain die.

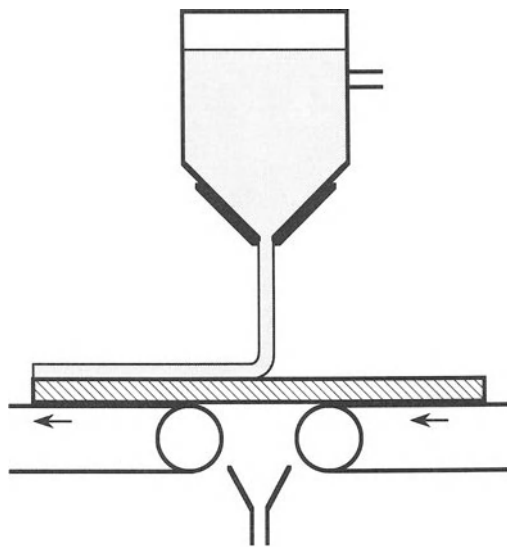


Figure 11c.2 Orifice type curtain die.

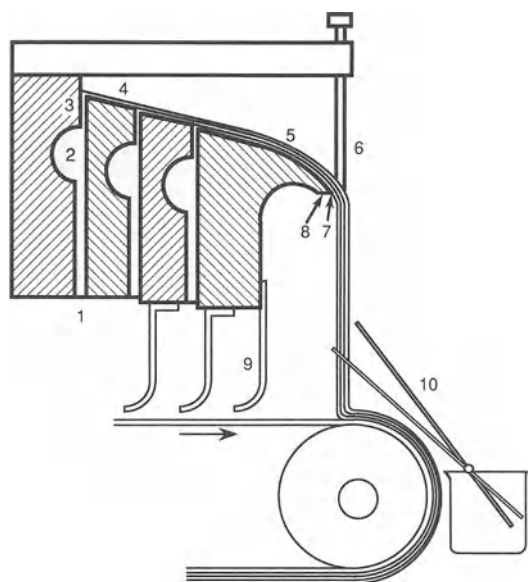


Figure 11c.3 Slide-fed type curtain die (after Hughes 1970) with feeding nozzle (1); cavity (2); slot (3); slide (4); elongated slide (5); edge guide (6); lip (7); underside of lip (8); air shield (9); and catch pan for start-up (10).

conditions. Section 11c.3 explains the phenomena and steady flow fields involved in successful curtain coating, as well as the effects of coater designs. Section 11c.4 addresses the susceptibility of curtain coating to external disturbances, including both the stability of a falling liquid curtain (Section 11c.4.1) and the response of curtain coating to ongoing disturbances (Section 11c.4.2). Section 11c.5 discusses instabilities of curtain-coating flows in the dynamic wetting region and related operability windows. Section 11c.6 provides a summary of important patents and other practical concerns.

11c.2 METHODS AND EQUIPMENT

Figures 11c.3 and 11c.4 show the essential parts of curtain coating devices according to the particular embodiments described in Hughes' (1970) patent. A first embodiment, the slide-fed curtain-coating die (Fig. 11c.3), consists of liquid feeder nozzles that are supplied at a constant rate by precision metering pumps; cavities that

distribute the liquid uniformly in a lateral direction; slots that discharge the liquid onto an included slide surface where one layer is stacked on top of the next; an extended curved slide portion along which the multilayered liquid film accelerates; a lip that forms a uniform liquid sheet; vertical edge guides that maintain a desired width of the falling sheet; and air shields that protect the liquid curtain from air currents and thereby enhance its stability. The curtain height can be changed by adjusting the vertical position of the die with respect to the substrate to be coated. A second embodiment of a multilayer curtain coating die, the slot-fed type (Fig. 11c.4), merges liquid layers within the die manifold and extrudes them together from a slot. The resulting flow field in the sheet forming zone is quite different from that in a slide-fed type die.

Another type of a curtain-coating die was disclosed by Miyake (1973). It is illustrated in Fig. 11c.5. The die has two slide surfaces, both with negative inclinations. As a result, there is no static contact line where the falling curtain forms. The patent claims that separating the

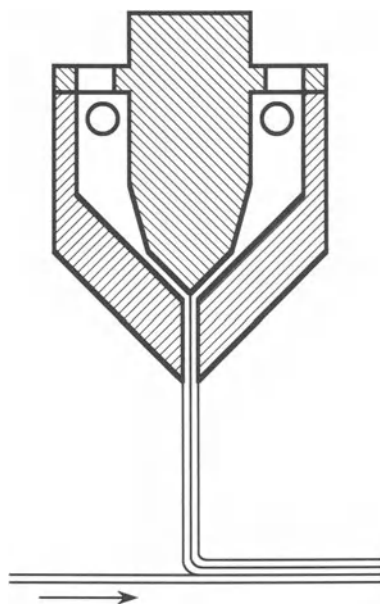


Figure 11c.4 Slot-fed type curtain die (after Hughes (1970)).

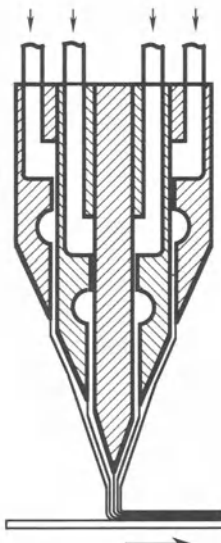


Figure 11c.5 Reversed slide type curtain die (Miyake, 1973).

static contact lines from the sheet-forming region prevents coating defects caused by the appearance of dried coating solution in the vicinity of the static contact line. Another variation yet is a combination of two slide-fed dies, shown in Fig. 11c.6 (Fahrni 1976). This configuration features two static contact lines in the sheet forming zone, as well as two static contact lines away from the lips where the liquid layers emerge from the feed slots. Fahrni's design produces a multilayered, symmetrically falling liquid sheet.

As is evident from the above descriptions, the key distinction between the four types of curtain dies is the number of static contact lines in the sheet forming zone. The slot-fed type and the Fahrni type have two, the slide-fed type has one, and the inverted-slide type has none. Practical implications of the different designs result from differences in the velocity profile in the sheet forming zone and differences in the adsorption time of surface active agents when present.

Hughes (1970) claimed a wide range of successful curtain coating conditions, including speeds from 0.75 m/s to 10 m/s; total coated weights from 13.8 g/m² to 233.5 g/m²; viscosities of the lower-most layer ranging from 4 to 80 mPa s; and curtain heights from 0.05 m to 0.2 m. Brown (1961), and later Greiller (1972), pointed out that a minimum flow rate is necessary in order to

maintain a stable curtain. This can limit the range of applicability of curtain coating operations. Greiller nevertheless highlighted the capability of curtain coating to apply thin layers at very high speeds by comparing the operable range of flow rate in curtain coating with that in slide coating. Further details on the operability of curtain coating are given in Section 11c.5 below.

11c.3 STEADY-STATE OPERATIONS

To organize the discussion of curtain coating, and also to facilitate a theoretical analysis of the process, the flow in curtain coating is best divided into several zones, namely a sheet forming zone, a curtain flow zone, and an impingement zone (Kistler 1983). These zones, shown in Fig. 11c.7, are common to all types of curtain coating devices. In curtain coating devices of the slide type, there is also a film-forming zone at the slot exit and a falling-film-flow zone along the inclined slide. The flows in these zones are the same as in slide coating, and are discussed in Chapter 11b. For that reason, they are not covered here again. Single- and multilayer falling-film flows

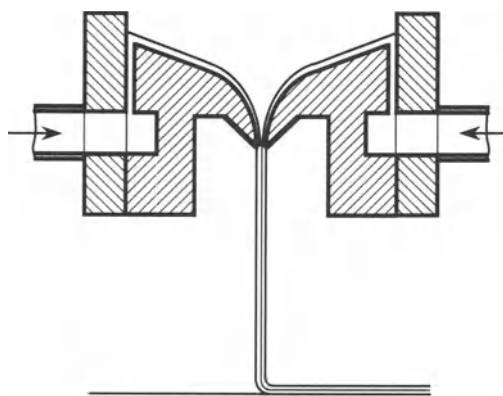


Figure 11c.6 Two merging, slide-fed curtain coating dies (Fahrni 1976).

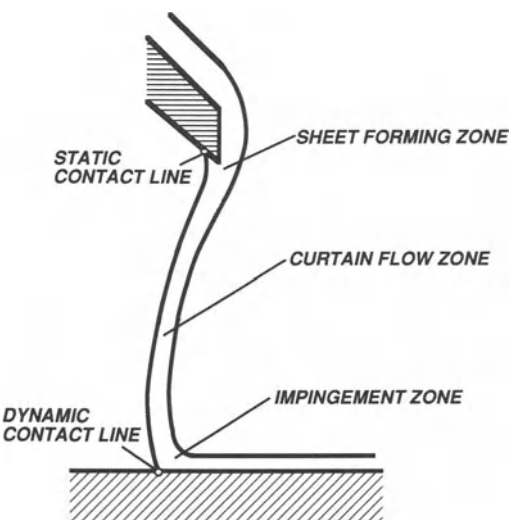


Figure 11c.7 Flow zones in curtain coating (Kistler 1983).

and their stability are also addressed in depth in Chapters 8 and 11d.

11c.3.1 SHEET FORMING ZONE

An important part of curtain coating is the formation of a freely falling liquid sheet. The flow fields in the sheet forming zone of symmetrical, slot-fed curtains have been calculated by Kistler (1983). Contours of shear stress and transverse velocity, shown in Fig. 11c.8, reveal that the transition from a shear flow to an extensional flow is confined to a rather small range of $-1 < x < 3$, where x is the distance from the die exit in units of half the slot clearance. Kistler (1983) analyzed not only the formation of a falling curtain of low or moderate viscosity, but also the extrusion of a highly viscous liquid for a sheet casting process, which makes use of a very similar slot-fed die. In extrusion, of course, there can be considerable die swell. In curtain coating, in contrast, there is very little or no die swell at all. Kistler found that a small amount of swelling can be promoted by very narrow slot clearances. His computed results show, however, that even when there is no die swell the separation angles of the liquid–air interface can be fairly high, ranging from 130° to 180° when measured from the die-internal slot surface. Unless the liquid wets the solid very poorly, such angles are likely to violate Gibbs' inequality (see Chapter 3), and the liquid is prone to wet the die lip past the sharp corner at the slot exit.

The flow fields of sheet formation from a slide-fed die have also been analyzed by Kistler (1983) (see also Kistler and Scriven (1994)), as shown in Fig. 11c.9. The trajectory of the liquid sheet where it leaves the slide lip is controlled by gravity, inertia, viscous and capillary forces. The computed pressure and stress contours indicate the existence of a singularity at the static contact line, where sudden acceleration takes place. The resulting maldistributions of stress near the lip cause the liquid sheet to deflect toward the underside of the lip.

The deflection of the falling curtain is one of the mechanisms at the root of a set of phenomena

sometimes referred to as the ‘teapot effect’ (Kistler 1983; Kistler and Scriven 1994). A second mechanism is wetting of the underside of the lip. It can give rise to hydrodynamic hysteresis which, in turn, stems from the nonlinearities inherent to viscous free-surface flows and permits multiple stable curtain shapes and flow fields at the same flow parameters. A third mechanism is conventional wetting hysteresis that arises from differences in advancing and receding contact angles (Chapter 3). It has its physical origins in surface roughness and inhomogeneities, and is confounded by the presence of a sharp corner. This set of phenomena is not only of theoretical interest but also of considerable practical importance in curtain coating with a slide-fed die – where formation of a straight wetting line without wetting past the sharp corner is key to maintaining a uniform curtain. Kistler and Scriven (1994) demonstrated all three mechanisms in experiments, and analyzed them theoretically by means of the finite element method.

As for the deflection of the falling liquid curtain when the static wetting line remains pinned at the sharp corner, the flow rate per unit width, Q , or equivalently the Reynolds number, $Re \equiv \rho Q / \mu$, is the key variable (ρ is the liquid density and μ the viscosity). The amount of deflection is not a monotonous function of flow rate, but exhibits a distinct maximum at an intermediate flow rate, as illustrated in Fig. 11c.10. Kistler and Scriven (1994) found that the angle of inclination of the slide, β , has a fairly weak influence. The effect of the property parameter $Po \equiv \sigma(\rho/\mu^4 g)^{1/3}$ is quite significant, but its influence is mostly confined to shifting the Reynolds number at which the maximum deflection occurs. In the definition of Po , σ is the surface tension and $g = 9.81 \text{ m/s}^2$ is the gravitational acceleration. Kistler and Scriven (1994) emphasized that the deflection comes from purely hydrodynamic effects and not from wetting and spreading phenomena associated with the static contact line.

When the Gibbs inequality condition is violated, the static contact line can move past the sharp corner and cause the liquid to wet the underside

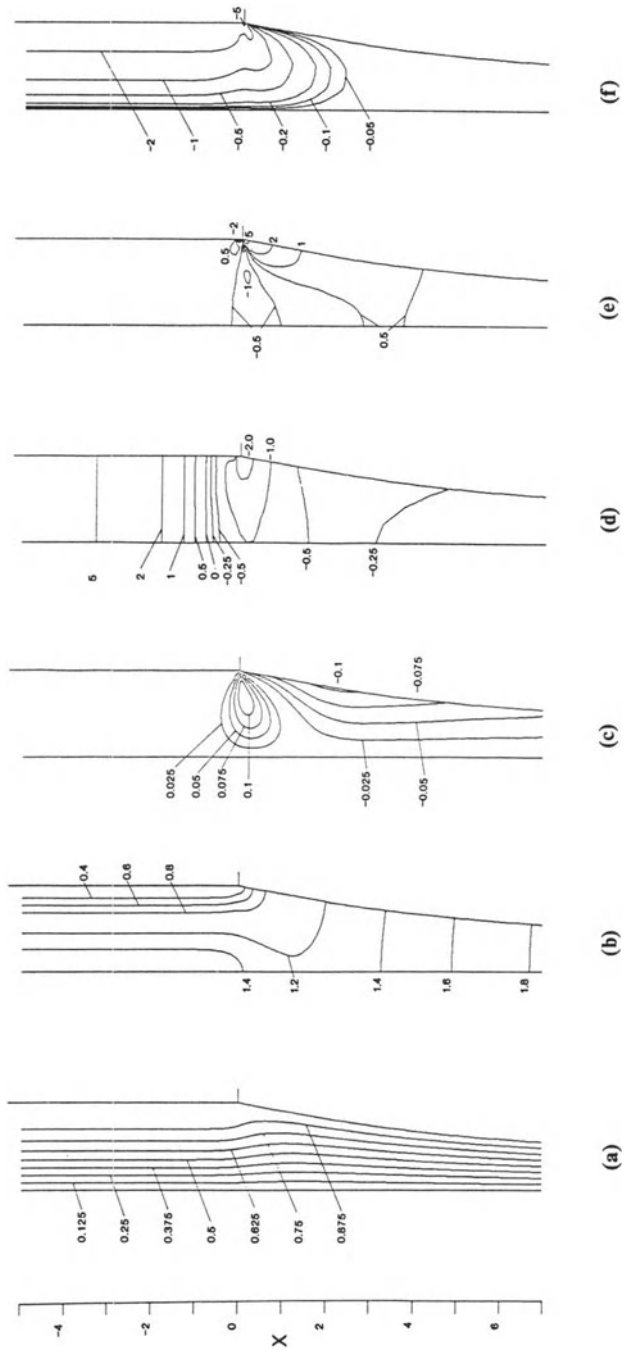


Figure 11c.8 Flow fields in sheet forming zone for slot-fed type curtain coating die (Kistler 1983; see also Kistler and Scriven 1994): (a) stream lines; (b) particle speed; (c) transverse velocity component; (d) normal stress difference; (e) pressure; (f) shear stress. $Re = \rho Q/\mu = 10$, $St = \rho g W^3/(\mu Q) = 0.5$, $Ca = \mu Q/(W\sigma) = 2$, where $g = 9.81 \text{ m/s}^2$, Q is the volumetric flow rate per unit width, W is half the slot width, ρ is the liquid viscosity, μ is the liquid density, and σ the surface tension. The horizontal scale is exaggerated by a factor of 2.

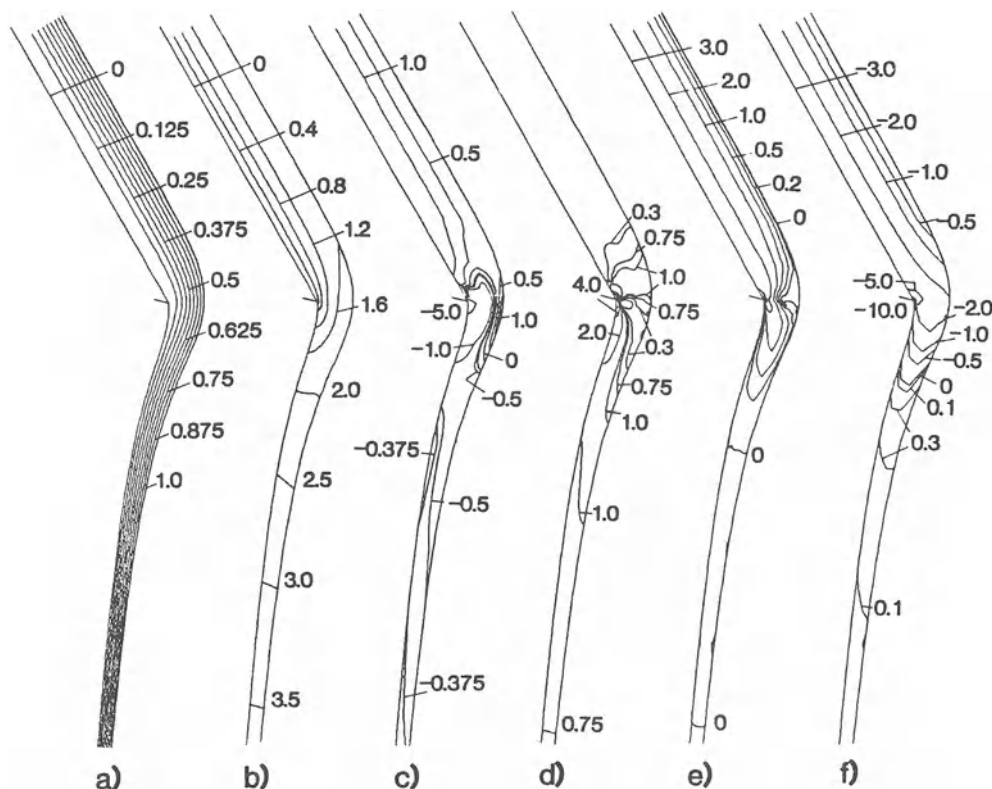


Figure 11c.9 Flow fields in sheet forming zone for slide-fed type curtain coating die (Kistler 1983; see also Kistler and Scriven 1994): (a) stream function; (b) particle speed; (c) pressure; (d) normal stress difference; (e) shear stress; (f) vorticity. $Re = \rho Q / \mu = 5$, $Po = \sigma / (\mu^4 g / \rho)^{1/3} = 7.30$, $\beta = 60^\circ$, where β is the angle of slide inclination measured from horizontal.

of the lip. According to the inequality, wetting depends on the static contact angle of the liquid–solid system θ_c , the cut-back angle γ between the inclined slide and the lip underside, and the separation angle of the interface that results from the trajectory of the deflected curtain and is a function of Re , Po and β . Kistler's finite element analysis with free movement of the contact line revealed how the equilibrium position of the static contact line is affected by the above-mentioned five parameters. In addition to the flow parameters that control the deflection, θ_c and γ have a strong influence on the contact line position, a phenomenon that is generally known and incorporated in patents explained

below. Further confounding whether and, if so, how far the liquid wets the lip past the sharp corner is contact angle hysteresis. This hysteresis, as well as the hydrodynamic hysteresis, makes the contact line position strongly dependent on the history of the preceding back-and-forth movement of the line.

The hydrodynamic hysteresis arises because the dependence of the contact line position on various parameters, especially the Reynolds number, is not a single-valued function but exhibits multiple steady states at the same parameter value. Even if a set of parameters corresponds to a pinned condition, operating at those parameters does not assure that the static

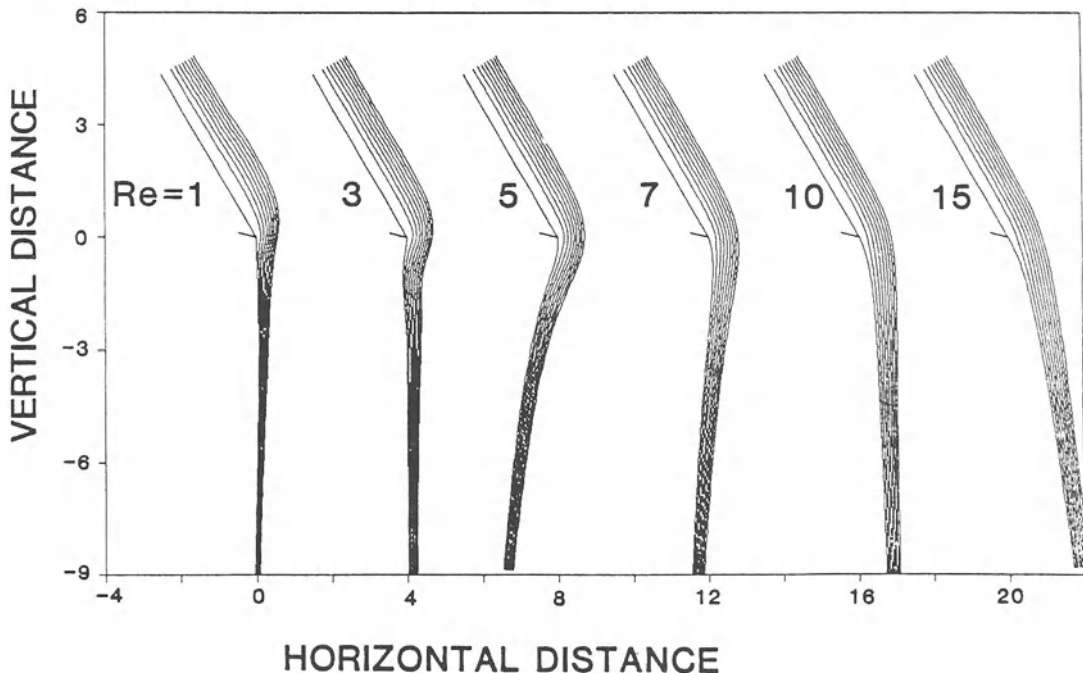


Figure 11c.10 Hydrodynamic deflection of the falling sheet at different flow rates (Kistler 1983; see also Kistler and Scriven 1994). $Po = \sigma/(\mu^4 g/\rho)^{1/3} = 6.35$, $\beta = 60^\circ$.

contact line is indeed pinned. Figure 11c.11 illustrates how the contact line migrates with changes in Reynolds number, and how hysteresis appears as a consequence of drastically different contact line positions for increasing and decreasing flow rates. At low rates, the contact line remains near the sharp corner but Gibbs' inequality is not satisfied and the lip underside is slightly wet. As the Reynolds number increases, the contact line advances further past the lip, until a critical Reynolds number is reached at an upper turning point. Beyond that Reynolds number, the contact line recedes in a jump-like manner back to the sharp corner and stays pinned with further increases in Re . When, on the other hand, the flow rate is decreased from high values that correspond to a pinned condition, the contact line remains pinned down to flow rates well below those at the upper turning point. When Gibbs' inequality can no longer be satisfied past

a lower critical flow rate, the contact line advances past the lip but, at first, does so very gradually until a critical Reynolds number is reached at a lower turning point. Below the lower critical Reynolds number, the contact line jumps past the lip to wet the underside again. Kistler and Scriven (1994) confirmed this characteristic behavior of the contact line position as calculated by the finite element method with experimental measurements.

In Figure 11c.11, for purposes of simplicity, the effects of contact angle hysteresis are ignored. Using different contact angles for advancing and receding situations, Kistler and Scriven (1994) were able to match their computed predictions with their experiments. Nonetheless, Kistler and Scriven (1994) stress that much of the hysteresis seen as part of the teapot effect is purely hydrodynamic in origin, even though it is influenced by a wetting parameter that exhibits

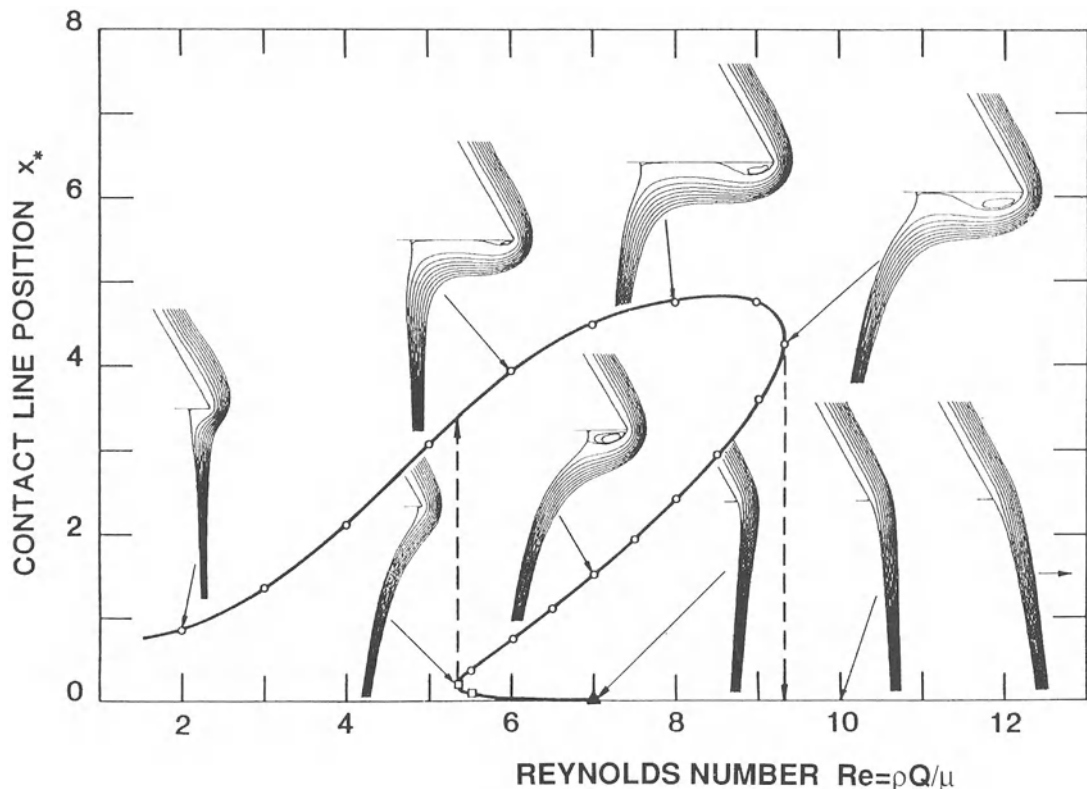


Figure 11c.11 Teapot effect: migration of the contact line and its hysteresis (Kistler 1983; see also Kistler and Scriven 1994). $Po = \sigma/(\mu^4 g/\rho)^{1/3} = 6.35$, $\beta = 60^\circ$, $\theta_C = 67^\circ$, $\gamma = 60^\circ$. The symbols are explained in the text.

hysteresis itself, namely the contact angle. Kistler and Scriven (1994) also examined the effect of contact angle on the hydrodynamic hysteresis of the contact line position. Their finite-element computations reveal that the contact line position becomes less and less sensitive to flow rate as the contact angle increases, but that an isolated hysteresis loop may separate from the main loop shown in Fig. 11c.11 before, above a critical angle, wetting no longer occurs over the entire range of flow rates because Gibbs' inequality is always satisfied.

These results are very relevant to practical aspects of successful operation of a slide-type curtain coating die because wetting of the lip underside can lead to degradation of the coating material trapped in the dead flow zones beneath

the lip and a wavy wetting line, both giving rise to down-web striations and streaks in the coated layers. Kistler and Scriven (1994) showed, by means of finite-element based design studies, that decreasing the cut-back angle γ between the inclined slide and lip underside is very effective in eliminating wetting past the sharp corner. Other lip designs aimed at preventing uneven wetting and related streaking are discussed in Section 11c.6.1 below.

Another practical issue intimately linked to the teapot effect relates to the curved trajectory of a deflected liquid sheet – which may deviate substantially from the vertical trajectory imposed by straight edge guides. When the curtain deflection is prominent, a ‘crease’ may form where the more or less uniformly deflected curtain

in the central portion of the coating width meets the standing wave that emanates from the point of initial contact of the curtain with the edge guide and delimits the portion of the falling sheet that is strongly influenced by the edge guide. This ‘crease’, in turn, causes a ‘kink’ in the dynamic wetting line that can become a major source for down-web striations or streaks. Ridley (1979) suggested that the use of a vertical edge guide in the form of a plane perpendicular to the curtain instead of the commonly used rod solves this problem. However, this solution is not always suitable. In fact, sometimes it may aggravate the unevenness of the coated layers near the edge guide, as mentioned below.

Curtain deflection from the teapot is not always harmful, however. Suga *et al.* (1991), for example, claimed that when the deflection is small and the flow rate is high, the three-dimensional flow resulting from the bowed shape of the dynamic contact line drives small bubbles toward the edges, and thereby prevents a special kind of air entrainment caused by bubbles that would otherwise get trapped in the impingement flow, especially when there is a heel (see Section 11c.3.3 below).

11c.3.2 CURTAIN FLOW ZONE

In successful curtain coating operation, the most significant influence of the flow in the freely falling curtain is the final velocity at which the liquid impinges onto the substrate. As discussed further in Section 11c.5 below, that velocity has a significant effect on the operating window. Brown (1961) measured the velocity within a curtain falling from a slot by means of a rotating mirror that projected the trajectories of bubbles in the falling liquid sheet. He found that the curtain reaches a free-fall regime a short distance below the slot exit and proposed an empirical formula for the curtain velocity V as a function of the vertical coordinate X in the form of a free-fall parabola that starts from the point X_0 below the slot:

$$V^2 = V_0^2 + 2g[X - 2(4\mu/\rho)^{2/3}g^{-1/3}] \quad (11c.1)$$

In this formula, V_0 is the average velocity at the slot exit. The distance X_0 is taken to be

$$X_0 = 2(4\mu/\rho)^{2/3}g^{-1/3} \quad (11c.2)$$

Brown’s data points show agreement between the measured and the calculated velocity only when the distance X is larger than two or three times X_0 . In addition, a comprehensive finite-element analysis of the sheet-forming region (Kistler 1983) reveals that the value of X_0 may not be a simple function of the liquid properties like $2(4\mu/\rho)^{2/3}g^{-1/3}$, as conjectured by Brown (1961).

For curtains with curved trajectories that result from hydrodynamic deflection at a slide lip, Kistler (1983) gave a generalized analysis to obtain a set of integrodifferential equations in terms of curvilinear, orthogonal coordinates. Those equations, applicable to all sorts of two-dimensional liquid sheets, are important as starting points for various approximations. However, they are also very complicated and can provide exact solutions only in special cases.

In the thin film approximation, the integrodifferential equations reduce to simple differential equations for the thickness profile and angle of inclination of a falling liquid sheet (Kistler 1983). This approximation assumes that the characteristic length scale over which significant changes in thickness or angle occur in the streamwise direction is much greater than that of the thickness. For a vertically falling sheet, for instance, the streamwise momentum balance reduces to

$$\frac{1}{4Ca} \left(\frac{(Re/4)^5}{2St} \right)^{1/3} \frac{d}{dx} \frac{h_{xx}}{[1 + (h_x Re/8)^2]^{3/2}} + \frac{h_x}{h^3} + 1 - \left(\frac{h_{xx}}{h^2} - \frac{h_x^2}{h^3} \right) = 0 \quad (11c.3)$$

Here, h is half the curtain thickness, measured in units of $(Re/8)(4\mu/\rho)^{2/3}g^{-1/3}$; x is the distance along the symmetry axis of the curtain, measured in units of $(4\mu/\rho)^{2/3}g^{-1/3}$; and h_x and h_{xx} are the first and second derivatives of h with respect to x . The Reynolds number is $Re = \rho Q/\mu$, the Stokes number is $St = \rho g W^3/\mu Q$, and the capillary

number is $Ca = \mu Q/W\sigma$, where $2W$ is the slit clearance. Kistler (1983) used equation (11c.3), and similar ones for deflected sheets, to provide outflow boundary conditions for finite-element analyses confined to sheet-forming zones.

Thus far, the formation and free fall of the curtain has been discussed independently of the impingement flow downstream. In certain flow regimes, however, capillarity can transmit a significant amount of upstream influence from the impingement region, and 'pull' the curtain in the direction of the substrate motion, resulting in a bent trajectory toward the substrate. This so-called 'pulled-film' phenomenon is observed when the flow rate is low or the curtain height is small. Because the phenomenon can cause film-breakage and hence limits operability, the exact range of conditions and countermeasures are discussed in Section 11c.5 on the coatability window.

11c.3.3 IMPINGEMENT ZONE

The flow in the impingement zone is, of course, at the heart of curtain coating, for it largely controls the operating behavior of the process. Kistler (1983) was the first to investigate the evolution of free-surface shape and associated flow field in the impingement region. He did so by performing finite-element calculations in the limit of very high capillary numbers where the Reynolds number $Re = \rho Q/\mu$ and the ratio U/V of the substrate speed U to the impingement speed V become the dominant parameters. Figure 11c.12 shows that high Reynolds numbers or, equivalently, high flow rates, and also low speed ratios promote the formation of a pronounced 'heel' that pushes the dynamic wetting line upstream. At small values of Re and large values of U/V , on the other hand, the dynamic wetting line tends to get pulled underneath the impinging curtain. Kistler (1983) generated the contours in Fig. 11c.13 of various flow variables in the impingement zone. The contours of pressure and stress clearly signal a singularity at the dynamic contact line. The pressure contours also reveal the buildup of an impact pressure right underneath the impinging curtain. Downstream, the flow

rapidly evolves into a parallel, fully developed flow. The rapid development of the flow is caused by the strong shear stress imparted by the substrate, which gives rise to a boundary layer that emanates from the vicinity of the dynamic wetting line. For cases with larger heels than those in Fig. 11c.12, Ogawa, Kashiwabara and Scriven (1992) demonstrated agreement between computed stream lines and experimental flow visualization employing hydrogen bubbles and fluorescent dyes, as illustrated in Fig. 11c.14.

Heel formation is closely associated with an operating bound because, as the heel grows large, it typically incorporates one or several recirculating eddies. These eddies may trap bubbles or degraded particles of the coating solution, which in turn can cause coating streaks. Large heels may also be susceptible to various instabilities, including instabilities that result in periodic flow structures in the cross-web direction, and a special kind of air-entrainment (Kistler 1983). Kistler (1983) explained how the position of the dynamic wetting line and the closely related size of the heel can be estimated from a boundary-layer theory for moving flat surfaces (Sakiadis 1961). Details of the model and specific results are described in Section 11c.5 below on the coating window.

The phenomenon of the dynamic wetting line getting pulled underneath the impinging curtain is also closely linked to an operating limit, namely massive, visible air entrainment. Not only this limit, however, but also dynamic wetting below that limit and its exact influence on successful curtain coating is associated with considerable quantitative uncertainty, especially as far as theoretical analysis is concerned. The reason is that the physics of the local liquid-air displacement process are not completely understood (for an in-depth discussion, see Chapter 3). Miyamoto and Scriven (1982) advanced the hypothesis that 'a thin air film is always entrained and subject to breakage and dissolution'. This hypothesis is supported by experimental evidence from works by Muës, Hens and Boij (1989) and Miyamoto (1991). However, quantitative sub-microscopic models are still lacking that can

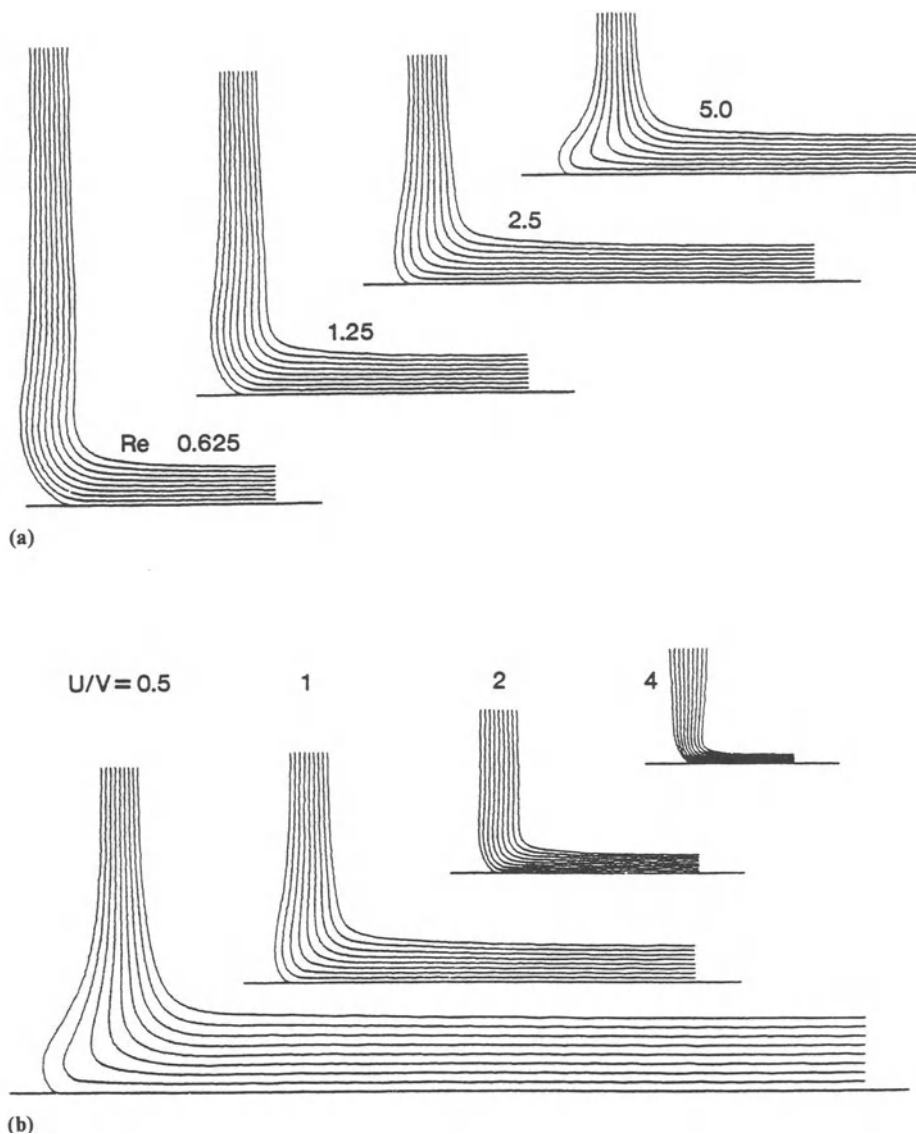


Figure 11c.12 Heel formation and pulled film for $Ca = 100$ (Kistler 1983). The symbols are explained in the text. (a) $U/V = 1$; (b) $Re = 2.5$.

predict both the apparent dynamic contact angle under successful coating conditions and the rate of momentum transfer through an entrained and collapsing air film.

In spite of the quantitative uncertainty at the dynamic wetting line, the steady, macroscopic flow field in the impingement zone is fairly well

understood, as evidenced by the results cited above (*cf.* Figs 11c.12 to 11c.14). The air entrainment that presumably occurs during successful coating is very local and does not affect the global flow as long as the air film is thin enough so as not to cause instability in the liquid layer. Nevertheless, in coating flow analyses at

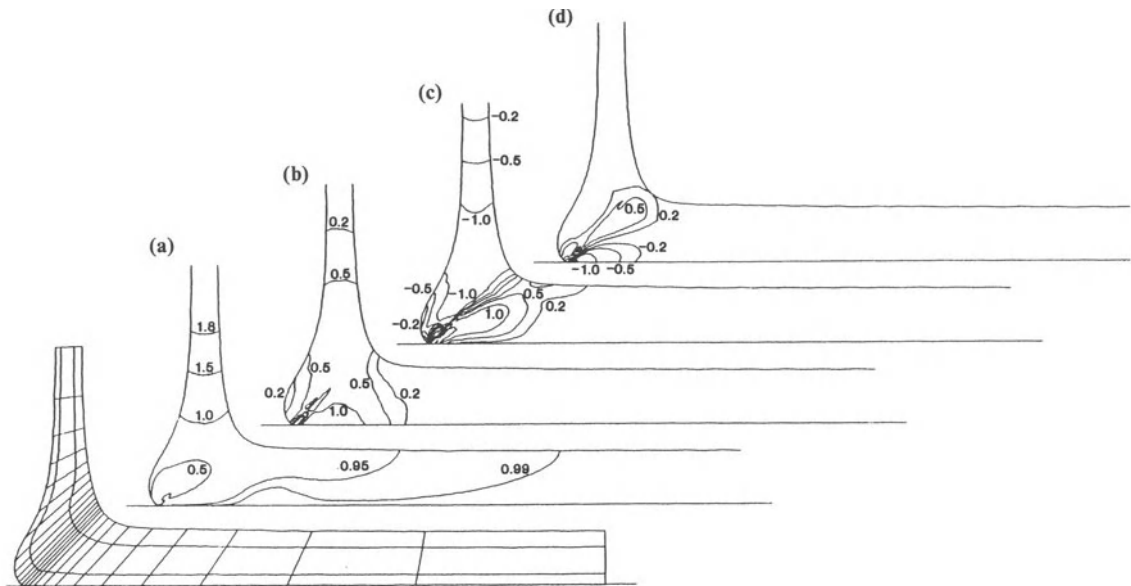


Figure 11c.13 Details of flow field in impingement zone (Kistler 1983): (a) particle speed; (b) pressure; (c) normal stress difference; (d) shear stress. $Re = 2.5$, $U/V = 0.5$, $Ca = 100$.

macroscopic length scales, the above-mentioned uncertainty manifests itself in two unsettled difficulties: one is the need to impose an apparent dynamic contact angle which remains an arbitrary input parameter unless taken from some experiment or empirical correlation; the other is the choice of an appropriate slip coefficient in an *ad hoc* boundary condition that removes the singularity at the dynamic contact line. Kistler (1983) avoided the first difficulty by computing in the limit of high capillary numbers and specifying no contact angle at all. This is feasible because a specified contact angle affects the computed free surface profile only in the immediate proximity of the contact line. Ogawa and Scriven (1994) examined the effects of specified dynamic contact angles by comparing four cases, namely, Kistler's formulation, one specifying 140° , one specifying 170° , and a hybrid of Kistler's and specifying 140° . The computed dynamic-contact-line positions showed insensitivity to both a specified contact angle and the slip coefficient.

11c.4 SENSITIVITY TO SMALL DISTURBANCES

11c.4.1 STABILITY OF A LIQUID CURTAIN

The formation of a stable liquid curtain is the first step in a successful curtain coating operation. At low flow rates, the liquid curtain tends to detach from the edge guides or break into individual streams. As the flow rate is reduced further, the liquid dribbles off in the form of individual droplets from various places at the lip of the coating die. Pritchard (1986) observed a number of unstable flow patterns in liquid films that fall from the end of a plate at low Reynolds numbers.

The film thickness at the foot of the curtain, which generally is at most several times the final coating thickness, is less than the thickness of the coating beads in other die coating methods. Consequently, the capability of curtain coating in depositing a thin film at low coating speeds falls well behind slide coating, which is also used

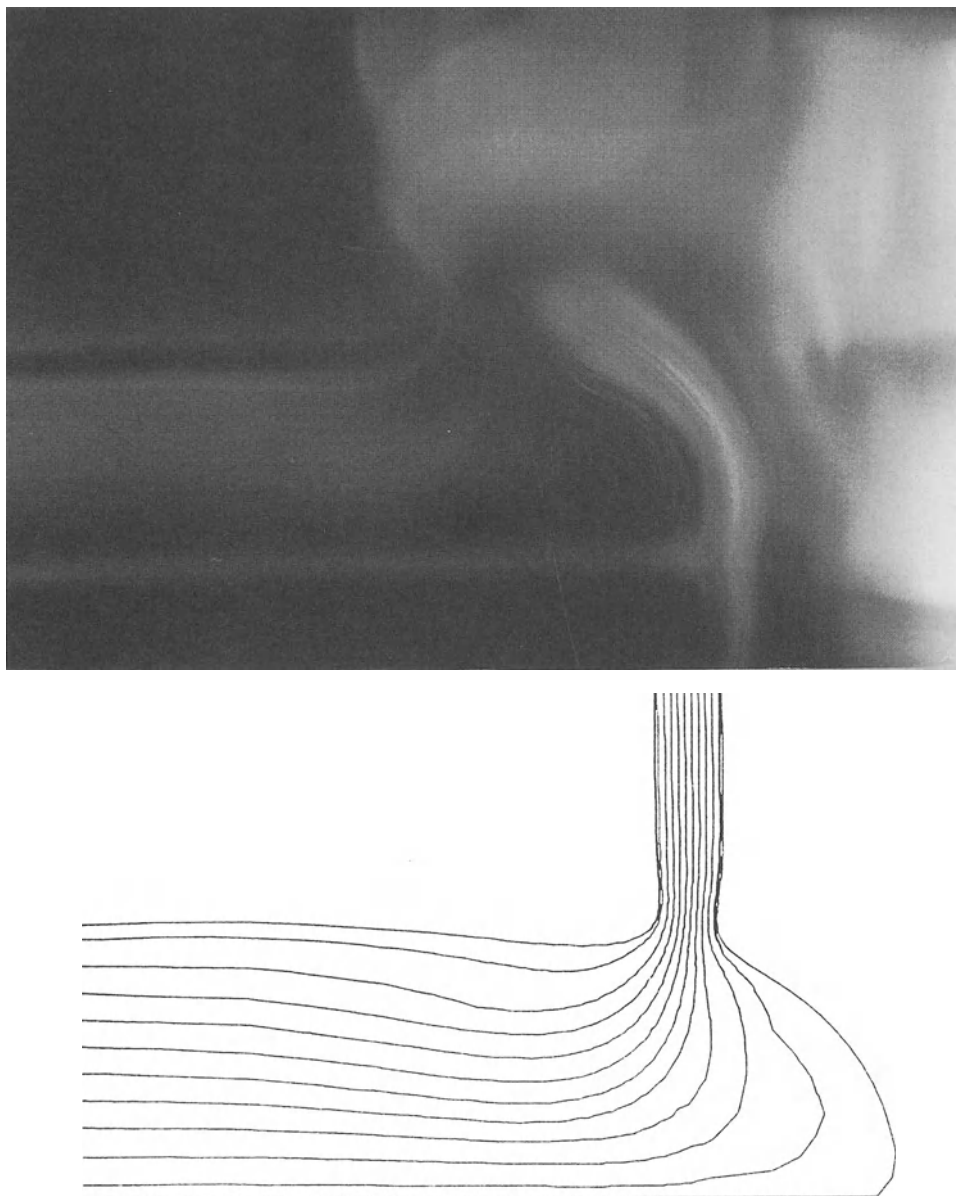


Figure 11c.14 Impingement flow: comparison of theory and experiment (Ogawa, Kashiwabara and Scriven 1992). $Re = \rho Q / \mu = 10$, $Ca = \mu U / \sigma = 0.08$, $U/V = 0.29$.

as a precision multilayer coating method. Greiller (1972) suggested that the minimum flow rate to form a stable curtain with an aqueous gelatin solution containing surfactants is around $0.5 \text{ cm}^2/\text{s}$ (per unit width of the curtain). Our experience has been that this value is close to the practical

limit. On the other hand, slide coating can be operated at a flow rate less than $0.1 \text{ cm}^2/\text{s}$ if the web runs slowly enough. Therefore, curtain coating is most suitable for high speed coating when moderate coating thicknesses are desired. A long curtain, which is advantageous in delaying the

onset of air entrainment (see Section 11c.5 below), is more difficult to form in practice than a short one. Curtain heights up to 250 mm are recommended, based on both stability and operability considerations.

Greiller's (1972) experimental results furthermore suggest that there is an optimum range for liquid viscosity, and that surfactants play an important role in stabilizing the curtain (Fig. 11c.15). Greiller did not offer an explanation for the optimum in viscosity. A possible scenario might be that increasing viscosity enhances damping of disturbances and thereby stabilizes the curtain but, at the same time, accelerates the boundary layer development along the edge guide and thereby promotes breakage of the curtain. The effect of surfactants may be attributed to the reduced surface tension and to surface elasticity, as is often the case in the stability of film flow down an inclined plane (see Chapters 4 and 11d). At the edge of the curtain, surfactants act either to prevent contraction of the curtain by enhancing the wettability of the edge guide, or promote contraction by the Marangoni effect. This point is discussed further in Section 11c.6.

Several authors have reported theoretical stability analyses of falling liquid curtains in attempts to describe the operating bound that arises from the low-flow limit. Brown (1961) followed Taylor's (1959) analysis of the stability of a water bell. Taylor's stability argument is based on a simple momentum balance on a free edge that would result from the formation of a hole in the liquid sheet (Fig. 11c.16). The inertia force $\rho V^2 H$ (or ρQV) must be greater than the surface tension force 2σ for such a hole not to grow and be carried away with the liquid stream. Here, H is the thickness of the curtain, and Q is again the volumetric flow rate per unit width. The resulting condition for stability is

$$\rho V^2 H > 2\sigma \text{ or } \rho QV > 2\sigma \quad (11c.4)$$

In dimensionless form, (11c.4) becomes

$$We > 2 \quad (11c.5)$$

where $We = \rho QV/\sigma$ is the Weber number which compares inertial forces with surface tension

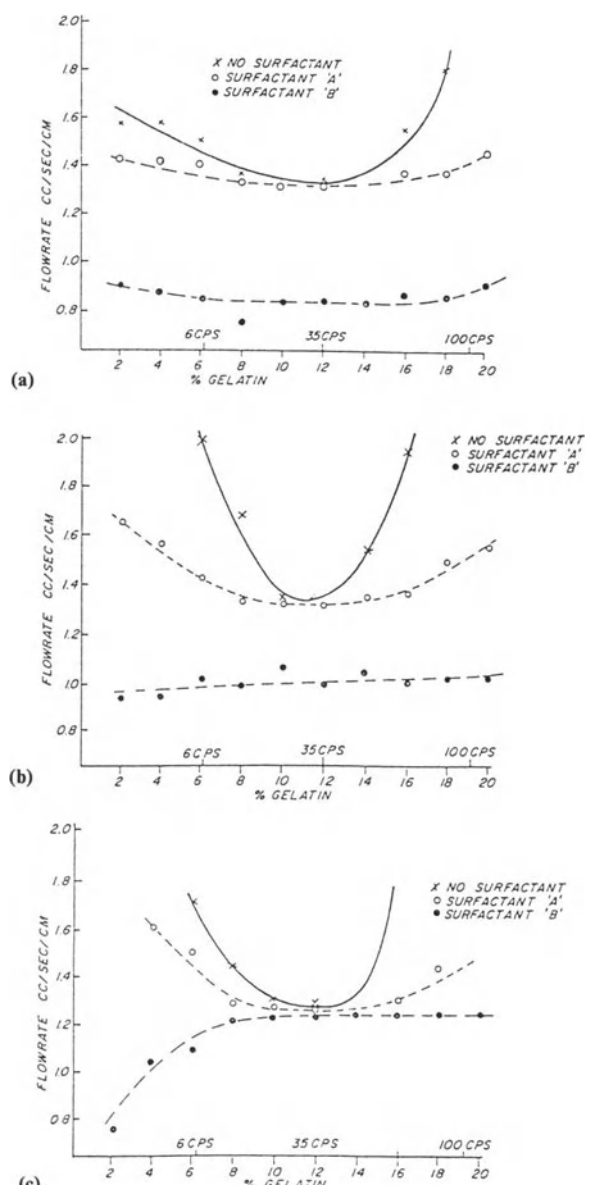


Figure 11c.15 Minimum flow rates for curtain stability (Greiller 1972): (a) flow rates to which a falling curtain, first established at a high flow rate, can be reduced without breaking; (b) flow rates at which the free-falling curtain is resistant to breaking upon introducing a solid object into the curtain and moving it about; (c) flow rates at which the free-falling curtain will reform on its own after being deliberately broken.

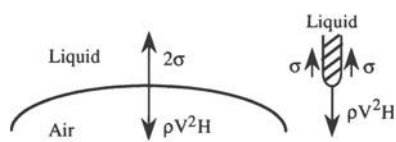


Figure 11c.16 Forces acting at the free edge that would result from breakage of a falling liquid sheet.

forces. Brown (1961) suggested that (11c.5) must hold right above the impingement zone where large disturbances may exist. Of course, this simple analysis cannot explain the whole story of curtain stability. In fact, Brown's experiments themselves showed that the region near the slot exit is apparently stable even though the simple stability criterion is not satisfied because of low speeds.

Lin (1981) carried out a linear stability analysis of falling liquid sheets, employing a first order approximation that takes into consideration both spatial and temporal disturbances. He predicted that only those spatially growing sinuous disturbances are unstable whose group velocity is in the upstream direction. In other words, they are unstable if the velocity of the wave propagation in the upstream direction is greater than the velocity of the fluid particle falling downstream. This turns out to be the case exactly when $We > 2$. However, a later analysis by Lin, Lian and Creighton (1990) shows that, when $We > 2$, the curtain is stable in a vacuum and is convectively unstable (i.e. asymptotically stable) in the presence of surrounding gas. When $We < 2$, the large-time asymptotic amplitudes of sinuous disturbances is nonvanishing but bounded. In conclusion, a falling curtain of finite length is stable to small disturbances in all cases, which contradicts Lin's earlier results.

Do and Christodoulou (1992) presented results from a full-fledged finite-element stability analysis (*cf.* Chapter 9) and found that curtain-coating flows are linearly stable for both two-dimensional and three-dimensional disturbances. Their finding supports the conclusion of the latest work of Lin and co-workers.

Finnicum, Weinstein and Ruschak (1993) tested

the stability of a falling curtain in experiments. They applied different pressures to each side of a falling curtain, and found that practically stable curtains can exist over wide ranges of flow conditions, including conditions that violate the simple stability criterion $We > 2$.

Altogether, recent theories and experiments concur in supporting the conclusion that falling curtains are linearly stable regardless of the Weber number. So how does a falling curtain disintegrate? Edge effects may be the key: they cause local thinning of the curtain near edge guides which could trigger break-up. Many solutions have been proposed to prevent such local thinning of the curtain. They include injection of an additional liquid stream to the edge region, or optimization of the edge guide designs (see Section 11c.6 for more details). Another likely cause for loss of curtain integrity comes from nonlinear effects such as those arising from contaminants and bubbles in the liquid, which may become nucleation sites for holes growing in the curtain (Do and Christodoulou 1992).

11c.4.2 RESPONSE TO SMALL DISTURBANCES

The study of coating sensitivity to small, ongoing disturbances is of great importance from a practical standpoint. Several computational analyses of curtain coating have been carried out, all based on the finite-element method (consult Chapter 9 for details on the various methodologies). Kaneko and Scriven (1988) analyzed the case of short curtains with an applied pressure difference. They used a linearized transient analysis, i.e. time integration of the governing Navier–Stokes system linearized about the steady state of interest. Katagiri (1990) compared slide and curtain coating in regard to their frequency responses with various kinds of disturbances by solving the fully nonlinear, time-dependent equations directly. Ogawa and Scriven (1990) reported results from a linearized frequency response analysis for single- and two-layer curtain coating. Do and Christodoulou (1992) performed a linear stability analysis of curtain coating with respect to two- and three-dimensional disturbances.

All the analyses suggest in essence the same general result, namely that curtain coating is highly susceptible to small disturbances acting on the unsupported liquid sheet. This is not surprising, as a very small difference in pressure between the two sides of a curtain will drastically alter the trajectory of the curtain (Finnicum, Weinstein and Ruschak 1993). If the applied pressure difference oscillates sinusoidally in time, the curtain undergoes a swinging motion like a pendulum. As a consequence, the coated film will suffer a large-amplitude unevenness in the down-web direction (i.e. 'barring'). Figure 11c.17 shows the frequency response of the coating thickness in curtain coating to sinusoidally varying disturbance in pressure at the upstream free surface of the curtain, and compares it with the response of slide coating to an oscillating disturbance in applied vacuum. The difference in amplitude reaches two orders of magnitude, curtain coating

evidently being much more sensitive to small pressure variations than slide coating.

In reality, air currents disturb a curtain randomly rather than pushing the curtain over its entire width simultaneously. As a result, the coated layer exhibits wide bands of streak-like unevenness. When the coating liquid contains a volatile solvent, the Marangoni effect originated by the irregular solvent evaporation magnifies the unevenness of the final coated layer. Therefore, the amount of volatile solvent in the lowermost and uppermost layers should be minimized. To protect the curtain from the air flow carried by the moving web, an air shield is essential. The influence of ambient air currents, such as the air flow used to condition the entire coating room, should also be minimized. Systems designed to contain the deleterious influence of air flows are reviewed in more detail in Section 11c.6.4.

Whereas the falling curtain is highly susceptible to ongoing external disturbances, the coating bead in the impingement zone is more tolerant of disturbances than the coating bead in other pre-metered coating methods. Examples of the second type of disturbances include fluctuations in coating speed (Fig. 11c.18), heterogeneous

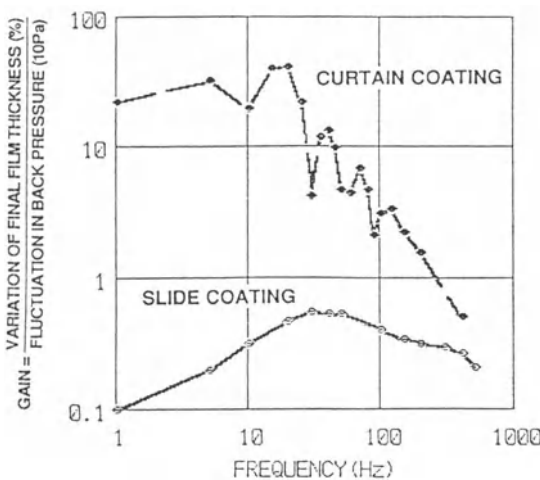


Figure 11c.17 Computed frequency responses of slide and curtain coating to perturbations in surrounding pressure (Katagiri 1990). The vacuum is perturbed by ± 40 Pa in slide coating; the pressure at the upstream free surface of the curtain is perturbed by ± 1 Pa. $\rho = 10^3$ kg/m 3 ; $\eta = 20$ mPa s; $\sigma = 40$ mN/m; H_∞ (final film thickness) = 1.05×10^{-4} m; $U = 1.67$ m/s; α_s (slide angle in slide coating) = 15° ; L (gap) = 2.5×10^{-4} m; ΔP (vacuum in slide coating) = 150 Pa; α_c (slide angle in curtain coating) = 45° ; H_c (curtain height) = 0.02 m.

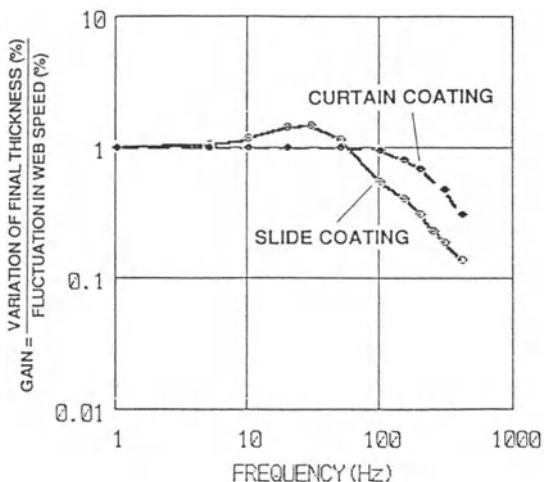


Figure 11c.18 Computed frequency responses of slide and curtain coating when the web speed is perturbed sinusoidally by $\pm 5\%$ (Katagiri 1990). The parameter values are the same as in Fig. 11c.17.

surface energy of substrates (Fig. 11c.19), wavy substrates, and splice passages. Such disturbances affect only a localized region around the dynamic contact line and immediately downstream. The curtain remains intact because the disturbances do not propagate upstream (see Lin (1981)). Figure 11c.20 shows the computed maximum

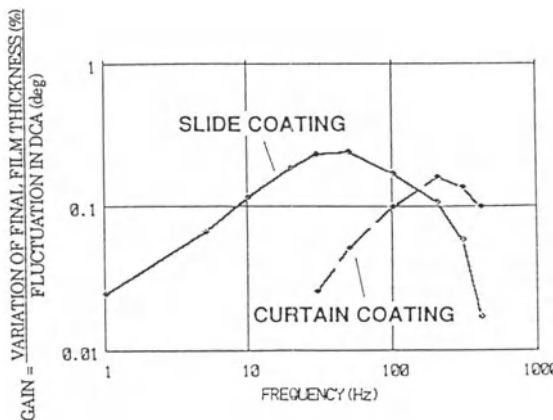


Figure 11c.19 Computed frequency responses of slide and curtain coating when the dynamic contact angle is perturbed sinusoidally by $\pm 5^\circ$ (Katagiri 1990). The parameter values are the same as in Fig. 11c.17.

movement of free surfaces in curtain coating when the web speed fluctuates by $\pm 5\%$ (Katagiri 1990). Clearly, a localized area, particularly inside the boundary layer along the web, is disturbed whereas the liquid curtain remains steady. This resilience to perturbations in the coating bead is the reason why curtain coating can be used to coat discontinuous materials or air-supported webs (see Fig. 11c.21, taken from Yoshida *et al.* (1978)). For the same reason, electrostatic assist works very well in combination with curtain coating: a heterogeneous electrostatic charge distribution on the web causes less unevenness in curtain coating than in slide or slot coating.

Ribbing, a corduroy-type pattern of regularly spaced lines in the down-web direction which is often seen in slide or slot coating (see Chapters 11a and 11b), is not normally observed in curtain coating. Ribbing results from an instability of a two-dimensional viscous free-surface flow to three-dimensional disturbances. Finite-element stability analysis corroborates that curtain coating is stable to such disturbances (Do and Christodoulou 1992). Rib-like streaks, however, are sometimes encountered in curtain coating of non-Newtonian liquids. A detailed analysis of this phenomenon has not yet been performed.

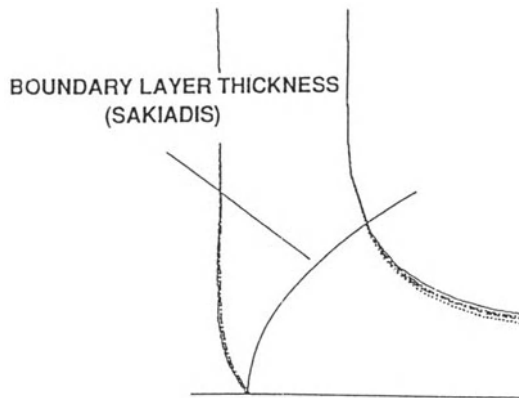


Figure 11c.20 Calculated maximum movement of free surfaces in curtain coating when the web speed is perturbed sinusoidally $\pm 5\%$ with a frequency of 30 Hz (Katagiri 1990). The parameter values are the same as in Fig. 11c.17.

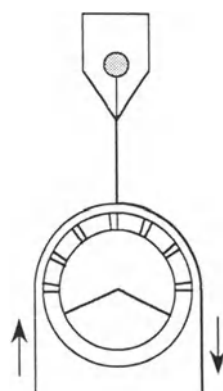


Figure 11c.21 Curtain coating on air supported substrate (Yoshida *et al.* 1978).

11c.5 OPERABILITY

11c.5.1 COATING WINDOW

The dimensionless groups which govern the flow field in the impingement region of curtain coating are the Reynolds number $Re = \rho Q / \mu$, the web speed normalized by impinging velocity, U/V , and the capillary number $Ca = \mu V / \sigma$. Kistler (1983) showed, by means of finite-element analysis, that the limiting regime of high capillary numbers provides a good approximation to curtain coating at high speeds, for it captures many of the essential characteristics of impingement flow. In the limit of $Ca \rightarrow \infty$, the coating window can be drawn in a plane of Re versus U/V , for it depends only on those two dimensionless groups. Figure 11c.22 shows a schematic of such a coating window; Fig. 11c.23 shows photographs of unsuccessful curtain coating past several of the limits. The phenomena limiting successful curtain-coating operation are:

- curtain disintegration at low flow rates (already discussed in Section 11c.4 and then taken up further in Section 11c.6);
- pulled film phenomenon at low flow rates and low coating speeds (see Fig. 11c.23a below);
- air entrainment at high coating speeds and relatively low flow rates (see Fig. 11c.23b);

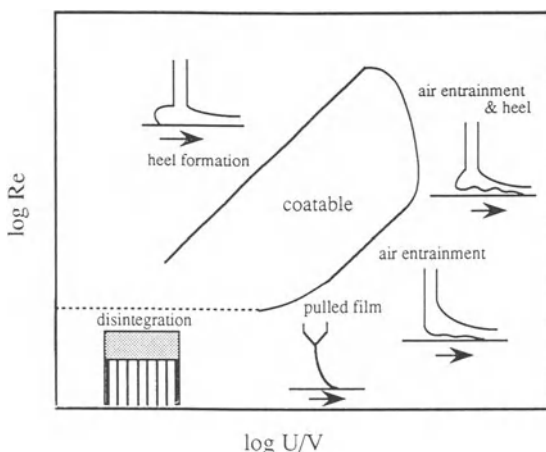


Figure 11c.22 Schematic of coating window in curtain coating.

- heel formation at high flow rates and low coating speeds (see Fig. 11c.23c);
- air entrainment with heel formation at high flow rates and high coating speeds (Fig. 11c.23d).

11c.5.2 PULLED FILM

A highly bent curtain without a freely falling part tends to form at low flow rates and low coating speeds (Fig. 11c.23a). The mechanism can be explained as follows. As the flow rate is reduced, the viscous drag imparted by the substrate shifts the dynamic contact line downstream and forces the curtain to bend near the impingement region. At the bent upstream meniscus, capillary forces balance the inertia force of the falling liquid. Below a certain flow rate, the capillary pressure dominates over the inertia force and the curtain starts to be pulled. The Weber number, which is the ratio of inertia forces to surface tension forces (cf. Section 11c.4.1), is the appropriate dimensionless index for this phenomenon. The pulled film is typically close to instability and a slight reduction of the flow rate causes the curtain to break up.

Ogawa, Kashiwabara and Scriven (1992) predicted the film pulling phenomenon from a finite-element analysis of one-phase flow, that is, they neglected air flow. Examples of their analysis are given in Fig. 11c.24. These authors also performed flow visualization, and confirmed that the free surface shapes are well predicted by the computational analysis. Their numerical predictions reveal that high surface tension and low curtain heights promote the pulled-curtain phenomenon (Fig. 11c.25), in accord with the explanation given above. In Fig. 11c.25, the criterion used to delineate the pulled-film regime is whether or not the dynamic contact line is located past the vertical extension of the downstream free surface of the curtain which, at the onset of the pulled-film regime, still exhibits a region of near-vertical fall. Experimental observations, corroborated by finite-element predictions, indicate that liquid viscosity and coating speed have a relatively small effect on preventing film

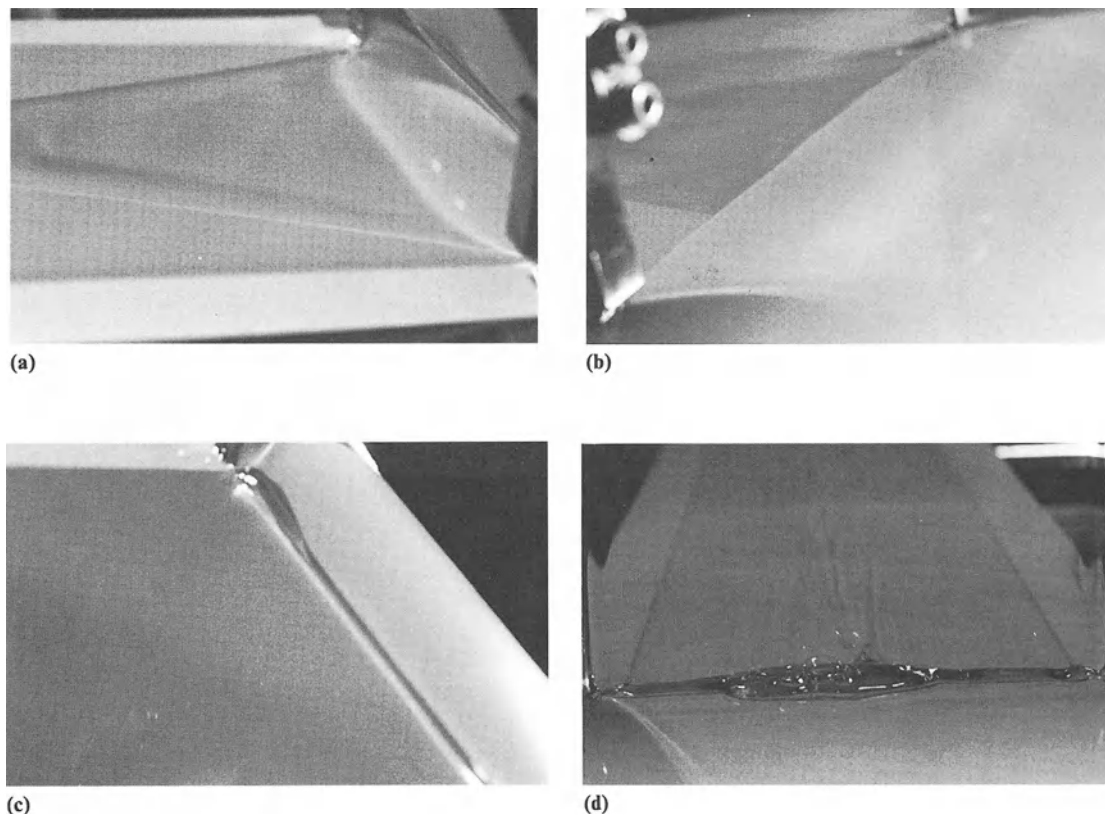


Figure 11c.23 Photographs of limiting phenomena in curtain coating: (a) pulled film; (b) air entrainment; (c) heel; (d) air entrainment with heel.

pulling. Likewise, air flow, which might be suspected to be highly influential, turns out to be insignificant in the pulled-curtain phenomenon.

The way to avoid the pulled-curtain effect and thereby widen the coating window is to increase curtain height if the curtain is sufficiently stable, or to lower the dynamic surface tension of the lowermost layer.

11c.5.3 AIR ENTRAINMENT

The large pressures created by the impingement of the freely falling liquid can suppress the intrusion of an incipient thin air film and thereby delay the onset of visible air entrainment in curtain coating. Brown (1961) reported that stable curtain coating can be accomplished at

speeds as high as 6 m/s with an impingement velocity of 1.4 m/s. The maximum coating speed claimed by Hughes (1970) is 10 m/s. These speeds are much higher than the speeds of dynamic wetting without deleterious air entrainment in plunging-tape experiments (cf. Chapter 3), and also the maximum operating speeds typically obtained with other die coating methods.

Nevertheless, air entrainment is still a key phenomenon in curtain coating, and can limit the maximum coating speed. Past the limit, V-shaped air pockets followed by streaks of entrained air bubbles are often seen, as shown in Fig. 11c.23(b). These features closely resemble those associated with air entrainment of a tape plunging into a pool (see Chapter 3). It is generally presumed that air entrainment sets in when the

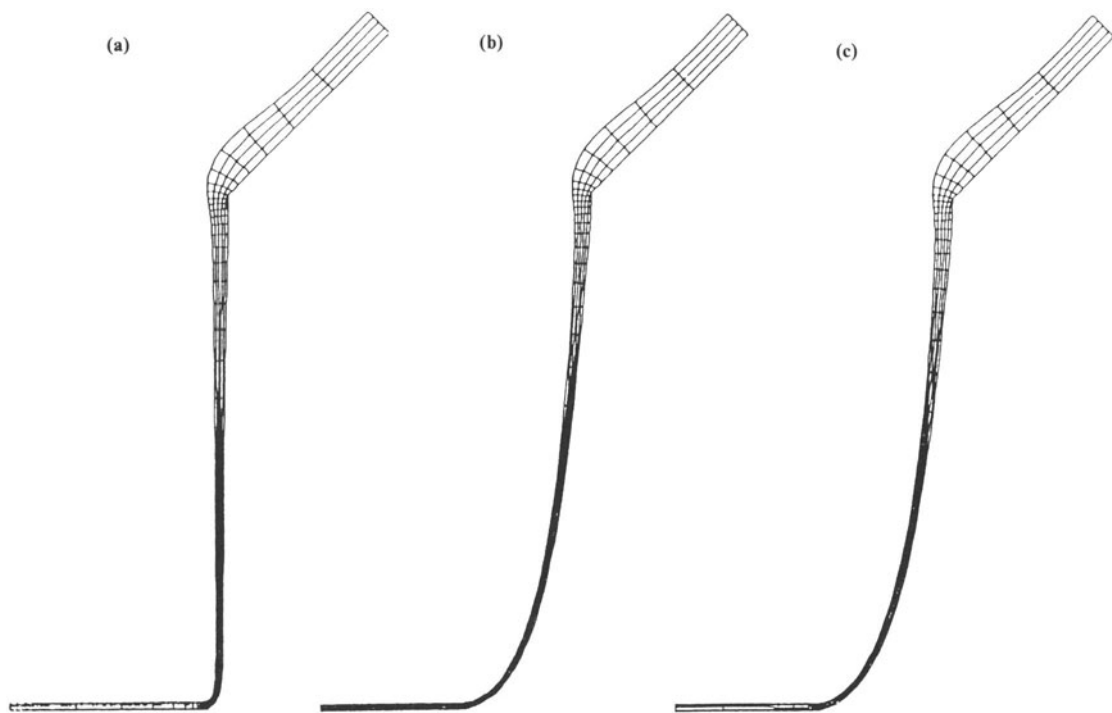


Figure 11c.24 Calculated effect of Re and Ca on pulled film phenomena (Ogawa, Kashiwabara and Scriven 1992): (a) not pulled ($Re = 7.4$, $Ca = 0.25$); (b) pulled (lower Q , viz. $Re = 6.7$, $Ca = 0.25$); (c) pulled (higher σ , viz. $Re = 7.4$, $Ca = 0.22$).

dynamic contact angle reaches 180° (see again Chapter 3).

Miyamoto (1986) observed two types of air entrainment with curtain coating: in the first, illustrated in Fig. 11c.26a, trails of bubbles and craters are visible in an otherwise well-coated film; in the second, on the other hand, the liquid layer is completely disrupted by the entrained air, as in Fig. 11c.26b. The first sample was obtained by coating a 122 mPa s aqueous gelatin solution on to a gelatin-subbed substrate. Miyamoto (1986) attributed the first type of air entrainment to a conjoining-pressure-driven collapse or a Rayleigh–Taylor type instability of a thin film of entrained air. According to the hypothesis by Teletzke, Davis and Scriven (1988), such a thin air film is always entrained between an advancing liquid and a substrate above a critical speed. Miyamoto and Scriven (1982)

suspected that the conjoining-force-driven instability breaks the air film into small bubbles. When the bubble number and size become excessive, visible air entrainment appears. Craters found in line together with bubbles were considered to be the outcome of the dissolution of small bubbles. The second type of air entrainment was obtained by coating a gelatin solution of a lower viscosity. Miyamoto (1986) attributed the resulting defect to a Kelvin–Helmholtz instability caused by the velocity difference between the liquid and the entrained air. However, all these hypotheses, which rationalize the two types of air entrainment by proposing two distinct mechanisms, have not yet been completely verified, and identification of the various mechanisms of air entrainment are still subject of ongoing research. A more detailed discussion can be found in Chapter 3.

Kistler (1983) obtained an operating window

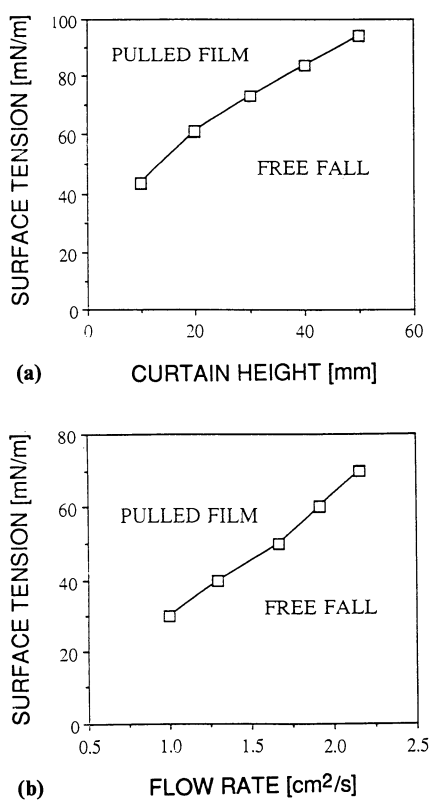


Figure 11c.25 Operating bounds arising from pulled film phenomenon (Ogawa, Kashiwabara and Scriven 1992): (a) effects of curtain height and surface tension; (b) effects of flow rate and surface tension. Base condition: $\rho = 10^3 \text{ kg/m}^3$, $\sigma = 60 \text{ mN/m}$, $Q = 1.9 \text{ cm}^2/\text{s}$, $\eta = 30 \text{ mPa s}$, H_C (curtain height) = 0.02 m, $U = 2 \text{ m/s}$.

for curtain coating from his finite-element analysis in the high-capillary-number regime and compared his predictions with experiments, as shown in Fig. 11c.27. He took computed solutions with an apparent dynamic contact angle of 180° to identify a hypothetical limit of air entrainment. This limit qualitatively captures the effect of the Reynolds number on air-entrainment velocity in experiments, as seen in the figure.

Blake, Clark and Ruschak (1994) rationalized the capability of curtain coating to coat at high coating speeds with the concept of ‘hydrodynamic assist’. Their starting point is the correlation

$U_s = 8.12[V \cos \alpha]^{0.81}/\eta_0^{0.19}$ that summarizes their experimental data for bone gelatin and a polyethylene terephthalate base. Here, U_s denotes the maximum coating speed, V is the impinging velocity, α is the inclination of the web from the horizontal plane at the point of impingement (α is positive when the web runs downward) and η_0 is the viscosity at zero shear rate (λ and n in the Carreau model are expressed as functions of η_0). Illustrative data are shown in Fig. 11c.28. The second ingredient in the explanation of Blake, Clarke and Ruschak (1994) is a simplified model that predicts the position of the dynamic contact line from boundary layer theory (see also Chapter 3). A comparison of experimental air-entrainment data and predicted dynamic-wetting-line positions revealed that the maximum coating speed without catastrophic air entrainment is highest when the wetting line is located beneath the impinging curtain. This finding suggests that the hydrodynamic forces resulting from the impact of the curtain delay the establishment of an air bearing between the liquid and the solid, and thereby ‘assist’ dynamic wetting.

The analyses of Kistler (1983) and Blake, Clarke and Ruschak (1994) make plain that long curtains and low-viscosity liquids are effective in delaying the onset of air entrainment. The rapid flow development near the dynamic wetting line suggests a positive effect of a shear-thinning coating liquid on delaying the onset of air entrainment (Kistler 1983; Ogawa and Scriven 1994). Another important parameter is the impingement angle of the curtain with respect to the substrate, as is also evident from the correlation obtained by Blake *et al.* Sone, Hanawa and Kageyama (1989) suggested that the preferred angle between the falling liquid sheet and the moving web ranges from 120° to 150° (the angle is measured on the upstream side of a curtain). The mechanism behind the impingement angle effect can be rationalized with the concept of ‘hydrodynamic assist’ but is not fully understood. The influence of surface energy of the solid substrate is weaker in curtain coating than in slide coating because hydrodynamic effects are so dominant in the impingement flow.

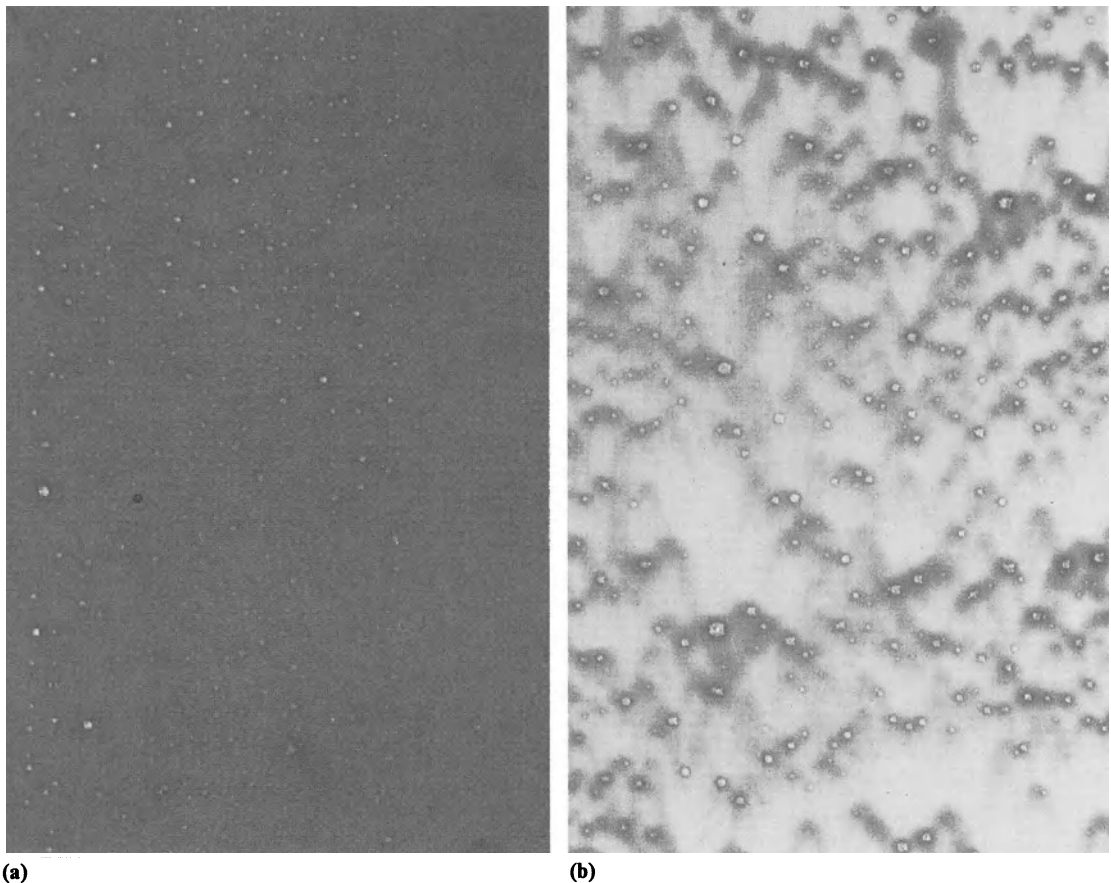


Figure 11c.26 Photographs of coated samples with air entrainment (Miyamoto 1986): (a) bubbles and craters on mostly well coated film (conjoining-force-driven instability); (b) completely disrupted layer (shear-driven instability).

11c.5.4 HEEL FORMATION

When the flow rate is increased, the dynamic contact line migrates upstream in proportion to the increase of the distance needed for the boundary layer to develop (see Fig. 11c.12). The resulting heel with its eddy often traps bubbles, agglomerates, gels, or other particles resulting from a deteriorated coating solution. Furthermore, in the presence of a heel, the dynamic contact line tends to not be straight, causing various types of down-web striations.

Kistler (1983) and Blake, Clarke and Ruschak (1994) explained heel formation by means of a simple model based on boundary layer theory

for moving flat surfaces (Sakiadis 1961). According to the model, the position of the dynamic wetting line is dictated by the development length needed for the displacement thickness of the boundary layer to reach the final film thickness. That development length is placed in the flow so that the corresponding nominal (99%) thickness of the boundary layer is reached at the vertical extension of the top free surface of the falling curtain. The final result for the dynamic contact line position x_* is

$$(1 - x_*) U/V = 0.383 Re \quad (11c.6)$$

where x_* is normalized by the thickness of the falling sheet and measured from the vertical

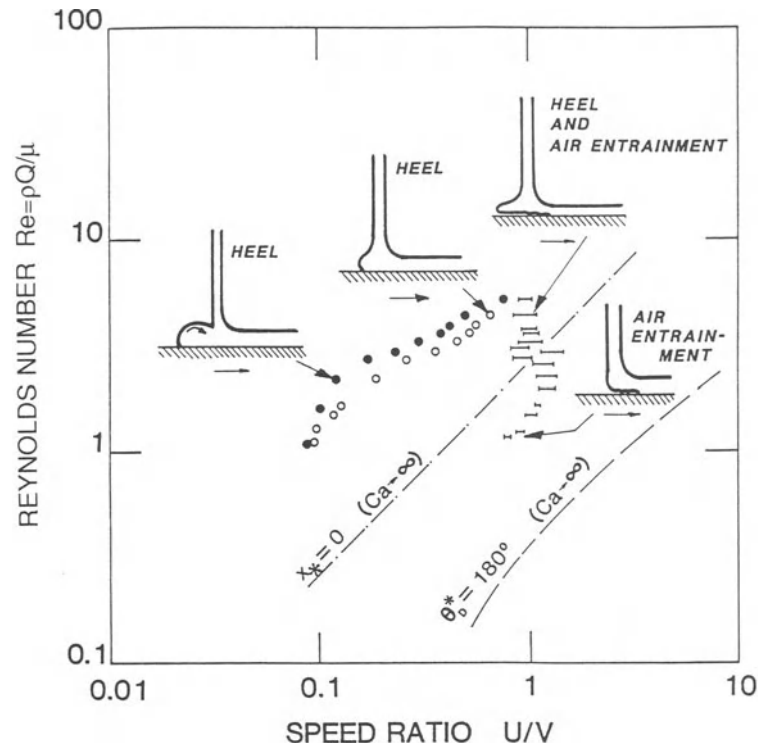


Figure 11c.27 Finite-element predictions of air entrainment and onset of heel formation, as well as comparison with operating limits measured in experiments (Kistler 1983). $Ca \cdot U/V = 3$; for definition of θ^* , see Section 11c.5.4 below.

portion of the rear free surface. Figure 11c.29 compares the contact line position estimated from equation (11c.6) with results obtained from finite-element calculations. The simple model suitably explains the mechanism of heel formation when the flow rate is increased. In Fig. 11c.27, experiments are compared with finite-element predictions. In spite of significant quantitative differences, the predictions approximately replicate the experimental trends. Altogether, the findings confirm that the dynamic wetting line position and associated heel formation are controlled by a balance between macroscopic, hydrodynamic mechanisms, namely the inertia of the impinging liquid and the momentum transfer that accelerates the liquid of the given volumetric flow to the final coating speed. At moderate capillary numbers, of course, surface tension also comes into play.

Measures to avoid large heels include increasing U/V and reducing Reynolds number. A higher surface tension shortens the length of the boundary layer through an increased pressure gradient in the bead and also makes the heel smaller.

11c.5.5 AIR ENTRAINMENT WITH HEEL FORMATION

At high flow rates, the maximum coating speed is bounded by massive air entrainment in the presence of a heel (Fig. 11c.23d). This regime of air entrainment is quite distinct from air entrainment at a low flow rate (Section 11c.5.3), and exhibits different flow characteristics. In particular, air entrainment in this regime seems to cause slip between the liquid and the substrate, which results in the formation of very large heels. A

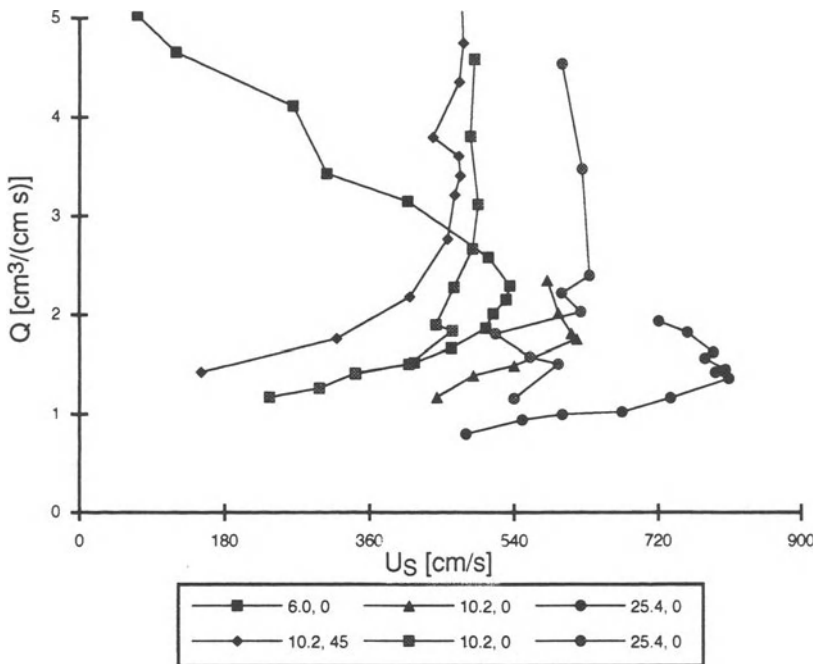


Figure 11c.28 Maximum coating speed of curtain coating (Blake, Clarke and Ruschak 1994). The data points indicate the conditions for clearing of air entrainment as coating speed is reduced. The liquids were aqueous solutions of bone gelatin with viscosities of 63 mPa s (black symbols) and 220 mPa s (gray symbols). The legend gives the curtain height H_c in centimeters, followed by the impingement angle in degrees (measured between the direction of web motion and the horizontal).

complete understanding of the mechanisms involved has yet to be reached. It is plausible, however, that air entrainment becomes massive in the presence of a heel because the heel lessens the hydrodynamic assist of wetting. The transition between flow states with and without air entrainment is very abrupt, and is accompanied by a dramatic change in heel size (in the regime described in Section 11c.5.4, in contrast, the heel changes size slowly and continuously as a function of flow parameters). There seems to be a nonlinear jump in the flow states, as is manifested by the existence of a hysteresis in air entrainment speed, reported by Blake, Clarke and Ruschak (1994). These authors found that the clearing speed of air entrainment when they decreased the flow rate is much lower than the speed at the onset of air entrainment when they increased the flow rate.

Kistler (1983) also noted bistable pairs of flow states with and without air entrainment, and plotted experimental limits of air entrainment in the presence of heels. Figure 11c.27 shows that, in that regime, the maximum coating speed decreases slightly when the flow rate is increased. At the time, finite element analysis was not developed enough to predict this phenomenon, which still awaits theoretical prediction.

Degrauwé and Hens (1986) coated a polyester base with aqueous gelatin solutions of various viscosities using a slide-fed curtain coating die. They found that the maximum coating speed is almost independent of the Reynolds number (which includes viscosity) and also curtain length (Fig. 11c.30). These findings suggest that, in the heel-flow regime, microscopic wetting mechanisms dominate over the macroscopic hydrodynamics.

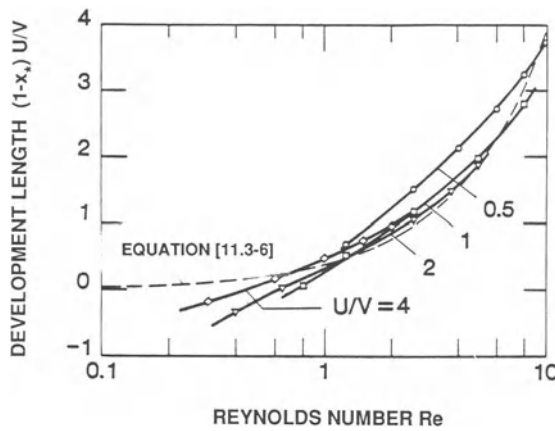


Figure 11c.29 Effect of Reynolds number and speed ratio on wetting line position: comparison of FEM calculation and a simple model based on Sakiadis' boundary layer theory (Kistler 1983).

Therefore, microscopic parameters such as surface energy of the substrate are important for maximizing coating speed. Surface roughness will have an effect as well, there being an optimal choice for surface roughness that is most effective in breaking up the entrained air. Hartman (1989), for example, showed that the maximum curtain coating speed of photographic materials on matt paper (rough) is higher than on glossy paper (smooth), in contrast to slide coating. Electrostatic assist is also effective to assist air displacement in the presence of a heel.

11c.6 PRACTICAL PROBLEMS

11c.6.1 LIP DESIGN

Curtain-coating dies of the slide-fed type usually incorporate an elongated, downward bent slide block along which the surface velocity of the falling film increases. This configuration involves numerous design factors, such as the inclination of the plane slide upstream, the radius of curvature of the elongated slide, the inclination of the slide at the terminating lip, and the angle at which the underside of the lip is cut back. Fahrni and Zimmermann (1978), in their patent, describe

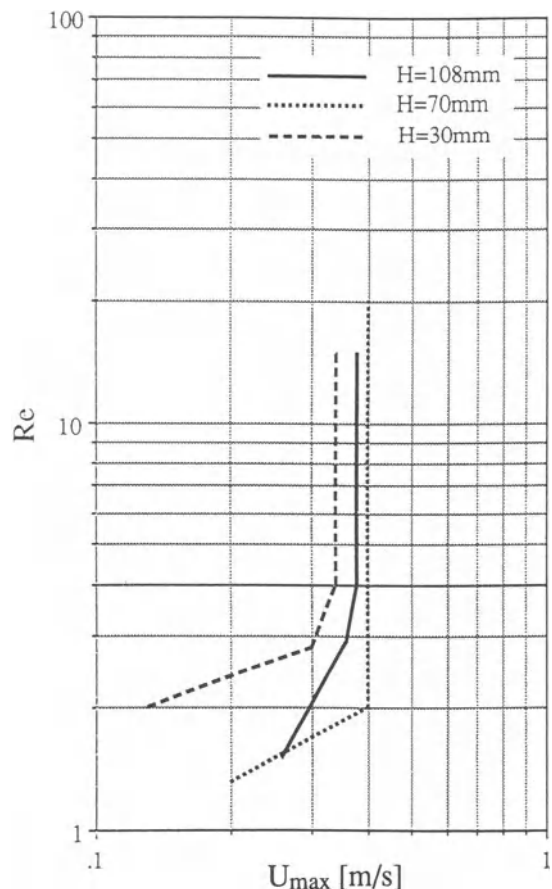


Figure 11c.30 Maximum coating speed of curtain coating (Degrauwé and Hens 1986). ν (kinematic viscosity) = 13, 25 and $38 \times 10^{-6} \text{ m}^2/\text{s}$, σ = 34 mN/m, H_C (curtain height) = 0.03, 0.07 and 0.108 m, Q = 1, 1.5, 2, and $2.5 \text{ cm}^2/\text{s}$.

suitable radii of curvature for the elongated slide surface, ranging from 20 to 40 mm. They claim that these radii reduce the minimum flow rate needed to maintain a stable curtain. Accelerating the liquid flow decreases the surface density of surfactants and increases the local surface tension, thereby reducing the difference in the surface tensions between the top and the bottom free surfaces. That way, the curtain is stabilized.

The inclination of the slide at the lip affects the teapot effect as mentioned in Section 11c.3.

So does the inclination of the cut-back of the lip underside, as is also explained in that section. In practice, of course, that inclination has an upper limit dictated by the shape of the lip and fabrication capabilities. Greiller (1975) showed an example of 30° from horizontal. Dittman *et al.* (1976) disclosed lip designs with a chamfered, overhanging slide and a cut-back on the underside, some of which Kistler and Scriven (1994) also analyzed. Fahrni and Zimmermann (1978) chamfered the lip to form a sharp edge.

11c.6.2 EDGE GUIDES

Edge guides are essential for maintaining the coating width of a curtain: without them, the curtain tends to contract into a triangular sheet and, sufficiently far downstream, forms a liquid cylinder. Edge guides can be a problem, however, because by necessity they involve three-dimensional flow fields that are prone to cause local variations in coating thickness. Edge guides can also significantly influence the stability of the curtain.

Several patents suggest the use of different liquids in the edge regions from those in the central region in order to obtain a stable curtain. Ridley (1977) proposed a system with three distinct partial curtains that together constitute an integrated curtain, as shown in Fig. 11c.31. In this system, the flow rate of the edge region can be increased independently to make the whole curtain stable, even when the central portion requires a lower flow rate. Improvements to this patent address the thick edge regions that are unattractive because they may delay drying. Watanabe, Tanaka and Yoshimura (1980), for instance, installed a jet of liquid adjacent to the edge guide as shown in Fig. 11c.32. They claim that a small amount of added liquid flowing in the direction of the curtain is sufficient to prevent shrinkage or breakage of the curtain. Recently, Reiter (1989) proposed an edge configuration that flushes the top part of the edge guides with a low-viscosity liquid, and then extracts most of that liquid by means of a suction device near the lower end of the edge guides. This improvement minimizes the drying load at the edges.

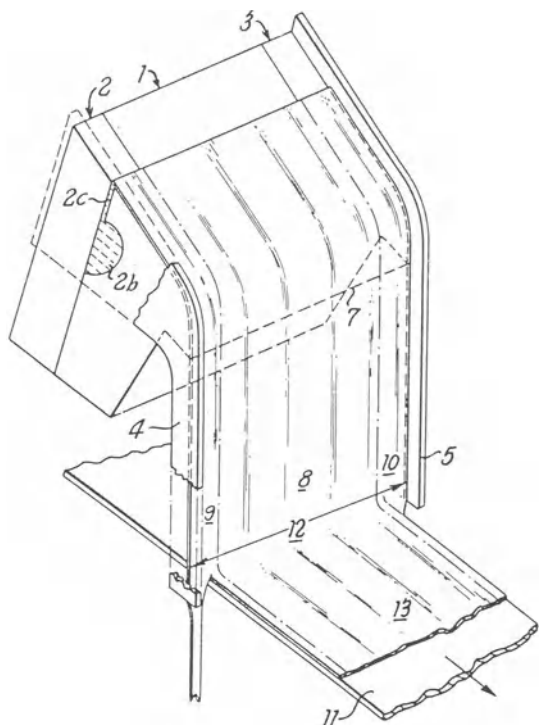


Figure 11c.31 Partial curtain at edge region (Ridley 1977).

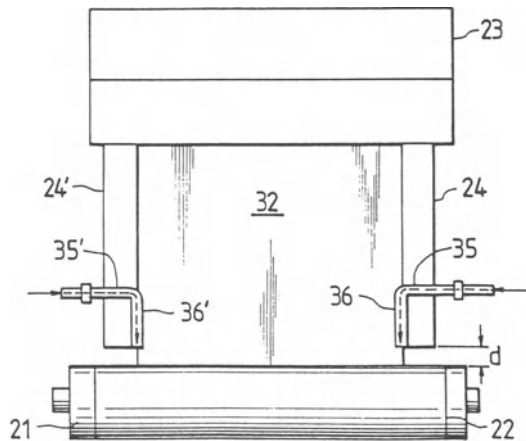


Figure 11c.32 Jet adjacent to guide bar (Watanabe *et al.* 1980).

A suitable choice of edge-guide material is also important for maintaining a stable curtain. Greiller (1975) used stainless steel rods which, since, have become standard. Other materials such as polyvinyl chloride and Teflon appear in examples of later patent embodiments. As a general rule of thumb, wettable materials assure a stable curtain but produce a thicker coated edge. Katagiri (1992) illustrated the effect of contact angle by means of fully three-dimensional finite-element calculations. His results suggest not only a strong influence on curtain thickness near the edge guide but also a danger of curtain break-up when the contact angle is large. The mechanism of the edge stability is quite complicated. Nishida (1990) measured the vertical and horizontal velocities in a curtain with a laser-Doppler velocimeter. He uncovered the development of a Blasius type boundary-layer along the edge guide, and a resulting flow toward the center of the curtain (Fig. 11c.33). This lateral flow creates a thin film near the edge guide. Katagiri (1992) analyzed the same flow field using the three-dimensional finite-element method mentioned already. His predictions (Fig. 11c.34) reveal the same flow characteristics as Nishida's measurements. The flow profile near the edges strongly depends on the capillary forces that arise from wetting of the edge guides by the liquid, and the forces coming from the surface tension gradient in the curtain caused by a difference of adsorption time between the central region and the edge region. The capillary force attracts the liquid toward the edge guides, and the surface tension gradient creates a flow toward the center of the curtain. Creating a balance of these effects is essential for preventing thinning of the curtain near the edge guides (Nishida, Katagiri and Suga 1992).

11c.6.3 START-UP

Two methods for starting up a curtain coating operation have appeared in patents. One method is to remove a catch pan that receives the falling liquid near the moving substrate during preparation or interruption of the coating machine, as shown in Fig. 11c.3. The other method is to

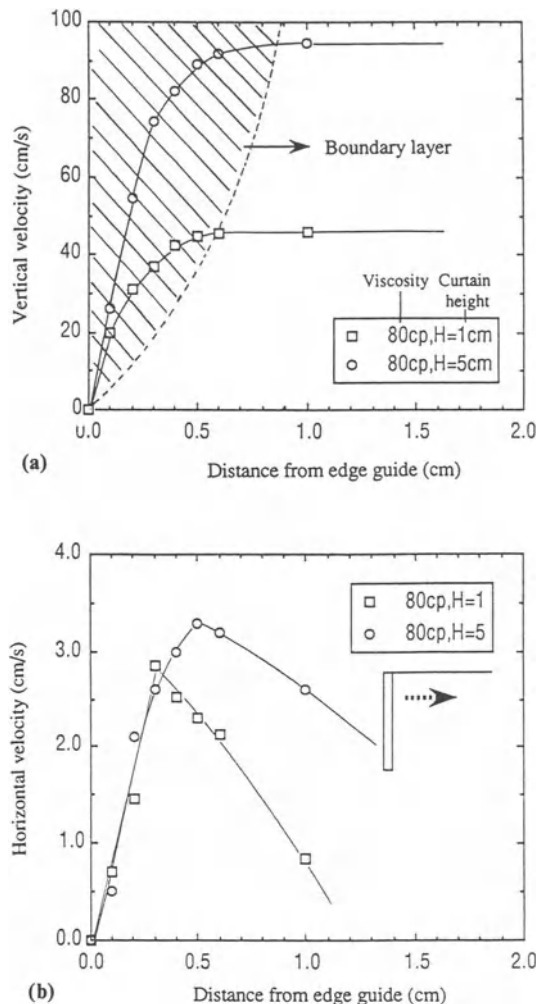


Figure 11c.33 Vertical and horizontal velocities obtained by laser-Doppler measurements in the curtain: (a) vertical velocities; (b) horizontal velocities (Nishida 1990).

move the curtain die from a holding station to the running web, as shown in Fig. 11c.35 (Kawahara and Yamagishi 1979). Several design improvements have appeared in patents. Reduction of the thickness at the very beginning of coating, where it is usually thicker than the subsequent normal position, is vital for high speed coating. Solutions have been proposed for improving the shape of the pan edge (Kozak 1989; Morikawa, Kobayashi and Miyamoto 1989).

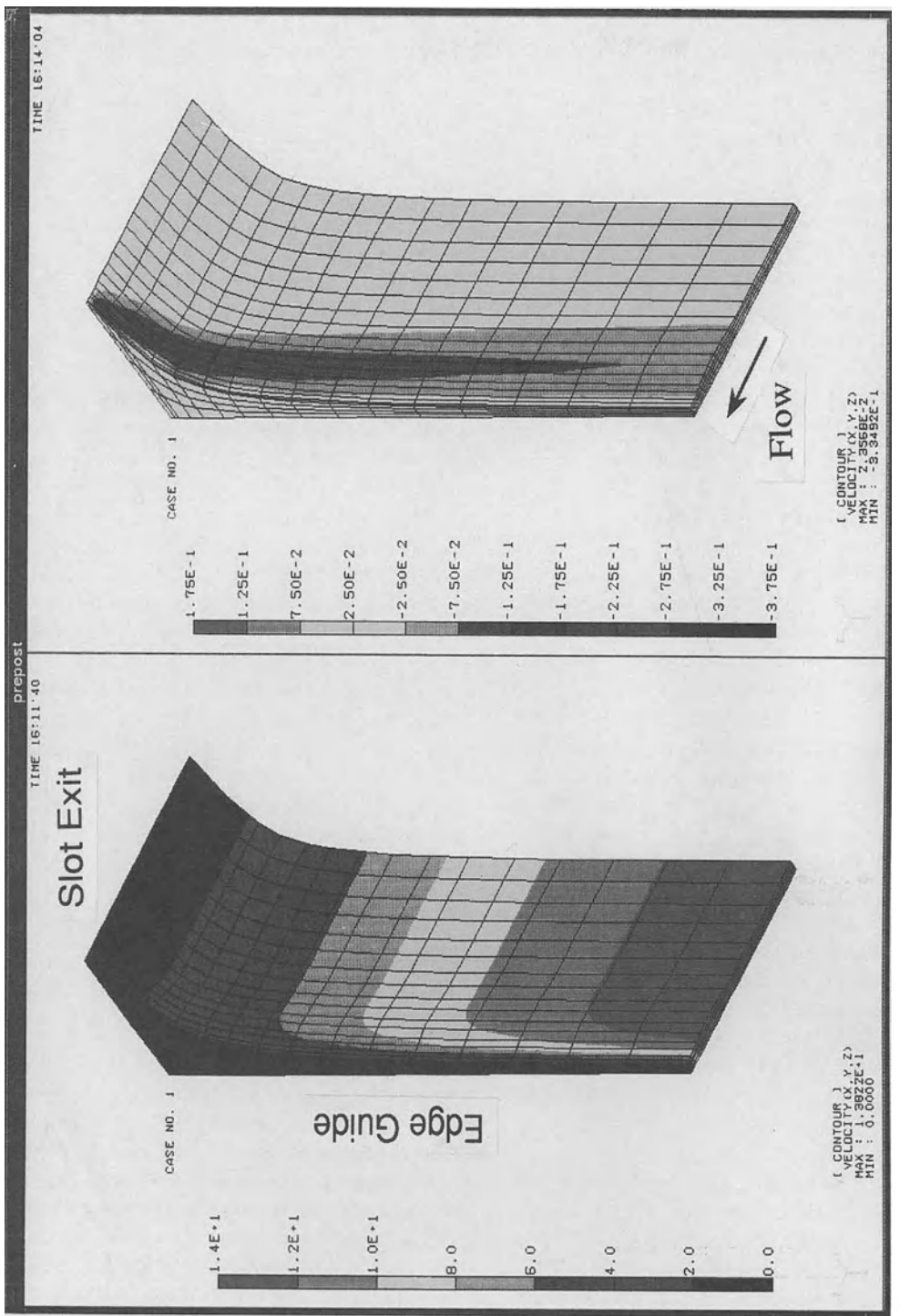


Figure 11c.34 Velocity contours obtained by three-dimensional finite-element analysis (Katagiri 1992); (a) vertical velocity contour; (b) horizontal velocity contour. $\rho = 10^3 \text{ kg/m}^3$, $\eta = 50 \text{ mPa s}$, $\sigma = 40 \text{ mN/m}$, $2W$ (slot clearance) = 0.04 m, $Q = 0.04 \text{ m}^3/\text{s}$, θ_c (contact angle at edge guide) = 90°, H_c (curtain height) = 0.1 m.

(a) (b)

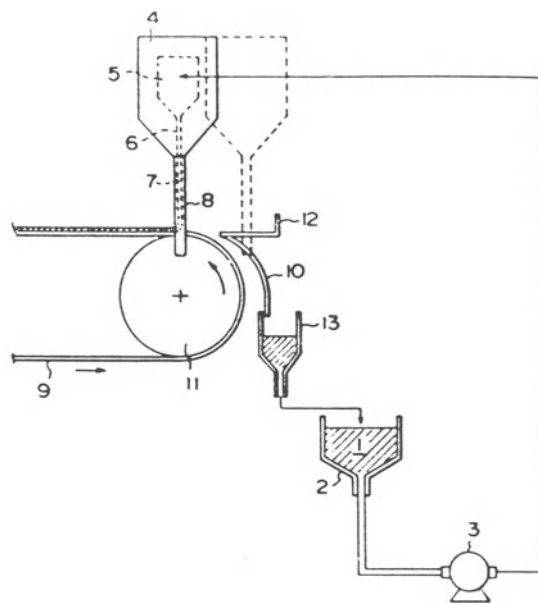


Figure 11c.35 Startup method of curtain coating (Kawahara and Yamagishi. 1979).

11c.6.4 AIR SHIELDS

Shielding the curtain sheet from ambient air flow and protecting the dynamic contact line from the impact of the air dragged towards the curtain by the substrate are important for achieving uniform coating. An air shield such as the one in Hughes' patent (Fig. 11c.3) is a basic way to prevent disturbances. Further refinements have been made since. Ridley, Denewtown and Stokes (1980) employed a curved rigid member placed in close proximity to the curtain and combined with a carefully controlled laminar gas flow to guide the trajectory of the falling liquid sheet over its entire height and thereby achieve a uniform wetting line. Morikawa and Kobayashi (1987) used a suction box as an air shield. Sone and Hanawa (1991) pressed a roller against the substrate just upstream of the impingement region. Ghys, Mues and Geerts (1992) used a concentric cover plate around a portion of the coating roll. All these designs are aimed at decreasing the impact of air flow on the falling

liquid sheet and the dynamic contact line. Another approach to preventing disturbances to the curtain is reducing the ambient air flow. O'Connor (1981) suggested shrouding the entire coater set-up with a porous, foam-like material.

11c.6.5 VARIABLE COATING WIDTH

A special feature of curtain coating is its ability to accommodate changes in coating width easily. A classic method employs a curtain that is wider than the substrate, unused liquid being caught in a pan (Greiller 1972). The coating width can even be made narrower than the web to leave uncoated parts on both sides. This may be important, for instance, when the substrate is a thin porous material such as paper that is weakened and prone to breakage when wet. Narrower coating widths can be achieved, for example, by folding the edge of the running web downward along both sides of a coating roll so that the liquid is attracted to the edge guide rather than the web (for a particular implementation, see Kawahara *et al.* (1983)). Further improvements in variable coating-width systems come from sliding catch pans, which are installed at both edges and slide in the cross-web direction to adjust the coating width (Kaneko and Naruse 1986). Another approach yet is to slant the die in the horizontal plane to reduce the effective coating width as described by Naruse (1985).

11c.7 CONCLUDING REMARKS

This chapter reviews theories, experiments and patents pertinent to curtain coating in order to give an overview of current curtain-coating technology, and to indicate directions for future developments.

Almost a century of continuous improvements and refinements have transformed curtain coating into a high-speed production process for multi-layered materials and many other precision-coated products. The outstanding feature of curtain coating is its operability at high speeds, mainly brought about by the impinging inertia of a freely falling liquid sheet. However, at the same time,

the unsupported liquid sheet is a source of many difficulties in practice. The intent of most of the patents reviewed in this chapter is to deal with these difficulties, and thereby facilitate operation of the process and improve coating quality. However, several patents typically exist for the same purpose, indicating a lack of a clearly optimal method as well as a lack of thorough understanding of the physics.

Complete understandings of air entrainment, air entrainment with heel formation, and start-up procedures are issues that will have to be addressed further in the future. The first two phenomena will require a two-phase flow analysis with molecular interaction between liquid and solid, breakdown of the entrained air film, and dissolution of the air. Analyses of the instabilities of the entrained air film and the coated liquid are keys to the physics of the problems. The third problem is fairly complicated because design factors, such as the edge shape of the catch pan, influence the phenomenon. Apart from steady-state analysis, stability and transient analyses will be important in solving these remaining problems.

With increasing demand for multilayer functional materials, the application of curtain coating will become more widespread, provided the difficulties in its operation can be solved with further improvements.

REFERENCES

- Blake, T. B., Clarke, A. and Ruschak, K. J. 1994. Hydrodynamic assist of dynamic wetting. *AIChE J.* **40**: 229–242.
- Booth, G. L. 1970. *Coating Equipment and Processes*. New York: Lockwood Publishing.
- Brown, D. R. 1961. A study of the behavior of a thin sheet of moving liquid. *J. Fluid Mech.* **10**: 297–305.
- Cox, E. R. 1968. Curtain coating of web stock with hot melts. *TAPPI*, **51**(7): 39A–42A.
- Degrauwé, D. and Hens, J. 1986. Limits of curtain coating: comparison of theory with experimental data. Paper read at AIChE Spring National Meeting, New Orleans, FL.
- Dittman, D. A., Griswold, G. L., Wright, S. E. and Winkler, D. E. 1976. Curtain coating apparatus. *Research Disclosure*. No. 14715.
- Do, D. V. and Christodoulou, K. N. 1992. Multilayer curtain coating flows: stability and sensitivity to small disturbances. Paper read at AIChE Spring National Meeting, New Orleans, LA.
- Fahrni, F. 1976. Coating device. US Patent 3,973,062.
- Fahrni, F. and Zimmermann, A. 1978. Coating device. US Patent 4,109,611.
- Finnicum, D. S., Weinstein, S. J. and Ruschak, K. J. 1993. The effect of applied pressure on the shape of a two-dimensional liquid curtain falling under the influence of gravity. *J. Fluid Mech.* **255**: 647–665.
- Ghys, J. J., Mues, W. and Geerts, H. J. 1992. Curtain coater. European Patent EP 0 489 978A1.
- Greiller, J. F. 1972. Method of making photographic elements. US Patent 3,632,374.
- Greiller, J. F. 1975. Apparatus for production of photographic elements. US Patent 3,867,901.
- Hartman, R. L. 1989. High speed curtain coating process and apparatus. World Patent 89/05477.
- Hughes, D. J. 1970. Method for simultaneously applying a plurality of coated layers by forming a stable multilayer free falling vertical curtain. US Patent 3,508,947.
- Kaneko, N. and Naruse, Y. 1986. Coating apparatus. Japanese Patent Publication JP 61-35880A.
- Kaneko, N. and Scriven, L. E. 1988. Transient analysis of a curtain coating flow. Paper read at AIChE Spring National Meeting, New Orleans, LA.
- Katagiri, Y. 1990. Comparative study of unsteady behavior in slide and curtain coating. Paper read at AIChE Spring National Meeting, Orlando, FL.
- Katagiri, Y. 1992. Analysis of edge effects in curtain coating. Paper read at AIChE Spring National Meeting, New Orleans, LA.
- Kawahara, S., Ogura, T., Isayama, S. and Hirose, M. 1983. Coating method. Japanese Patent Publication JP 58-3672A.
- Kawahara, S. and Yamagishi, K. 1979. Process for thermosensitive recording sheet. Japanese Patent Publication JP 54-74761A.
- Kistler, S. F. 1983. The fluid mechanics of curtain coating and related viscous free surface flows with contact lines. PhD thesis, University of Minnesota, Minneapolis. Ann Arbor, MI: University Microfilms International.
- Kistler, S. F. and Scriven, L. E. 1994. The teapot effect: sheet-forming flows with deflection, wetting and hysteresis. *J. Fluid Mech.* **263**: 19–62.
- Kozak, S. J. 1989. Curtain coating start-up method and apparatus. World Patent WO 89/07283.
- Lin, S. P. 1981. Stability of a viscous liquid curtain. *J. Fluid Mech.* **104**: 111–118.

- Lin, S. P., Lian, Z. W. and Creighton, B. J. 1990. Absolute and convective instability of a liquid sheet. *J. Fluid Mech.* **220**: 673–689.
- Miyake, A. 1973. Coating die. Japanese Patent Publication JP 48-34946A.
- Miyamoto, K. 1986. On the nature of entrained air bubbles in coating. Paper read at AIChE Spring National Meeting, New Orleans, LA.
- Miyamoto, K. 1991. On the mechanism of air entrainment. *Industrial Coating Research* **1**: 71–88.
- Miyamoto, K. and Scriven, L. E. 1982. Breakdown of air film entrained by liquid coated on web. Paper read at AIChE Annual Meeting, Los Angeles, CA.
- Morikawa, M. and Kobayashi, K. 1987. Coating method and apparatus. Japanese Patent Publication JP 62-289264A.
- Morikawa, M., Kobayashi, K. and Miyamoto, K. 1989. Coating apparatus. Japanese Patent Publication JP 1-304076A.
- Mues, W., Hens, J. and Buij, L. 1989. Observation of a dynamic wetting process using laser-Doppler velocimetry. *AICHE J.* **35**: 1521–1526.
- Naruse, Y. 1985. Coating method. Japanese Patent Publication JP 60-44077A.
- Nishida, S. 1990. The formation of flow rate distribution near the edge guide of liquid curtain. Paper read at the SCEJ 55th Meeting, Nagoya, Japan.
- Nishida, S., Katagiri, Y. and Suga, Y. 1992. Coating method. European Patent EP 0 517 170A2.
- O'Connor, T. R. 1981. Coating apparatus provided with a protective shield. US Patent 4,287,240.
- Ogawa, S. and Scriven, L. E. 1990. Analysis of curtain coating flow. Paper read at AIChE Spring National Meeting, Orlando, FL.
- Ogawa, S. and Scriven, L. E. 1994. An analysis of curtain coating flow. *AICHE J.* (to be published).
- Ogawa, S., Kashiwabara, Y. and Scriven, L. E. 1992. Theoretical and experimental study of curtain coating flow. Paper read at AIChE Spring National Meeting, New Orleans, LA.
- Poirier, C. C. 1966. Curtain coating of corrugated paper board. *TAPPI*. **49**(10): 66A–67A.
- Pritchard, W. G. 1986. Instability and chaotic behavior in a free-surface flow. *J. Fluid Mech.* **165**: 1–60.
- Reiter, T. C. 1989. Curtain coating method and apparatus. World Patent WO 89/10583.
- Ridley, K. A. 1977. Curtain coating method. US Patent 4,019,906.
- Ridley, K. A. 1979. Curtain coating apparatus. US Patent 4,135,477.
- Ridley, K. A., Denewtown, J. E. and Stokes, L. R. 1980. Curtain coating. Great Britain Patent GB 1 559 701.
- Sakiadis, B. C. 1961. Boundary-layer behavior on continuous solid surfaces. *AICHE J.* **7**: 26–31, 221–224, 467–470.
- Sone, Y. and Hanawa, T. 1991. Coating method. Japanese Patent Publication JP 3-94870A.
- Sone, Y., Hanawa, T. and Kageyama, T. 1989. Coating method. Japanese Patent Publication JP 64-51170A.
- Suga, Y., Kobayashi, K., Sasahara, T. and Miyamoto, M. 1991. Coating method. European Patent EP 426 122 A2.
- Taylor, G. I. 1959. The dynamics of thin sheets of fluid. Part III: disintegration of fluid sheets. *Proc. Roy. Soc. London A.* **253**: 313.
- Taylor, L. H. 1903. Machine for production of solidification forming nutriment with whole cover as confectionery and pie. German Patent Publication DE 145517.
- Teletzke, G. F., Davis, H. T. and Scriven, L. E. 1988. Wetting hydrodynamics. *Rev. Phys. Appl.* **12**: 1473–1484.
- Wandtke, L. A. 1964. Curtain coating machine. US Patent 3,132,968.
- Watanabe, T., Tanaka, K. and Yoshimura, Y. 1980. Coating method and apparatus. Japanese Patent Publication JP 55-73365A.
- Yoshida, T., Ujihara, M., Watanabe, K. and Takagi, A. 1978. Method to coat onto both sides of web. Japanese Patent Publication JP 53-115754A.

SURFACTANT EFFECTS IN COATING PROCESSES

11d

P. Randall Schunk and L. E. Scriven†*

11d.1 INTRODUCTION

Free surfaces and laminar viscous flow are the features common to all coating flows which are susceptible to the effects of surfactant additives. Surfactants can change drastically the interfacial physics and chemistry of aqueous solution – and more rarely organic solutions – because they preferentially concentrate, or adsorb, at interfaces. The surfactant concentration there can be orders of magnitude larger than in the bulk liquid, depressing surface tension far below that of the solvent. If the liquid flows in such a way that fluid elements moving along the surface undergo rapid compression or expansion (area change), then the surface composition changes. If the surface deformation is not everywhere the same, neither is the surface concentration: there are concentration gradients. Concentration gradients make surface tension gradients. The consequence is in the balance of forces at the interface: the depression of capillary forces and the induction of surface tension gradients can stabilize the flow, lead to large changes in interfacial shape, and sometimes induce unsteady flow.

Surfactants are often dissolved in liquids to be coated to serve sundry purposes, the nature of which depends on the type of coating. For

example, in aqueous coatings of photosensitive materials, surfactants are employed as solubilizers, sensitizers and dispersants, or to influence specific characteristics of the final product, such as surface roughness and permeability to processing solutions (Sturge 1977; Knox 1970). But as long as surfactants have been used for these purposes, they have also been used as real or imagined coating aids, ostensibly to make the coating method more operable, or operable over a wider range of operating conditions. It is made plain in Chapter 4 that surfactants play a significant role in controlling and sometimes causing coating defects, both through a static (equilibrium) effect and through a so-called dynamic surface tension effect.

The concept of dynamic surface tension, however, is often misunderstood. If a surface-active substance is dissolved in a liquid, the surface tension is lower than that of the pure liquid. Surface tension is a local equilibrium property and is most reliably measured when the whole body of solution is at equilibrium, i.e. uniform in composition and temperature, and at rest. The dynamic surface tension is the local tension measured or estimated somewhere in a solution and surface that are not at rest, but flowing, and flowing in such a way that parcels of liquid moving along the surface are deforming. When the surface is expanding or contracting, the amount of surfactant adsorbed per unit area changes by diffusion and adsorption, or desorption, to re-establish equilibrium. Thus

* Current address: Sandia National Laboratories, Department of Incompressible Fluid Dynamics, Albuquerque, NM 87185, USA.

† Current address: University of Minnesota, Department of Chemical Engineering and Materials Science, Minneapolis, Minnesota, 55455.

dynamic surface tension is a result of a local non-equilibrium process of surface area change, adsorption and desorption, diffusion and convective transport, and even micellization as well. In contrast, (static) surface tension is a well-defined thermodynamic property.

The primary goal of this chapter is to reconcile the concept of dynamic surface tension with the physical mechanisms by which surfactants exert effects and then to identify what surfactant properties are relevant so that practical extensions of this research can be made. As such what is presented here complements Chapter 4, which focuses on methods of measuring the relevant surfactant properties (e.g., static surface tension, dynamic surface tension, diffusion coefficients, etc.). Together we hope these chapters will provide a guide, as well as valuable insight, towards the correct selection of surfactant systems to aid in the production of single and multilayer coatings.

Mechanisms by which surfactants affect free-surface flows hinge on the complex interplay of surfactant convection, diffusion, adsorption and even micellization (aggregation). The governing principles of conservation of mass, conservation

of momentum, and models and constitutive equations of surfactant equilibria provide the framework for analyzing the mechanisms; these principles are described in Section 11d.2. Applications of published theories to coating and related flows is the subject of Section 11d.3. The highlights there are several analyses of the effects of surfactant at static and dynamic wetting lines. In the remainder of the chapter (Section 11d.4) we examine three viscous free surface flows that serve as coating-related case studies. The first is of film flow down an inclined plane (Section 11d.4.2), the simplest of all viscous free surface flows. The second is of an overflowing pool (Section 11d.4.3), a method which epitomizes the difficulties of interpreting measurements of apparent surface tension of a flowing liquid. The third is of slide coating flow (Section 11d.4.4), the most widely used method of depositing multilayered photographic films.

11d.2 THE THEORY OF SURFACTANT ACTION

The theory describing surfactant action must, of course, include the principles that govern small

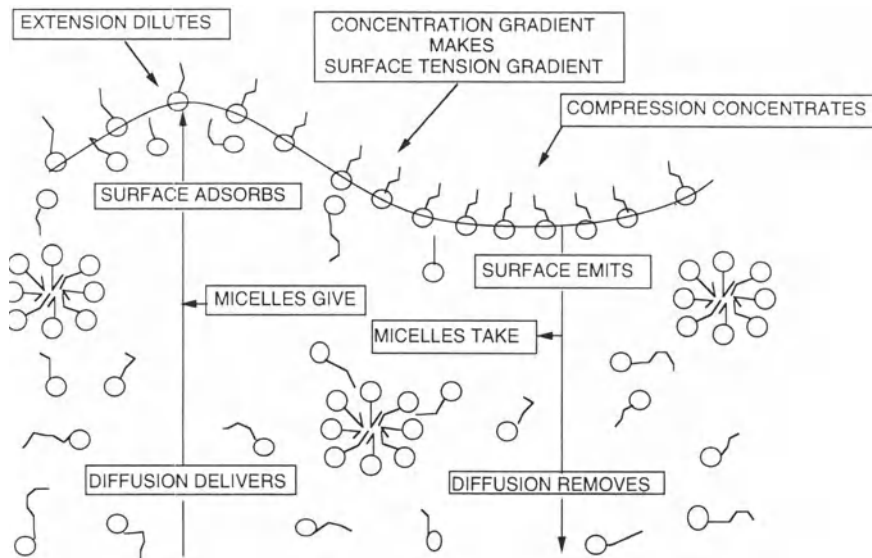


Figure 11d.1 Surfactant action at and near a free surface.

scale viscous free surface flow. The relevant equations and boundary conditions are the Navier–Stokes equations, which govern the flow in the bulk liquid, the kinematic and traction boundary conditions, which account for mass and momentum conservation at gas/liquid surfaces and liquid/liquid surfaces, and special conditions which control the behavior of gas/liquid/solid lines of contact (Chapter 2). In addition, the theory must account for the surfactant inventory, an inventory generally made up of individual surfactant molecules in solution, which are surface-active and are free ‘monomers’ with respect to aggregation; molecules, or monomers, adsorbed at the surface; and molecules aggregated in micelles. The mechanisms by which surfactant moves into and out of the surface and through which micelles affect that movement are portrayed in Fig. 11d.1. Those mechanisms and the underlying theory have three parts: convective diffusion, adsorption–desorption, and micelle-solution exchange of surface active monomers.

11d.2.1 THEORY OF CONVECTIVE DIFFUSION

The movement of surfactant monomers and micelles in the bulk liquid is described by the convective diffusion equations. In dimensionless form these equations are

$$\frac{\partial c_i}{\partial t} + \mathbf{u} \cdot \nabla c_i = \frac{1}{Re Sc_i} \nabla^2 c_i + q_i$$

for $i = 1, 2, \dots, N$ (11d.1)

where c_i is the bulk concentration of surfactant species i in units of C_i^* , the initial concentration of the same. Sc_i is the Schmidt number, $\mu/(\rho D_i)$, with μ being the viscosity, ρ the density, and D_i the diffusivity (diffusion coefficient) of species i . \mathbf{u} is the velocity vector and Re is the Reynolds number, $\rho U L / \mu$, with U being the chosen unit of velocity and L the chosen unit of length. q_i is the rate of generation of species i in units of $C_i^* U / L$. C_i is the concentration of surface-active monomers and C_i , $i = 2, 3, \dots, N$ are the concentrations of surface-inactive aggregates, the sub-

script referring to the aggregation number. Expressions for q_i come from the model of micelle–solution exchange equilibrium, an example of which is described below.

Boundary conditions on (11d.1) are

$$\mathbf{n} \cdot \nabla c_i = 0 \text{ for } i = 1, 2, \dots, N \text{ at solid surfaces}$$

(11d.2)

$$\begin{aligned} \mathbf{n} \cdot \nabla c_1 &= Sc_1 Re \left(\frac{\Gamma^*}{C_1^* L} \right) \\ &\times \left[\frac{\partial \Gamma}{\partial t} + 2H \mathbf{n} \cdot (\mathbf{u} - \mathbf{u}_s) \Gamma + \nabla_s \cdot (\mathbf{u}_{II} \Gamma) \right] \\ &+ \frac{Sc_1}{Sc_s} \left(\frac{\Gamma^*}{C_1^* L} \right) \nabla_s^2 \Gamma \text{ at free surfaces} \end{aligned} \quad (11d.3)$$

Γ is the surface concentration (moles of adsorbed material per unit area) in units of the surface concentration, Γ^* , that is in equilibrium with the initial concentration of monomers in the liquid C_1^* . $Sc_s \equiv \mu/(\rho D_s)$ is the surface Schmidt number, D_s being the surface diffusion coefficient. $2H$ is the mean curvature of the surface, $\mathbf{u}_{II} \equiv (\mathbf{I} - \mathbf{n}\mathbf{n}) \cdot \mathbf{u}$ is the velocity vector tangent to the surface, and \mathbf{u}_s is the velocity of the surface.

The first condition (11d.2) makes solid surfaces impenetrable to surfactant. The second condition (11d.3) allows bounding free surfaces to take up surfactant from the liquid and hold a significant inventory of surfactant monomers (Gibbs' definition of so-called ‘surface excess’, (Gibbs 1906); see also Edwards *et al.* (1991)). Condition (11d.3) says that the diffusive flux of surfactant monomers normal to the surface is controlled by four factors: (1) the rate of accumulation of surfactant per unit area $\partial \Gamma / \partial t$; (2) the rate of local creation of surface owing to motion of a curved surface normal to itself $2H \mathbf{n} \cdot (\mathbf{u} - \mathbf{u}_s) \Gamma$ (a small effect and contributes only for unsteady flows or evaporating solvents); (3) the rate of local redistribution by surface convection $\nabla_s \cdot (\mathbf{u}_{II} \Gamma)$, and (4) movement within the surface by diffusion relative to mass-average motion $D_s \nabla_s^2 \Gamma$. The third term contains the effect of surface expansion and contraction – that is, free surfaces are mathematically compressible, unlike the liquid itself, because the

surface velocity field may have nonzero divergence, i.e., $\nabla_s \cdot \mathbf{u}_{II} \neq 0$. The fourth contribution can be a delicate matter when diffusion itself induces mass-average motion. Because surface diffusivities are immeasurable this contribution is neglected here except near dynamic contact lines, where the surface concentration gradients are so steep that some diffusion is required to stabilize the concentration field at affordable levels of computation.

11d.2.2 SURFACE CONSTITUTIVE RELATION – ADSORPTION MODEL

To complete the theory of surfactant transport in free surface flows, what is needed is a constitutive equation that relates surface excess per unit area, Γ , and bulk concentration, C_1 , in the liquid next to the surface. Here, as an approximation, only the monomers are allowed to concentrate at the surface. Generalizations that allow for dimers and small aggregates to do the same are given by Franses (1979). These are not accounted for in the present analysis.

The Langmuir–Syszkowski equation of surface state (equation (4.5)) is a reasonably accurate description of equilibrium adsorption of many surfactants. Combining it with equation (4.1) and integrating yields the equation for surface tension in terms of surfactant concentration:

$$\sigma = \sigma_s - RT\Gamma_\infty \ln\left(1 + \frac{C_1}{a}\right) \quad (11d.4)$$

σ_s is the surface tension when the surfactant concentration is zero, or equivalently the surface tension of the solvent; R is the ideal gas constant; T is the temperature; and Γ_∞ is the surface concentration under saturated conditions. That (11d.4) is a reasonably accurate description of equilibrium surface tension data of many aqueous surfactant systems is discussed in Chapter 4.

When the constitutive equation (11d.4) is combined with the balance of traction at the free surface, (*cf.* Chapter 2), a working condition results on momentum transport in which appears explicitly the surface concentration:

$$\begin{aligned} \mathbf{n} \cdot \mathbb{T} &= 2H\mathbf{n} \left[\frac{1}{Ca} - Es \ln\left(1 + \frac{c_s}{a^*}\right) \right] \\ &\quad - Es \left(\frac{1}{a^* + c_s} \right) \nabla_s c_s \end{aligned} \quad (11d.5)$$

Here $Es \equiv (RT\Gamma_\infty)/\mu U$ is the surface elasticity number, which measures the relative importance of viscous force and the decrement of capillary force owing to surface tension lowering by surfactant; and Ca is the capillary number (see Chapter 2). $a^* \equiv a/C_1^*$ is the dimensionless Langmuir constant, or the concentration at which $\Gamma = \Gamma_\infty/2$ in units of C_1^* (Chapter 4). c_s denotes the dimensionless concentration just below the surface, in units of C_1^* . What is called Gibbs elasticity of a surface is defined as (Rusanov and Krotov 1979)

$$E \equiv \left(\frac{d\sigma}{d \ln \Gamma} \right) \quad (11d.6)$$

Gibbs elasticity is a property of an interface that acts through interfacial (surface) tension gradients that, in turn, develop as a result of differential amounts of expansion or contraction of neighboring elements of the interface:

$$\nabla_s \sigma = E \nabla_s (\ln \Gamma) \quad (11d.7)$$

Gibbs elasticity E is a true mechanical property only if it is measured in the absence of bulk-surface exchange of surfactant. Only in that case does the shear stress in the surface respond instantaneously to a surface deformation, without diffusion-induced stress relaxation. With some rearrangement the last term in equation (11d.5) can be combined with equation (4.1) to give

$$Es \left(\frac{1}{a^* + c_1} \right) \nabla_s c_1 = \frac{Es}{a^*} c_s \nabla_s (\ln \Gamma) \quad (11d.8)$$

By comparing (11d.7) with (11d.8), it is clear that Gibbs elasticity implied by the Langmuir–Szyszkowski equation is $(Es/a^*)c_s$. So the surface elasticity can be determined from input parameters to the adsorption model, i.e. a^* and Γ_∞ . A review of many attempts to measure surface elasticity directly is given by Lucassen–Reynders (1981); see also Chapter 4.

11d.2.3 MICELLE-SOLUTION SURFACTANT INVENTORY

Not all surfactants form micelles in water. When they do, the micelles normally show up above a certain range of surfactant concentration. This range is often narrow and can resemble a phase transition. For this reason it is termed Critical Micellization Concentration, or simply CMC (Mukerjee and Mysels 1971). Many thermodynamic properties, surfactant monomer activity, or chemical potential, solvent activity, surface tension, etc., change more or less abruptly at the CMC.

Micelles are equilibrium aggregates of colloidal dimension, i.e., they are made up of 10 to 100 monomers, and are stabilized by physical forces. They tend strongly to stay in equilibrium with the remaining molecules, or monomers, from which they are formed. Various models to account for this equilibrium have been put forward. The oldest one by Bury (1927) and Hartley (1936) regards a micelle as a colloidal entity, made up of n monomers of surfactant, that is in equilibrium with the individual molecules in solution:

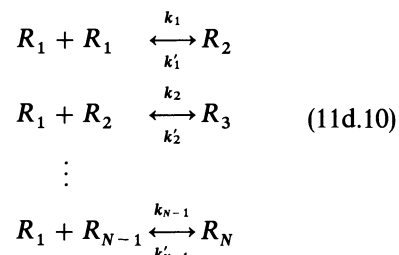
$$nR \leftrightarrow R_n; \quad C_n/C_1^n = \exp(-\Delta G_n/RT) \quad (11d.9)$$

Here C_n is the concentration of micelles of size n , i.e., made up of n monomers, C_1 is the concentration of monomers in solution and ΔG_n is the free energy of micelle formation. Typically in aqueous solutions n , the aggregation number, is greater than 20 – often it is around 100.

In this so called Bury–Hartley model a micelle is formed supposedly by an n -molecule encounter. This is disconcerting because even a three-molecule encounter is improbable and a simultaneous encounter of twenty or more molecules is so unlikely as to be practically impossible. Nevertheless, the Bury–Hartley model describes qualitatively the CMC, predicting an abrupt change in many physical properties of the solution at the CMC (see Kamrath 1984). For this reason it has found widespread use in the study of surfactant transport near surfaces at which monomers concentrate (for example, Miller 1981 and Lucassen-Reynders 1981).

What the Bury–Hartley model cannot explain is that the critical concentration of different properties is often different; that in some cases at least there is substantial preaggregation below the critical micelle concentration; that micelle sizes, as measured by aggregation numbers, are distributed over a definite range; and that equilibrium is established in much less time than the waiting time for simultaneous encounter of n surfactant molecules.

Physically a micelle must be built up by a succession of binary encounters, as recognized first by Meyer and Van der Wyk (1937). At equilibrium the distribution of aggregates is governed by a set of stepwise-addition reactions (Hall and Pethica 1967):



Here k_i is the rate constant for the i th forward step and k'_i is the rate constant for the i th reverse step. $K_i \equiv C_i/(C_{i-1}C_1)$ is the equilibrium constant for the i th addition reaction. In reality the i different steps could have i distinct equilibrium constants. But unless some simple functional relationship can be established among all of the constants this is not practicable.

Bidner, Larson and Scriven (1976) examined a simpler model with just two different equilibrium constants, and two additional constants which define the range of aggregation numbers of micelles in contrast to premicelles, or submicelles, as depicted in Fig. 11d.2. The ‘floor’ N is the lowest degree of aggregation at which a complete micelle exists. The aggregates that contain less than N monomers are referred to as premicelles. The ‘ceiling’ $N + p$ is the maximum possible degree of aggregation. The aggregates that contain more than N but less than $N + p$ monomers are referred to as micelles. The $N - 1$ reaction steps needed to form a micelle are supposed to be

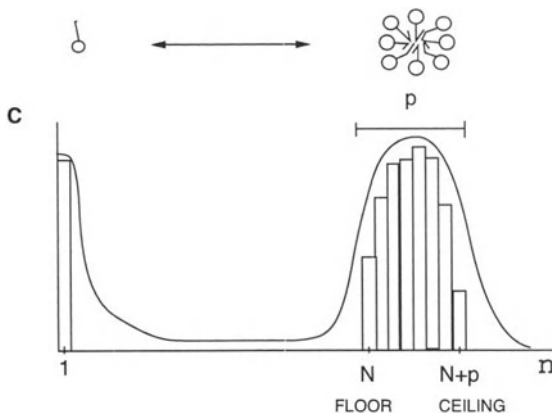


Figure 11d.2 Micelle–solution inventory typical of surfactant systems (Bidner, Larson and Scriven 1976).

unfavorable equilibria and are characterized by a relatively small equilibrium constant K_i , at least small compared with those $K \equiv K_i$ which characterize the p micelle–solution exchange steps. Consequently the distribution statistically favors micelles, and the concentration of premicelles is insignificant. Bidner, Larson and Scriven (1976) suggest characteristic values of p should be 20 or 30, more-or-less in accord with a thermodynamic treatment by Ruckenstein and Nagarajan (1975) and experimental evidence by Shinoda *et al.* (1963).

Hereafter the usually small concentration of submicelles is neglected and the entire inventory is contained between the monomers and the p different species of micelles:

$$C_T = C_1 + NC_N + (N+1)C_{N+1} + \dots + (N+p)C_{N+p} \quad (11d.11)$$

C_T is the total concentration of individual monomers that would be in solution if no micelles were formed.

Because the equilibrium constants of the i th step, for $i > N$, are all the same we take $k_N = k_{N+1} = \dots = k_{N+p}$, and likewise $k'_N = k'_{N+1} = \dots = k'_{N+p}$, i.e. the rate of monomer emission or adsorption is the same for each micelle. The same assumptions are made for the unfavorable steps

$1, 2, \dots, N-1$. If the equilibrium constants for the latter are all $K \equiv K_i$, then at equilibrium

$$(KC_1)C_1 = C_2, (KC_1)^2C_1 = C_3, \dots, (KC_1)^{N-1}C_1 = C_N$$

or, equivalently,

$$\frac{C_N}{C_1} = K_{eq} C_1^{N-1} \quad (11d.12)$$

where $K_{eq} \equiv K^{N-1}$ is the effective equilibrium constant between the monomers and the micelles of aggregation number N . The dimensional rate of formation of each species, $Q_i \equiv (C_i^* U/L)q_i$ (see equation (11d.1)), can now be expressed with mass-action principles:

$$\begin{aligned} Q_1 &= \frac{dC_1}{dt} = k'_{N-1}C_N + k'_NC_{N+1} \\ &\quad + k'_{N+1}C_{N+2} + \dots + k'_{N+p-1}C_{N+p} \\ &\quad - k_NC_1 - \dots - k_{N+p-1}C_{N+p-1}C_1 \\ Q_N &= \frac{dC_N}{dt} = k'_NC_{N+1} - k_NC_NC_1 \\ Q_{N+1} &= \frac{dC_{N+1}}{dt} = k_NC_NC_1 + k'_{N+1}C_{N+2} \\ &\quad - k'_NC_{N+1} - k_{N+1}C_1C_{N+1} \\ Q_{N+p} &= \frac{dC_{N+p}}{dt} = k_{N+p-1}C_{N+p-1}C_1 \\ &\quad - k'_{N+p-1}C_{N+p} \end{aligned} \quad (11d.13)$$

Physically, the difficult reaction steps are the first $N-1$. Hereafter we account for the division of surfactant monomers between those free in solution and those which make up a micelle with the equilibrium constraint (11d.12). The kinetic expressions (11d.13) describe the monomer–micelle exchange process.

With the model of Bidner, Larson and Scriven (1976) six additional physical parameters must be specified in order to account for micellization in any mathematical model of a flow field: one for micelle diffusion, i.e. D_N , three for micelle–solution equilibria, i.e. $N, p, C_N^*/C_1^*$, and two for micelle–monomer exchange kinetics, i.e. k' and

k. To predict physical realizable values of each requires measurement of kinetic exchange rates of monomers among the micelles and the distribution of aggregation sizes that accounts for the entire inventory of surfactant monomers. Although numerous theoretical studies have been made to elucidate the equilibrium aspects of micellization by models that predict the behavior of physical properties, e.g. surface tension, kinetics of micellization have received much less attention (Kreshek *et al.* 1966; Muller 1972; Hall 1987); however, insight has been gained through measurements of micellar equilibration rates (Mijnlieff and Ditmarsch 1965; Leung and Shah 1986).

As equilibrium between micelles and monomers is established very rapidly, fast-reaction-techniques are required to study them. Among those which have been applied successfully to micellar solutions are temperature jump, pressure jump, and ultrasound adsorption. These methods lead to the relaxation time for a micellar system: the time needed for micelles, and monomers that make them up, to re-establish equilibrium after equilibrium has been upset. The relative (relaxation) step in the present model is the relatively slow dissociation of monomers from the micelles. The characteristic relaxation time of these steps is (Kreshek *et al.* 1966)

$$\tau \equiv [k(C_1 + C_N) + k']^{-1} \quad (11d.14)$$

Diffusivities of surfactants in solution, both monomers and micelles, must also be measured, or predicted, to complete the theory. The task is difficult and only a few methods have been successful (see Chapter 4). This is especially the case when the surfactant is ionic and its concentration is above the CMC. Experimental evidence suggests that even when the surfactant is nonionic the micelle diffusivities are as much as 30% smaller than that of the monomers (Weinheimer, Evans and Cussler 1980). When the surfactant is ionic the micelle diffusivity can rise with concentration above the CMC due to electrostatic interactions (Weinheimer, Evans and Cussler 1981). In this chapter, diffusion coefficients are left as empirical parameters and independent of concentration.

11d.3 THEORETICAL TREATMENTS OF COATING AND RELATED FLOWS

Although experimental studies on the effects of surfactant in viscous free surface flows abound in the open literature, there has been relatively little in the way of theoretical analysis. The majority of the theoretical treatments have been limited to insoluble surfactant systems, the effects of surfactant being relegated to a free boundary equation akin to equation (11d.3) and the balance of normal and tangential stress at the free surface (Chapter 2). When surfactants are allowed to be appreciably soluble, theoretical analysis can become much more difficult: the main problem is the relatively low diffusivity of surfactants in liquid compared with the kinematic viscosity of the liquid, i.e., high Schmidt numbers, which leads to exceedingly thin concentration boundary layers. The challenge, analytically, has been to handle the momentum transport in the flow simultaneously with surface tension gradients and surfactant convection and diffusion.

In this section we make no attempt to cover the voluminous literature available on dynamic surface tension, but instead we review the most significant analyses of surfactant effects in coating and related flows, in both the insoluble and more importantly the soluble regimes. Most research on the hydrodynamic effects of surfactant has focused on the motion of drops and bubbles, the spreading of liquids on solid surfaces, and the damping of waves on films. Below we highlight the analytical treatments most significant to each of these areas. We then discuss the few contributions available that directly address the effects of surfactants in coating flows.

Two-phase flow in porous media (e.g., Ginly and Radke 1988) and the dynamic behavior of foams (e.g., Hirasaki and Lawson 1985; Edwards *et al.* 1991) have interested researchers in the effects of surfactants on the motion of bubbles through channels of various shapes. Analytical treatments of the problem are usually approached by simplifying the bulk momentum equations with lubrication theory, which results in surface evolution equations that can be integrated (e.g.,

Hirasaki and Lawson 1985; Ginley and Radke 1988; Ratulowski and Chang 1990).

Unfortunately, the lubrication approach precludes the analysis of complex flow patterns, i.e., recirculations, and for the most part has been applied to insoluble systems. For flows dominated by viscous and capillary forces the boundary-element method is an efficient route to a solution and has been applied extensively to drop and bubble hydrodynamics (see Chapter 9; Stone and Leal 1990; Lu and Chang 1988); unfortunately, the method does not lend itself to convective diffusion analysis and hence its use has been mostly confined to insoluble systems. Wassmuth *et al.* (1993) have recently made a significant advance with their numerical treatment of the moving bubble problem that is general enough to handle complex flow regimes and convective-diffusion of surfactant. Like the work we present in this chapter, they solve the full two-dimensional Navier–Stokes and convective diffusion problem.

The motion of drops in a uniform stream of fluid under the influence of surfactant has also been the subject of extensive research (e.g., Oguz and Sadhal 1988; Argrawal and Wasan 1979; LeVan and Newman 1976). In fact, this problem benefited from one of the first numerical treatments of bulk diffusion of surfactant in more than one space dimension (LeVan and Newman 1976); in that work, however, the effect of surfactant on the velocity field was not considered. Sadhal and Johnson (1986) have since put forward an exact solution to the mixed boundary-value problem for the case of insoluble surfactants. The case of soluble surfactants in the continuous phase have been treated by Holbrook and LeVan (1983a,b) who used the collocation method to solve the convection-diffusion problem for realistic surfactant properties. Their results showed an appreciable amount of interfacial velocity retardation. Oguz and Sadhal (1988) used the method of matched asymptotic expansions to generalize the theory for insoluble as well as slightly soluble surfactants. The results of their treatment graphically exhibit the physical phenomena involved in the mass transport within the drop and lead to quantitative agreement with experimental meas-

urements. They also give a historical review of all previous attempts at solving the problem.

The effect of surfactants on the ability of liquids to spread on solids has also been a popular subject of research. Much of the work in this area is closely related to the hydrodynamics of wetting, the essential part of most coating processes. In Section 11d.4.4 we cite the analytical treatments of spreading where they are relevant to our analysis. The interested reader should consult reviews given by Kistler (1993) and Bose (1993).

That surfactants have a significant damping effect on waves in quiescent pools and in films flowing down inclined surfaces has been known for some time (*cf.* Lamb 1879; Emmert and Pigford 1954; Whitaker 1964). Thin film coating is just one area of technology that has kept interest in this problem alive. Early theoretical studies of the wave-damping effect were made with quiescent liquid pools. The first to explain the damping mechanism was Lamb (1879) who deduced the behavior of small-amplitude sinusoidal waves by what amounts to linear stability analysis. Although his analysis was limited to insoluble and inextensible films of surface active material, his predictions were accurate as was his insight to the underlying physical principles. Nearly a century later Dorrestein (1959) extended Lamb's analysis to include extensible films but then Levich (1945) and independently Hansen and Mann (1964) gave the first explanations of the effects of soluble surfactants, i.e., diffusion and adsorption effects included. Finally, Lucassen (1975) added micellization to the picture (*cf.* Lucassen 1975, Rillaerts and Joos 1982, Lucassen-Reynders 1987), but the more complex interplay of the underlying principles which control stability was not laid bare.

Beyond quiescent pools there are falling liquid films, and waves running down them in many circumstances grow, as is well established; that is, the flow can be unstable (Benjamin 1957, Krantz and Goren 1971). That adding soluble surfactant to the liquid can dampen waves, i.e. stabilize the flow, is also well established (Emmert and Pigford 1954; Whitaker and Jones 1966).

Linear stability analysis still pertains to the evolution of disturbances up to visible wave inception, but is complicated by the main flow of the liquid film, the 'base flow', which ramifies Lamb's approach into a combination of the Orr–Sommerfeld equation of linear flow stability theory and the linearized convective diffusion equation. This combination has been solved without major restrictions on the range of validity of predictions only by Whitaker (1964) and Sterzi (1982); however, the still more complex interplay of underlying phenomena remains unexamined in the literature, so far as the authors are aware. Among the approximate analyses that apply to limiting cases, those of Anshus and Acrivos (1966) and Lin (1970) for waves that are much longer than the film is thick are noteworthy, because they verify that Whitaker's (1964) results are accurate in the long-wave limit. But neither have they shed light on how stability is controlled by the interplay of underlying phenomena. We return to this problem in Section 11d.4.2, where we show that the damping effect can be explained by the phasing of the surface tension gradient-induced shear stress relative to the wave amplitude.

Direct analysis of the effects of surfactant in coating flows includes research in the area of Langmuir–Blodgett film deposition (see Chapter 13 for review; Rame 1988; Park 1991). Park (1991) used the method of matched asymptotic expansions to solve the governing equations and found that the surface speed profile is greatly affected by the presence of an adsorbed monolayer. He built on the analysis of the effects of surfactant monolayers on the movement of a bubble front confined in a channel, which takes on a similar appearance to dip coating (see Ratulowski and Chang 1990; and Chapter 13). Rame (1988) also examined Langmuir–Blodgett film deposition. With similar analytical techniques he examined the effects of the monolayer on the moving contact line which is present in the plunging mode (advancing contact angle; see Chapter 13), as opposed to the withdrawal mode (receding contact angle). Like Park (1991) he focused on insoluble surfactant systems but proposed several mechanisms which allow for transfer of the

surfactant monolayer to the substrate. One mechanism involves dissolution of the monolayer into the bulk phase followed by re-adsorption to the substrate. He concluded that two hydrodynamic parameters are needed to make the problem well posed: the dynamic contact angle and a surfactant transfer ratio. Cox (1986) also analyzed the effect of insoluble surfactant on moving contact lines; however, he did not allow for transfer of surfactant to the substrate. More recently, Bose (1993) considered soluble systems. His modeling results show that Rame's surfactant transfer ratio can be used to get both buildup and depletion of surfactant at an advancing dynamic contact line.

The work of Bose and his colleagues is significant because most practical coating applications, with the exception of Langmuir–Blodgett films (see Chapter 13), involve surfactants that are appreciably soluble. Ruschak (1987), in one of the few other available treatments of soluble systems, studied the effects of several surfactant properties on the undesirable flow induced by air currents after the liquid is coated. Wu and Whitaker (1986) examined the effects of surfactant at and near static separation lines. They deduced that secondary flows (recirculations) near such lines provide a convective mechanism by which surfactant molecules are brought to the surface much more rapidly than those delivered by diffusion, and, consequently, steep surface concentration gradients there are unlikely. Goetmackers and Scriven (1992), following the work we present below, probed the effects of surfactant on the steady operating states and the dynamics of curtain coating. Most recently Giavedoni and Saita (1992) examined the effects of surfactant-induced interfacial viscosity on location of the dynamic contact line terminating the upstream meniscus in slot coating.

Like Giavedoni and Saita (1992) many researchers are now reverting back to a science called 'interfacial rheology' as a means of modeling the effects of surfactants in capillary hydrodynamics (see Edwards *et al.* (1991)). The idea is to develop constitutive equations that describe how the state of surface stress depends on surface

deformation and the rate of surface deformation; effectively, the surfactant transport mechanisms are lumped into the mechanical properties of the surface. Before some pioneering work by Scriven (1960), the term ‘interfacial rheology’ had been employed mostly in reference to experimental studies devoted to qualitatively elucidating the rigidity and viscoelasticity of adsorbed monolayers at fluid interfaces. Gibbs elasticity, as we defined it in Section 11d.2.2, is used to describe the elastic response, and surface dilatational viscosity and shear viscosity are used to capture the effects of rate of surface strain. All of these properties can be built into surface constitutive equations, as was demonstrated originally by Scriven (1960). This approach has been used in the study of drops and bubbles (*cf.* Argrawal and Wasan 1979 and LeVan 1981), the motion waves on a monolayer-covered surface (e.g., Lucassen and Hansen 1967), the stability of liquid threads (e.g., Rusanov and Krotov 1979), the behavior of foams (e.g., Edwards *et al.* 1991) and even recently in coating flows (Giavedoni and Saita 1992).

Other than the work we present in this chapter there have been only a few other numerical treatments of the effects of surfactant on viscous free surface flow, at least without significant approximation. Three of them are mentioned above (Bose 1993; Holbrook and LeVan 1983a,b; Wassmuth *et al.* 1993). Another one that we cover in Section 11d.4.3 is the finite difference work by Bergink-Martens *et al.* (1990), who examined the effects of surfactant in an overflowing liquid pool.

11d.4 CASE STUDIES OF SURFACTANT EFFECT

11d.4.1 METHODS OF ANALYSIS

In the coming subsections, the Navier–Stokes system (Chapter 2) and the convective-diffusion system (equations (11d.1)–(11d.3)) are solved together to investigate the physics of surfactant effects in three prototypical flows. Flow down an inclined plane is the first and possesses a simple, analytically tractable base flow. We

examine the stability around the base flow, which is accessible through a fourth-order differential equation, i.e., the celebrated Orr–Sommerfeld equation (Benjamin 1957). In the other two cases, an overflowing liquid pool and a slide coating process, the flow is too complex to fit any standard coordinate system. The culprits are the free surfaces that bound the flow but relocate and reshape in response to changes in properties and operating parameters, e.g., flow rate, surface tension and so on. The changes usually require robust parameterization techniques to follow them successfully. These aspects make the Galerkin/finite-element technique, suitably augmented to handle free boundaries (Chapter 9, Kistler 1984; Christodoulou and Scriven 1992) and the intense surfactant concentration gradients normal to those boundaries (Schunk 1989; Chapter 13), the method of choice for an efficient route to a suitable solution.

The results of the first case study, which come from a numerical solution of a differential equation in a single space dimension, were found to be converged with respect to mesh refinement, i.e. the results proved to be virtually insensitive to the further addition of elements to the mesh (see Chapter 9). Unfortunately the same cannot be rigorously claimed for the second and third case studies (overflow cell and slide coating flow), although we did find in most cases that the solutions agreed qualitatively, and even sometimes quantitatively, to published experimental data (see Section 11d.4.3). We believe that sufficient resolution is lacking only near static and dynamic contact lines (see Section 11d.4.4) and in regions where the solution is unimportant (flow over the rim in the overflow cell). We are confident that we use sufficient resolution of the steep concentration gradients that occur normal to deforming free surfaces. Moreover, most of the conclusions we draw agree with published experience, as we bring out as often as possible in the following discussion.

The reader should be cautioned, however, when interpreting the results regarding the effects of the *ad hoc* models employed at the dynamic contact line, models which have never been

substantiated by careful comparisons with experimental data. Because the traditional hydrodynamic assumptions break down at the dynamic contact line, the results obtained with any approach are subject to scrutiny. The reader is urged to take the results as no more than the demonstration that, whatever the correct model, the solutions are extremely sensitive to the physics near the dynamic contact line. The reader is also urged to consult several authoritative references on the subject (Kistler 1993; Bose 1993).

11d.4.2 FLOW DOWN AN INCLINED SLIDE

It is well known that the wave-damping capability of surface active substances, or surfactants, must hinge on surface tension gradients. Incipient disturbances, which can be viewed as propagating waves, tend to compress and extend periodically the adsorbed layer of surfactant at the free surface, thereby inducing a surface tension gradient that aids or opposes the disturbance. The gradient is reduced and shifted by diffusion, the more soluble the surfactant, and can be further altered by uptake and discharge of soluble surfactant from micelles, if they are present. This section uses the theory put forth in Section 11d.2 to predict how nonequilibrium processes of diffusion and micellar exchange of surfactant affect the stability of liquid films running down inclined planes – ‘falling liquid films’.

The key to understanding the mechanism behind the damping effect of surfactant is the magnitude and phase angle of the surface concentration response relative to wave height. These of course determine the surface tension response and the phasing of surface tension gradients relative to the disturbance. The latter induces a shear stress on the underlying liquid and through it couples the hydrodynamic stability problem with surfactant transport. Smith (1990) reconciled these phasing concepts in the surfactant-free case, arguing that shear stress, properly phased relative to wave amplitude, heightened disturbance growth rate. However, few have recognized that the magnitude and phase of the

surface concentration can also be used to explain how surfactants temper wave growth.

Given below is a complete assessment of the mechanisms of instability (and stability) within the bounds of the linear theory for small disturbances on flowing liquid films which hold a significant inventory of surface-active material in the surface layer. Surfactants that are soluble are also allowed to diffuse and aggregate (form micelles).

11d.4.2.1 Linear stability analysis

The tools we use are normal mode analysis of the linearized vorticity equation, i.e. the Orr–Sommerfeld equation, and the principles which govern surfactant inventory, i.e. convective-diffusion equations for both the monomer and the micelles. Disturbances that are small enough to justify the linearization of the vorticity equation can be represented mathematically in terms of combinations of sinusoids, or Fourier modes. Because most dangerous modes are two-dimensional (Squire 1933) it suffices to restrict disturbances to the type shown in Fig. 11d.3.

When the temporal form of the Fourier modes is substituted into the Navier–Stokes equations, the stability formulation results in the Orr–Sommerfeld equation (see for example Whitaker

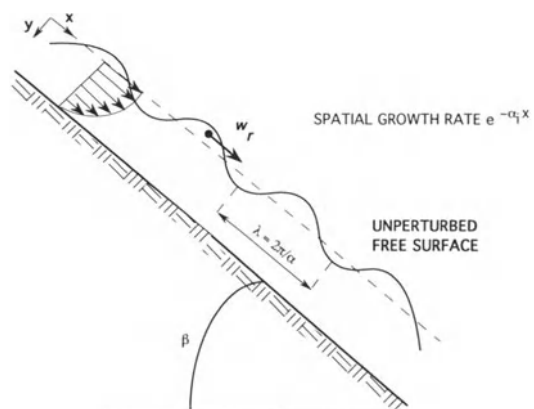


Figure 11d.3 Flow down an inclined surface: definition sketch.

1964, Yih 1963). The Orr–Sommerfeld equation is a fourth-order ordinary differential equation and hence requires four boundary conditions: two at the solid wall and two at the free surface. At the wall the two conditions are those of impenetrability and no-slip (Chapter 2). At the free surface the balance of normal and tangential forces (equation (11d.5)) is employed.

In steady flows of films down inclined surfaces there are no surface tension gradients; the system is in complete chemical equilibrium and bulk concentrations of each species are everywhere the same. When this base flow is perturbed sinusoidally, surface compression and expansion by each normal mode cause small departures from equilibrium. The convective diffusion equations, i.e. equation (11d.1), can be linearized accordingly, and the solution can be represented with the same generic Fourier modes as used for the velocity and pressure, necessarily of the same frequency because the source of the concentration disturbance is wave expansion and contraction. A second-order ordinary differential equation system results for each species. The boundary conditions as described earlier enforce impenetrability at the substrate surface and a species balance between the excess surfactant at the surface and that just underneath (*cf.* equations (11d.2)–(11d.3)). The stability formulation of

these equations can be found elsewhere (Whitaker 1964; Schunk 1989).

The relevant parameters in the Navier–Stokes system are the Reynolds number, Re , the capillary number, Ca , and the angle of inclination β . The first two of these are described in Chapter 2. The relevant parameters in the convective diffusion system are the Schmidt number of each species (monomer and micelle), $Sc_i \equiv \mu/(\rho D_i)$, the recruitment depth (or strength of adsorption), $d_e \equiv (d\Gamma/dC_1)/h$, and the elasticity number, $Es \equiv (1/\mu U_m) d\sigma/d \ln \Gamma$. Here we specialized to a linearized version of the Langmuir adsorption model (equation (4.5)): $\Gamma = (d\Gamma/dC_1)C_1$. The elasticity and Schmidt numbers are described in Section 11d.2. The recruitment depth is based on surface–subsurface equilibrium and is the depth of liquid which contains the same amount of surfactant as the surface, measured in units of the film thickness h . The remaining parameters appear in the source and sink terms of the convective diffusion equations and are used to account for the surfactant monomer–micelle exchange process. These are also described in Section 11d.2. The physical and material properties needed to determine these dimensionless groups are given in Table 11d.1.

The Orr–Sommerfeld equation and its boundary conditions together with the linearized form

Table 11d.1 Surfactant liquid properties corresponding to sodium-dodecyl sulfate in water at 20°C

Parameter		Value	Source
Monomer diffusivity	D_1	$0.4 \times 10^{-9} \text{ m}^2/\text{s}$	Weinheimer <i>et al.</i> (1981)
Dimensional recruitment depth	$d_e L$	10^{-2} cm	Mysels and Florence (1970)
Langmuir constant	a	34.3 mol/m^3	Prins <i>et al.</i> (1967)
Saturation adsorption	Γ_∞	$18 \times 10^{-6} \text{ mol/m}^2$	Prins <i>et al.</i> (1967)
Aggregation number of smallest micelle	N	98	Ruckenstein and Nagarajan (1975) Corkill and Walker (1972)
Micelle size distribution	p	3	Corkill and Walker (1972)
Micelle diffusivity	D_N	$0.5 \times 10^{-9} \text{ m}^2/\text{s}$	Weinheimer <i>et al.</i> (1981)
Micelle/monomer concentration ratio	C_N^*/C_1^*	1	Kamrath (1984)
Rate constant	k	$1 \leftrightarrow 1 \times 10^8 \text{ s}^{-1}$	Leung and Shah (1986)
Rate constant	k'	$1 \leftrightarrow 1 \times 10^8 \text{ molar}^{-1} \text{ s}^{-1}$	Leung and Shah (1986)

of the convective-diffusion equations and their boundary conditions are homogeneous. As such they constitute a complex eigenproblem, the eigenvalues of which depend on the disturbance forms of interest, i.e., either temporal or spatial or even some combination of the two. In the temporal formulation, complex values of the wave speed w (the eigenvalue) are sought at a specified real wave number α so as to avoid a trivial solution. The temporal growth rate in this case is $e^{\alpha w_i t}$, where w_i is the imaginary part of w . In the spatial formulation, complex values of α are sought given the real frequency, $\omega \equiv \alpha_i w_r$. The spatial growth rate is $e^{\alpha_i x}$, α_i being the imaginary part of α . The corresponding eigenfunctions physically represent the variation of the stream function disturbances and the concentration disturbances across the base flow direction as well as the unknown disturbance amplitude at the free surface.

With the use of the finite element method (e.g., Schunk 1989) or the finite difference method (e.g., Whitaker 1964) the system of complex differential equations can be transformed into an algebraic eigenproblem. Of interest are those solutions to the eigenproblem which correspond to marginally stable and most dangerous states with respect to wave number or frequency. The most useful result, however, is the curve of most dangerous perturbations, that is the wave number or frequency of the most rapidly amplified perturbation at each value of a specified physical parameter.

11d.4.2.2 Results

Effects of surface elasticity

Figure 11d.4a shows predictions of the effect of surface elasticity on the growth rate of the most dangerous temporal disturbance in the limit of negligible bulk-surface interchange of surfactant (this ideal situation is approached as either $d_e \rightarrow \infty$ or $D_1 \rightarrow 0$ ($Sc_1 \rightarrow \infty$)). We divided the elasticity number in Fig. 11d.4a by the Reynolds number in order to compare our results with those of Whitaker, who scaled the surface tension

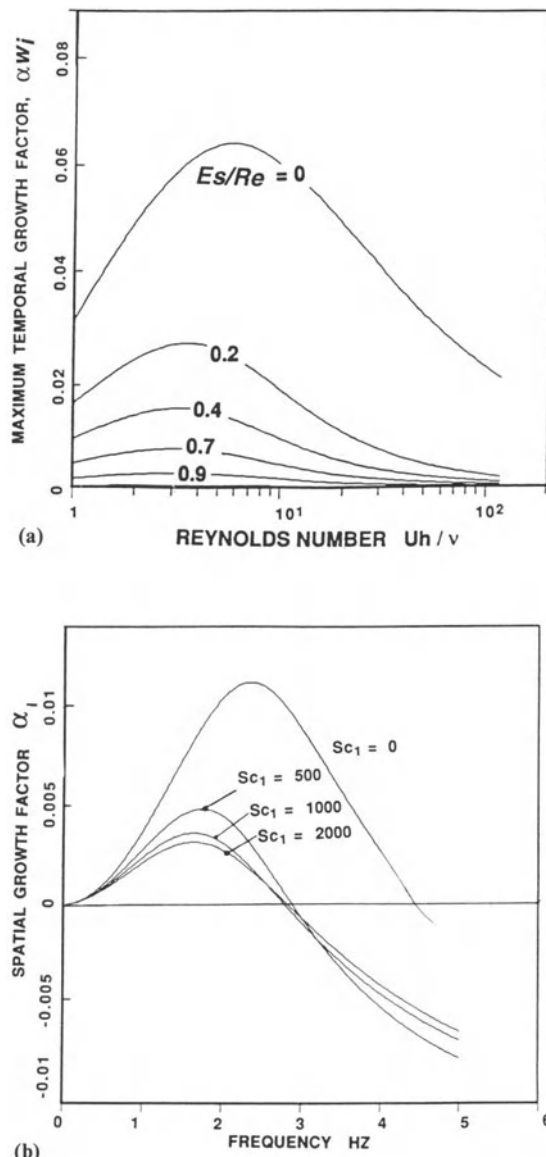


Figure 11d.4 (a) Temporal growth rate (αc_i) of the most dangerous disturbance, $d_e \rightarrow \infty$ (insoluble limit). $Ca = 1$, $\beta = \pi/2$. (b) Spatial growth factor $-\alpha_i$ vs. disturbance frequency ω with varying Schmidt number Sc_1 (diffusivity). $d_e = 10^{-2}$, $Ca = 1$, $\beta = \pi/2$.

gradient forces with inertial forces. The curves show that tangential surface forces owing to surface tension gradients tend to delay at a given

wave number the onset of instability to higher Reynolds number and, moreover, decrease the growth rate of the most dangerous disturbances, provided that $Es > 0$; for $Es < 0$ these forces are destabilizing. Surface elasticity supports the stabilizing effect of capillary pressure, and both have a greater stabilizing effect for shorter waves, i.e. larger wave numbers.

In the limit approached as the wavelength becomes large, i.e., as the wave number approaches zero, the disturbances at the surface penetrate deeper and the influence of the base flow profile curvature is greater. Schunk (1989) showed that temporal growth rates of long-waves (small α) go as $e^{\alpha(6Re/5 - Es - \cot\beta - \alpha^2/3Ca)}$. This stability result applies to insoluble, spread monolayers and is accurate to first order in α . It shows that surface elasticity has an effect at leading order in α ; capillary pressure, on the other hand, enters as a third-order effect. Thus for $\alpha = 10^{-2}$ surface tension would have to increase 100-fold more than surface elasticity to achieve the same degree of stabilization. For film flow down vertical planes, or $\beta = \pi/2$, the flow becomes completely stable to disturbances of all wave numbers as the elasticity number exceeds $6Re/5$. This result agrees well with the authors' predictions (to within 1%) and to a lesser extent with those of Whitaker (1964) (to within 20%) who reported a critical value of $1.03Re$.

Effects of diffusion

When diffusion is added to the story, the surface tension variations no longer respond instantaneously to surface deformation. In this case the mechanism by which surfactant affects stability is most easily explained in terms of time scales, not only those of surface deformation but also those characteristic to diffusion.

The characteristic time scale of surface deformation goes as the reciprocal of the wave frequency, $1/\omega$. By imposing the disturbance frequency ω as a parameter the time scale becomes a physical parameter. Figure 11d.4b shows the spatial growth factor α_i (growth rate $e^{\alpha_i x}$) as a function of disturbance frequency. The various curves show

how the Schmidt number Sc_1 affects the rate at which disturbances of a given frequency amplify or decay in the downstream direction. Actually these curves describe the frequency response, appearing similar to those of the output of a band-selective amplifier. As diffusion coefficients fall, unstable modes are confined to lower frequencies and the growth rates in the unstable band decrease.

The time scale $\tau_d \equiv (Sc_1 h^2/v)d_e^2$ characteristic of diffusional interchange is the time needed for diffusion to extend over a distance of order of the recruitment depth $d_e \equiv (d\Gamma/dC_1)/h$ (see Cussler 1984). Plainly τ_d depends on the concentration of surfactant when the Szyszkowski–Langmuir equation for Γ (equation (4.5)) is employed. For a dilute surfactant–water system and a base flow film thickness h of 0.1 cm, Sc_1 is of the order of 1000 and d_e is of the order of 10^{-2} (Mysels and Florence 1970). The time scale τ_d is then of the order of 0.1 s. Hence, for frequencies of surface deformation considerably less than 10 Hz diffusional transport has a noticeable influence on surface tension gradients.

Effects of micellization

Because an exhaustive study of the effect of each micellization parameter in the model of micelle–solution exchange is beyond the scope of this work, the authors chose here a representative case study based on micelle kinetic studies of sodium dodecyl sulfate (SDS) in water described in the work of Leung and Shah (1986) and in the earlier work of Mijnlieff and Ditmarsch (1965). The parameters needed to describe the micelle dynamics are the last six given in Table 11d.1. Of these, the micelle–solution exchange rates k and k' and the micelle/monomer concentration ratio are the most sensitive to the presence of other additives (Leung and Shah 1986). For instance, electrolytic, organic, and even polymeric additives can change characteristic aggregation rates by several orders of magnitude. Because of this sensitivity, parameter studies were focused on k , k' , and C_N^*/C_1^* .

Figure 11d.5 shows how sensitive the maximum

spatial growth factors are to the characteristic relaxation time τ_m of the micelle–monomer exchange process; τ_m^{-1} depends linearly on the rate constants k and k' (equation (11d.14)). The results indicate that the more rapid the exchange of monomers between the micelles and solution the more rapid equilibrium between the surface and the bulk is re-established, and hence the more unstable the flow because of the reduction of stabilizing surface tension gradients. Rapid micelle–solution exchange clearly facilitates transport of the monomer species to and from the surface.

The degree to which micelles help re-establish equilibrium, and thereby the degree to which gradients along the surface are reduced, depends on the time scale over which micelles, which are surface-inactive, re-establish equilibrium in solution relative to the time scale over which movement of monomers, which are surface active, by diffusion re-establishes equilibrium between the surface and the bulk. The degree to which equilibrium is upset in the first place depends on the time scale of surface expansion, or 2π divided by the frequency.

Figure 11d.5 shows that when k' and k are such that $\tau_m = 10^{-2}$ s (equation (11d.14); $C_1 = 0.003$ molar, $k' = 100$ molar $^{-1}$ s $^{-1}$, $k = 100$ s $^{-1}$, and $C_N/C_1 = 1$), the dependence of spatial growth rate on frequency is nearly the same as that when no micelles are present. Clearly micelle–solution exchange is inconsequential during the time scale of surface deformation, which is longer than 0.1 s in the range of frequencies covered. The diffusion time scale $(d\Gamma/dC_1)^2/D_1$ of all curves in Fig. 11d.5 is of the order of 0.01 s; it is shorter than that of surface deformation. Figure 11d.5 also indicates that spatial growth factors corresponding to each relaxation time fall on the same curve at frequencies less than about 1 Hz. In that range micelle effects appear to be small, or at least small compared with diffusion effects. In any case, at frequencies greater than 1 Hz, micelle–solution exchange speeds up the diffusion process, surface tension gradients are smoothed, and stability is diminished: bands of unstable frequencies become broader and the

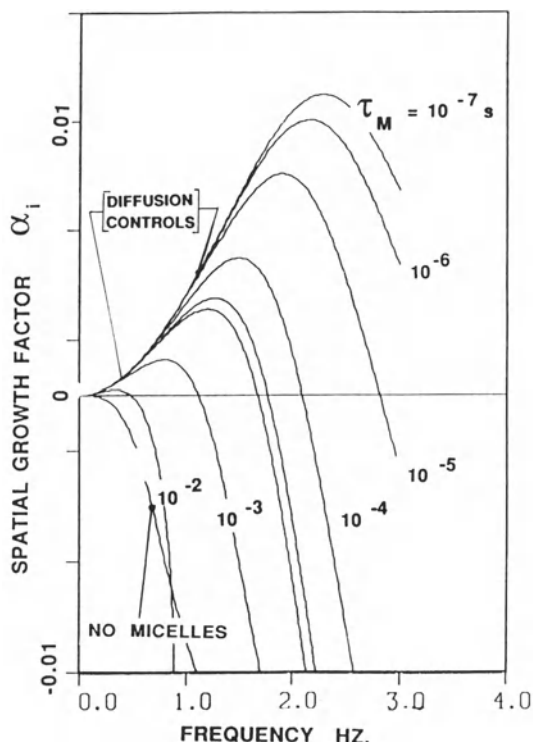


Figure 11d.5 Effect of micelle-monomer relaxation time on the spatial growth factor vs. disturbance frequency ω . $Sc_1 = 1000$, $d_e = 10^{-2}$, $Sc_N = 4000$, $\beta = \pi/2$, $Ca = 1$, $Re = 1$.

maximum spatial growth factors higher. In the high frequency limit, it is expected that all curves in Fig. 11d.5 will again become independent of micelle dynamics, because in that range the system behaves as if it were insoluble.

11d.4.2.3 Mechanism of the stabilizing effect

The predictions in the preceding section indicate, in the range of parameters examined, that surfactants tend to stabilize film flow. The sensitivity of surface tension to concentration is responsible, the magnitude of which is set by the surface elasticity number Es . The physical mechanism begins with local surface expansion and compression. Expansion dilutes and compression concentrates any surfactant deposited

or adsorbed at the liquid surface. If the expansion or compression is not everywhere the same, neither is the surface concentration. Through surface elasticity, concentration gradients make surface tension gradients.

The damping effect of surfactant rests on the phase lag of surfactant response behind the disturbing wave. Conveniently the phasing is explicit in each normal mode of the stability analysis described above. By virtue of the way complex variables are used to represent sinusoidally periodic change, the normal modes of surface expansion rate $\nabla_s \cdot \mathbf{u} \equiv (\mathbf{I} - \mathbf{nn}) \cdot \nabla \cdot \mathbf{u}$, surface concentration response $c_1|_{y=0}$, and surface tension gradient response $\nabla_s \sigma$ can be readily evaluated. Because each normal disturbance mode varies sinusoidally in space and time, the rate of change of any quantity necessarily, in time, lags 90°, or $\pi/2$ radians, behind its amplitude; and the gradient of any quantity necessarily leads 90° ahead of its amplitude.

The phase lag of surface expansion rate behind wave amplitude depends on the flow near the surface. The phase lag of surface concentration depends on the flow, and hence the phase lag of surface expansion, and the convective diffusion process in the liquid beneath the surface: were there no diffusion, the location of minimum surface concentration would coincide with that of maximum surface expansion, which is a quarter-wavelength out of phase with that of maximum surface expansion rate. The phase lag of the surface tension gradient is exactly $\pi/2$ behind the surface concentration: wherever the location of maximum surface concentration will also be the location of minimum surface tension; likewise, wherever the location of minimum surface concentration will be the location of maximum surface tension.

Figure 11d.6 portrays the surfactant response on a film flowing down a vertical wall when the surfactant is insoluble, i.e., $D_1 \rightarrow 0$. The left of Fig. 11d.6 shows the disturbance velocity field over 1.5 wavelengths. Disturbances travel from left to right, as does the direction of flow. The Reynolds number is 0.001 and the disturbance decays with time. Surfactant molecules tend to

gather near the crests and scatter near the troughs, by virtue of surface compression being least near the crests and surface expansion being greatest near the troughs; the maximum and minimum rate of strain is of course a quarter-wavelength displaced, which in this case is at the wave nodes where $\nabla_s \cdot \mathbf{u}$ is either a maximum or a minimum. The phase lag of surface expansion rate behind the wave is $-\pi/2$ and maximum surface expansion rate coincides with the rear quarter-wave points; the maximum surface compression rate coincides with the forward quarter-wave points. Because there is no diffusion, the surface concentration is in phase with wave amplitude, and the surface tension gradient is in phase with the forward quarter-wave point. The surface tension gradient is directed from the crests towards the troughs and in that way tends to support effects of capillary pressure, which acts downwards on the crests and upwards on the troughs.

As the Reynolds number Re of the base flow increases, the locations of maximum surface compression and expansion shift relative to wave amplitude; so does the surface tension gradient. On the right of Fig. 11d.6 the Reynolds number is 10 and the flow was found to be neutrally stable, although it would be unstable were it not for the surfactant – vertical falling films are unstable to any disturbance when no surfactant is present (Krantz and Goren 1971). The phase shift relative to the low-Reynolds number case on the left is roughly $\pi/4$. What this shift does to the stabilizing effect of surface tension gradients is discussed below. First diffusion is added to the story.

Diffusion affects the stabilizing action of surfactant in two ways: the first is by causing the phase of the surface tension to lag the wave crest; the second is by reducing the magnitude of the surface tension gradient. Figure 11d.7 illustrates the effect of surfactant diffusivity on surface concentration response. The Reynolds number Re is 0.001 and the recruitment depth d_e is 0.01. The contours of constant monomer concentration are shown at a diffusivity of $10^{-6} \text{ cm}^2/\text{s}$; the Schmidt number is 1000. The lower the diffusivity,

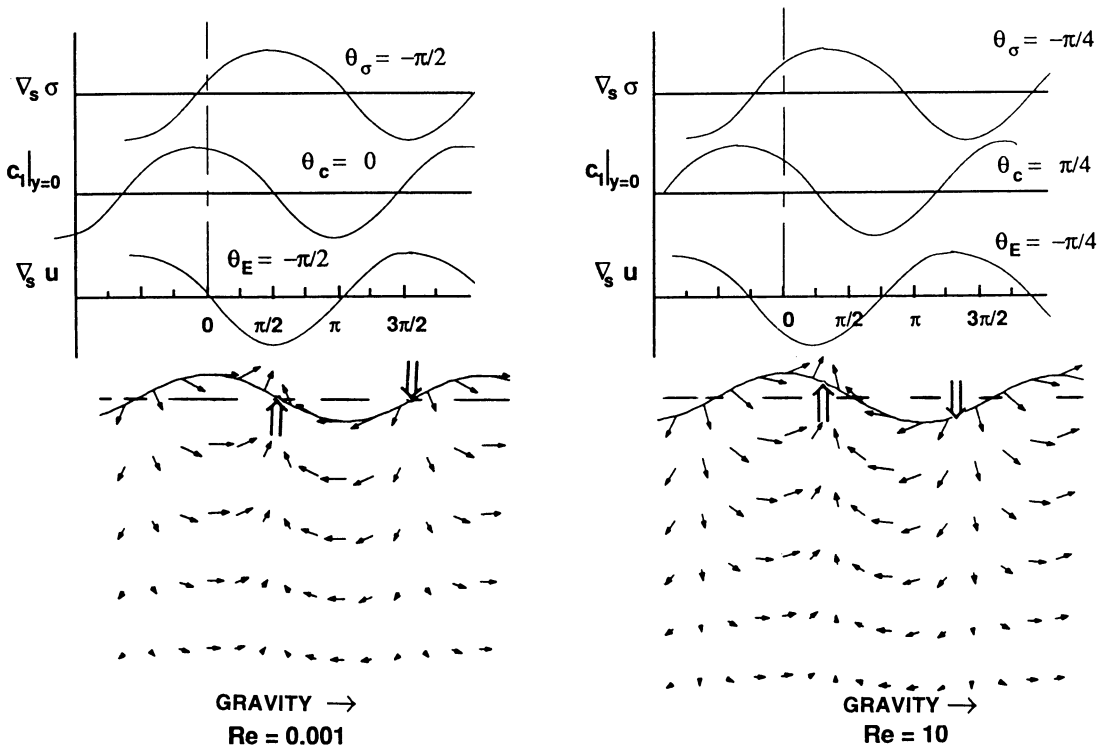


Figure 11d.6 Phasing of surface expansion rate, surface concentration and surface tension gradient relative to a passing disturbance. Predictions are for a liquid film running down a vertical wall with insoluble surfactant. The capillary number Ca is unity; the surface elasticity number Es is 10.

the less the disturbances in concentration penetrate into the film. The surface concentration is a maximum near the wave crests, the exact location of the maximum being shifted slightly forward on the wave. The phase lag of concentration relative to the wave crest is about $\pi/8$. Were there no diffusion, i.e., if $D_1 \rightarrow 0$, the phase lag would be 0 at this Reynolds number (*cf.* Fig. 11d.6). Because there is diffusion, surfactant moves to replenish local surface deficits of surfactant near the troughs and relieve local surface excess of the same near the crests, thereby tending to restore equilibrium. At larger diffusivities, diffusion is much more effective at re-establishing equilibrium during the period of the disturbance: gradients normal to the surface broaden as do those along the surface. The higher the diffusivity, the more the concentration response lags behind the

disturbing wave: diffusion replenishes faster the local surface deficit of molecules in the surface layer after that layer undergoes maximum expansion in the wave troughs. When the diffusivity is raised to $0.001 \text{ cm}^2/\text{s}$, the phase lag of surface concentration is nearly $\pi/2$, the point of maximum concentration being near the forward quarter-wave point.

The matter of how surface tension gradients stabilize is settled by considering the magnitude and phase of the shear stress loading induced by those gradients. The phasing idea takes on a similar form in the problem of wind first raising water waves, as Lamb (1879) discovered. He deduced, from what amounts to a linear stability analysis of waves on still pools, that two requirements of a purely tangential force must be met to generate and maintain waves: first, the

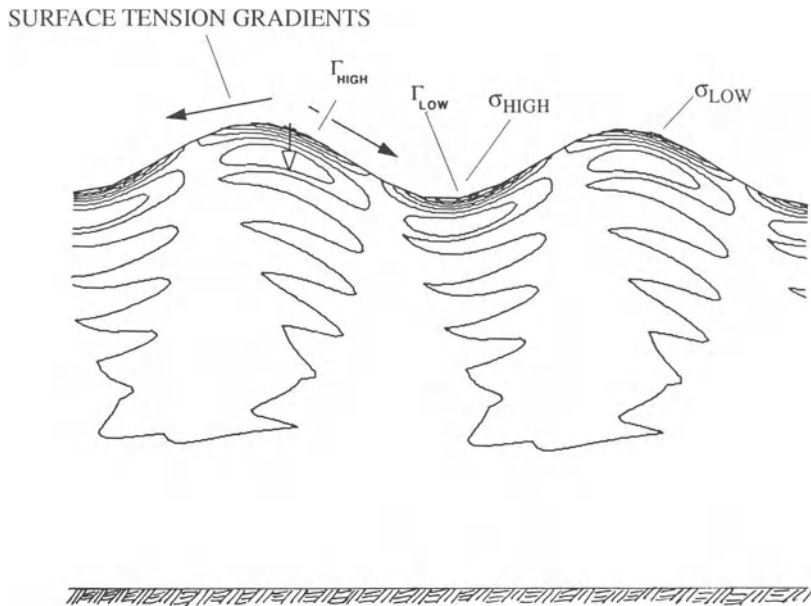


Figure 11d.7 Contours of constant concentration of surface-active free monomer. Calculations are for a film running down a vertical wall (from left to right). $d_e = 10^{-2}$, $\beta = \pi/2$, $Ca = 1$, $Re = 1$.

tangential force must be strong enough to offset the damping effect of viscous forces; second, the tangential force must be distributed so as to act forward on the wave crests, in the direction of wave propagation, and backward on the wave troughs, changing signs at the nodes. He also showed that a tangential force having an opposite sign, i.e., one that lags the first case by 180° , would temper growth or accelerate decay. The situation with surfactant is no different; surface tension gradients act entirely within, and therefore tangential to, the surface. In the case under study here, however, the liquid is flowing and maintenance of waves is by forces generated from gravitational potential and not by wind blowing over the surface. Nevertheless, surface tension gradients exert a tangential force, part of which acts backward on the wave crests and forward on the wave troughs – though this is not so much the case the higher the diffusivity (cf. Fig. 11d.7).

There is also the issue of normal stress loading. Lamb and more recently Smith (1990) examined this as well. Surfactant affects normal stress

loading because it reduces surface tension, and thereby capillary force, which acts downward at the wave crests and upwards at the wave troughs. Surfactants can also affect normal viscous stress in the liquid beneath, insofar as surface tension gradients alter the flow. Although not illustrated here, this research revealed that surfactants do not alter significantly the magnitude or phase of the normal stress loading relative to the waves, at least in the range of flow and surfactant parameters examined (Re from 0 to 100, E_s from 0 to 110, Sc_1 from 0 to 1×10^6 , and d_e from 0 to 1×10^6).

The way in which surfactant distributes along a surface deformed by normal modes is contrary to what many have speculated. Levich (1945) and later Lin (1970) proposed that crests tend to stretch films and troughs tend to compress them. This would actually give rise to a destabilizing mechanism similar to the one proposed by Lamb (1879) and others for wind over water. The correct picture is given in Fig. 11d.7: the kinematics of a passing wave tend to gather surfactant, and

thereby depress surface tension, near its crest and scatter surfactant near its troughs.

11d.4.3 THE OVERFLOWING LIQUID POOL

Predictions of surfactant effects in flow down an inclined surface demonstrate that a complete theory provides a means to probe relevant mechanisms of surfactant action. But how can specific surfactant systems be characterized in terms of the degree to which they can exert dynamic effects? One way is simply to measure all the relevant properties, i.e., equilibrium surface tension versus surfactant concentration, surfactant molecular diffusivity, and micellar coefficients if concentrations above the critical micellization range are of interest. An alternative, although harder to interpret, is to measure a so-called dynamic surface tension, as described in detail in Chapter 4.

To interpret dynamic surface tension requires a complete theory of the physical rate processes involved, i.e. diffusion, adsorption and micellization. The ultimate goal of measuring dynamic surface tension is to deduce basic physical properties needed to complete that theory. To date few methods have emerged with that capability because the flow field is usually too complex for simplified analyses to be accurate, especially when surface tension gradients are important. Possible exceptions are those methods designed to detect falling surface tension over the course of several minutes (see Defay and Petre 1971; Chapter 4). On that time scale, well established static methods are suitable, e.g., spinning drop, Du Nouy ring, etc. (see Adamson 1982), and there is no flow field to contend with.

Available methods of measuring dynamic surface tension – or otherwise measuring or inferring the surface tension as a function of time or of surface deformation rate – are categorized most appropriately by their relevant time scales: that is, time scales on which measurements can be interpreted. Coating flows, as well as many other processing flows, pose an outstanding challenge because surface deformation time scales can be exceedingly small – often they are less

than one millisecond. Because dynamic surface tension is so difficult to interpret only a small number of techniques have proved to be practicable. Some of them are detailed in Chapter 4.

It appears that one method seeing at least some use in the aqueous coating industry is that in which liquid wells up in a small circular pool and overflows the edge, called the overflow technique. Although it is easier to operate than any other method, the flow field is complex and poorly understood. As near as the author can tell, a study with the method was first published by Piccardi and Ferroni (1951). The approach appears to have originated with M. Mclean, a researcher with Kodak Limited Research in the United Kingdom, in 1951 (Orem 1988). One overflow cell design is shown in Fig. 11d.8. In it liquid is pumped into the bottom of an upright dish and allowed to overflow the rim. As an area element associated with a parcel of surface liquid moves radially outward to flow over the rim it expands. As this happens any adsorbed surfactant has to cover more area, and so the surface concentration falls locally. Correspondingly, the

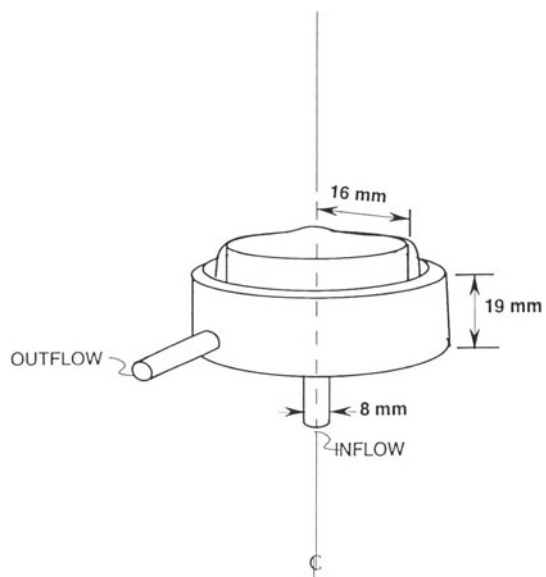


Figure 11d.8 Overflow cell design from Schunk (1989).

surface tension rises. What is often called the dynamic surface tension is the apparent surface tension inferred from the capillary force that the expanding surface exerts on a Du Nouy ring, Wilhelmy plate, or the like.

Although some related techniques have been described (e.g., Fainerman 1986; Imaishi *et al.* 1982), only several other published accounts of the overflow cell exist: Defay and Roba-Thilly (1954), Padday (1957), and most recently Bergink-Martens *et al.* (1990) are examples (more can be found in Chapter 4). Defay and Roba-Thilly used a funnel-shaped dish and measured the apparent surface tension with a Du Nouy ring, concentric with the rim of the cell. Padday used a cylindrical vessel like that in Fig. 11d.8 and attempted to equidistribute the flow by placing a glass sinter a few millimeters below the surface. Although this reduces the required inventory of liquid and confines the flow so the flow is better controlled, it does not change the basic aspects. Bergink-Martens *et al.* combined a theoretical and experimental treatment of a funnel-like design to examine the effects of surfactant on the surface speed profile.

Interpreting measurements of dynamic surface tension by the overflow cell or any related method is difficult, chiefly because of an unknown flow field. Based on existing data and the author's experience, a few disconcerting aspects of the method need to be analyzed before its usefulness as a dynamic tensiometer can be assessed. These aspects are (1) the heretofore unknown nature (strength) and extent of the surface deformations and how these depend on flow rate and cell dimensions, (2) the possibility of inferring from the measurements basic physical properties, e.g., diffusivities, micellization kinetics, etc., and (3) the effect of surface tension gradients on the flow field.

11d.4.3.1 Analysis

Insofar as the cell sits upright, the flow is rotationally symmetric around the cell axis (z -axis); see Fig. 11d.8. Accordingly we needed to solve only an axisymmetric flow problem. The

relevant Navier-Stokes system and species conservation equations are summarized in Chapter 2 and earlier in the present chapter. Here only the specializations are made for this particular flow; most pertain to the parameters that define the flow configuration and the boundary conditions at the inflow and outflow surfaces; those parameters that pertain to surfactant transport remain for the most part unchanged. Again we use the Galerkin/finite-element technique to solve the governing equations, with an automatic mesh generation scheme based on solving an elliptic partial differential equation system; for details see Schunk (1989).

11d.4.3.2 Results and discussion: parameter studies

The dimensions and geometrical features of the prototype cell match those of the laboratory cell shown in Fig. 11d.8. Physical properties and parameters are specified for sodium-dodecyl sulfate (SDS) in water at a temperature of 20°C. This is the same surfactant system studied earlier in the flow down an inclined surface. The relevant properties of the system are given in Table 11d.1.

The equations of overall mass and momentum transfer were solved first over a range of flow rates bounded by those attainable with the experimental setup, i.e. 0.1 to 3 cm³/s. Figure 11d.9 shows the flow structure at 3 cm³/s; the basic aspects are the same at lower flow rates. The liquid stream entering the bottom of the cell broadens under the action of viscosity. A momentum boundary layer builds up from the stagnation point and grows along the free surface. Much of the liquid is turned back into a large toroidal recirculation in the upper, outer part of the cell. The liquid stream jets upward, welling up the surface around the center line.

The surface speed profile is of particular interest because it determines the characteristic time scale of surface deformation, and hence the depth to which diffusion can penetrate in the act of re-establishing equilibrium. For example, the slope of the speed profile determines the rate of surface expansion (or compression) and hence

the time scale over which equilibrium between the surface and the bulk is upset. Figure 11d.9 also shows the speed profiles at five different flow rates. The rate of surface expansion is the relative rate of change of surface area per unit of fiducial mass. It is governed by the differential equation of area change: $d[\ln(dA)]/dt = \nabla \cdot v_s dA$ is any infinitesimal control area and v_s is the velocity field by which elements of the surface that defines the system move. In terms of a coordinate basis that lies within an axisymmetric surface the surface divergence of the surface velocity, $\nabla \cdot v_s$, is $[d(sv_s)/ds]/s$, where s is a measure of arc length along the surface in the radial direction.

The speed profiles reveal that the kinematics of the surface flow is radially uneven; the top of Fig. 11d.9 shows that its nature can be described in two zones. The innermost zone, which surrounds the center stagnation point, is the one with the most intense surface expansion as parcels of liquid accelerate rapidly away from the center. There the surface expansion is intense and localized (200 s^{-1} at a flow rate of $1.4\text{ cm}^3/\text{s}$), taking on the greatest value at the stagnation point which is ordinarily at (or near) the center of the surface. Hereafter, this region is referred to as the impingement zone. In this zone the surface speed increases linearly with radial distance, indicating that the flow is irrotational in nature (Batchelor 1967). The surface accelerates to a peak speed at a distance that is between one-tenth and one-fifth of the distance from the center to the rim. Then the surface expansion abates so that adsorption simply controlled by diffusion can move surfactant into the surface to bring it toward equilibrium with the liquid beneath. In this region the speed falls with radial distance as $1/s$ and the expansion factor falls to nearly zero. Hereafter, this region is called the radial-outflow zone. Both surface zones are shown schematically in Fig. 11d.9.

The speed profiles also reveal that the concept of 'surface age' has no physical basis in an

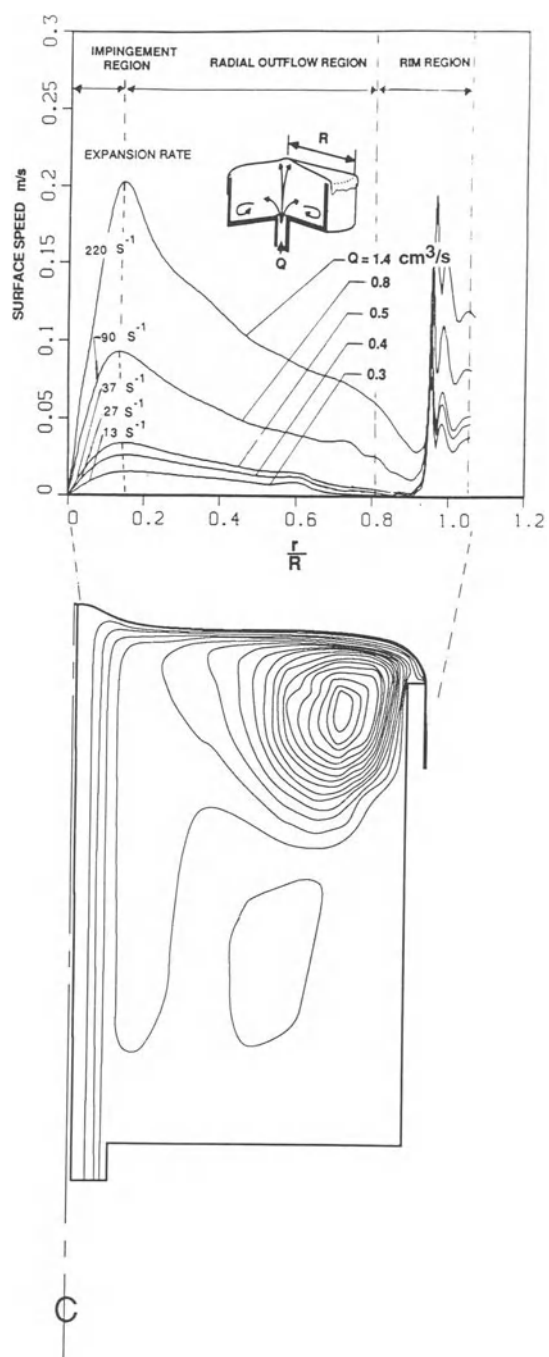


Figure 11d.9 Predicted flow field without surfactant. Lower part shows pattern of streamlines at a flow rate of $3\text{ cm}^3/\text{s}$. Upper part shows the surface speed profiles at five different flow rates.

overflow cell of this shape and dimension. Surface age is usually defined as the time elapsed from the creation of a surface, without any excess of adsorbed material (surfactant), and a time during which there is no surface deformation (Defay and Petre 1971). Defay and Roba-Thilly (1954) and Padday (1957) referred to the transit time from the center of the surface to the edge as the 'surface age', but the speed profiles in Fig. 11d.9 reveal that the extent of effective surface expansion ('renewal') spans a large portion of the surface surrounding the center, especially at low flow rates. In fact, in the funnel-like cell design examined by Bergink-Martens *et al.* (1990), the impingement zone spans more than half the cell radius.

Figure 11d.10 shows a sampling of computed results at different concentrations and flow rates for SDS in water at 20°C. Figure 11d.10a shows the difference between the dynamic surface tension and the equilibrium surface tension at four concentrations. The flow rate is 0.6 cm³/s. Departures from equilibrium surface concentration are greatest when the bulk concentration is the smallest. The highest bulk concentration, 10⁻³ molar, is just below the CMC; at this concentration departures from equilibrium are small if not negligible, even near the stagnation point. Time scales over which diffusion works to re-establish equilibrium are proportional to $(\Gamma/C_1^*)^2/D_1$ and this is of the order of 1 ms for SDS at concentrations above 10⁻³ molar (Mysels and Florence 1970). The rate of surface expansion is 100 s⁻¹ in the impingement region and so the time scale over which equilibrium is being upset is about 0.01 s. Hence diffusion is able to re-establish equilibrium much faster than surface expansion can destroy it. For concentrations less than 10⁻⁴ molar, however, diffusion time scales are greater than 0.01 s. In this case diffusion between the surface and the bulk is too slow to re-establish equilibrium. In all cases, the surface expansion rate is small in the radial-outflow zone and the transport of surfactant is controlled by diffusion. Correspondingly, the surface tension falls towards equilibrium. As the surface passes over the rim, however, rapid surface expansion again dilutes the surface and surface tension rises sharply.

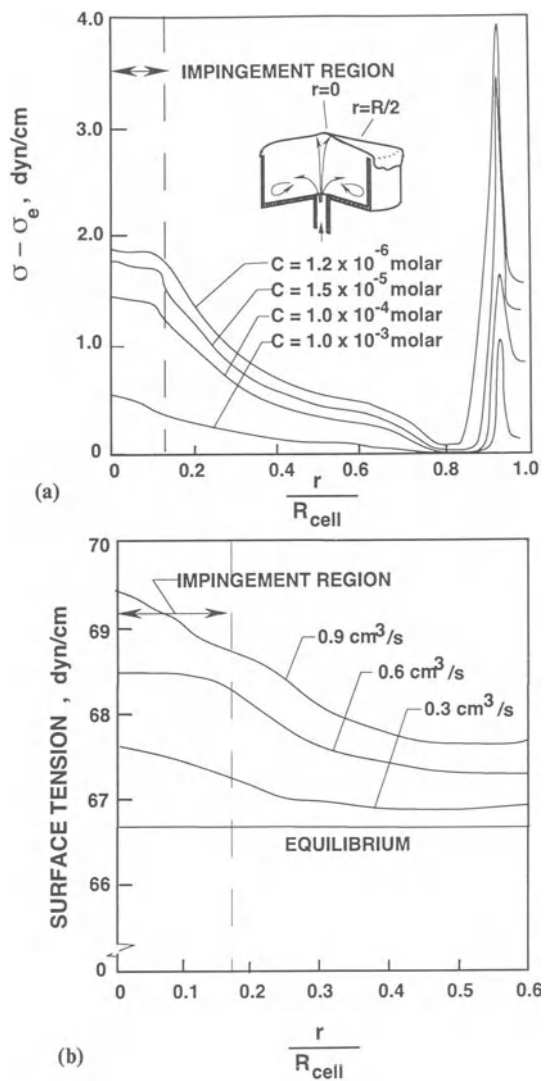


Figure 11d.10 Predictions for SDS in water at 24°C. (a) Effect of bulk concentration on the surface tension profile. The flow rate is 0.6 cm³/s. (b) Effect of flow rate on the same. The solution is 2 × 10⁻⁵ molar.

Figure 11d.10b shows the effect of flow rate on surface tension profiles. The predictions are computed for 2 × 10⁻⁵ molar SDS in water. The diffusion time scale, $(\Gamma/C_1^*)^2/D_1$, at this concentration is of the order of 1 s. It is clear from the speed profiles in Fig. 11d.9 that the surface

expansion rate is the greatest when the flow rate is the greatest. At each of the flow rates for which predictions are shown in Fig. 11d.10 the reciprocal of the expansion rate is less than the characteristic time scale for diffusion. The result is a subequilibrium surface concentration across the cell, even at the lowest flow rate, $0.3 \text{ cm}^3/\text{s}$, because diffusion is too slow to re-establish equilibrium.

The predictions of local surface tension for a 2×10^{-5} molar SDS solution agree to within 5% with the measurements of the same with the wire probe (Schunk 1989). Propagation of the uncertainties in the force measurement, wire diameter, and contact angle sets the upper bound of random error at about 3%. One possible source of the discrepancy is the surface constitutive equation (11d.4); the theory is reliable inasmuch as that equation is accurate. Other possible sources are uncertainty in the physical properties with which the predictions were made and computational error caused by insufficient mesh refinement.

The effects of micelles on local surface adsorption, and hence local surface tension, is difficult to extract from measurements of surface tension in the overflow cell. At concentrations near that at which surfactant aggregation is thought to occur for SDS (about 3×10^{-3} molar on the basis of the equilibrium measurements of surface tension; see Schunk 1989) little sensitivity of local surface tension to flow rate is observed. So the predictions to follow cannot be corroborated by the measurements. Nevertheless they are exceedingly useful for studying the effect of micelles on the rate at which rapidly expanding surfaces re-establish equilibrium. That micelles can indeed exert effects has been confirmed in controlled experiments (Lucassen and Giles 1975).

For the same micellar system we examined in the previous section on slide flows we again focus our parameter studies on the rate constants k and k' and the inventory C_N^*/C_1^* . Figure 11d.11 shows the profiles of monomer and micelle

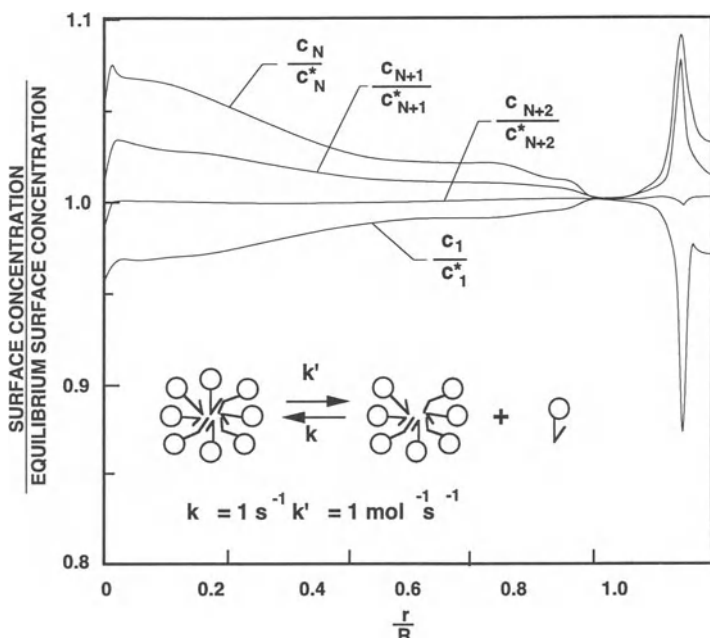


Figure 11d.11 Surface concentration profiles of monomer and micelle species. The flow rate is $0.5 \text{ cm}^3/\text{s}$. Predictions are for 0.003 molar SDS-water solution.

concentration along the free surface at a flow rate of $0.5 \text{ cm}^3/\text{s}$. Evidently the distribution of concentrations of surface active monomers and micelles shifts when chemical equilibrium is disrupted by the expanding surface of the overflow cell. Near the cell center micelles emit monomers in an attempt to replenish the free surface deficit of the latter. The result is a concentration distribution that shifts to favor the 'floor' species C_N . A distribution shift that favors the ceiling species $N + p$ would be the case if the surface were being compressed.

Figure 11d.12a shows how sensitive the monomer surface concentration profile is to micelle–solution exchange rate constants k and k' . The concentration ratio C_N^*/C_1^* is set to unity. The results indicate that the more rapid the exchange of monomers between the micelles and solution the more rapidly the equilibrium between the surface and the bulk is re-established, and hence the more uniform the surface concentration and surface tension are across the cell. Rapid

micelle–solution exchange clearly facilitates transport of the monomer species towards the avid surface.

The characteristic micelle relaxation time is given by equation (11d.14) and its magnitude for the case in which $k = 100 \text{ mol}^{-1} \text{s}^{-1}$, $k' = 100 \text{ s}^{-1}$ and $C_N^*/C_1^* = 1$, is $2 \times 10^{-4} \text{ s}$. The time scale for diffusion to and from the surface is 0.01 s for a SDS-water solution that is 3×10^{-3} molar (Mysels and Florence 1970). The time scale of surface expansion at a flow rate of $0.5 \text{ cm}^3/\text{s}$ is $(25 \text{ s}^{-1})^{-1}$, or 0.04 s ; see Fig. 11d.9. Hence micelles and monomers re-establish equilibrium amongst themselves much faster than equilibrium is upset by surface expansion. In so doing they must speed up the much slower diffusion process in a way that keeps the surface more uniform in concentration and nearer to equilibrium, more so than would be the case if micelles were absent.

Finally, Fig. 11d.12b shows how the micelle to monomer concentration ratio affects the surface monomer concentration profile. Increasing the

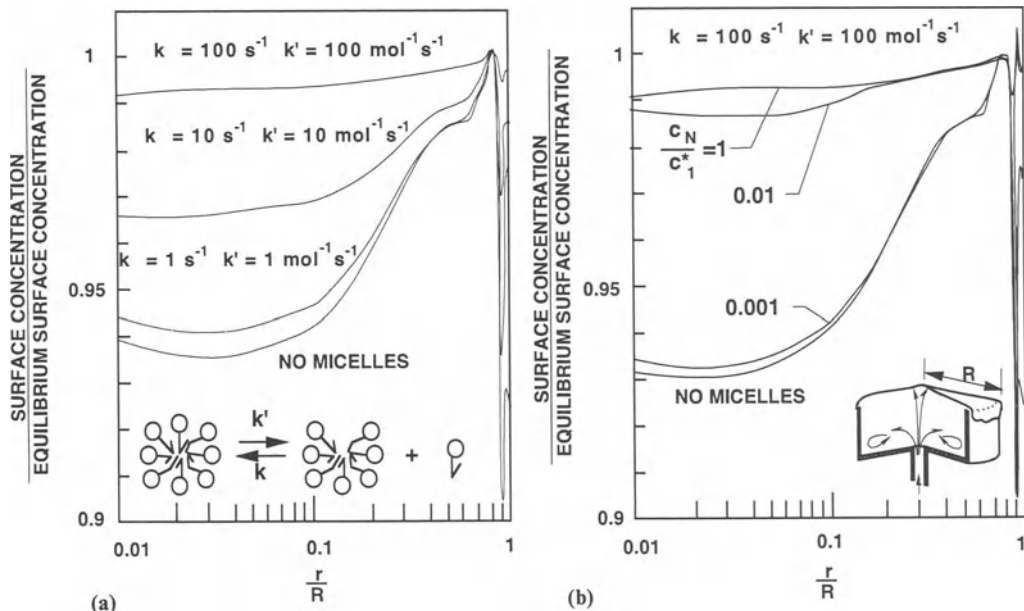


Figure 11d.12 Predictions for 0.003 molar SDS in water at 24°C . The flow rate is $0.5 \text{ cm}^3/\text{s}$. (a) Effect of micelle–solution exchange rate constants on the profiles of monomer concentration along the surface. The micelle to monomer concentration ratio is unity. (b) Effect of monomer to micelle concentration ratio on the same. $k' = 10 \text{ mol}^{-1} \text{s}^{-1}$ and $k = 10 \text{ s}^{-1}$.

concentration of surfactant when the system is above the CMC usually raises the ratio of micelle concentration to monomer concentration (Kamrath 1984). What is most significant is that the greater the ratio C_N/C_1 , i.e. the more the total inventory of surfactant is in micellar form, the closer the system stays to equilibrium. Again, the mere presence of rapidly exchanging micelles tends to drive the system towards equilibrium.

11d.4.3.3 Conclusions

The essential result of this analysis is the finding that the surface speed changes rapidly across the free surface in the overflow cell and this makes for highly nonuniform surface expansion (deformation). To complicate matters further, the extent of the regions of surface expansion change with flow rate. Because of this, the so called ‘surface age’ – defined by many researchers as a measure of elapsed time during which surfactant molecules arrive at the surface in the act of re-establishing equilibrium – is indeterminate without reliable theory. Moreover, the material parameters for the mechanisms proposed in the theory cannot be deduced from the measurements in an overflow cell, unless those measurements are interpreted with a detailed analysis of the sort we present here, i.e. the material parameters are determined by matching theory to experiment.

There is a possibility that the cell design can be altered in such a way to make the measurement easier to interpret. For example, Bergink-Martens *et al.* (1990) proposed one particular design which results in appreciable surface expansion across more than half the cell radius. Unfortunately, the expansion rates they report are all less than 5 s^{-1} .

11d.4.4 SLIDE COATING FLOW

Nearly any coating flow could serve as a case study of the potential effects of surfactant additives. Here the focus is slide coating (Chapter 11b). This process is the workhorse of the photographic films industry, and the use of surfactant additives is nowhere deeper entrenched than in multilayer photographic coating technology (see for example

Knox 1970). Though surfactants are routinely used as coating aids, the zones where they act and the mechanisms by which they work are still matters of controversy. To settle some aspects of this controversy is the main objective of this case study.

Over the years many surfactants have been tested and their effects have been correlated with their chemical natures and, often, capacities for lowering surface tension. In this way has grown an art of picking a surfactant to cope with a specific difficulty, and to be compatible with the rest of the coating formulation. An early report came from Deryagin and Levi (1964). They tested surfactant additives for their ability to improve dynamic wetting in a roll-coating process, i.e. their ability to increase the maximum speed at which the substrate can be successfully coated without excessive air-entrainment. They also predicted from a crude analysis what their experiments confirmed: that only certain surfactants can improve dynamic wetting, and those surfactants have a common chemical structure and interaction with gelatin. Their experiments were limited to low coating speeds – at least by today’s standards – and it is unclear what criterion for ‘successful’ wetting they used.

In a landmark patent, Knox (1970) revealed a particular combination of surfactant (hydroxy propylene oxide) and gelatin, and other additives too, that resulted in improved quality and uniformity of the coated layers in the final product. In other words, the surfactant made the formulation easier to coat successfully, or at least that was Knox’s claim.

Before Knox’s patent, it appears that the most common coating aid was saponin, a surfactant prepared from quillara bark (Sturge 1977; cf. Sterzi 1982). Being of natural origin, saponin varies in composition according to the source and method of extraction and is often plagued by the presence of impurities. Growing demands for higher coating speeds and increased number of coated layers, together with the growing complexity of the coating formulation, rendered saponin alone insufficient as a coating aid. Consequently, there came a proliferation of

synthetic surfactants developed for the same purpose, the first of which appears to be that by Knox (1970).

The art has remained highly proprietary and little attention is given to it in the scientific literature. Since Knox (1970), only a few reports have been published on the matter, at least with any direct mention of coating. Zvanut and Cohen (1978) investigated the physical properties of gelatin–surfactant combinations, including surface tension and dynamic surface tension, and claimed that these correlated well with the ability of certain surfactants to aid the coating process. They published no proof of this claim, however. Greener *et al.* (1980) found that a certain surfactant (Atlox 2081) delayed the onset of the ribbing imperfection to higher coating speeds in a two-roll coating process. Their case study did not employ gelatin mixtures, but rather a glycerin–water mixture. Hempt *et al.* (1985), though citing no particular coating method, claimed that improvements in ‘coating operability’ can be made when the right surfactants are added to gelatin mixtures. Again their claim is not substantiated with careful coating experiments but instead is based on experience and on measurements of a relevant surface mechanical property known as surface elasticity. Zeldes (1985), in a more recent US patent, demonstrated clearly the improvement in slide coating operability by adding surfactants of the fluorocarbon type. His claim is that such additives promote defect-free coating at higher coating speeds. But the nature of the defect to which he refers is unclear. Fruhner, Kragel and Kretzschmar (1989, 1991) examined the effects of several surfactants on the stability of the liquid bridging the gap between the die face and web and demonstrated a clear improvement in coating quality at higher web speeds. The degree of improvement, however, was highly dependent on surfactant type and its interaction with gelatin. Valentini *et al.* (1991) attempted to correlate measurements of dynamic surface tension with the range of applied vacuum over which defect-free coating can be achieved. Though he claimed that dynamic surface tension does affect the so-called ‘coatability window’, the

characteristic time scales of most defect formation phenomena are far less than that on which he measured dynamic surface tension. Padmanabhan and Bose (1988) measured the dynamic contact angle with a simple plunging tape apparatus (see Chapter 3) in the presence of surfactants. Although their measurements were at speeds much lower than those found in a typical coating operation ($< 1 \text{ cm/s}$), they found strong evidence of nonequilibrium values of surface tension at the dynamic contact line, over a certain range of concentration.

A computer-aided theoretical analysis of surfactant effects in steady and unsteady two-dimensional flow of Newtonian coating liquid in a slide coater is reported below. The details of the techniques can be found in Chapter 9 and Chapter 13. Of course, as we pointed out earlier, there have been several significant theoretical developments, the most noteworthy coming from Park (1991), Cox (1986), Giavedoni and Saita (1992), Ruschak (1987) and Bose (1993). The phenomena of interest here are shown in Fig. 11d.13. Clearly, surfactant can act by various mechanisms in each zone. Surfactant action on surface waves on the liquid flowing down the slide of indefinite length is well understood now from the linear stability analysis earlier; however, it remains unclear how end effects, where the flow may not be rectilinear, alter this action – as in the case when the liquid runs off the end of the slide into the bead region. Possibilities of surfactant action on the rapidly deforming upper and lower menisci between the slide and substrate – that is, around the ‘coating bead’ – are complex and barely identified. Whether surfactant transport to and from the lower meniscus is fast enough to have a significant impact on the static and dynamic wetting process is also unclear.

Other issues arise when more than one layer is coated, the most notable one being edge control after the liquid has been coated. In practice, surfactants are added to each layer in varying amounts, so that the bottom layer has the highest apparent (dynamic) tension, and each layer above that has a successively diminishing apparent tension (see Chapter 4 for complete

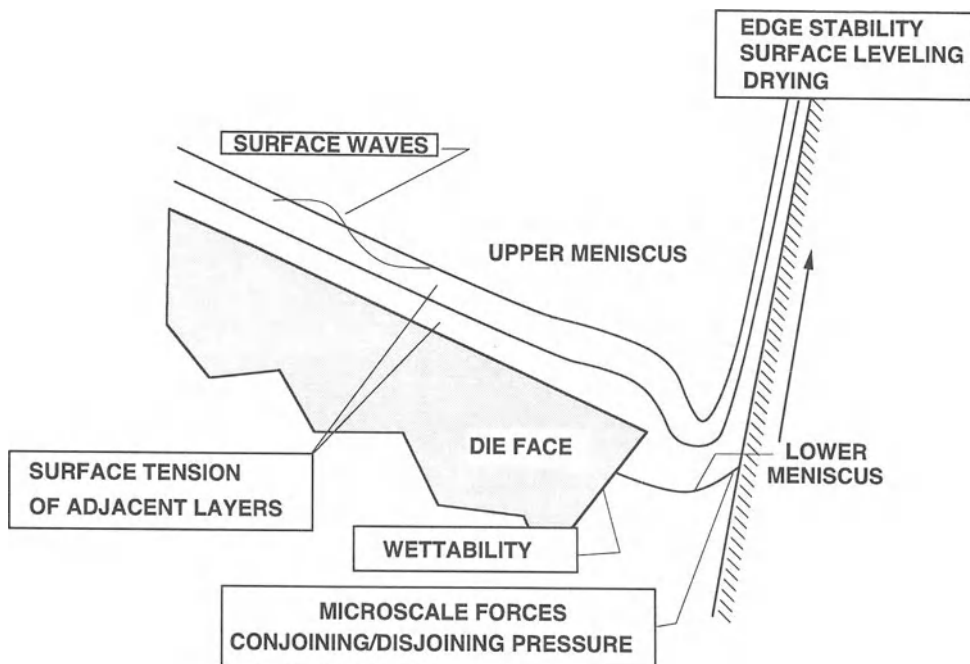


Figure 11d.13 Zones of surfactant action in multilayer slide coating.

discussion). In that way the exposed edges of the upper layers cannot contract and drag lower layers with them after being deposited. But when equilibrium conditions are not attained immediately this simple argument fails, especially when adjacent layers contain different surfactants and their equilibrium tensions are nearly the same (Orem 1988). A quantitative understanding requires a three-dimensional, or at least a specialized two-dimensional, transient analysis and is not pursued here. However, predictions below reveal the extent to which equilibrium is achieved after the liquid has been coated, thereby providing a test for the argument above.

11d.4.4.1 Results and discussion: effect of surfactant on steady operating states

The many surfactant solution properties and coater design specifications in Table 11d.2 define a case of a slide coating process. Despite lacking the effects of gelable polymer, which too can have

a surface-tension lowering effect, we believe this study is typical of slide coating in the photographic film industry. As in the previous case studies, an aqueous sodium-dodecyl sulfonate (SDS) solution was chosen as a model system, and its relevant properties are given in Table 11d.1.

Figure 11d.14 shows the computed velocity field, streamlines and surfactant concentration contours corresponding to the base case. The liquid is seen to wet the die face. The expansions and compressions that material elements undergo while moving along the surfaces in the slide coating flow can be inferred from the streamline structure in the adjacent liquid: where the streamlines are converging in the direction of flow, the liquid on the surface speeds up along its path and initially, at least, any adsorbed surfactant has to cover more area. In other words, any surface excess concentration per unit area of the surface is lowered. Conversely where the streamlines are diverging in the direction of flow the surface slows down along its path,

Table 11d.2 Dimensional operating parameters and surfactant liquid properties representative of a slide coating system. Solution is sodium-dodecyl sulfate in water at 20°C

Webspeed	U_w	2 m/s
Gapwidth	L_{gap}	250 μm
Vacuum	p_b	-150 Pa
Gravity-web angle	β	0°
Slide-web angle	α	70°
Dynamic contact angle	θ_d	155°
Static contact angle	θ_s	70°
		Layer A (lower)
		Layer B (upper)
Final film thickness	—	45 μm 25 μm
Initial film thickness	—	940.3 μm 283.38 μm
Viscosity	—	15 mPa s 5 mPa s
Density	—	1000 kg/m ³ 1000 kg/m ³
Solvent surface tension	σ_0	70 mN/m 60 mN/m
Surfactant concentration		20 mol/m ³ 20 mol/m ³
Equilibrium surface tension		42 mN/m 38 mN/m

surface elements are compressed and initially, at least, any surface excess concentration per unit area is raised. In each event equilibrium between the surface and the bulk is upset, and surfactant tends to move from the solution to the surface, or vice versa, to restore equilibrium. The concentration contours show how the straining motion of the surface causes movement of surfactant by diffusion in the adjacent liquid. It is noteworthy that the concentration boundary layers adjacent to the surface are extremely thin.

Figure 11d.15a shows the speed profiles along the upper and lower menisci at four surfactant concentrations, ranging from 0.002 molar to 0.05 molar. Figure 11d.15b shows the corre-

sponding surface concentration profiles. If soluble surfactant is to act dynamically in the coating bead, there must be places on the menisci of the bead where the time scale of surface strain is shorter than the characteristic diffusion and adsorption times. Figure 11d.15b shows that such places evidently exist on the upper meniscus in the bead region and on the lower meniscus close to the dynamic wetting line, as the surface concentration deviates from its equilibrium value by as much as 20%. Because surface tension depends strongly on surfactant concentration, concentration gradients make surface tension gradients, as depicted in Fig. 11d.15c. These in turn exert a shearing stress on the liquid beneath and can alter the flow.

What matters is how this diffusion time scale, $(\Gamma_\infty/C_1^*)^2/D_1$ (Mysels and Florence 1970), compares with the time allowed for surfactant to re-establish equilibrium. If the surface is undergoing no strain, such as on the slide or far downstream on the web, that time scale is the transit time of the surface from the point at which equilibrium is destroyed. If the surface is being strained, such as between the slide and the substrate – that is, around the coating bead – then that time scale is of the order of the inverse of the strain rate. Evidently, from Fig. 11d.15, the diffusion time scale is much larger than the inverse of surface strain rate on the upper meniscus, as long as the concentration is less than 0.05 molar; that is, diffusion cannot deliver surfactant to or remove surfactant from the surface fast enough to maintain equilibrium. On the lower meniscus diffusion is fast enough to establish equilibrium over a small portion of the surface near the static contact line, as long as the concentration is greater than about 0.02 molar.

The surface strain rate is simply the gradient of surface speed. On the upper meniscus, in the bead region, the surface strain rate is of the order of 1500 s^{-1} where the surface is expanded and of the order of 2000 s^{-1} where the surface is compressed; on the lower meniscus it is of the order of 1000 s^{-1} where the surface is expanded near the static contact line and of the order of $20,000\text{ s}^{-1}$ where the surface is compressed near

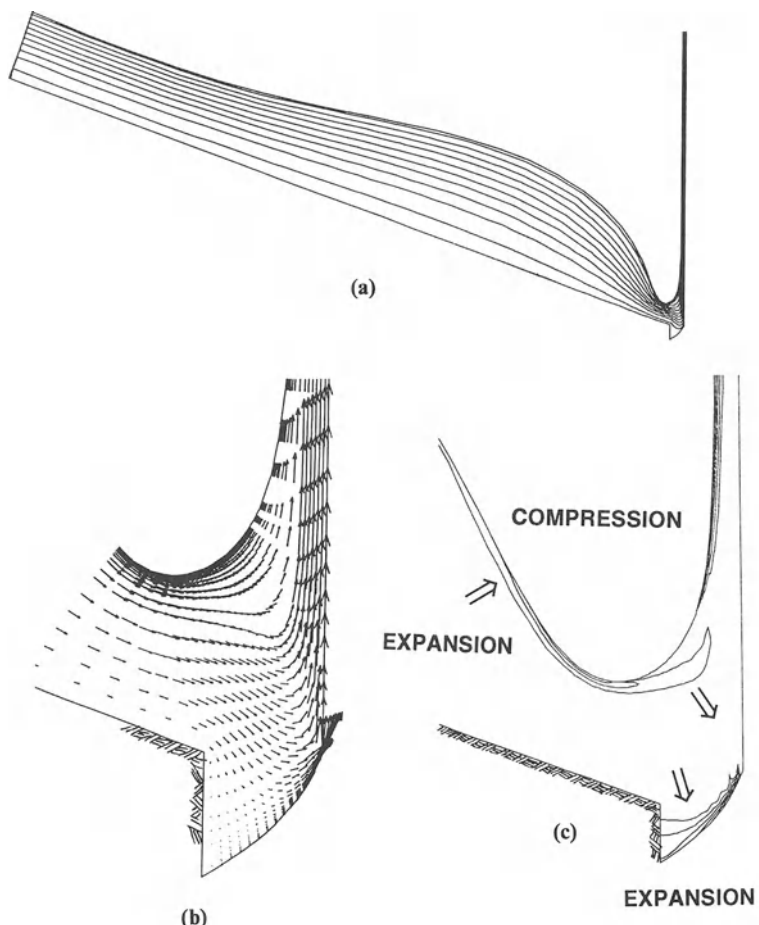


Figure 11d.14 Base case (a) streamlines, (b) velocity field and (c) concentration contours of surfactant in bead region with arrows indicating surfactant movement in an out of the surface (vacuum reduced to 300 Pa).

the dynamic contact line. Whether the surface liquid undergoes compression near the contact line is an unsettled matter, as we discuss below. Figure 11d.15 shows that equilibrium is nearly maintained across the entire lower meniscus at concentrations greater than 0.02 molar, and so the time scales of diffusion at those concentrations must be less than $(10,000 \text{ s}^{-1})^{-1}$, or 0.1 ms. This is in accord with the characteristic recruitment time, $(\Gamma_\infty/C_1^*)^2/D_1$, which falls below 0.1 ms at concentrations greater than 0.025 molar.

Far upstream on the slide the surface and the

bulk are in equilibrium. There the surface and the bulk are assumed to have ample time to establish equilibrium after they emerge from the feed slot; Fig. 11d.15. Whether equilibrium is attained before the liquid exits the flow domain downstream depends on how the transit time of the liquid from the base of the slide to the outflow plane compares to the characteristic equilibration time of the surface and the bulk, i.e., $(\Gamma_\infty/C_1^*)^2/D_1$. The former is about 1.6 ms when the web speed is 2 m/s; the latter depends on the bulk concentration. At concentrations less than 0.01 molar

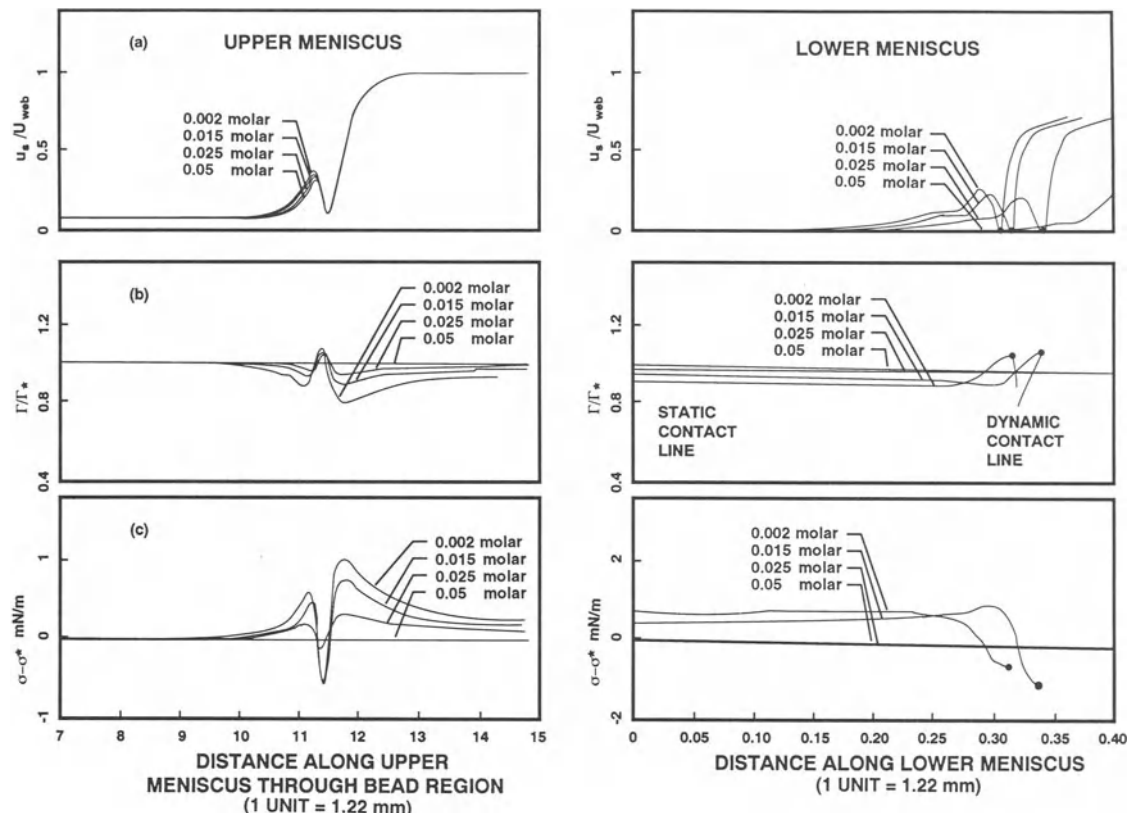
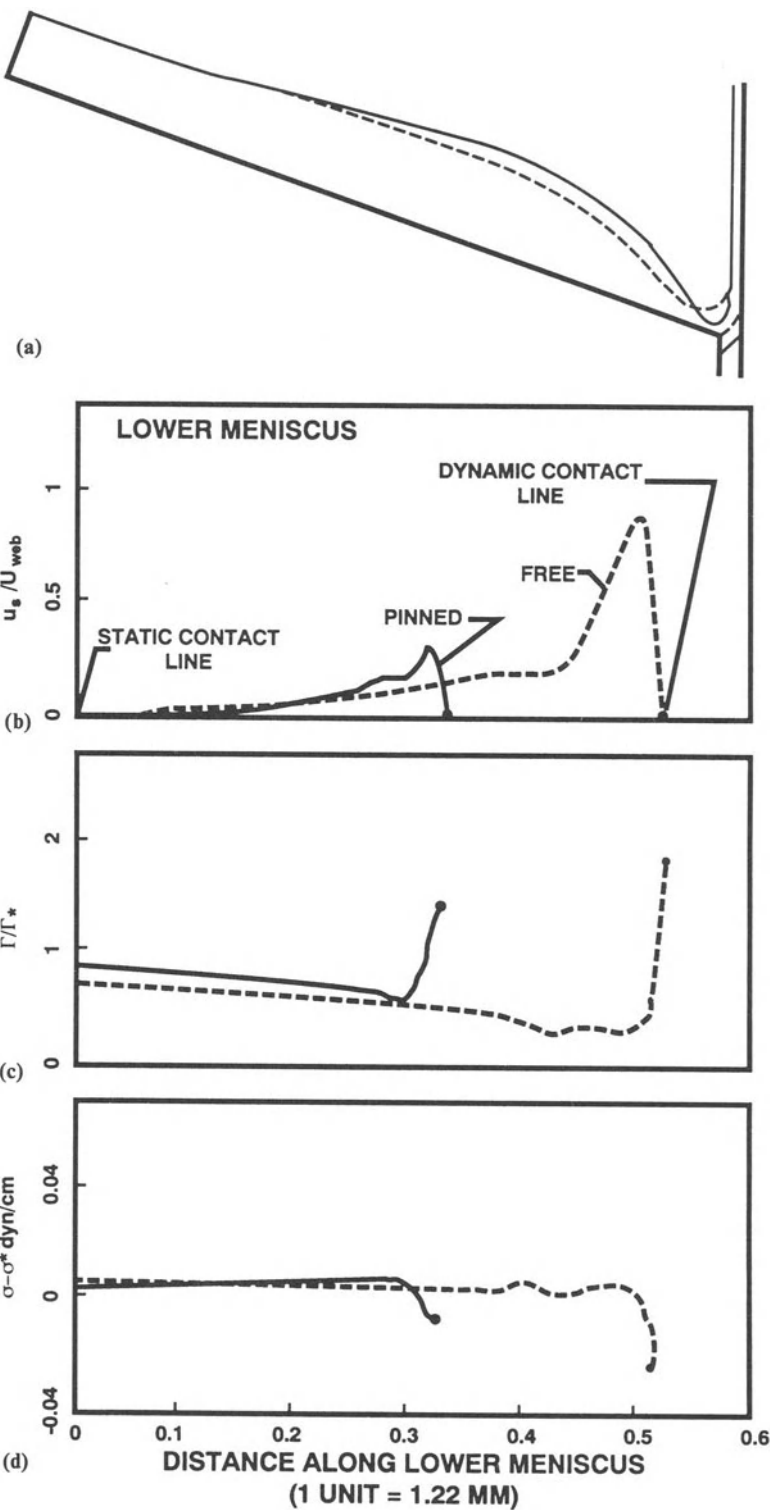


Figure 11d.15 Profiles along upper and lower meniscus in the bead region: (a) surface speed, (b) surface concentration, and (c) difference between local surface tension and equilibrium tension. System is SDS in water at 20°C.

the equilibration length can be many times the film thickness, e.g., with 0.005 molar solutions equilibrium is not attained between the liquid and the surface until the deposited film is about 5 cm downstream. That the surface and the bulk have not established equilibrium just after the film is deposited may change the widely accepted hypothesis that equilibrium surface tension controls edge stability in multilayer coating and is apparently one reason why measurement of so-called dynamic surface tension is important to edge control in a multilayer coating (Chapter 4).

The situation on the lower meniscus depends on the position of the meniscus relative to the sharp corner at the base of the slide and on the flow kinematics at and near the contact lines. Reducing the vacuum from 350 Pa to 150 Pa raises the meniscus from the position of the base case to a pinned position, as depicted in Fig. 11d.16. When the meniscus is pinned the surface strain rates are more intense. Although the surface is effectively ‘created’ at the static contact line, it maintains a near equilibrium inventory of surfactant, even when the solution is as dilute

Figure 11d.16 Pinned vs. free lower meniscus. (a) Surface shape, (b) surface speed measured in units of web speed, (c) surface concentration, measured in units of equilibrium concentration, of 0.001 molar SDS in water at 20°C, and (d) difference between dynamic surface tension and equilibrium surface tension.



as 0.001 molar. Presumably the infinite residence time of the surface elements immediately at the static contact line allows the surface to recruit surfactant from a broad region like that between the die lip and lower meniscus; see Fig. 11d.14c (*cf.* Whitaker and Wu 1985). Still the concentration at the static contact line is slightly depressed because of the slight surface expansion there.

Figures 11d.14–11d.16 indicate that surfactant adsorbed to the lower meniscus is apparently not being transferred to the web at a significant rate (see Cox 1986; Rame 1988). Instead it holds up there and diffuses back into the bulk, contradicting the fundamental idea of a coating process (Kistler 1984). It is perhaps relevant that recent experimental evidence indicates ‘surfactant hold-up’ might occur at speeds much slower than we employ here (Padmanabhan and Bose 1990). The boundary condition on liquid motion used so far requires that the velocity of the liquid at the dynamic contact line be equal to the velocity of the dynamic contact line. This condition results in perfect slip and effectively relieves the stress singularity that otherwise occurs with the conventional no-slip boundary condition (Kistler 1984). But only certain slip models allow transfer of surfactant from the free surface to the substrate (Dussan V. 1976). Rame (1988) proposed several indirect mechanisms that promote transfer of surfactant: these include surface diffusion or imposition of at least a limited amount of solubility, thus providing for dissolution then reabsorption through the bulk phase. The only other way to remedy this problem is by allowing a multivalued velocity at the dynamic contact line, which would allow surfactant to pass freely to the substrate but brings back the nonintegrable stress singularity. As it happens, such a condition brings about dramatic changes in the response of the lower meniscus to small disturbances, changes which warrant further investigation. What effect the unresolved stress singularity has on the validity of any solution computed with a multivalued velocity is unknown. We return to this matter in the following subsection.

There has been a long-standing controversy

whether surfactant is capable of exerting any effects on the lower meniscus, as it has been thought that the flow is too rapid and the residence time of liquid between the die and the web is too short for the meniscus to recruit a significant excess of surfactant from the bulk liquid. This controversy is settled above where it is shown that the lower meniscus is capable of recruiting surfactant molecules fast enough to depress its tension significantly.

Another way surfactant can affect the lower meniscus is through the apparent static contact angle, θ_s^c , the meniscus makes with the die face. The equilibrium value – for the composition of the solid surface and the composition of the adjacent coating liquid – is crucial in positioning the static contact line (see Chapter 3). If the contact angle is within a certain range – less than 60° in this study – that line can attach to the edge of the die lip, which has been shown to be desirable for uniform coating. Otherwise the line may locate on the face below the edge. The positioning is also influenced by the pressure field in the coating bead, which responds to the vacuum being applied to the underside. All else being fixed, the higher the contact angle, the more likely the coating bead is to wet the die lip.

The static contact angle is an outward measure of the tendency of the liquid L to form a film on or adsorb to the solid S in the presence of a gas G . Young’s equation relates the angle to the surface tension σ and to hypothetical excess free energies per unit area of the solid exposed to the gas, σ_{SG} and the liquid, σ_{SL} : $\cos \theta_s^c = (\sigma_{SG} - \sigma_{SL})/\sigma$. σ_{SG} and σ_{SL} both diminish when the surfactant adsorbs to the solid, as σ is likely to do, and they are sensitive to unintended contamination as well (Chapter 3; Bose 1993; Blake 1984). Surface roughness and compositional heterogeneity of the solid can be additional complicating factors, because they can lead to multivalued contact angles, a phenomenon known as ‘contact angle hysteresis’ (Chapter 3). The contact angle depends on whether the liquid is in a receding or advancing situation (see Johnson and Dettre 1969; Bose 1993). Moreover, the presence of surfactant can change the range of the hysteresis between

advancing and receding values. To incorporate the effect of contact angle hysteresis in this analysis would require some knowledge of how the liquid originally came into contact with the solid. At the very least this issue begs for a parameter study within the advancing/receding contact angle range, although we do not pursue that here.

Here we assume that the current surfactant system is ‘inert’ to the substrate and is not volatile so that changes in σ_{SG} and σ_{SL} are negligible (Bose 1993). Surfactant adsorption at the gas–liquid interface lowers the contact angle and therefore promotes wetting. Although contact

angle data are sparse for materials with which coating dies are often fabricated, e.g., stainless steel, this effect is accounted for qualitatively here through Young’s equation and an empirical relationship among σ , σ_{SG} , and σ_{SL} : $\sigma_{SG} - \sigma_{SL} = 72.5 - \sigma$ (Fowkes 1962). Here σ , σ_{SG} , and σ_{SL} are in units of mN/m and the relationship is an approximation for aqueous solutions of ionic surfactants on metals such as copper, iron, and silver (Johnson and Dettre 1969).

Figure 11d.17a shows the effect of the amount of added surfactant on the position of the lower meniscus, using the empirical relationship given

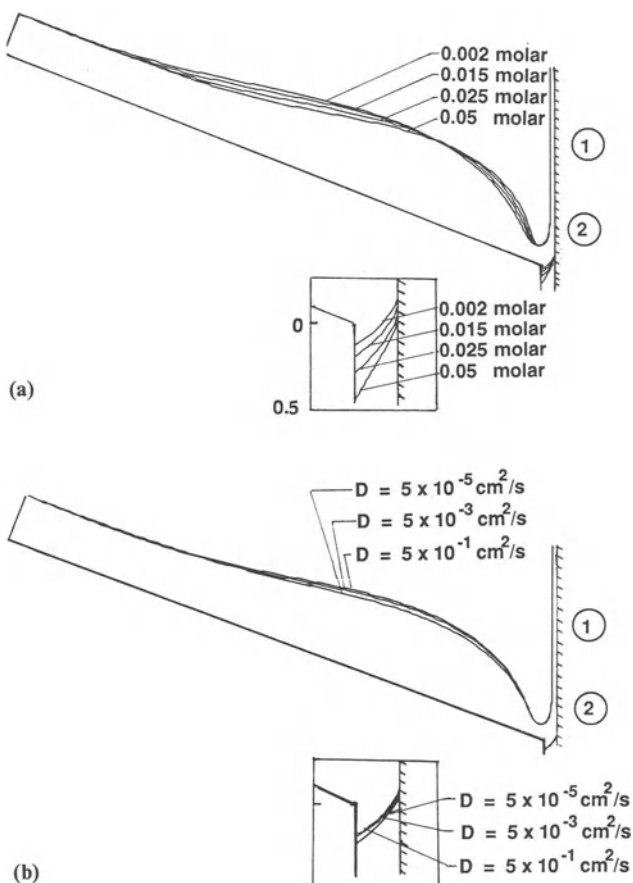


Figure 11d.17 (a) Surfactant concentration effect on the free surface shape. (b) Surfactant diffusivity effect on the free surface shape. The system is 0.025 molar SDS in water at 20°C.

by Fowkes (1962). The greater the concentration the more the liquid wets the solid. The change in location of the lower meniscus can be attributed partly to the depression of tension, and hence to the reduction in static contact angle. To assess how much dynamic surface tension is involved, the meniscus position is predicted when equilibrium is maintained and compared with that when equilibrium is not maintained, as in Fig. 11d.17a. This is done by simply specifying a large diffusivity, of the order of $1 \text{ cm}^2/\text{s}$.

The results of doing so are shown in Fig. 11d.17b. Clearly the dynamic effects of surfactant are important, but not as important as the equilibrium effect. The movement of the lower meniscus is seen to be slightly less than would be the case if equilibrium were always maintained.

The apparent dynamic contact angle in this study remains an empirical parameter. Unfortunately, the fate of adsorbed surfactant on menisci which terminate at a dynamic contact line is uncertain, as is the physics of dynamic wetting itself. Several studies suggest that surfactant can affect the macro-scale features of the dynamic wetting process. Cox (1986) demonstrates that the macroscopic contact angle depends on contact line velocity and surfactant concentration under certain conditions. Unfortunately, he did not allow transfer of surfactant from the liquid surface to the substrate, and his analysis is limited to insoluble surfactants. Hopf and Geidel (1987) and Hopf and Volke (1987) investigated the effects of surfactant on advancing and receding contact angles. They found poor agreement with the results of several noteworthy theories (e.g., Blake 1988), which they attributed to the effect of surfactant transfer from the surface to the substrate. They also claimed that surfactant can change the macro-scale dynamic contact angle, at least at speeds less than 1 cm/s . So far we have adopted Cox's idea of not allowing surfactant to pass across the dynamic contact line. When we do allow surfactant transfer, as suggested by Hopf and co-workers and in a different way than advocated by Rame (1988), we find a dramatic effect of surfactant on unwanted disturbances in slide coating. We describe this below.

The profiles of surface concentration of SDS in Fig. 11d.15 show that the surface concentration gradients can be steep on the upper meniscus, especially in the bead zone. The corresponding steep surface tension gradients do not appear in earlier versions of coating theory but must be reckoned with because they can alter the flow, as Fig. 11d.17 indicates. In Fig. 11d.17a the surface elasticity E_s is changed by varying the concentration. Plainly the surface tension-lowering effect of surfactants together with the surface tension gradients they induce can reduce the size of the standing capillary wave on the upper meniscus. It is perhaps relevant that a Dupont Patent (Zeldes 1985) is based on experimental observations of such an effect. The patent claims that reducing the amplitude of this wave expands the bounds of operability with respect to the ribbing instability.

The mechanism underlying this amplitude reduction hinges on the local reduction of capillary forces by the surface tension lowering effect. The forces that operate beneath the standing wave are pressure, which rises in the streamwise direction due primarily to a velocity decrease, and the capillary pressure, the resultant of surface tension in the curved meniscus. The streamwise viscous stress immediately beneath the peak of the wave is about 10% of both forces and rises to about 40% at the foot of the slide. Reduced capillary pressure by surfactant leads to a reduced wavelength and a less pronounced thinning of the film just upstream of the bead. On the other hand, the curvature of the lower meniscus increases to compensate for the lower surface tension under the applied vacuum.

A small part of the amplitude reduction can be attributed to the surface tension gradient that the surfactant causes. This is indicated in Fig. 11d.17b, where the strength of the surface tension gradient is varied while the equilibrium tension is kept the same. This is accomplished by varying the surfactant diffusivity over the range of $0.5 \text{ cm}^2/\text{s}$ to $5 \times 10^{-5} \text{ cm}^2/\text{s}$. The locally rising tension of the meniscus on the backside of the standing wave, just downstream of its crest, is part of a surface tension gradient that is directed towards

the trough of the concave meniscus. That gradient steepens with falling diffusivity and exerts a stress that accelerates the liquid underneath the wave towards the bead, thereby reducing the liquid deceleration upstream that leads to the standing wave.

11d.4.4.2 Surfactant effects on the dynamics of slide coating

We examine the effects of surfactant on the dynamics of slide coating by imposing small disturbances in various parameters describing the flow and measuring the response in the take-away zone on the web, because thickness variations there may become permanent defects downstream. As far as theoretical predictions are concerned that position is the outflow plane that terminates the flow actually computed. When the disturbance amplitude is small enough, the resulting variations in the final coated thickness can be inferred with a frequency response analysis (see Chapter 9 for details).

The frequency response to five disturbance sources in a two-layer slide coating process of constant viscosity, surface tension, and density was established in the work of Van Abbenyen *et al.* (1989). The operating conditions they chose are used for the base case in this study. Here the effect of surfactant on the frequency response is examined, mainly to determine if dynamic surface tension can dampen the response of the uniformity in final thickness to ongoing sinusoidal disturbances. In this section, one surfactant-related parameter is varied, the concentration, and one physical property is varied, the surfactant diffusivity. A comparison of the response of the system with varying concentration and realistic surfactant diffusivity to that with varying concentration and an unrealistically large diffusivity resolves the importance of dynamic surface tension. Of course were the diffusivity large enough, the time scale of re-equilibration would be so short as to make it improbable for the surface and the bulk to stray from equilibrium.

In the results we report here only one operating parameter has been changed from the base case,

and that is the vacuum. Here it is reduced to 150 Pa (from 350 Pa) so that the meniscus pins at the sharp edge at the end of the slide (the equilibrium contact angle is taken to be 60°). Figure 11d.18 shows the frequency response of the total film thickness to small disturbances in two of the same parameters chosen by Van Abbenyen *et al.*; namely, (1) vacuum, and (2) dynamic contact angle. We also tested four other parameters (gap width, flow rate of the upper layer, flow rate of the lower layer, and webspeed) but found no major differences, at least when the meniscus is pinned. The first parameter (vacuum) is an operating condition; the second reflects the surface characteristics of the web being coated and the fluid mechanics of the liquid flow as it contacts the web at the apparent dynamic wetting line. On the left of Fig. 11d.18 the response is shown at a large surfactant diffusivity, $1 \text{ cm}^2/\text{s}$, and at three different surfactant concentrations – 0.00036 molar, 0.015 molar, and 0.05 molar, corresponding to equilibrium tensions of 69 mN/m, 55 mN/m and 35 mN/m, respectively; on the right the response is shown at a realistic surfactant diffusivity, $1 \times 10^{-6} \text{ cm}^2/\text{s}$, and at the same three concentrations. The results in Fig. 11d.18 are all for the customary ‘zero’ velocity formulation at the dynamic wetting line (Kistler 1984). Results of the new ‘discontinuous’ velocity formulation (Schunk 1989) when they are perceptibly different are given below.

The effect of varying equilibrium tension without the effect of dynamic surface tension, or equivalently varying concentration at a high surfactant diffusivity, is such that disturbances in vacuum and dynamic contact angle are less amplified (or more damped) by falling tension (see for example graphs on left side of Fig. 11d.18). The opposite effect is seen for disturbances that produce motion on the slide and cause vibration in the upper layer thickness, e.g., those excited by variations in the flow rate of the upper layer (not shown here), the damping effect of rising tension is likely caused by increased capillary pressure gradients – that go along with rising tension – which tend to fill the wave troughs by driving liquid from underneath the crests. This is the

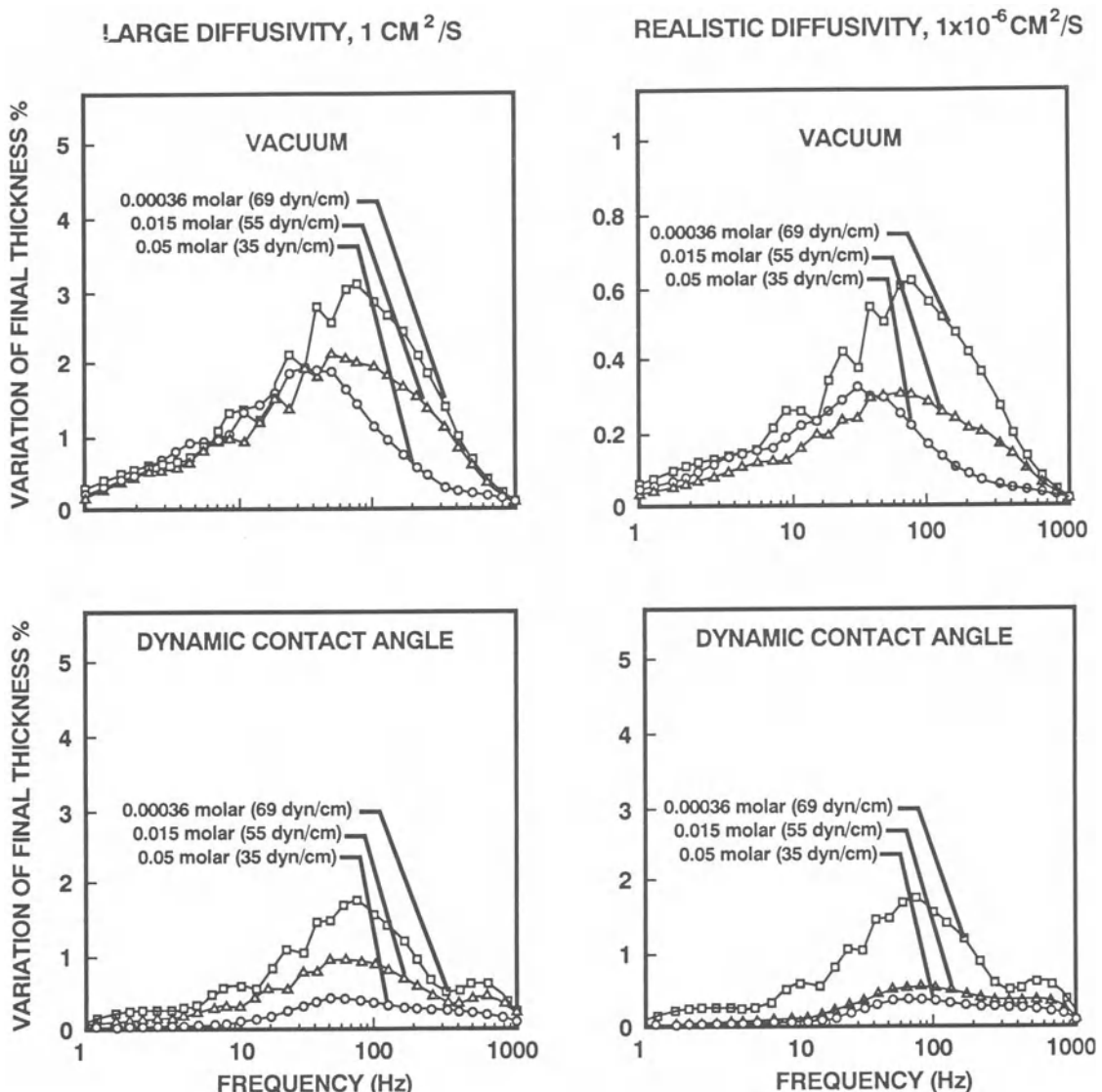


Figure 11d.18 Frequency response of a two-layer flow. Variation of final layer thickness caused by 1% perturbation of backpressure (upper half), and dynamic contact angle (lower half).

same mechanism as that which damps capillary waves on the surface of the slide flow examined earlier.

The picture can be different when the surfactant diffusivity takes on a realistic value, as shown on the right in Fig. 11d.18. When the dynamic

contact angle fluctuates sinusoidally, whatever the cause, the effect of surfactant is such that the least concentrated solution, 0.00036 molar, allows the most amplification, the amplification factor being a little less than 2 at a frequency of 70 Hz, but for more concentrated solutions, 0.015 molar

and 0.05 molar, there is damping at all frequencies, the peak amplification factor being only 0.2 at a frequency of 50 Hz for the most concentrated solution. The mechanism evidently involves surface tension gradients, because raising the concentration but maintaining equilibrium (graph on the lower left in Fig. 11d.18) lowers the amplification factor far less than when equilibrium is not established (graph on the lower right in Fig. 11d.18), especially at the intermediate concentration where the amplification factor at 50 Hz is 0.8 on the left and 0.4 on the right. The same effects of dynamic surface tension can be seen in the response to fluctuations in vacuum (see Fig. 11d.18), for which significantly more damping occurs at the highest and intermediate concentrations, 0.05 and 0.015 molar, when the diffusivity is lowered to a realistic level. So the right amount of surfactant can have a desired effect but too much or too little produces little or no effect. In the limit of zero frequency, the same response is seen at both low and high diffusivity, as they should because in that limit the surfactant has ample time to equilibrate over the infinitely long period of the fluctuation.

Results so far presented are for the customary zero-velocity expedient at the dynamic contact line (see Kistler 1984). Earlier we demonstrated that this leads to a large hold-up of adsorbed surfactant on the surface just upstream, creating a locally lower tension there (see Figs 11d.15 and 11d.16). Schunk (1989) proposed a different formulation that allows a nonzero (discontinuous, actually) velocity at the dynamic contact line and results in a steep acceleration and hence a higher surface tension at the same place. Moreover, it effectively allows more rapid transfer of surfactant from the liquid/gas surface to the solid surface, as advocated by Hopf and Volke (1987). Unfortunately the condition results in a nonintegrable stress singularity, the effects of which are only as severe as the discretization allows, i.e., the finer the discretization in the contact line region, the stronger the singularity. Nonetheless, it is relevant to compare the dynamic response of the coating flow with the zero-velocity formulation and the multivalued velocity formulation, not

necessarily because one is more realistic than the other, but because each represents an extreme case, as we made clear above.

Large differences are seen in the sensitivity to ongoing fluctuations in vacuum and dynamic contact angle. These differences are illustrated in Fig. 11d.19. The lower right half of Fig. 11d.19 shows the effect of the new velocity condition on the fate of fluctuations in vacuum. The most dangerous frequency remains unchanged at about 70 Hz, but the sensitivity of the flow is far greater when the velocity is nonzero at the contact line. At the lowest concentration, 0.00036 molar, the amplification factor at the most dangerous frequency is 1.1 when the velocity is discontinuous and about 0.7 when the velocity is zero, so that the disturbances are amplified instead of damped. Adding more surfactant results in damping at all frequencies, however, reducing the peak amplification factor to 0.4 for concentrations of 0.015 molar and 0.05 molar.

The effect of the 'discontinuous velocity condition' on fluctuations in dynamic contact angle is illustrated in the left half of Fig. 11d.19. This condition has the largest effect on the response of the least concentrated solution, 0.00036 molar, sharpening and heightening the peak around the most dangerous frequency to about 2.5, from 2.0 in the 'zero velocity' case. The 'nonzero velocity' condition also increases the sensitivity of the response to the bulk concentration of surfactant, i.e., increasing the bulk surfactant concentration from 0.00036 molar to 0.05 molar reduces the peak amplification factor from 1.5 to less than 0.1, making the flow nearly insensitive to dynamic contact angle disturbances. So strong an effect warrants further investigation.

11d.5 SUMMARY

Experimental evidence in the form of surface tension measurements in dynamic situations (Chapter 4) and flow visualization (Valentini *et al.* 1991; Zeldes 1985; Knox 1970) reveal potentially important effects of surfactant additives in coating

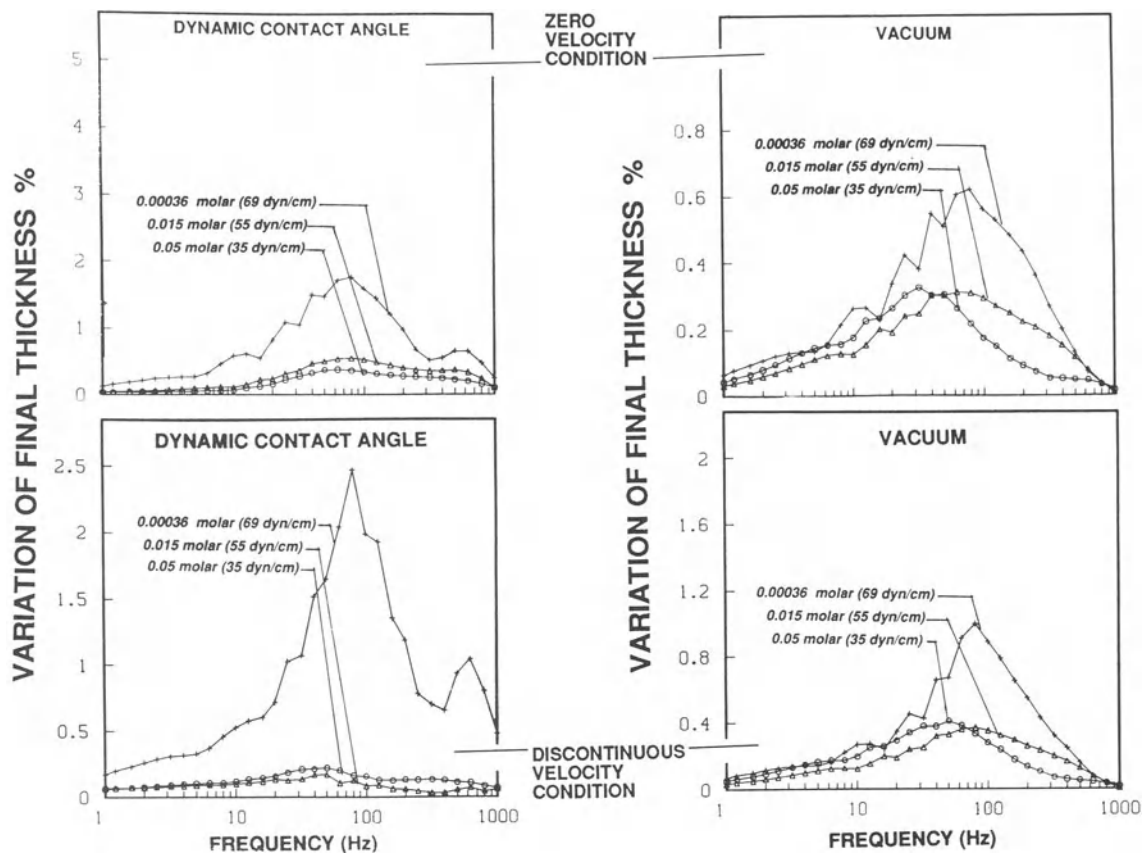


Figure 11d.19 Effect of velocity at the dynamic contact line on frequency response. Upper half is response of zero velocity; lower half is response of nonzero, discontinuous velocity. Left half is the response to ongoing fluctuations in dynamic contact angle; right half is the response to ongoing fluctuations in vacuum.

flows – and indeed many closely related flows. Some of those effects prove to be desirable in coating because they increase ‘coating latitude’, or expand the operability to a wider range of operating parameters. But some of those effects prove to be detrimental because they lead to unacceptable nonuniformities in the final coated film (Chapter 4). A comprehensive understanding of the underlying mechanisms will enable more efficient choice of surfactant additives to cope with specific difficulties and to expand the bounds of operability.

In this chapter we have demonstrated potential effects of surfactant in three prototypical flows,

beginning with the simplest of all free surface flows: film flow down an inclined surface (Section 11d.4.2). An important understanding of the mechanisms by which surfactant dampens waves has been developed. Although these mechanisms have long been known to hinge on surfactant-induced surface tension gradients, we found that diffusion and micellization undermine those gradients, and shift the phase of the surface tension response relative to the wave crests and troughs. This analysis extends what went before (Whitaker 1964; Sterzi 1982) to include effects of soluble surfactant that aggregate, or form micelles.

An overflowing liquid pool represents the

second situation examined above (Section 11d.4.3). Selection of this flow as a case study stems from its use in making dynamic surface tension measurements, which are accomplished with a Du Nouy ring or Wilhelmy plate inserted into the expanding surface. The outstanding challenge, however, is to interpret the measurements in terms of the variable processes, and ultimately to deduce from those processes surface-bulk re-equilibration rates that are independent of the flow field. This would of course lead to relevant physical properties such as surfactant diffusivities and micelle relaxation times for specific surfactant solutions, properties that are necessary to make theoretical predictions. Without reliable theory to predict the complex flow field and the effect of surfactant-induced surface tension gradients on it, however, ambiguous interpretation is inevitable. Only such a theory with reliable constitutive equations – the latter involving the effect of surfactants on equilibrium properties which must also be measured – will enable physical properties of surfactant solutions to be inferred from the surface tension measurements with the overflow device. Part of this program is carried out above.

Finally we tested the theory in slide coating flow (Section 11d.4.4). This process is the workhorse of the photographic films industry, and the use of surfactant additives is nowhere deeper entrenched than in multilayer photographic coating technology. Under steady operating conditions surfactant acts mainly through its ability to lower equilibrium surface tension. If present in high enough concentrations, surfactants can significantly depress the surface tension of the lower and upper menisci, thereby changing the shape of the coating bead as it bridges the narrow gap between the slide die and the moving web. Surfactant can also act dynamically on the coating bead, inducing flow-altering surface tension gradients where the menisci deform rapidly; however, these effects in steady operation are much smaller than those caused by the depression of equilibrium tension. It appears that dynamic effects of surfactant on transient phenomena are more noticeable, such as in tempering unwanted

disturbances that arise as a result of ongoing fluctuations in dynamic contact angle and webspeed. These strong effects warrant further investigation.

REFERENCES

- Adamson, A. W. 1982. *Physical Chemistry of Surfaces*. 4th edn. New York: Wiley.
- Agrawal, S. K. and Wasan, D. T. 1979. The effect of interfacial viscosities on the motion of drops and bubbles. *Chem. Engng J.* **18**: 215.
- Anshus, B. E. and Acrivos, A. 1967. Effect of surface active agents on the stability characteristics of falling liquid films. *Chem. Eng. Sci.* **22**: 389–393.
- Batchelor, G. K. 1967. *An Introduction to Fluid Dynamics*. Cambridge University Press.
- Benjamin, B. T. 1957. Wave formation in laminar flow down an inclined plane. *J. Fluid Mech.*, **2**: 554–574.
- Bergink-Martens, D. J. M. et al. 1990. Surface dilation and fluid-dynamical behavior of Newtonian liquids in an overflowing cylinder. *J. Coll. Interf. Sci.* **138**: 1–9.
- Bidner, M. S., Larson, R. G. and Scriven, L. E. 1976. On the theory of micellization with reference to petroleum recovery. *Lat. Am. J. Chem. Eng. Appl. Chem.* **6**: 1–32.
- Blake, T. D. 1984. Wetting. In *Surfactants*. London: Academic Press. pp. 222–275.
- Blake, T. D. 1988. Wetting kinetics – how do wetting lines move? 1988 Spring National Meeting of the AIChE. 6–10 March 1989, New Orleans, LA.
- Bose, A. 1993. Wetting by solutions. In *Wettability*, ed. J. Berg. New York: Marcel Dekker.
- Bury, L. R. 1927. Adsorption of butyric acid on water surfaces. *Phil. Mag.* **4**: 980–997.
- Christodoulou, K. N. and Scriven, L. E. 1992. Discretization of free surface flows and other moving boundary problems. *J. Comp. Phys.* **99**: 39–55.
- Corkill, J. M. and Walker, T. 1972. Light scattering and diffusion studies in nonionic micellar systems. *J. Coll. Interf. Sci.* **39**: 621–631.
- Cox, R. G. 1986. The dynamics of the spreading of liquids on a solid surface. Part 2. Surfactants. *J. Fluid Mech.* **168**: 195–220.
- Cussler, E. L. 1984. *Diffusion: Mass Transfer in Fluid Systems*. Cambridge University Press.
- Defay, R. and Petre, G. 1971. Dynamic surface tension. In *Surface and Colloid Science – Vol. 3*, ed. E. Matijevic. Wiley-Interscience. pp. 27–81.
- Defay, R. and Roba-Thilly, J. 1954. Sur l'existence d'un palier dans la courbe d'évolution aci cours der temps de la tension superficielle d'une solution. *J. Coll. Sci. Suppl.* **1**: 36–52.

- Deryagin, J. and Levi, S. M. 1964. *Film Coating Theory*. London: Focal Press.
- Dorrestein, R. 1961. General linearized theory of the effect of surface films on water ripples. *Ned. Akad. Wetens.* **54**: 260–271.
- Dussan, V., E. B. 1976. The moving contact line: the slip boundary condition. *J. Fluid Mech.* **67**: 665.
- Edwards, D. A., Brenner, H. and Wasan, D. T. 1991. *Interfacial Transport Processes and Rheology*. MA: Butterworth-Heinemann.
- Emmert, B. and Pigford, R. L. 1954. A study of gas adsorption in falling liquid films. *Chem. Eng. Prog.* **50**: 87–93.
- Fainerman, V. B. 1986. Dynamic surface tension and the viscosity of an expanding adsorbed layer. *Kolloidnyi Zhurnal*. **48**: 758–763.
- Fowkes, F. M. 1962. Determination of interfacial tensions, contact angles and dispersion forces in surfaces by assuming additivity of intermolecular interactions in surfaces. *J. Phys. Chem.* **66**: 382–399.
- Frances, E. I. 1979. Phase behavior and interfacial tension studies of surfactant systems. PhD thesis, University of Minnesota.
- Fruhner, H., Kragel, J. and Kretzschmar, G. 1989. Investigation on the stability of the liquid bridge of the slide hopper type coating technique. Part 2: Stability criteria for coating bead in slide coating. *J. Inf. Rec. Mater.* **17**: 273.
- Fruhner, H., Kragel, J. and Kretzschmar, G. 1991. Investigation on the stability of the liquid bridge of the slide hopper type coating technique. Part 3: Mechanism of the effect of surfactants for the stabilization of the liquid bridge. *J. Inf. Rec. Mater.* **17**: 273.
- Giavedoni, M. D. and Saita, F. A. 1992. Interfacial viscosity in viscous free surface flows. A sample case. *Ind. Eng. Chem. Res.* **31**: 2222–2231.
- Gibbs, J. W. 1906. *The Scientific Papers of J. Willard Gibbs. Vol. I Thermodynamics*. New York: Longmans Green & Co. 1931; New York: Dover reprint. 1961.
- Ginley, G. M. and Radke, C. J. 1988. Influence of soluble surfactants on the flow of long bubbles through a cylindrical capillary. *ACS Symp. Ser.* **396**: 480.
- Goetmackers, B. and Scriven, L. E. 1992. Multilayer curtain coating: Modeling surfactant and rheological effects. Semiannual meeting of the AIChE, New Orleans, LA.
- Greener, J., Sullivan, T., Turner, B. and Middleman, S. 1980. Ribbing instability of a two-roll coater: Newtonian fluids. *Chem. Eng. Commun.* **5**: 73–82.
- Hall, D. G. 1987. A phenomenological approach to micellisation kinetics. *J. Chem. Soc. Faraday Trans.* **83**: 967–983.
- Hall, D. G. and Pethica, B. A. 1967. Thermodynamics of micelle formation. In *Nonionic Surfactants*, ed. M. J. Schick, pp. 517–557. New York: Marcel Dekker.
- Hansen, R. S. and Mann, J. A. 1964. Propagation characteristics of capillary ripples, I: theory of velocity dispersion and amplitude attenuation of plane capillary waves. *J. Appl. Phys.* **35**: 152–171.
- Hartley, G. S. 1936. *Aqueous Solutions of Paraffin Chain Salts*. Paris: Hermann et Cie.
- Hempt, C., Lunkenheimer, K. and Miller, R. 1985. On the experimental determination of the dilational surface elasticity and the exchange of matter of mixed gelatin surfactant adsorption layers. *Z. Phys. Chemie*. Leipzig. **266**: 713–720.
- Hirasaki, G. J. and Lawson, J. B. 1985. Mechanism of foam flow in porous media: Apparent viscosity in smooth capillaries. *Soc. Pet. Eng. J.* **25**: 176.
- Holbrook, J. A. and LeVan, M. D. 1983a. Retardation of droplet motion by surfactant. Part 1. Theoretical development and asymptotic solutions. *Chem. Engng. Commun.* **20**: 191.
- Holbrook, J. A. and LeVan, M. D. 1983b. Retardation of droplet motion by surfactant. Part 2. Numerical solutions for exterior diffusion, surface diffusion, and adsorption kinetics. *Chem. Engng. Commun.* **20**: 273.
- Hopf, W. and Geidel, Th. 1987. The dynamic contact angle I. Dependence of the receding contact angle on velocity in the surfactant-containing three-phase system. *Colloid and Polymer Sci.* **265**: 1075–1084.
- Hopf, W. and Volke, K. 1987. The dynamic contact angle II. Investigation of the adsorption mechanism based on the measurement of the preceding contact angles. *Colloid and Polymer Sci.* **265**: 1085–1089.
- Imaiishi, N. et al. 1982. Surface hydrodynamics of surfactant solutions. *J. Chem. Eng. Japan*. **8**: 143–149.
- Johnson, R. E. and Dettre, R. 1969. Wettability and contact angles. In *Surface and Colloid Science*, ed. E. Matijevic. **2**: pp. 85–120.
- Kamrath, R. F. 1984. Thermodynamics and phase behavior of single and binary surfactant systems. PhD thesis, Purdue University.
- Kistler, S. F. 1984. The fluid mechanics of curtain coating and related viscous free surface flows with contact lines. PhD thesis, University of Minnesota.
- Kistler, S. F. 1993. Hydrodynamics of wetting. In *Wettability*, ed. J. Berg. New York: Marcel Dekker.
- Kistler, S. F. and Scriven, L. E. 1983. Coating flows. In *Computational Analysis of Polymer Processing*. Eds J. A. Pearson and S. M. Richardson. London: Applied Science Publishers.
- Knox, W. J. 1970. Photographic surfactant compositions. US Patent 3,514,213.

- Krantz, W. B. and Goren, L. S. 1971. Stability of thin liquid films flowing down a plane. *Ind. Eng. Chem. Fundam.* **10**: 91–99.
- Kreshek, G. C. et al. 1966. Determination of the dissociation rate of dodecylpyridinium iodide micelles by a temperature-jump technique. *J. Amer. Chem. Soc.* **188**: 246–253.
- Lamb, H. S. 1879. *Hydrodynamics*. 6th edn. New York: Dover reprint. 1945.
- Leaist, D. G. 1986. Binary diffusion of micellar electrolytes. *J. Coll. Interf. Sci.* **111**: 230–239.
- Leung, R. and Shah, D. O. 1986. Dynamic properties of micellar solutions. I. Effects of short-chain alcohols and polymers on micellar stability. *J. Coll. Interf. Sci.* **113**: 484–498.
- LeVan, M. D. 1981. Motion of a droplet with a Newtonian interface. *J. Coll. Interf. Sci.* **83**: 11.
- LeVan, M. D. and Newman, J. 1976. The effect of surfactants on the terminal and interfacial velocities of bubbles or drops. *AICHE J.* **22**: 695.
- Levich, V. G. 1945. *Physicochemical Hydrodynamics*. Reprinted in 1962. Englewood Cliffs, NJ: Prentice-Hall.
- Lin, S. P. 1970. Stabilizing effects of surface active agents on a film flow. *AICHE J.* **16**: 375–379.
- Lu, W. Q. and Chang, H. C. 1988. An extension of the biharmonic boundary integral method to free surface flow in channels. *J. Comput. Phys.* **77**: 340.
- Lucassen, J. 1975. Adsorption kinetics in micellar systems. *Faraday Disc. Chem. Soc.* **59**: 76–92.
- Lucassen, J. and Giles, D. 1975. Dynamic surface properties of nonionic surfactant solutions. *J. Chem. Soc. Faraday J.* **71**: 217–230.
- Lucassen, J. and Hansen, R. S. 1967. Damping of waves on monolayer-covered surfaces I. Systems with negligible surface dilatational viscosity. *J. Coll. Interf. Sci.* **22**: 32–44.
- Lucassen-Reynders, E. H. 1981. *Anionic Surfactants*. New York: Marcel Dekker.
- Lucassen-Reynders, E. H. 1987. Effects of surfactant aggregation in soluble monolayers on dynamic surface properties. *Colloids and Surfaces* **25**: 231–249.
- Meyer, K. H. and Van der Wyk, A. 1937. Properties of polymers in solution, VII. *Helv. Chim. Acta* **20**: 1321–1329.
- Mijnlieff, P. F. and Ditmarsch, R. 1965. Rate of micelle formation of sodium alkyl sulphates in water. *Nature* **5013**: 889–891.
- Miller, R. 1981. Adsorption kinetics of surfactants from micellar solutions. *Coll. Polym. Sci.* **259**: 1124–1128.
- Mukerjee, P. and Mysels, K. J. 1971. Critical micelle concentrations of aqueous surfactant systems. NSRDS-NBS-36, Superintendent of Documents, US Government printing office, Washington, D.C.
- Muller, N. 1972. Kinetics of micelle dissociation by temperature-jump techniques. A reinterpretation. *J. Phys. Chem.* **76**: 3017–3024.
- Mysels, K. J. and Florence, A. T. 1970. Techniques and criteria in the purification of aqueous surfaces. In *Clean Surfaces: Their preparation and characterization for interfacial studies*. Ed. G. Goldfinger. New York: Marcel Dekker.
- Oguz, H. N. and Sadhal, S. S. 1988. Effects of soluble and insoluble surfactants on the motion of drops. *J. Fluid Mech.* **194**: 563–579.
- Orem, M. W. 1988. Private communication.
- Padday, J. F. 1957. A direct reading, electrically operated balance for static and dynamic surface tension measurement. *Proc. 2nd Intl. Congr. Surface Activity*. London: Butterworth.
- Padmanabhan, S. and Bose, A. 1988. The importance of direct measurement of dynamic contact angles during the wetting of solids by surfactant solutions. *J. Coll. Interf. Sci.* **126**(1): 164–170.
- Padmanabhan, S. and Bose, A. 1990. On the anomalous behavior of surfactant contaminated drops. *J. Coll. Interf. Sci.* **139**(2): 535–540.
- Park, C. W. 1991. Effects of insoluble surfactants on dip coating. *J. Coll. Interf. Sci.* **146**: 382–394.
- Piccardi, G. and Ferroni, E. 1951. Surface tension of liquids in movement. *Annali De Chimica (Rome)* **41**: 3–23.
- Prins, A., Arcuri, C. and Van Den Temple, M. 1967. Elasticity of thin liquid films. *J. Coll. Interf. Sci.* **24**: 84–90.
- Rame, E. 1988. On the spreading of liquids in the presence of surfactants. PhD thesis, University of Pennsylvania.
- Ratulowski, J. and Chang, H. C. 1990. Marangoni effects of trace impurities on the motion of long gas bubbles in capillaries. *J. Fluid Mech.* **210**: 303.
- Rillaerts, E. and Joos, P. 1982. Rate of demicellization from dynamic surface tensions of micellar solutions. *J. Phys. Chem.* **86**: 3471–3478.
- Ruckenstein, E. and Nagarajan, R. 1975. Critical micelle concentration. A transition point for micellar size distribution. *J. Phys. Chem.* **79**: 2622–2626.
- Rusanov, A. I. and Krotov, V. V. 1979. Gibbs elasticity of liquid films, threads, and foams. In *Progress in Surface and Membrane Science*, 13. Eds D. A. Cadenhead and J. F. Danielli. Academic Press.
- Ruschak, K. J. 1987. Flow of a thin liquid layer due to ambient disturbances. *AICHE J.* **33**(5): 801.
- Sadhal, S. S. and Johnson, R. E. 1986. On the

- deformation of drops and bubbles with varying interfacial tension. *Chem. Engng. Commun.* **46**: 97.
- Schunk, P. R. 1989. Surfactant and polymer additives in coating and related flows. PhD thesis, University of Minnesota. Available from University Microfilms International, Ann Arbor, MI.
- Scriven, L. E. 1960. Dynamics of a fluid interface. *Chem. Eng. Sci.* **12**: 98–105.
- Shinoda, K. et al. 1963. *Colloidal Surfactants*. New York: Academic Press.
- Smith, M. K. 1990. The mechanism for the long-wave instability in thin liquid films. *J. Fluid Mech.* **217**: 469–485.
- Squire, H. B. 1933. On the stability for three-dimensional disturbances of viscous fluid flow between parallel walls. *Proc. Roy. Soc. London. A* **142**: 621–628.
- Sterzi, G. S. 1982. Surfactant effect in film flow. MS thesis, University of Minnesota.
- Stone, H. A. and Leal, L. G. 1990. The effects of surfactants on drop deformation and breakup. *J. Fluid Mech.* **220**: 161–186.
- Sturge, J. M. 1977. *Neblette's Handbook of Photography and Reprography. Materials, Processes, and Systems*. 7th edn. New York: Van Nostrand Reinhold.
- Valentini, J. E. et al. 1991. Role of dynamic surface tension in slide coating. *Ind. Eng. Chem. Res.* **30**: 453–461.
- Van Abbenyen, W., Christodoulou, K. N. and Scriven, L. E. 1989. Frequency response of a coating flow: predictions for slide coating. Submitted to *AIChE J.*
- Wassmuth, F., Laidlaw, W. G. and Coombe, D. A. 1993. Calculation of interfacial flows and surfactant redistribution as a gas/liquid interface moves between two parallel plates. *Phys. Fluids A.* **5**(7): 1533–1548.
- Weinheimer, L. E., Evans, D. F. and Cussler, E. L. 1981. Diffusion in surfactant solutions. *J. Coll. Interf. Sci.* **80**: 524–531.
- Whitaker, S. 1964. Effect of surface active agents on the stability of falling liquid films. *Ind. Eng. Chem. Fundam.* **3**: 131–142.
- Whitaker, S. and Jones, L. O. 1966. Stability of falling liquid films: effects of interface and interfacial mass transport. *AIChE J.* **12**: 524–531.
- Wu, A. and Whitaker, S. 1986. The recirculation zone at the entrance of a falling liquid film: consequences for the surfactant adsorption problem. *J. Coll. Interf. Sci.* **110**: 389–397.
- Yih, C. S. 1963. Stability of liquid flow down an inclined plane. *Phys. Fluids* **6**: 321–334.
- Zeldes, M. D. 1985. Coating process employs surfactants. US Patent 4,508,764.
- Zvanut, C. W. and Cohen, E. D. 1978. High shear-rate viscosity and dynamic surface tension of photographic emulsions. *Int. Cong. Photo. Sci.* August 1978.

Dennis J. Coyle

This chapter describes the processes of knife and roll coating from a fluid-mechanical point of view. It combines a critical review of what is known, along with some speculation aimed at stimulating new lines of research. Physical mechanisms underlying the flow phenomena are emphasized, along with their practical implications. Section 12a.1 describes a variety of coaters and presents a logical scheme for their classification. Section 12a.2 introduces the fluid-mechanical mechanisms important in determining the operability of these coaters. The remaining sections deal specifically with knife coating, forward roll coating, and reverse roll coating.

12a.1 CLASSIFICATION OF KNIFE AND ROLL COATING PROCESSES

Knife coating is a process by which a thin liquid coating is formed on a continuous web by the application of an excess of coating liquid which is subsequently metered by a rigid knife held in close proximity to a rigidly supported web. Figure 12a.1a depicts a typical roller-fed knife coater. The thickness of the coating depends primarily on the clearance, or gap, between the knife and the web, and upon the geometry of the gap (bevel angle, length, etc.).

Roll coating is a process by which a thin liquid film is formed on a continuous web by the use of two or more rotating rolls, such that the fluid

flow in a small gap between a pair of rotating rolls is the primary factor controlling the thickness and uniformity of the coated film. The thickness of the coating depends primarily on the gap between adjacent rolls and their relative speeds. Two basic types of roll coaters are distinguished by the relative direction of roll surface motion in the gap: in forward roll coating the roll surfaces move in the same direction and in reverse roll coating they move in opposite directions. The simplest versions of each are depicted in Fig. 12a.1b,c. In terms of the flow fields, knife coating is a subset of forward roll coating where one surface is stationary.

12a.1.1 ILLUSTRATIVE EXAMPLES

There are several types of knife coaters, and a multitude of machines considered to be roll coaters (Higgins 1965; Booth 1970; Satas 1984; Scharenberg 1985; Zink 1979). Figure 12a.1 shows selected examples. These machines tend to be simple, inexpensive, and extremely versatile; able to coat over a wide range of thicknesses, speeds and viscosities. In general, these devices are not as precise nor do they coat films of as high uniformity as premetered devices such as extrusion, slide, or curtain coaters (Chapter 11). A notable exception to these generalizations are so-called 'precision' roll coaters, which are capable of uniformity comparable to the premetered devices, and which can be complex and expensive.

Knife coaters, one example of which is shown in Fig. 12a.1a, are simple, low-cost, compact coaters used for applying thick coatings of high viscosity liquids. Typical operating parameters are 3–120 m/min speed, 1000–10 000 mPa s viscosity, and 50–2500 µm wet coating thickness (Zink 1979). The main disadvantages of this method are its propensity for streaking and the fact that the coating thickness is sensitive to web thickness variations.

Forward roll coating, sometimes referred to as ‘meniscus roll coating’, is most commonly used to apply thin optical-quality coatings of low-viscosity liquids (Satas 1984; Zink 1979). Typical operating parameters are 3–60 m/min speed, 1–50 mPa s viscosity, and 25–60 µm wet thickness. The main disadvantages of this method are the limitations of low speed and viscosity, and that the coating thickness is sensitive to speed and viscosity as well as gap. Reverse roll coating is probably the most versatile coating method in use today (Booth 1990; Satas 1984). A reverse roll coater can apply uniform wet coatings of 10–1000 µm thickness at speeds of 3–600 m/min, and can handle coatings of 1–500 000 mPa s viscosity. The primary disadvantages are complexity, cost, and solvent evaporation (Zink 1979).

This chapter deals only with roll and knife coaters with rigid rolls and knives. Flexible blade coaters, kiss coaters, squeeze-roll (deformable-roll) coaters, and gravure coaters are considered separately with elastohydrodynamic systems (Chapter 12c).

12a.1.2 CLASSIFICATION – PRIMARY AND AUXILIARY FLOWS

There are several variations of knife coating. In the simplest case the knife, in addition to its metering function, also serves the function of cross-web distribution of coating by forming a rolling puddle upstream. A roller-fed knife coater applies excess coating to the web by either dipping, roll transfer, or a puddle-feed, and the knife causes excess coating to run back toward the applicator. If there is a structure for containing

a liquid supply upstream of the knife, it is referred to as pond-fed or hopper-fed knife coating.

The various rolls in a roll coater are given common names associated with their function, and these names are included in Fig. 12a.1. The applicator roll applies the coating to the web. The back-up roll supports and often drives the web at the point of coating application. If a gap is maintained between applicator roll and web, the back-up roll is usually rigid. If the web is forced into near-contact with the applicator roll (forming a nip), the back-up roll is rubber-covered and sometimes referred to as the impression roll. The metering roll is a reverse-moving roll that removes (‘meters’) excess coating from the surface of the applicator roll. Its surface must be scraped (doctored) clean by a blade before contacting the coating on the applicator roll. A fountain roll picks up coating solution from a pan and transfers it to the applicator roll, and may be run in a forward or reverse direction.

The simple two-roll forward roll coater in Fig. 12a.1b is fed by dip-coating from a pan, after which the coating is metered by its passage through the narrow gap between applicator and back-up rolls and then splitting downstream. Addition of a third roll to pick up the coating and transfer it to the applicator roll gives more flexibility in coating thickness and speed (Zink 1979).

Figures 12a.1c–f show four versions of reverse roll coaters, but there are many other variants (Booth 1970, 1990; Satas 1984). All types use a reverse-acting metering roll to control the coating thickness, and the region between these rolls is called the metering gap. There are two major classes of reverse-roll coaters. The first, shown in Fig. 12a.1c, uses the transferred film as the final product. The film on the applicator roll is first formed by dip coating or fountain roll transfer. The second, shown in Figs 12a.1d–f, uses the metered film as the final product. The implications of this significant difference, in terms of thickness and uniformity, are discussed later. Reverse roll coaters can be pan-fed (Fig. 12a.1d), fountain-roll-fed (Fig. 12a.1e), die-fed, or nip-fed (Fig. 12a.1f), depending upon the means of coating supply to the applicator roll.

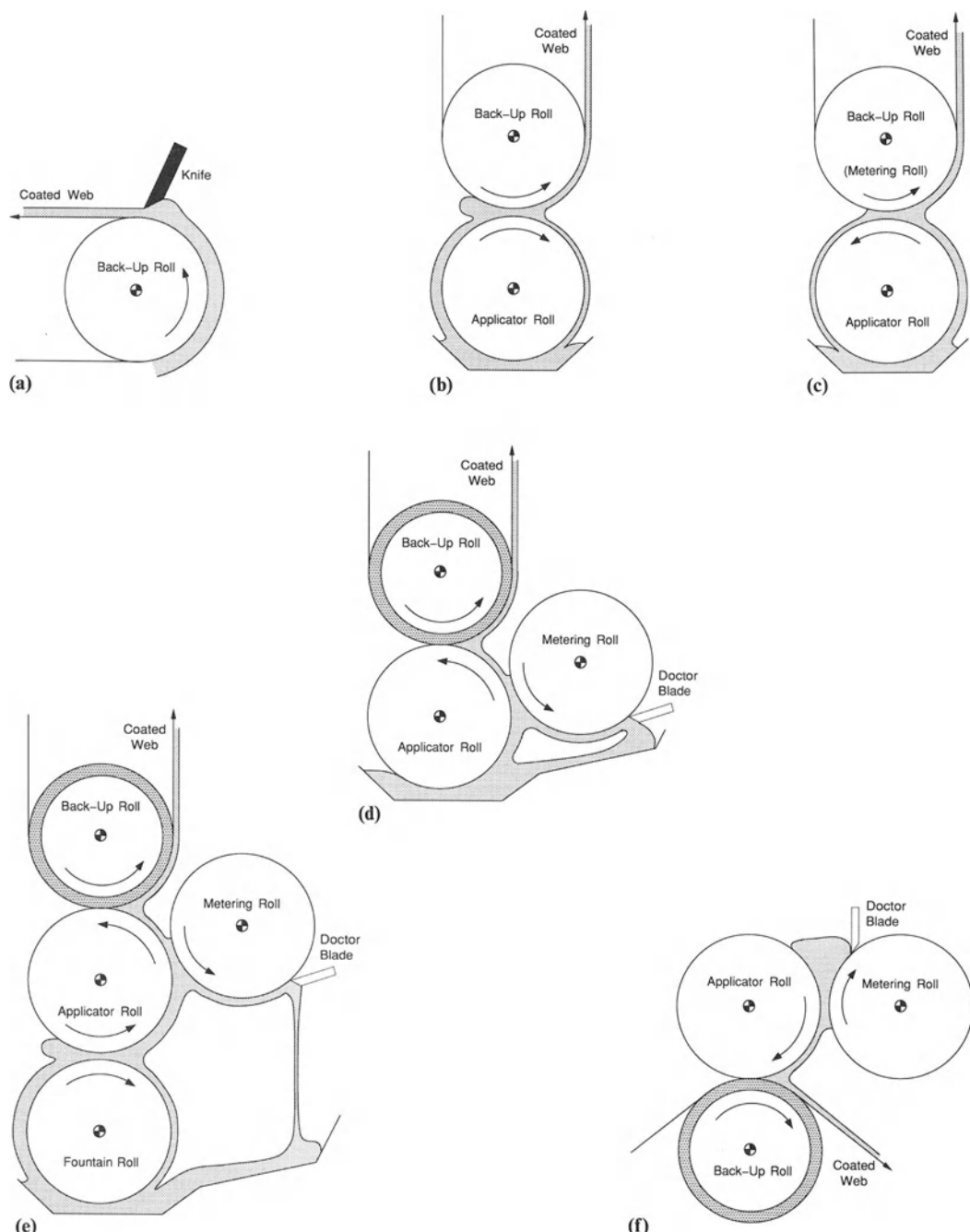


Figure 12a.1 Common types of knife and roll coaters. The coating thicknesses and gaps between rolls are magnified for clarity. (a) Roller-fed knife (knife-over-roll) coating; (b) two-roll pan-fed forward roll coater; (c) two-roll pan-fed reverse roll coater; (d) three-roll pan-fed reverse roll coater; (e) four-roll pan-fed reverse roll coater; and (f) three-roll nip-fed reverse roll coater.

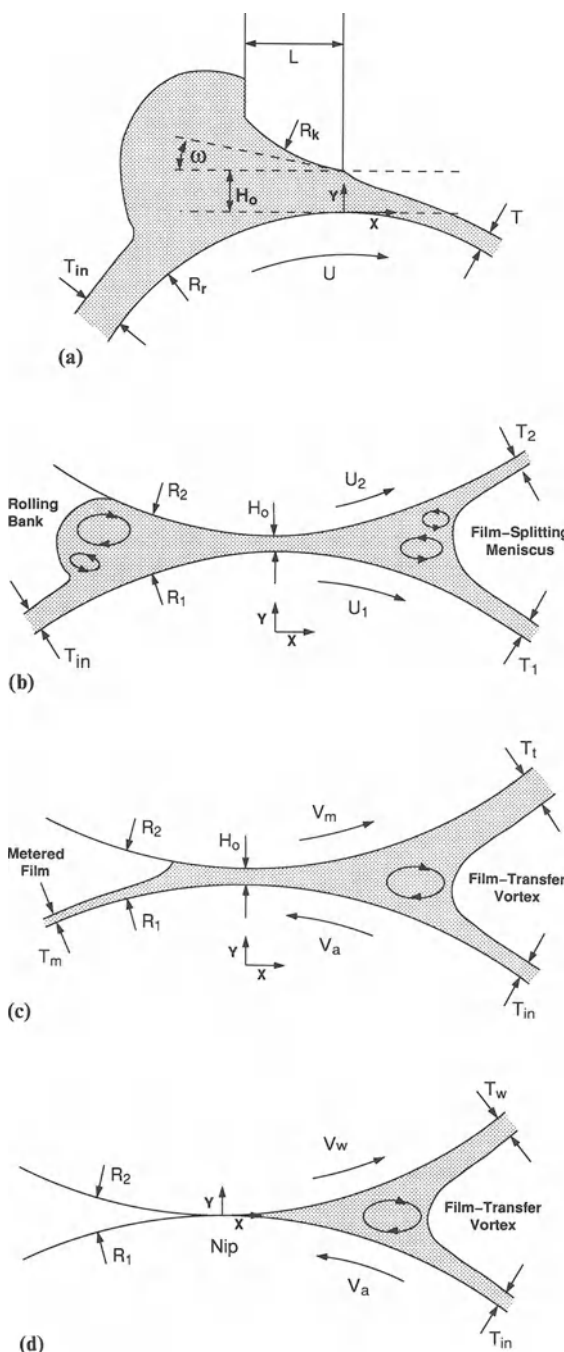


Figure 12a.2 Definition sketches of primary flows in knife and roll coating. (a) Knife coating gap flow; (b) forward roll film-splitting flow; (c) reverse roll metering flow; and (d) reverse roll nip transfer flow.

While there are many knife and roll coating configurations, the situation can be simplified by realizing that all such coaters can be described as a series of separate flows, each between a single pair of rolls (or a knife and a roll). This leaves only four types of flow fields, herein called primary flows, that need to be analyzed. These are: (1) knife coating gap flow, Fig. 12a.2a; (2) forward roll film-splitting flow, Fig. 12a.2b; (3) reverse-roll metering gap flow, Fig. 12a.2c; and (4) reverse-roll nip-transfer flow, Fig. 12a.2d. All knife and roll-coating configurations are simply a combination of these ‘building-blocks’ with other non-roll-coating flows, herein called auxiliary flows, such as dip coating and extrusion coating. While the auxiliary flows are usually ignored in analyzing knife and roll coaters, they can be a source of coating nonuniformity and operating limits.

The primary flows depicted in Fig. 12a.2 are often referred to as the coating bead. Preferably, these flows are laminar, steady, and two-dimensional, but under certain conditions they become three-dimensional and/or unsteady and the coating is nonuniform. The following section describes the physical mechanisms of the primary flows, the appropriate scalings and dimensionless groups, and the major bead failure modes.

12a.2 FLOW MECHANISMS IN KNIFE AND ROLL COATING

12a.2.1 STEADY BASE FLOWS

12a.2.1.1 Lubrication flows

The primary mechanism of flow between rigid rolls and knives is that of hydrodynamic lubrication – the combined drag and pressure-driven flow in a slowly converging/diverging geometry (Cameron (1976); see also Chapter 8 in this volume). The nearly one-dimensional flow in the gap is therefore governed by the integrated Reynolds equation:

$$\frac{dP}{dX} = 12\mu \left(\frac{(U_2 + U_1)/2}{H^2} - \frac{Q}{H^3} \right) \quad (12a.1)$$

where P is the pressure, μ is the viscosity, U_1 and U_2 are the roll speeds, Q is the volumetric flow rate per unit width and H is the separation between roll surfaces as a function of main-flow coordinate X . It is standard practice in lubrication theory and contact mechanics to define an equivalent radius of a roll against a flat plate which gives an identical geometric description of any two-roll or roll-knife configuration (Johnson 1985). Using this approach, the equivalent radius R_e and the roll surface separation or gap profile H are

$$\frac{1}{R_e} = \frac{1}{R_1} + \frac{1}{R_2} \quad (12a.2a)$$

$$H = H_0 + \frac{X^2}{2R_e} \quad (12a.2b)$$

where H_0 is the minimum clearance (gap) between two surfaces of radii R_1 and R_2 . This leads to the introduction of the main controlling dimensionless geometric parameter H_0/R_e , which is a measure of the converging/diverging nature of the gap profile. In the gap the pressure scales with lubrication viscous force

$$P_{\text{lub}} = \frac{\mu \bar{U}}{H_0} \left(\frac{R_e}{H_0} \right)^{1/2} \quad (12a.3)$$

where \bar{U} is the average roll velocity. The solution of the Reynolds equation for roll coating flows has been the subject of numerous papers with various approximate boundary conditions applied at the upstream and downstream menisci.

12a.2.1.2 2D free surface flows

G. I. Taylor (1963) pointed out that roll coating (and journal bearing) flows naturally separate into two distinct regions: lubrication-type flow in the vicinity of the gap center and two-dimensional free-surface flow in the vicinity of the coating menisci. Ruschak (1982) formalized Taylor's basic idea in terms of matched asymptotic expansions for the case of forward roll coating with a fully flooded upstream region (see Chapter 8). The outer problem is the lubrication flow described by the Reynolds equation. The inner

problem is the two-dimensional free-surface flow near the film-splitting meniscus governed by the Navier–Stokes equations, though the simpler film-profile equations of Kheshgi, Kistler and Scriven (1992) could be used to describe this region. Matching the pressure gradient of the inner and outer solutions determines the flow rate and meniscus position. The same technique could be used to solve the other primary flows in roll coating.

Finite-element analysis allows the complete calculation of two-dimensional free-surface flow fields for many coating processes (Kistler and Scriven 1983, 1984). The predictions from these computations are often very accurate but can be tedious to do, so that the asymptotic approach is more efficient at capturing the essence of the underlying mechanisms.

In the meniscus region of the flow there are several possible mechanisms controlling the flow and its stability. There are three choices of pressure scaling: viscous, surface tension, and inertial

$$P_v = \frac{\mu \bar{U}}{H_0} \quad (12a.4a)$$

$$P_{\text{st}} = \frac{\sigma}{R_c} \quad (12a.4b)$$

$$P_i = \rho U^2 \quad (12a.4c)$$

where σ is the surface tension, R_c is the meniscus' radius of curvature, and ρ is the density. The relevant dimensionless groups are the capillary number, Reynolds number, and the Weber number:

$$Ca = \frac{\mu U}{\sigma}$$

$$Re = \frac{\rho U L}{\mu}$$

$$We = \frac{\rho U^2 L}{\sigma} = Re Ca$$

where U and L are appropriate characteristic velocity and length scales.

12a.2.2 THE RIBBING INSTABILITY

Roll coating flows are especially susceptible to a bead failure mode called ribbing. The thickness of the coated film varies in a sinusoidal fashion across the web, such that 'stripes' or 'ribs' appear to run along the machine direction. This defect is also referred to as 'corduroy', 'rake-lines', or 'phonographing', and can also occur in extrusion, slide, and knife coating (see Chapters 11a and 11b). Figure 12a.3 is a photograph of ribbing in forward roll coating film-splitting of a viscoelastic liquid. The defect occurs even with Newtonian liquids. This instability was first observed in flows created by rolls and spreaders by Chalmers and Hoare (1941), Pearson (1960), Sone and Fukushima (1960), and Pitts and Greiller (1961). Ribbing is similar to the phenomena of viscous fingering, which is observed when a low viscosity liquid displaces a high viscosity one from a confined passageway (Saffman and Taylor 1958). It is also seen in the peeling of an adhesive film (McEwan and Taylor 1966) and in the splitting of an oil film in a ventilated journal bearing

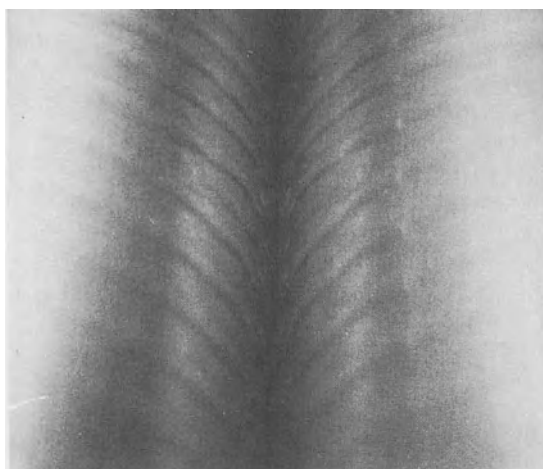


Figure 12a.3 Photograph of the ribbing instability in forward roll coating with rigid rolls and flooded inlet. The roll surfaces move upwards at the center of the photograph. The fluid is a viscoelastic polyacrylamide/water solution (from Coyle 1984).

(Dowson and Taylor 1979). The same type of coating defect is also found on films on rotating rolls, such as those in a paper-making machine (Yih 1960).

12a.2.2.1 Interfacial force balance

Ribbing is a manifestation of the instability of the two-dimensional base flow to a perturbation of the coating meniscus. The mechanism of ribbing can be understood from a simple force balance on the air–liquid interface that forms the coating meniscus (Pitts and Greiller 1961; Savage 1977b). Consider the meniscus perturbation of infinitesimal amplitude ϵ depicted in Fig. 12a.4. The pressure under the 'bump' or 'rib' (point 2) is different from the pressure in the unperturbed region (point 1) for two reasons: there is a pressure gradient in the flow, and the radius of curvature of the meniscus has been changed. If the pressure under the perturbation is the greater of the two, it will generate lateral flow out of the perturbation, causing it to level. If the pressure under the perturbation is the lesser of the two, it will generate lateral flow into the perturbation, causing it to grow. This latter situation corresponds to a flow which is unstable to a ribbing disturbance. Evaluating the pressures at points 1–3 (Savage 1977b) results in the criterion that the flow is

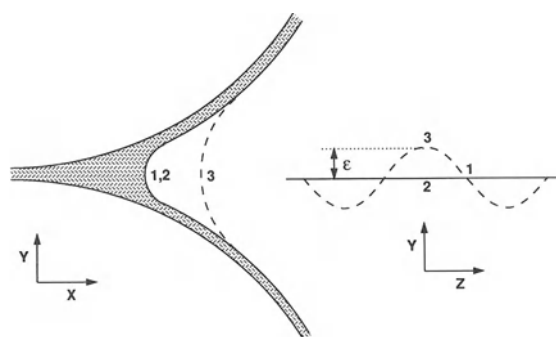


Figure 12a.4 Schematic of a sinusoidal perturbation to a coating meniscus, from which an approximate stability criterion can be derived. The magnitude (ϵ) of the perturbation is greatly magnified.

unstable to ribbing if

$$\frac{dP}{dX} - \sigma \left(\frac{1}{R_c^2} \frac{dR_c}{dX} + N^2 \right) > 0 \quad (12a.5)$$

where N is the wavenumber of the ribs and X increases as the meniscus is approached from the liquid side. Surface tension stabilizes the meniscus, while a positive pressure gradient is destabilizing. The sign and relative magnitude of these terms, and thus the stability of the flow to ribbing, depends on the specific geometry and operating conditions. In addition, the pressure gradient can arise from either viscous forces (lubrication flow) or inertial forces, depending on the viscosity of the liquid under consideration.

Equation (12a.5) can be used to evaluate the stability of all knife and roll coating flows to ribbing. To obtain information on the shape of the unstable disturbances and their initial growth rate, a more rigorous linear stability analysis is required. Neither approach predicts the shape of the meniscus at finite amplitude or whether the new three-dimensional flow state is steady or time-dependent.

12a.2.2.2 Viscous mechanism for ribbing

Viscosity can be the driving force for the ribbing instability as the converging/diverging geometry creates pressure gradients. This is the ‘classical’ ribbing mechanism studied by Pearson (1960) and many others since. Using a viscous pressure scaling such as equation (12a.4a), the interfacial force balance can be nondimensionalized and so the capillary number appears. The pressure gradient depends on the solution to the Reynolds equation (equation (12a.1)), so the parameter H_0/R_e arises. Thus there is a critical capillary number, which is a function of the gap/radius ratio, above which the flow is unstable to ribbing. In reverse roll coating the critical capillary number will also depend on roll speed ratio. If the pressure gradient is negative, which can be the case in knife and reverse roll coating, the flow is stable at any value of capillary number. If the pressure gradient is positive, which is often

the case, surface tension is the main stabilizing force and stable operation is typically limited to low speed. The ribbing instability in the specific geometries are reviewed in Sections 12a.3, 12a.4, and 12a.5.

12a.2.2.3 Inertial mechanism for ribbing

Inertia can also be the driving force for the ribbing instability, as it too can create a pressure gradient. The simplest case is the stability of a liquid film on a rotating roll (Yih 1960). For a film of thickness D on a roll of radius R rotating with a surface speed of U , the inertial pressure gradient at the free surface is $\rho U^2 (1 + D/R)/R$, the radius of curvature of the meniscus is $-(R + D)$, and $dR_c/dX = -1$. Inserting these expressions into equation (12a.5) gives the criterion that the flow is unstable if

$$1 + D/R - \frac{\sigma}{\rho U^2 R} \left[N^2 - \frac{1}{(1 + D/R)^2} \right] > 0 \quad (12a.6)$$

which is equivalent to the result derived by Yih (1960, equation (46)). Equation (12a.6) can be rearranged in terms of the critical Weber number above which the flow is unstable

$$We^* = \frac{n^2}{1 + D/R} - \frac{1}{(1 + D/R)^3} \quad (12a.7)$$

As the base flow meniscus radius of curvature is negative, surface tension destabilizes the flow for long enough waves (small n), and so a rotating film is always unstable. Yih performed a linear stability analysis to predict growth rates. At low Reynolds number (high viscosity) they are small, so that the ribs might never be seen in a coater where the film spends a very short time on the rotating roll. At high Reynolds number the growth rate is proportional to \sqrt{U} , while the residence time is proportional to $1/U$, so that the total growth scales with $1/\sqrt{U}$. This poses the interesting possibility that for low-viscosity liquids, inertial ribs could appear at low speed but then seemingly disappear at higher speeds.

The contention that this mechanism is only

important for very low viscosity liquids is supported by the experimental observations that for liquids of roughly 10 mPa s or higher viscosity, the apparent onset of ribbing in roll coating correlates with the capillary number (see Section 12a.4), such that increasing viscosity lowers the critical speed, which is opposite of what the inertial mechanism would predict. In addition, if one computes the Reynolds number based on a lubrication length scale (equation (12a.3) divided by equation (12a.4c)), the viscosity would need to be on the order of 5 mPa s or lower to make the Reynolds number greater than one. But for special cases where the viscosity is low and the gap is large, this inertial mechanism could become significant.

Another mode of inertially-driven instability could result from the instability of rotating vortices in the coating bead, similar to those visualized in a blade-coating pond (Triantafillopoulos and Aidun 1990; Aidun, Triantafillopoulos and Benson 1991) or other rotating flows discussed by Aidun (1991a,b). The manifestation in a free surface flow could be similar in appearance to the classical viscous-driven ribs, though the wavelength should be longer. The basic mechanism is an unstable stratification of angular momentum in a rotating flow (Chandrasekhar 1961). The free surface bounding the flow could render it much more unstable than the corresponding confined flow, such as is the case when one compares the rotating film with the problem of Taylor vortices.

Yih (1960) also presented experimental data showing the existence of inertially-driven ribbing. Since then there has been no study of this aspect of ribbing in coating flows. This is surprising considering that the ranges of coating conditions claimed for some roll coaters would fall into this regime.

12a.2.3 AIR ENTRAINMENT AND STARVATION

Air entrainment is another mode of coating bead failure (see Chapter 3). The three-phase dynamic contact lines present in the primary roll coating flow fields are susceptible to air entrainment at

high enough coating speeds, though there may be hydrodynamic assist of wetting in these flows. Even though this limit must exist, there are no published studies.

There is also possible air entrainment in the auxiliary flows, most notably where the wet surface of an applicator or fountain roll plunges back into the coating pan. If the roll has a relatively deep submersion, the critical capillary number for air entrainment is (Bolton and Middleman 1980):

$$Ca^* = 3.3 Po^{-0.3}; \quad Po < 3 \quad (12a.8a)$$

$$Ca^* = 5.0 Po^{-0.7}; \quad Po > 3 \quad (12a.8b)$$

where $Po = \sigma \left(\frac{\rho}{\mu U g} \right)^{1/3}$ is the property number.

If the roll has a very shallow immersion depth, critical speeds of air entrainment are much lower. This occurs if the immersion depth is less than the characteristic interfacial displacement depth, which is on the order of 1–5 mm (Ghannam and Esmail 1990).

Another bead failure mode is called starvation. If the auxiliary flow, such as dip coating, does not deliver enough flow to the gap of the primary flow, the coating bead will break. This mode of failure is most common in processes such as meniscus roll coating (Chapter 12b) where both speed and viscosity are low.

12a.2.4 SOURCES OF COATING NONUNIFORMITY

There are other sources of coating nonuniformity which are not failure modes of the coating bead, but are subtleties of the coating process and its sensitivity to disturbances which can lead to defects such as streaks and cross-bars.

12a.2.4.1 Auxiliary flows

The first category of defects are those that arise due to the auxiliary flows. Any nonuniformity in a coated film formed by an auxiliary flow corresponds to a disturbance of the inlet of the primary flow. These disturbances are damped if

they must traverse a long lubrication-type flow in a narrow gap between rigid surfaces before impacting the coated film of interest (Pearson 1985). Such is the case for a knife coater, a forward roll coater, and a reverse roll coater where the metered film becomes the product. In contrast, in a reverse roll coater using the transferred film for the product (Fig. 12a.1c) the disturbance will be transferred directly to the product with little or no damping.

There are several types of disturbances. Ribbing may occur on the applicator roll, either inertially driven or viscous-driven from a previous film-split between fountain and applicator roll. Cross-bar type waves could form due to the instability of a thick rising film flow (Yih 1963). The pond in a nip-fed reverse roll coater becomes unstable at high Reynolds number causing the rolling vortex to become three-dimensional (Aidun 1991b). None of these effects have received much study.

For reverse roll coaters (Fig. 12a.1d–f), the doctoring of the metering roll is another auxiliary flow. The metered film uniformity is dependent on the complete removal of coating from the metering roll. Incomplete or nonuniform doctoring will generate streaks in the metered film. Doctored blades can be thin (~ 0.1 mm) flexible steel or thick (> 1 mm) plastic material. Trailing configurations (acute angle between blade tip and roll surface tangent) are the same as flexible blade coating covered in Chapter 12c. Extremely thin films ('clean doctoring') require stiff blades at the proper application angle and loading. Reverse-angle doctoring is akin to knife coating (covered in Section 12a.3) with a short knife length and a nearly zero gap which is controlled by the applied load. Neither process has been studied systematically as related to reverse roll coating.

12a.2.4.2 Process perturbations

The second category of defects are those that arise due to perturbation of the process. As the flow rate in a self-metered coating process is primarily determined by the gap spacing, any variation in gap directly translates into coating thickness variability. Such nonuniformity can be

cross-web variation due to mechanical misalignment or variation in roll diameter along its axis. It can also be time-dependent in nature, caused by roll run-out, vibrations, and speed fluctuations. The sensitivity of the bead to perturbations can be evaluated by computing the frequency response (as described in Chapter 9 and illustrated for slide coating in Chapter 11b). No such studies have been done for roll coating.

12a.2.4.3 Bubbles and contamination

The third category of defect mechanisms arises from subtleties of the steady-state primary flow field. Roll coating flows often have regions of closed recirculation, or vortices. These can trap bubbles and particulate contaminants and cause streaks. The liquid in the vortices has a very long residence time in the process which could lead to degradation of the coating, again producing streaks or point defects.

12a.3 KNIFE COATING

12a.3.1 STEADY FLOW

Flow in a knife coater is governed predominantly by hydrodynamic lubrication, sometimes with inertia being important as well. Available models are either derived for a special case (Greener and Middleman 1974), or define redundant dimensionless geometric groups and are thus confusing (Sullivan and Middleman 1986; Hsu *et al.* 1985). An analytic model for the creeping flow of a Newtonian liquid in a knife coater has been derived for this book.

As pointed out by Secor (1991), the geometry of a knife coater (Fig. 12a.2a) can be described in terms of two dimensionless parameters, the inclination and the curvature:

$$\iota = \frac{L}{H_0} \tan(\omega); \quad \kappa = \frac{1}{2} \frac{L}{R_e} \frac{L}{H_0} \quad (12a.9a, b)$$

where $1/R_e = 1/R_r + 1/R_k$ is the equivalent curvature in terms of the roll and knife radii, L is the length of the knife, H_0 is the gap, and ω

is the inclination angle. In terms of the dimensionless flow direction coordinate $\zeta = X/L$, the dimensionless gap profile $h = H/H_0$, and the dimensionless coating thickness (flow rate) $t = T/H_0$, the gap profile and the Reynolds equation (equation (12a.1)) can be written as

$$h = 1 - \iota\zeta + \kappa\zeta^2 \quad (12a.10)$$

$$\frac{dp}{d\zeta} = \frac{6}{h^2} - \frac{12t}{h^3} \quad (12a.11)$$

where the dimensionless pressure is $p = \frac{PH_0^2}{\mu UL}$.

The Reynolds equation can be integrated, boundary conditions of ambient pressure at both inlet and outlet imposed, as the result rearranged to solve for the dimensionless flow rate

$$t = \left[\frac{\frac{2\kappa + \iota}{(\kappa + \iota + 1)^2}}{\frac{2\kappa + \iota}{\kappa + \iota + 1} - 2\kappa T_1} - \frac{6\kappa}{D} \right]^{-1} \quad (12a.12a)$$

where $D = \iota^2 - 4\kappa$ and T_1 is the integral of $1/h$ which is

$$T_1 = \begin{cases} \frac{2}{\sqrt{-D}} \left[\tan^{-1} \left(\frac{2\kappa + \iota}{\sqrt{-D}} \right) \right. \\ \left. - \tan^{-1} \left(\frac{\iota}{\sqrt{-D}} \right) \right]; & D < 0 \\ \frac{2}{\iota} - \frac{2}{2\kappa + \iota}; & D = 0 \\ \frac{1}{\sqrt{D}} \ln \left[\frac{\iota + \sqrt{D}}{\iota - \sqrt{D}} \frac{2\kappa + \iota - \sqrt{D}}{2\kappa + \iota + \sqrt{D}} \right]; & D > 0 \end{cases} \quad (12a.12b)$$

There are several limiting cases of interest. As curvature effects become negligible ($\kappa = 0$), the dimensionless flow rate becomes

$$t = \frac{\iota + 1}{\iota + 2} \quad (\kappa = 0) \quad (12a.13)$$

If, in addition, the surfaces are parallel ($\iota = 0$) then $t = 1/2$, while if the surfaces are steeply inclined ($\omega = \infty$) or the blade level very long ($L/H_0 = \infty$) then $\iota = \infty$ and $t = 1$.

The case of $\iota = 0$ gives the limiting flow rate of

$$t = \left[\frac{1}{\kappa + 1 + \frac{(\kappa + 1)^2}{\sqrt{\kappa}} \tan^{-1}(\sqrt{\kappa})} + \frac{3}{2} \right]^{-1} \quad (\iota = 0) \quad (12a.14)$$

If $L/H_0 = \infty$ then $t = 2/3$, which is the limit of a roll rotating in close proximity to a stationary wall under flooded conditions.

The limit of $t = 0$ is obtained when the two surfaces touch, which occurs when $\iota < -1 - \kappa$ if $\kappa < 1$ or when $\iota < -2\sqrt{\kappa}$ if $\kappa > 1$.

The flow rate as a function of inclination and curvature is shown in Fig. 12a.5, alongside results of finite-element calculations of the full two-dimensional free-surface flow field. The calculations were done in the same manner as those of Sullivan, Middleman and Keunings (1987), incorporating the downstream free surface and applying no-traction boundary conditions far upstream of the knife. Lubrication theory tends to underestimate the flow rate for short blades ($L/H_0 < 10-100$), mainly due to an entrance effect shown in the pressure profiles in Fig. 12a.6a. This entrance effect was also calculated and experimentally verified by Sullivan, Middleman and Keunings (1987). Lubrication theory accurately predicts both flow rate and pressure profiles for long blades (Fig. 12a.6b), even when the blade inclination angle is steep. When inertial forces become significant the entrance is more important due to an inertial impact pressure (Fig. 12a.6b), which is common under conditions of high speed flexible blade coaters (Chapter 12c).

The effects of shear-thinning and viscoelasticity on the flow rate were studied by Sullivan, Middleman and Keunings (1987). A 1.25% CMC/water solution, which shear-thins with a power-law index $n = 0.5$, gave lower pressures

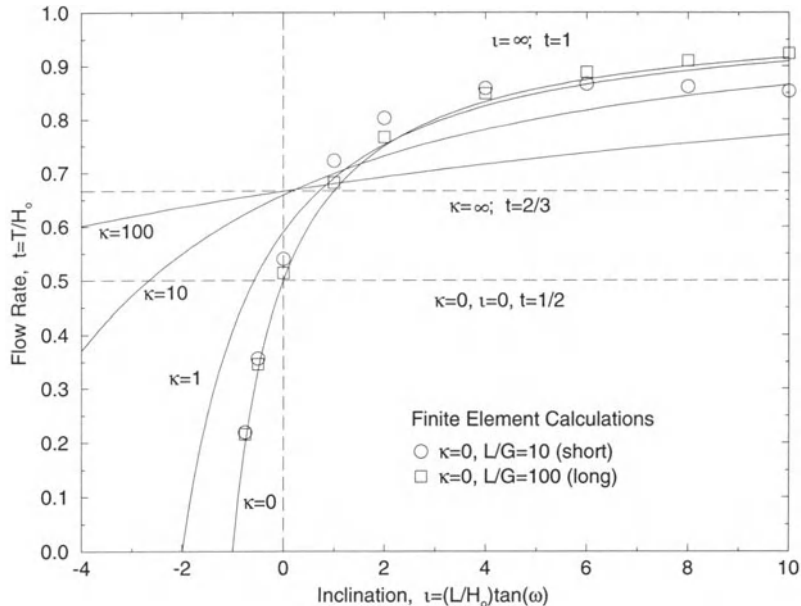


Figure 12a.5 Knife coater flow rate versus inclination and curvature as predicted by lubrication theory, with comparison to numerical model. Experimental data (not shown) agree with numerical results.

and the flow rate was increased by 10–15%. Their numerical model was consistent with these observations. A constant-viscosity viscoelastic Boger fluid gave experimental flow rates reduced by about 40%.

12a.3.2 RIBBING INSTABILITY

The primary fluid-mechanical instability in knife coating is ribbing. The operating diagram has been studied theoretically and experimentally by Strenger, Secor and Sramek (1992). For Newtonian and shear-thinning liquids, ribbing appears above some low value of capillary number only for diverging-tip geometries ($i < 0$). As the liquid is made more viscoelastic, ribbing also occurs at highly converging geometries ($i \gg 1$) due to the development of elastic normal stresses.

A number of studies of a roll rotating next to a stationary plate, which can be thought of as a

knife coater where the downstream geometry diverges and the downstream static contact line is not pinned at a corner, have reported the critical capillary number for ribbing (Savage 1977a; Sullivan and Middleman 1979; Dowson *et al.* 1980; Bauman *et al.* 1982; Adachi *et al.* 1988). At low capillary number the flow field is sensitive to the contact line where the downstream meniscus separates from the stationary plate at some static contact angle (Coyle *et al.* 1986). In fact, Adachi *et al.* (1988) reported that at much higher capillary number, the contact line passes through the nip center and the ribs disappear. These results seem to indicate that increasing knife gap divergence destabilizes the flow to ribbing. In a related geometry, Bixler (1982) reported that increasing the divergence of the flow channel stabilized the flow to ribbing, and similar results exist for forward roll coating (see Section 12a.4); which would seem to contradict knife coating results.

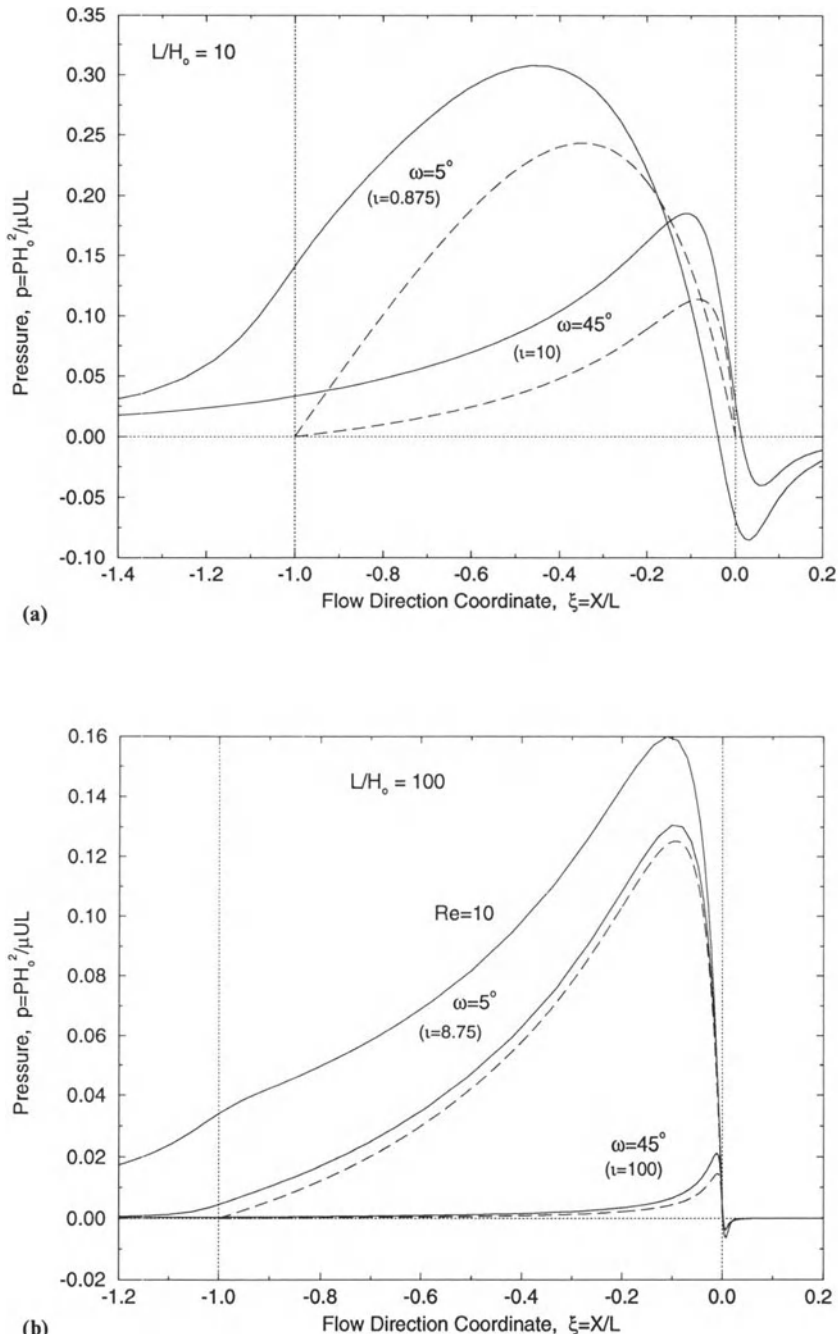


Figure 12a.6 Knife coater pressure profiles at small and large inclinations, comparing lubrication theory (dashed lines) and finite-element calculations (solid lines), for: (a) short blades; (b) long blades, and (c) diverging tip geometries.

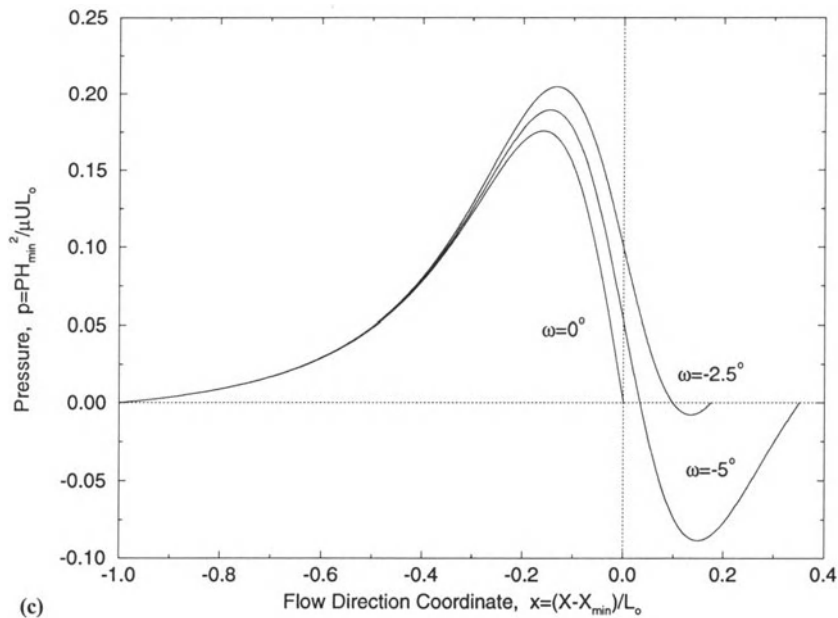


Figure 12a.6 *Continued.*

The stability of these flows is determined by the interfacial force balance (equation (12a.5)), not just by the degree of flow channel divergence. To make comparisons based on minimum (not tip) gap, equation (12a.11) can be re-arranged to give the pressure gradient at the meniscus in terms of the minimum gap

$$\frac{dP}{dX} = \frac{6\mu U}{H_{\min}^2} \left(1 - \frac{\iota^2}{4\kappa}\right)^2 (1 - 2t) \quad (12a.15)$$

This equation indicates that the pressure gradient at the meniscus is negative as long as $t > 1/2$, so that the flow is always stable to ribbing if $t > 1/2$. If $t < 1/2$, ribbing will appear at some critical capillary number. Figure 12a.5 shows that the flow rate t can be greater than $1/2$ for small negative inclinations (diverging tips) depending on the curvature. Equation (12a.12) can be used to find the inclination at which $t = 1/2(\iota_{1/2})$. Any diverging-tip geometry with $\iota > \iota_{1/2}$ will be stable to ribbing. If the inclination is less, the tip is more diverging and ribbing will occur at some

critical capillary number. Figure 12a.6c shows pressure profiles for constant minimum gap clearance H_{\min} for three different diverging tip lengths (i.e. $\omega = -5^\circ$ corresponds to the knife tip extending 5° past the point of minimum clearance around the roll). These profiles clearly show that increasing the diverging tip region causes the pressure gradient at the downstream meniscus to go from negative (stabilizing) to positive (destabilizing).

Adachi's results can be explained as follows. At the lowest speeds the meniscus locates far downstream from the gap center so that the pressure gradient is destabilizing but low enough in magnitude that surface tension dominates. As speed is increased, the meniscus recedes into the gap and ribbing occurs. At the highest speed the wetting line moves far enough into the gap that $t \sim 1/2$ and the flow becomes stable again. Bixler's results can be explained as follows. His flow was premetered with $t < 1/2$ held constant. He increased the divergence by increasing κ which according to equation (12a.15) decreases the

pressure gradient and so stabilizes the flow. A similar effect takes place in forward roll coating, and is discussed in Section 12a.5.

12a.3.3 OPERABILITY DIAGRAMS

Figure 12a.7, adapted from the work of Strenger, Secor and Sramek (1992), shows operability diagrams for a roller-fed knife coater. The main failure modes are starvation, where the auxiliary feed flow does not supply enough coating to the knife; flooding, where too much flow is supplied; and ribbing. The window is large when the inclination is positive (converging) and the fluid

Newtonian or shear-thinning. If the fluid is viscoelastic, the window shrinks considerably because viscous normal stresses at high inclination generate another region of ribbing. Experiments indicated there was no window with viscoelastic polyacrylamide solutions, rather, some degree of ribbing was always observed.

12a.3.4 PRACTICAL IMPLICATIONS

There are several practical implications of the above analysis and results. The coating thickness in a knife coater is primarily determined by the clearance between knife and web, and is typically 1/2 to 1 times the gap which necessitates small gaps for thin coatings. This makes the coating thickness sensitive to mechanical tolerances, web thickness variations, knife deflections and physical damage to the knife tip. Contamination can be trapped in this gap leading to streaks.

As the coating thickness is comparable in magnitude to the gap, it might be difficult to pin the static contact line to the downstream corner of the knife as drawn in Fig. 12a.2a. The liquid will have a natural tendency to wet up the downstream surface of the knife, possibly causing streaky coatings. The wedge spreader (Pearson 1960) is an extreme example of this phenomenon, where ribbing results.

Finally, ribbing is a problem if the geometry is too diverging or the fluid viscoelastic. The former simply requires proper knife installation, while the latter might require reformulation, dilution, or a change in coating method.

12a.4 FORWARD ROLL COATING

The simplest forward roll coater is shown in Fig. 12a.1b. The coating thickness applied to the web is governed by the flow in the nip between the bottom applicator roll and the top back-up roll around which the web is wrapped. The coating liquid is initially deposited on the applicator roll by dip coating from the coating pan, although a fountain roll or die could also be used. The most-commonly analyzed case is where an excess of coating reaches the gap so that it is flooded,

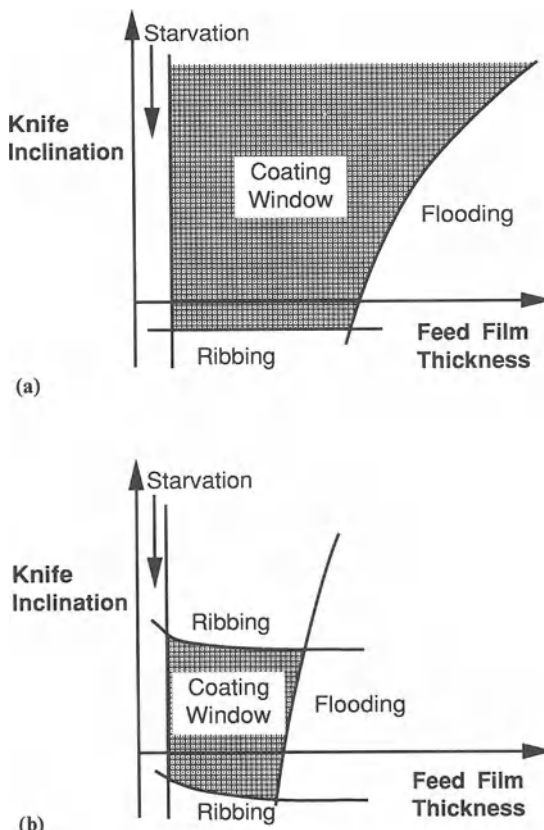


Figure 12a.7 Schematic operability diagram for a roller-fed knife coater, showing major failure modes for: (a) Newtonian and (b) viscoelastic liquids (adapted from Strenger, Secor and Sramek (1992)).

and so the details of the inlet region can be neglected. The case where the gap is ‘starve-fed’ is only briefly covered in this section and is dealt with in detail in Chapter 12b.

12a.4.1 FILM-SPLITTING MENISCUS REGION – STEADY FLOW

The lubrication of journal and slider bearings (Dowson and Taylor 1979) and gear teeth (Martin 1916; Gatcombe 1945), along with the knife coater of the previous section, are all special cases of the geometry of Fig. 12a.2b. Flow in the region of the gap center is therefore governed by the Reynolds equation (equation (12a.1)). Fluid is dragged into the gap by the moving roll surfaces through the action of viscosity. As the geometry is converging, the ‘squeezing’ action generates high pressures on the inlet side of the gap. Conversely, the drag flow in a diverging geometry results in low pressures (below atmospheric) on the downstream side of the gap. In fact, if the

rolls were completely submerged, the pressure profile on the downstream side of the gap would be an inverted image of the upstream profile in Fig. 12a.8. Downstream of the gap center the liquid film splits into two films, each coating one of the rolls. In the vicinity of the film-splitting liquid/air interface (the coating meniscus) the flow is two-dimensional.

A number of analyses of forward roll coating flow are based on lubrication theory with various *ad hoc* boundary conditions which either ignore or crudely approximate the influence of the flow near the film-split meniscus. The primary focus of these models is the prediction of the dimensionless flow rate, defined as $\lambda = Q/(H_0 \bar{U})$ where Q is the total flow rate (per unit width) through the gap and H_0 is the minimum total gap spacing. Martin (1916) used the Reynolds condition that the film splits at a point downstream where both the pressure and its gradient are zero, predicting $\lambda = 1.226$. Gatcombe (1945) assumed the rolls were completely submerged, predicting $\lambda = 4/3$,

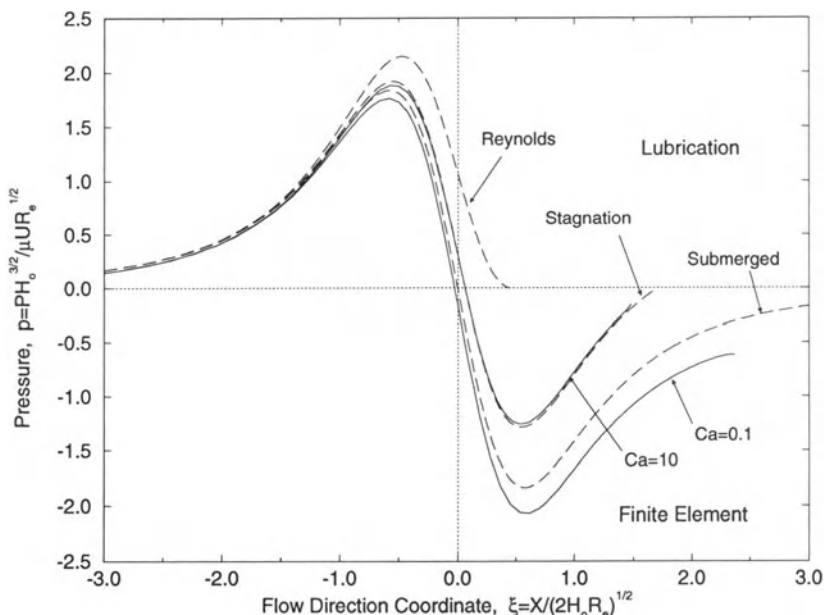


Figure 12a.8 Computed pressure along the main flow direction in forward roll coating as a function of capillary number. The dashed lines are lubrication theory results for different downstream pressure boundary conditions.

while Hopkins (1957) proposed the separation hypothesis that the film splits at the first stagnation point downstream of the nip center, thus predicting $\lambda = 1.3015$. Pitts and Greiller (1961) attempted an approximate solution to the difficult problem of the two-dimensional flow near the meniscus with some success, as did Coyne and Elrod (1970a,b), who essentially solved approximate film profile equations. Williamson (1972) obtained an approximate numerical solution to the downstream free-surface flow. Savage (1977a) and Dowson and Taylor (1979) have reviewed some of these earlier boundary conditions. Ruschak (1982) solved the problem accurately (for small H_0/R_e) using matched asymptotic expansions, while Coyle *et al.* (1986) used the finite element method to solve the full Navier–Stokes equations for the flow field.

Several authors have attempted to develop simpler analytical models that crudely incorporate the film-split meniscus into a lubrication model of the flow (Greener and Middleman 1975, 1979; Taylor 1974a,b,c; Benkreira *et al.* 1981a). Unfortunately, these models give totally inaccurate predictions of flow rate and meniscus location at small capillary number. The exception are those that patch together lubrication pressure profiles with Coyne and Elrod's (1970a,b) approximate solution, which give more accurate behavior (Greener and Middleman 1979).

Finite-element solutions of the Navier–Stokes equations show details of the flow field (Coyle *et al.* 1986). Streamlines as a function of roll speed ratio and capillary number are plotted in Fig. 12a.9. As capillary number is decreased, the meniscus locates farther from the gap center and

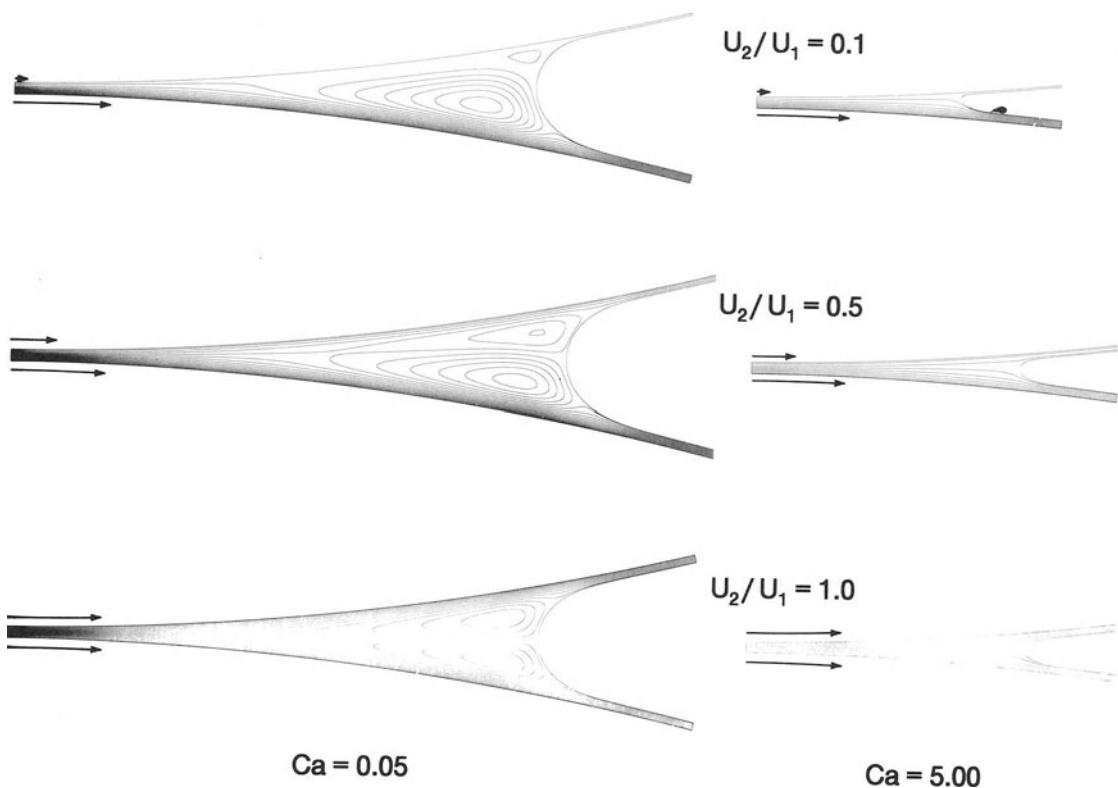


Figure 12a.9 Computed stream lines for forward roll coating flow as a function of capillary number and speed ratio ($H_0/R_e = 0.001$).

a pair of recirculations grow. This is due to surface tension forces at low capillary number limiting the curvature of the meniscus and so forcing it to locate at a point of larger roll surface separation. The positive pressure gradient (Fig. 12a.8) combines with this larger roll surface separation to drive the recirculations.

The computed (Coyle *et al.* 1986) dimensionless flow rate λ varies from 1.33 to 1.29 as capillary number is increased from 0.01 to infinity for equal roll speeds, in agreement with experiments (Pitts and Greiller 1961; Schneider 1962; Hintermaier and White 1965; Benkreira *et al.* 1981b). The computed value of λ is also relatively insensitive to roll speed ratio, having a value of $\lambda = 1.23$ for $U_2/U_1 = 0$ and $Ca = \infty$, which is also in agreement with experiments (Sullivan and Middleman 1979; Adachi *et al.* 1988). The film-split meniscus location has been measured by several authors for both symmetric (Pitts and Greiller 1961; Coyle *et al.* 1986), and zero speed ratio roll/plane configurations (Dowson *et al.* 1980; Adachi *et al.* 1988), and agreement with finite-element solutions is good (Coyle *et al.* 1986).

Theory and experiment for shear-thinning viscous fluids give values of the dimensionless flow rate λ that increase to around 1.4 as the power law index (n) decreases (Coyle *et al.* 1987; Benkreira *et al.* (1981b). Doremus and Piau (1981, 1983) measured greatly reduced flow rates with viscoelastic polyethylene oxide solutions. This effect is a result of the high elongational viscosity of these fluids interacting with the rapid accelerating/decelerating flow kinematics when the gaps are large and Newtonian viscous forces weak. These effects are analogous to those reported for knife coating (Section 12a.3).

When the rolls are moving at unequal speeds the faster roll carries away the thicker coating (Fig. 12a.10). Combining lubrication theory with the hypothesis that the flow splits at the first stagnation point simply predicts that the ratio of coating thicknesses on the rolls is equal to the square root of the speed ratio (Savage 1982). Computations (Coyle *et al.* 1986) indicate that the exponent should be roughly 0.65, which is in agreement with the data of Benkreira *et al.*

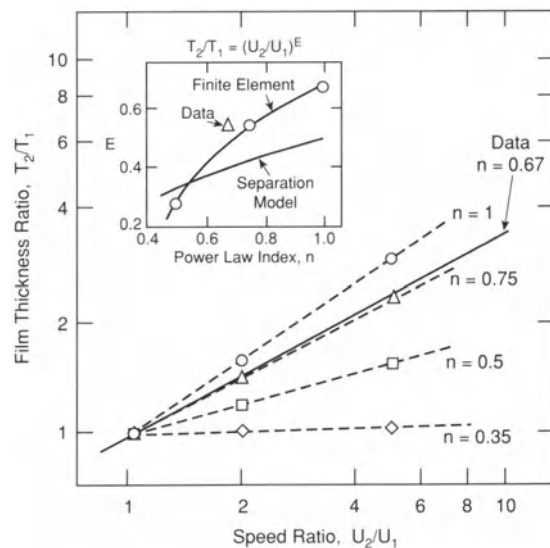


Figure 12a.10 Effect of shear-thinning on film thickness ratio in forward roll coating at infinite capillary number, compared with experiments. Decreasing n causes the film to split more symmetrically (reproduced from Coyle *et al.* (1987), by permission).

(1981b). If the liquid is shear-thinning, decreasing the power law index at a given speed ratio causes the film to split much more symmetrically, so that the faster roll gets more nearly the same coating thickness as the slower one (Coyle *et al.* 1987; Benkreira *et al.* 1981b). This is primarily due to the action of the shear-thinning viscosity which partially nullifies the asymmetry in the velocity boundary conditions.

The pressure field is one-dimensional except in the immediate vicinity of the film-split meniscus. At high capillary number, the positive portion of the pressure curve is much larger in magnitude than the negative portion, producing a roll-separating force. As the capillary number is decreased, the negative portion of the pressure curve expands and becomes comparable in magnitude to the positive part, as shown in the computed pressure profiles of Fig. 12a.8. Similar profiles were measured by Dowson *et al.* (1980).

12a.4.2 FILM-SPLITTING MENISCUS REGION – RIBBING

The most-studied aspect of roll coating instability is ribbing due to the viscous mechanism described in Section 12a.2.2. The pressure gradient at the film-splitting meniscus is always positive (Fig. 12a.8) and thus always destabilizing according to equation (12a.5). Therefore the avoidance of ribbing in roll coating requires low capillary numbers and large gaps such that the surface tension forces generated by the curved interface can dominate the viscous pressure forces generated by the lubrication flow.

Many authors have proposed simple models to predict the onset of ribbing (Pitts and Greiller 1961; Fall 1978, 1982, 1985; Savage 1977a, b, 1984, 1991; Gokhale 1981, 1983a,b; Benkreira *et al.* 1982a). The following illustrates the basic approach.

The critical capillary number for the onset of ribbing can be simply predicted by equation (12a.5) by considering the flow between linearly diverging surfaces (Ruschak, 1985). The terms in equation (12a.5) are evaluated by assuming that:

- (1) $\lambda \sim 4/3$, so that the coating thickness on each roll is given by $T = 2H_0/3$;
- (2) the roll separation at the film-split location is given by the geometric relationship $H_1 = 2R_e \cos(\alpha/2)$ where α is the diverging angle at the split point;
- (3) $dR_e/dX = \sin(\alpha/2)$;
- (4) the meniscus radius of curvature and film thickness are related by the Landau–Levich approximation $T/R_e = 1.34 Ca^{2/3}$;
- (5) the pressure gradient given by equation (12a.1) is $dp/dx = 12(1/h_1^2 - \lambda/h_1^3)$ where $p = PH_0/\mu U$, $x = X/H_0$, and $h_1 = H_1/H_0$.

Combining these expressions gives a neutral stability curve determined by

$$Ca - \frac{1.34}{\cos(\alpha/2)} Ca^{5/3} - \frac{1}{3} \cos^2(\alpha/2) \sin(\alpha/2) = 0 \quad (12a.16)$$

which, for small α and Ca , has the approximate solution

$$Ca = \alpha/6 \quad (12a.17)$$

These neutral stability curves are similar to those shown by Ruschak (1985, Fig. 9). The slope between roll surfaces is

$$\alpha = \left(\frac{H_0}{R_e} \right)^{1/2} \sqrt{2 \left(\frac{\lambda}{q} - 1 \right)}; \quad q = \frac{2T}{H_1} = \frac{1.34 Ca^{2/3}}{\cos(\alpha/2)} \quad (12a.18)$$

Equations (12a.16) and (12a.18) represent the neutral stability curve. Combining equations (12a.17) and (12a.18) for $Ca \rightarrow 0$ gives

$$Ca = 0.338 \left(\frac{H_0}{R_e} \right)^{3/8} \quad (12a.19)$$

which is included in Fig. 12a.11. This expression has the correct limiting behavior for $Ca \rightarrow 0$, but underestimates the critical capillary number over the range of H_0/R_e of interest. The accuracy can be improved by changing assumption (4) regarding the meniscus shape (Savage 1991).

An alternative approach is that of Ruschak (1985), who combined his asymptotic analysis of the steady base flow with Pearson's (1960) linear stability analysis to achieve an accurate prediction of the onset of ribbing. A more rigorous approach was taken by Coyle *et al.* (1990), who used 2D base flow calculations and 3D normal-mode linear stability analysis to obtain more accurate predictions for large gap/radius ratios.

Figure 12a.11 shows measurements of the critical capillary number for ribbing in roll coating systems, summarizing results of a number of workers (Pitts and Greiller 1961; Mill and South 1967; Greener *et al.* 1980; Benkreira *et al.* 1982a; Carter and Savage 1987; Couder *et al.* 1989; Rabaud *et al.* 1989, 1990; Coyle *et al.* 1990a; Rabaud 1990), and the data is consistent within the range of experimental uncertainty. The theoretical curves, both finite-element and asymptotic, agree well with the experiments over more than two orders of magnitude of gap/radius ratio. Both data and theory indicate that speed ratio itself has little effect on the critical capillary number when defined with the average roll speed (Carter and Savage 1987). In addition, Hasegawa and Sorimachi (1993) showed that ribbing could be eliminated by placing a string acrosss the gap

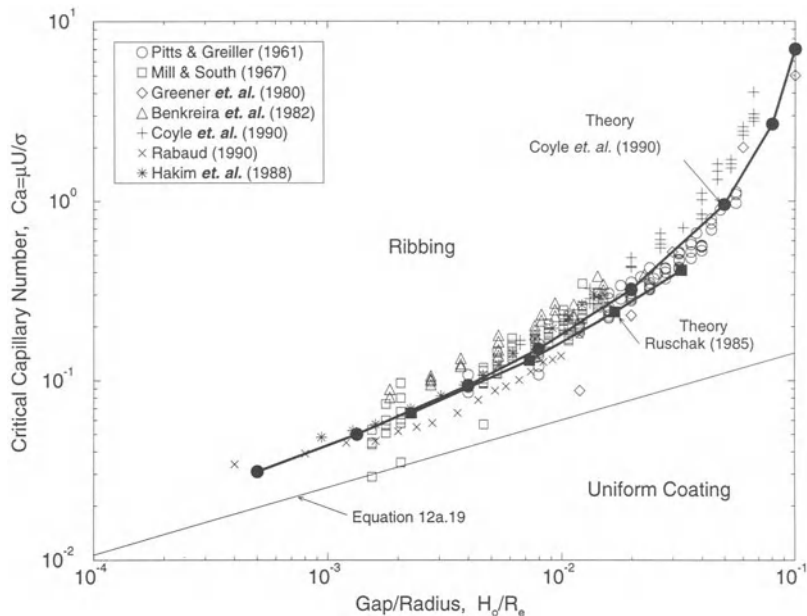


Figure 12a.11 Critical capillary number for the onset of ribbing in forward roll coating as a function of gap/radius ratio, showing comparison of experiments and theory.

touching the meniscus. This causes the meniscus to pin to the string at a larger distance from the gap center which reduces the destabilizing viscous pressure gradient.

Linear stability analysis does not predict what the new steady or time-dependent flow pattern will be beyond the critical capillary number, it merely predicts the fastest-growing mode at criticality. Experiments indicate that the steady ribbed flows are stable for some range of higher capillary number, though no detailed data exists (Mill and South 1967; Coyle 1984). Recently, Gurfinkel and Patera (1996) computed the evolution from the unstable two-dimensional steady states to the stable three-dimensional steady ribbed states by numerical solution of the unsteady three-dimensional free-surface fluid flow problem using periodic boundary conditions in the cross-web direction. The results in Fig. 12a.12 show the evolution of a nonsinusoidal steady-state ribbing pattern similar to that of Fig. 12a.3.

Unusual ribbing patterns have been observed

in non-Newtonian liquids such as butter and printing inks (Fukushima 1976). For non-Newtonian paints, ribbing, filamentation, and 'spatter' is observed (Glass 1978a-d). Bauman *et al.* (1982) report that adding 10 ppm of high molecular weight polyacrylamide reduced the critical capillary number by a factor of 2–5, even though there was no measurable change in steady shear viscosity nor could normal stresses in steady shear flow be measured. Adding 100 ppm reduced the critical capillary number by a factor of 10–30. Similar results were obtained by Hasegawa and Sorimachi (1993). To quantify the effect of rheology on the onset of ribbing, Soules *et al.* (1988) and Fernando and Glass (1988) studied a series of aqueous blends of hydrolyzed polyacrylamide (flexible backbone, high extensional viscosity) and hydroxyethyl cellulose (more rigid backbone, low extensional viscosity). All blends had the same steady shear viscosity, but differed greatly in extensional viscosity. Dramatic reduction of the critical capillary number for the onset of

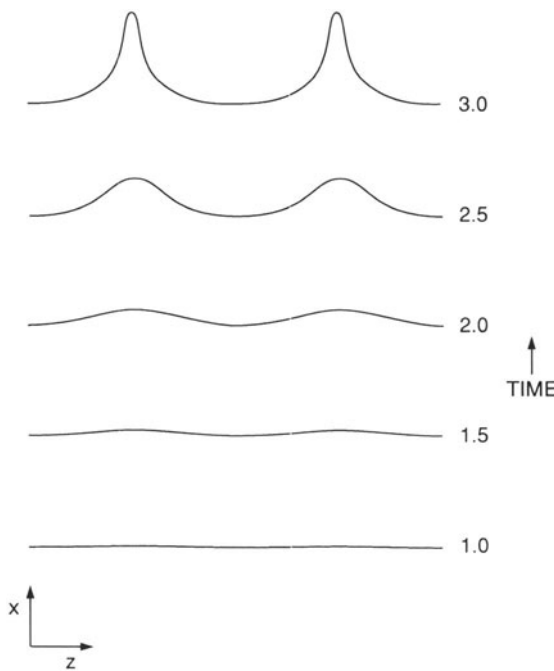


Figure 12a.12 Free surface profiles across symmetry plane for film-splitting flow in forward roll coating, showing computed evolution to a stable three-dimensional non-sinusoidal ribbed flow state. ($Ca = 0.5$, $U_2/U_1 = 1$, $H_0/Re = 0.02$, wavelength = $15H_0$, and time is in units of $\mu/\rho U^2$ (reproduced from Gurfinkel Castillo and Patera (1996), by permission).

ribbing was correlated with the magnitude of the extensional viscosity.

Finally, a number of authors have postulated that under extreme conditions (high viscosity, high speed, small gap), the sub-ambient pressure downstream of the gap center in forward roll coating causes vaporous cavitation within the liquid, and therefore represents a fundamentally different mechanism of film-splitting (Banks and Mill 1954; Floberg 1964; Miller and Myers 1958; Myers *et al.* 1959; Myers and Hoffman 1961; Hoffman and Myers 1962; Dowson and Taylor 1979). A different point of view is as follows (Kistler 1994). For high viscosity liquids and small gaps, the critical speed for the onset of ribbing is extremely low. As speed is increased

past criticality the ribs get shorter in wavelength, become time-dependent, and take on filament-like structure. The ultimate chaotic filamentation film-splitting mode is simply the natural state of the system which is very far beyond criticality, not the result of vaporous cavitation.

12a.4.3 ROLLING BANK INLET REGION

The flow field in the upstream rolling bank region was qualitatively described by Pearson (1985) and experimentally determined by Agassant and Espy (1985) for calendering of high-viscosity polymer melts. The flow field may consist of up to two vortices under the free surface, shown in Fig. 12a.13. These have been computed for a limited number of cases at low capillary number (Kistler and Scriven 1984; Chen and Higgins 1988). Benjamin and Scriven (1992) computationally mapped out the flow rate versus capillary number parameter space. For a given capillary number, reducing the flow rate below the flooded-gap limit gives two-vortex flows, followed by one-vortex flows, followed by vortex-free flows, below which the bead breaks at the 'starvation' limit. These computations were all for conditions of small enough gap that a one-dimensional lubrication pressure profile developed near the gap center. Chapter 12b examines cases outside this regime, where the structure of the flow is much more complex and more vortices can be present (Gaskell, Savage and Summers 1994; Benjamin and Scriven 1994).

The stability of this flow has not been studied. It is suspected that these vortices will become unstable to three-dimensional disturbances at high enough Reynolds number as discussed in Chapter 12a.2.2. Air entrainment at the wetting line might occur at high enough speeds, but this too has not been studied. Air entrainment might also occur due to formation of a cusp where the incoming free surface meets the rolling bank (see Section 12a.2.3). Finally, excessive feed could lead to excessive runback and film instabilities which could perturb the flow and give coating nonuniformities.

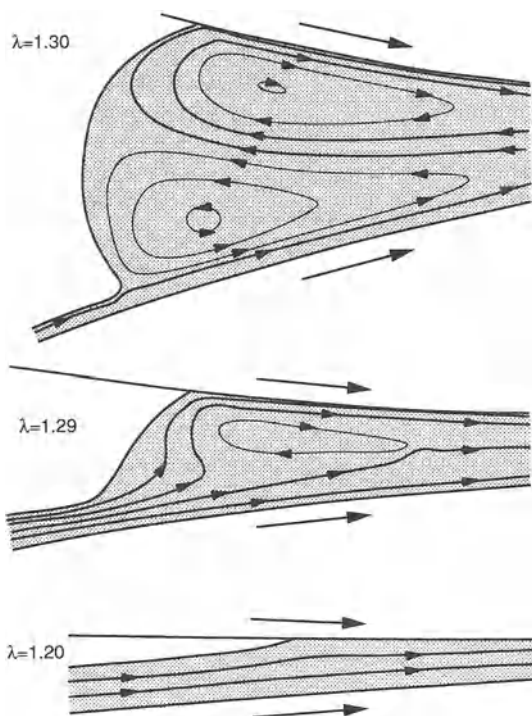


Figure 12a.13 Streamlines in the rolling bank of a forward roll coater, showing transition between: (a) two-vortex regime; (b) one-vortex regime, and (c) no-vortex regime as the inlet film thickness is decreased. ($Ca = 0.51$, $U_2/U_1 = 1$, $H_0/Re = 0.004$ (reproduced from Benjamin (1992), by permission).

12a.4.4 OPERABILITY DIAGRAMS

Figure 12a.14 attempts to capture the operability diagram of the simple forward roll coater of Fig. 12a.1b. Two hypothetical diagrams are shown, since the high-viscosity behavior will be quite different from the low-viscosity behavior. At high viscosity, ribbing imposes a severe limit on speed, while starvation should not be a problem. Air entrainment, either on the web or in a cusp, could also be high-speed limits. At low viscosity starvation can be a limit because dip coating will supply a thin film to the gap and so low capillary number (low speed) will be needed to stabilize the bead. Air entrainment and/or inertial vortex

instability could be high-speed limits. Inertial ribbing such as seen by Yih (1960) might also be present. Of all these limits, only the high-viscosity ribbing limit has been mapped out thoroughly.

12a.4.5 PRACTICAL IMPLICATIONS

There are several practical implications of the above analysis and results. As in knife coating, the coating thickness in a forward roll coater is primarily determined by the minimum gap, which necessitates small gaps for thin coatings and makes the coating thickness sensitive to mechanical tolerances, web thickness variations, and roll deflection. In addition, viscosity and surface tension (Ca) affect the flow field and its stability. Forward roll coating is especially susceptible to ribbing, requiring either large gaps, low speed, low viscosity, rapid leveling after coating, or less-stringent product uniformity requirements.

12a.5 REVERSE ROLL COATING

Figure 12a.1c–f shows four types of reverse roll coaters. The flow in the metering gap, between the applicator roll and the reverse-acting metering roll, is the primary flow field all reverse roll coaters share. This flow is the main focus of this section. The reverse-roll nip transfer flow of Fig. 12a.2d is also discussed here because it can also strongly affect the coating uniformity achieved with a reverse roll coater.

12a.5.1 METERING GAP FLOW – STEADY FLOW

Simple lubrication-theory models of flow in the metering gap, ignoring the metered film meniscus and the dynamic wetting line, predict a simple linear relationship between the metered film thickness and the speed ratio and gap thickness:

$$t_m = \frac{T_m}{H_0} = \frac{\lambda}{2} \left(1 - \frac{V_m}{V_a} \right) \quad (12a.20)$$

where the applicator and metering roll surface speeds, V_a and V_m , are taken as positive numbers,

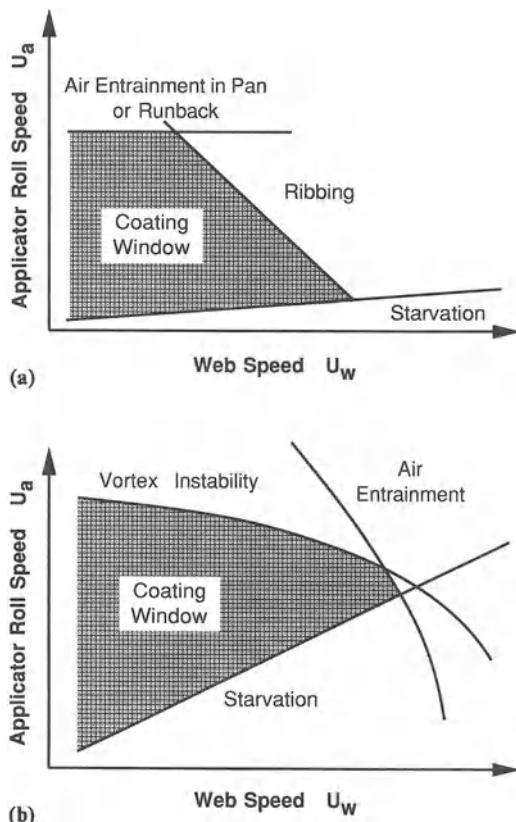


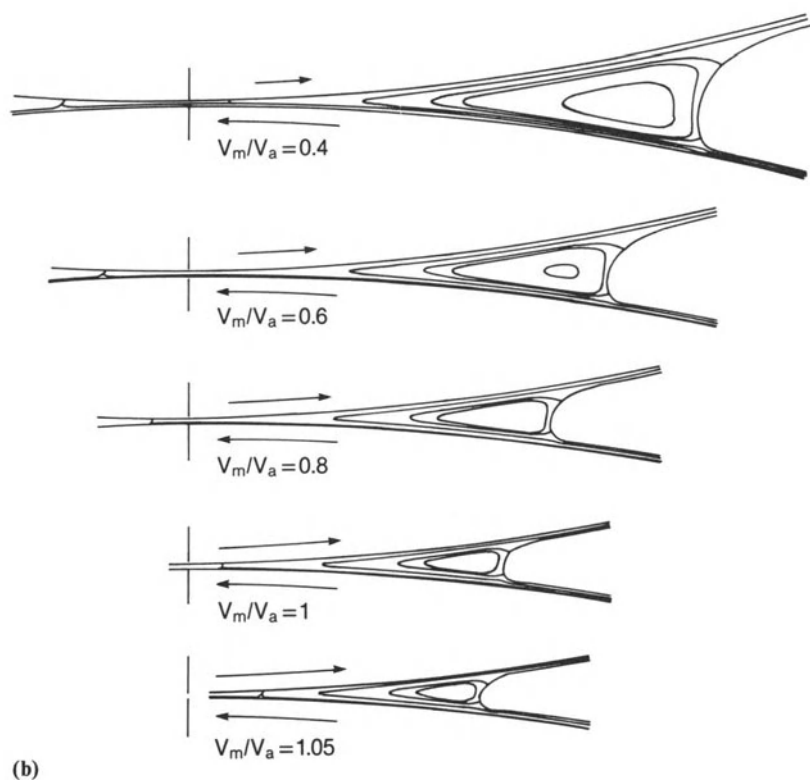
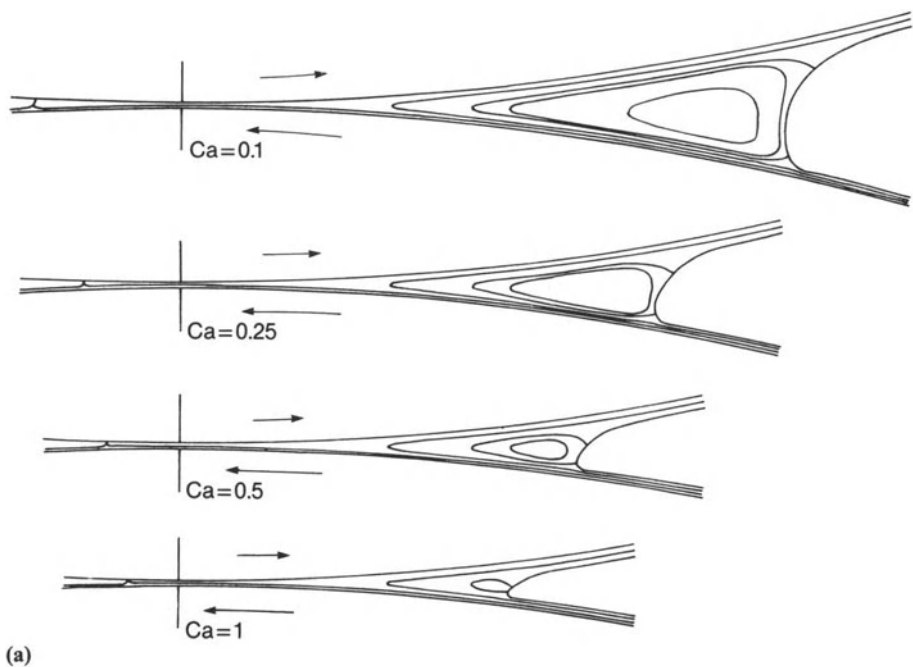
Figure 12a.14 Operability diagrams for the two-roll forward roll coater of Fig. 12a.1b: (a) viscous regime; (b) inertial regime.

and λ , as in forward roll coating, is 1.3 (Ho and Holland 1978; Greener and Middleman 1981; Benkreira *et al.* 1982b; Coyle *et al.* 1990c). Experimental data of Ho and Holland (1978) and Benkreira *et al.* (1981b), which are restricted to low speed ratio, agree with this expression, with the extensive data of the latter authors yielding a value of $\lambda = 1.26$ for equation (12a.20). Equation (12a.20) predicts negative metered film thicknesses at speed ratios above unity, which is not possible.

Figure 12a.15 shows computed streamlines for

the flow as a function of capillary number and speed ratio (Coyle *et al.* 1990b). Similar to forward roll coating, decreasing the capillary number causes the menisci to be less-tightly curved and in doing so move to where the roll surfaces are farther apart. Therefore the bead gets larger and a recirculation appears in the upstream film-transfer flow. Increasing the speed ratio causes the wetting line to become located on the upstream side of the gap (the right-hand side of the figure), rather than on the downstream

Figure 12a.15 Computed streamlines for metering gap flow as a function of: (a) capillary number and (b) speed ratio. Increasing either causes the bead to shrink and the wetting line to invade the gap ($H_0/R_e = 0.004$, a – $Ca = 0.1$, b – $V_m/V_a = 0.4$). As drawn, the metering roll is directly above the applicator roll (reproduced from Coyle *et al.* (1990b), by permission).



side as one might intuitively expect. The recirculation on the upstream side of the gap shrinks, and the coating bead becomes small and tightly curved. In all knife and roll coating flows, lubrication theory predicts that the net flow is in the direction of the faster surface, and this sets up a pressure gradient that augments the flow rate by roughly 30% (i.e. $\lambda = 1.3$). The reverse-roll metering gap must always have a net flow in the direction of the applicator roll, so that as speed ratio approaches and passes unity there must be significant deviations from the predictions of lubrication theory due to the curved menisci and surface tension.

Figure 12a.16 shows the dependence of the metered film thickness on speed ratio and capillary number. As speed ratio is increased both the

experimental and computed coating thickness pass through a minimum beyond which they increase sharply. The minimum film thickness corresponds to the point where the wetting line is at the gap center. At this point the gap has effectively lost its metering ability since the region of minimum roll surface clearance is no longer filled with liquid. Instead, the metering is being done further upstream where the clearance is larger and thus the metered film is thicker. Further increasing speed ratio worsens this situation, and the steep upturn in metered film thickness corresponds to the wetting line moving further into the upstream side of the gap. Lowering the capillary number has little effect at low speed ratios, but it shifts the minimum metered film thickness to higher speed ratio values.

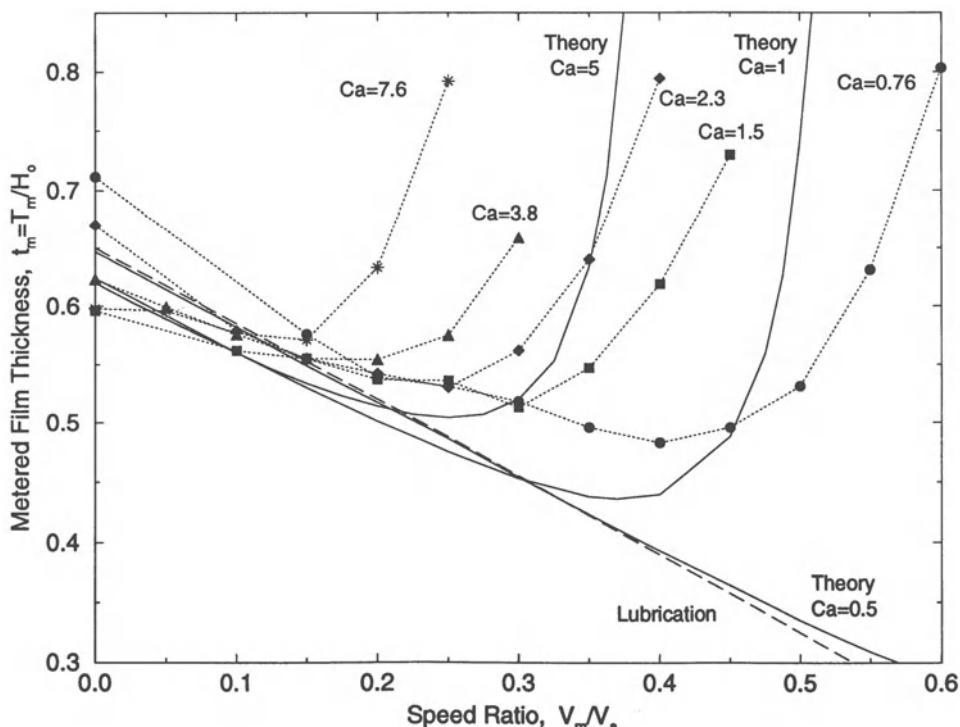


Figure 12a.16 Reverse roll metered film thickness as a function of speed ratio and capillary number, comparing experiments (dashed lines) and theory. The point of minimum film thickness corresponds to the wetting line located at the gap center ($H_0 = 500 \mu\text{m}$, $R_1 = R_2 = 0.1 \text{ m}$).

Kang and Liu (1991) report the speed ratio at which the film thickness attains its minimum as

$$V_m/V_a = 0.29 Ca^{-0.55}; \quad 0.12 \leq Ca \leq 12 \quad (12a.21)$$

Unfortunately they do not report a correlation for minimum coating thickness, which would be of interest since significant positive deviations from equation (12a.20) are present at the minimum, especially for low capillary number.

Fukazawa (1993) matched lubrication pressure profiles to the Landau and Levich condition for radius of curvature of the metered film meniscus to create a simple model which captures the essential physics of this flow, thus predicting the presence of a minimum in the film-thickness versus speed ratio curve.

Theory for shear-thinning viscous fluids predicts that there is little change, as compared with Newtonian theory, in metered film thickness as a function of speed ratio and capillary number, providing the latter is defined using the viscosity at the characteristic process shear rate $\dot{\gamma} = 2V_a/H_0$ (Coyle *et al.* 1990d). Experiments with shear-thinning polymer solutions confirm this (Benkreira *et al.* 1981b). The biggest difference is a predicted 5–7% increase in film thickness at low speed ratios. The data confirm that the dimensionless flow rate λ increases to 1.34 (a 6% increase from its Newtonian value of 1.26).

12a.5.2 METERING GAP FLOW – FAILURE MODES

The stability of the metering gap transferred film has not been examined closely. The metered film in a reverse roll coater is subject to two instabilities. The first is the classical viscous ribbing, while the second is a three-dimensional time-periodic disturbance called ‘cascade’, ‘herringbone’, or ‘seashore’ (Babchin *et al.* 1981; Coyle *et al.* 1990b). This latter disturbance, shown in the photograph of Fig. 12a.17, consists of irregular saw-tooth cross-web bars on the film coinciding with periodic bead oscillation and air entrapment on the metering roll. The latter gives a nonuniform transferred film containing large air bubbles.

The mechanism of ribbing in reverse roll coating is the same as that in forward roll coating. Surface tension stabilizes the flow to ribbing. The hydrodynamic pressure gradient at the metered film meniscus destabilizes the flow if it is positive. Whereas in forward roll coating this pressure gradient is always destabilizing, in reverse roll coating the pressure gradient can be reversed by increasing the speed ratio (Fig. 12b.18) and in this way the pressure gradient becomes stabilizing. Thus ribbing can be eliminated in a reverse roll coater even at high capillary number when surface tension is no longer a significant stabilizing influence.

The mechanism of cascade stems from the intrusion through the gap of the dynamic wetting line, as shown in Fig. 12a.15. When the wetting line is located on the upstream side of the gap, the region of minimum roll surface clearance does not affect the metering of the coating, and increasing speed ratio increases the coating thickness. At high enough speed ratios, the metered film becomes as thick as the minimum roll surface clearance through which it tries to pass. It periodically re-attaches to the metering roll at the gap center, entraps a large bubble of air on the metering roll, and is suddenly much thinner because the gap at the re-attachment point (which does the metering) is much smaller. The wetting line then moves back into the upstream region and the film becomes thicker and the cycle repeats itself. Flow visualization experiments have confirmed this mechanism (DiCarlo 1986).

Two typical operability diagrams are shown in Fig. 12a.19. At very low capillary number the flow is uniform and stable at any value of speed ratio. What makes a reverse roll coater so useful is that at high capillary number there exists a stable ‘window’ of operation: if the speed ratio (V_m/V_a) is within a certain range, the metered film is uniform and stable. If the speed ratio is below this range, the metered film exhibits ribbing of the sort seen in a forward roll coater. At speed ratio values above the stable range, the cascade instability sets in. Transition to ribbing as the speed ratio is lowered out of the stable range is

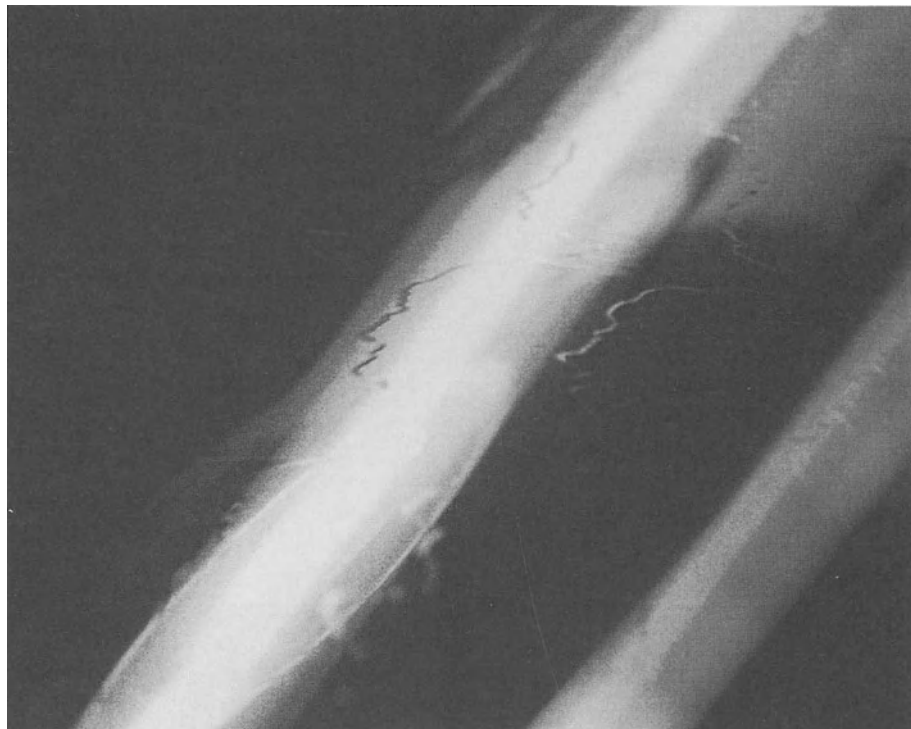


Figure 12a.17 Photograph of the cascade instability on the metered film (top view, roll surface moves from bottom right to top left). The irregular cross-web waves are regularly spaced in the downweb direction (reproduced from Coyle *et al.* (1990b), by permission).

gradual, but the transition to cascade is sharp, occurring just beyond the speed ratio which produces the minimum metered film thickness. The onset of cascade shifts to slightly higher values of speed ratio as the gap is decreased, but this onset can be approximated for gap widths of 25–250 µm as (Coyle 1984)

$$V_m/V_a = 0.43 Ca^{-0.46}; \quad 0.2 \leq Ca \leq 4 \quad (12a.22)$$

As one would expect, this curve is above and roughly parallel to the correlation of maximum speed ratio for minimum coating thickness (equation (12a.21)) defined by Kang and Liu (1991).

It is interesting to note that for small gaps there is an intermediate range of capillary numbers over which there is no stable window of operation. This leads to the counter-intuitive fact that in some cases one must increase the speed of the

coater in order to eliminate ribbing. In addition, as Reynolds number increases, the stable operating window widens and shifts to higher speed ratios (Coyle *et al.* 1990b).

Experiments and computations for non-Newtonian liquids have been carried out by Coyle *et al.* (1990d). Experiments with shear-thinning polymer solutions show that the onset of cascade is unchanged from Newtonian results if capillary number is based on the process shear rate as above ($\dot{\gamma} = 2V_a/H_0$), which is in agreement with theory. Ribbing was aggravated, and the stable window disappeared at high polymer concentrations. Experiments with highly elastic polymer solutions gave no stable operating window due to ribbing. At high concentrations, there was no longer a clear transition to cascade, but rather the metered film gradually became more ‘mottled’

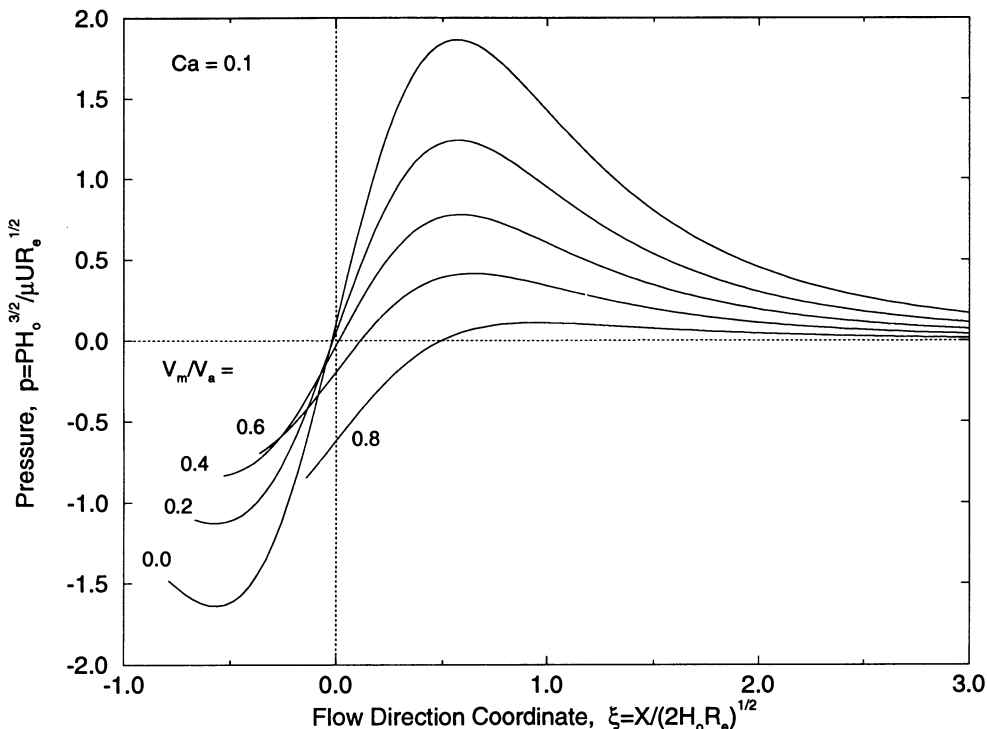


Figure 12a.18 Computed pressure along the main flow direction (X) as a function of speed ratio for reverse roll coating. The metered film forms on the left side of the figure.

in appearance as speed ratio was increased. Deformation rates computed from Newtonian kinematics illustrate the severity of the deformation rates in a reverse roll coater, and how rapidly a fluid element experiences these deformations. For example, shear rates of 10^5 s^{-1} and extension rates of 10^4 s^{-1} are not uncommon, and occur over a time scale of milliseconds. Considering the extreme nature of the deformation one might expect that rheology will be important in determining the operability of a reverse roll coater.

12a.5.3 REVERSE ROLL NIP TRANSFER

The operability of reverse roll nip transfer, shown in Fig. 12a.2d, has been studied by Kang, Lee and Liu (1990). If the web is moved too fast with respect to the applicator roll, ribbing is observed. The limiting wipe ratio (V_w/V_a) for the onset of

ribbing is approximately 1.2 for Newtonian liquids and 1.6 for viscoelastic polymer solutions. Broughton *et al.* (1950) found a limiting wipe ratio of roughly unity. This general behavior can be explained according to the viscous mechanism for ribbing (Section 12a.2.2). The Reynolds equation predicts a positive pressure gradient at the film transfer meniscus if the wipe ratio exceeds 1.0, so that this meniscus becomes potentially unstable to ribbing according to equation (12a.5), and this result is consistent with the viscous mechanism of ribbing. A curious aspect of Kang, Lee and Liu's results is the insensitivity of the limiting wipe ratio to capillary number and inlet film thickness. The stabilizing effect of viscoelasticity can perhaps be explained by considering a polymer solution's extensional response. Increasing the wipe ratio increases the relative stretch rate of the coated film, so that a

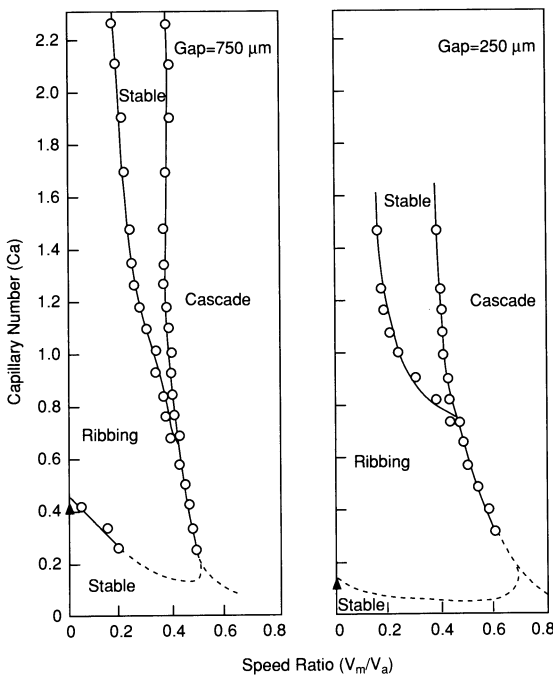


Figure 12a.19 Experimental operability diagrams for metering gap flow with a Newtonian liquid, showing operating regions of defect-free coating, ribbing, and cascade. The triangles on the y -axis are data for a roll against a stationary plate (reproduced from Coyle (1992), by permission).

viscoelastic solution might develop locally lower pressures near the meniscus which could partially counteract the positive pressure gradient due to viscous forces.

12a.5.4 OPERABILITY DIAGRAMS – TWO-ROLL REVERSE ROLL COATER

Figure 12a.20 attempts to map the operating diagram for the simple two-roll reverse roll coater of Fig. 12a.1c, for both high and low viscosity liquids. At high viscosity the main failure modes are metered film ribbing and cascade, which are just mapped from Fig. 12a.19. It should be noted that there is no evidence, pro or con, indicating that ribbing on the metered film is associated with a defect on the transferred

film. Rising film flow instability could also be a limit, as high coverages from dip coating could result in run-back, which would introduce a defect directly onto the coated product. Air entrainment in the pond will occur at high enough viscosity and applicator roll speed (equation (12a.8)). Air entrainment on the web might occur, but has not been studied. At low enough viscosity, metered film ribbing and cascade are absent and starvation becomes the main limit. Inertially-driven ribs and vortex instabilities might also come into play, but have not been studied.

12a.5.5 OPERABILITY DIAGRAMS – THREE-ROLL REVERSE ROLL COATER

The operability limits of a three-roll reverse roll coater would be those of the two-roll version above, with the extra variable of the wipe ratio as a third dimension to the diagram. In this case, the main extra failure mode that limits operability is reverse nip transfer ribbing, avoidance of which requires a wipe ratio of 1.2 or less. Once again, inertially driven ribs and vortex instabilities may also come into play, but have not been studied.

12a.5.6 PRACTICAL IMPLICATIONS

There are several practical implications of the above analysis and results. As in knife and forward roll coating, the coating thickness in a reverse roll coater is primarily determined by the minimum gap, which necessitates small gaps for thin coatings and makes the coating thickness sensitive to mechanical tolerances and roll deflection. As in forward roll coating, viscosity and surface tension affect the flow field and its stability through the capillary number. Reverse roll coating adds an extra degree of freedom, the speed ratio, which can be adjusted to control the coating thickness, flow field, and its stability. At low capillary number coating thicknesses much smaller than the minimum gap can be obtained, while stable flows can be achieved with proper

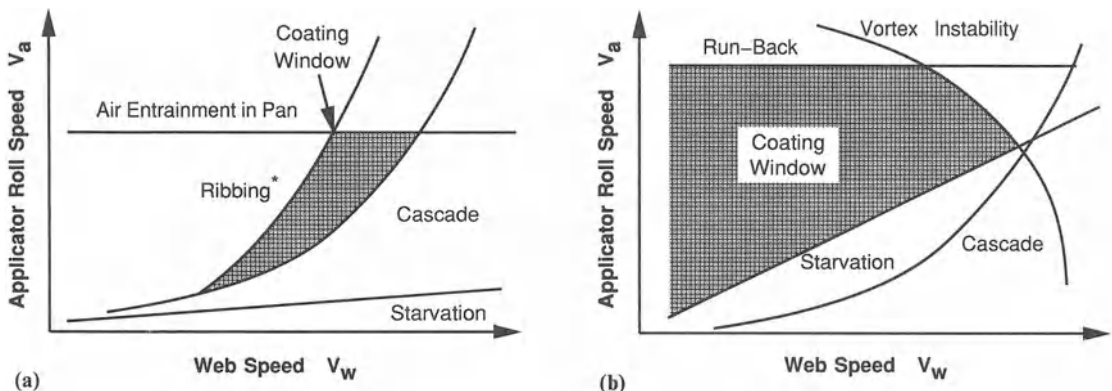


Figure 12a.20 Operability diagrams for the two-roll reverse roll coater of Fig. 12a.1c: (a) viscous regime, (b) inertial regime.

speed ratio adjustment even at high capillary number. Both of these effects illustrate the advantages of reverse roll coating over knife coating and forward roll coating.

12a.6 SUMMARY AND CONCLUDING REMARKS

The above summarizes most of what is known about the fluid mechanics of knife and roll coating. There are many gaps in our understanding. The phenomena of inertially driven instability in low-viscosity systems has not been studied, nor has the sensitivity of these coating devices to perturbations. The subject of dynamic wetting and air entrainment in these coaters is not documented. Doctoring in reverse roll coating needs further understanding. The dynamics and stability of the rolling bank in forward roll coating is not understood. Perhaps the least understood and most practically significant problem in all of these coaters is the effect of non-Newtonian fluid rheology on their steady operation and stability. These and other specific aspects need further research, but we also need detailed systematic studies of the operating limits of specific coating configurations in order to understand how all the building-block flows fit together and interact.

REFERENCES

- Adachi, K., Murata, Y., Morikawa, T. and Nakamura, R. 1990. Thin film coating with a knife or blade. *AICHE Spring National Meeting*, New Orleans, March.
- Adachi, K., Tamura, T. and Nakamura, R. 1988. Coating flows in a nip region and various critical phenomena. *AICHE J.* **34**(3): 456–464.
- Aidun, C. K. 1991a. Principles of hydrodynamic instability: application in coating systems Part 1: Background. *Tappi J.* **74**(2): 213–219.
- Aidun, C. K. 1991b. Principles of hydrodynamic instability: application in coating systems Part 2: Examples of flow instability. *Tappi J.* **74**(3): 213–220.
- Aidun, C. K., Triantafillopoulos, N. G. and Benson, J. D. 1991. Global stability of a lid-driven cavity with throughflow: Flow visualization studies. *Phys. Fluids A.* **3**(9): 2081–2091.
- Babchin, A. J., Clish, R. J. and Wahren, D. 1981. Stability and disturbance of coating films. *Adv. Coll. Int. Sci.* **14**: 251–280.
- Banks, W. H. and Mill, C. C. 1954. Some observations on the behavior of liquids between rotating rollers. *Proc. Royal Soc. A.* **223**: 414–419.
- Bauman, T. M., Sullivan, T. M. and Middleman, S. 1982. Ribbing instability in coating flows: effect of polymer additives. *Chem. Eng. Commun.* **14**: 35–46.
- Benjamin, D. F. 1994. Roll coating flows and multiple roll systems. PhD thesis, University of Minnesota, Minneapolis.
- Benjamin, D. F. and Scriven, L. E. 1992. Forward roll coating: effect of feed condition. *AICHE Spring National Meeting*, New Orleans, April.

- Benjamin, D. F. and Scriven, L. E. 1994. Stability of forward roll coating flows. AIChE Spring National Meeting, Atlanta, April.
- Benkreira, H., Edwards, M. F. and Wilkinson, W. L. 1981a. A semi-empirical model of the forward roll coating flow of Newtonian fluids. *Chem. Eng. Sci.* **36**: 423–427.
- Benkreira, H., Edwards, M. F. and Wilkinson, W. L. 1981b. Roll coating of purely viscous liquids. *Chem. Eng. Sci.* **36**: 429–434.
- Benkreira, H., Edwards, M. F. and Wilkinson, W. L. 1982a. Ribbing instability in the roll coating of Newtonian fluids. *Plastics Rubber Proc. Appl.* **2**: 137–144.
- Benkreira, H., Edwards, M. F. and Wilkinson, W. L. 1982b. Mathematical modelling of the reverse and metering roll coating flow of Newtonian fluids. *Chem. Eng. Sci.* **37**(2): 277–282.
- Bixler, N. E. 1982. Stability of a coating flow. PhD thesis, University of Minnesota, Minneapolis.
- Bolton, B. and Middleman, S. 1980. Air entrainment in a roll coating system. *Chem. Eng. Sci.* **35**(3): 597–601.
- Booth, G. L. 1970. *Coating Equipment and Processes*. New York: Lockwood Publishing Company.
- Booth, G. L. 1990. Coating converting processes: Traditional methods and new uses. 21st Annual IGC Coating Systems Conference, Boston, August, Bis-Cap International, Newtonville, MA.
- Broughton, G., Egan, L. W. and Sturken, C. 1950. The reverse roll principle of coating. *Tappi J.* **33**(7): 314–317.
- Cameron, A. 1976. *Basic Lubrication Theory*. New York: Wiley.
- Carter, G. C. and Savage, M. D. 1987. Ribbing in a variable speed two-roll coater. *Math. Eng. Ind.* **1**(1): 83–95.
- Chalmers, B. and Hoare, W. E. 1941. *J. Iron St. Inst.* **144**: 127.
- Chandrasekhar, S. 1961. *Hydrodynamic and Hydromagnetic Stability*. Oxford: Oxford University Press.
- Chen, K. and Higgins, B. G. 1988. Study of the flow in the upstream bank of liquid in a forward roll coater by the finite element method. *Chem. Eng. Sci.* **43**(10): 2867–2875.
- Couder, Y., Michalland, S., Rabaud, M. and Thome, H. 1989. The printer's instability: The dynamical regimes of directional viscous fingering. In *Nonlinear Evolution of Spatio-temporal Structures in Dissipative Continuous Systems*, eds F. H. Busse and L. Kramer. Proceedings of the NATO Advanced Research Workshop, Streitberg, September.
- Coyle, D. J. 1984. The fluid mechanics of roll coating: steady flows, stability, and rheology. PhD thesis, University of Minnesota, Minneapolis.
- Coyle, D. J. 1992. Roll Coating. In *Modern Coating and Drying Technology*, eds E. Cohen and E. Gutoff. New York: VCH Publishers. pp. 63–116.
- Coyle, D. J., Macosko, C. W. and Scriven, L. E. 1986. Film-splitting flows in forward roll coating. *J. Fluid Mech.* **171**: 183–207.
- Coyle, D. J., Macosko, C. W. and Scriven, L. E. 1987. Film-splitting flows of shear-thinning liquids in forward roll coating. *AIChE J.* **33**(5): 741–746.
- Coyle, D. J., Macosko, C. W. and Scriven, L. E. 1990a. Stability of symmetric film-splitting between counter-rotating cylinders. *J. Fluid Mech.* **216**: 437–458.
- Coyle, D. J., Macosko, C. W. and Scriven, L. E. 1990b. The fluid dynamics of reverse roll coating. *AIChE J.* **36**(2): 161–174.
- Coyle, D. J., Macosko, C. W. and Scriven, L. E. 1990c. A simple model of reverse roll coating. *Ind. Eng. Chem. Res.* **29**: 1416–1419.
- Coyle, D. J., Macosko, C. W. and Scriven, L. E. 1990d. Reverse roll coating of non-Newtonian liquids. *J. Rheol.* **34**(5): 615–636.
- Coyne, J. C. and Elrod, H. G. 1970a. Conditions for the rupture of a lubricating film. Part 1: Theoretical model. *J. Lubric. Technol.* **92**: 451–456.
- Coyne, J. C. and Elrod, H. G. 1970b. Conditions for the rupture of a lubricating film. Part 2: New boundary conditions for the Reynolds equation. *J. Lubric. Technol.* **93**: 156–167.
- DiCarlo, M. J. 1986. Reverse roll coating – experiments and theory. MS thesis, University of Minnesota, Minneapolis.
- Doremus, P. and Piau, J.-M. 1981. Viscoelastic elongational lubrication. *J. Non-Newtonian Fluid Mech.* **9**: 389–400.
- Doremus, P. and Piau, J.-M. 1983. Experimental study of viscoelastic effects in a cylinder-plane lubricated contact. *J. Non-Newtonian Fluid Mech.* **13**: 79–91.
- Dowson, D. and Higginson, G. R. 1966. *Elasto-Hydrodynamic Lubrication*. Oxford: Pergamon Press.
- Dowson, D., Smith, E. H. and Taylor, C. M. 1980. An experimental study of hydrodynamic film rupture in steadily-loaded, non-conformal contact. *J. Mech. Eng. Sci.* **22**(2): 71–78.
- Dowson, D. and Taylor, C. M. 1979. Cavitation in bearings. *Ann. Rev. Fluid Mech.* **11**: 35–66.
- Fall, C. 1978. Surface ribbing of a thin viscous fluid film emerging from a spreader or roller. *J. Lubric. Technol.* **100**: 462–466.
- Fall, C. 1982. A theoretical model of striated film-rupture. *J. Lubric. Technol.* **104**: 164–167.
- Fall, C. 1985. A theoretical model of striated film-

- rupture applied to the cylinder-plane. *J. Tribol.* **107**: 419–422.
- Fernando, R. H. and Glass, J. E. 1988. Dynamic uniaxial extensional viscosity (DEUV) effects in roll application. Part 2. Polymer blend studies. *J. Rheol.* **32**(2): 199–213.
- Floberg, L. 1964. Cavitation in lubricating oil films. In *Cavitation in Real Liquids*, ed. R. Davies. Amsterdam: Elsevier Publishing Company. pp. 138–146.
- Fukazawa, K. 1993. Reverse roll coater model. MS thesis, University of Minnesota, Minneapolis.
- Fukushima, M. 1976. Study of an anomalous flow during rolling of viscoelastic fluid. Part 1. Experimental. *Jap. J. Appl. Phys.* **15**(3): 525–530.
- Gaskell, P. H., Savage, M. D. and Summers, J. L. 1994. Flow transformation from classical to meniscus roll coating. AIChE Spring National Meeting, Atlanta, April.
- Gatcombe, E. K. 1945. Lubrication characteristics of involute spur gears – a theoretical investigation. *Trans. ASME* **67**: 177–188.
- Ghannam, M. T. and Esmail, M. N. 1990. Air entrainment and dynamic contact angles in hydrodynamics of liquid coating. *Canadian J. Chem. Eng.* **68**(2): 197–203.
- Glass, J. E. 1978a. Dynamics of roll spatter and tracking. Part 1: Commercial latex trade paints. *J. Coatings Technol.* **50**(640): 53–60.
- Glass, J. E. 1978b. Dynamics of roll spatter and tracking. Part 2: Formulation effects in experimental paints. *J. Coatings Technol.* **50**(640): 61–68.
- Glass, J. E. 1978c. Dynamics of roll spatter and tracking. Part 3: Importance of extensional viscosities. *J. Coatings Technol.* **50**(641): 56–71.
- Glass, J. E. 1978d. Dynamics of roll spatter and tracking. Part 4: Importance of G^* recovery and N_1 in tracking. *J. Coatings Technol.* **50**(641): 72–78.
- Gokhale, V. V. 1981. Bounds for region of ribbing instability in some free surface coating flows. *J. Rheol.* **25**(4): 421–432.
- Gokhale, V. V. 1983a. Improved stability criterion for lubrication flow between counterrotating rollers. *AIChE J.* **29**(5): 865–866.
- Gokhale, V. V. 1983b. Exact solution to the ribbing instability problem in lubrication flow by invariant imbedding. *Chem. Eng. Commun.* **21**: 81–87.
- Greener, J. and Middleman, S. 1974. Blade coating of a viscoelastic fluid. *Polymer Eng. Sci.* **14**: 791–796.
- Greener, J. and Middleman, S. 1975. A theory of roll coating of viscous and viscoelastic fluids. *Polymer Eng. Sci.* **15**(1): 1–10.
- Greener, J. and Middleman, S. 1979. Theoretical and experimental studies of the fluid dynamics of a two-roll coater. *Ind. Eng. Chem. Fundam.* **18**: 35–41.
- Greener, J. and Middleman, S. 1981. Reverse roll coating of viscous and viscoelastic liquids. *Ind. Eng. Chem. Fundam.* **20**: 63–66.
- Greener, J., Sullivan, T., Turner, B. and Middleman, S. 1980. Ribbing instability of a two-roll coater: Newtonian fluids. *Chem. Eng. Commun.* **5**: 73–83.
- Gurfinkle Castillo, M. E. and Patera, A. T. 1996. Three-dimensional ribbing in forward-roll film coating processes. *J. Fluid Mech.*, in press.
- Hakim, V., Rabaud, M., Thome, H. and Couder, Y. 1988. Directional growth in viscous fingering. In *New Trends in Nonlinear Dynamics and Pattern Forming Phenomena: The Geometry of Nonequilibrium*. Proceedings of the NATO Advanced Research Workshop, Cargese, August.
- Hasegawa, T. and Sorimachi, K. 1993. Wavelength and depth of ribbing in roll coating and its elimination. *AIChE J.* **39**(6): 935–945.
- Higgins, D. G. 1965. Coating methods. In *Encyclopedia of Polym. Sci. Tech.* John Wiley, Vol. 3, pp. 765–807.
- Hintermaier, J. C. and White, R. E. 1965. The splitting of a water film between rotating rolls. *Tappi J.* **48**(11): 617–625.
- Ho, W. S. and Holland, F. A. 1978. Between-rolls metering coating technique, a theoretical and experimental study. *Tappi J.* **61**(2): 53–56.
- Hoffman, R. D. and Myers, R. R. 1962. The splitting of thin liquid films. II. Cavitation dynamics. *Trans. Soc. Rheol.* **6**: 197–207.
- Hopkins, M. R. 1957. Viscous flow between rotating cylinders and a sheet moving between them. *Brit. J. Appl. Phys.* **8**: 442–444.
- Hsu, T. C., Malone, M., Laurence, R. L. and Middleman, S. 1985. Separating forces in blade coating of viscous and viscoelastic liquids. *J. Non-Newtonian Fluid Mech.* **18**: 273–294.
- Johnson, K. L. 1985. *Contact Mechanics*. Cambridge University Press.
- Kang, Y.-T., Lee, K. Y. and Liu, T.-J. 1991. The effect of polymer additives on the performance of a two-roll coater. *J. Appl. Polymer Sci.* **43**: 1187–1195.
- Kang, Y.-T. and Liu, T.-J. 1991. Minimum film thickness for reverse roll coating. *Chem. Eng. Sci.* **46**(11): 2958–2960.
- Khesghi, H. S., Kistler, S. F. and Scriven, L. E. 1992. Rising and falling film flows: viewed from a first-order approximation. *Chem. Eng. Sci.* **47**(3): 683–694.
- Kistler, S. F. 1994. Personal communication.
- Kistler, S. F. and Scriven, L. E. 1983. Coating flows.

- In *Computational Analysis of Polymer Processing*, eds J. R. A. Pearson and S. M. Richardson. London and New York: Applied Science Publishers, pp. 243–299.
- Kistler, S. F. and Scriven, L. E. 1984. Coating flow theory by finite element and asymptotic analysis of the Navier–Stokes system. *Int. J. Num. Meth. Fluids.* **4:** 207.
- Martin, H. M. 1916. The lubrication of gear teeth. *Engineering.* **102:** 119–121.
- McEwan, A. D. and Taylor, G. I. 1966. The peeling of a flexible strip attached by a viscous adhesive. *J. Fluid Mech.* **26:** 1–15.
- Mill, C. C. and South, G. R. 1967. Formation of ribs on rotating rollers. *J. Fluid Mech.* **28:** 523–529.
- Miller, J. C. and Myers, R. R. 1958. A photographic study of liquid flow in a roll nip. *Trans. Soc. Rheol.* **2:** 77–93.
- Myers, R. R. and Hoffman, R. D. 1961. The distribution of pressures in the roll application of Newtonian fluids. *Trans. Soc. Rheol.* **5:** 317–328.
- Myers, R. R., Miller, J. C. and Zettlemoyer, A. C. 1959. The splitting of thin liquid films. I. Kinematics. *J. Colloid Sci.* **14:** 287–299.
- Pearson, J. R. A. 1960. The instability of uniform viscous flow under rollers and spreaders. *J. Fluid Mech.* **7:** 481–500.
- Pearson, J. R. A. 1985. *Mechanics of Polymer Processing*. London: Elsevier Applied Science Publishers.
- Pitts, E. and Greiller, J. 1961. The flow of thin liquid films between rollers. *J. Fluid Mech.* **11:** 33–50.
- Rabaud, M. 1990. Personal communication.
- Rabaud, M. and Hakim, V. 1989. Shape of stationary and travelling cells in the printer's instability. In *Proceedings of the Third International Workshop on Instabilities and Nonequilibrium Structures*, eds E. Tirapegui and W. Zeller. Kluwer Academic Publishers.
- Rabaud, M., Michalland, S. and Couder, Y. 1990. Dynamical regimes of directional viscous fingering: spatiotemporal chaos and wave propagation. *Phys. Rev. Lett.* **64**(2): 184–187.
- Reynolds, O. 1886. On the theory of lubrication and its application to Mr Beauchamp Tower's experiments, including an experimental determination of the viscosity of olive oil. *Philos. Trans. R. Soc. Lond. A.* **177:** 157–234.
- Ruschak, K. J. 1982. Boundary conditions at a liquid/air interface in lubrication flows. *J. Fluid Mech.* **119:** 107–120.
- Ruschak, K. J. 1985. Coating flows. *Ann. Rev. Fluid Mech.* **17:** 65–89.
- Saffman, P. G. and Taylor, G. I. 1958. The penetration of a fluid into a porous medium or Hele-Shaw cell containing a more viscous liquid. *Proc. R. Soc. Lond. A.* **245:** 312–329.
- Satas, D. (ed.) 1984. *Web Processing and Converting Technology and Equipment*. New York: Van Nostrand Reinhold.
- Savage, M. D. 1977a. Cavitation in lubrication. Part 1. On boundary conditions and cavity-fluid interfaces. *J. Fluid Mech.* **80:** 743–755.
- Savage, M. D. 1977b. Cavitation in lubrication. Part 2. Analysis of wavy interfaces. *J. Fluid Mech.* **80:** 757–767.
- Savage, M. D. 1982. Mathematical models for coating processes. *J. Fluid Mech.* **117:** 443–455.
- Savage, M. D. 1984. Mathematical model for the onset of ribbing. *AICHE J.* **30**(6): 999–1002.
- Savage, M. D. 1991. Meniscus instability and ribbing. *Industrial Coating Research.* **2:** 47–58.
- Savage, M. D. and Gaskell, P. 1990. Meniscus coating. AICHE Spring National Meeting, Orlando, March.
- Scharenberg, R. T. 1985. Coating methods. In *Encyclopedia of Polym. Sci. Eng.* 2nd edn. John Wiley, Vol. 3, pp. 552–567.
- Schneider, G. B. 1962. Analysis of forces causing flow in roll coaters. *Trans. Soc. Rheol.* **6:** 209–221.
- Secor, R. B. 1991. Process modeling of contact extrusion and coextrusion. *Tappi J.* **74**(11): 168–174.
- Sone, T. and Fukushima, M. 1960. On the stripe pattern during rolling of viscous materials. *J. Phys. Soc. Japan.* **15:** 1708.
- Soules, D. A., Fernando, R. H. and Glass, J. E. 1988. Dynamic uniaxial extensional viscosity (DUEV) effects in roll application. Part 1. Rib and web growth in commercial coating. *J. Rheol.* **32**(2): 181–198.
- Strenger, M. R., Secor, R. B. and Sramek, R. J. 1992. Knife coating of a viscoelastic material. AICHE Spring National Meeting, New Orleans, March.
- Sullivan, T. M. and Middleman, S. 1979. Roll coating in the presence of a fixed constraining boundary. *Chem. Eng. Commun.* **3**(6): 469–482.
- Sullivan, T. M. and Middleman, S. 1986. Film thickness in blade coating of viscous and viscoelastic liquids. *J. Non-Newtonian Fluid Mech.* **21:** 13–38.
- Sullivan, T. M., Middleman, S. and Keunings, R. 1987. Use of a finite-element method to interpret rheological effects in blade coating. *AICHE J.* **33**(12): 2047–2056.
- Taylor, C. M. 1974a. Separation cavitation in lightly loaded fluid film bearings with both surfaces in motion. Part 1. Theoretical considerations. *J. Mech. Eng. Sci.* **16**(4): 147–150.

- Taylor, C. M. 1974b. Separation cavitation in lightly loaded fluid film bearings with both surfaces in motion. Part 2. Analysis of the cylinder plane and journal bearing configurations. *J. Mech. Eng. Sci.* **16**(4): 150–155.
- Taylor, C. M. 1974c. Film rupture for a lubricated cylinder lightly loaded against a plane. *J. Mech. Eng. Sci.* **16**(4): 225–231.
- Taylor, G. I. 1963. Cavitation of a viscous fluid in narrow passages. *J. Fluid Mech.* **16**: 595–619.
- Triantafillopoulos, N. G. and Aidun, C. K. 1990. Relationship between flow instability in short-dwell ponds and cross directional coat weight nonuniformities. *Tappi J.* **73**(6): 127–136.
- Weiss, H. L. 1977. *Coating and Laminating Machines*. Converting Technology Co., Milwaukee.
- Williamson, A. S. 1972. The tearing of an adhesive layer between flexible tapes pulled apart. *J. Fluid Mech.* **52**: 639–656.
- Yih, C. S. 1960. Instability of a rotating liquid film with a free surface. *Proc. Roy. Soc. A.* **258**: 63–89.
- Yih, C. S. 1963. Stability of liquid flow down an inclined plane. *Phys. Fluids.* **6**(3): 321–334.
- Zink, S. C. 1979. Coating processes. In *Encyclopedia of Chem. Tech.* 3rd edn. Vol. 6, John Wiley, pp. 386–426.

Philip H. Gaskell and Michael D. Savage

12b.1 INTRODUCTION

The reader may well be wondering ‘What is Meniscus Roll-Coating?’ This is not altogether surprising because, as far as we are aware, there are no references to this form of coating in the open literature and yet it has been around in various industries for several decades. Meniscus roll-coating is used to produce high quality, ultra-thin films at line speeds of the order of tens of meters per minute and is characterized by two key features:

- coating is in the low capillary number range where capillarity plays a dominant role in determining the pressure field;
- inlets are starved; the incoming film is much thinner than the roll separation.

One reason for the lack of references in the literature is perhaps a tacit assumption by practitioners and theoreticians alike that this coating process was essentially the same as the more familiar inlet-flooded, coating process. In fact this assumption falls quite wide of the mark; the two are, in reality if not appearance, quite different with their own characteristic pressure and velocity fields.

This chapter aims to review the results of a five year investigation into forward mode, meniscus roll-coating. A tripartite scientific approach has been used combining experimental methods, mathematical modeling and computational simulations (Gaskell *et al.* 1995b, 1996a). This combination has indeed proved a very powerful and

effective means for unraveling the mysteries of forward mode, meniscus roll-coating.

The two regimes of forward roll coating are introduced and contrasted in Section 12b.2. An experimental and theoretical investigation of the flow structure in meniscus roll coating is the subject of Section 12b.3 which concludes with the identification of three critical flow rates. These correspond to three key events which arise as the feed condition is varied. Section 12b.4 identifies the part of parameter space corresponding to the meniscus roll coating regime while Section 12b.5 discusses various instabilities to the coating bead.

12b.2 FORWARD ROLL COATING

In forward roll coating two regimes of practical interest can be identified according to their inlet feed condition; these are the classical (inlet-flooded) and the meniscus (inlet-starved) coating regimes. They are shown in Fig. 12b.1 for forward roll coating where the rolls are contra-rotating and therefore move in the same direction through the nip. The lower roll is partially submerged in a bath and fluid is transferred to the nip by the action of viscous lifting, prior to being deposited on a moving substrate. The meniscus coating bead is formed in one of two ways:

1. beginning with a small minimum gap and a flooded inlet, a starved inlet condition is produced by increasing the roll separation;

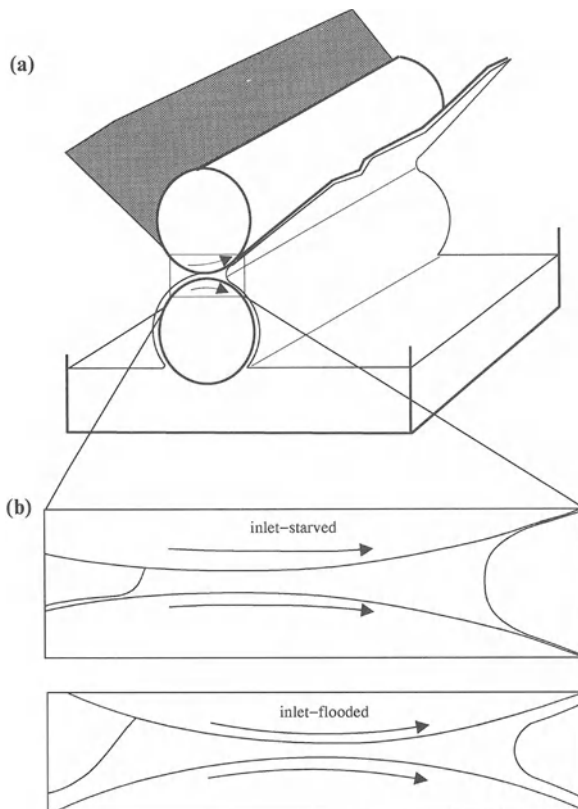


Figure 12b.1 (a) A two-roll coater operating in forward mode; (b) exploded view of the nip region showing a flooded and starved inlet.

2. beginning with a suitable gap and a flooded inlet the incoming flux is decreased by reducing the speed of the lower roll.

A key feature of inlet-flooded roll coating is the location of the upstream meniscus – far from the nip – where it has negligible influence on both the flow and the pressure field. In addition, fluid pressures in the nip region are much greater than those due to capillary action at the menisci. In the starved inlet regime the upstream meniscus is seen to be much closer to the nip where capillary action plays the crucial role in generating a sub-ambient pressure field. Characteristic flow patterns are shown in Fig. 12b.2a and 2b for speed ratios $S_p = 1$ and $S_p = 2$, where $S_p = U_1/U_2$

and U_1, U_2 are the speeds of the upper and lower rolls. A thin fluid stream can be seen snaking between and around a pair of eddies occupying most of the flow region – the relative size of the eddies being determined by the speed ratio. This flow pattern contrasts sharply with that typical of the inlet-flooded regime, where the flow is essentially unidirectional ahead of the downstream recirculation region, see Fig. 12b.3.

Two nondimensional parameters which help to distinguish these coating regimes are capillary number, Ca , and nondimensional flow rate, q , defined as follows:

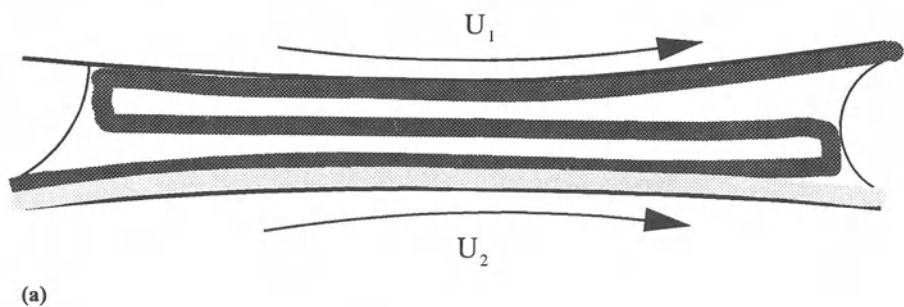
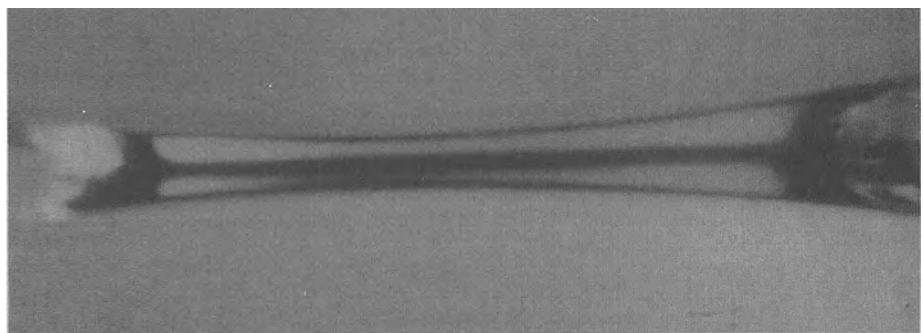
$$Ca = \frac{\mu U_m}{\sigma}, \quad q = \frac{Q}{2H_0 U_m} \quad (12b.1)$$

where μ and σ represent fluid viscosity and surface tension; Q is the actual flow rate per unit axial length, $2H_0$ the minimum gap separation and $U_m = (U_1 + U_2)/2$ is the average roll speed.

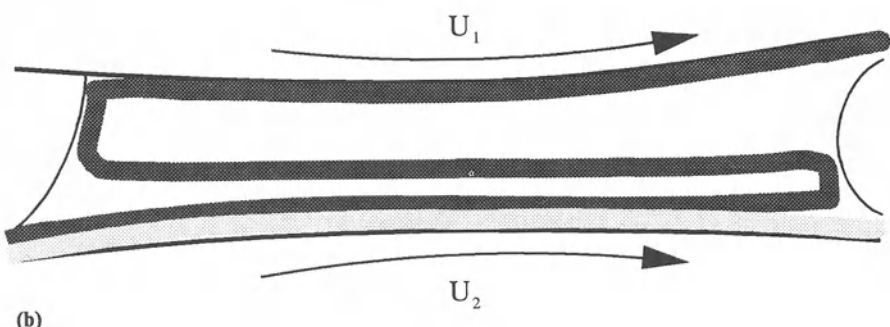
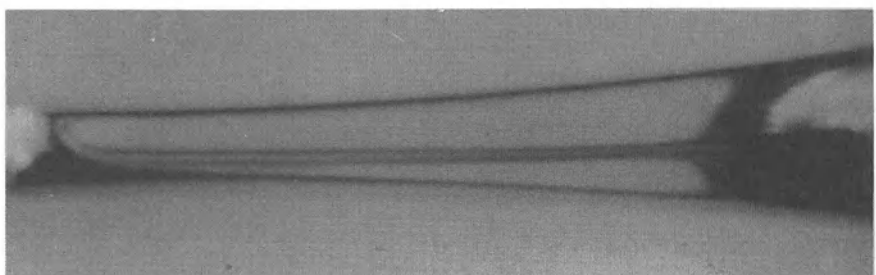
When inlets are fully flooded q has its maximum value, q_{\max} , which depends on speed ratio and capillary number. In particular, q_{\max} varies from 1.33 to 1.29 as capillary number is increased from 10^{-2} to ∞ for equal roll speeds (Coyle *et al.* 1986). Classical roll-coating with flooded inlets is a self-metered coating process in which the geometry and roll speed determine the flow rate, Q – which is accordingly nondimensionalized by means of the average roll speed, U_m , and the gap thickness, $2H_0$. In meniscus roll coating neither the gap nor the upper roll speed play any part in determining the flow rate Q as all the fluid approaching the inlet is transferred through the nip. Nevertheless it may still be regarded as a self-metered process as the coating thickness applied to the web is determined by the roll speeds. The flow rate Q is given by:

$$Q = U_2 H_i \quad (12b.2)$$

where H_i is the thickness of the inlet film attached to the lower roll. For meniscus roll coating therefore, it is useful to introduce a new dimen-



(a)



(b)

Figure 12b.2 Streamline flows in the bead of a meniscus roll coater with $R_m/H_0 = 125$ and rolls moving left to right: (a) $Ca = 10^{-2}$, $S_p = 1$; (b) $Ca = 1.5 \times 10^{-2}$, $S_p = 2$.

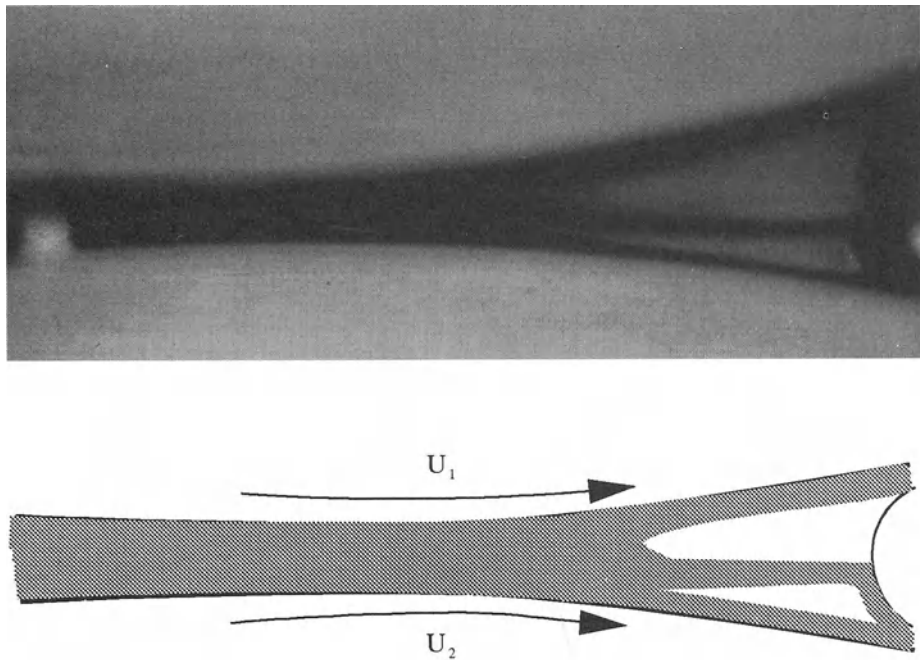


Figure 12b.3 A characteristic flow for inlet flooded roll coating with rolls moving left to right and $R_m/H_0 = 110$, $Ca = 0.2$, $S_p = 2$.

sionless flow rate, q^m , defined by:

$$q^m = \frac{Q}{U_2(2H_0)} = \frac{U_2 H_i}{U_2 2H_0} = \frac{H_i}{2H_0} \quad (12b.3)$$

where q^m provides a measure of the degree of inlet starvation. Typically $q^m \sim 10^{-1}$ and is related to q via the equation:

$$q = \left(\frac{2}{1 + S_p} \right) q^m \quad (12b.4)$$

Table 12b.1 presents a summary of the two coating regimes with their associated inlet conditions and flow rates.

12b.3 FLOW STRUCTURE

12b.3.1 EXPERIMENTAL INVESTIGATION

The first investigation of the fluid dynamics of meniscus roll coating (Malone 1992) was purely

experimental. Its aim was to identify the characteristic velocity and pressure fields and also to measure various quantities such as film thicknesses and free surface locations for comparison with theoretical predictions. The work involved a combination of state-of-the-art high speed video photography, image processing and computerized particle tracking software allied to both dye injection and particle seeding of the flow – two of the oldest methods for determining the motion of a fluid known to experimental fluid dynamicists. This marriage of old and new was not easily arranged and a number of major hurdles had to be overcome – not least the sheer practical difficulties of making observations and obtaining physical measurements of such a small scale flow confined within a restricted geometry comprised of two stationary free surfaces and two moving solid boundaries.

An important feature of the flow visualization

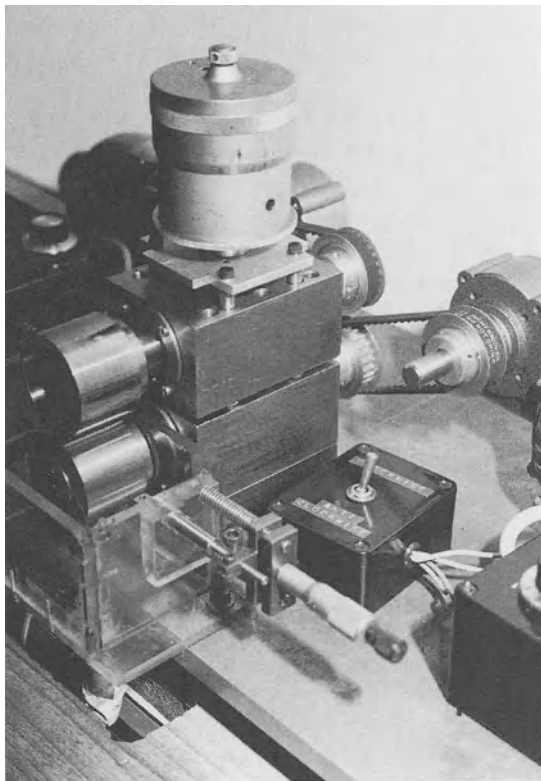
Table 12b.1 Coating regimes in a forward roll coater

<i>Coating regime</i>	<i>Feed/Inlet condition</i>	<i>Flow rate</i>
Classical	Inlet-flooded	Maximum flow rate, $q = q_{\max}$
Meniscus	Inlet-starved/Ultra-starved	Substantially reduced flow rate, $q^m = (1 + S_p)q/2 \ll 1$

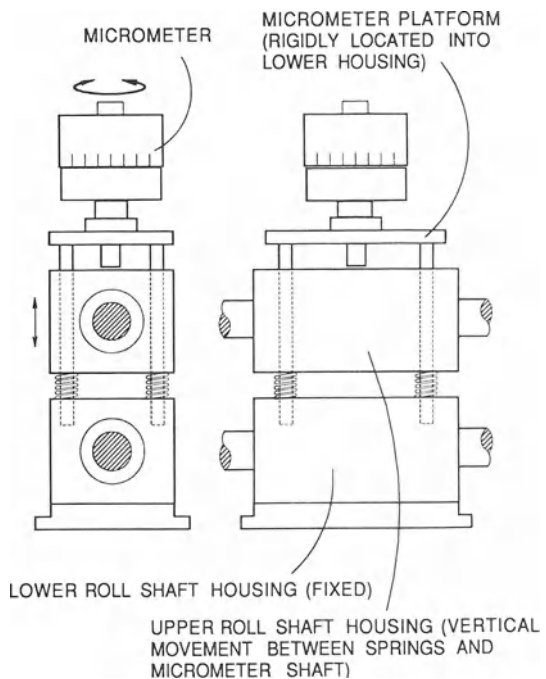
techniques employed is their ability to provide information about the complete flow field without physical intrusion. In addition to giving a qualitative picture of the associated fluid dynamics involved, quantitative information may be derived by analyzing recorded images of the flow. In order to view the fluid motion in the very small region between the two rolls it was necessary to

look along the axis at an illuminated cross-section of the flow.

The generation of meaningful, rigorous experimental results required the design and development of specialized equipment and procedures. Figure 12b.4a shows the cantilevered roll system adopted for the study. Its major advantage is ease of accessibility to the nip region while retaining the



(a)



(b)

Figure 12b.4 (a) Photograph of the experimental setup showing a cantilevered roll system; (b) schematic of roll shaft housing showing micrometer assembly.

essential features of an industrial process in the meniscus coating regime.

For the purposes of flow visualization several lower/upper roll configurations could be achieved: steel/steel; steel/acrylic; acrylic/hollow acrylic. The steel rolls were manufactured from stainless steel, ground and polished to achieve a high quality surface finish. The use of acrylic rolls allowed the nip region to be illuminated more effectively. Their surfaces were polished (including the inner surface in the case of the hollow roll) to obtain a glass-like finish.

Steel support shafts of 25 mm diameter were ground on the roll location diameter and the rolls bored to obtain a precision H6 fit (BS 4500) in order to eliminate effectively roll runout. Similarly, all roll diameters were finished on their respective support shafts to ensure concentricity – the maximum indicated roll run-out was found to be less than 5 µm. The rolls can be detached from the steel support shafts allowing ease of roll interchange – each shaft is supported in a housing by two high precision roller bearings, separated by a suitable distance (100 mm) so as to minimize bending and vibration of the shafts.

The rolls are of sufficient diameter (50 mm) to give the radius of curvature required to produce a reasonably high aspect ratio of bead width to minimum gap thickness over a wide range of operating conditions and enable clear images of the flow within the nip to be obtained. Three factors were considered in choosing the length of the rolls:

1. the optimum viewing depth for flow visualization;
2. accurate representation of the industrial process;
3. moderate roll weight to minimize deflection and vibration at high speeds.

The chosen length of 35 mm gave a more than adequate bead length to gap ratio (e.g. 100, for a typical gap setting of 350 µm) as well as a very compact design.

The rolls are driven and controlled independently for maximum versatility. Each motor has a control unit for continuous speed variation and is connected to the roll shaft via a 27:1 worm

reduction gearbox, pulley and toothed rubber belt. The latter requires very little tension during operation and therefore loading on each roll shaft is negligible. Vibration from the drive system was also minimal.

The lower roll bearing/shaft housing is bolted to an aluminum base plate while four steel columns are press-fitted into the lower housing onto which the upper housing is located with a precision slide fit (see Fig. 12b.4b). The control of the proximity of the upper and lower housings is achieved by a micrometer assembly – the precision slide fit on the columns ensures that the movement of the upper housing remains parallel. The bearing end-caps are used to adjust independently the axial position of the shafts to facilitate alignment. In addition they are used to retain and pre-load the bearings via the shaft collars which reduces any internal clearance and takes up any play in the shaft, either axially or radially. Also, as the end caps are secured using four diagonally positioned screws it is possible to make precise independent adjustments to ensure that the roll ends are aligned.

Although the separation of the rolls can be adjusted accurately (to within 1 µm) using the micrometer arrangement outlined above, the actual gap setting relies on accurate calibration of this device. This was done using specialist plastic wrapping film which is available in thicknesses as low as 6 µm. The film was pulled between the rolls as the gap size was decreased until resistance was encountered, in much the same way as is experienced with a feeler gauge. However, unlike the latter, film has the advantage that there is less of a problem in ensuring horizontal alignment. Error in setting the gap size was estimated to be in the region of 10 µm (e.g. 3.5%, for a typical gap setting of 350 µm).

The viscosity of fluids used in industrial applications of meniscus roll coating is relatively low, i.e. in the region of 10^{-3} Pa s when compared with fluids used in classical roll coating where viscosity ranges from 5×10^{-2} to 500 Pa s. This posed a problem in the sense that a compromise has to be reached between choosing a fluid with a viscosity representative of the industrial process

and one which will enable the use of a minimum roll separation large enough for good quality images of the flow within the bead.

Silicone oils meet the above requirements; viscosity ranges from 0.65×10^{-3} to 5.0×10^{-3} Pa s upwards. These oils are Newtonian at shear rates less than 10^4 s $^{-1}$ and optically clear. A less expensive, alternative used for this study, was Shell Tellus R5 oil (a light organic oil). The fluid properties of these oils are given in Table 12b.2.

The action of the web in removing fluid from the nip is mimicked by the use of a scraper blade mechanism. The scraper material has to be rigid enough not to deform under its own weight but flexible enough to be clamped up against the roll for the efficient removal of fluid. Both plastic (polyester) and metal (brass shim, thickness 0.3 mm) scrapers were assessed and although they both performed well the latter was found to remove fluid more effectively. With a metal scraper it is easier to achieve a uniform knife-edge finish along its length whereas plastic tends to score or become fibrous. The efficiency of scraping was determined using filter paper to absorb any excess fluid left on the roll. The paper was weighed after being in contact with the roll for measured periods of time and fluid removal for the metal scraper was found to be between 95 and 98% efficient.

The use of an oil soluble, powder dye namely grasol blue (solvent blue 27) dispensed with the need to match the properties of the liquid dye to those of the working fluid. The dissolved dye was injected via a hypodermic needle into the incoming fluid film, far upstream of the nip so as not to influence the flow in the cross-sectional

region of interest. A useful variant to continuous dye injection was to 'pulse' the injection sequence. For particle tracking, a number of different materials were examined but only one, Sephasord, a material used for gel filtration was found to meet the necessary criteria of sphericity, opacity, neutral buoyancy, mono-dispersiveness and size (5 µm), and produce consistent results when suitably illuminated.

In order to achieve high quality flow visualization the light sensitivity of the system is of prime importance because of the difficulties encountered in illuminating a two-dimensional plane in the constricted area of a two-roll coater. The dye injection studies were performed using a combination of acrylic rolls together with powerful white light sources (two 250 W studio lamps), one positioned each side of the nip. However for the particle tracking work the white light sources had to be replaced by low power (10 mW) lasers. Also, to obtain consecutive images in which the movement of particles from one frame to the next is sufficiently small so as to be less than half the mean distance between particles distributed in the flow field required a high recording frame rate, typically 250 to 1000 full frames per second. A Kodak Ektapro 1000 high speed video system and imaged intensified camera proved more than adequate in this respect.

Obtaining qualitative discrete measurements of velocities within complex flows presents a challenging and difficult problem to the experimentalist. The imaging technique employed was developed in close collaboration with R. J. Perkins (1991), specifically for use with high speed video equipment. The software behaves in effect as two separate programs – the first analyzes a digitized

Table 12b.2 Fluid properties at 20°C

Liquid	Viscosity (Pa s)	Surface tension (N m $^{-1}$)	Density (kg m $^{-3}$)
R5 oil	8.4×10^{-3}	30.4×10^{-3}	839
Silicone oil 200/0.65	0.72×10^{-3}	16.1×10^{-3}	761
Silicone oil 200/1	1.12×10^{-3}	17.5×10^{-3}	818
Silicone oil 200/5	5.45×10^{-3}	19.7×10^{-3}	920

image and identifies and locates all the particles, the second uses this information to match particles frame-by-frame.

Figures 12b.5a–5d illustrate the path taken by the injected dye as it progresses through the flow field (the rolls are moving left to right with equal speed). The dye enters on the lower roll (Fig. 5a) and moves with the roll surface until it splits in the bottom right-hand corner of the bead (Fig. 5b); some of the dye continues along the lower roll to form the outlet film thickness, the remainder makes a ‘U-turn’ to travel in the reverse direction through the flow field (Fig. 5c). Once the dye reaches the upstream free surface (by now it has traveled two bead lengths) it experiences a second ‘U-turn’ and then moves with the upper roll, eventually leaving the bead in the fluid layer attached to the upper roll.

A typical associated velocity field, generated by particle tracking, is illustrated in Fig. 12b.6. It shows quite clearly the presence of the reverse jet along the centre of the bead. The velocity of this jet can be measured and in the case of symmetric rolling is found to be approximately half that of the roll speeds. This is in good agreement with the theoretical and computational results of a meniscus roll coating model outlined in the next section.

12b.3.2 MATHEMATICAL MODELS – ANALYTICAL AND NUMERICAL SOLUTIONS

Three mathematical models have been developed for analyzing and understanding meniscus (inlet-starved) roll coating; two are solved analytically and one numerically. In the first, the ‘zero-flux’ model, an idealized situation is considered in which flux into and out of the flow domain, or bead, is neglected, i.e. $q = 0$. The cross-section of the bead is assumed to be rectangular with the curvature of the rolls neglected and the menisci modeled as planes on which shear stress is zero. The governing equations are Stokes’ equations for an incompressible fluid:

$$\begin{aligned} 0 &= \nabla P - \mu \nabla^2 \mathbf{U} \\ 0 &= \nabla \cdot \mathbf{U} \end{aligned} \quad (12b.5)$$

where P is the pressure and the velocity field $\mathbf{U} = (U, W)$ is assumed to be in the two-dimensional (X, Z) plane. The penalty for neglecting the curvature of the menisci is that the normal stress condition on each meniscus has to be relaxed. Mathematically, the model reduces to the solution of the biharmonic equation for the streamfunction Ψ :

$$\nabla^4 \Psi = 0 \quad (12b.6)$$

subject to appropriate boundary conditions, as shown in Fig. 12b.7 where the bead, of length $2A$ and depth $2H$, is assumed to be rectangular ($-A \leq X \leq A$, $-H \leq Z \leq H$). This boundary value problem is similar to the lid-driven cavity flows studied by Joseph (1977) and Canedo and Denson (1989). A solution for the streamfunction is derived analytically in the form of a truncated series of eigenfunctions, and also computationally using a streamfunction-vorticity, finite-element technique (Gaskell *et al.* 1991).

Results show (Thompson 1992) that the streamline patterns obtained, analytically and computationally, are in agreement with each other and in qualitative agreement with the experimentally observed streamline flow (Fig. 12b.5) for various speed ratios. An important result from this zero flux model concerns the horizontal pressure gradient dP/dX which has negligible variation with respect to the cross film coordinate, Z – indicating that fluid pressure depends only upon the X coordinate i.e. $P = P(X)$. Also, in the central core of the bead, sufficiently far away from either meniscus, the pressure gradient, dP/dX , is effectively constant:

$$\frac{dP}{dX} = \text{constant} \quad (12b.7)$$

– a result which suggests a linear profile for pressure, quite different from the distribution in the inlet-flooded regime with its characteristic maximum and minimum, see Coyle (1996).

A more refined mathematical model is the ‘small flux’ model which takes into account the small non-zero flux q transported through the bead. It makes use of results from the ‘zero flux’

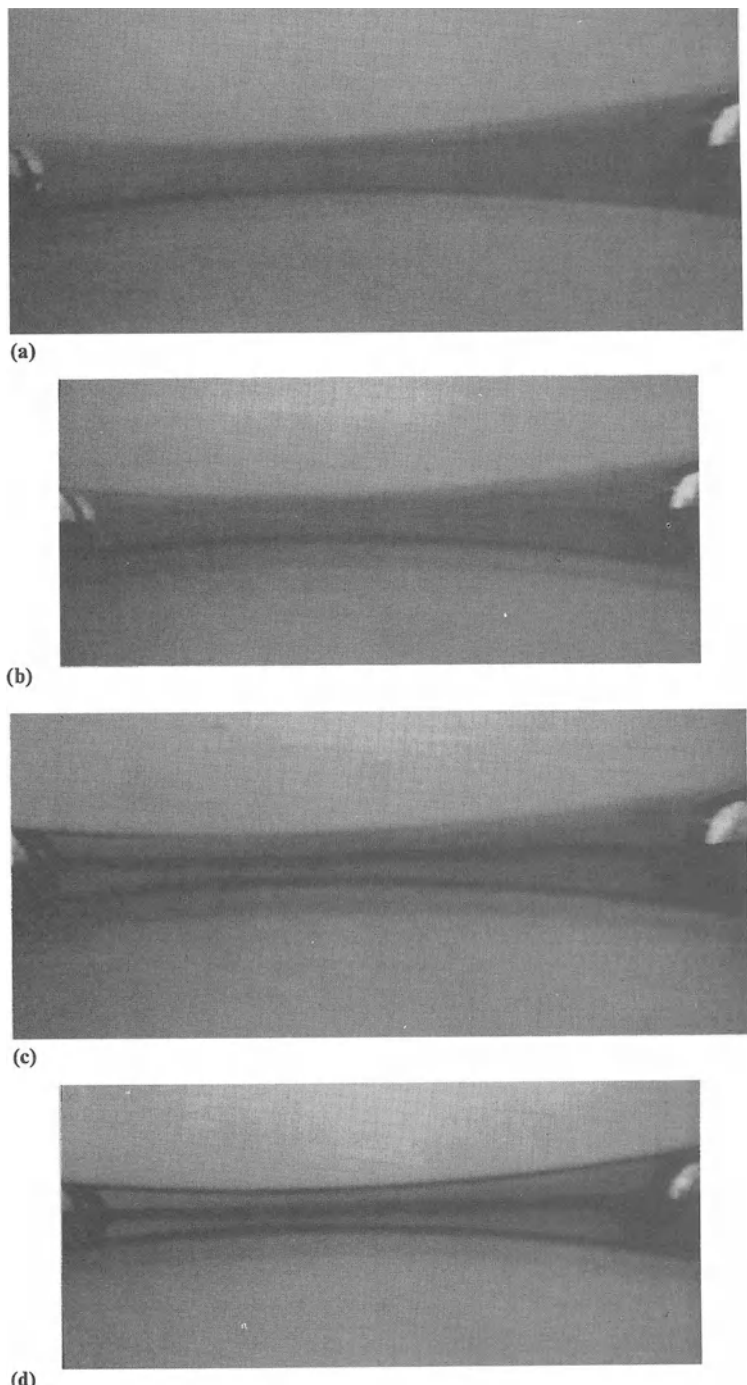


Figure 12b.5(a)–(d) Dye entering into the bead of a meniscus roll coater identifies the ‘snake’ – the path followed by the inlet fluid which is transferred to the upper roll (rolls moving left to right with $R_m/H_0 = 125$, $Ca = 10^{-2}$, $S_p = 1$).

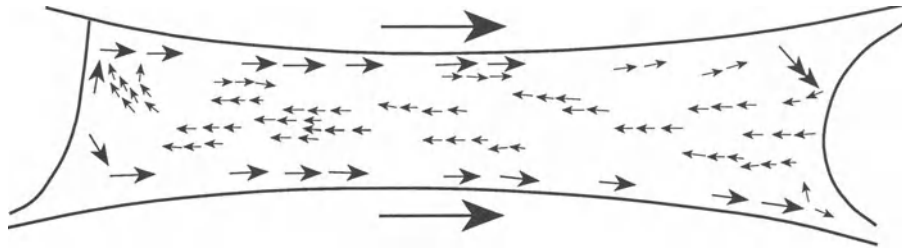


Figure 12b.6 The velocity field in the bead of a meniscus roll coater generated by computerized particle tracking methods (rolls moving left to right with $R_m/H_0 = 125$, $Ca = 10^{-2}$, $S_p = 1$).

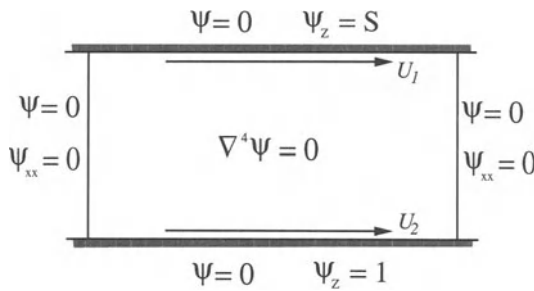


Figure 12b.7 Boundary conditions for Stokes flow in an idealized rectangular bead with zero flux, bounded by two free surfaces and two moving plates.

model that the fluid flow in the central core is essentially one-dimensional with fluid pressure constant across the bead. It is precisely these results which indicate that lubrication theory will model the flow in the central core with the velocity distribution $U(X, Z)$ expressed as a combination of Poiseuille and Couette flow:

$$U(X, Z) = \frac{1}{2\mu} \frac{dP}{dX} (Z^2 - H^2) + \frac{(U_1 - U_2)}{2} \frac{Z}{H(X)} + \frac{(U_2 + U_1)}{2} \quad (12b.8)$$

$H(X)$, the semi-gap width at station X , is given by:

$$H(X) = H_0 + \frac{X^2}{2R_m} \quad (12b.9)$$

where R_m is an average roll radius defined by:

$$\frac{2}{R_m} = \frac{1}{R_1} + \frac{1}{R_2} \quad (12b.10)$$

and R_1, R_2 represent the radii of the upper and lower rolls, respectively. The velocity distribution is quadratic in Z and $U(X, Z) = 0$ has two roots in $-H(X) \leq Z \leq H(X)$ for all speed ratios. Hence there are two positions across the gap at which the flow is stationary. It can therefore describe the unidirectional flow in the central core of the bead consisting of a fluid transfer jet snaking around a pair of eddies. This jet is the mechanism for transferring fluid to the upper roll in order to coat the web and, as such, is similar to the transfer jet operating in the upstream recirculation region of an inlet flooded roll coater, Pearson (1985).

At this point it is convenient to introduce the following nondimensional variables:

$$x = \frac{X}{\sqrt{2R_m H_0}}; \quad z = \frac{Z}{H_0}; \quad p = \frac{P}{\mu U_m} \frac{H_0^2}{\sqrt{2R_m H_0}}; \\ h_1 = \frac{H_1}{H_0}; \quad h_2 = \frac{H_2}{H_0}; \quad h_i = \frac{H_i}{H_0}$$

Figure 12b.8 shows a schematic for flow in a bead extending from $x = -b$ to $x = d$. Fluid approaches the bead in a uniform layer of thickness h_i and exits by way of two uniform layers h_1 and h_2 attached to the web and lower roll, respectively. Continuity of flux requires that $U_2 H_i = U_1 H_2 + U_1 H_1$, which in nondimensional

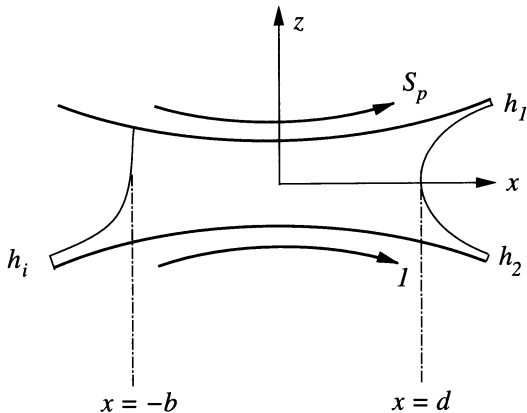


Figure 12b.8 Schematic of the bead with small flux q and bounded by two menisci and two moving rolls.

form becomes:

$$h_i = h_2 + S_p h_1 \quad (12b.11)$$

As flow rate is constant, equation (12b.8) yields Reynolds' equation:

$$\frac{dp}{dx} = \frac{3}{(1+x^2)^2} \left[1 - \frac{q}{(1+x^2)} \right] \quad (12b.12)$$

which is solved for pressure by introducing the change of variable $x = \tan\alpha$:

$$p(\alpha) = 3 \int (\cos^2\alpha - q \cos^4\alpha) d\alpha \quad (12b.13)$$

If R_b and R_d are the radii of curvature of the upstream and downstream menisci then the corresponding fluid pressures are $-\sigma/R_b$ and $-\sigma/R_d$, respectively, where σ is surface tension.

It is clear from Fig. 12b.8 that suitable approximations for R_d and R_b are the semi-gap width and the full gap width, respectively:

$$R_d = H_0(1+d^2); \quad R_b = 2H_0(1+b^2) \quad (12b.14)$$

By writing $b = \tan\alpha_b$, $d = \tan\alpha_d$ and imposing (12b.14), equation (12b.13) yields:

$$\begin{aligned} & \frac{\sqrt{2}}{3} \left(\frac{Ca}{\sqrt{H_0/R_m}} \right)^{-1} (\cos^2\alpha_b - 2\cos^2\alpha_d) \\ &= (\sin 2\alpha_b + 2\alpha_b + \sin 2\alpha_d + 2\alpha_d) \\ & \quad - q \left(\frac{\sin 4\alpha_b}{8} + \frac{3\alpha_b}{2} + \sin 2\alpha_b \right) \\ & \quad - q \left(\frac{\sin 4\alpha_d}{8} + \frac{3\alpha_d}{2} + \sin 2\alpha_d \right) \end{aligned} \quad (12b.15)$$

There are a number of observations to be made.

1. Equation (12b.15) identifies $(Ca\sqrt{R_m/H_0})$ as the important nondimensional parameter in meniscus roll coating. In order to obtain solutions of (12b.15) this parameter must be of order 1, in order to ensure that the left-hand side balances the dominant term on the right-hand side, which is of order 1. Therefore:

$$Ca \approx \sqrt{\frac{H_0}{R_m}} \quad (12b.16)$$

2. Once $\sqrt{H_0/R_m}$, Ca and q are specified, equation (12b.15) gives a relation between the angles α_b , α_d which locate the positions of the free surfaces. If α_d is known then α_b can be determined. In fact α_d can be obtained via results from Landau and Levich (1942) which enable the thickness of the uniform film on each roll to be related to the radius of curvature of the downstream meniscus:

$$h_1 = 1.34 \frac{R_d}{H_0} \left(\frac{\mu U_1}{\sigma} \right)^{2/3} \quad (12b.17)$$

$$h_2 = 1.34 \frac{R_d}{H_0} \left(\frac{\mu U_2}{\sigma} \right)^{2/3} \quad (12b.18)$$

Taking for example $U_1 = U_2 = U$, $Ca = \mu U / \sigma$ and $q = q^m$, equations (12b.14) and (12b.18) give:

$$1 + d^2 = \sec^2 \alpha_d = \frac{q^m}{1.34(Ca)^{2/3}} \quad (12b.19)$$

Clearly, α_d is known once q^m and Ca are specified.

The case $U_1 \neq U_2$ is a natural extension of the above.

3. Figure 12b.9 shows a typical pressure distribution for $H_0/R_m = 10^{-2}$, $Ca = 1.3 \times 10^{-3}$, $U_1 = U_2$, $b = \tan \alpha_b = 1.55$ and $d = \tan \alpha_d = 3.5$. The pressure field is entirely subambient as a result of capillary action at the menisci. The sharp reduction in pressure over the upstream meniscus is followed by a linear rise through the central core (i.e. a constant pressure

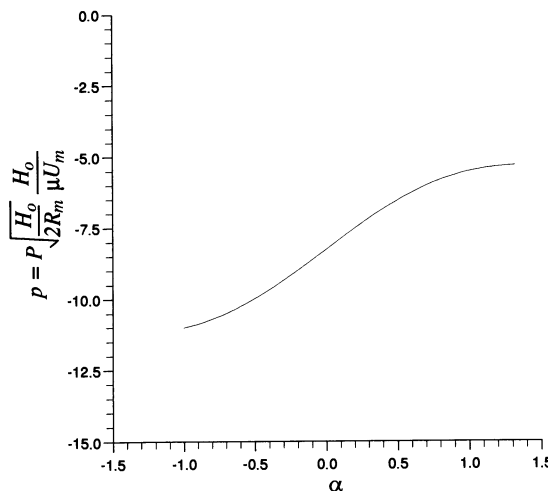


Figure 12b.9 A nondimensional pressure profile for $R_m/H_0 = 100$, $S_p = 1$, $Ca = 1.3 \times 10^{-3}$, $q = 0.075$, $b = 1.55$ and $d = 3.5$ as predicted via the small flux model.

gradient as suggested by the zero flux model) and then a more gradual rise to the downstream meniscus.

This subambient pressure field was verified by Malone (1992) who took pressure measurements in a plate-roll configuration. The plate-roll set-up may be regarded as a two-roll system in which the upper roll is stationary and of infinite radius.

4. Of particular interest to the coating specialist are the film thicknesses h_1 and h_2 attached to the upper and lower rolls. Equations (12b.17) and (12b.18) suggests a two-thirds power law for film thickness ratio:

$$\frac{h_1}{h_2} = S_p^{2/3} \quad (12b.20)$$

This is the relation derived by Ruschak (1985) for flooded inlets. Similarly Coyle *et al.* (1986) obtained a 0.65 power law relationship over a range of speed ratio, $0 < S_p < 10$ using a finite-element analysis, which was found to be in accord with the findings of Benkreira *et al.* (1981). However, for meniscus roll coating, i.e.

starved inlets and small flow rates, the validity of expression (12b.20) needs to be established experimentally and also computationally using a more refined mathematical model.

Such a refined model incorporating the effects of curved menisci, wetting lines and nonlinear boundary conditions is shown in Fig. 12b.10. Numerical solutions were found to this nonlinear boundary value problem using a Galerkin, weighted residual, finite-element, formulation of the governing equations together with a spinal representation for the free-surface, as defined by Kistler and Scriven (1983). The region of interest was tessellated into 1615 triangular V6/P3 elements (see Fig. 12b.11) which are taken to satisfy the LBB stability condition (Babuska and Aziz 1972), discussed more fully in Chapter 11. With the pressure interpolation one order lower than that for velocity, the rate of convergence is ‘optimal’ and no ‘locking’ (Hughes 1987) occurs. The reader is referred elsewhere (Gaskell *et al.* 1995a), for a fuller description of the computational details.

Finite-element solutions were obtained for a two roll coater with $H_0/R_m = 10^{-2}$, flow rates in the range $0.075 < q^m < 0.333$ and an apparent contact angle of 90° at the dynamic wetting line. There are two points to be noted regarding the apparent contact angle employed. The value of 90° was suggested from experiment whilst computationally finite-element solutions were ob-

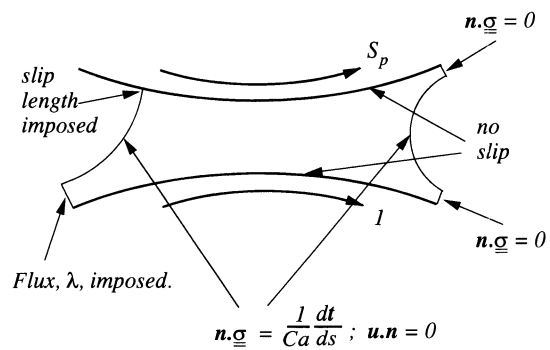


Figure 12b.10 Nonlinear boundary conditions for Stokes flow in a bead incorporating the effects of a dynamic wetting line and curved menisci.

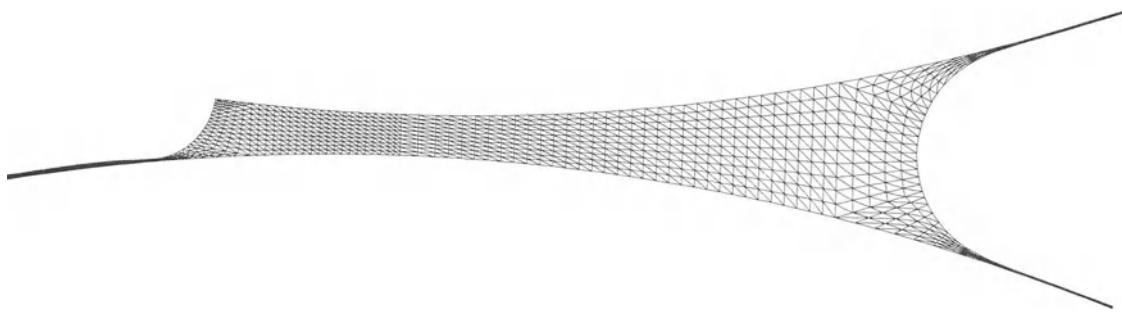


Figure 12b.11 Tessellation of the flow domain shown in Fig. 12b.10 containing 1615 six node triangular elements.

tainable for a contact angle in the range 80° to 100° with negligible change to the overall solution. Figure 12b.12a–12c show streamline plots for $q^m = 0.075$ and speed ratios $S_p = 1/2, 1$ and 2 with corresponding capillary numbers $Ca = 1.69 \times 10^{-3}, 1.8 \times 10^{-3}$ and 1.05×10^{-3} , respectively. (In Section 12b.4 it will become clear that, for a given flow rate of q^m and geometry ratio H_0/R_m , speed ratio and capillary number are not independent parameters).

Figure 12b.12a–c reveal a ‘double eddy’ structure with eddy thickness dependent on S_p – in qualitative agreement with experiment and the predictions of the zero flux model. The flux of fluid in the transfer jet, subsequently referred to as the ‘snake’, is seen to increase with S_p . Corresponding subambient pressure fields are displayed in Fig. 12b.13 which are in accord with the predictions from the small flux lubrication model.

Flow rate, q^m , is seen to have no effect on film thickness ratio as illustrated in Fig. 12b.14 for various speed ratios from $S_p = 1/5$ to $5/2$. Figure 12b.15 shows the variation of h_1/h_2 with S_p for a constant flow rate including a comparison with $h_1/h_2 = S_p^{2/3}$ obtained from the analysis of Landau and Levich, equation (12b.18). Agreement is remarkably close over the whole speed ratio range.

12b.3.3 CRITICAL FLOW RATES

In this section the aim is to vary the feed condition and examine its effect on the flow

structure. Three critical flow rates will be identified corresponding to three key developments in the flow.

12b.3.3.1 Pressure field transformation ($q = 1$)

First it is shown that $q < 1$ is a necessary condition for obtaining pressure profiles, typical of meniscus roll coating, Fig. 12b.13, for which capillarity at the upstream meniscus plays a dominant role.

If the feed condition is such that the inlet is flooded or moderately starved then the pressure profile will exhibit stationary points where pressure has either a local maximum or minimum value. At a stationary point $dp/dx = 0$ and therefore this condition together with Reynolds equation, equation (12b.12), predicts stationary points where:

$$x^2 = q - 1 \quad (12b.21)$$

and the nondimensional flux, q , is given by equation (12b.1).

Provided $q > 1$ stationary points will be symmetrically located about the nip. When $q < 1$, equation (12b.21) has no real solutions and therefore no stationary points occur. Hence $q = 1$ is the critical flow rate at which there is a smooth transformation in the shape of the pressure profile to one which exhibits no stationary points, is everywhere subambient and is dominated by capillary action at the menisci. Furthermore equation (12b.21) implies that the critical flow

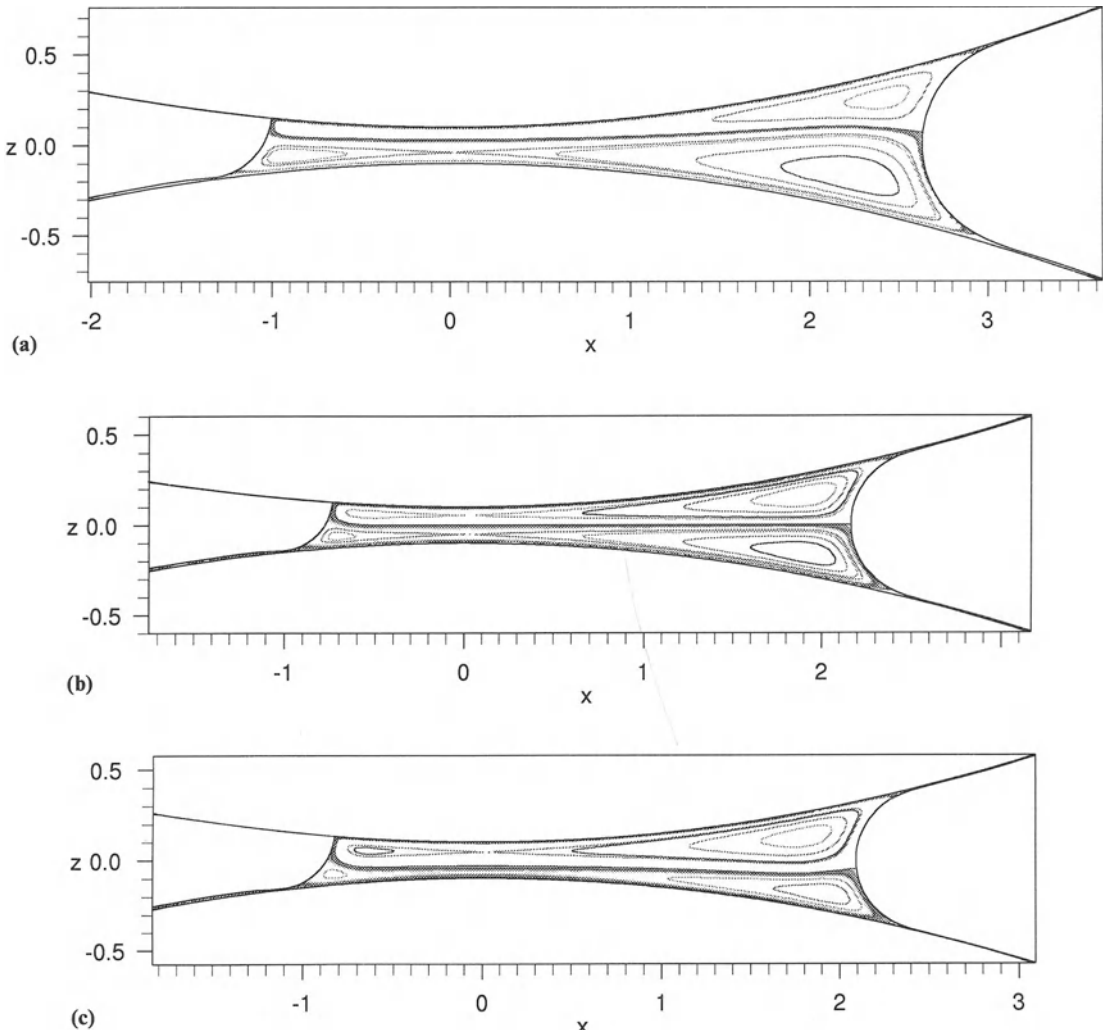


Figure 12b.12(a)–(c) Flow structures in the bead for $R_m/H_0 = 100$ and $q^m = 0.075$; (a) $S_p = 1/2$, $Ca = 1.69 \times 10^{-3}$; (b) $S_p = 1$, $Ca = 1.80 \times 10^{-3}$; (c) $S_p = 2$, $Ca = 1.05 \times 10^{-3}$.

rate, $q = 1$, is independent of capillary number, speed ratio and geometry ratio, H_0/R_m .

The above results, derived from lubrication theory, have been confirmed computationally and also by experiment with a plate-roll geometry (Malone 1992). Figure 12b.16 shows the evolution of the pressure profile (with pressures measured along the centre line) for $q = 0.8, 0.9, 1.0, 1.1, 1.2$ and 1.3 , obtained using the finite-element method

and a two roll coater with $H_0/R_m = 10^{-2}$ and $S_p = 1$.

12b.3.3.2 Effect of feed condition on velocity field

So one may conclude that $q < 1$ is a necessary condition for meniscus roll coating. It is not sufficient however because, in practice, inlets are

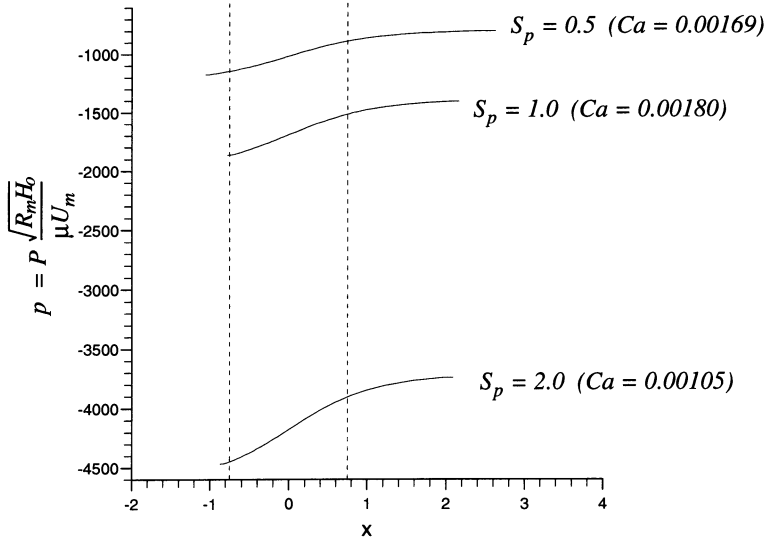


Figure 12b.13 Pressure distributions, taken along the centre line, $z = 0$, for $R_m/H_0 = 100$, $q^m = 0.075$ and corresponding to each of the flows in Fig. 12b.12a–c.

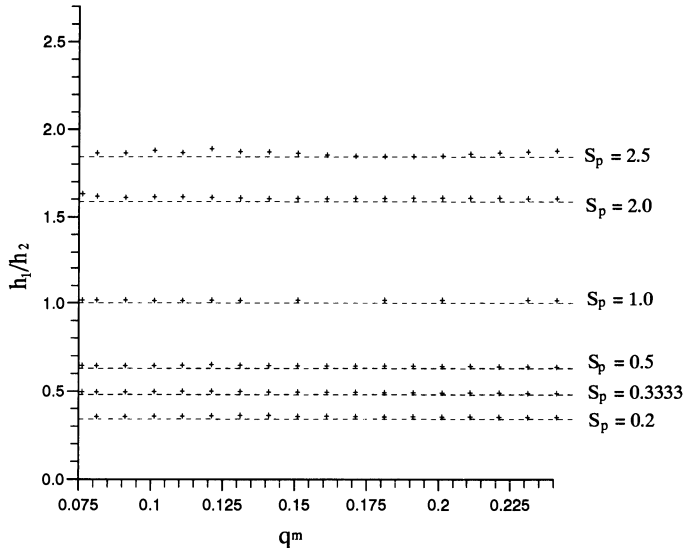


Figure 12b.14 The effect of flow rate, q^m , on film thickness ratio, h_1/h_2 , for $R_m/H_0 = 100$ and various speed ratios: + finite element solutions; ----- Landau Levich, equation (12b.18).

starved with $q \ll 1$. In order to specify that part of parameter space corresponding to the meniscus coating regime, computational solutions for the

velocity field are needed as the flow rate is varied. In fact such results reveal flow transitions between the different velocity fields and the critical

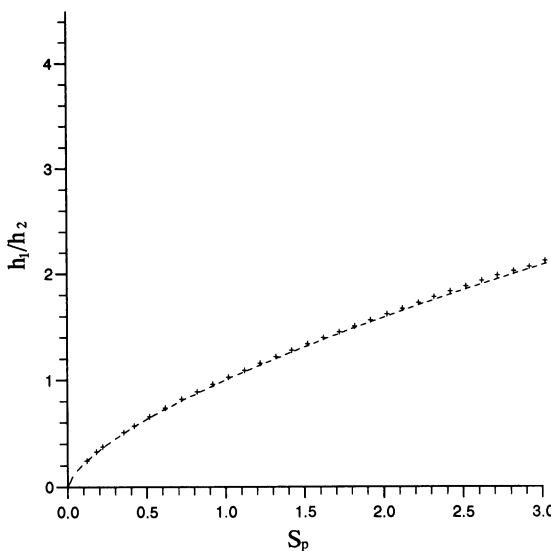


Figure 12b.15 The variation of h_1/h_2 with speed ratio for $R_m/H_0 = 100$ and constant flow rate, $q^m = 0.075$; + finite element solutions; ----- Landau-Levich, equation (12b.18).

parameters associated with them including two additional critical flow rates.

Figures 12b.12a–12c illustrate meniscus coating with an ultra-starved inlet, $q = 0.075$, and a characteristic snake carrying fluid to the upper roll. Each solution exhibits two large eddies, both of which consist of a bounding streamline pinned to a free surface, an outer circulation, a separatrix and saddle point, and two sub-eddies as clearly illustrated in Fig. 12b.17 for the case $S_p = 1/2$.

As q is increased gradually the additional flux will cause a pinching of the lower eddy such that streamlines in its outer circulation including the bounding streamline are successively drawn into the saddle point. Figure 12b.18a shows a flow pattern at a critical flow rate, $q = 1/9$, $S_p = 1$, at which the bounding streamline is also a separatrix passing through three stagnation points P_1 , P_2 and P_3 . Also shown is a streamline (part of the snake) located immediately below the separatrix which will be the next streamline to be drawn into the saddle point as q is increased further.

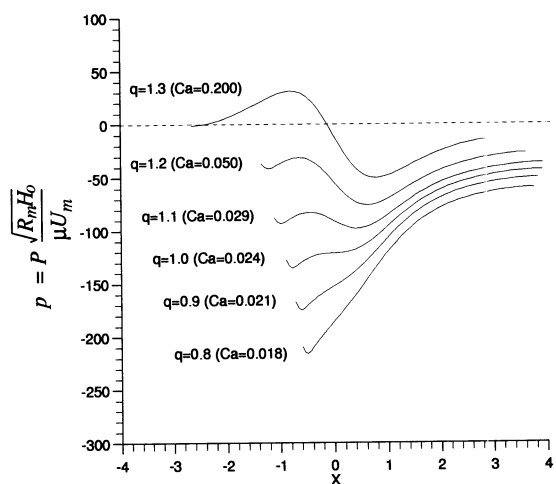


Figure 12b.16 Pressure profiles for $R_m/H_0 = 100$, $S_p = 1$ and $q = 0.8, 0.9, 1.0, 1.1, 1.2$ and 1.3 illustrating the transformation in shape at $q = 1$.

Figure 12b.18b shows this streamline as the separatrix and the former separatrix/bounding streamline is now detached from the saddle point P_3 giving rise to a ‘mini-snake’ or ‘back-jet’ in the lower left of the picture. Fluid entering the bead is now able to reach the upper roll via either the large snake or the mini-snake and in the latter case it circumnavigates the now isolated, lower left, eddy and flows between its bounding streamline and the separatrix.

The above situation marks the emergence of a back-jet, the intensity of which increases with flow rate. In fact, as q increases, the flux in the back-jet increases while that in the snake diminishes, and the lower left eddy is observed to contract and eventually disappear, Fig. 12b.19a and 19b. Flow in the snake will decrease to zero at a critical flow rate when the dividing streamline separating inlet fluid which reaches the upper roll from that which remains attached to the lower roll – rises and is attracted to the saddle point, Fig. 12b.20a and 20b. This causes flow in the snake to switch off and so fluid transfer to the upper roll is entirely by means of the fully developed back-jet. Mathematically it is possible

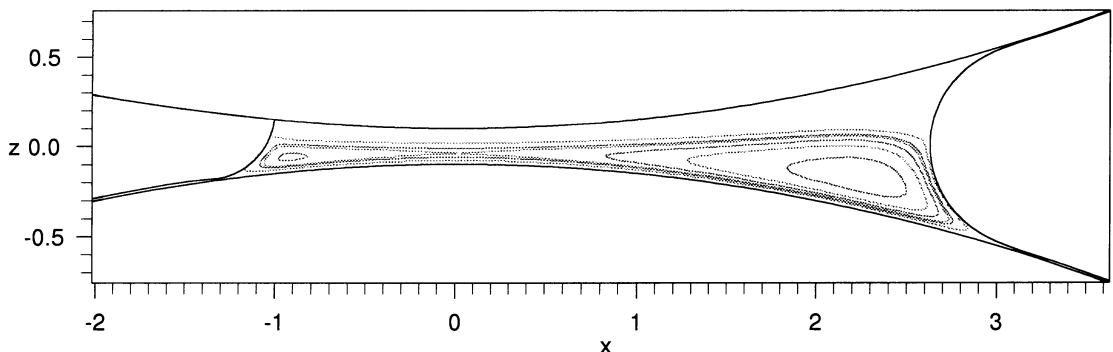
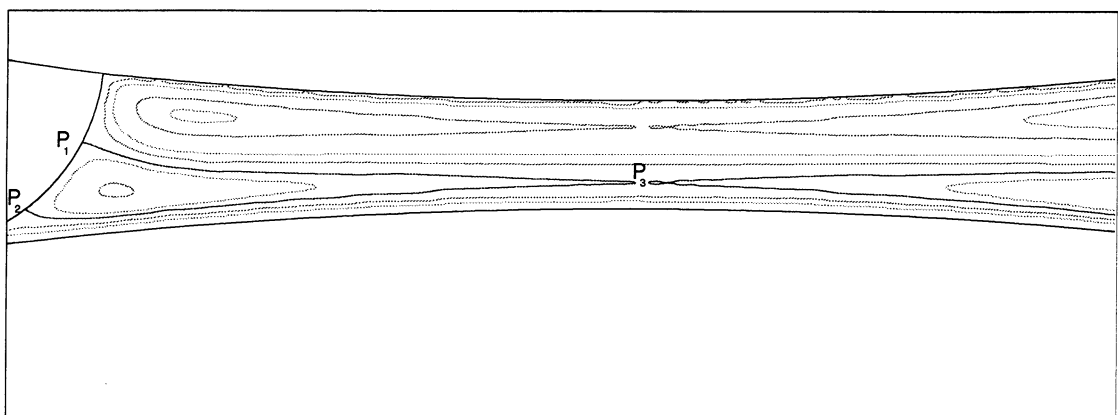
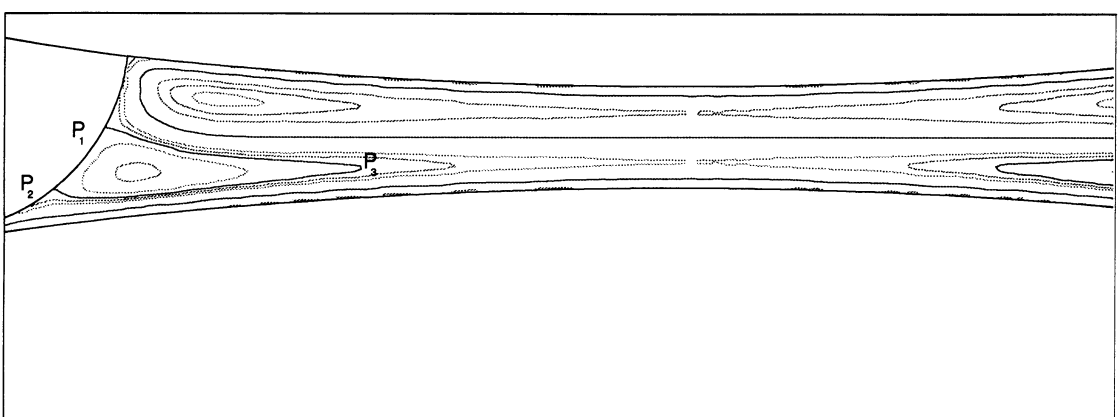


Figure 12b.17 An illustration of the important streamlines and features which make up the ‘lower eddy’ for $R_m/H_0 = 100$, $Ca = 2.25 \times 10^{-3}$, $q^m = 0.025$ and $S_p = 0.5$.



(a)



(b)

Figure 12b.18 The onset of the back-jet for $R_m/H_0 = 100$, $Ca = 2 \times 10^{-3}$ and $S_p = 1.0$: (a) critical flow rate $\bar{q} = 1/9$; (b) $q = 0.13$ the back-jet is established.

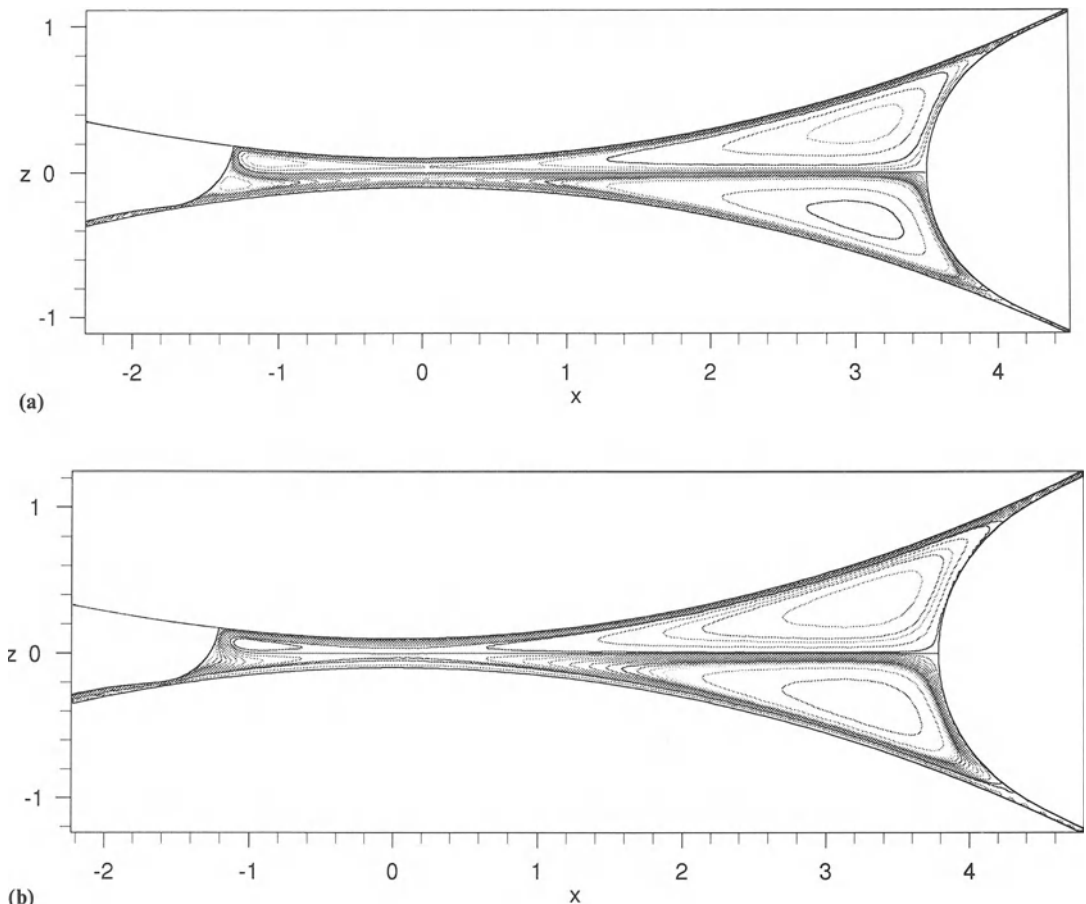


Figure 12b.19 The effect of increasing the flux for $R_m/H_0 = 100$, $S_p = 1.0$ showing that flux in the back-jet increases while that in the snake diminishes: (a) $q^m = 0.18$, $Ca = 2 \times 10^{-3}$; (b) $q^m = 0.3$, $Ca = 3.25 \times 10^{-3}$.

to use lubrication theory to predict these two critical flow rates.

12b.3.3.3 Switching on the back-jet ($q = \bar{q}$)

The first step is to locate the z -coordinates of the two saddle points, Fig. 12b.18a. As they are stagnation points, equations (12b.8) and (12b.12) with $H(X) \approx H_0$ give:

$$(1 - q)(z^2 - 1) + \frac{2}{3} \left(\frac{S_p - 1}{S_p + 1} \right) z + \frac{2}{3} = 0 \quad (12b.22)$$

that is, the nondimensional coordinates z_1 and z_2 are solutions of a quadratic equation and functions of S_p and q .

The second step is to calculate the flux, Q , of fluid flowing between the lower roll and the lower of the two saddle points ($z = z_1$):

$$Q = \int_{-H_0}^{z_1} U dZ \quad (12b.23)$$

When conditions are critical and the back-jet is switched on the flux Q is identically the total inlet flux, $Q = U_2 H_i$ and so equations (12b.8),

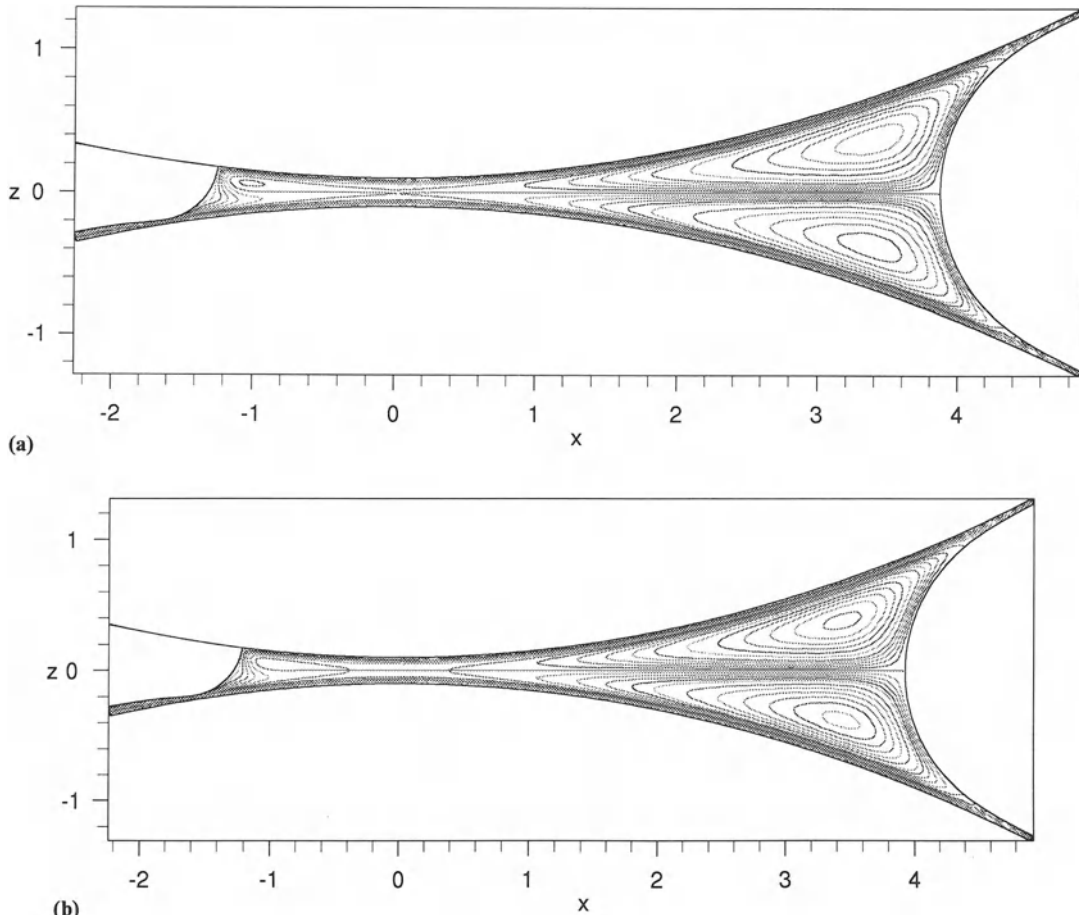


Figure 12b.20 Switching off the snake when $R_m/H_0 = 100$ and $S_p = 1$: (a) critical flow rate $q^* = 1/3$, $Ca = 3.25 \times 10^{-3}$; (b) $q^m = 0.35$, $Ca = 3.6 \times 10^{-3}$, fluid transfer to the upper roll is entirely via the back-jet and the saddle points have now moved apart.

(12b.12) and (12b.23) yield:

$$\frac{3}{4}(1-q)\left[\frac{z_1^3}{3} - z_1 - \frac{2}{3}\right] + \left(\frac{S_p - 1}{S_p + 1}\right)\left(\frac{z_1^2 - 1}{4}\right) + \frac{(z_1 + 1)}{2} = q \quad (12b.24)$$

great deal of tortuous algebra the following solution is obtained:

$$z_1 = [3(1-q)(3q(1+S_p) - (1-S_p)) - (1-S_p)](1+S_p)/[3(1-q)(3q-1)(1+S_p)^2 - (1-S_p)^2] \quad (12b.25)$$

$$q = \bar{q} = \frac{2}{9} \left[\frac{3 + 2S_p - 2\sqrt{S_p^2 + 3S_p}}{1 + S_p} \right] \quad (12b.26)$$

Equation (12b.24) is a cubic in z_1 which has to be solved simultaneously with equation (12b.22) to produce a solution for both z_1 and q . After a

This critical flow rate, \bar{q} , is speed ratio dependent, yet independent of capillary number and geometry ratio.

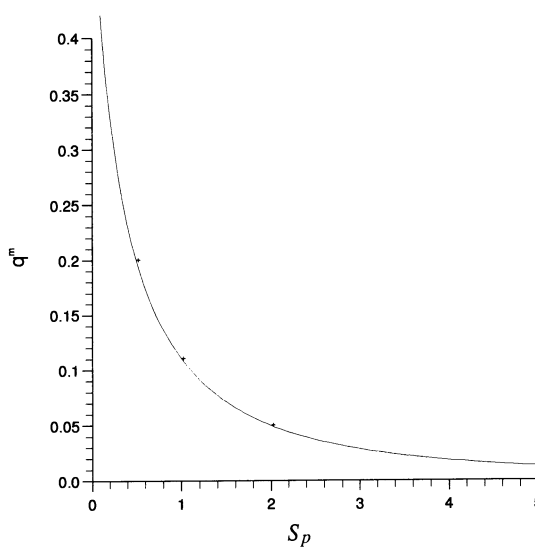


Figure 12b.21 The onset of the back-jet for $R_m/H_0 = 100$. Theoretical curve for critical flow rate \bar{q} as a function of S_p ; + indicate data points obtained from finite-element solutions; the curve is that predicted via lubrication theory, equation (12b.26).

Figure 12b.21 shows a plot of \bar{q} against S_p as given by equation (12b.26) together with a number of data points for the onset of the back-jet obtained computationally.

12b.3.3.4 Switching off the snake ($q = q^*$)

Once again the starting point is to consider the flux, Q , flowing between the lower roll and the lower of the two saddle points ($z = z_1$), as given by equation (12b.23). When conditions become critical, the snake is switched off and the flux Q is carried away on the lower roll. Therefore, $Q = U_2 H_2$, and equation (12b.23) along with (12b.8) and (12b.12) give:

$$\begin{aligned} \frac{3}{4}(1 - q^*)\left(\frac{z_1^3}{3} - z_1 - \frac{2}{3}\right) - \frac{S_p - 1}{S_p + 1}\left(\frac{z_1^2 - 1}{4}\right) \\ + \left(\frac{z_1 + 1}{2}\right) = \frac{h_2}{(1 + S_p)} \end{aligned} \quad (12b.27)$$

Solving equations (12b.27) and (12b.22) will, in principle, determine z_1 and the critical flow rate q^* . The problem, however, is that we do not have a general expression for h_2 except for the particular case $S_p = 1$ when $h_2/[(1 + S)] = h_i/[2(1 + S)] = q/2$.

The case of equal roll speeds is the only one for which q^* can be predicted. The solutions for (12b.27) and (12b.22) are:

$$z_1 = 0 \quad \text{and} \quad q^* = \frac{1}{3} \quad (12b.28)$$

Computations reveal this critical flow rate to be $q^* = 0.3327$, Fig. 12b.20a, showing yet again the ability of simple lubrication theory to predict important features accurately.

For unequal roll speeds q^* has to be determined computationally and thus far an overall pattern has not emerged.

12b.4 THE MENISCUS ROLL COATING REGIME

In summary, meniscus roll coating is an inlet starved process, $q \ll 1$, for which it is useful to distinguish between two degrees of starvation according to the fluid transfer mechanism. If the inlet is ultra-starved ($q < \bar{q}$), fluid is transferred only via the snake, whereas if the inlet is starved ($\bar{q} < q \ll 1$) fluid is transferred by both the snake and the back-jet. This distinction is summarized in Table 12b.3.

The remaining problem is to determine that part of parameter space, i.e. the range of capillary numbers and geometry ratios, in which meniscus roll coating can arise.

Table 12b.3 The meniscus coating regime

Inlet condition	Fluid transfer mechanism	Flow rate
Ultra-starved	Snake	$q \leq \bar{q}$
Starved	Snake and back-jet	$\bar{q} < q \ll 1$

$$\frac{3\sqrt{2}}{4} Ca \sqrt{\frac{R_m}{H_0}} = \left[\frac{\cos^2 \alpha_b - 2 \cos^2 \alpha_d}{(\sin 2\alpha_b + \sin 2\alpha_d)(1-q) + 2(\alpha_b + \alpha_d)(1-3q/4) - \frac{1}{8}(\sin 4\alpha_b + \sin 4\alpha_d)} \right] \quad (12b.29)$$

Because a two roll coater operates in a three-dimensional parameter space defined by capillary number, Ca , geometry ratio, H_0/R_m and flow rate, q , it is highly desirable to have a relationship involving these parameters – a relationship which defines the meniscus roll coating regime. With so many parameters involved, it would be difficult to obtain such a relationship from computational data alone. However, the small flux model provides such a relationship in the form of equation (12b.15), as shown in equation (12b.29), above. This gives valuable insight into the delicate balance between the governing parameters. The following observations can be made.

1. For meniscus coating with $q \ll 1$ it is clear that Ca and H_0/R_m cannot be chosen randomly. As mentioned previously with regard to equation (12b.15) $Ca(R_m/H_0)^{1/2}$ must be of order unity for the equation to have a solution. If a solution cannot be found for a given set of parameter values it means that the coating bead does not exist for these values.
2. It is observed both experimentally and computationally that once an equilibrium flow is established with Ca , H_0/R_m and q all fixed then if any one of these parameters is varied, the position of the upstream meniscus changes immediately whereas the downstream meniscus changes its position more slowly. Furthermore it is found that the upstream meniscus is restricted in the sense that it cannot move too far in towards the nip nor too far out. This behavior can be predicted via equation (12b.29).

As an illustration consider those flows in which the downstream meniscus is far from the nip so that $\alpha_d \approx \pi/2$. For each flow rate q , equation (12b.29) gives capillary number as a function of b , ($b = \tan \alpha_b$), the position of the upstream meniscus. Figure 12b.22a shows a curve of $Ca(R_m/H_0)^{1/2}$ against b for flow rates $q = 0.075$ and $q = 0.2$ and $\alpha_d = \pi/2$. As Ca increases b decreases and the upstream

meniscus moves inwards. Experiments by Malone (1992), suggest that once the meniscus reaches the minimum gap position it loses stability giving rise to the phenomena of the bead break described in the next section. Similarly b increases when Ca is reduced and the upstream meniscus moves away from the nip. In practice, however, the meniscus only moves out so far. There is a point, beyond which, solutions predicted by equation (12b.29), are not realized nor are they obtainable computationally.

The remaining problem now is to explain why the meniscus only moves out so far when Ca is reduced and why a certain class of solutions is not realized in practice. In fact such solutions correspond to flows in which capillary pressure at the upstream meniscus is comparable to that at the downstream one and so the pressure field has ‘essentially collapsed’, i.e. the assumption on which the small flux model is based – that pressure and viscous forces are in balance, with inertia negligible – is no longer valid and therefore such equilibrium flows do not exist. Both experiments and computations suggest that the position of the upstream meniscus, $b = \tan \alpha_b$, usually lies within the range $0 < b < 1.75$.

3. Equation (12b.29) can be written in the form:

$$Ca \left(\frac{R_m}{H_0} \right)^{1/2} = f(q, \alpha_b, \alpha_d) \quad (12b.30)$$

where f is a function of the variables q , α_b and α_d ; then one way of displaying results is to fix q and plot solutions as data points on a graph of $Ca(R_m/H_0)^{1/2}$ against b , ($b = \tan \alpha_b$). Figure 12b.22b identifies a corner of parameter space, bounded by the axes and the curve AB, in which solutions are to be found. The data points correspond to finite-element solutions for which $q^m = 0.2$, $0.1 < S_p < 2.5$ and $2.2 < d < 3.9$ where $d = \tan \alpha_d$. The curves

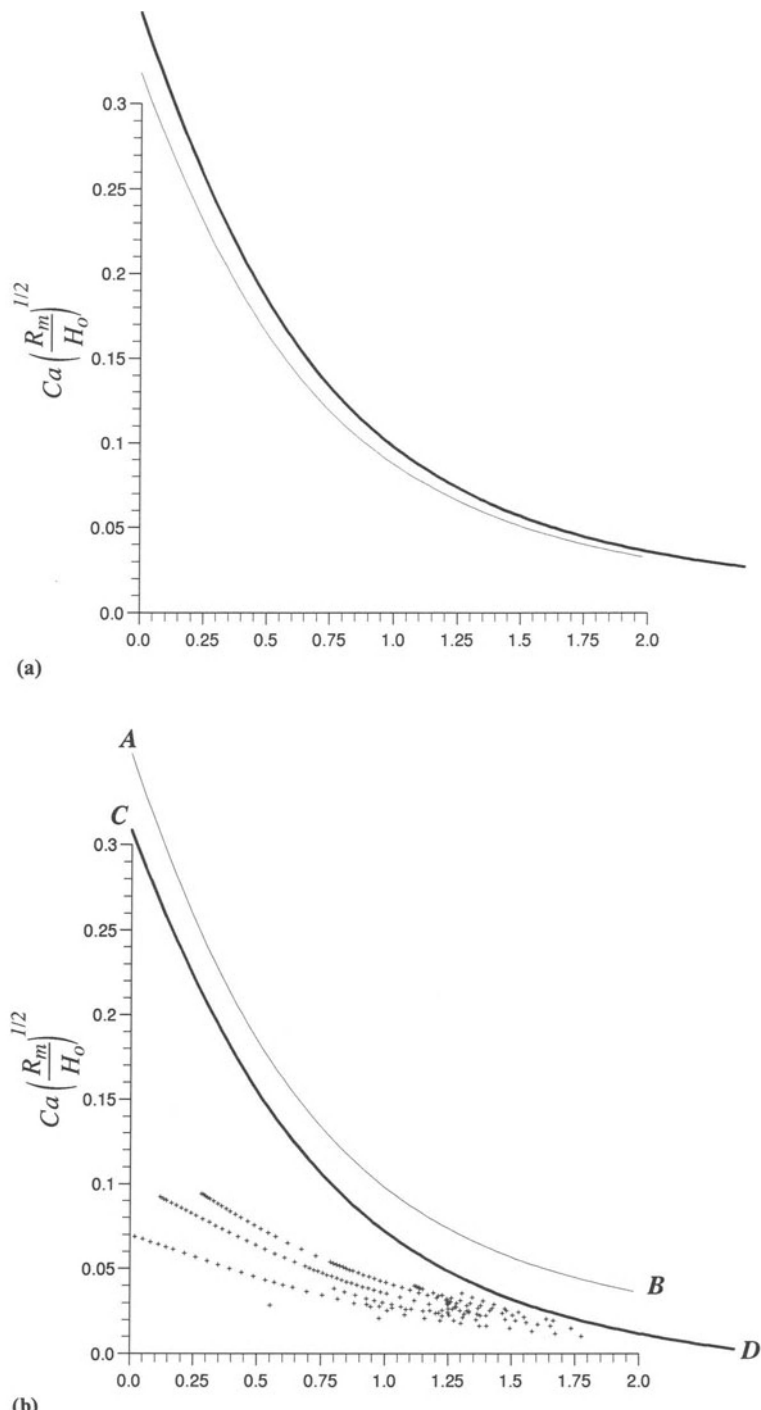


Figure 12b.22 (a) Theoretical curves of $Ca(R_m/H_0)^{1/2}$ against b for $\alpha_d = \pi/2$ and flow rates $q^m = 0.075$ and 0.2 ; (b) + data points obtained from finite-element solutions for the latter flow rate, AB and CD are theoretical curves derived from equation (12b.29) when $\alpha_d = \pi/2$ and $5\pi/12$, respectively.

AB and CD represent solution curves obtained analytically via equation (12b.29) when $\alpha_d = \pi/2$ and $5\pi/12$, respectively.

12b.5 INSTABILITIES

In meniscus roll coating Malone (1992) identified a number of characteristic instabilities and their associated coating defects, including bead-break, bead-collapse and bubble generation which are described below. Little is known about the mechanisms causing these instabilities and what is reported here are the results of that preliminary investigation.

12b.5.1 BEAD-BREAK

This instability manifests when speed ratio is increased from a stable operating condition where the bead has uniform free surfaces upstream and downstream of the nip. As the speed of the upper roll increases, the upstream free surface moves towards the nip and subsequently exhibits a local indentation or 'necking', see Fig. 12b.23a. However, there is evidence to suggest that the free surface can pass through the nip before losing stability. The necking may then lead to either a local form of bead-break, Fig. 12b.23b, or several bead-breaks producing a cellular array of beads, Fig. 12b.23c. As U_1 is further increased, additional neckings arise until a quasi-stable situation is reached with equispaced beads distributed along the axis of the rolls in the nip region. The effect is to produce alternate wet and dry stripes on the upper roll – which in practice would be the web. When developed fully this form of instability bears some similarity to 'ribbing' by virtue of its regular, periodic pattern along the axis. Unlike ribbing however, it appears to arise as a result of a two-dimensional disturbance to the upstream meniscus, Gaskell *et al.* (1996b). In pre-metered bead coating operations such as slide or slot coating this instability is very common and is referred to as 'rivulets'. Other defects, observed on the web, have been referred to as coating misses or 'cigar misses' due to their

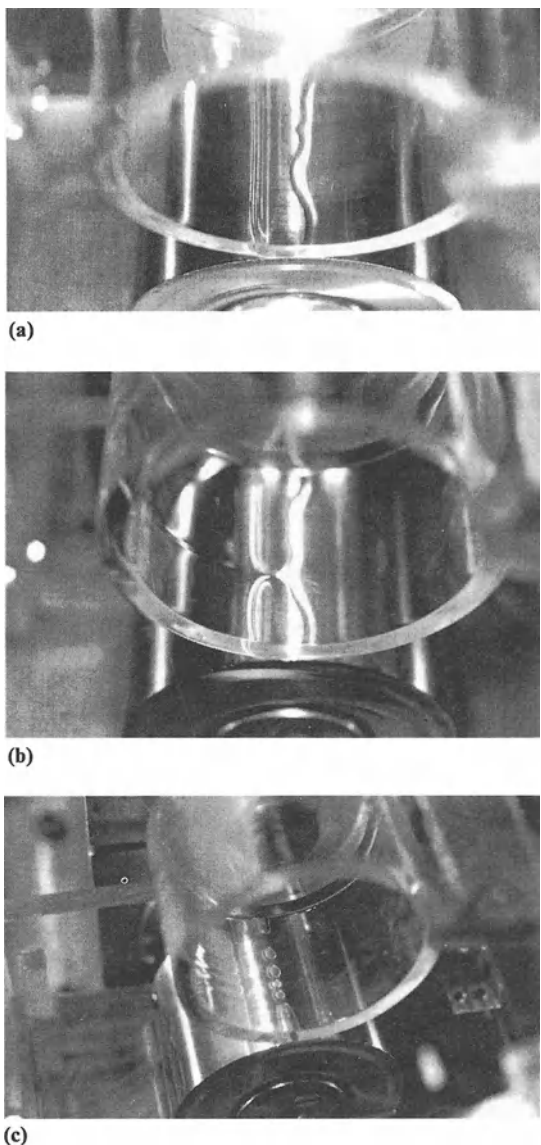


Figure 12b.23 (a) Local indentation of the upstream free surface; (b) bead-break; (c) multi-bead-break (rolls moving right to left).

characteristic shape. It is conceivable that these may be due to the onset of bead-break when the bead may well be alternately breaking and reforming, i.e. alternating between Fig. 12b.23a and 12b.23b.

12b.5.2 BEAD-COLLAPSE

Excessive inlet starvation would appear to be the cause of this particular instability. If flow rate q^m is reduced beyond a critical value or if S_p is increased by reducing U_2 and simultaneously reducing flow rate then the bead will break somewhere along its length followed by the disintegration of the remainder of the bead – leaving a layer of fluid on the lower roll only.

12b.5.3 BUBBLE GENERATION

A common defect in meniscus roll coating is the appearance of bubble lines on the coated web arising from the presence of bubbles in the fluid bead. When they first appear they tend to grow in size and wander axially along the nip. A bubble may lodge up against the free surface at the downstream side of the nip, Fig. 12b.24, giving the appearance of a local indentation of the surface and giving rise to a bubble line which is a down web line of localized, low coat weight. As the fluid bead is a region of subambient pressure, as a result of capillary action at the menisci, it is not surprising that it should provide a source of attraction and a resting place for any bubble that might emerge. Two possible sources of bubble generation have been suggested; vaporous cavitation and degassing as dissolved gas is expelled from the solution. However the measured pressures (Malone 1992) appear to be an order of magnitude smaller than those required for vapourization (for example, the vapour pressure of a typical industrial fluid, toluene, is -23 mm Hg

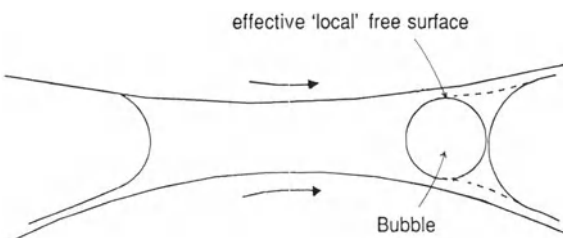


Figure 12b.24 A bubble in the bead giving rise to a bubble line defect.

which is equivalent to -3000 Pa) and therefore degassing is the most likely cause, although further work needs to be done.

ACKNOWLEDGMENTS

The authors wish to record their gratitude to Dr J. L. Summers (of the University of Leeds) who collaborated in the preparation of this manuscript and kindly generated many of the finite-element results. Thanks are also due to ICI for their generous sponsorship of this work.

REFERENCES

- Babuska, I. and Aziz, A. K. 1977. *Lectures on the Mathematical Foundations of the Finite Element Method*, ed. A. K. Aziz. New York: Academic Press. p. 1.
- Benkreira, H., Edwards, M. F. and Wilkinson, W. L. 1981. A semi-empirical model of the forward roll coating flow of Newtonian fluids. *Chem. Eng. Sci.* **36**: 423.
- Canedo, E. L. and Denson, C. D. 1989. Flows in driven cavities with a free surface. *AIChE J.* **35**(1).
- Coyle, D. 1996. *Liquid Film Coating*, (eds S. F. Kistler and P. M. Schweizer). Chapman and Hall, Ch. 12a.
- Coyle, D., Makasko, C. W. and Scriven, L. E. 1986. Film-splitting flows in forward roll coating. *J. Fluid Mech.* **171**: 183.
- Gaskell, P. H., Savage, M. D. and Thompson, H. M. 1991. Creeping flow: novel analytic and finite element solutions. *Proc. 7th Int. Conf. Num. Meth. Lam. and Turb. Flow*, eds Taylor, Chin, Homsy, pp. 1743.
- Gaskell, P. H., Innes, G. E. and Savage, M. D. 1996a. An experimental investigation of meniscus roll coating. *J. Fluid Mech.*, in press.
- Gaskell, P. H., Innes, G. E. and Savage, M. D. 1996b. Bead break instability in meniscus roll coating. Submitted to *J. Fluid Mech.*
- Gaskell, P. H., Savage, M. D., Summers, J. L. and Thompson, H. M. 1995a. Flow topology and transformation in fixed gap symmetric forward roll coating systems. *Proc. 9th Int. Conf. Num. Meth. Lam. and Turb. Flow*, eds Taylor, Durbetaki. pp. 984.
- Gaskell, P. H., Savage, M. D., Summers, J. L. and Thompson, H. M. 1995b. Modeling and analysis of meniscus roll coating. *J. Fluid Mech.* **298**: 113.
- Hughes, T. J. R. 1987. *The Finite Element Method: Linear Static and Dynamic Finite Element Analysis*.
- Joseph, D. D. 1977. The convergence of biorthogonal

series for biharmonic and Stokes flow edge problems: Part 1. <i>SIAM J. Appl. Math.</i> 33 : 337.	h_1, h_2	nondimensional outlet film thicknesses
Kistler, S. F. and Scriven, L. E. 1983. Coating flows. <i>Computational Analysis of Polymers</i> . pp. 343.	\mathbf{n}	unit normal vector
Landau, L. D. and Levich, V. G. 1942. Dragging of liquid by a moving plate. <i>Acta Physchim, URSS.</i> XVII (1–2): 42.	P	pressure
Malone, B. 1992. An experimental investigation of roll coating phenomena. PhD thesis, University of Leeds.	p	nondimensional pressure
Pearson, J. R. A. 1985. <i>Mechanics of Polymer Processing</i> . pp. 378–380. London and New York: Elsevier Applied Science Publications.	Q	flow rate per unit axial length
Perkins, R. J. 1991. Department of Applied Mathematics and Theoretical Physics, Cambridge. Private com- munication.	q	nondimensional flow rate
Ruschak, K. J. 1985. Coating Flows. <i>Ann. Rev. Fluid Mech.</i> 17 : 65.	q_{\max}	maximum value of q
Thompson, H. M. 1992. A theoretical investigation of roll coating phenomena. PhD thesis, University of Leeds.	q^m	modified nondimensional flow rate
	\bar{q}, q^*	critical, nondimensional flow rates
	R_1, R_2	upper and lower roll radii
	R_b, R_d	radius of curvature of upstream and downstream menisci
	R_m	average roll radius
	s	nondimensional surface coordinate
	S_p	speed ratio (nondimensional)
	\mathbf{t}	unit tangent vector
	U_1, U_2	upper and lower roll speeds
	U_m	average roll speed
	U, W	velocity components
	X, Z	coordinate directions
	x, z	nondimensional coordinate directions

NOTATION

A	bead half length
b	a nondimensional length, defined by $b = \tan \alpha_b$
Ca	capillary number
d	a nondimensional length, defined by $d = \tan \alpha_d$
H	bead half depth
H_0	half minimum gap separation
H_i	inlet film thickness on lower roll
H_1, H_2	outlet film thicknesses on upper and lower roll
h_i	nondimensional inlet film thickness

Greek letters

α	nondimensional angular coordinate, defined by $x = \tan \alpha$
∇	del operator $\left(\frac{\partial}{\partial x}, \frac{\partial}{\partial y}, \frac{\partial}{\partial z} \right)$
μ	fluid viscosity
π	pi
Ψ	streamfunction
σ	surface tension
$\underline{\sigma}$	shear stress tensor

ELASTOHYDRODYNAMIC COATING SYSTEMS

12c

Ferdinand R. Pranckh and Dennis J. Coyle

12c.1 INTRODUCTION

Elastohydrodynamics is the interaction between hydrodynamic traction forces exerted by a flowing fluid and elastic restoring forces imparted by a deformable solid that forms part of the confinement of the flow. Elastohydrodynamic effects are negligible in most coating flows. However, some coating methods rely on elastohydrodynamic interactions for coated film metering, formation, and transfer. Figure 12c.1 depicts six of the most common elastohydrodynamic coating methods. In all but the tensioned-web slot coater and the gravure coater, the thickness of the coated film depends primarily on the balance between the hydrodynamic forces exerted by the liquid and the internal elastic restoring forces and external loads resisting the deflection of the deformable flow confinement. In general, therefore, elastohydrodynamic coating configurations are self-metered (see Chapter 1 for a systematic classification of coating processes). In the two noted exceptions, the coating flow is nearly pre-metered, but the elastohydrodynamic effects avoid the need to build coating devices with extremely narrow, pre-set gaps between a stationary applicator and the moving substrate and thereby allow deposition of much thinner liquid films than are achievable by their rigid counterparts of die and roll coating. This points to the major reason for using elastohydrodynamic coating systems, namely their ability to apply greatly

reduced coating thicknesses with less sensitivity to mechanical tolerances. Reduced sensitivity to operating parameters and process perturbations is an additional bonus. As will become apparent throughout this chapter, however, this is not always achieved. For that reason, there are distinct trade-offs between rigid and elastohydrodynamic coating applicators.

The various elastohydrodynamic coating systems illustrated in Fig. 12c.1 are distinguished by the type of elastic confinement they incorporate. Flexible-blade and membrane coaters employ static plates, or sheets, of metal or plastic as metering elements. In flexible-blade coating (Fig. 12c.1a), the upstream edge of a rather thin strip of metal or plastic is clamped in a rigid holder and loaded against a liquid-laden, moving substrate backed up by a roll so that the blade and substrate form a converging wedge. The liquid supplied to that wedge typically is dip-coated upstream or applied with a more sophisticated device, such as a confined-flow feed box that becomes an integral part of the blade installation (see Chapter 12d). In membrane coating (Fig. 12c.1b), the applicator is a compliant trailing wiper film that is wrapped around and extends past a cylindrical, inflatable 'air bag' or membrane. The membrane-backed wiper together with the moving substrate form a converging, wedge-shaped region very similar to that in blade coating. That region is typically fed from a puddle that sits

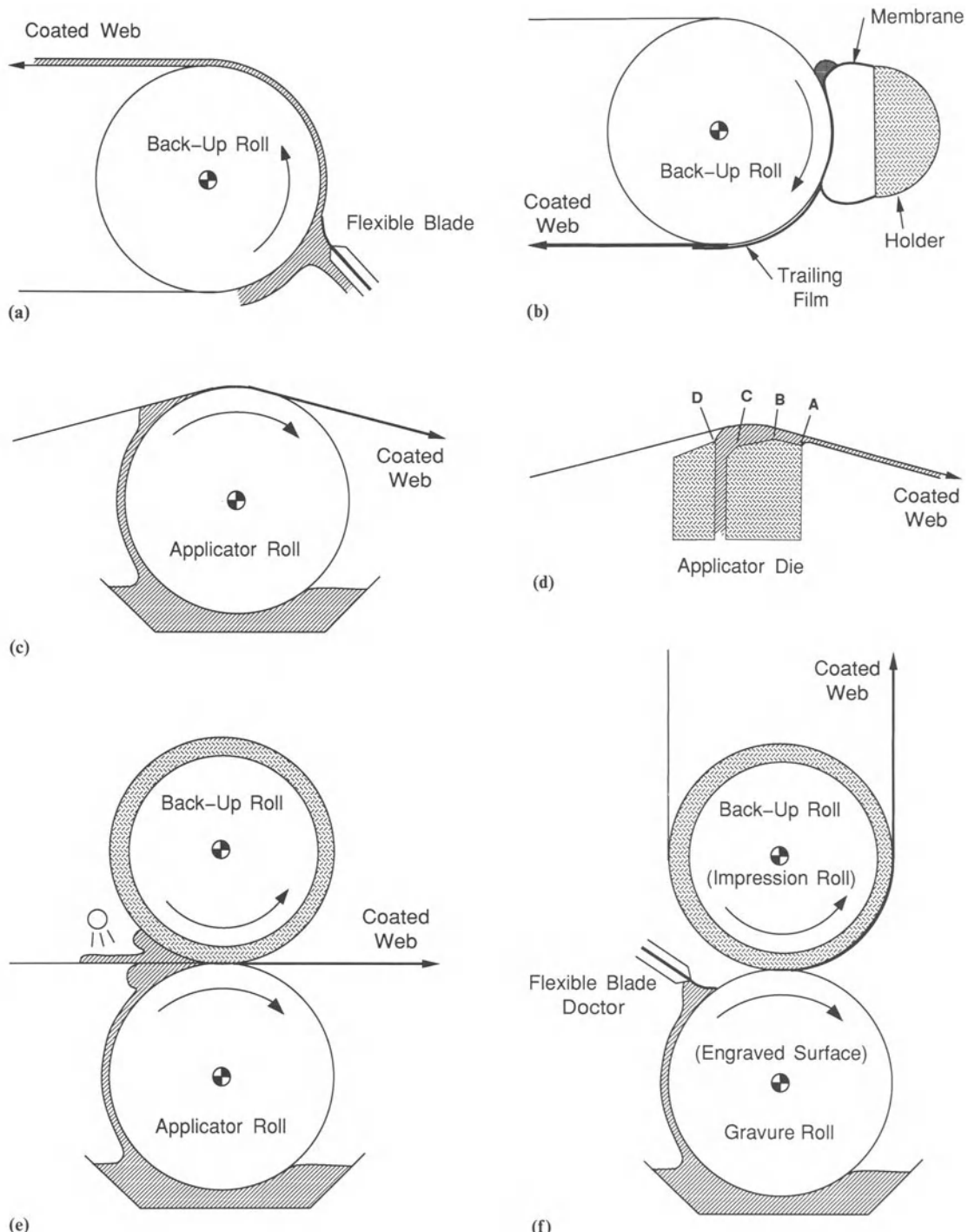


Figure 12c.1 Common types of elastohydrodynamic coating methods: (a) flexible-blade coater; (b) membrane coater; (c) tensioned-web roll coater (forward mode); (d) tensioned-web slot coater; (e) squeeze-roll coater; (f) direct gravure coater. The coating thickness and gaps between elastic flow confinements are magnified for clarity.

right above the wedge and is supplied by a pipe or a more elaborate flow distributor.

In both coating configurations, the wedge-shaped region between the metering element and the substrate is key to setting the coating thickness. The hydrodynamic lubrication forces generated by the drag flow into the converging wedge tend to bend and lift the metering element. This action is opposed by the external load which, in flexible-blade coating, comes from rotating or translating the blade holder or from forcing a pressurized bladder or some mechanical device against the blade; in membrane coating, the load comes from the pneumatic pressure within the membrane, and is transmitted through the compliant wiper. As a result of the similarities between flexible-blade and membrane coating, the elastohydrodynamic balance between hydrodynamic forces and external load produces an operating response that is quite comparable in both configurations: the metered coating thickness depends primarily on the external load, the bending stiffness of the flexible plates or sheets involved, the liquid viscosity and possibly other rheological properties, and the coating speed. At sufficiently high speeds, inertia effects can also come into play (see Chapter 12d).

Tensioned-web roll and slot coaters, illustrated in Figs 12c.1c and 12c.1d, rely solely on the deformable substrate without any external mechanical support to provide the elastic flow confinement and imposed load in the coating application step. In tensioned-web roll coating, often also called kiss coating, liquid is transferred onto a tensioned web as the web passes over a rotating applicator roll. The liquid film on the applicator roll is typically supplied by dip coating, sometimes reduced in thickness with additional metering roll steps of the sort described in Chapter 12a. In tensioned-web slot coating, a liquid film is applied directly out of a slot of a coating die onto a web that travels in free span between two idler rolls.

In both tensioned-web coating configurations, wrapping the substrate over a certain, albeit sometimes small, angle around the roll or slot-coating die loads the substrate against those rigid

parts of the coating devices. The normal load that arises from the resultant of the tension in the curved substrate presses the substrate against the roll or die. In kiss roll coating, the normal load together with speed, viscosity and possibly substrate stiffness meter the amount of liquid that passes through the nip between the roll and substrate in a manner very similar to that of the pneumatic air load controlling coating thickness in membrane coating. Running the roll and substrate at differential or opposite speeds provides additional options to influence the final coating thickness. In tensioned-web slot coating, in contrast, the final coating thickness is premetered with the pump that supplies liquid to the die. Changes in normal load, resulting from adjustments in tension, modifications in die-lip design, or alterations in speed or viscosity are now used to ensure that the elastohydrodynamic floating height of the substrate above the die lips can accommodate the desired, pre-metered amount of liquid. The basic elastohydrodynamic action, nevertheless, is quite similar in both tensioned-web coating systems.

Squeeze roll and gravure coaters, shown schematically in Figs 12c.1e and 12c.1f, incorporate compliant elastic layers of rubber or rubber-like elastomers bonded to steel rolls as metering elements. Some substrates, like paper, are compressible and hence also interact elastically with the coating process. Squeeze-roll coaters, sometimes referred to as nip-roll coaters, are in essence configured like forward roll coaters, with either one or both rolls being rubber covered. Nip control is achieved by either direct pressure loading of the rolls, or by setting a gap or a positive engagement with mechanical stops. To achieve thin coatings, several nips can be arranged in sequence in multi-roll configurations. The liquid supply system to the nip can be rather crude, as illustrated by the pipe-fed puddle or dip coating systems shown in Fig. 12c.1e. Gravure coaters are quite similar to nip roll coaters, except that the rigid roll has cells, grooves or other patterns of a specific volume engraved into its surface. The liquid supply system is also more sophisticated. An excess of coating solution is

applied to the gravure roll, usually by dipping the roll into a pan or by using a more precise orifice- or fountain-type applicator. This excess is then doctored by a flexible blade which leaves the cells only partially full with liquid. This doctoring step, of course, constitutes an additional elastohydrodynamic coating system very similar to the flexible-blade coater introduced above.

As for the basic elastohydrodynamic mechanisms at work, the nip interface between the rolls is quite similar in squeeze-roll and gravure coating. The mechanical deformation resulting from the positive engagement, or at least close proximity, between the rolls builds a pressure hump akin to that in Hertzian contact between two elastic rolls in dry contact. This pressure hump must be balanced by the hydrodynamic lubrication flow pressures in the liquid, and the thickness of the liquid film between the rolls is a direct consequence of that balance. The purpose of the elastohydrodynamic interaction is quite different, however, in the two coating configurations. In squeeze roll coating, the intent is to allow the elastohydrodynamics to meter the coating thickness. The thickness depends primarily on the liquid viscosity, coating speed, load, and elastic modulus as well as thickness of the rubber layer. In gravure coating, in contrast, the wet coating thickness is premetered in the sense that it is dominated by the engraved volume and is relatively insensitive to the adjustable process and fluid variables. The main task of the elastohydrodynamic interaction is to allow the substrate wrapped around the rubber-covered nip roll – or the nip roll directly in offset-gravure configurations in which that roll serves as transfer roll – to conform to the textured surface of the gravure cylinder and thereby ensure proper pick-out of part of the liquid from the cells or grooves.

The main purpose of this chapter is to provide a critical review of the published literature on elastohydrodynamic coating operations. Section 12c.2 recounts the mechanisms of elastohydrodynamics and outlines the governing equations. The remaining sections discuss each of the coating methods in turn, covering flexible-

blade (Section 12c.3), membrane (Section 12c.4), tensioned-web roll (Section 12c.5), tensioned-web slot (Section 12c.6), squeeze roll (Section 12c.7), and gravure coating (Section 12c.8). Throughout, the main emphasis is on identifying the physical mechanisms of viscous flow and elastic deformation, and explaining how their interaction results in the observed operating behavior. Where sufficient information is available, the chapter also comments on instabilities and how these affect uniformity and operability limits.

Many of the hydrodynamic instabilities that are seen in elastohydrodynamic coating systems are the same as those encountered in other coating configurations and discussed throughout the entire volume. Most prominent are perhaps air entrainment (e.g., Chapter 3) and ribbing (e.g., Chapter 12a). Ribbing, for instance, tends to occur in flexible-blade coating under highly loaded conditions that cause the blade tip to lift off the substrate wrapped around the back-up roll. A related defect in squeeze-roll and tensioned-web roll coating is the film-split pattern shown in the photograph of Fig. 12c.2. Its amplitude and wavelength change with coating thickness but, for all practical purposes, the defect cannot be avoided in squeeze-roll and tensioned-web roll coaters when operated in the forward mode. In this case – and in quite a few other elastohydrodynamic coating applications – acceptable coating uniformity depends on leveling before solidification or a lax criterion of what is ‘acceptable’.

Other flow instabilities are more peculiar to elastohydrodynamic, or at least self-metered, coating systems. Many originate in the puddle or rolling bank of liquid that builds upstream of the metering element. This puddle, similar to that discussed for forward roll coating with rigid rolls in Chapter 12a but possibly considerably larger, contains one or more vortices. At high Reynolds numbers, these might become unstable and form a three-dimensional vortex structure or even undergo transition to turbulent flow. Even at low and moderate Reynolds numbers, rolling banks are susceptible to air entrainment and also to entrapment of dirt, particle agglomerates,

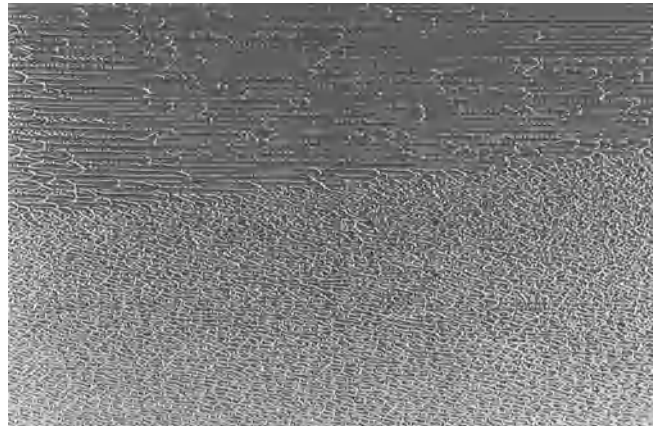


Figure 12c.2 Photograph of film-split pattern in squeeze-roll coating of a Newtonian liquid. The coating direction is left-to-right; the upper region has a thicker wet coverage than the lower.

bubbles, and other sources of defects. The puddles can also have a particularly strong influence on the coating near the edges of the web. If too little fluid is supplied to an upstream puddle, the coater becomes ‘starved’ and the coating width shrinks while maintaining a near constant thickness at the center of the web. If too much is supplied, the puddle can overflow, resulting in excessive edge beads, run-back, or other problems.

In addition to hydrodynamic instabilities, mechanical instabilities can also degrade the coating quality resulting from elastohydrodynamic coating processes. Examples include vibrations of doctor blades, or tension fluctuations, fluttering and buckling in tensioned webs.

12c.2 ELASTOHYDRODYNAMIC MECHANISMS

12c.2.1 LIQUID FLOW

Steady, two-dimensional coating flows of inelastic liquids, to which this section is restricted, are governed by the continuity equation (2.7) (Chapter 2), the momentum conservation equation (2.19), and an appropriate constitutive equation to describe non-Newtonian viscous behavior. For Newtonian liquids, the last two reduce to the Navier–Stokes equation (2.21), and the traction

that the coating liquid exerts on elastically deformable flow confinement arise from both the isotropic pressure and viscous stresses:

$$T_{nn} \equiv \mathbf{n}\mathbf{n} : \mathbf{T} = -p + \mathbf{n}\mathbf{n} : \mathbf{D} \quad (12c.1a)$$

$$T_{nt} \equiv \mathbf{t}\mathbf{n} : \mathbf{T} = \mathbf{t}\mathbf{n} : \mathbf{D} \quad (12c.1b)$$

Here, T_{nn} and T_{nt} are the normal and the tangential traction components made non-dimensional with $\mu U/L$, where μ is the characteristic viscosity, U is the characteristic speed, usually the substrate or coating speed, and L is a characteristic length; \mathbf{n} and \mathbf{t} are the local normal and tangent unit vector to the boundary; p is the pressure and \mathbf{T} is the total stress tensor, both measured in units of $\mu U/L$; and $\mathbf{D} \equiv \nabla\mathbf{v} + \nabla\mathbf{v}^T$ is the rate of strain tensor, where \mathbf{v} is the dimensionless velocity field.

If the narrow clearance of the flow confinement that results from the elastohydrodynamic interaction varies slowly in the stream-wise direction, the lubrication approximation applies and the Navier–Stokes system (2.7) and (2.21) reduces to the much simpler Reynolds equation which describes the pressure distribution along the flow channel (see Chapter 8 for details). With the deformable boundary as the reference surface, the non-dimensional form of this equation is:

$$\frac{d}{ds} \left(\frac{h^3}{12} \frac{dp}{ds} \right) = \frac{d}{ds} \left(h \frac{v_1 + v_2}{2} \right) \quad (12c.2)$$

Here, s is the arc length along the reference surface measured in units of L ; h is the channel height measured in units of L ; and v_1 and v_2 are the projections of the boundary velocities onto the reference surface, both measured in units of U . In the lubrication approximation, the normal and tangential traction components on the deformable flow confinement depend only on the pressure profile along the narrow flow channel and reduce to:

$$\begin{aligned} T_{nn} &= -p \\ T_{nt} &= -\left(\frac{h}{2} \frac{dp}{ds} - \frac{1}{h}\right) \end{aligned} \quad (12c.3)$$

From the pressure distribution, it is nonetheless straightforward to calculate the stream-wise velocity $u(s, z)$ or the shear rate $\dot{\gamma}(s, z)$ at any point (s, z) if desired:

$$\begin{aligned} u(s, z) &= -\frac{1}{2} \frac{dp}{dz} (zh - z^2) + \left(\frac{h-z}{h}\right) \\ \dot{\gamma}(s, z) &\equiv \frac{du}{dz} = -\frac{1}{2} \frac{dp}{ds} (h - 2z) - \frac{1}{h} \end{aligned}$$

Here, z is the coordinate perpendicular to the reference surface measured in units of L , u is measured in units of U , and $\dot{\gamma}$ in units of U/L .

For the purpose of comparing and assessing different coating flows, it is sometimes useful to calculate the total shear suffered by the fastest moving 95% of coated liquid as it passes through the coating device, Γ_{95} , and the total pressure load that the liquid exerts on the substrate or the deformable coating device, P_s (for complete details, see Pranckh and Scriven (1990)). These quantities are defined as

$$\Gamma_{95} \equiv \int_0^L -\frac{1}{h_{95}(s)} \left[\int_0^{h_{95}(s)} \frac{\dot{\gamma}(s, z)}{u(s, z)} dz \right] ds \quad (12c.4)$$

$$P_s \equiv \int_0^L p(s) ds \quad (12c.5)$$

where $h_{95}(s)$ is the dimensionless height from the moving substrate to the streamline that demarcates 95% of the total liquid flow Q , i.e., $0.95Q = \int_0^{h_{95}(s)} u(s, z) dz$. Γ_{95} is measured in units of U , and P_s in units of μU .

12c.2.2 ELASTIC LAYERS

The simplest approach to modeling solid layers of rubber, rubber-like elastomers or compressible materials such as paper is to assume their deformation is purely elastic (Section 12c.7 briefly addresses the complications that arise from viscoelastic behavior of solid layers). In most coating configurations, the deformation of elastic layers has no cross-web component nor any cross-web gradients. It is therefore governed by the equations of plain-strain elasticity. Deformation is measured by the Finger strain tensor \mathbf{F} whose components are

$$F_{ij} = \frac{\partial x_i}{\partial X_j} \quad (12c.6)$$

where $x_i = X_i + u_i$ are the deformed coordinates written as the sum of the reference coordinates X_i and the displacements u_i . The equation of continuity requires that the determinant of the Finger tensor (or its inverse \mathbf{F}^{-1}) minus one equal the volume dilation

$$\frac{\partial u_1}{\partial x_1} + \frac{\partial u_2}{\partial x_2} + \frac{\partial u_1}{\partial x_1} \frac{\partial u_2}{\partial x_2} + \frac{\partial u_1}{\partial x_2} \frac{\partial u_2}{\partial x_1} = -\frac{3(1-2\nu)}{E} P \quad (12c.7)$$

Here, E is Young's modulus, ν is Poisson's ratio, and P is the isotropic pressure. The equation of mechanical equilibrium (momentum balance) is simply

$$\nabla \cdot \sigma = 0 \quad (12c.8)$$

where σ is the Eulerian stress tensor. For a solid that follows Hooke's law, the stress is proportional to strain so that

$$\sigma_{ij} = -P \delta_{ij} + 2G e_{ij} \quad (12c.9)$$

Here, e_{ij} are the components

$$e_{ij} = \frac{1}{2} \left(\frac{\partial u_i}{\partial x_j} + \frac{\partial u_j}{\partial x_i} - \frac{\partial u_\alpha}{\partial x_i} \frac{\partial u_\alpha}{\partial x_j} \right) \quad (12c.10)$$

of \mathbf{e} , the Almansi (Eulerian) strain tensor, and G is the shear modulus, which is related to Young's modulus via $E = 2(1+\nu)G$.

Equations (12c.7)–(12c.10) are readily solved by the finite-element method as part of a coating-flow simulation algorithm (*cf.* Chapter 9). The hydrodynamic boundary loads can be determined from the full Navier–Stokes system or the Reynolds equation. For sufficiently small deformations, the gradients can be evaluated in the undeformed reference state and the quadratic terms become negligible. The mathematical form of the resulting linear plain-strain equations is identical to that of the Navier–Stokes system in the limit of zero Reynolds number (see equation (2.27) in Chapter 2). If the deformable layer can be regarded as a deep elastic slab, i.e. a semi-infinite Hookean solid, its local indentation can be expressed as an integral of the pressure distribution, thereby further simplifying the analysis as discussed in Section 12c.7 (see equation (12c.18) and also Carvalho and Scriven (1993)).

If the normal tractions that act on the elastic layer have no steep gradients, an additional, dramatic simplification arises from the so called Winkler elastic foundation approximation (Johnson 1985): the elastic layer is taken to act like an array of infinitesimally narrow springs, with the displacement of a particular spring having no effect on its neighbors. With non-local effects ignored, the displacement at any point along the deformable layer is simply proportional to the loading at that point:

$$H - H_0 = K P_n \quad (12c.11)$$

Here, H and H_0 are the loaded and unloaded elevations, P_n is the local normal load, and K is the bulk modulus of the material. Johnson (1985) shows how K relates to the Young's E modulus for several limiting cases. The Winkler approximation in the form (12c.11) has been successfully applied to squeeze-roll coating (Coyle 1988b; see also Section 12c.7) and high speed blade coating of a compliant paper substrate (Pranckh and Scriven 1988).

When the normal load arises from the coating flow alone, as described by the Navier–Stokes equations or the Reynolds equation, equation (12c.11) becomes

$$h - h_0 = El T_{nn}$$

Here, h and h_0 are measured in units of L ; T_{nn} is the normal traction component, given by equation (12c.1) or (12c.3); and $El \equiv \mu U/(LK)$ is the elasticity number that compares the relative importance of characteristic viscous stresses with that of characteristic elastic stresses.

12c.2.3 THIN PLATES, SHELLS AND MEMBRANES

Flexible metering devices in blade, roll or gravure coaters and the webs in tensioned-web roll or tensioned-web die coaters typically start out flat in their undeformed state and thus are, in mechanical terms, plates or membranes. Because they are most often very thin compared with their overall length, the local deformations of infinitesimally small segments remain small, even in highly bent states during coater operation. Hence, the resistance to bending and stretching can be described by linear elastic models, as in standard thin-plate theory (Fluegge 1960). On a macroscopic scale, however, the deformations can be large, i.e. the changes in position of the deformable members can be of the same magnitude as their characteristic length or larger, giving rise to large curvatures and associated geometric nonlinearities. These nonlinearities can be accounted for by what the solid mechanics literature refers to as cylindrical shell theory (Fluegge 1960). In its simplest form typically used in coating flow analysis, that theory is limited to thin, inextensible shells and thereby retains the linear bending model of thin-plate theory. In the context of viscous free surface flows, shells can be thought of as interfaces that not only have surface tension but also have surface bending stiffness.

If there is no misalignment or buckling in the cross-web direction in the first place, and variations of the viscous tractions in the cross-machine direction are negligible so that the base flow is two-dimensional or has, compared with the elastic forces, only small cross-machine disturbances like those resulting from a ribbing instability, the blade or web shapes are two-dimensional. In

this idealization, the governing equations for the shells become one-dimensional:

$$\frac{dN}{ds} - \kappa Q + P_t = 0$$

$$\frac{dQ}{ds} + \kappa N + P_n = 0$$

$$\frac{dM}{ds} - Q = 0$$

$$M = -\kappa$$

Here, P_t and P_n are the tangential and normal load distributions along the shell; N is the local resultant of the internal normal stresses acting in the direction of the tangent t to the shell which, if positive, is in effect the tension in the blade or web; M is the bending moment resulting from those normal stresses; Q is the resultant of the shear stresses in the direction of the normal n to the thin shell; κ is the local curvature; and s is the arc length along the shell. Some of the variables are displayed in Fig. 12c.3a. N and Q are measured in units of D/L^2 and M in units of D/L , where L is a characteristic length of the shell and D its bending stiffness $D \equiv E\delta^3/[12(1 - \nu^2)]$; δ , in turn, is the shell thickness, and E and ν are Young's modulus and Poisson's ratio respectively of the shell material. κ is made nondimensional with $1/L$; P_t and P_n with D/L^3 ; and s with L .

The equations listed above represent the tangential force balance, the normal force balance, the moment balance, and the constitutive equation that relates the bending moment to curvature. The contributions κQ and κN are a direct consequence of the geometric nonlinearities that result from the large deflections. The constitutive equation describes the linear response of a Hookean solid under the Kirchhoff–Love assumptions for thin plates and thin shells (for an in-depth discussion, see Fluegge (1960)). For computational purposes, it is convenient to eliminate Q which, given the load distributions along the shell, yields two coupled nonlinear ordinary differential equations κ and N :

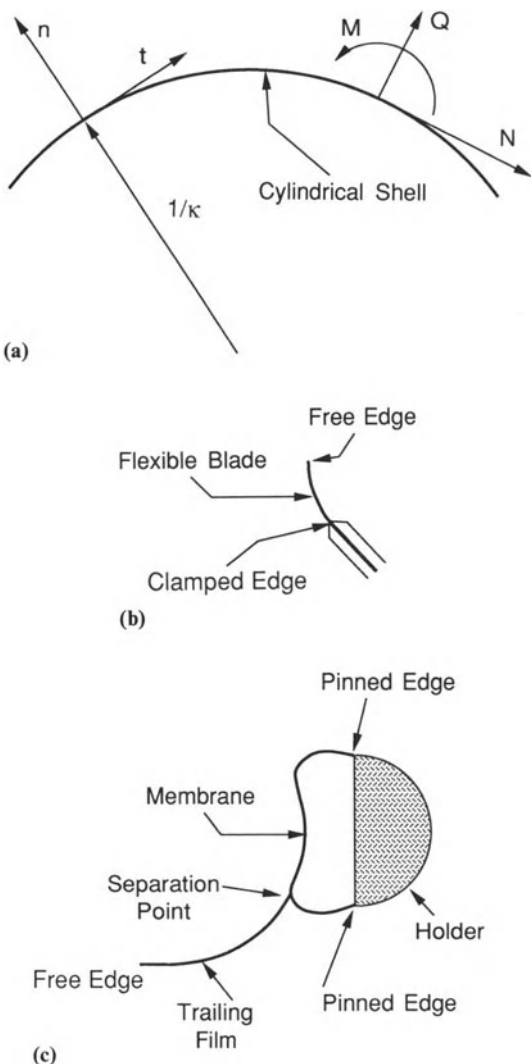


Figure 12c.3 Definition sketches for theory of deformation of thin plates, sheets, and membranes into cylindrical shells: (a) definition of tangent, t , normal, n , radius of curvature $1/\kappa$, tangential force, N , normal force, Q , and bending moment, M ; (b) boundary conditions for analysis of flexible-blade coater; (c) boundary conditions for analysis of membrane coater.

$$\begin{aligned} \frac{dN}{ds} + \kappa \frac{d\kappa}{ds} + P_t(s) &= 0 \\ -\frac{d^2\kappa}{ds^2} + \kappa N + P_n(s) &= 0 \end{aligned} \quad (12c.12)$$

From the curvature, the x - and y -coordinates of the shell, measured in units of L , are readily calculated from:

$$\frac{d\beta}{ds} = \kappa, \quad \frac{dx}{ds} = \cos\beta, \quad \frac{dy}{ds} = \sin\beta$$

Here, the auxiliary variable β is the local angle of inclination of the blade or web. Eliminating this variable reduces the three first-order equations to two second-order equations:

$$\begin{aligned} \frac{d^2x}{ds^2} + \kappa \frac{dy}{ds} &= 0 \\ \frac{d^2y}{ds^2} - \kappa \frac{dx}{ds} &= 0 \end{aligned} \quad (12c.13)$$

The appropriate boundary conditions for the force balances (12c.12) and the geometric relations (12c.13) depend on the physics of the situation, illustrated for a blade coater and a membrane coater in Figs 12c.3b and 12c.3c respectively. When a flexible blade is rigidly clamped, its position given by the coordinates x_c and y_c at the clamp and the slope β_c at the clamp must be prescribed:

$$\frac{dx}{ds} = \cos\beta_c, \quad \frac{dy}{ds} = \sin\beta_c, \quad x = x_c, \quad y = y_c$$

When the edge of an elastically deformable member is pinned along a line but free to rotate along that line, as is approximately the case for the membrane wrapped around the holder in membrane coating, the boundary conditions are:

$$\kappa = 0, \quad x = x_p, \quad y = y_p$$

The first condition expresses that, due to unconstrained rotation, there is no clamping moment. At a free edge of a trailing blade, there is no bending moment nor any tension or normal load and, hence, the boundary conditions are

$$\frac{d\kappa}{ds} = 0, \quad \kappa = 0, \quad N = 0$$

When two elastically deformable members are in contact, as is the case for the trailing film wrapped around the inflated membrane in

membrane coating, the force and momentum balances that govern each are coupled via a set of conditions that describe the contact mechanics. The simplest approach is to assume that the two members can freely slide over one another without any friction, as discussed by Pranckh and Scriven (1989b). Special attention must be paid to the end points of contact zones where two elastically deformable members join or part. At such points, a concentrated force of reaction gives rise to a jump, or discontinuity, of $d\kappa/ds$ or, equivalently, Q for both members. This must be accounted for with a special set of end point conditions (for details, see Pranckh and Scriven (1989b)).

The tangential and normal load distributions P_t and P_n in equations (12c.12) can have contributions from both hydrodynamic forces and from externally imposed forces such as the loading that a pressurized air hose exerts on a coating blade, viz.,

$$P_t = El T_{nt} + P_{t,ext}$$

$$P_n = El T_{nn} + P_{n,ext}$$

Here, El is the elasticity number, $El \equiv \mu UL^2/D$, and $P_{t,ext}$ and $P_{n,ext}$ are additional distributed external loads, measured in units of D/L^3 ; T_{nt} and T_{nn} are the tangential and normal traction components as defined at equations (12c.1).

Equations (12c.12) and (12c.13) or equivalent forms were used by Saita and Scriven (1985) and Pranckh and Scriven (1990) with the Reynolds equation to describe blade coating; by Shibata and Scriven (1986) with the full Navier–Stokes equations to describe tensioned web slot coating; by Pranckh and Scriven (1988) with the Navier–Stokes equations to describe high-speed blade coating; and by Pranckh and Scriven (1989a,b) with the Reynolds and the Navier–Stokes equations to describe membrane coating.

12c.3 FLEXIBLE-BLADE COATING

In flexible-blade coating, introduced already in Section 12c.1 above, a liquid film of controlled thickness is metered onto a moving, roll-supported substrate by means of a blade that is loaded

against an over-supply of liquid applied upstream (see Fig. 12c.1a). Flexible-blade coaters are most commonly used to apply mineral pigmented, latex, or functional coatings onto paper at very high speeds. Chapter 12d focuses in depth on this particular industrial application, whereas this section is limited to describing the elastohydrodynamic mechanisms of flexible-blade coating in detail. Other examples of the use of flexible blades in liquid film coating come from the doctoring elements in gravure and roll coating; these are discussed further in Section 12c.8 and Chapter 12a respectively.

The central component in all flexible-blade configurations is the coating or metering blade, which can range from easily bent plastic strips to fairly stiff spring-steel plates. Typical steel blades are 0.25 to 0.5 mm thick and 20 to 100 mm long. External loading can be applied in several ways. Simplest is to pivot the blade about the clamp to a working angle ϕ_w which is larger than the initial installation angle ϕ_0 at which the tip of the undeflected blade first touches the substrate: see Fig. 12c.4. Alternatively, the blade can be

loaded with an air bladder or hose that is mounted in a rigid holder and positioned against the blade away from the clamping point. Controlling the bladder or hose pressure sets the external loading $P_{n,ext}$. The air hose can also be replaced with bar or fulcrum that is loaded mechanically or pneumatically to deliver a controllable normal force $F_{n,ext}$ per unit length in the cross-web direction at a fixed distance s_F from the clamping axis. Figure 12c.4 illustrates the latter two loading configuration schematically. Yet another loading method is to press the blade against a fixed stop, which acts as a secondary pivot axis as the entire blade holder is translated and forces the blade tip against the substrate (Sommer *et al.* 1987; Nakazawana *et al.* 1987; Akesson and Olsson 1988). The feed system in a blade coater can be a dip-coated applicator roll positioned upstream of the blade coating station, a confined feed box (often referred to as 'fountain applicator' – see Chapter 12d), or simply a puddle feed between the blade and the moving substrate.

The key strength of blade coating is its capability

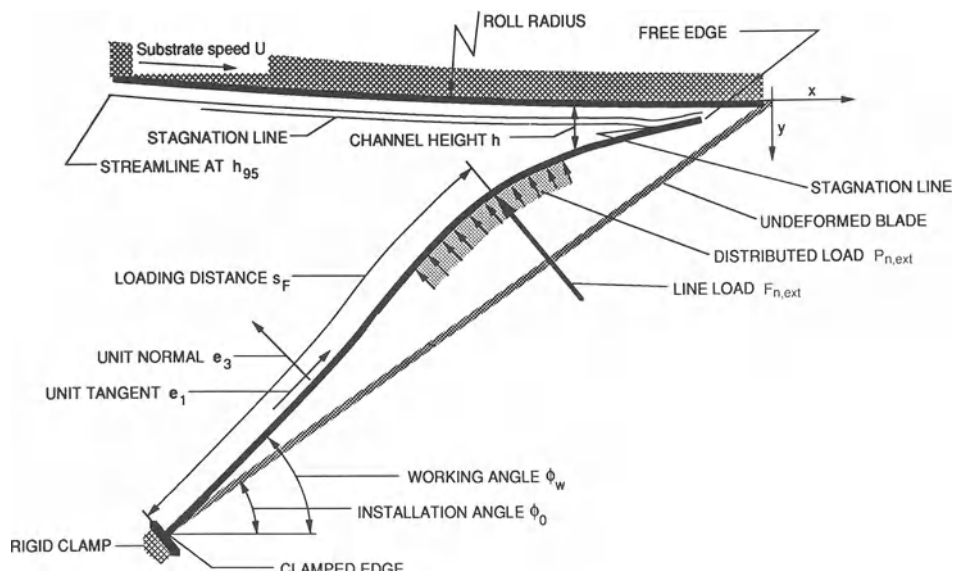


Figure 12c.4 Schematic of flexible-blade coater, including geometric parameters and loading variables needed for modeling blade deformation and flow (see text for further explanation of the variables).

to lay down fairly thin layers at very high speeds. In paper coating, for instance, speeds can be in excess of 10 or even 20 m/s, with viscosities of 0.05 to 20 Pa s and wet coating thicknesses of 15 to 150 μm being typical (*cf.* Chapter 12d). The main weakness of blade coating is related to the tendency of particles to get trapped under the blade, thereby producing streaks or scratches. The resulting coating flaws can limit the usefulness of blade coating for demanding precision coating applications. Nevertheless, special configurations of flexible blades are used with great success to smooth the overall uniform but locally patterned coatings of magnetic suspensions or viscous adhesives metered onto a substrate by means of a gravure roll.

12c.3.1 BLADE COATING ACTION AND OPERATING RESPONSE

Blade coaters can operate in two distinct regimes. In the so called stiff-blade, beveled blade, straight-blade or trailing-blade regime – which is the most common mode of operating a high-speed coater for particulate suspensions in the paper industry – the metering blade in its mounting is deformable but its angle of attack remains rather high. In this regime, the metered film thickness is dominated by the dynamics in the immediate vicinity of the blade tip. The ultimate limit where the metering blade is practically rigid, often encountered in household and laboratory spreading applications, is of course the same as the knife coating discussed in Chapter 12a. On the other hand, in the so called flexible-blade, low-angle-blade, or bent-blade regime, the blade is quite highly flexed and more or less conforms to the substrate over an extended region, which controls the elastohydrodynamic response of the blade coating system.

Much of the older literature on blade coating postulates *a priori* that the blade operates in one or the other of these two regimes. However, whether a blade should be classified as ‘stiff’ or ‘flexible’ depends not only on its flexural rigidity as given by its elastic properties and thickness, but also on the way the blade is mounted and

loaded, and the strength of the hydrodynamic forces.

Motivated by observations of Munter (1981) and Eklund (1984), Saita and Scriven (1985) were the first to elucidate, from first principles, that there is a continuous progression from stiff-blade to flexible-blade coating. That progression gives rise to a characteristic non-monotonic operating curve for coating thickness as a function of blade loading, as shown in Fig. 12c.5 and to be explained in more detail below. Saita and Scriven’s (1985) insights are based on a finite-element analysis of elastic bending and viscous flow in flexible-blade coaters operating at moderate speeds and low blade angles. In this regime, the hydrodynamic action in blade coating is often dominated by viscous lubrication effects, as described by the Reynolds equation (12c.2). If the coating speed is high and the angle of attack of the blade is large, inertia effects can give rise to significant impact pressures that can be understood in terms of inviscid flow theory. Chapter 12d discusses this regime at great length (see also Kahila and Eklund (1978) and Pranckh and Scriven (1988)).

The elastohydrodynamic action in a blade coater is as follows (Saita and Scriven 1985). The moving substrate, supported by a back-up roll, carries liquid into the wedge-shaped region between the blade and the substrate, causing the lubrication pressure to rise. The resulting adverse pressure gradient induces a flow component that opposes the flow driven by viscous drag from the moving substrate, and much if not most of the liquid supplied to the blade is rejected. Only a small fraction passes through the narrow gap between the blade and the substrate to become the coated layer. By necessity, rejected and coated liquid are separated by a stream surface that terminates at a stagnation line on the blade (for a schematic representation, see Fig. 12c.4). Both hydrodynamic pressures and viscous shear stresses act as loads on the blade and deform it elastically. The configuration of the deformed blade changes the shape of the flow passage, which in turn alters the flow field and the hydrodynamic pressure and the viscous stresses

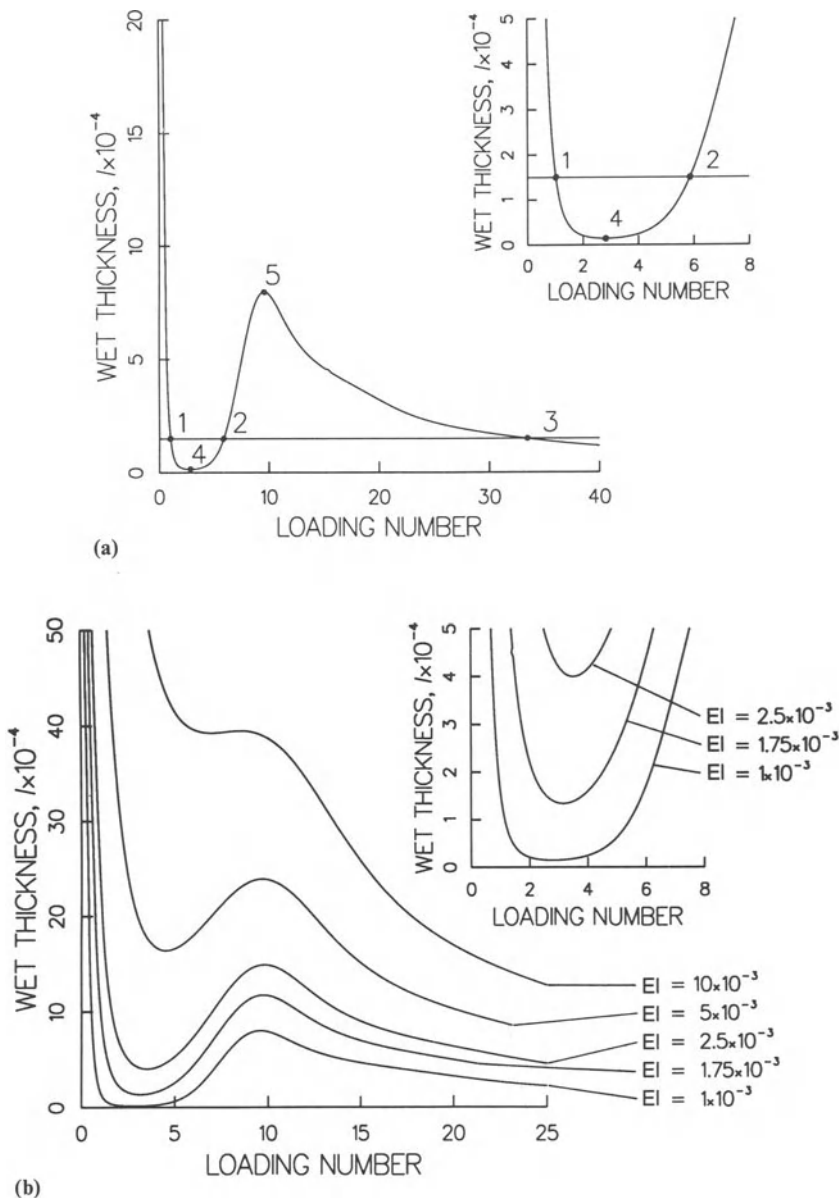


Figure 12c.5 Operating response of a flexible-blade coater: (a) characteristic curve of coating thickness versus blade loading ($EI \equiv \mu UL^2/D = 10^{-3}$); (b) effect of elasticity number on characteristic response curve (for a complete listing of all the design and operating parameters, see Pranckh and Scriven (1990)).

in it – resulting in a quintessential elastohydrodynamic interaction. In an equilibrium operating state, the blade-internal restoring forces that result from the elastic deformations, together

with any externally applied loads, balance the hydrodynamic pressure and the viscous shear stress on the blade. This balance controls the amount of coated liquid that passes under the

blade. Thus, for a given speed and viscosity, the final coating thickness is readily adjusted by changes in blade stiffness, blade mounting and positioning, and external blade loading.

When the external load on a deformable blade is first increased past the point of initial contact with the liquid-laden substrate, the coating thickness falls abruptly. Figure 12c.5a illustrates this behavior for a blade with a fixed clamp installed at 15° and a normal load $F_{n,\text{ext}}$ applied at a distance of $0.65 L$ from the clamp. Here, L is the blade length, and the dimensionless loading parameter used in the figure is $F_{n,\text{ext}} L^2 / D$, where $D \equiv E\delta^3 / [12(1 - \nu^2)]$ is the bending stiffness as defined in Section 12c.2 above. The initial decay of the wet coating thickness is so rapid because, at low loads, the blade deflects little and the hydrodynamic pressure forces concentrate very close to the blade tip where the flow channel between the blade and the substrate needs to tighten to build the pressures necessary to compensate for a higher external load. As the load increases further, however, the blade deforms more and more, expanding the range of the narrow flow channel that contributes to the buildup of hydrodynamic lubrication pressure. Eventually, the net load from hydrodynamic pressure increases more rapidly than the external load, giving rise to a minimum in wet coating thickness and a subsequent, seemingly counter-intuitive increase of coating thickness with higher blade loads. In this regime, the slope of the flow channel near the blade tip continues to decrease, and the pressure peak broadens and shifts upstream, i.e. away from the blade tip. Eventually, the blade deforms so much that the portion close to the tip is nearly parallel to the substrate, reducing the pressure forces around the tip. This gives rise to the maximum in the coating-thickness versus load curve (point 5 in Fig. 12c.5a). Past the maximum, the blade tip forms a diverging flow channel with the moving substrate. In this flow geometry, hydrodynamic pressure oscillates close to the blade tip and can become sub ambient, possibly pulling the blade toward the substrate.

Because the operating curve is non-monotonic, different blade loadings can, of course, give rise

to the same coating thickness. In Fig. 12c.5a, for example, a wet coating thickness of $h_w = 1.5 \times 10^{-4}$ (measured in units of blade length L) can be produced with loading numbers of 1.02, 5.85, or 33.4. These are marked as points 1–3 in the figure. With a 40 mm long, 0.381 mm thick steel blade at a line speed of 13.33 m/s and a 50 mPa s liquid, the wet thickness would be 6 μm and the three line loads F_N would be 680, 3900 and 22300 N/m, applied here at 14 mm from the tip of the blade.

The extrema in the operating curve mark the boundaries between the operating modes of the blade. Point 4 in Fig. 12c.5a divides the stiff-blade mode, or beveled-blade mode, to the left from the flexible-blade mode, or bent-blade mode, to the right. The region from the minimum at point 4 to the inflection in the vicinity of point 2 is sometimes called the intermediate region. The term bent-blade mode is often reserved for the region to the right of the inflection, and highly bent-blade for the region to the right of the maximum at point 5.

For practical applications, it is important to know the mode in which the blade operates, because of the different response to changes in blade loading. For a blade operated in the beveled mode, small errors in the blade-to-roll alignment or small variations in cross-web load distribution can have pronounced effects on the cross-web coat weight distribution because the coating thickness is so sensitive to blade coating. In the bent-blade mode, in contrast, deficiencies in blade alignment or load distribution have less pronounced effects on the cross-web coating uniformity because the increase and subsequent decrease in coating thickness require more substantial increases in blade loading.

In the bent mode, the details of the blade-tip shape can also have a significant effect, for the blade tip itself becomes part of the narrow flow channel between the blade and the substrate. This effect was not accounted for by Saita and Scriven (1985), but was included in a follow-up analysis by Pranckh and Scriven (1988) (see also Chapter 12d). Another coating configuration in which the tip geometry of a deformable blade is

all important is that of a reverse-angle doctor blade, i.e. a blade with an angle of attack larger than 90°. This setup is quite common in situations where complete wiping of a roller surface is desired, such as in reverse-roll coating, gravure coating, or rotogravure printing (e.g., Weiss (1985)), but no rigorous elastohydrodynamic analyses have appeared in the published literature. In either the beveled mode or the reverse-angle mode, blade-tip wear can be significant and can alter blade coater performance over time.

Changing from one blade operating regime to another can also have a substantial effect on the amount of liquid driven into a porous substrate, such as paper. For the example given in Fig. 12c.5a, the total pressure load P_s that acts on the substrate rises from 570 dimensionless units in the beveled mode to 3180 in the bent mode, and climbs to 27100 in the highly bent mode. This illustration suggests that the pressure driving force for penetration into a porous substrate would be nearly nine times greater in the highly bent mode than in the bent mode.

The distribution of average shear along the blade reveals further differences between the flow regimes (Pranckh and Scriven 1990). In the beveled mode of the example given in Fig. 12c.5a, nearly all of the shear is concentrated close to the blade tip. The total shear strain suffered is 107 dimensionless units. In the bent mode the shear distributes more evenly, the maximum in average shear shifts upstream, and the total shear suffered mounts to 236. In the highly bent mode the last quarter of the blade is nearly parallel to the substrate, the average shear rises to a maximum at 70% of the total blade length and decreases little from there to the blade tip, so that the total shear climbs to 2110.

12c.3.2 SENSITIVITY TO BLADE DESIGN, INSTALLATION AND OPERATION

The characteristic operating curve of a blade coater is quite sensitive to the value of the elasticity number, $El \equiv \mu UL^2/D$. This is illustrated in Fig. 12c.5b, again for a blade with a fixed

clamp installed at 15° and a normal load F_n applied at a distance of 0.65 blade lengths from the clamp (Pranckh and Scriven 1990). At elasticity numbers above a certain value (10^{-2} for the example in Fig. 12c.6), the coating thickness is rather high and its operating response to increasing load becomes monotonically decreasing. On the other hand, toward lower elasticity numbers, i.e. smaller viscosities, lower speeds or stiffer and shorter blades, the coated films become thinner and the extrema in the operating curve become more pronounced. In particular, near the minimum, the wet film thicknesses can become extremely thin, amounting to a nearly complete wiping by the stiff blade (see inset in Fig. 12c.5b).

Reductions in coating thickness can also come from shifting the external blade load toward the blade tip, or increasing the initial blade installation angle (Pranckh and Scriven 1990). Both changes reduce the distance between the normal force load and the blade tip, where viscous forces concentrate, and hence have the same effect as shortening and stiffening the blade. Decreasing the radius of the substrate-wrapped back-up roll also can decrease the coating thickness, but the effect is significant only for radii less than two blade lengths (Pranckh and Scriven 1990). The reduced roller radius steepens the wedge between the blade and the substrate close to the blade tip, which has an effect similar to that of increasing the installation angle.

Alternative blade mounting and loading mechanisms can also influence the final coating thickness for a given blade speed, viscosity and blade length and stiffness, but do not change the characteristic operating response (Saita and Scriven 1985; Pranckh and Scriven 1990). Pivoting the blade about its clamp induces an external torque at the blade clamp. Elastic restoring forces, which are internal reaction forces induced by the blade deformation, transmit the torque along the blade to the regions of high hydrodynamic pressure and high wall shear. Increasing the working angle leads to an operating curve that is similar to that of increasing the normal force loading of a blade with a normal force loading mechanism (Pranckh and Scriven

1990). In the beveled mode in particular, the differences in operating curve are small because the blade remains nearly straight and thus the moment of the normal force about the clamp is equivalent to the external torque applied at the clamp. In the bent and highly bent modes, on the other hand, blades loaded by an external torque at the clamp deform more in the upstream half as they transmit the torque from the clamp to the regions of high viscous forces downstream. Thus the pivoting mechanism, while effective at low loadings, is not as effective as normal force loading closer to the tip in the bent and the highly bent modes (Pranckh and Scriven 1990).

12c.3.3 COATING OPERABILITY AND UNIFORMITY

Once the characteristic operating response is understood, a flexible-blade coater is fairly simple to set up, operate and control. Also, unless the blade is very stiff and operated near the minimum in coating thickness, it is unlikely to fail completely in putting down some layer of liquid on the substrate. Still, flexible-blade coating can suffer from several instabilities that can seriously degrade coating uniformity. For instance, if a puddle of liquid occupies part of the wedge region instead of a turnaround flow that cleanly rejects the excess liquid supplied to the blade, the resulting rotating flow is susceptible to instabilities, in particular break-up into cells in the cross-web direction that can cause down-web striations. This sort of coating flaw has been investigated most thoroughly in the context of high-speed paper coating (Chapter 12d). If improperly shaped, installed, or loaded, flexible coating blades are also prone to cause ribbing. In the stiff or beveled blade-coating mode, ribbing can occur when the beveled edge at the blade tip is at the wrong angle and forms a diverging flow channel with the substrate. In the highly bent mode, ribbing arises when the blade is bent so much that its extremity near the tip forms a diverging section with the substrate wrapped around the curved back-up roll. In either case, at sufficiently high speeds, more chaotic instability modes take over,

including cavitation (Eklund 1984). These can even eject liquid from the blade tip (*cf.* Chapter 12d).

Flexible-blade coating is also quite prone to cause coating defects. Its propensity for streak formation in particular is perhaps the primary reason why simple blade-coating configurations are not used more often for demanding precision coating application – in spite of their flexibility and low cost. Streaks possibly originate from particles or bubbles trapped in recirculating flows on the upstream side of the blade. Saita and Scriven (1985) linked streaking and scratching defects in coating of shear-thinning suspensions to the region around the stagnation line (*cf.* Fig. 12c.4) where shear rates are small and shear-thinning viscosities are high. They contend that close to the stagnation line particles can get trapped, which leads to streaks, and suspensions can form particle aggregates, which leads to coating defects if aggregates get dislodged and the shear they suffer downstream does not suffice to break them up. In the bent mode, the stagnation line is away from the blade tip and the coated liquid is subsequently subjected to prolonged shear which may break-up dislodged particle aggregates. In the beveled mode, in contrast, the stagnation line is very close to the blade tip and downstream of the stagnation line the liquid is scarcely sheared at all. This is presumably why the beveled mode is more susceptible to streaks. Another reason may be that a blade in the beveled mode is more susceptible to irregular and erratic wetting past the tip which, in either mode, could also induce striations and streaks.

12c.4 MEMBRANE COATING

In membrane coating, also known as hydro-pneumatic coating (Pipkin 1986), a thin, uniform liquid film is metered by a highly flexible sheet, or membrane, that is bent round to form a sector of a cylinder and is pressurized pneumatically to force a compliant trailing wiper against the liquid to be coated, as described in Section 12c.1 above. This simple, yet surprisingly effective coating configuration seems to have evolved in parallel in two different industries. For magnetic media

coating, Pipkin (1982a,b) started from an applicator that consisted of a wiping film equipped with a loading mechanism (Eichler and Brueck 1972) to develop a practical membrane coater that can even be adapted for simultaneous two-sided coating (Pipkin 1982b, 1984). For coating suspensions of clay and other materials on paper, meanwhile, Taylor and Fridhandler (1985) modified a conventional blade coater loaded by a pressure hose by substituting a thin plastic film for the stiff blade.

The key components of a membrane coater, shown in Fig. 12c.1b, are an inflatable membrane with provision for pneumatic pressurization; a wiping film that wraps around the membrane and trails past it; a positionable mounting fixture that holds both the membrane and the trailing film; and a rigid back-up roll that carries and supports the coating substrate. On the upstream side of the membrane, the film may separate from the membrane and is then attached separately. The upper part of the trailing film together with the substrate from a wedge-shaped hopper into which the coating liquid is supplied, either with a simple feed pipe or a more sophisticated feed device (e.g., Pipkin (1983); Berdinner and Throckmorton (1984)). Not shown in Fig. 12c.1b are the end dams or other provisions that prevent the resulting liquid puddle from leaking out sideways and thereby maintain a certain coating width. Also not shown are the edges of the rigid holder that seal the pressurized membrane.

In comparison with other coating devices that must rely on precision machined parts, the strengths and weaknesses of membrane coating are quite similar to those of flexible blade coating (*cf.* Section 12c.3). A particularly attractive feature of the membrane configuration is that the liquid supply and distribution system is directly incorporated in the coater head assembly (see Fig. 12c.1b). Also, the membrane and trailing film are inexpensive and are fairly easily and quickly replaced. Moreover, the shearing strain to which the coating liquid is subjected can be increased or lessened merely by changing the length of the trailing film. This can be used to great advantage for achieving uniform coatings of suspensions

that are shear-thinning, for orienting nonspherical particles, and for breaking up weak flocs in a suspension. On the other hand, if the coating liquid degrades under prolonged shear, short trailing films may be required.

12c.4.1 MEMBRANE COATING ACTION

The basic action of a membrane coater is the elastohydrodynamic metering that takes place when the membrane is pressurized and forces a portion of the wiper film against the substrate which, in turn, is pressed against the rotating back-up roll. Pranckh and Scriven (1989a,b) (see also Pranckh 1989) have analyzed the elastohydrodynamics of membrane coating in some detail, and this entire section is largely based on their work.

Where the wiper film and the substrate converge, a wedge-shaped region forms that dominates the thickness of the liquid film coated downstream very much in the same manner as in blade coating (see Section 12c.3 above). As a result, the rate at which the liquid actually passes into the narrow passage between the membrane-backed film and rigid-roll-backed substrate depends primarily on the viscosity and possibly other rheological properties of the liquid, the speed of the substrate, and the pneumatic membrane loading which, together with the hydrodynamic loads, determines the shape of the converging wedge.

What is different from flexible-blade coating – and what causes a different operating response to increasing loading – is that the metering action in the converging wedge zone can be made independent of the flow features downstream. Depending on membrane pressurization and the membrane position, the membrane-backed film can conform to the rigid-roll-backed substrate over a sector of considerable length, as described in detail by Pranckh and Scriven (1989a). In this so-called contact zone, the channel height between the trailing wiper film and the substrate is nearly constant. If the contact zone is sufficiently long, a Couette flow establishes itself at a relatively constant, elevated hydrodynamic pressure that balances the membrane pressure. The contact

zone ends near the place where membrane curves back to its downstream attachment on the rigid holder. The trailing film conforms to the membrane over a short separation region over which the pressure falls to ambient. Downstream, the membrane and film split and the remainder of the trailing film adheres to the coated liquid layer. In this trailing film zone, the film is kept under tension by viscous drag transmitted through the liquid layer from the moving substrate.

12c.4.2 OPERATING BEHAVIOR

The operating behavior of the membrane coating process is quite simple, and makes for easy process control. Figure 12c.6 shows predicted and measured coating thicknesses as a function of elasticity number El at different membrane pressures. Elevated viscosities, higher coating speeds or more pliable membranes – which all increase the elasticity number – produce thicker coatings. So do more pliable wiper films. Toward higher elasticity numbers, the sensitivity of coating thickness to El diminishes. Increasing the pneumatic pressure load shifts the curves of coating thickness versus elasticity number to thinner coatings, but does not alter the monotonic character of the operating curves. Thus, in applications where a constant film thickness is desired, changes in speed or viscosity are quickly compensated with changes in air pressure, making for a robust and readily automated coating process.

The operating behavior of a membrane coater and associated control strategy can easily be understood by analogy with a lubricated slider bearing: in the case of constant inclination, the load carrying capacity of such a bearing rises as the lubricant thickness falls. In a membrane coater, this effect is advantageously adopted to lower the coating thickness by raising the air pressure load in the membrane (see Fig. 12c.6). The higher that pressure, the more the liquid pressure must increase in the converging wedge leading to the contact zone and, hence, the steeper the positive pressure gradient becomes. Therefore, a larger fraction of the liquid gets rejected and the coated layer becomes thinner.

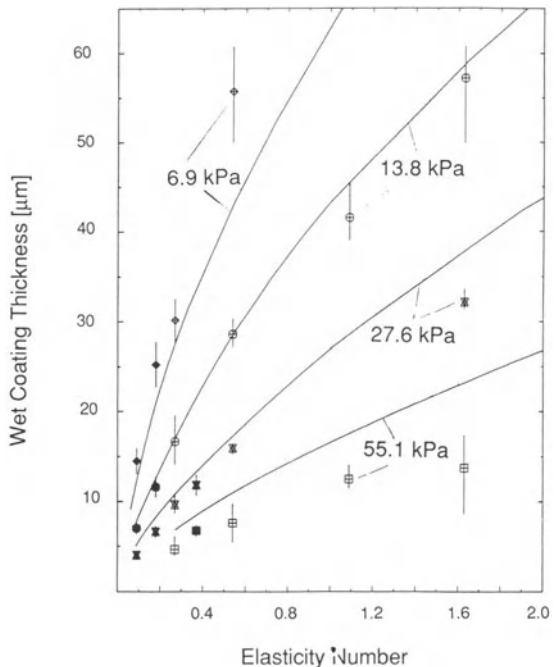


Figure 12c.6 Characteristic operating behavior of membrane coating: wet coating thickness versus elasticity number at different membrane pressures. The curves are theoretical predictions, the vertical bars connect the highest and lowest of three measured coating thicknesses, and the symbols indicate their average. The elasticity numbers $Es = \mu UL^2(1 - v^2)/E\delta^3$ is defined here with the unsupported arc length L of the membrane between its clamping points, the modulus E of the membrane, and its thickness δ (for a complete listing of all the design and operating parameters, see Pranckh and Scriven (1989a)).

Changing the position of the membrane holder with respect to the back-up roll alters the amount of engagement (i.e., the hypothetical interference of the undeformed, pressurized membrane and the back-up roll), but has little effect on the coating thickness, unless the engagement is so small that the liquid forces are too weak to deform the membrane substantially and make it conform to the curved shape of the back-up roll. In that case, the membrane acts more like a rigid metering element and coating thickness does become dependent on engagement (Pranckh and Scriven

1989a). Another exception arises when the substrate being coated is porous. In that case, the elevated pressure in the contact zone over which the membrane and the trailing film conform to the roll tends to impregnate the substrate with coating liquid by pushing the liquid into the pore spaces. The amount of impregnation depends, of course, on contact length. This length, in turn, is readily controlled by changes in membrane-to-roll engagement.

Changing the length of the trailing wiper film past the membrane also has little effect on the final coating thickness (Pranckh and Scriven 1989a). This finding is consistent with the notion that the elastohydrodynamic interaction in the converging wedge zone sets the coating thickness, as explained above. However, extending the trailing film lengthens the trailing film zone in which the liquid undergoes simple shearing flow and thus raises the total shear strain imparted on the liquid. Hence, if the final properties of the coated film depend on the total shear, they can be controlled independently of coating thickness.

12c.4.3 COATING UNIFORMITY AND OPERABILITY

A major attraction of membrane coating is its potential to generate uniform coatings (Pipkin 1982a,b; Pipkin 1984). Basic elastohydrodynamic concepts suggest that, where the flow channel converges more because of faulty applicator fabrication, substrate imperfections, or blemishes or debris on the back-up roll, the liquid pressure rises, causing the highly deformable applicator to widen the passage locally and to increase the flow rate there. The resulting more or less self-equilibrating action epitomizes the desired ability of elastohydrodynamic coating devices to compensate for less stringent mechanical tolerances than are typically built into rigid coating applicators. Pranckh (1989) (see also Pranckh and Scriven 1989b) attempted to quantify this action with a highly simplified model in which the membrane/film structure is approximated by linear two-dimensional plate theory. His preliminary results confirm that, for substrates with

down-web ridges of wavelengths substantially larger than the wet film thickness, a film of nearly uniform thickness can emerge, with the amplitude in thickness variations depending on elasticity number.

Even though the basic operating behavior of membrane coating is simple and the resilience to cross-web nonuniformities seems robust, the window of successful operation can be limited by several factors. For one, the dynamic wetting line at which the liquid in the pool must push away the air in contact with the moving substrate is quite unprotected and hence susceptible to massive air entrainment past a critical speed (the data given in Chapter 3 for the plunge-tank configuration probably provide a good first estimate for that speed). As in many other coating configurations, air entrainment may preferentially start at the edges where some sort of mechanical barriers delimit the pool in the cross-web direction and thereby put an additional restriction on practicable coating speeds. Depending on pool size and viscosity, the maximum coating speed may be further limited by inertia-driven pool-flow instabilities similar to those seen in so-called short-dwell applicators used for high-speed paper coating (Aidun 1990) (see also Chapter 12d). Such instabilities cause a segmentation of the recirculating flow in the pool into three-dimensional cells. These, in turn, are prone to cause down-web striations of coating nonuniformity (Triantafillopoulos and Aidun 1990). The recirculating flow in the pool may also allow suspensions to flocculate or agglomerate, and volatile solvents to evaporate from quiescent parts of the free surface. The resulting, unwanted concentration of inhomogeneities may intermittently be entrained by the liquid being coated and cause unacceptable coating defects. A membrane-coated liquid film may even be susceptible to the ubiquitous ribbing instability because, toward the trailing edge of the wiper film, the pressure gradient can be slightly positive (Pranckh and Scriven 1989b) (for a detailed discussion of the ribbing instability in general, see Chapter 12a). A further limit on the practical applicability of membrane coating may be related to difficulties in coating very thin

liquid layers, associated for instance with inordinately high membrane pressures needed to overcome the hydrodynamic lubrication pressures, or with abrasive wear and scratching from particulate-filled coatings.

12c.5 TENSIONED-WEB ROLL COATING

As previewed in Section 12c.1, the essence of tensioned-web roll coating, often also called kiss coating, is the elastohydrodynamic transfer of part or all of a liquid film from a rotating applicator roll onto a moving web that ‘kisses’ the roll without back-up support. Figure 12c.1c shows the roll running in a forward mode, but a kiss coater can also be operated in a reverse transfer mode. The positioning of upstream and downstream idler rolls (not included in the figure) controls the angle over which the substrate wraps the applicator roll, usually between 5° and 15° (Grant and Satas 1984). Common applications include adhesives, hot melts, and silicone coatings on paper and plastic film (Booth 1970; Zink 1979; Grant and Satas 1984). Compared with other roll coating configurations – which typically require expensive mechanisms accurately to maintain a close gap between two high-precision rolls and, at a given gap, are limited to a rather narrow range of coating thickness (*cf.* Chapter 12a) – a primary attraction of kiss coating is its simplicity. In lieu of the gap, web tension and wrap angle provide readily adjusted control variables in kiss coating. They allow successful operation over wide parameter ranges, especially for coating thickness. Standard handbooks suggest speeds up to 5 m/s with viscosities between 50 and 1000 mPa s and wet coating thicknesses as low as 25 µm (e.g., Zink (1979); Grant and Satas (1984)). A potentially serious drawback of tensioned-web roll coating, on the other hand, is that the unsupported web becomes part of the metering device. Hence, variations in web characteristics, such as its thickness or stiffness, or web instabilities, such as flutter or buckling, tend to degrade coating uniformity.

In spite of its simplicity and practical importance, tensioned-web roll coating has received

curiously little attention in the published literature. For that reason, only a sketchy overview of the operating principles can be given in what follows.

The elastohydrodynamic interaction between the tensioned web and the viscous liquid film determines the height at which the web floats above the coating roll. An estimate for that height can be found in the literature for so called foil bearings in which a thin flexible film replaces one of the (nearly) rigid components of a conventional bearing, forming an elastohydrodynamic system very similar to a kiss coater. Foil bearings have been studied extensively, as summarized by Gross (1980). Practical applications include, for instance, magnetic recording devices in which the magnetic tape is the moving foil and the recording/playback head acts as the shaft or roll. Foil bearings are also a common occurrence – and possibly a nuisance – on web lines where, at sufficiently high speeds, the web can become ‘air-borne’ on smooth idler rolls. The characteristic regions in foil bearings and in tensioned-web roll coaters are in essence the same: a wedge shaped entrance zone that constitutes a high pressure-gradient metering zone, as explained for a blade coater in Section 12c.3 above; a constant channel zone of Couette flow at an elevated pressure; and an exit zone. In kiss coating, of course, the flow in the entrance and exit zones is complicated by the presence of a meniscus which could possibly have some influence. Eshel and Elrod (1965) calculated the constant channel height H for a perfectly flexible foil bearing as

$$H = 0.64 R \left(\frac{6\mu U}{T} \right)^{2/3} \quad (12c.14)$$

where R is the roll radius, U the foil speed, μ the fluid viscosity, and T the foil tension. In 12c.14, the influence of bending stiffness of the foil is taken to be negligible. With rising stiffness, the internal stresses in the direction normal to the foil start to carry some of the load (*cf.* equation (12c.12)), lowering the constant floating height H . However, the effect typically is small (Gross 1980).

Given the lack of more refined models that account for the details of the free-surface flows

at the inlet and outlet, the simple relation (12c.14) furnishes at least a leading-order estimate for the lubricating film thickness between web and roll in a tensioned-web roll coater, provided the angle of wrap is sufficiently large to allow for a constant-channel zone between the inlet and outlet regions. As is to be expected for an elastohydrodynamic coating system with given geometry, the film thickness is set by the competition between viscous pressure forces, μU , and mechanical restoring forces, in this case primarily the normal resultant from the externally imposed web tension T (in 12c.14, variations in the tangential shear resultant N due to viscous shear tractions are taken to be negligible). In the case of kiss coating, both the foil and the roll are moving, and the speed that enters (12c.14) is $U = U_{\text{web}} + U_{\text{roll}}$, i.e., the sum of the web and roll speed. In either the forward or the reverse mode, the thickness of the coated film that is metered through the contact region between the web and the roll is closely linked to the floating height H via the linear Couette velocity profile between the two moving surfaces. A noteworthy special case arises for reverse kiss coating at a speed ratio near 1:1 for which, according to equation (12c.14) the floating height and hence the metered film thickness tend toward zero. This result provides a simple explanation for why a reverse kiss coater can be used to transfer a liquid film completely from a smooth roll to a web while wiping the roll almost perfectly clean, as mentioned by Grant and Satas (1984).

It is to be expected that kiss coaters have several operating limits. For one, there are practical limits to the web tension T that can be applied, which limits the minimum coating thickness for a given liquid and a given line speed, in particular in the forward mode. Also, tensioned-web roll coating most likely suffers from some of the same instabilities as conventional rigid roll coating (*cf.* Chapter 12a), but little has been documented in the open literature. Ribbing, for instance, is probably equally prominent, especially in forward kiss coating; and reverse kiss coating must exhibit some sort of ‘cascade’ instability. Tensioned-web roll coating is furthermore sus-

ceptible to additional instabilities related to flexibility and deformability of the substrate. Pearson (1985) investigated the stability of the liquid flow in forward kiss coating. He approximated the web as perfectly flexible, accounting only for the tangential stress resultants in equation (12c.12). He described the flow with the lubrication approximation, imposing ambient pressure and an *ad hoc* approximation to the film split as boundary conditions. For stream-wise disturbances in the inlet zone, he calculated an amplification factor of

$$e^{-\frac{THk\phi R}{12\mu Uv}}$$

where ϕR is the length of the constant gap zone, and k and v are the real wavenumber and the wave speed of the disturbance respectively. According to Pearson’s result, disturbances in the machine direction introduced in the inlet zone are always damped. For cross-web disturbances, in contrast, Pearson (1985) found an appreciable positive amplification factor, i.e., cross-web disturbances grow with distance downstream.

12c.6 TENSIONED-WEB SLOT COATING

In tensioned-web slot coating, a liquid film is metered out of a slot of a coating die onto a web in free span between two idler rolls (see Fig. 12c.1d). The web is wrapped around at least the downstream lip of the die, forming an elastohydrodynamic system with a viscous coating layer between the die lip(s) and the web.

Tensioned-web slot coating shares many similarities with tensioned-web roll coating discussed in Section 12c.5 above, for it merely replaces the applicator roll with a slot-coating die. The main advantage of the die over the roll is that the liquid distribution system is fully enclosed and the final coating thickness is set by the liquid supply pump to the die, as in other pre-metered coating systems.

Tensioned-web slot coating is also very closely related to conventional slot coating, discussed at length in Chapter 11a. A major advantage of

tensioned-web slot coating over standard slot coating is the simplicity of the overall setup: there is no precision back-up roll, nor is there a need for a vacuum system to stabilize the coating bead. Moreover, the positioning of the die with respect to the web path can be considerably less precise. Instead of the narrow gap between a slot-coating die and the back-up roll – which must be pre-set and maintained with tight tolerances – the clearance between the web and the die lip that is necessary to coat a certain film thickness is automatically accommodated by the elastohydrodynamics. Changes in tension, angle of wrap, and possibly even lip design may be necessary to cover wide ranges of film thickness, viscosity, or speed but, if judiciously managed, allow for thinner coatings and higher speeds than may be feasible with conventional slot coaters. Tanaka and Noda (1984), for instance, claim to have achieved coating speeds of 5 m/s for dry coatings only 5 µm thick whereas, with a conventional slot coater for the same liquid, the minimum thickness was 20 µm and the maximum speed 1.7–2.5 m/s. The main disadvantage of tensioned-web slot coating is similar to that of tensioned-web roll coating: the web becomes part of the coating device and any nonuniformity, tension variation, vibration, or instability in the web directly translates into poor coating uniformity.

Tensioned-web slot coating devices have been in use for quite some time for less demanding applications (e.g., Van Guelpen (1946)), but have more recently achieved prominence for precision coating, especially of magnetic tapes and diskettes (e.g., Pipkin and Schaefer (1979); Tanaka and Noda (1984)). Very recently, tensioned-web slot coating technology has been extended to allow simultaneous deposition of two or more layers (e.g., Chino, Hiraki and Sato (1988); Shibata *et al.* (1992)).

In relation to the large number of patent publications on tensioned-web slot coating, the patents and other published literature provide disappointingly limited insights into the elastohydrodynamic mechanisms at work. Shibata and Scriven's (1986) (see also Shibata *et al.* (1992)) finite-element analysis of a few selected case

studies, nevertheless, captures some of the essential design and operating considerations. For instance, the analysis shows how changes in web tension, which alter the normal resultant forces generated by the curved web, must be offset by changes in the liquid tractions. With increasing tension, the lubrication-flow pressures generated by the die lip downstream of the slot exit rise and the upstream free surface with its dynamic wetting line is pushed further upstream. Changes in the flexural rigidity of the web also considerably influence the pressure field, and resulting web deformation and upstream meniscus position. Likewise, changes in downstream lip design and the relative position of the two lips normal to the web have a significant effect. Tanaka and Noda (1984), for instance, claim that for the particular design shown in Fig. 12c.1c the angles between the points ABC and ABD and the distances AB and BC are of particular importance because they all control the pressure profile under the substrate from D to A.

Proper control of the position and shape of the upstream meniscus seems to be key to keeping the coating bead within the window of successful operation (Chino, Hiraki, Sato and Chikamasa 1988a; Shibata 1988). If the bead is starved, for example due to an insufficient pumping rate or too low a web tension, the meniscus with the dynamic wetting line is pulled downstream and triggers premature air entrainment. On the other hand, the bead swells if the pumping rate or the tension is too high, pushing the upstream meniscus, including the static contact line, well past the slot exit (e.g., point D in Fig. 12c.1d). Eventually, part of the liquid that is supplied to the die flows over and dribbles down on the upstream side of the die. A substantial part of the range between these two operating limits if not the entire range can presumably also be covered with relatively minor changes in the angle at which the incoming web arrives. In fact, careful control of that angle – and elimination of unacceptable web vibrations and instabilities – may be the crux to making a tensioned-web slot coater work: if the angle is too large, the bead starves and breaks up; if the angle is too

small, the bead flows over or, if there is insufficient flow supplied to the die, the upstream lip contacts and scars the incoming dry web.

The sensitivity of the tensioned-web slot-coating process to web tension suggests that cross-web tension variations can produce substantial coating thickness variations and even local coating failure. On the other hand, controlled tension variations could also be used to compensate for skewed cross-web flow profiles generated by the die manifold, as demonstrated by Chino *et al.* (1988b). These authors employed idler rolls that could be tilted by as much as 25 mm per meter width upstream and downstream of the coating head. Downstream of the coating head, another idler was tilted to cancel out the induced variation in tension across the web.

12c.7 SQUEEZE-ROLL COATING

The essence of any squeeze-roll coater is the deformable nip between two cylinders, one or both of which have an elastomeric covering. One version is illustrated in Fig. 12c.1e. Squeeze-roll coaters are widely used to apply waxes, hot melts, adhesives, silicone fluids, and the like onto paper or plastic films. Another common example is the size press on a paper making machine, which is used to impregnate the paper with water, binder and pigment. Speeds up to 6 m/s, viscosities in the range from 10 to 5000 mPa s, and wet coating thicknesses as low as 5 µm and as high as 100 µm are possible (Booth 1970; Zink 1979; Satas 1984). The main attraction of these coaters is that they are simple to operate and inexpensive. Some disadvantages are that the coating thickness is sensitive to viscosity and speed, and the coated layers exhibit a rough pattern that results from film-split instabilities (see Fig. 12c.2 above).

The mechanisms governing the metering action of the roll nip are in essence the same as those governing the elastohydrodynamic lubrication of bearings and gears (Dowson and Higginson 1966). Fluid is dragged into the nip by the moving roll surfaces through the action of viscosity, and as the geometry is converging the squeezing

action generates high pressures. These pressures cause elastic deformation of the roll surfaces, which alters the converging geometry and thus affects the hydrodynamic pressure. It is the relative balance of viscous pressure force and elastic restoring force that controls the flow in the nip. Compared with these forces, surface tension is insignificant in determining the flow rate and can be ignored for all cases but the rigid roll limit at low capillary number.

12c.7.1 NIP MECHANICS

There are two ways of operating a deformable nip – preset position (gap) or preset load (force). The first fixes the distance between the roll axes using mechanical stops, such that the distance between undeformed roll surfaces (gap) is specified (the gap can be negative). The load which tries to force the rolls apart is a function of the operating parameters. The second method of nip control is constant applied load (usually expressed as pli, pounds/lineal inch, or N/m). One of the rolls can slide towards or away from the opposite fixed roll, and is loaded either hydraulically or pneumatically up against the fixed roll. The gap between the rolls is now a function of operating parameters.

In a manner analogous to Section 12a.2.1 for the case of lubrication between two rigid roll surfaces, the elastohydrodynamic lubrication of two cylinders can be approximated by a cylinder loaded against a semi-infinite elastic half-space, where again we define an effective radius R_e (*cf.* equation (12a.2a)) and an effective plane strain modulus E_e

$$\frac{1}{E_e} = \frac{1 - v_1^2}{E_1} + \frac{1 - v_2^2}{E_2}$$

The competition between forces is quantified by two dimensionless parameters: the elasticity number and the load parameter,

$$El = \frac{\mu \bar{U}}{E_e R_e}, \quad Wa = \frac{W}{E_e R_e} \quad (12c.14)$$

The elasticity number is the ratio of viscous and elastic force, while the load parameter is the ratio of applied load (W) and elastic restoring force. For a constant gap operation, the load parameter is replaced by the geometric factor H_0/R_e , where H_0 is the gap between undeformed roll surfaces and takes on negative values for most cases of practical interest. The dependent variable of primary interest in coating operations is the flow rate through the nip. It is equal to the local gap between deformed roll surfaces at the point of maximum pressure, usually expressed as the dimensionless group H_m/R_e . Two other variables of interest are the pressure and gap profiles, $P(X)/E_e$ and $H(X)/R_e$, both as a function of the flow direction coordinate X .

There are two limiting behaviors which are helpful to understand. The first is the rigid roll limit, where hydrodynamic (viscous) forces dominate and elastic deformation is negligible so that the theory of Section 12a applies. The second is the elastic dry contact limit, where elastic forces dominate and hydrodynamic forces are negligible so that Hertz contact theory, or an improvement upon it, applies. The relative importance of hydrodynamic and elastic forces can be measured by a single dimensionless group g_3 , which is the ratio of the pressure generated hydrodynamically in the liquid film to the pressure to produce elastic deformation (Johnson 1985). The hydrodynamic pressure scale is derived from lubrication theory (see equation (12a.3)). As the gap can be expressed in terms of the load as $H_0 = 4.9 \mu \bar{U} R_e / W$ (Coyle 1992), the hydrodynamic pressure scales as

$$P_{\text{lub}} = \frac{W^{3/2}}{(\mu \bar{U})^{1/2} R_e} \quad (12c.15)$$

The pressure for dry contact can be approximated by Hertz's contact theory

$$P = P_{\max} \left(1 - \left(\frac{X}{A} \right)^2 \right)^{1/2}, \quad P_{\max} = \left(\frac{WE_e}{\pi R_e} \right)^{1/2},$$

$$A = \left(\frac{4WR_e}{\pi E_e} \right)^{1/2} \quad (12c.16a, b, c)$$

Thus the ratio of hydrodynamic to elastic pressure is proportional to

$$g_3 = \frac{W}{(\mu \bar{U} E_e R_e)^{1/2}} = \frac{Wa}{El^{1/2}} \quad (12c.17)$$

The rigid roll limit is $g_3 = 0$, while the dry contact limit is $g_3 \gg 1$.

In general, both hydrodynamic and elastic contributions must be accounted for. The flow in the gap between roll surfaces determines the pressure in the liquid which in turn enters the normal traction boundary condition for the equations governing the elastic deformation of the solid boundary, summarized in Section 12c.2. For infinitesimal deformation of a Hookean solid, the gap profile becomes

$$H(X) = H_0 + \frac{X^2}{2R_e} - \frac{2}{\pi E_e} \int_{-\infty}^{\infty} P(s) \ln \left| \frac{X-s}{s} \right| ds \quad (12c.18)$$

This can be combined with the Reynolds equation to get a single integral equation for $H(X)$ which can be solved numerically (Herrebrugh 1968). The solution depends on the single dimensionless parameter g_3 , and results in the dimensionless gap profile

$$\bar{h} = \frac{H(X)W}{R_e \mu \bar{U}} = \frac{H(X)}{R_e} \frac{Wa}{El} \quad (12c.19)$$

An accurate large- g_3 solution can be obtained if one assumes a nearly parallel gap profile combined with approximate analysis of the wedge-shaped inlet zone to give (Hooke and O'Donoghue 1972)

$$\bar{h}_m = 3.12 g_3^{0.8} \quad (12c.20)$$

where \bar{h}_m is the value of \bar{h} at the point of maximum pressure and thus the dimensionless film thickness. Equation (12c.20) agrees with Herrebrugh's solution for $g_3 > 1$. Later studies by Cudworth and Higginson (1976) and Hall and Savage (1988a,b) used improved numerical methods but did not note a significant difference in the results. A simple one-dimensional spring model has also been shown to give similar predictions (Coyle 1988b). Comparison with rigid roll theory of Chapter 12a (*cf.* Coyle (1988b))

shows that the low- g_3 limit gives $\bar{h}_m = 6.0$ if the Reynolds boundary condition is used, $\bar{h}_m = 0.0$ if the submerged boundary condition is used, $\bar{h}_m = 3.8$ if the high-capillary number numerical solution to the flow is used.

Another parameter which can be important is the thickness of the deformable cover of the rolls (L/R_e). If the surface deformations are of the same order of magnitude as the cover thickness, the contact width will be reduced, the load more concentrated, and the coating thinner. The relative importance of the cover thickness can be evaluated by calculating the Hertzian dry contact half-width (A in equation (12c.16c)). For example, consider a coater where $R_1 = R_2 = 10$ cm, and only one roll is rubber-covered. For soft covers, typical conditions would be $E = 1$ MPa and $W = 1750$ N/m (10 pli) so $A = 0.91$ cm. Typical roll cover thicknesses are 1.2 cm, so that the cover thickness should be important. Hooke (1986a) produced solutions of the appropriate equations over a wide range of loads and layer thicknesses by compiling and extending earlier results (Gupta 1976; Hooke 1977, 1986b). Jaffar (1990) produced similar results. Finite-element calculations of Coyle (1990) incorporated the effects of nonlinear finite deformation of the elastic solid layer, and gave a thickness dependence somewhat weaker than Jaffar's.

As roll covers for coating applications are typically made of rubber, which is a viscoelastic solid rather than a Hookean elastic solid, theory based on the latter may not be adequate in describing a roll coating nip. The dry rolling contact of viscoelastic solids has been investigated (Bapat and Batra 1984), but the only corresponding analysis for the lubricated contact so far attempted failed due to lack of numerical convergence at relaxation times much lower than those of experimental interest (Coyle 1990).

Results of finite-element calculations (Coyle 1990), which happen to be for the case of an elastic roll against a rigid one, can be used to show the details of the pressure and gap profiles. Figure 12c.7 shows such profiles for a constant load operation. At high load (low El , high g_3) there is an extended nearly parallel gap region

over which the pressure profile is nearly Hertzian. These are the classic elastohydrodynamic gap profiles first measured by Crook (1961a,b). If, at constant load, the viscosity or speed (contained in El) is increased (reducing g_3), the pressure in the inlet region increases and, as the area under each pressure curve is equal, the pressure in the central nip region falls. At the same time the rolls move apart and the inlet region takes on a less sharp gap profile.

The limiting cases for constant gap setting are different. Figure 12c.8 shows the pressure and gap profiles for two constant gap settings. At positive gaps, low values of El reduce to the rigid roll limit, while increasing El increases pressure and deformation of the roll surface. At negative gaps, the low El limit is dry contact, while increasing the viscosity or speed (increasing El) again increases the pressures and deformations.

12c.7.2 COMPARISON WITH DATA

Equation (12c.20) can be rearranged in terms of the operating variables as

$$H_m = 3.12(\mu\bar{U})^{0.6} W^{-0.2} E_e^{-0.4} R_e^{0.6} \quad (12c.21)$$

to give a dimensionally consistent theoretical prediction of coating thickness.

Several authors have performed experiments using constant force operation of the nip and Newtonian oils. The most extensive data are those of Smith and Maloney (1966), which can be correlated (in SI units) by

$$H_m = 4.0\mu^{0.64}\bar{U}^{0.58} W^{-0.34} E_e^{-0.35} R_e^{0.58} \quad (12c.22a)$$

but can also be correlated by

$$\bar{h}_m = 3.13 g_3^{0.71} \quad (12c.22b)$$

with a correlation coefficient of 0.997. Coyle (1988a), presented data which are significantly lower and can be correlated (in SI units) by

$$H_m = 4.1(\mu\bar{U})^{0.49} W^{-0.43} E_e^{-0.41} R_e^{0.42} \quad (12c.23)$$

but which can not be correlated in terms of \bar{h}_m

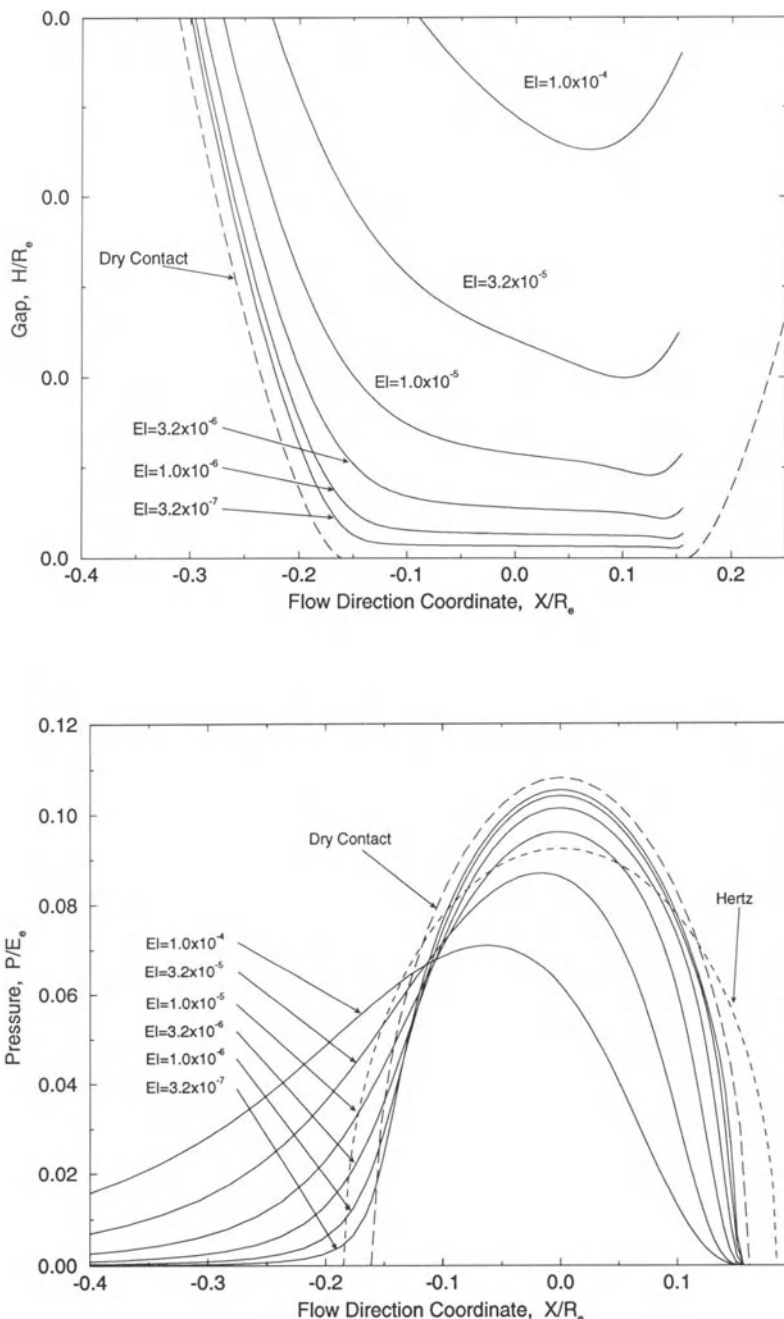


Figure 12c.7 Computed pressure and gap profiles in a squeeze-roll nip as a function of elasticity number at constant load. The dry contact limit is approached as El is decreased ($W = 0.0268$, $E_2/E_1 = \infty$, $R_2/R_1 = 1.67$, $U_2/U_1 = 1$, $L/R_1 = 0.167$).

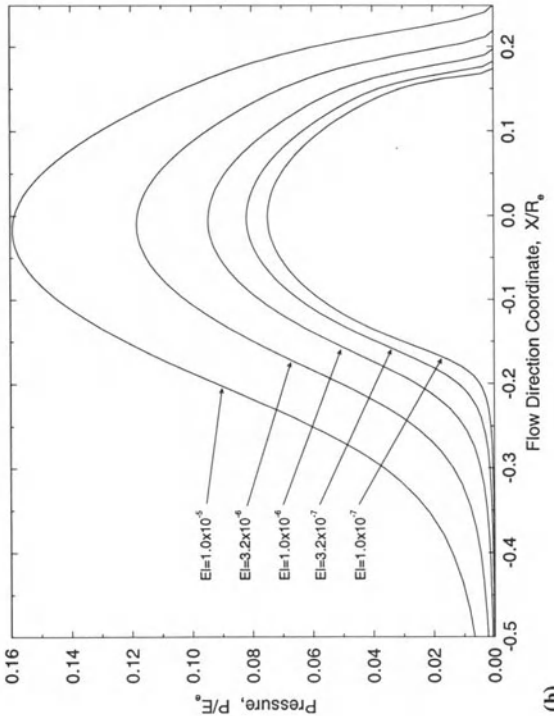
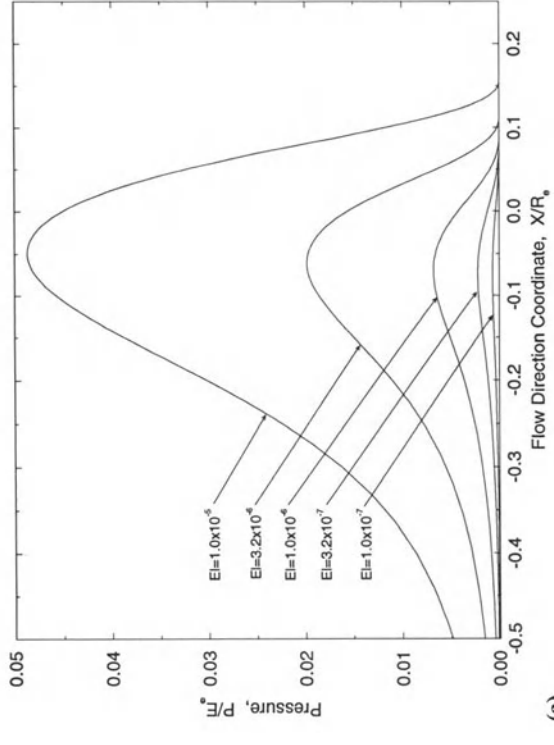
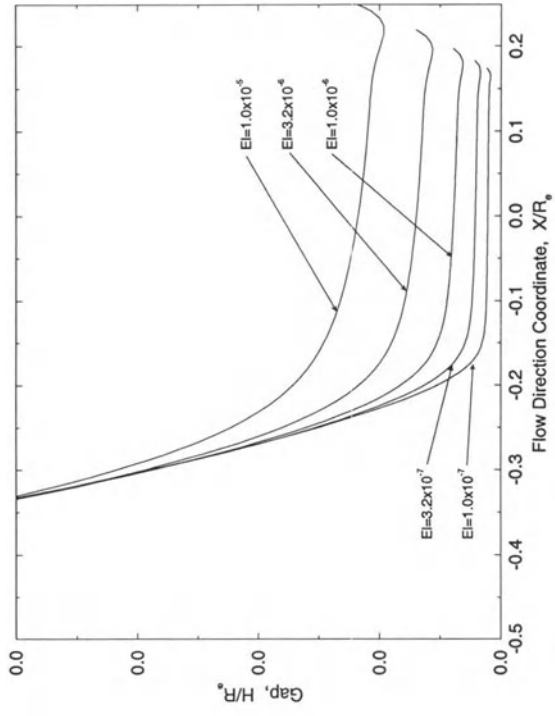
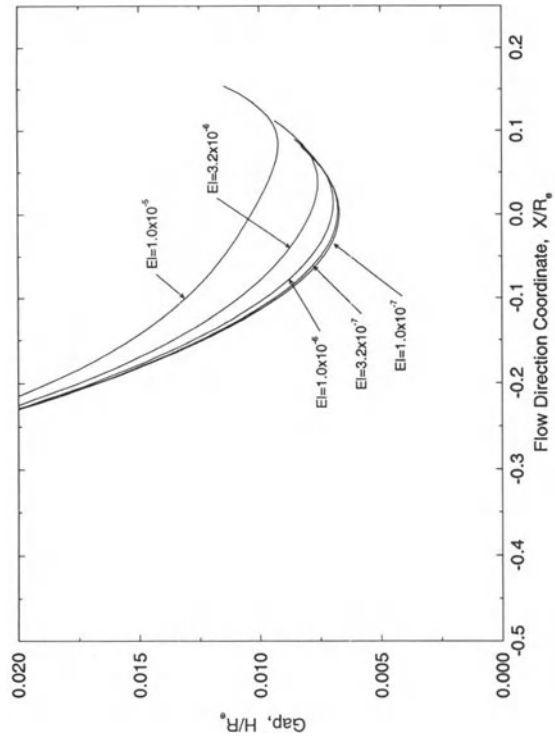


Figure 12c.8 Computed pressure and gap profiles in a squeeze-roll nip as a function of elasticity number at constant gap ($E_2/E_1 = \infty$, $R_2/R_1 = \infty$, $U_2/U_1 = 0$, $L/R_1 = 0.1$). (a) At positive gap settings, the rigid roll limit is approached as El is decreased ($H_o/R_1 = +0.033$). (b) At negative gap settings, the dry contact limit is approached as El is decreased ($H_o/R_1 = -0.033$).

versus g_3 nor as h_m versus Wa and El . The exponents in the correlations are all quite similar, indicating agreement in terms of the sensitivity of coating thickness to changes in the parameters. Varnam and Hooke (1977) and Swales *et al.* (1972) present limited data which also fall significantly lower than equation 12c.22.

Figure 12c.9 shows a direct comparison of results of finite element calculations (Coyle 1990) with some of the experimental data. The agreement between theory and data of Smith and Maloney (1966) is excellent. The data of Coyle (1988a) show the same sensitivity to viscosity, speed and load, but the coating thicknesses are lower. The latter data do not correlate with the three dimensionless groups available (Wa , El , L/R_e), indicating that there is another parameter of importance. An obvious candidate is viscoelasticity of the rubber roll covers. As the deflection of the solid boundaries is large compared to the film thickness, small changes in the elastic response of the solid, and thus small differences in the

amount of elastic deflection, may correspond to large relative changes in the film thickness.

Adachi *et al.* (1988) and Kang, Lee and Liu (1991) present coating thickness data for squeeze-roll nips operated at pre-set constant gaps. Their results, alongside theoretical predictions (Coyle 1990), are plotted in Fig. 12c.10. For fixed positive gaps, the rigid roll limit is evident as the plateau of coating thickness at low elasticity number ($H_m = 0.65 H_0$). At high elasticity number the coating thickness begins to increase as viscous forces overcome the resistance to elastic deformation. For fixed negative gaps there is, of course, no rigid roll limit and the coating thickness steadily decreases as elasticity number decreases. Making the gap setting more negative reduces the coating thickness, though the sensitivity to even further reductions in gap decreases. The agreement of theory and experiment is good, except for one set of data.

For negative gaps and low El , equation (12c.20) can be rearranged, eliminating the load W in

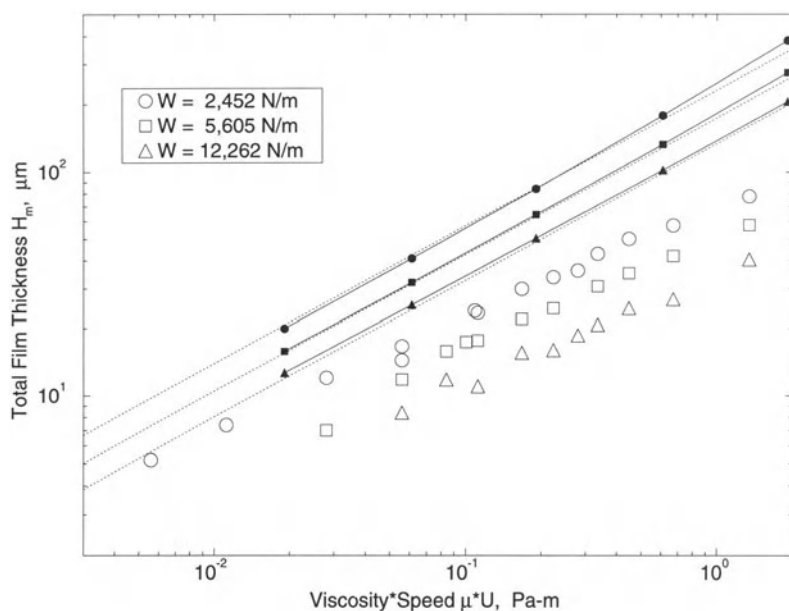


Figure 12c.9 Computed (lines) and measured (symbols) flow rate in a squeeze-roll coater as a function of viscosity, speed, and load; ($E_1 = 3 \text{ MPa}$, $E_2/E_1 = \infty$, $R_2/R_1 = 1.67$, $U_2/U_1 = 1$). The dotted lines represent data of Smith and Maloney (1966), equation (12c.22b).

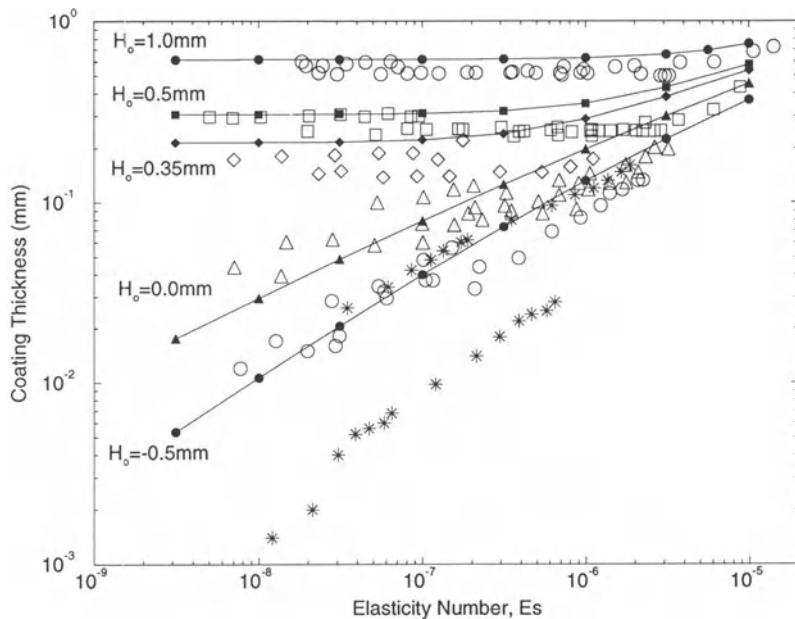


Figure 12c.10 Computed (curves) and measured (symbols) flow rate in a squeeze-roll coater as a function of elasticity number and gap setting. The data of Adachi (1988), represented by open symbols, are for a rubber-covered roll against a stationary flat plate. The data of Kang, Lee and Liu (1991) (*) are for a rubber-covered roll and a steel roll at equal speeds ($H_0 = -0.3$ mm, upper set for 60 durometer, lower set for 90 durometer).

favor of the gap setting H_0

$$H_m \sim (\mu \bar{U})^{0.6} (-H_0)^{-0.2} E_e^{-0.6} R_e^{0.2} \quad (12c.24)$$

Kang, Lee and Liu's data fit the expression

$$H_m \sim (\mu \bar{U})^{0.5} (-H_0)^{-0.47} E_e^{-1.6} \quad (12c.25)$$

where the latter gap and modulus exponents are a result of the one data set that deviates significantly from theoretical predictions.

Kang, Lee and Liu (1991) also present data for non-Newtonian fluids. Shear-thinning lowers both the coating thickness and the sensitivity to speed – trends that would be expected. Viscoelasticity of the liquid increases both the coating thickness and the sensitivity to speed, but also causes large ribbing defects; results analogous to those for rigid rollers.

12c.7.3 OPERABILITY

Operability limits for a squeeze-roll coater are not as clear-cut as for its rigid-roll counterpart. As mentioned earlier, there is always a film-split pattern (similar to ribbing) for loaded systems producing thin coatings. Starvation of the nip is nearly impossible for pan-fed systems, although puddle-fed devices will tend to coat a narrower width stripe of constant coating thickness if the feed rate is too low. Flooding of the nip is possible, which might result in excessive edge beads or overflow of the ends of the roll nip. As nips always tend to produce a rolling bead or puddle of excess coating liquid upstream, the possibility of vortex instability and air entrainment exists, similar to the rigid roll cases in Chapter 12a. For example, a horizontal size press on a paper-making machine can have turbulent

splashing flow in the puddle, leading to coating defects.

12c.7.4 PRACTICAL IMPLICATIONS

The most obvious difference between squeeze-roll and rigid-roll coating, besides the much thinner coatings, are the difference in exponents in the above coating thickness equations. For example, the coating thickness is proportional to the gap for rigid rolls, but only depends on the 0.47 power of the gap (experimentally) for a deformable-roll system. These exponents indicate reduced sensitivity to operating parameters, roll misalignment, roll run-out and other inaccuracies and perturbations to the system. These improvements are analogous to those of blade or membrane coating compared with rigid knife coating.

12c.8 GRAVURE COATING

As described in Section 12c.1, the essence of gravure coating is the filling of cells or grooves on a gravure cylinder with liquid, and the transfer of part of that liquid onto a substrate or intermediate transfer roll. Gravure coating has its origins in rotogravure printing, but has since evolved into many configurations (Booth 1970, 1990; Satas 1984). In direct gravure coating, illustrated in Figure 12c.1f, the liquid is transferred directly to the substrate backed up by the rubber nip roll. In offset gravure coating, the gravure cylinder transfers liquid to an intermediate, so-called offset roller which, in turn, applies the coating to the substrate at a second nip. Both modes can furthermore be operated with counter-rotating rolls at matching nip surface speeds (forward gravure) or at differential speeds (differential gravure). The rolls can even be co-rotating to generate speeds at the nip in the opposite direction (reverse gravure). Gravure techniques are very common for applying silicones, adhesives, magnetic recording layers and many other coatings (Booth 1970, 1990; Satas 1984). Typical conditions are 1 to 50 µm for coating thickness, 15 to 1500 mPa s for viscosity, and up to 10 m/s for

speed. The primary advantage of gravure coating is that very thin films are attainable at high speeds and with consistent overall uniformity. The main disadvantage is that it is difficult to get films free of local nonuniformities related to the engraved pattern.

In all configurations, the key component that distinguishes gravure coating from other roll coating methods is the gravure cylinder, whose chrome-plated or ceramic surface is engraved with cells or grooves of a specific, precisely maintained volume. Because the coating thickness applied to the web is strongly tied to the engraved volume, gravure could be classified as a pre-metered coating technique. It is nonetheless included in this chapter here because it includes two elastohydrodynamic processes: flexible-blade doctoring and squeeze-roll nip transfer. Both can have a dramatic effect on the appearance of the remnant gravure pattern in the coated layer, and can also be used to adjust coating thickness to some extent. In differential speed and reverse gravure coating, moreover, adjustments in speed ratio provide the option for substantial changes in coating thickness at a fixed cell or groove volume.

The pattern of cells or grooves is engraved onto the surface of the roll either by mechanical engraving (knurling), by chemical etching, or by electromechanical engraving (Satas 1984). Figure 12c.11 shows two versions of mechanical engraving (trihelical grooves and quadrangular cells) and one example of electromechanical (or electronic) engraving. Knurling uses a rotating tool which is run over the surface of the cylinder under pressure to mechanically form depressions in the surface that are an image of the tool surface. Electronic engraving uses a radially vibrating diamond stylus to cut cells into the roll surface as the roll is rotated on a lathe and the stylus slowly translated across the roll's axis. The 'pitch', 'cell count', or 'screen' is the number of grooves or cells per unit length measured perpendicular to the pattern angle, and typically ranges from 4 to 160 cells/cm. The 'volume factor' is the volume of the cells per unit surface area of the roll, and typically ranges from 4 to 300 µm

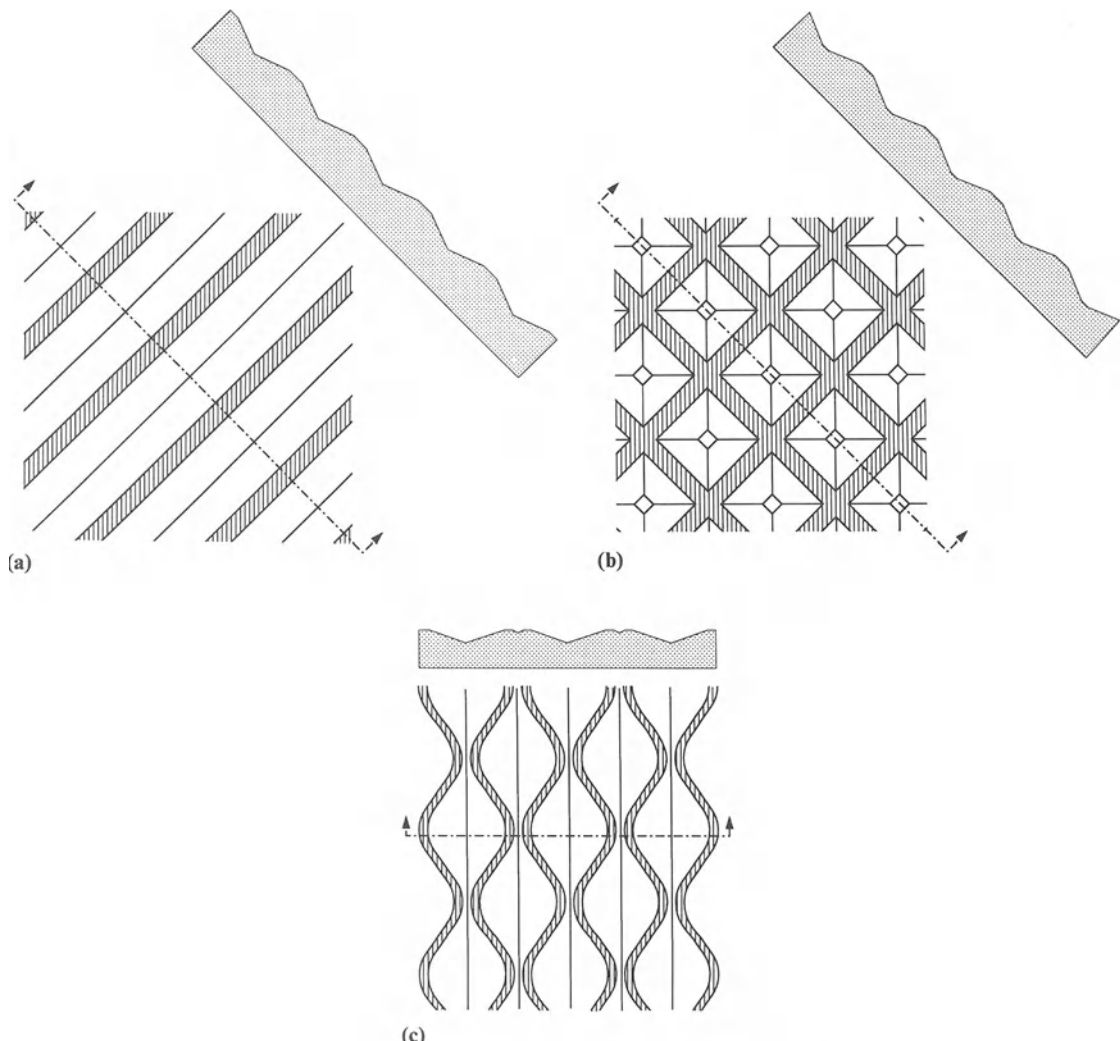


Figure 12c.11 Common cell patterns used for gravure rolls, showing top views and cross-sections. The land areas are shaded, and as shown here the roll axes are horizontal: (a) tri-helical, knurled; (b) quadrangular, knurled; and (c) electro-mechanical engraving.

(cubic microns per square micron of surface). The flat surface between the cells is called the land area, and the angle between the sides of the cells is called the stylus or tooth angle.

No matter what the machine configuration or engraving type, there are three fundamental operations in gravure coating that must be understood. The first is the feed, which is the

initial application of excess coating liquid to fill the cells. The second is the doctoring of the gravure roll by the flexible blade, which removes excess coating from the land areas. The third is the nip flow and cell transfer process by which part of the coating liquid in the cells is applied to the web. These three processes are discussed below. The book *Gravure Process and Technology*

(Gravure Association of America 1991) provides detailed descriptions of machine configurations and gravure applications.

12c.8.1 FEED

The purpose of a feed system is simply to fill the cells with coating liquid. The simplest method is a pan of liquid in which the gravure cylinder is partially immersed. Entrapment of air in the cells will determine the upper limit of speed and viscosity with the feed system. The limit will depend on the cell geometry and the rheology of the coating liquid. Enclosed feed systems and fountain dies have been developed to overcome pan feed problems associated with high speeds, such as air entrainment, foam generation, large volume liquid holdup and excessive solvent evaporation (Gravure Association of America 1991). There exists no published fundamental understanding, experimental or theoretical, of the feed step.

12c.8.2 DOCTORING

The doctoring of a coating from a smooth surface using a flexible steel blade is covered in detail in Section 12c.3, and is also addressed in Chapter 12d. On smooth surfaces, the response of coating thickness to increases in blade loading follows a characteristic, nonmonotonic pattern with a minimum followed by a maximum (Fig. 12c.5a). At any load, increasing the elasticity number (i.e. the ratio of viscous to elastic forces) lifts the blade and increases the coating thickness (Fig. 12c.5b). In gravure coating, it is often desired that the land areas of the cylinder are doctored cleanly. The insights gained from Section 12c.3 suggest that wiping of the lands would be most complete toward the upper end of the stiff-blade regime where blade-coated films on flat surfaces can become extremely thin.

The theory of flexible blade doctoring has been extended to include trihelical engraved roll surfaces (Kistler 1988). The shape of the blade is only weakly affected by the presence of the grooves, but the grooves are important in determining

the average coating thickness and the closest approach distance between the land and the blade. The theory predicts two fundamental regimes of operation which depend on the balance between roll roughness and blade stiffness. For shallow grooves or a highly-flexible blade, there is a large clearance between blade and land, a significant amount of coating is left on top of the land, and the response of the system is in essence the same as for a smooth roll. This regime corresponds to either small volume factors (and high pitch) or high elasticity numbers. For deep grooves or a stiff blade, there is a very small clearance between blade and land, all the hydrodynamic force on the blade is concentrated over the land, and the flow is metered almost exclusively by the cell volume. In this regime, which corresponds to large volume factors (and low pitch) or low elasticity numbers, the average film thickness no longer passes through a pronounced minimum and a maximum as the blade loading is increased. Rather, as the blade tip approaches the land surface the average coating thickness on the gravure roll becomes much less sensitive to the load and is more or less equal to the cell volume per unit area. Toward higher loads, the cells are left only partially filled. The results for tri-helical patterns should be qualitatively valid for other patterns, though the exact amount of liquid remaining in the cells depends on a pressure-driven component of flow, and thus will be different for discrete cells and continuous grooves.

Some of this behavior has been observed experimentally. Lindblad, Tift and Watson (1988) observed the minimum in coating thickness as blade force increases for high pitch engravings and flexible (high EI) elastomeric doctor blades. Their data at high loads showed a much steeper increase in thickness than would be expected from their data of blade penetration into dry grooves, illustrating the significant hydrodynamic lifting of the blade which occurs when operating in the bent-blade mode. They also measured the poorer doctoring (thicker coated films) achieved with longer blades and with blades made from an elastomer with a slower relaxation time.

The data of Patel and Benkreira (1991) illustrate similar effects but also include variations in elasticity number and volume factor. A normalized excess coating thickness can be defined as the difference between liquid and engraved volume/area, normalized by the engraved volume/area. Figure 12c.12 shows the approximate excess coating thickness as a function of blade loading and elasticity number, replotted from Patel and Benkreira's original data. At low elasticity numbers, here corresponding to low viscosity and speed, there is no excess coating thickness and the coating volume is determined solely by the cell volume. At high elasticity numbers there is substantial excess coating on the roll, and the increase in thickness with blade coating indicates that conditions correspond to the intermediate region of bent-blade operation. The high elasticity number curves also show how rolls with higher volume factors tend to operate more towards the regime where the lands are scraped clean.

The amount of coating carried by the gravure roll into the transfer nip is thus controlled by the metering action of the doctor blade. This amount of metering and its sensitivity to changes in operating conditions can be large or small, depending on the regime in which the doctor blade is operating. In this manner the doctoring can affect both quantity and quality of the coating transferred to the web.

12c.8.3 CELL TRANSFER OR PICK-OUT

The transfer of the coating from the gravure roll to the web can be thought of in terms of two limiting regimes. If an excess of coating is supplied to the nip, a rolling bank of liquid is formed, the coating on the web is continuous, and the process is closely related to squeeze-roll coating. If the proper amount of coating is supplied to the nip, printing of the gravure pattern will occur. This leads to two limiting views of the fluid flow. The first case is the splitting of a continuous liquid

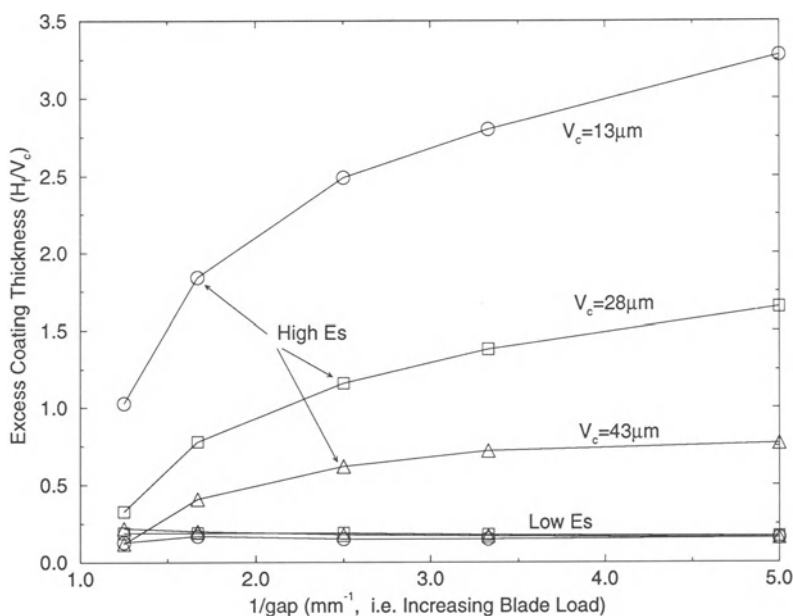


Figure 12c.12 Experimental measurements of excess coating thickness on three gravure rolls as a function of blade loading and elasticity number (data replotted from Patel and Benkreira (1991)).

film that occurs in all roll coating processes. The second is the uniaxial stretching and rupture of discrete liquid filaments. The second view especially emphasizes the importance of viscoelastic and elongational response of the coating liquid. In reality, this view is somewhat simplistic because other more subtle effects complicate matters.

The experimental work of Pulkrabek and Munter (1983) and Munter (1990) describes the transfer operation and the effects of design and operating variables. While this work concentrated on tri-helical patterns, there is likely to be some parallels with other patterns, such as cells. Most of the results are furthermore limited to direct forward gravure coating. They illustrate the two modes of transfer, referred to as merged and printing. There are three major problems which can arise during transfer leading to flaws on the coated product. The first, called flashing, occurs when one or more grooves are only partially picked out, leaving a bare region on the web. The second, called combined or multiple-line pick-out, occurs when liquid from two or more adjacent grooves is combined to form a single line of coating on the web, thus doubling (or tripling) the line spacing on the web. This type of pick-out is not stable, does not level properly, and can lead to other flaws such as pinholes and craters. The third problem occurring at high speed is misting, where fine droplets of coating are ejected from the nip.

The most important parameter for controlling the type and stability of pick-out is the engraving pattern design (Pulkrabek and Munter 1983; Kistler and Munter 1986; Munter 1990). Three design variables are critical. First, the volume factor is the primary means of controlling the average coating thickness. The amount of coating transferred to the web is around 60% of the cell volume for forward direct gravure coating (see also Lindblad, Tift and Watson (1988)). If excess coating is supplied to the nip, a rolling bank is formed on the upstream side. In most cases the web is actually pressed into the grooves or cells to contact the liquid. Second, the pitch (for a given volume factor) is the primary means of controlling the type and stability of pickout. For

a given volume factor, an equivalent gap between smooth rolls which would give the same coating thickness as calculated, and from this gap a natural frequency of ribbing is found. If the pitch is chosen to match that ribbing frequency, single-line pickout will occur up to a critical speed. If the pitch is much higher than the natural ribbing frequency, the competition between the natural ribbing frequency and roll pattern will result in unstable multiple-line pick-out. Third, the ratio of land to volume factor is important. High values encourage printing, and worsen the leveling process (small lines of coating that are widely spaced).

Cell-transfer is also affected by operational variables, though these are secondary compared with the gravure pattern design. Operating with a rolling bank on the upstream of the nip is the primary means of adjusting the pick-out, creating merged pick-out patterns which level best. The bank can be adjusted by supplying excess coating from the doctor blade or by increasing the nip pressure to increase the penetration of the web into the grooves. The pick-out can also be adjusted by changing the take-off angle of the web or the viscosity of the coating, both of which can affect the natural ribbing frequency (Kistler and Munter 1986). Generally, operational variables are more useful in controlling pick-out stability than in controlling coating thickness. Further evidence of insensitivity of coating thickness to operational parameters is found in the results of a study of reverse gravure coating with a tensioned web (Benkreira and Patel 1993). Their data suggest that the thickness of the coating liquid applied to the web is about 33% of the engraved volume, independent of engraving type (tri-helical, pyrimidal or quadrangular), ratio of web to gravure roll speed, or liquid viscosity. The large difference in applied coating thickness from that obtained in forward direct gravure coating needs further investigation. Limited data at low speeds, obtained for forward gravure and reverse gravure with an impression roll, are consistent in terms of low sensitivity of coating thickness to operating variables (Stasyuk and Peglovskii 1981; Stasyuk, Peglovskii and Fedotkin 1983).

Model studies have also been performed using fluids that do not level and thus preserve the pick-out pattern for subsequent analysis (Munter 1990). In terms of amplitude of the remnant engraving pattern, the coating quality is improved by: (1) increasing the pitch; (2) flooding the inlet; (3) not running a highly loaded nip, or (4) running reverse rather than forward gravure coating.

While many of the above results are limited to tri-helical engravings in forward direct gravure coating, they nevertheless illustrate the limiting regimes of operation and the general effects of engraving design and operating parameters. In addition, the strong influence of coating rheology on the operation of gravure coating is well recognized in the trade literature but is not well understood.

12c.8.4 PRACTICAL IMPLICATIONS

The main strength of gravure coating is its ability to apply thin coatings at high speed. The coating thickness is nearly proportional to the engraved volume, so that changing coating thickness more than a small amount requires changing the gravure roll. The uniformity of the coating is strongly influenced by engraving design and coating formulation rheology, but there are few published guiding rules to assist the practitioner in specifying either. This uncertainty is compounded by the additional influences of doctoring, feeding, solvent evaporation and rubber roll response, among other factors.

12c.9 SUMMARY AND CONCLUSIONS

This chapter describes and analyzes some of the most common elastohydrodynamic coating methods. Their behavior, in terms of coating thickness and sensitivity to operating conditions, is fairly well understood. It results from the balance between viscous hydrodynamic forces generated in converging drag flows and elastic restoring forces of the deformable boundaries confining the flow field. The understanding gained from the theoretical and experimental study of

elastohydrodynamic coating methods also sheds light on when and why these methods are advantageous over their rigid counterparts.

In general, there are three main advantages to using an elastohydrodynamic coating method rather than rigid-type applicators. First, elastohydrodynamic systems are less sensitive to mechanical tolerances, both spacial and time-dependent. The former results in less sensitivity of cross-web coating uniformity to variables such as roll alignment or bowing. The latter results in lower sensitivity to roller run-out, vibration, web thickness variations, etc. This decreased sensitivity also means that the acceptable range of machine settings and variability in setup is larger than in other coating methods. The second advantage is the ability of elastohydrodynamic coating methods to coat very thin coatings with simpler, easier to operate, and less expensive machinery than is needed for other precision coating techniques. The third advantage of elastohydrodynamic systems is their development of a long extended high-pressure nip region, which is primarily responsible for the lower sensitivity cited above. This region also serves to damp unsteady planar inlet disturbances (Pearson 1985) and thus helps coating uniformity.

Elastohydrodynamic coating methods also have some disadvantages. The most severe is coating uniformity, especially for demanding product applications. Squeeze-roll and tensioned-web roll coating always result in a film-split pattern on the coated surface, and may not damp steady ribbing-type inlet disturbances (Pearson 1985). Flexible-blade coaters and membrane coaters tend to trap particles that create streaks in the coating. Gravure coaters create a patterned coating depending on the engraving pattern and fluid rheology. All elastohydrodynamic coating methods are sensitive to variations in elastic properties. Rubber covers on rolls will age, embrittle or swell in response to exposure to solvent, oils or ozone. Tensioned web coaters are sensitive to web tension control and the stiffness uniformity and straightness of the web. In addition, application of thin coatings requires higher tensions which can stretch or tear the web.

Ultimately, the advantages and disadvantages of every coating method must be carefully weighed in terms of the requirements of the specific product to be manufactured.

Even though the basic mechanisms, advantages, and disadvantages are quite well laid out, several essential gaps remain in our knowledge of elastohydrodynamic coating systems. The operation of a squeeze-roll coater depends on the nonlinear, time-dependent elastic deformation of an elastomer layer, which remains poorly understood. The details of the operability of a tensioned web coater with respect to geometry has not been thoroughly explored. Most aspects of gravure coating are poorly understood, including filling, doctoring, and 'pick-out' of cells of both Newtonian and non-Newtonian liquids. As all elastohydrodynamic coating methods have a converging wedge inlet region on which the coating thickness depends, all should be sensitive to the viscoelastic forces developed by liquids in such a rapidly accelerating velocity field. Finally, the details controlling the uniformity of the coated films are not well understood.

REFERENCES

- Adachi, K., Ishuzu, Y. and Nakamura, R. 1988. Coating flows between a rotating deformable roller and a stationary flat plate. AIChE Spring National Meeting, New Orleans, March.
- Aidun, C. K. 1990. Principles of hydrodynamic instability in coating systems. *1990 TAPPI Coating Conference Proceedings*. pp. 275–298. Atlanta: TAPPI Press.
- Akesson, R. and Olsson, A. 1988. Neue Billiblade-Konstruktion verbesselter Qualität und Runnability, *Wochenblatt Papierfabrikation*. 8: 352.
- Bapat, C. N. and Batra, R. C. 1984. Finite plane strain deformations of nonlinear viscoelastic rubber-covered rolls. *Int. J. Num. Meth. Eng.* **20**: 1911–1927.
- Benkreira, H. and Patel, R. 1993. Direct gravure roll coating. *Chem. Eng. Sci.* **48**(12): 2329–2335.
- Berdinner, E. J. and Throckmorton, J. P. 1984. Coating apparatus. US Patent 4,475,478.
- Booth, G. L. 1970. *Coating Equipment and Processes*. New York: Lockwood Publishing Company.
- Booth, G. L. 1990. Coating converting processes: Traditional methods and new uses. 21st Annual IGC Coating Systems Conference, Boston, August, Bis-Cap International, Newtonville, MA.
- Carvalho, M. S. and Scriven, L. E. 1993. Effect of deformable roll cover on roll coating. *Proceedings of 1993 TAPPI Polymers, Lamination, and Coating Conference*. Atlanta: TAPPI Press.
- Chino, N., Hiraki, Y. and Sato, T. 1988. Coating apparatus. US Patent 4,854,262.
- Chino, N., Hiraki, Y., Sato, T. and Chikamasa, N. 1988a. Method of applying a liquid to a moving web. US Patent 4,717,603.
- Chino, N., Sato, T., Tanaka, F., Fukumura, K. and Hiraki, Y. 1988b. Thickness correcting coating method. US Patent 4,776,997.
- Coyle, D. J. 1988a. Experimental studies of flow between deformable rolls. AIChE Spring National Meeting, New Orleans, March.
- Coyle, D. J. 1988b. Forward roll coating with deformable rolls: A simple one-dimensional elastohydrodynamic model. *Chem. Eng. Sci.* **43**(10): 2673–2684.
- Coyle, D. J. 1990. Nonlinear theory of squeeze-roll coating. AIChE Spring National Meeting, Orlando, March.
- Coyle, D. J. 1992. Roll coating. In *Modern Coating and Drying Technology*, eds E. Cohen and E. Gutoff. New York: VCH Publishers.
- Crook, A. W. 1961a. Elastohydrodynamic lubrication of rollers. *Nature*. **190**: 1182–1183.
- Crook, A. W. 1961b. The lubrication of rollers. II. Film thickness with relation to viscosity and speed. *Phil. Trans. R. Soc. Lond.* **254**: 223–236.
- Cudworth, C. J. and Higginson, G. R. 1976. Friction of lubricated soft surface layers. *Wear*. **37**: 299–312.
- Dowson, D. and Higginson, G. R. 1966. *Elastohydrodynamic Lubrication*. Oxford: Pergamon Press.
- Eichler, W. and Brueck, R. 1972. Casting apparatus with flexible wiper film. US Patent 3,688,738.
- Eklund, D. E. 1984. Influence of blade geometry and blade pressure on the appearance of a coated surface. *TAPPI J.* **67**(5): 66–70.
- Eshel, A. and Elrod, H. G. 1965. The theory of the infinitely wide, perfectly flexible foil bearing. *Trans. ASME, J. of Basic Eng.* **87**: 831–836.
- Fluegge, W. 1960. *Stresses in Shells*. Berlin: Springer.
- Grant, O. W. and Satas, D. 1984. Other knife and roll coaters. In *Web Processing and Converting Technology and Equipment*, ed. D. Satas. pp. 60–80. New York: Van Nostrand Rheinhold.
- Gravure Association of America. 1991. *Gravure Process and Technology*. Rochester NY: Gravure Association of America.
- Gross, W. 1980. *Fluid Film Lubrication*. New York: Wiley.

- Gupta, P. K. 1976. On the heavily loaded elastohydrodynamic contacts of layered solids. *J. Lubric. Technol.* **98**: 367–374.
- Hall, R. W. and Savage, M. D. 1988a. Two-dimensional elastohydrodynamic lubrication. Part 1: The associated dry contact problem. *Proc. Instn. Mech. Engrs.* **202**(C5): 347–353.
- Hall, R. W. and Savage, M. D. 1988b. Two-dimensional elastohydrodynamic lubrication. Part 2: Solution of the line contact problem. *Proc. Instn. Mech. Engrs.* **202**(C5): 354–360.
- Herrebrugh, K. 1968. Solving the incompressible and isothermal problem in elastohydrodynamics through an integral equation. *J. Lubric. Technol.* **90**: 266.
- Hooke, C. J. 1977. The elastohydrodynamic lubrication of heavily loaded contacts. *J. Mech. Eng. Sci.* **19**(4): 149–156.
- Hooke, C. J. 1986a. The elastohydrodynamic lubrication of a cylinder on an elastomeric layer. *Wear* **111**: 83–99.
- Hooke, C. J. 1986b. A note on the elastohydrodynamic lubrication of soft contacts. *Proc. Instn. Mech. Engrs.* **200**(C3): 189–194.
- Hooke, C. J. and O'Donoghue, J. P. 1972. Elastohydrodynamic lubrication of soft, highly deformed contacts. *J. Mech. Eng. Sci.* **14**(1): 34–48.
- Jaffar, M. J. 1990. Two-dimensional elastohydrodynamic lubrication of elastic strips. *Wear* **139**: 335–350.
- Johnson, K. L. 1985. *Contact Mechanics*. Cambridge University Press.
- Kahila, S. J. and Eklund, D. E. 1978. Factors influencing the coat weight in blade coating with beveled blades: theory and practice. *1978 TAPPI Coating Conference Proceedings*. pp. 13–29. Atlanta: TAPPI Press.
- Kang, Y.-T., Lee, K. Y. and Liu, T.-J. 1991. The effect of polymer additives on the performance of a two-roll coater. *J. Appl. Polymer Sci.* **43**: 1187–1195.
- Kistler, S. F. 1988. Flexible-blade doctoring in gravure coating. AIChE Spring National Meeting, New Orleans, March.
- Kistler, S. F. and Munter, J. D. 1986. Effect of take-up angle and substrate deformation in forward roll coating. AIChE Spring National Meeting, New Orleans, April.
- Lindblad, N. R., Tift, R. and Watson, P. K. 1988. The metering of ink in the grooves of a gravure roll. *J. Imaging Tech.* **14**: 140–143.
- Malvern, L. E. 1969. *The Mechanics of a Continuous Medium*. Englewood Cliffs, NJ: Prentice-Hall.
- Munter, J. D. 1981. Personal communications to Saita and Scriven (1985).
- Munter, J. D. 1990. Attenuation of cell patterns for gravure coating. AIChE Spring National Meeting, Orlando, March.
- Nakazawana, T., Morita, H. and Booth, G. L. 1987. The vari-dwell-time blade coater. *1987 TAPPI Coating Conference Proceedings*. Atlanta: TAPPI Press.
- Patel, R. and Benkreira, H. 1991. Gravure roll coating of Newtonian liquids. *Chem. Eng. Sci.* **46**(3): 751–756.
- Pearson, J. R. A. 1985. *Mechanics of Polymer Processing*. London and New York: Elsevier.
- Pipkin, D. J. 1982a. Apparatus for forming a coating on a substrate. US Patent 4,345,543.
- Pipkin, D. J. 1982b. Method and apparatus for forming a coating on both sides of a substrate. US Patent 4,327,130.
- Pipkin, D. J. 1983. Coating apparatus and method. US Patent 4,387,124.
- Pipkin, D. J. 1984. Method for forming a coating on a substrate. US Patent 4,442,144.
- Pipkin, D. J. 1986. Membrane coating. AIChE Spring National Meeting, New Orleans, April 7–10, 1986.
- Pipkin, D. J. and Schaefer, D. W. 1979. Method for applying a viscous liquid to a substrate. US Patent 4,142,010.
- Pranckh, F. R. 1989. Elastohydrodynamics in coating flows. PhD thesis, University of Minnesota, Minneapolis, MN.
- Pranckh, F. R. and Scriven, L. E. 1988. The physics of blade coating of a deformable substrate. *TAPPI J.* **73**(1): 163–173.
- Pranckh, F. R. and Scriven, L. E. 1989a. *Elastohydrodynamics of membrane coating*. University of Minnesota Supercomputer Institute Report No. 89/83.
- Pranckh, F. R. and Scriven, L. E. 1989b. *Analysis of membrane coating*. University of Minnesota Supercomputer Institute Report No. 89/85.
- Pranckh, F. R. and Scriven, L. E. 1990. Elastohydrodynamics of blade coating. *AIChE J.* **36**(4): 587–597.
- Pulkabek, W. W. and Munter, J. D. 1983. Knurl roll design for stable rotogravure coating. *Chem. Eng. Sci.* **38**(8): 1309–1314.
- Saita, F. A. 1984. Elastohydrodynamics and flexible blade coating. PhD thesis, University of Minnesota, Minneapolis.
- Saita, F. A. and Scriven, L. E. 1983. Analysis of the flexible blade coater. *Lat. Am. J. Chem. Eng. Appl. Chem.* **36**: 587–597.
- Saita, F. A. and Scriven, L. E. 1985. Coating flow analysis and the physics of flexible blade coating. *1985 TAPPI Coating Conference Proceedings*. pp. 13–21. Atlanta: TAPPI Press.
- Satas, D. (ed.) 1984. *Web Processing and Converting Technology and Equipment*. New York: Van Nostrand Reinhold.

- Scharenberg, R. T. 1985. Coating methods. In *Encyclopedia of Polym. Sci. Eng.* 2nd edn. Vol. 3, pp. 552–567. New York: John Wiley.
- Shibata, N., Chino, N., Sato, A. and Chikamasa, H. 1992. Simultaneous video tape dual-layer coating technology. *Fujifilm Research and Development*. **37**: 107–111.
- Shibata, N. and Scriven, L. E. 1986. Theory of coating unsupported web by a slot die. AIChE Spring National Meeting, New Orleans, April.
- Smith, J. W. and Maloney, J. D. 1966. Flow of fluids between rotating rollers. *Tappi*. **49**(11): 63–66.
- Sommer, H. 1985. Influence of metering element geometry on coat quality. *1985 TAPPI Coating Conference Proceedings*, pp. 23–34. Atlanta: TAPPI Press.
- Stasyuk, I. A. and Peglovskii, V. I. 1981. Thickness of polymer coats laid by raster rollers. *Khim. Neft.* **9**: 9.
- Stasyuk, I. A., Peglovskii, V. I. and Fedotkin, I. M. 1983. Polymer coating on roll substrates by a screened spindle. *Khim. Neft.* **2**: 22–23.
- Swales, P. D., Dowson, D. and Latham, J. L. 1972. Theoretical and experimental observations of the behavior of soft elastic materials under elastohydrodynamic conditions. *Proceedings of the 1972 Symposium on Elastohydrodynamic Lubrication*, Inst. Mech. Eng., pp. 22–28.
- Tanaka, Y. and Noda, S. 1984. Coating apparatus. US Patent 4,480,583.
- Taylor, J. A. and Fridhandler, R. M. 1985. Apparatus for and method of metering of coating on a moving web. US Patent 4,532,158.
- Triantafillopoulos, N. G. and Aidun, C. K. 1990. Relationship between flow instability in short-dwell ponds and cross-directional coat weight nonuniformities. *1990 TAPPI Coating Conference Proceedings*, pp. 309–324. Atlanta: TAPPI Press.
- Van Guelpen, L. J. 1946. Apparatus for coating webs. US Patent 2,464,771.
- Varnam, C. J. and Hooke, C. J. 1977. Non-Hertzian elastohydrodynamic contacts: an experimental investigation. *J. Mech. Eng. Sci.* **19**(5): 189–192.
- Weiss, H. L. 1985. *Rotogravure and Flexographic Printing Presses*. Milwaukee, Wisconsin: Converting Technology Corp.
- Zink, S. C. 1979. Coating processes. In *Kirk-Othmer Encyclopedia of Chemical Technology*. Vol. 6, pp. 386–426. New York: Wiley.

Cyrus K. Aidun and Nick G. Triantafillopoulos

12d.1 INTRODUCTION

Blade coating is a popular method among the many techniques used to apply a uniformly thin film of liquid continuously onto moving webs. Although still a self-metered, as opposed to a pre-metered process, blade coating falls within the class of processes where the coating layer is metered prior to the meniscus. In that sense, the blade acts as a precise smoothing device which removes excess coating – applied onto the web upstream with some kind of a mechanical feeding system or puddle – and lets a thin coating film pass through the narrow channel formed between the blade and the moving substrate (Fig. 12d.1).

The flow is primarily due to the shear stress induced by the substrate motion which is dragging coating in the channel formed between the substrate and the blade, the so-called blade nip. In contrast to the meniscus-metered class of coating processes, such as dip coating (see Chapter 13), where the coating thickness is determined by the shape of the meniscus, parameters independent of the meniscus control the coating film thickness of blade-metered coating systems. Generally, the film thickness, its uniformity and overall quality, depend on the characteristic blade nip geometry, the rheology of the coating and properties of the web. Difficulties encountered

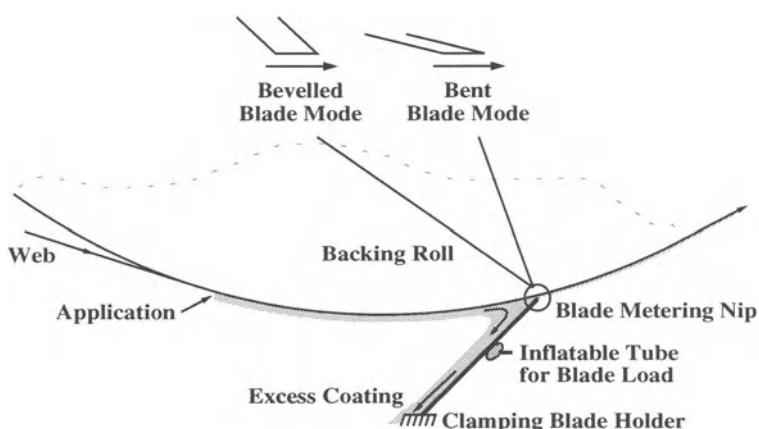


Figure 12d.1 Schematic of the flow approaching the blade in a coater with an applicator roll.

in understanding, predicting, and controlling the blade-metering process arise from interactions of complex phenomena, which will be discussed in more detail in the following sections.

Blade coating refers to the broad family of processes where a liquid layer emanates from the shallow channel formed between a stationary blade and a moving substrate supported against a roll. The liquid may be a dispersion or suspension of solid particles; the blade can be rigid or flexible; and the supporting roll can be hard or soft. The subject of rigid knife coating is covered in Chapter 12a. Here we focus on flexible blade coating, where the blade can be loaded with a mechanical member or an inflatable pressured hose located at some distance from the edge of the blade – the blade tip (Fig. 12d.1). The blade may also be loaded by rotating the blade holding assembly, so that the blade bends against the substrate and the supporting (backing) roll. Industrial applications of this process include addition of adhesives and coating to paper, paperboard and films, as well as oxide coatings onto magnetic recording tapes.

Although flexible blades are commonly used to apply liquid films onto smooth and incompressible polymeric substrates (e.g., in magnetic suspension technology), they are most popular in surface application of coatings for publication papers and paperboard. The reason for surface treatment of paper and paperboard is to develop a uniformly smooth surface for printing and superior appearance. Blade coating generates a smooth surface with improved optical properties, gloss, and printed ink density, while capturing halftone dot highlights during printing. However, these substrates are rough, porous and compressible, properties which make the physics of this blade coating process particularly challenging.

Blade metering is the coating process of choice for paper and paperboard applications because it is conductive to relatively high machine speeds and coating viscosities. Blade coaters for paper run at speeds above 5 m/s, while the steady shear viscosity of mineral dispersions for paper coatings varies from several hundred to over a thousand mPa s. The discussion in this chapter concentrates

on the high-speed blade coating process for paper webs.

Similar to many other coating techniques, blade coating technology has evolved from simple and basic applications. Many day-to-day applications are, in principle, forms of blade coating. A simple process of spreading butter by knife over a piece of toast is a simple example. In fact, Booth (1970) uses this example to describe the effect of coat weight in relation to the angle formed between the blade tip and the tangent to the substrate, i.e., the so-called blade angle. The original coating apparatus appeared in two forms (Trist 1945). In one form, a coating head or trough was used to contain the coating, hence the flexible blade formed the boundary at the leading edge of the trough. This is a 'puddle' type of coater, which was common during the early development and use of the blade coating process (Fig. 12d.2). In a second form, excess coating was applied onto the moving web with an applicator roll and metered downstream with the blade. The excess coating was then recycled back into the pad feeding the applicator roll. This configuration was termed the 'inverted' blade coater. In both cases the substrate was drawn around a rubber covered supporting roll, also called the backing roll, which drives and supports the substrate.

Continual upgrading of the blade coater process, however, was needed as machine speeds increased for productivity and film thicknesses decreased

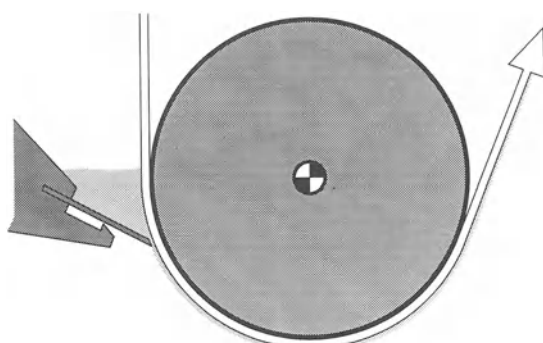


Figure 12d.2 Schematic of a puddle coater.

due to rising mailing costs. Nowadays, there is a whole family of newer blade coaters where differences exist on: (1) the application of excess coating (or pre-metering) with roll applicators or jets; (2) variability in the dwell time between application and metering; (3) pre-metering with one blade first before final metering with a second blade, or (4) utilization of a short (2.5–5.0 cm in length) pressurized pond for application of the coating before metering, hence the flexible blade itself acts as a boundary that keeps the coating in contact with the substrate and as a metering device. This latter design is the popular type of blade coater known in the paper industry as the ‘short-dwell coater’. These and other blade coater designs are discussed in detail in Section 12d.2.

Blade coaters for paper are also classified into two categories, depending on their operational mode. In the first configuration the tip of the blade remains nearly tangent to the web surface and the backing roll at the area of contact between the blade and the web. This is the so-called straight, trailing, or bevelled blade (Fig. 12d.1). The blade angle, formed between the blade and the tangent to the backing roll (Fig. 12d.3), is comparatively large, typically varying between 25° and 50°. In practice, blades are prehoned to nominal bevel angles – typically, 45°, 40°, 35°, etc., so that one needs to set the blade angle to the bevel angle of the blade in order to run the blade on its bevelled mode. However, metallic blades wear out over time during normal operation and the bevel angle changes. When this occurs, the blade is not running anymore on its bevel, resulting in configurations (b) and (c), as illustrated in Fig.

12d.3. In cases (b) and (c) the blade runs on its trailing (heel) or leading (toe) edge, respectively, something which may lead to coating defects. Therefore, the exact blade geometry is a critical issue in bevelled blade coating, as will be discussed in more detail in Section 12d.7.

In the second configuration the underside of the blade is parallel to the web over a finite area (Fig. 12d.1). This is the so-called flexed, low-angle or bent blade mode. The blade angle in this case varies from almost 0° to 25°. The main difference between these two blade modes is the operational window of the process, i.e., the range of machine speed and film thickness, or coat weight, for which satisfactory coating is feasible. (The papermakers use coat weight to express coating film thickness in grams per unit area, in square meters of paper). The bent mode is preferred for comparatively high film thicknesses and low coater speeds (e.g., paperboard coating), while the bevelled blade is selected for applying thin films at relatively high speeds (e.g., light-weight coated publication papers).

There are several process parameters in high-speed blade coating systems which influence the surface quantity and quality of coating applied onto a substrate. Generally, the coating film thickness, or coat weight, depends on the interaction between the various operating parameters; namely, the coater geometry, coating rheology, and properties of the substrate. Usually the mechanical or pneumatic load on the blade is adjusted to control the final coating film thickness of coat weight. The blade thickness is typically between 0.1 to 1.0 mm and the blade length (i.e. the distance between the edge of the blade, or blade tip, and the location where the blade load is being applied) is about 2 to 10 cm. A typical time scale of the metering process at the blade nip is 0.01 milliseconds for 17 m/s coater speed (Gane, Watters and McGenity 1992). Although most of the commercially utilized blades are made out of steel, newer blades are manufactured with ceramic tips which resist wear and provide a better control of coating film thickness in the long run. The manner by which these parameters influence, and therefore can be

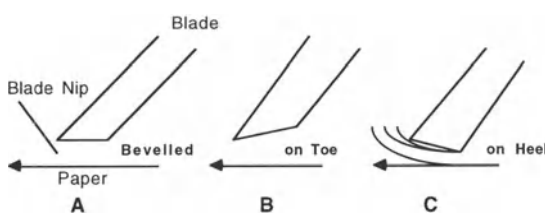


Figure 12d.3 Schematic of a bevelled blade running on (a) parallel, (b) toe, and (c) heel.

manipulated to predict, the coating film thickness is discussed in Section 12d.3.

Blade metering is a simple and rather primitive process flow, but presents a complex hydrodynamic system which has been under investigation since its original recognition as a superior coating system, as early as the 1950s. Originally blade coaters for paper operated at relatively low speeds, i.e., 5 to 10 m/s, but modern blade coating systems operate at speeds in excess of 20 m/s. The coating fluid (or dispersion) is forced from one extreme of flow conditions to another, while the fluid and dispersed particles experience changes in the shear rate from almost zero upstream of the blade to nearly 10^6 s^{-1} inside the passage under the blade tip in a period of time less than one millisecond. In the convergent flow through the blade nip, regions with high pressure gradients are adjacent to nearly constant pressure areas (or pressure plateau). Furthermore, the coating materials are non-Newtonian, exhibiting complex rheological behavior including dilatancy, yield stress, thixotropic recovery and viscoelasticity. Paper coatings, for example, comprise highly concentrated dispersions (i.e., 30–40% by volume) of anisometric, orientable particles suspended in an aqueous phase containing polymeric additives. Therefore, the ability to predict and control the coating process many times becomes a formidable task.

In addition to the above complications, one could hardly design a process which, with respect to modeling, involves more complex boundaries. The blade is flexible, the substrate is generally deformable and permeable, and there are free-surfaces with static and dynamic contact lines. On the other hand, the requirements for a successful coating process are also extreme. The flow needs to remain steady and two-dimensional at high machine speeds for maintaining a uniformly thin coating film. Uniformity needs to be sustained in both the machine line and the cross machine directions, as film thickness nonuniformities would not be acceptable from the standpoint of both visual appearance and physical attributes. Furthermore, anomalies occurring at the bounding walls, as well as the bulk of the process flow,

would cause coating film defects and deposits appearing at the blade surfaces. In practice, consistent and sustained productivity requires adequate knowledge of the physics of the blade coating flows, as well as the characteristics of both the substrate and the coating material.

The focus in this chapter is on high-speed blade coating of paper webs. Section 12d.2 describes the various designs and their evolution over the years to the high-speed precision coaters of today. Section 12d.3 discusses how the different process parameters interact to determine the film thickness, or coat weight. It also includes a review of analyses and experimental studies on the physics of blade-metering. Although the emphasis is on blade-metering on rough, porous and compressible substrates, limited reference is made to rigid knife coating of smooth, incompressible substrates to illustrate qualitative differences between the two processes. Sections 12d.4 through 12d.5 deal with hydrodynamic and other phenomena which influence the process and the uniformity of the film thickness. Finally, Sections 12d.6 and 12d.7 cover respectively aspects of paper coating rheology and blade coating defects, their appearance and origins.

12d.2 BLADE COATER DESIGNS

The first blade metering on a continuous coating machine is credited to the system designed by Trist (1945) which was primarily used for coating an oil phase emulsion on bread wrapping paper. The superior potential of this technique was recognized in the 1950s when a growing number of applications started to adopt the blade coating system. A wide variety of blade coating equipment has been invented since then. Richardson (1957) and Booth (1970) review the earlier blade coaters and their designs.

There are in general three important regions in an application system: (1) the wetting or the dynamic contact line (see Section 12d.5) where the fluid first comes into contact with the substrate; (2) the dwell region where the coating liquid remains usually undisturbed adjacent to the solid

surface, and (3) close to the metering region where the fluid layer approaches the blade.

The flow in an ideal application process should be steady state and two-dimensional. If the coated layer approaching the blade has uniform thickness and if the blade has no defects, then the resulting coated film would have a constant thickness. However, nonuniformities or unsteadiness upstream of the blade may result in coating defects. The mechanisms whereby flow nonuniformities upstream of the blade could result in coating defects have been analyzed by Miura and Aidun (1992).

The maximum coating speed is determined primarily by limitations set by the application unit. The fundamental limit on the coating speed depends on the maximum speed at which the air adjacent to the solid surface can be replaced by liquid at the wetting region. This is sometimes referred to as the maximum wetting speed and depends on the flow field in the vicinity of the dynamic contact line. Above the maximum wetting speed, small air bubbles entrain into the liquid and result in coating defects, as explained in Section 12d.5. Flow instabilities in the application unit upstream of the blade sometimes impose more severe limitations on the coating speed than air entrainment. These instabilities, as discussed in Sections 12d.4 and 12d.5, result in operational difficulties and coating defects. Therefore, air entrainment and flow instabilities are the main issues of concern in the development of modern high speed coating systems.

There are four different categories of blade coating systems that depend on the coating

application method before metering. These comprise the puddle, roll, jet (slot), and contact application systems. The common process involved in all of these systems is that they supply the blade with excess coating fluid which is, subsequently, metered by the blade. Typically, fifteen to twenty parts of the applied coating are removed by the blade for every part applied on the moving web. Each one of these application systems can be combined with any blade mode, i.e., bevelled or bent. A list of the different commercially available types of blade coaters are listed in Table 12d.1. Figure 12d.4 presents schematics of the different blade coating equipment for paper.

Currently, many of the high speed blade coating systems operate with a roll applicator where a thick layer of coating fluid is transferred to the surface of the substrate. The coating layer, which is typically between 100 µm to 1 mm thick, is metered downstream by the blade to provide a final film thickness in the range of 10 to 50 µm. This operation is commonly referred to as the inverted blade coater; also known as the flooded-nip™ blade coater. Although this is a quite common blade coating system, it is now clear that other techniques such as jet and pond application systems are superior. In particular, the so-called short-dwell coaters have recently found wide acceptance by the paper industry due to their compactness, ease of operation, and capability to keep the equipment clean, as well as their ability to apply comparatively thin coating films at high machine speeds (i.e., greater than 25 m/s). The main advantage of the short-dwell coater is that it can provide the same coat

Table 12d.1 Classification of commercial blade coating application systems

<i>Coater type</i>	<i>Coating application mode</i>	<i>Blade configuration</i>
Inverted blade	Roll applicator Slot orifice Jet fountain Contact applicator	Bevelled (stiff) blade Bent blade Zero-angle blade Billblade™
Puddle coater		
Short-dwell coater		
Simultaneous two-sided coater		

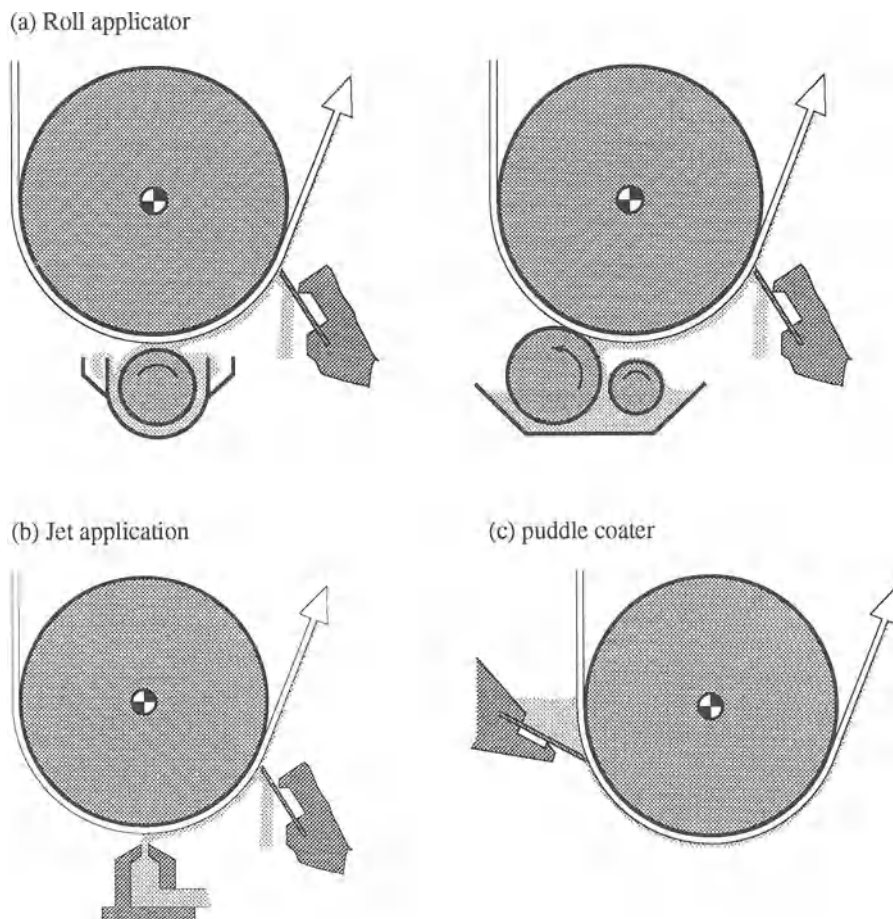


Figure 12d.4 Schematic of (a) roll, (b) jet, and pond application systems which include (c) puddle coater and pressurized pond application systems with (d) short-dwell time and (e) long-dwell time modes of operation.

weight onto a paper web as a system with an applicator roll but at substantially lower blade pressures, something which significantly improves productivity because it minimizes the possibility for web breaks. The different application systems, presented schematically in Fig. 12d.4, are discussed in the following sections.

12d.2.1 PUDDLE-TYPE COATERS

There are a variety of coating application systems in this class. The two principal categories are one-sided and two-sided coating systems (Figs

12d.4 and 12d.5) where both sides of the substrate are coated and dried simultaneously. In principle, these coaters cannot operate at high speed because of air entrainment at the wetting line which results in foaming of the puddle and, in extreme cases, prevents contact of the fluid with the substrate.

These coaters are commonly used today in various applications, such as speciality paper and board coating. The pond level in normal operation is between 150 to 170 mm high and the backing roll has a soft rubber cover (~ 70 P&J). The two-sided puddle coaters (Fig. 12d.5), such as, the

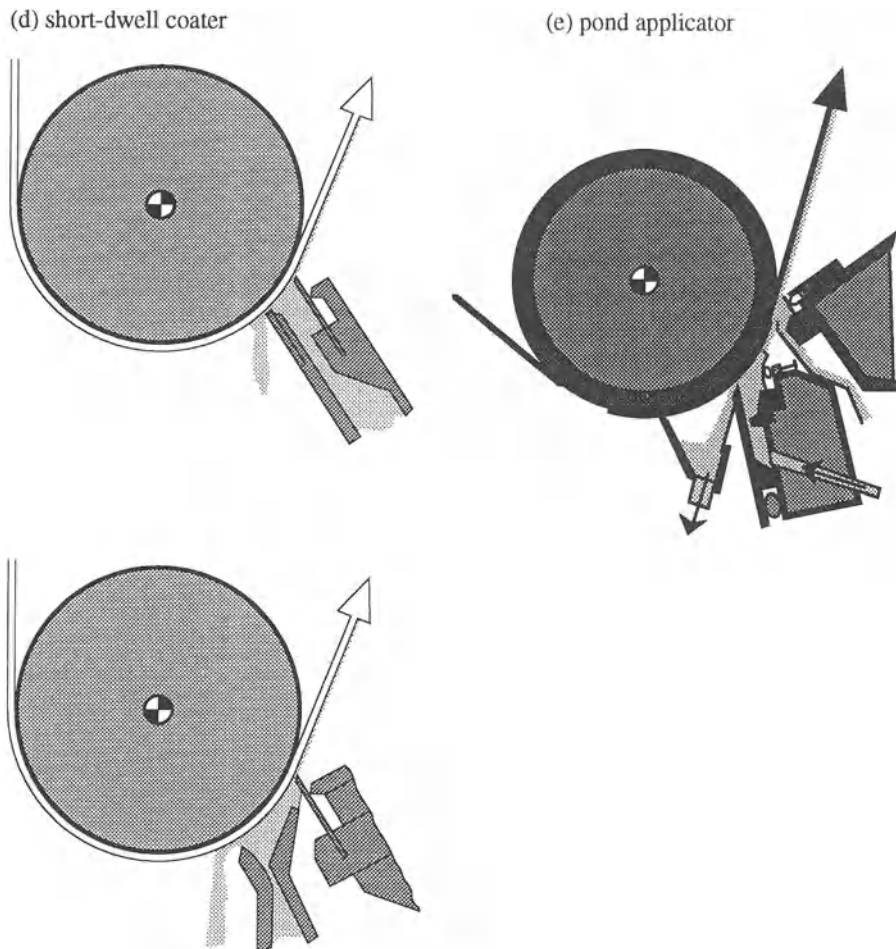


Figure 12d.4 *Continued.*

Billingsfors-Langed, better known as the Billblade™ system (Holton and Klass 1986), have remained in operation despite their limitations in speed and film thickness control. In addition to air entrainment, misting is also a problem with these coaters. At high speed, coating droplets form a mist of coating fluid, usually at the diverging region between the substrate and the roll where a meniscus forms. Misting occurs because of meniscus instability and breakup (film split), similar to the spraying mechanism in roll applicators. It is reported (Holton and Klass 1986) that by running the backing roll 3–5%

faster than the web and forming a ‘take-off’ angle of the web away from the roll completely eliminates film split and the misting problems on the roll side.

12d.2.2 ROLL COATERS

Roll applicators are perhaps the most popular and traditional form of coating systems. The transfer or applicator roll picks up the coating fluid from a supply pan or reservoir, as shown in Fig. 12d.4a, and transfers the fluid to the substrate being carried by the backing roll. The clearance between the surface of the two rolls

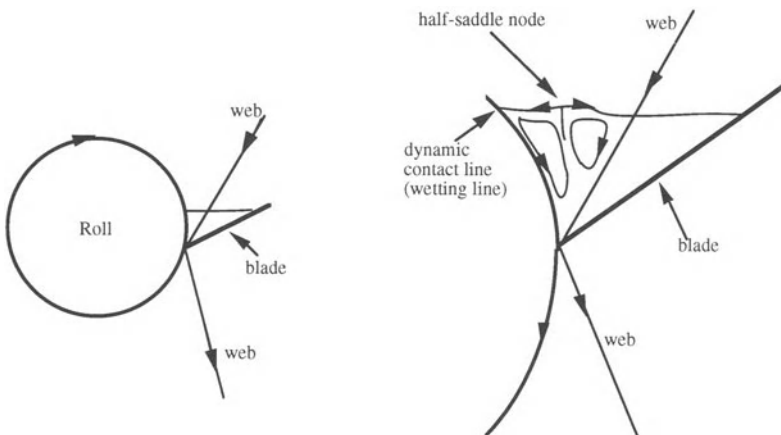


Figure 12d.5 Double-sided puddle or (Billingsfors-Langed) BillbladeTM coater.

can vary from 100 µm to 1 mm depending on the particular operation. The roll coating modes can be forward where the two rolls rotate counter to each other, or reverse, where the rolls rotate in the same direction. The amount of coating fluid transferred to the substrate by the applicator roll depends on the fluid properties, the gap, and the relative speed between the substrate and the roll.

There are a number of roll applicator systems with multi-roll metering units which have been developed by various companies. For examples of these systems, the reader is encouraged to see the review by Booth (1970). For a more extensive analysis of the mechanics and instabilities in roll applicators, see Section 12d.4 and Chapter 12a.

Roll applicators with blade metering units, in general, provide a good quality coated surface. However, because of flow instabilities and ribbing, roll applicators have limited use in high-speed blade coating. Also, as speed increases, the meniscus splits forming droplets. This spraying action causes difficulties in maintaining a clean and smooth layer of coating fluid prior to the blade. As indicated above, it is important that the coating layer remains smooth and uniform, as a nonuniform layer approaching the blade results in coated film thickness nonuniformities and other defects. In addition to this problem, from a practical point of view, roll applicators

are difficult to operate, clean and maintain. Manufacturing light-weight coated paper and film requires metering most of the applied coating from the surface by exerting a relatively large pressure on the blade. This causes frequent web breaks with an enormous waste in coating fluid and substrate material. Because of these difficulties with roll applicator systems, a number of more advanced application systems are being developed. These fall within the class of jet and pressurized application systems.

12d.2.3 JET COATERS

These systems, as the name implies, consist of a rectangular liquid jet which comes into direct contact with the substrate, as shown in Fig. 12d.4b. We confine the term 'jet coaters' to those systems in which a liquid jet emanating from the nozzle directly impacts the substrate. Some in the industry refer to the pressurized pond system of Fig. 12d.4c as jet coaters, as well. However, the fluid flow characteristics and the coating features between the two systems presented in Figs 12d.4b and 12d.4c are substantially different. With a jet coating system, the entire fluid leaving the nozzle is transferred to the substrate and supplied to the doctor blade. In contrast, in pressurized pond application systems some of

the fluid is always rejected from the pond. Also, jet coaters are usually used for thicker liquid film application on the surface. Thinner film applications can better be achieved with short-dwell time or other pressurized pond application coaters.

To ensure a uniform coated surface, the jet must have uniform constant momentum across the coater. This is achieved, in practice, by injecting the coating fluid from a large reservoir into a long channel before forming a two-dimensional free-surface jet. As the volume of the reservoir is relatively large, the pressure inside will be essentially static and uniform across the nozzle (see Chapter 10 for a more detailed discussion of manifold design). A long slightly converging nozzle will allow the flow to develop fully and stay attached to the wall. In other words, a converging nozzle ensures that pressure drops in the flow direction and therefore, the shear stress retarding the flow near the walls will not cause flow separation or flow reversal at the wall.

The control parameters are the opening gap of the jet, d , the jet angle relative to the substrate, α , the velocity of the substrate, U , and the jet Reynolds number, $Re \equiv \rho dV/\mu$, the capillary number $Ca \equiv \mu V/\sigma$ where ρ , μ , and σ are the fluid density, viscosity, and surface tension, respectively. The jet velocity scale, V , is defined as the mass flux divided by the jet's cross-sectional area. The jet could swell or contract depending on Re and Ca . Here we are assuming that the coating liquid behaves like a Newtonian fluid, although at low shear the viscosity of coating fluids usually depend on the rate of shear. In practice, the jet is usually from 1 to 1.8 mm thick at the vena contracta and extends about 12 to 25 mm in length. The coating flow rate per unit width is in the range of 1.3 to 3 m/s. The relative velocity of the jet to the substrate, V/U , varies from 0.1 to 0.5 depending on the coating thickness and other parameters.

12d.2.4 PRESSURIZED POND COATERS

In this class of coating application systems, the coating fluid comes into contact with the substrate

in a pressurized reservoir adjacent to a metering blade. The main purpose of increasing the pressure inside the coating reservoir is to avoid 'skip coating', that is to force the fluid to remain in contact with the substrate at high speed and avoid air entrainment at the wetting line (see Section 12d.5 for more detail).

This system of coaters has received considerable attention in the industry for several reasons. The coating head is compact and easy to operate and maintain. These pressurized pond systems are frequently used in short-dwell mode (referred to as Short-Dwell Coaters) where a very thin layer of coating is applied on the surface of a substrate without causing excessive web breaks.

With these coaters, the pond is adjacent to the blade and the coating liquid is transferred to the surface of the substrate immediately prior to the metering section. In contrast to the long-dwell time coaters where the coating layer travels adjacent to the substrate for a relatively long time before being metered off, the coating in short-dwell coaters has little time to penetrate into the substrate. These coaters are particularly used for light-weight printing and publication grade of papers as well as many other products including pre-metered size press applications. These coaters have several advantages over other coating application systems. The main advantages of these coaters as compared with roll applicators are the compactness, operational efficiency, and increased productivity of thinner coated film and, therefore, lighter-weight coated layers. It is reported (Closset 1986) that with these coaters, blade pressure can be reduced by 40% resulting in a considerable reduction in web breaks. This increases productivity by reducing the loss time due to web breaks by as much as 28% as compared with blade metering systems with roll applicators. Furthermore, a 40% reduction in coating liquid loss is reported by the industry. The lower blade pressure results in a 60% longer blade life time.

As the coating speed is increased, problems appear in all coaters. Although the short-dwell coater can operate at speeds in excess of 20 m/s, the coated surface quality deteriorates quickly

beyond a critical speed which depends on several factors including the coating rheology. Usually these problems appear in the form of long streaks which have a coating thickness deficit of about 20 to 60%. Section 12d.7 describes the various coating defects in blade coating systems. The most severe coating defect with short-dwell coaters are long streaks about 1–3 cm wide and 10 to 100 cm long. Extensive experiments (Triantafillopoulos and Aidun 1990) have shown that the parameters which have the most significant influence in generating streaks are coating speed, low shear viscosity of the coating liquid, and consequently, the concentration of the suspension. Suspensions with larger particle aspect ratio (thin disk-shaped) and larger shear viscosity tend to be more susceptible to coating defects, in general.

Additional problems for short-dwell and other pressurized pond application coaters are the instabilities that occur inside the pond as well as air entrainment issues at the dynamic contact line. These problems are fundamental to any pressurized pond application system. Sections 12d.4 and 12d.5 treat these issues in more detail.

It is also possible simultaneously to coat both sides of a moving web passing between two blades located one against each other. A Bill-blade™ is the configuration where the web passes through the nip of a bent blade, on one side, and a roll on the other side. Two separate puddles of coating exist, one on the roll side and the other one of the blade side. These puddles allow for application of coating onto the moving web from both sides simultaneously.

12d.3 BLADE METERING PROCESS

The physics of high-speed flexible blade coating has been the subject of interest in many studies over the years. The motivation was to document the interaction of the various forces acting on the blade and to determine how process variables affect coat weight. Most of the work focused on development of semi-empirical relationships which can be readily used to manipulate the process and control coat weight. These relationships were based on rather simplistic analyses which

incorporated only a limited number of the physical phenomena involved. Fundamental understanding of the blade metering process for paper has only recently been attained with the help of both computational models and experiments.

In the present section we review key relationships between operational variables and coat weight, with a focus on high-speed blade metering of paper webs. We will refer to previous analyses and experiments which shed light on the physics of this process. Both the bevel and bent blade operating modes are discussed. Topics covered in detail in other chapters of the book, i.e., elastohydrodynamic coating systems covered in Chapter 12c, are only briefly mentioned here. Differences in the operational behavior of high-speed blade metering and low-speed blade and knife coatings are also discussed in order to point out qualitative difference between the two systems.

The mechanism of low-speed blade coating has been studied by several authors (Middleman 1977; Hwang 1979; Sullivan 1986). When inertia effects are neglected, lubrication theory is an acceptable first approximation to describe the viscous forces in the gap between the blade and the web (or roller in the case of knife-over-roll coating). The lubrication model predicts both the pressure profiles and the coating thickness.

Generally, the coating film thickness for Newtonian fluids is approximately equal to one half the minimum separation between the blade and the moving web. As shown by Sullivan (1986) and Strenger, Secor and Sramek (1992), the final coating thickness also depends on the size, curvature, inclination and inlet conditions of the upstream (feeding) region of flow. The key characteristic of this process is that coat weight decreases with increasing viscosity and web speed. In contrast, coat weight increases with viscosity and web speed in high-speed blade metering of paper coatings with bevelled blades (Kahila and Eklund 1978b). These differences suggest that, at least for the case of high-speed bevelled blade coating, inertia effects, which are ignored in pure lubrication flows, may be important.

Typically, the development of coat weight, of

wet film thickness, as a function of blade pressure in high-speed flexible blade metering follows the behavior depicted in Fig. 12d.6. In the bevelled mode, the blade pressure lowers the coat weight (region I), up to a point where pressure changes bring a minimal change in coat weight. When the flexible blade runs on its bent or low blade angle (i.e., blade angles below 20°) mode, coat weight increases with increasing blade pressure (region III). As the blade pressure of a bent blade increases, the operating blade angle decreases and, consequently, coat weight increases. In well-flexed blades, the coat weight passes through a maximum upon continual increase in blade pressure, as shown in Fig. 12d.6. Beyond this point (region IV), coat weight decreases with rising pressure because the excessive bending on the blade causes formation of a divergent nip between the blade tip and the surface of the moving web. Under these circumstances, the final film thickness may acquire a film-splitting pattern due to instabilities developed at the free surface of the coating film emerging from the channel between the blade tip and the web (Eklund 1984). This is similar to the film-splitting phenomenon that occurs in roll coating.

The relationship between coat weight and blade pressure depicted in Fig. 12d.6 was first reported by Eklund (1984) and it was analyzed by Saita (1984) using elastohydrodynamic principles (see Chapter 12c). Although this relationship applies to coating any type of a web, experimental data presented by Eklund (1984) were based on a paper web. In practice, it takes a wide range of blade pressures, irrespectively of how these are applied (i.e., with an inflatable hose or a mechanical device), to generate this graph. A key observation, however, is that a certain coat weight can be achieved with the flexible blade operating at two, or even three, different conditions. To understand the behavior of this system one needs to consider the forces involved in flexible blade metering.

Several dynamic forces develop as the coating fluid is dragged by the moving web onto the converging flow under the blade (Kahila and Eklund 1978a–c; Saita and Scriven 1985). First

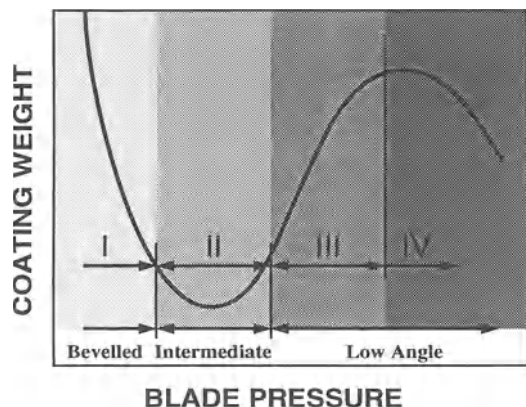


Figure 12d.6 Schematic illustrating change in coating weight as a function of the blade pressure in blade coating of paper webs (Eklund 1984).

are the shear and normal viscous stresses arising from the coating dragged into the converging region under the blade and through the blade nip. Coating fluid in these regions also develops a pressure and pressure gradient, similar to those occurring in purely lubrication flows. In turn, the viscous and pressure forces exerted on the blade cause it to deflect due to generation of elastic forces. In addition to the above, inertia forces are also present. These forces arise from the impact pressure of the upstream coating fluid layer, which contacts the blade and changes momentum to be expelled away from the blade nip. It is worth noting that other forces, such as gravity, surface tension, colloidal, etc., are present but play a minor role in high-speed blade metering.

The mechanism of blade metering is based on the balance of all the forces described above. As the moving web drags coating between it and the blade, hydrodynamic forces – in conjunction with inertial forces – stress the blade, which deforms proportionally to its flexural rigidity. Internal elastic forces and external loading (i.e., tube pressure) oppose blade deformation, so that finally the blade assumes a shape that balances all forces acting on it. In turn, the flow re-organizes to balance the hydrodynamic forces in the coating field of flow, while the paper web (and the backing roll) compresses under the

influence of the pressure pulse under the blade. As a result, at least for the case of paper coating, the non-Newtonian rheology of the coating and the compressibility and absorptive properties of the web also influence coat weight development. Both these and the fluid dynamic phenomena occurring during blade metering of paper coatings are discussed in more detail in the following paragraphs.

Many attempts have been made over the years to analyze and understand blade coating of paper. These led to deriving models of the physics of blade coating and to developing semi-empirical relationships which connect operational parameters, coating and substrate properties to coating film thickness or coat weight. These analyses and models considered three basic kinds of fundamental phenomena: (1) the hydrodynamic and inertial phenomena at the vicinity of the blade nip which are responsible for development of the forces described above; (2) the filling of pores in the substrate, which depends on the surface roughness and compressibility of the web; and (3) the penetration of the continuous (dispersing) phase of a coating dispersion into the substrate. It should be emphasized that most paper coating applications are considered high speed, i.e., in excess of 5 m/s, and the substrates are viscoelastic networks of cellulosic fibers which can rapidly absorb water and swell.

The simplest models are based on hydrodynamic lubrication at the blade nip. This phenomenon, more or less influenced by paper absorption, is considered the principle mechanism for coating deposition (Follette and Fowells 1960; Böhmer 1969; Bliesner 1971; Turai 1971; Modrak 1973; Hayward 1973). In these analyses the blade is considered as a cantilever beam that deflects under load, while the flow through the blade nip is based on hydrodynamic lubrication. Coating in the region close to and under the blade tip is assumed to develop a load-bearing capacity that lifts the blade in the normal direction to the web movement. The hydrodynamic lift exerted by the coating is counteracted by the applied blade load. According to this model, the net force acting on the blade is that of the hydrodynamic lubrication

lift which has been considered either inside the blade nip or upstream of the nip entrance on the underside boundary of the blade. This lubrication flow is similar to the one occurring in a rotating slider or a journal bearing, which has been a benchmark flow in fluid mechanics.

For the case of bevelled blade coating, the blade nip geometry has been considered as both a converging (Böhmer 1969; Bliesner 1971; Modrak 1973; Hayward 1973) and a parallel (Turai 1971) channel. In the former configuration, the hydrodynamic lubrication lift developed in the convergent flow is considered responsible for blade lifting. In the latter configuration, the blade tip is supposed to remain parallel to the paper surface at all times, so that the gap between the blade tip and the paper surface is equal to the final film thickness. As the drag flow induced by the moving web can only account for half the coating film thickness, a pressure gradient is needed to derive the other half. That pressure gradient leads to calculating the pressure force which lifts the blade. Experimental results based on lubrication (Follette and Fowells 1960) indicated that coat weight is inversely proportional to blade load. Coating weight increases with increasing machine speed; solids concentration and steady shear viscosity of the coating; the absorbancy and roughness of the paper; and blade extension. It decreases with increasing blade load and the blade thickness, and a backing roll made out of a harder rubber. (Extension here means the distance from the tip to the location on a blade beam where the blade load is being applied). In addition, coat weight decreases with an increasing blade angle.

Gartaganis, Cleland and Wairegi (1977) studied the connection between various operating parameters and coat weight in both bevelled and bent blade coating of paper. For the case of a bent blade mode, coat weight increases with increasing machine speed, blade extension, coating solids content and steady shear viscosity, the roughness and absorbancy of the web and the backing roll radius. Coat weight decreases with increasing blade angle and decreasing blade thickness. These authors also documented the

relationship between coat weight and blade load. Coat weight initially increases with blade load, up to a limiting load, thereafter decreasing as the load continues to increase. The two regimes before and after the maximum coat weight correspond to regions III and IV in Fig. 12d.6.

Early studies demonstrated that, in both the bevelled and bent operational modes, coat weight strongly depends on properties of the substrate. As some fibers at the paper surface cross over other underlying fibers and air voids exist between fiber crossings, paper webs have rough surfaces and are porous. Under the same blade configuration and load, more porous and compressible substrates provide comparatively high coat weights (Luciani and Galloni 1978). Among many variables, the porosity of the web depends on the papermaking furnish, mineral additives, paper formation and surface treatment. In particular, externally applied surface treatments onto paper webs are a practical way to improve their coatability. Paper compressibility, on the other hand, is primarily dependent on the papermaking furnish, formation, and consolidation of the fibrous network forming the paper web.

The simple lubrication model cannot fully explain the physics of high-speed blade coating. The blade boundary may not be parallel to the web under all possible operating conditions. The paper may deform under the pressure applied on it by the blade tip and the blade nip gap may therefore be far from parallel. The uniformity of the pressure gradient upstream of the blade nip is questionable, so is the assumption that the blade can be analyzed as a cantilevered beam. Lubrication approximation does not take into account physical phenomena arising from the free surfaces upstream of the blade and the coating penetration into the substrate. Finally, there is no consideration of the pressure (inertial) force upstream from the blade nip where the excess coating is deflected away. Because of all these complications, more advanced models are required to describe the blade metering process of paper.

All of the previous lubrication flow analyses are based on a one-dimensional model which

does not take into consideration the free surfaces, both upstream and at the terminating edge of the blade. The pressure drop across the blade nip has been considered nonexistent as both the upstream and downstream pressures are considered atmospheric. This assumption, however, may not always be valid, especially for the case of pond-type of blade coaters where a puddle is used to feed the blade nip (Fig. 12d.4c–e). Guzy and Higgins (1982) considered a nonzero pressure differential across the blade nip. These authors studied the effect of pressure differential on the load bearing capacity of the blade and found that, for the case of a negative differential, there is no bound on film thickness. However, when the differential is positive, there is a limit on the final film thickness.

Drawing from elastohydrodynamic computations, which are discussed in detail in Chapter 12c, Saita and Scriven (1985) developed a lubrication model which accounts for both the shear-driven (Couette) flow through the blade nip and the pressure-driven (Poissonneille) flow for convergent gaps. In addition to hydrodynamics, these authors considered the elastic forces of the blade, but excluded inertial effects and effects arising from free surfaces and the compressibility and permeability of the web. This model covers the operational behavior of both a low-angle stiff blade and a highly bent blade at moderate speeds (i.e., 4.5 m/s). The coating thickness in the bevelled blade mode was found to be approximately equal to the blade nip gap, i.e., the clearance between the tip of the blade and the surface of the substrate. In the bent blade mode, the coating thickness was about one half the width of the blade nip. In addition to predicting the qualitative physics of flow (Fig. 12d.6), this model provided quantitative results which were in agreement with measurements (Saita 1984) of relatively moderate-speed coating of Newtonian and shear-thinning fluids onto smooth, nonporous and incompressible webs. Based on this work, hydrodynamic lubrication dominates coating deposition in bent blade metering.

The above model was advanced by Pranckh and Scriven (1988, 1990) to incorporate the two-

dimensional flow in high-speed (i.e., 15 m/s) bevelled blade coating. It accounted for the fluid inertia upstream of the blade nip, the viscous forces on the face and side of the blade, and the pressure force in the blade nip. Computations based on this physical model illustrated that blade load and the working blade angle influence coating deposition in bevelled blade metering, where coating fluid inertia becomes important at high speeds (Pranckh 1989). Derived qualitative relationships are in agreement with experimental results published by Kahila and Eklund (1978b,c), Eklund (1984) and Kuzmak (1986a,b). This model was further expanded to incorporate porous substrates, hence laden air is being displaced by the coating due to pressure- and capillary-driven penetration of the coating into the porous substrate (Chen and Scriven 1989).

Computations illustrated that the amount of air trapped within the substrate is critical for determining the hydrodynamic pressure profile at the blade nip. More detail on the elastohydrodynamic models appear in Chapter 12c. However, quantitative results of these models remain to be verified by controlled experiments.

Key issues in high-speed blade metering of coatings for paper are the role of inertia, from the excess coating striking the underside of the blade upstream of the blade nip, and the roughness and compressibility of the web. Windle and Beazley (1967) and Kahila and Eklund (1978a) emphasized these phenomena, instead of the viscous forces and pressure gradient at the blade nip. According to these authors, high-speed metering evolves by filling depressions (or cavities) of the web, while the blade rides almost in contact with fiber crossings at the web surface. Hydrodynamic lift develops only in the convergent flow upstream of the blade nip entrance, so that lubrication flow exists only in this region. According to these authors, the focal phenomenon involves the coating layer which comes in contact with the blade and changes direction of flow as excess coating is removed from the blade. In doing so, the coating layer transfers momentum to the rigid blade, causing it to deflect.

In the case of bevelled blades, hydrodynamic

lift under the tip of the blade may exist temporally and only under unsteady conditions, i.e., when the blade tip is not exactly parallel to the web surface. Eventually, over an extended period of operation, the process attains equilibrium as the steel blade wears out to assume a parallel-plate geometry under the blade tip. Thus, studies by Kahila and Eklund (1978a–c) neglect the fluid viscosity and use potential theory with a simple momentum balance over a control volume at the blade to estimate the force exerted by the coating onto the blade. The inertia generates an ‘impulse’ force which is similar to the stagnation pressure incorporated in the elastohydrodynamic model (Pranckh and Scriven 1988, 1990). This force is significant at high-speed blade metering, i.e., the impulse force is by two orders of magnitude greater than the hydrodynamic lubrication when the blade angle is greater than 28° (Kahila and Eklund 1978b,c; Eklund 1984). Triantafillopoulos and Altug (1991) found that the inertial phenomenon is dominant for determining coat weight in bevelled blade coating of paper at speeds between 3 and 5 m/s. The impulse force accounted for more than 90% of the dynamic forces acting on a blade. The strong influence of the impulse force was also verified by Lyons (1993) who analyzed blade metering in a pond-type laboratory coater. Computations showed that the impulse force was by an order of magnitude greater than the hydrodynamic lubrication force. It is therefore important to realize that inertial effects are significant in high-speed bevelled blade coating of paper.

Besides the blade forces acting in the normal direction to web travel, there is the shear force which is parallel to web movement. Kartovaara (1991) showed that the lateral shear force can be as high as 30% of the dynamic forces acting on the blade for coater speeds between 5 and 16 m/s. The lateral force is proportional to coater speed, coating viscosity and length of the blade tip (i.e., blade thickness).

Practical experience has shown that, for bevelled blades, coat weight is directly proportional to steady shear viscosity of paper coatings and machine speed. When viscosity increases, i.e., by

raising the volumetric concentration of paper coatings, the blade load to obtain a certain coat weight also increases. Although coating viscosity does not appear in the impulse force equation, it influences the mass flow rate approaching the blade which is proportional to the impulse force. Comparatively high viscosity increases the amount of coating picked up by the web at the applicator roll nip and, consequently, raises the impulse force. Another observation from practice is that, under a constant load, coat weight increases proportionally with the coater speed (Fig. 12d.7). This is because the impulse force is directly proportional to the momentum of the coating layer dragged by the web into the region under the blade. Both trends for coating viscosity and speed observed at high-speed blade metering of paper are the opposite of those observed in low-speed knife coating where lubrication flow is predominant.

The contribution of the excess coating layer carried by the web onto bevelled blade nip was also considered by Kuzmak (1986a,b). In contrast to Kahila and Eklund, Kuzmak considered lubrication flow inside the blade nip, i.e., between the web surface and the blade tip. This work emphasized the effects of running the blade on its leading (toe) or trailing (heel) edge on coat weight and blade loading (Fig. 12d.3). In particular, it is necessary to continually increase blade load over an extended period of operation when running on the heel, or decrease the load when

running on the toe in order to maintain a certain coat weight. Under constant loading, an increase of the blade tip length, i.e., by using a thicker blade or running at the heel, would increase coat weight because the effective loading force at the blade tip decreases. When the blade tip area increases, blade loading is distributed over a wider area, the force per unit area decreases and, consequently, coat weight decreases. A constant coat weight in bevelled blade coating is maintained only when the tip of the blade is running parallel to the web surface.

The sensitivity of the system to the exact geometry at the blade tip is an important issue in bevelled blade coating of paper. This issue was discussed by Ramp (1983) and Roper and Attal (1993) who pointed out that running the blade on its toe or heel may lead to web breaks and coating defects, as discussed in more detail in Section 12d.7. The parallel nip geometry is usually the physical state of operation of bevelled blades in practice. Even though sometimes the blade tip is not set up correctly, the steel blade wears out to attain the parallel nip geometry. Under a certain blade load and blade angle, there is only one blade position where the blade nip is a parallel channel and the process remains in equilibrium. Changes in blade loading (i.e., tube) pressure to change coat weight lead to deviations from the parallel nip geometry, something which may increase the possibility for coating defects (Roper and Attal 1993). When the blade loading pressure increases, the blade tip shifts closer to the moving web at the toe and reduces coat weight. However, this configuration causes the blade tip to form a converging channel with the web, as depicted in Fig. 12d.3b. A decrease in the blade loading, on the other hand, allows the blade tip to run on its heel and apply more or less coating on the web, depending on the sharpness of the blade tip at its heel (Ramp 1983). This is illustrated in Fig. 12d.3c. The parallel channel geometry between the blade tip and the web can be maintained only if the mechanical mounting mechanism of the flexible blade is adjusted to compensate for changes in blade loading. It is therefore important to recognize

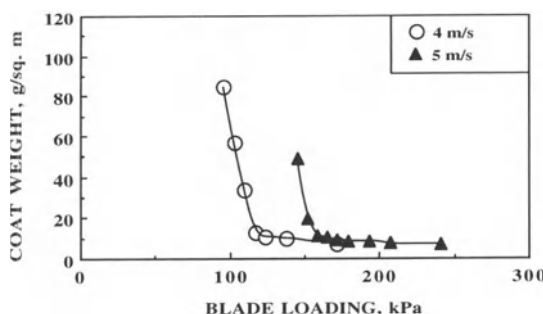


Figure 12d.7 Coat weight increases with machine speed in a bevelled blade coater. Experiments by Triantafillopoulos and Altug (1991).

that, when one changes blade pressure to influence coat weight, one also needs to adjust the blade mounting device accordingly to maintain parallel nip geometry at the blade tip.

Although blade wear during the operation of steel blades is an important subject, it has drawn little attention. Hassell (1981) illustrated that blade wear is proportional to the mass flow rate of the coating transferred under the blade and, therefore, depends mainly on coater speed and coat weight. Under a constant load, wear reduces as speed increases, the difference increasing at high blade pressures. Wear also decreases at high coat weights. However, it increases with the abrasiveness of the mineral pigment used in the coating formulation and the roughness of the web. This data indicated that blade wear is independent of the coating viscosity. As a result of wear, which changes the blade nip geometry, new steel blades require readjustment of blade pressure and holder positioning after a few minutes in operation. Recently, ceramic tip blades are used for paper coatings which are free of wear. However, these blades require proper initial setting because they have tips with multiple bevels. Under normal operational conditions, ceramic tip blades have a longer life than steel blades, although care is needed to avoid chipping the brittle tip of the blade.

In addition to fluid dynamics, properties of the coating fluids and the web influence coat weight development in blade metering of paper webs. One consideration is the penetration of the dispersing phase, i.e., the water with all soluble components and small colloidal particles such as latex, into the porous and absorbent paper substrate. This takes place prior to metering and when the coating contacts the moving web for the first time. This process fills in the voids in the paper surface and forms a relatively immobilized layer, referred to as the 'filtercake', through capillary and pressure penetration. This filtercake has a much higher solids content than the bulk of the coating which is fed into the process. Pressure penetration seems to be the more important mechanism (Sandås and Salminen 1987) as substantial pressure pulses apply onto

the web, in particular at the nip of an applicator roll. These pressures can be as high as 200 kPa in roll applicators, and about 100 kPa in fountain applicators (Eklund 1984). In contrast, the pressure in the case of a pond or short-dwell coater is less than 7 kPa (Korpela, Palsanen and Pitkanen 1986), which is the reason for the widespread preference of this application technique. The low pressure, in combination with the comparatively short coating-paper contact time period in short-dwell coaters, minimizes water absorption by the paper (cellulose) fibers prior to metering. In contrast, substantial absorption occurs before the blade in the case of a coater with an applicator roll.

An indirect consequence of water leaving the coating and entering the substrate is that cellulose fibers absorb water from the coating and swell. Swelling influences both the coat weight pickup at the blade, as well as paper properties dependent on changes occurring at the paper surface. Qualitative differences which exist between papers coated with an applicator roll and a short-dwell coater have been attributed to fiber swelling and its occurrence before or after the blade metering process (Eklund 1984). For coating with an applicator roll, fiber swelling occurs prior to metering. When the fibers swell, the web surface becomes rougher, requiring heavier blade loading to deposit a certain coat weight as the blade fills in the volume of the surface voids of the web. The blade acts as a smoothing device by covering the surface contour of paper. In contrast, fiber puffing and swelling take place after the blade metering step in the case of a short-dwell coater. This leads to a relatively rough final coated surface which adversely affects optical and printing properties. Consequently, papers coated with a short-dwell coater have inferior surface characteristics to those coated in a blade coater with an applicator roll.

In addition to substrate properties, the non-Newtonian flow behavior of paper coatings influences coat weight. Typically, higher steady shear viscosity leads to higher coat weight under a constant blade load, or higher load to obtain a targeted coat weight. A complication is that

the blade metering process involves regions with a wide range of shear rates (Pranckh and Scriven 1988). Stagnation regions appear next to areas where the shear rate is substantially high. Typical paper coating dispersions are shear thinning, while they exhibit significant yield stress and thixotropic recovery. They also demonstrate viscoelastic behavior, at least at low strain rates. When the volumetric concentration of the dispersion exceeds a certain level, paper coatings become dilatant. Low shear viscosity – obtained with single-point, rotating spindle type of instruments – is used to determine the ability to bring paper coatings to the metering zone, while high shear viscosity – obtained with a concentric cylinder's viscometer – is used to determine the required blade load to attain a certain coat weight. Böhmer (1969) was the first to estimate that, when considering the coating film thickness at the blade nip to be about $10\text{ }\mu\text{m}$, the shear rates in the blade nip of a coater running at speeds of practical interest can be as high as 10^6 s^{-1} . Viscometric data at these high shear rates are not readily available for paper coatings, although measurements with capillary viscometers have recently appeared in the literature (Roper and Attal 1993). Considerations of the non-Newtonian rheology of paper coatings are discussed in more detail in Section 12d.6.

In summary, the physics of high-speed blade metering of paper webs involve complex phenomena and their interactions. Viscous forces, developing in the blade nip and at the underside of the blade, and pressure forces in the blade nip, contribute to deflecting the blade, but the inertia of the coating layer reaching the blade also plays a significant role. Although lubrication flow seems to be the dominant mechanism for bent blades, the impulse of the coating layer striking the side of the blade is an important mechanism for deflecting bevelled blades. The interaction of the blade forces under conditions of practical interest, i.e., where non-Newtonian effects of the coating fluid and the absorbancy of the web come into the picture, is still an issue for investigation. Although computational fluid dynamics shed light on the mechanisms of high-speed blade

metering, there has not yet been a comprehensive model which also incorporates phenomena occurring during the application of the coating prior to metering. In addition, the influence of the paper absorbancy and compressibility to the final film thickness need to be further investigated, in particular as these properties influence formation of a filtercake prior to metering and correlate with swelling of paper fibers and roughening of the sheet. The exact mechanism of filtercake formation has not yet been studied in depth, so that the operational behavior of the process is difficult to predict and control. A point worth noting in the case of bevelled blade coating is the influence of blade nip geometry. The blade remains in equilibrium only when the geometry is a parallel channel. When the channel is convergent or divergent, coating defects appear, even though the rheology of the coating fluid has been optimized. Rheological phenomena occurring during the high-speed blade metering process and coating defects are discussed in Sections 12d.6 and 12d.7, respectively.

12d.4 HYDRODYNAMIC INSTABILITY IN BLADE COATING

The ideal coating flow is steady state and two-dimensional, that is, there are no temporal or cross-stream flow variations. Any instability would almost always result in a transition to a three-dimensional or unsteady state. Consequently, the film thickness becomes nonuniform. If the transition is to a two-dimensional time dependent state, there will be coating film thickness nonuniformity in the streamwise (machine) direction. Transition to three-dimensional flow will result in cross-stream variations referred to as streaks.

There are a number of regions in high-speed blade coating where the flow could become unstable. The most critical modes of instability are the transitions from a two-dimensional to a three-dimensional state (i.e., a symmetry breaking bifurcation). This transition could take place at the blade nip, in the case of a diverging gap, or

at other locations upstream of the blade (Aidun 1991a–c).

In pond application systems, the most serious instabilities are of a centrifugal type which occur inside the pond. In the pond, the base state consists of recirculating eddies which are almost two-dimensional over most of the coater width, except near the side walls where the Eckman-type layer forms. In actual coaters, the coater width is at least two orders of magnitude larger than the pond depth. Therefore, the effects of the sidewalls on the flow can be assumed to be a perturbation of the two-dimensional flow.

In this section, we focus on the pond of these coaters which is very similar to a lid-driven cavity, a rectangular section where the top surface moves with a constant speed. In practice, the top surface is the substrate that is being coated. As we are interested in the stability of the flow inside the cavity, we assume that all of the surfaces are smooth and impermeable. The substrate is usually being transported by circular rolls. However, as the radius of the roll is much larger than the streamwise length of the cavity, we assume that the top surface is flat. In the experiments outlined below, the roll diameter is 61 cm where the streamwise length of the cavity is only 5.08 cm long.

The parameters that govern the flow characteristics are the cavity aspect ratio and the cavity Reynolds number

$$Re = \frac{\rho U D}{\mu}$$

where U is the lid velocity, D is the cavity depth, μ and ρ are the fluid viscosity and density. Let us begin with the simplest case – a lid-driven cavity with infinite span. The Navier–Stokes and Continuity equations given by

$$\mathbf{u}_t + Re \left(\mathbf{u} \cdot \nabla \mathbf{u} \right) = \nabla p + \nabla^2 \mathbf{u} \quad \text{in } \Omega \quad (12d.1a)$$

$$\nabla \cdot \mathbf{u} = 0 \quad \text{in } \Omega \quad (12d.1b)$$

govern the flow in the cavity domain defined by Ω . The velocity vector, \mathbf{u} , pressure, p , and time, t , are scaled with the lid velocity, V , pressure scale, $\rho v V/D$, and time scale, D^2/v , respectively, and the cavity depth, D , is used as the length

scale. The boundary conditions are no slip walls, given by

$$\mathbf{u}|_{\partial\Omega_i} = (V, 0, 0) \quad \text{and} \quad \mathbf{u}|_{\partial\Omega - \partial\Omega_i} = (0, 0, 0) \quad (12d.2)$$

where $\partial\Omega$ is the boundary of Ω and $\partial\Omega_i$ represents the top surface. At a sufficiently small value of Re , the solution to this system represents a two-dimensional (2-D) flow given by

$$\mathbf{u}_{2D} = [u(x, y), v(x, y), 0] \quad (12d.3)$$

The boundary integral form of this solution is available for creeping flows, and in numerical form, for a wide range of Re by many investigators (for example see Bozeman and Dalton 1973; or Nallasamy and Krishna Prasad (1977)). In practice, however, this solution becomes unstable at a critical Reynolds number, Re_C , and most likely gives rise to a steady cellular flow (symmetry breaking pitchfork bifurcation). The value of Re_C and the wavelength of the critical mode, λ_C , depend on the length, H , to depth, D , aspect ratio, H/D . The three-dimensional (3-D) solution near onset can be approximated by separating variables in the linearized disturbance equation (see Chapter 8 for more information on linear stability analysis) and using a trigonometric representation in the z -direction. The critical disturbance mode at onset is then given by

$$\mathbf{u}' = [u'(x, y) \cos Z, v'(x, y) \sin Z, w'(x, y) \sin Z] \quad (12d.4)$$

where $Z = 2\pi(z - \alpha)/\lambda$, λ is the wavelength of the periodic cellular flow, and α represents an arbitrary phase of the disturbance structure. As the flow close to the critical Reynolds number is a superposition of the two-dimensional base flow and the critical disturbance mode, represented in (12d.4), the new state is a three-dimensional flow pattern with periodicity in the spanwise direction.

Now consider a cavity with finite span, L , and free-slip end walls where the boundary conditions at the end-wall planes, $\partial\Omega_e$, are given by

$$w = 0 \quad \text{and} \quad \frac{\partial u}{\partial z} = \frac{\partial v}{\partial z} = 0 \quad \text{on} \quad \partial\Omega_e \quad (12d.2')$$

Here also the steady two-dimensional solution (12d.3) satisfies the boundary conditions (12d.2'). The bifurcating 3-D solution at onset can be represented by (12d.4) with the eigenfunction, Z , modified to $n\pi z/L$, where n is the wavenumber of the disturbance structure inside the container, and the phase angle, α , being no longer arbitrary, is set to zero. Modes representing an even or odd number of cellular patterns can become critical and destabilize the 2-D base solution as shown in Fig. 12d.8. Here the vertical (horizontal) plane represents solutions with an odd (even) number of cellular patterns.

As the slip condition at the end wall given by (12d.2') is also a symmetry condition, the similarity mapping used by Aidun (1987) applies. Therefore, from the stability boundary for a single cell pattern, $R_c^1(L)$, the entire stability boundary for the initial bifurcation point can be mapped by the transformation

$$R_c^n(L) = R_c^1\left(\frac{L}{n}\right) \quad \text{where } n = 1, 2, \dots \quad (12d.5)$$

The expected form of the stability boundary predicted by equation (12d.5) is shown in Fig. 12d.9. This figure shows the effect of the cavity span on the critical Reynolds number for

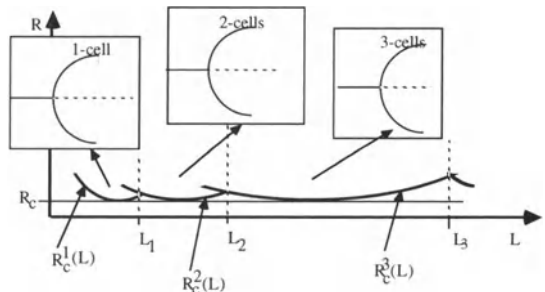


Figure 12d.9 An example of the stability boundary showing the self-similarity of various cellular patterns (Aidun, Triantafillopoulos and Benson 1991).

transitions from a two-dimensional flow, ideal for coating systems, to a three-dimensional flow which results in coating nonuniformities.

Let us next discuss the real driven cavity system where the no-slip condition applies to the end wall as well as any other solid boundary.

In a series of experiments, Aidun, Triantafillopoulos and Benson (1991) and Benson and Aidun (1992) investigated the stability of flow in a driven cavity with span to depth aspect ratio of 3 to 1. Their experiment setup consisted of a roll driving the fluid inside a rectangular cavity, as shown in Fig. 12d.10. This is similar to the

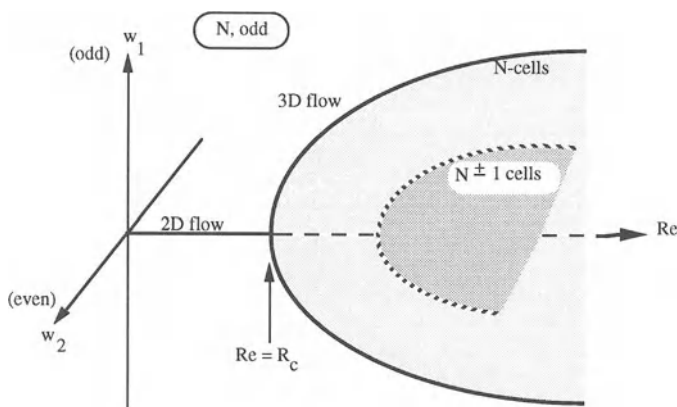


Figure 12d.8 The state diagram for a lid-driven cavity with free-slip end walls, an ideal representation of a pond application coater.

setup of Pan and Acrivos (1967), although in these experiments, the roll diameter is considerably larger than the cavity and, therefore, the penetration is about 2% compared with 8.5% (of the cavity width) in Pan and Acrivos' experiments.

The cavity, placed on top of a lower compartment (Fig. 12d.10a), makes contact with the roll and has length $H = 5.08$ cm in the direction of roll motion, depth $D = 5.08$ cm, and span $S = 15.24$ cm transverse to the direction of roll motion. Thus, the characteristic geometric parameters are 1:1 and 3:1 for depth- and span-to-length aspect ratios, respectively. The lower compartment has the same dimensions but a depth of only 2.54 cm and serves the purpose of feeding fluid uniformly into the cavity.

A very thin film of fluid adheres to the roll and escapes the cavity through the downstream lip EC. This layer of fluid is scraped off the roll by a sharp blade downstream of the cavity. At the bottom of the cavity adjacent to the GK corner, a narrow slot (3 mm opening) opens into the lower section which is connected to a pump and acts as a reservoir for replenishing the fluid that escapes the cavity.

Fluid is supplied to the lower section of the cavity via a 1.00 cm pipe tap from one side. The observed flow patterns show that the flow through the slot into the cavity is uniform over the span.

At a low Reynolds number, the flow is steady and almost two-dimensional. However, as the Reynolds number increases above 825, the steady flow destabilizes and gives rise to a time periodic state with an oscillation frequency of about $0.1 U/\ell$. Flow visualization of the time periodic state shows small-amplitude time periodic waves appearing on the downstream secondary eddy starting out at the middle symmetry plane and traveling towards the side walls. As Re increases, these traveling waves become more clearly visible (see Fig. 12d.11b) until a second incommensurate frequency, $0.0056 U/\ell$, appears at Re above 990.

Benson and Aidun (1992) show that the flow remains quasiperiodic up to $Re = 1055$ where many other modes are excited and a broad band of frequencies appear signaling the existence of a low dimensional chaotic state. Figure 12d.11d, shows the flow at $Re = 1900$. At this state, the mushroom shaped vortices appear and disappear randomly inside the cavity. These structures are similar to Gortler-like vortices that Koseff and Street (1984a–c) have reported at higher Reynolds numbers.

The length scale of the vortices presented in Fig. 12d.11d is comparable to a class of streaks that are observed at high speed with pond application systems such as the short-dwell coater. However, other issues such as air entrainment become important mechanisms which promote defects in coaters of this type. Recent experiments (Veverka and Aidun, 1991; Li and Burns, 1992) indicate that air entrainment is another significant cause of coating streaks.

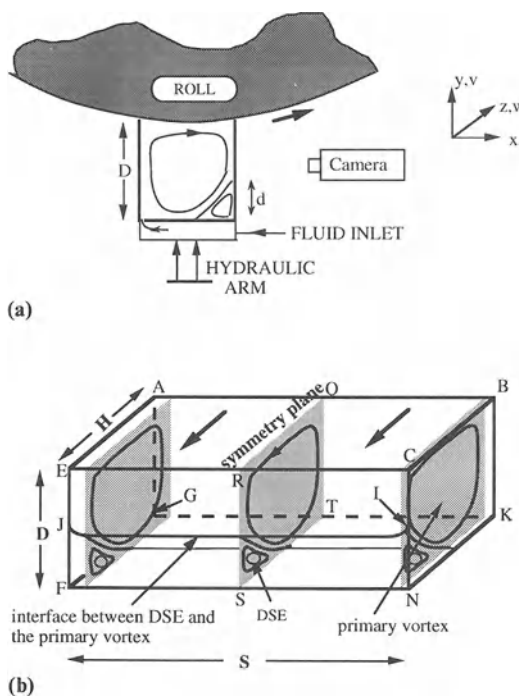


Figure 12d.10 Schematic of the experimental setup showing (a) the coordinate system x , y , z and the corresponding velocity components u , v , w , and (b) recirculating primary and secondary eddies of the steady state primary mode.

12d.5 AIR ENTRAINMENT

Application of a thin liquid film on a flat substrate involves displacement of air by liquid. With flexible substrates, such as paper, photographic films, or magnetic tapes, the coating is continuously applied

to a moving substrate. The speed of the substrate and, therefore, the rate of coating is limited by the maximum critical speed of displacing the air. Beyond the maximum wetting speed, air cannot be effectively displaced, and some patches of air remain on the surface or entrain into the liquid.

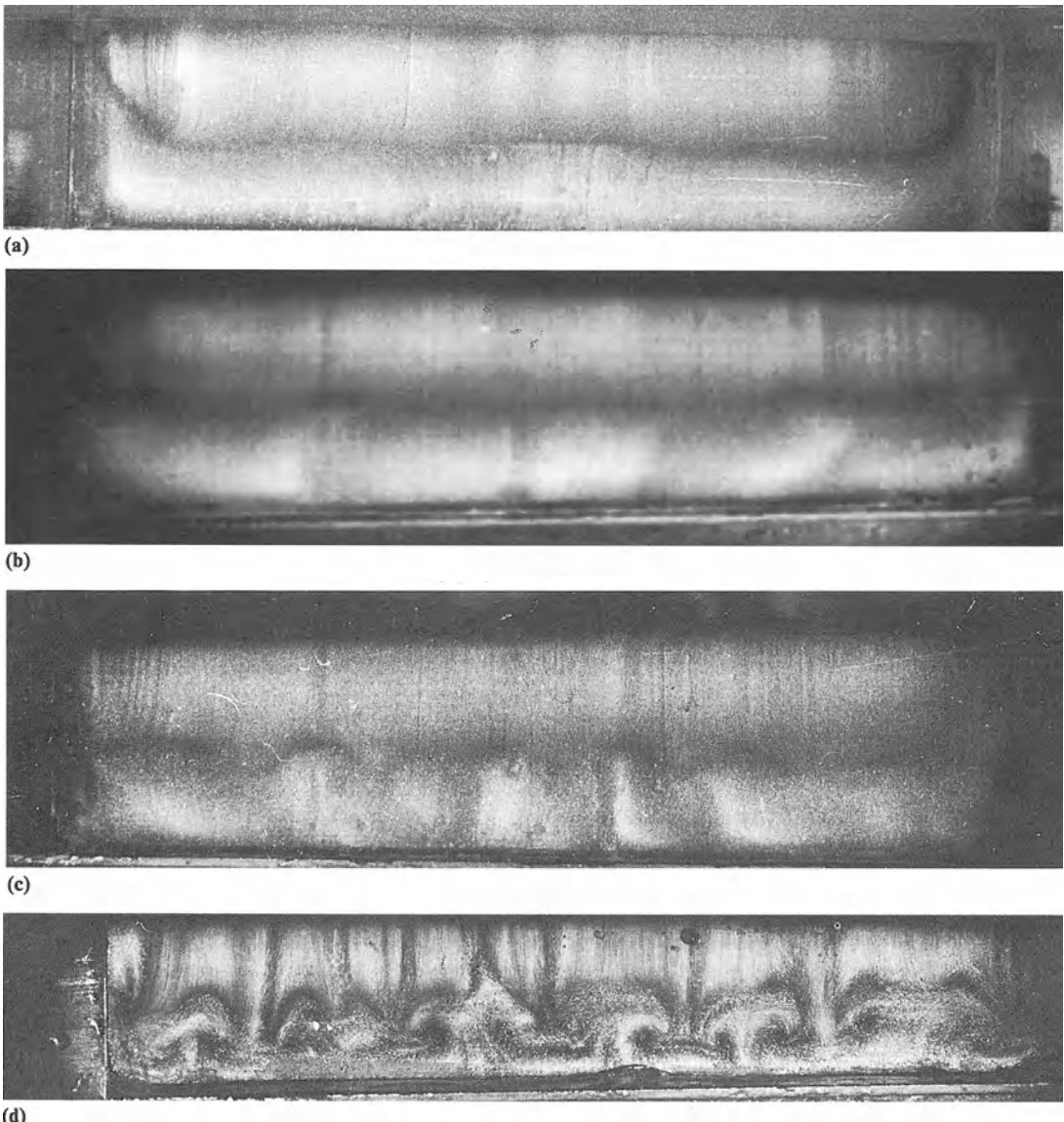


Figure 12d.11 Front-view photographs of flow patterns. From top to bottom: (a) two-dimensional steady flow with primary and secondary rolls at $Re = 500$ (notice the straight separation line); (b) wavy separation line for $Re = 700\text{--}1000$ (time-periodic flow); (c) appearance of mushroom-like structures for $Re = 1100$; (d) unsteady state at $Re = 1900$ (Aidun, Triantafillopoulos and Benson 1991).

With the increasing demand for higher production rates, air entrainment has emerged as one of the leading problems in the coating industry. By air entrainment we mean a physically isolated patch of air or bubble that enters into the liquid phase. In pond application systems, the air gradually accumulates in low pressure areas. These air pockets interact with the substrate and generate coating defects mostly in the form of streaks on the surface (Aidun 1989).

The critical speed for onset of air entrainment has been measured by many investigators (Kennedy and Burley 1977; Burley and Kennedy 1976; Bolton and Middleman 1976; Blake and Ruschak 1979; Burley and Jolly 1984; Sullivan and Middleman 1979), see Chapter 3 for more detail. Some of these measurements, however, are subjective and show inconsistent behavior. For example, some studies (Kennedy and Burley 1977; Burley and Kennedy 1976) indicate that the substrate entry angle significantly affects the critical air entrainment speed, while other studies (Bolton and Middleman 1976; Blake and Ruschak 1979) show no relation between the two. The effect of surface roughness on the critical speed for air entrainment has also remained unclear; some studies (Burley and Jolly 1984) show a strong interdependence, while others (Sullivan and Middleman 1979) indicate otherwise. It is probably the different experimental setups and substrate materials that are responsible for some of the inconsistencies.

In this section, we focus on the physical mechanism of air entrainment in blade coating systems. In particular, we investigate the sequence of events which leads to formation of air bubbles and their entrainment into the liquid. We recognize at least two regimes of air entrainment (Scriven 1982): (1) a microscopic regime, proposed by Miyamoto and Scriven (1982) and further investigated by Miyamoto (1991), and (2) a second regime at macroscopic scale where air bubbles in the order of few hundred microns and larger form at the wetting line and penetrate into the liquid.

In the microscopic regime, it is hypothesized that a thin air layer, less than a micron, forms

at the dynamic contact line. Miyamoto and Scriven (1982) analyzed the two-dimensional idealization of this flow and concluded that Kelvin–Helmholtz-type instabilities are likely to occur for thicker gas films, while a ‘disjoining collapse’ instability at the interface will dominate for thinner air layers. Miyamoto (1991) presents some experimental evidence of massive shear instability of the air film and formation of ‘craters’.

This section focuses on the macroscopic regime of air entrainment where the entrained bubbles are too large to dissolve in the liquid and, therefore, remain as air bubbles in the liquid.

To study the kinetics of wetting, Deryagin and Levi (1964) used a simple slot-like coating apparatus to reproduce the process of coating an emulsion on a flexible substrate. They used a wetting hopper with a square cross-section with sides equal to 2.4 cm. Using visualization techniques, they observed the deformation of the wetting line as they increased the substrate speed. At low base velocity of a wettable liquid/solid system, the contact angle is small, and ‘perfect wetting’ is observed. As the coating speed increases, the meniscus deforms, and the contact angle increases to 180° as shown in Fig. 12d.12. They report that at this critical speed, a shift in the contact line is observed by the appearance of a triangle where contact between the liquid and the substrate is broken. As the substrate speed increases further, the triangular area grows to a point where the break extends over the entire length of the contact as illustrated in Fig. 12d.12b.

The pioneering work of Deryagin and Levi (1964) reveals an important event and limitation in the wetting of solids by liquid. A contact line, originally straight, breaks into a sawtooth pattern at a critical speed where the contact angle reaches 180°. In the ideal situation where the contact line is infinitely long, this behavior can be viewed as a transition from a two-dimensional flow to a three-dimensional state.

Blake and Ruschak (1979) attribute this behavior to a maximum wetting speed above which the contact line has to break into a V-shaped pattern so that the effective wetting speed falls below the maximum value. A rigorous analysis of the

contact line instability and formation of triangular air pockets remains to be undertaken.

Many experiments, as outlined above, show that the prerequisite for air entrainment in the wetting process of a smooth surface is the formation of these structures. The events that follow this transition and lead to air entrainment in low-speed roll coating systems are discussed by Veverka and Aidun (1991) and Aidun, Veverka and Scriven (1992). There is some evidence that the same sequence of events also leads to air entrainment with high-speed pressurized pond application blade coating systems. The difference is that with pressurized pond systems, the fluid is forced out of the cavity at the overflow baffle near the contact line (see Fig. 12d.4e), substantially delaying air entrainment to higher speeds.

There is now direct evidence of the serious adverse effects of air entrainment in pond application systems. In a series of experiments with actual pressurized pond coating systems, Li and Burns (1992) showed that the accumulation of air inside the coating cavity results in streaks at speeds much below the 'skip' coating regime. They used typical paper coating liquids with a small amount of fluorescent dye. The dye was added to detect the nonuniform coating thickness

patterns under ultraviolet light after the coated samples were dried. The substrate used was paper and the coating speed was varied from 15 m/s to a maximum of 25 m/s. To examine the effect of air accumulation in the pond, Li and Burns (1992) placed a ventilation tube inside the pond. A series of experiments was completed with the ventilation tube extracting air from the pond. A second set of experiments was conducted under the same conditions with the ventilation tube blocked so that no air could be extracted from the pond. In their experiments Li and Burns (1992) clearly document that in every case, extraction of air significantly reduced the coating thickness nonuniformity and streaks on the surface.

12d.6 NON-NEWTONIAN RHEOLOGY IN BLADE COATING

Paper coatings comprise highly concentrated dispersions of mineral particles, with volumetric concentrations in excess of 40% by volume. Flow characteristics are generally determined by the volume fraction of the disperse phase, the magnitude of interparticle forces and the structure of the flocculates formed. In addition, the dispersing phase of paper coatings contains

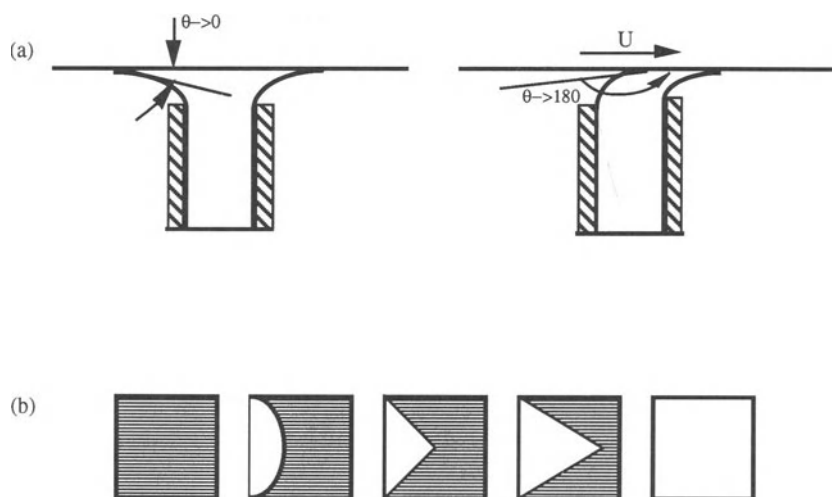


Figure 12d.12 Schematic of the boundary displacement during wetting (Deryagin and Levi 1964).

polymers which may or may not be water soluble. Although these polymers are added at small amounts (typically 0.1% to 5%), they substantially affect coating rheology. Polymers function by inducing a network structure which physically bounds polymer molecules and/or dispersed particles. This structure leads to development of yield stress and viscoelasticity at low shear. At high shear rates, forces holding the network structure are disrupted leading to shear thinning. This structural breakdown is also associated with time-dependent rheological behavior, known as thixotropy. Typical coating dispersions, therefore, have high viscosity at low shear rates and low viscosity at high shear rates. At increased particle concentrations, however, paper dispersions become increasingly non-Newtonian, independent of the flow behavior of the dispersing phase.

At low stresses, coating dispersions show not only plastic behavior but also viscoelasticity. In addition to polymeric network structures, these rheological phenomena arise from three-dimensional network structures due to intermolecular interactions between pigment particles. When subjected to low shear stresses, these structures attain a dynamic equilibrium between structural breakdown and re-formation under the applied shear stress and exhibit primarily elastic deformation and a high viscosity. Consequently, in addition to flow curves which describe the relationship between shear rate and shear stress, rheological characterization of paper coatings requires controlled-stress and dynamic viscoelastic measurements.

The rheological behavior of paper coatings plays an important role during processing and application in a high-speed blade coater. It determines not only the coating flow at the blade nip, but also the flow feeding the application zone. Rheology influences the hydrodynamics upstream of the blade through the steady shear viscosity and plastic yield. Once at the blade nip, high-shear viscosity and, possibly, viscoelasticity affect the blade deflection and the final film thickness (or coat weight). After the blade nip, thixotropic recovery contributes to the post metering behavior of the coating layer. Although

the effect of rheology on high-speed blade coating for paper is an evolving field of research, there exist some documented correlations between coating rheology and coatability. The following paragraphs point these out, while addressing the main unresolved issues. For comparison, reference is also made to rheological effects in the relatively low-speed blade (or knife) coating.

Viscoelasticity in high-speed blade coating of paper can be assessed from the Deborah number, $De = \lambda/t$, where λ is the characteristic relaxation time of the coating liquid or dispersion, and t is the characteristic residence time in the process flow. Most coating materials have a very broad relaxation behavior and, therefore, exhibit a slow change of storage and loss moduli with frequency (Goodwin 1989). For example, typical values of the relaxation time for paper coatings are in the range of 0.1 to 5.0 s (Roper 1990; Salminen and Förs 1992). These values correspond to the time period for the shear modulus to decrease half of its value at 0.01 s in a dynamic rheometer. Values obtained with this method represent quantitative approximations of the characteristic relaxation spectra. Considering that a typical residency period at the blade nip is approximately in the order of magnitude of 10^{-5} s (Kline 1985), the De is much larger than 1. Such high Deborah numbers suggest that paper coating dispersions could behave like elastic solids rather than mobile liquids during their application.

Similar or larger Deborah numbers are common in coating of polymeric liquids onto smooth and impermeable substrates. The effect of viscoelasticity on coating film thickness has been well documented for the case of lubrication flow in rigid blade coating (Middleman 1981). Prediction of the film thickness (or coat weight) requires consideration of the normal forces arising from the viscoelasticity of the polymeric liquid in addition to viscous forces (Hsu, Malone and Laurence 1985). Theoretical and experimental studies have shown that, while the non-Newtonian shear viscosity influences the flow and pressure distributions at the nip, viscoelasticity affects blade loading (Greener and Middleman 1974; Hsu, Malone and Laurence 1985; Hsu 1986). In

particular, viscoelasticity contributes to the separating (normal) force which tends to push the bounding surfaces of the web and blade apart. The separating force increases with flow velocity, i.e., the speed of the backing roll (Hsu 1986). For relatively high flow velocities, the load capacity on a stationary blade over a moving plate can be up to fifty times greater for a non-Newtonian viscoelastic lubricant than for a Newtonian fluid (Doremus and Piau 1981). In addition, much less fluid is carried through the gap in the case of viscoelastic fluids, while both the stagnation point of the flow and the maximum normal stress abscissa move closer to the gap (formed between the blade and the plate) center (Doremus and Piau 1983). Theoretical analysis (Greener and Middleman 1974) of the lubrication flow in a blade nip indicates that, as compared with a Newtonian fluid, the pressure developed under the blade decreases for a polymeric viscoelastic fluid and increases for an elastic Newtonian (Boger) fluid. Sullivan (1986) demonstrated that film thickness increases with purely viscous shear-thinning fluids, while viscoelastic fluids, which have both viscous (shear-thinning) and elastic behavior, cause the film thickness to either increase or decrease depending on the relative contributions of shear-thinning and elastic effects. For the case of fluids with the same viscosity but different elasticity, film thickness decreases as elasticity increases. This trend is also valid for a Newtonian fluid having elastic properties, i.e., a Boger fluid. In a blade-over-roll geometry, the coating film thickness increases with both the blade angle and blade extension, although coating films of highly elastic Boger fluids are independent of blade nip configuration (Sullivan, Middleman and Keunings 1987). Furthermore, the operability window of blade coaters shrinks with viscoelastic liquids (Strenger, Secor and Sramek 1992). The limiting factor is the appearance of ribbing instability on the coating film. This defect is associated with converging blade geometries where inclusion of elastic normal stresses in the lubrication model predicts, for high inclinations (i.e., large blade angles), a rising pressure at the exit from the channel. Because of the complex

rheology of polymeric liquids, which exhibit both viscous and elastic behavior, it is difficult exclusively to attribute their flow behavior at blade nips to elasticity. Many times elastic effects compete with viscous behavior (shear thinning), making prediction and control of the final film thickness difficult to achieve.

The role of viscoelasticity in high-speed blade coating of paper is further complicated. The highly concentrated coating dispersion contains orientable particles and polymeric additives which interact with the dispersed phase in many different ways to affect rheology. In addition, paper webs are compressible, nonuniform, permeable and filled with air. Water soluble binders and additives – such as starch, carboxymethylcellulose, hydroxyethylcellulose, polyvinyl alcohol, etc. – added to paper coatings induce viscoelasticity and increase viscosity at low shear rates. However, they also make the coatings shear thinning at high shear rates. Therefore, it is difficult to separately assess the viscous and elastic contributions of rheology to the flow at the blade. Results by Sullivan (1986) suggest that shear thinning, characteristic of paper coatings, may offset the effect of elasticity in the case of viscoelastic coatings.

Normal forces due to viscoelasticity could influence the flow and the force balance in and around the blade nip during high-speed blade metering of paper coatings. This, in turn, could affect the final coat weight obtained under a given set of process conditions. Elasticity is expected to generate substantial normal forces perpendicular to the flow direction when the coating is flowing out from the restricted channel under the blade and the relaxation time is sufficiently long (Ginn 1974, 1977). Then, normal forces and viscoelasticity need to be taken into account when setting up the operating parameters of the process. Windle and Beazley (1967, 1968) analyzed the flow beneath a bevelled blade based on the hydrodynamic lubrication flow in a converging wedge and considered paper compressibility and roughness in determining coat weight. These authors suggested that the hydrodynamic lift acting on the blade arises, at

least partially, from the normal forces of coating viscoelasticity which contributes to the total thrust of the flow through the nip. However, laboratory coater experiments with coatings containing clay, styrene butadiene latex and starch, and having the same low-shear viscosity but different low-strain elasticity did not yield significantly different coat weights. Windle and Beazley (1968) attributed their inability to document the effect of viscoelasticity to (1) failure to separate the viscous from the elastic contributions to the dynamic forces acting on the blade, and (2) the possibility that the passage of the coating through the blade nip might be viewed as fracture of a weak elastic solid rather than flow of a viscous liquid.

It is important here to recognize that characterization of coating viscoelasticity is usually based on oscillatory dynamic measurements at low deformations. These measurements are not sufficient to characterize the behavior of coatings at the very fast deformation process in the blade nip. Similar to steady-shear viscosity measurements, viscoelastic measurements cannot be extrapolated from low to high deformations. The problem is that it is difficult to measure viscoelastic properties at shear rates of the order of 10^5 to 10^6 s^{-1} which are experienced under the blade and inside the blade nip.

Attempts to measure the normal forces exerted by paper coatings are based on viscometric measurements in capillary flows. Kurath (1965, 1974) documented that normal stresses are much larger than shear stresses for clay dispersions in a starch solution, increasing with the shear rate and volumetric concentration. However, the dependence of normal stresses on concentration was limited to clay/starch coatings and did not make any difference in a coating containing clay, calcium carbonate and starch. It is also worth noting that the magnitude of normal stresses depends not only on the type of mineral pigment used, but also the size and shape of the pigment. Kurath (1974) found that, when a fine particle clay was substituted with a delaminated (platey) clay in a starch formulation, both shear and normal stresses increased substantially under

constant shear rate (i.e. $17.4 \times 10^4 \text{ s}^{-1}$). For the clay/carboxymethylcellulose coatings tested by Grankvist and Sandås (1990), normal forces increased exponentially with shear rate above 10^5 s^{-1} . At constant shear rate, normal forces increase with the molecular weight of the carboxymethylcellulose and its addition level. Laun and Hirsch (1990) investigated the normal forces of two coatings (64% solids by weight), one of the coatings demonstrating absence of any normal forces, while the second one – which was dilatant at shear rates between 10^3 and 10^5 s^{-1} – had normal stress differences which were five times greater than the corresponding shear stresses. It is possible, therefore, for high-solids coatings which are dilatant, and consequently behave like elastic solids as shear rate increases, to demonstrate substantial normal forces in shear flows when the shear rate is sufficiently high, i.e., above 10^5 s^{-1} . The dependence of normal forces on shear rate follows the well-known relationship of normal stresses being proportional to the square of shear velocity (Grankvist and Sandås 1990).

Normal forces may also arise from shear induced structures (Brady and Bossis 1988) formed across shear planes existing between the blade and the web. Computer simulations (Bousfield 1990) illustrated that shear in the gap, formed between the paper and the blade surface, can cause an ordered arrangement of pigment particles such that 'bridging' between the two boundaries occurs. Formation of bridges develops an additional normal force, which can be as much as four times the normal force occurring originally. Bridging frequency increases rapidly with increasing solids content of the coating.

The recent growth of interest in understanding the physics of blade metering and coating rheology is partly due to higher machine speeds and lower coat weights. Currently, many industrial coaters run in excess of 24 m/s and apply from 4 to 10 grams of coating per square meter of paper. When the machine speed increases, the deformation process under the blade becomes faster and the Deborah number increases, while large transient stresses develop due to the relatively high blade loadings. Such process conditions,

coupled with the trend toward coatings with high volumetric concentrations, make consideration of normal forces in high-speed blade metering of paper webs more realistic.

In summary, the non-Newtonian behavior of paper coating dispersions arises from interparticle interactions and the network structure of polymeric additives. Most paper coatings are viscoelastic at low strain rates, demonstrate substantial yield stress, and are shear thinning thixotropic over a broad range of shear rates. The magnitude of the characteristic rheological parameters depends primarily on volumetric concentration and the amount and type of polymeric additives and, secondarily, on the particle size and shape of the mineral pigments used. The viscoelasticity of paper coating dispersions is substantially lower than that of polymers. Although viscoelasticity prevails at low strain rates, the elastic network structures breakdown with shear so that, at high shear rates, paper coatings behave like viscous suspensions. The degree of shear thinning depends on the coating formulation, i.e., coatings with soluble polymers have relatively high low-shear viscosity and low high-shear viscosity. Suspensions of coarse, highly anisometric pigment particles demonstrate comparatively high elasticity at low shear and viscosity at high shear. Although most paper coatings do not demonstrate significant elasticity at high shear rates, coatings with extremely high volumetric concentration become dilatant and behave like weakly elastic materials. The large Deborah number makes processing of these type of coatings in a high-speed blade coater problematic. However, there is not yet a clear connection between rheological properties of coatings and their processability as high-speed coaters. This is partly due to interactions between the coating dispersion and the substrate, such as formation of a filtercake on top of the web prior to metering and the swelling of cellulosic fiber of paper when they come in contact with a coating dispersion. Furthermore, it is not yet known how the coating layer rheology after metering and before drying influences the appearance of coated surface defects and the end-use properties of paper.

12d.7 BLADE COATING DEFECTS

As with any coating operation, a defect free surface is important in maintaining consistent and sustainable productivity and product quality in high-speed blade coating. Although there are many different types of defects appearing in the various applications of the blade coating process, here we concentrate only on blade coating defects on paper webs. Furthermore, the focus is on defects arising from process flow dynamics and properties of paper coating dispersions.

Good runnability usually means coating without visual film defects on the coated surface and a uniform coat weight (or film thickness) in both the machine and cross-machine directions. In the development of a coating formulation strategy, good runnability also means being able to obtain a certain coat weight at comparatively lower blade loads. This leads to lower blade forces acting onto the web, thus minimizing the possibility for web breaks. Indeed coater runnability becomes more important as the speed of commercial coaters increases beyond 24 m/s and the coating film thickness continually reduces.

Most of the common visual defects in blade coating appear in the form of scratches, skips or streaks on the coated surface. Scratches usually appear in the form of fine hair-like indentations (less than 3 mm in width) in the coating layer running along the machine line direction. Skips are associated with a patterned surface appearance because of areas devoid or depleted of coating. The appearance of skips is associated with air inclusion or entrapment into the coating pond or in a region upstream the metering blade. Streaks, on the other hand, appear in various forms. Narrow streaks take the form of relatively narrow indentations, 5 mm and up to a few centimeters in width. Wider streaks can be as broad as several centimeters and form bands of heavier coat weight running along the machine direction. All of these defects are easy to observe when paper samples are viewed with transmitted ultraviolet light. Streaks appear as variation of opacity across the web, while scratches appear as thin, less opaque lines. The origin and

mechanisms responsible for these defects are numerous, some of them discussed in more detail in the sections about air entrainment and hydrodynamic defects (Sections 12d.4 and 12d.5).

The appearance of scratches depends on properties of all three components in a blade coating operation; namely, the base paper, the coating dispersion, and process parameters or blade nip geometry. Usually this defect is a problem with bevelled but not bent blades. Huang (1984) separated scratches into mechanical and rheological based on their origin. 'Mechanical' scratches are attributed to the entrapment of foreign matter in the blade nip. These materials may be loose fibers from the web, contaminants in the coating stream, nondispersed or aggregated mineral pigments in the coating, poorly prepared soluble binders or thickeners, etc. Additionally, hard spots on the bevel of the blade or chipping of a ceramic blade can cause scratching of the coated surface.

'Rheological' scratches are associated with properties of both the coating dispersion and the basesheet. The coating needs to have good 'water holding', also known as water retention. Water holding defines the capability of a coating dispersion to control release of its dispersing phase when it makes contact with the porous web during processing (Eklund 1981). Water and solubilized materials are released from the coating by capillary and pressure penetration, but the dominant mechanism for dewatering is pressure penetration experienced by the coating dispersion at the nip of the applicator roll and under the blade (Sandås and Salminen 1987). Water retention is associated with the physical and chemical state of network structure present in the dispersion due to interparticle interaction and the presence of polymeric additives. Consequently, it depends on the type of mineral pigment used, and its ability to form an array of closely packed particles under the influence of an external pressure pulse; the low shear viscosity of the coating and the liquid phase; and the nature of structure networks due to the presence of polymeric additives. Water holding additives used in paper coatings may be soluble or insoluble in water. Typical additives

are carboxymethylcellulose, hydroxyethylcellulose (and their associative derivatives), alginates, polyvinyl alcohol, polyurethane associative thickeners, alkali swellable lattices, etc. Soluble binders and their modification, such as starch and proteins, are also inducing some water retention in paper coatings.

Experiments by Gane, Watters, and McGenity (1992) illustrated that the coating layer, or filtercake, formed next to the web prior to metering has a higher solids concentration than the coating at the application station or feeding stream. Coatings with good water retention, however, do not lose substantial water and soluble material into the basesheet at the applicator roll and the blade nips. Because of that, the filtercake build onto the web before metering maintains a solids content close to that at the application zone.

Associated with water retention is the term 'immobilization solids', which represents the volumetric concentration at which a coating dispersion has almost infinite shear viscosity – the coating becomes dilatant. For a coating dispersion with a certain solids content, the characteristic immobilization solids are closely connected to water retention. Ideally, coating immobilization should occur after the blade metering step of the application process (Eklund 1981). Excessive dewatering prior to metering can cause the filtercake formed onto the web to become dilatant. In turn, a dilatant filtercake reaching the blade nip can generate scratches and narrow streaks (Huang 1984, 1986).

Coating dewatering also depends on properties of the basesheet; namely its surface pore structure, compressibility, smoothness and absorbancy. An 'open', absorbant basesheet tends to take up more water from the coating and, therefore, increases the solids content of the filtercake layer formed prior to metering next to the web. Coating immobilization before the blade nip is responsible for the appearance of scratches or narrow streaks due to entrapment of particles or particle agglomerates at the blade nip. Furthermore, scratches and streaks can be generated from poor water retention at the stagnation line, appearing on the

blade boundary, of the converging flow upstream from the blade nip (Pranckh and Scriven 1988). Eventually, new coating material reaching the blade will push large agglomerates deposited at the stagnation line through the blade nip. As a result, streaks and scratches due to this mechanism are temporal in nature, disappearing over a long time of operation.

The exact mechanism of interaction between water retention and the substrate is not yet completely understood. Water leaving the coating layer on top of the traveling web is absorbed by cellulosic fibers of the web, thus causing them to swell and rise. Fiber rising, in turn, influences the quality of the coated surface and properties like gloss. In systems with an applicator roll, fiber swelling takes place prior to the blade nip, while in the case of a short-dwell coater, swelling takes place after the blade since the fibers do not have enough time and the coating does not experience high normal pressures prior to metering. Consequently, there are differences in the final quality of papers coated with each one of these two types of coaters (Eklund 1984). Although the rise in coating solids concentration between the application and metering steps has been documented, little is known about the exact mechanism of the dewatering process. Recent computational work suggests that dewatering occurs through a filtration process (Letzelter and Eklund 1993).

The origins of visual coating defects and large scale (i.e., several centimeters in width) coat weight nonuniformities at high coater speeds are still under investigation. In addition to other blade coating variables, such as the basesheet and blade nip geometry, the coating formulation plays an important role. The major formulation variables are: the choice of platy pigment particles (i.e., delaminated clays) and their size distributions, the continuous (dispersion) phase rheology, and the solids content of coatings.

Experimental evidence suggests that the ability of highly anisometric particles to orient parallel to the flow direction in the blade nip might be critical (Gane and Coggon 1987). Among other variables, particle orientation depends on rheologi-

cal and viscoelastic properties of the continuous phase. Furthermore, it seems that the rapidly accelerating flow at the converging geometry near the blade nip would generate elongation (or stretching) along the streamlines of the flow, thus introducing the elongation viscosity of the coating as an additional variable. In that sense, the flow in the blade nip can be viewed as a time-dependent extensional deformation. Usually, the elongational viscosity is at least three times greater than the steady shear viscosity. This rule may also apply for highly concentrated dispersions of paper coatings containing soluble polymers (Schurz 1984). However, recent measurements at shear rates of $5 \times 10^5 \text{ s}^{-1}$ demonstrated that paper coatings without soluble additives (i.e., starch, carboxymethyl or hydroxyethyl cellulose, associative thickness, polyvinyl alcohol, etc.) do not have a measurable elongational viscosity (Carreau and Lavoie 1993). These coatings flow as Newtonian fluids at high shear rates. Elastic structures in suspension, which prevail at small rates of deformation, are destroyed at high shear rates, i.e., structures are sensitive to shear and disappear at high strains or shear rates.

In addition to the above defects a common problem in many blade coating operations with paper webs is the appearance of almost dried out coating extruded from under the blade at the outgoing nip. This defect is known as feathering, weeping, whiskering, or bleeding, and is more common in the bevelled than the bent blade mode. Many times, bleeding leads to localized wet deposits at the exit from the blade nip which grow over time to eventually form dried out deposits, known as stalagmites, hanging onto the upper side of the blade. Therefore, often bleeding is qualitatively classified as wet or dry, depending on its appearance. Stalagmites as long as several centimeters have been observed in practice. Their appearance is a localized phenomenon which may not adversely affect the coated paper quality until stalagmites detach from the blade and deposit on top of the paper, or grow to a size where they start scratching the surface. When this happens, wet and dry bleeding lead to visually observed coating surface defects.

There have been numerous attempts over the years to correlate coating and process variables with the occurrence of wet and dry bleeding. Generally, bleeding is promoted by high coater speeds; highly concentrated coating, i.e., the solids content of coatings; poor water retention; increased coating viscoelasticity; the type of mineral pigment particles used, i.e., clays are more susceptible to bleeding than calcium carbonates (Hofmann and von Raven 1986; Eklund and Förs 1988; Gane, Watters and McGenity 1992; Triantafillopoulos and Grankvist 1992). Additionally, bleeding reduces with high blade angles and decreased blade thickness and blade extension in the case of bevelled blades (Engström and Rigidahl 1987). Although many of these conditions are sufficient for the occurrence of bleeding, they are not always necessary. For example, it was frequently thought before that shear thickening in the form of dilatancy under the blade tip could cause formation of aggregates and the appearance of bleeding. However, experimental work has demonstrated that this is not always a requirement (Engström 1984). Many times, shear thinning coatings are associated with the buildup of stalagmites at the blade. Gane and Coggon (1987) speculated that plug flow or slippage at the blade tip of a bevelled blade cause bleeding and stalagmites formation. Furthermore, the coating film at the exit of the nip fractures, thus causing emission of coating droplets and aggregates. Gane and Coggon (1987) gave no explanation of the mechanism which causes the film fracture.

Recent studies with high-speed visualization and microphotography have shed light on the phenomenon of blade bleeding, or weeping. Stalagmites are initially formed by a stepwise process which involves formation of small columns of nucleation, or trunks, which then branch out (Branston *et al.* 1993). The appearance and disappearance of new growths is a continuous process. Two ways that weeps grow are through trunks which continually acquire coating that flows up their web sides, and crowns that acquire coating during temporary contact with the moving web. Overgrown weeps eventually are propelling

away with the web. Scanning electron microphotography (Vodnick *et al.* 1993) indicated that all weeps have a bulbous crown atop a comb of separate trunks which join, two-by-two, in their upper reaches. Evidence from these observations suggests that trunks and crowns grow through different mechanisms and that, at least partly, trunks grow by blockage of large pigment particle booklets or lumps trapped at the blade nip.

The viscoelastic character of paper coating formulations can also cause the appearance of coating surface defects. These defects in turn influence the aesthetic appearance, properties and quality of the coating layer. The 'memory' induced by viscoelasticity at low deformations can dramatically change the spreading response and consolidation of coatings after metering. Immediately upon cessation of shear stresses and other forces acting during the fast deformation at the blade nip, the stored energy in the coating begins to relax. The coating layer would then return, at least partially, to its previous state of rest. Expansion (or spreading) of the coating layer after the blade tip, due to removal of external stress, promotes coverage of the substrate. The recoverable strain may be related to coating patterns and defects, such as scratches and various types of streaks (Engström and Rigidahl 1987). This phenomenon would be more pronounced for coatings with a more elastic character because, to some extent, levelling-out of blade induced streaks is controlled by viscoelastic properties of the coating (Adolfsson, Engström and Rigidahl 1989). The relaxation time, which characterizes coating viscoelasticity, is often comparable to the time available before the coating layer has been immobilized due to dewatering into the substrate. This is especially true in the case of coaters which run at high speeds. When one compares the relaxation times of different coatings – determined by stress relaxation measurements – with the residual width of an initially rather broad streak deliberately induced into the wet coating layer, the longer the relaxation time the wider is the remaining streak (Adolfsson, Engström and Rigidahl 1989). Appearance of this type of coating defect at the surface of paper can

be, at least partially, attributed to the inability of the coating film to spread and level out after metering and before drying. Furthermore, at high coater speeds, viscoelastic coating formulations have a strong tendency to form stalagmites at the blade surface upstream of the blade nip exit (Engström and Rigidahl 1989). The correlation of the presence of blade defects to the characteristic relaxation time of a coating has also been illustrated recently with measurements of stress relaxation of paper coatings (Young and Fu 1990, 1991). Paper coatings containing soluble thickeners exhibit substantial viscoelasticity. These coatings which have comparatively slow relaxation would most likely exhibit formation of streaks in the final coated paper.

A few experimental studies have been made over the years to investigate the influence of the viscoelasticity on defect-free runnability and bleeding in high-speed blade coaters. Sandås and Salminen (1991) investigated the effect of starch, carboxymethylcellulose, polyvinyl alcohol and an alkali-swellable thickener on rheological properties, including viscoelasticity, and on coating performance (the pigment was a platey English china clay). The oxidized starch, which had the lowest elastic modulus at low deformations, showed the best performance at the coater. A similar study (Triantafillopoulos and Grankvist 1992) with a variety of pigments and three different starches demonstrated that wet bleeding and scratches appear when the low-strain elasticity is relatively high. Particularly, coatings with cationic starch have high elasticity which substantially reduces at high strains and develops to excessive shear thinning. Dry bleeding, on the other hand, does not seem to depend on elasticity but rather the geometry of the blade nip.

Sustained and consistent coater runnability without defects and a uniform coat weight does not only relate to viscoelasticity. It is also a function of a combination of formulation parameters including: steady shear viscosity at low and high shear rates, water retention, and immobilization solids. In addition, the blade nip geometry in the case of a bevelled blade plays an important role. Preferably, the blade tip has

to be as close as possible to parallel to the web surface (or tangent to the backing roll at the blade nip region). Under this configuration the blade is truly running on its bevel, as shown in Fig. 12d.3a, and the coat weight is proportional to high-shear viscosity measured with a capillary viscometer (Roper and Attal 1993). When the blade is off its bevel, the system is not in equilibrium and coating defects are more likely to occur. Running on the toe of the blade (Fig. 12d.3b) can lead to dry bleeding, formation of stalagmites at the blade surface and web breaks at high blade loading. Running on the heel (Fig. 12d.3c), on the other hand, generates a divergent nip where film splitting at the exit from the blade induces visual defects, even though the coating rheology may be acceptable (Hofmann and von Raven 1986; Roper and Attal 1993). It is therefore important to recognize that, in addition to all the other variables discussed earlier, the blade geometry is a critical variable which needs to be monitored and controlled.

In summary, the appearance of surface defects in high-speed blade coating depends on all three components of the process: the paper web, coating rheology, and the metering geometry of the blade. Although the exact mechanisms leading to coating surface defects have only recently been explored, many cause-and-effect relationships have been established through practical experience. For instance, too porous and absorbent webs are detrimental to defect-free runnability because of excessive dewatering of the coating dispersion prior to metering and an increase in the solids content of the filtercake reaching the blade. Water entering the fibrous matrix of paper causes fibers to swell, a phenomenon which influences both the coat weight and end-use properties of paper. Generally, coatings with comparatively high elastic moduli at low strain rates and high plastic yield are more difficult to process up to the application zone and are associated with the appearance of visual defects, appearing both on the blade and the web. In addition, relatively high high-shear viscosity is often associated with poor runnability because it requires higher blade pressures to obtain a certain coat weight,

something which may lead to coating defects because the stresses applied onto the web also increase. Beyond the rheological parameters, the water retention property of a particular formulation plays a role in its processability. Coatings with the ability to hold water, particularly under the influence of a pressure pulse, can be processed trouble free at high coater speeds. Furthermore, the parallel channel geometry needs to be always maintained at the tip of a bevelled blade, as convergent or divergent flows at the blade nip will lead to coating defects. If this requirement is not met, coating defects may appear even though the substrate and coating rheology have been optimized for good runnability.

12d.8 CONCLUSION

High-speed blade metering of paper webs is a qualitatively different process from knife coating. Blade coating of paper is a precision process where the blade is flexible, the substrate is porous and compressible, and the speeds are three to four times faster than those prevailing in knife coating. This process comprises mass transfer phenomena coupled with inertia and viscous effects, flow through porous media, nip dynamics of resilient rolls, and non-Newtonian fluid dynamics of highly concentrated dispersions. The forces at the blade nip and the interaction of the coating material with the web are the principal mechanisms for coating deposition. Because of the high speed involved, inertia effects at the blade nip may become important, as do viscous and elastic effects. Furthermore, the quality and uniformity of the coating layer also depends on coating dewatering prior to metering and the roughening of the web at the application zone due to capillary penetration and fiber swelling. Therefore, the strong interaction between coating rheology, paper web and process variables make prediction and control of the process difficult to sustain.

In addition, there are physical differences between the operational modes of the blade (i.e., bevelled versus bent) and coating feeding systems into the metering zone. Bevelled blades are preferred for high speeds and relatively low

coated film thicknesses (10–25 µm), while bent blades are commonly used at lower speeds (below 7 m/s) for heavier coat weights. However, bevelled blades are more susceptible to visual coating defects and web breaks as the blade loading pressure – and, therefore, the stress applied onto the web – continually increases. It is also important to realize that the operation of bevelled blades is very sensitive to the geometry under the blade tip. Deviations from a parallel channel geometry lead to convergent or divergent flows at the blade nip which are responsible for the appearance of coating surface defects, even when both coating rheology and web properties have been optimized. Bent blades are generally less susceptible to coating defects.

Variations in the feeding system to the metering blade are also responsible for qualitative differences in the coating film. Systems with an applicator roll generate a substantial nip pressure which causes coating dewatering, fiber swelling and web roughening prior to metering. The blade acts as a metering device which also compresses the web, filling in its surface voids with coating and, therefore, creating a smooth contour of coating. In contrast, pond type and short-dwell blade coaters induce little dewatering prior to metering, but fiber swelling and web roughening take place after metering. Consequently, the coating contour is more nonuniform than in the previous case, an effect which may lead to inferior surface properties. Although pressurized pond coaters are superior coaters compared with roll applicators, these coaters also have limitations in terms of hydrodynamic instabilities and air entrainment in the pond. Both of these phenomena may generate coat weight nonuniformities across the machine line direction, manifested as bands or streaks when the web is viewed with transmitted light. These nonuniformities impose limits in the processability of high-speed blade coaters for paper, with respect to both the coater speed and shear viscosity.

Non-Newtonian fluid dynamics introduce an additional complexity in the physics of high-speed metering of paper coatings. Coating formulations, comprising highly concentrated

dispersions of anisometric mineral particles and including polymeric additives, demonstrate a whole range of non-Newtonian effects under the large strains occurring during the coating process. Interparticle interactions and network structure due to the presence of polymers are responsible for plastic yield and viscoelastic behavior at low strain rates. At high shear, most coatings are shear thinning and exhibit thixotropic recovery. When the concentration of pigment particles increases, coatings become dilatant and impose strong viscoelastic effects at high rates of shear. However, most coatings do not demonstrate viscoelasticity at high shear rates. Particle orientation and packing under the high shear flow conditions prevailing close and inside the blade nip determine the rheological behavior of paper coatings. Orientation of platelike pigment particles parallel to the machine line direction reduces the effective shear viscosity in the blade nip. However, slipping phenomena at the blade tip surface may lead to coating defects as film fracture occurs at the exit from the blade nip. In addition to rheology, the dewatering properties of paper coatings influence their processability. Poor water retention is detrimental to coater runnability, as water leaving the coating layer prior to metering increase the effective solids content of the filtercake reaching the blade.

The physics of high-speed flexible blade metering remains an active field for research. Practical experience has played a significant role in establishing many of the relationships existing today between application variables and final film thickness and properties. Semi-empirical relationships, however, are not sufficient to explain the complex physics involved, as these relationships often do not find universal application to all different types of coating formulations and paper webs. For instance, many relationships connecting coating rheology and web properties with the appearance of visual coating defects and film nonuniformities are not always accurate. A good example of this is dilatant coatings which have often been associated with the buildup of blade deposits (stalagmites). However, many shear thinning coatings can also lead to stalagmites

and surface scratches on the coated web. It is only with thorough, systematic studies based on mathematical analyses and experimentation that understanding of the process can yield useful results to predict and control the appearance of these and other coating defects.

The high-speed blade metering of paper is an area rich with opportunity for advancement. Conceptual models are needed to explain the interaction of coatings with the paper web to better describe the dewatering process and the local nonuniformity in coating coverage. The physical phenomena occurring at the blade nip are still not well understood as there are only a few experiments that have been executed under well controlled conditions. Furthermore, there needs to be a more systematic approach in establishing relationships between rheological and dewatering parameters of coatings and their processability at high-speed coating operations. These relationships should also include the influence of the various coating components. Finally, the mechanisms for hydrodynamic instabilities and air entrainment need to be investigated in depth in order to assess their contribution to process limitations and to the appearance of coating defects. However, successful contributions to part or all of these areas would require the combination of theoretical analyses with carefully designed experiments.

REFERENCES

- Adolfsson, M., Engström, G. and Rigidahl, M., 1989. The effect of the relaxation time of coating colours on the elimination of blade streaks. *Coating Conference Proceedings*, pp. 55–58. Atlanta: TAPPI Press.
- Aidun, C. K. 1987. Stability of convection rolls in porous media, bifurcation phenomena in thermal processes and convection. *AMD*, 89, eds H. H. Bau, L. A. Bertram and S. A. Korpeila.
- Aidun, C. K. 1989. *Fundamentals of Coating Systems*. Technical Report to the Project Advisory Committee, Institute of Paper Science and Technology, Atlanta, GA.
- Aidun, C. K. 1991a. Principles of hydrodynamic instability: applications to coating systems – Part I: Background. *Tappi J.* 74(2): 213.
- Aidun, C. K. 1991b. Principles of hydrodynamic

- instability: applications to coating systems – Part II: Examples of coating flow instability. *Tappi J.* **74**(3): 213.
- Aidun, C. K. 1991c. Principles of hydrodynamic instability: applications to coating systems – Part III: Generalization of coating flows as dynamical systems. *Tappi J.* **74**(4): 209.
- Aidun, C. K., Triantafillopoulos, N. G. and Benson, J. 1991. Global stability of a lid-driven cavity with throughflow: flow visualization studies. *Phys. Fluid A.* **3**(9): 2081.
- Aidun, C. K., Veerka, P. J. and Scriven, L. E. 1992. Onset of air entrainment: effects of surface characteristics. Paper presented at the International Symposium on Thin-Film Coating, Spring National AIChE Meeting, March 30–April 1, paper no. 55.
- Benson, J. and Aidun, C. K. 1992. Transition to unsteady nonperiodic flow in a lid-driven cavity via torus bifurcation. *Phys. Fluid A.* **4**(10): 2316.
- Blake, T. D. and Ruschak, K. J. 1979. A maximum speed of wetting. *Nature.* **282**: 489.
- Bliesner, W. C. 1971. Basic mechanisms in blade coating. *Tappi J.* **54**(10): 1673–1679.
- Böhmer, E. 1969. The relationship between coating weight and other variables during blade coating. *Norsk Skogindustri.* **23**: 308–324.
- Bolton, B. and Middleman, S. 1976. Air entrainment in a roll coating system. *Chem. Eng. Sci.* **35**: 597.
- Booth, G. L. 1970. *Coating Equipment and Processes*. New York: Lockwood Publishing.
- Bousfield, D. W. 1990. The simulation of pigment motion during blade coating. *Coating Conference Proceedings*. pp. 325–334. Atlanta: TAPPI Press.
- Bozeman, J. D. and Dalton, C. 1973. Numerical study of viscous flow in a cavity. *J. Comp. Physics.* **12**(348).
- Brady, J. F. and Bossis, G. 1988. Stokesian dynamics. *Annual Rev. Fluid Mech.* **20**: 111–157.
- Branston, R. E. et al. 1993. Weeping in blade coating. Part I: High-speed video and still macro photography. *Coating Conference Proceedings*. pp. 79–86. Atlanta: TAPPI Press.
- Burley, R. and Jolly, R. P. S. 1984. Entrainment of air into liquids by a high speed continuous solid surface. *Chem. Eng. Sci.* **39**: 1357.
- Burley, R. and Kennedy, B. S. 1976. An experimental study of air entrainment at a solid/liquid/gas interface. *Chem. Eng. Sci.* **31**: 901.
- Carreau, P. J. and Lavoie, P. A. 1993. Rheology of coating colors: A rheologist point of view. *2nd Coating Fundamentals Symposium Proceedings*. pp. 1–18. Atlanta: TAPPI Press.
- Chen, K. S. A. and Scriven, L. E. 1989. On the physics of liquid penetration into a deformable porous substrate. *Coating Conference Proceedings*. pp. 93–106. Atlanta: TAPPI Press.
- Cloosset, G. P. 1986. Recent advances in coating technology. *TAPPI Annual Meeting Proceedings*. pp. 57–62. Atlanta: TAPPI Press.
- Deryagin, B. M. and Levi, S. M. 1964. *Film Coating Theory*. London: Focal Press.
- Doremus, P. and Piau, J.-M. 1981. Viscoelastic elongational lubrication. *J. Non-Newtonian Fluid Mech.* **9**: 389–400.
- Doremus, P. and Piau, J.-M. 1983. Experimental study of viscoelastic effects in a cylinder-plane lubricated contact. *J. Non-Newtonian Fluid Mech.* **13**: 79–91.
- Eklund, D. E. 1981. Rheology and water retention of high-solids coating colors. *Coating Conference Proceedings*. Atlanta: TAPPI Press. pp. 49–57.
- Eklund, D. E. 1984. Influence of blade geometry and blade pressure on the appearance of a coated surface. *Coating Conference Proceedings*. pp. 37–43. Atlanta: TAPPI Press. *Tappi J.* **67**(5): 66–70.
- Eklund, D. and Förss, S. 1988. Observation on stalagmite formation and blade bleeding. *Wochbl. Papierfabrik.* **116**(10): 400–404.
- Engström, G. 1984. Coating colors with high solids content: runnability on the blade coater. *Wochbl. Papierfabrik.* **112**(6): 184–187.
- Engström, G. and Rigidahl, M. 1987. The implication of viscoelasticity on coating rheology and structure. *Tappi J.* **70**(5): 91–94.
- Engström, G. and Rigidahl, M. 1989. Stalagmite formation during blade coating – effects of process conditions. *Coating Conference Proceedings*. pp. 59–63. Atlanta: TAPPI Press.
- Follette, W. J. and Fowells, R. W. 1960. Operating variables of a blade coater. *Tappi J.* **43**(11): 953–957.
- Gane, P. A. C. and Coggon, L. 1987. Coating blade geometry: its effect on coating color dynamics and coated sheet properties. *Coating Conference Proceedings*, pp. 7–18. Atlanta: TAPPI Press. *Tappi J.* **70**(12): 87–96.
- Gane, P. A. C., Watters, P. and McGenity. 1992. Factors influencing the runnability of coating colours at high speeds. *Coating Conference Proceedings*. pp. 117–132. Atlanta: TAPPI Press.
- Gartaganis, P. A., Cleland, A. J. and Wairegi, T. 1977. Blade mechanics of extended blade coaters: theory and practice. *Coating Conference Proceedings*. pp. 145–155. Atlanta: TAPPI Press. *Tappi J.* **61**(4): 77–81.
- Ginn, R. F. 1974. *A Fundamental Rheological Study of the Blade Coating Process*. Project 3069. Progress Report Four, The Institute of Paper Chemistry, Appleton, WI.
- Ginn, R. F. 1977. Fundamentals of flow. In *Physical Chemistry of Pigments in Paper Coating*. Ed. C. L. Garey. pp. 233–253. Atlanta: TAPPI Press.
- Goodwin, J. 1989. *Coating Rheology*. Technical Information Brochure. Bohlin Rheology.
- Grankvist, T. O. and Sandås, S. E. 1990. Measurement of viscoelasticity at low and high shear rates.

- Coating Conference Proceedings.* pp. 473–478. Atlanta: TAPPI Press.
- Greener, Y. and Middleman, S. 1974. Blade-coating of a viscoelastic fluid. *Pol. Eng. Sci.* **14**(11): 791–796.
- Guzy, C. J. and Higgins, B. G. 1982. Viscous pressure across the nip of a blade coater and its effect on the final coated film thickness. *Coating Conference Proceedings.* pp. 63–71. Atlanta: TAPPI Press.
- Hassell, M. V. 1981. A study of coater blade wear. Paper read at the 2nd Latin-American Congress on Pulp and Paper, June 22–26, Torremolinos, Malaga, Spain.
- Hayward, G. 1973. Factors affecting the metering characteristics of a blade coater. *Coating Conference Proceedings.* pp. 61–71. Atlanta: TAPPI Press.
- Hofmann, H. P. and von Raven, A. 1986. Production problems from stalagmite-like buildups of coating colors on the blades of high-speed coaters. *Wochbl. Papierfabrik.* **114**(8): 261–266.
- Holton, J. E. and Klass, C. P. 1986. Simultaneous two-sided on-machine coating with bilblade blade coating. *TAPPI Seminar Notes.* pp. 115–124. Atlanta: TAPPI Press.
- Hsu, T. 1986. The role of fluid viscoelasticity in the dynamics of bounded coating flows. PhD dissertation, University of Massachusetts.
- Hsu, T. C., Malone, M. and Laurence, R. L. 1985. Separating forces in blade coating of viscous and viscoelastic liquids. *J. Non-Newtonian Fluid Mech.* **18**: 273–294.
- Huang, D. K. 1984. Blade streak and scratch problem. *Blade Coating Seminar.* pp. 59–70. Atlanta: TAPPI Press.
- Huang, D. K. 1986. Blade streak and scratch problem. *Blade Coating Seminar.* pp. 175–186. Atlanta: TAPPI Press.
- Hwang, S. S. 1979. Hydrodynamic analyses of blade coaters. *Chem. Eng. Sci.* **34**: 181–189.
- Kahila, S. J. and Eklund, D. E. 1978a. Processes occurring under the blade during blade coating: (1) Theory. *Wochbl. Papierfabrik.* **106**(17): 661–665.
- Kahila, S. J., Eklund, D. E. and Obetko, D. 1978b. Processes occurring under the blade during blade coating: (2) Practical tests. *Wochbl. Papierfabrik.* **106**(18): 709–714.
- Kahila, S. J. and Eklund, D. E. 1978c. Factors influencing the coat weight in blade coating with bevelled blades: theory and practice. *Coating Conference Proceedings.* pp. 13–25. Atlanta: TAPPI Press.
- Kartovaara, A. 1991. Lateral force under the blade tip of bevelled-blade coating. *Coating Conference Proceedings.* pp. 13–21. Atlanta: TAPPI Press.
- Kennedy, B. S. and Burley, R. 1977. Dynamic fluid interface displacement and prediction of air entrainment. *J. Colloid Interface Sci.* **62**(1): 48.
- Korpela, M., Palsanen, J. and Pitkanen, S. 1986. Practical experience with the short dwell coater. *Wochbl. Papierfabrik.* **114**(8): 267–271.
- Koseff, J. R. and Street, R. L. 1984a. Visualization studies of a shear driven three-dimensional recirculating flow. *J. Fluid Eng.* **106**: 21.
- Koseff, J. R. and Street, R. L. 1984b. On end wall effects in a lid-driven cavity flow. *J. Fluid Eng.* **106**: 385.
- Koseff, J. R. and Street, R. L. 1984c. The lid-driven cavity flow: a synthesis of qualitative and quantitative observations. *J. Fluid Eng.* **106**: 390.
- Kurath, S. 1965. *A Fundamental Study of Coating of Paper and Paperboard: The Rheological Behavior of Coating Colors.* Project 2495. Progress Report Two, The Institute of Paper Chemistry, Appleton, WI.
- Kurath, S. A. 1974. Viscosity of coating colors at high shear rates. *Technical Information Sheet 408-1.* Atlanta: TAPPI Press.
- Kuzmak, J. M. 1986a. Bevelled-blade coating. *Tappi J.* **69**(2): 72–75.
- Kuzmak, J. M. 1986b. Bevelled-blade coating: factors affecting coat weight. *Blade Coating Seminar Notes.* pp. 72–75. Atlanta: TAPPI Press.
- Laun, H. M. and Hirsch, G. L. 1990. High shear rheometry of paper coatings including normal stress measurements. *Coating Conference Proceedings.* pp. 445–452. Atlanta: TAPPI Press.
- Letzelter, P. and Eklund, D. 1993. Coating colour dewatering in blade coaters. *Coating Conference Proceedings.* pp. 247–257. Atlanta: TAPPI Press.
- Li, A. and Burns, J. 1992. Effects of air entrainment on coat weight distribution with an enclosed pond application. *Proc. Tappi Coating Conf.* pp. 173–184. Atlanta: TAPPI Press.
- Luciani, M. and Galloni, M. 1978. Base paper and coating colour in the trailing blade process: dependence of coating weight on raw stock smoothness. *Paper.* **190**(4): 183–189.
- Lyons, A. V. 1993. A mathematical model of coat weight control on the CLC. Presented at 2nd CLC Users' Forum, May 2, Minneapolis, MN.
- Middleman, S. 1977. Blade coating. *Fundamentals of Polymer Processing.* Ch. 8, pp. 199–211. New York: McGraw-Hill.
- Middleman, S. 1981. Elastic phenomena. *Fundamentals of Polymer Processing.* Ch. 4, pp. 463–480. New York: McGraw Hill.
- Miura, H. and Aidun, C. 1992. Pressure fluctuations and coat-weight nonuniformities in blade coating. *Coating Conference Proceedings.* pp. 193–216. Atlanta: TAPPI Press.
- Miyamoto, K. 1991. On the mechanism of air entrainment. *J. Industrial Coating Research.* **1**: 71.
- Miyamoto, K. and Scriven, L. E. 1982. Breakdown of air film entrained by liquid coated on web. Presented

- at the AIChE Annual Meeting, Paper 106F, Los Angeles, CA.
- Modrak, J. P. 1973. Effect of coating color rheology on the blade coating process. *Tappi J.* **56**(10): 70–73.
- Nallasamy, M. and Krishna Prasad, K. 1977. On the cavity flow at high Reynolds numbers. *J. Fluid Mech.* **79**: 391.
- Pan, F. and Acrivos, A. 1967. Steady flows in rectangular cavities. *J. Fluid Mech.* **28**: 643.
- Pranckh, F. R. 1989. Elastohydrodynamics of blade coating. PhD dissertation, Department of Chemical Engineering and Material Sciences, University of Minnesota.
- Pranckh, F. R. and Scriven, L. E. 1988. The physics of blade coating of deformable substrate. *Coating Conference Proceedings*. pp. 217–238. Atlanta: TAPPI Press.
- Pranckh, F. R. and Scriven, L. E. 1990. Elastohydrodynamics of blade coating. *AIChE J.* **36**(4): 587–597.
- Ramp, J. W. 1983. The angles of tip tube blade coating. *Coating Conference Proceedings*. pp. 83–95. Atlanta: TAPPI Press.
- Richardson, C. A. 1957. The trailing blade coater. *Tappi J.* **40**(8): 155A.
- Roper, J., III. 1990. Viscoelastic measurements and their significance. Presented at the Coating Advances Seminar, August 11–14, Western Michigan University, Kalamazoo, MI.
- Roper, J., III and Attal, J. F. 1993. Evaluations of high-speed runnability using pilot coater data, rheological measurements, and computer modeling. *Coating Conference Proceedings*. pp. 107–114. Atlanta: TAPPI Press.
- Saita, F. A. 1984. Elastohydrodynamics and flexible blade coating. PhD dissertation. University of Minnesota.
- Saita, F. A. and Scriven, L. E. 1985. Elastohydrodynamics and flexible blade coating. *Coating Conference Proceedings*. pp. 13–21. Atlanta: TAPPI Press.
- Salminen, P. J. and Förs, S. 1992. Fundamental approaches for optimizing fibre coverage in blade coating. *Coating Conference Proceedings*. pp. 7–22. Atlanta: TAPPI Press.
- Sandås, S. E. and Salminen, P. J. 1987. Water penetration in coated papers. *Coating Conference Proceedings*. pp. 97–101. Atlanta: TAPPI Press.
- Sandås, S. E. and Salminen, P. J. 1991. The influence of the interaction between pigment and various cobinders on rheology, dewatering and coating performance. *Coating Conference Proceedings*. pp. 51–59. Atlanta: TAPPI Press.
- Schurz, J. 1984. The rheology of paper coatings. *Wochbl. Papierfabrik.* **112**(8): 275–280.
- Scriven, L. E. 1982. How does air entrain at wetting lines. Paper read at the International Symposium on Thin Film Coating, AIChE Spring National Meeting, Orlando, FL.
- Strenger, M. R., Secor, R. B. and Sramek, R. J. 1992. Knife coating of a viscoelastic material. Presented at the 6th International Coating Process Science and Technology Symposium, AIChE Spring National Meeting, March 30–April 2, New Orleans, LA.
- Sullivan, T. M. 1986. An experimental and computational investigation of rheological effects in blade coating. Doctoral dissertation, Department of Chemical Engineering, University of California at San Diego.
- Sullivan, T. M. and Middleman, S. 1979. Roll coating in the presence of a fixed constraining boundary. *Chem. Eng. Commun.* **3**(469).
- Sullivan, T., Middleman, S. and Keunings, R. 1987. Use of a finite-element method to interpret rheological effects in blade coating. *AIChE J.* **33**(12): 2047–2056.
- Triantafillopoulos, N. G. and Aidun, C. K. 1990. Relationship between flow instability in short-dwell ponds and cross-directional coat weight nonuniformities. *Tappi J.* **73**(6): 127.
- Triantafillopoulos, N. G. and Altug, N. 1991. A comparative study of forces in blade coating. *AIChE Forest Products Symposium Proceedings*. pp. 141–158. Atlanta: TAPPI Press.
- Triantafillopoulos, N. and Grankvist, T. 1992. Viscoelasticity and high-shear rheology in relationship to short dwell coater runnability. *Coating Conference Proceedings*. pp. 23–36. Atlanta: TAPPI Press.
- Trist, A. R. 1945. US Patents 2,368,176, 2,593,074 and 2,796,846.
- Turai, L. L. 1971. Analysis of the blade coating process. *Tappi J.* **54**(8): 1315–1318.
- Verkerk, P. J. and Aidun, C. K. 1991. Flow visualization of air entrainment and dynamic contact line instability in low-speed roll coating. *Proc. TAPPI Engineering Conference*. **2**: 719; *Tappi J.* **74**(9): 203.
- Vodnick, J. L. et al. 1993. Weeping in blade coating. Part II: SEM and X-ray microanalysis of microtome-sectioned weeps. *Coating Conference Proceedings*. pp. 87–96. Atlanta: TAPPI Press.
- Windle, W. and Beazley, K. M. 1967. The mechanics of blade coating. *Tappi J.* **50**(1): 1–7.
- Windle, W. and Beazley, K. M. 1968. The role of viscoelasticity in blade coating. *Tappi J.* **51**(8): 340–348.
- Young, T. and Fu, E. 1990. Associative behavior of cellulosic thickeners and its implication on coating structure and rheology. *Coating Conference Proceedings*. pp. 395–404. Atlanta: TAPPI Press.
- Young, T. and Fu, E. 1991. Rheological behavior of LWC coatings containing associative cellulosic thickeners. *Coating Conference Proceedings*. pp. 61–70. Atlanta: TAPPI Press.

P. Randall Schunk, Alan J. Hurd and C. Jeffrey Brinker

13.1 INTRODUCTION

When faced with depositing a liquid film on a surface, laboratory scientists usually rely on free coating by withdrawal or drainage, or so-called free-meniscus coating. Simplistic and inexpensive, these techniques abound in the research and development of materials that can be deposited in the liquid state. What has come to be known as dip coating (Deryagin and Levi 1964; Ruschak 1976; Scriven 1988), viscous lifting (Van Rossum 1958), or drag-out (Landau and Levich 1942) begins with immersing a substrate in a vessel filled with liquid. Withdrawal of the substrate from the liquid, if managed properly, can result in a thin coherent liquid film, as shown in Fig. 13.1b. Alternatively, the liquid in the vessel can be drained around the substrate. This technique is often referred to as coating-by-drainage (Jeffreys 1930; Van Rossum 1958; Groenveld 1971) and is diagrammed in Fig. 13.1c. Recourse is sometimes taken from dip coating to coating-by-drainage when limited vertical space prevents substrate withdrawal (*cf.* Ashley and Reed 1984) or when coating small, short substrates to avoid the local thickening obtained when the trailing edge is withdrawn (Schroeder 1969). Although most often dip coating is operated as a batch process, it can be made continuous (Fig. 13.1d) when the substrate is a long, flexible sheet or filament (Deryagin and Levi 1964; Scriven 1988); however, sustaining a continuous coating process requires the addition of make-up liquid to the vessel. In any case, the physics of batch dip coating,

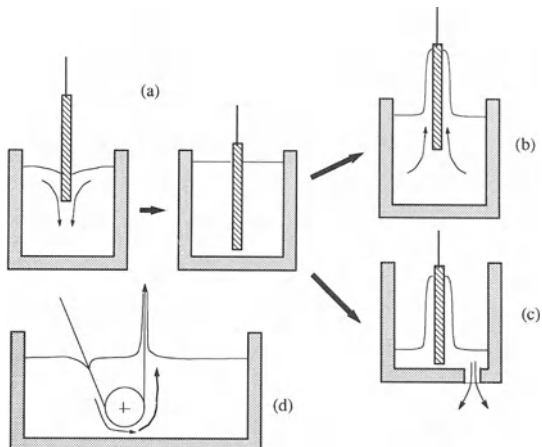


Figure 13.1 (a) Substrate immersion. (b) Coating by substrate withdrawal. (c) Coating-by-drainage. (d) Continuous dip coating.

continuous dip coating, and coating-by-drainage are essentially the same, differing only in the frame of reference in which the flat part of the meniscus is stationary.

Even though dip coating is one of the oldest coating techniques, it is still used widely to form thin films. Dip coating is one of only several means of coating irregularly shaped (non-planar) and rigid objects. The others include spin coating (*cf.* Chapter 14), which can be used when the substrate is a disk, plate or bowl, and spray coating (*cf.* Prescher 1991), which can be used on objects of simple enough shape that adequate

coverage be line-of-sight can be achieved. Thin films with remarkable uniformity (20 nm with thickness variations of less than 10%) can be achieved with spin coating over as much as 100 cm². Spray coating is often adequate for thick films but usually falls short of dip and spin coating in uniformity.

Free-meniscus coating techniques are encountered in many manufacturing applications. Before the discovery of pre-metered coating techniques dip coating was the most common way of producing photographic films (Deryagin and Levi 1964). For decades, primers for protective or cosmetic coatings were applied to automobile bodies by dipping and withdrawal (Rosenberg and Beiter 1989). Wax replicas are dip coated with a ceramic slurry to form mold housings in the investment casting industry (Horton 1990). Solid reflective coatings on plate glass windows are currently applied with dip coating followed by heat treatment (Dislich 1988). Electron-beam resist is often applied to nonplanar objects with dip coating as a part of nonplanar lithography processes (e.g., Jacobsen *et al.* 1991). The term 'hot-dip galvanizing' implies dip coating iron or steel parts in molten zinc to protect against corrosion (Tuck 1983; Bablik 1950). In the recent surge of research on advanced materials, dipping and withdrawal are not only used to apply the coatings, but also to control the final microstructure (e.g., Brinker and Scherer 1990).

Flows that share many essential features with free-meniscus coating can also be found in a great variety of situations in technology. Dip coating is the essential part of a process known as Marangoni drying, which is used to cleanse microelectronics substrates of small particulates (Leenaars, Huethorst and van Oekel 1990; O'Brien and Van Den Brule 1991). Arrangements that resemble dip coating are also encountered as part of many high-speed self-metered coating techniques, such as 'roll-pan pick up' whereby a film is lifted out of a reservoir by an applicator roll and then split or stripped (Chapter 12). Together with these situations, many applications beg for the proper principles underlying coating-by-drainage, especially when these principles can be

used to predict the thickness and the stability of the layer left behind. One example is the draining films on the walls of nuclear reactors for which proper cooling depends on the evolution of the film thickness (Bankoff 1983); another example is the amount of liquid left behind for accurate measurement of liquid volume in burettes and pipettes, or in the accurate determination of viscosity in capillary viscometers (Deryagin and Levi 1964).

In applications of free-meniscus coating the nature of the substrate can vary widely. For instance, in the manufacture of membranes and sensors the porous substrate is invaded by the liquid during the process. In the manufacture of multilayer laser reflectors, substrates are rigid and flat but are often as large as 0.2 m² (Britten and Thomas 1992). In the automobile and casting industries the substrate shape is highly irregular and usually complex; clearly in these cases design considerations favor adequate coverage over film uniformity. Cylindrical shapes such as wire are also common. In this case a high degree of uniformity can be managed but the range in film thickness is limited by the additional capillary pressure due to the circumferential curvature when the radius is small. The substrate can be long and flexible, as in most premetered coating applications (Chapter 11). In most present-day applications for which film quality is crucial the substrates are usually flat, rigid and short.

The physics underlying free-meniscus coating processes have seen heightened attention in the last several years, stemming mainly from recent interest in coatings of materials whose microstructure can be controlled with the process conditions. Tailored coatings of advanced materials for low-volume applications are the most noteworthy; in particular, coatings with controlled porosity (Brinker and Scherer 1990) and Langmuir–Blodgett monolayers and bilayers (Tredgold 1987) are discussed in this chapter. We emphasize the former, paying particular attention to sol-gels, materials for which a combined dip-coating flow and drying environment can be managed to form films for a wide variety of applications. The dip-coating technique is key

to the versatility in these applications because the fluid mechanics and drying occur simultaneously, unlike in most high-speed techniques.

Section 13.2 below puts free-meniscus coating into perspective by relating it to slot coating (Chapter 11), its closest pre-metered relative. Applications with varying effects of inertial and capillary forces are categorized and described in Section 13.3 together with the available theories and experimental findings in the literature. The highlights here are the several extensions of the landmark analysis by Landau and Levich (1942). These include both successful and unsuccessful attempts at theories for high speeds and low surface tension, as well as analyses of evaporation effects, with and without a condensed phase. Microstructure control with coating conditions is the subject of Section 13.4. There we introduce two applications which drive our research: Langmuir–Blodgett film deposition and sol-gel processing. Our discussion emphasizes sol-gel processing, a subject more familiar to the authors. The focus of Section 13.5 is the special methods needed to analyze coating and drying. Drying of the multicomponent solvents peculiar to sol-gel materials can drastically change the interfacial physics of a film; components with different volatilities and different surface tensions can lead to surface tension gradients that alter the flow. These phenomena complicate conventional analysis of coating flows. In this section we generalize classical coating theories (*cf.* Kistler and Scriven 1983) to include two-phase flow with evaporation. In Section 13.6 we consider a case study in sol-gel coating, to which we apply the complete two-phase flow theory. The results are validated against measurements of concentration along the film and reveal potential effects of the drying environment on the final film microstructure.

13.2 PRE-METERED VERSUS SELF-METERED COATING FLOWS

In dip coating the substrate is normally withdrawn vertically from the coating bath, entraining the liquid in a viscous boundary layer that splits in

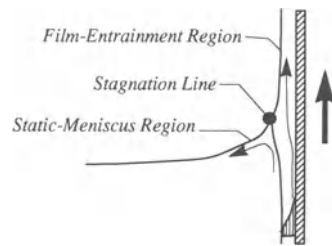


Figure 13.2 Dip coating.

two at the free surface (see Fig. 13.2). Between the two parts of the flow is a dividing streamline, hereafter referred to as the stagnation line. The liquid next to the substrate ends up in the final film, whereas the liquid on the other side of the stagnation line is returned to the bath by gravity. In effect, this line is analogous to a metering element (blade, knife, roll) as discussed in Chapter 12a. Its location can be linked to the thickness of the deposited film and is governed by several factors (see Scriven 1988).

Clearly operating conditions such as coating speed and angle of substrate withdrawal affect the meniscus shape and hence the position of the stagnation line. In addition, however, surface tension lowers the pressure in the liquid underneath the concave meniscus, viscosity thickens the boundary layer along the substrate, and inertia in the liquid boundary layer arriving at the deposition region can potentially induce a significant hydrodynamic pressure. So the position of the stagnation line and hence the coating thickness depend not only on the operating conditions, but also on the physical properties of the liquid (Ruschak 1985; Scriven 1988). Unfortunately, coating at higher speeds leads to thicker films, as does withdrawal at any angle other than vertical (Tallmadge 1971). Hence, if dip coating is the method of choice for a particular application then coating speed may be a limiting factor to achieve thin films (e.g., for high throughput). If the substrate is flexible and thin, i.e., capable of being wound into a roll for compact storage, then dip coating is usually not a practical coating technique; in this case the

pre- and self-metered techniques covered in Chapter 11 are the methods of choice.

Of all the pre-metered coating techniques, slot coating is the closest relative to dip coating, especially when the coating web is drawn upward against gravity (*cf.* Figs 13.2 and 13.3). In slot coating, a slot-fed die delivers liquid to a moving substrate at a prescribed volumetric flow rate V^* . The resulting film thickness is simply V^*/WU , where U is the substrate speed and W is the width of the coated layer. So simple adjustments of the flow rate can be used to determine the coating thickness, although that flow rate can only be varied between limits, as is indicated in the lower part of Fig. 13.3. If the flow rate is too high, the bead 'floods' if the lifting force imparted by the moving substrate is incapable of taking away liquid at the same rate. If the flow rate ceases, or becomes too slow, the coating bead (liquid bridging the coating gap) starves and the coating fails. The only way to regain a continuous coating is to lower the coating speed, a situation

that begins to look like dip coating. In fact a slot coating arrangement can be operated in the usual slot coating mode or in the continuous dip coating mode. The latter can be achieved from a slot coating arrangement simply by widening the separation between the die lips and the substrate (coating gap) and sealing the upstream lip against the substrate, as shown in Fig. 13.3 (Sartor and Scriven 1990). As the gap grows wider the film thickness becomes less sensitive to the inlet flow rate. Although this multimode capability may be impractical, it points out that a pre-metered coating apparatus can be managed to coat in the free-meniscus mode, and that there must be some parametric relationship between the steady operating states of both modes.

That such a relationship exists was demonstrated by Sartor and Scriven (1990) and earlier by Ruschak (1976). The explanation hinges on the competition between several forces, the major players being capillary forces (surface tension), viscous forces, inertial forces and gravitational forces. The competition between viscous forces and surface tension is conveniently measured with the capillary number, $Ca \equiv \mu U / \sigma$ (Chapter 1). Here μ is the viscosity of the liquid, and σ is the surface tension of the same. The competition between inertial forces and viscous forces is measured with the Reynolds number, $Re \equiv UL\rho/\mu$. Here L is a characteristic length (usually taken as the coating gap), and ρ is the density of the liquid. The competition between gravitational forces and viscous forces is measured by the Stokes number $St \equiv gL^2\rho/\mu U$, and the competition between gravitational forces and surface tension forces is measured by the Bond number, $Bo \equiv gL^2\rho/\sigma$.

Table 13.1 shows the values of these dimensionless numbers for slot coating of a glycerine–water solution (Sartor 1990) and for dip coating of a sol–gel solution (Hurd and Brinker 1988), both under arbitrary but representative operating conditions. It is noteworthy that gravity is far less important than surface tension in slot coating, as the Bond number is far less than unity. A small capillary number also indicates that surface tension dominates viscous forces. In

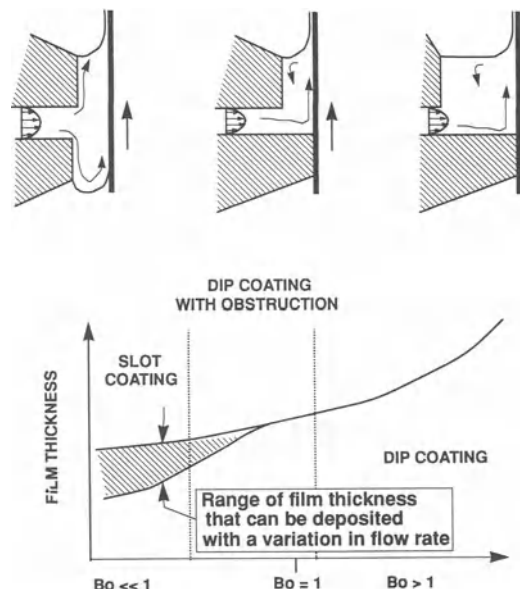


Figure 13.3 Slot-fed die taken from a pre-metered slot coating arrangement to dip coating flow (printed with permission from Sartor and Scriven (1990)).

Table 13.1 Parameters for slot coating and dip coating

Parameter	Dip coating	Slot coating
Length scale	$\sim 2 \text{ mm}$ (capillary length)	Coating gap $\sim 0.5 \text{ mm}$
U	0.5 cm/s	13.3 cm/s
μ	0.001 Pa s	0.029 Pa s
h	10 μm	82 μm
σ	50 mN/m	61 mN/m
Re	10	2.75
Ca	10^{-3}	0.0632
St	784	0.762
Bo	0.784	0.048

dip coating, viscous forces can be important, although in practice they are usually far less consequential than surface tension, at least under these operating conditions. Gravity also dominates viscous forces ($St \gg 1$) and has the same order effect as surface tension ($Bo \sim 1$).

One aspect that slot coating and dip coating can have in common is the capillary number. At low capillary numbers the gross shape of the meniscus is controlled by surface tension and the hydrostatic pressure field. Landau and Levich (1942) showed that the pressure jump across this meniscus is related to the film thickness H by

$$\Delta P = 1.34 Ca^{2/3} \sigma / H \quad (13.1)$$

This result can be derived by equating the curvature of the meniscus in the film-entrainment region (cf. Fig. 13.2) to that in the 'static' meniscus near that region (cf. Landau and Levich 1942; Ruschak 1985). This equation was derived for dip coating on the premise that the static meniscus is an arc of a circle, and so it is useful only when inertial and gravitational effects are negligible. This is often the case in slot coating because the menisci are so small ($Bo \ll 1$) that gravity does not affect their shape. Under a two-sided balance between capillary forces and viscous forces, the whole concept of pre-metered coating can be explained on purely geometric grounds by equation (13.1) (Ruschak 1976): the curvature of the upstream and downstream menisci in a slot

coating configuration adjust in response to any factor influencing ΔP , and adjust through the film thickness H so that equation (13.1) is satisfied. These factors include the flow rate and any applied pressure differential across the bead (cf. vacuum stabilization in Chapters 11a and 11b). Finite element calculations by Ruschak (1982) show that equation (13.1) fails at about $Ca = 0.01$. In fact, Ruschak (1976) showed that equation (13.1) is inapplicable if $Bo Ca^{1/3} \ll 1$.

Gravity usually plays an important role in dip coating. Correspondingly, the Bond number is of order one or greater. The free surface sags and is far from circular. Although this shape determines the final film thickness uniquely, as was argued above that at low Ca , the curvature cannot vary in response to a pressure change within the reservoir. In fact the surface shape is largely determined by the hydrostatic pressure field, at least at small capillary numbers. Effectively this means that the film thickness cannot be controlled with forced flow into the reservoir, as it is in slot coating. In fact, in most dip coating situations the substrate is withdrawn from a quiescent bath with no inflow at all. Sartor and Scriven (1990) studied the sensitivity of the final film thickness along the parametric path from slot coating to dip coating, i.e., from low Bo to high Bo . Their results show that a wider range in film thickness is possible at low Bond numbers, where the meniscus shape can be controlled by external pressure or internal flow rate. They also point out that at high Bond numbers, as in dip coating, this lack of control can be advantageous because of lower sensitivity of the final thickness to external disturbances, even though the process may be self-metered. Their results are summarized in Fig. 13.3.

Kheshgi, Kistler and Scriven (1992) recently explored the effects of bath configuration. In what they call dip coating with an obstruction they found that moving the far wall of a coating bath close to the curved part of the meniscus leads to a decrease in film thickness, all else being the same. Deryagin and Levi (1964) exploited this effect to allow faster coating at a given film thickness.

13.3 DIP COATING AND DRYING

13.3.1 CLASSICAL THEORIES AND RELEVANT EXTENSIONS

The velocity profile of the entrained film, regardless of the physical parameters, can be described by the classic Nusselt solution for gravitational flow of a liquid film. That solution, however, is parameterized by the flow rate, which can be determined only by analyzing the region around the stagnation line. Theories applicable at low capillary numbers, i.e. less than 0.01, in this region were for a long time the only ones available, the most noteworthy arising from the analysis of Landau and Levich (1942). Invoking the lubrication concept (Chapter 8), they treated the rising film as nearly one-dimensional and the meniscus near the reservoir as static. Using what amounts to the classical lubrication equations together and the differential equation of hydrostatics they identified a matching condition for the film-entrainment and the static-meniscus regions. For vertical withdrawal they used that condition to get an expression for the film thickness in terms of the key parameters and physical properties:

$$H = c_1 \frac{(\mu U)^{2/3}}{\sigma^{1/6}} (\rho g)^{1/2} \quad (13.2)$$

The constant c_1 has been determined to be about 0.944 (Newtonian liquids). At about the same time Deryagin and Levi (1964) derived equation (13.2) independently, and then extended the theory to simple non-Newtonian liquids. Ruschak (1974, 1976) and Wilson (1982) have since shown that equation (13.2) is asymptotically valid as $Ca \rightarrow 0$. Experiments accord with equation (13.2) provided that Ca is less than 10^{-2} (see for example Spiers, Subbaraman and Wilkinson 1974).

Many have used the theory of Landau and Levich. Groenveld (1971) applied it to expand Jeffrey's (1930) classical drainage result to include the effects of surface tension. Ruschak (1976, 1985) extended it to explain the relationship between pre-metered and self-metered coating flows at low capillary number. He also compared

the low capillary number theory with the data of Morey (1940) and found good agreement at Ca less than 0.01 (Ruschak 1976). Countless applications of equation (13.2) have been made in research on coatings of advanced materials, which are normally applied at low Ca (Brinker and Scherer 1990; Hurd and Brinker 1990; Park 1991).

White and Tallmadge (1965) were among the first to attempt the extension of equation (13.2) to higher capillary numbers. They did so by accounting for the effect of gravity in the film-entrainment region. Unfortunately, like many of their successors (Esmail and Hummel 1975; Spiers, Subbaraman and Wilkinson 1974), their extension was to add gravity, but gravity alone does not extend the validity of the theory of Landau and Levich, as Ruschak (1985) pointed out in his review on coating flows. Moreover, whenever gravity or other higher-order effects are included, Landau and Levich's procedure for matching curvature breaks down (see Ruschak (1985) for discussion). These analyses have nevertheless led to reasonable agreement with the experimental data reported by Gutfinger and Tallmadge (1965) and Spiers, Subbaraman and Wilkinson (1974) – see for example the analyses of White and Tallmadge (1965); Spiers, Subbaraman and Wilkinson (1974); Tekic and Jovanovic (1982); and Nigam and Esmail (1980).

Successful attempts to solve the problem at higher capillary numbers are now commonplace. Lee and Tallmadge (1974) solved the complete two-dimensional equations with the finite-difference method and explored the effect of inertia and of bath dimensions. They found good agreement with experimental data at capillary numbers greater than one. Wilson (1982) used the method of matched asymptotic expansions to obtain a closed form solution for the film profile applicable at all capillary numbers. Kheshgi, Kistler and Scriven (1992) integrated a film profile equation, similar to the one derived by Ruschak (1978) and Tekic and Jovanovic (1982), to obtain first-order approximations of film profiles for a variety of situations geometrically similar to dip coating.

Several theories, including the one of White and Tallmadge (1965), are graphed in Fig. 13.4. The ordinate represents the film thickness in units of $(\mu U/\rho g)^{1/2}$. In several of these theories an upper limit to the film thickness that can be withdrawn is evident. The reason for this can be explained by the diminishing effects of surface tension. When the liquid viscosity and the web-speed are high enough to straighten out the curved meniscus, then the resulting film thickness is determined by the balance between viscous drag and gravity. As the drag force is proportional to μU and the gravity force to ρgh (for vertical withdrawal) the film thickness should follow $h = c(\mu U/\rho g)^{1/2}$, hence the choice of units on film thickness in Fig. 13.4. Tuck (1983) and Homsey and Geyling (1977) believe that the proportionality constant c should be unity if the capillary number grows large but inertial effects remain negligible. Experiments have shown that c is typically around 0.8 (e.g., Spiers, Subbaraman and Wilkinson 1974). Our analysis, the details of

which are discussed in Section 13.5, suggests $c = 0.74$.

Early on, Morey (1940) made film thickness measurements at capillary numbers as high as 0.1. Van Rossum (1949) extended Morey's results to Ca of order 1 and found that the maximum flux obtainable corresponds to $c = 0.54$. Non-invasive capacitance probes were used by Spiers, Subbaraman and Wilkinson (1974) to measure film thicknesses over the Ca range 0.003 to 18. They built on the work of Tallmadge and Gutfinger (1967) who used micrometer probes. The data of Spiers *et al.* and Gutfinger and Tallmadge (1965) show an upper limit in the film thickness parameter to be about 0.8 (see Fig. 13.4), just above what we predict. Experiments with roll-pan pickup were performed by Tharmalingam and Wilkinson (1978), Nigam and Esmail (1980) and others, with capillary numbers as high as 50 being achieved.

Modern computer-aided techniques of solving the complete Navier-Stokes system have made full theories of free-meniscus coating possible

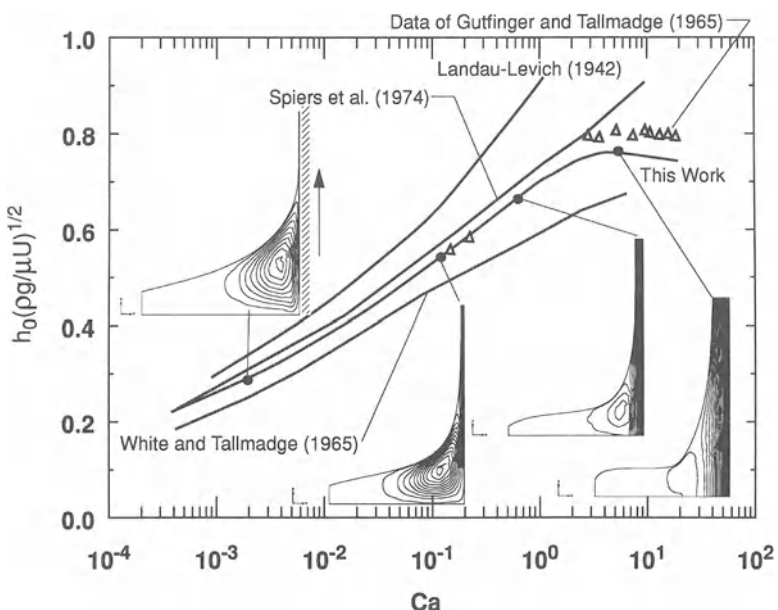


Figure 13.4 Variation of dimensionless film thickness with capillary number. Comparison of previous analyses with that by the present authors.

(Chapter 9), as Fig. 13.4 makes plain. Besides the analysis of Lee and Tallmadge (1974), Marques, Costanza and Cerro (1978) also used a finite-difference technique to solve the high capillary number limit. Ruschak (1982) applied the finite-element technique to approximate the two-dimensional flow between partially submerged, counter-rotating rollers. He used that solution to help determine the inlet boundary condition on an outer expansion of the film-entrainment region. The situation was basically free-meniscus coating but did not include gravity. Tanguy, Fortin and Choplin (1984) also applied the finite-element method. Even though they concentrated on capillary numbers above 0.01, their analysis was extended to dip coating wires and cylinders and also to non-Newtonian liquids. Unfortunately their resolution was not sufficient in the region of high meniscus curvature, the necessity of which was made clear by Sartor (1990). Sartor applied modern free-surface parameterization techniques (Chapter 9) to solve the complete set of operating states between slot coating and dip coating.

As capillary number rises and entrained films become thicker, the base flow state becomes more susceptible to disturbances that can grow appreciably. Falling liquid films on vertical surfaces are unstable to all two-dimensional disturbances (see Chapter 11d), so it is likely to expect that rising films akin to those in dip coating are unstable as well. Several attempts at measuring entrained film thicknesses at high capillary numbers ($Ca > 10$) have been hampered by the appearance of transverse waves that are falling with respect to the bath (see Soroka and Tallmadge 1971; White and Tallmadge 1965). Some researchers have discussed the stability of rising film flows (e.g., Tuck 1983; Kheshgi, Kistler and Scriven 1992), but the subject has yet to receive direct theoretical treatment, so far as the authors are aware. Fortunately, the voluminous literature available on the stability of falling liquid films is highly relevant (e.g., Benjamin 1957; Chapter 11d), mainly because the same forces are at play and the shape of the velocity profile takes on the same parabolic functional form. From this analogy

we can expect that vertically rising films are always unstable. So how can dip coating operations, even at slow speeds, produce acceptable films? It may be that disturbance growth rates are small enough that growing waves can escape detection, at least until the film is cured or solidified. It may also be that rising films in effect can carry wavy disturbances upward and away from the bath, as suggested by Kheshgi, Kistler and Scriven (1992).

It is perhaps relevant that film thickness measurements at capillary numbers greater than about unity have been successful only for higher viscosity fluids, i.e., at viscosities at least two-orders of magnitude greater than that of water, or around 0.1 to 1 Pa s (e.g., Soroka and Tallmadge 1971; Spiers, Subbaraman and Wilkinson 1974). The stability of the solutions at $Ca > 1$ reported in this work and represented in Fig. 13.4 were attainable only if the viscosity was increased to at least 0.1 Pa s, in which case the Reynolds number remained less than about 100.

13.3.2 DIP COATING WITH CONCOMITANT EVAPORATION

The potential for evaporation to affect the dip coating process was first recognized by Slattely and Givens (1933) while attempting to explain discrepancies between Jeffrey's (1930) theory and experiment. Interest in evaporation effects has reappeared in sol-gel dip coating because the fluid mechanics of film deposition overlaps with evaporation, a phenomena that is prevalent when coating liquids are volatile and the coating speed is small, i.e., low capillary numbers. An important feature observed in this case is the existence of a stationary 'drying line' at which the volatile mass becomes exhausted. In this area the most recent extension of the low Ca theory of Landau and Levich (1942) was made by Hurd and Brinker (1990) who explored the effects of evaporation on the entrained film, focusing on a region within several millimeters of the drying line. They found that the evaporation rate diverges at the drying line, although the amount of vaporized mass remained finite (see Fig. 13.6).

This led to a parabolic film profile of the form

$$h(x) = cx^{1/2} \quad (13.3)$$

Here x is the distance from the drying line measured along the substrate; the constant c depends on the diffusion coefficient of the vapor. For single component systems, equation (13.3) accords with ellipsometric measurements of film thickness made by Hurd and Brinker (1988). Below we summarize the theory (Section 13.6.1) and experimental program (Section 13.4.2) developed by Hurd and Brinker (1988, 1990) before extending the theory and analysis to multicomponent systems.

Leenaars, Huethorst and van Oekel (1990) exploited the overlap of drying and deposition in a process they contrived to clean substrates in microelectronics applications. The key to the process is to create surface tension gradients along the meniscus while dip coating. They did so through the gas phase by feeding organic vapor down the film. The organic vapor condenses on the film and creates a surface tension gradient directed toward the water-rich reservoir. The shear forces created by this movement are evidently enough to dislodge unwanted particles from the substrate.

Some effort has been made to understand the detailed physics of thin drying films whose shape is dictated by surface tension (low Ca and low Bo). Parks and Wayner (1987) analyzed a vertically extended meniscus wetting a stationary substrate, a situation that shares many features with dip coating. Even though the substrate is stationary, flow is induced by evaporation and surface tension gradients. To predict which force drives the most flow they measured the film thickness profile and then applied lubrication-type equations to determine the mass flux induced by each factor. For binary systems they found that concentration-induced surface tension gradients tend to be more important than thermally induced ones and that the former draws liquid into the thin film region if the less volatile species has a higher surface tension. Their theory encompassed extremely thin films which are controlled by liquid–solid–vapor interfacial forces, e.g., dis-

joining pressure. A review of this work by Wayner (1991) makes plain that the thermodynamics of evaporation are important to the understanding of the wetting of thin films. Where applicable we consider his ideas in our development of a complete free-meniscus coating theory (Section 13.5).

13.3.3 DRYING IN THE PRESENCE OF A NON-VOLATILE PHASE

Several one-dimensional analyses of film drying that pertain to dip coating downstream of the two-dimensional metering region are available. The intent in most of these is to determine the effect of increased volume fraction of non-volatile species on the drying rate (*cf.* Poehlein, Vanderhoff and Wit-Meyer 1975). An analysis by Cairncross, Francis and Scriven (1992) considers the effect of concentration- and temperature-dependent diffusivity, which tends to drop precipitously as the residual solvent is drawn off. The most common phenomenon in these studies is the concentration of the condensed phase near the free surface, or so-called skin effect (Bornside, Macosko and Scriven 1989; Tu and Drake 1990). In fact, Cairncross, Francis and Scriven model the effect of a gelling front which originates at the free surface in the drying of silica sol-gel films. Not surprisingly the same ‘skinning’ phenomenon has been predicted in spin coating of polymeric and colloidal systems (Chapter 14; Bornside 1989; Rehg and Higgins 1992).

Taking these analyses to two or three dimensions enables the assessment of drying stresses in a film. One of the few attempts at understanding drying-induced stresses in gelled films was made by Emery and Egolf (1989). With the finite-element method they predicted moisture distributions and moisture stresses in boehmite gels by solving the corresponding thermal-mechanical stress problem. They found that thinner films have less propensity to crack. Tam, Stolarski and Scriven (1992) applied the finite-element method in two dimensions to study viscoplastic stress development in a drying film. Their analysis focuses on the warping of flexible substrates and

on the interaction of stress development around neighboring defects. Significant theoretical work towards understanding the drying stress problem in sol-gels has also been made by Scherer (1988). Cairncross and co-workers (e.g. Cairncross *et al.* 1995) have recently extended this analysis to examine the shrinkage and residual stress development in gelled films with a complex theory of partially saturated, deformable porous media. Several other analyses exist, but they deal with other materials (e.g., Cooper 1977; Lewis, Morgan and Thomas 1983).

13.4 MICROSTRUCTURE CONTROL WITH DIP COATING

It has recently become apparent that the microstructure of films coated from solutions of polymeric precursors or of nonreactive but flocculating particles can be controlled with operating conditions in dip coating (Brinker *et al.* 1991b). That dip coating is amenable to such control is a direct consequence of the concurrent fluid mechanics of deposition and drying of the film, an effect that is usually absent from most high speed coating techniques. Because advanced materials are often coated at low capillary number (Ca less than about 0.01), the coating rate is usually slow enough for the fluid mechanics of the deposition process and the film-drying process to interact. Thin ceramic coatings of sol-gel materials and Langmuir–Blodgett (L–B) coatings of surfactants fall into this category.

In the following discussion we use several terms which need to be defined. The condensed phase of a sol-gel refers to the inorganic or metal organic precursors which polymerize into a network; in a Langmuir–Blodgett formulation that phase is made up of amphiphilic molecules, or surfactants (see Chapter 4), that form a monolayer or bilayer structure. A drying line is a mathematical line at which the meniscus formed by the solvent recedes into the network of polymers in a sol-gel. If no condensed phase is present, the drying line is simply the line at which the solvent disappears. In a Langmuir–Blodgett film the drying line defines the locale of the last

trace of solvent to evaporate. The mass fractal dimension d of a growing polymer relates its molecular mass M to its characteristic radius r , i.e., $M \sim r^d$. The mass fractal dimension is by definition less than the imbedding dimension of space (Brinker and Scherer 1990).

13.4.1 LANGMUIR–BLODGETT (L–B) FILMS

Because L–B films are composed of one or several coherent molecular monolayers, they represent the ultimate challenge of microstructure control (*cf.* Roberts 1990). These organic films are formed layer-by-layer via the transfer of amphiphiles, i.e., molecules having polar hydrophilic ends and nonpolar hydrophobic chains, from a liquid surface to a substrate through multi-pass immersion and withdrawal (Fig. 13.5). The subphase liquid is usually a polar solvent, such as water, and the molecules are surfactants that are more-or-less insoluble in the liquid. As Fig. 13.5 makes clear, the Langmuir–Blodgett (L–B) technique in its simplest form is free-meniscus coating.

Since the development of this technique (Langmuir 1938; Blodgett 1935), it has been used as a tool of surface chemistry for the study of surface interactions and wetting (Swalen 1992). L–B films have consistently attracted interest because of their applicability in microelectronics,

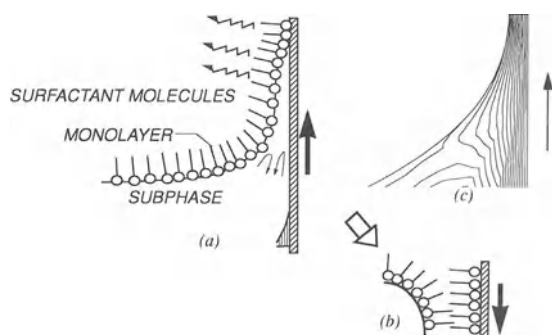


Figure 13.5 (a) Single- and (b) double-pass Langmuir–Blodgett film deposition. (c) Computed streamline pattern for an inextensible surface (from Schunk *et al.* (1992)).

integrated optics, microlithography, and in a new field known as molecular electronics. The most comprehensive reviews of these applications are given by Tredgold (1987) and Roberts (1990). Research activity in the last several years has heightened because one can now polymerize L-B films of various materials to provide the long-sought mechanical rigidity and thermal stability (Agarwal 1988).

The L-B process begins with a monolayer of surface active molecules (amphiphiles) initially spread at the interface between water and air. The support liquid is contained in what has become known as a Langmuir trough, which is equipped with a movable barrier for monolayer compression. After the monolayer is compressed against the substrate to a desired surface pressure (this quantity is the reduction of surface tension below that of clean water; see Adamson 1982), as measured by a Wilhelmy plate or du Nouy ring (see Chapter 4), the substrate is withdrawn slowly, depositing the delicate monolayer on the substrate. Subsequent immersion (down stroke) can then be used to deposit a second layer of molecules whose hydrophobic tails are directed toward those of the first layer. During deposition it is important to keep the surface pressure and therefore the packing of the molecules constant so the microstructure of the film is uniform on the substrate. Control of solvent drying is also crucial: rapid drying can lead to film defects (Sugi 1985). In fact it is common practice to maintain slow withdrawal so that the subphase can drain away (Tredgold 1987). Speeds of 4 mm/min are typical, with maximum speeds of about one to 60 mm/min attainable. Capillary numbers for these processing conditions are obviously small ($\sim 10^{-5}$) despite the substantial reduction in surface tension induced by monolayer compression.

Controlling the mechanical response of the surface to the stretching motion of the deposition process is important to film quality (Tredgold 1987). Several mechanical properties of the monolayer have been used to characterize this response. Some investigators have ventured to define a surface viscosity to measure the resistance

to shearing of the monolayer (Chapter 11d; Gaines 1966; Tschoegl 1962). The consequences of film viscosity to L-B film formation have been studied by Malcolm (1985) and Daniel and Hart (1985). Extensibility of the film is also important to the success of the deposition process. Several mechanical properties that measure extensibility are known to affect the fluid mechanics of deposition. The most common is surface elasticity, or the sensitivity of surface tension to the change in surface area per molecule (Chapter 4; Chapter 11d). In fact, the effects of large surface elasticities can be simulated in free meniscus coating with a steep surface tension gradient directed from the bath to the film. Figure 13.5c shows the consequence: both substrate and surface forces draw liquid upward. Were it not for evaporation or drainage, the entrained film would be much thicker than in the absence of surface tension gradients.

Film profiles during L-B deposition have been measured recently by Butler (1993). They used an imaging ellipsometry technique, similar to the one described in Section 13.4.2, to probe the film thickness in the dynamic contact region. Unfortunately, a quantitative comparison between those measurements and the available theories of film deposition (e.g., Park 1991) has not been completed.

Still an outstanding issue in dip coating monolayers is that of tolerable microstructure control. Because there is usually considerable interaction between the monolayer and the substrate, the microstructure of L-B films of simple straight-chained molecules is rarely the same as the crystalline structure of the same materials. Moreover, the L-B technique allows one to produce films of a precisely determined number of layers, which ordinary crystallization methods do not. Short-range order in the plane of the film can usually be achieved, but long-range order in this plane has only been produced over distances of 1 mm or less. Much of the current art of microstructure control hinges on the physics of dynamic contact (e.g., Petrov, Kuhn and Möbius 1979) and the synthesis of compatible amphiphile/solvent/substrate combinations (Petty 1987) of which little is known.

13.4.2 SOL-GEL FILMS

Sol-gel films have also enjoyed recent attention because they are suitable for a wide range of applications (Brinker and Scherer 1990). This versatility stems from the wide range of porosity and thermophysical properties (e.g., dielectric constant, conductivity, etc.) that can be tailored into thin films simply by varying the processing conditions. By 'sol' is meant a colloidal dispersion of particles in a liquid; by 'gel' is meant a giant aggregate or molecule that extends throughout the sol. Typically the particles are inorganic or metalorganic precursors which participate in a polymerization (gelation) process. Processing a sol usually includes this gelation stage; dip coating processes are no exception.

The most commonly used organic precursors for sol-gel film formation are metal alkoxides (Brinker and Scherer 1990). Normally the alkoxides are dissolved in alcohol and hydrolyzed by the addition of water. This step produces hydroxyl ligands on the precursors. Condensation reactions involving these ligands result in polymers composed of metal–oxygen–metal or metal–hydroxyl–metal bonds plus, in most cases, the by-products water and alcohol. Condensation reactions that are reserved in the presence of excess water or alcohol promote bond breaking and reformation processes that, if extensive, permit complete restructuring of the growing polymer. Thus controlling the growth of the inorganic polymers is a means of controlling its fractal dimension. This in turn provides a means of controlling density, and hence porosity, of the gels.

The production of so-called 'monolithic' or bulk ceramics make up a portion of the applications of sol-gels, but thin films have shown the greatest commercial success due to the ability to control both chemical composition and microstructure in either single or multilayer depositions (Dislich 1988). Today sol-gel film coatings are being studied intensively for such diverse applications as protective and optical coatings, passivation and planarization layers, sensors, high or low dielectric constant films, inorganic

membranes, semiconducting anti-static coatings, electro-optic and nonlinear optical films, superconducting films, strengthening layers and ferroelectrics. In most of these applications the sol is applied to the substrate with dip coating or a related technique, and process conditions are such that the capillary number is usually less than 10^{-3} . Several sections below are devoted to the details of sol-gel dip coating.

13.4.2.1 Factors influencing microstructure in sol-gel films

The dependence of molecular growth rate on solvent composition, extent of polymerization, and kinematic factors in the flow field provides the coupling between the physical chemistry of gel formation and the physics of the flow. The physical mechanism by which the polymerization process affects the fluid mechanics of deposition hinges on two phenomena. The first is the capacity of polymers which are growing in molecular weight to alter the rheological response of the solution in which they are dissolved. The second is the impedance effect of a branching polymer on the diffusive transport of a solvent (Cairncross, Francis and Scriven 1992), and hence the rate of evaporation, which itself can induce flow (*cf.* Parks and Wayner 1987). Although these effects are important to the thickness of films that can be deposited, far more important to the microstructural evolution in the film is the reverse effect, i.e., the effect of the flow on final microstructure. This mechanism has several parts (see Fig. 13.6).

Dip coating sol-gel materials involves more than a competition between viscous, capillary and gravitational forces; the mechanism which controls final film thickness and microstructure is considerably more complex. Film thinning by gravitational draining is assisted by vigorous evaporation, which also acts to decrease the amount of liquid that can be withdrawn. To make matters even more complicated, sols are typically formulated with several solvents, each of which usually differs in volatility and surface tension. Sometimes the relative volatilities are

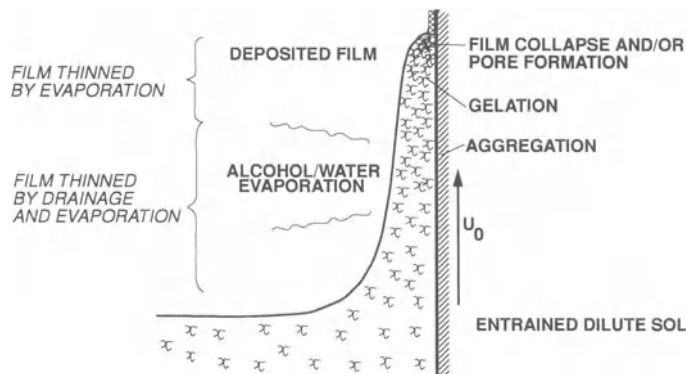


Figure 13.6 Schematic of the steady state dip-coating process, showing the sequential stages of structural development that result from draining accompanied by solvent evaporation and continued condensation reactions.

different enough to lead to differential solvent evaporation and ultimately to concentration variations along the film. An exception here might occur if there were an azeotrope-like composition at which the drying can be carried out (Dillon 1977). Differential evaporation triggers several other events at and beneath the liquid–gas interface. First it may lead to concentration variations along the interface; these variations make surface tension gradients which contribute to the surface stress and alter the flow. Second, differential evaporation leads to diffusion of the volatile species towards the surface and non-volatile ones away from the surface.

As the film thins, entrained particles or molecules of the condensed phase are forced together (Fig. 13.6). Above the stagnation point (*cf.* Fig. 13.2), where all entrained inorganic species are incorporated in the final deposited film, a simple balance of the flux of non-volatile material over a horizontal slice leads to

$$h(x)\phi(x) = \text{constant} + \text{terms of order} \left(\frac{h^2}{\lambda^2} \right) \quad (13.4)$$

where $\phi(x)$ is the volume fraction of solids and $\lambda \equiv (\mu U / \rho g)^{1/2}$. We see that ϕ varies inversely with h if $h \ll \lambda$. Hurd and Brinker (1990) found that film profiles of a single evaporating solvent

being coated on a planar substrate are parabolic in shape (equation (13.3)), and that ϕ should vary as $(1/h) \sim x^{-1/2}$ in the thinning film, x being the distance in the upstream direction from the drying line.

The rapid concentration of the entrained inorganic species by evaporation is more evident from consideration of the mean particle (polymer) separation distance $\langle r \rangle$, which varies as the inverse cube root of ϕ , or $\langle r \rangle \sim x^{1/6}$. This precipitous function implies that half the distance between particle (polymer) neighbors is traveled in the last 2% of the deposition process, which translates to a time scale of about 0.1 s. The evaporation-driven transport may be viewed like that induced by centrifugation or electrophoresis: the centrifugal acceleration needed to cause an equivalent rate of crowding is as much as 10^6 times the acceleration of gravity (this assumes that there exists no steric barriers to concentration; often aggregation/network formation will interrupt this dramatic compaction process).

Of course as the film becomes more concentrated in the condensed phase the rheological response of the liquid film changes from Newtonian to shear-thinning (aggregated systems) or thixotropic (ordered systems) and then to viscoelastic. Eventually the gelation extends throughout the film and the material no longer yields, i.e., the film behaves as an elastic solid. As the residual

solvent is drawn off, receding menisci in the micropores of the film create extreme capillary pressures which put the liquid into tension and the network into compression. This can have a significant effect on the pore structure and pore volume of the final film. (See Cairncross *et al.* 1996.)

From the preceding discussion we expect that the final film structure should depend on the competition between such phenomena as evaporation and capillary pressure, which tend to compact the structure, and condensation reactions and aggregation processes which tend to stiffen the structure. The fluid mechanics of the deposition process influence the rate of evaporation and hence the solvent composition when the structure is forming, thus influencing the compressive capillary pressure (surface tension) forces once the network has been formed. The chemistry of the polymerization and aggregation processes is also influenced by the deposition process, as is described next.

The short time of the deposition process (~ 10 s) and, more importantly, the extremely short time in which the inorganic species are in close proximity ($\ll 1$ s) establish important time scales for the dip coating process and distinguish sol-gel thin film formation from bulk (monolithic) gel formation. For bulk systems, the gelling sol is normally maintained at a constant concentration; the gelation, aging and drying stages occur sequentially. Often the time required to prepare a monolithic bulk gel is on the order of days to weeks. During dip coating the drying stage completely overlaps the gelation and aging stages. The deposited sol remains rather dilute until the final stage of the deposition process at which point it is rapidly concentrated. There are only fractions of seconds available for condensation reactions to occur.

We anticipate several consequences for the short time scale of the film deposition process. (1) There is little time available for networks to 'find' low energy configurations. Thus (for reactive systems) the dominant aggregation process responsible for network formation may change from reaction-limited near the reservoir surface to transport limited near the drying line. The

reduced fractal dimensionality of transport-limited aggregates should result in more porous network. (2) For sols composed of repulsive particles, there is little time available for the particles to order as they are concentrated in the thinning film. (3) There is little time available for condensation reactions to occur. Thus gelation may actually occur by a physical process rather than a chemical process – in some systems, this is evident by the rapid resolubilization after immersion in the solvent (Brinker and Scherer 1990). (4) As the gels in thin films are weakly condensed compared with bulk gels, they are more easily compacted; first by evaporation and then by the capillary pressure exerted at the final stage of the deposition (drying) process. Furthermore the maximum capillary pressure is likely to be higher due to the collapse of the network (and hence reduction in pore size) that precedes the final stage of drying. Of course, greater capillary pressure also promotes greater compaction of films, which leads to smaller pore size, larger index of refraction, and higher mechanical rigidity.

All things considered, it is surprising that the condensed phase has relatively little effect on the deposition process, at least to within several millimeters of the drying line. Figure 13.7 shows the product of refractive index and film thickness versus the logarithm of the withdrawal speed U

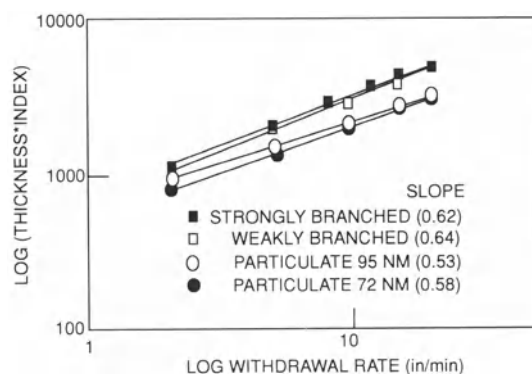


Figure 13.7 Product of thickness and refractive index (proportional to film mass/unit area) versus withdrawal rate (from Brinker *et al.* (1991b)).

for films prepared from a variety of silicate sols in which the precursor structures ranged from weakly branched polymers, characterized by a mass fractal dimension, to highly condensed particles (Brinker *et al.* 1991a). The slopes range from 0.53 to 0.64, values near those expected from equation (13.2), i.e., slope of 0.5. This correspondence between the thicknesses of the deposited films and a theory developed for low *Ca* coating of pure fluids (Landau and Levich 1942) suggests that the entrainment of the inorganic species has little effect on the hydrodynamics of dip coating, at least in the early stages of deposition where the entrained sol is quite dilute. Thus some insight into sol-gel film deposition may be gained by closer examination of the details of dip coating of multicomponent systems without the condensed phase reactions.

13.4.2.2 Film profiling with imaging ellipsometry and fluorescence spectroscopy

It is evident from the discussion above that microstructure is influenced heavily by evaporative film thinning. However, quantifying this effect experimentally is difficult; the refractive index varies with composition and, under typical operating conditions, films are usually less than 5 μm thick in the regime in which the evaporative-thinning is most rapid. Moreover, there is a need to measure the rate of film thinning, as well as the local thickness. In order to address these challenges, Hurd and Brinker (1988) developed an imaging ellipsometer that allows acquisition of spatially resolved thickness and refractive index data over the entire area of the film being deposited.

A beam of light from a surface suffers different amplitude and phase shifts depending on its polarization. In ellipsometry these amplitude and phase shifts are measured and interpreted by an appropriate model (Azzam and Bashara 1977). A typical ellipsometer consists of a laser, a polarizer to prepare a known polarization, the reflecting sample, a quarter-wave compensator plate that resolves the polarization parallel to the surface and perpendicular to the surface, and

an analyzing polarizer. In null ellipsometry, the analyzer and polarizer are adjusted until the reflected beam is distinguished. With the polarizer angles measured as extinction, it is possible to calculate both the index *n* and the thickness *H* of a film covering a substrate with a known index.

In initial attempts to study films, Hurd and Brinker found that the usual methods of narrow-beam ellipsometry were unsatisfactory because of fluctuations in thickness. Furthermore, it was desirable to obtain data from many points on the film at once rather than one point per dip coating. Hence, the laser was expanded and collimated to illuminate approximately 1 cm^2 of the film, thereby creating an image that can be analyzed for thickness variations.

A thickness profile of an ethanol film obtained by imaging ellipsometry is shown in Fig. 13.8 together with a thickness profile of a propanol–water film and that of a toluene–methanol film. Noteworthy in all cases is the blunt shape near the drying line, which turns out to be parabolic in functional form, in accord with equation (13.3). The double parabolic shape is a result of successive evaporation of more- and less-volatile components and of surface tension gradients directed toward the drying line. The ‘pile-up’ feature in the methanol–toluene case is an extreme example. The detailed mechanisms are discussed later.

A related approach is to use various fluorescent molecules, ions or crystals, as photophysical or

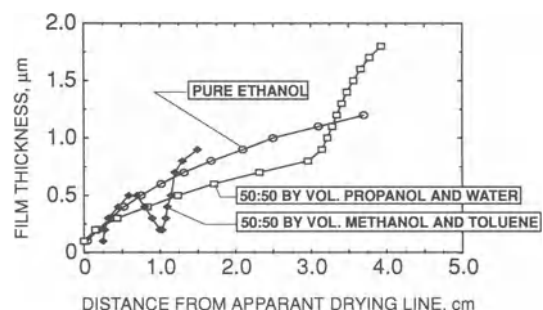


Figure 13.8 Thickness profiles measured with imaging ellipsometry (from Hurd and Brinker (1988)).

photochemical probes. The probes are entrained in the depositing film and transported to the drying line along with the dispersed inorganic phase. Acquisition of emission spectra as a function of height along the reservoir surface provides structural information related to the surroundings of the probe on a length scale of one to several nanometers. This approach has been used successfully to characterize gelation, aging and drying in bulk systems (Kaufman and Avnir 1986; Pouixviel, Dunn and Zink 1989) and thin films (Nishida *et al.* 1994). It benefits from the availability of literally thousands of potential probes that are sensitive to changes in viscosity, solvent polarity, local geometry, rigidity, pressure, etc.

A sample result from the fluorescence spectroscopy experiments is shown in Fig. 13.9. A mixture of ethanol and water with a low concentration of organic optical molecules is coated at 0.4 cm/s. Using an argon laser excitation source with spatial resolution of about 100 µm, fluorescence spectra are acquired from the probe molecules at various heights above the reservoir

surface. Thus far pyranine has been used to sense the changing solvent composition (and hence surface tension) in the binary fluid mixture due to preferential evaporation of ethanol. Figure 13.9 (left) shows clearly in a plan view that the concentration varies along the film, especially in the last 20% or so of the entrained film. In that portion concentration varies from that of the alcohol-rich liquid to that of nearly pure water at the drying line. On the right we show a profile view of the concentration variation as predicted from the theory described in Section 13.5. These predictions appear to be qualitatively similar. At this time we have not quantified the concentrations in the experiments.

Film thickness and concentration profiling provide a means of determining the film thinning rate and film composition at the drying line; both factors are known to affect final microstructure; but what about measuring film microstructure itself? We characterize the film microstructure (surface area, percentage porosity, and pore size distribution) *in situ* by analyzing N₂ adsorption-desorption isotherms acquired using a surface

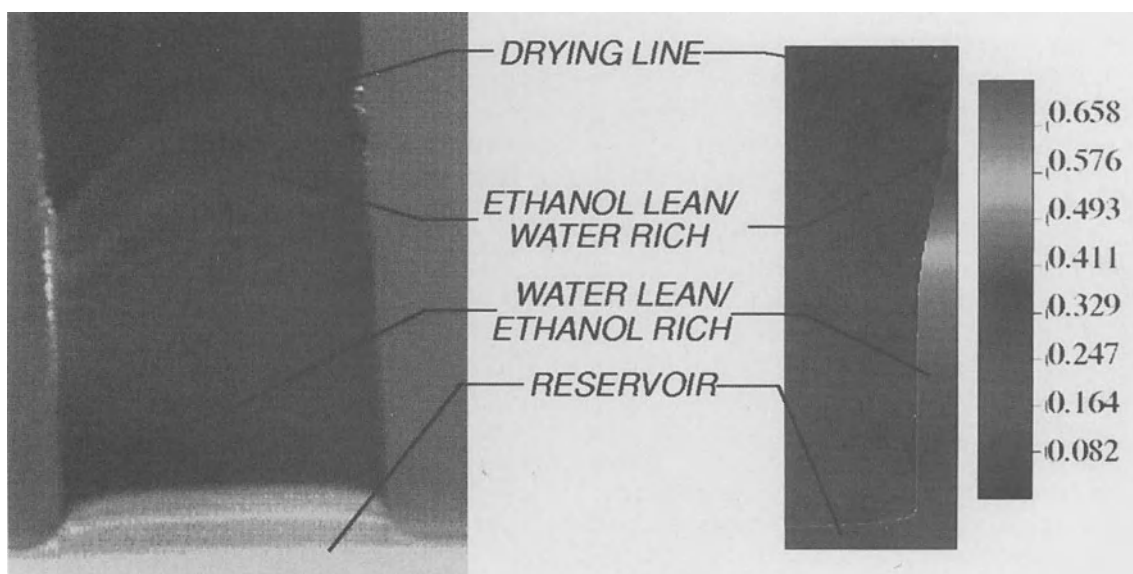


Figure 13.9 Plan view of concentration variations measured with fluorescence spectroscopy (left). Mass fraction of ethanol predicted from theory (right, horizontal axis magnified 100×).

acoustic wave (SAW) technique developed by Frye *et al.* (1988). The effects of processing conditions on film microstructure determined with the SAW devices are reported elsewhere (Brinker *et al.* 1991b). There it is shown a striking variation in film porosity achieved with silica based sols is created with simple adjustments to the pH and pre-deposition aging.

13.5 THEORY AND ANALYSIS OF FREE-MENISCUS COATING AND DRYING

The purpose of this section is to augment the theory developed in Chapter 2 to account for coating of multicomponent solvents, differential evaporation and surface tension gradients, thereby enabling the realistic analysis of sol-gel dip coating. Although most drying theories available today include coupled momentum, energy and species transport in the liquid phase, they lump the same theory for the gas phase into mass-transfer coefficients (e.g., Emery and Egolf 1989; Bornside 1989; Tu and Drake 1990). This was

our initial approach, but we found no available theory for mass transfer in the gas phase to be adequate (Schunk, Hurd and Brinker 1992). We proceeded to analyze the coupled physics in both phases, employing the proper interphase boundary conditions. This approach, although more costly, was far more successful at realistically predicting the sol-gel dip coating and drying process.

The development below pertains to the geometry pictured in Fig. 13.10a. How that geometry relates to the pilot coating setup with which we performed the benchmarking experiments is shown in Fig. 13.10b. The diffusivities, viscosities and densities of both phases were taken as constant and the process was considered to be isothermal. The first assumption is appropriate because we do not attempt to apply our theory to the regime in which the thermophysical properties depend on concentration, i.e., we do not extend calculations to high enough solid content where significant dependencies are noticed. With regard to the assumption of isothermal flow, evaporation can depress the temperature of the film and condensation can raise the temperature of the film, but initial calculations with the energy equation have shown that the temperature variations (a fraction of a degree K) do not have a significant effect on the phenomena we investigate here (*cf.* Schunk and Rao 1994). In fact Parks and Wayner (1987) found that concentration effects on surface tension were far more important than thermal effects in a setup similar to dip coating.

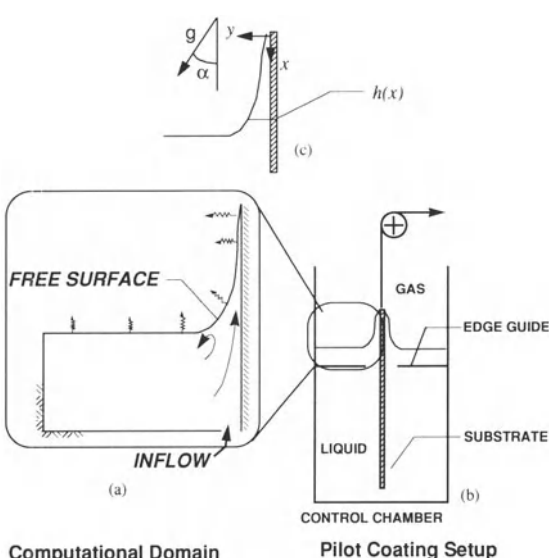


Figure 13.10 Computational domain of pilot dip coating setup: (a) system geometry; (b) pilot coating setup; (c) geometry around drying line.

13.5.1 TWO-PHASE MULTICOMPONENT SYSTEMS

Fluid flow in the gas and liquid phase is governed by the principles of conservation of mass and momentum in the bulk liquid, i.e., the Navier–Stokes system (Chapter 2). This system is coupled to the convective diffusion equations for species transport in several ways. First, diffusion itself can induce mass-average motion and hence influence the balance of momentum, although this effect is not present with the constant densities we assume here. Second, evaporation or condensation at a free surface

introduces fluid motion in the bounding phases; this happens to be the basis of the boundary condition on velocity we apply at the free surface. Third, species transport near a free surface of each solvent component possessing a unique surface tension can change the surface tension of that surface. This upsets the balance of forces at the free surface: local excursions of surface tension away from its equilibrium value affect the normal balance of forces, and variations of surface tension along the surface affect the tangential balance of forces.

13.5.1.1 Theory for mass exchange across interface

In addition to the Navier–Stokes system and the energy equation outlined in Chapter 2, the relevant convective diffusion equations are

$$\frac{\partial \rho^l X_i^l}{\partial t} + \mathbf{u} \cdot \nabla \rho^l X_i^l = \nabla \cdot \rho^l D_i^l \nabla X_i^l + q_i \quad \text{for } i = 1, 2, 3, \dots, N \quad (13.5)$$

$$\frac{\partial \rho^g X_i^g}{\partial t} + \mathbf{u} \cdot \nabla \rho^g X_i^g = \nabla \cdot \rho^g D_i^g \nabla X_i^g + q_i \quad \text{for } i = 1, 2, 3, \dots, N \quad (13.6)$$

where X_i is the bulk mass fraction of species i ; D_i is the pseudo-binary diffusivity of species i ; and q_i is the rate of generation of species i . \mathbf{u} represents the vector of mass-average velocity. The superscripts l and g denote liquid phase and gas phase, respectively. Expressions for q_i will depend on the reactivity of species i with other species. For now we consider nonreactive systems for which $q_i = 0$. When more than two species are included in any phase we ignore the effects of cross-term diffusion coefficients and assume every species behaves as if it were dilute (pseudo-binary diffusion). The equation of local overall mass conservation, the continuity equation $\nabla \cdot \mathbf{u} = 0$, which is already a part of the Navier–Stokes system is used in place of one of the components of equation (13.5) and equation (13.6). These equations can be rewritten in terms of volume fractions and volume-average quantities

(cf. Cairncross, Francis and Scriven 1992), but we see no major advantage gained in this case by doing so.

Boundary conditions on equation (13.5) and equation (13.6) are

$$\mathbf{n} \cdot \nabla X_i = 0$$

for $i = 1, 2, 3, \dots, N$ at solid surfaces (13.7)

$$\mathbf{n} \cdot [(\mathbf{u}_s - \mathbf{u}) X_i^l \rho^l - \mathbf{j}_i^l] = \mathbf{n} \cdot [(\mathbf{u}_s - \mathbf{u}) X_i^g \rho^g - \mathbf{j}_i^g]$$

for $i = 1, 2, 3, \dots, N$ at free surfaces (13.8)

\mathbf{j}_i is the diffusive contribution to the total flux $\mathbf{N}_i \equiv \rho X_i \mathbf{u} + \mathbf{j}_i$ of species i . \mathbf{j}_i is given by Fick's law: i.e., $\mathbf{j}_i \equiv -\rho D_i \nabla X_i$. \mathbf{u}_s is the velocity of the free surface. Equation (13.7) implies that all solid surfaces are impermeable to all species. Equation (13.8) allows bounding free surfaces to exchange species: the diffusive and convective flux of component i normal to the surface in the liquid must be balanced by the diffusive and convective flux of component i normal to the surface in the gas. Of course we assume that the surface is incapable of holding a significant inventory of any species in excess of the bulk, under equilibrium conditions. That is, no species here is taken to be surface active (see Chapter 11d).

Analogous to the bulk equations above, we replace one of the species kinematic conditions (equation (13.8)) with the overall kinematic condition (the sum of all equations in equation (13.8)) which states that the overall mass flux across the surface be continuous, i.e.,

$$\mathbf{n} \cdot (\mathbf{u} - \mathbf{u}_s) \rho^l = \mathbf{n} \cdot (\mathbf{u} - \mathbf{u}_s) \rho^g \quad (13.9)$$

It is common practice to replace the right-hand sides of equations (13.8) and (13.9) with terms of the form $K_i(X_i - X_i^0)$ (see, for example, Bornside 1989). Here X_i is the mass fraction i at the free surface in the gas phase; under equilibrium conditions it can be related to the mass fraction at the same locale but in the liquid phase. X_i^0 is a parameter used to set the overlying concentration of component i far away from the surface in the gas. K_i is known as a mass-transfer coefficient and is responsible for approximating the gas-

phase mass transport of component i . It is usually deduced from experimental correlations or from simplified theories and models of flow and convective diffusion fields.

The mass-transfer modeling approach can be highly successful if the gas-phase fluid mechanics can be controlled or constrained to some known pattern (e.g., Bornside 1989) and the overlying saturation can be controlled. Trouble arises when the pattern of gas flow is changed, for which K_i must be rederived or recomputed. Moreover, simplified theories that enable the evaluation of K_i are often inadequate approximations to the true physics. In this case the only alternative is to solve the complete theory in the gas phase as well, which is often only accessible through computer-aided mathematics, a route we chose in the work reported here.

The remaining boundary conditions needed on equation (13.5) and equation (13.6) must provide a datum which sets a concentration level for each species. In the dip coating case study below, that datum in the liquid phase is set at an inflow boundary:

$$X_i = X_i^0 \quad \text{at inflow surfaces.} \quad (13.10)$$

Equation (13.10) might apply in the gas phase if gas of a known saturation of each component is being blown into the system. Otherwise the datum is set at the free surface with the conditions of vapor–liquid equilibrium.

The solvent in the gas phase at the free surface is taken to be in equilibrium with the solvent in the liquid at the free surface. In this work we approximate this equilibrium behavior with Raoult's law:

$$p_i = p_i^V \tilde{x}_i|_h \quad (13.11)$$

where p_i^V is the saturation vapor pressure of solvent component i at a specific temperature and \tilde{x}_i is the mole fraction of the same in the liquid at the free surface. p_i is the partial pressure of component i in the gas phase at the free surface. Raoult's law usually holds for the component present in excess or when the system can be taken as thermodynamically ideal. For many systems,

however, Raoult's law is satisfactory over a wide range of concentrations (Denbigh 1981). We plan on taking this simplified approach here.

To make equation (13.11) computationally convenient we express p_i in terms of mole fraction \tilde{x}_i in the gas phase with Dalton's law that $p_i/p_{\text{tot}} = \tilde{x}_i^g$. The remaining challenge is to convert mass fractions into mole fractions so that equation (13.5) and equation (13.6) can be used together with equation (13.11). This can be accomplished by solving all but one of the following definition equations for the mole fraction of component i

$$X_i = \frac{\tilde{x}_i M_i}{\tilde{x}_1 M_1 + \tilde{x}_2 M_2 + \cdots + \tilde{x}_N M_N} \quad \text{for } i = 1, 2, 3, \dots, N \quad (13.12)$$

together with the constraint that $\tilde{x}_1 + \tilde{x}_2 + \tilde{x}_3 + \cdots + \tilde{x}_N = 1$. Another alternative to solving equation (13.12) is to use a volume fraction-based formulation, a situation for which Amagat's law states that volume fractions equal mole fractions in ideal gases.

At each locale on the free surface the number of unknown concentrations is twice the number of volatile species – the species in the liquid that are taken as nonvolatile and the species in the gas that are taken as insoluble in the liquid are accounted for by no-penetration conditions of the form $N_i = \rho X_i \mathbf{u} + \mathbf{j}_i = 0$. To account for the unknown concentrations we use the conditions given by equation (13.8) for the liquid phase and the vapor–liquid equilibrium conditions given by equation (13.11) and equation (13.12) in the gas phase.

13.5.1.2 Coupling of momentum conservation to species conservation

When mass exchange is allowed across the free surface the velocity will be discontinuous there if the material undergoes a density change. In two dimensions, at a given locale on the free surface, there will be four velocity components from a double-valued vector velocity. The corresponding conditions at the free surface that

we use to determine these components are

$$\mathbf{n} \cdot \mathbf{T}|_l = \mathbf{n} \cdot \mathbf{T}|_g + 2H\sigma\mathbf{n} + \mathbf{n} \cdot \rho^l(\mathbf{u}^l - \mathbf{u}_s)(\mathbf{u}^l - \mathbf{u}^g) + \nabla_s \sigma \quad (13.13)$$

$$\mathbf{t} \cdot \mathbf{u}|_{\text{gas}} = \mathbf{t} \cdot \mathbf{u}|_{\text{liquid}} \quad (13.14)$$

$$\rho^g(1 - X_1^g - X_2^g - \cdots - X_{N-1}^g)\mathbf{n} \cdot (\mathbf{u} - \mathbf{u}_s) \\ = -\rho^g D^g \nabla(X_1^g - X_2^g + \cdots + X_{N-1}^g) \quad (13.15)$$

Here \mathbf{t} represents the unit tangent vector to the free surface; σ is the surface tension; $2H$ is the mean curvature of the surface; and \mathbf{T} is the total stress of a Newtonian liquid (*cf.* Chapter 2). Each of these conditions is applied at the free surface, the vector condition (13.13) being applied as a boundary condition on Navier–Stokes' equations in the liquid phase and the scalar conditions (13.14) and (13.15) being applied as boundary conditions on the Navier–Stokes' equations in the gas phase.

Equation (13.13) is a vector condition that balances the normal and tangential components of the viscous forces and the hydrodynamic pressure in both adjacent phases with the capillary pressure, the vapor recoil by volume expansion, and the surface tension gradients at the interface. We neglect vapor recoil effects (the third term on the right) because it scales with the Reynolds number, which can be shown to make the term insignificant with the small evaporation rates occurring here. Equation (13.14) enforces the continuity of tangential velocity at the interface. Equation (13.15) expresses the gas phase velocity component normal to the interface as a function of the gradients in concentration in the gas phase next to the surface. It is derived on the premise that the N th component in the gas is effectively insoluble in the liquid and that all binary diffusivities are equal. In this work the insoluble component is taken to be air. All other volatile components are allowed to enter the gas phase by evaporation or re-enter the liquid phase by condensation.

In this work we have taken the surface tension σ to be a function of concentration alone. Future work will include temperature. In any case what is needed is a constitutive equation that relates the surface tension to the concentration of all

components in the liquid next to the surface, at least those components which affect the surface tension. One approach is to use a linear mixing law to describe the surface tension:

$$\sigma = \frac{\sigma_1 X_1 + \sigma_2 X_2 + \cdots + \sigma_m X_m}{X_1 + X_2 + \cdots + X_m} \quad (13.16)$$

Here m is the number of components which affect the surface tension. σ_i is the surface tension of that component if it were pure. A better constitutive equation arises from fitting a higher order function, e.g., cubic, to the actual data. We used both approaches and found the latter necessary to achieve qualitative agreement with the dip coating process. An example of this is shown below with ethanol–water as solvents.

13.5.2 COMPUTATIONAL STRATEGIES FOR SIMULTANEOUS MOMENTUM AND SPECIES TRANSPORT

As we show in Section 13.6.1, the equations simplified for single-phase, single-component flow are analytically tractable when the meniscus curvature is small and the film is thin and flat. Predictions for multicomponent systems without the same restrictions come from solving the Navier–Stokes system (Chapter 2) together with equations (13.5) to (13.10) without approximation. We use the techniques based on the earlier work of Christodoulou and Scriven (1992) and Kistler and Scriven (1983) to accomplish this task. These techniques, also described in Chapter 9, are based on subdomaining, Galerkin's method, and finite-element basis functions. In order to cope efficiently with the thin boundary layers in concentration that develop next to the free surface we employed a two-level discretization scheme designed by Schunk (1989). The coarse subdomain structure, or mesh, was designed with the elliptic generation scheme described in Chapter 9 (Christodoulou and Scriven 1992). This scheme produced meshes that automatically conform to changes in boundary shape when physical parameters are varied. Figure 13.11 shows a sample of the two levels of discretization used in this chapter. The fine level was formed by algebraically 'sub-dividing' four

times the rows of elements adjacent to the free surface on each side of the interface, with a geometric progression in element thickness perpendicular to the free surface. The meshes contain 1883 biquadratic elements in the coarse grid and 2435 biquadratic elements in the fine grid, and gives rise to a total of 46 394 unknown coefficients for ternary systems in both phases.

The resulting equations, which are a discretized version of the physical ones being solved, are nonlinear and algebraic. They are solved as is common practice in coating-flow analysis with Newton's method, as described in Chapter 9. The discontinuities in velocity and concentration at the free surface, owing to the volume change on evaporation and vapor–liquid equilibrium, were handled with two nodes assigned to the same physical location on the surface. One node was assigned to the liquid-phase element and one to the gas-phase element. Multiplying the weighted residual equations applied at those nodes with the proper liquid/gas property ratios makes for convenient cancellation of the diffusive flux contributions and eliminates the need to evaluate normal derivatives at the boundary (see Schunk and Rao 1994).

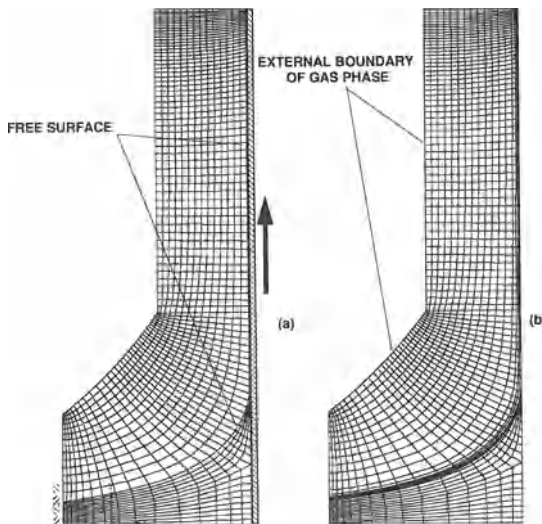


Figure 13.11 Sample meshes for two-phase flow: (a) coarse mesh; (b) fine mesh.

13.6 CASE STUDY: SOL-GEL THIN FILMS

13.6.1 ASYMPTOTIC ANALYSIS FOR SINGLE-COMPONENT SOLVENT

The first attempt at a theory for dip coating and evaporation was made by Hurd and Brinker (1988) for single component (pure) solvents. They assumed that the evaporation rate was constant along the entrained liquid film and ignored the effects of surface tension. They predicted a linear thinning thickness profile, i.e., wedge-shaped. In the same work, however, experiments indicated that the evaporation rate was not constant and that the film profile was blunt (parabolic) in shape, presumably due to an accelerated evaporation rate near the drying line; see Fig. 13.8. In the following development, we show that the evaporation rate is controlled by the vapor diffusion away from the film.

Because experiments show that the film is much thinner than its width and breadth, and its slope is relatively small compared with the distance on the substrate over which it dries, the flow is slow enough that a lubrication approximation applies in which flow is parallel to the substrate and only gradients normal to the substrate are important, i.e., $\mathbf{u} \cdot \nabla \mathbf{u} \approx 0$. The film cannot be considered thin near the static reservoir, however, but there the fluid mechanics is negligible; in this region surface tension and gravity control meniscus shape.

In the development we present here, the effects of long-range molecular forces (e.g., disjoining pressure) that can be important when films are thin have been neglected. Here x measures the distance along the substrate from the drying line toward the reservoir, and y measures the distance normal to the film, as shown in Fig. 13.10. If the substrate is pulled from the reservoir at an angle α from vertical, the Navier–Stokes equations, duly simplified with the lubrication approximation, can be integrated to give

$$u = -U[1 + f(x)h(x)y - \frac{1}{2}f(x)y^2] \quad (13.17)$$

where the appropriate boundary conditions of non-slip at the substrate surface ($y = 0$), vanishing

shear stress at the meniscus ($y = h(x)$), and the balance of capillary pressure with hydrodynamic pressure at the free surface have been applied. $f(x)$ is defined as

$$f(x) \equiv \left(\frac{\rho g}{\mu U} \right) \left[(\sin \alpha) \frac{dh}{dx} - \cos \alpha \right] - \left(\frac{\sigma}{\mu U} \right) \frac{dk}{dx} \quad (13.18)$$

κ being the mean curvature of the meniscus. An equation for the steady state $h(x)$ can be found by equating the mass flux $J(x) \equiv \int_0^h \rho u dy$ to the evaporative loss between x and the drying line, i.e.,

$$J(x) \equiv - \int_0^x E(x) dy \quad (13.19)$$

where the quantity $E(x)$ is the local evaporation rate at point x . If we take $\Pi \equiv \frac{h(x)}{Ca^{1/6}} \left(\frac{\rho g}{\mu U} \right)^{1/2}$, the equation for $h(x)$ is

$$\begin{aligned} \Pi^3 \frac{d}{d\xi} \left(\frac{d^2 \Pi / d\xi^2}{(1 + Ca^{2/3} (d\Pi/d\xi)^2)^{3/2}} \right) &= 3[\Pi - j(\xi)] \\ + \Pi^3 \frac{d\Pi}{d\xi} Ca^{2/3} \sin \alpha - \Pi^3 Ca^{1/3} \cos(\alpha) \end{aligned} \quad (13.20)$$

Here

$$x \equiv \xi / Ca^{1/6}$$

and

$$j(\xi) = (\rho U)^{-1} \left(\frac{\rho g}{\mu U} \right)^{1/2} Ca^{-1/6} \int_0^x E(x) dx$$

The local evaporation rate $E(x)$ is assumed to be equal to the diffusive flux of vapor in the gas phase at the interface, i.e., $-D \frac{\partial X}{\partial y} \Big|_{y=h}$, X being the mass fraction solvent in the gas phase. Neglecting convection effects in the gas phase, Equation (13.6) becomes

$$\nabla^2 X = 0 \quad (13.21)$$

$$X = X_0 \text{ at } y = h(x) \quad (13.22)$$

$$\frac{dX}{dy} = 0 \text{ at } y = 0 \text{ on dry substrate.} \quad (13.23)$$

Equation (13.22) and equation (13.23) represent boundary conditions on the solvent concentration

in the gas. Equation (13.22) is actually a statement of vapor–liquid equilibrium (Raoult's law, equation (13.11)); equation (13.23) is a simplification of equation (13.7) and ensures no evaporative source above the drying line. Equation (13.21) is equivalent to that for the electrostatic potential around a conductive object, with the electric field at the surface being analogous to the evaporation rate $E(x)$ and the flux $J(x)$ analogous to the charge accumulation between 0 and x . Near any sharp boundaries, the electric field (evaporation rate) diverges but the charge (vaporized mass) must remain integrable. This divergence in evaporation accounts for the blunt profiles depicted in Fig. (13.8).

As the profile $h(x)$ is not known *a priori*, equations (13.21) to (13.25) constitute a free boundary problem. However, because the entrained film is very thin compared with its breadth and length, the vapor sees it as infinitely thin; hence, its detailed shape is inconsequential. The solution for the potential and field near the edge of a thin sheet is (Jackson 1975):

$$X \approx X_0 - a_1 r^{1/2} \sin\left(\frac{\theta}{2}\right) \quad (13.24)$$

$$E = -D \frac{\partial X}{\partial y} \Big|_{y=0} = Da_1 x^{-1/2} \quad (13.25)$$

where (r, θ) are cylindrical coordinates defined by $r \sin \theta = y$ and $r \cos \theta = x$. The constant a_1 must be determined from boundary conditions. Equation (13.25) can be used to evaluate $j(\xi)$ in equation (13.20). Solving equation (13.20) near the drying line where curvature effects are assumed negligible and Π and $d\Pi/d\xi$ are small gives (Hurd and Brinker 1990)

$$h(x) = \frac{Da_1}{\rho U} x^{1/2} \quad (13.26)$$

Fitting the pure ethanol data in Fig. 13.8 to the form $h = cx^\nu$ yields $\nu = 0.5 \pm 0.01$, which holds over the experimentally observable range $50 \mu\text{m} < x < 1 \text{ cm}$. It can be shown that the curvature is small in this range (radius of curvature of order 1 km).

The singularity strength (exponent) in equation (13.25) is sensitive to the geometry of the film. For coating a cylinder of decreasing radius, the

strength passes from $-1/2$ for large radius to -1 as the radius vanishes. This change can be demonstrated experimentally (Hurd 1992).

13.6.2 COMPUTER-AIDED RESULTS FOR MULTICOMPONENT ONE- AND TWO-PHASE SYSTEMS

13.6.2.1 Base case

The thermophysical properties and coater design specifications in Table 13.2 define a case of a dip coating process. This base case is of a typical process in sol-gel dip coating and is the one, with the exception of the liquid composition and substrate speed, for which the experiments summarized in Section 13.4 were performed. A solution of ethanol in water with a dispersed, non-volatile phase was chosen as a model system because it is typical of a silica-based sol. The density and viscosity of the liquid were taken to be independent of the initial concentration of all species. The surface tensions at different ethanol concentrations are shown in Fig. 13.12. We fit a hyperbolic cosine function to the data in the range 0 to 0.2 mass fraction ethanol and a linear function in the range 0.2 to 1. The fit served as the constitutive equation for surface tension.

Table 13.2 Operating conditions and thermophysical properties for dip coating base case

Operating conditions	
Liquid composition (volume %)	74:16:10 ethanol/water/ non-volatile
Substrate speed	1.0 cm/s
Substrate withdrawal angle	Vertical
Reservoir width	7 mm
Reservoir depth	3 mm
Thermophysical properties	
Liquid viscosity	2×10^{-3} Pa s
Gas viscosity	1.8×10^{-5} Pa s
Liquid density	1000 kg/m ³
Gas density	1 kg/m ³
Surface tension (equilibrium 20°C)	30 mN/m
Liquid diffusivity	1×10^{-8} m ² /s
Gas diffusivity	1.6×10^{-4} m ² /s

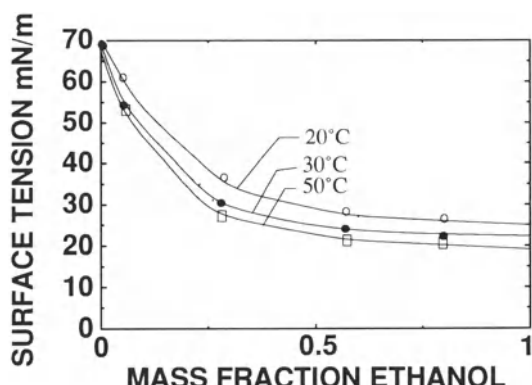


Figure 13.12 Surface tension versus mass fraction ethanol in water–ethanol solutions at several different temperatures (from Weast (1974)).

It is important to mention that the flow was observed to be essentially steady under the conditions given in Table 13.2 (Hurd 1992). Moreover, the flow was visibly stable when we varied the substrate speed and coating liquid composition, with the exception of a three-dimensional ribbing-like phenomenon that appeared over a narrow range of coating rates (Hurd 1992). This instability was likely connected to temperature- or concentration-induced surface tension variations because it rarely occurred in single-component systems. Interestingly, the rib-like pattern decayed rapidly with distance downstream, and the final film was apparently flat and unaffected. Because our analysis is strictly two-dimensional, we cannot pick up any evidence of this flow state. However, we are confident that the flow and mass-transport fields we report herein are stable with respect to two-dimensional disturbances, unless instabilities arise because of lack of sufficient resolution in the computational mesh.

13.6.2.2 Single-phase flow with mass transfer model

The equations of overall mass, momentum and species transfer were solved first for the liquid phase only, with a mass-transfer model accounting

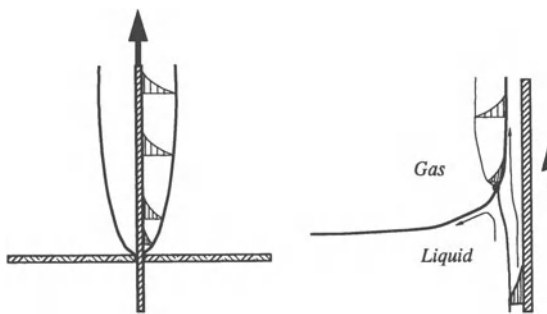


Figure 13.13 Similarity of the boundary layer between moving flat plate and free surface movement in dip coating.

for the fluid mechanics and mass transport in the gas phase. In this approach, equation (13.6) and the right-hand sides of equations (13.8) and (13.9) were replaced with expressions based on the effective flux of each species across the interface (*cf.* Bornside (1989)). These expressions were of the form $N_i = K_i(X_i - X_i^0)$, for each species i . The constants K_i were estimated from classic boundary-layer theory of semi-infinite flow driven by a moving flat plate emanating from a slit (Sakiadis 1961). Figure 13.13 suggests that the boundary layer in gas flow that builds up downstream of the stagnation point in dip coating is of the Sakiadis type, except near the stagnation point. In this boundary layer approach, functional forms for the velocity components and the concentration are substituted into the Navier–Stokes system and the convective-diffusion equations in the gas phase. The resulting equation set is then solved for the rate of mass transfer in terms of the concentrations (partial pressure) of the transported species at the surface of the film. The average gas-phase coefficient of mass transfer K_i resulting from this approach is

$$K_i = \frac{D_i}{L} (0.56 Sc_g^{1/2} Re_g^{1/2}) \quad (13.27)$$

Here Re_g is the effective Reynolds number in the gas phase based on the substrate speed and a development length L along the film. Sc_g is the Schmidt number in the gas phase based on the binary diffusivity D_i , taken in this case to be the

same for all species. It is noteworthy here that K_i is independent of the local interfacial concentration, and that only through the mass transfer model for the flux, i.e., $n_i = K_i(X_i - X_i^0)$, can it depend on the local concentration X_i^0 in the ‘far field’ of the gas phase. Furthermore, the local mass transfer coefficient decreases with increasing distance downstream (Cussler 1984), which leads to lower mass transfer rates. The simplified lubrication approach in the previous section suggests that the mass transfer rates must increase with distance downstream to give rise to the parabolic-type meniscus shapes.

Figure 13.14 shows the pattern of streamlines for a composition of 82:8:10 by weight ethanol/water/non-volatile. Figure 13.15 shows the corresponding mass fractions of ethanol (right) and of non-volatile species (left) in the film region above the level of the reservoir. The pattern of streamlines shows a counterclockwise recirculation driven by the upward movement of the substrate. Because we are approximating the process as steady, the balance of material leaving the system by evaporation and film entrainment (upper right) is the liquid brought into the reservoir to maintain its level. The streamlines

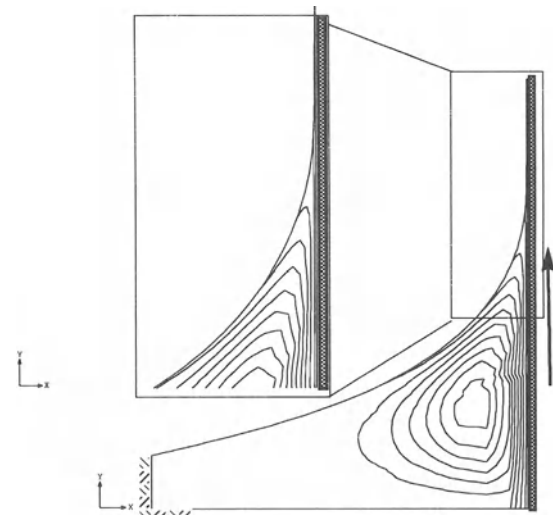


Figure 13.14 Pattern of streamlines predicted with boundary-layer type mass transfer model. Composition is 82:8:10 by weight ethanol/water/non-volatile.

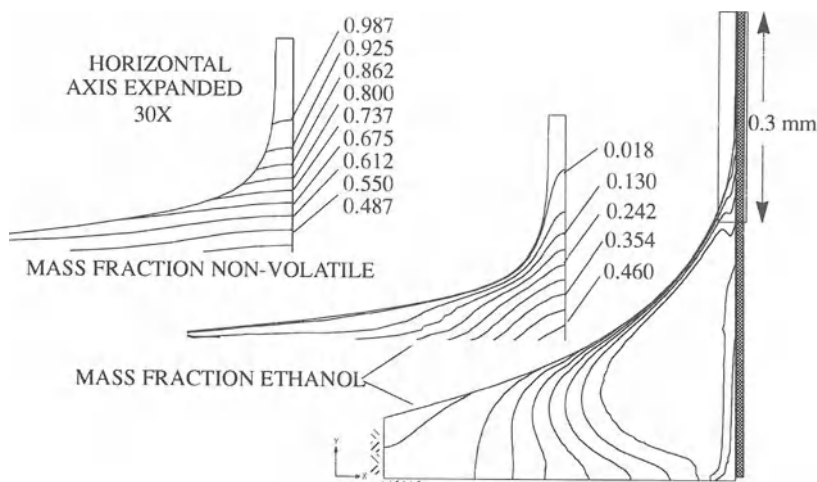


Figure 13.15 Concentration contours predicted with mass-transfer model. Left side shows the mass fraction of non-volatile material and the right side shows the mass fraction of ethanol. The mass transfer coefficient (given by equation (13.27)) is constant along the free surface. Conditions are the same as Fig. 13.14.

indicate this inflow along the substrate at the bottom of the reservoir. Near the free surface the streamlines also indicate vigorous evaporation, as several intersect the surface. The corresponding concentration contours (Fig. 13.15) show streamwise depletion of the more volatile species (ethanol) and a boundary layer of ethanol lean (water-rich) solution along the free surface overlying the more-or-less static reservoir. That boundary layer turns parallel to the film direction when the film becomes so thin that the substrate presence influences the evaporation-induced concentration gradients. Streamwise enrichment of the non-volatile species is also evident in Fig. 13.15. The concentration contours in this case are largely perpendicular to the interface where the film is thin.

The results in Fig. 13.15 show small variations in volatile species concentration along the free surface. In fact, the ratio of water to ethanol remains large (water-rich) and unchanged near the surface, although the absolute mass fractions of these species change as the non-volatile species concentrates along the substrate. This result is an artifact of the constant mass transfer coefficient used so far, which outweighs any mechanism in the liquid phase that might cause the concentration

at the surface to vary. Unfortunately, the simplified boundary layer theory we employ does not account for variations in the overlying concentration of volatile mass – X_i^0 must be set in an *ad hoc* fashion as a parameter – and possible dependencies of the local mass transfer coefficient K_i on local concentration at the interface. With this approach we found no way to reproduce the experimentally measured profiles of ethanol–water films.

To investigate the effect of a varying coefficient we presumed that the evaporation rate must increase with distance downstream, as suggested by the geometrical effects observed in experiments near the drying line. Correspondingly we tried ramping in an *ad hoc* manner the mass transfer coefficient with distance along the surface from the pool to the outflow plane. The results of one case are shown in Fig. 13.16 (left). In this case the mass transfer coefficient was ramped from a low value (one tenth of that given by equation (13.27)) to the value used in Fig. 13.15 over the last 0.2 mm of the entrained film. Now not only is a substantial gradient of ethanol concentration apparent along the free surface, but the corresponding surface tension gradient directed upward

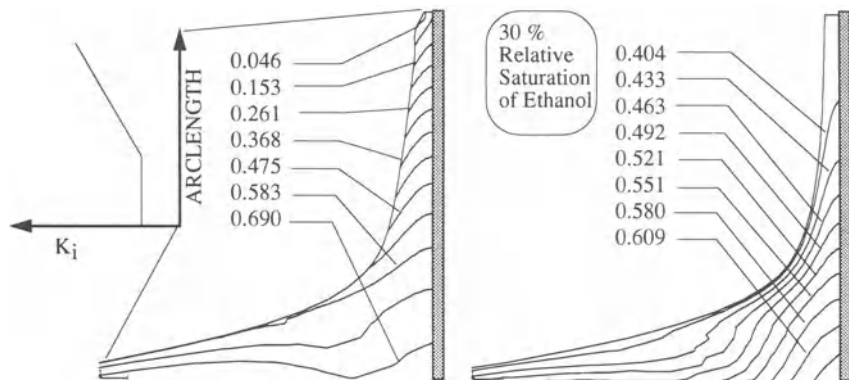


Figure 13.16 Effect of ramping of mass-transfer coefficient (left) and humidity change (right) on the contours of constant mass fraction of ethanol. All other conditions are the same as in Fig. 13.14. The horizontal axis is expanded thirty-fold.

is strong enough to create a small pile-up of water-rich liquid near the outflow plane. Instead of varying the mass transfer coefficient we also tried adjusting the overlying concentration through the parameter X_i^0 . On the right of Fig. 13.16 we show the effect of adding a 30% overlying saturation of ethanol in the overlying gas, i.e., we set the partial pressure of ethanol to be 30% of its equilibrium vapor pressure. In this case we notice that evaporation of ethanol is impeded enough to undermine the streamwise depletion of ethanol. In fact, the mass fraction ethanol is still 0.4 at the outflow plane.

13.6.2.3 Model of two-phase flow

In place of the mass-transfer model in the gas phase we solved the mass-transport system given by equations (13.5) to (13.12) together with the Navier–Stokes system in both gas and liquid phases (see Schunk and Rao 1994 for details). This eliminates the need to lump the gas-phase physics into a single but variable coefficient, albeit at a greater cost. The problem then is no longer one of the accuracy of the mass transport coefficient, but of the accuracy of the boundary conditions on the gas flow. The advantage of this approach, however, is that it enables us to explore the effects of air conditioning, i.e., the

effects of humidity and the effects of forced convection, on the final film quality. Another advantage is that it circumvents the need to search for gas-phase mass transport theories that account for realistic variations in mass-transfer coefficient, and especially theories that are analytically tractable.

The base case here is the same as that outlined in Table 13.2, but the coating composition is taken to be 74:16:10 by weight ethanol/water/non-volatile so that the water to alcohol ratio was identical to that in the experiments performed by Hurd and Brinker (1988), cf. Fig. 13.8.

The boundary conditions we impose on the gas flow in the base case force dry air into the domain over a portion of the artificial boundary that overlies the reservoir (see Fig. 13.17). The velocity of the gas over this portion was taken to be 0.1 cm/s, which is of the order of the substrate speed, i.e., 0.2 cm/s, but far less than the evaporation-induced velocity in the gas phase (order of 10 cm/s). Over the same portion of the boundary we specified the incoming gas composition to be void of water and ethanol vapor. The remaining external boundary in the gas-phase we presumed to be free of viscous traction and of diffusive flux of each species, except for the solid boundary that contains the coating liquid on the left-hand part of the domain, which is

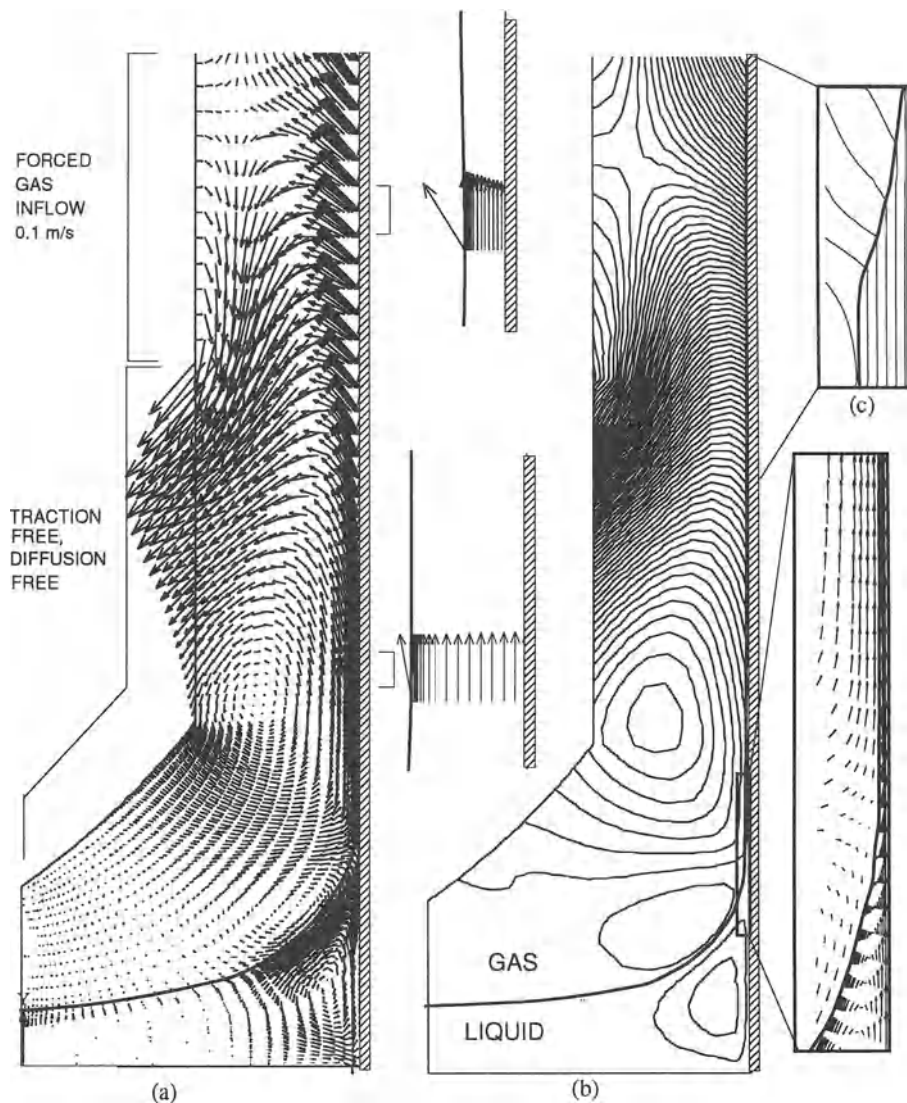


Figure 13.17 (a) Velocity vectors (absolute) in gas and liquid phases. (b) Pattern of streamlines. (c) Pattern of streamlines in film region with horizontal axis expanded 100 times (multiplied by density).

taken to extend into the gas as well. Of course these conditions are arbitrary, but they provide a means of matching the experimental conditions. Unfortunately the experimental data we have available for comparison were performed with no knowledge of the details of the gas flow.

Figure 13.17 shows the pattern of streamlines

and the velocity vectors corresponding to the base case operating conditions. Between any two adjacent streamlines in Fig. 13.17b the volumetric flow rate is the same, but the mass flow rate changes if the streamlines cross the free surface. Both the pattern of streamlines and the velocity vectors in the gas phase show a clockwise vortex

driven by the counter-clockwise recirculation in the liquid phase reservoir. This is a direct consequence of no-slip boundary condition (equation (13.14)) at the interface. Over this portion of the free surface the evaporation rate is relatively small, due mostly to a higher concentration of ethanol and water vapor in the overlying gas. Far above the reservoir surface the streamlines indicate a strong vapor current emanating from the thin liquid film. This heightened evaporation is also evident in plots of velocity vectors: the component of velocity normal to the surface, governed by equation (13.15), increases with distance downstream. Also noteworthy is the viscous boundary layer in the gas phase building downstream of the deposition region on the free surface (right side, bottom, of Fig. 13.17). It is this boundary layer on which we based our model of mass transfer in the previous section. The two-phase flow calculations indicate that the mass transfer model we employed earlier may be inaccurate in part because of strong convection normal to the free surface. If we extract the local mass transfer coefficient from the two-phase flow calculations we find that the portion of the evaporation rate coming from a vapor diffusion model is 20% too large (*cf.* Schunk and Rao 1994).

Vapor–liquid equilibrium conditions make for a concentration discontinuity at the free surface. This discontinuity defines the free surface, as shown in Fig. 13.18. Unfortunately, owing to relatively high vapor pressures, the concentration levels of ethanol and water in the gas phase, and hence the gradients in concentration there, are too small to be resolved by the color spectrum. For that reason we show an overlay of the concentration contours in the gas phase. Note-worthy is the gradient in concentration normal to the free surface which grows larger with distance downstream (i.e., contour lines in the gas phase become more parallel to the film downstream), and an apparent layer of relatively high vapor concentration overlying the reservoir (mass fraction 0.095). Correspondingly, we see little enrichment of water and non-volatile species near the reservoir. Well above the reservoir,

however, the film becomes depleted in ethanol, and the water concentration rises. But the water too is evaporating, and near the outflow plane (projected to be about 2 mm from the drying line) the concentration of the non-volatile species begins to concentrate precipitously. Figure 13.18 shows the mass fraction non-volatile species rising from 0.4 to 0.7 in the last 1 cm of the film.

When coating binary solvent-based sols, the meniscus shape usually exhibits a peculiar plateau region followed by a region of rapid thinning and a second, lower plateau. This shape has been observed in earlier experiments (Hurd 1992) where it was conjectured to be a consequence of differential volatilities and surface tensions of ethanol and water. This mechanism is corroborated by the theory and is shown in Fig. 13.18. Below the second plateau (or ‘foot’) is a water-rich phase that outlasts the alcohol due to a lower volatility. This apparent ‘phase separation’ appears regardless of the original composition of the liquid and over a wide range of drying conditions we tried through alterations in the gas-phase boundary conditions. It even appears at the evaporation-azeotrope composition at which the mixture evaporates at constant concentration.

Surface tension gradients between the alcohol-rich and water-rich portions of the film enhance this plateau region. The velocity vectors in Fig. 13.17 (center inset) show a rapid acceleration of the surface, and hence of the underlying liquid, towards the downstream plateau, thereby lengthening the foot feature. With other solvent mixtures this can be even more dramatic. For instance, in toluene–methanol systems the surface-tension-gradient driven flow is strong enough to thicken the lower plateau, creating a pile-up of the less volatile toluene near the drying line (Fig. 13.18). This phenomenon, which is known as Marangoni flow (Sternling and Scriven 1959), is akin to the famous example of wine tears, where evaporation in the thin film region of a glass induces a climbing motion of the wine (Walker 1983). It has also been observed widely in spreading drops of binary liquids, for which it is found that

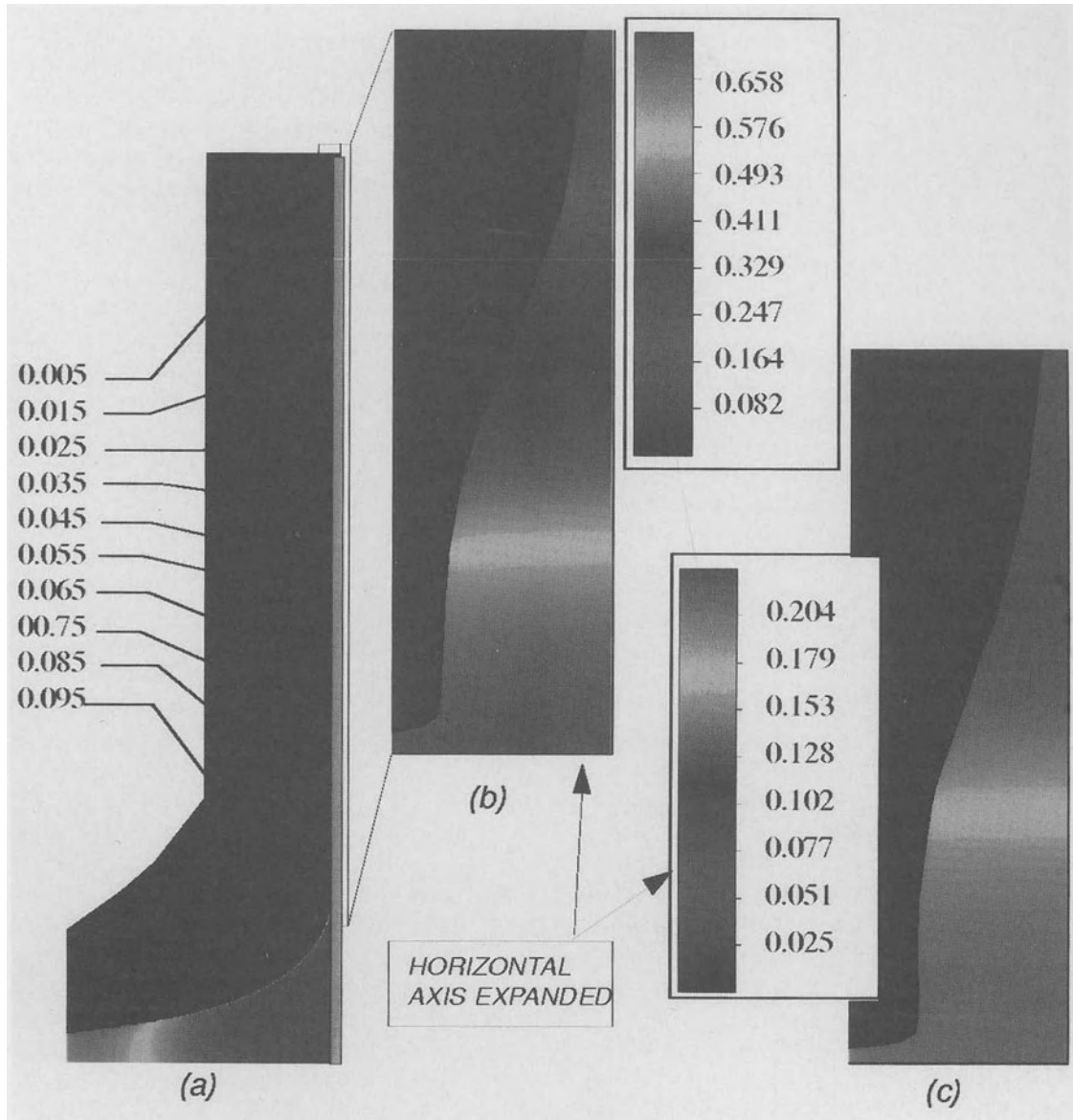


Figure 13.18 Concentration contours for two-phase flows: (a) mass fraction ethanol; (b) mass fraction ethanol in film region; (c) mass fraction water in film region. The difference between one and the sum of (b) and (c) is the mass fraction non-volatile at the same location.

when the more volatile component has a lower surface tension, the drop will spread faster due to surface tension gradients. A first-hand example of this with ethanol–water systems was observed by Pesach and Marmur (1987).

The shape of the drying film can have enormous implications on the development of the gel microstructure. One way is through the kinematic effect associated with rapid film thinning, which brings gelling molecules close together at high

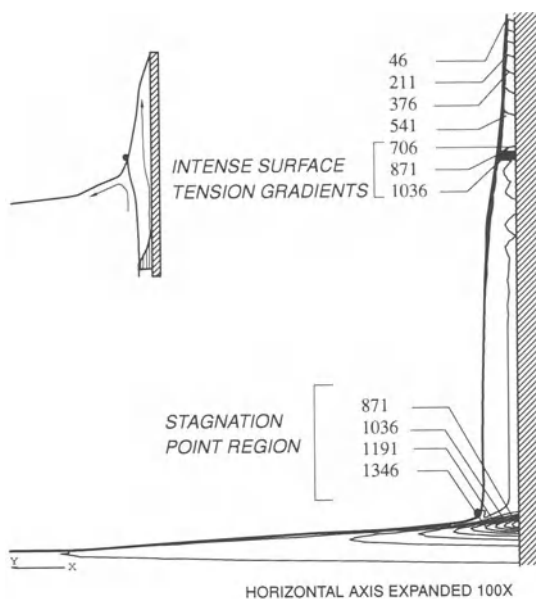


Figure 13.19 Shear rates in dip coating, s^{-1} .

rates (cf. equation (13.4)). Another way is through the large velocity gradients created by the variations in surface tensions. Figure 13.19 shows that shear rates in the liquid underneath the rapidly thinning menisci can reach 1000 s^{-1} . Locale where the rates are highest lie underneath the stagnation point, which terminates a dividing line between the entrained film and the draining film, and near the most intense surface tension gradients between the water-rich region (downstream) and the ethanol-rich region (upstream).

The two-dimensional model of sol-gel dip coating described in Section 13.6 was tested against the experimentally measured film thickness profiles and concentrations profiles described earlier. The coating liquid in the theory was composed of 74% by weight ethanol, 16% by weight water, and 10% by weight non-volatile, the last having a molecular weight of 46 g/mol. In the experiments the liquid was 82% ethanol and 18% water, so the ratio of ethanol to water was the same. The non-volatile component was included in the theory to prevent complete evaporation of the film, a phenomenon the

current numerical scheme is incapable of handling. Experiments were performed at coating speeds of 0.2 cm/s; the computations ranged from 2 cm/s to 1 cm/s. Solutions to the theory at lower coating speeds could not be attained due to insufficient streamwise resolution in the computational mesh needed to resolve film thickness of less than 1 μm .

Figure 13.20 shows a comparison between film thickness profiles predicted with the theory and the profile measured with imaging ellipsometry (Fig. 13.8). Clearly there is a large discrepancy in the magnitude of the film thickness at any point along the substrate. But the solution family parameterized by web speed shows that the correct magnitude is apparently being approached with a reduction in substrate speed, which is encouraging. Even more encouraging is that the shape features we predict are similar to the experimental data, both of which show a reasonable fit to equation (13.26). It is also reasonable to expect quantitative agreement had we been able to match the conditions of the experiment. We do not expect, however, to be able to predict the exact location of the drying line with the theory, unless we can match the drying environment in the experiments and account for the microscale physics which dominate when the film

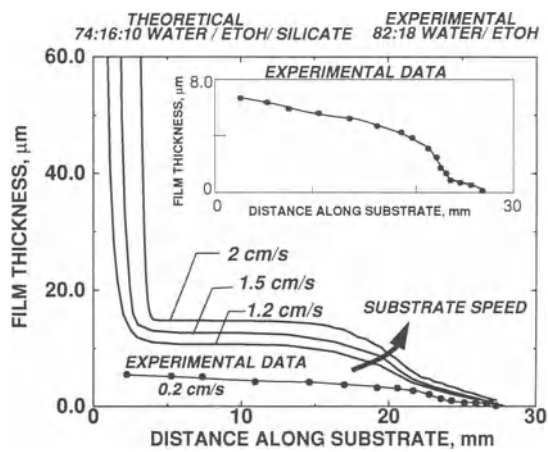


Figure 13.20 Comparison between theory and experiment

becomes thinner than 100 Å. Unfortunately, at the time of the experiments, little effort was made to characterize the gas flow. This clearly leaves room for future work.

We also checked the predicted concentration profiles against those inferred from the fluorescence spectroscopy measurements, as shown in Fig. 13.9. Even though the experiments were performed under different conditions, we see similar concentration variations along the film, with much of the ethanol depletion taking place well above the reservoir surface. Unfortunately, at the time of this writing, we had no quantitative measurements available indicating the magnitude of these variations.

13.6.2.4 Drying control

Because the gas phase plays an important role in the development of film microstructure, it is possible to control microstructure with the drying environment. There are several means of doing so, the simplest being the humidity. With the more-simplified mass transfer theory for the gas phase, humidity adjustments can be made to the overlying saturation of species i , through X_i^0 , as we demonstrated in Fig. 13.16. Unfortunately, changing the overlying saturation probably alters the flow field, and should be accompanied by the appropriate adjustments to the mass-transfer coefficient K_i . Rather than search for the appropriate coefficients we again opted for the two-phase flow approach, for which humidity control is a simple matter of conditions on the volatile species at the external boundaries of the domain.

As an example, we show in Fig. 13.21 the effects of drying control with a narrow jet of dry air impinging on the liquid film just above the level of the reservoir. This approach, often termed air-knife control, is usually employed to accelerate the drying of films after they are deposited and solidified. Air knives are also commonly employed to control the film thickness, through an air-stripping process. Here an air knife was employed to achieve both effects.

The air is blown from a nozzle at 1 m/s and the coating conditions correspond to the base

case outlined in Table 13.2; however, the composition in this case is 40:40:20 water/ethanol/non-volatile. Figure 13.21 (right side) shows the velocity field under and around the air knife. Noteworthy is the stagnation-like flow pattern under the jet where it impinges on the film. In this figure, the velocity vectors in either phase are multiplied by density, and so they indicate a mass flow rate, and the vectors on the free surface in the gas phase have been magnified over the others to show the heightened evaporation underneath the air knife. Figure 13.21 (left side and top) shows the concentration contours of ethanol in both the gas and the liquid. Here the stagnant layer of gas with high ethanol vapor content is visible beneath the air knife. Up on the substrate the concentration of ethanol in the gas is much less and, correspondingly, the evaporation rates are much higher. The highest evaporation rates are directly under the air jet at the film surface, as expected. Correspondingly the volatile components are drawn off the film more rapidly, with the film becoming virtually depleted of the more volatile ethanol underneath the air jet. Of course this affects the final film thickness, but not as much as the metering effect through impingement pressure. This is also evident in Fig. 13.21 (top right) where there appears a depression in the film underneath the jet.

Clearly the film concentration and thickness evolution can be controlled with the air knife. If the results we present here are not desirable to a coating practitioner, we are free to vary the concentration of the air blown through the jet. In fact it is possible to enrich the film in a condensable solvent component, as has been demonstrated in the Marangoni drying technique (*cf.* Leenaars, Huethorst and van Oekel 1990; O'Brien and van den Brule 1991).

13.7 SUMMARY/FUTURE PROSPECTS

Dip coating epitomizes free-meniscus coating. Of all coating processes covered in this book, it is probably the oldest and most studied. It is also perhaps the most unique. Film thickness can be controlled only through substrate speed, angle

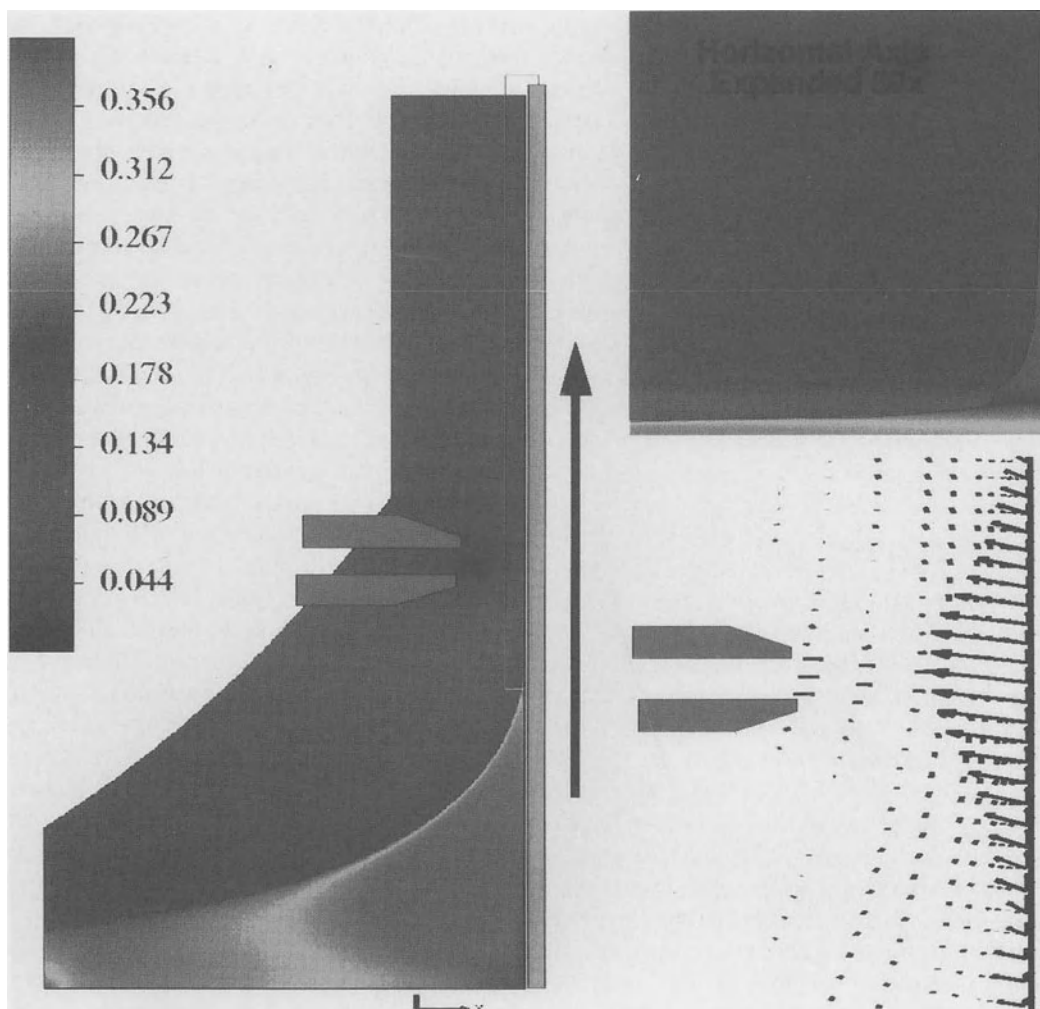


Figure 13.21 Drying control with air knife. Concentrations are mass fraction ethanol. Conditions are the same as in previous figures.

of withdrawal, and various thermophysical properties of the liquid to be coated (i.e., viscosity, density, surface tension, vapor pressure, etc.). Interestingly, even though ambient back pressure, inlet flow rate, and coating gap are crucial to the operability of most pre-metered techniques, they have little or no effect on the range of film thicknesses that can be deposited successfully with dip coating.

When substrate speeds are slow (i.e., low capillary number) film drying makes free-meniscus

coating even more unique: the mass transport by evaporation and the fluid mechanics of deposition take place simultaneously, so any realistic analysis must consider both phenomena. We believe this chapter accomplishes this task, and points out that there is still much to be learned about dip coating and drying.

We attack dip coating in its simplest form and with the complicating effects of concomitant drying with a realistic theory based on conservation laws of overall mass, momentum, species

and energy transport. The theory encompasses both gas and liquid phases, with proper interphase boundary conditions applied where appropriate. Multiple components and multiple phases together with the volume change accompanying evaporation or condensation makes any numerical scheme of solving the governing equations more challenging. The problem is that velocity and concentration are discontinuous (multivalued) at the surface, the first being a result of a volume expansion that accompanies interphase transfer, and the second stemming from vapor–liquid equilibrium laws.

In this chapter we focus on the dip coating of sol-gel materials, which are normally composed of a condensed phase component, which may polymerize or aggregate, and one or more solvent components which are volatile (e.g., alcohol and water). In most cases we solved the corresponding nonlinear differential equations with the Galerkin/finite-element method. We employed the best techniques available for mesh generation and free surface parameterization.

The solutions contain detailed information on the meniscus shape and the distribution of solute in both phases during deposition. We found that differential volatility leads to surface concentration gradients, and hence surface tension gradients that alter the flow and change the meniscus shape. For the first time the peculiar thinning profile that has been observed experimentally in alcohol–water systems is predicted theoretically. Moreover, the predictions agree qualitatively with profiles measured with imaging ellipsometry. Because of this agreement we extended the calculations to different drying environments to demonstrate how drying strategies might be used to control sol-gel microstructure. This portion of the analysis was made feasible only by extending the theory to two-phase flow, rather than relying on a mass transfer coefficient to account completely for the gas-phase fluid mechanics and convective diffusion regimes.

Understanding how to control the microstructure of sol-gel films with the drying regime is the main goal of the research program summarized in this chapter. The work presented here happens

to be part of a much broader program on the physical chemistry and processing of sol-gel materials. However, quantitative predictions of the effects of processing conditions on microstructure are not accessible with the current theory, at least at this stage. What is still needed is a detailed model of the transport phenomena at the drying line, near which the fleeting formation of the gel network will require a detailed model of the chemistry of gelation. We are currently addressing the detailed physics which dictate the final pore structure of the film, but only once the film has been deposited (Brinker *et al.* 1994 and Cairncross *et al.* 1995).

This chapter points out that it is perhaps unfortunate that our research is not more closely allied with that of Langmuir–Blodgett (L–B) films, for the techniques and goals of both are often similar. In fact many of the experimental techniques we use have also been applied in a similar way to the dip coating of L–B monolayers, e.g., fluorescence spectroscopy (Ahlers *et al.* 1989). In L–B films the control of monolayer and bilayer microstructure is the ultimate goal, made challenging by the delicate nature of films only one or several molecules thick. Even though our coverage of L–B films is sparse, we felt it deserved attention because the same processing issues apply, e.g., drying control.

ACKNOWLEDGMENTS

The authors thank Terri Butler, University of Minnesota, for providing valuable advice on Langmuir–Blodgett coating. This research was supported in part by the Basic Energy Sciences program of the DOE and was performed under the contract DE-AC04-76-DP00789.

REFERENCES

- Adamson, A. W. 1982. *Physical Chemistry of Surfaces*. 4th edn. New York: Wiley.
- Agarwal, V. K. 1988. Langmuir–Blodgett films. *Physics Today*, **40**: 40–46.
- Ahlers, M. *et al.* 1989. Specific recognition and formation of two-dimensional streptavidin domains in mono-

- layers: application to molecular devices. *Thin Solid Films.* **180:** 93–99.
- Ashley, C. S. and Reed, S. T. 1984. *Sol-Gel-Derived AR Coatings for Solar Receivers*. Sandia National Laboratories Internal Report SAND84-0662.
- Azzam, R. M. A. and Bashara, N. M. 1977. *Ellipsometry and Polarized Light*. Amsterdam: Elsevier, Ch. 4.
- Bablik, H. 1950. *Hot-Dip Galvanizing*. London: Spon.
- Bankoff, S. G. 1983. Problems in interfacial instability. *Proceedings of the 4th International Conference on Physicochemical Hydrodynamics*, ed. R. Pfeffer. **404:** 405–419.
- Bein, T. et al. 1989. Molecular sieve sensors for selective detection at the nanogram level. *J. Am. Chem. Soc.* **111:** 7640–7641.
- Benjamin, B. T. 1957. Wave formation in laminar flow down an inclined plane. *J. Fluid Mech.* **2:** 554–574.
- Blodgett, K. B. 1935. Films built by depositing successive mono-molecular layers on a solid surface. *J. Amer. Chem. Soc.* **57:** 1007.
- Bornside, D. E. 1989. Spin coating. PhD thesis, University of Minnesota. Available from University Microfilms International, Ann Arbor, MI.
- Bornside, D. E., Macosko, C. W. and Scriven, L. E. 1989. Spin coating: one-dimensional model. *J. Appl. Phys.* **66:** 5185–5193.
- Brinker, C. J., Frye, G. C., Hurd, A. J. and Ashley, C. S. 1991a. Fundamentals of sol-gel dip coating. *Thin Solid Films.* **201:** 97–108.
- Brinker, C. J., Hurd, A. J., Frye, G. C., Schunk, P. R. and Ashley, C. S. 1991b. Sol-gel thin film formation. Centennial Memorial Issue of the *Journal of the Ceramics Society of Japan*. **99:** 862–877.
- Brinker, C. J. and Scherer, G. W. 1990. *Sol-Gel Science*. San Diego: Academic Press.
- Brinker, C. J., Sehgal, R., Raman, N., Schunk, P. R. and Headley, T. J. 1994. Polymer approach to supported silica membranes. *J. Sol-Gel Science and Technology.* **2:** 469.
- Britten, J. A. and Thomas, I. M. 1992. *Large-area Sol-gel Multilayer Laser Reflectors Applied By Meniscus Coating*. Technical Report, Lawrence Livermore National Laboratory, UCRL-JC-109389.
- Butler, T. L. 1993. Mechanisms of Langmuir–Blodgett film deposition and the development of polymeric film materials. PhD thesis, University of Minnesota.
- Cairncross, R. A., Chen, K. S., Schunk, P. R., Brinker, C. J. and Hurd, A. J. 1995. Recent advances in theoretical modeling of deposition, drying, and shrinkage in sol-gel coating processes. *Proceedings of the American Ceramic Society National Meeting*, Cincinnati, OH, 30 April–3 May.
- Cairncross, R. A., Francis, L. F. and Scriven, L. E. 1992. Competing drying and reaction mechanisms in the formation of sol-to-gel films, fibers, and spheres. 10th Anniversary issue of *Drying Technology* **10**(4).
- Christodoulou, K. N. and Scriven, L. E. 1992. Discretization of free surface flows and other moving boundary problems. *J. Comp. Phys.* **99:** 39–55.
- Cooper, A. R. 1977. *Quantitative Theory of Cracking and Warping During the Drying of Clay Bodies*, ed. L. Hench. pp. 261–276.
- Cussler, E. L. 1984. *Diffusion: Mass Transfer in Fluid Systems*. New York: Cambridge University Press.
- Daniel, M. F. and Hart, J. T. T. 1985. Effect of surface flow on the morphology of Langmuir–Blodgett films. *J. Mol. Electron.* **1:** 97–104.
- Denbigh, K. 1981. *The Principles of Chemical Equilibrium*. Cambridge University Press.
- Deryagin, B. V. and Levi, S. M. 1964. *Film Coating Theory*. London: Focal Press.
- Dillon, P. W. 1977. Application of critical relative humidity, an evaporation analog of azeotropy, to the drying of water-borne coatings. *J. of Coatings Technology*. **49:** 38–49.
- Dislich, H. 1988. Thin films from the sol-gel process. In *Sol-Gel Technology for Thin Films, Fibers, Preforms, Electronics, and Special Shapes*, ed. L. C. Klein. pp. 50–79. Park Ridge, NJ: Noyes.
- Emery, A. F. and Egolf, J. R. 1989. Finite element analysis of the stresses and consolidation of boehmite gel during the constant rate drying period. *Proceedings of the 1989 National Heat Transfer Conference*. HTD-113: 95–104.
- Esmail, M. N. and Hummel, R. L. 1975. A note on linear solutions to free coating onto a vertical surface. *Chem. Eng. Sci.* **30:** 1195–1196.
- Frye, G. C., Ricco, A. J., Martin, S. J. and Brinker, C. J. 1988. Characterization of surface area and pore size of sol-gel films using SAW devices. In *Better Ceramics Through Chemistry III*, eds C. J. Brinker, D. E. Clark and D. R. Ulrich. Materials Research Society, Pittsburgh. pp. 349–354.
- Gaines, G. L. 1966. *Insoluble Monolayers at Liquid–Gas Interfaces*. New York: Interscience.
- Groenveld, P. 1971. Drainage and withdrawal of liquid films. *AIChE J.* **17:** 489–490.
- Gutfinger, C. and Tallmadge, J. A. 1965. Films of non-Newtonian fluids adhering to flat plates. *AIChE J.* **11:** 403.
- Homsy, G. M. and Geyling, F. T. 1977. A note on instabilities in rapid coating of cylinders. *AIChE J.* **23:** 587–590.
- Horton, R. A. 1990. Investment casting. In *Metals*

- Handbook 15.* Prepared by ASM International. p. 257.
- Hurd, A. J. 1992. Evaporation and surface tension effects in dip coating. *Adv. Chem. Series*, No. 234. *Colloid Chemistry of Silica*, ed. H. Bergna (Amer. Chem. Soc., Washington DC).
- Hurd, A. J. and Brinker, C. J. 1988. Optical sol-gel coatings: ellipsometry of film formation. *J. de Physique*. **49**: 1017–1025.
- Hurd, A. J. and Brinker, C. J. 1990. Sol-gel film formation by dip coating. In *Better Ceramics Through Chemistry IV*, eds B. J. J. Zelinski, C. J. Brinker, D. E. Clark and D. R. Ulrich, Materials Research Society, Pittsburgh. pp. 575–581.
- Jackson, J. D. 1975. *Classical Electrodynamics*. New York: Wiley.
- Jacobsen, S. C., Wells, D. L., Davis, C. C. and Wood, J. E. 1991. Fabrication of micro-structures using non-planar lithography (NPL). *Proceedings of the IEEE Workshop on Micro Electro Mechanical Systems*, Nara, Japan, 31 Jan–2 Feb.
- Jeffreys, H. 1930. Draining of a vertical plate. *Proc. Camb. Phil. Soc.* **26**: 204–205.
- Kaufman, V. R. and Avnir, D. 1986. Structural changes along the sol-gel-xerogel transition in silica as probed by pyrene excited-state emission. *Langmuir*. **2**: 717–722.
- Kheshgi, H. S., Kistler, S. F. and Scriven, L. E. 1992. Rising and falling film flows: viewed from a first-order approximation. *Chem. Eng. Sci.* **47**: 683–694.
- Kistler, S. F. and Scriven, L. E. 1983. Coating flows. In *Computational Analysis of Polymer Processing*, eds J. R. A. Pearson and S. M. Richardson. Essex: Applied Science Publishers. pp. 244–299.
- Landau, L. D. and Levich, V. G. 1942. Dragging of a liquid by a moving plate. *Acta Phys. Chim. URSS.* **17**: 42–54.
- Langmuir, I. 1938. Overturning and anchoring of monolayers. *Science*. **87**: 493–500.
- Lee, C. Y. and Tallmadge, J. A. 1974. Dynamic meniscus profiles in free coating III: predictions based on two-dimensional flow fields. *AIChE J.* **20**: 1079–1086.
- Leenaars, A. F. M., Huethorst, J. A. M. and van Oekel, J. J. 1990. Marangoni drying: A new extremely clean drying process. *Langmuir*. **6**: 1701–1703.
- Lewis, R. W., Morgan, K. and Thomas, H. R. 1983. The nonlinear modeling of drying induced stresses in porous bodies. In *Advances in Drying*, ed. A. S. Mujumdar. Washington: Hemisphere.
- Malcolm, B. R. 1985. The flow and deformation of synthetic polypeptide monolayers during compression. *J. Coll. Interf. Sci.* **104**: 520–528.
- Marques, D., Constanza, V. and Cerro, R. L. 1978. Dip coating at large capillary number: an initial value problem. *Chem. Eng. Sci.* **33**: 87.
- Morey, F. C. 1940. Thickness of a liquid film adhering to a surface slowly withdrawn from the liquid. *J. Res. Natl. Bur. Stand.* **25**: 385–393.
- Nigam, K. D. P. and Esmail, M. N. 1980. Liquid flow over a rotating dip coater. *Canadian J. Chem. Engng.* **58**: 564–568.
- Nishida, F., McKiernan, J. M., Dunn, B., Zink, J. I., Brinker, C. J. and Hurd, A. J. 1994. In situ fluorescence imaging of sol-gel thin film deposition. *J. Sol-Gel Sci. and Tech.* **2**: 477–482.
- O'Brien, S. B. G. and Van Den Brule, B. H. A. A. 1991. A mathematical model for the cleansing of silicon substrates by fluid immersion. *J. Coll. Interf. Sci.* **144**: 210–221.
- Park, C. 1991. Effects of insoluble surfactants on dip coating. *J. Coll. Interf. Sci.* **146**: 382–394.
- Parks, C. J. and Wayner, P. C. 1987. Surface shear near the contact line of a binary evaporating curved thin film. *AIChE J.* **33**: 1–10.
- Pesach, D. and Marmur, A. 1987. Marangoni effects in the spreading of liquid mixtures on a solid. *Langmuir*. **3**: 519–524.
- Petrov, J. G., Kuhn, H. and Möbius, D. 1979. Three-phase contact line motion in the deposition of spread monolayers. *J. Coll. Interf. Sci.* **73**: 66–74.
- Petty, M. C. 1987. Molecular engineering using the Langmuir–Blodgett technique. In *Polymer Surfaces and Interfaces*, eds W. J. Feast and H. S. Munro. pp. 163–185. John Wiley.
- Poehlein, G. W., Vanderhoff, J. W. and Wit-Meyer, R. J. 1975. Drying of latex films. *Polym. Prepr., Am. Chem. Soc., Div. Polym. Chem.*, **16**: 268.
- Pouxviel, J. C., Dunn, B. and Zink, J. I. 1989. Fluorescence study of aluminosilicate sols and gels doped with hydroxy trisulfonated pyrene. *J. Phys. Chem.* **93**: 2134–2139.
- Prescher, M. 1991. Paint technology and the environment. *EuroCoat*. **1**: 50–53.
- Rehg, T. J. and Higgins, B. G. 1992. Spin coating of colloidal suspensions. *AIChE J.* **38**: 489–501.
- Roberts, G. 1990. *Langmuir–Blodgett Films*. New York: Plenum Press.
- Rosenberg, L. D. and Beiter, R. L. 1989. *Impact of New Technology and Changing Practices in the Automotive Coatings Business*. AIChE Symposium Series on New Polymer Technology for Auto Body Exteriors. pp. 33–36.
- Ruschak, K. J. 1974. The fluid mechanics of coating flows. PhD thesis, University of Minnesota.

- Ruschak, K. J. 1976. Limiting flow in a pre-metered coating device. *Chem. Eng. Sci.* **31**: 1057–1066.
- Ruschak, K. J. 1978. Flow of a falling film into a pool. *AICHE J.* **24**: 705–709.
- Ruschak, K. J. 1982. Boundary conditions at a liquid/air interface in lubrication flows. *J. Fluid Mech.* **119**: 107–120.
- Ruschak, K. J. 1985. Coating flows. *Ann. Rev. Fluid Mech.* **17**: 65–89.
- Sakiadis, B. C. 1961. Boundary-layer behavior on continuous solid surfaces. *AICHE J.* **7**: 26–35.
- Sartor, L. 1990. Slot coating: fluid mechanics and die design. PhD thesis, University of Minnesota.
- Sartor, L. and Scriven, L. E. 1990. The progression from dip coating to slot coating: What controls film thickness? Presented at the Fall Annual Meeting of the AIChE, Chicago, IL.
- Scherer, G. W. 1988. Aging and drying of gels. *J. Non-Crystalline Solids.* **100**: 77–92.
- Schroeder, H. 1969. Oxide layers deposited from organic solutions. In *Physics of Thin Films 5*, ed. G. Haas. pp. 87–141. New York: Academic Press.
- Schunk, P. R. 1989. Surfactant and polymer additives in coating and related flows. PhD thesis, University of Minnesota.
- Schunk, P. R., Hurd, A. J. and Brinker, C. J. 1992. Surface tension gradient effects in sol-gel dip coating. Presented at the 1992 Spring National Meeting of the AIChE, 29 March–2 April, New Orleans, LA.
- Schunk, P. R. and Rao, R. R. 1994. Finite element modeling of evaporation and condensation processes in film and fiber formation. *Int. J. Numer. Meth. Fluids.* **18**: 821–842.
- Scriven, L. E. 1988. Physics and applications of dip coating and spin coating. In *Better Ceramics Through Chemistry III*, eds C. J. Brinker, D. E. Clark and D. R. Ullrich. pp. 717–729. Materials Research Society, Pittsburgh.
- Slatterly, J. and Givens, H. 1933. The shape of the profile of a liquid film draining on a vertical, clean, wetted glass plate and the combined effects of gravity, viscosity, surface tension and evaporation on the same. *Trans. Roy. Soc. Canada.* **27**: 145.
- Soroka, A. J. and Tallmadge, J. A. 1971. A test of the inertial theory for plate withdrawal. *AICHE J.* **17**: 505–509.
- Spiers, R. P., Subbaraman, C. V. and Wilkinson, W. L. 1974. Free coating of a Newtonian liquid onto a vertical surface. *Chem. Eng. Sci.* **29**: 389–396.
- Sternling, C. V. and Scriven, L. E. 1959. Interfacial turbulence: hydrodynamic stability and the Marangoni effect. *AICHE J.* **18**: 231–240.
- Sugi, M. 1985. Langmuir–Blodgett films – a course towards molecular electronics: a review. *J. Molec. Elec.* **1**: 3–17.
- Swalen, J. D. 1992. Molecular films. *Ann. Rev. Mater. Sci.* **21**: 373–408.
- Tallmadge, J. A. 1971. A theory of entrainment for angular withdrawal of flat supports. *AICHE J.* **17**: 243–246.
- Tallmadge, J. A. and Gutfinger, C. 1967. Entrainment of liquid films. *Ind. Eng. Chem.* **59**: 18–34.
- Tam, S., Stolarski, H. K. and Scriven, L. E. 1992. Defect-related stresses in drying films. AIChE Spring National Meeting, New Orleans, LA, 1992.
- Tanguy, P., Fortin, M. and Choplin, L. 1984. Finite element simulation of dip coating, II: non-Newtonian fluids. *Int. J. for Num. Meth. Fluids.* **4**: 441–457.
- Tekic, M. N. and Jovanovic, S. 1982. Liquid coating onto a rotating roll. *Chem. Eng. Sci.* **37**: 1815–1817.
- Tharmalingam, S. and Wilkinson, W. L. 1978. The coating of Newtonian liquids onto a rotating roll. *Chem. Eng. Sci.* **33**: 1481–1487.
- Tredgold, R. H. 1987. The physics of Langmuir–Blodgett films. *Rep. Prog. Phys.* **50**: 1609–1656.
- Tschoegl, N. W. 1962. Mathematical relations of torsion pendulum in study of surface films. *Kolloid Z.* **181**: 19–29.
- Tu, Y. and Drake, R. L. 1990. Heat and mass transfer during evaporation in coating formation. *J. Coll. Interf. Sci.* **135**: 562–572.
- Tuck, E. O. 1983. Continuous coating with gravity and jet stripping. *Phys. Fluids.* **26**: 2352.
- Van Rossum, J. 1958. Viscous lifting and drainage of liquid. *Appl. Sci. Res. A.* **7**: 121–144.
- Walker, J. 1983. The amateur scientist: What causes the ‘tears’ that form on the inside of a glass of wine? *Scientific American.* May: 161–169.
- Wayner, P. C. 1982. The interfacial profile in the contact line region and the Young–Dupre equation. *J. Coll. Interf. Sci.* **88**: 294–295.
- Wayner, P. C. 1991. The effect of interfacial mass transport on flow in thin liquid films. *Coll. Surf.* **52**: 71–84.
- Wayner, P. C., Kao, Y. K. and LaCroix, L. V. 1976. The interline heat-transfer coefficient of an evaporating wetting film. *Int. J. Heat Mass Transfer.* **19**: 487–492.
- Weast, R. C. 1974. *Handbook of Chemistry and Physics*. 55th edn. CRC Press.
- White, D. A. and Tallmadge, J. A. 1965. Theory of drag out of liquids on flat plates. *Chem. Eng. Sci.* **20**: 33–37.
- Wilson, S. D. R. 1982. The drag-out problem in film coating theory. *J. Eng. Math.* **16**: 209.

Ronald G. Larson and Timothy J. Rehg

14.1 INTRODUCTION

Spin coating is a batch process in which a liquid film is spread by centrifugal force onto a rotating substrate. A typical spin-coating system for microelectronic wafers is shown in Fig. 14.1. At high rotation speeds, around 1000 to 10 000 rpm,

such devices spin low-viscosity liquids to thicknesses from a few microns down to a few nanometers, with thickness nonuniformities no greater than 1% (Moreau 1988). Solidified films are obtained when the spin-coated liquid contains polymers or colloids in a volatile solvent. Solvent evaporation is greatly accelerated by the air flow induced by high spinning speeds; thus, the application, coating and drying of a film can be accomplished in less than a minute. Because of its speed, combined with its simplicity and low cost, spin coating is unusual as a batch coating process that is useful even in high capacity industrial applications. Although in simplicity it is bested by batch dip coating (see Chapter 13), the uniformity and thinness of spin-coated layers far exceed dip coated ones, and are unmatched by all but relatively exotic methods such as vacuum or Langmuir deposition. As a result, spin coating has long been widely used in high-volume production of advanced electronics devices. It was used as long ago as the 1950s, for example, to deposit phosphor onto the curved glass surfaces of color television tubes.

Nowadays, spin coating is ubiquitous in the microelectronics industry as a means of depositing polymer resist layers for photolithographic processing of integrated circuits (Thompson, Wilson and Bowden 1983; Moreau 1988). Another important modern application of spin coating is the deposition of transparent or reflective inorganic colloidal surface coatings on laser optical components, such as highly reflecting mirrors.

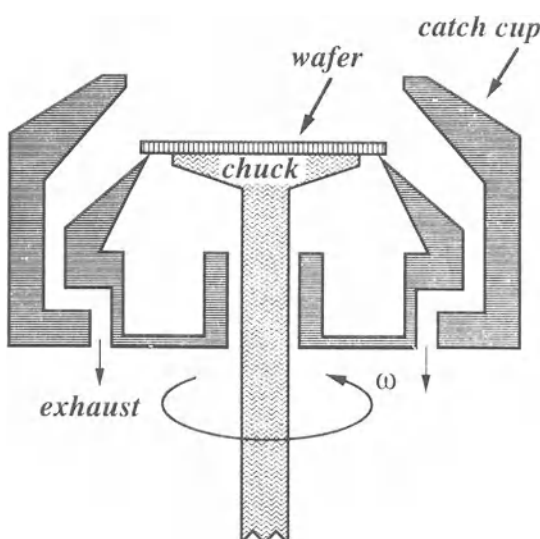


Figure 14.1 Schematic diagram of a typical spin coating system. Air is drawn down and across the wafer by centrifugal forces. The catch-cup traps solvent droplets that are flung from the wafer, preventing their unwanted release into the environment. An exhaust suction assists this, and prevents droplets from re-circulating and hitting the wafer, which would mar the coating (from Bornside *et al.* (1993)).

14.1.1 APPLICATIONS OF SPIN-COATED FILMS

Polymeric resist films are used to delineate device patterns of silicon wafers. Light is shone through a mask to cast a fine pattern of light and shadow on the photosensitive resist that overlies a silicon wafer. In areas exposed to light, photo-catalyzed reactions render the resist either more (positive tone) or less (negative tone) susceptible to subsequent removal during development. For positive resists, the exposed polymer is removed during development by plasma etching or solvent dissolution, while the unexposed polymer remains; the opposite is true for negative resists. In either case, the areas of substrate that remain covered by resist are protected from attack by etchants, thereby transferring a pattern from the resist layer to the underlying silicon wafer. After the etching is complete, the remaining polymer is removed, and the wafer is ready for further lithographic processing steps, including deposition of additional resist layers by spin coating. Frequently, therefore, resist solutions must be spin coated onto wafers that contain micron-scale unevenness because of the previous etching steps to which they have been subjected, a fact with important consequences that we explore in Section 14.3.

Great attention is paid to the chemical design of resist polymers, as these must be highly photosensitive, so that a sharp change in the reactivity of the polymer occurs with only a small change in the total light exposure. With a highly sensitive resist, sharp lines can be produced even when the boundaries of the pattern of illumination are somewhat fuzzy, as is inevitably the case because of wavelength limits to optical resolution. Further discussion of the chemistry of these highly specialized polymeric resists is beyond the scope of this text. The motivated reader should consult Moreau (1988).

Inorganic colloidal coatings are important in high-energy laser-optic systems because they exhibit considerable resistance to laser damage and are less expensive to fabricate than are the traditional electron beam evaporated coatings

(Thomas 1986). This is especially true when the desired optical component is a highly reflecting mirror. In this application, one deposits layers of a material with high refractive index n_h and thickness $D_h = \lambda/(4n_h)$, alternating with layers of a material with low refractive index n_l and thickness $D_l = \lambda/(4n_l)$. In this way, Thomas (1986) has used spin coating to fabricate a laser mirror ($\lambda = 1.06$ mm) with 18 alternating layers each of colloidal alumina ($D_h = 185$ nm, $n_h = 1.43$) and silica ($D_l = 217$ nm, $n_l = 1.22$), producing a surface with 99% reflectivity. Coating uniformity is critical in these systems; small thickness variations induce losses that can accumulate to significant levels when many optical components are present. Unfortunately, the film uniformity achieved by spin coating, although high, may not always be high enough for these applications. This topic is discussed further in Section 14.2.

The volatility of the coating solvent in which the resist polymer is dissolved or the inorganic colloidal particles are suspended is an important concern. Obviously, extremely low volatilities are undesirable, because evaporation times will then be long. But very high volatility, which is usually correlated to low viscosity, can lead to uneven film thicknesses, because of inertial or evaporation-related Marangoni instabilities discussed below. In addition, if the resist solution poorly wets the substrate, pinhole defects and other manifestations of dewetting can be the result; see Chapter 6.

14.1.2 OVERVIEW OF THE SPIN-COATING PROCESS

An excellent overview of the spin-coating process is provided by Bornside, Macosko and Scriven (1987) and by Scriven (1988). They describe four stages of spin coating: deposition, spin-up, spin-off and evaporation. Deposition and spin-up occur quickly; the substrate is usually brought to its final rotation rate within a fraction of a second. Spin-off and evaporation occur concurrently; however, in the first seconds after spin-up, the film is many microns thick, and the fluid has little time to evaporate as it is flung from the

disk into the ‘catch-cup’ shown in Fig. 14.1. Later, the film (by then only a few microns thick) flows so slowly that it thins mainly by solvent evaporation.

In the next section, we consider spin coating over level substrates, both with and without evaporation, and discuss briefly the instabilities that can degrade film thickness uniformity. In the subsequent section, the effects of substrate unevenness on the leveling of the film profiles are discussed in detail, including the practical impact of departures from levelness on the performance of the film in microlithography. Finally, a brief summary of the state of understanding of spin coating is offered.

14.2 SPIN COATING OVER LEVEL SUBSTRATES

14.2.1 WITH EVAPORATION NEGLECTED: THE ANALYSIS OF EMSLIE, BONNER AND PECK

The earliest analysis of spin coating over a flat, rotating, substrate is that of Emslie, Bonner and Peck (1958). Their analysis considers only Newtonian fluids, and takes advantage of the thinness of the film, compared with the radial expanse of the substrate, which justifies the use of a lubrication analysis. (For a detailed discussion of the lubrication approximation, see Chapter 8). Emslie, Bonner and Peck neglect all forces except centrifugal and viscous; thus, gravitational, Coriolis, and capillary forces are ignored, as is air-drag on the free surface. Neglect of these forces is usually justified, except that for uneven substrates capillary forces must be re-introduced; see Section 14.3. Less justifiable is the constancy of fluid properties; this stipulation is derived from a completely unrealistic assumption: the neglect of solvent evaporation. Neglect of solvent evaporation renders the analysis unsuitable for quantitative predictions. Still, the model of Emslie, Bonner and Peck (1958) gives a simple estimate of the time required to spin a film down to a given thickness and, more importantly, it shows

why spin coating generally produces such highly uniform films.

Under the above assumptions, the equation of fluid motion in the film is simply

$$-\mu \frac{\partial^2 V}{\partial Y^2} = \rho \Omega^2 R \quad (14.1)$$

where V is the radial velocity, μ is the viscosity, and ρ is the density of the fluid; Ω is the angular rotation rate, and R is the radial position (distance from the axis of rotation). The boundary conditions on equation (14.1) are $V = 0$ at $Y = 0$, and $\partial V / \partial Y = 0$ at $Y = H$; these correspond, respectively, to the no-slip and the stress-free boundary conditions at the substrate (where $Y = 0$) and at the film-air interface (where $Y = H$). Integrating equation (14.1), we obtain a parabolic velocity profile:

$$V = \frac{\rho \Omega^2 R}{\mu} \left(HY - \frac{1}{2} Y^2 \right) \quad (14.2)$$

The volumetric flow rate, Q , per unit length of film circumference is then

$$Q = \int_0^H V dY = \frac{\rho \Omega^2 R H^3}{3\mu} \quad (14.3)$$

The mass continuity equation, when combined with equation (14.3), implies that

$$\frac{\partial H}{\partial t} = -\frac{1}{R} \frac{\partial (RQ)}{\partial R} = -\frac{\rho \Omega^2}{3\mu} \frac{1}{R} \frac{\partial}{\partial R} (R^2 H^3) \quad (14.4)$$

Equation (14.4) describes the time evolution of the film thickness profile over the spinning substrate.

To solve equation (14.4), one must specify an initial film thickness profile. This initial profile is influenced by the method of dispensing liquid onto the substrate, which is often not well defined. Fortunately, however, Emslie, Bonner and Peck showed that for Newtonian liquids, the initial nonuniformities tend to disappear rapidly after start-up of spin coating. Figure 14.2 shows a typical calculation by Emslie, Bonner and Peck: a film with an initially sinusoidally

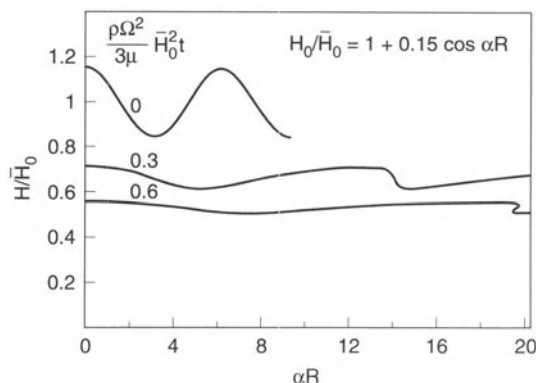


Figure 14.2 Flattening of an initially oscillatory film thickness profile during spin coating of a non-volatile fluid at three different dimensionless times, $(\rho\Omega^2/3\mu)\bar{H}_0^2 t$. In the above, $H_0(R)$ is the initial film profile, \bar{H}_0 is the initial average film thickness, and α is a constant controlling the wavelength of the initial film profile (from Emslie, Bonner and Peck (1958)).

varying thickness quickly becomes nearly uniformly thick as a result of spin-coating flow. The thickness becomes uniform, in part, because of the cubic dependence on thickness of the flow rate Q in equation (14.3). The flow rate in a locally thick area of the film is higher than in surrounding thinner areas, and thus the thick area thins faster than the surrounding areas, making the film thickness more uniform. Once the film has become uniformly thick, with thickness H_i , the rate of uniform thinning of the film can be obtained from a simple solution of equation (14.4):

$$H = H_i [1 + \frac{4\rho\Omega^2}{3\mu} H_i^2 t]^{-1/2} \quad (14.5)$$

Acrivos, Shah and Petersen (1960) extended the analysis of Emslie, Bonner and Peck (1958) to power-law shear thinning fluids. For a power-law fluid, the viscosity is infinite at the center of the disk ($R = 0$), because the shear rate there is zero; this leads to the unrealistic film thickness profiles shown in Fig. 14.3. Jenekhe and Schuldt (1984) considered the more realistic Carreau model for shear-thinning fluids, whose viscosity approaches a constant at low shear rates. Similar

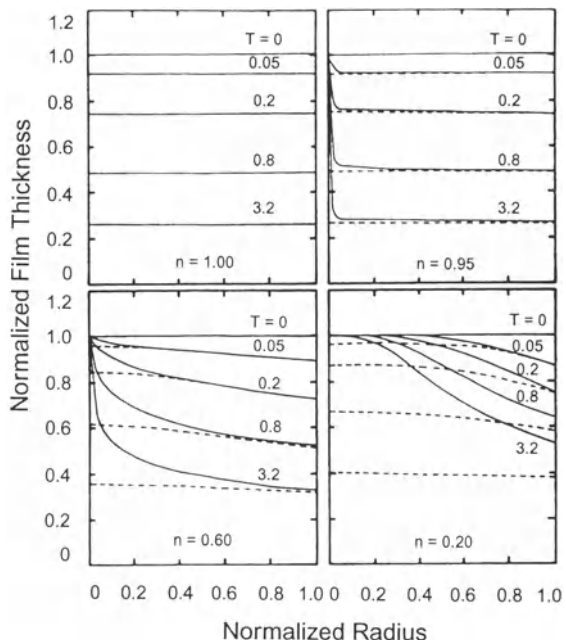


Figure 14.3 Evolution of the thickness profile of an initially uniform, non-volatile, shear-thinning fluid film during spin coating. The solid lines are for the power law fluid, whose shear-rate-dependent viscosity is $\eta = K\dot{\gamma}^{n-1}$ and $\dot{\gamma}$ is the local shear rate, while the dashed line are for the Carreau model with $\eta = \mu_0(1 + \lambda^2\dot{\gamma}^2)^{(n-1)/2}$. Here n is the power law index. The dimensionless time T is t/t_{char} with $t_{\text{char}} \equiv ((2n+1)/n)(\rho\Omega^2/C)R_0^{1-n}H_0^{1+n})^{-1/n}$. The constant C is given by K for the power-law model and by $\mu_0\lambda^{n-1}$ for the Carreau model (reprinted with permission from Jenekhe and Schuldt (1984); © 1984 American Chemical Society).

to the findings of Emslie, Bonner and Peck, Jenekhe and Schuldt found for Carreau fluids that films that are initially nonuniform will tend toward uniformity for long enough spinning times. However, one important distinction from the work of Emslie, Bonner and Peck is that a Carreau-type shear-thinning fluid that is initially uniform will tend to become nonuniform, and then return to a uniform state at long spinning times; see Fig. 14.3. The departure from uniformity occurs because the shear rate is higher near the edge of the substrate than it is near the center. Hence the viscosity near the edge is lower than

at the center, and thus the film will thin more quickly near the edge than at the center. As the film thins, however, the average shear rate decreases, eventually becoming low enough everywhere that the coating solution behaves as a Newtonian fluid, and Emslie, Bonner and Peck's prediction of a uniformly thick film is recovered at long times.

Whether a spin-coated film will in the end be uniform depends on the magnitude of non-Newtonian effects, the time period over which the film returns to uniformity, and the time period over which the film ceases to flow due to solvent evaporation. Evaporative effects are taken up in the next section.

14.2.2 THE EFFECTS OF EVAPORATION

As discussed in the Introduction (Section 14.1) to this chapter, the spin-coated liquid usually contains a volatile solvent that evaporates during spinning, leaving behind a thin solid film. As the analysis of Emslie, Bonner and Peck does not account for evaporation, it cannot, for example, predict the final dry film thickness. Hence, many practitioners have relied on empirical correlations between final film thickness H_f and spinning speed Ω . These correlations are typically expressed as a power law,

$$H_f = K\Omega^{-b} \quad (14.6)$$

The exponent b usually is close to 0.5 (Sukanek 1985), but higher values are sometimes found; the most notorious example is that of Daughton and Givens (1982), who report $b = 0.81$ for a solution of polyamic acid. The correlation (14.6) is adequate for many practical purposes, although the constants K and b must be measured for each spin coating fluid.

Solvent evaporation couples liquid-phase diffusive transport of solvent toward the interface to gas-phase convective mass transport of solvent away from the interface. The solvent vapor is carried away in a stream of air that is drawn down axially toward the surface and driven radially across it by a 'centrifugal pumping action' created by the spinning substrate (Bornside

et al. 1993). The flow pattern generated by an infinite spinning disk was analyzed long ago by von Kármán (1921). Under laminar flow conditions, there is an Ekman momentum boundary layer of thickness $\sim \sqrt{(v_G/\Omega)} \approx 0.25$ mm, for a typical rotation speed (2000 rpm). Here $v_G = 0.16$ cm²/s is the kinematic viscosity of air. Above this boundary layer there is a downward axial flow of air with velocity $\approx 0.89\sqrt{(v_G/\Omega)} \approx 5$ cm/s.

Evaporation of the volatile solvent produces a mass-transfer boundary layer whose thickness is similar to that of the momentum boundary layer, when, as usual, the Schmidt number $Sc \equiv v_G/D_G$ is near unity, where D_G is the gas-phase diffusivity. Most importantly, the thicknesses of these boundary layers, and hence the evaporation rate, are predicted to be independent of the radial position. In practice, of course, some nonuniformity arises from the finite radius of the substrate and the air flow pattern in the catch-cup and the exhaust; see Fig. 14.1. However, a finite-element analysis of the air flow and mass transport in the typical spin-coating device shows that the evaporation rate is remarkably uniform and insensitive to the inlet and outlet flow conditions (Bornside *et al.* 1993). The high degree of uniformity in the evaporation rate leads to a similar uniformity in the final film thickness. This uniformity, as mentioned in the Introduction (Section 14.1), is responsible for the commercial usefulness of spin coating.

Nonuniformities of the film thickness can occur very near the edge of the spinning wafer, because of higher evaporation rates caused by the combination of both radial and axial flow (Bornside *et al.* 1993). The result is a thick edge bead confined to a few unused millimeters at the wafer's edge, which is of no practical consequence.

The uniformity of the evaporation rate across the substrate was intuited years ago by Meyerhofer (1978). He modified the analysis of Emslie, Bonner and Peck by including in the mass balance equation (14.4) a uniform solvent evaporation rate E ; thus

$$\frac{\partial H}{\partial t} = -\frac{2\rho\Omega^2}{3\mu} H^3 - E \quad (14.7)$$

where E is in units of solvent volume evaporated per unit area per unit time. If the film is thin enough that the solvent concentration remains uniform throughout the depth of the film, a mass balance equation for the nonvolatile solute can be written:

$$\frac{\partial}{\partial t}(CH) = -C \frac{1}{R} \frac{\partial(RQ)}{\partial R} = -C \frac{2\Omega^2 H^3}{3\mu(C)} \quad (14.8)$$

where C is the volume fraction of solute in the film, and equation (14.4) has been used.

Equations (14.7) and (14.8) can be solved for a specified initial condition to obtain $C(t)$ and $H(t)$, if the dependencies of the viscosity μ and evaporation rate E on concentration C are known. Meyerhofer measured the dependence $\mu(C)$ and fit this dependence to a simple power law; and he took E to be constant in time as well as position. Then, integrating equations (14.7) and (14.8), Meyerhofer found, not surprisingly, that for typical spinning speeds, the final film thickness H_f is nearly independent of the initial film thickness as long as the initial thickness is at least as large as 100 μm or so. The numerical solution confirmed that early in spin coating, when the film is thick, flow dominates the thinning, but later, when the film has become much thinner, flow is slow, and thinning is due mainly to evaporation.

Meyerhofer showed that if there is an abrupt transition from thinning by flow only, to thinning by evaporation only, then the final film thickness can be estimated analytically. The transition point is defined to be the point at which the rate of solvent loss by flow equals the rate of loss by evaporation; that is

$$\frac{(1-C)2\Omega^2\rho H_0^3}{3\mu} = E \quad (14.9)$$

where H_0 is the film thickness at the transition between flow-dominated and evaporation-dominated thinning. This gives for the final film thickness:

$$H_f = C_0 H_0 = C_0 \left(\frac{3\mu_0 E}{2(1-C_0)\rho\Omega^2} \right)^{1/3} \quad (14.10)$$

where C_0 is the initial concentration of solute,

and $\mu_0 \equiv \mu(C_0)$. The concentration is assumed to depart from C_0 only after the transition to evaporation-dominated thinning.

If the air flow remains laminar, and if the vapor-phase resistance to mass transfer dominates the liquid-phase resistance, then for an infinite disk, the von Kármán boundary-layer flow implies that the rate of evaporation E depends on the spinning speed Ω as

$$E = k\Omega^{1/2} \quad (14.11)$$

where k is a constant determined by the coating solvent; an equation for it is given shortly. With equation (14.11), equation (14.10) becomes (Meyerhofer 1978):

$$H_f = \left(\frac{3}{2} \right)^{1/3} k^{1/3} C_0 (1 - C_0)^{-1/3} \rho^{-1/3} \mu_0^{1/3} \Omega^{-1/2} \quad (14.12)$$

The proportionality $H_f \propto \Omega^{-1/2}$ predicted by equation (14.12) agrees with Meyerhofer's data, and data obtained in other spin-coating studies with polymer resist solutions (Sukanek 1985). Also agreeing with experiments is Meyerhofer's prediction that the time to dry the film is proportional to Ω^{-1} . The measured concentration dependence of H_f also agrees with that predicted by equation (14.10), if the measured concentration dependence of the viscosity is used, and the constant k is obtained by a fit to one of the data points.

Bornside, Macosko and Scriven (1991), see also Lawrence (1988, 1990), recently showed that k can be computed *a priori*; for vapor-phase-limited mass transfer, k is given by

$$k = \left(\frac{cD_G}{v_G^{1/2} \rho} \right) \left(\frac{p^* M}{RT} \right) \quad (14.13)$$

where p^* is the vapor pressure of the pure solvent, M is its molecular weight, D_G is its diffusivity in the vapor phase, and $c \approx 0.55$ is a prefactor with a weak dependence on Sc . Equation (14.13) yields a value of $k \approx 10^{-5} \text{ cm s}^{-1/2}$ for typical spin-coating solvents. Using equation (14.13), Bornside, Macosko and Scriven were able to predict *a priori* the film thicknesses measured by Flack *et*

al. (1984) for PMMA polymer films spun from chlorobenzene solvent.

The assumptions underlying Meyerhofer's simple prediction, equation (14.12), then, are that there is an abrupt transition from flow with negligible evaporation, to evaporation with negligible flow, and that this occurs when the rate of thinning by flow is equal to the rate of thinning by evaporation; and that the rate of evaporation is controlled by vapor phase convective mass transport, which, in turn, is set by a boundary-layer mass transport rate proportional to $\Omega^{1/2}$. The qualitative correctness of these idealizations, and hence of equation (14.12), for spin coating of resist solutions, has been supported not only by experiments, but also by analyses more complete than that of Meyerhofer. Ohara, Matsumoto and Ohashi (1989), in particular, start from the general two-dimensional equations for axisymmetric fluid, mass and energy transport in the laminar liquid and gas phases, and reduce these to one-dimensional equations by using the von Kármán similarity forms for the radial dependencies. They then integrate the one-dimensional equations numerically to obtain the time-dependent concentration and velocity fields in the liquid and gas phases. Figure 14.4 shows the numerical predictions obtained by Ohara, Matsumoto and Ohashi (1989) for an experiment of Flack *et al.*, in which a 9% solution of PMMA in chlorobenzene was spin-coated at 2000 rpm. Figure 14.4b shows that at early times, convective thinning dominates, while the rate of evaporative thinning is roughly constant, and much slower than convective thinning. Roughly 10 s after the start of spin coating, the rate of convective thinning quickly drops below the rate of evaporative thinning, and only after this occurs does the solute concentration rise greatly above its initial value. Thus, these simulations support Meyerhofer's assumption that the transition from flow-dominated to evaporation-dominated transport is abrupt. Note from Fig. 14.4c that the solute concentration remains roughly uniform throughout the liquid film, as assumed by Meyerhofer. Ohara, Matsumoto and Ohashi also found for their numerical solution the same

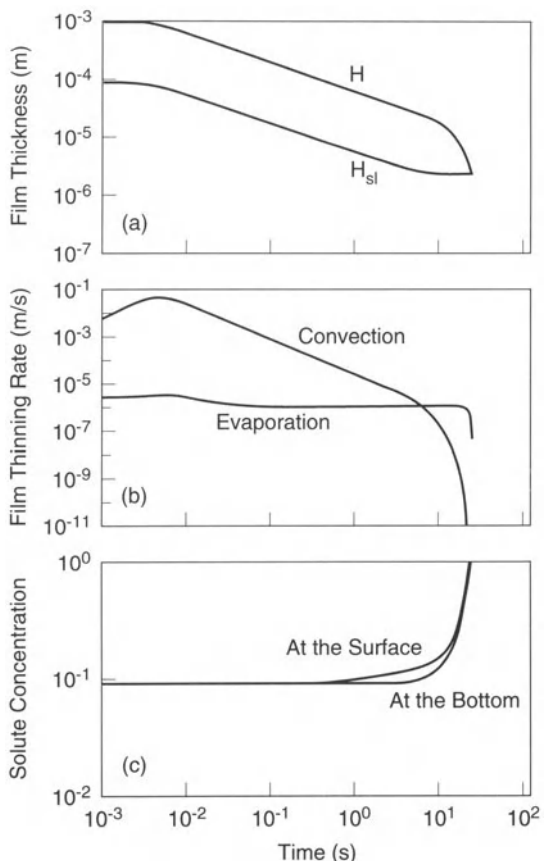


Figure 14.4 Simulated spin coating of a solution of PMMA in chlorobenzene onto an infinite disk spinning at 2000 rpm. (a) The film thickness H and the solute portion of that thickness H_{sl} . (b) The contributions of convection and evaporation to the overall rate of thinning. (c) The solute concentration at the free surface of the liquid and at the bottom of the liquid film, next to the substrate (from Ohara, Matsumoto and Ohashi (1989)).

scaling, $H_f \propto \Omega^{-1/2}$, obtained in Meyerhofer's simple analysis. The numerical simulation therefore supports the assumptions of Meyerhofer's simplified analysis in almost every respect. The only significant failure of the simple theory is a failure that is shared by the numerical solution of Ohara, Matsumoto and Ohashi, namely that when the initial polymer concentration is low, 2% or so, the theory does not predict an experimentally

observed deviation from the scaling $h_f \propto \Omega^{-1/2}$ (Meyerhofer 1978; Ohara, Matsumoto and Ohashi 1989).

Other analyses of spin coating of resist solutions have been presented; in rigor and complexity these are intermediate between Meyerhofer's simple analysis and the numerical solution of Ohara, Matsumoto and Ohashi. Notable are the analyses of Sukanek (1985) and of Lawrence (1988, 1990). These, like the study of Ohara, Matsumoto and Ohashi, show that typically the rate of thinning by flow drops quickly during the early stages of spin coating so that the cross-over to evaporation-dominated thinning is abrupt, and when it occurs, the solute concentration is still near its initial value. As the volume of solute that is finally trapped on the substrate is largely determined at this cross-over point, more complex effects that might occur later in spin coating have little or no effect on the final film thickness.

When spinning is terminated before the cross-over, and the film is allowed to dry in the absence of spinning, both Lawrence and Zhou (1991) and Yonkoski and Soane (1992) have found theoretically that equation (14.6) still holds for the final film thickness, although with $b > 0.5$. Yonkoski and Soane conducted experiments with a polyimide photoresist to verify this predicted result. They found best fits to equation (14.6) for $b = 0.5$ when the spinning time was 200 seconds, and $b = 1$ when the spinning time was reduced to 30 s. Skrobis, Denton and Skrobis (1990), in spin-coating experiments with a thermosetting isoimide oligomer, found that the exponent b depended on the coating-solution solvent when the spinning time was held to 15 s. They found $b = 0.57$ for the solvent of highest volatility, and $b = 0.97$ for the one with lowest volatility. For the latter, spinning was terminated well before the film had become thin enough for the cross-over to evaporation-dominated thinning to occur. These findings suggest an explanation for the Daughton and Givens' exponent of 0.8 mentioned earlier, as in their experiments spinning was terminated after only 20 s. A larger spinning time might well have yielded an exponent closer to 0.5, for their

solutions of polyamic acid. Thus, if spinning is continued until evaporation becomes the dominant cause of thinning, Meyerhofer's simple analysis is typically qualitatively, and frequently quantitatively, correct for spin coating of polymer resist solutions.

For the spin coating of colloidal suspensions, Meyerhofer's analysis is not as satisfactory. Rehg and Higgins (1992) examined the spin coating of colloidal suspensions with a model essentially identical to that of Ohara, Matsumoto and Ohashi (1989). This numerical study shows that for colloidal suspensions Meyerhofer's analysis has two significant failings; namely, it under-predicts the coated film thickness, and it does not capture the correct concentration dependence of the film thickness. These departures are especially evident for colloidal suspensions with solids loading near the solidification point. Near this point, the viscosity is strongly concentration dependent, and even the small increase in solids concentration that occurs early during spin coating changes the solution viscosity enough to invalidate Meyerhofer's assumption of a constant viscosity during the convection-dominated stage of spin coating. As a result of this early increase in film viscosity, the convective thinning decreases more rapidly, and becomes small compared with evaporation sooner than predicted by Meyerhofer's analysis; the result is a film that is thicker than Meyerhofer's analysis would predict. Nevertheless, the numerical analysis does support Meyerhofer's assumption that thinning abruptly changes from being convection to being evaporation dominated and the oft observed scaling $H_f \propto \Omega^{-1/2}$ is still obtained. In fact, equation (14.12) should still hold if one could somehow determine the solution viscosity μ at the transition between convection and evaporation dominated thinning, and use this to replace the initial solution viscosity μ_0 .

When the viscosity of the coating solution is both shear thinning and sensitive to small changes in concentration, the coated film will be susceptible to nonuniformities. This is shown theoretically by Sukanek (1991) and Britten and Thomas (1992), who extended Sukanek's Newtonian model

(Sukane 1985) to the cases of shear-thinning polymer solutions and shear-thinning colloidal suspensions, respectively. Britten and Thomas (1992) also demonstrated this phenomenon in spin-coating experiments with colloidal alumina/water suspensions. Their experimental results, shown in Fig. 14.5, are in qualitative agreement with the theory; the film thickness decreases from the substrate center to the edge. The observed quantitative disparity is due to some uncertainty in the shear-rate-dependent solution viscosity. Despite this disparity, the qualitative agreement supports the inference drawn in Section 14.2.1 that nonuniformities in film thickness occur when the cross-over from non-Newtonian to Newtonian flow occurs too late to restore uniformity to the film before evaporation renders the film immobile. (As mentioned in Section 14.2.1, a cross-over to Newtonian flow occurs when the film is thin enough that the shear rate drops into a regime of Newtonian behavior).

For polymer solutions, the absence of experimental data showing nonuniformities induced by shear thinning is consistent with our earlier discussion. The analysis of Ohara, Matsumoto and Ohashi (1989) shows that the solvent

concentration in the film decreases only slightly during the stage when convective thinning is important (see Fig. 14.4). Thus, it is likely that a shear-thinning film will have enough time to become uniform before the flow stops (see Fig. 14.3), a conclusion supported by the universal experience of practitioners that spin-coated polymer films are uniform. Indeed, Lawrence and Zhou (1991), in an extension of Lawrence's earlier work (1988, 1990) on shear thinning systems, conclude that nonuniformities will be present only for large Deborah numbers De , where $De \equiv \Omega^2 \rho H_0 R_s / \mu_0 \dot{\gamma}_c$, and R_s is the substrate radius and $\dot{\gamma}_c$ is the shear rate above which shear thinning is important. For large Deborah numbers, $De \gg 1$, shear thinning will persist even at very low shear rates and the film may not become Newtonian before convective thinning becomes unimportant.

As non-Newtonian effects are generally not important, unless the coating solution is close in concentration to a gel or solidification point, the equation for film thickness, equation (14.12), should be adequate in many commercial settings to predict the spinning speed required to obtain a desired film thickness. This is rarely done, however. In practice, it is usually easier to spin-coat resist solutions at various spinning speeds and measure the resulting film thicknesses to obtain a correlation between film thickness and spinning speed for a given spin-coating solution, as discussed at the beginning of this section.

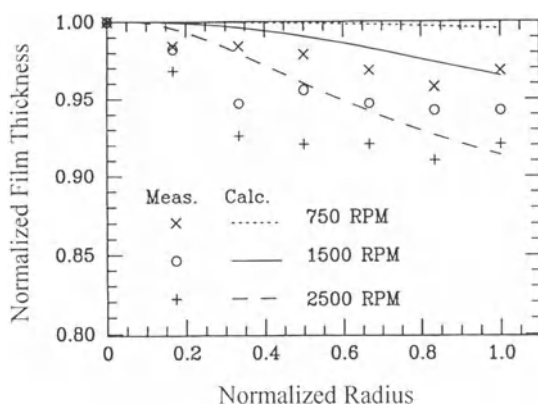


Figure 14.5 Calculated and measured film thickness profiles, normalized with the film thickness at the substrate center, for coatings deposited from colloidal alumina/water suspensions (from Britten and Thomas (1992)).

14.2.3 STABILITY OF SPIN COATING

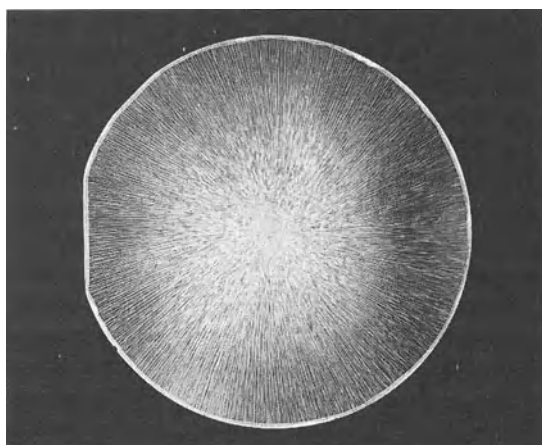
Spin coating is, by and large, a rather stable coating method, as evidenced by the reliably uniform films that it produces. However, as most practitioners of spin coating have experienced, surface features are occasionally exhibited in the spin-coated films that render the coatings unacceptable for their intended purpose. Three principal features characterizing these unacceptable films are cloudiness (Lai 1979), orange peel (Lai 1979), and radial striations (Elliott and Hockey 1979). Cloudy films, characterized by an opaque ap-

pearance, seem to be produced when the solvent and polymer are only partially miscible; when solvent evaporation drives the polymer concentration up beyond its solubility limit in the solvent, the polymer precipitates. Selection of a solvent/polymer system that does not phase separate is an obvious remedy for this condition. Lai suggests that, even with this remedy, water contamination of the coating solution can lead to phase separation, especially if the solvent has a higher volatility than water. Preferential evaporation of the solvent will concentrate the residual water, thereby increasing the likelihood of phase separation. Therefore, selection of a solvent in which water is insoluble is also a valuable strategy for avoiding cloudy films.

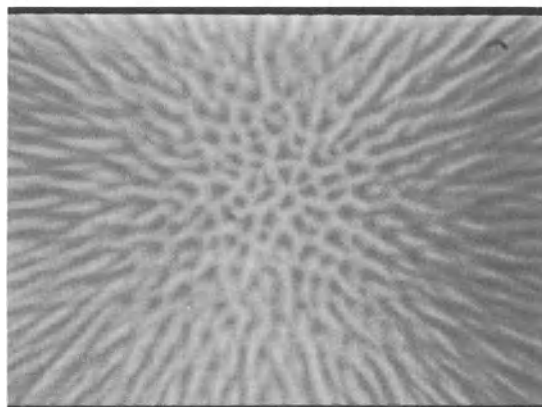
Both orange peel and radial striations are less well understood. To date, formal stability analyses have not been undertaken that clearly identify the mechanisms that induce these surface features. Nevertheless, experimental studies have identified means of avoiding them. Orange peel, which is characterized by randomly positioned surface dimples, has been examined by Lai (1979) and Spangler, Torkelson and Royal (1990) in spin coating. (Orange peel also occurs in other coating flows, as discussed in Chapter 6). Both of the above experimental studies find that the incidence of orange peel correlates with solvent volatility; nonuniform spin coated films are obtained when the solvent has a low boiling point, and uniform films are obtained for high-boiling solvents. Spangler, Torkelson and Royal also found that uniform films can be spin coated if the coating solution is viscous enough, even for highly volatile solvents. In practice, photoresist producers use relatively high boiling solvents in their formulations, such as xylene ($T_b = 140^\circ\text{C}$) and orange peel is rarely observed nowadays in commercial spin coating. It is noteworthy that water is only sparingly soluble in xylene and that the vapor pressure of water is nearly four times that of xylene at room temperature; thus xylene-containing coating solutions can also be expected to avoid precipitation-induced cloudiness.

Radial striations have been observed in both spin-coated photoresists (Elliott and Hockey

1979; Leers 1981; Frasch and Saremski 1982), and colloidal films (Rehg 1992; Rehg and Higgins 1992). Figure 14.6 shows a photograph of a colloidal coating exhibiting radial striations. At the substrate center, where the magnitude of the bulk flow is small, the striations give way to polygonal cells. Daniels *et al.* (1986), Rehg (1992), and Rehg and Higgins (1992) all postulate that the striations and polygonal cells are a consequence of a Marangoni flow, the secondary flow driven by temperature-induced surface-tension gradients that spontaneously develop in volatile thin films (see Chapters 2, 6 and 13). The structures of both



(a)



(b)

Figure 14.6 Surface topography of a film spin coated from a colloidal silica/ethanol suspension. (a) Radial striations on a wafer, 6 cm in diameter. (b) Polygonal cells on an enlarged view of the substrate center (from Rehg (1992)).

the polygonal cells and the striations are consistent with those of other film flows that are susceptible to Marangoni convection. Quiescent films have long been known to develop polygonal convection cells (Pearson 1958), and films draining under gravity have been observed experimentally – and predicted theoretically – to develop longitudinal roll cells (Ludviksson and Lightfoot 1968), due to the Marangoni instability. In spin coating, surface-tension gradients can be induced either by temperature gradients (due to evaporative cooling) or by concentration gradients.

Rehg (1992) demonstrated experimentally that the spin coating conditions that give rise to striations are consistent with Marangoni convection. In particular, he found that films spin coated from both high- and low-viscosity polymethylmethacrylate/1,2-dichloroethane coating solutions are free of striations; Figure 14.7 shows that only solutions of intermediate viscosity show the striations. The lack of striations for high-viscosity solutions is readily explained: when the coating solution viscosity is large, Marangoni convection is suppressed by large viscous forces. Recall that the Marangoni number, defined as $Ma \equiv (\partial\sigma/\partial T)H\Delta T/(\mu\alpha)$, is a measure of the

ratio of surface-tension-gradient forces to viscous stabilizing forces; see Chapter 6. Here α is the thermal diffusivity, and ΔT is the temperature difference between the top and the bottom of the film.

For low-viscosity films, the Marangoni number is initially large, so the absence of striations in this case (see Fig. 14.7) is less obvious. Rehg (1992) and Rehg and Higgins (1992) argue, however, that films spin coated from low-viscosity coating solutions are stabilized by the dynamic thinning process; that is, even if a film is initially susceptible to Marangoni convection, the striations do not grow to appreciable magnitude before the flow is restabilized by viscous forces that become increasingly important as the film rapidly thins. Thus, while μ is small, the film thickness H quickly becomes small, and the Marangoni number is therefore small as well. An analogous phenomenon, the formation and suppression of inertial circumferential waves, has been predicted by Reisfeld, Bankoff and Davis (1991a). Using a linear stability analysis, they show that spin-coated films are unstable to formation of these waves during spin up; but as the film thins, the stabilizing effect of viscosity intervenes, and the disturbance decays. (To the authors' knowledge, in experimental spin-coated films, circumferential waves have never been observed. For further discussion, see Reisfeld, Bankoff and Davis (1991a,b).)

Other data have been reported that support Rehg's (1992) and Rehg and Higgins' (1992) assertion. Rehg (1992) performed spin coating experiments with a colloidal silica/ethanol coating solution known to produce polygonal convection cells in quiescent films and striations in films spin coated at 2000 rpm. Films free of striations were obtained when the substrate rotation rate was increased to 3500 rpm. When the substrate acceleration rate was reduced from 10 krpm/s to 1 krpm/s and the rotation rate was maintained at 3500 rpm, striations were again evident in the coated film. Slow rotation and slow acceleration are known to reduce the rate of film thinning (Rehg and Higgins 1988), thereby prolonging the spinning time before the stabilizing effect of viscosity becomes important and dampens Maran-

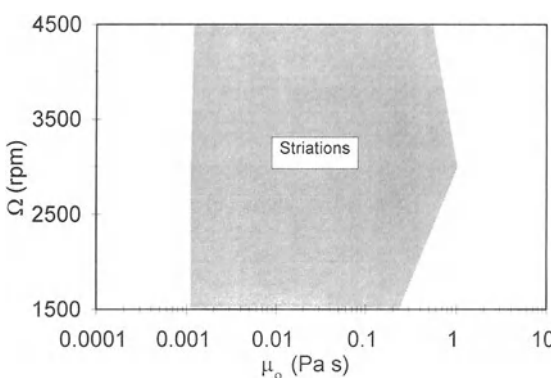


Figure 14.7 ‘Operability diagram’ showing conditions where films free of striations can be spin coated from polymethylmethacrylate/1,2-dichloroethane solutions whose viscosities μ_0 were controlled by varying the polymer concentration. The unshaded region represents conditions yielding striation-free coatings (adapted from Rehg (1992)).

goni flow. High spinning speeds (Leers 1981; Daniels *et al.* 1986) and high acceleration rates (Frasch and Saremski 1982) are both found to attenuate striations in experiments with photoresists although, for the particular solutions used by Leers and Daniels *et al.*, the striations could not be completely eliminated. Both Elliott and Hockey (1979) and Daniels *et al.* (1986) report that striations can be suppressed by saturating the ambient environment with the spin-coating solvent. This reduces the rate of solvent evaporation and therefore decreases both the temperature and concentration gradients that can induce Marangoni convection. Rehg and Higgins (1992) used their model to reproduce qualitatively these experiments and found, without exception, that the instantaneous Marangoni number is reduced when the spin coating conditions are changed to those less likely to yield striations; see Fig. 14.8.

While these results give insight into the mechanism that induces striations, they do not provide practical means of avoiding them.

Measures that lend themselves to rapid thinning of the film (low viscosity, rapid acceleration and rapid rotation rate) are not universal in their ability to eliminate the instability. When large-viscosity coating solutions are used, only thick films are attainable. Health and flammability issues make it undesirable to saturate the atmosphere with solvent, unless shields (Chiba *et al.* 1982), air barriers (Peugh and Ward 1984), or other means of gas handling are used; these, of course, add complication and expense. Surfactants have been shown to suppress striations (Daniel *et al.* 1986; Rehg 1992), as shown in Fig. 14.9, but their use may not be tolerable in all applications (i.e., high energy laser systems). Fortunately, practitioners have found that a more robust solution than these is simply to use solvents with low volatility. Such solvents generate less severe temperature and concentration gradients that can drive the Marangoni secondary flow. In photoresist systems, at least, striations are rarely observed nowadays.

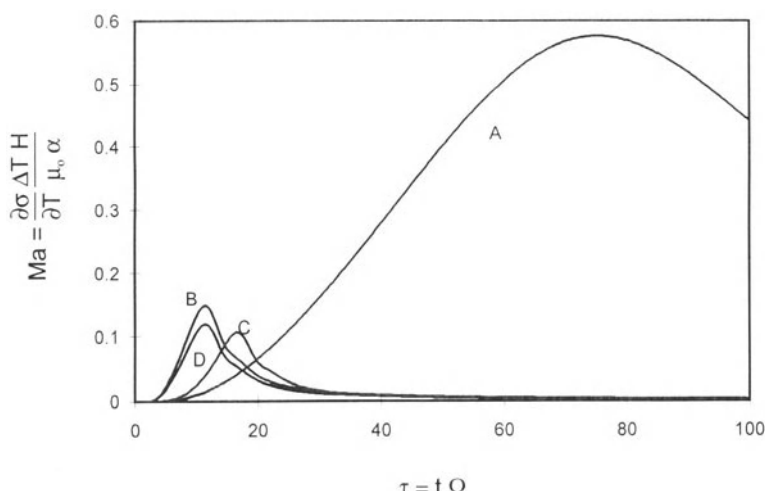


Figure 14.8 The calculated instantaneous Marangoni number versus dimensionless spinning time. The coating solution is a suspension of colloidal hard spheres in ethanol. Spinning conditions: (A) $\Omega = 5000$ rpm, 2000 rpm/s substrate acceleration, 0% saturation of the atmosphere with ethanol; (B) $\Omega = 5000$ rpm, impulsive substrate acceleration, 0% saturation of the atmosphere with ethanol; (C) $\Omega = 10\,000$ rpm, impulsive substrate acceleration, 0% saturation of the atmosphere with ethanol; (D) $\Omega = 5000$ rpm, impulsive substrate acceleration, 30% saturation of the atmosphere with ethanol (from Rehg (1992), and Rehg and Higgins (1992); (A), (B) and (D) reproduced with permission of the American Institute of Chemical Engineers, © 1992 AIChE. All rights reversed).

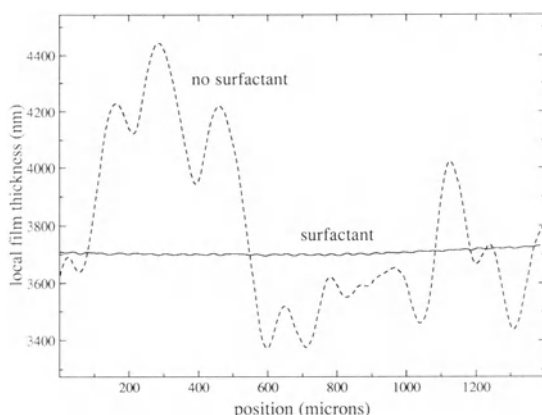


Figure 14.9 Film profiles with and without surfactant in a 14 wt.% polymethylmethacrylate/1,2-dichloroethane solution spin coated at 2000 rpm. The coating solution that produced the striation-free film contained 0.14 vol.% FC-431 surfactant. The film profiles were measured by profilometry (3M Corporation; from Rehg (1992)).

Another instability, usually a fairly benign one, occurs when the vapor phase Reynolds number $Re \equiv R^2\Omega/v_G$ becomes high enough, $Re \approx 10^5$, that laminar air flow is no longer maintained (Wahal *et al.* 1993, and references therein). For a large disk spinning at high speed Ω , there will then be a critical radius R_2 such that for $R > R_2$, the flow is turbulent. Laminar flow is found only when $R < R_1$. For intermediate R , $R_1 < R < R_2$, laminar flow is disrupted by three-dimensional spiral vortices known as Ekman spirals. Experiments have shown that the Reynolds numbers corresponding to R_2 and R_1 are $Re_2 \approx 3 \times 10^5$ and $Re_1 \approx 10^5$.

In a spin-coating apparatus using smoke trails for visualization, Wahal *et al.* (1993) observed Ekman spirals, with negative winding direction; i.e., opposite direction to those reported by others. For these spirals of negative winding, Wahal *et al.* found $Re_1 \approx 0.2 \times 10^5$. Linear stability analyses predict that spirals of either winding direction can occur, but the negative ones should occur at the lowest Reynolds number, namely at $Re \approx 0.037 \times 10^5$. In their experiments with 6-inch diameter substrates, Wahal *et al.* find the

uniformity of the spin coated film to be only slightly degraded by the presence of these Ekman spirals; the coating thickness only varied by 0.2%.

When larger substrates are coated, such as in the spin coating of magnetic media, film uniformity is degraded by the gas-phase turbulence; the spin coated film exhibits 'spokes' that prevent the magnetic head from traveling as smoothly over the medium as is desirable (Scheffel and Richter 1978; Hagan, Maloy and Wilke 1986). Scheffel and Richter discovered that the inertial instability is suppressed if a co-rotating, parallel plate, called an air barrier, is positioned 2 to 20 mm above the substrate to be coated. With this method, the gas flow between the air barrier and the substrate is then largely just solid-body rotation. Hagan, Maloy and Wilke found that a stationary barrier, combined with the use of helium as the ambient gas adequately suppresses the 'spoke' instability. Because the kinematic viscosity of helium is nearly eight times that of air, the Reynold's number is approximately eight times smaller, and the critical radius beyond which the gas flow is turbulent is correspondingly larger, when helium is substituted for air.

14.3 SPIN COATING OVER UNEVEN SUBSTRATES

As discussed in Section 14.2, spin coating tends to produce films of uniform thickness; hence on flat substrates the films are flat. On an uneven substrate, however, the surface of the film tends not to be flat, but to conform to the topography of the underlying substrate; see Fig. 14.10. Unevenness in the film-air surface can have deleterious consequences in further lithographic processing steps. In particular, as the sizes of microelectronic devices are decreased to submicron dimensions, sharper focusing is required of the radiation that exposes the resist film; and this cannot always be obtained over all areas of an uneven surface. Thus, it is desirable to level, or 'planarize' the polymer film, either during, or after, spin coating (Rothman 1980; Burggraf 1986; Stillwagon, Larson and Taylor 1987).

Leveling is also required in the etch-back

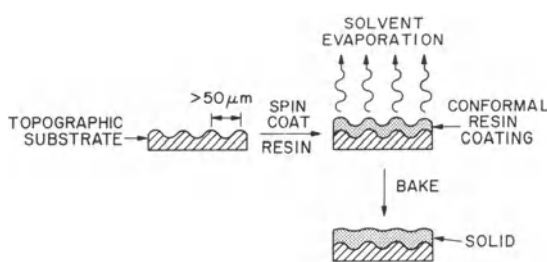


Figure 14.10 Stages of spin coating over uneven substrates. Thin conformal coatings are produced over features that are wider than about 50 μm ; these coatings can be leveled to some extent during the baking step, which melts the polymer film, allowing reflow to occur (from Stillwagon and Larson (1990)).

method (Sato *et al.* 1973; Adams and Capio 1981) for producing inter-layer metal contacts. In this scheme, metal pillars are formed on top of a metal layer. Onto this uneven substrate, a conformal dielectric layer is spin coated. A resist overlayer is then added, which is planarized. The resist and dielectric are then etched by a process that removes both at the same rate, eventually exposing the metal pillars, which then jut out from the remaining dielectric layer. These are used to form contacts to a second metal layer, which, apart from the contacts, is insulated from the first layer by the dielectric. In this etch-back process, both a conformal and a planarized layer must be deposited; to achieve both types of coverage over the same substrate (i.e., a conformal layer in one step of the process and a planarized one in another step), the factors that control the leveling process must be understood and controlled.

In a series of spin-coating experiments, Rothman (1980) and others (Adams and Capio 1981; White 1985a,b; Bassous *et al.* 1983; Wilson and Piacente 1986; Stillwagon and Larson 1988, 1990; Peurrung and Graves 1991) have established the conditions required to maximize planarization. These experiments, reviewed by Stillwagon (1987), show that fine features are more readily planarized; films over features smaller than 10 μm are typically planar, while those over features wider than 50 μm are often quite conformal (Rothman 1980;

Adams and Capio 1981; White 1985a). However, the degree of planarization depends not only on the width and shape of the feature, but also on the surrounding topography; closely spaced features are planarized better than isolated ones, other things being equal (Rothman 1980, White 1985b; Stillwagon and Larson 1988). White (1985b) found that planarization and the film profiles over line features depend on the orientation of those lines on the wafer, and on their distance from the center of rotation. Planarization also depends strongly on the properties of the resist solutions; in particular, leveling is enhanced by increasing the concentration of polymer in the resist, and by decreasing the polymer molecular weight (Rothman 1980; Bassous *et al.* 1983; LaVergne and Hofer 1985; Stillwagon and Larson 1992). Resist solutions whose viscosity increases rapidly as solvent evaporates, planarize poorly. Thicker films planarize better. However, for a given thickness of resist, better planarization is achieved if the resist is applied in several layers, rather than just one (Bassous *et al.* 1983).

White (1985a,b) has developed an empirical method for estimating film profiles and planarization of resist films over complex topologies. He measures the degree of planarization of a given resist over a series of isolated features of varying widths under given spinning conditions, and thus obtains an empirical correlation between film thickness and feature width. Using a Fourier transform, he then represents the uncoated surface topography by a two-dimensional series of sine and cosine functions. The coated surface topography is obtained by multiplying the coefficients of the sine and cosine functions in the series for the uncoated substrate by weighting parameters; these weighting factors are obtained from the measured correlation between film thickness and feature width. The weighting factors for long wavelength topographies ($> 50 \mu\text{m}$) are near unity, implying little planarization for these features, while for short wavelengths, the weighting factors are close to zero, implying nearly perfect planarization. In this way, White obtains reasonable predictions of the film profiles over complex two-dimensional topographies. This empirical

method needs to be supplemented, however, by a more fundamental approach to provide understanding of the role of resist fluid properties or processing conditions on planarization.

A more fundamental approach to planarization is taken in the lubrication analyses of Stillwagon and Larson (1988; 1990; 1992), of Brodkorb, Köhler and Ritzel (1989), and Sukanek (1989). These theories, which follow earlier work on the leveling of paints by Smith, Orchard and Rhind-Tutt (1961) and by Overdiep (1977), account for the influence of capillary forces on the film profile. The theories have several simplifying approximations in common, including the assumptions of uniform rate of solvent evaporation, film properties that are uniform throughout the film thickness, isothermal conditions, neglect of gravitational forces, and a shear-rate independent viscosity.

Most importantly, these analyses use the lubrication approximation (see Chapter 8), which is valid when $W/D \gtrsim 10$, where W is the width of the feature and D its depth. Under the lubrication approximation, the vertical component of velocity is taken to be negligible; and the profile of lateral velocity versus height is parabolic. While this approximation is expected to fail near the steep walls of sharply defined features, the wall regions are a small fraction of the total substrate area, and the lubrication approximation can provide a good estimate of the average resistance to flow experienced by a fluid particle.

The assumption that fluid properties (such as viscosity) are constant throughout the thickness of the film requires that the rate of polymer–solvent interdiffusion be fast enough compared with the rate of thinning of the film that the polymer concentration remains vertically uniform. Because of the thinness of the films, this assumption seems to be a good one, except late in spin coating when the polymer concentration becomes high enough that the polymer–solvent binary diffusion coefficient becomes small. At this point it is possible that a skin of concentrated polymer forms on the surface of the film, which blocks evaporation of the remaining solvent. Typically, at the conclusion of spin coating, a residual

solvent volume fraction of perhaps 10–20% remains in the film (Shaw, Frisch and Dill 1977). The residual solvent is driven off by a baking step after spin coating; the film shrinkage produced by solvent evaporation during the baking step can reduce the degree of planarization of the film (Schiltz, Abraham and Dechenaux 1987). The baking step can also melt the dried polymer and enhance planarization (Fig. 14.10), as will be discussed in more detail below.

If, as often assumed, the rate of evaporation remains uniform across the wafer, then thicker portions of the film, such as those over planarized features, will retain higher solvent concentrations than surrounding thinner portions. Although vertical diffusive equilibrium is maintained throughout most of the spin coating process because of the thinness of the film, the degree to which lateral diffusion occurs over a feature depends on the width of the feature. For features less than about 10 µm wide, lateral diffusion cannot be neglected. Bornside (1990) has simulated both lateral and vertical diffusion over fine grooves with $W \leq 5 \mu\text{m}$ during the late stages of spin coating when flow is assumed to have stopped. He used a two-dimensional finite-element analysis, and showed that lateral polymer diffusion can enhance planarization of small features by transporting polymer into the fluid over the grooves, so that less shrinkage occurs during the final, drying stage of spin coating. This analysis neglects capillary driven flow, which is reasonable when the film becomes very viscous. However, because the diffusivity decreases as the solution viscosity increases, it is not clear that there will be a regime in which lateral diffusion is important, while viscous flow is negligible.

As discussed above, lateral concentration gradients exist late in spin coating, at least for wide features. As a result, if the surface tension depends on concentration, surface tension gradients can develop; and this induces bulk flow by the Marangoni effect. Sukanek (1989) investigated theoretically the effect of surface tension gradients, using a hypothetical relationship between surface tension and polymer concentration, and found that the gradients of surface tension promote

conformal films and therefore reduce leveling. The magnitude of the effect is sensitive not only to geometric parameters such as film thickness and feature width, but also to the concentration dependence of the surface tension, however, and this dependence is often unknown. Overdiep (1977) found that Marangoni flow is important in the leveling of paint brushmarks. However, the characteristic unevenness of these brushmarks was around 4 mm, and the paint film thickness was around 100 μm ; these length scales are much larger than the corresponding length scales for spin coating. The effect of Marangoni flow on leveling during spin coating has yet to be assessed.

The above discussion indicates that many phenomena can in principle occur during spin coating over uneven substrates, including capillary flow, Marangoni flow, and vertical and lateral diffusion of polymer and solvent. Understanding the interplay of all of them would require numerical simulation of the coupled multidimensional transport equations for mass and momentum. However, experiments described below show that, in many cases, a satisfactory understanding of the leveling process in spin coating can be achieved using a simplified lubrication analysis that neglects Marangoni flow and lateral diffusion of polymer. The leveling that is simplest to understand is that which occurs during the baking step at the conclusion of spin coating, and we consider it first.

14.3.1 LEVELING AFTER SPINNING

When a spin-coated wafer is heated, the polymer layer can be liquified and can level itself by capillary flow; see Fig. 14.10. Some materials, such as polyimides, undergo reactions during the heating step that increase the viscosity of the film and limit the time available for leveling of the film (Stillwagon and Larson 1990). Even for films that are not subject to such reactions, leveling after spin coating is only feasible economically if the time t_L for capillarity to induce the required leveling is not too large. This leveling time t_L , which is set by a balance of capillary and viscous

forces, is given by

$$t_L \sim \frac{\mu W^4}{\sigma H_f^3} \quad (14.14)$$

where W is the width of the feature, μ is the film viscosity, H_f is a characteristic film thickness, and σ is the liquid–air surface tension of the film. Notice that the leveling time increases rapidly with increasing feature width W . Essentially the same equation was obtained years ago by Smith, Orchard and Rhind-Tutt (1961), and generalized by Overdiep (1977), for leveling of paint brushmarks over flat substrates.

Often a feature of an uneven substrate is much wider than it is deep; i.e., $W/D \gtrsim 10$, where D is the depth of the feature. When this is the case, a lubrication analysis accurately predicts the film thickness during the leveling process. From the lubrication analysis, one obtains a differential equation describing the evolution of the film thickness profile over an uneven substrate. For a two-dimensional groove or trench, we define the depth of the trench D , its width W , and the local heights of the substrate $S(X)$ and the film $\Phi(X)$; see Fig. 14.11. The local thickness of the film, $H(X)$, is $\Phi(X) - S(X)$. The lubrication analysis then gives (Stillwagon and Larson 1988; Brodkorb, Köhler and Ritzel 1989)

$$\frac{\partial H}{\partial t} = \frac{1}{3} \frac{\sigma}{\mu} \frac{\partial}{\partial X} \left[\left(\frac{\partial^3 H}{\partial X^3} + \frac{\partial^3 S}{\partial X^3} \right) H^3 \right] \quad (14.15)$$

where X is the coordinate in the plane of the substrate that is perpendicular to the trench.

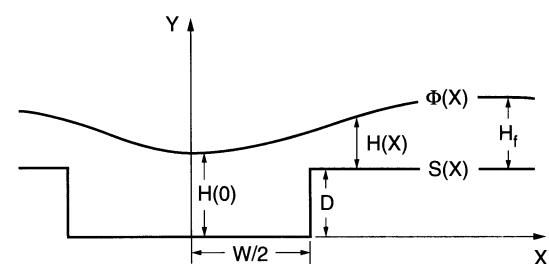


Figure 14.11 Sketch of a film profile over a trench-like feature (from Stillwagon and Larson (1990)).

When we make equation (14.15) dimensionless using $x \equiv X/H_f$, $h \equiv H/H_f$, $s \equiv S/H_f$, and $\phi \equiv \Phi/H_f$, where H_f is the initial uniform film thickness, we obtain

$$\frac{\partial h}{\partial T} = \frac{1}{3} \frac{\partial}{\partial x} \left[\left(\frac{\partial^3 h}{\partial x^3} + \frac{\partial^3 s}{\partial x^3} \right) h^3 \right] \quad (14.16)$$

Here T is the dimensionless time given by

$$T \equiv \frac{t \sigma H_f^3}{W^4 \mu} \quad (14.17)$$

For simplicity, we take the viscosity μ to be a constant. Figure 14.12 shows film profiles calculated from equation (14.16) for leveling over an isolated trench with steep walls represented by arctangent functions. In these calculations, the film is assumed to be initially uniformly thick; i.e., perfectly conforming to the underlying substrate. Notice in Fig. 14.12 that near the center of the trench at $x = 0$, the film initially

thins as fluid is drawn from the center toward the walls to reduce the large film curvature that initially exists near the walls. The thinning of the film near the center of the feature quickly comes to an end, however, and for $T \gtrsim 5 \times 10^{-3}$, the film thickens with time over the entire trench by drawing fluid in from the plateau regions that neighbor the trench.

We here define the degree of planarization P to be the film thickness in the center of the trench, normalized so that it is zero when the film is of uniform thickness (and hence conformal) and unity when the film is level. For an isolated feature, this definition is equivalent to

$$P \equiv \frac{H(0) - H(\infty)}{D} \quad (14.18)$$

where $H(0)$ is the film thickness in the center of the feature and $H(\infty)$ is the film thickness far from the isolated feature.

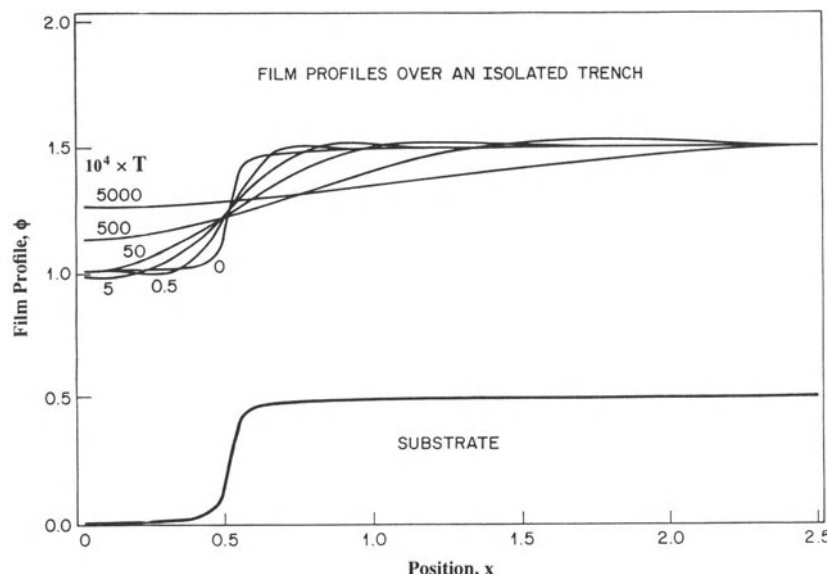


Figure 14.12 Predictions from the lubrication equation of the film profile over an isolated trench-like feature, at various dimensionless times T after cessation of spin coating of non-volatile liquids. At the end of spin coating, the film profile is assumed to be conformal. The width W of a typical feature is much greater than its depth D , and thus for the typical feature, the vertical scale of this figure is greatly expanded compared with the horizontal scale (from Stillwagon and Larson (1988)).

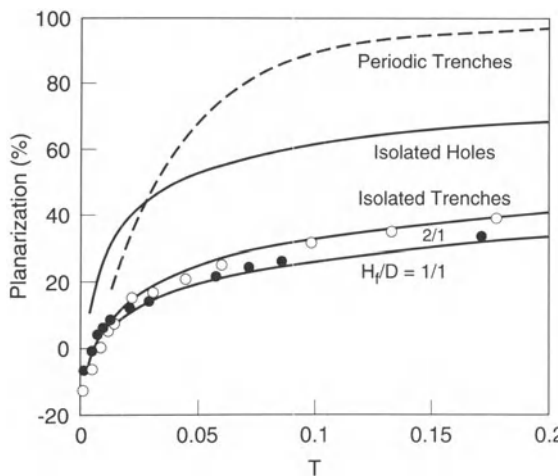


Figure 14.13 The degree of planarization P versus dimensionless time T after cessation of spinning of non-volatile liquids. Data are given for isolated trench-like features with H_f/D ratios of 1 and 2 (closed and open circles, respectively). Theoretical predictions from the lubrication equation (14.22) are given for isolated trenches with H_f/D of 1 and 2, and for periodic trenches and isolated round holes with $H_f/D = 2$ (from Stillwagon and Larson (1988)).

Figure 14.13 shows the predicted dependence of the degree of planarization on dimensionless time T after cessation of spin coating for isolated trenches, for isolated circular holes, and for periodic trenches separated from each other by plateaus of width equal to the trench width W . The ratio H_f/D of the film thickness to the feature depth has a small effect on the degree of planarization; this is shown in Fig. 14.13 for isolated trenches. Figure 14.13 also shows interferometry measurements of the degree of planarization versus dimensionless time for the leveling of non-volatile silicon liquids over isolated trenches. In these and similar experiments, the feature width W , the film thickness H_f , the fluid viscosity μ , and the feature depth D were all varied; Fig. 14.13 shows that the data agree well with the lubrication theory. At very small T , the degree of planarization is negative, because in the initial stages of leveling, fluid is drawn from the center of the feature toward the steep walls,

as discussed earlier. Not surprisingly, the planarization is greater for a hole than for a trench with width W equal to the hole's diameter. Also, planarization is more rapid for periodic trenches than for isolated ones, as the former can be leveled in part by the erosion of the neighboring plateaus. For periodic trenches, the definition of P in equation (14.18) is changed by replacing $H(\infty)$ by the film thickness at the center of a plateau. For photoresists, during the baking step the viscosity can change with time because of evaporation of residual solvent, or because of curing reactions. This effect is not included in Fig. 14.13, but is accounted for in the equations of Brodkorb, Köhler and Ritzel (1989).

The most important conclusions from these results are that the time required for a film of thickness H_f to level a feature of width W is proportional to W^4/H_f^3 . Hence, for typical films of thickness 2 μm or less, impractically long times can be required to level features with widths of 200 μm or more. And as the degree of planarization is negative at small T , attempts to level features that are too wide may, in the leveling time available, actually make the film less level. Thus, if planar films are desired, wide features should be avoided.

14.3.2 LEVELING DURING SPINNING

If the feature is narrow enough, the film over it can be partially leveled during spin coating; this might in some cases eliminate the need for leveling after spinning. Above, we stated that partial leveling could typically be expected for feature widths of about 50 μm or less. We can justify this estimate, and calculate film profiles during spin coating, by extending the lubrication analysis presented above to include the centrifugal forces generated by the rotation of the substrate, and to include the influence of the solvent evaporation that occurs during spinning.

For the moment, let us neglect the solvent evaporation, while accounting for centrifugal forces. Hwang and Ma (1989), Brodkorb, Köhler and Ritzel (1989), and Stillwagon and Larson (1990) derived lubrication equations for film flow over

a spinning substrate with axisymmetric unevenness. For a trench-like feature whose long dimension is perpendicular to the radial coordinate, and whose width W is much smaller than the distance R_0 of the trench center from the center of rotation of the wafer, the lubrication equation is

$$t_c \frac{\partial h}{\partial t} = -\frac{1}{3} \frac{\partial}{\partial x} \left[\omega^{-2} \left(\frac{\partial^3 h}{\partial x^3} + \frac{\partial^3 s}{\partial x^3} \right) h^3 + h^3 \right] \quad (14.19)$$

where

$$\omega^2 \equiv \frac{\rho \Omega^2 W^3 R_0}{\sigma H_f} \quad (14.20)$$

and

$$t_c \equiv \frac{W \mu}{H_f^2 \rho \Omega^2 R_0} \quad (14.21)$$

is the ‘centrifugal time’ required for the local film profile to come into local equilibrium with the centrifugal force. In equations (14.20) and (14.21), H_f is a characteristic film thickness that we define below. Except for the centrifugal term, equation (14.19) neglects inertia. From equation (14.5) of Emslie, Bonner and Peck (1958), we find that far from any topographic features the relative rate of thinning of the film, namely $-(dH/dt)/H$, is roughly given by $W/(R_0 t_c)$. Thus the rate, $1/t_c$, at which the film profile over a feature comes into local equilibrium with the centrifugal force is faster by a factor R_0/W than the rate at which the film thickness far from the feature changes by a significant percentage. Thus, except for large features that are close to the center of the spinning wafer, a local equilibrium approximation is warranted. As the film thins, the profile over the feature can then be assumed to adjust rapidly to changes in the film thickness far from the feature, so that at each instant, the film profile is in a state of local equilibrium between the surface tension and the centrifugal forces.

With this local equilibrium approximation, the time derivative in equation (14.19) can be dropped, and the characteristic film thickness H_f can be defined as the slowly changing film thickness far

from the feature. Then we integrate the right side of equation (14.19), and obtain

$$\text{constant} = \omega^{-2} \left(\frac{\partial^3 h}{\partial x^3} + \frac{\partial^3 s}{\partial x^3} \right) h^3 + h^3 \quad (14.22)$$

The profiles computed from equation (14.22) are in excellent agreement with experimental profiles; see Fig. 14.14. These experimental profiles were measured by spin coating non-volatile epoxy liquids that were cured during spinning by exposure to ultraviolet radiation; the height profiles of the hardened films were then determined by mechanical profilometry (Stillwagon and Larson 1990). Notice that the profiles are asymmetric; at high ω^2 there is a bump just upstream of the trench. The mechanism by which these asymmetries occur is discussed by Peurrung and Graves (1991).

The degree of planarization P was obtained from these profiles; Fig. 14.15 is a plot of P versus dimensionless spinning speed ω^2 , for $H_f/D = 2$. The relationship between P and ω^2 predicted by equation (14.22) is also plotted in Fig. 14.15; agreement with the measurements is good. In the experiments, a universal curve was obtained when data for varying Ω , W , R_0 , H_f and D were plotted against ω^2 with H_f/D held fixed. One of the dashed lines in Fig. 14.15 was obtained by linearizing equation (14.22) about a conformal profile; the other was obtained by linearizing about a level profile. These two linearizations are accurate, respectively, at large ω^2 and at small ω^2 . As in leveling after spinning, during spinning there is also a dependence of the degree of planarization on the ratio H_f/D (Stillwagon and Larson 1990). Figure 14.15 shows that some planarization is achieved at $\omega^2 = 10$, and almost complete planarization is obtained for $\omega^2 = 0.1$. In typical applications, $\Omega = 4000$ rpm, $\rho = 1$ g/cm³, $R_0 = 2.5$ cm, $\sigma = 30$ mN/m, and $H_f = 1$ μm. We then find from the definition of ω^2 in equation (14.20) that planarization improves significantly as W decreases from 50 μm to 10 μm; this agrees with the conclusions drawn from other experiments, mentioned earlier.

Because of the neglect of solvent evaporation,

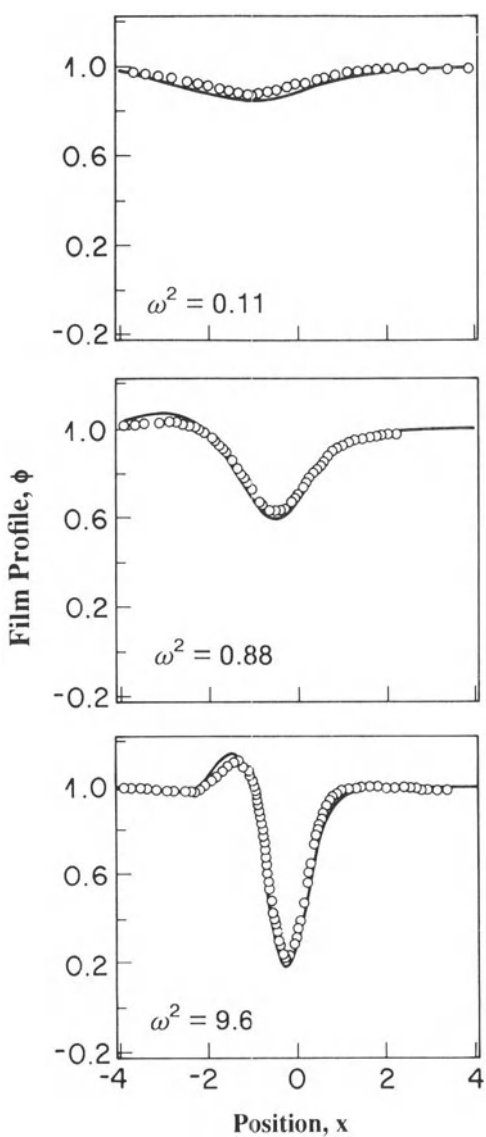


Figure 14.14 Film profiles over isolated trench-like features during spin coating of non-volatile liquids. The points are experimental data for epoxy liquids suddenly solidified during spin coating and the lines are the predictions of the lubrication equation (14.22). The vertical scale of this figure is greatly expanded compared with the horizontal (from Stillwagon and Larson (1990)).

Fig. 14.15 does not directly apply to most spin coating applications. Solvent evaporation increases the viscosity of the liquid film and slows its flow across the substrate. When the film viscosity becomes high enough, flow becomes negligible, and the thinning of the film occurs mainly by evaporation. However, earlier in spin coating, the film is mobile and we expect that its thickness profile will achieve local equilibrium over a feature, just as it does when evaporation is absent. Peurrung and Graves (1991) have measured film profiles during spin coating by using stroboscopic interferometry, and have shown that local equilibration does occur during the early stages of spin coating. Figure 14.16 shows the film profiles that they measured over long rectangular bumps during spin coating. Solving equation (14.22), these profiles can be predicted. Note that ω^2 changes with time, as ω^2 depends on H_f , and H_f decreases continuously during spinning. If ω^2 at each instant in time is computed from the instantaneous value of H_f , then from equation (14.22) the film profile at that instant can be accurately computed. Thus equation (14.22) holds not only for non-volatile fluids, but also for volatile liquids early in spin coating.

A two-dimensional version of equation (14.22) for features of arbitrary two-dimensional shape has been presented recently by Peurrung and Graves (1993). They solved the two-dimensional equation by a finite-element method for features such as the square bump shown in Fig. 14.17, and obtained iso-thickness profiles during spinning that have the same shapes as those seen in their experiments. Note in Fig. 14.17 the peculiarly shaped 'wake' in the film profile downstream of the square bump; the predicted and measured wake profiles are similar, showing that the two-dimensional lubrication theory is valid.

During spin coating, so much solvent eventually evaporates that the film becomes very viscous, and its flow rate becomes so low that it thins mainly by evaporation. When this point is reached, the film profile can no longer equilibrate over the feature, and equation (14.22), and its two-dimensional analog, no longer hold. Accurate analysis of leveling during the final stages of spin

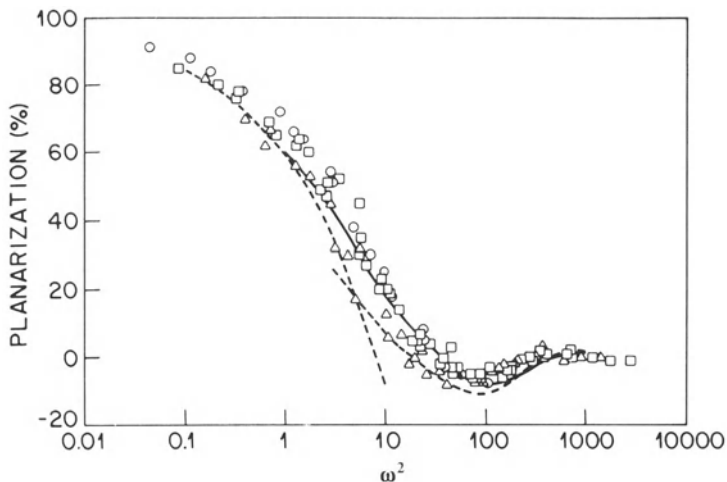


Figure 14.15 Plot of the degree planarization versus dimensionless spinning speed ω^2 . The data points are for epoxy liquids hardened during spin coating with $H_f/D = 2$, and W , R_0 , H_f , D , and Ω all varied. For (\square), H_f and D are fixed; for (\triangle), Ω is fixed; and for (\circ), Ω , H_f , and D are fixed. The solid line is from the lubrication equation solved numerically, and the dashed lines are for linearizations of the lubrication equation, valid at large and small ω^2 (from Stillwagon and Larson (1990)).

coating therefore requires that evaporation and its effects on film viscosity be accounted for.

Brodkorb, Köhler and Ritzel (1989) and Stillwagon and Larson (1990; 1992) have developed methods of estimating the effects of solvent evaporation. Stillwagon and Larson, extending the ideas of Meyerhofer (1978) and LaVergne and Hofer (1985), assume that the film profile remains in local equilibrium until the polymer volume fraction C in the film reaches a value C_1 high enough that the film can be assumed to be immobile. At this point, fluid rearrangement over the feature is assumed to stop, and the film thereafter changes its local thickness only by evaporation. Thus, during the final evaporative stage, the film thickness merely shrinks because of the loss of solvent. Thicker portions of the film, such as those over narrow, leveled features, contain more solvent and hence shrink more than thinner parts of the film. Thus the leveling achieved earlier in the spin coating process is partially lost. As a result, if P_1 is the degree of planarization achieved over a feature at the moment the fluid becomes immobile, and if all

solvent is finally evaporated, the final degree of planarization P_2 over that feature is given by

$$P_2 = C_1 P_1 \quad (14.23)$$

where, as mentioned above, C_1 is the polymer volume fraction at the instant the film becomes immobile. Equation (14.23) neglects any effect of lateral diffusion of polymer during the final evaporation stage. As the film profile is assumed to remain in local equilibrium over the feature until the polymer concentration reaches C_1 , P_1 is given by the theory for non-volatile solvents. Thus P_1 is a function of ω_1^2 and H_1/D , where H_1 is the film thickness far from the feature when the polymer concentration reaches C_1 , and $\omega_1^2 \equiv \rho\Omega^2 W^3 R_0 / \sigma H_1$, is defined as in equation (14.20), except that H_f is replaced by H_1 .

Stillwagon and Larson (1992) estimated the concentration at which the film is effectively immobilized to be that at which the rate of thinning of the film by evaporation equals $1/t_c$, the rate of equilibration given by equation (14.21). The rate of evaporation has been estimated by Lawrence (1988, 1990) and by Ohara, Matsumoto

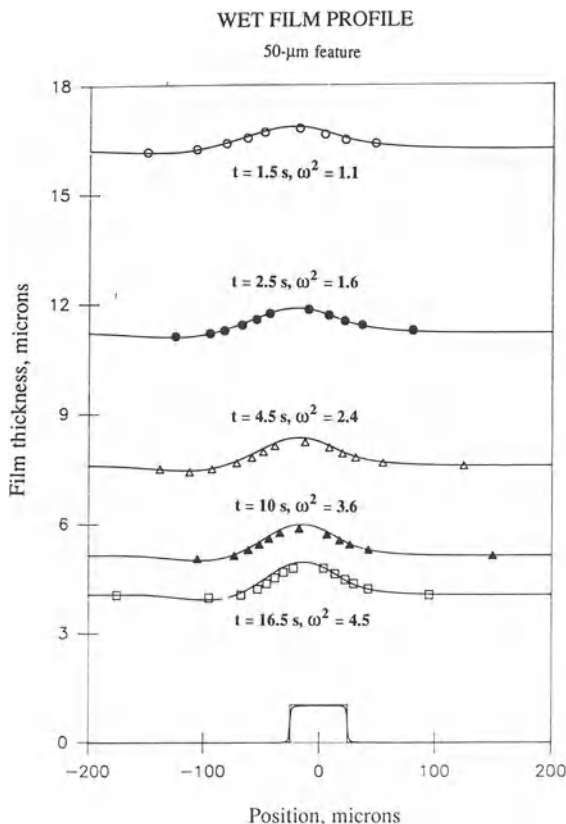


Figure 14.16 The data points are film profiles over a 50 μm rectangular bump measured by interferometry during spin coating of an evaporating polymer solution. The lines are the predictions of the lubrication equation, where ω^2 varies with the instantaneous film thickness H_f (from Peurrung and Graves 1991; reprinted by permission of the publisher, The Electrochemical Society, Inc.).

and Ohashi (1989), who assumed that the slow step in evaporation is the diffusive transport in the vapor phase; see Section 14.2.2. In this way, Larson and Stillwagon estimated C_1 and found that it depends on the initial polymer concentration C_0 , on the concentration–viscosity curve for the solution, and on the ratio W/R_0 . Thus

$$P_2 \approx C_1(C_0, M, W/R_0) \times P_1(\omega_1^2, H_1/D) \quad (14.24)$$

Here M is the molecular weight of the polymer; for a given type of polymer, M controls the

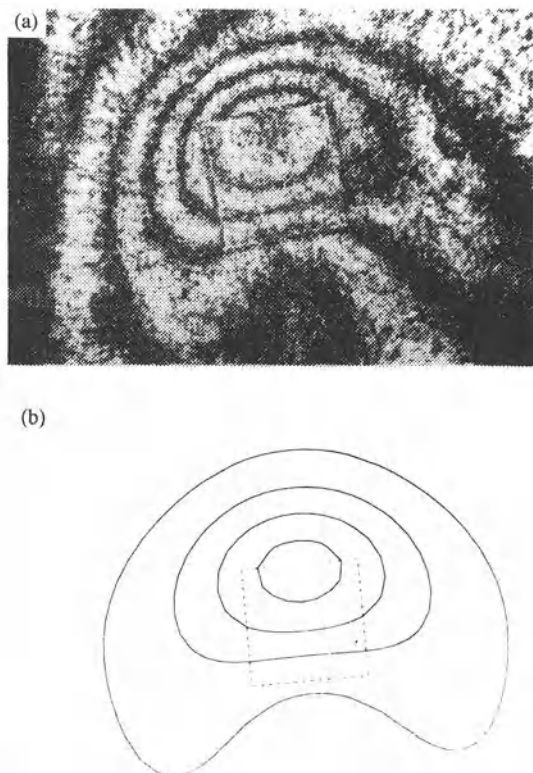


Figure 14.17 (a) Interferometric picture of a 100 μm square bump over which fluid is flowing during spin coating, with flow from top to bottom. The picture was taken 1 s after start-up of spin coating. (b) The dashed line shows the shape of the square ‘bump’, and the solid lines are the predicted iso-thickness contours of the film over the bump. The contours represent thickness variations of 0.157 μm , which also corresponds to the thickness variations between dark fringes on the left (from Peurrung and Graves 1993; reprinted with permission from *IEEE Trans. Semicond. Manuf.* 6(1): 72–76; © 1993 IEEE).

relationship between viscosity and polymer concentration. $P_1(\omega_1^2, H_1/D)$ is obtained by solving equation (14.22). A dependence of C_1 on W/R_0 exists because wide features near the center of the wafer have a longer equilibration time t_c than smaller features that are farther from the center of the wafer; see equation (14.21).

Stillwagon and Larson spin coated a series of polystyrene solutions of varying concentration

and molecular weight and generally found that, by adjusting C_1 , the measured dependence of degree of planarization P_2 on spinning speed ω_2^2 could be fit to equation (14.24); see Fig. 14.18. Here ω_2^2 is defined in terms of the measurable final film thickness H_2 , and is related to ω_1^2 by $\omega_1^2 = \omega_2^2 C_1$. Qualitative agreement was found between predicted and measured dependencies of C_1 on C_0 , M and W/R_0 . However, the predicted values of C_1 were higher than the experimental values; quantitative agreement could only be attained by introducing a large arbitrary parameter, as suggested earlier by Brodkorb, Köhler and Ritzel (1989). Also, Peurrung and Graves (1991) found that the shapes of the dried film profiles were significantly different in some cases from the shapes predicted by assuming

uniform shrinkage during the evaporation stage. Evidently, the assumption of a sharp transition between flow and evaporation stages of the level process, with perfect equilibration before the transition and no flow and no transverse diffusion after the transition, does not lead to completely satisfactory predictions.

14.4 SUMMARY AND PERSPECTIVE

Using intuition and seat-of-the-pants engineering, early practitioners made the process of spin coating thin films over level substrates into a highly successful industrial coating method over fifty years ago. Modeling and analyses developed since then have served mainly to explain why spin coating works so well, and to delineate some theoretical limits, should future generations find reason to optimize the technique to obtain even better performance. Simple analyses of spin coating assume uniform evaporation, and then predict film thicknesses. These analyses, backed by experimental results, show that thicker films are obtained by increasing the viscosity of the solution, the solids concentration, or the volatility of the solvent, or by decreasing the spinning speed. As long as overly volatile solvents are avoided (these can lead to Marangoni-type instabilities), the uniformity of the film thickness in spin coating is usually less than a percent and often a few tenths of a percent or better. If for some reason one wants to improve on this uniformity, spinning conditions must be carefully controlled so that other instabilities, including Ekman spirals, are avoided.

Often, because of previous microelectronic processing, the wafers over which solutions are spin coated contain topographic unevenness of a micron or so in depth, and tens to hundreds of microns or more in width. Most of the factors that control leveling or planarization of the spin-coated film over such topography both during and after spin coating are well understood, thanks to recent efforts, and can be predicted, at least qualitatively, by simple lubrication models. The most important of these factors is the width W of the topographic feature underlying the fluid

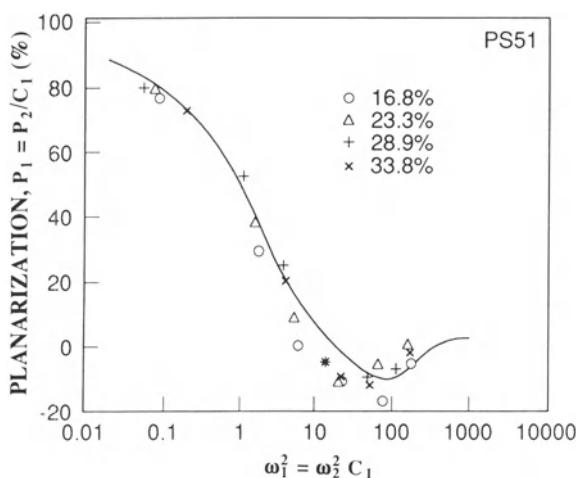


Figure 14.18 Planarization $P_1 = P_2/C_1$ versus dimensionless spinning speed ω_1^2 for 16.8%, 23.3%, 28.9% and 33.8% solutions of polystyrene (molecular weight = 51 000) in the solvent propylene glycol monomethyl ether acetate. The degree of planarization P_2 and the spinning speed ω_2^2 were calculated using the final film thickness H_2 . P_1 and ω_1^2 are defined in terms of the film thickness $H_1 \equiv H_2/C_1$ at the transition from the flow to the drying stage of spin coating. By adjusting C_1 , the data for all concentrations collapse onto a single curve that agrees with the line given by the lubrication theory for $H_1/D = 4$ (from Stillwagon and Larson (1992)).

film. Some planarization during spinning can be expected if $W \lesssim 50 \mu\text{m}$, and a high degree of planarization can be expected if $W \lesssim 10 \mu\text{m}$. The degree of planarization depends also on the topography surrounding the feature; isolated features are more poorly planarized than closely spaced ones. The properties of the resist solution affect planarization. Solutions that remain fluid at high solids concentration planarize best; also the higher the initial polymer concentration, the better the planarization. Following spin coating, further planarization is possible if the film's mobility can be restored by heating. The dependence on feature width of the time to achieve leveling by surface-tension-driven flow is so severe, however, that it may be impractical to level features wider than about $200 \mu\text{m}$, unless the film is unusually thick.

In sum, spin coating over level substrates is a well developed practice, which usually produces satisfactory results for commercial purposes. The most serious problems seem to occur when the substrate is uneven, and the spin-coated film is sometimes not level enough for high-resolution photolithography. The conditions under which such problems will occur are now well understood and can be modeled semi-quantitatively. Future work might be directed toward making these predictions completely quantitative, or toward developing new ways to improve leveling.

REFERENCES

- Acrivos, A., Shah, J. J. and Petersen, E. E. 1960. On the flow of a non-Newtonian liquid on a rotating disk. *J. Appl. Phys.* **31**(6): 963–968.
- Adams, A. C. and Capio, C. D. 1981. Planarization of phosphorus-doped silicon dioxide. *J. Electrochem. Soc.* **128**(2): 423–429.
- Bassous, E., Ephrath, L. M., Pepper, G. and Mikalsen, D. J. 1983. A three-layer resist system for deep u.v. and RIE microlithography on nonplanar surfaces. *J. Electrochem. Soc.* **130**(2): 478–484.
- Bornside, D. E. (1990). Mechanism for the local planarization of microscopically rough surfaces by drying thin films of spin-coated polymer/solvent solutions. *J. Electrochem. Soc.* **137**(8): 2589–2595.
- Bornside, D. E., Macosko, C. W. and Scriven, L. E. 1987. On the modelling of spin coating. *J. Imag. Technol.* **13**(4): 122–130.
- Bornside, D. E., Macosko, C. W. and Scriven, L. E. 1991. Spin coating of a PMMA/chlorobenzene solution. *J. Electrochem. Soc.* **138**(1): 317–320.
- Bornside, D. E., Brown, R. A., Ackmann, P. W., Frank, J. R., Tryba, A. A. and Geyling, F. T. 1993. The effects of gas phase convection on mass transfer in spin coating. *J. Appl. Phys.* **73**(2): 585–600.
- Brodkorb, W., Köhler, J. M. and Ritzel, O. 1989. A hydrodynamic model for the spin-coated substrate topography. Parts I and II, *Experimentelle Technik der Physik*. **37**(6): 519–525; 527–540.
- Burggraaf, P. 1986. Wafer steppers and lens options. *Semicond. Int.* **9**(3): 56–63.
- Chiba, K., Tsunoda, T., Kato, Y., Endo, M., Sawase, F., Itikawa, K. and Imamura, M.-A. 1982. Coating method. US Patent 4,353,937.
- Daniels, B. K., Szmunda, C. R., Templeton, M. K. and Trefonas III, P. 1986. Surface tension effects in microlithography – striations. *Proc. SPIE*. **631**: 192–201.
- Daughton, W. J. and Givens, F. L. 1982. An investigation of the thickness variation of the spun-on thin films commonly associated with the semiconductor industry. *J. Electrochem. Soc.* **129**(1): 173–179.
- Elliott, D. J. and Hockey, M. A. 1979. One micron range photoresist imaging: a practical approach. *Solid State Technology*. **22**(6): 53–60.
- Emslie, A. G., Bonner, F. T. and Peck, L. G. 1958. Flow of a viscous liquid on a rotating disk. *J. Appl. Phys.* **29**(5): 858–862.
- Flack, W. W., Soong, D. S., Bell, A. T. and Hess, D. W. 1984. A mathematical model for spin coating of polymer resists. *J. Appl. Phys.* **56**(4): 1199–1206.
- Frasch, P. and Saremski, K. H. 1982. Feature size control in IC manufacturing. *IBM J. Res. Develop.* **26**(5): 561–567.
- Hagan, J. A., Maloy, J. E. and Wilke, M. A. W. 1986. Magnetic disk coating method and apparatus. US Patent 4,589,139.
- Hwang, J. H. and Ma, F. 1989. On the flow of a thin liquid film over a rough rotating disk. *J. Appl. Phys.* **66**(1): 388–394.
- Jenekhe, S. A. and Schuldt, S. B. 1984. Coating flow of non-Newtonian fluids on a flat rotating disk. *Ind. Eng. Chem. Fundam.* **23**(4): 432–436.
- Lai, J. H. 1979. An investigation of spin coating of electron resists. *Polym. Eng. Sci.* **19**(15): 1117–1121.
- LaVergne, D. B. and Hofer, D. C. 1985. Modeling planarization with polymers. *Proc. SPIE*. **539**: 115.
- Lawrence, C. J. 1988. The mechanics of spin coating of polymer films. *Phys. Fluids*. **31**(10): 2786–2795.

- Lawrence, C. J. 1990. Spin coating with slow evaporation. *Phys. Fluids A.* **2**(3): 453–456.
- Lawrence, C. J. and Zhou, W. 1991. Spin coating of non-Newtonian fluids. *J. Non-Newt. Fluid Mech.* **39**: 137–138.
- Leers, D. 1981. Investigation of different resists for far and deep UV-exposure. *Solid State Technology*. **24**(3): 90–92.
- Ludviksson, V. and Lightfoot, E. N. 1968. Hydrodynamic stability of Marangoni films. *AIChE J.* **14**(4): 620–626.
- Meyerhofer, D. 1978. Characteristics of resist films produced by spinning. *J. Appl. Phys.* **49**(7): 3993–3997.
- Moreau, W. M. 1988. *Semi-Conductor Lithography*. New York: Plenum Press.
- Ohara, T., Matsumoto, Y. and Ohashi, H. 1989. The film formation dynamics in spin coating. *Phys. Fluids A.* **1**(12): 1949–1959.
- Overdiep, W. S. 1977. Levelling of paints. In *Physicochemical Hydrodynamics*, ed. D. B. Spalding. New York: Advance Publications Ltd. pp. 683–697.
- Pearson, J. R. A. 1958. On convection cells induced by surface tension. *J. Fluid Mech.* **4**(5): 489–500.
- Peugh, H. V. and Ward, A. W. 1984. Coating thickness and wedge geometry control for magnetic disks. US Patent 4,485,758.
- Peurrung, L. M. and Graves, D. B. 1991. Film thickness profiles over topography in spin coating. *J. Electrochem. Soc.* **138**(7): 2115–2124.
- Peurrung, L. M. and Graves, D. B. 1993. Spin coating over topography. *IEEE Trans. Semicond. Manuf.* **6**(1): 72–76.
- Rehg, T. J. 1992. Spin coating of monodisperse colloidal suspensions: evidence of evaporative convection. PhD dissertation, University of California Davis.
- Rehg, T. J. and Higgins, B. G. 1988. The effects of inertia and interfacial shear on film flow on a rotating disk. *Phys. Fluids*. **31**(6): 1360–1371.
- Rehg, T. J. and Higgins, B. G. 1992. Spin coating of colloidal suspension. *AIChE J.* **38**(4): 489–501.
- Reisfeld, B., Bankoff, S. G. and Davis, S. H. 1991a. The dynamics and stability of thin liquid films during spin coating. I. Films with constant rates of evaporation or absorption. *J. Appl. Phys.* **70**(10): 5259–5266.
- Reisfeld, B., Bankoff, S. G. and Davis, S. H. 1991b. The dynamics and stability of thin liquid films during spin coating. II. Films with unit-order and large Peclet number. *J. Appl. Phys.* **70**(10): 5267–5277.
- Rothman, L. B. 1980. Properties of thin polyimide films. *J. Electrochem. Soc.* **127**(10): 2216–2220.
- Sato, K., Harada, S., Saiki, A., Kimmura, T., Okubo, T. and Mulai, K. 1973. A novel planar multilevel interconnection technology utilizing polyimide. *IEEE Trans. Parts, Hybrids Packaging*. **9**: 176–180.
- Scheffel, D. and Richter, V. 1978. Apparatus for the manufacture of the magnetic coatings of magnetic disks. US Patent 4,073,262.
- Schiltz, A., Abraham, P. and Dechenaux, E. 1987. Improvement of photoresist planarization properties by thermal cure. *J. Electrochem. Soc.* **134**(1): 190–194.
- Scriven, L. E. 1988. Physics and applications of dip coating and spin coating. *Mat. Res. Soc. Symp. Proc.* **121**: 717–729.
- Shaw, J. M., Frisch, M. A. and Dill, F. H. 1977. Thermal analysis of positive photoresist films by mass spectrometry. *IBM J. Res. Dev.* **21**(3): 219–226.
- Skrobis, K. J., Denton, D. D. and Skrobis, A. V. 1990. Effect of early solvent evaporation on the mechanism of the spin coating of polymeric solutions. *Polym. Engng Sci.* **30**(3): 193–196.
- Smith, N. D. P., Orchard, S. E. and Rhind-Tutt, A. J. 1961. The physics of brush marks. *J. Oil and Colour Chemists Assoc.* **44**(9): 618–633.
- Spangler, L. L., Torkelson, J. M. and Royal, J. S. 1990. Influence of solvent and molecular weight on thickness and surface topography of spin-coated polymer films. *Polym. Eng. Sci.* **30**(11): 644–653.
- Stillwagon, L. E. 1987. Planarization of substrate topography by spin-coated films: a review. *Solid State Technol.* **30**(6): 67–71.
- Stillwagon, L. E., Larson, R. G. and Taylor, G. N. 1987. Planarization of substrate topography by spin coating. *J. Electrochem. Soc.* **13**(8): 2030–2037.
- Stillwagon, L. E. and Larson, R. G. 1988. Fundamentals of topographic substrate leveling. *J. Appl. Phys.* **63**(11): 5251–5258.
- Stillwagon, L. E. and Larson, R. G. 1990. Leveling of thin films over uneven substrates during spin coating. *Phys. Fluids A.* **2**(11): 1937–1944.
- Stillwagon, L. E. and Larson, R. G. 1992. Planarization during spin coating. *Phys. Fluids A.* **4**(5): 895–903.
- Sukanek, P. C. 1985. Spin coating. *J. Imag. Technol.* **11**(4): 184–190.
- Sukanek, P. C. 1989. A model for spin coating with topography. *J. Electrochem. Soc.* **136**(10): 3019–3026.
- Sukanek, P. C. 1991. Dependence of film thickness on spin speed in spin coating. *J. Electrochem. Soc.* **138**(6): 1712–1719.
- Thomas, I. M. 1986. High laser damage threshold porous silica antireflective coating. *Applied Optics*. **25**(9): 1481–1483.
- Thompson, L. F., Willson, C. G. and Bowden, M. J. 1983. *Introduction to Microlithography*. Washington, DC: American Chemical Society.

- von Kármán, Th. 1921. Über laminare und turbulente Reibung. *Z. Angew. Math. Mech.* 1: 233–252.
- Wahal, S., Oztekin, A., Bornside, D. E., Brown, R. A., Seidel, P. K., Ackmann, P. W. and Geyling, F. T. 1993. Visualization of a gas flow instability in spin coating systems. *Appl. Phys. Lett.* 62(20): 2584–2586.
- White, L. K. 1985a. Approximating spun-on, thin film planarization properties on complex topographies. *J. Electrochem. Soc.* 132(1): 168–172.
- White, L. K. 1985b. A model study of superficial topography for improved lithography. *J. Electrochem. Soc.* 132(12): 3037–3041.
- Wilson, R. H. and Piacente, P. A. 1986. Effect of circuit structure on planarization resist thickness. *J. Electrochem. Soc.* 133(5): 981–984.
- Yonkoski, R. K. and Soane, D. S. 1992. Model for spin coating in microelectronic applications. *J. Appl. Physics.* 72(2): 725–740.

INDEX

Page numbers in **bold** refer to figures and page numbers in *italic* refer to tables.

Accommodation coefficient 196
Adams–Bashforth/trapezoid-rule integration 332
Adhesion 105–6
Adsorption, *see* Surfactants
Aerosol OT 117, 121, 127
Air entrainment 6, 86, 89, 93–5, **93**, 446–7, 473–4, 482–4, **482**, **485**, 486–8, **486**, 546, 641, 657–9
air bubble collapse 87, 483
air film 87, 92, 473, 483, 658
empirical correlations 88–9, 446
hydrodynamic theories 92
hysteresis 90, 487
macroscopic flow effect 86–7
macroscopic regime 658–9
microscopic regime 92, 473, 483, 658
models for entrained air film 90–2, 93–5
molecular-kinetic theory 93
prevention with hydrodynamic assist 89–90, 463, 484
sawtooth-shaped wetting line 86–7, **87**, 88, 95, 658, **659**
shear-thinning viscosity effect 89, 484
surface roughness effect 89, 658
surface wettability effect 89
see also specific coating methods
Amphiphilic molecules 682
Analysis of variance (ANOVA) 215
Arbitrary Lagrangian–Eulerian (ALE) methods 299–300, 305, 348–9
comparison with standard finite-element method 349
Architectural paints 138, 141, 160–75
see also Latex coatings
Arnoldi’s algorithm 322
Asymptotic methods 8, 72, 251–94
composite expansion 256
inner expansion 256
inner region 256, 267–9, 273
linearization 257
matching 256, 269, 275, 279–80

outer expansion 256
outer region 256, 266–7, 272
stretching transformation 256, 267, 273
see also Domain perturbation methods; Regular perturbation methods; Singular perturbation methods
Auto-focus method 227
Back-diffusion 108
Bandedness 429, 456
Bank rolling 157, **311**, 558–9, **559**, 630–1
instabilities 602–3
Barring 418, 421, 448–51, 479
Bead coating, *see* Slide coating
Beer’s law 222
Bent blade, *see* Flexible blade coating
Bernoulli’s equation 29–31
Beveled blade, *see* Flexible blade coating
Bifurcation 655
symmetry-breaking 653
Bifurcation points 320, 328, 338, **655**
Bingham model 155, 337
Bingham–Carreau–Yasuda model 375
Blade coating 10, 637, **637**
inverted 638
of paper 138
see also Flexible-blade coating; Knife coating; High-speed blade coating
Blasius boundary layer 490
Bleeding 444, 665–6
Blotchiness 458
Bond number 48–51, **51**, 52, **53**, 63, 73, 86, 406, 676–7
limit of low values 50, 51, 676
limit of high values 50, 676
Boundary conditions 31–47, 301–3
complete set 47, 301–3
distinguished 306, 315
essential 305

finite-element implementation 305–6
free 303
inflow 303
natural 305
outflow 303
traction 302
see also Dynamic boundary condition; Interfacial boundary conditions; Kinematic boundary condition; No-slip condition
Boundary-element methods 352
Boundary integral techniques 351–2
Boundary layer 28
in curtain coating bead 31, 473, 480, 484, 485–6, **488**, 747–8
in overflow cell 414, **515**
for mass transfer 713
in slide-coating bead 434, 435
in surfactant concentration 522, **524**
Box–Wilson method 742
Bright-field detector 231
Brushmarks 187
Bubbles 547, 596
as defect source 458, 546
static pressure inside 39
trapped in recirculation 472, 547, 596, 755
see also Maximum bubble pressure method
Buckingham theorem 215
Bury–Hartley model 499
Calcium carbonate 141
Calendering 12
Capacitance gauging
of film thickness 225–6
of thin gaps and slots 226
Capillary forces 63, 71
Capillary hydrodynamics 7, 19–62
Capillary length 52, 63, 272
Capillary number 48, 64, 71, 75, 80, 81, 85, 86, 91–4, 158, 303, 406, 439, 481, 511, 543, 574, 620, 676, 679, **679**, 680

- Capillary number (*contd*)
 limit of low values 48–52, 573
 limit of high values 52–3, 336, 475, 484
- Capillary pressure 38, 686
- Capillary rheometer 147, 662
- Capillary rise 66–7, 112
 for measuring surface tension 112
- Capillary statics 66–8, 272
- Capillary tube, meniscus advancing in 72–3
- Carrier layer 447
- Carreau(–Yasuda) model 154, 213, 337, 375
- Cascade instability 563–6, 564, 566
- Casson model 154
- Cavitation 157, 557, 596
- Cavity design, *see* Coating dies
- CCD arrays 237, 238
- CCD video camera 217, 230
- Characteristic equation 276, 279
- Chatter 457
 see also Barring
- Chebichev methods 318
- Chemical potential 192
- Chemical vapor deposition 3
- Chevrons 457
- Choker bar 369, 371
- Clay 141, 175
- Cleaning-in-place (CIP) system 736
- Cloudy films 717–18
- Coagulation, shear induced 395
- Coathanger manifold 369, 386–93, 388
 design 386–93, 390–2
 tapered 386, 387
- Coating bead 73, 401–2, 427, 450–1, 542, 744
 see also Slide coating; Slot coating
- Coating by drainage 673, 673
- Coating by withdrawal 673, 673
- Coating defects, *see* Defects
- Coating dies 25
 adjustment mechanisms for slot 369, 371, 741
 capacitance gauging of slot uniformity 226
 cavity 369
 cavity cross-sections 370
 cavity flow analysis 29, 373–5
 cavity-slot transition analysis 378–9
 contamination and cleaning 547, 753–5
 control of cross-web uniformity 741
 cross-web flow distribution 379, 380, 756–9
- design configurations 370, 403–4, 404
- design considerations 8, 383–96, 752
- design optimization 752–61, 752, 760
- dimensional analysis 379–82
- distribution chamber, *see* Manifold
- elastic deflections 381
- feed 372–3, 373
 center 372
 end 372
 multiple 372
 recycle 395
- inertial effects 386, 387
- internal flow analysis 372–83, 393
- manifolds 369, 372, 645
- multilayer manifold design 394–5
- nonuniformity from flow-split in center-fed cavity 373
- pressure distribution 374–5, 376
- reactive flows 395
- secondary cavities 393–4, 752
- sensitivity to small variations in slot 379, 395, 760
- slot 369
 accuracy 760
- slot flow analysis 376–9, 377
- streak formation 755
- temperature uniformity 395, 760
- thermal analysis 382–3
- viscoelastic effects 381
- see also* Choker bar; Coathanger manifold; T-manifold; Wall shear stress
- Coating equipment, *see* Pilot coating equipment
- Coating failure 6
- Coating flows 42, 301–8, 501–5
 album of 243–6, 243
 boundary conditions 31–48, 301–3
 governing equations 20–31, 301–3
 mathematical analysis 252–4
- Coating fluids 137
 test fluids for pilot experiments 212–13
- Coating formulations 139–42
 effect on defects 184
- Coating gap 401
 control 422
- Coating industry 4
- Coating irregularities, *see* Defects
- Coating machine
 capacity 763
 change-over time 764
 down time 764
 specific machine utilization 763
- Coating processes
 dynamics, or transient behavior 739–40
- industrial and academic research 4
- overview 3–15
- robustness 741, 746
- yield 763
- Coating rheology 66, 137–82, 659–63
 interplay among components and application performance 157–77
 numerical analysis 337–9
 rheometric flows 142–9
- Coating technology, origins 4
- Coating uniformity 216–22, 334, 546–7, 641, 659, 741, 756–9, 757, 758
 control 740–1
 power spectrum 220
 quality index 218
 quantification 216–22
 threshold level as quality criterion 222
- Coating window 745–6
 computational analysis 327–8, 331
- feasibility 745
- quality 329–30, 745
- sensitivity 745
 see also specific coating methods
- Coextrusion 323, 394
 interfacial instability 323
 critical layer thickness ratio 394
- Cohesion 105–6
- Colloidal coatings 710, 716, 718–20, 720
 shear-thinning 717
 see also Sol-gel films
- Compressive flow 144
- Computational methods 8, 297–366
- Cone-and-plate rheometer 147, 164
- Conjoining pressure 190, 193
 see also Disjoining pressure
- Conjugate gradient (CG) method 318, 351
- Conjugate residual (CR) method 318
- Conservation laws 20–31, 301–3
 linear momentum 22–4, 691–2
 mass 20–2, 32–5
 solute 43
 species 43, 690
- Consistent pressure Poisson equation (CPPE) 308
- Constitutive equations 24, 38, 138, 154–5

- generalized Newtonian fluid 24, 154, 337
 interfacial stress 37
 Newtonian fluid 154, 302
 surface 504
 surface excess concentration 498
 viscoelastic fluid 155
see also Bingham model; Carreau model; Cusson model; Maxwell model; Power-law model
- Constitutive theory 7
 Contact angle 45–7, 45, 64, 64
 advancing 46, 65, 66
 apparent 45, 65
 boundary condition 70, 302
 hysteresis 46, 65–6, 335, 467, 526
 interface between miscible fluids 335
 measurement 65
 receding 46, 65, 66
 submicroscopic, or actual 45
 surfactant effects 526–8
see also Dynamic contact angle; Static contact angle
- Contact line, *see* Wetting line
 Contamination 100, 547, 753–5
 airborne particles 58
 particulate 547
 Continuation procedures 319–21, 327
 arc-length 320, 350
 around singular points 320
 first order 319
 step-size control 320
 Continuity equation 22, 259–60, 302, 307, 654
see also Conservation law
 Control 11, 735–41
 algorithm 739
 feed-back 735–6, 735
 feed-forward 735–6, 736
 loops 740
 on-line 740
 Control volume 21, 286, 433
 Convective diffusion 497–8, 504
 in computational methods 339–40, 692–3
 equations for 690
 Corduroy, *see* Ribbing
 Corner
 flow in 245
 wetting-line mobility at 66
see also Gibbs' inequality
 Couette flow 582
 Couette–Poiseuille flow 442
 Couette rheometer 147
 Cracking 199, 201
 Craters 192, 458
- Crazing 199, 201
 Creeping flow 28
 Critical micelle concentration 101, 499, 501, 516, 519
 Critical pigment volume concentration (CPVC) 141
 Critical point tracking 327–8
 Critical points 320, 327
see also Bifurcation point; Hopf point; Turning point
 Curling 199
 Curtain coating 9, 463–93, 744–52
 air boundary layer 747
 air current effect 479
 air entrainment 463, 473, 482–4, 482, 485, 745
 with heel 486–8, 486
 air shields 479, 491–2
 applications 463, 466
 applied pressure difference 477, 479
 barring 479
 coating window 481–2, 481, 486, 745, 745, 750
 curtain flow zone, *see* Falling curtain
 dynamic contact angle 69, 70
 dynamic wetting 336, 473–5, 744–52
 edge effects 471–2, 478, 490
see also Edge guides
 equipment configurations and design 464–6, 464, 465, 466
 finite-element analysis 473, 474, 475, 476, 481, 483
 fixed-grid simulation 344
 frequency response 479, 480
 heel formation 310, 310, 473, 474, 476, 485–8, 746–7
 impingement angle 484
 impingement flow 70, 463, 473–5, 475, 476, 746, 748, 749, 751
 impingement velocity 463, 472
 linear finite-element stability analysis 326
 lip design 488–9
 maximum coating speed 466, 487, 488
 minimum coating thickness 326, 463, 481
 multilayer 464, 465
 non-Newtonian effects 484
 operability 481–8
 optimization dynamic of wetting line position 744–52
 puddling (vortex in heel) 745
 pulled-film phenomenon 473, 474, 481–2, 483, 484
- sheet-forming flow 467–72, 468, 469
see also Teapot effect
 sensitivity to disturbances 475–80
 start-up 490–1, 492
 steady-state operation 466–75
 variable coating width 492
- Curvature
 mean radius 38, 39, 40, 64
 principal radii 39
 sign 39
- Deborah number 660
 Defects 6, 7, 13, 199, 201, 217, 219, 221, 448–51, 456–8, 544, 546–7, 616, 663–8, 755
 classification 231
 frequency spectrum of 221
 healing 184–9
 on-line detection 230–2
 prevention 735, 736
 quantification 216–22
see also Laser scanners
 Deflection number 381
 Deformable roll coating, *see* Squeeze-roll coating
 Deformation rate, *see* Rate of strain
 Degassing 596, 735, 755
 Derivative, substantial 23
 Dewatering 664
 Dewetting 8, 104, 189–96, 191, 192
Die coating, see Extrusion Coating; Slot coating
Die design, see Coating dies
Die swell 467
 Differential/algebraic equation system (DAES) 331
 numerical solvers 332
 Diffusion 43, 108–10, 125, 197–9, 497–8, 508, 690, 713
 interlayer in multilayer coating 450
 within surface or interface 42, 497
see also Convective diffusion; Surfactants
 Diffusion coefficient, *see* Diffusivity
 Diffusion limited transport 197–8, 713
 Diffusivity 108, 109, 125, 127, 127, 128, 198, 497
 concentration and temperature dependence 681
 for micelles 500
 in polymer films 198
 pseudo-binary 690
 Dimensional analysis 48
see also Buckingham theorem

- Dip coating 11, 271, 673, 675, 678–82
 applications 673–4
 batch 673, 673
 continuous 673, 673
 evaporation, concomitant 680–1
 film thickness 678–80, 678, 686–7, 686
 film uniformity 674
 irregularly shaped substrates 673, 674
 Landau–Levich analysis 678
 non-Newtonian liquids 680
 obstruction to control film thickness 677
 operating parameters 677, 695
 stability 547, 566, 680
 stagnation line 675
 two-phase flow model 689–92, 698–703, 699, 701
 versus slot coating 676–7, 676
see also Rising film flow
- Discontinuous velocity condition 531
- Discretization, *see* Finite-element method; Mesh
- Disjoining pressure 43–5, 43, 64, 72, 190, 192–3, 194
 profiles 193
- Disperse polymer coatings, *see* Polymer dispersions
- Dispersion
 particle intersections in 149
 viscosity of 149
- Dissipation, viscous 382
- Disturbance 283
 amplitude 283
 phase speed 283
 wave number 283
- Divergence theorem 21, 23, 33, 305
 for surfaces 36, 306, 325
- Doctor blade 540
- Doctoring 546, 629–30
 coating thickness 629, 630
 in gravure coating 629–30
 regimes 629
 reverse-angle 546, 612
 trailing-blade 546
- Domain perturbation methods 256–8, 271–80, 282
 for slowly varying deformation 257–8, 258, 271–80
 for small deformation 256–7, 257, 275
see also Asymptotic methods
- Drag-out, *see* Dip coating
- Drop
 in flow with surfactants 502
 pendant 115
- pressure inside 64
 sessile 115
- Dry patches, growth or healing 194–6
- Drying 7, 13, 196–9, 678–82
 air flow effects 503
 control 703, 704
 defects 197
 at die lips 422, 466
 diffusion limited in film 197–9
 gas-side mass transfer resistance 196–7
 microstructure control 703
 in presence of non-volatile phase 681–2
 of sol-gels 682
 of suspension of solid particles 201
 of thin films 681
 two-phase flow model 689–93
see also Dip coating; Evaporation;
 Spin coating; Stress buildup in coatings
- Drying line 680–1, 682, 694
 film profile at 681
- Du Nouÿ Ring 112, 117–19, 533, 683
- Dye-injection as flow tracer 240–1, 576, 579
- Dynamic boundary condition 36–41, 38, 43–5, 47, 49, 55, 58–60
- Dynamic contact angle 45, 69, 69, 70, 71–3, 73, 75–86, 92, 95, 531
 apparent 70
 boundary condition 70, 73
 empirical correlations 80
 experimental data 79–86
 flow geometry effect 85
 hydrodynamic bending and shaping of meniscus 70, 335, 336
 hydrodynamic theory 76–8
 low-speed effects 80
 maximum value of 180° 69, 70
 measurement techniques 69
 molecular-kinetic theory 76
 speed dependence 46, 69, 70, 79–86
 surface roughness effects 85
- Dynamic mechanical measurements 144, 151
- Dynamic surface tension 99–100, 108–10, 109, 131, 132–3, 132, 495, 513, 514, 524
 measurement 100, 111–16, 513–14
 parametric simulation 110
 for selected surfactants in water/gelatin 124–8
- Dynamic uniaxial extensional viscosity (DUEV) 146, 150, 151, 178–9
- Dynamic wetting 6, 7, 63–4, 69, 90–3, 95
 driving force 76
 failure 63, 70, 86–95
 finite-element analysis 335–7, 473, 484, 526, 528
 hydrodynamic models 71, 76–8, 79
- laser-Doppler velocimetry 87, 235
- line, *see* Dynamic wetting line
- matched asymptotic analysis 77
- molecular forces 72
- molecular-kinetic theory 76
- multi-valued velocity 336, 526
- slip models 77, 335
- speed limit 63
- stick-slip behavior 83, 85
- three-phase zone 87
- with surfactants 335–6, 525, 526
- wedge flow 76
- see also* Air entrainment
- Dynamic wetting line 9, 69–75, 531, 532, 659, 744–52
 optimization of position 484, 744–52
- sawtooth-shaped 86–7, 87, 88, 95, 658, 659
- singularity 71
- Edge effects 490, 491
- Edge guides
 slide coating 457
 curtain coating 471–2, 489–90, 489
- Edge of liquid film
 meniscus shape 68
 retraction of 189
 necking-in in coating bead 457
- Eigenvalue problem 283, 322, 325
 computational solution 322–3
- Ekman layer 713
- Ekman spirals 721
- Elastic layers 604–5
 elastic foundation approximation 605
 plain-strain theory 604–5
 spring model 605
- Elastic-viscous split stress (EVSS) formulation 339
- Elasticity number 605, 607, 620
- Elastohydrodynamic coating
 methods 10, 599–635
 common types 599–603, 600
 mechanical instabilities 603

- Elastohydrodynamics 599, 603–7
 finite-element analysis 340–1, 604
 traction boundary conditions 607
see also Elastic layers; Plates
- Electrostatic assist 6, 12, 404, 447, 480, 484
- Electrostatic charges 12
- Elongational viscosity 146, 150, 151, 169–73
- Electrostatic double layer 193
- Emcol 5130 117, 122, 123
- Empimin LSM30 117, 123, 125, 125, 126
- Empirical model building 215
- Emulsion polymerization 140
- Endoscope 237, 243
- Energy absorption as a function of film thickness 222
- Entrance length 27
- Entrance pressure loss 378
- Equations of motion 49, 265
see also Conservation laws; Navier–Stokes equations
- Euler–Newton continuation 319
- Eulerian–Lagrangian methods, *see* Lagrangian–Eulerian methods
- Euler's equation 28, 29, 30
- Evaporation 289, 680–1, 693, 713–17
 concomitant with coating 680–1
 differential 684–5
 singularity at drying line 694
see also Sol–gel film dip coating
- Evaporation cooling 197
- Evolutionary operation (EVOP) 743
- Experimental methods 8, 209–50, 297
see also Statistical experimental design
- Explicit interface tracking 345–6
- Explicitly elliptic momentum equations 338
- Extension number 381
- Extensional flow 144
- Extension-thickening behavior 338
- Extrusion coating 401, 402
 flow visualization 414
- Factorial design 215, 742
- Falling curtain 472–3, 475–8
 capillary waves 113
 finite-element stability analysis 326, 478
 film-profile equations 472
 free-fall velocity 31, 113, 472
 low-flow limit 326, 464, 475–8, 477, 745
 Marangoni effect 479
 sensitivity to disturbances 463
 stability 326, 475–8, 745
- surfactant effects 477
 trajectory 467, 470, 472
see also Curtain coating; Teapot effect
- Falling curtain method, for measuring dynamic surface tension 113–14
- Falling film flow 271–80, 271
 domain perturbation analysis 271–80
 film profile equation 275, 278
 inertia effects 277
 standing waves 278, 280, 432
 surfactant effects on stability 502–3
see also Film flow down an incline
- FAN method 376, 378
- Fast Fourier transform (FFT) 217, 220, 238
- Fat edges 457
- Feathering 665
- Fenopon CO-433 117, 123
- Fiber coating
 stability of coated film 289
see also Dip coating
- Fiber plunging into pool
 dynamic contact angle 78, 79
- Fibonacci search method 742
- Fick's law 43, 198, 690
- Filamentation 157, 173, 557
- Film, *see* Liquid film
- Film flow, *see* Falling film flow; Film flow down incline; Rising film flow; Rotating film flow
- Film flow down incline 280–92, 281, 429, 448–50, 505–12
 critical Reynolds number for long-wave instability 285
 density stratification 291
 equipment vibrations 289
 film thickness 429
 flow around local disturbance 352
 frequency response of two layers 530
 heated from below 289
 linear stability analysis 281–92, 505–7
 as method for measuring dynamic surface tension 119–20, 120
 mechanisms controlling stability 285–8, 509–13
 nonlinear stability 288
 non-Newtonian effects on stability 289, 291, 339, 449
 slot exit design 244–5, 428–9, 429
 solitary waves 289
 stability of single layer 280–9, 281, 351, 352
- stability of multiple layers 290–2, 448–50
- surfactant effects on stability 449, 502–3, 505–12, 505, 511, 512
 diffusion 450, 507, 508
 micellization 508–9, 509
 phase lag 510–12
 surface elasticity 507–8, 507
- viscosity stratification 291, 448–50
- visualization of slot-exit flow 243, 244–5
 visualization of merging of two layers 243, 245
- Film pressure 106
- Film profile equation 193, 275–9, 472
- Film profile evolution equation 711, 724–5
 for uneven substrate 727
- Film profiling, *see* Fluorescence spectroscopy; Imaging ellipsometry
- Film retraction, at edge 189
- Film rupture 189, 191, 192–4, 195
- Film split, *see* Forward roll coating
- Film thickness measurement 222–6, 224
- Film thickness uniformity, *see* Coating uniformity
- Film thinning 190–2, 191
 surface-tension gradient driven 191–2, 192
- Film viscosity 193
- Filtercake formation 652, 664
- Filtering
 of fluids 735, 755
 of signals 217, 219
- Finger strain tensor 604
- Finite-difference method
 for free-surface flow 350–1
 for time discretization 332
- Finite-element method 299, 300, 301–34, 543
 basis function 304
 discretization 304–8
 discretization errors 308
 imposition of boundary conditions 305–6
 steady-state problems 315–19
 three-dimensional problems 304, 308, 490
see also Frequency response analysis; Linear stability analysis; Mesh; Mesh generation; Transient analysis
- Finite-volume method 350–1

- Fixed-grid methods 341–6
 dynamic boundary conditions 343–4, 345
 local grid adjustment 345
Flexible blade coating 599, **600**,
 601, 607–13, **608**, **637**, 638,
 646–53
 bent-blade regime 609, 611, **637**,
 639, 647
 beveled-blade regime 609, 611,
637, 639, **639**, 647
 blade design 608
 blade-tip geometry 611
 elastohydrodynamic action 601,
 609–12, 647–8
 feed systems 608
 film-splitting instability 647
 inertia effects 609, 647, 650
 loading configurations 608
 low-angle-blade regime, *see* Bent-
 blade regime
 operability 613
 operating response 609, **610**, 611,
 612–13, **647**
 on porous substrate 612
 puddle-flow instabilities 613
 ribbing 602, 613
 streaks 609, 613
 trailing-blade regime, *see* Beveled-
 blade regime
see also High-speed blade
 coating
Flow 20–47
 fully developed 27
 laminar 27
 turbulent 27
see also Flow visualization; Fluid
 velocity measurement; Free-
 surface flow
Flow forming zone 303
Flow separation, *see* Recirculation
Flow visualization 90, 237, 238,
 239–43, **240**, **241**, 576–9, 721
 examples – album of coating
 flows 216–22, **243**
 high-speed 174, 666
 illumination 238
 tracers 238, 240, 242, 576, 579
 inside vortices 241
Fluid
 definition 18
 incompressible 22
see also Newtonian fluid; Non-
 Newtonian fluid
Fluid delivery 12
Fluid handling 736
Fluid preparation 12, 736
Fluid velocity measurement 232–6
Fluorad FX-1002 117, 123
Fluorescence spectroscopy 687–8,
687
Foams 104, 501
Foil bearing 617
Force balance 23, 40, **51**, 52, 55, **57**
Force singularity 71
Forces
 centrifugal 709, 727
 body 22
 surface 22
Forward kiss coater, *see* Tensioned-
 web roll coater
Forward roll coater 10, 157–60,
 261–71, 539, 540, **541**, 552–9
 air entrainment 538
 applications 540
 asymmetric 264, 555
 bank, rolling 157, 558–9, **559**
 deformable rolls, *see* Squeeze-roll
 coating
 cavitation 157, 557
 filamentation 157, 173, 557
 film-split flow 553–5
 film-split instabilities 157, 556–8
 film-split location 264, 266, 268,
 269, 270, 554–5
 finite-element analysis 554–5, **554**
 inlet flooded 552, 573, **574**, **576**
 inlet starved 553, 558, 573, **574**
see also Meniscus roll coating
 linear stability analysis 556–7
 lubrication analysis 261–5, 553–5
 metered film thickness 270, 555,
555, 574
 misting 157
 non-Newtonian effects 555, **555**,
 557–8
 operability window of 559, **560**
 pressure distribution 157, 262,
263, 553, **553**
 primary flows 540, **542**
 ribbing 157, 556–8
 singular perturbation analysis
 265–71, 543
 string to eliminate ribbing 556–7
Fountain applicator, *see* Jet fountain
 applicator
 Fourier analysis 217
 Fractal dimension 682, 686
 Free-boundary parameterization
 308–15, 341–6
 Free-falling flow 31, 472
 Free-Lagrangian methods 347
 Free-meniscus coating 673–705
see also Coating by drainage;
 Coating by withdrawal; Dip
 coating
 Free-surface flows 5, 31–45, 47–62,
 300–1, **301**
- Free-volume theory of polymer/
 solvent diffusion 198
Frequency-response analysis
 329–30
 three-dimensional disturbances
 330
 two-dimensional disturbances
 329–30
Front capturing methods 342
Front tracking 341–6
Frontal method 317
Frumkin equation of state 107
Function optimization 742
Galerkin weighted residuals 253,
 305, 306, 307
Gauss elimination 317
Gaussian quadrature 306
Gel slugs 458
Gelatin 213, 452, 483, 484, 487
 subbing layer of 65
 surface activity 125
Gellation 685
Generator lines 308
Gibbs' adsorption equation 41, 107
Gibbs' complementary condition, *see*
 Gibbs' inequality
Gibbs' inequality 66, 246, 302, 432,
 467, 470, 471
 in finite-element algorithms 320,
 334
Gibbs' surface elasticity 110–11,
 498, 504, 507–8, **507**
Giordano roll coater 139, **139**, 159
Glass transition 200
Glassy regime 153
Glycerin, aqueous solution 213, 452
Graetz number 382
Gravity number 380
Gravure coating 10, **600**, 601,
 627–32
 bank 630–1
 cell patterns 627, **628**
 cell transfer, or pick-out 630–2
 differential 627
 direct **600**, 627
 elastohydrodynamic action 602
 feed systems 629
 forward **600**, 627
 offset 627
 reverse 627
 ribbing 631
 stability 631
 volume factor 627
see also Doctoring
Grid, *see* Mesh
Grid reconnection 347
Hamaker constant 44

- Hansen approximation 109
 Healing of coating irregularities 184–9
 Hele-Shaw flow 326
 Hertz contact theory 621
 Hexagonal cell pattern, *see* Orange peel
 High-speed blade coating 637–69
 air entrainment 641, 657–9
 applicator configurations 640–6, 641
 blade design and loading 639
 blade tip geometry 639, 651, 667
 blade wear 651–2
 computational analysis 650
 cross-web uniformity 334, 641, 659
 control 740–1
 defects 663–8
 deformation rates 640, 660, 662
 equipment 640–6, 641
 inertia effects 650
 instabilities 641, 653–6
 lubrication-flow models 648–9
 maximum coating speed 641, 657
 metered coating thickness in 646, 648, 650–1, 651
 metering action 646–53
 non-Newtonian effects 652–3, 660–3
 normal forces 661–2
 streaks and striations 658, 659
 time scales 639, 660
 viscoelastic effects 660, 661
 see also Flexible-blade coating;
 Inverted blade coater; Jet coater; Paper coating process;
 Pressurized pond coater;
 Puddle-type blade coater; Roll applicator; Short-dwell coater
 High-speed photography 174, 237
 High-speed video 237, 576, 579
 High-solids coatings 141
 Hookean solid 341
 Hopf points 320, 323, 327
 Hopkins flow-separation condition 262, 263, 270
 Hopper, *see* Coating die
 Hydraulic radius 375
 Hydrodynamic assist 89–90, 463, 484
 Hydrogen bubble method 235–6, 240, 241, 241
 cathodic corrosion protection 241
 Hydrostatic pressure distribution 25
 Hydrophile-hydrophobe balance (HLB) number 101
 Hydrophobically-modified, alkali-swelling emulsion (HASE) thickeners 175
 Hydrophobically-modified, ethoxylated urethane 173–5, 178
 Hydroxyethyl cellulose 161, 163, 167, 168, 172, 557, 664
 Hysteresis
 contact angle 46, 65–6, 335, 467, 526
 hydrodynamic 469
 Igepal CA-720 117, 123
 Image processing 238–9, 244, 576, 579
 Imaging ellipsometry 687, 687
 Imaging techniques 236–9, 579
 Immersion of substrate 673
 Immobilization solids 664
 Implicit time integration 331
 Implicit volume tracking 342–5
 Inclined film flow, *see* Film flow down incline
 Inclined plane method for measuring dynamic surface tension 119–20, 120
 Infrared absorption, for measuring film thickness 222–3, 223, 224
 Initialization of finite-element calculation 321
 Instabilities 6, 403
 centrifugal 654–6
 free-surface, or wave 285
 interfacial wave 290, 394
 long-wave 285
 shear-flow 284
 spatial 283
 symmetry-breaking 323, 653–4
 temporal 283
 Integral methods 253, 289, 351–2
 Interface 19, 31–45, 47–62
 air–liquid 44, 48, 54, 59, 61
 fluid–fluid 31, 34, 35, 47
 impermeable 34, 497
 Interface reconstruction 343
 Interfacial boundary conditions 31–45, 301–3, 302, 690–2
 mass balance 32
 normal stress balance 48–54
 species balance 42, 690, 691–2
 stress balance 36–41, 58–62, 302, 691
 tangential stress balance 54–61
 see also Dynamic boundary condition; Kinematic boundary condition
 Interfacial phenomena 19–62, 107–11, 498, 689–92
 Interfacial rheology 503
 Interfacial tension, *see* Surface tension
 Interferometry
 mechanical, *see* Moiré technique
 optical 228, 728
 stroboscopic 728, 730
 Internal design of coating dies, *see* Coating dies
 Invariant, of tensor 154
 Inventory control, of product 762–3
 Inverse iteration 322, 325
 Inverse problem 333–4
 Inverted blade coater 638, 641
 Irrotational flow 29
 Iterative matrix solvers 318–19
 Iterative solution of non-linear problems 315–17, 742
 Jacobian, of mapping 313
 Jacobian matrix 316, 320, 322
 Jet coater, *see* Jet fountain applicator
 Jet fountain applicator 642, 644–5
 manifold design 645
 Kelvin–Helmholtz instability 342, 483
 Kinematic boundary condition 32–5, 47, 55, 60, 61, 302, 690
 Kirchhoff–Love assumptions 606
 Kiss coating, *see* Tensioned-web roll coating
 Knife coating 258–61, 539, 540, 541, 547–552
 applications 540
 configurations 540
 finite-element analysis 548
 flooding 552
 lubrication theory 258–61, 547–9
 metered film thickness 260, 548–9, 549, 646, 660–1
 non-Newtonian viscosity effects 548–9
 operability window of 552, 552
 pond-feed 540
 pressure profiles 260, 549, 550, 551
 ribbing instability 549, 551, 661
 separating forces 660–1
 starvation 552
 steady flow 547–9
 streaks 552
 viscoelastic effects 548–9, 552, 660–1
 Krebs units 149, 161, 162, 164
 Ladyzhenskaya–Babuska–Brezzi (LBB) condition 304

- Lagrangian methods 343, 346–50, 354
 Lagrangian mesh generation 315
 Lagrangian–Eulerian methods 305, 345, 348–9
see also Arbitrary Lagrangian–Eulerian (ALE) methods
 Lambert's law 222
 Landau–Levich theory of film deposition 279–80, 583, 677, 678
 Langmuir adsorption isotherm 108
 Langmuir constant 107, 108, 115, 498
 Langmuir–Blodgett films 11, 682–3, 682
 applications 682
 deposition 503, 683, 709
 microstructure control 683
 Langmuir–Knudsen equation 196
 Langmuir–von Szyszkowski equation 107, 108, 498
 Laplace equation, *see* Young–Laplace equation
 Laser–Doppler anemometry (LDA), *see* Laser–Doppler velocimetry
 Laser–Doppler velocimetry 87, 233–6, 233, 490
 applications to coating flows 234–5, 490
 Laser scanners 230–2, 230, 232, 735
 Laser strobe 238
 Latex 140–1
 as additive to alter rheology 213
 coalescence 140
 preparation 140
 stability 141
 Latex coatings 160–75
 drying 200
 effective volume fraction in 163, 164
 elastic response 167–9
 elongational viscosity 169–73, 172
 formulation 141, 160–1, 161
 leveling of 167–9
 particle size effect on rheology 161, 163, 163, 164
 roll sputter 169–73, 171
 thickener effect on rheology 161–4, 173
 transient structure formation and rheology 167, 167, 168, 169, 176
 viscosity at high shear rates 161–2, 162
 viscosity at low shear rates 164–7, 163
 Leveling of coated films 8, 53, 54, 159–60, 184–9, 185, 186, 724–6
 capillary-pressure driving force 54, 186
 film-thickness effect 161
 inverted films 188
 mechanisms 185–6
 Newtonian liquids 185–8
 non-Newtonian liquids 167–9, 188, 339
 surface-tension gradient effects 188–9
 time requirements 186–7, 188, 725
 uneven substrates 724–6
 viscosity effect 162
see also Spin coating
 Lid-driven cavity 580, 654
 cellular flow 655
 stability of flow 654–5
 Light-guide rod collector 231
 Light-sheet illumination 238
 Limit points, *see* Turning points
 Linear equations, solution of 317–19
 Linear stability analysis 280–92, 300, 321–7, 505–7, 654–5
 finite-element method 321–7
 method of normal modes 283, 505
 quasi-static condensation method 325
 three-dimensional disturbances 323–7, 654–5
 two-dimensional disturbances 321–3
see also Orr–Sommerfeld equation
 Liquid film
 fate after coating 183–205, 183
 healing of irregularities 184–9, 185, 186, 194–6
 non-wetting 192, 196
 rupture 189, 191, 192–4, 195
see also Film flow down incline; Leveling; Thin liquid film
 Lodyne S-103 117, 123
 London–van der Waals dispersion forces 44, 107
 Lot size, of coated product 762
 LU factorization 317, 319, 320, 328
 Lubrication approximation 93, 94, 259, 376, 603, 693, 723
 Lubrication flows 30, 258–61, 542–3
 Lubrication theory 258–62, 542–3, 582–4, 603–4
 boundary conditions 260, 262, 553–4, 583
 derivation with domain perturbation method 265–7
 failure of ad-hoc boundary conditions in 264, 270–1, 554
 for flow in liquid film 274
 for flow between solid surfaces 259–60, 542–3
 requirement for success 260, 264
 two-dimensional 376, 377
see also Reynolds equation
 Magnetic assist 404, 414
 Manifold design, *see* Coathanger manifold; Coating dies; Jet fountain applicator; T-manifold
 Mapping 308
 iso-parametric 305, 349
 sub-parametric 305, 313
 Marangoni drying 674
 Marangoni elasticity 111
 Marangoni flow 38, 41–3, 54–62, 103, 104, 192, 477, 699, 700, 718–20, 723–4
 Marangoni instability 198, 718–20
 Marangoni number 198, 719, 720
 Marker-and-cell (MAC) method 344
 Mass transfer 196–7, 688–91, 695–91, 695–8, 695–8, 713
 Mass transfer coefficient 197, 690, 696
 Mass transfer models 197, 690, 696
 Material function 138, 142
 Matrix solver 317–19
 direct 317–18
 iterative 318–19
 Maximum bubble pressure method 114
 Maxwell model 155, 156, 339
 Membranes, *see* Plates
 Membrane coating 10, 599, 600, 601, 613–17
 air entrainment 616
 coating uniformity 616–17
 configuration and components 600, 614
 defects 616
 elastohydrodynamic action 601, 614–15
 finite-element analysis 615–16
 minimum film thickness 617
 operating response 615–16, 615
 pool-flow instabilities 616
 shearing action 613
 Meniscus
 advancing in capillary tube 72–3
 asymptotically planar, against flat plate 50–2, 51, 67–8, 68
 in coating bead 73–4, 73, 74, 402, 524
 dynamic 68–9

- hydrodynamic bending near dynamic wetting line 71, 77
- between parallel plates 48–52, 48, 53
- quasi-static 50
- rise in capillary tube 66–7, 67, 112
- static 64, 66–8
- for tape entering pool 69, 75
- Meniscus roll coating 11, 540, 573–97
- applications 540
- back jet 588, 589, 590–2, 590, 591
- bead break-up 595
- bead collapse 596
- bubble generation 596
- capillary action 574
- double eddy structure 585, 586
- feed condition effect 586–90
- finite-element analysis 584–5, 584, 585
- film thickness ratio 584, 585, 587
- flow structure 576–85
- flow transitions 585–92
- flow visualization 575, 576–7, 578, 579
- lubrication theory 582–3
- parameter ranges 592–5, 592
- pressure distribution 580, 584, 587
- pressure field transformation 585–6
- small-flux model 580–4
- snaking fluid stream 574, 575, 581, 588, 590, 591, 592
- start-up 573–4
- streamline pattern 580, 581, 586
- ultra-starved inlet 588, 592
- zero-flux model 580
- Mesh 308
- boundary conforming 299, 308
 - two-level 340, 692–3
 - unstructured 349
- Mesh generation 308–15, 341–6
- adaptive 313
 - algebraic 308–11
 - elliptic, or differential 311–15
 - generalized algebraic 309–10
 - Lagrangian pseudo-solid 315
- Mesh orthogonality 312
- Mesh refinement 72, 313, 692–3
- Mesh smoothness 312
- Methyl methacrylate 140
- Micelles 101, 102, 496, 499–501, 500, 508–9, 509
- kinetics of formation 499–501
- Microscopes 237
- mono zoom 242
- Microstructure of coatings 11, 674
- control in dip coating 682–7
 - control through drying 703
 - see also* Langmuir–Blodgett films; Sol-gel films
- Microwave absorption
- for measuring film thickness 223–4
 - for measuring moisture content 223
- Misting 157, 643
- Mixed-mapping method 313
- Modulus
- complex 145
 - dilatational surface elasticity 110
 - dynamic 146
 - loss 145, 152
 - shear 604
 - storage 145, 152
- see also* Young's modulus
- Moiré technique 227–30, 228, 229
- Moisture content, measurement with microwave absorption 223
- Molecular forces 43, 65, 190, 193
- Molecular-kinetic theory 76, 80, 93
- Molecular-rate process, *see* Dynamic wetting
- Momentum equations 305, 307
- see also* Conservation laws; Navier–Stokes equations
- Momentum number 380
- Mottle 197, 221, 458
- Mudcracking 201
- Multidimensional scaling method 217
- Multilayer coating
- choice of surface tensions 106, 458
 - edge control 520–1, 525
 - leveling 189
 - surfactant optimization 130–3, 520–1
- see also* Coating dies; Curtain coating; Film flow down incline; Slide coating; Tensioned-web slot coating
- Multiphase flow 20, 20
- Nahme number 382
- Navier–Stokes equation 24, 25–6, 93, 259, 265, 269, 302, 304, 315, 432, 505, 605, 607, 654, 691–3
- Navier's slip boundary condition 302
- Nekal BX 117, 123, 127
- Neural networks 744
- Neutral curve for stability 284, 556
- Newtonian fluid 24, 154, 157, 158, 185, 188, 235, 288, 603
- Newton's iteration method 306, 316–17, 319, 320, 327, 340, 350
- basin of attraction 319
 - derivation of Jacobian matrix 316
- Niaproof #4 117, 121, 122, 123, 127
- Nodes 304, 308
- spacing 309, 312
- Non-Newtonian fluids 6, 7, 85, 89, 137, 138, 158, 289, 445, 668–9
- examples 149–53
 - in finite-element computations 337–9
- Nonwetting liquid 191
- Normal stresses 142, 374, 380–1, 661–2
- Normal stress coefficient 144, 381
- Normal stress number 381
- Normal vector to surface 34
- No-slip condition 35, 47, 60, 61, 71, 302
- Nucleation, of dry patches 189–90, 191
- Numerical methods, *see* Computational methods
- Nusselt film flow 281–2, 431, 678
- Original equipment manufacturer (OEM) coatings 138, 139, 141–2, 159, 175–7, 177
- formulation 141–2
 - rheological response 175–7, 177
- Olin 10G 117, 123, 124, 124
- Operability analysis
- three-dimensional disturbances 328
 - two-dimensional disturbances 327
- Operability window, *see* Coating window
- Operations model 762, 765–6, 766
- Optical sectioning technique 239–42, 240, 241
- Optimization 11, 215, 333–4, 736–8, 741–66
- algorithms 741–4
 - applications 744–66
 - constraints 741
 - criteria 741
 - macro 738
 - micro 737
 - of operability latitude 334
 - of shape of coating device 334
- Orange peel 198, 718
- Ordinary differential equations system (ODES) 331
- Orr–Sommerfeld equation 283, 448–9, 503, 505, 506, 505–7

- Oscillating jet method for measuring dynamic surface tension 112–13, 118–19
- Oscillatory shear flow 144, 151
- Overflow cell for measuring dynamic surface tension 114–115, 513–19
- cell design 513
- computational analysis 514–19
- flow structure 515
- Paint, *see* Latex coating
- Paper coating process 138–9, 637–69
- air entrapment in pores 650
- compressibility effects 649, 650
- liquid penetration into pores 175, 652
- non-Newtonian effects 659–63
- porosity effects 649, 650
- relaxation after application 666
- roughness effects 649, 650
- swelling 652
- see also* High-speed blade coating
- Paper coatings 141, 175, 638, 640
- formulation 141, 640, 659, 664
- rheology 175, 659–60, 661–3, 666
- runnability 175, 663
- structure formation and break-up 175, 660, 662
- transient rheological response 176, 660
- Parallel-plate rheometer 147
- Parameter optimization 741
- Particle defects 458
- Particle image velocimetry (PIV) 236, 576, 580, 582
- Particle-in-cell (PIC) method 343, 349
- Particle methods, computational 349–50
- Particle orientation 665
- Particle tracking 238, 242, 576, 579
- Péclet number 328
- Peeling of coating 199
- Penalty function formulation 307
- Perturbation methods, *see*
- Asymptotic methods; Domain perturbation methods; Regular perturbation methods; Singular perturbation methods
- Petrov–Galerkin method 306
- Phase inversion method 198
- Phase separation in coatings 198–9, 199, 717–18
- Phonographing, *see* Ribbing
- Photolithographic process 709, 710
- Photography 237, 238
- high-speed 174, 237
- Picard iteration, *see* Trial method
- PID control system 740
- Pigment 140
- chemical pretreatment 173–4
- extender 141
- Pilot coating equipment 211–13, 211, 212
- Pinholes 194
- Pinning of wetting line, *see* Static wetting line
- Pipe flow, pressure drop 26
- Pivoting 317
- Plates 605–7
- bending stiffness 606
- clamping conditions 607
- contact between 607
- finite-element analysis 606–7
- linear elastic theory 605–7
- Plug flow 30, 31
- PMMA solution 715, 715
- Poiseuille flow 26–7, 29, 30, 582
- Poisson equation 313
- Poisson's ratio 201, 604
- Poly(ethylene oxide) thickeners 164, 173
- Poly(ethylene terephthalate) 69, 81, 81, 82, 83, 84, 87, 87, 88, 88, 89, 92, 484
- Polymer additives for enhanced coating performance 137, 160–77, 213, 448
- Polymer dispersions 141–2, 175–7
- Polymer melts, dynamic uniaxial extensional viscosity 150
- Polymer solutions
- dynamic mechanical analysis 152
 - elastic effects 564
 - rheology during gelation 145
 - shear-thinning 564, 717
- Polymeric resist films 710
- Polymers
- amorphous 152
 - cross-linked 152
 - grafted 140
 - water reducible 141–2, 175–7
 - water-soluble 140, 163–7, 173–5
- Polystyrene solutions 730–1, 731
- Poly(vinyl alcohol) 165, 452, 664
- Polyurethane based, aqueous dispersion (PURAD) 176–7, 178
- Potential flow 29
- Powder coating 189, 189
- Power-law index 154, 213, 375
- Power-law liquids 375, 376, 384, 385
- Power-law model 154, 337, 375
- Preconditioning of matrix 318–19
- Precursor film 65, 77
- Predictor-corrector scheme 319, 332
- Pre-metered coating methods 9, 399–536
- versus self-metered methods 675–7
- Premicelles 499
- Pressure–Poisson equation (PPE) formulation 304, 307–8, 319, 333
- Pressurized pond coater 643, 645–6
- air entrainment 646, 656, 659
- cellular flow 655–6, 657
- centrifugal instabilities 646, 655–6
- see also* Short-dwell coater
- Priming layer 12
- Primitive-variable formulation 304–7
- Process capability 739
- Process control, *see* Control
- Process optimization, *see* Optimization
- Product
- application 3
 - design 333–4
 - fabrication 737, 738
 - specifications 739
 - unit-cost minimization 761–6, 765
- Profilometry 226–7
- Property parameter 467
- Puddle coater 638, 638, 641, 642–3, 642, 644
- air entrainment 642
 - misting 643
 - one-sided 642
 - two-sided 642, 644
- II-theorem, *see* Buckingham theorem
- Quality assessment 216
- Quality control 217
- Quality index (QI) 220
- Quasi-Newton methods 316
- Radial striations 718–20
- Rakelines, *see* Ribbing
- Raoult's law 691
- Rate of deformation, *see* Rate of strain
- Rate of strain 142
- in coating processes 160, 337, 565, 640, 660, 662
 - extensional 144
 - shear 143
- Rate-of-strain tensor 24, 154
- Rayleigh instabilities 159
- Rayleigh–Taylor instability 342, 483

- Real-time imaging 239
 Recirculation, or flow separation
 defects generated by 546,
 755
 Refractive index 233, 686–7, **686**
 Regular perturbation methods
 254–5, **255**, 268, 282, 285
 Relaxation time 153, 155, 660
 for micellization 500
 Repellency spots 458
 see also De-wetting
 Residence time 385
 Resins, *see* Water-reducible resin
 coatings
 Reverse roll coating 10, 539, 540,
 547, 559–67
 air entrainment 566
 applications 540
 cascade instability 563
 coating window 566, **567**
 configurations 541
 dynamic wetting line position
 560, **561**
 failure modes 563–5, **563–6**
 finite-element analysis 561
 lubrication-flow analysis
 559–60
 metered film thickness 562, **562**
 metering gap flow 559–63, **560**
 nip-transfer flow 565–6
 non-Newtonian effects 563, 564,
 565
 pressure profiles 565
 primary flows 540, **542**
 ribbing instability 563, 565
 Reynolds equation 260, 341, 380,
 542, 565, 583, 603, 605, 607,
 609, 621
 derivation of 259–60
 Reynolds number 27, 28, 30, 48, 49,
 185, 197, 284, 285, 287, 289,
 303, 326, 406, 439, 467, 473,
 481, 507, 510, 511, 543, 654,
 721, 758
 Reynolds transport theorem 20, 23,
 33
 Rezoning 347
 Rheology 137–79
 see also Rheometry
 Rheometers, *see* Capillary rheometer;
 Cone-and-plate rheometer;
 Couette rheometer; Parallel-plate
 rheometer
 Rheometric flows 142–9
 Rheometry 7, 137, 662
 simulation of deformations in
 coating processes 160, 662
 see also Dynamic mechanical
 measurements
- Ribbing 157, 158, **158**, 159, 323–7,
 418, 447–8, 480, 544–6, **544**,
 549–52, 556–8, **557**, 563, **566**, 613
 critical capillary number 158,
 545, 549, 556–7, **557**
 effect of divergence of flow
 channel 549
 elongational viscosity effect 159,
 557–8
 frequency as a function of
 capillary number 158
 inertial mechanism for 545–6
 interface profiling 227
 interfacial force balance 544–5,
 544, 551
 linear finite-element stability
 analysis 326, 420, 448
 lubrication theory 326
 mechanisms 157–8, 544–6, 563
 with static wetting line 549
 string to eliminate 556–7
 surfactant effects 447
 three-dimensional analysis for
 large amplitudes 557, **558**
 viscoelastic effects 410
 viscous mechanism 545
 see also Forward roll coating; Slide
 coating
 Rising film flow 271–80, **271**,
 678–80
 domain perturbation analysis
 271–80
 film profile equation 275, 278
 stability 547, 566
 see also Dip coating
 Rivulets 418, 595
 Robin boundary condition 303
 Robustness of coating process 751,
 759
 Roll
 applicator 540, **541**, 638
 back-up 540, **541**
 cantilevered 577, **577**
 fountain 540, **541**
 impression 540, **541**
 metering 540, **541**
 transparent 243, 416, 578
 Roll applicators
 for high-speed paper coating 641,
 642, 643–4
 limitations 644
 for paints (mat roll) 138
 Roll coating 539, 540, **541**
 air entrainment 546
 auxiliary flows 542
 common configurations 539–42,
 541
 dampening of inlet disturbances
 546–7
- dip coating in 547, 566, 679
 falling film flow 271
 feed systems 540, **541**
 gap setting 577, 578
 primary flows 540–2, **542**
 sensitivity to process
 perturbations 546
 scraping, or wiping 579, 612
 starvation 546
see also Forward roll coating;
 Meniscus roll coating; Reverse
 roll coating; Squeeze roll
 coating; Tension-web roll
 coating
 Rotating film flow
 inertia-driven ribbing instability
 545
 Rotating flow, stability 546
 Rubber
 deformable roll cover 341
 dynamic mechanical analysis 152
 Rubbery regime 153
 Runnability 175, 663
 Sakiadis boundary layer 480, 484,
 485–6, **488**, 696, 748
 Sagging 188, 450
 Schmidt number 197, 497
 Schur–Wielandt deflation 322
 Scraper blade 579
 see also Doctor blade
 Scratches 663, 664
 Screening experiments 215
 Search methods 742
 Segregated solver approach 319
 Self-metered coating methods 10,
 537–672
 versus pre-metered methods 574,
 637, 675–7
 Sensitivity analysis
 three-dimensional disturbances
 330
 two-dimensional disturbances
 329–30
 Sensors 213–14
 Shape factor 374, 375, 754
 Shear-thinning behavior 24, **151**,
 154, **165**, **166**, 337, 375, **376**
 Shell theory, cylindrical 605–7
 in finite-element method 341
 Sherwood number 197
 Short-dwell coater 639, 641, **643**
 defects 646
 maximum speed 646
 see also Pressurized pond coater
 Silicone oils 579, 579
 Simple-line interface calculation
 (SLIC) 343
 Simplex method 740, **742**, 743

- Singular points, *see* Critical points
 Singular perturbation methods
 255–6, 256, 265–71, 272
 Skinning 197, 681
 Skips 663
 Slide coating 9, 427–62, 519–31
 air entrainment 446–7
 application angle 246, 430–1, 430
 applicability 428
 approximate force-balance
 analysis 433–40
 barring 448–51
 bead 450–1, 432, 433
 bead break-up 74, 546
 bead oscillations 451
 bead vacuum effect 245–6, 428
 bleeding, or weeping 444
 coating gap 431
 coating window 330, 331, 451–3,
 451, 452, 453
 critical point tracking 328
 die-lip design and its effects 246,
 431–2, 448
 die-lip edge sharpness 431–2
 dynamics, or frequency response
 329, 454–6, 455, 479, 480,
 529–31, 530
 flow 314, 314, 443, 521–31, 521
 flow visualization 243–6, 243, 440
 free-surface profiling 227
 finite-element mesh 314
 largest gap 73
 linear finite-element stability
 analysis 323, 324, 326
 maximum bead vacuum, or
 pressure difference 328
 minimum film thickness, or low-
 flow limit 246, 437–8, 438,
 446–7
 multilayer 427, 445
 non-Newtonian effects 445
 operating limits 328, 445–53
 quality window 330, 331
 ribbing 326, 328, 447–8, 528
 sensitivity to disturbances 453–6
 slide inclination 431
 slide length 431
 slot-exit design 244–5, 428–30,
 429
 standing waves 432
 static wetting line position 431–2
 steady-state operation 432–45,
 521–9
 streaks 429, 456
 surfactant effects 445, 521–31
 surface-age time scales in 103,
 103
 three-phase zone 87
 vacuum box 432
 viscosity stratification 328
 velocity field near dynamic wetting
 line 336
 vortex formation, or recirculating
 flow 429, 439–43, 440
 wetting meniscus in 73, 74, 74
 see also Film flow down an incline
 Slip model, *see* Dynamic wetting;
 Navier's slip boundary
 condition
 Slot coating 9, 401–26, 401
 air entrainment 422
 applications 402
 barring 418, 421
 critical point tracking 328
 coating window 403, 417, 419,
 420, 421
 die-lip design 403–4, 404, 406
 die-lip edge sharpness 404, 422
 dynamic behavior 421
 equipment 403–5
 flow regimes 407
 flow visualization 414–16
 maximum gap 419
 meniscus shapes 406, 408–10,
 677
 multilayer 402, 404–5, 405, 415
 numerical simulations 411–13,
 411, 412
 operating modes 409
 operating parameters 406–7, 677
 operating limits 328, 408–10,
 416–20
 pressure control with vacuum
 box 404, 412
 pressure distribution 408–9, 412
 recirculating flow 410, 412, 413,
 415
 ribbing instability 410, 418, 420
 rivulets 418
 sensitivity to small disturbances
 420
 starvation, or low-flow limit 418,
 419
 steady-state operation 405–16
 streaks 421
 surfactant effects 503
 versus dip coating 676–7, 676
 viscoelastic effects 411, 415
 weeping 418
 see also Tensioned-web slot
 coating
 Slot flow 376–8
 pressure drop 29
 Slurry coatings 198
 Soap film, axisymmetric 40
 Sodium dodecyl sulfate (SDS) 117,
 121, 123, 128, 130, 506, 516–17,
 516–18, 522, 524
 Sol-gel film dip coating 680–1,
 684–7, 685, 688–93
 asymptotic analysis for single-
 component solvent 693–4
 compaction 686
 computational analysis 694–703
 single-phase flow 694–7
 two-phase flow 698–703
 evaporation effects 684–7,
 693–703
 film thickness 686
 film profiles 685, 687–9, 687, 689,
 702
 flow and concentration fields
 696–8, 701
 gellation 685, 700
 mass transfer model 696–7
 microstructure control via drying
 703
 microstructure formation 684–7,
 685, 700–2
 multi-component systems
 694–703, 695–9, 701–2
 ribbing-like instability 695
 shear rates 701, 702
 Sol-gel films 11, 683–8
 applications 684
 drying stresses 682
 formulation 684
 polymerization 684
 pore structure 686
 refractive index versus withdrawal
 speed 686–7, 686
 SOLA-VOF method 344
 Solidification 13
 Solvent evaporation 684, 713–17,
 728–30
 Solvents
 multiple 684
 organic 141
 Spattering 169, 171
 Spectral element method 351
 Spectral methods 283, 339, 351
 Spin coating 11, 709–34, 709
 air flow effects 713, 721
 air flow instabilities 721
 air flow visualization 721
 applications 709, 710
 circumferential waves 719
 colloidal suspensions 716,
 718–20, 720
 concentration-dependent viscosity
 effects 716–17
 defects 717–21
 deposition 710
 diffusive transport 713
 edge effects 713
 evaporation 710, 711, 713–17,
 728–9

- film profile evolution 712, 728, 730
final film thickness 714, 715
mass transfer 713, 714
Marangoni effect 718–20, 723–4
Meyerhofer's analysis 714–16
non-Newtonian effects 712, 716–17
operability diagram 719
planarization 721–4, 725, 726, 727–9, 729, 731
processing stages 710–11
spin-off 710
spin-up 710
stability 717–21
surfactant effects 720, 721
thinness of coatings 709
uneven substrates 721–31, 722
 leveling after spinning 724–6
 leveling during spinning 726–31
 rectangular bump 728, 730
 rectangular trench 724, 724, 725
uniformity of coatings 709, 712–13, 716–17
Spines 309
Splice passage 330, 431, 456, 480, 745
Spray coating 12, 674
Spreading 105–6, 458, 502
 halting at corner 66
 see also Dynamic wetting; Gibbs' inequality
Spreading coefficient 106
Spreading pressure 107
Sputtering 3
Squeeze-roll coating 10, 600, 601, 620–7
 dry contact limit 621, 622, 624
elastohydrodynamic action 602, 620
elastic roll models 604–5, 621–2
film-split patterns 602, 603
gap profiles 623, 624
metered coating thickness 625, 626
nip adjustment or loading 620
nip mechanics 620–2
operability limits 626–7
pressure profiles 623, 624
rigid-roll limit 621, 624
sensitivity 627
viscoelastic roll models 622
Stability 280–1
 spatial 283
 temporal 283
 see also Linear stability analysis
Stalagmites 665, 666
Starry night defect 201
Start-up of coating process 330, 402, 430, 456, 490, 573–4
Static contact angle 45, 64–5, 75
 see also Contact angle; Gibbs' inequality
Static surface tension 99–100, 107–8, 131
 measurement methods 111–16
for selected surfactants in water and gelatin 120–3, 121
Static wetting 7, 63, 64–8
 finite-element analysis 334–5
 with flow 64, 68
Static wetting line 9, 66–8, 744
mobility 66
of interface between miscible fluids 335
pinning at corner 66, 404, 422, 431–2, 467, 552
Statistical clustering analysis 743–4
Statistical experimental design (SED) 214–16, 742
Statistical process control 739
Steady-shear flow 142–4
Step-in-strain flow 145
Step-in-strain-rate flow 146
Stick-slip behavior, *see* Dynamic wetting
Stochastic fluctuations 741, 756
Stock of coated material, flow through 762–3, 763
Stokes flow 277, 580, 582, 584
Stokes number 53, 303, 380
Stormer viscometer 149, 162, 164
Strain hardening 150
Streaks, or streaklines 219, 421, 429, 456, 471, 547, 552, 608, 613, 663, 666, 755
Streamlined finite-element method 309, 349
Streamline visualization 238–40
Stress 23–4, 142
 anisotropic, at interface 43
 interfacial 36
 normal 142, 374, 380–1, 661–2
 shear 142, 145, 155
 yield 155, 660
Stress buildup in coatings 8, 199–201, 681–2
 defects from 199
Stress growth function 145, 153
Stress overshoot 153
Stress ratio 381
Stress tensor 23, 24
Striations, *see* Bandedness; Radial striations
Stroboscope 238
Styrene 140
Subbing layer 12
 swelling of 65
Subdomain 304
Substrate 12
 air supported 480
 primed 12
 subbed 12
 uneven 721–31
 wavy 480
Successive overrelaxation (SOR) 319
Successive substitution, *see* Trial method
Surface acoustic wave (SAW) technique 688
Surface-active agents, *see* Surfactants
Surface age 120, 124, 515–16
 for surfactants in water 129
Surface compression 103, 111, 497
Surface convection 497
Surface diffusion 497
Surface dilation, or expansion 103, 111, 115, 497
Surface elasticity, *see* Gibbs' surface elasticity
Surface elasticity number 498, 511
Surface heterogeneity 65
Surface porosity 65
Surface pressure 683
Surface profilometry 226–7
 mechanical 226
 optical 227
Surface roughness 65, 85, 89
Surface tension 38, 44, 51–4, 54, 55, 56, 105, 106
 concentration dependence 41, 56–8, 108, 120–3, 122, 123, 498, 692, 695
 in interfacial stress tensor 38
 measurement techniques 111–16
 of mixtures 692
 molecular contributions to 106–7
 temperature dependence 41, 54, 59
 see also Dynamic surface tension; Static surface tension
Surface-tension-gradient driven flow, *see* Marangoni flows
Surface tension gradients 41–3, 55, 57, 59, 191, 198, 531, 681
Surface topography measurement 226–32
Surface traction vector 23
Surface viscosity, dilational 110–11, 504
Surfactant actions 495–533
 coating aid for defect control 104, 495

- Surfactant actions (*contd*)
 in coating flows 42, 101, 102–3,
 103, 496–501, 496, 501–5,
 519–21, 521
 at dynamic wetting lines 525, 526
 finite-element analysis 339–40,
 504–5
 immobilization of interface 42
 influence on product properties
 104–5, 495
 promotion of wetting and
 spreading 99, 502
 retardation of interfacial flow 56
 stabilization of coating flows
 505–13
 stabilization of coating solutions
 104, 495
 theory 496–501
 time scales, characteristic 99, 103,
 124–8, 508, 509, 514–15, 522–8
see also Surfactants
- Surfactant modified water-soluble polymers 173–5
- Surfactants 7, 99–136, 289, 445,
 494–536, 682–3
 adsorption at interface 99, 101,
 107–8, 498, 523–4
 adsorption density 109
 adsorption isotherm 107
 aggregate structures 101, 102
 classification 101, 116
 convective diffusion 339–40,
 497–8
 convective redistribution 42
 diffusion 108–10, 508
 diffusion-controlled adsorption
 108–10, 125
 in emulsion polymerization of
 latex 140, 161
 excess surface concentration 41,
 107, 497
 inventory in solution and micelles
 496, 499–501, 500
 patents 105
 properties of 101–2, 116, 506, 522
 recruitment depth 506
 selection criteria 128–30
see also Critical micelle
 concentration; Langmuir–
 Blodgett films; Micelles;
 Surface elasticity
- Swift–Steiber conditions 262–3, 270
- T-manifold 369, 380
 design 383–6, 386
- Tape plunging into pool 69, 75
 air entrainment 86–9, 87, 88, 446
 dynamic contact angle 69, 69, 75,
 75, 81–4
- meniscus 69, 75
- Teapot effect 467–71
 deflection of liquid stream 467,
 470
 finite-element analysis 469, 470,
 471
 fixed-grid simulations 344
 hydrodynamic hysteresis 467
 lip design to prevent 471
- Tensioned-web roll coating 10, 600,
 601, 617–18
 elastohydrodynamic action 601,
 617
 film-split patterns 602
 finite-element analysis 310, 311
 foil-bearing theory 617
 forward mode 310, 311, 600, 617
 operating limits 618
 reverse mode 617
 reverse wiping with complete liquid
 transfer 618
 rolling bank 311
 stability 618
 web instabilities 617
- Tensioned-web slot coating 10, 405,
 600, 601, 618–20
 control of coating bead stability
 620
 die-lip design 619
 elastohydrodynamic action 601,
 619
 multilayer configuration 619
- Texapon K-12 117, 122, 123, 123,
 128
- Thermocapillarity 59, 59, 289
- Thick edges 457
- Thickeners 163–9, 172–5, 213, 740
see also Latex coating
- Thin air film 87, 92, 473, 483, 658
 finite-element analysis 336–7
 lubrication-flow model 93–6
 molecular forces 71–2
 stability and collapse 45, 483
see also Air entrainment
- Thin liquid film 43–5, 44
 drying 681
 left behind after dewetting 194
 molecular forces 71–2
 overlap of interfacial regions 44
 stability and break-up 45, 192–4
- Thixotropy 146, 660
- Titanium dioxide 141
- Total linearization method (TLM)
 317
- Transfinite interpolation 310–11
- Transient analysis 330–4
 implicit scheme 331
 large amplitudes 301
 linearized equation set 329
- semi-implicit scheme 333
 time discretization 332, 348
 time-step size control 332
- Transport theorem 32, 33
see also Reynolds transport
 theorem
- Traube's Rule 42
- Trial method 315–16, 350
- Triangulation method 227
- Triton 770 116, 123
- Triton X-100 121
- Triton X-102 117, 121
- Triton X-200 117, 123
- Turning points 320, 323, 327, 338,
 470, 471
- Upwinding 306, 338
- Uniformity index 383
- Van Karman similarity solution
 714, 715
- Video techniques 237
 high-speed 237, 576, 579
- Vinyl acetate 120
- Viscoelasticity 24, 66, 167–9, 175,
 188, 660, 667, 669
 constitutive models 154
 deformable roll covers 341
 die-internal flows 374, 381
 in finite-element computations
 338–9
 linear regime 144
- Viscosity 24, 143
 complex 144
 concentration-dependent 756
 dynamic 144–5
 elongational 146, 150, 151,
 169–73
 planar elongational 144
 shear 143
 temperature dependent 382, 756
 uniaxial elongational 144, 150,
 178–9
- Viscous number 380
- Volume factor 627
- Volume-of-fluid (VOF) method 343,
 344
- Vortex instabilities 566, 567
- Vortex methods 350
- Wall shear stress 375, 389, 395,
 753–5, 754
- Water bell 477
- Water retention 664, 665, 666, 668
- Water-reducible resin coatings
 141–2, 175
 formulation 141–2
 rheological response 175–7
- Wave instability 285

- Wave number 283
- Waves
- damped, with surfactants 111, 502, 505–13
 - interfacial 290
 - solitary 289
 - standing 278, 280, 432
- Web cleaning 12
- Web handling 12
- Web instabilities 617
- Weber number 48, 49, 64, 70, 73, 75, 85, 86, 90, 93, 326, 477–8, 543
- Wedge, flow in 245
- Weeping
- paper coating 175, 665–6
 - slide coating 444
 - slot coating 418
- Weissenberg number 153
- Wetting 63–97, 105–6
- complete 64, 105
 - kinetics 658
 - maximum speed of 86, 641, 658
 - partial 105
 - see also* Air entrainment; Dynamic wetting; Static wetting
- Wetting lines 63, 64
- in computational analysis 334–7
 - stationary with flow 64, 68
 - see also* Dynamic wetting line; Static wetting line
- Wicking 66–7
- Wilhelmy plate 111–12, 119–20, 533, 683
- Winkler approximation 605
- Wire coating, *see* Fiber coating
- WFL equation 382
- X-ray fluorescence (XRF) 224–5, 224, 225
- Yield stress 155, 376, 660
- Young–Laplace equation 29, 38, 64–9, 77, 112, 114
- disjoining pressure contribution to 44
- Young's equation 64, 70, 105, 106, 526
- Young's modulus 145, 201, 604

CONTROL AND OPTIMIZATION OF COATING PROCESSES

15

Peter M. Schweizer

15.1 INTRODUCTION – THE IMPORTANCE OF CONTROL AND OPTIMIZATION

One of the focal points of many quality improvement programs is the concept of prevention. Within the scope of coating, prevention refers to ‘do it right the first time’ by avoiding defects which would have to be removed at a later stage of the manufacturing process. For example, producing coating solutions free of bubbles and other unwanted particles would make it unnecessary to install excessive and costly de-gassing and filtering systems. Furthermore, the finishing operation would be more efficient because there would be no need to cut out spot defects.

In its purest sense, the manufacturing philosophy of prevention excludes the use of traditional process control with feed-back loops, because, as is schematically shown in Fig. 15.1, such

control systems are only necessary, if something went wrong upstream in the process.

The use of feed-back control is most meaningful during the learning and development phase of a new process. One could even postulate that the purpose of feed-back control is ‘to put itself out of business’ by constantly climbing up along the learning curve, and by changing know-how into know-why, thereby approaching the philosophy of prevention. An example is a laser scanner installed downstream from the coating point. In its traditional use, it is an element of a feed-back control loop. However, it can also be used to help eliminate defect-generating processes upstream from the coating point by searching for the problem causes every time the scanner signal exceeds its threshold level. In this fashion, fewer and fewer defects will occur until, ideally, there will no longer be a need for a scanner on the coating machine.

An alternative control algorithm which is more in line with the concept of prevention is feed-forward control. In contrast to feed-back control where the effect of a disturbance is measured downstream from the process and the corrective action is fed back upstream to manipulate a suitable variable, the disturbance in feed-forward control is detected upstream from the process, and the corrective action is imposed on a suitable variable also upstream, so as to avoid a disruption of the process by the disturbance, see schematic diagram in Fig. 15.2.

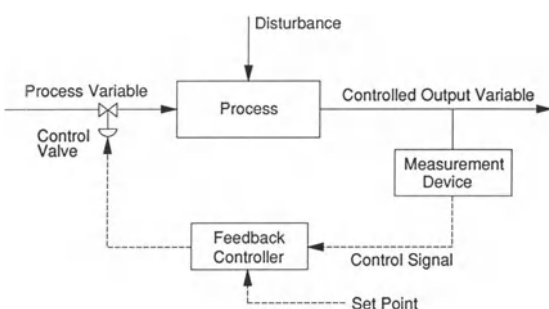


Figure 15.1 Schematic diagram of feedback control.

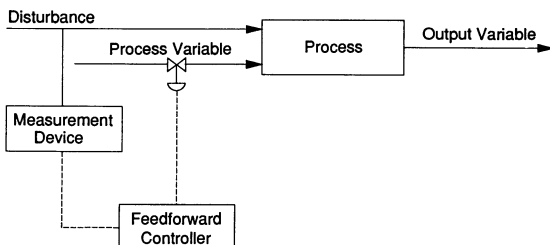


Figure 15.2 Schematic diagram of feedforward control.

Feed-forward control may be encountered in the fluid preparation and handling system of a coating plant. Here, vessels, delivery lines, pumps, filter housings, etc. are often cleaned with automated CIP systems (CIP = Cleaning In Place). In the photographic industry, for example, cleaning efficiency is high, if the temperature of the detergent solution is kept at an elevated level, thus requiring a recirculation loop which comprises a heat exchanger and a reservoir. The challenge for the control loop is to maintain a constant detergent temperature under conditions of randomly and suddenly changing detergent flow rate, depending on the cleaning needs throughout the system. Upon increased cleaning demand, warm detergent from the reservoir is mixed with fresh, cold detergent, and heated by the heat exchanger before entering the system. A temporary drop in detergent temperature after the heat exchanger can now be prevented, if a temperature sensor installed upstream from the heat exchanger detects the forthcoming load change for the heat exchanger and triggers an increase of the heat source supplied to the heat exchanger. The amount of source increase is controlled by a second temperature sensor installed downstream from the heat exchanger, which compares the detergent temperature with a given set point.

Process control in feed-back or feed-forward mode is justified in many instances, for example where process sensitivity to small changes of parameters is very high. In addition, prevention can rarely be applied to its full extent, because many processes are too complex to be perfectly optimized. Important examples of controlled

parameters, where feed-back or feed-forward loops have reached a high degree of sophistication, include the web speed and flow rate in premetered coating processes, as well as the speed ratio between two rolls and the load on the doctoring blade in self-metered coating operations. The aim of control is to maintain variations of relevant process parameters at 'acceptable' levels. This will result in significant benefits such as more consistent product uniformity, increased productivity, raw material savings, timely and accurate process information, improved operator and management decision tools, etc. (Swain 1985; Shapiro 1993).

In contrast to process control, optimization provides a framework for implementing the concept of prevention by designing effects of parameter variations out of the system. The purpose of process optimization is to determine (optimize) those operating conditions (independent process parameters, p_i) which lead to extreme values (maxima or minima) of selected dependent variables x_j . With regard to coating processes, one might ask to set values for the viscosity, surface tension, roll diameters, roll separation, roll speed ratio, etc. of a roll coating operation such as to maximize the web speed without entraining excessive air, or such as to minimize the level of a particular defect, ribbing lines, for example (see Chapter 12).

As will be shown below, process optimization can be carried out whether or not a functional relationship between independent process parameters and dependent variables is known. However, optimization works particularly well if the process can be represented by one or several analytical expressions which are either derived from theoretical models, or from empirical fits to experimental data, i.e., $x_j = f(p_i), j = 1, 2 \dots, m, i = 1, 2, \dots, n$. For the simple case of $j = 1$, the optimum value for the parameter p_k , which will lead to an extreme value of x , can be found by forcing

$$\frac{\partial x}{\partial p_k} = 0 \quad (15.1)$$

It can be concluded from the sign of the

second derivative of x , whether the extreme value corresponds to a minimum ($\partial^2 x / \partial p_k^2 > 0$), a maximum ($\partial^2 x / \partial p_k^2 < 0$), or an inflection point ($\partial^2 x / \partial p_k^2 = 0$). Moreover, process optimization is typically subject to boundary conditions and constraints, and extreme values of dependent variables may only be valid locally, within the parameter range considered. In any case, optimization by mathematical modeling is generally the last step in the development cycle of a specific process because it requires much basic knowledge of the process.

Optimization of coating processes can be carried out on different levels with increasing degrees of scope and complexity. The simplest scenario is called micro-optimization which focuses on a single detail of a coating flow, for example optimizing the geometry for flow around a corner inside a coating die to prevent flow separation, or optimizing the position of the dynamic wetting line in curtain coating to reduce the sensitivity with regard to external disturbances, see Section 3.3.1.

The next level of optimization addresses specific process steps, sub-processes, or unit-operations. Any coating process encompasses several of them, including fluid preparation and handling, web handling, formation of a liquid film (die or hopper design, see Section 3.3.2 and Chapter 10), film flow along solid surfaces, unsupported flow in short coating beads or extended liquid curtains, dynamic wetting, flow after coating (leveling), setting, curing, drying, etc.

Expanding the scope of optimization to the next level, the purpose then becomes to maximize the efficiency and effectiveness of the entire coating process (or, more generally, the entire manufacturing process) by simultaneously optimizing each of the relevant sub-processes. Invariably, the complexity of such a system will lead to conflicting requirements for the quantitative levels of the process parameters which are available. These include viscosity, surface tension, flow rate, coating speed, various geometric variables and others. In slide and curtain coating, for example, the viscosity should be low to promote high coating speeds without entraining air between

the impinging curtain and the web, but the viscosity should also be high to prevent cross-waves on the hopper slide, particularly because the onset of such waves is promoted by high flow rates needed for high coating speeds.

As a consequence, process optimization will most likely result in some kind of a compromise with regard to assigning values to process parameters. How to arrive at this compromise is not a trivial task; it is determined by how the optimizations of the sub-processes are weighted against one another, which in turn depends on the particular application. For simple systems, the optimization compromise may occasionally be eliminated, if parameter conflicts caused in subsequent sub-processes by the optimization of the first sub-process can be eliminated or shifted forward to the next sub-process (domino syndrome). Success of this procedure necessitates manipulating only those parameters which are particular to the sub-process under consideration, and which do not occur in subsequent sub-processes (often geometrical parameters).

The primary objective of an industrial coating company, however, is not to design and optimize manufacturing processes, but to produce coated goods with a high value for the consumer. The making of a coated product can schematically be described as the simultaneous interaction between a recipe (e.g., prescription of how raw materials have to be combined to form the coating solution), one or several processes that act on the coating solution, one or several machines on which the processes are implemented, and a set of ever-present disturbances, see Fig. 15.3.

Many of the available parameters are simultaneously fundamental to the recipe, to the process, and to the machine. The available parameters can be grouped into the following three classes:

- physical fluid or material properties, such as rheological properties, surface tension, density, contact angles, modulus of elasticity, etc;
- operating parameters, such as coating speed, meniscus vacuum, film thickness, fluid temperature, etc.;

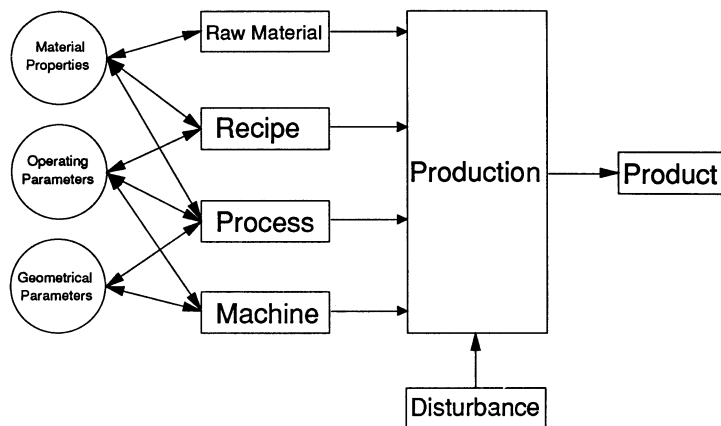


Figure 15.3 Relevant elements of the making of coated products.

- geometrical parameters, such as die dimensions, roller diameter, nip or gap dimension, slide angle, application angle, curtain height, etc.

It is apparent that the development of new products is most effectively carried out as an interactive team effort between chemists who typically design new raw materials and formulate recipes, chemical engineers who typically are responsible for coating and other unit processes, and mechanical engineers who typically design and construct the machinery necessary to run the processes.

Sometimes, circumstances require that priorities in product design are directed toward the recipe in order to affect chemical, physical, or mechanical product properties other than film thickness or film thickness uniformity, for example, speed and contrast of photographic products, surface texture and tribological parameters of magnetic recording media, electrical conductivity of polymeric coatings, etc. This can be achieved by manipulating physical fluid properties and operating parameters. Consequently, these two parameter classes may no longer be available for the engineers to optimize the coating and other processes, as well as machinery. Now, if possible at all, the challenge for the engineers lays in optimizing product design by optimizing processes and machinery

via manipulating geometrical parameters only, for that is the only class of parameters which is completely separated from the product recipe, see Fig. 15.3. In such a scenario, the design freedom for the formulation chemist is unlimited.

The above described scenario is called combined process/product optimization. Its complexity is still higher, because it aims at optimizing product properties (including chemical and physical properties, etc.) and not only the recipe, or the process, or the machine itself.

From an industrial viewpoint, process optimization ultimately must be carried out with respect to economics. The goal of this level of optimization (macro-optimization) is to minimize the total manufacturing costs in terms of product unit costs. Here, the scope includes not only coating and manufacturing processes, but also stock levels, and costs associated with distribution, marketing, research, engineering, administration, etc. Obviously, optimizations at lower levels affect the outcome of higher level optimizations, and ideally, they should be carried out first. However, high level optimization may still be meaningful, even if not all technical aspects of coating flows are known and optimized in detail.

The above description of optimization takes us back to the essence of this book, which is the explanation of scientific principles of coating

processes, as well as their technological (and economical) implications. The knowledge of these principles, and the associated theoretical models provide a useful framework for optimizations on the first and second level (micro-optimization and optimization of specific process steps or unit operations).

Section 15.2 addresses process control as it is applied to coating processes. In particular, statistical issues and the time-dependent behavior of the process are discussed. Section 15.3 is devoted to process optimization. In the first part, optimization criteria and an overview of optimization algorithms are presented in general form. In the second part, three examples of optimizing specific aspects of coating technology are provided. Section 15.3.3.1 exemplifies micro-optimization by focusing on the position of the dynamic wetting line for premetered coating processes. Section 15.3.3.2 illuminates the optimization of die or hopper design, which is a specific process step. In Section 15.3.3.3, a modest attempt is presented to model and optimize an entire coating company in order to minimize product unit costs. Finally, the chapter closes with an outlook on interesting issues yet to be conquered.

Owing to the professional experience of the author, the view points and examples presented in this chapter tend to be biased toward the photographic industry and toward premetered coating processes. However, it is hoped that the reader will be able to recognize the essential statements and apply them to other specific coating situations. As will become clear below, there is no 'once and for all' solution to control and optimization problems, as they are always subject to a particular set of boundary conditions and constraints.

15.2 CONTROL OF COATING PROCESSES

Process control in general is part of any engineering education, and its essence has been published in a great number of books and scientific papers. Therefore, the discussion in this chapter is focused

on a few issues where process control is specifically applied to coating processes.

Process control can be divided into two main areas. The first one, statistical process control, is a method to learn and visualize when a process is in control. Being in control means the process is operating within its capabilities, and any fluctuations are due only to sources of natural variability. Statistical process control also allows one to detect sources of abnormal variability which cause the process to go out of control. Should the variability exceed a given, statistically calculated limit, then corrective actions are required to bring the process back into control.

Process capability must be distinguished from product specifications. If product specifications are tighter than process capabilities, the product is not properly manufacturable. An acceptable product can only be obtained through intensive inspection after the fact by the quality control department. Naturally, these activities and the accompanying loss of yield will not only lead to excessive manufacturing costs but also to customer dissatisfaction, because there is no guarantee that a defective product will not slip through the inspection process.

These and many more issues relevant to coating processes are discussed in detail by Frost and Gutfoff (1991).

The second main area of process control concerns the dynamics, or the time-dependent behavior, of a process. The objective is to develop controllers (software algorithms and hardware) which will allow the process to run automatically and in the desired way. Apart from the above mentioned feed-back and feed-forward controllers, process stability is of major concern, both for open-loop processes with no controllers in the system, and for closed-loop processes with controllers present. Luyben (1973) is just one example of a textbook where these issues are described in detail.

The determination of optimum values for the parameters of the control algorithm can easily be achieved, so long as the process can be described by a mathematical model. However, it is not an easy task if the process is too complex

to be modeled, and if the optimization of the controller must be accomplished during normal process operations. For such cases, Skormin (1991) has developed an experimental procedure employing a signal analyzer and a simplex optimization algorithm to adjust the parameters of industrial PID control systems. In particular, he used the speed control of a coating machine as an example. Variation of web speed can be associated with certain types of coating defects, which explains the rather strict requirements on the accuracy of web speed controllers (typically $<0.1\%$). Hence, optimum controller parameters can be obtained by minimizing the variance of web speed with respect to the parameter values.

Today, modern coating plants in all areas of the coating industry are highly automated and comprise a great number of control loops. Many applications are found in the coating solution preparation area and in the delivery system, but also in the coating machine itself as well as in the dryer. Parameters to be controlled include coating speed, flow rate, fluid temperature, fluid pressure, concentrations of various chemical compounds added to the coating solution, air temperature and humidity, web tension, web direction, coating gap, roll separation distance, roll separation force, etc. These parameters may not only be held constant, but they may follow complex curves as a function of time, for example temperature profiles during the making of silver-halide emulsions for photographic products, or speed profiles during acceleration and deceleration of the coating machine.

One area that provides some degree of difficulty is the on-line control of fluid properties like viscosity or other rheological parameters and surface tension. This is unfortunate because fluid properties directly affect the coating process. While several manufacturers of viscometers offer equipment for on-line measurements, the relevant geometrical dimensions are not always suitable for mounting in small-diameter delivery lines. Hence, on-line viscosity measurement is preferably used in solution preparation and holding vessels, the location of which is typically far upstream from the coating point. In addition, correcting

an out-of-spec viscosity value is often limited to adding solvent. This is a one-way procedure because solvent removal is usually not possible. Furthermore, on-line changes of solvent quantities will affect the performance of the coating process, the wet film thickness, and the set points for the setting and drying zones, all of which will make overall control and operation of the coating process very difficult. Finally, the addition of polymers in the form of thickening agents may not be a viable option to control viscosities. Thickeners often increase the viscosity only in the low shear rate range, while in the high shear rate range they promote non-Newtonian rheological behavior, particularly shear thinning. In pre-metered coating methods, the viscosity in the boundary layer just downstream from the dynamic wetting line may actually become lower if a thickener is present than if the solution contained no thickening agent. This feature may not be desirable, because it may move the position of the dynamic wetting line too far upstream, thereby increasing the sensitivity of the coating process with respect to external disturbances, see Section 15.3.3.1.

For some coating processes, it is possible to control the chief parameter, the lateral film thickness distribution. In blade coating during paper manufacturing, for example, cross-directional film thickness nonuniformity is often caused by blade beam deflection, which in nearly all cases is a result of nonuniform blade beam temperature. The problem is amplified during the start-up phase (unsteady non-isothermal operating conditions), and by the very large coating widths ($>8\text{ m}$) that are encountered in the paper industry. To solve the problem, Sollinger (1990) presented a control mechanism called thermal anti-deflection system. Ducts for water flow are installed at the inside front and rear surfaces of the blade beam which is of square cross-section. The front and rear ducts are connected to separate water circulation systems. The duct adjacent to the coating roll is operated at a constant temperature. In contrast, the water temperature of the second duct is controlled by a laser measurement, which determines the blade

beam deflection in the center of the beam. With such a system, any blade beam deflection vertical to the blade level can be adjusted, regardless of whether the coater is in operation or at rest, and regardless of the temperature of the coating fluid.

In another example, the control of film thickness uniformity for slot or extrusion coating is described by Braatz *et al.* (1992). In this case of single-layer pre-metered coating, the height of the metering slot of the coating die, which is crucial for determining the final film thickness distribution, can be adjusted by means of several equally spaced bolts. Cross directional control is aimed at maintaining a uniform thickness profile by measuring the film thickness downstream from the coating point (after the dryer in this case), and by feeding a corrective signal back to adjust the position of (some of) the bolts. The mathematical model used to design the control algorithm does not account for detailed process dynamics because of the large time delay between change of slot height and the resulting change in film thickness, owing to the large distance between coating die and sensor. Even though this control can only eliminate slowly acting disturbances, it was shown experimentally to perform well within the given constraints, for example, as related to excessive mechanical stress in the coating die.

15.3 OPTIMIZATION OF COATING PROCESSES

Before embarking on optimization, the variable(s) to be optimized must be defined, boundary conditions and constraints must be identified, and optimization strategies and algorithms must be chosen. These aspects are discussed below.

15.3.1 OPTIMIZATION CRITERIA

The choice for variables to be optimized is large. As explained in Section 15.1, it depends on the level of optimization one is interested in, and it ranges from minimizing the corner radius of a flow boundary, to minimizing the residence time for liquid flow through a coating die, to maximizing

the coating speed, to maximizing the film thickness uniformity, to minimizing the product unit costs, etc. While the choice of these kinds of variables may be meaningful and justifiable in many instances, we propose also to consider the following optimization philosophy.

Process optimization shall be aimed at defining and quantifying as many constraints for independent process parameters and dependent process variables as appropriate. The parameter to be optimized shall not be a particular dependent variable such as those described above, but rather the sensitivity of such a dependent process variable to process fluctuations. The sensitivity is a measure for the robustness of the process. Minimizing the sensitivity is equivalent to a flat response surface around the optimum. Moreover, sensitivity is related to stochastic effects which are natural and always present in any process; hence, they are predestined to be minimized.

Appropriate constraints for independent and dependent process parameters will vary from application to application. Consider the fictive example, where, for coating speeds of up to 2 m/s and viscosities of up to 100 mPa s, the cross-directional film thickness nonuniformity is required to be <1%. The variable to be minimized is not the film thickness nonuniformity itself, but the sensitivity of the film thickness nonuniformity to stochastic fluctuations of parameters such as viscosity, coating speed, coating gap, wetting characteristics of the web, etc.

Two specific examples of this optimization philosophy are presented in Sections 15.3.3.1 and 15.3.3.2.

15.3.2 OPTIMIZATION ALGORITHMS

The selection of an optimization strategy, i.e. the choice of the most appropriate optimization procedure that leads to the desired result, depends on whether or not a relationship between the variable to be optimized and the process parameters is known, and on whether the optimum values for independent variables of a stationary process are sought (parameter optimization), or optimum functions for control variables of a

non-stationary process are to be determined (function optimization), Wilde (1964), Wilde and Beightler (1967).

Function optimization requires a functional description of the process by differential equations. Most often, it is applied to unsteady processes such as chemical reactions. Apart from drying and curing, coating operations are steady processes and therefore, parameter optimization is the method of choice. The distinction here is between one-dimensional (the optimum depends on only one variable) and multidimensional (the optimum is determined by several independent variables) systems (Bandermann 1972).

As mentioned above, for simple cases where the process can be modelled with analytical functions, the method of differential analysis according to equation (15.1) allows one to optimize the process quite easily.

Perhaps more important than differential analysis are iterative strategies or so-called search methods, which are applicable without analytical models, as long as the goal parameter assumes an optimum within the range of interest for the process variables. The location of the optimum must be evaluated experimentally, and so the design of suitable experimental plans is of major importance, see Chapter 7 in this book, as well as Montgomery (1984) and Reklaitis, Ravindran and Ragsdell (1983) for general references.

In the case of one-dimensional systems, simultaneous search methods are called for if all experiments should be carried out at the same time, for example in order to save time (Wilde 1964). However, more efficient search methods can be applied, if the experiments can be carried out sequentially, because experience gained in earlier trials can be used to design later ones. A well known and very efficient procedure in this class is the Fibonacci search method (Wilde and Beightler 1967; Denn 1969). With only ten experiments, the size of the interval in which the optimum is located can be reduced by a factor of 100 compared with the initial interval size.

In the field of coating technology, parameter optimization within multidimensional systems is a more realistic scenario. Here, the purpose of

optimization is the determination of a low-order polynomial regression model over specified ranges for the independent parameters, and the calculation of response surfaces (equidistant lines) that represent constant values of the variable to be optimized. At the same time, the experimental efforts to carry out this procedure shall be minimized by utilizing suitable experimental design plans.

The choices are numerous. A sure method for finding an optimum is the full factorial plan, where the entire parameter space is covered with a sufficiently fine grid and the variable to be optimized is determined at each grid point. As the number of required experiments is given by n^p with p being the number of independent parameters and n being the number of levels for each parameter, the method is rather laborious and not recommended for problems with $p > 3$.

A far more superior and efficient approach is the Box–Wilson method (Box and Wilson 1951; Box and Hunter 1957). The procedure is schematically depicted in Fig. 15.4 for the case of two independent variables. The starting point is an arbitrary area on the response surface of the variable to be optimized that is sufficiently remote from the optimum. It is assumed that in this region, the response surface can be approxi-

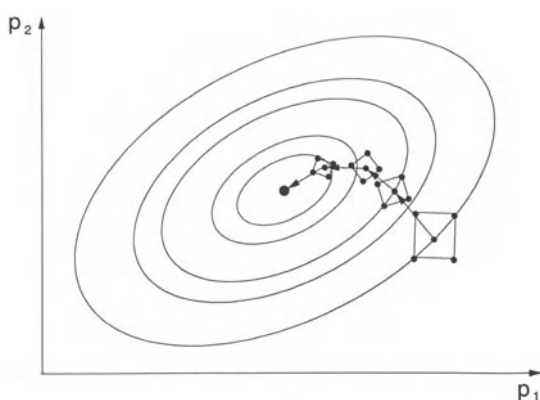


Figure 15.4 Schematic diagram of the simplex method: well designed local experimental plans (—●—) define the path toward the optimum.

mated by first-order polynomial models. The coefficients of these models are determined by way of experiments (orthogonal first-order designs like full or fractional factorial plans).

The above models provide the basis for applying the method of steepest ascent (steepest descent, if a minimum is searched). It is a procedure for moving sequentially toward the optimum, along the path with maximum increase in response. In this context, a frequently used procedure is the simplex method, which is a first-order orthogonal experimental design (Spendley, Hext and Himmsworth 1962; Nelder and Mead 1965). A simplex is a regularly sided structure with $k + 1$ vertices in k dimensions. Thus, for $k = 2$ the simplex is an equilateral triangle, while for $k = 3$ it is a regular tetrahedron. If well designed, the simplex method adapts itself to the local landscape and changes step size according to the local slope of the landscape. Most importantly, it generates the coordinates for a new local experimental plan along the path toward the optimum, see Fig. 15.4.

The sequence of local experimental plans is repeated until the goal parameter is sufficiently near the optimum. Here, the response surface can no longer be accurately described by first-order models; its curvature requires the use of high-order polynomial functions which can account for parameter interactions. The associated experimental design plans must have at least three levels for each independent variable so that the model parameters can be estimated. The preferred class of second-order response surface designs is the class of composite and rotatable designs. These designs are based on 2^p factorial or fractional factorial plans, which are augmented by $2p$ axial points and by several center points. Rotatable refers to the feature that the variance of the predicted response at some point x is only a function of the distance between the point x and the design center, but not a function of the direction between the design center and the point x (Montgomery 1984). Frequently used composite designs include names like central composite, star, Box–Behnken, etc. (Box and Behnken 1960).

In practice, optimization techniques as described above are often applied in laboratory environ-

ments. However, due to imperfect scale-up conditions, the optimum of a full-scale production process may not exactly be located at the same parameter values as in the laboratory. To overcome this discrepancy, Box developed a method called Evolutionary Operation (EVOP), allowing the routine plant operating conditions to be moved toward the optimum (Box and Draper 1969). The principle of the method consists of carrying out a 2^2 or at most a 2^3 factorial design plan around the current operating point. The variations of the independent parameter levels must be chosen to be small enough so as to prevent excessive loss of yield, but large enough so that the variation of the variable to be optimized exceeds its standard deviation, and that the potential improvements in process performance will eventually be discovered. EVOP is continually applied in the direction of presumed process improvement until the experimental costs exceed the expected gains in revenues.

The main advantages of EVOP include process optimization based on routine operating data, while the risk of excessive losses is kept low. Moreover, the optimization can be carried out by the operating personnel if the procedure is well specified. The main disadvantage, on the other hand, is the rather slow progress toward the optimum. This is particularly cumbersome if, for some reason, such as changes in equipment or process, the location of the initial optimum has been changed to other operating conditions during the course of the experiment, rendering previously obtained results practically useless. Some of the disadvantages can be avoided, however, by using the above described sequential simplex method (Nelder and Mead 1965).

There may be situations where neither the method of differential analysis nor experimental search procedures are applicable for process optimization, due either to a large number of independent process parameters or to the unavailability of accurate and automatic sensing devices. In such cases, statistical clustering analysis of process variables may be of help. This technique is widely used in pattern recognition. A pattern, described by a large number of continuous

variables, can be recognized as a pattern of a particular class by analyzing only a small group of dominant variables. These groups of key variables, associated with particular classes, can be selected by processing available statistical data. Skormin and Siciliano (1991) have formulated such a clustering procedure for the film coating process, aimed at analyzing the product quality as well as optimizing and controlling the process.

Skormin and Siciliano chose the quality of the coated film as the variable to be optimized: it was visually assessed by the quality inspector and assigned a value 'A' if acceptable, or a value 'B' if unacceptable. Unacceptable quality may be caused by typical defects like streaks, repellencies, mottle, bubbles, cross bars, remelt, etc. Clustering analysis provides a means for identifying relevant process parameters like viscosity, surface tension, emulsion temperature, etc., which determine the product quality. Moreover, if distinct clusters are present, lines separating acceptable from unacceptable quality can be identified and quantified. These lines form the boundaries of the operating window. In that sense, clustering analysis of the available experimental data provides a reliable alternative to the direct investigation of particular defect mechanisms.

Another diagnostic method that has become popular in recent years is called artificial neural networks. Based on available data, neural networks are able to 'learn' nonlinear but empirical relationships (regression models) between input and output parameters of a process. They have been applied to process and product design, as well as to process operations (optimization) and control. More specifically, networks have been used to design fixed or adaptive model-predictive control systems, to diagnose process faults and to identify patterns and root causes, and to monitor process trends in order to assess process performance or product quality. Applications of this method to coating processes, however, are not known to the author. An overview of artificial neural networks and an entry point to the vast literature can be found in the paper by Bakshi and Stephanopoulos (1993).

15.3.3 APPLICATIONS

Examples of optimization, such as the ones presented below, cannot provide general solutions to particular types of optimization problems, e.g. die design, because inherently, a process can only run at an optimum for exactly one set of operating conditions (combination of physical fluid or material properties, operating parameters, and geometrical parameters). As soon as one of these parameters is changed, another parameter should be adjusted for the process to remain at the same optimum. Alternatively, a process may be optimized such that the variable to be optimized remains within a specified but acceptable range, while some of the operating conditions vary within specified limits.

Section 15.3.3.1 on the position of the dynamic wetting line belongs to the former type of process optimization, and Section 15.3.3.2 on die or hopper design represents an example of the latter class of optimization problems. Finally, Section 15.3.3.3 shows how product unit costs can be minimized by modeling an entire coating company. The purpose of presenting these applications is to lay out procedures, and to stimulate interest by offering new ideas about optimizing certain aspects of coating processes.

15.3.3.1 Position of the dynamic wetting line for premetered coating processes

The class of premetered coating processes comprises the slot or extrusion, slide and curtain modes. Many of their characteristic features have been described in the scientific literature (Sartor 1990; Christodoulou and Scriven 1989; Kistler 1983) and in Chapter 11 of this book. In spite of distinct differences with regard to operating conditions and operating behavior between the three main modes, they have in common the fact that ultimately a liquid sheet or bridge or 'bead' is formed by the coating head and subsequently deposited onto the moving substrate. This liquid bridge is characterized by two static contact lines located on the coating head where the two free surfaces of the bridge are formed, and by a

dynamic contact line situated where the bridge first touches the web. The three coating modes distinguish themselves in the design of the coating head, i.e. in the way the liquid bridge is formed (be it single- or multilayered), in the length of the liquid bridge, and in the orientation of the liquid bridge with respect to the gravity vector.

In practice, operating conditions of coating processes are depicted in so called coating windows where the multidimensional space of relevant process parameters is divided into a region (or regions) of admissible operating conditions leading to acceptable product uniformity, and into a region of unacceptable product uniformity. The boundaries of the coating window, which separate areas of high and low uniformity, are associated with the onset of flow instabilities or other undesirable features, which in turn cause coating defects. The names of these defects depend on the selected parameters of the coordinate system of the coating window and on the descriptive colloquialisms which vary from company to company. Figure 15.5 shows a schematic example of a coating window for the curtain mode (Kistler 1983; Blake, Clarke and Ruschak 1994). In the plane of coating speed versus volumetric flow rate per unit width, the area of admissible operating conditions is bound by the onset of air entrainment, the onset of 'puddling' (vortex in curtain heel), and the loss of stability of the falling curtain.

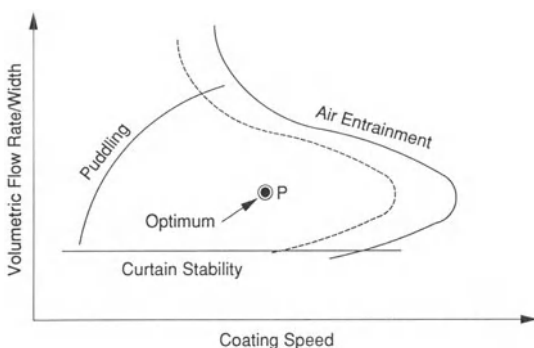


Figure 15.5 Schematic diagram of the coating window for curtain coating. Air entrainment: —— detected on undisturbed web; - - - - detected after splice passage.

A coating window such as the one in Fig. 15.5 applies only when all other relevant process parameters are held constant, e.g. viscosity, surface tension, bead vacuum and geometric parameters such as curtain height, slide angle, impingement angle, application angle, lip design, etc. Any variation of any of these parameters will alter the shape and location of the coating window. If, for example, the fluid viscosity is increased, the onset of air entrainment will shift towards lower speeds, thereby decreasing the size of the parameter space leading to acceptable product uniformity.

Operating conditions of industrial coating processes are often situated close to one of the boundaries of the coating window. While such conditions may offer advantages, for example with respect to the maximum attainable coating speed for a given set of parameters, they may also be characterized by increased process uncertainty, i.e. any small deviation in any of the process parameters from its nominal value may shift the operating point across the boundary of the coating window into an area of decreased product quality. Such a shift is particularly objectionable if the coating defect depicted by that boundary is characterized by an 'on/off' mechanism which will immediately lead to catastrophic process failure.

The goal of modern product design is not only to build in distinct product features but also to make the product manufacturable. In the context of a coating window, this means the operating conditions should not be located close to one of the boundaries but should be sufficiently remote from it so as to guarantee maximum process certainty.

Chen and Scriven (1992) expanded on the idea of the coating window by introducing the feasibility window (range of relevant parameters within which a coating can be established and maintained at all), the sensitivity window (range in which the coating is stable to spontaneous disturbances triggered by process fluctuations and unresponsive to forced disturbances from the surroundings), and the quality window (range without vortices in the flow field, and static wetting lines pinned to straight edges on the coating die). The idea

of relating quality or optimum flow conditions to the absence of vortices was already mentioned by Schweizer (1988). In Fig. 15.5, the line depicting the onset of 'puddling' is a boundary of the quality window, while the solid line depicting the onset of air entrainment belongs to the feasibility window as long as air entrainment is detected on the undisturbed web by simply increasing the coating speed. If, on the other hand, the onset of air entrainment is measured after the passage of a splice beneath the impinging curtain (representing a large disturbance), the respective boundary of the coating window moves left towards lower coating speeds (dashed line). This boundary is now part of the sensitivity window.

The purpose of this section is to show how one may go beyond the onion-like structure of coating windows, which define increasing product uniformity from outer layers toward the center, by identifying a single operating point inside the coating window (schematically indicated as point P in Fig. 15.5), for which the product uniformity becomes optimum for a given set of relevant process parameters. Conversely, the goal of such an optimization strategy is also to shift the coating window around a desired operating point such that the resulting product uniformity will be the best possible.

The variable to be optimized was chosen to be the position of the dynamic wetting line which, beside gross defects such as air entrainment, 'puddling', ribbing lines, vortices, etc., has been shown – according to our experience – to affect the uniformity of the coated product. In particular, product uniformity decreases if the wetting line is not straight across the coating width but wavy as a result of perturbing forces occurring randomly and sporadically. The optimum position of the dynamic wetting line is characterized by maximum robustness with respect to ambient disturbances. The arguments are presented by using the impingement zone of a falling curtain as an exemplary flow field. The results, however, will only be qualitative and can, in principle, also be applied to slide, slot, and extrusion coating.

Consider a plane liquid jet (curtain) impinging on a horizontal and stationary surface. The

momentum of the liquid will cause the jet to split into two symmetrical films which will flow away from each other along the surface. If the surface is set in motion, it will exert a force (viscous drag) on the liquid which tends to pull all the fluid in the direction of the motion. The above arguments are also valid if the jet impinges on the surface at an angle other than perpendicular. Successful coating, that is the formation of a dynamic wetting line, is achieved if the net change in momentum parallel to the substrate is balanced by the sum of all forces acting on the fluid in the plane of the substrate, and if the net change of momentum in the direction perpendicular to the substrate exceeds a critical value in order to avoid air entrainment. Depending on the position of the dynamic wetting line relative to the front or back surface of the falling curtain, the impingement zone may assume a heel form.

Referring to Fig. 15.6, the integral form of the momentum equation in X- and Y-directions, using a control volume whose boundaries coincide with a cut through the curtain upstream of the impingement zone, with the substrate surface, and with a cut through the fully developed film downstream of the impingement zone, can be written as

$$\rho Q(U - V \sin \alpha) = \sum F_x \quad (15.2a)$$

$$\rho QV \cos \alpha = \sum F_y \quad (15.2b)$$

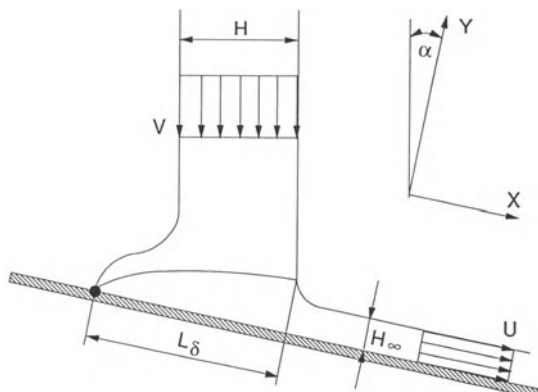


Figure 15.6 Schematic diagram of the curtain impingement zone.

where ρ is the density, Q is the volumetric flow rate/width, U is the coating speed, V is the curtain impingement velocity, H is the thickness of the impinging curtain, H_∞ is the final wet thickness of the coated film, and α is the impingement angle. The types of forces F_x and F_y in the X - and Y -direction include viscous drag, pressure (static, dynamic, or pressure difference across the curtain), gravity, surface tension and molecular interactions. In addition, there are force disturbances stemming from variations of any of the relevant process parameters. One important disturbing force, that is generally not included in the model of equation (15.2), is the pressure exerted on the curtain heel by the air boundary layer carried along by the uncoated web. The air boundary layer cannot be avoided and, according to our experience, it is characterized by some degree of nonuniformity across the coating width. The resulting effect on the coating uniformity is manifested by broad bands in the down-web direction, whose occurrence is random in time and cross-web position. Another important disturbance is given by the passage of the tape used to splice subsequent rolls of substrate. Often, the tape is fastened over both ends of adjacent rolls, thus providing a step-like sudden change of web thickness, which has been observed to trigger excessive air entrainment. Both of the above described disturbances act in the coating direction.

Any change of any force in the coating (X)-direction and near the plane of the substrate will result in a small displacement of the dynamic wetting line. The sum of all forces in the X -direction can only be balanced within certain limits. These limits mark the boundaries of the coating window, i.e., air entrainment.

Equation (15.2) describes the conservation of momentum for the fluid contained in the defined control volume. As the equation is written in integral form, it does not suffice to accurately reveal the details of the momentum and force distributions along the boundaries of the control volume. With regard to the optimum position of the dynamic wetting line, the distribution of the X -momentum near the plane of the substrate

is of particular interest. To a first approximation, the change of X -momentum there is mainly balanced by viscous drag and pressure forces. According to the boundary layer theory of Sakiadis (Sakiadis 1961; Kistler 1983), the viscous drag force, or wall shear stress, is strongly negative in the vicinity of the dynamic wetting line and increases in the downstream direction with $(X)^{-1/2}$. For large heels, i.e., when the dynamic wetting line is located far upstream of the rear curtain surface, therefore, the change of viscous drag force underneath the curtain is weak. Pressure forces, on the other hand, arise from a transformation of the Y -momentum into a stagnation pressure, qualitatively characterized by a bell-shaped distribution whose maximum value is proportional to the square of the normal component of the curtain impingement velocity, $(V \cos \alpha)^2$ (Blake, Clarke and Ruschak 1994), and whose tails approach low values far downstream from the impingement zone and far upstream, particularly if the heel is large. Evidence to support this statement is given by the special case of a jet impinging onto a horizontal and stationary wall (Deshpande and Vaishnav 1982), and by Kistler (1983) and Gilbert, Wagner and Nagel (1994) who both used the finite-element method to compute the flow field (pressure field in terms of isobars) in the curtain impingement zone.

On the grounds of the above arguments, it can be stated that the distribution of X -momentum along the substrate surface and beneath the impinging curtain is mainly characterized by the bell-shaped curve of the stagnation pressure, particularly if the curtain heel is large. In the light of this flow characteristic, the optimum position of the dynamic wetting line is postulated as the point P of maximum slope on the upstream tail of the pressure (momentum) distribution curve, see Fig. 15.7. At that point, any disturbing force in the coating direction, such as those described above, tending to displace the dynamic contact line by the distance ΔX can only do so, if it overcomes the resisting change of X -momentum ΔM .

Owing to the bell-shaped momentum distribu-

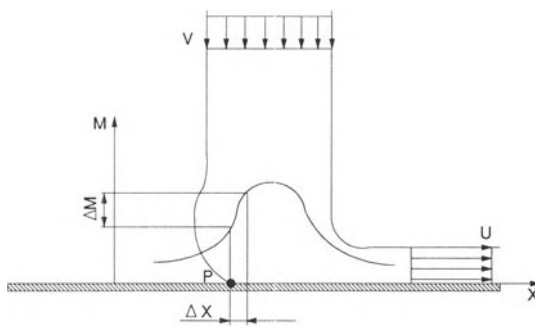


Figure 15.7 Schematic diagram of the curtain impingement zone with a bell-shaped momentum distribution along the substrate. The optimum location, P, for the dynamic wetting line is postulated to be at the steepest slope of the momentum distribution.

tion curve, the resistance to contact line displacement will be smaller if the wetting line is located at any other point than P. The only exception is a point P' located at the steepest slope on the downstream branch of the momentum distribution. P' will be the optimum position only if the disturbing force is acting in a direction opposite to the web motion. However, it is assumed that such forces are less important compared with disturbances stemming from the splice passage and from the air boundary layer, which are both acting in the direction of web motion.

A convenient way of quantitatively describing the position of the dynamic wetting line has been presented by Blake, Clarke and Ruschak (1994). They defined a dimensionless ratio l , called the relative wetting line position (see Fig. 15.6).

$$l = \frac{L_\delta}{(H/\cos \alpha)} \quad (15.3)$$

where L_δ is the length of the boundary layer which originates at the dynamic wetting line and extends to the front surface of the curtain, and $H/\cos \alpha$ is the thickness of the curtain as projected onto the plane of the substrate. Consequently, for $l = 1$, the dynamic wetting line is in the plane of the rear curtain surface. For $l < 1$, the wetting line is located further downstream, while for $l > 1$, the curtain impingement zone is charac-

terized by a heel. The relative wetting line position has been shown to depend on all relevant process parameters, and it can be approximated by way of an analytical expression based on the Sakiadis boundary layer theory (Blake, Clarke and Ruschak 1994). While this expression is quite successful in predicting the position of the dynamic wetting line, it does not provide the necessary information to determine the optimum value for l according to the above criterion, because the Sakiadis-type boundary layer model does not account for shock-like disturbances from splice tapes nor for the effects of the impinging air boundary layer, both of which are considered important here.

In order to validate the above described optimization criterion, numerical solutions of the full Navier–Stokes system and associated investigations of the sensitivity of the flow to ever present disturbances are needed. The most attractive and efficient method is frequency response analysis, see Chapter 9. This tool was not available to the author at the time of writing. One piece of evidence, however, was provided by Stadler (1993), who used the finite-element method to calculate an exemplary flow field of the curtain impingement zone, see Fig. 15.8.

Flow parameters were chosen such that the resulting curtain heel became relatively large ($l = 3.10$). This situation is not considered optimum, because the dynamic wetting line is located too far upstream in a region of relatively low pressure and low pressure gradients. This fact is indicated in Fig. 15.8 by the pressure distribution along the substrate surface (bell-shaped curve superimposed on the streamline pattern). The left tail of the curve clearly starts to flatten toward the dynamic wetting line. Notice that the pressure curve is not shown all the way to the dynamic wetting line due to unreliable values owing to the singularity there (see Chapter 9), and that the origin of the pressure coordinate system coincides with the substrate plane. The maximum point on the pressure curve corresponds to a pressure of 1982 Pa for a curtain impingement velocity of 2 m/s, which is nearly equal to the stagnation pressure $\rho V^2/2$ if the

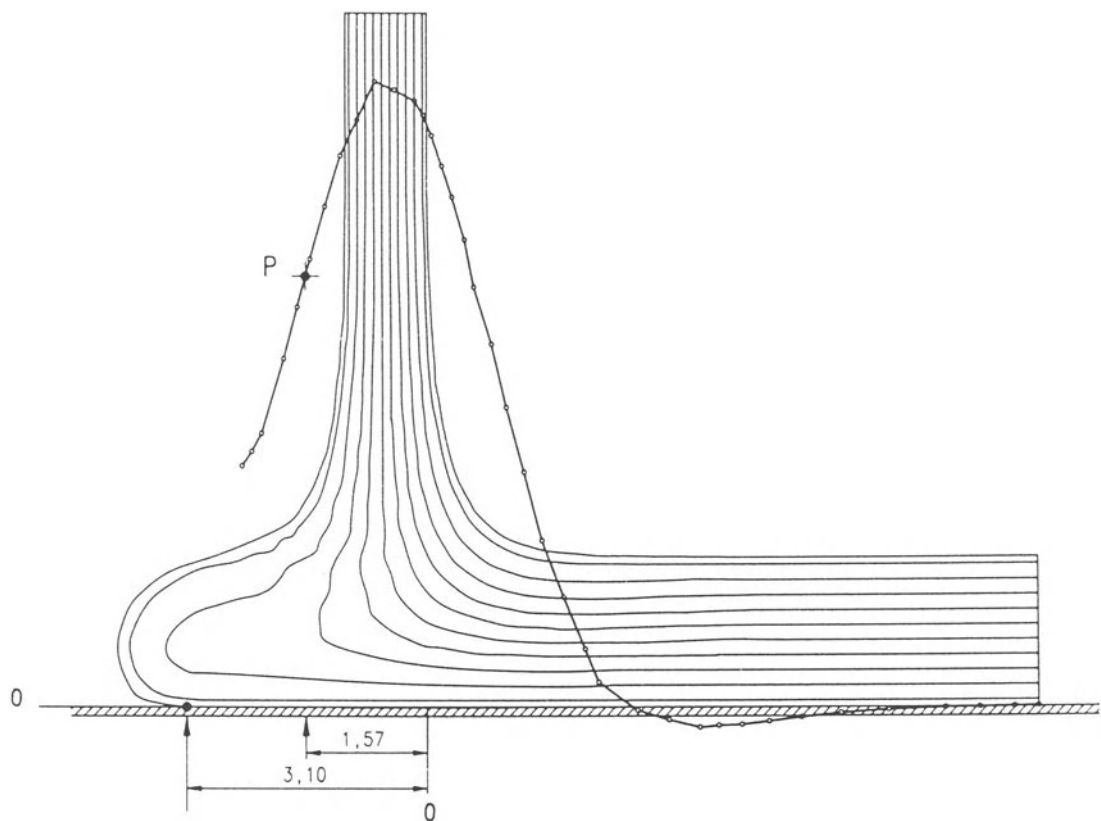


Figure 15.8 Streamline pattern of the curtain impingement zone with superimposed pressure distribution along the substrate. The value for the relative wetting line position is 3.17. The point P of steepest slope on the pressure curve (= proposed optimum position for the dynamic wetting line) is located at 1.57 curtain thicknesses behind the front surface of the curtain. Reynolds number $Re = 4.5$, capillary number $Ca = 18.0$, speed ratio $V/U = 1.8$, curtain impingement angle $\alpha = 0^\circ$, apparent dynamic contact angle $\Theta_D = 170^\circ$ (from Stadler 1993).

density assumes a value of 1000 kg/m^3 . The steepest slope on the pressure curve is located at point P, which is considered the optimum position for the dynamic wetting line, resulting in maximum robustness with respect to disturbing forces acting on the heel in the coating direction. For the flow parameters chosen in this example, the value for the dynamic wetting line position at P equals 1.57. Barring qualitative results for other values of the flow parameters, it is assumed that the optimum value for the relative wetting line position lies in the range of $1 < l < 2$. Moreover, it is apparent from Fig. 15.8 that the

slope of the pressure curve is fairly constant in the range of about $1 < l < 2$, indicating a flat optimum. Therefore, the robustness of the flow system is not expected to change much, as long as the dynamic wetting line is located in that range.

Blake, Clarke and Ruschak (1994) have presented a different criterion for the optimum wetting line position by stating that the pressure generated by the impinging curtain can act as a load and thus may delay the onset of air entrainment. Based on a balance of the Y-momentum, they found a maximum for the impingement pressure if $l = 2$. Referring to Fig. 15.8, the maximum

impingement pressure on the substrate occurs inside the projection of the curtain ($l < 1$), at least for the parameters chosen in the example. While the maximum pressure criterion proposed by Blake, Clarke and Ruschak presents an optimum with respect to the impingement pressure which presumably is related to the maximum speed of wetting, it is not an optimum with respect to the stability of the wetting line position in response to perturbations which in turn is related to the uniformity of the coated film. For either argument, however, optimum conditions seem obtained if the relative wetting line position l is of order unity. This opinion is also shared by Van Abbenyen, Mues and Goetmaeckers (1992) who postulate optimum conditions for $l = 1$. Their argument is based on the maximum speed of wetting, but they do not present a refined physical model to support it.

As an illustration, the air entrainment boundary of the curtain coating window has been drawn from the data published by Blake, Clarke and Ruschak (1994), see Fig. 15.9. The curve is valid for an aqueous gelatin solution characterized by a low shear viscosity of 30 mPa s, a power law index of 0.85, and a time constant of 0.000 248 s⁻¹

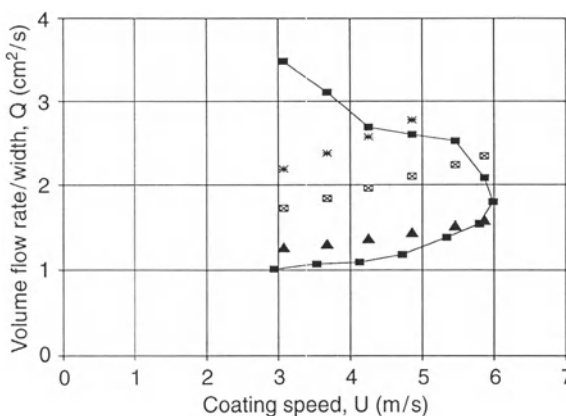


Figure 15.9 Curtain coating window in the U - Q plane showing experimental data (—■—) of the boundary for air entrainment (from Blake, Clarke and Ruschak 1994). Legend: Calculated values for the position of the relative dynamic wetting line, $l = 1.0$ ▲; 1.5 ◻; 2.0 ✕.

(Carreau model). In addition, the surface tension has been set to 40 mN/m, the application angle to 0°, and the curtain height to 100 mm. Three locations of constant relative wetting line position are depicted inside the area of acceptable coating uniformity. The values for l are of order unity, hence the symbols drawn in the figure point toward the area of maximized process robustness inside the coating window. The l -values have been calculated with the formula based on the Sakiadis boundary layer model and published by Blake, Clarke and Ruschak (1994). As l increases beyond a value of about 2 a sizable heel is formed, indicating a departure from optimum operating conditions and an approach of the ‘puddling’ boundary of the coating window (Fig. 15.5; Kistler 1983). On the other hand, if l decreases below a value of 1 the air entrainment boundary is approached, and operating conditions in this area of the coating window are characterized by increased process uncertainty.

With the help of the optimization criterion described above (dynamic wetting line located at steepest slope of pressure distribution), the area inside the coating window has been reduced to a line of preferred operating conditions, described by $l = \text{constant}$ and of order unity. A further reduction to a single optimum point as depicted in Fig. 15.5 is achieved by selecting the thickness of the coated film. In the Q - U plane (Fig. 15.9), conditions of constant film thickness are given by straight lines through the origin.

It may occur that curtain coating suffers from excessive air entrainment, even if the operating parameters are chosen such that the relative wetting line position is at its optimum value near unity. Under these circumstances, it may be possible to clear the air entrainment by changing the operating parameters such that the relative wetting line position moves from the steepest slope to the maximum of the pressure distribution. This approach satisfies the optimization criterion put forth by Blake, Clarke and Ruschak (1994). It is, however, associated with a reduction of process robustness according to the arguments presented above. We propose a different approach to clear the air entrainment by changing the

operating parameters such that l remains at the location of steepest pressure gradient, but that the pressure at the location of steepest slope increases sufficiently by increasing the curtain impingement velocity (increasing the curtain height). As is shown in Fig. 15.10, the result is not only a higher peak of the momentum distribution curve, but also a steeper maximum slope, and therefore an increased resistance to wetting line displacement in response to stronger perturbations.

Thus, the robustness of premetered coating processes can be increased by increasing the Y-momentum while keeping the wetting line at its optimum position. High impingement speed, high coating speed at constant thickness of the coated film, and a liquid jet impinging perpendicularly onto the substrate ($\alpha = 0^\circ$) favor such conditions. One might even question the existence of an absolute maximum speed of wetting, because there is no conceivable limit to increasing the Y-momentum.

In this light, curtain coating is superior to slide and slot coating, because the momentum of the impinging jet is one order of magnitude larger

(free falling curtain versus liquid film on an inclined plane and flow in a narrow slot).

In slide and slot coating, the position of the dynamic wetting line can effectively be controlled by the pressure difference across the bead. However, the relationship between wetting line position and pressure difference is difficult to obtain experimentally and is often not known for real applications, which is why these coating modes are characterized with a great deal of uncertainty.

Furthermore in slide and slot coating, the position of the dynamic wetting line determines the separation angle of the lower meniscus from the die lip which in turn controls the migration of the static wetting line along the face of the lip (Kistler 1983). A flow field where the static wetting line is not pinned to a sharp corner of the die lip but wets the die face is similar to a large heel in the impingement zone of a falling curtain. The optimum position of the dynamic wetting line (l near unity) promotes a static wetting line that is pinned to the die lip, thereby reducing the chances for streaks and lines.

In summary, the optimum position of the dynamic wetting line for premetered coating processes is postulated to coincide with the steepest slope of the pressure distribution in the plane of the substrate. It is argued that the process robustness with respect to random disturbances in coating direction is maximized at this operating point. Today, computer-aided methods of frequency response analysis exist to calculate the optimum position of the dynamic wetting line in the presence of process perturbations for any arbitrary combination of process parameters. However, such methods were not available to the author. Nevertheless, it is reasoned that the optimum value for the relative dynamic wetting line position, l , must be of order unity. For curtain coating, l can be calculated with sufficient accuracy for practical applications using a model based on the Sakiadis boundary layer theory and published by Blake, Clarke and Ruschak (1994). Finally, the optimization criterion can qualitatively also be applied to slide and slot coating. For slide coating in particular, operating

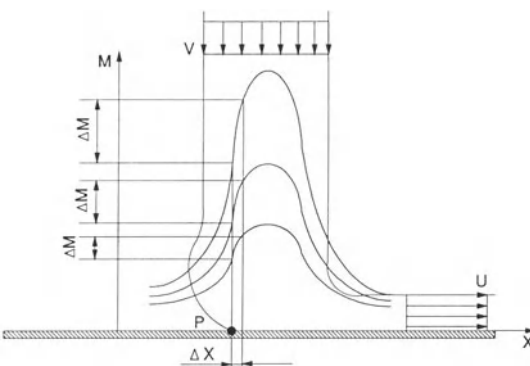


Figure 15.10 Schematic diagram of the curtain impingement zone with bell-shaped momentum distributions along the substrate. The steepest slope of the momentum distribution increases with increasing momentum, M , of the impinging curtain, and so does the robustness of the location P for the dynamic wetting line with respect to external disturbances.

conditions with l near unity promote a flow field with the static wetting line pinned at the corner of the die lip, which in turn reduces the propensity for lines and streaks in the down-web direction.

15.3.3.2 Die design

The physical principles and specific details of die or hopper design are presented in Chapter 10 and in the scientific literature, for example Durst, Lange and Raszillier (1994) and Ruschak and Weinstein (1996). The purpose of this section is to complement Chapter 10 by showing how these principles can be combined with some of the optimization procedures described above to determine which die performs the best for a set of boundary conditions.

The issues considered here are confined to internal die design and to simple applications. In particular, liquids will be Newtonian, and fluid flow will be modeled analytically for ease of presentation. These issues, however, can easily be applied to more complex and realistic situations such as non-Newtonian rheology, but at the expense of more complex modeling efforts.

A side-fed dual cavity hopper will serve to discuss the examples below. As sketched in Fig. 15.11, the fluid flow portion of such a hopper is defined by twelve geometrical parameters, namely the coating width or cavity length, W , the bar thickness, T , the lengths of the inner and outer metering slots, L_1 and L_2 , the heights of the inner

and outer metering slots, H_1 and H_2 , the shapes of the inner and outer cavities, β_1 and β_2 (see Chapter 10, and Liu 1983), the sizes (cross-sectional area) of the inner and outer cavities, $A_{1,0}$ and $A_{2,0}$, the size of the inner cavity at $X = W$, $A_{1,1}$, and the taper index, m , indicating how the size of the inner cavity cross-section changes with X , see equation (15.7). L is the total length of the fluid flow portion of the die element; for given values of the above defined parameters, L is not independent.

The goal of die design optimization is to assign numerical values to each of these geometrical parameters such that die performance criteria meet given quality specifications.

The purpose of a die is to create a liquid film by redistributing fluid from a point source (feed pipe) to a line source (metering slot). The performance of a die has traditionally been judged by only one quality criteria, namely the uniformity of the film thickness. While this is undoubtedly an important criterion, it is insufficient because the overall die performance must be assessed by several criteria, depending on the particular application. The list of performance criteria may include:

- uniformity of film thickness;
- tendency to form streaks in the liquid film;
- tendency to contaminate the die;
- ease of die cleaning;
- residence time characteristics;
- fluid pressure at die inlet;
- weight of die.

In addition to judging the performance, these criteria may also serve as boundary conditions or constraints during die design optimization by requiring them to respect specified values. In any case, the criteria must first be translated into suitable parameters that are accessible to fluid flow modeling, before they can be used for quality assessment or as guidelines for design optimization. Further arguments about die design optimization and design constraints have been presented by Winter and Fritz (1986), Sartor (1990) and Durst, Lange and Raszillier (1996).

The following discussion will be restricted to

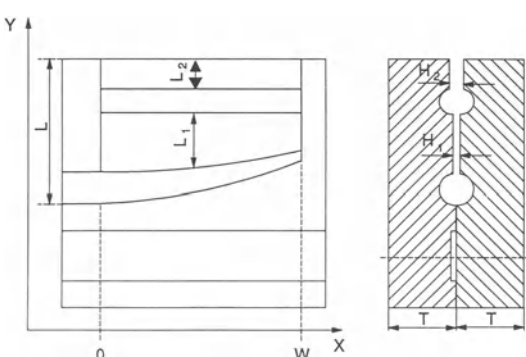


Figure 15.11 Schematic diagram of a side-fed dual cavity die. Left: front view; right: cross-section.

the first four criteria in the above list. The issue of residence time has been addressed in the literature (Winter and Fritz 1986; Lee and Liu 1989). However, according to our own experience, models relying on one-dimensional fluid flow are insufficient for accurately predicting residence time parameters. Fluid pressure at the die entrance will only become important if gravity is the driving force to feed the coating solution, or if the pressure is high enough to mechanically deform the die.

Die contamination and cleaning

Many dies are being used to coat not only one but several different products, each of which is characterized by its own specific chemical and physical properties. Thus, it is imperative to prevent cross-contamination during product change-over by removing and purging any residual material of the previous product. Better yet, cleaning would not be necessary if the die did not contaminate in the first place.

Contamination of solid surfaces may take several forms such as thin films of soluble or insoluble liquid or gel, crusts and particles adhering to the surface (Schweizer 1992). Here, the word particle is used as a generic name, standing for solid particle, gas bubble, droplet, or any other inhomogeneous part in the otherwise homogeneous coating solution.

The mechanisms by which contamination builds up on a solid surface are complex. Factors that affect contamination include surface roughness, flow state (laminar or turbulent), kinetic forces (form and friction drag), surface tension forces, adhesion forces, etc. In any case, if contamination is present, the forces making it stick to the surface are greater than the forces required to remove it from the surface. Conversely, if contamination is to be prevented, the removing forces must be greater than the adhesive forces everywhere inside the hopper and at all times of operation.

If a die is not taken apart during a product change, mechanical devices such as brushes cannot be used to scrub dirty surfaces. The only cleaning aid available are kinetic forces supplied by the coating fluid itself or by a cleaning solution.

Prevention of contamination and cleaning of flow systems, particularly the removal of particles, is not specific to flow inside dies. In fact, the food processing industry has been dealing with these issues for many years, and the scientific literature is extensive, for example Grasshoff and Reuter (1983); Barouch, Wright and Matijevic (1987); Dussan V. (1987); Yeckel and Middleman (1987); Sharma *et al.* (1992). Some important results of these investigations can be summarized as follows.

- The complex process of removing particles from a solid surface can be simplified and characterized by a single parameter, namely the wall shear stress.
- There is an exponential relationship between the wall shear stress supplied to the flow system and the diameter of the smallest particle that can be removed from the flow system.

From the die designer's point of view, the wall shear stress is a convenient parameter, because it is not only proportional to the product of viscosity times flow rate, but it also depends on geometrical parameters of the flow configuration, and thus it can be controlled by appropriate die design. Consequently, cleaning efficiency and prevention of contamination can be optimized by choosing appropriate dimensions for distribution cavities, metering slots and cavity inlets. What exactly these dimensions should be depends on the level of wall shear stress required to remove any particles of unacceptable size which, for a given range of viscosities and flow rates, is determined by the quality requirements of the particular products under consideration.

In summary, a design constraint relating to cleaning efficiency or prevention of contamination can be formulated and requires that the wall shear stress, τ_w must exceed a minimum value τ_0 anywhere inside the die at all times of operation.

$$\tau_w > \tau_0 \quad (15.4)$$

Based on experience, the value of τ_0 is on the order of 1.0 N/m² for many coating applications.

The flow in the inner cavity is predominantly along the cavity axis, and the average wall shear stress can be approximated by equation (15.5)

which was derived by Miller (1972) and is valid for ducts with arbitrary cross-section.

$$\tau_w = \frac{\mu V^*}{\beta AS} \quad (15.5)$$

Here, μ is the viscosity, β is the shape factor (Liu 1983), V^* is the volumetric flow rate which decreases linearly along the cavity axis according to

$$V^* = V_0^* \left(1 - \frac{X}{W}\right) \quad (15.6)$$

where V_0^* is the volumetric flow rate at the cavity inlet ($X = 0$), S is the wetted perimeter and A the cross-sectional area of the duct. In the most general case, S and A are both functions of X , and A is conveniently represented by

$$A = A_{1,0} \left(1 - \frac{X}{bW}\right)^m \quad (15.7)$$

with b being defined as $A_{1,0}/(A_{1,0} - A_{1,1})$. In our example, both cavities have circular cross-sections, and b is chosen to be 1.0 ($A_{1,1} = 0.0$).

To satisfy the design criterion (15.4), both the wall shear stress at the cavity entrance, $\tau_{w,0}$, and the wall shear stress distribution along the cavity axis must be above the minimum value, τ_0 , for all products to be considered. Thus, for a given range of viscosities and flow rates, the shape and size of the cavity cross-section must be chosen accordingly. Values of the shape factor β have been published by Liu (1983), and Liu and Hong (1988) for several duct shapes. β is largest for a circular cross-section ($\beta = 1/8\pi$); corners with small included angles are disadvantageous. It follows that by choosing a cavity shape, the size of the cross-section at the cavity inlet ($X = 0$) is determined by equation (15.4). The choice of shape may be a compromise between high wall shear stress and manufacturing costs of the die, because symmetrical shapes (e.g., circle) require more machining time than nonsymmetrical shapes (e.g., semi-circle).

For circular cross-sections, the wall shear stress distribution normalized with the value at

the cavity entrance can be calculated to give

$$\frac{\tau_w}{\tau_{w,0}} = \frac{\left(1 - \frac{X}{W}\right)}{\left(1 - \frac{X}{bW}\right)^{3m/2}} \quad (15.8)$$

For $b = 1.0$, as is the case in our example, the wall shear stress distribution depends on m , and several curves are drawn in Fig. 15.12. Obviously, the design criterion (15.4) is satisfied for $m \geq 2/3$.

The condition $b = 1.0$ has been chosen to keep the mathematics simple. In reality, $b > 1.0$, resulting in enhanced three-dimensional flow and, as known from experience, in reduced cleaning efficiency near the cavity end. Consequently, equation (15.8) is not accurate near $X/W = 1.0$.

Turning the attention to the metering slots, the flow there is mainly along the Y-axis, and the wall shear stress can be calculated according to

$$\tau_w = \frac{6\mu Q_0}{H^2} \quad (15.9)$$

where Q_0 is the uniform volumetric flow rate per unit width, and H is the slot height. Owing to the characteristic dimensions, the wall shear stress in the slot is typically one to two orders of magnitude higher than in the inner distribution

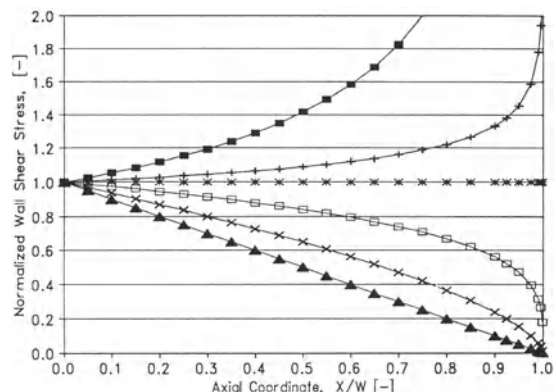


Figure 15.12 Wall shear stress distribution for a tapered cavity of circular cross-section. Legend: taper index $m = 1.0$ ■; 0.75 ▼; 0.66 *; 0.5 □; 0.25 ×; 0.0 ▲.

cavity, and therefore, equation (15.4) is much easier to satisfy.

Finally, the flow in the outer distribution cavity is also mainly in the Y-direction. In general, the wall shear stress here must be computed numerically. Except for shallow cavities, the level of wall shear stress will be low due to suddenly expanding or at least diverging flow boundaries. In spite of this disadvantage, the presence of an outer cavity may be useful to dampen excessive flow nonuniformities produced by the inner cavity/metering slot, see Chapter 10.

In summary, the shapes and sizes of both distribution cavities are determined by the criterion (15.4). In contrast, the criterion is easily satisfied by a wide range of slot heights, so they are still open for optimization. In general, high wall shear stress is obtained by small characteristic dimensions of the flow domains which, as will be seen below, is in conflict with achieving uniform film thickness distributions. The solution to this conflict is high-viscosity fluids.

Streak formation

Based on experimental work involving flow visualization (Schweizer 1988), the origin of streaks can be attributed to an interaction between a 'particle' and a 'particle trap' anywhere in the flow field. Here, streaks refers to narrow lines in the downweb direction with steep property gradients along their sides; it does not include broad diffuse streaks nor flow instabilities such as ribbing lines.

The word 'particle' is used in a generic sense; it can be a solid particle, a gas bubble, a nick in a corner of the flow boundary, or any other inhomogeneous part in the otherwise homogeneous coating fluid. The principal types of 'particle traps' have been identified as flow separation or vortices, areas of low wall shear stress, and rough surfaces.

The mechanism which leads to the formation of streaks depends on the type of particle trap. If a particle is stuck to a rough surface or if it adheres to an area of low wall shear stress, then a streak is the result of the wake behind the

particle, possibly accompanied by phase separation. However, if a particle is trapped inside a vortex, it will spin around owing to the circular or helical fluid motion, thereby disturbing the liquid, and particularly interfaces and/or free surfaces outside the separating streamline. In any case, the strength and the optical appearance of the streak in the coated film depends on the relative size and type of particle and particle trap, and on the distance of the particle trap from the coating point. Moreover, particles alone, or particle traps alone, will not cause streaks, only the interaction of both will.

To prevent streaks, the number of particles must be reduced, and the particle traps must be eliminated. While the first item is an operational problem related to filtering and de-gassing of fluids (Schweizer 1992), the second item is of interest to the die designer. Since vortices are characterized by a separating streamline that begins and ends at separation points on the flow boundary where the wall shear stress is zero, equation (15.4) is a suitable design criterion for the prevention of streaks. Requiring the wall shear stress to be above a minimal level does not allow particles to adhere to the flow boundary, and it implies the absence of stagnation points, and hence the absence of vortices.

The issue of vortices is also closely related to the design of the entrance to the inner distribution cavity. Many dies are of the 'coat-hanger' type where the cavity is center-fed. Consequently, the liquid arriving in the feed section must turn a sharp corner of 90° to enter both arms of the cavity. If the feed section has a small cross-section, the resulting peak from the stagnation pressure may translate into a local thickness nonuniformity in the coated film, and the liquid may separate from the cavity wall downstream of the corners. If, on the other hand, the feed section has a large cross-section or is diverging, the wall shear stress may be too low, even to the point where vortices start to form in the feed section. All of these features are potential causes for hopper contamination and streak formation. They can be reduced by feeding the cavity from the side.

Film thickness uniformity

The thickness uniformity of the liquid film exiting the die is a measure of the die performance. It may also be a measure of the quality of the coated film further downstream. In any case, it is strongly determined by the outer metering slot which is the last of a series of flow elements comprising the die. More specifically, the film thickness uniformity at the slot exit is proportional to the volumetric flow rate distribution across the coating width, which in turn is proportional to the pressure profile in the outer cavity according to

$$Q(X) = \frac{\Delta P(X)H(X)^3}{12\mu(X)L(X)} \quad (15.10)$$

Equation (15.10) is valid for Newtonian fluids. Q is the volumetric flow rate per unit width, ΔP is the pressure difference across the slot, and L and H are the length and height of the slot, respectively. If the pressure at the slot exit is arbitrarily set to zero then ΔP reduces to the pressure, P , at the slot entrance which is approximately equal to the pressure distribution in the outer distribution cavity. The other variables have been defined above.

An analytical expression for the variation of Q , and hence for the variation of the film thickness, is obtained by taking the total derivative of equation (15.10) (Schweizer 1992). If normalized with the uniform volumetric flow rate per unit width, Q_0 , the derivative takes the form

$$\frac{dQ(X)}{Q_0} = \frac{dP(X)}{P} + \frac{3dH(X)}{H} - \frac{d\mu(X)}{\mu} - \frac{dL(X)}{L}$$

term	(1)	(2)	(3)	(4)
------	-----	-----	-----	-----

(15.11)

Term (1) represents the lateral variation of the pressure drop across the metering slot, term (2) is the variation of the slot height, term (3) is the variation of the viscosity and term (4) indicates the variation of the slot length.

As has been shown by Schweizer (1992), equation (15.11) can be further expanded to visualize that each of the four terms is composed of a

deterministic and a stochastic contribution. Let us take term (3) and give more details. In many applications, the viscosity of the coating fluid is a function of concentration, C , and temperature, T , both of which may vary with time, t , and along the cavity axis, X . Hence, term (3) must be replaced by its total derivative according to

$$term \ (3) = -\frac{1}{\mu} \left\{ \frac{\partial \mu}{\partial C} \left[\frac{\partial C}{\partial X} dX + \frac{\partial C}{\partial t} dt \right] \right\}$$

$$\text{term } + \frac{\partial \mu}{\partial T} \left[\frac{\partial T}{\partial X} dX + \frac{\partial T}{\partial t} dt \right] \} \quad (6) \quad (15.12)$$

Terms (5) and (6) describe the variation of viscosity due to spatial and temporal variations of the fluid concentration and temperature, respectively. The partial derivatives $\partial\mu/\partial C$ and $\partial\mu/\partial T$ are fluid properties; they are always positive and can be determined experimentally (Schweizer 1992). $\partial T/\partial X$ stands for the variation of fluid temperature along the cavity axis. If the fluid temperature at the die entrance is not equal to the die temperature, then the die will act as a heat exchanger, and consequently, the fluid will change its temperature as it flows along the distribution cavity. This temperature difference between fluid and die at the inlet is a measure for the degree of isothermal operating condition. Any values other than zero will cause flow rate nonuniformity. The effect and its resulting contribution to nonuniformity is called systematic or deterministic, if the temperature distribution $T(X)$ can be calculated (Schweizer 1992).

On the other hand, even if the process is nominally operated isothermally, there will still be a slight contribution to nonuniformity due to random or stochastic fluctuations of the fluid temperature as a result of imperfect process control capabilities ($\partial T/\partial t$ in term (6) will not exactly be zero). Similar arguments can be developed for term (5), which is related to mixing and fluid homogeneity.

In summary, deterministic contributions to nonuniformity arise when the die is operated at nominal conditions other than those assumed as

boundary conditions during the design stage. Their effects are additive. In contrast, stochastic contributions express process control capabilities, and their combined effect is equal to plus or minus the square root of the sum of their variances. The variance is the square of the standard deviation, s , and the value of the standard deviation can be multiplied by 1, 2, or 3, depending on the desired confidence level (Box, Hunter and Hunter 1978). It follows that the flow rate nonuniformity (equation (15.11)) is more correctly expressed as

$$\frac{\Delta Q(X)}{Q_0} = \sum_i \Omega_i \pm \sqrt{\left(\sum_j s_j^2 \right)} \quad (15.13)$$

where Ω_i and s_j denote, respectively, any deterministic and stochastic contribution which can be quantified, e.g., terms (1) to (6) in equations (15.11) and (15.12). Notice that in contrast to equations (15.11) and (15.12), the flow rate nonuniformity is now expressed in terms of a finite difference and not as a differential in the true mathematical sense (i.e., $dQ \rightarrow 0$), because variations of independent process parameters are finite in reality.

As shown in Fig. 15.13, the widthwise flow rate uniformity (or nonuniformity) is thus characterized by a band whose overall slope is determined by the sum of the deterministic

contributions Ω_i , and whose width is indicative of all stochastic contributions s_j . For a side-fed hopper, the band is wedge-shaped or sigmoidal, while for a center-fed die, it is symmetrical about the inlet. Moreover, the banded profile is a theoretical limit within which a real profile would come to lay.

The curves in Fig. 15.13 have been calculated using equations (15.11) to (15.13), but merely for illustrative purposes. Moreover, the meaning of ε_{tot} will be explained further below.

The task of the die designer is to determine accurately the magnitude of the four terms in equation (15.11) (or of the right-hand side of equation (15.13)) in order to predict the flow rate distribution for a particular die design, or, better yet, to optimize the geometrical die parameters so that the right-hand side of equation (15.11) remains below a specified value for a given range of operating conditions and a given level of process control capabilities (inverse die design problem).

Traditional die design as disclosed in the published literature has been focused on term (1) in equation (15.11), which is representative of the pressure drop in the distribution cavity. One possible approach is to construct a simple cavity with constant cross-section, and make it large enough so that its pressure drop becomes much smaller than the pressure drop across the metering slot. A more refined strategy is to calculate the pressure distribution in the cavity, and to compensate its nonuniformity with the pressure drop across the metering slot by appropriately varying either the slot length (term (4)) or the slot height (term (2)).

The latter procedure with the slot length (term (4)) as the parameter to be modified was followed in order to prepare the examples below (for details see Chapter 10). A simple analytical model for a side-fed dual cavity die has been used to calculate the flow rate uniformity. The model is one-dimensional and valid for Newtonian rheology. Inertia (Leonard 1985) and viscous (Liu 1983; Lee and Liu 1989) effects are accounted for in the flow rate/pressure drop relationship for the flow in the inner distribution cavity, but

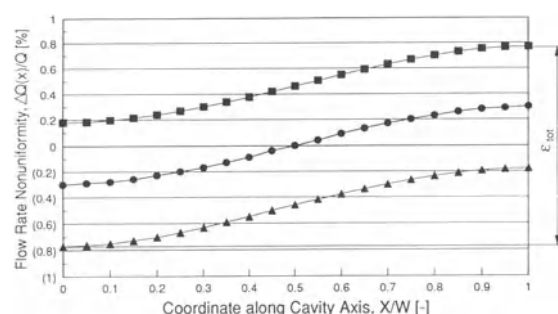


Figure 15.13 Cross profile (widthwise flow rate nonuniformity) characterized by band with overall slope stemming from deterministic contributions (—●—) and width stemming from stochastic contributions (■ + s; —▲— s).

gravitational effects are neglected. The flow in both metering slots and also in the outer cavity is assumed to be purely viscous. Both cavities have circular cross-sections, and the dimensions of the outer system (cavity plus slot) remain constant across the coating width. The situation is schematically depicted in Fig. 15.14.

The essence of the model is to solve a differential equation for the length of the inner metering slot according to equation (15.14), and the result is the so called taper function for the inner slot length.

$$\frac{dL_1}{dX} = \frac{H_1^3}{12\mu Q} \left(\frac{dP}{dX} \right)_{\text{cavity}} \quad (15.14)$$

Within the scope of the model, the taper function for L_1 , and therefore the flow rate distribution at the slot exit depend on the Reynolds number defined as $Re = \rho Q_0 / \mu$ (ρ = fluid density), as well as on additional parameters such as power law index and time constant, if the fluid is non-Newtonian (Lee and Liu 1989). The value of the Reynolds number is associated with a particular fluid being pumped through the die, and as such it is indicative of fluid properties and operating conditions. As is typical for many companies, coating equipment including dies is used for manufacturing not only one but several different products. However, it is expected that the equipment perform equally well for all products. This requirement presents a problem in die design, because optimized geometrical parameters are generally fixed and cannot be adjusted if fluid properties or operating parameters vary from one product to the next. It is therefore necessary to define optimum die performance by allowing a small but acceptable amount of nonuniformity which is not to be exceeded by any operating conditions within the specified range.

$L_1(X)$ will be optimum (and the flow rate distribution $Q(X)$ will be perfectly uniform) for exactly one Reynolds number, namely Re_D , the Reynolds number for which the die has been designed. For any other Reynolds number, $L_1(X)$ should have been designed differently, and this discrepancy will cause a flow rate nonuniformity

(deterministic contribution to the cross profile). For an optimized die according to the present example, terms (1) and (4) in equation (15.11) can thus be reduced to

$$\frac{dQ(X)}{Q_0} = \left[-\frac{1}{L_1} \frac{\partial L_1}{\partial X} dX \right]_{(Re - Re_D)} \quad (15.15)$$

As from term (3), there will also be a stochastic contribution to the cross profile from terms (1) and (4). Even if the die is operated at Re_D , the Reynolds number will still slightly vary with time, either from batch to batch due to inconsistencies in solution preparation, or within a batch due to pump rate fluctuations or due to viscosity variations as a result of hardener addition which triggers a chemical reaction in the coating fluid, for example.

Machining imperfections during the manufacturing of the slot height and slot length will also contribute to the cross profile. The effect is particularly serious for the slot height because it is multiplied by a factor of 3 owing to the 3rd power of the slot height in equation (15.10). While slot height and length can be measured and hence should be treated as deterministic contributions, we chose to consider them as stochastic, because appropriate data is not always readily available.

Additional deterministic contributions to the cross profile can be attributed to the terms (2) and (4) in equation (15.11). If, for example, an existing die is operated at significantly different conditions from those assumed during the design, the resulting strongly nonuniform cross profile can be empirically reduced by appropriately modifying the length of the outer metering slot (retailoring). Another case refers to multi-slot dies which are often used in the photographic industry for simultaneously coating multilayer films (see Chapters 11b and 11c). Here, the individual die bars can be considered as cantilevered plates which deflect under the action of fluid pressure in the metering slots on each side of the bar. If a die is used for coating more than one product, the resulting pressures in the slots will differ from product to product, and so will the bar deflection and the modification of the nominal slot height.

As is discussed above, any die will always produce some small amount of nonuniformity. Let its magnitude be ε_{tot} ; it is obtained by integrating equation (15.13) over the coating width, W . ε_{tot} can be looked at as the difference between the highest and the lowest point of the nonuniformity band, see Fig. 15.13. Conversely, ε_{tot} can be used as a boundary condition for the optimization procedure by forcing it to be less than a given maximum value

$$\varepsilon_{\text{tot}} \leq \varepsilon_{\text{max}} \quad (15.16)$$

Optimization procedure

So far, it has been shown that the values of some of the geometrical die parameters can be optimized based on wall shear stress requirements. The values of the remaining geometrical die parameters are obtained by applying an optimization procedure for which an optimization criterion must first be defined. Clearly, all geometrical parameters affect the magnitude of ε_{tot} which in turn must satisfy equation (15.16).

The criterion of choice optimizes the robustness of the cross profile with respect to random process fluctuations. In Fig. 15.14, two sigmoidal nonuniformity bands are drawn schematically;

ε_{tot} is the same for both bands and consequently, they are acceptable as long as equation (15.16) is satisfied. One band is wide and has a negative slope of small magnitude, indicating small contributions from deterministic factors and large contributions from stochastic factors. In contrast, the band with the larger but positive slope is narrower, indicating large deterministic contributions but small contributions from factors related to random process fluctuations. It is this feature which is most important, because the real cross profile, which lies inside the band, will be much more consistent within a batch, and from batch to batch, and product consistency is crucial to customer satisfaction.

The optimization criterion can thus be formulated analytically as

$$\text{minimum} \left[\sum_j s_j^2 \right] \quad (15.17)$$

Note that the criterion corresponds to the second term on the right-hand side of equation (15.13). The optimum design is now found via one of the search procedures described above. If analytical fluid flow models are used, computational efforts will not be excessive, and a full-factorial plan is convenient. More specifically, each of the remaining geometrical parameters to be optimized (inner and outer slot height, inner and outer slot length, position of the outer cavity, bar width) is taken at several levels within a predetermined range, and equation (15.13) is calculated for each case subject to equation (15.16). The parameter configuration that satisfies equation (15.17) will be taken as optimum design.

Three partial results of this multidimensional optimization process are presented below. The purpose is to visualize qualitatively how certain geometrical parameters affect the cross profile. Therefore, details on the other parameters are less important and are not given. Similar examples have also been published by Sartor (1990).

In Fig. 15.15, ε_{tot} is shown to depend on the ratio of inner to outer slot length, L_1/L_2 . This ratio indicates the position of the outer cavity for a given value of L (see Fig. 15.11). Depending on the ratio of inner to outer slot height, H_1/H_2 ,

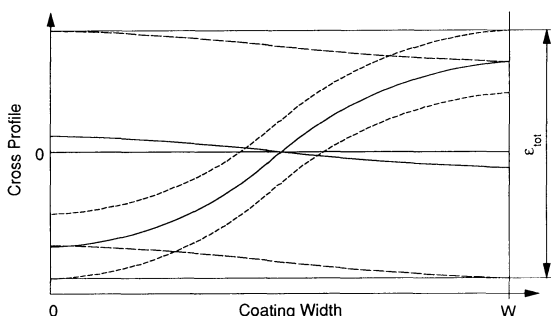


Figure 15.14 Comparison of characteristic cross profile bands. --- small deterministic and large stochastic contributions leading to a wide band susceptible to disturbances. - - - large deterministic and small stochastic contributions resulting in a narrow but robust band.

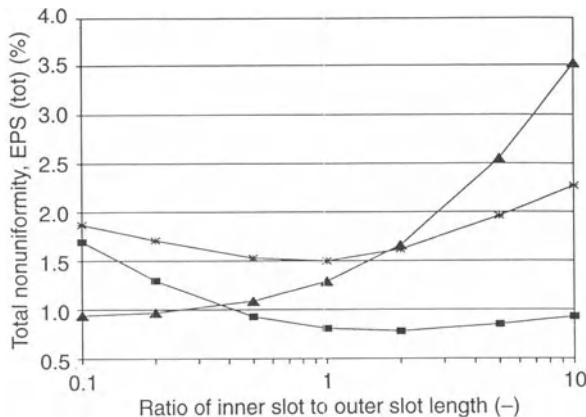


Figure 15.15 Optimum position of outer cavity. Total flow rate nonuniformity as a function of ratio of inner to outer slot length. Legend: ratio of inner to outer slot height $H_1/H_2 = 0.25$ —■—; 0.43 —*—; 1.0 —▲—.

the optimum value for L_1/L_2 is either on the edge or inside the allocated range for the search procedure.

The effect of the outer slot height, H_2 , on the cross profile, ε_{tot} , is shown in Fig. 15.16. For small values of H_2 , the damping capability of the outer cavity/metering slot is large, resulting in small deterministic contributions (only inertia effects are accounted for in this example), but the random effects of machining accuracy ($3\Delta H_2/H_2$) are considerable. For large values of H_2 , on the other hand, these trends are reversed, leading to a distinct minimum for ε_{tot} and hence, to an optimum value for H_2 . In both examples, the nonuniformity curves in the vicinity of the optimum point are fairly flat, indicating low sensitivity to changes in the respective independent parameters.

Finally, the effects of random process fluctuations on ε_{tot} are shown in Fig. 15.17. In particular, the effects of slot accuracy (machining capability), ΔH , dominate the effects of temperature fluctuations, ΔT , for small values of ΔT , i.e., for operating conditions that are nearly isothermal. On the other hand, slot accuracy becomes less important, if temperature control capabilities are

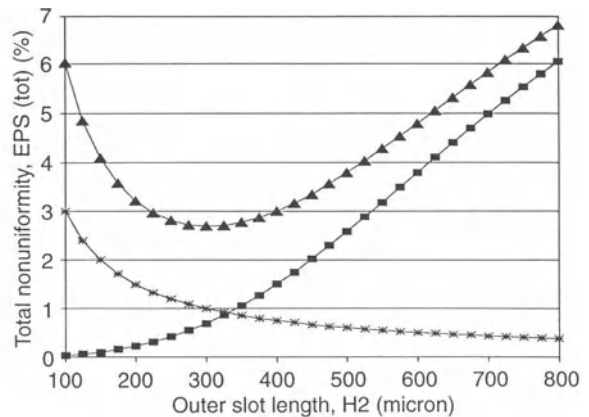


Figure 15.16 Optimum outer slot height. Total flow rate nonuniformity as a function of outer slot height. Legend: —■— inertia effects; —*— mechanical slot accuracy; —▲— sum of both effects (total flow rate nonuniformity).

inadequate, resulting in considerable nonisothermal operating conditions. In any case, owing to the absence of perfection in real manufacturing processes, there will always be some amount of

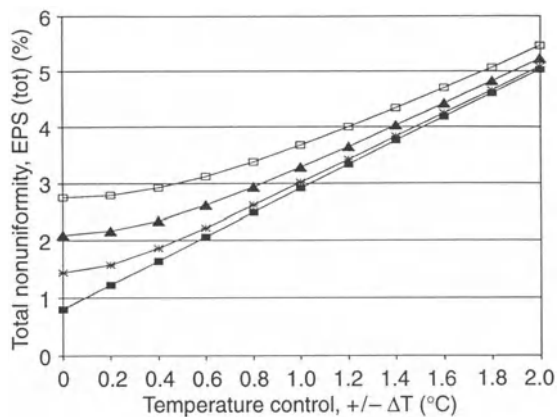


Figure 15.17 Process control capabilities. Total flow rate nonuniformity as a function of temperature control capability. Legend: mechanical slot accuracy $\Delta H = 0.0 \mu\text{m}$ —■—; $0.5 \mu\text{m}$ —*—; $1.0 \mu\text{m}$ —▲—; $1.5 \mu\text{m}$ —□—.

flow rate nonuniformity, even if all deterministic contributions are zero.

In reality, it may often be difficult if not impossible to reach the optimum design because of conflicts among various design constraints. A typical scenario is described as follows. The demand for high wall shear stress requires the inner and outer cavity cross-sections to be small, which in turn makes the die sensitive to changes in Reynolds number and rheological properties, particularly if the operating ranges of these two parameters are large. The sensitivity can be diminished if the heights of the metering slots are small or the lengths of the slots are large. The slot heights cannot be too small, in order to prevent mechanical slot accuracy from becoming important. If the slot lengths are too large, deformations of the slot heights may occur due to excessive bending of the die bars as a result of differential pressures in adjacent slots of a multilayer hopper. The bending can be controlled by making the bars thicker, which leads to a longer hopper slide and hence promotes the inception and growth of slide waves, if the multilayer film is ill designed. Moreover, in slide coating, for example, long metering slots may not be acceptable, if the new hopper must fit on the old hopper mount, and if it must meet the coating roll at the same application point as the old hopper.

Such a situation either requires solutions to newly formed problems such as well designed multilayer films that are not susceptible to slide waves even on a long slide, or it necessitates a compromise (departure from the optimum design) by relaxing one or several design constraints. Which constraints can best be relaxed depends on the particular application and must be considered carefully. Often, the choice is between high wall shear stress and good flow rate uniformity, with the uniformity taking priority.

To close this section, it must be mentioned that film thickness uniformity is not always controlled by design as described above, but often by choosing appropriate operating procedures, particularly if the coating width is large. Such procedures include varying the flow rate

in the distribution chamber by recirculating liquid through the sides of the die (Tanaka and Chikamasa 1983), and adjusting the height of the metering slot via choker bar (Anderson et al. 1975) or flexible hopper plate (Nissel 1976), see also Section 15.2, and Braatz *et al.* 1992.

15.3.3.3 Minimization of product unit costs

In a competitive market one of the foremost goals of any manufacturing company is to minimize product unit costs, because it provides maximum leverage in terms of product pricing, profit margins, and control of market share. For a typical coating company the total product unit costs, C_U , expressed as currency per unit area, e.g., (\$/m²), depend on several factors according to

$$C_U = C_P + C_L + C_O \quad (15.18)$$

where C_P are the production costs, C_L are called logistics costs, and C_O denote overhead costs or operating expenses. All three cost factors on the right-hand side of equation (15.18) depend in turn on a variety of other factors, namely

$$C_P = C_{RM} + C_C + C_{FP} + C_{QC} \quad (15.19a)$$

$$C_L = C_S + C_{DT} \quad (15.19b)$$

$$C_O = C_{MR} + C_{CI} + C_{RD} + C_{MS} + C_A \quad (15.19c)$$

Where C_{RM} are raw material costs which, as in the photographic industry, may include costs for operating elaborate manufacturing processes, e.g., the making of light-sensitive silver-halide emulsions; C_C are coating costs; C_{FP} are finishing and packaging costs; C_{QC} are quality control costs; C_S are stock or inventory costs for raw materials, intermediates and finished goods; C_{DT} are distribution and transport costs; C_{MR} are maintenance and repair costs; C_{CI} are capital investment costs; C_{RD} are research and development costs; C_{MS} are marketing and sales costs and C_A are administration costs such as finance and control, human resources, senior management, etc. Production costs, C_P , are sometimes divided into direct and indirect costs, whereby direct costs are generated by work directly related to

the manufacturing process, e.g., operating a coating machine, and indirect costs are associated with activities not directly related to the manufacturing process, e.g., supervision, laboratory services, etc. Furthermore, many of the cost factors are split into fixed and variable costs, the latter one indicating a dependency of the cost factor on the production volume. Variable costs may include direct labour costs, energy costs, etc. For many coated products the production volume is expressed as ‘area coated per unit time.’

The income of a coating company is generated by the sale of consumables, i.e. coated products. Therefore, the sum of production and logistics costs are often called ‘cost of sales.’ Overhead costs, on the other hand, are not directly related to the manufacturing process, but they must be absorbed by it. Typically, overhead costs are allocated to the unit costs of the product or products being manufactured in indirect proportion to their respective production volumes.

As will be shown below, production and logistics costs, and to a lesser degree overhead costs, depend on a great number of independent parameters which are characteristic of the manufacturing processes, of the products being coated, and of other relevant activities being carried out in the company. In this light, equations (15.18) and (15.19) provide the basis for what we call a comprehensive operations model. Such a model is a powerful management tool for the decision making process, because it relates specific product and operation parameters to the product unit costs. Consequently, it allows one to test various manufacturing scenarios and, most importantly, to minimize product unit costs by choosing appropriate values for the independent parameters. The model is also invaluable, for it allows one to take a view of the entire manufacturing process and of how it affects the product unit costs by simultaneously considering all relevant parameters. This feature is significant, because without such help most human mental capabilities are unable to process the very large number of independent parameters (several tens, or more) contained in the model. Moreover, the feature is essential for finding the global optimum

(i.e., minimum product unit costs) instead of just local sub-optima.

The level of resolution of the operations model can be developed to any desired degree. As soon as the dependency of a particular process and its related costs upon independent parameters is known from data, or at least can be described in words, it can also be translated into an analytical expression which will become part of the operations model. The degree of uncertainty associated with model predictions is directly related to the basic understanding of the processes to be modeled: if a process is well understood, it can be modeled with high resolution and the confidence in predicted results will be high.

It is beyond the scope of this chapter to develop the complete operations model to any practical degree of resolution, because such a task strongly depends on the boundary conditions of a particular application. Nevertheless, the power of the model is demonstrated below by way of a selected example.

Suppose that the annual net sales volume (in terms of coated area) of a particular product is $A_{0,\text{net}}$. It is then interesting to know how many times this product has to be coated per year such that its unit costs are minimized. The net lot size per coating, $A_{L,\text{net}}$, and the number of annual coating events (coating campaigns), N , are related to $A_{0,\text{net}}$ according to

$$A_{L,\text{net}} = \frac{A_{0,\text{net}}}{N} \quad (15.20)$$

It is known from our experience that at least raw material, coating and stock costs depend on the size of the coating lot, see equation (15.19). If we succeed in modeling these three cost factors as a function of independent parameters, we can predict the dependence of the unit costs upon the lot size.

Focusing on inventory, a typical stock cycle is depicted in Fig. 15.18. When discussing issues of inventory it is useful to measure time in units of (day). At time t_0 a lot of the product is coated, finished, packaged, and put in stock. However, the product may not be sold yet during the time period t_T , because its properties must first be

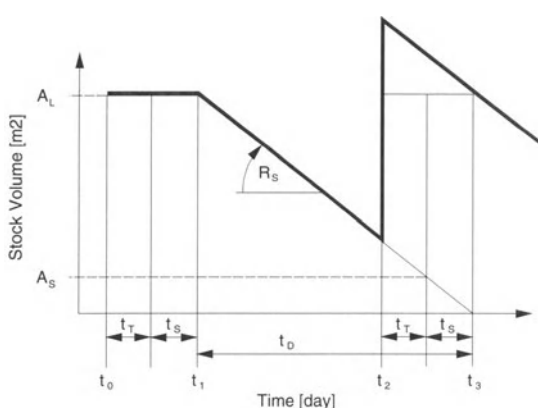


Figure 15.18 Material flow through stock: typical periodic sawtooth-like dependency of finished goods inventory upon time.

tested, or because the product properties have not yet reached equilibrium. In addition, the Marketing Department may request to maintain a certain volume of safety stock, $A_{S,\text{net}}$, in order to absorb unpredictable sales fluctuations. It may be appropriate to link the safety stock to the size of the coating lot according to $A_{S,\text{net}} = \varepsilon \cdot A_{L,\text{net}}$, with ε being a small suitable number. The safety stock is equivalent to another waiting period of length t_S . Now, at time t_1 , the product can be sold at a rate R_S , which is measured in units of (m^2/day), and which can approximately be quantified by $R_S = A_{0,\text{net}}/365$. After the period t_D the stock is depleted and the product cycle comes to an end at t_3 . The next lot must not be coated at t_3 , but at $t_2 = t_3 - t_T - t_S$ in order to account for the waiting periods associated with testing and safety stock. Consequently, product flow through stock is characterized by a periodic, saw tooth-like curve whose cycle time is equal to the product depletion time t_D , see thick line in Fig. 15.18. The first (start-up) cycle is different from all subsequent (equilibrium) cycles, because no product can be sold during the waiting period between t_0 and t_1 .

The time periods t_S and t_D are calculated according to

$$t_S = \frac{A_{S,\text{net}}}{R_S} = 365 \cdot \varepsilon \cdot \frac{A_{L,\text{net}}}{A_{0,\text{net}}} \quad (15.21)$$

$$t_D = \frac{A_{L,\text{net}}}{R_S} = 365 \cdot \frac{A_{L,\text{net}}}{A_{0,\text{net}}} \quad (15.22)$$

The area underneath the saw tooth curve in Fig. 15.18 represents the material value of the stock. This value itself does not contribute to the product unit costs. What does contribute, however, is the interest of the money equivalent to the stock value that either is lost because the money is temporarily blocked in inventory instead of invested elsewhere, or must be paid to a bank in exchange for a loan.

Product unit costs accounting for the variable portion of stock costs can thus be modeled by

$$C_S = i \cdot C_{FG} \left[\frac{t_T}{365} + \frac{A_{L,\text{net}}}{A_{0,\text{net}}} \left(\varepsilon + \frac{1}{2} \right) \right] \quad (15.23)$$

where C_{FG} is the specific value of the (finished) goods residing in stock, e.g., the sales price expressed in currency per unit area, and i is the annual interest rate.

Turning the attention to the coating process, the product unit costs associated with the coating process, C_C , and with the costs of raw materials, C_{RM} , may be approximated by

$$C_C = \frac{1}{y_B} \cdot SMU \cdot C_{CM} \quad (15.24)$$

$$C_{RM} = \frac{1}{y_B} \left[C_B + \sum_j \left(\frac{M_j \cdot C_{MJ}}{y_{MJ}} \right) \right] \quad (15.25)$$

where y_B is the base yield of the coating process with respect to the uncoated raw base. The variable SMU is called specific machine utilization; it is defined as the time required to coat a certain volume of a particular product, and it is expressed in units of (h/m^2). SMU is equal to the inverse of the coating machine capacity, CMC ; SMU is preferred over CMC , because the analytical expression of its model is slightly simpler. C_{CM} in units of ($$/\text{h}$) is called the specific costs or hourly rate of the coating machine. For the sake of simplicity, C_{CM} is held constant in this example. In reality, however, C_{CM} is a complex variable

that depends on the annual gross coating volume and on fixed and variable cost contributions from labor, energy and auxiliary materials consumption, etc. Materials costs that apply to the coating solution must be summed over the number of components, j , that comprise the coating solution. M is the specific material coverage (kg/m^2), C_M is the specific material cost (\$/kg), and y_M is the material yield, i.e. the ratio of coating solution being coated onto the web to coating solution being initially prepared in the kettle. C_B is the specific base cost (\$/ m^2).

Apart from the coating time proper, the variable SMU also contains nonproductive times that can be allocated to a specific product, such as change-over time, time for coating trials during product development, down time due to machine breakdowns or operating errors, time for preventive maintenance, etc. The specific machine utilization can be calculated according to

$$SMU = n \left[\frac{1}{W \cdot U} + \frac{(t_{\text{change-over}} + t_{\text{nonproductive}})}{A_{L,\text{gross}}} \right] \quad (15.26)$$

Here, n is the number of coating passes for the product, W is the coating width, U is the coating speed, averaged over the number of passes according to

$$\frac{1}{U} = \frac{1}{n} \sum_{i=1}^n \frac{1}{U_i} \quad (15.27)$$

If $n > 1$, y_B in equations (15.24) and (15.25) must also be averaged over the number of passes. $t_{\text{change-over}}$ is the change-over time between successive products or coating passes, and $t_{\text{nonproductive}}$ is the balance of nonproductive time per product or pass. Note that in contrast to the above discussion about inventory, the lot size to be coated per campaign is taken as gross value, $A_{L,\text{gross}}$, whereby

$$A_{L,\text{net}} = y_B \cdot A_{L,\text{gross}} \quad (15.28)$$

Typically, the value of the base yield y_B is less than 1.0, because not all of the raw base that is moved through the coating machine will be covered with usable product due to edge losses, start and finish losses, as well as losses caused

by various coating defects. y_B can accurately be determined by measuring the area of raw base entering the coating machine and the area of finished goods entering the stock. However, y_B can also be modeled by identifying and quantifying as many events as possible that lead to a loss of raw base (loss of yield). In particular, base losses occurring once per coating campaign and losses occurring on every coated roll can be distinguished. In the present example, we shall account for start losses, $A_{St} = t_{St} \cdot U \cdot W$, where t_{St} is the time period between the coating start and the establishment of an acceptable coating uniformity; losses in length direction stemming, for example, from sample taking, coating defects, splice passage, etc., $A_L = L_L \cdot W$, where L_L is the total length of full-width cuts per roll, and the number of rolls per campaign is equal to $A_{L,\text{gross}}/(L_R \cdot W)$ with L_R being the length of the roll; and losses in cross-web direction resulting from uncoated margins on the substrate, coated edge regions with unacceptable thickness profile, etc., $A_C = W_Q \cdot L_R$, where W_Q is the total width of wasted edge area per roll. With the above information the following approximate model for the base yield can be constructed

$$y_B = 1 - n \left(\frac{t_{St} \cdot U \cdot W}{A_{L,\text{gross}}} + \frac{L_L}{L_R} + \frac{W_Q}{W} \right) \quad (15.29)$$

Similar arguments as presented for the base yield y_B apply also to the material yield y_M . Its value is less than 1.0 due to losses during start, finish and unplanned machine breakdowns. A simple model for y_M relates V_L , the total lost volume of coating solution, to the volume of solution coated onto the web (H_∞ is the final wet thickness of the coated film)

$$y_M = 1 - \frac{V_L}{H_\infty \cdot A_{L,\text{gross}}} \quad (15.30)$$

Finally, the specific base cost C_B may also depend on the lot size, if the base supplier offers price reductions for buying large base quantities. In the present example a linear dependency is assumed according to

$$C_B = C_{B,0} - R_D \cdot A_{L,\text{gross}} \quad (15.31)$$

where $C_{B,0}$ is a reference base cost and R_D is the rate of discount offered by the supplier.

Equations (15.18) to (15.31) form a simple operations model whose main intent is to study the effect of the coating lot size upon the product unit costs. The model as it stands contains a total of 22 independent parameters, relating raw material costs, product properties, process capacity, process capability, and financial parameters to the resulting product unit costs. Investigating such complex multidimensional relationships without the help of a mathematical model clearly exceeds human capabilities.

Figure 15.19 shows the product unit costs, C_U , as well as coating, stock and raw materials costs as a function of the gross coating lot size, $A_{L,gross}$ for the arbitrary chosen parameter values in Table 15.1. The number of components in the coating solution, j , has been set to 1 for reasons of simplicity. Some of the units do not conform with the SI norm, but they work well in practice or match other units in a particular equation.

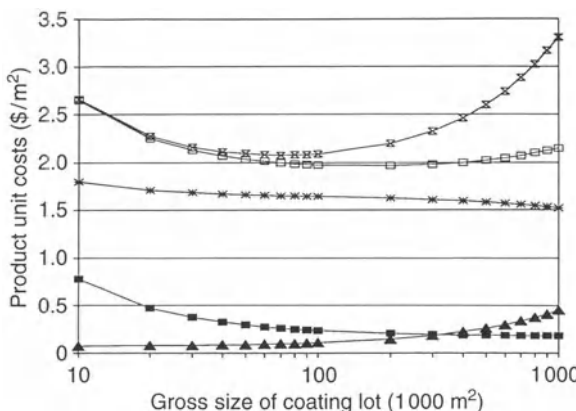


Figure 15.19 Product cost contributions as a function of the gross size of the coating lot. —■—: coating costs; —▲—: stock costs; —*—: raw materials costs; —□—: resulting product unit costs for an annual product volume of $A_{0,net} = 4 \text{ mio. m}^2$; —◇—: resulting product unit costs for an annual product volume of $A_{0,net} = 1 \text{ mio. m}^2$; the values of all other independent parameters are given in Table 15.1.

According to the operations model and the values of the independent parameters as defined in Table 15.1, coating costs decrease hyperbolically, stock costs increase linearly, and raw materials costs decrease at varying rates with increasing gross size of the coating lot. The resulting product unit costs reach a minimum for $A_{L,gross} = 200\,000 \text{ m}^2$ if the annual product volume equals 4 mio. m^2 . However, the optimum coating lot size decreases to $70\,000 \text{ m}^2$ if the annual product volume is only 1 mio. m^2 . In general, the minimum of the product unit costs is shifted towards larger coating lot sizes if coating and materials costs dominate stock costs; the opposite is true if inventory costs are larger than coating and raw material costs. The minimum of the product unit costs curve as a function of the coating lot size may not be very pronounced as is the case for the conditions in Fig. 15.19. Nevertheless, a small reduction in production costs may just make a significant difference in terms of sales volume and market share in a highly competitive market place, and the operations model is the necessary tool to realize this difference. In practice, the realization of the minimum product unit costs may be hindered by additional boundary conditions such as restricted product shelf life, particularly if the rate of sale is low and the operations model calls for large coating lot sizes.

In summary, an operations model has been presented that provides a means for relating financial business parameters (product unit costs) to technological performance criteria of the manufacturing process. In particular, issues of raw material costs, process capacity and process capability have been accounted for. The latter is a measure of the ability of the process to produce products of acceptable quality. The ability to avoid various coating defects, edge nonuniformities, and other losses is implicitly contained in the yield factors for raw base and coating solution. The description of the current state of basic knowledge of coating processes and their technological implications necessary to achieve high process capacities and capabilities is the subject matter of this book.

Table 15.1 Values of independent parameters for operations model

$A_{0,\text{net}}$ (m ²) $4 \cdot 10^6$	$C_{B,0}$ (\$/m ²) 1	C_{CM} (\$/h) 1000	C_{FG} (\$/m ²) 20	C_M (\$/kg) 4	ε (–) 0.25	H_∞ (μm) 100
i (–) 0.12	L_L (m) 20	L_R (m) 3500	M (kg/m ³) 0.1	n (–) 2	R_D (\$/m ⁴) $1 \cdot 10^{-7}$	t_{C-O} (h) 1
t_{N-P} (h) 1.5	t_{st} (s) 30	t_T (day) 10	U (m/s) 2.5	V_L (m ³) 0.2	W (m) 1.5	W_Q (m) 0.1

The strength of the operational model lies in its ability to evaluate various action scenarios in terms of return on investment, i.e., it allows one to quantify the necessary efforts of a particular scenario (human and financial resources) to achieve the resulting reduction in product unit costs.

The operations model also visualizes the relationship of various levels of optimization. While equations (15.18) and (15.19) may be regarded as a model for optimization on the macro-level, parameters such as the specific machine utilization (equation (15.26)) point to the level of optimization of entire sub-process, e.g., the coating process, and still other parameters such as the base and material yields (equations (15.29) and (15.30)) can be maximized by optimization on the micro- and unit operation level.

The practical usefulness of the operations model can and should be increased by modeling additional terms in equations (15.18) and (15.19), and by increasing the resolution of some of the terms modeled above. The latter can easily be achieved for the prediction of the yield factors by accounting for other contributions to the loss of yield. Another example is the hourly rate of the coating machine. In reality, this parameter depends on the total annual production volume of the coating machine; it is therefore tied to parameters such as manned machine time, direct and indirect labor costs, boundary conditions in union contracts, etc. The possibilities appear unlimited.

15.4 OUTLOOK

Optimization and control is the ultimate goal of any research and development activity. The basis for optimization is a fundamental and complete understanding of the process under consideration, which in turn requires well educated scientists and engineers who have the best tools available to carry out experimental and theoretical investigations. Consequently, process optimization can only be realized effectively if the underlying technology has reached a fairly mature stage. In coating technology, this stage has been reached in certain areas as is evidenced by the examples above, but additional interesting problems remain to be investigated.

Another consequence of optimization is the difficulty of presenting results in a general and broadly useful form. The reason is the complexity and the multidimensional aspects of most coating flow problems, and thus the inability of expressing the relationship between relevant process parameters in analytical form. Moreover, optimum operating conditions can only be maintained for exactly one configuration of process parameters. Optima for one particular application are therefore of limited use if one or several parameters are changed for another application. There is a need for scientists to develop or acquire the necessary knowledge and tools to perform the optimization for local boundary conditions and constraints. In some applications, there is a need to depart from the true optimum by allowing a certain

amount of imperfection, so that the optimum can be reached from within a specified range of the input parameters. There is also a need to find flat optima, where the sensitivity of the optimum with respect to changes of process parameters is small.

Optimization is an expression of the philosophy of prevention. It is the foremost means of achieving and improving manufacturing productivity; one of the most important challenges of industrial companies. For scientists and engineers, optimization is an opportunity to strive for the best by fulfilling the ultimate goal of coating flow research. More yet: the development of useful optimization models in terms of economic parameters such as the one expressed by equation (15.18) goes beyond coating technology. It requires interdisciplinary collaboration among experts from all aspects of manufacturing technology and logistics. The attempt to model and optimize a manufacturing company as an entity is a formidable task that still awaits successful completion.

ACKNOWLEDGMENT

I am grateful to J. Bruce Ikin, Ken A. Ridley, and David J. Nield from ILFORD Limited, and John DeNewton formerly from ILFORD Limited for challenging discussions and valuable contributions to the issue of optimum wetting line position. I am also thankful to Dirk Stadler from the Lehrstuhl für Strömungsmechanik at the University of Erlangen for his spontaneous willingness to calculate an example of the flow field of the curtain impingement zone.

REFERENCES

- Anderson, J. W., et al. 1975. US Patent 3,884,611.
- Bakshi, B. R. and Stephanopoulos, G. 1993. Wave-net: a multiresolution, hierarchical neural network with localized learning. *AICHE J.* **39**(1): 57–81.
- Bandermann, F. 1972. Optimierung chemischer Reaktionen. In *Ullmanns Encyklopädie der technischen Chemie, Band 1*. pp. 362–418. Weinheim: Verlag Chemie.
- Barouch, E., Wright, T. H. and Matijevic, E. 1987. Kinetics of particle detachment. *J. Colloid Interface Science*. **118**(2): 473–481.
- Blake, T. D., Clarke A. and Ruschak, K. J. 1994. Hydrodynamic assist of dynamic wetting. *AICHE J.* **40**(2): 229–242.
- Box, G. E. P. and Behnken, D. W. 1960. *Technometrics*. **2**(4): 455.
- Box, G. E. P. and Draper, N. R. 1969. *Evolutionary Operation*. New York: John Wiley.
- Box, G. E. P. and Hunter, J. S. 1957. Multifactor experimental designs for exploring response surfaces. *Annals of Mathematical Statistics*. **28**: 195–242.
- Box, G. E. P., Hunter, W. G. and Hunter, J. S. 1978. *Statistics for Experimenters*. New York: John Wiley.
- Box, G. E. P. and Wilson, K. B. 1951. *J. Roy. Statist. Soc. Ser. B (London)*. **13**: 1.
- Braatz, R. D., Tyler, M. L., Morari, M., Pranckh, F. R. and Sartor, L. 1992. Identification and cross-directional control of coating processes. *AICHE J.* **38**(9): 1329–1339.
- Chen, K. S. A. and Scriven, L. E. 1992. Two views of multilayer coating beads. *Industrial Coating Research, Volume 2*.
- Christodoulou, K. N. and Scriven, L. E. 1989. The fluid mechanics of slide coating. *J. Fluid Mech.* **208**: 321–354.
- Denn, M. M. 1969. *Optimization by Variational Methods*. New York: McGraw-Hill.
- Deshpande, M. D. and Vaishnav, R. N. 1982. Submerged laminar jet impingement on a plane. *J. Fluid Mech.* **114**: 213–236.
- Durst, F., Lange, U. and Raszillier, H. 1994. Optimization of distribution chambers of coating facilities. *Chem. Eng. Sci.* **49**(2): 161–170.
- Durst, F., Lange, U. and Raszillier, H. 1996. Minimization and control of random effects on film thickness uniformity by optimized design of coating die internals. *Proceedings of the 1st European Coating Symposium on the Mechanics of Thin Film Coatings*, eds P. H. Gaskell, M. D. Savage and J. L. Summers, pp. 85–94. Singapore: World Scientific Publishing.
- Dussan V., E. B. 1987. On the ability of drops to stick to surfaces of solids. Part 3. The influences of the motion of the surrounding fluid on dislodging drops. *J. Fluid Mech.* **174**: 381–397.
- Frost, P. J. and Gutoff, E. B. 1991. *The Application of Statistical Process Control to Roll Products*. 2nd edn. PJ Associates, 1001 Marina Drive, Suite 605E, North Quincy, MA 02171.
- Gibbs, J. W. 1906. *The Scientific Papers of J. W. Gibbs. Volume I, Thermodynamics*. Longmans, Green. pp. 314–331.
- Gilbert, N., Wagner, H. G. and Nagel, P. 1994. Slot

- extrusion coating in the presence of magnetic forces. Paper 2c, presented at the 7th International Coating Process Science and Technology Symposium of the AIChE Spring National Meeting, Atlanta, GA, April 17–21, 1994.
- Grasshoff, A. and Reuter, H. 1983. Untersuchungen zum Reinigungsverhalten zylindrischer Toträume. *Chemie-Ingenieur-Technik.* **55**(5): 406–407.
- Kistler, S. F. 1983. The fluid mechanics of curtain coating and related viscous free surface flows with contact lines. PhD thesis, University of Minnesota. Available from University Microfilms International, Ann Arbor, MI.
- Lee, K.-W. and Liu T. J. 1989. Design and analysis of a dual-cavity coat-hanger die. *Polymer Engng Sci.* **29**(15): 1066–1075.
- Leonard, W. K. 1985. Inertia and gravitational effects in extrusion dies for non-Newtonian fluids. *Polymer Engng Sci.* **25**(9): 570–576.
- Liu, T. J. 1983. Fully developed flow of power-law fluids in ducts. *I&EC Fundamentals.* **22**: 183–186.
- Liu, T. J. and Hong, C.-N. 1988. The pressure drop/flow rate equation for non-Newtonian flow in channels of irregular cross-section. *Polymer Engng Sci.* **28**(23): 1559–1564.
- Luyben, W. L. 1973. *Process Modeling, Simulation, and Control for Chemical Engineers*. New York: McGraw-Hill.
- Miller, C. 1972. *Ind. Eng. Chem. Fundam.* **11**: 524.
- Montgomery, D. C. 1984. *Design and Analysis of Experiments*. 2nd edn New York: John Wiley.
- Nelder, J. A. and Mead, R. 1965. A simplex method for function minimization. *The Computer Journal.* **8**: 308–313.
- Nissel, F. R. 1976. Thickness control system for an extrusion die. US Patent 3,940,221.
- Reklaitis, G. V., Ravindran, A. and Ragsdell, K. M. 1983. *Engineering Optimization: Methods and Applications*. New York: John Wiley.
- Ruschak, K. J. and Weinstein, S. J. 1996. Mathematical modeling of fluid dies. *Proceedings of the 1st European Coating Symposium on the Mechanics of Thin Film Coatings*, eds P. H. Gaskell, M. D. Savage and J. L. Summers, pp. 3–22. Singapore: World Scientific Publishing.
- Sakiadis, B. C. 1961. Boundary layer behaviour on continuous solid surfaces: II. The boundary layer on a continuous flat surface. *AIChE J.* **7**: 221.
- Sartor, L. 1990. Slot coating: fluid mechanics and die design. PhD thesis, University of Minnesota.
- Schweizer, P. M. 1988. Visualization of coating flows. *J. Fluid Mech.* **193**: 285–302.
- Schweizer, P. M. 1992. Fluid handling and preparation. In *Modern Coating and Drying Technology*, eds E. D. Cohen and E. B. Gutoff. pp. 23–61. New York: VCH Publishers.
- Shapiro, S. I. 1993. Process control. Chapter 5 in *The Coating Processes*, ed. J. C. Walter. pp. 175–180. TAPPI Press, Atlanta, Georgia.
- Sharma, M. M., Chamoun, H., Sita Rama Sarma, D. S. H. and Schechter, R. S. 1992. Factors controlling the hydrodynamic detachment of particles from solids. *J. Colloid Interface Science.* **149**(1): 121–134.
- Skormin, V. A. 1991. A simple solution to PID controller adjustment. *Power Conversion and Intelligent Motion (PCIM).* **17**(3): 44–48.
- Skormin, V. A. and Siciliano, R. J. 1991. Novel approach to quality analysis, optimization, and control of film coating process. *J. Coatings Technol.* **63**: 103–110.
- Sollinger, H. P. 1990. New developments in coating CD profile control. *TAPPI Proceedings of the 1990 Coating Conference*. pp. 347–351.
- Spendley, W., Hext, G. R. and Himsorth, F. R. 1962. Sequential application of simplex designs in optimization and evolutionary operation. *Technometrics.* **4**: 441.
- Stadler, D. 1993. Lehrstuhl für Strömungsmechanik, University of Erlangen/Nürnberg, Cauerstrasse 4, D-91058 Erlangen, Germany. Finite element calculations of the curtain impingement zone performed specifically for this work.
- Swain, R. H. 1985. Closing the loop on coating processes. *Paper, Film and Foil Converter* (6,7).
- Tanaka, Y. and Chikamasa, H. of Fuji Photo Film Co. Ltd. US Patent 4,416,214.
- Van Abbenen, W., Mues, W. and Goetmaeckers, B. 1992. Explaining limits of operability in curtain coating. Paper 43a, presented at the 6th International Coating Process Science and Technology Symposium of the AIChE Spring National Meeting, New Orleans, LA, March 29–April 2, 1992.
- Wilde, D. J. 1964. *Optimum Seeking Methods*. Englewood Cliffs, NJ: Prentice-Hall.
- Wilde, D. J. and Beightler, C. S. 1967. *Foundations of Optimization*. Englewood Cliffs, NJ: Prentice-Hall.
- Winter, H. H. and Fritz, H. G. 1986. Design of dies for the extrusion of sheet and annular parisons: the distribution problem. *Polymer Engng Sci.* **26**(8): 543–553.
- Yeckel, A. and Middleman, S. 1987. Removal of a viscous film from a rigid plane surface by an impinging liquid jet. *Chem. Eng. Comm.* **50**: 165–175.